

AD639982

AD

USAAVLABS TECHNICAL REPORT 66-40

2

**HIGH-SPEED WIND TUNNEL TESTS OF A
HIGH BYPASS LIFT/CRUISE FAN PROPULSION SYSTEM**

By

E. G. Smith

CLEARINGHOUSE
FOR FEDERAL SCIENTIFIC AND
TECHNICAL INFORMATION

Hardcopy

Microfiche

\$10.80

\$3.00

778 38
SP

ARCHIVE COPY

Code 1

July 1966

**U. S. ARMY AVIATION MATERIEL LABORATORIES
FORT EUSTIS, VIRGINIA**

CONTRACT DA 44-177-AMC-10(T)

GENERAL ELECTRIC COMPANY

CINCINNATI, OHIO



Distribution of this
document is unlimited

RECEIVED
OCT 12 1966
B

Disclaimers

The findings in this report are not to be construed as an official Department of the Army position unless so designated by other authorized documents.

When Government drawings, specifications, or other data are used for any purpose other than in connection with a definitely related Government procurement operation, the United States Government thereby incurs no responsibility nor any obligation whatsoever; and the fact that the Government may have formulated, furnished, or in any way supplied the said drawings, specifications, or other data is not to be regarded by implication or otherwise as in any manner licensing the holder or any other person or corporation, or conveying any rights or permission, to manufacture, use, or sell any patented invention that may in any way be related thereto.

Trade names cited in this report do not constitute an official endorsement or approval of the use of such commercial hardware or software.

Disposition Instructions

Destroy this report when no longer needed. Do not return it to the originator.

ACCESSION FOR		
CFSTI	WHITE SECTION	<input checked="" type="checkbox"/>
DDC	DIFF SECTION	<input type="checkbox"/>
UNANNOUNCED		<input type="checkbox"/>
JUSTIFICATION		
BY		
DISTRIBUCTION/AVAILABILITY CODES		
DIST.	AVAIL.	and/or SPECIAL
/		



DEPARTMENT OF THE ARMY
U. S. ARMY AVIATION MATERIEL LABORATORIES
FORT EUSTIS, VIRGINIA 23604

This report, covering the results of performance tests of a 36-inch high bypass lift/cruise fan conducted in the NASA-Langley 16-foot high-speed tunnel, has been reviewed by the U. S. Army Aviation Materiel Laboratories and is considered to be technically sound.

The data are reproduced for the information of industry and Government agencies and for the stimulation of ideas.

Task 1D131201D159
Contract DA 44-177-AMC-10(T)
USAAVLABS Technical Report 66-40
July 1966

**HIGH-SPEED WIND TUNNEL TESTS OF A
HIGH BYPASS LIFT/CRUISE FAN PROPULSION SYSTEM**

by

E.G. Smith

Prepared by

General Electric Company
Flight Propulsion Division
Advanced Technology and Demonstrator Programs Department
Lift Fan Systems Operation
Cincinnati, Ohio

for

U.S. ARMY AVIATION MATERIEL LABORATORIES
FORT EUSTIS, VIRGINIA

*Distribution of this
document is unlimited*

SUMMARY

An investigation was carried out in the NASA-Langley 16-foot high-speed tunnel to determine the aerothermodynamic characteristics of a family of close-coupled lift/cruise fan installations. The lift/cruise installation consisted of the General Electric X376 tip turbine fan system driven by a T58-6A core engine acting as a gas producer, and a nacelle system comprised of a family of interchangeable inlet and exhaust systems. The characteristics were obtained for Mach numbers between 0.0 and 0.85.

The test results showed that the low-speed drag coefficient (C_D) of the nacelle system (including core engine) was between 0.04 and 0.88, depending on the nacelle geometry and the inlet mass flow ratio. Drag rise or drag divergence occurred at lower than predicted test Mach numbers because of premature critical flow in the region of a nacelle fairing between fan and engine. The axisymmetric regions of the fan nacelle and the core engine nacelle demonstrated critical Mach number performance as obtained using standard nacelle design procedures. The test results provide criteria for redesign of the fairing regions to eliminate the premature critical flow conditions in this region of the installation. Analysis and recommendations for fairing and inlet lip design changes are provided; small scale unpowered model tests would be needed to verify the analysis.

Propulsion system performance was satisfactory throughout the test range. Certain off-design operating conditions produced high fan blade stresses which limited the test range for several of the configurations. Propulsion system performance confirmed present prediction methods and provided experimental data in previously unexplored regions of fan operation.

FOREWORD

This report describes an experimental investigation to determine the aerothermodynamic characteristics of a family of close-coupled lift/cruise fan installations.

The investigation was conducted by the Flight Propulsion Division of the General Electric Company, Cincinnati, Ohio, under United States Army Contract DA 44-177-AMC-10(T). The test equipment was designed and manufactured under the direction of General Electric personnel. Testing was conducted in the 16-foot high-speed wind tunnel facilities of the NASA-Langley Research Center. Reduction of the test data was jointly directed by NASA and General Electric personnel. Analysis of the test data and preparation of the final report were performed by General Electric personnel.

The program was initiated in March 1963, with first tests in the wind tunnel occurring in December 1963. The first phase of the test program was prematurely terminated in February 1964, when failure of the X376 fan system occurred, apparently due to failure and subsequent ingestion of a part of the inlet bullethead assembly. The program was reinitiated in June 1964, the assembly was rebuilt, and the first test of the second phase of the program was conducted in May 1965. Tests were terminated in June 1965, after completion of the objective test program.

BLANK PAGE

CONTENTS

	<u>Page</u>
SUMMARY	iii
FOREWORD	v
LIST OF ILLUSTRATIONS	viii
LIST OF TABLES	xlii
LIST OF SYMBOLS	xliv
INTRODUCTION	1
DESCRIPTION OF TEST EQUIPMENT	2
PROCEDURES	5
TEST RESULTS	6
ANALYSIS OF TEST RESULTS	15
APPLICATION OF TEST RESULTS TO CRUISE FAN NACELLE DESIGNS	40
CONCLUSIONS	45
BIBLIOGRAPHY	47
DISTRIBUTION	48
APPENDIXES	
I. Data Reduction and Analysis Procedures	50
II. Tests To Measure Sound Vibration in Cruise Fan	
Inlets	65
III. Model Description	71

ILLUSTRATIONS

<u>Figure</u>		<u>Page</u>
1	Typical Model Mounted in Test Section of Langley 16-Foot Tunnel	107
2	Installation Drawing of Model in Wind Tunnel	108
3	Cruise Fan Model Nomenclature	109
4	Geometry and Dimensional Data for Models 1 and 2	110
5	Geometry and Dimensional Data for Models 3 and 4	111
6	Geometry and Dimensional Data for Models 5 and 6	112
7	Geometry and Dimensional Data for Models 7 and 8	113
8	Internal Area Distribution - Inlet 1	114
9	Internal Area Distribution - Inlet 2	115
10	Internal Area Distribution - Inlet 3	116
11	Nozzle Area Distribution for Model Using Afterbody 1 and Plug 2	117
12	Nozzle Area Distribution for Model Using Afterbody 1 and Plug 3	118
13	Nozzle Area Distribution for Model Using Afterbody 2 and Plug 2	119
14	Nozzle Area Distribution for Model Using Afterbody 2 and Plug 3	120
15	Nozzle Area Distribution for Model Using Afterbody 4 and Plug 3	121
16	Nozzle Area Distribution for Model Using Afterbody 4 and Plug 4	122
17	Internal Area Distribution for Engine Inlet	123
18	Instrumentation Plane Nomenclature	124
19	Model Axial Plane Notation	125
20	Variation of Speed Ratio Parameter with Mach Number and Corrected Fan Speed	126

<u>Figure</u>		<u>Page</u>
21	Relationship of Fan and Conventional Coefficients	127
22	Engine Airflow Characteristics - Model 1	128
23	Engine Turbine Discharge Total Pressure - Model 1	129
24	Engine Exhaust Gas Temperature - Model 1	130
25	Engine Ideal Gas Horsepower Characteristics - Model 1 . .	131
26	Engine Airflow Characteristics - Model 2	132
27	Engine Turbine Discharge Total Pressure - Model 2	133
28	Engine Exhaust Gas Temperature - Model 2	134
29	Engine Ideal Gas Horsepower Characteristics - Model 2 . .	135
30	Engine Airflow Characteristics - Model 3	136
31	Engine Turbine Discharge Total Pressure - Model 3	137
32	Engine Exhaust Gas Temperature - Model 3	138
33	Engine Ideal Gas Horsepower Characteristics - Model 3 . .	139
34	Engine Airflow Characteristics - Model 4	140
35	Engine Turbine Discharge Total Pressure - Model 4	141
36	Engine Exhaust Gas Temperature - Model 4	142
37	Engine Ideal Gas Horsepower Characteristics - Model 4 . .	143
38	Engine Airflow Characteristics - Model 5	144
39	Engine Turbine Discharge Total Pressure - Model 5	145
40	Engine Exhaust Gas Temperature - Model 5	146
41	Engine Ideal Gas Horsepower Characteristics - Model 5 . .	147
42	Engine Airflow Characteristics - Model 6	148
43	Engine Turbine Discharge Total Pressure - Model 6	149
44	Engine Exhaust Gas Temperature - Model 6	150
45	Engine Ideal Gas Horsepower Characteristics - Model 6 . .	151

<u>Figure</u>		<u>Page</u>
46	Engine Airflow Characteristics - Model 7	152
47	Engine Turbine Discharge Total Pressure - Model 7	153
48	Engine Exhaust Gas Temperature - Model 7	154
49	Engine Ideal Gas Horsepower Characteristics - Model 7	155
50	Engine Airflow Characteristics - Model 8	156
51	Engine Turbine Discharge Total Pressure - Model 8	157
52	Engine Exhaust Gas Temperature - Model 8	158
53	Engine Ideal Gas Horsepower Characteristics - Model 8	159
54	Fan Airflow Characteristics - Model 1	160
55	Fan Total Pressure Ratio - Model 1	161
56	Fan Stream Ideal Gross Thrust - Model 1	162
57	Fan Turbine Residual Ideal Gross Thrust - Model 1	163
58	Fan System Ideal Gross Thrust - Model 1	164
59	Total Ram Drag - Model 1	165
60	Fan System Ideal Net Thrust - Model 1	166
61	Fan Flow Function Characteristics - Model 1	167
62	Fan Pressure Coefficient Characteristics - Model 1	168
63	Fan Ideal Net Thrust Coefficient - Model 1	169
64	Fan Net Thrust Coefficient with a Nozzle Coefficient of 0.95 - Model 1	170
65	Fan Airflow Characteristics - Model 2	171
66	Fan Total Pressure Ratio - Model 2	172
67	Fan Stream Ideal Gross Thrust - Model 2	173
68	Fan Turbine Residual Ideal Gross Thrust - Model 2	174
69	Fan System Ideal Gross Thrust - Model 2	175

<u>Figure</u>		<u>Page</u>
70	Total Ram Drag - Model 2	176
71	Fan System Ideal Net Thrust - Model 2	177
72	Fan Flow Function Characteristics - Model 2	178
73	Fan Pressure Coefficient Characteristics - Model 2	179
74	Fan Ideal Net Thrust Coefficient - Model 2	180
75	Fan Net Thrust Coefficient with a Nozzle Coefficient of 0.95 - Model 2	181
76	Fan Airflow Characteristics - Model 3	182
77	Fan Total Pressure Ratio - Model 3	183
78	Fan System Ideal Gross Thrust - Model 3	184
79	Fan Turbine Residual Ideal Gross Thrust - Model 3	185
80	Fan System Ideal Gross Thrust - Model 3	186
81	Total Ram Drag - Model 3	187
82	Fan System Ideal Net Thrust - Model 3	188
83	Fan Flow Coefficient Characteristics - Model 3	189
84	Fan Pressure Coefficient Characteristics - Model 3	190
85	Fan Ideal Net Thrust Coefficient - Model 3	191
86	Fan Net Thrust Coefficient with a Nozzle Coefficient of 0.95 - Model 3	192
87	Fan Airflow Characteristics - Model 4	193
88	Fan Total Pressure Ratio - Model 4	194
89	Fan Stream Ideal Gross Thrust - Model 4	195
90	Fan Turbine Residual Ideal Gross Thrust - Model 4	196
91	Fan System Ideal Gross Thrust - Model 4	197
92	Total Ram Drag - Model 4	198
93	Fan System Ideal Net Thrust - Model 4	199

<u>Figure</u>		<u>Page</u>
94	Fan Flow Coefficient Characteristics - Model 4	200
95	Fan Pressure Coefficient Characteristics - Model 4	201
96	Fan Ideal Net Thrust Coefficient - Model 4	202
97	Fan Net Thrust Coefficient with a Nozzle Coefficient of 0.95 - Model 4	203
98	Fan Airflow Characteristics - Model 5	204
99	Fan Total Pressure Ratio - Model 5	205
100	Fan Stream Ideal Gross Thrust - Model 5	206
101	Fan Turbine Residual Ideal Gross Thrust - Model 5	207
102	Fan System Ideal Gross Thrust - Model 5	208
103	Total Ram Drag - Model 5	209
104	Fan System Ideal Net Thrust - Model 5	210
105	Fan Flow Coefficient Characteristics - Model 5	211
106	Fan Pressure Coefficient Characteristics - Model 5	212
107	Fan Ideal Net Thrust Coefficient - Model 5	213
108	Fan Net Thrust Coefficient with a Nozzle Coefficient of 0.95 - Model 5	214
109	Fan Airflow Characteristics - Model 6	215
110	Fan Total Pressure Ratio - Model 6	216
111	Fan Stream Ideal Gross Thrust - Model 6	217
112	Fan Turbine Residual Ideal Gross Thrust - Model 6	218
113	Fan System Ideal Gross Thrust - Model 6	219
114	Total Ram Drag - Model 6	220
115	Fan System Ideal Net Thrust - Model 6	221
116	Fan Flow Function Characteristics - Model 6	222
117	Fan Pressure Coefficient Characteristics - Model 6	223

<u>Figure</u>		<u>Page</u>
118	Fan Ideal Net Thrust Coefficient - Model 6	224
119	Fan Net Thrust Coefficient with a Nozzle Coefficient of 0.95 - Model 6	225
120	Fan Airflow Characteristics - Model 7	226
121	Fan Total Pressure Ratio - Model 7	227
122	Fan Stream Ideal Gross Thrust - Model 7	228
123	Fan Turbine Residual Ideal Gross Thrust - Model 7	229
124	Fan System Ideal Gross Thrust - Model 7	230
125	Total Ram Drag - Model 7	231
126	Fan System Ideal Net Thrust - Model 7	232
127	Fan Flow Function Characteristics - Model 7	233
128	Fan Pressure Coefficient Characteristics - Model 7	234
129	Fan Ideal Net Thrust Coefficient - Model 7	235
130	Fan Net Thrust Coefficient with a Nozzle Coefficient of 0.95 - Model 7	236
131	Fan Airflow Characteristics - Model 8	237
132	Fan Total Pressure Ratio - Model 8	238
133	Fan Stream Ideal Gross Thrust - Model 8	239
134	Fan Turbine Residual Ideal Gross Thrust - Model 8	240
135	Fan System Ideal Gross Thrust - Model 8	241
136	Total Ram Drag - Model 8	242
137	Fan System Ideal Net Thrust - Model 8	243
138	Fan Flow Function Characteristics - Model 8	244
139	Fan Pressure Coefficient Characteristics - Model 8	245
140	Fan Ideal Net Thrust Coefficient - Model 8	246

<u>Figure</u>		<u>Page</u>
141	Fan Net Thrust Coefficient with a Nozzle Coefficient of 0.95 - Model 8	247
142	Fan Turbine Pressure and Temperature Ratios - Model 1 . .	248
143	Fan Speed - Horsepower Characteristics - Model 1	249
144	Engine Horsepower Absorbed by Fan Turbine - Model 1 . . .	250
145	Fan Turbine Pressure and Temperature Ratios - Model 2 . .	251
146	Fan Speed - Horsepower Characteristics - Model 2	252
147	Engine Horsepower Absorbed by Fan Turbine - Model 2 . . .	253
148	Fan Turbine Pressure and Temperature Ratios - Model 3 . .	254
149	Fan Speed - Horsepower Characteristics - Model 3	255
150	Engine Horsepower Absorbed by Fan Turbine - Model 3 . . .	256
151	Fan Turbine Pressure and Temperature Ratios - Model 4 . .	257
152	Fan Speed - Horsepower Characteristics - Model 4	258
153	Engine Horsepower Absorbed by Fan Turbine - Model 4 . . .	259
154	Fan Turbine Pressure and Temperature Ratios - Model 5 . .	260
155	Fan Speed - Horsepower Characteristics - Model 5	261
156	Engine Horsepower Absorbed by Fan Turbine - Model 5 . . .	262
157	Fan Turbine Pressure and Temperature Ratios - Model 6 . .	263
158	Fan Speed - Horsepower Characteristics - Model 6	264
159	Engine Horsepower Absorbed by Fan Turbine - Model 6 . . .	265
160	Fan Turbine Pressure and Temperature Ratios - Model 7 . .	266
161	Fan Speed - Horsepower Characteristics - Model 7	267
162	Engine Horsepower Absorbed by Fan Turbine - Model 7 . . .	268
163	Fan Turbine Pressure and Temperature Ratios - Model 8 . .	269
164	Fan Speed - Horsepower Characteristics - Model 8	270

<u>Figure</u>		<u>Page</u>
165	Engine Horsepower Absorbed by Fan Turbine - Model 8	271
166	Static Forces from Balance Measurements - Model 1	272
167	Static Forces from Balance Measurements - Model 2	273
168	Static Forces from Balance Measurements - Model 3	274
169	Static Forces from Balance Measurements - Model 4	275
170	Static Forces from Balance Measurements - Model 5	276
171	Static Forces from Balance Measurements - Model 6	277
172	Static Forces from Balance Measurements - Model 7	278
173	Static Forces from Balance Measurements - Model 8	279
174	Variation of Net System Forces with Speed Based on Force Measurements - Model 1	280
175	Variation of Net System Forces with Speed Based on Force Measurements - Model 2	281
176	Variation of Net System Forces with Speed Based on Force Measurements - Model 3	282
177	Variation of Net System Forces with Speed Based on Force Measurements - Model 4	283
178	Variation of Net System Forces with Speed Based on Force Measurements - Model 5	284
179	Variation of Net System Forces with Speed Based on Force Measurements - Model 6	285
180	Variation of Net System Forces with Speed Based on Force Measurements - Model 7	286
181	Variation of Net System Forces with Speed Based on Force Measurements - Model 8	287
182	Typical Engine Inlet Stream Pressure Distributions at Station 2.0	288
183	Typical Engine Inlet Stream Pressure Distributions at Station 2.0	289

<u>Figure</u>		<u>Page</u>
184	Typical Engine Inlet Stream Pressure Distributions at Station 2.0	290
185	Typical Engine Inlet Stream Pressure Distributions at Station 2.0	291
186	Typical Engine Inlet Stream Pressure Distributions at Station 2.0	292
187	Typical Engine Discharge Total Pressure Distributions - Model 3, $M_0 = 0.50$	293
188	Typical Engine Discharge Total Pressure Distributions During Windmill	294
189	Fan Rotor Inlet Pressure Distributions - Model 1, $M_0 = 0.0$	295
190	Fan Rotor Inlet Pressure Distributions - Model 1, $M_0 = 0.3$	296
191	Fan Rotor Inlet Pressure Distributions - Model 1, $M_0 = 0.6$	297
192	Fan Rotor Inlet Pressure Distributions - Model 1, $M_0 = 0.8$	298
193	Fan Rotor Inlet Pressure Distributions - Model 2, $M_0 = 0.0$	299
194	Fan Rotor Inlet Pressure Distributions - Model 2, $M_0 = 0.3$	300
195	Fan Rotor Inlet Pressure Distributions - Model 2, $M_0 = 0.6$	301
196	Fan Rotor Inlet Pressure Distributions - Model 2, $M_0 = 0.8$	302
197	Fan Rotor Inlet Pressure Distributions - Model 4, $M_0 = 0.0$	303
198	Fan Rotor Inlet Pressure Distributions - Model 4, $M_0 = 0.3$	304
199	Fan Rotor Inlet Pressure Distributions - Model 4, $M_0 = 0.5$	305

<u>Figure</u>		<u>Page</u>
200	Fan Rotor Inlet Pressure Distributions - Model 4, $M_0 = 0.65$	306
201	Fan Rotor Inlet Pressure Distributions - Model 3, $M_0 = 0.0$	307
202	Fan Rotor Inlet Pressure Distributions - Model 3, $M_0 = 0.2$	308
203	Fan Rotor Inlet Pressure Distributions - Model 3, $M_0 = 0.3$	309
204	Fan Rotor Inlet Pressure Distributions - Model 3, $M_0 = 0.4$	310
205	Fan Rotor Inlet Pressure Distributions During Wind- milling - $M_0 = 0.3$	311
206	Fan Rotor Inlet Pressure Distributions During Wind- milling - $M_0 = 0.8$	312
207	Fan Rotor Discharge Total Pressure Distributions - Model 1	313
208	Fan Rotor Discharge Total Pressure Distributions - Model 2	314
209	Fan Rotor Discharge Total Pressure Distributions - Model 4	315
210	Fan Rotor Discharge Total Pressure Distributions - Model 3	316
211	Fan Discharge Total Pressure Distributions During Wind- milling	317
212	Fan Discharge Total Pressure Distributions - Model 1 . .	318
213	Fan Discharge Total Pressure Distributions - Model 2 . .	319
214	Fan Discharge Total Pressure Distributions - Model 4 . .	320
215	Fan Discharge Total Pressure Distributions - Model 3 . .	321
216	Typical Engine Inlet Internal Pressure Distributions - $M_0 = 0.0, N_E = 92.8\%$ $\sqrt{\theta_2}$	322

<u>Figure</u>		<u>Page</u>
217	Typical Engine Inlet Internal Pressure Distributions - $M_0 = 0.3, N_E = 95.0\%$ $\sqrt{\theta_2}$	323
218	Typical Engine Inlet Internal Pressure Distributions - $M_0 = 0.6, N_E = 94.3\%$ $\sqrt{\theta_2}$	324
219	Typical Engine Inlet Internal Pressure Distributions - $M_0 = 0.8, N_E = 92.0\%$ $\sqrt{\theta_2}$	325
220	Typical Fan Inlet Internal Pressure Distributions for Inlet 1 - $M_0 = 0.0, N_F = 98.5\%$ $\sqrt{\theta_{10}}$	326
221	Typical Fan Inlet Internal Pressure Distributions for Inlet 1 - $M_0 = 0.3, N_F = 32.2\%$ (Windmill) $\sqrt{\theta_{10}}$	327
222	Typical Fan Inlet Internal Pressure Distributions for Inlet 1 - $M_0 = 0.3, N_F = 97.0\%$ $\sqrt{\theta_{10}}$	328
223	Typical Fan Inlet Internal Pressure Distributions for Inlet 1 - $M_0 = 0.8, N_F = 64.2\%$ (Windmill) $\sqrt{\theta_{10}}$	329
224	Typical Fan Inlet Internal Pressure Distributions for Inlet 1 - $M_0 = 0.8, N_F = 87.6\%$ $\sqrt{\theta_{10}}$	330
225	Typical Fan Inlet Internal Pressure Distributions for Inlet 2 - $M_0 = 0.0, N_F = 97.4\%$ $\sqrt{\theta_{10}}$	331
226	Typical Fan Inlet Internal Pressure Distributions for Inlet 2 - $M_0 = 0.2, N_F = 32.0\%$ (Windmill) $\sqrt{\theta_{10}}$	332

<u>Figure</u>		<u>Page</u>
227	Typical Fan Inlet Internal Pressure Distributions for Inlet 2 - $M_0 = 0.2$, $N_F = 59.9\%$ $\sqrt{\theta_{10}}$	333
228	Typical Fan Inlet Internal Pressure Distributions for Inlet 2 - $M_0 = 0.2$, $N_F = 97.2\%$ $\sqrt{\theta_{10}}$	334
229	Typical Fan Inlet Internal Pressure Distributions for Inlet 2 - $M_0 = 0.4$, $N_F = 60.2\%$ (Windmill) $\sqrt{\theta_{10}}$	335
230	Typical Fan Inlet Internal Pressure Distributions for Inlet 2 - $M_0 = 0.4$, $N_F = 97.1\%$ $\sqrt{\theta_{10}}$	336
231	Typical Fan Inlet Internal Pressure Distributions for Inlet 3 - $M_0 = 0.0$, $N_F = 97.2\%$ $\sqrt{\theta_{10}}$	337
232	Typical Fan Inlet Internal Pressure Distributions for Inlet 3 - $M_0 = 0.2$, $N_F = 24.0\%$ (Windmill) $\sqrt{\theta_{10}}$	338
233	Typical Fan Inlet Internal Pressure Distributions for Inlet 3 - $M_0 = 0.2$, $N_F = 94.8\%$ $\sqrt{\theta_{10}}$	339
234	Typical Fan Inlet Internal Pressure Distributions for Inlet 3 - $M_0 = 0.4$, $N_F = 45.3\%$ (Windmill) $\sqrt{\theta_{10}}$	340
235	Typical Fan Inlet Internal Pressure Distributions for Inlet 3 - $M_0 = 0.4$, $N_F = 95.2\%$ $\sqrt{\theta_{10}}$	341
236	Typical Fan Inlet Internal Pressure Distributions for Inlet 3 - $M_0 = 0.6$, $N_F = 62.3\%$ (Windmill) $\sqrt{\theta_{10}}$	342

<u>Figure</u>		<u>Page</u>
237	Typical Fan Inlet Internal Pressure Distributions for Inlet 3 - $M_0 = 0.6$, $N_F = 94.5\%$ $\frac{\sqrt{\theta_{10}}}{\sqrt{\theta_2}}$	343
238	Typical Engine Nacelle Pressure Distributions - $M_0 = 0.3$, $N_E = 57.0\%$ $\frac{\sqrt{\theta_2}}{\sqrt{\theta_2}}$	344
239	Typical Engine Nacelle Pressure Distributions - $M_0 = 0.3$, $N_E = 87.6\%$ $\frac{\sqrt{\theta_2}}{\sqrt{\theta_2}}$	345
240	Typical Engine Nacelle Pressure Distributions - $M_0 = 0.3$, $N_E = 95.0\%$ $\frac{\sqrt{\theta_2}}{\sqrt{\theta_2}}$	346
241	Typical Engine Nacelle Pressure Distributions - $M_0 = 0.6$, $N_E = 54.0\%$ $\frac{\sqrt{\theta_2}}{\sqrt{\theta_2}}$	347
242	Typical Engine Nacelle Pressure Distributions - $M_0 = 0.6$, $N_E = 87.2\%$ $\frac{\sqrt{\theta_2}}{\sqrt{\theta_2}}$	348
243	Typical Engine Nacelle Pressure Distributions - $M_0 = 0.6$, $N_E = 94.3\%$ $\frac{\sqrt{\theta_2}}{\sqrt{\theta_2}}$	349
244	Typical Engine Nacelle Pressure Distributions - $M_0 = 0.7$, $N_E = 54.9\%$ $\frac{\sqrt{\theta_2}}{\sqrt{\theta_2}}$	350
245	Typical Engine Nacelle Pressure Distributions - $M_0 = 0.7$, $N_E = 85.8\%$ $\frac{\sqrt{\theta_2}}{\sqrt{\theta_2}}$	351
246	Typical Engine Nacelle Pressure Distributions - $M_0 = 0.7$, $N_E = 93.8\%$ $\frac{\sqrt{\theta_2}}{\sqrt{\theta_2}}$	352

<u>Figure</u>		<u>Page</u>
247	Typical Engine Nacelle Pressure Distributions - $M_0 = 0.8$, $N_E = 54.5\%$ $\frac{N_E}{\sqrt{\theta_2}}$	353
248	Typical Engine Nacelle Pressure Distributions - $M_0 = 0.8$, $N_E = 83.9\%$ $\frac{N_E}{\sqrt{\theta_2}}$	354
249	Typical Engine Nacelle Pressure Distributions - $M_0 = 0.8$, $N_E = 92.0\%$ $\frac{N_E}{\sqrt{\theta_2}}$	355
250	Nacelle External Pressure Distributions - Model 1, $M_0 =$ 0.301, $N_F = 32.2\%$ (Windmill) $\frac{N_F}{\sqrt{\theta_{10}}}$	356
251	Nacelle External Pressure Distributions - Model 1, $M_0 =$ 0.300, $N_F = 97.0\%$ $\frac{N_F}{\sqrt{\theta_{10}}}$	357
252	Nacelle External Pressure Distributions - Model 1, $M_0 =$ 0.601, $N_F = 56.4\%$ $\frac{N_F}{\sqrt{\theta_{10}}}$	358
253	Nacelle External Pressure Distributions - Model 1, $M_0 =$ 0.600, $N_F = 94.2\%$ $\frac{N_F}{\sqrt{\theta_{10}}}$	359
254	Nacelle External Pressure Distributions - Model 1, $M_0 =$ 0.797, $N_F = 64.2\%$ (Windmill) $\frac{N_F}{\sqrt{\theta_{10}}}$	360
255	Nacelle External Pressure Distributions - Model 1, $M_0 =$ 0.800, $N_F = 87.6\%$ $\frac{N_F}{\sqrt{\theta_{10}}}$	361
256	Nacelle External Pressure Distributions - Model 2, $M_0 =$ 0.301, $N_F = 32.3\%$ (Windmill) $\frac{N_F}{\sqrt{\theta_{10}}}$	362

<u>Figure</u>		<u>Page</u>
257	Nacelle External Pressure Distributions - Model 2, $M_0 = 0.300$, $N_F = 98.4\%$ $\frac{\sqrt{\theta_{10}}}{\sqrt{\theta_{10}}}$	363
258	Nacelle External Pressure Distributions - Model 2, $M_0 = 0.598$, $N_F = 56.7\%$ (Windmill) $\frac{\sqrt{\theta_{10}}}{\sqrt{\theta_{10}}}$	364
259	Nacelle External Pressure Distributions - Model 2, $M_0 = 0.599$, $N_F = 91.5\%$ $\frac{\sqrt{\theta_{10}}}{\sqrt{\theta_{10}}}$	365
260	Nacelle External Pressure Distributions - Model 2, $M_0 = 0.800$, $N_F = 61.3\%$ (Windmill) $\frac{\sqrt{\theta_{10}}}{\sqrt{\theta_{10}}}$	366
261	Nacelle External Pressure Distributions - Model 2, $M_0 = 0.799$, $N_F = 85.1\%$ $\frac{\sqrt{\theta_{10}}}{\sqrt{\theta_{10}}}$	367
262	Nacelle External Pressure Distributions - Model 3, $M_0 = 0.202$, $N_F = 32.0\%$ (Windmill) $\frac{\sqrt{\theta_{10}}}{\sqrt{\theta_{10}}}$	368
263	Nacelle External Pressure Distributions - Model 3, $M_0 = 0.202$, $N_F = 97.2\%$ $\frac{\sqrt{\theta_{10}}}{\sqrt{\theta_{10}}}$	369
264	Nacelle External Pressure Distributions - Model 3, $M_0 = 0.301$, $N_F = 47.0\%$ (Windmill) $\frac{\sqrt{\theta_{10}}}{\sqrt{\theta_{10}}}$	370
265	Nacelle External Pressure Distributions - Model 3, $M_0 = 0.301$, $N_F = 97.7\%$ $\frac{\sqrt{\theta_{10}}}{\sqrt{\theta_{10}}}$	371
266	Nacelle External Pressure Distributions - Model 3, $M_0 = 0.400$, $N_F = 60.2\%$ (Windmill) $\frac{\sqrt{\theta_{10}}}{\sqrt{\theta_{10}}}$	372

<u>Figure</u>		<u>Page</u>
267	Nacelle External Pressure Distributions - Model 3, $M_0 = 0.401$, $N_F = 97.1\%$ $\frac{\sqrt{\theta_{10}}}{\sqrt{\theta_{10}}}$	373
268	Nacelle External Pressure Distributions - Model 4, $M_0 = 0.203$, $N_F = 22.3\%$ (Windmill) $\frac{\sqrt{\theta_{10}}}{\sqrt{\theta_{10}}}$	374
269	Nacelle External Pressure Distributions - Model 4, $M_0 = 0.202$, $N_F = 95.3\%$ $\frac{\sqrt{\theta_{10}}}{\sqrt{\theta_{10}}}$	375
270	Nacelle External Pressure Distributions - Model 4, $M_0 = 0.501$, $N_F = 49.9\%$ (Windmill) $\frac{\sqrt{\theta_{10}}}{\sqrt{\theta_{10}}}$	376
271	Nacelle External Pressure Distributions - Model 4, $M_0 = 0.500$, $N_F = 93.5\%$ $\frac{\sqrt{\theta_{10}}}{\sqrt{\theta_{10}}}$	377
272	Nacelle External Pressure Distributions - Model 4, $M_0 = 0.649$, $N_F = 58.8\%$ (Windmill) $\frac{\sqrt{\theta_{10}}}{\sqrt{\theta_{10}}}$	378
273	Nacelle External Pressure Distributions - Model 4, $M_0 = 0.650$, $N_F = 91.7\%$ $\frac{\sqrt{\theta_{10}}}{\sqrt{\theta_{10}}}$	379
274	Nacelle External Pressure Distributions - Model 5, $M_0 = 0.202$, $N_F = 24.0\%$ (Windmill) $\frac{\sqrt{\theta_{10}}}{\sqrt{\theta_{10}}}$	380
275	Nacelle External Pressure Distributions - Model 5, $M_0 = 0.200$, $N_F = 97.8\%$ $\frac{\sqrt{\theta_{10}}}{\sqrt{\theta_{10}}}$	381
276	Nacelle External Pressure Distributions - Model 5, $M_0 = 0.400$, $N_F = 45.3\%$ (Windmill) $\frac{\sqrt{\theta_{10}}}{\sqrt{\theta_{10}}}$	382

<u>Figure</u>		<u>Page</u>
277	Nacelle External Pressure Distributions - Model 5, $M_0 = 0.400$, $N_F = 95.2\%$ $\sqrt{\theta_{10}}$	383
278	Nacelle External Pressure Distributions - Model 5, $M_0 = 0.650$, $N_F = 65.9\%$ (Windmill) $\sqrt{\theta_{10}}$	384
279	Nacelle External Pressure Distributions - Model 6, $M_0 = 0.301$, $N_F = 30.1\%$ (Windmill) $\sqrt{\theta_{10}}$	385
280	Nacelle External Pressure Distributions - Model 6, $M_0 = 0.299$, $N_F = 98.1\%$ $\sqrt{\theta_{10}}$	386
281	Nacelle External Pressure Distributions - Model 6, $M_0 = 0.598$, $N_F = 51.7\%$ (Windmill) $\sqrt{\theta_{10}}$	387
282	Nacelle External Pressure Distributions - Model 6, $M_0 = 0.599$, $N_F = 92.4\%$ $\sqrt{\theta_{10}}$	388
283	Nacelle External Pressure Distributions - Model 6, $M_0 = 0.800$, $N_F = 59.9\%$ (Windmill) $\sqrt{\theta_{10}}$	389
284	Nacelle External Pressure Distributions - Model 7, $M_0 = 0.200$, $N_F = 23.2\%$ (Windmill) $\sqrt{\theta_{10}}$	390
285	Nacelle External Pressure Distributions - Model 7, $M_0 = 0.202$, $N_F = 99.6\%$ $\sqrt{\theta_{10}}$	391
286	Nacelle External Pressure Distributions - Model 7, $M_0 = 0.400$, $N_F = 44.7\%$ (Windmill) $\sqrt{\theta_{10}}$	392

<u>Figure</u>		<u>Page</u>
287	Nacelle External Pressure Distributions - Model 7, $M_0 = 0.400$, $N_F = 93.3\%$ $\sqrt{\theta_{10}}$	393
288	Nacelle External Pressure Distributions - Model 7, $M_0 = 0.649$, $N_F = 64.6$ (Windmill) $\sqrt{\theta_{10}}$	394
289	Nacelle External Pressure Distributions - Model 8, $M_0 = 0.301$, $N_F = 29.3\%$ (Windmill) $\sqrt{\theta_{10}}$	395
290	Nacelle External Pressure Distributions - Model 8, $M_0 = 0.301$, $N_F = 95.8\%$ $\sqrt{\theta_{10}}$	396
291	Nacelle External Pressure Distributions - Model 8, $M_0 = 0.500$, $N_F = 44.8\%$ (Windmill) $\sqrt{\theta_{10}}$	397
292	Nacelle External Pressure Distributions - Model 8, $M_0 = 0.500$, $N_F = 98.0\%$ $\sqrt{\theta_{10}}$	398
293	Nacelle External Pressure Distributions - Model 8, $M_0 = 0.699$, $N_F = 56.0\%$ (Windmill) $\sqrt{\theta_{10}}$	399
294	Nacelle External Pressure Distributions - Model 8, $M_0 = 0.699$, $N_F = 93.0\%$ $\sqrt{\theta_{10}}$	400
295	Nozzle Pressure Distribution - Model 1, $M_0 = 0.301$, $N_F = 32.2\%$ (Windmill) $\sqrt{\theta_{10}}$	401
296	Nozzle Pressure Distribution - Model 1, $M_0 = 0.300$, $N_F = 97.0\%$ $\sqrt{\theta_{10}}$	402

<u>Figure</u>		<u>Page</u>
297	Nozzle Pressure Distribution - Model 1, $M_0 = 0.601$, $N_F = 56.4\%$ $\frac{N_F}{\sqrt{\theta_{10}}}$	403
298	Nozzle Pressure Distribution - Model 1, $M_0 = 0.600$, $N_F = 94.2\%$ $\frac{N_F}{\sqrt{\theta_{10}}}$	404
299	Nozzle Pressure Distribution - Model 1, $M_0 = 0.797$, $N_F = 64.2\%$ (Windmill) $\frac{N_F}{\sqrt{\theta_{10}}}$	405
300	Nozzle Pressure Distribution - Model 1, $M_0 = 0.800$, $N_F = 87.6\%$ $\frac{N_F}{\sqrt{\theta_{10}}}$	406
301	Nozzle Pressure Distribution - Model 2, $M_0 = 0.301$, $N_F = 32.3\%$ (Windmill) $\frac{N_F}{\sqrt{\theta_{10}}}$	407
302	Nozzle Pressure Distribution - Model 2, $M_0 = 0.300$, $N_F = 98.4\%$ $\frac{N_F}{\sqrt{\theta_{10}}}$	408
303	Nozzle Pressure Distribution - Model 2, $M_0 = 0.598$, $N_F = 56.7\%$ (Windmill) $\frac{N_F}{\sqrt{\theta_{10}}}$	409
304	Nozzle Pressure Distribution - Model 2, $M_0 = 0.599$, $N_F = 91.5\%$ $\frac{N_F}{\sqrt{\theta_{10}}}$	410
305	Nozzle Pressure Distribution - Model 2, $M_0 = 0.800$, $N_F = 61.3\%$ (Windmill) $\frac{N_F}{\sqrt{\theta_{10}}}$	411
306	Nozzle Pressure Distribution - Model 2, $M_0 = 0.799$, $N_F = 85.1\%$ $\frac{N_F}{\sqrt{\theta_{10}}}$	412

<u>Figure</u>		<u>Page</u>
307	Nozzle Pressure Distribution - Model 3, $M_0 = 0.202$, $N_F = 32.0\%$ (Windmill) $\frac{N_F}{\sqrt{\theta_{10}}}$	413
308	Nozzle Pressure Distribution - Model 3, $M_0 = 0.202$, $N_F = 97.2\%$ $\frac{N_F}{\sqrt{\theta_{10}}}$	414
309	Nozzle Pressure Distribution - Model 3, $M_0 = 0.301$, $N_F = 47.0\%$ (Windmill) $\frac{N_F}{\sqrt{\theta_{10}}}$	415
310	Nozzle Pressure Distribution - Model 3, $M_0 = 0.301$, $N_F = 97.7\%$ $\frac{N_F}{\sqrt{\theta_{10}}}$	416
311	Nozzle Pressure Distribution - Model 3, $M_0 = 0.400$, $N_F = 60.2\%$ (Windmill) $\frac{N_F}{\sqrt{\theta_{10}}}$	417
312	Nozzle Pressure Distribution - Model 3, $M_0 = 0.401$, $N_F = 97.1\%$ $\frac{N_F}{\sqrt{\theta_{10}}}$	418
313	Nozzle Pressure Distribution - Model 4, $M_0 = 0.203$, $N_F = 22.3\%$ (Windmill) $\frac{N_F}{\sqrt{\theta_{10}}}$	419
314	Nozzle Pressure Distribution - Model 4, $M_0 = 0.202$, $N_F = 95.3\%$ $\frac{N_F}{\sqrt{\theta_{10}}}$	420
315	Nozzle Pressure Distribution - Model 4, $M_0 = 0.501$, $N_F = 49.9\%$ (Windmill) $\frac{N_F}{\sqrt{\theta_{10}}}$	421
316	Nozzle Pressure Distribution - Model 4, $M_0 = 0.500$, $N_F = 93.5\%$ $\frac{N_F}{\sqrt{\theta_{10}}}$	422

<u>Figure</u>		<u>Page</u>
317	Nozzle Pressure Distribution - Model 4, $M_0 = 0.649$, $N_F = 58.8\%$ (Windmill) $\frac{N_F}{\sqrt{\theta_{10}}}$	423
318	Nozzle Pressure Distribution - Model 4, $M_0 = 0.650$, $N_F = 91.7\%$ $\frac{N_F}{\sqrt{\theta_{10}}}$	424
319	Nozzle Pressure Distribution - Model 5, $M_0 = 0.202$, $N_F = 24.0\%$ (Windmill) $\frac{N_F}{\sqrt{\theta_{10}}}$	425
320	Nozzle Pressure Distribution - Model 5, $M_0 = 0.200$, $N_F = 97.8\%$ $\frac{N_F}{\sqrt{\theta_{10}}}$	426
321	Nozzle Pressure Distribution - Model 5, $M_0 = 0.400$, $N_F = 45.3\%$ (Windmill) $\frac{N_F}{\sqrt{\theta_{10}}}$	427
322	Nozzle Pressure Distribution - Model 5, $M_0 = 0.400$, $N_F = 95.2\%$ $\frac{N_F}{\sqrt{\theta_{10}}}$	428
323	Nozzle Pressure Distribution - Model 5, $M_0 = 0.650$, $N_F = 65.9\%$ (Windmill) $\frac{N_F}{\sqrt{\theta_{10}}}$	429
324	Nozzle Pressure Distribution - Model 6, $M_0 = 0.301$, $N_F = 30.1\%$ (Windmill) $\frac{N_F}{\sqrt{\theta_{10}}}$	430
325	Nozzle Pressure Distribution - Model 6, $M_0 = 0.299$, $N_F = 98.1\%$ $\frac{N_F}{\sqrt{\theta_{10}}}$	431
326	Nozzle Pressure Distribution - Model 6, $M_0 = 0.598$, $N_F = 51.6\%$ (Windmill) $\frac{N_F}{\sqrt{\theta_{10}}}$	432

<u>Figure</u>		<u>Page</u>
327	Nozzle Pressure Distribution - Model 6, $M_0 = 0.599$, $N_F = 92.4\%$ $\frac{N_F}{\sqrt{\theta_{10}}}$	433
328	Nozzle Pressure Distribution - Model 6, $M_0 = 0.800$, $N_F = 59.9\%$ (Windmill) $\frac{N_F}{\sqrt{\theta_{10}}}$	434
329	Nozzle Pressure Distribution - Model 7, $M_0 = 0.200$, $N_F = 23.2\%$ (Windmill) $\frac{N_F}{\sqrt{\theta_{10}}}$	435
330	Nozzle Pressure Distribution - Model 7, $M_0 = 0.202$, $N_F = 99.6\%$ $\frac{N_F}{\sqrt{\theta_{10}}}$	436
331	Nozzle Pressure Distribution - Model 7, $M_0 = 0.400$, $N_F = 44.7\%$ (Windmill) $\frac{N_F}{\sqrt{\theta_{10}}}$	437
332	Nozzle Pressure Distribution - Model 7, $M_0 = 0.400$, $N_F = 93.3\%$ $\frac{N_F}{\sqrt{\theta_{10}}}$	438
333	Nozzle Pressure Distribution - Model 7, $M_0 = 0.649$, $N_F = 64.6\%$ (Windmill) $\frac{N_F}{\sqrt{\theta_{10}}}$	439
334	Nozzle Pressure Distribution - Model 8, $M_0 = 0.301$, $N_F = 29.3\%$ (Windmill) $\frac{N_F}{\sqrt{\theta_{10}}}$	440
335	Nozzle Pressure Distribution - Model 8, $M_0 = 0.301$, $N_F = 95.8\%$ $\frac{N_F}{\sqrt{\theta_{10}}}$	441
336	Nozzle Pressure Distribution - Model 8, $M_0 = 0.500$, $N_F = 44.8\%$ (Windmill) $\frac{N_F}{\sqrt{\theta_{10}}}$	442

<u>Figure</u>		<u>Page</u>
337	Nozzle Pressure Distribution - Model 8, $M_0 = 0.500$, $N_F = 98.0\%$ $\frac{N_F}{\sqrt{\theta_{10}}}$	443
338	Nozzle Pressure Distribution - Model 8, $M_0 = 0.699$, $N_F = 56.0\%$ (Windmill) $\frac{N_F}{\sqrt{\theta_{10}}}$	444
339	Nozzle Pressure Distribution - Model 8, $M_0 = 0.699$, $N_F = 93.0\%$ $\frac{N_F}{\sqrt{\theta_{10}}}$	445
340	Nozzle Pressure Distribution - Model 1, $M_0 = 0.0$, $N_F = 83.6\%$ $\frac{N_F}{\sqrt{\theta_{10}}}$	446
341	Nozzle Pressure Distribution - Model 2, $M_0 = 0.0$, $N_F = 98.8\%$ $\frac{N_F}{\sqrt{\theta_{10}}}$	447
342	Nozzle Pressure Distribution - Model 3, $M_0 = 0.0$, $N_F = 97.4\%$ $\frac{N_F}{\sqrt{\theta_{10}}}$	448
343	Nozzle Pressure Distribution - Model 4, $M_0 = 0.0$, $N_F = 95.2\%$ $\frac{N_F}{\sqrt{\theta_{10}}}$	449
344	Nozzle Pressure Distribution - Model 5, $M_0 = 0.0$, $N_F = 97.2\%$ $\frac{N_F}{\sqrt{\theta_{10}}}$	450
345	Nozzle Pressure Distribution - Model 6, $M_0 = 0.0$, $N_F = 99.1\%$ $\frac{N_F}{\sqrt{\theta_{10}}}$	451
346	Nozzle Pressure Distribution - Model 7, $M_0 = 0.0$, $N_F = 99.6\%$ $\frac{N_F}{\sqrt{\theta_{10}}}$	452

<u>Figure</u>		<u>Page</u>
347	Nozzle Pressure Distribution - Model 8, $M_0 = 0.0$, $N_F = 72.7\%$ $\frac{N_F}{\sqrt{\theta_{10}}}$	453
348	Wind Tunnel Axial Mach Number Distributions	454
349	Variation of System Lift with Angle of Attack and Speed, $M_0 = 0.30$ - Model 8	455
350	Variation of System Axial Thrust with Angle of Attack and Speed, $M_0 = 0.30$ - Model 8	456
351	Variation of System Pitching Moment with Angle of Attack and Speed, $M_0 = 0.30$ - Model 8	457
352	Variation of System Lift with Angle of Attack and Speed, $M_0 = 0.50$ - Model 8	458
353	Variation of System Axial Thrust with Angle of Attack and Speed, $M_0 = 0.50$ - Model 8	459
354	Variation of System Pitching Moment with Angle of Attack and Speed, $M_0 = 0.50$ - Model 8	460
355	Variation of System Lift with Angle of Attack and Speed, $M_0 = 0.70$ - Model 8	461
356	Variation of System Axial Thrust with Angle of Attack and Speed, $M_0 = 0.70$ - Model 8	462
357	Variation of System Pitching Moment with Angle of Attack and Speed, $M_0 = 0.70$ - Model 8	463
358	Engine Nacelle Pressure Distributions Showing Effects of Angle of Attack, $M_0 = 0.30$	464
359	Engine Nacelle Pressure Distributions Showing Effects of Angle of Attack, $M_0 = 0.70$	465
360	Nacelle External Pressure Distributions Showing Effects of Angle of Attack, $M_0 = 0.30$	466
361	Nacelle External Pressure Distributions Showing Effects of Angle of Attack, $M_0 = 0.70$	467
362	Nacelle Internal Pressure Distributions Showing Effects of Angle of Attack, $M_0 = 0.30$	468

<u>Figure</u>		<u>Page</u>
363	Nacelle Internal Pressure Distributions Showing Effects of Angle of Attack, $M_0 = 0.70$	469
364	Nozzle Plug Distributions Showing Effects of Angle of Attack, $M_0 = 0.30$ and 0.70	470
365	Fan Turbine Operating Characteristics - Model 3, $M_0 = 0.0$	471
366	Fan Turbine Operating Characteristics - Model 3, $M_0 = 0.2$	472
367	Fan Turbine Operating Characteristics - Model 3, $M_0 = 0.3$	473
368	Fan Turbine Operating Characteristics - Model 3, $M_0 = 0.4$	474
369	Fan Turbine Operating Characteristics - Model 6, $M_0 = 0.0$	475
370	Fan Turbine Operating Characteristics - Model 6, $M_0 = 0.3$	476
371	Fan Turbine Operating Characteristics - Model 6, $M_0 = 0.4$	477
372	Fan Turbine Operating Characteristics - Model 6, $M_0 = 0.5$	478
373	Fan Turbine Operating Characteristics - Model 6, $M_0 = 0.6$	479
374	Fan Turbine Operating Characteristics - Model 6, $M_0 = 0.7$	480
375	Comparison of Predicted and Measured Fan Turbine Performance - Model 3	481
376	Comparison of Predicted and Measured Fan Turbine Performance - Model 6	482
377	Fan Performance Characteristics - Model 1	483
378	Fan Performance Characteristics - Model 2	484
379	Fan Performance Characteristics - Model 3	485
380	Fan Performance Characteristics - Model 4	486

<u>Figure</u>		<u>Page</u>
381	Fan Performance Characteristics - Model 5	487
382	Fan Performance Characteristics - Model 6	488
383	Fan Performance Characteristics - Model 7	489
384	Fan Performance Characteristics - Model 8	490
385	Variation of Fan and Fan Turbine Pressure with Fan Speed for the Eight Models	491
386	Variation of Fan Inlet Loss Coefficient with Mass Flow Ratio	492
387	Variation of Static Inlet Loss Coefficient with Inlet Length to Diameter Ratio	493
388	Correlation of Effects of Mass Flow Ratio on Inlet Loss Coefficients	494
389	Variation of Engine Inlet Loss Coefficient with Mass Flow Ratio	495
390	Effects of Mass Flow Ratio on Inlet Maximum Internal Velocity - Inlet 1	496
391	Effects of Mass Flow Ratio on Inlet Maximum Internal Velocity - Inlet 2	497
392	Effects of Mass Flow Ratio on Inlet Maximum Internal Velocity - Inlet 3	498
393	Effects of Inlet Internal Lip Radius on Maximum Surface Velocity at Static ($M_0 = 0.0$) Conditions	499
394	Variation of Inlet Lip Maximum Velocity with Angle of Attack	500
395	Variation of Peak External Pressure Coefficient with Mach Number and Mass Flow Ratio for Model 1 (Inlet 1)	501
396	Variation of Peak External Pressure Coefficient with Mach Number and Mass Flow Ratio for Model 2 (Inlet 2)	502
397	Variation of Peak External Pressure Coefficient with Mach Number and Mass Flow Ratio for Model 3 (Inlet 2)	503
398	Variation of Peak External Pressure Coefficient with Mach Number and Mass Flow Ratio for Model 4 (Inlet 3)	504

<u>Figure</u>		<u>Page</u>
399	Variation of Peak External Pressure Coefficient with Mach Number and Mass Flow Ratio for Model 5 (Inlet 3)	505
400	Variation of Peak External Pressure Coefficient with Mach Number and Mass Flow Ratio for Model 6 (Inlet 1)	506
401	Variation of Peak External Pressure Coefficient with Mach Number and Mass Flow Ratio for Model 7 (Inlet 1)	507
402	Variation of Peak External Pressure Coefficient with Mach Number and Mass Flow Ratio for Model 8 (Inlet 1)	508
403	Variation of Peak External Pressure Coefficient with Mach Number for Inlet 1 at a Mass Flow Ratio of 0.5	509
404	Variation of Peak External Pressure Coefficient with Mach Number for Inlet 2 at a Mass Flow Ratio of 0.50	510
405	Variation of Peak External Pressure Coefficient with Mach Number for Inlet 3 at a Mass Flow Ratio of 0.4	511
406	Variation of Peak External Pressure Coefficient on Inlet Leading Edge with Angle of Attack at a Mach Number of 0.30	512
407	Variation of Peak External Pressure Coefficient on Inlet Leading Edge with Angle of Attack at a Mach Number of 0.50	513
408	Variation of Peak External Pressure Coefficient on Inlet Leading Edge with Angle of Attack at a Mach Number of 0.70	514
409	Effects of Angle of Attack on Peak External Pressure Coefficient at a Mass Flow Ratio of 0.50	515
410	Effects of Angle of Attack on Free-Stream Mach Number for Critical Flow in Area of Fairing - Model 8	516
411	Variation of Peak External Pressure Coefficient with Mach Number and Mass Flow Ratio for Engine Nacelle - 0° Plane	517
412	Variation of Peak External Pressure Coefficient with Mach Number and Mass Flow Ratio for Engine Nacelle - 180° Plane	518

<u>Figure</u>		<u>Page</u>
413	Variation of Engine Nacelle Peak External Pressure Coefficient with Mach Number at a Mass Flow Ratio of 0.32	519
414	Nozzle Static Thrust Coefficients Based on Force Balance Data	520
415	Definition of Surfaces of Integration of Nozzle Forces	521
416	Exhaust Nozzle Effective Area Characteristics - Model 1	522
417	Exhaust Nozzle Effective Area Characteristics - Model 2	523
418	Exhaust Nozzle Effective Area Characteristics - Model 3	524
419	Exhaust Nozzle Effective Area Characteristics - Model 4	525
420	Exhaust Nozzle Effective Area Characteristics - Model 5	526
421	Exhaust Nozzle Effective Area Characteristics - Model 6	527
422	Exhaust Nozzle Effective Area Characteristics - Model 7	528
423	Exhaust Nozzle Effective Area Characteristics - Model 8	529
424	Nacelle Drag Coefficients Based on Force Measurements and an Ideal Exhaust Nozzle - Model 1	530
425	Nacelle Drag Coefficients Based on Force Measurements and an Ideal Exhaust Nozzle - Model 2	531
426	Nacelle Drag Coefficients Based on Force Measurements and an Ideal Exhaust Nozzle - Model 3	532
427	Nacelle Drag Coefficients Based on Force Measurements and an Ideal Exhaust Nozzle - Model 4	533
428	Nacelle Drag Coefficients Based on Force Measurements and an Ideal Exhaust Nozzle - Model 5	534

<u>Figure</u>		<u>Page</u>
429	Nacelle Drag Coefficients Based on Force Measurements and an Ideal Exhaust Nozzle - Model 6	535
430	Nacelle Drag Coefficients Based on Force Measurements and an Ideal Exhaust Nozzle - Model 7	536
431	Nacelle Drag Coefficients Based on Force Measurements and an Ideal Exhaust Nozzle - Model 8	537
432	Nacelle Drag Coefficients Based on Force Measurements and a Nozzle with a 0.95 Thrust Coefficient - Model 1	538
433	Nacelle Drag Coefficients Based on Force Measurements and a Nozzle with a 0.95 Thrust Coefficient - Model 2	539
434	Nacelle Drag Coefficients Based on Force Measurements and a Nozzle with a 0.95 Thrust Coefficient - Model 3	540
435	Nacelle Drag Coefficients Based on Force Measurements and a Nozzle with a 0.95 Thrust Coefficient - Model 4	541
436	Nacelle Drag Coefficients Based on Force Measurements and a Nozzle with a 0.95 Thrust Coefficient - Model 5	542
437	Nacelle Drag Coefficients Based on Force Measurements and a Nozzle with a 0.95 Thrust Coefficient - Model 6	543
438	Nacelle Drag Coefficients Based on Force Measurements and a Nozzle with a 0.95 Thrust Coefficient - Model 7	544
439	Nacelle Drag Coefficients Based on Force Measurements and a Nozzle with a 0.95 Thrust Coefficient - Model 8	545
440	Variation of Drag Coefficient with Mach Number for the Three Inlet Systems	546
441	Circumferential Variation of Pressure Coefficient for Model 6 (Inlet 1)	547
442	Circumferential Variation of Pressure Coefficient for Model 2 (Inlet 2)	548
443	Variation of Afterbody Drag with Mach Number Based on Pressure Integrations	549
444	Effects of Inlet Length on Nacelle Drag Coefficients	550
445	Summary of Nacelle Total Drag Coefficients Based on Balance Measurements	551

<u>Figure</u>		<u>Page</u>
446	Variation of Nacelle Contribution to Lift with Angle of Attack and Speed, $M_0 = 0.3$	552
447	Variation of Nacelle Contribution to Drag with Angle of Attack and Speed, $M_0 = 0.3$	553
448	Variation of Nacelle Contribution to Pitching Moment with Angle of Attack and Speed, $M_0 = 0.3$	554
449	Variation of Nacelle Contribution to Lift with Angle of Attack and Speed, $M_0 = 0.50$	555
450	Variation of Nacelle Contribution to Drag with Angle of Attack and Speed, $M_0 = 0.50$	556
451	Variation of Nacelle Contribution to Pitching Moment with Angle of Attack and Speed, $M_0 = 0.50$	557
452	Variation of Nacelle Contribution to Lift with Angle of Attack and Speed, $M_0 = 0.70$	558
453	Variation of Nacelle Contribution to Drag with Angle of Attack and Speed, $M_0 = 0.70$	559
454	Variation of Nacelle Contribution to Pitching Moment with Angle of Attack and Speed, $M_0 = 0.70$	560
455	Variation of Nacelle Contribution to Pitching Moments with Speed - No Correction for Fan Thrust Alignment . . .	561
456	Variation of Nacelle Contribution to Pitching Moments with Speed - Corrected for Static Fan Thrust Alignment . .	562
457	Comparison of Lift Curve Slope of Model 8 and Ring Wing Data	563
458	Comparison of Pitching Moment Curve Slope of Model 8 and Ring Wing Data	564
459	Ratio of Absorbed to Ideal Horsepower - Model 1	565
460	Ratio of Absorbed to Ideal Horsepower - Model 2	566
461	Ratio of Absorbed to Ideal Horsepower - Model 3	567
462	Ratio of Absorbed to Ideal Horsepower - Model 4	568
463	Ratio of Absorbed to Ideal Horsepower - Model 5	569

<u>Figure</u>		<u>Page</u>
464	Ratio of Absorbed to Ideal Horsepower - Model 6	570
465	Ratio of Absorbed to Ideal Horsepower - Model 7	571
466	Ratio of Absorbed to Ideal Horsepower - Model 8	572
467	Variation of Horsepower Ratio with Speed and Nozzle Area	573
468	Variation of Flow Coefficient with Speed and Nozzle Area	574
469	Variation of Ideal Net Thrust with Speed and Nozzle Area	575
470	Variation of Net Thrust with Speed and Nozzle Area for a 0.95 Nozzle Thrust Coefficient	576
471	Fan Operating Characteristics for Optimum Nozzle Trim and 100% Fan Speed	577
472	Fan Horsepower Requirements as a Function of Speed and Mach Number for Optimum Trim Area	578
473	Variation of Fan Horsepower Requirements with Speed and Nozzle Area at a Fan Speed of 90%	579
474	Predicted Nacelle Critical Mach Number as a Function of Inlet Length and Inlet Diameter	580
475	Predicted Minimum Mass Flow and Velocity Ratios as a Function of Inlet Length and Inlet Diameter	581
476	Estimated Correction to Critical Mach Number for Angle of Attack	582
477	Comparison of Predicted and Measured Critical Mach Numbers for the Three Inlets	583
478	Variation of Low Speed Pressure Coefficient with Mass Flow Ratio for the Three Inlets Tested	584
479	Compressibility Correction of Low Speed Pressure Coefficients	585
480	Comparison of Inlet Peak Pressure Coefficients for the Fairing and Axisymmetric Regions of Inlets	586

<u>Figure</u>		<u>Page</u>
481	Geometric Constants for Design of Fan-Engine Nacelle Fairing	587
482	Sketch of Model 8 Showing Original and Modified Nacelle Designs	588
483	Microphone Installation in Model 3 Inlet	589
484	Schematic Diagram of Instrumentation and Data Reduction Systems	590
485	Conversion Chart - Output Level Versus Pressure Level in Decibels	591
486	Conversion Chart - Output Level Versus Pressure Level in Pounds per Square Inch	592
487	Wave Form of Pressure Signal Data Point Number 1, $M_0 = 0.3$, $N_F = 1900$ Revolutions per Minute	593
488	Amplitude and Frequency Analysis for Microphone Located at 337.5 Degrees, Data Point Number 1, $M_0 = 0.3$, $N_F = 1900$ Revolutions per Minute	594
489	Wave Form of Pressure Signal Data Point Number 2, $M_0 = 0.4$, $N_F = 2450$ Revolutions per Minute	595
490	Amplitude and Frequency Analysis for Microphone Located at 270 Degrees, Data Point Number 2, $M_0 = 0.4$, $N_F = 1900$ Revolutions per Minute	596
491	Amplitude and Frequency Analysis for Microphone Located at 337.5 Degrees, Data Point Number 2, $M_0 = 0.4$, $N_F = 1900$ Revolutions per Minute	597
492	Wave Form of Pressure Signal Data Point Number 3, $M_0 = 0.5$, $N_F = 2950$ Revolutions per Minute	598
493	Amplitude and Frequency Analysis for Microphone Located at 270 Degrees, Data Point Number 3, $M_0 = 0.5$, $N_F = 2950$ Revolutions per Minute	599
494	Amplitude and Frequency Analysis for Microphone Located at 337.5 Degrees, Data Point Number 3, $M_0 = 0.5$, $N_F = 2950$ Revolutions per Minute	600
495	Wave Form of Pressure Signal Data Point Number 4, $M_0 = 0.6$, $N_F = 3410$ Revolutions per Minute	601

<u>Figure</u>		<u>Page</u>
496	Amplitude and Frequency Analysis for Microphone Located at 370 Degrees, Data Point Number 4, $M_0 = 0.6$, $N_F = 3410$ Revolutions per Minute	602
497	Amplitude and Frequency Analysis for Microphone Located at 337.5 Degrees, Data Point Number 4, $M_0 = 0.6$, $N_F = 3410$ Revolutions per Minute	603
498	Wave Form of Pressure Signal Data Point Number 5, $M_0 = 0.7$, $N_F = 3760$ Revolutions per Minute	604
499	Amplitude and Frequency Analysis for Microphone Located at 270 Degrees, Data Point Number 5, $M_0 = 0.7$, $N_F = 3760$ Revolutions per Minute	605
500	Amplitude and Frequency Analysis for Microphone Located at 337.5 Degrees, Data Point Number 5, $M_0 = 0.7$, $N_F = 3760$ Revolutions per Minute	606
501	Wave Form of Pressure Signal Data Point Number 6, $M_0 = 0.8$, $N_F = 4050$ Revolutions per Minute	607
502	Amplitude and Frequency Analysis for Microphone Located at 270 Degrees, Data Point Number 6, $M_0 = 0.8$, $N_F = 4050$ Revolutions per Minute	608
503	Amplitude and Frequency Analysis for Microphone Located at 337.5 Degrees, Data Point Number 6, $M_0 = 0.8$, $N_F = 4050$ Revolutions per Minute	609
504	Wave Form of Pressure Signal Data Point Number 7, $M_0 = 0.3$, $N_F = 1920$ Revolutions per Minute	610
505	Amplitude and Frequency Analysis for Microphone Located at 270 Degrees, Data Point Number 7, $M_0 = 0.3$, $N_F = 1920$ Revolutions per Minute	611
506	Amplitude and Frequency Analysis for Microphone Located at 337.5 Degrees, Data Point Number 7, $M_0 = 0.3$, $N_F = 1920$ Revolutions per Minute	612
507	Data Showing Correlation of Microphone Frequencies with Harmonics of the Blade Passing Frequency	613
508	Amplitude of Overall Signal and Primary Source Signal Due to Pressure Fluctuations Shown as a Function of Mach Number	614

<u>Figure</u>		<u>Page</u>
509	Amplitude of Overall Signal and Primary Source Signal Due to Pressure Fluctuations Expressed in Decibels and Shown as a Function of Mach Number	615
510	Local Dynamic Pressure at Axial Plane of Microphone Shown as a Function of Tunnel Mach Number	616
511	Amplitude of Pressure Fluctuations Shown as a Function of Local Dynamic Pressure	617
512	Photograph of Sting or Support Beam for Cruise Fan Model	618
513	Photograph of Balance Adapter	619
514	Photographs of Main Support Frame	620
515	Photograph of T58-6A Engine Mounted in Engine Support Beams	621
516	Photographs of X376 Fan Mounted in Main Support Frame . .	622
517	Photograph of Nozzle Plug for Cruise Fan Model	623
518	Model Assembly Drawing	625
519	Detail Drawing of Main Frame	633
520	Detail Drawing of Nacelle Inlets	639
521	Detail Drawing of Aft Nacelle 1	643
522	Detail Drawing of Aft Nacelle 2	649
523	Detail Drawing of Aft Nacelle 4	655
524	Detail Drawing of Nozzle Plugs	661
525	Detail Drawing of Engine Inlet	665

TABLES

<u>Table</u>		<u>Page</u>
I	Model Coordinates, Inlet Cowl Internal Surface	76
II	Model Coordinates, Inlet Cowl External Surface	77
III	Model Coordinates, Fan Bullethead	78
IV	Model Coordinates, Afterbody Outer Contour	79
V	Model Coordinates, Nozzle Outer Shroud	80
VI	Model Coordinates, Engine Cowl Outer Surface	82
VII	Model Coordinates, Engine Inlet Internal Surface	83
VIII	Model Coordinates, Engine Bullethead	84
IX	Model Coordinates, Nozzle Plug	85
X	Model Coordinates, Fan Inlet to Engine Nacelle Fairing . .	88
XI	Model Coordinates, Afterbody to Engine Nacelle Fairing . .	90
XII	Surface Pressure Instrumentation Location, Inlet Cowl Internal Surface	92
XIII	Surface Pressure Instrumentation Location, Inlet Cowl External Surface	93
XIV	Surface Pressure Instrumentation Location, Fan Bullet- nose	95
XV	Surface Pressure Instrumentation Location, Afterbody Outer Contour	95
XVI	Surface Pressure Instrumentation Location, Nozzle Outer Shroud	97
XVII	Surface Pressure Instrumentation Location, Engine Nacelle Outer Contour	98
XVIII	Surface Pressure Instrumentation Location, Engine Nacelle Inner Contour	99
XIX	Surface Pressure Instrumentation Location, Plug Con- tour	99

<u>Table</u>		<u>Page</u>
XX	Gas Stream Pressure Instrumentation Location	102
XXI	Summary of Test Points During Noise Studies - Model 3 . .	106

SYMBOLS

A	area or axial force
A _e	effective one-dimensional flow area
A _I	inlet leading edge area
A _O	free stream area of inlet mass flow
A _π	area based on nacelle maximum diameter
C	chord of ring wing
C _{Dπ}	drag coefficient, $\frac{D}{q_0 A_\pi}$
C _F	local skin friction coefficient
C _L	lift coefficient, $\frac{L}{q_0 A_\pi}$
C _m	pitching moment coefficient, $\frac{m}{q_0 A_\pi D_F}$
C _P	pressure coefficient, $\frac{P_L - P_0}{q_0}$, or specific heat of gas
C _T	thrust coefficient
D	diameter or drag
f	stream thrust, $P_S A + \frac{w}{g} V$
F	axial force or thrust
g	gravitational constant
H _D	drag coefficient, $\frac{D}{\rho_{10.0} U_T^2 A_F}$
H _L	lift coefficient, $\frac{L}{\rho_{10.0} U_T^2 A_F}$

H_m	pitching moment coefficient, $\frac{m}{\rho_{10.0} U_T^2 A_F D_F}$
H_N	net thrust coefficient, $\frac{F_N}{\rho_{10.0} U_T^2 A_F}$
HP	ideal gas horsepower
K	geometric constant
L	lift or length of model component
M	Mach number
m	pitching moment
\bar{m}	flow function parameter, $\frac{W\sqrt{T_T}}{P_T A}$
N	rotational speed or normal force
P_L	local surface static pressure
P_O	ambient static pressure
P_S	stream static pressure
P_T	stream total pressure
q	dynamic pressure, $\frac{\rho v^2}{2}$
R	radius or gas constant
S_w	wetted surface area
T_T	total temperature
U_T	fan tip speed
V	velocity
W	airflow
W_f	engine fuel flow

x	axial distance
α	angle of attack
θ_p	nozzle plug angle
γ	ratio of specific heats
δ	pressure correction based on standard pressure
η	efficiency
θ	temperature correction based on standard temperature
λ	nozzle pressure ratio
ρ	density
ϕ	circumferential angle around model ($\phi = 0^\circ$ at top of model opposite engine nacelle)
Φ	flow coefficient
ψ	pressure coefficient
\overline{w}	loss coefficient

SUBSCRIPTS

0	ambient, free stream, or at $\alpha = 0^\circ$
1.0	engine nacelle inlet leading edge station
2 or 2.0	engine compressor inlet station
2.1	engine inlet midstream
2.2	engine inlet boundary layer
5.1	engine turbine discharge station
5.6	fan turbine discharge station
9.0	fan nacelle inlet leading edge station
10 or 10.0	fan rotor inlet station
10.1	fan inlet midstream
10.2	fan inlet tip boundary layer
10.3	fan inlet hub boundary layer
10.6	fan rotor discharge station
11 or 11.0	fan discharge station
11.1	fan discharge midstream
11.2	fan discharge tip boundary layer
11.3	fan discharge hub boundary layer
12.0	fan nozzle throat station
13.0	end of plug
5.1 - 0	engine turbine discharge referred to ambient or free stream
5.1 - 5.6	engine turbine discharge referred to fan turbine discharge
AB	afterbody
AVG	average
B	force balance or engine nacelle body

C	plug crown or cold arc of fan discharge
CR	critical or at $M_0 = 1.0$
D	drag, or diameter
DR	ram drag
E	engine, engine nacelle or effective
F	fan or friction
G	gross
H	fan hub or hot arc of fan discharge
I	nacelle inlet or inlet
J	jet (ring wing data)
L	lift, local or length
m	pitching moment
MAX or max	maximum
MIN	minimum
N	nacelle, net or nozzle throat
S	nozzle shroud, system or product
T	fan tip, or thrust (negative drag)
TH	inlet throat

INTRODUCTION

In recent years increased emphasis has been placed on the design and development of V/STOL aircraft systems. One of the promising propulsion systems in the high bypass category is the lift/cruise fan. This system incorporates the turbomachinery from the tip-turbine-driven lift fan, which is an outgrowth of the X353 and X376 lift fans presently powering the XV-5A research aircraft. Present advanced design studies of tip turbine lift/cruise fans indicate probable fan bypass ratios of between 5 and 10, as compared to the X353 and X376 lift fans with a bypass ratio of 12.

Shifting the tip turbine fan from its low axial profile lift fan installation to a minimum diameter cruise installation required totally different inlet and exhaust systems.

Review of existing test data for nacelle and nozzle systems applicable for use with these families of lift/cruise turbofans showed that very little data was available. As a result, extensive scale model programs were then initiated to investigate the aerodynamics in these previously unexplored regions. Reference 3 gives a summary of one such program designed to obtain nacelle and nozzle aerodynamic performance by use of small scale models. The tests were conducted within the bypass and pressure ratio ranges applicable to the lift/cruise fan systems. A logical next step in the development of performance data is the design, test, and flight of a full-scale propulsion system. As an interim program to fill the gap between scale-model and full-scale performance data, a test program utilizing the existing X376 fan system was proposed and conducted. This system uses a fan which has a bypass ratio of about 12, powered by a modified T58-6A core engine as the basic propulsion system. This report summarizes the aerothermodynamic performance that was obtained during the test program.

The test model consisted of the basic propulsion system and a family of inlet and nozzle systems. The inlet systems provided a means of determining effects of length and diameter on performance. The nozzles provided changes in discharge area, as well as length and diameter. Eight different models were assembled using various combinations of the inlet and nozzle systems. The tests were performed in the NASA-Langley 16-foot wind tunnel. Tests were conducted within a range of propulsion system power settings and tunnel Mach numbers commensurate with lift/cruise fan operating envelopes.

The results presented in this report should provide useful performance data to fill the gap between the small-scale model and full-scale tests. Presentation of the test results in parametric non-dimensional form provides a means of estimating nacelle internal and external performance representative of these high pressure ratio lift/cruise fan systems.

DESCRIPTION OF TEST EQUIPMENT

TEST FACILITY

The tests during this investigation were made in the Langley 16-foot high-speed tunnel. The tunnel is a single return, atmospheric type with a test section Mach number range continuously variable from about 0.2 to about 1.3. During this test program, the maximum test Mach number was 0.85.

The model was sting supported on a single vertical strut. Model attachment to the sting was through a strain gage balance capable of measuring six force components. The strut is mounted on shoes that slide on a circular arc to provide angle of attack variation. The model angle of attack was varied from 8.0 degrees nose down to 2.0 degrees nose up. The model was mounted in the inverted position in the tunnel such that the 8.0 nose down condition is equivalent to a positive angle of attack. The center of rotation of the model during angle of attack changes was at wind tunnel station 134.

Photographs of a typical model configuration installed in the tunnel test section are shown in Figure 1. The top portion of the test section has been raised, as required during model installation and setup, for these photographs. Figure 2 is a sketch of a typical model installed in the wind tunnel test section showing pertinent installation and model dimensions.

FAN AND CORE ENGINE

The propulsion system of the model consisted of an X376 fan system driven by a T58-6A engine modified for use as a core engine. A sketch of the major propulsion system components is identified and shown in Figure 3.

The X-376 fan is a 1.1 pressure ratio, tip-turbine-driven fan. The fan tip diameter is 36 inches with a hub diameter of 16.2 inches. The fan design speed is 4074 revolutions per minute. The tip turbine is located radially outboard of the fan tip and absorbs power over about 167 degrees of the circumferential arc; the remaining part of the turbine arc remains inactive.

The engine used to provide gas power to the fan turbine was the T58-6A engine converted from a turboshaft engine to a conventional jet engine. Conversion was accomplished by removing the power turbine assembly and by modifying the power turbine nozzles to reduce the flow restrictions at that location in the engine.

Ducting, bellows, and flow straightening sections provided the flow path for routing the engine exhaust gases to the fan scroll inlet. The gas drives the fan turbine over the 167 degrees of active arc. The fan and turbine exhaust flows were then discharged into a common annulus before entering the exhaust nozzle system.

MODEL

The complete cruise fan model consisted of the fan and core engine and all necessary inlet and exhaust systems as identified in Figure 3. These included the fan inlet cowl, engine nacelle, the afterbody, the fan and engine bulletnoses and the nozzle plug. Changes of model configurations were obtained by using three each of interchangeable fan inlets, afterbodies and nozzle plugs. These components were matched to provide eight separate complete nacelle configurations for testing in this program. Figures 4, 5, 6, and 7 show sketches of each of these test configurations and significant applicable geometric data. This range of configurations was tested to investigate inlet cowl design for a range of nozzle exit areas and afterbody lengths.

Internal and external duct coordinates for each of the model components are listed in detail in Tables I through XI. Area distributions through the three inlet and six nozzle systems are shown in Figures 8 through 16. Area distributions through the engine inlet are shown in Figure 17.

A description of the test hardware, including design descriptions and detailed drawings of the major test components, is given in Appendix III.

INSTRUMENTATION

Pressure instrumentation was provided in the model for measurement of surface and air stream pressures. About 500 individual pressure measurements were provided on the model and recorded during each test point reading. Recording of the pressures was accomplished using twelve scanivalves with the measurements stored on punched cards. This recording system, which is the standard equipment used by NASA-Langley for pressure measurements, was capable of reading and recording all pressures in less than 40 seconds.

The pressure sensors, wall static taps, and stream total and static probes were located at several angular positions and at different axial stations in the model. The location of each angular measurement position was assigned a letter designation as shown in Figure 18. Similarly, a number designation was assigned to each axial plane or station, as in Figure 19. These angular and axial plane designations will be used in discussion and identification of pressure measurements throughout this report.

The location, both axial and radial, for each of the surface pressure measurements provided in the model is given in Tables XII through XIX. The tabulations are given according to model component where applicable. The numbers listed in the tables are code numbers assigned to each pressure probe. The absence of a code number denotes a pressure location that is not applicable. The code numbers provided identification of tabulated data and test results.

The listing of pressure measurements provided for determining flow conditions throughout the model is given in Table XX. The planes where measurements were provided are:

- o Engine Compression Inlet - Station 2.0
- o Engine Turbine Discharge - Station 5.1
- o Fan Turbine Discharge - Station 5.6
- o Fan Rotor Inlet - Station 10.0
- o Fan Rotor Discharge - Station 10.6
- o Fan Stage Discharge - Station 11.0
- o Model Base at Sting Mount - Station 14.0

The radial location of each of the pressure probes varied with test configuration as listed.

In addition to the pressure measurements, temperature probes were provided in the engine discharge flow stream for measurement of gas total temperature. The conventional engine exhaust gas temperature harness was used for engine turbine discharge measurements. This system resulted in a single average gas temperature. An array of eight temperature probes was provided in the fan turbine discharge flow path at station 5.6 (Figure 19). These probes were located at the same positions as the fan turbine discharge pressures listed in Table XX. Each temperature measurement was individually recorded.

In addition to the above described pressure measurements and the normal tunnel test condition measurements, the following were also recorded:

- o Engine and fan rotational speeds
- o Engine and fan vibrations
- o Engine oil pressure and temperature
- o Fan blade vibratory stress levels
- o Numerous structural and cavity temperatures as required to insure that the model was performing satisfactorily and not overheating

SOUND VIBRATION MEASUREMENTS

A special part of the test program was devoted to the measurement of pressure fluctuations and noise levels at the surfaces of the nacelle inlet internal duct. These measurements were taken by microphones installed in the nacelle surface and were recorded on magnetic tape. The results of this phase of the test program are summarized in Appendix II.

PROCEDURES

EXPERIMENTAL TEST

A typical test run in the wind tunnel consisted of setting two or three different wind tunnel Mach numbers. At each Mach number the engine power was varied between "off" and the maximum possible setting as determined by either engine or fan design speeds. Five or six engine power settings were taken at each tunnel Mach number. After both the wind tunnel and the propulsion system had stabilized at a set of test conditions, a reading of all data was taken. This reading included all force measurements, pressures, temperatures, and propulsion system vibrations and stresses. A complete reading would normally take about 60 seconds. Following completion of the reading, the tunnel or engine was adjusted to the next set of test requirements.

During tests of several of the models, a limit test Mach number was attained when fan blade stresses exceeded normal operating limits. These high stress levels were attributed to operation of the fan at off design conditions not normally encountered in a typical fan operating envelope. The limit Mach numbers established by these conditions are reflected in the range of test Mach numbers used for each model.

DATA REDUCTION

Reduction of experimental data into usable engineering units and parameters was performed on electronic computing machines. The data reduction procedure first converted all measurements from coded units as stored on punched cards into engineering units using the appropriate calibration and correction factors. Each individual measurement was then printed out in absolute units as well as coefficients based on free-stream velocity head.

The next step of the data analysis procedures was to use the basic measurements to compute propulsion system and nacelle performance. A detailed breakdown of the equations and methods used in analysis of the test data is given in Appendix I.

TEST RESULTS

USEFUL CONVERSION CHARTS

Throughout the presentation of test results and analysis of the data, several coefficient forms will be used that exhibit unique relationships among one another. Figures 20 and 21 show two of the most useful of these relationships. Figure 20 shows the variation of the speed ratio parameter, free-stream Mach number divided by fan tip Mach number, with free-stream Mach number and corrected fan speed. Figure 21 shows the multiplying factor required for conversion between the conventional force coefficient systems, referenced to free-stream velocity heads, and the fan coefficient form, referenced to fan rotational speed. This conversion parameter is primarily a function of the speed ratio, free-stream Mach number divided by fan tip Mach number, with a second-order correction due to Mach number.

PROPULSION SYSTEM PERFORMANCE

A major part of the test results involve the aerothermodynamics of the propulsion system. The propulsion system, consisting of the fan, core engine and ducting, develops thrust levels in the model that must be well defined in order to determine the nacelle internal and external performance. The propulsion system performance is presented for each of the eight test configurations. In the analysis section, the effects of test variables on this performance are analyzed.

Core Engine Performance

Figures 22 through 25 present the measured engine parameters as a function of engine speed for Model 1. The figures show engine inlet airflow, turbine discharge total pressure, exhaust gas temperature, and ideal gas horsepower. Engine airflow was computed using measured average pressures at the engine inlet station. Gas horsepower was calculated based on average turbine discharge flow conditions expanded isentropically to ambient pressure. All engine performance is standardized using measured engine inlet total pressure and temperature. Similar engine performance characteristics for the seven other models are given in Figures 27 through 53.

Fan Performance

Typical fan performance characteristics for Model 1 are shown in Figures 54 through 64. Figures 54 and 55 present fan airflow and pressure ratio versus speed and wind tunnel Mach number. Figures 56 through 60 show the various ideal thrusts and drags of the fan system for the range of test Mach numbers and fan speeds. Fan operating characteristics in coefficient form are given in Figures 61 and 62. Variations of fan flow coefficient with Mach number and speed ratio, and free-stream Mach number divided by fan tip Mach number, are shown in Figure 61. Figure 62 gives the values of fan pressure coefficient for the same range of operating conditions.

Figures 63 and 64 present fan net thrust variations with Mach number and speed ratio. The thrust in these curves is presented in fan coefficient notation for an assumed nozzle thrust coefficient of 0.95, as well as for an ideal nozzle system. Detailed procedures used in calculating these parameters are given in Appendix I.

Similar performance for the seven other test models is given in Figures 65 through 141.

Fan Power Absorption

Since the propulsion system had a confluent exhaust nozzle system, the power absorbed by the fan system is an important test result. A confluent nozzle system in this case combines the exhausts of both the fan discharge and fan turbine discharge streams into a single flow area prior to acceleration at the nozzle throat. The power extraction in the fan turbine is then established by the conditions where the two streams unite. These conditions are discussed later. The data required to provide the future analysis are shown in Figures 142 through 165 for the eight test models. The figures depict fan turbine pressure ratio and temperature ratio as a function of fan rotational speed and test Mach number. Fan horsepower requirements are presented as the ideal gas horsepower required for a given fan speed and Mach number. The procedures used in calculating the gas horsepower are given in Appendix I. The third characteristic shown for each model is the variation of gas horsepower being extracted by the fan turbine as a function of engine corrected speed. This horsepower parameter will be required in analysis of the power requirements of the fan system.

Balance Data

For each set of test conditions, net forces acting on the model were recorded on the strain gaged balance system. The forces were recorded for three axes, axial force, normal force, and longitudinal moments.

Static Performance

Each test model was run in the tunnel under conditions of near zero velocity. The axial and normal forces and pitching moments for each test model as measured on the balance system are shown in Figures 166 through 173. Forces and fan speed are corrected to standard atmospheric conditions.

Performance With Tunnel Speed

Net forces acting on the models, as obtained from balance measurements, are shown in Figures 174 through 181. These figures present the forces in coefficient form using free-stream velocity head as the reference speed. Tunnel speed is standardized using the speed ratio parameter, free-stream Mach number divided by fan tip Mach number. It is interesting that the

characteristics appear to converge to a single curve, independent of Mach number and fan rotational speed. Similar coefficient notations have succeeded in correlating results of other low speed tests of the fan system.

PRESSURE DISTRIBUTIONS

Pressure measurements were taken to determine surface static pressure distributions and flow conditions throughout the model. The following discussion will present representative pressure distributions for each of the test models. The characteristics presented were selected to show significant effects of each test variable.

Flow Conditions

Flow conditions were measured at the inlet and discharge planes of both the core engine and the fan system. These measurements were taken by arrays of total and static probes, as defined in the instrumentation listings given in the appendixes. The following discussion will present typical total and static pressure distribution along the engine and fan flow paths.

Engine Inlet

Figures 182 through 186 show measured total and static pressure distributions at the engine inlet, station 2.0. These figures show a relatively uniform velocity profile, as indicated by the static pressure levels, with a fairly thick boundary layer adjacent to the outer wall or tip. A slight circumferential variation of static pressure, and consequently velocity, is apparent in comparing pressures for the 22-degree and 202-degree planes. This variation probably results from the slight flow turning that occurs in the engine inlet just upstream of the measurement plane.

Engine Turbine Discharge

Engine discharge total pressure was measured in the ducting system between the core engine and the fan turbine scroll inlet. The measurement plane is located downstream of the transition duct, flow straightener, and bellows systems. Figure 187 shows the total pressure distribution at the core engine discharge for a range of engine speeds. Figure 188 shows these distributions under windmill conditions. As is apparent, these total pressure profiles are practically constant across the duct area.

Fan Inlet

Fan inlet total and static pressure profiles were measured by an array of Pitot-static probes located about 9 $\frac{1}{4}$ inches forward of the fan rotor center line. For inlet configurations 1 and 2, this location is well inside the inlet contours. For inlet configuration 3, this measurement station is less than three inches aft of the inlet leading edge. At this

location, the flow included both radial and axial components; therefore, these pressure measurements may exhibit possible errors that may affect the inlet airflow calculation. Caution should be used when performing analysis using inlet 3 airflow measurements.

Typical fan inlet total and static pressure distributions are shown in Figures 189 through 204. Inlet pressure distributions for Model 1, Model 2, and Model 4, Figures 189 through 200, show effects of the inlet geometry on rotor inlet velocity profiles with a fixed fan discharge geometry. Effects of Mach number are shown by a series of four figures for each model.

The trend of the pressure distributions shows that the rotor inlet velocity decreases from the hub to the tip for the cases where the long inlets are used. The short inlet appears to reverse this trend for static conditions where Mach number equals zero. It is also apparent that increases in tunnel speed produce small changes in the inlet velocity distributions. From these observations, it becomes apparent that the fan rotor inlet velocity distributions are nearly insensitive to inlet geometry and tunnel speed. This infers that the fan system operation may be invariant with Mach number and configuration.

Figures 201 through 204 present fan inlet pressure profiles for the model with the maximum fan nozzle discharge area. The primary difference between these and the previously described profiles may be observed at static condition. Here, the rotor inlet velocity profile is more uniform from hub to tip than for the case in which the fan is throttled because of a small discharge area.

Fan inlet pressure distributions during windmilling conditions are shown in Figures 205 and 206 for two extreme Mach numbers, 0.30 and 0.80. These pressure distributions are very similar to the cases described above, when the fan was operating at near maximum power.

Observation of the total pressure distribution for each test configuration shows a boundary layer adjacent to the outer wall or tip. This boundary layer increases in thickness or depth proportional to the inlet length. Model 1 has the thickest boundary layer and Model 3, the thinnest. The pressure losses associated with these boundary layers were calculated using the methods described in Appendix I. Analysis of the associated loss coefficients is performed later.

Rotor Discharge

In following the flow through the fan system, the next logical measurement plane is at the fan rotor discharge. Typical fan rotor discharge pressure distributions for Models 1, 2, 4, and 3 are shown in Figures 207 through 210. Each figure shows the radial and circumferential variation of rotor

discharge pressure for a range of Mach numbers. Each of these curves represents the same test conditions as used for the fan inlet distributions in Figures 189 through 204.

For the case when the fan is throttled by a small nozzle area, Models 1, 2 and 4, the rotor discharge pressures appear to be low at the static conditions, especially at the tip region. Apparently, the rotor inlet flow conditions are such that the tip is near stall and operating with excessive losses. It should be noted, as will be discussed later, that a small nozzle area at static conditions makes the fan operate way off design and this effect is normal.

As the Mach number is increased, the rotor pressures tend to increase to a certain level as the fan system reaches its normal operating point. The operating point movement is indicated by changes in the flow coefficient. A flow coefficient of about 0.50 is the design point. At Mach numbers above this level, the rotor discharge pressures drop off sharply as the fan again begins to operate off design in regions of high losses.

Figure 210 shows rotor discharge profiles for Model 3, which has the maximum nozzle area. Here the rotor pressure is high at static conditions, since the fan is operating near design conditions. Increases in Mach number produce reduced rotor discharge pressures as the fan flow coefficient moves above the design value.

Figure 211 presents both rotor and fan discharge total pressure distributions under conditions of windmilling. Total pressure losses are observed as an average total pressure at the rotor discharge that is less than the fan inlet pressure. However, the radial distributions indicate that the hub puts energy into the flow, while the tip extracts sufficient energy to drive the hub, plus that necessary to compensate for losses.

Fan Discharge

Fan discharge pressure distributions taken downstream of the fan stator row are shown in Figures 212 through 215. These distributions are similar to the rotor discharge described above, but modified because of fan stator losses.

Surface Pressure Distributions

Axial and circumferential pressure distributions were measured on each surface of the models by wall static pressure taps. Representative surface pressure distributions will be presented to show trends of the data or specific flow effects.

Engine Nacelle Internal Pressure Distributions

Typical engine inlet pressure distributions along the internal surfaces are shown in Figures 216 through 219. The data presented in these figures were obtained during the tests of Model 2, and are representative of the other seven models. No abnormal flow conditions are indicated by these pressure distributions.

Fan Inlet Internal Pressure Distributions

Typical pressure distributions for the fan inlet internal surfaces are presented in Figures 220 through 237. Pressure distributions are shown for each of the three inlet configurations for a range of Mach numbers and mass flow ratios. Pressure distribution along the bullethead surface is also shown on each figure. Changes in the level of the peak pressure coefficient occur as a function of Mach number and power setting. These pressure distributions are discussed in the analysis section.

Engine Nacelle External Pressure Distributions

The engine nacelle and inlet system were assumed to represent the complete cylindrical surface along the lower part of the model. This surface extends from the engine inlet leading edge back to the most aft edge of the model. Typical engine nacelle pressure distributions taken along the five axial planes on the inlet are shown in Figures 238 through 249 for a range of Mach numbers and engine speed settings. The zero-degree or top plane is in line with the fan inlet; therefore, the aft part of this pressure distribution reflects the effects of the fan inlet as a coefficient approaching a stagnation pressure level. The bottom pressure distribution extends from the leading edge to the extreme aft edge of the model. Near an axial distance of 0.60 to 0.80, a negative pressure coefficient exists, reflecting effects of the fan nacelle thickness distribution.

Fan Nacelle External Pressure Distributions

Fan nacelle external pressure distributions were obtained by numerous surface pressure taps located on both radial and axial planes along the model. Typical axial pressure distributions along four different planes of Model 1 are shown in Figures 250 through 255. The distributions are presented for three test Mach numbers: one at the lowest speed, another at the highest test Mach number, and the third at some intermediate value. Whenever possible, two values of engine or fan power setting are shown: windmill and near maximum power. These pressure distributions show a relatively high negative pressure coefficient near the leading edge and a gradual recovery of pressure toward a pressure coefficient near zero at the aft part of the nacelle. Circumferential variations in pressure coefficient are also shown, with the largest coefficients occurring in the region of the fan to engine nacelle fairing.

When the pressure coefficient level for critical flow, that is, a local Mach number of 1.0, is within the scales of the figures, the level is shown and identified. Nacelle pressure distributions, covering the same range of test conditions, are presented in Figures 256 through 294 for the other seven test configurations. Comparison of these pressure coefficient distributions for each test model is performed later in this report.

Nozzle and Plug Pressure Distributions

The exhaust nozzle used in the nacelle system consists of an outer shroud and a plug that extends aft of the plane of the nozzle throat. The pressure levels on the plug downstream regions are affected by both the nozzle jet flow and the nacelle external flow and are therefore a function of both the free-stream Mach number and fan power settings. Figures 295 through 339 present plug pressure distributions for the eight test models. The data shown are at the same test conditions that existed for the nacelle external pressure distribution shown in Figures 250 through 294.

Pressure coefficient values equivalent to nozzle inlet total pressure and critical flow conditions are shown on each figure when possible.

Pressure distributions along the nozzle surfaces during static conditions are shown in Figures 340 through 347. These pressure distributions are presented as a pressure coefficient, referenced to rotor discharge total pressure. The pressure distributions are shown for the maximum power setting tested for each model.

TUNNEL WALL PRESSURES

Tunnel static pressure was measured by a row of static pressure taps located along the center of one of the tunnel flats. This static pressure, along with the tunnel total pressure, was then used to compute the axial Mach number distribution. Figure 348 presents typical Mach number distributions along the tunnel flat of a range of nominal test Mach numbers from 0.2 through 0.8. Each distribution shows a deceleration of the flow upstream of the model inlet, then an acceleration to a level greater than nominal at the model maximum diameter. Downstream of the model, the flow decelerates as it enters the diffuser section of the tunnel. The slight rise in velocity near tunnel station 139 is apparently caused by the effects of termination of the wind tunnel slots and beginning of the diffuser. Similar Mach number distributions with the model not installed in the wind tunnel show an almost constant value of Mach number throughout the test section.

The non-uniformity of these Mach number distributions caused considerable concern and doubt as to the accuracy of the test results and possible large wind tunnel interaction effects. Because of this concern, a 1/5 scale size of Model 7 was constructed and tested in this same wind tunnel. The model was sufficiently instrumented with static pressure probes for determination

of surface pressure distribution. Comparison of surface pressure distributions of both the full size and 1/5 scale models showed excellent agreement, well within normal repeatability of the same model during two different tests at the same conditions. The conclusions, as a result of this comparison, are that the wall pressure distributions are the result of normal streamline curvature at a distance out from the model equivalent to the location of the wind tunnel walls.

PERFORMANCE WITH VARIABLE ANGLE OF ATTACK

Tests to determine the effects of angle of attack were conducted on Model 8. The range of angle of attack, as determined by balance load limits, was from -2.0 degrees to +8.0 degrees at Mach numbers of 0.30 and 0.50 and from -2.0 degrees to +5.0 degrees at a Mach number of 0.70. The results showed that, within the test accuracy, the performance of the propulsion system did not change for the range of this test. Therefore, the previously presented propulsion system performance for Model 8 is applicable; that is, angle of attack had no effect on internal performance. The following test results show the variables that were affected significantly by changes in angle of attack.

Balance Data

At each angle of attack and speed setting, the balance forces were recorded, along with all pressure data. Figures 349 through 357 show the measured lift, drag and moments for the three test Mach numbers as a function of angle of attack. The balance data is presented in fan coefficient notation, using fan tip speed as the reference parameter. The zero angle of attack data for Model 8 were converted to this coefficient form and are included in the figures. The data presented in this form show clearly the effects of angle of attack. An explanation of the trends of these forces and moments will follow later in this report.

Surface Pressure Distributions

All surface pressures were recorded for each angle of attack setting. Representative internal and external pressure distribution showing the extremes of angle of attack and Mach number are shown in Figures 358 through 364. Figures 358 and 359 present the engine nacelle external pressure distribution for Mach numbers of 0.30 and 0.70. Pressure distributions for the extreme angle of attack are compared. Figures 360 and 361 present similar external pressure distributions for the fan nacelle. These pressure distributions show the increases in local pressure coefficient with angle of attack. Figures 362 and 363 show fan inlet internal pressure distribution, again for the same range in test variables. These distributions show that angle of attack causes large increases in local lip velocities, but all these irregularities are absent at the fan inlet station. This smoothing of the flow profiles results in consistent fan performance with variable

angle of attack. Nozzle plug pressure distributions are shown in Figure 364. These characteristics show that the plug pressure distributions were not affected by angle of attack, within the range of this test program.

ANALYSIS OF TEST RESULTS

The following discussion will present analysis and evaluation of the test results. The analysis will be treated as four classes or categories:

1. Propulsion system aerothermodynamic performance
2. Nacelle internal aerodynamic performance
3. Nacelle external aerodynamic performance
4. System performance including nacelle drag and effects of angle of attack

PROPULSION SYSTEM PERFORMANCE

The propulsion system includes the fan, the fan turbine system, and the core engine. Analysis of the core engine will be limited to evaluation of the turbine discharge conditions as they apply to fan system performance. The basic measured conditions at the core engine discharge have previously been presented in the test results. Analysis of fan system performance will include definition of both the fan system and fan turbine operating characteristics. Analysis of a set of boundary conditions used to establish performance of the confluent nozzle system will also be presented.

Fan Turbine Performance

During the test, measurements for determination of fan turbine performance included flow conditions at the fan turbine inlet and pressure and temperature measurements at the fan turbine discharge plane. These measurements were used to determine the fan turbine performance shown in Figures 365 through 374. The curves present variation of turbine flow function and total to total pressure ratio, with respect to fan turbine speed. Representative data are shown for two test models, Model 3 and Model 6. These two models represent extremes of turbine operating conditions, Model 3 being the maximum nozzle area configuration and Model 6 being a typical minimum area. Turbine efficiency based on the turbine pressure ratio and temperature ratio is not shown, because the measurement system was not set up with the intention of obtaining this performance indicator.

Comparison of the measured turbine performance characteristics with predicted performance is accomplished in Figures 375 and 376. These characteristics show predicted and measured performance as changes of turbine flow function with turbine pressure ratio at constant values of turbine speed. Figures 375 and 376 show data obtained from Model 3 and Model 6, respectively. Comparison of the measured and predicted performance shows excellent agreement. Maximum differences between measured and predicted flow functions, at a given pressure ratio, are about two percent. This deviation is well within the test accuracy, and for practical purposes, the fan turbine performance in the model verified predicted performance. One additional comment should be made concerning turbine performance for Model 6.

as shown in Figure 376. Here, the slope of the flow function curve is steeper than predicted. This difference in slope may possibly be the result of the following step-by-step description:

- o At a given turbine speed, turbine pressure ratio increases as the result of higher tunnel Mach numbers.
- o As the tunnel Mach number is increased, the ambient static pressure reduces to produce the increased Mach number, tunnel total pressure remaining nearly equal to atmospheric pressure.
- o This reduction in static pressure causes similar decreases in pressure levels inside the model cavities; for example, the engine and fan system bay areas.
- o The pressure ratio across seals between the fan scroll and mating static parts therefore increases, because the turbine inlet pressure remains nearly constant.
- o Since these seals do leak small amounts of flow upstream of the fan turbine system, the increased pressure ratio across the seals results in proportioned increases in leakage relative to the turbine flow.
- o This leakage flow is part of the turbine flow function as presented in curves, and does not really pass through the fan turbine system; thus it appears as a higher than predicted flow function.
- o The differences are greater for Model 6 than for Model 3 because of the higher test Mach numbers.

The data do show this trend, and the above discussion is a plausible explanation of the apparent small differences between predicted and measured performance.

Fan Performance

Basic fan performance data are usually presented as a flow coefficient versus pressure coefficient characteristic. A second characteristic showing system or product efficiency, turbine efficiency multiplied by fan efficiency, versus flow coefficient then provides a means of determining the power required to operate the fan at a given operating condition.

These characteristics were measured or calculated directly from the test results and are presented in Figures 377 through 384 for each of the test models. In obtaining this performance, the operating conditions of the fan, that is, flow coefficient, were varied by changing nozzle area, Mach number and fan speed in numerous combinations. The values of pressure coefficient and flow coefficient were obtained directly from the

figures shown in the test results. Stage efficiency was calculated based on ratio of gas horsepower developed in the fan stream to power absorbed in the fan turbine system. The equations and relationships used in this calculation are given in Appendix I.

Numerous comparisons of the eight sets of characteristics may be made to show any possible effects due to changes in nacelle geometry in either the fan inlet or nozzle system.

Comparison of the curves for Models 1, 2 and 4 shows the effects of changing the inlet geometry. Model 1 has the longest inlet system and Model 4 the shortest. For a flow coefficient of 0.5 and below, all three sets of performance are basically the same, indicating no effect due to inlet geometry. This range of flow coefficients is representative of low Mach number and high fan power levels. In the high flow coefficient regions greater than 0.5, the pressure coefficient for a given flow coefficient is highest for the longest inlet and lowest for the shortest inlet. This indicates that the inlet does have some effect, and is possibly the result of rotor inlet velocity distributions. At these values of flow coefficient, the shortest inlet has low tip and high hub axial velocities at the rotor inlet, as compared to the long inlet. This is observed by comparison of the rotor inlet static pressure distributions in Figures 189 through 206. Since the rotor is operating at high flow coefficient conditions, the fan blading is at negative incidence angles and operating with high losses. For the short inlet, the reduced axial velocity at the tip brings the local blade incidence angle more nearly to the design value, and consequently the blade losses are decreased. However, at the hub, the axial velocity is higher and the blading in this region operates still further off design. Therefore, the hub losses increase considerably, since variation of losses with changes of incidence angle from design values is a quadratic or high power. The increase in losses far overshadows the decrease, and consequently the pressure ratio is lower for the short inlet system.

Effects of nozzle geometry, both area and length behind the fan discharge, may be observed by comparison of the performance of several different models. Models 3 and 4 represent the smallest and largest nozzle area range, the only geometry change being the plug system. Models 6 and 8 have the same area, Model 6 having a short afterbody or nozzle and Model 8 having the longest one. Models 4 and 5 represent a change in nozzle area with no change in the inlet. The diameter of the nozzle is also different between the two models.

Comparison of the above sets of performance characteristics shows that there is no appreciable change in performance due to nozzle area changes or nozzle geometry, either length or diameter.

Based on the above discussions and the general characteristics of fan operation, the following statements may be made concerning fan operation and performance:

1. Peak system product efficiency is about 62 percent and occurs at a flow coefficient of 0.55. This efficiency is the total product efficiency and accounts for fan efficiency, turbine efficiency, scroll losses, and seal leakage.
2. Fan performance, pressure coefficient and efficiency, is unaffected by the levels of external Mach number at a given flow coefficient.
3. Changes in exhaust nozzle area and geometry, within the ranges of this test, do not affect fan performance at a given operating condition.
4. Changes of inlet geometry, in particular length, appear to affect fan performance at high flow coefficient regions greater than 0.6. The fan pressure rise was lower for the short inlet than for the long inlet. These differences in performance are of little concern, since off design flow coefficients in this region would be typical only of high speed, deceleration or let-down flight of a vehicle powered by a cruise fan type propulsion system.
5. Based on all of these data, it is possible to select a probable fan performance characteristic that best defines the X376 fan system. The recommended typical average characteristic is Model 2, Figure 378.

Power Balance

The exhaust nozzle system used on each test model uses the principle of confluent flow in a single nozzle throat. This system combines both the cold fan and the hot fan turbine streams into a single flow system just downstream of the stage discharge planes. The flow is then allowed to perform a free mixing process and is discharged through a single annular nozzle throat. The unique problem of this type of nozzle system is how to determine the flow split in the nozzle throat, which in turn then establishes the interdependent operating conditions of both the fan and the fan turbine.

The combined operating conditions then establish the rotational speed of the fan by maintaining power balance between the fan and the fan turbine, taking into consideration the appropriate efficiencies.

Performance predictions of the fan with a confluent nozzle system force the power balance by assuming the discharge static pressures to be equal at the plane where mixing is initiated. Referring to Figure 3, the plane in question is at the downstream end of the flow splitter. The results obtained during this test program were used to validate this assumption of equal static pressures of the two streams.

Direct measurements of the stream static pressures were not taken for either the fan or the fan turbine streams. However sufficient measurements were taken to permit the calculation of an effective static pressure for each of the

streams. A comparison of these pressures then was used as a basis for checking the assumptions. The effective static pressures were computed using one-dimensional compressible flow relationships and measured values of total pressure, temperature and mass flow of the two streams. The measured values of these parameters for the fan turbine, denoted by subscripts 2.0, 5.1 and 5.6, and for the fan stream, denoted by 10.0 and 11.0, have been presented in the test results. The area used in the calculations was the geometric flow area at the plane of the flow splitter trailing edge, with no flow coefficient correction. These areas were different for each model and are listed below:

<u>Model(s)</u>	<u>Fan Area</u>	<u>Fan Turbine Area</u>
1, 2 and 4	768	128
3	910	128
5	844	128
6	852	128
7 and 8	860	128

The results of this analysis are presented in Figure 385 as a ratio of the two pressures and as a function of fan rotational speed. Data for all eight test models and each Mach number are shown. The data show that the assumption of equal static pressures of the two flows is verified by the test data to within plus or minus one percent.

These differences may be due to the assumption of a unity flow coefficient for the flow areas and the distortion levels in the two streams. In any case, cycle calculations have shown that these small differences in pressure level produce negligible changes in predicted performance. A discussion of the flow areas occupied by each stream in the nozzle throat is provided in the section which discusses exhaust nozzle system performance.

NACELLE INTERNAL PERFORMANCE

Nacelle internal performance analysis includes a discussion of losses associated with both the fan and engine inlet system and performance of the exhaust nozzle system.

Inlet Performance

Measurements taken during the test program included surface static pressure distributions and total pressure distributions at the inlet to the respective propulsion system component. Typical pressure distributions as measured have been presented in the test results for both the surface and the inlet profiles.

Inlet losses were obtained by calculating an average total pressure at the fan or engine inlet and comparing this to ambient or free stream total pressure. The calculation procedures used in obtaining the losses and the definition of the loss coefficient are given in Appendix I. Representative measured loss coefficients for each of the eight test models are shown in

Figure 386. The losses are presented as a function of the inverse of mass flow ratio. This parameter approaches zero at static, Mach number of 0.0, conditions. The inlet configuration for each model is also listed on the figure. The plotted data clearly show the effects of both inlet configuration and mass flow ratio on the loss coefficient. The highest losses are exhibited by the longest inlet at static conditions. The trends of the data suggest that there is a possible correlation of inlet losses as a function of inlet length.

Such a correlation was found to be as follows:

$$\bar{x}_{10} = \left(0.017 \frac{L}{D_{TH}} \right) \left(\frac{A_{TH}}{A_{10.0}} \right)^2 (K)$$

This equation is plotted as the dashed curve in Figure 386 and shows good correlation of the test results.

The first term of the equation represents the effects of inlet length on losses, as shown in Figure 387. The loss coefficient in this case is based on the velocity at the inlet throat rather than at the fan inlet, Station 10.0. The second term is an area correction that accounts for the ratio of throat to fan inlet areas, while the third term is a factor that is a function of mass flow ratio. The variation of the multiplier K with mass flow ratio is shown in Figure 388.

Similar data for the engine inlet system are presented in Figure 389, and the static loss coefficient is also included in the correlation shown in Figure 388. For this inlet, the total pressure measurements were not as complete as those used in the fan inlet, and the loss coefficients are questionable. Comparison with the losses for the fan inlets shows reasonable agreement.

It may be concluded that the above correlation is accurate for inlet performance predictions, provided that the inlet geometry is similar to that used in the test model. In particular, the ratio of inlet diameter to throat diameter should be approximately 1.13.

Another significant parameter depicting performance of the inlet system is the level of the peak velocities that occur on the inlet near the throat. These peak velocities then determine at what average Mach number the flow over the inlet will become critical with possible increases in loss. Critical flow on the inlet lip could produce considerable losses if the resulting shock produces flow separation.

Figures 390 through 392 show the variation of the peak velocity on the inlet internal surface with mass flow ratio. The data are presented as the ratio of measured velocity to ideal velocity heads. This ideal velocity was computed using one-dimensional compressible flow, the measured airflow, and the physical minimum flow area at the inlet throat. The data clearly

show that the peak velocity occurs at static conditions at an inverse mass flow ratio of zero. The peak velocities then decrease rapidly as the inverse mass flow ratio is increased. The peak velocity for Inlets 1 and 2 approach the ideal velocity, as predicted by one-dimensional flow for mass flow ratios less than about 0.6.

The measured velocity for Inlet 3 approaches a value about 25 percent higher than ideal at high inverse mass flow ratios. This difference is about the level that would be predicted if the flow area were reduced by an amount equal to the bulletnose area. This is a reasonable result, since the inlet is short and the bulletnose protrudes forward of the inlet leading edge.

The above velocities are based on measurements at the zero-degree plane of the inlet. These data were selected to reflect a near axisymmetric inlet system. Pressure distribution at the 180-degree plane was influenced considerably by the proximity of the engine nacelle system, and the velocities were usually higher than the levels as shown in the figures.

Using these results at static conditions, a peak velocity about 50 percent higher than the ideal one-dimensional prediction can be expected, equivalent to a pressure coefficient of 1.3. Assuming that there are no changes in pressure coefficient due to increased Mach number, critical flow should occur somewhere on the inlet lip radius when the calculated average Mach number reaches about 0.58 at the inlet throat or an inlet mass flow of 83 percent of choke based on one-dimensional flow at the inlet throat.

Tests showing the effects of inlet radius on static performance as reported in reference 7 are presented in Figure 393. The results of these tests are also shown. For the range of lip diameter variation used in reference 7 tests, the peak internal velocity varied with the square root of the inlet lip diameter. This function is shown on the figure as the solid line. The static velocity levels for the three inlets used in this test fall slightly below reference 7 results. This difference may be attributed to effects of the bulletnose on the outer surface velocities.

The model used in reference 7 had a bulletnose that extended to the leading edge of each inlet and is the probable cause of the higher surface velocities. The bulletnose extending ahead of the leading edge of Inlet 3 is the reason for better agreement with results of reference 7. Therefore, the dashed curve in Figure 393 shows the estimated effects of inlet radius on an inlet system where the bulletnose is behind the inlet throat, and the solid curve shows where the bulletnose extends into the throat.

The above data present maximum inlet lip velocity at zero-degree angle of attack. Model 8 was used to investigate the effects of angle of attack on system performance, and the variation of inlet lip maximum velocity is shown in Figure 394. These characteristics show that within the range of test variables, the peak lip velocity occurs at zero speed. Extrapolation of the data shows that an angle of attack of 13 to 14 degrees is required to

produce inlet velocities equal to the static values. These results tend to indicate that maximum inlet lip velocities will occur, for an inlet system of the type tested, at the static or zero speed condition.

NACELLE EXTERNAL PERFORMANCE

Nacelle external performance analysis concerns primarily the effects of geometry on the flow conditions along the nacelle outer surface. Analysis of total nacelle drag is presented later during discussion of system performance. Flow conditions along the nacelle were obtained by measurement of static pressure distributions using arrays of wall static pressures. Typical pressure distribution for each of the test models has been presented in the test results. The level of the peak pressure coefficient near the inlet leading edge is one of the significant parameters in presenting nacelle performance. Pressure coefficients equal to critical, Mach number equal to one, are usually used in determining the design point Mach number for low-speed nacelles of this type. Local Mach numbers in excess of critical may result in drag divergence.

Using the measured pressure distributions for each model, the peak pressure coefficient at three circumferential locations around the nacelle was obtained and is presented in Figures 395 through 402. The three circumferential planes in question are:

- o The zero-degree or top plane opposite the engine nacelle
- o The 90-degree plane at the side of the model
- o The 150-degree plane located at the center of the engine-fan nacelle fairing

The peak pressure coefficients are presented for the range of test Mach numbers and mass flow ratios. Each figure shows that there was considerable circumferential distortion of the pressure coefficients for each inlet system. In general, the data show that the pressure coefficient is highest at the zero-degree plane and minimum at the 150-degree plane, or in the fairing region.

To show the effects of Mach number and the conditions for critical flow on the nacelle surface, local pressures at constant mass flow ratio were plotted for each inlet system. These data are shown in Figures 403 through 405 for the three inlets. Also shown on each figure is the pressure coefficient required for critical flow as a function of free-stream Mach number. The point where the local pressure coefficient, as measured, exceeds the critical pressure coefficient should be the so-called design Mach number for the nacelle. The data for Inlets 1 and 2 show that critical flow occurs at much lower Mach numbers in the fairing region than at the top of the nacelle. For example, at the zero-degree plane of Inlet 1, critical flow occurs at a Mach number of 0.79, and in the fairing region at a Mach number of 0.70. Based on the inlet design, the point for critical flow should have been a Mach number of 0.8. The fairing region, as well as the 90-degree side of the nacelle, exhibits critical Mach numbers lower than design. This

result is indicative of large interference effects due to the proximity of the engine nacelle system, resulting in premature critical flow over most of the nacelle external surface. This effect will produce drag rise or divergence at a lower Mach number than predicted. This effect will be discussed later during presentation of system performance.

Inlet 3 is the only inlet system that showed critical flow occurring at all measurement planes at approximately the same free stream Mach number. Comparison of the Mach number of 0.54, for critical flow, with the predicted value of 0.55 shows excellent agreement.

Summarized below are the design and measured Mach numbers for each inlet system:

<u>Inlet</u>	<u>M_{Design}</u>	<u>M_{CR} ($\phi = 0^\circ$)</u>	<u>M_{CR} ($\phi = 90^\circ$)</u>	<u>M_{CR} ($\phi = 150^\circ$)</u>
1	0.8	0.79	0.74	0.70
2	0.7	0.70	0.67	0.64
3	0.55	0.54	0.55	0.57

This tabulation shows that the zero-degree or top plane of the inlets does exhibit a Mach number capability as predicted. However, the lower half of the nacelle, from 90 degrees to 180 degrees, does not meet design requirements for Inlets 1 and 2, apparently because of the large engine to fan nacelle interference effects.

Investigation of the effects of nacelle angle of attack was made using Model 8. A similar analysis method as presented at zero-degree angle of attack for the eight models is used to show the effects of angle of attack. Variation of the peak pressure coefficient, near the inlet leading edge, with mass flow ratio and angle of attack is presented in Figures 406 through 408. Each figure shows data for a constant free-stream Mach number ranging from 0.30 to 0.70.

At each test Mach number, effects of angle of attack on the peak pressure coefficient are apparent. Plotting the data at a constant mass flow ratio of 0.50 results in the characteristics shown in Figure 409. These curves show that large changes in conditions for critical pressure coefficient occur with changes in angle of attack. These changes appear to be largest in the fairing region. Cross plotting free-stream Mach number and angle of attack for critical pressure coefficient in the fairing region results in the curve shown in Figure 410. This increase in Mach number for critical flow at negative angles of attack may be a clue to possible nacelle design changes that would increase the Mach number for drag rise or divergence. These changes will be discussed later in system analysis and conclusions.

Similar pressure coefficient data for the engine nacelle system are presented in Figures 411 through 413. The data show that the engine nacelle system meets or exceeds the design Mach number of 0.8. This shows that the

design methods used apply to an axisymmetric system, such as the engine nacelle, but must be used with caution when designing a nonsymmetrical system.

SYSTEM PERFORMANCE

This section of the analysis of test results will be concerned with performance of the complete system as a component. Typical results that will be discussed include:

- o Nozzle static thrust performance and effective flow area
- o System total drag
- o Fan system internal performance
- o Effects of angle of attack on nacelle performance

Nozzle Static Thrust

In order to provide a thrust and drag bookkeeping system, an evaluation of nozzle thrust coefficient is required. During this test, nozzle thrust performance could be determined only at static conditions. The tests were run with the model installed in the wind tunnel on the standard force balance system. The test data were taken in rapid succession in order to minimize induced flow effects due to the wind tunnel. However, as analysis of the data progresses, it will become apparent that there were considerable tunnel effects even though efforts were made to minimize them.

Performance of a nozzle system is presented in terms of thrust and flow coefficients. Thrust coefficient in this case is defined as the actual thrust of the nozzle system divided by the total ideal thrust. In this case, the ideal thrust is the sum of both the fan and the fan turbine streams, calculated as if there were no flow mixing. Detailed procedures and equations used in calculating this ideal thrust are given in Appendix I.

Flow coefficient is defined as the ratio of the measured nozzle effective area to the measured physical flow area at the nozzle throat. The nozzle effective area is that calculated using the measured nozzle flow, pressure and temperature, and one-dimensional flow analysis. The two exhaust streams are assumed to be unmixed, and the detailed calculation procedures are given in Appendix I.

Using the static force data as measured on the balance system and the measured fan discharge conditions, nozzle static thrust coefficients were calculated and are shown in Figure 414 for seven of the test models. Data for Model 8 were not obtained during the test program because of instability of the fan flow. Model 8 has the smallest nozzle area, and caused the fan to operate at a flow coefficient near the fan surge condition. As a result, only low fan speed static data could be taken, and the resulting force measurements were of too low a level for evaluation of a static nozzle thrust coefficient.

The measured thrust coefficients for the seven models shown varied from about 0.85 to 0.905. These levels of nozzle performance are below any predicted values and will be assumed erroneous because of wind tunnel interaction effects. It should be noted that observers inside the wind tunnel during conduct of these static tests observed an induced tunnel flow of about 30 to 40 feet per second. This flow could very easily reduce the thrust level due to ram drag and tunnel interaction effects by the amounts shown. However, a comparison of thrust coefficient levels proves interesting. Models 1, 2 and 4 have the same nozzle geometry, differing only in the inlet. The thrust coefficient for each of these models was between 0.855 and 0.87, which is well within expected test accuracy.

Models 5, 6 and 7 also have similar nozzle system geometry and yield similar thrust coefficients. The only significantly different nozzle system was used on Model 3. This model had a thrust coefficient of 0.91, which is definitely higher than the other six systems. Model 3 had the largest nozzle area, and this higher thrust coefficient is expected, based on the ratio of wetted to nozzle throat area. This relationship is used in another method of determining nozzle thrust coefficients.

In conclusion it may be stated that the balance data at static test conditions gave erroneous thrust coefficients, because of ram drag and tunnel interaction effects owing to induced tunnel velocities. However, comparing relative levels of data, six of the models have almost the same thrust coefficient, with only Model 3 having a thrust coefficient about 3 or 4 percent higher.

A second method for evaluating the nozzle thrust coefficient utilizes evaluation of the momentum of the nozzle discharge stream by integrating forces throughout the nozzle internal surface. Referring to Figure 415, the integration of all momentum and pressure area terms for the nozzle internal surface yields the following summation:

$$(F_G)_{INT} = (P_{S11.0} - P_0) A_{11.0} + \frac{W_{11.0}}{g} V_{11.0} +$$

$$(P_{S5.6} - P_0) A_{5.6} + \frac{W_{5.6}}{g} V_{5.6} - \int_{INT} (P_L - P_0) dA$$

$$(F_G)_{INT} = f_{11.0} + f_{5.6} - f_{INT}$$

The first two terms represent the pressure force and momentum of the fan discharge and fan turbine discharge streams. The velocities and pressures were calculated using measured total pressure, temperature and flow, and one-dimensional flow analysis. The integral term represents the pressure area integration in the axial direction throughout the complete nozzle

internal surface. Referring to Figure 415, the integral is as follows:

$$\int_{\text{INT}} (P_L - P_O) dA = \int_a^b \pi (P_L - P_O) dR^2 - \int_b^c \pi (P_L - P_O) dR^2 -$$

$$0.48 \int_d^e \pi (P_L - P_O) dR^2 - 0.52 \int \pi (P_L - P_O) dR^2 + \int_e^f \pi (P_L - P_O) dR^2$$

The gross thrust as calculated above represents the nozzle thrust, not including friction losses. These calculations were performed on seven of the test models at static conditions, and the following results were obtained. The nozzle thrust coefficient was also calculated using the ratio of integrated thrust to the calculated ideal isentropic thrust.

Model	$(P_{T11.0})_E$	$f_{11.0}$	$f_{5.6}$	f_{INT}	$(F_G)_{\text{INT}}$	F_G	$(C_T)_{\text{INT}}$
1	1.047	662	153	187	628	676	0.93
2	1.048	681	157	167	671	695	0.97
	1.064	898	212	227	683	910	0.97
3	1.053	1100	139	66	1173	1209	0.97
	1.072	1461	129	62	1578	1592	0.99
4	1.048	690	159	180	669	704	0.95
	1.060	835	197	234	798	847	0.94
5	1.049	777	143	141	779	785	0.99
	1.065	1031	193	198	992	1035	0.99
6	1.065	948	216	334	830	851	0.98
7	1.050	783	156	161	778	785	0.99
	1.067	1047	206	225	1028	1040	0.99

The above results yield thrust coefficients near expected values, when compared to the lower values previously obtained by force balance calculations. It is interesting to note that Models 1, 2 and 4 all have the same nozzle system and exhibit thrust coefficients about 2 or 3 percent lower than the other models. This lower thrust coefficient may be a real thrust decrement or just the inaccuracies of the calculation procedure. Looking at the nozzle pressure distributions for these models, it may be observed that the static pressure levels at both the nozzle shroud tip and plug maximum diameter are below ambient pressure. This low pressure level is indicative of over-expansion in the nozzle, apparently because of the rapid turning near the plug crown and the lack of sufficient straight flow path directing the nozzle exhaust flow down the plug surface. As for the possibility of calculation inaccuracies, this nozzle system is the only

one of the configurations in which there is not a straight section in the flow path immediately downstream of the fan discharge. The lack of a constant area section may result in static pressure distortions in this region which were not accounted for when calculating the momentum at stations 11.0 and 4.5, using the one-dimensional flow analysis. In either case, based on these results, it appears that the nozzle thrust coefficients are 0.99 for Models 3, 5, 6 and 7, and 0.96 for Models 1, 2 and 4. Because of skin friction losses, it should be noted that these thrust coefficients are greater than the actual values.

The following discussion will present estimates of the nozzle skin friction, and losses that may be used with the above results in making estimates of nozzle thrust coefficient levels. Nozzle skin friction drag is as follows:

$$D_F = \int C_F q_L dA$$

where

C_F is the local skin friction coefficient

q_L is the local velocity head

dA is the axial surface area projection

Referring to typical pressure distributions for the nozzle systems, the following general comments concerning the velocity distributions are possible:

- o Velocity from the plug maximum diameter to the tip is equal to nozzle discharge velocity.
- o Velocity on the forward part of the plug and nozzle shroud is a function of ratio of nozzle area to fan discharge area.

Making use of these relationships, it is possible to develop an approximate expression for the product of velocity head and wetted area for a nozzle system of this type.

The wetted area on the downstream part of the plug may be expressed as follows:

$$A_1 = \frac{\pi R_C^2}{2 \tan \beta_p}$$

where

R_C is plug crown radius

β_p is plug half cone angle

The above area assumes a small plug crown radius relative to total plug length. Making use of the assumption of constant skin friction coefficient and uniform velocity equal to nozzle discharge, the drag of the plug downstream surface is as follows:

$$D_1 = C_F \left[(P_{T11.0})_E - P_0 \right] \frac{\pi R_C^2}{\tan \beta_p}$$

The wetted area of the nozzle shroud may be expressed as follows by assuming that the nozzle discharge diameter is not too different from the fan tip diameter. This is usually the case for this type of exhaust system.

$$A_2 = (2 \pi R_T) L_S$$

where

R_T is fan discharge tip diameter

Assuming incompressible flow as an approximation for simplification, the velocity along the shroud surface is related to nozzle discharge velocity as follows:

$$q_S = \left(\frac{A_N}{A_{11.0}} \right)^2 \left[(P_{T11.0})_E - P_0 \right]$$

Therefore, the drag on the nozzle shroud surface is as follows:

$$D_2 = C_F \left[(P_{T11.0})_E - P_0 \right] \left(\frac{A_N}{A_{11.0}} \right)^2 (2 \pi R_T) L_S$$

The surface area of the upstream part of the plug may be approximated by assuming a conical surface with a minimum diameter equal to the fan hub and a maximum diameter equal to the plug crown. The length is about equal to the nozzle shroud length. Therefore, the surface area is approximately:

$$A_3 = \pi (R_H + R_C) L_S$$

where

R_H is the fan hub diameter

Using the velocity expression derived for the shroud in the above analysis, the plug upstream drag is as follows:

$$D_3 = C_F \left[(P_{T11.0})_E - P_0 \right] \left(\frac{A_N}{A_{11.0}} \right)^2 \pi (R_H + R_C) L_S$$

Therefore, in summation of the above drag expressions, the total nozzle drag is as follows:

$$D_F = C_F \left[(P_{T11.0})_E - P_0 \right] \left[\frac{\pi R_C^2}{\tan \beta_P} + \left(\frac{A_N}{A_{11.0}} \right)^2 (2\pi R_T) L_S + \left(\frac{A_N}{A_{11.0}} \right)^2 \pi (R_N + R_C) L_S \right]$$

The above expression was evaluated for each of the test models using the following geometric data:

Model	R_C (inches)	R_T (inches)	R_H (inches)	L_S (inches)	β_P (degrees)	$\frac{A_N}{A_{11.0}}$
1	18.6	18.00	8.10	44.7	12.5	0.58
2	18.6	18.00	8.10	44.7	12.5	0.58
3	16.1	18.00	8.10	44.7	12.5	0.96
4	18.6	18.00	8.10	44.7	12.5	0.58
5	15.1	18.00	8.10	44.7	12.5	0.67
6	16.1	18.00	8.10	44.7	12.5	0.54
7	15.1	18.00	8.10	54.1	12.5	0.67
8	16.1	18.00	8.10	54.1	12.5	0.54

The resulting nozzle drags, as listed in the following table, were computed using a skin friction coefficient of 0.003.

Model	D_F $(P_{T11.0})_E - P_0$
1	24
2	24
3	34
4	24
5	21
6	18
7	23
8	20

Integration of nozzle pressure distributions checked out the above approximate equation to within 10 percent; therefore, this method appears acceptable for evaluation of nozzle skin friction drag. In particular,

this relationship may prove useful in optimization of future plug nozzle designs.

This drag due to skin friction may now be used in estimating the gross thrust coefficient of the nozzles for use in further evaluation. From the pressure integration analysis, the nozzle thrust coefficients, neglecting friction, ranged between about 0.96 for Models 1, 2 and 4 and 0.99 for all other models. Assuming that these thrust coefficients are applicable and using the friction drags previously estimated, it is possible to estimate nozzle gross thrust coefficients for a range of pressure ratios. The friction drag expressed as a coefficient, non-dimensionalized by nozzle total pressure times area, is as follows:

$$\frac{D_F}{(P_{T11.0})_E A_N} = \frac{D_F}{[(P_{T11.0})_E - P_0]} \left(1 - \frac{1}{\lambda} \right) \frac{1}{A_N}$$

where

λ is nozzle pressure ratio

A_N is nozzle throat area

The above expression shows that the nozzle drag is equal to a constant divided by nozzle throat area and multiplied by a function of nozzle pressure ratio. However, when corrected to a change in nozzle thrust coefficient, the term that is a function of pressure almost reaches a constant value, increasing only slightly with increased pressure ratio. As a result, the thrust coefficient for each nozzle may be assumed to be a constant. Listed below are the thrust coefficient decrements due to skin friction and the best estimate of the gross thrust coefficient for each model:

<u>Model</u>	<u>ΔC_T (friction)</u>	<u>C_T (estimate)</u>
1	.030	0.95
2	.030	0.95
3	.024	0.96
4	.030	0.95
5	.022	0.97
6	.023	0.97
7	.024	0.97
8	.025	0.97

The effects of thrust coefficient levels on system performance are discussed later.

Effective Flow Area

Nozzle effective flow area was computed using the measured flow, temperature and pressure of the fan and turbine discharge streams. One-dimensional compressible flow analysis was used in computing the area, as

described in Appendix I. Figures 416 through 423 show the variation of nozzle effective area with nozzle pressure ratio. The upper curves show the total nozzle area, which is the sum of the areas occupied by the fan flow and fan turbine flow. The solid symbols denote conditions of windmill. For these conditions, only a small amount of engine flow occupies the nozzle, as most of the area is cold fan discharge flow.

The most important fact to observe in the data is that in most cases the nozzle total area is invariant with nozzle pressure ratio, core engine power setting and free-stream Mach number. The nozzle area for Model 3 is the only case in which a trend with engine power setting appeared; low core engine power settings showed small nozzle flow areas. The nozzle flow phenomenon that produced this trend in data could not be determined from the measurements taken during this test program.

The lower curve is included in the figures to show the relative percentage of the nozzle area occupied by the core engine discharge flow. This flow area is the consequence of the static pressure balance at fan discharge plane. This pressure balance phenomenon has previously been discussed and the results presented in Figure 385.

An attempt was made to measure the physical area of the hardware, and this area is presented on the figures. It should be noted that these measurements are taken cold, but during engine operation about half the shroud runs hot. However, the cold area is applicable for the windmill case. Comparison of the effective and physical flow areas is inconclusive in predicting a flow coefficient for this type of nozzle system.

System Total Drag

One of the prime purposes of this test was to obtain the external drag coefficients of a complete nacelle system. The balance data will be used primarily for evaluation of this drag. The drag due to the external nacelle system is the difference between the balance force and the propulsion net thrust, as shown below:

$$D_N = D_B - F_N$$

where

F_N is the propulsion system net thrust

D_B is the measured balance force corrected for the balance base pressure effects

Calculation procedures are described in Appendix I.

In Appendix I the propulsion system net thrust is defined as:

$$F_N = C_T F_G - F_{DR}$$

Both the gross thrust and the ram drag forces are based on direct measurements. It now becomes apparent that the nozzle thrust coefficient is an unknown variable in evaluation of nacelle drag. In the previous discussion, considerable effort was devoted to the evaluation of the nozzle gross thrust coefficient, but still there is some question concerning the absolute level. Therefore, the analysis of nacelle drag has been accomplished using two extremes of nozzle thrust coefficient: a maximum value of 1.0, which assumes an ideal friction-free nozzle, and a minimum value of 0.95. These two levels encompass the range of estimated thrust coefficients.

The nacelle total drag coefficient using force balance data is then as follows:

$$C_{D\pi} = \frac{D_B - [C_T F_G - F_{DR}]}{q_0 A_\pi}$$

The above expression is a linear function of nozzle thrust coefficient, so by evaluating the expression at two extreme levels, interpolation at different thrust coefficients is possible.

Calculated nacelle total drag coefficients for each of the test models are shown in Figures 424 through 439. Nacelle drag is presented as a function of inlet mass flow ratio for the range of test Mach numbers. Figures 424 through 431 present data for the ideal nozzle assumption, and Figures 432 through 439 are data for the lower level of thrust coefficient. In general, the measured drag coefficients for each model show a rise in drag at the higher Mach numbers. Drag also either increases or decreases with mass flow ratio, depending on the nozzle thrust coefficient. The increasing drag with increased mass flow ratio, as indicated by the data assuming an ideal nozzle, tends to contradict similar results of other test programs. The lower level of thrust coefficient more closely follows the expected trends.

Using these test results, it is now possible to determine two indicators of nacelle performance: the low speed drag coefficients and the Mach number for drag rise or drag divergence. The low speed drag coefficient is a function of nozzle thrust coefficient, but the speed for drag rise is independent of this assumption.

Figure 440 shows the change in drag coefficient as a function of free-stream Mach number for each of the inlets tested. This figure is a composite of all eight models, and within the normal test accuracy, variations in after-body and plug geometry did not affect the conditions for drag rise. The drag data are presented at mass flow ratios where most of the test data were obtained. These three characteristics show drag rise of the three inlets occurring at Mach numbers of 0.6, 0.55 and 0.4 for Inlets 1 through 3, respectively. These conditions for drag rise, when compared to conditions for critical flow, differ significantly as summarized below:

<u>Inlet</u>	<u>M_{CR}</u>	<u>M_{drag rise}</u>
1	0.70	0.6
2	0.64	0.55
3	0.57	0.4

The difference in Mach number levels may be due to either of the following:

1. Pressure instrumentation not located to indicate maximum velocity regions.
2. Afterbody drag contributing to the increase in drag.

If circumferential variations of surface static pressures are the cause of the increased drag, a look at these pressure distributions at several axial stations along the nacelle may prove interesting. Figures 441 and 442 show the circumferential variation of pressure coefficient at several axial stations for Inlets 1 and 2. It immediately becomes apparent that extrapolation of the pressure distributions to about 160 degrees in the fairing region will yield pressure coefficients about 0.2 to 0.3 larger than the instrumentation plane at 150 degrees. These higher pressure coefficients reduce the Mach number for critical flow by about 0.10, which is the level of difference between force and pressure data previously discussed. It is difficult to understand how such a local effect can cause such a severe drag rise.

Another potential reason for the low drag rise Mach numbers may be large changes in afterbody drag as a function of free-stream Mach number. True afterbody drag cannot be calculated because of the plug nozzle system. The flow distribution over the plug surface is influenced by both the propulsion system discharge flow and the external flow. Because the nozzle could not be tested statically to pressure ratios comparable to those existing during free-stream flow, it is not possible to separate the two effects. However, a look at the afterbody drag within the region between the nacelle maximum diameter and the nozzle discharge will indicate possible trends. These drags were computed for Models 1, 2 and 4 and are shown in Figure 443. Each of these models has the same nozzle afterbody configuration; only the inlets are different. The data show that, within the test accuracy, the drag of the three models is the same. Noting that the three models have considerably different inlet contours, it is interesting that the afterbody drag does not change. This being the case, apparently most of the drag increase as shown in Figure 440 is attributed to the inlet and inlet fairing geometry.

Based on this analysis, including afterbody drag and circumferential variations of inlet pressure, it seems reasonable to assume that the drag rise is caused by the local velocity distributions in the region of the fan to engine nacelle fairing, and possibly an increase in interference drag as a result of these increased velocities.

The remaining analysis that may be performed using the balance data is an evaluation of effects of nacelle geometry on drag. Several comparisons may be made and are summarized below:

<u>Comparison Showing Effects of:</u>	<u>Models</u>
Inlet length - afterbody and nozzle unchanged	1, 2 and 4
Afterbody length - inlet, nozzle diameter, and area unchanged	6 and 8
Nozzle area - inlet and afterbody unchanged	2 and 3 7 and 8

Comparison of effects of inlet length are shown in Figure 444. Low-speed nacelle total drag is plotted versus inlet length and total nacelle length as a constant mass flow ratio of 0.55. The data are shown for a nozzle thrust coefficient of 0.95, consistent with that estimated in the previous analysis.

The problem remains to attempt to separate this drag into friction effects and nacelle drag, both afterbody and inlet. Friction drag is estimated using the following methods.

The skin friction drag of the nacelle may be estimated based on wetted area and local velocities. Referring to pressure distributions for the nacelles, it may be observed that the local velocity, on an average over the complete nacelle, varies with nacelle length as tabulated below:

<u>Model</u>	$\frac{L_N}{D_{MAX}}$	$\frac{q_{AVG}}{q_0}$
1	1.87	1.25
2	1.43	1.45
4	1.13	1.60

These data correlate quite well using the following relationship:

$$\frac{q}{q_0} = 1 + \left(\frac{D_{MAX}}{L_N} \right)^2$$

The fan nacelle friction drag is then approximated by the following equation:

$$(C_D)_F = \frac{C_F q S_W}{q_0 A_{MAX}} = 2 C_F \left[1 + \left(\frac{D_{MAX}}{L_N} \right)^2 \right] \frac{L_N}{D_{MAX}}$$

This friction drag does not include drag on the plug surface, since it is included in the nozzle thrust coefficient decrement. There is also a friction drag due to the engine nacelle system. Assuming an average local velocity of 1.10 times free stream and referring to nacelle geometry, engine nacelle friction drag is as follows:

$$(C_D)_E = 5.3 C_F$$

At the low speeds, with Mach number equal to values from 0.2 to 0.4, the Reynolds number based on nacelle length was about 1 times 10^7 to 2 times 10^7 . At these Reynolds numbers, the skin friction coefficient is about 0.003. Therefore, the estimated friction drag for the total models is:

$$(C_D)_F = 0.016 + 0.006 \left[\frac{L_N}{D_{MAX}} + \frac{D_{MAX}}{L_N} \right]$$

This equation of estimated friction drag is shown in Figure 444 and accounts for about one-half the total drag. It should be noted that this friction drag as estimated is consistent with the measured drag levels of similar nacelles, as presented in reference 3. These tests were run with a simulated mass flow ratio of unity, where most of the drag should be skin friction. The difference between the skin friction and total drag in Figure 444 is probably the result of inlet additive drag. However, because of the nonsymmetry of the model and the problems in the fairing regions, an evaluation of additive drag using balance data appears impractical. In either case, it does appear that the additive drag of the shorter inlet system is much lower than that of the longer inlet.

The second comparison showing the effects of afterbody length uses the results obtained for Models 6 and 8. The afterbody length for these two models was 0.89 and 1.08, respectively, and represented a relatively small change. Comparison of the data shows that there is no difference in the level of measured drag or the rate of change of drag with mass flow ratio of these two models.

Comparison of effects of nozzle area on performance was accomplished by changing the plug geometry in two of the models. Comparison of measured drags of Models 2 and 3, and Models 7 and 8 is inconclusive in showing trends due to changing nozzle area only.

In summary, it may be concluded that the measured nacelle drags as obtained during this test program showed only small effects owing to model geometry, noting that the geometric differences between the models were not very large. A complete summary of the measured low-speed drag coefficients is shown in Figure 445 for all eight models. The drags as shown were evaluated at the previously estimated nozzle thrust coefficients. A band is shown including most of the measured drags. This band represents about two points (0.02) of drag coefficient. In general, it appears that the shorter nacelles

have the lowest drags and the longest nacelles the highest, as shown in Figure 444. Also shown on the figure is the estimated skin friction drag of the engine nacelle system based on skin friction estimates.

The data show a rise of drag coefficient with a decrease in mass flow ratio, characteristic of an additive drag effect. The drag coefficient at a mass flow ratio near unity is about 0.05 to 0.06, including 0.016 of engine drag. This 0.035 to 0.045 value of drag coefficient is about 1.5 to 2.0 times the estimated friction drag and is probably a combination of boattail and interference drags.

Effects of Angle of Attack

Tests under conditions of variable angle of attack were run using Model 8. Variable angle of attack data were obtained at Mach numbers of 0.3, 0.5 and 0.7. The measured test results showed typical variations of lift, drag, and moments with angle of attack. Analysis of this part of the test program will be concerned with a study of the test results in an attempt to determine the major contributors to these variations.

In Appendix I, the detailed equations relating total lift and drag as a sum of the nacelle and propulsion system components are presented. Using these relationships, the induced lift, drag, and pitching moments attributed to the nacelle system were computed and are shown in Figures 446 through 454 for the three test Mach numbers. The data are presented in conventional lift, drag, and moment coefficients using the nacelle maximum area and fan diameter as the reference geometric parameters.

Comparison of the lift and drag data shows that the breakdown as used is invariant with mass flow ratio. However, there is a small change of the angle of attack for zero lift and the lift curve slope with Mach number. This may be the result of normal test accuracy or a true effect due to Mach number.

Figures 455 and 456 show variation of pitching moments at zero angle of attack with mass flow ratio. Figure 455 is the case for no correction due to thrust alignment, and shows considerable variation of moments with cross flow ratio. Figure 456 shows the same data corrected for thrust alignment as described in Appendix I. Although not a perfect correlation is shown, the case including correction for thrust alignment tends to reduce the variation of moments with speed ratio.

An interesting comparison of these test data with ring wing performance may clarify any effects of nacelle geometry, and at the same time provide a means of extrapolating the data. Ring wing lift, drag and moments are presented in reference 4 for a range of length-to-diameter ratios. However, before these data are used, they must be corrected to a comparable book-keeping system as described in Appendix I. The major difference in ring wing data as presented is in the accounting for the thrust and ram drag

caused by the internal flow. For nacelle tests and performance, the effects of internal flow are usually treated separately from the external flow. A similar treatment is possible using the ring wing data if ideal flow is assumed for the internal stream. This assumption of ideal flow implies that the nozzle total pressure is equal to the free-stream total pressure. Therefore, the jet velocity is equal to the free-stream velocity, and the lift and drag components caused by these are:

$$L = \rho V_0^2 A_j \sin \alpha$$

$$D = \rho V_0^2 A_j - \rho V_0^2 A_j \cos \alpha$$

where

A_j is the nozzle discharge area

Similarly, if the ram drag is assumed to act at the face of the inlet lip, then the moment due to ram drag is:

$$m = \rho V_0^2 A_j \frac{C}{4} (\sin \alpha)$$

where

the moment center is assumed to be at the quarter chord location.

These relationships were used to correct lift and moment data for the ring wing to a system comparable to nacelle data, and are presented in Figures 457 and 458. Drag data are not presented because the angle of attack excursion in this test was not sufficient to produce significant drag increases and no correlation with ring wing performance is possible.

Figure 457 shows the variation of the lift curve slope with nacelle length-to-diameter ratio. The data have been converted to coefficients consistent with this report in all cases. Shown on the figure are the measured slope as obtained from reference 4 data, the correction due to thrust inclination, and the resulting induced effect. The measured lift curve slope at a Mach number of 0.3 for Model 8 is also shown and is slightly higher than the comparable ring wing data. Part of this difference in lift may be due to the engine nacelle system and the nozzle plug. Neither of these two potential lifting surfaces exists in the ring wing, and the differences as shown in the figure are reasonable. Using this ring wing data and the performance as measured for Model 8, effects of nacelle length are estimated as shown in Figure 457.

Some comments about the shape of the induced lift as shown for the ring wing system should be made concerning the drop-off in lift for low length nacelles. This drop-off is not caused by changes in lift, but seems to be a result of the assumption concerning thrust axis inclination. The above

derivation of the lift, due to the center stream thrust, assumed the flow angle of the discharge to be along the axis of the nacelle. For the low length models, it is apparent that this assumption is no longer true. The drop-off of the lift curve slope for the complete ring wing is probably caused by a change in thrust angle, and the slope for the induced lift component would then continue to increase at low nacelle lengths.

A similar comparison of Model 8 and ring wing data is shown in Figure 458 for the change of moments with angle of attack. Here the agreement between the two sets of test data is very good, especially since the moments due to the engine nacelle and nozzle plug tend to cancel one another. (It should be noted that this figure uses nacelle maximum diameter as the reference dimension, whereas fan diameter was used in the previous analysis. This is necessary to provide a consistent set of reference dimensions. Also, the moment center has been moved from the fan center line, 48 percent chord, to the 25 percent chord point to make it consistent with the ring wing data.)

The remaining effect due to angle of attack is the drag caused by induced lift. With the meager amount of data, it looks as if a reasonable drag to lift relationship is as follows:

$$(C_D)_I = (C_L)^2$$

In addition to the above effects, it is significant that there was no appreciable change of the system internal performance under conditions of variable angle of attack within the range of test conditions explored. This includes the inlet systems, the turbofan hardware, and the exhaust nozzle system.

Propulsion System Performance

This part of the data evaluation will be concerned with performance of the X376 system when used in a cruise fan application. The procedures presented are applicable to a general type of cruise fan system, but the absolute levels of performance as shown are applicable to only the X376 fan when used in a cruise fan application.

In the analysis of the propulsion system performance, it was shown that the power balance of the fan turbine system appears to be determined by a static pressure balance of the fan and turbine streams at the fan discharge plane. This balance then determines the percentage of total gas power extracted by the fan turbine. Figures 459 through 466 present measured values of this power ratio as a function of the speed ratio parameter for the eight models. Since nozzle area is different for the eight models, a different characteristic of power balance exists. These data are then cross plotted in Figure 467 as a function of nozzle area for a range of speed ratios from zero to 1.35. Both the variation of power

extraction with area and the largest percentage of power extraction occurring at the largest areas are apparent. Also shown on these curves is a trim area schedule. This trim area is defined as the area required for maximum net thrust, the determination of which follows.

The fan operating point is first specified by assigning a fan flow coefficient. Then by use of the fan operating characteristics previously shown in Figures 377 through 384, the fan pressure coefficient and stage efficiency can be determined. Using the measured test results for the eight models, the variation of flow coefficient with nozzle area and speed ratio was obtained and is shown in Figure 468.

A similar procedure using measured fan net thrust provides the characteristics shown in Figures 469 and 470. Figure 469 assumes an ideal nozzle with a thrust coefficient of unity, and Figure 470 assumes a 0.95 coefficient. These two values are consistent with the previous assumed maximum and minimum nozzle performance levels.

It is apparent in both figures that the net thrust peaks at a maximum value as a function of the speed ratio parameter. The trim area is, therefore, determined as the area for maximum net thrust. At static conditions, Mach number of 0.0, fan net thrust does not attain a maximum value. This may be explained by the fact that the thrust per unit area of a lifting device increases proportionately to the discharge area. However, losses due to diffusion usually overcome these increased thrust levels for small diffusion ratios. For this case, a maximum trim area equal to the combined fan and fan turbine discharge areas was established. This trim area is shown at a speed ratio of zero.

A composite set of characteristics presenting fan performance parameters for the optimum area trim schedule is shown in Figure 471. Effective area for trim and all other previously discussed fan performance parameters are presented as a function of speed ratio. Also shown is the Mach number that satisfies the speed ratio for the fan operating at 100 percent corrected speed.

To complete the fan performance story, a correlation for total horsepower required to drive the fan system at a given rotational speed should be obtained. Such a presentation is given in Figure 472. Here, both total horsepower and extracted horsepower are shown as a function of fan speed and speed ratio. The percentage horsepower extraction is also shown. These characteristics were obtained by cross plotting the total horsepower as a function of nozzle area, as shown by Figure 473. This figure shows data that are typical for a corrected fan speed of 90 percent. The total horsepower is then obtained as a function of the speed ratio and fan corrected speed; the combined characteristics are then as shown in Figure 472.

The above characteristics represent the measured performance of the X376 fan system. Similar predicted fan performance agrees almost exactly with these experimental results.

APPLICATION OF TEST RESULTS TO CRUISE FAN NACELLE DESIGNS

The following discussion will summarize a set of procedures that utilize the results of these tests for the aerodynamic design of low-pressure cruise fan nacelle systems. The design procedures should be applicable to either close coupled or remote cruise fan installations. Close coupled cruise fan installations represent systems where the core engine is located in proximity to the fan. The engine nacelle system blends into the fan nacelle. The models used in this test were a type of close coupled system. The remote cruise fan installation incorporates separate fan and core engine locations, such that the fan nacelle shape and flow are not influenced by the core engine.

INLET INTERNAL PERFORMANCE

The two performance indicators used in this part of the design procedure are the inlet total pressure losses and the peak velocities on the inlet near the throat. The inlet losses are calculated using the following relationship derived empirically using the test results. The following equation assumes a non-separating diffuser system in the inlet. Possible diffuser separation should be checked using conventional diffuser data. A diffuser including an angle of less than 12 degrees is recommended to avoid separation and the attendant increase in losses. For a non-separating inlet, the losses are:

$$\bar{w}_{10} = \left(0.017 \frac{L}{D_{TH}} \right) \left(\frac{A_{TH}}{A_{10.0}} \right)^2 (K)$$

where \bar{w}_{10} = loss coefficient based on fan inlet velocity head at station 10.0

$\frac{L}{D_{TH}}$ = ratio of inlet length to inlet throat diameter. Inlet length is distance from inlet leading edge to fan face.

K = correction accounting for effects of speed as shown in Figure 388.

The level of peak velocity near the inlet leading edge should be checked to insure less than local critical flow. Figure 393 shows the ratio of local peak velocity to the effective one-dimensional velocity in the inlet throat at static conditions. The ratio of throat to inlet diameter should be established using this criterion and the inlet diameter as dictated by nacelle external design.

Similar local peak velocity data taken during this program and the Ames program, reference 10, show that the design conditions for peak inlet lip velocity is the static condition as described above.

NOZZLE PERFORMANCE

Performance of the exhaust nozzle system should be obtained by referring to test results of similar configurations. However, based on these tests, a first-order approximation is suggested, making use of an assumed thrust loss due to flow angularity and then a correction for estimated nozzle skin friction. For a good nozzle system, a thrust decrement due to angularity equal to one percent is reasonable; therefore, the nozzle thrust coefficient may be estimated as follows:

$$C_T = 0.99 - (\Delta C_T)_F$$

where

$$(\Delta C_T)_F = \frac{D_F}{(F_G)_I}$$

D_F = friction drag of nozzle

$(F_G)_I$ = nozzle ideal gross thrust evaluated at the nozzle pressure ratio.

The nozzle friction may be obtained by integration of the local velocity times area term, and may be estimated based on nozzle geometry using the following:

$$D_F = C_F \left[(P_{T11.0})_E - P_0 \right] \left[\frac{\pi R_C^2}{\tan \beta_P} + \left(\frac{A_N}{A_{11.0}} \right)^2 (2\pi R_T) L_S + \left(\frac{A_N}{A_{11.0}} \right)^2 \pi (R_N + R_C) L_S \right]$$

The above expression is a function of nozzle throat velocity head and the geometric constants of the nozzle system.

NACELLE CRITICAL MACH NUMBER AND DRAG

Reference 1 developed a method of predicting nacelle performance as a function of the free-stream Mach number for critical flow and a mass flow ratio, above which small gains in critical Mach number may be obtained and below which large penalties occur. These data have been presented in Figures 474 and 475, including an extension of the characteristics to relatively short nacelle length based on these test results.

Knowing the design flight conditions and propulsion system operating characteristics, the following design requirements must first be obtained:

- o Design Mach number - M_{DES}

- o Stream tube area of fan flow at design flight speed and altitude - A_0
- o Limiting nacelle dimensions such as inlet length, maximum diameter, or throat diameter as required by inlet internal design considerations
- o Inlet radius specified by static design requirements such that the inlet leading edge diameter is restricted to a given value

Using the above design requirements, it is possible to iterate on a nacelle design such that the mass flow ratio is either equal to or above the curve, as shown in Figure 475, and the critical Mach number, as determined by Figure 474, is above the design Mach number. Usual design techniques as presented in reference 1 recommend the design selection to be obtained at 0.02 lower than design mass flow ratio and at least 0.02 higher than design Mach number. The above design characteristics are presented for zero angle of attack. If the design conditions required the nacelle to operate at an angle of attack, the critical Mach number from Figure 474 should be reduced by the correction shown in Figure 476. Once a nacelle design has been determined to fulfil the initial design requirements and installation geometry, other conditions throughout the operating envelope should be checked for limiting design conditions.

A comparison of the predicted critical Mach numbers for the three test inlets and the measured values is shown in Figure 477. The dotted lines show the predicted critical Mach number, using Figures 474 and 475, with a vertical line denoting the minimum mass flow ratio at the design Mach number. The predicted characteristics do not include any correction factors as described above for either the Mach number or the mass flow ratio. The agreement of the test and predicted data is very good and is within 0.03 Mach number.

A discussion of the methods used in obtaining the measured characteristics based on low-speed data is as follows. Limitations of fan operating characteristics, especially fan pressure ratio, restricted the tests at high Mach numbers to basically one mass flow ratio for each inlet system. However, mass flow ratio could be varied over a suitable range at low Mach numbers. Combining the measured low-speed peak pressure coefficients for the eight models, Figures 395 through 402, the variation of pressure coefficient with mass flow ratio shown in Figure 478 is obtained. These characteristics are for the side opposite the engine nacelle system. The critical Mach number characteristics are then predicted using the compressibility corrections shown in Figure 479, and yield the curves shown in Figure 477.

The high-speed test data for each inlet system are also shown in Figure 477. Inlets 1 and 3 agree exactly with the low-speed data, but Inlet 2 is slightly higher. This difference may be because of the conservative method used in extrapolating the low-speed data, or just an inaccuracy of the test results. The measured effects of angle of attack on critical Mach number for Model 8 are compared with those predicted in Figure 476.

Note that this design procedure applies to an axisymmetric nacelle system only, or that part of the nacelle system remote from possible external interference effects. Other design techniques should be approached in the design of the nacelle systems close to possible interference effects, such as the engine nacelle for a close coupled cruise fan system.

Once the inlet design has been estimated, the total nacelle drag for conditions less than the critical Mach number can be estimated using the characteristics shown in Figure 445. These characteristics show nacelle drag coefficient variation with inlet mass flow ratio. A band of nacelle drag coefficients is shown for each mass flow ratio. The lower part of the band is representative of nacelle length to diameter ratios of about 1.0 and the upper part for nacelle lengths of about 2.0. This characteristic implies that the nacelle system should be made as short as possible for minimum drag levels. Also, the mass flow ratios should be as high as possible, commensurate with the inlet design, as dictated by the critical Mach number requirement. Note that the drag coefficients include engine nacelle as well as the fan nacelle drags. Corrections using estimated engine nacelle friction should be used for a remote fan installation.

FAN-ENGINE NACELLE FAIRING

These tests have shown that design of the fairing region between the engine and fan nacelles is a critical problem. The resulting test data provide some insight concerning possible design changes which may be required to improve performance of the system in this region.

A comparison of the peak pressure coefficients of the fairing and the axisymmetric regions of the nacelle for Inlets 1 and 2 is shown in Figure 480. Comparison of the pressure coefficient variation with mass flow ratio for the two regions of the nacelle shows that equivalent characteristics occur when the fairing mass flow ratio is reduced by a factor of 1.4. This factor infers that the inlet in the fairing region is spilling 40 percent more flow than the remainder of the nacelle. Using this ratio as a design value for modifying the mass flow ratio, design changes of the inlet lip geometry in the fairing region were obtained and are shown in Figure 481. The characteristics shown in Figures 474 and 475 were used to determine the inlet geometry. The inlet geometry changes in Figure 481 are presented as the following constants:

$$K_L = \frac{\text{length of nacelle in fairing region}}{\text{length of axisymmetric nacelle}}$$

$$K_D = \frac{\text{center line radius of fairing inlet lip}}{\text{center line radius of axisymmetric nacelle}}$$

The resulting redesigned fairing regions for the three test models, using the data shown in Figure 481, are as follows:

<u>Inlet</u>	<u>Axisymmetric Region</u>		<u>Fairing Region</u>	
	<u>L_I</u> <u>(inches)</u>	<u>R_I</u> <u>(inches)</u>	<u>L_I</u> <u>(inches)</u>	<u>R_I</u> <u>(inches)</u>
1	49	16.23	57.3	14.52
2	27	18.17	29.3	17.08
3	12	20.40	13.4	19.07

These lengths and diameters denote the geometry of the nacelle at the 150-degree location. The increased length and radius should blend into the axisymmetric nacelle at the top part of the model. These changes would produce an inlet with a swept-back leading edge. The sweep angle would be about 10 degrees for the Inlet 1 configuration. These proposed geometric changes for a typical nacelle are shown by the sketches in Figure 482. The configuration is Model 8, and both the original and modified nacelles are shown.

PROPULSION SYSTEM PERFORMANCE

The propulsion system used in this test was the X376 fan system. As a result, only general comments concerning propulsion system performance can be presented here.

One of the more important results is that within the test measurement accuracy, the propulsion system can be represented by a single set of performance characteristics. The fan system performance was unaffected, other than predicted, based on one-dimensional flow analysis, by either the inlet or the nozzle system geometry.

The second conclusion concerns the power extraction or absorption characteristics of the fan turbine. The level of power absorption in previous theoretical calculations of fan performance was established by assuming equal static pressures of the fan and fan turbine streams in the discharge plane. Measurements during this test verified that this was a correct assumption, and its continued use in performance evaluation is suggested.

CONCLUSIONS

Analysis of the results of this experimental investigation of cruise fan system performance indicated the following conclusions, applicable for the range of parameters investigated:

1. Propulsion system performance of the X376 fan and core engine followed previous predictions based on methods using a single set of operating characteristics for each component and one-dimensional flow analysis.
2. Low-speed drag coefficients for the complete nacelle system ranged from 0.040 to 0.060 at mass flow ratios near 1.0 and from 0.060 to 0.085 at a mass flow ratio of about 0.5.
3. Only small changes in nacelle low-speed drag were observed for the eight test models. Nacelle length was the only significant geometric variable that influenced the nacelle drag levels. The shortest nacelles had the lowest total drag.
4. Nacelle pressure distributions for the axisymmetric sections of the model demonstrated critical Mach numbers consistent with predicted values.
5. Free-stream Mach numbers for critical flow in the regions of the nacelle system near the fan-engine fairing were below predicted levels. Fan-engine nacelle interference effects caused excessive flow spillage in this region, with the attendant reduction in free-stream Mach numbers for critical flow.
6. Possible redesigns of the nacelle geometry for reduction of the interference effects of the fan and engine systems were developed using the test results. The redesigns suggest an increase in both the nacelle length and thickness in the vicinity of the fan and engine nacelle junction.
7. Nacelle inlet loss coefficients varied with inlet length and free-stream Mach number in a systematic manner, permitting evaluation of an empirical expression to predict the variation of inlet loss coefficient.
8. Nozzle thrust coefficients based on momentum integration and estimated friction drags varied between 0.95 and 0.97. One nozzle configuration used in Models 1, 2 and 4 had a low coefficient, apparently because of insufficient nozzle shroud length aft of the plug maximum diameter. For the other nozzles, the thrust coefficient decrements are primarily caused by skin friction drag losses. The nozzle systems tested in this program had high ratios of surface area to nozzle thrust area. This condition

contributed to the low thrust coefficients, and it will not exist in the plug nozzle of a typical high-pressure-ratio cruise fan system. For the high-pressure-ratio nozzle configurations, higher thrust coefficients are predicted.

9. Performance of Model 8 under conditions of variable angle of attack showed that the longitudinal stability derivatives of the lift and pitching moments are very similar to those obtained for a ring wing configuration.

BIBLIOGRAPHY

1. Baals, Donald O., Smith, Norman F., and Wright, John B., The Development and Application of High-Critical-Speed Nose Inlets, NACA Report No. 920, National Advisory Committee for Aeronautics, Langley Aeronautical Laboratory, Langley Field, Virginia, June 8, 1945.
2. Brüel and Kjaer, Instruction and Applications Manual, Models 4133 and 4134, Brüel and Kjaer Precision Instruments, Copenhagen, Denmark, October 1960.
3. Fasching, W.A., and Kutney, J.T., Lift/Cruise Fan Exhaust System Research Program, TRECOM Technical Report 64-49, U.S. Army Aviation Materiel Laboratories, Ft. Eustis, Virginia, September 1964.
4. Fletcher, Herman S., Experimental Investigation of Lift, Drag, and Pitching Moments of Five Annular Airfoils, NACA Report No. TN 4117, National Advisory Committee for Aeronautics, Langley Aeronautical Laboratory, Langley Field, Virginia, October 1957.
5. Hoerner, Sigward F., Fluid-Dynamic Drag, Published by Author, Library of Congress Catalog Card No. 57-13009, 1958.
6. Hough, Gary R., A Feasibility Study on the Measurement of the Time Dependent Shroud Pressure of a Ducted Propeller, TAR-TR612, Therm Incorporated, Ithaca, New York, August 1961.
7. King, R.C., Test Results of Three Low Speed Inlet Cowls with NACA 1-Series Centerbody and Outer Profiles and Elliptical Inner Lips, General Electric Report No. R62FPD168, Cincinnati, Ohio, April 1962.
8. Nichols, Mark R., and Keith, Arvid L., Jr., Investigation of a Systematic Group of NASA 1-Series Cowlings With and Without Spinners, NACA Report No. 950, National Advisory Committee for Aeronautics, Langley Aeronautical Laboratory, Langley Field, Virginia, February 8, 1948.
9. Ordway, D.E., and Greenberg, M.D., General Harmonic Solutions for the Ducted Propeller, TAR-TR613, Therm Incorporated, Ithaca, New York, August 1961.
10. Przedpelski, Z.J., Heikkinen, A.H., and Vacek, L., Aerodynamic Investigation of Low Speed VTOL Transition Characteristics of X353-5B Cruise Fan, General Electric Report No. R63FPD426, Cincinnati, Ohio, December 12, 1963.
11. Von Kármán, Th., "Compressibility Effects in Aerodynamics", Journal Aeronautical Sciences, Volume 8, Number 9, July 1941, pp. 337-356.

DISTRIBUTION

US Army Materiel Command	8
US Army Mobility Command	5
US Army Aviation Materiel Command	6
First United States Army	1
United States Army, Pacific	1
US Army Forces Southern Command	1
United States Army, Hawaii	1
Chief of R&D, DA	1
US Army Aviation Materiel Laboratories	30
US Army R&D Group (Europe)	2
US Army Limited War Laboratory	1
US Army Human Engineering Laboratories	1
US Army Research Office-Durham	1
US Army Test and Evaluation Command	1
Plastics Technical Evaluation Center	1
US Army Medical R&D Command	1
US Army Engineer Waterways Experiment Station	1
US Army Combat Developments Command, Fort Belvoir	2
US Army Combat Developments Command Transportation Agency	1
US Army Combat Developments Command Experimentation Command	3
US Army War College	1
US Army Command and General Staff College	1
US Army Transportation School	1
US Army Aviation School	1
Deputy Chief of Staff for Logistics, DA	1
US Army Infantry Center	2
US Army Tank-Automotive Center	2
US Army Aviation Maintenance Center	2
US Army Armor and Engineer Board	1
US Army Aviation Test Board	3
US Army Electronics Command	2
US Army Aviation Test Activity	2
Air Force Flight Test Center, Edwards AFB	1
US Army Field Office, AFSC, Andrews AFB	1
Air Force Aeropropulsion Laboratory, Wright-Patterson AFB	1
Air Force Flight Dynamics Laboratory, Wright-Patterson AFB	1
Systems Engineering Group, Wright-Patterson AFB	4
Bureau of Ships, DN	1
Bureau of Naval Weapons, DN	7
Chief of Naval Research	5
US Naval Air Station, Patuxent River	1
US Naval Air Station, Norfolk	1
David Taylor Model Basin	1
Commandant of the Marine Corps	1

Marine Corps Liaison Officer, US Army Transportation School	1
Ames Research Center, NASA	1
Lewis Research Center, NASA	1
Manned Spacecraft Center, NASA	1
NASA Representative, Scientific and Technical Information Facility	2
NAFEC Library (FAA)	2
US Army Aviation Human Research Unit	2
US Army Board for Aviation Accident Research	1
Bureau of Safety, Civil Aeronautics Board	2
US Naval Aviation Safety Center, Norfolk	1
Federal Aviation Agency, Washington, D. C.	1
Civil Aeromedical Research Institute, FAA	2
The Surgeon General	1
Defense Documentation Center	20

APPENDIX I

DATA REDUCTION AND ANALYSIS PROCEDURES

AVERAGE TOTAL AND STATIC PRESSURES

Pressure measurements of the flow conditions throughout the model were taken by arrays of total and static pressure probes. These arrays were arranged in such a way that the probes were located on centers of approximately equal areas with additional provisions for measurement of boundary layers where applicable. The following equations define the pressure probe numbers used in determining the particular average pressure. Pressures are computed as an arithmetic average which results in an approximate area average by virtue of the probe arrangements. (Reference Table XX, Figures 8 and 9.)

The equation used in computing these average pressures may be written in a general form as follows:

$$P_x = \frac{1}{N} \sum P_n$$

<u>Measurement</u>	<u>P_x</u>	<u>N</u>	<u>n</u>
Engine Inlet Static	P _{S2.0}	9	(432-440)
Engine Inlet Total	P _{T2.1}	15	(413-417), (420-424), (427-431)
Engine Inlet Boundary Layer	P _{S2.2}	6	(411-412), (418-419), (425-426)
Engine Discharge Pressure	P _{T5.1}	6	(405-410)
Fan Turbine Discharge	P _{T5.6}	8	(543-550)
Fan Inlet Static	P _{S10.0}	24	(465-488)
Fan Inlet Total	P _{T10.1}	24	(441-464)
Fan Inlet Tip Boundary Layer	P _{T10.2}	12	(491-502)
Fan Inlet Hub Boundary Layer	P _{T10.3}	4	(126-129)
Rotor Discharge Total	P _{T10.6}	24	(561-584)
Fan Discharge Total	P _{T11.1}	24	(507-530)
Fan Discharge Tip Boundary Layer	P _{T11.2}	8	(531-538)
Fan Discharge Hub Boundary Layer	P _{T11.3}	4	(539-542)
Balance Base Pressure	P _{14.0}	8	(553-560)

Missing or inoperative pressure probes, in the above averaging method, are replaced by a suitable measurement from adjacent probes.

FORCE BALANCE DATA

The force balance data consist of the three longitudinal forces; that is, drag, lift and pitching moments. The sign convention of these forces is as follows:

Normal (lift): positive downward

Axial (drag): positive rearward

Pitching Moments: positive nose down

These sign conventions appear reversed, but are the result of mounting the model inverted in the wind tunnel.

The force balance measurements are used directly as recorded after conversion to engineering units, with only one small correction. This correction accounts for any pressure area force that exists at the base of the sting support and is reflected as an axial force on the "live" part of the balance system. The correction factor is a simple addition to the axial force measurement as follows:

$$A = A_{\text{measured}} - A_B (P_0 - P_{14.0})$$

where

$A_B (P_0 - P_{14.0})$ is base force correction using measured base pressures at station 14.0.

For conditions of zero-degree angle of attack, the body axis forces, normal and axial, are identical to the wind axis forces. During test conditions where angle of attack was varied, wind axis forces were computed using the measured body axis forces and conventional trigonometric relationships with angle of attack.

The balance data were non-dimensionalized using free-stream velocity head, fan nacelle maximum area, and nacelle diameter as follows:

$$(C_L)_B = \frac{L_B}{q_0 A_{\pi}}$$

$$(C_D)_B = \frac{D_B}{q_0 A_{\pi}}$$

$$(C_m)_B = \frac{m_B}{q_0 A_{\pi} D_{\text{MAX}}}$$

PRESSURE COEFFICIENTS

Pressure data are presented in coefficient form using several values of velocity head measurements.

Plug and nacelle pressures are presented using the following conventional coefficient:

$$C_P = \frac{P_L - P_0}{q_0}$$

Internal pressures, that is, for the fan and engine inlet internal contours, as well as the flow conditions at Station 2.0 and 10.0, are presented in coefficients using the following:

$$\frac{P_L - P_{T0}}{P_{T0} - P_{S2.0}} \text{ or } \frac{P_L - P_{T0}}{P_{T0} - P_{S10.0}}$$

Other pressures, such as fan and rotor discharge, are presented as pressure ratios based on free-stream total pressure, P_{T0} .

ENGINE AND FAN AIRFLOWS

Both engine and fan airflow were computed using measured pressure at the inlet stations. The calculation procedure uses a pseudo mass-averaged method by treating the boundary layer separately from the free-stream measurements. The boundary layer areas for each inlet that was surveyed by an array of boundary layer probes are as follows:

Fan Inlet 1 - $A_{10.1}$ = 756.4 (midstream)
 $A_{10.2}$ = 81.9 (tip boundary layer)
 $A_{10.3}$ = 31.1 (hub boundary layer)
 $A_{10.0}$ = 869.4 (total area)

Fan Inlet 2 - $A_{10.1}$ = 753.1 (midstream)
 $A_{10.2}$ = 80.7 (tip boundary layer)
 $A_{10.3}$ = 31.1 (hub boundary layer)
 $A_{10.0}$ = 864.9 (total area)

Fan Inlet 3 - $A_{10.1}$ = 808.4 (midstream)
 $A_{10.2}$ = 84.1 (tip boundary layer)
 $A_{10.3}$ = 31.1 (hub boundary layer)
 $A_{10.0}$ = 923.6 (total area)

Engine Inlet - $A_{2.1} = 54.8$ (midstream)
 $A_{2.2} = 15.8$ (hub and tip boundary layers)
 $A_{2.0} = 70.6$ (total area)

(all areas in square inches)

The average or effective inlet total pressure was computed using the following:

$$(P_{T10.0})_E = \frac{(P_{T10.1}) (A_{10.1}) + (P_{T10.2}) (A_{10.2}) + (P_{T10.3}) (A_{10.3})}{A_{10.0}}$$

An inlet flow coefficient or effective area was also defined based on the boundary layer measurements and a mass-averaging technique:

$$\frac{(A_{10.0})_E}{A_{10.0}} = \frac{(M_{10.1}) (A_{10.1}) + (M_{10.2}) (A_{10.2}) + (M_{10.3}) (A_{10.3})}{A_{10.0}}$$

In the above equation, $M_{10.1}$, $M_{10.2}$ and $M_{10.3}$ represent the respective boundary layers and midstream Mach numbers computed, using the following:

$$M_{10.1} = \sqrt{\frac{\gamma-1}{2} \left(\frac{P_{S10.0}}{P_{T10.1}} \right)^{\frac{\gamma}{\gamma-1}} - 1}$$

$$M_{10.2} = \sqrt{\frac{\gamma-1}{2} \left(\frac{P_{S10.0}}{P_{T10.2}} \right)^{\frac{\gamma}{\gamma-1}} - 1}$$

$$M_{10.3} = \sqrt{\frac{\gamma-1}{2} \left(\frac{P_{S10.0}}{P_{T10.3}} \right)^{\frac{\gamma}{\gamma-1}} - 1}$$

The fan inlet airflow was then calculated using conventional compressible flow relationships and the computed values of $(P_{T10.0})_E$, $(P_{S10.0})$, $\frac{(A_{10.0})_E}{A_{10.0}}$ and T_{T0} .

Similar flow calculations were performed for the engine inlet airflow with station 2.0 measurements and areas used instead of station 10.0.

Engine discharge mass flow, that is, $W_{5.1}$, includes the engine inlet airflow with an additional mass flow due to fuel addition during combustion. Since fuel flow was not a measured parameter, assumed fuel flows, based on nominal engine characteristics, were used. The engine discharge flow is then as follows:

$$W_{5.1} = W_{2.0} + W_f$$

where

W_f is obtained using the following relationship between inlet airflow and fuel flow:

$W_{2.0}$	W_f
4.0	0.031
6.0	0.057
8.0	0.091
10.0	0.132
12.0	0.181
14.0	0.237

INLET LOSS COEFFICIENT

The inlet loss coefficient is used to define the losses in the fan and engine inlet systems between free-stream conditions and the measurement plane. The inlet loss coefficients for the fan and engine inlets are defined as follows:

$$\bar{\omega}_{10.0} = \frac{P_{T0} - (P_{T10.0})_E}{P_{T0} - P_{S10.0}}$$

and

$$\bar{\omega}_{2.0} = \frac{P_{T0} - (P_{T2.0})_E}{P_{T0} - P_{S2.0}}$$

FAN AND ROTOR DISCHARGE TOTAL PRESSURES

Rotor discharge total pressure was measured by an array of 24 probes, with no provisions for boundary layer measurements as used in the inlet systems. Rotor discharge pressure, $P_{T10.6}$, was then calculated as an arithmetic average of the probe measurements. This results in an area averaged pressure, since probes were spaced according to equal areas along the the radial stations. Rotor pressure ratio is therefore defined as follows:

$$(PR)_R = \frac{P_{T10.6}}{(P_{T10.0})_E}$$

However, the fan discharge total pressure measurements included provisions for measurement of midstream pressure and boundary layers at both the fan hub and tip regions. The effective total pressure was then calculated using:

$$(P_{T11.0})_E = \frac{(P_{T11.1}) (A_{11.1}) + (P_{T11.2}) (A_{11.2}) + (P_{T11.3}) (A_{11.3})}{A_{11.0}}$$

In this equation, subscript notations are as follows:

- 11.1 - fan discharge, midstream
- 11.2 - fan discharge, tip boundary layer
- 11.3 - fan discharge, hub boundary layer

These areas are a function of the particular afterbody and plug configuration as listed below:

<u>Afterbody</u>	<u>Plug</u>	<u>A_{11.1}</u>	<u>A_{11.2}</u>	<u>A_{11.3}</u>	<u>A_{11.0}</u>
1	2	736.7	83.0	40.2	859.9
1	3	736.7	83.0	40.2	859.9
2	2	728.2	83.0	43.0	854.2
2	3	720.5	83.0	48.7	852.2
4	3	772.9	88.0	48.7	909.6
4	4	627.5	88.0	52.1	767.6

Fan pressure ratio is then defined as:

$$(PR)_F = \frac{(P_{T11.0})_E}{(P_{T10.0})_E}$$

CORRECTION PARAMETERS

Throughout the data analysis and presentation, measured parameters were corrected to standard atmospheric conditions. These corrections are similar to those used in all parametric presentation of jet engine performance. The correction factors are defined as follows:

$$\theta_0 = \frac{T_{T0}}{518.69} \quad (T_{T0} \text{ in degrees Rankine})$$

$$\delta_0 = \frac{P_{T0}}{14.696} \quad (P_{T0} \text{ in pounds per square inch})$$

$$\delta_2 = \frac{P_{T2.0}}{14.696} \quad (P_{T2.0} \text{ in pounds per square inch})$$

$$\delta_{10} = \frac{P_{T10.0}}{14.696} \quad (P_{T10.0} \text{ in pounds per square inch})$$

Also, because both fan and engine inlet are basically identical to free stream temperature, the following equality is also used:

$$\theta_0 = \theta_2 = \theta_{10}$$

CORRECTED PERFORMANCE

The above correction parameters, referred to standard temperature and pressure, were then used in computing corrected performance as listed below:

Corrected rotational speed:	$\frac{N}{\sqrt{\sigma}}$
Corrected airflow:	$\frac{W\sqrt{\sigma}}{\delta}$
Corrected thrust or drag:	$\frac{F}{\delta}$
Corrected temperature:	$\frac{T}{\theta}$
Corrected pressure:	$\frac{P}{\delta}$
Corrected horsepower:	$\frac{HP}{\delta\sqrt{\sigma}}$

Subscripts assigned to the correction factors are used for identification of the reference conditions in all data presentations.

GROSS AND NET THRUST

In the process of thrust-drag bookkeeping, it is necessary to know the thrust contribution of the fan and engine systems. The following procedures and equations were used in calculating these parameters.

Fan exhaust flow ideal gross thrust was calculated as the potential ideal thrust available in expanding the gas from fan discharge pressure to ambient or free-stream static pressure.

$$F_{11.0} = W_{10} \sqrt{\frac{2(778.26)C_p}{g} (T_{11.0}) \left\{ 1 - \left[\frac{P_{S0}}{(P_{11.0})_E} \right]^{\frac{\gamma}{\gamma-1}} \right\}}$$

$$= W_{10} \sqrt{11.756 T_{11.0} \left\{ 1 - \left[\frac{P_{S0}}{(P_{11.0})_E} \right]^{\frac{\gamma}{\gamma-1}} \right\}}$$

All parameters in the above equation are either measured or calculated in previous discussion, with the exception of $T_{11.0}$. This parameter was computed using a constant fan efficiency of 0.82 and the following relationship between temperature and pressure rise across the rotor:

$$\left(\frac{T_{11.0}}{T_{10.0}} - 1 \right) (\eta_F) = \left\{ \left[\frac{(P_{11.0})_E}{(P_{10.0})_E} \right]^{\frac{\gamma-1}{\gamma}} - 1 \right\}$$

Fan turbine discharge ideal thrust was obtained similarly to the fan ideal thrust using conditions at station 5.6, the fan turbine discharge plane.

$$F_{5.6} = W_{5.1} \sqrt{\frac{2(778.26)C_p}{g} (T_{5.6}) \left[1 - \left(\frac{P_{S0}}{P_{5.6}} \right)^{\frac{\gamma}{\gamma-1}} \right]}$$

$$= W_{5.1} \sqrt{13.377 T_{5.6} \left[1 - \left(\frac{P_{S0}}{P_{5.6}} \right)^{\frac{\gamma}{\gamma-1}} \right]}$$

In the above equation, $W_{5.1}$ is computed as above, and both $T_{5.6}$ and $P_{5.6}$ are average values from the array of probes located in the fan turbine discharge annulus.

Fan and engine ram drag were computed using free-stream velocity and measured system airflows.

$$F_{DR} = \left(\frac{W_{10.0} + W_{2.0}}{g} \right) V_0$$

Free-stream velocity was computed using tunnel Mach number and temperature and compressible flow as follows:

$$V_0 = M_0 \sqrt{\gamma g R \frac{T_{T0}}{1 + \left(\frac{\gamma-1}{2} \right) M_0^2}}$$

Total propulsion system net thrust, that is, gross thrust minus ram drag, was computed using a nozzle thrust coefficient to account for a non-ideal exhaust nozzle system. Net thrust was calculated as follows:

$$F_N = C_T F_G - F_{DR}$$

GAS HORSEPOWER RELATIONSHIPS

In presentation of fan system performance, the energy levels are usually presented in terms of gas horsepower parameters. Ideal gas horsepower is the power that could be utilized in an ideal isentropic expansion of the gas from one set of conditions to another; for example, the engine discharge flow when expanding from turbine discharge pressure to ambient pressure. The general equation for this ideal horsepower used in the calculations is:

$$HP = \frac{778.26}{550} C_P T_T W \left[1 - \left(\frac{P_2}{P_1} \right)^{\frac{\gamma-1}{\gamma}} \right]$$

where

P_1 is the initial gas pressure and P_2 is the final pressure.

This equation was used to compute the following gas horsepower:

<u>Horsepower</u>	<u>Initial Pressure</u>	<u>Final Pressure</u>
HP _{5.1 - 0}	Turbine Discharge - $P_{T5.1}$	Ambient - P_{S0}
HP _{5.1 - 5.6}	Turbine Discharge - $P_{T5.1}$	Fan Turbine Discharge - $P_{T5.6}$
HP _{10.0 - 11.0}	Fan Inlet - $P_{T10.0}$	Fan Discharge - $P_{T11.0}$

For each horsepower calculation, the appropriate flows and total temperatures were used.

SYSTEM EFFICIENCIES

Two types of fan system efficiencies were calculated in the analysis. One is the term called "product efficiency", which is the resulting efficiency including both the fan and turbine systems. This efficiency is defined as:

$$\eta_S = \frac{HP_{10.0 - 11.0}}{HP_{5.1 - 5.6}}$$

The second is not a true efficiency, but is a ratio of horsepower absorbed in the fan turbine as compared to the total ideal in the core engine discharge flow. This relationship is:

$$\text{HP Ratio} = \frac{\text{HP}_{5.1 - 5.6}}{\text{HP}_{5.1 - 0}}$$

FAN OPERATING CHARACTERISTICS

The aerodynamic performance of the fan system is usually presented as a pressure-coefficient flow-coefficient map. These parameters were computed in the analysis of the data using the following equations:

$$\text{Pressure Coefficient: } \psi_{11.0} = \frac{2}{(M_T)^2 (\gamma-1)} \left[\left(\frac{P_{T11.1}}{P_{T10.1}} \right)^{\frac{\gamma-1}{\gamma}} - 1 \right]$$

$$\text{Flow Coefficient: } \phi_{10.0} = \frac{V_{10.0}}{U_T}$$

Note that the pressure coefficient is calculated using midstream pressures with no boundary layer allowances. The only new parameters used in these equations are M_T , U_T , and $V_{10.0}$, which are fan tip Mach number and speed, and fan inlet velocity. These were calculated using:

$$U_T = \left(\frac{N_F}{100} \right) \left(\frac{4074}{60} \right) (\pi D_F)$$

$$M_T = \frac{U_T}{\sqrt{\gamma g R \left[\frac{T_{T10.0}}{1 + \left(\frac{\gamma-1}{2} \right) (M_{10.1})^2} \right]}}$$

$$V_{10.0} = M_{10.1} \sqrt{\gamma g R \left[\frac{T_{T10.0}}{1 + \frac{\gamma-1}{2} (M_{10.1})^2} \right]}}$$

These two parameters, $\psi_{11.0}$ and $\phi_{10.0}$, along with product efficiency, η_S , are all that are necessary to define the normal fan operating characteristics.

INLET CAPTURE RATIO

Inlet capture ratio is a parameter commonly used in describing or correlating inlet and nacelle performance. In this analysis the inlet area used is the projected area of the inlet leading edge. For the fan inlet, the mass flow ratio is defined as:

$$\left(\frac{A_0}{A_I} \right)_{10.0} = \frac{(W_{10.0}) V_0}{2g q_0 (A_I)_{10.0}}$$

A similar parameter is used for the engine inlet system; that is,

$$\left(\frac{A_0}{A_I} \right)_{2.0} = \frac{W_{2.0} V_0}{2g q_0 (A_I)_{2.0}}$$

NACELLE DRAG COEFFICIENT - FORCE BALANCE METHOD

One method that can be used in evaluating the total system drag coefficient utilizes the axial forces measured on the balance and the fan system thrusts and drags based on internal flow measurements.

The net drag forces attributed to the complete nacelle system were computed as follows:

$$D_N = D_B + \left[C_T (F_{11.0} + F_{5.6}) - F_{DR} \right]$$

The term C_T is the nozzle thrust coefficient and was assumed to be two different extreme values: 0.95 as a minimum and 1.00 as a maximum.

The nacelle drag as calculated was converted to coefficient form using:

$$C_{D\pi} = \frac{D_N}{q_0 A_\pi}$$

ANGLE OF ATTACK ANALYSIS

Under conditions of variable angle of attack, the model forces may be attributed to effects due to the nacelle, forces due to the propulsion system, and any type of interactions on any or all the three force components. In order to investigate these effects, an analysis which attempts to separate the propulsion system forces from the total measured forces was used in reduction of the test data. The following is a discussion of these procedures and techniques.

In previous discussions, fan system gross thrust was calculated as:

$$F_G = C_T (F_{11.0} + F_{5.6})$$

The lift and drag components, due to the inclination of the thrust axis, are then related to angle of attack as follows:

$$\begin{aligned} L_{FG} &= + F_G \sin \alpha \\ D_{FG} &= - F_G \cos \alpha \\ m_{FG} &= 0 \end{aligned}$$

No moment contribution due to gross thrust was assumed, since the thrust axis should not change relative to the reference moment center. However, a moment contribution due to inlet ram drag of both the engine and fan inlet flows does exist. This moment was calculated assuming that the ram drag force acts at the centerline of the fan and engine inlet at the leading edges. The moments are then as follows:

$$\Delta m_F = (\bar{X}_N \sin \alpha) \left(\frac{W_{10.0}}{g} \right) (v_0)$$

$$\Delta m_E = (29.0 \cos \alpha + \bar{X}_E \sin \alpha) \left(\frac{W_{2.0}}{g} \right) (v_0)$$

where

\bar{X}_N and \bar{X}_E are axial distances from reference moment center and the fan and engine inlets. The number 29.0 is the vertical distance between the fan and engine inlet centerlines. These moments are a pitch up for a positive angle of attack change.

There is also a small pitching moment that exists in the fan system because of partial admission scroll system. Since the fan scroll system exhausts only on about 165 degrees of the fan tip arc, a moment is developed, because part of the nozzle exhaust flow is all cold and the other part is mixed hot and cold. Static test results showed that this moment is proportional to fan speed as follows:

$$m_0 = 0.18 \rho_{10.0} U_T^2 A_F D_F$$

where

$\rho_{10.0}$, U_T , A_F and D_F are expressions that will be described later in this analysis.

If the above forces and moments are assumed to represent all the contributions of the propulsion system, the remainder must be the nacelle contribution plus any interaction effects. Therefore, this part of the total is as follows:

$$\begin{aligned}L_I &= L_B - \Delta L_{FG} \\D_I &= D_B - (D_{FG} + F_{DR}) \\m_I &= m_B - \Delta m_F - \Delta m_E\end{aligned}$$

where

subscript B denotes balance measurements and F_{DR} denotes fan and engine ram drag forces as previously defined.

These remaining lift, drag and moments were then converted to coefficients using:

$$\begin{aligned}C_{LI} &= \frac{L_I}{q_0 A_\pi} \\C_{DI} &= \frac{D_I}{q_0 A_\pi} \\C_{mI} &= \frac{m_I}{q_0 A_\pi D_F}\end{aligned}$$

SPEED RATIO

Analysis of previous fan systems, as well as propellers, shows that speed, both tunnel and rotational, may be correlated using a parameter, $\frac{V_0}{U_T}$, where V_0 is tunnel speed and U_T is rotational tip speed.

In this analysis, the parameter is slightly modified to the following, using Mach numbers rather than speeds:

$$\text{Speed Ratio} = \frac{M_0}{M_T}$$

Both M_0 and M_T have been previously defined.

FAN COEFFICIENTS

Presentation of the test results in coefficient form, using free-stream velocity head as the correlating parameter, has the disadvantage of approaching infinite values at low tunnel speeds. Therefore, a second set or type of coefficient system based on fan parameters is sometimes more applicable in presenting performance. These parameters are defined as follows:

$$H_X = \frac{X}{\rho_{10.0} U_T^2 A_F}$$

where

X may be any force component, such as lift, net thrust or drag.

The density term $\rho_{10.0}$ is total density at the fan inlet and is:

$$\rho_{10.0} = \frac{P_{T10.0}}{R T_{10.0}}$$

The speed parameter, U_T , is fan tip speed and has previously been defined. The area term is fan annulus or thrust area and does not include the hub or turbine tip areas.

When presenting moments in this coefficient system, the length factor is usually taken as fan diameter, such that:

$$H_m = \frac{m}{\rho_{10.0} U_T^2 A_F D_F}$$

NOZZLE AREAS

Nozzle effective area for this system is an important parameter, since the test was one of the first using a confluent exhaust system. This system exhausts both the fan exit and turbojet flows into a single nozzle system. The procedure used in calculating the nozzle areas was to assume no mixing of the two flow streams within the nozzle system.

Nozzle pressure ratio for each flow stream was computed using nozzle base pressure rather than free-stream static pressure. This pressure was used because the nozzle system is not choked, and base pressure determines nozzle flow rather than ambient static pressure. Therefore, the nozzle pressure ratios are:

$$\lambda_{11.0} = \frac{(P_{T11.0}) E}{P_B}$$

$$\lambda_{5.6} = \frac{P_{T5.6}}{P_B}$$

$$P_B = \frac{P_{588} + P_{589} + P_{590}}{3}$$

where

P_{588} , P_{589} , and P_{590} are nacelle afterbody static pressures at one inch forward of the nozzle trailing edge.

These nozzle pressure ratios were then used to compute the ideal flow function for both the fan and fan turbine streams separately using the following relationships:

$$\bar{m} = \frac{W \sqrt{T_T}}{P_T A} = \frac{M \sqrt{\frac{\gamma g}{R}}}{\left[1 + \frac{\gamma-1}{2} M^2 \right]^{\frac{\gamma}{\gamma-1}}}$$

$$\text{and } M = \sqrt{\frac{\gamma-1}{2} \left(\frac{1}{\lambda} \right)^{\frac{\gamma}{\gamma-1}} - 1}$$

The effective flow area for each gas stream is then as follows:

$$A_{e5.6} = \frac{W_{5.1} \sqrt{T_{T5.6}}}{P_{T5.6} \bar{m}_{5.6}}$$

$$\text{and } A_{e11.0} = \frac{W_{10.0} \sqrt{T_{T11.0}}}{(P_{T11.0}) E \bar{m}_{11.0}}$$

The total nozzle effective flow area so reflected in both flow streams is:

$$A_{e12.0} = A_{e5.6} + A_{e11.0}$$

APPENDIX II

TESTS TO MEASURE SOUND VIBRATIONS IN CRUISE FAN INLETS

SUMMARY

Two microphones were installed in the inner wall of the X376 cruise fan model inlet during Phase I testing in the NASA 16-foot transonic tunnel. These microphones measured the time varying component of wall static pressure during windmill operation of the fan up to a tunnel Mach number of 0.8.

The first or second harmonic of the blade passing frequency was the primary disturbance source for the pressure fluctuations. The amplitude of the pressure fluctuation appears to be a linear function of the local dynamic pressure. For this test configuration, the measured pressure fluctuation had an amplitude of approximately 12 percent of the local dynamic pressure.

INTRODUCTION

Theoretical and experimental studies of ducted propellers or fans have indicated that the time-varying component of internal nacelle pressures may be of significant magnitude, as discussed in references 6 and 9. This varying pressure could affect cruise fan design in the areas of fan noise, structural fatigue, and inlet aerodynamics. To appraise the design considerations that should be given to this effect, it is necessary to ascertain the magnitude.

The instantaneous pressure was measured at the inner wall of the nacelle of model 3 during this test. Because this measurement was considered an initial exploratory step in obtaining such data, no attempt is made to determine methods for using the data in cruise fan design; instead, the potential influence on design is implied by the presentation of the data.

METHOD OF TEST

The measurements of instantaneous pressures were made only during the first test series, while running model 3. This model has the medium length inlet, Inlet 2, with a nozzle discharge area of about 96 percent of the fan annulus area.

The inlet is 27 inches long (measured forward from the rotor center line), and two microphones were flush mounted on the inner surface at an axial distance of 13.5 inches forward of the rotor center line. The circumferential locations of the microphones were at 270 degrees and 337.5 degrees. Figure 483 shows the location of the microphones. Details of the nacelle contour are given in Tables I and II.

Test data were obtained during windmilling fan operation over a large range of fan speeds and tunnel Mach number. Table XXI identifies the data points and lists pertinent test parameters.

A schematic of the instrumentation arrangement is shown in Figure 484. The microphones were Brüel and Kjaer Instruments, Incorporated, Model 4134, with a Brüel and Kjaer cathode follower, Model 2615. These microphones have a flat frequency response curve from 20 cycles per second to 20,000 cycles per second, with a basic sensitivity of approximately one millivolt per microbar, as discussed in reference 2. These variable capacitance microphones were chosen because they offer the following advantages:

- o Sensitivity is very good.
- o Electrical noise output is small.
- o Influence of mechanical vibration is small.

The output of the standard variable reluctance fan speed pickup was recorded along with the microphone signals. A sixty-tooth gear on the fan rotor provides the variable gap at the sensor. For the speed pickup signal, one cycle per second is equal to one revolution per minute.

The data were recorded on an Ampex SR-100 tape recorder at a tape speed of 60 inches per second. Microphone signals were de-coupled with an Aerovox, Type P88, 0.1 microfarad capacitor. Tape calibrations were made before and after the test runs.

TEST RESULTS

In presenting the data, the microphones will be identified by their respective circumferential location angles, that is, 270 degrees and 337.5 degrees. The amplitude of pressure variation is recorded as an equivalent voltage based upon microphone sensitivity and recording amplification. The test data shown in the report are presented in terms of this voltage. Figure 485 shows the conversion chart from output voltage to pressure level expressed as decibels. Figure 486 shows a similar conversion chart from output voltage to pressure level expressed in pounds per square inch.

The microphone at position 337.5 degrees was damaged during installation, with the result that its sensitivity was changed. The data from this microphone are presented since the frequency response did not change and since it shows the same trends as does the undamaged microphone. Amplitude values shown for this microphone are low.

Three types of data are presented for each data point:

- o Representative wave forms produced by the pressure signal
- o The overall or combined amplitude of the signal, including the contribution of all frequencies
- o A panoramic analysis of the signal to identify frequencies and the amplitude of each frequency

These data are shown in Figures 487 through 507.

For the wave form oscillograph traces, the tape playback speed was 1.5 inches per second (40 to 1 reduction in tape speed). The oscillograph chart speed was 16 inches per second; thus each inch of chart represents 0.00156 second of microphone data. The reference oscillator signal was recorded at 50 cycles per second, which represents a 2000-cycles-per-second signal when the 40 to 1 reduction factor is considered. Included with each figure of wave form data is the output of the sixty-tooth gear on the fan speed pickup. The wave form of the output from the two microphones is useful in displaying the periodic nature of the signal, but it cannot be used for comparative amplitudes.

The combined signal data and the panoramic analysis data are shown on the same charts, along with a trace showing fan speed in revolutions per minute.

For the frequency analysis data, each frequency sweep shown on the strip charts represents a period of one second. The tape playback was at 60 inches per second. The panoramic frequency chart shows an essentially linear sweep in frequency from the higher value shown at the bottom of the chart to the lower value shown at the top of the chart. The amplitude chart displays the amplitude of each signal component in the range of frequencies covered by the frequency sweep. By reading directly from one chart to the other, the amplitude of any frequency component can be determined. In several cases, the data are shown two times on different frequency sweeps. The 1000-cycles-per-second to 11,000-cycles-per-second frequency is intended to identify blade passing frequency and its harmonics. The 50-cycles-per-second to 2050-cycles-per-second frequency sweep is to show any sources with frequencies that are multiples of the fan rotation speed and result in one, two, three, or more cycles per revolution of the fan.

While examining these data, special attention should be given to the range and scale on each chart. The scale is changed quite often to improve sensitivity.

DISCUSSION

Data from the panoramic frequency analysis were used to identify disturbance sources. For most data points, a predominant frequency can be identified by the corresponding maximum peak in component amplitude. A second and third significant frequency can usually be identified by distinct component amplitude peaks which are somewhat smaller than that of the predominant frequency. Frequencies or modes will be called primary source, secondary source, and third-order source in order of descending amplitude. The most distinct identification of the three named sources can be made in Figure 493. In that figure the primary source has a frequency of about 3500 cycles per second; the secondary source has a frequency of about 1700 cycles per second; the third-order source has a frequency of about 5200 cycles per second.

In Figure 507, data on the three sources are shown along with lines representing the first three harmonics of the blade passing frequency. For the 36-blade fan, the blade passing harmonics are given by:

$$f_n = 0.6 \eta N_F$$

where

- η = order of the harmonic (first, second, third, etc.)
- N_F = fan rotational speed, revolutions per minute
- f_n = harmonic frequency, cycles per second

Examination of Figure 507 shows that the blade passing frequency and its harmonics are identifiable as disturbance sources for the measured pressure fluctuations. Either the first or second harmonic may be the primary source. The decay rate is such that the third harmonic is never greater than a third-order source, while higher harmonics are considered to have a negligible effect.

The data are inconclusive in identifying a predominance of either the first or the second harmonic. At the higher fan speeds, corresponding to higher tunnel Mach numbers, the primary source seems to occur at a lower frequency than the first harmonic. This source is not identified, but two possibilities listed below:

- o Increased turbulence in the boundary layer, perhaps induced by local shocks near the inlet leading edge
- o Reflection from the eight fan frame struts leading to a source of excitation corresponding to 24 cycles per revolution (note the dashed line in Figure 507)

The test data are more difficult to interpret for the high fan speeds. More sources of disturbance seem to be influencing the measurements, and the amplitude distribution changes fairly rapidly with time.

The amplitude of the combined or overall pressure fluctuation and the amplitude of the primary source are shown as a function of tunnel Mach number in Figures 508 and 509. The data in the figures are the same, except that the amplitude is expressed in pounds per square inch in Figure 508 and is expressed in decibels in Figure 509.

Two important points are shown in these figures:

- o The levels of pressure fluctuations measured by the two microphones are different. This difference is largely caused by the damage to the 337.5-degree microphone.
- o The trend of the data shows a relationship to the tunnel Mach number.

Static pressure taps in the nacelle wall at the axial plane of the microphone allow calculation of the dynamic pressure of the inlet airflow at the measuring plane. Figure 510 shows the local dynamic pressure as a function of tunnel Mach number.

Next, the overall level of pressure fluctuation, pounds per square inch, is shown as an essentially linear function of the local dynamic pressure in Figure 511. The data for the 270-degree microphone can be extrapolated to pass through the origin when the local dynamic pressure is zero. Extrapolation of the data from the 337.5-degree microphone does not intersect the origin, which confirms the error in the amplitude data from this microphone.

Referring to the 270-degree curve in Figure 511, it can be seen that for this particular set of conditions:

$$\Delta P \approx K q_L$$

where

ΔP = amplitude of the time-varying component of pressure

q_L = local dynamic pressure

K = slope of curve of ΔP versus q_L (from Figure 511, $K \approx 0.12$)

Referring to Figure 508, the amplitude of the primary source ranges from 40 percent to 50 percent of the amplitude of the overall pressure fluctuation. The part of the overall level which is due to the primary source decreases slightly as the tunnel Mach number increases. This is due to the increasing influence of factors other than fan blading.

It must be remembered that these data are gathered at one location in the nacelle for a fan windmilling case, and the effects of disc loading and tip speed to flight speed ratio have not been included. Many other influences should be investigated before any universally applicable rules can be stated. This is especially true as local air velocities in the nacelle approach the speed of sound.

Model tests could apparently be used to measure this phenomenon at many locations in a nacelle and under varied test conditions to map the locations of any areas of severe pressure fluctuations.

CONCLUSIONS

Either the first or the second harmonic of the blade passing frequency can be the primary source of disturbance for pressure fluctuations measured at the inner wall of a ducted fan nacelle. For this test, the third harmonic had a small effect and higher harmonics were negligible.

The amplitude of pressure fluctuation appears to be a linear function of the local dynamic pressure. The relationship probably depends upon location in the nacelle relative to any struts, distance from blades, disc loading, tunnel Mach number, and aerodynamic effects such as flow separation or shocks. At the 270-degree measuring point, the amplitude of pressure fluctuations was about 12 percent of the local dynamic pressure.

More extensive testing using many sensors and varied test conditions is necessary to experimentally evaluate and understand the entire nature of these pressure fluctuations.

APPENDIX III

MODEL DESCRIPTION

The cruise fan model was designed and assembled by contractor personnel. Fabrication of some model components was by sub-contractors, while others were fabricated by the contractor.

The model was installed in the wind tunnel by NASA and contractor personnel.

The description of the cruise fan model includes all items mounted ahead of the sting attachment face. An assembly drawing is shown in Figure 518.

STING

The sting or support beam (See Figure 512) is cantilevered from the strut head and supports the model in the air stream. The sting is a schedule 80 pipe with a 14-inch outside diameter. A 7-degree angle bend in the vertical plane is necessary to give the angle-of-attack range desired.

At the forward end of the sting, a machined fixture for holding the SRO-1 balance is welded to the pipe. The fixture has an internal taper to match the tapered end of the balance. The taper has a key slot for locking the balance in place. A spanner nut is used to pull the tapered surfaces together, after which the nut is locked to the sting.

Restraining cables are attached to the sting at the center of rotation for the strut system. Cables from each side of the sting are connected to the tunnel tank wall to prevent excessive deflections.

SRO-1 BALANCE

NASA supplied the SRO-1 six-component balance used to measure forces and moments on the cruise fan model. For this test, the balance was calibrated for normal force, axial force, and pitching moment only. The maximum allowable values for these three components are listed below:

Normal Force	-	\pm 15,000 pounds
Axial Force	-	\pm 5,000 pounds
Pitching Moment	-	\pm 25,000 foot-pounds

The forward end of the balance supports the cruise fan model. The balance adapter (Figure 513) slips over the forward end of the balance and is attached to it with 28 bolts. All model forces and moments are transmitted through the balance to the sting.

MAIN FRAME

The main frame (Figures 514 and 519) is a welded steel fabrication which forms the basic model structure. The balance adapter is a shrink fit assembly into the main frame base.

A circular frame above the main frame base supports the X376 fan and provides mounting surfaces for the nacelle inlets and nacelle afterbodies. Support beams running fore and aft of the main frame base support the T58 engine, its inlet, and its cowling.

T58-6A ENGINE (MODIFIED)

A T58-6A engine is modified for use as a core engine in the cruise fan model (Figure 515). This modification includes removing the power turbine and its casing, cutting back the trailing edge of the third stage nozzle diaphragm, and changing the engine lube system. The engine used (SN GE-E200357) and a spare engine (SN GE-E200342) were furnished by NASA-Ames Research Center. Fuel lines, electrical leads, and starter cables are routed through the sting to the engine.

The oil tank is mounted at the aft end of the main frame support beams, and the lines are routed along the beams to the engine. Electric actuators are used for the main and emergency throttles.

Two sections of transition ducting are used to carry the engine discharge gas to the fan. The first section mounts on the aft flange of the second stage nozzle casing. It contains a diffusing cone and anti-swirl vanes. A bellows to allow thermal growth is located at the aft end of the first section and is terminated with a marman flange. The mating second section has provisions for installing an instrument rake, and its aft flange bolts directly to the scroll flange of the fan.

X376

The X376 cruise fan is a slightly modified version of the X376 pitch control fan. The basic X376 fan is a high thrust-to-weight ratio, single stage, tip-turbine-driven lift fan.

The test scroll has a 180-degree active arc with a single inlet. The inlet, originally facing radially away from the fan, is turned 90 degrees to face forward. This allows installation with fan and engine axes parallel, but requires the use of new scroll mounts because of redistributed loading.

The test bulletnose is a Hastelloy "X" spinning which is attached to the fan frame by 24 radial bolts.

The scroll accepts the engine exhaust gas and distributes it through turbine inlet nozzles around the 180-degree admission arc. The front frame

of the fan provides the structural support for the scroll mounts, for fan mounting bosses, and for the rotor bearing sump. The rotor consists of 36 fan blades and the tip mounted turbine. The fan rear frame contains the fan and turbine stator vanes. The fan is shown installed in the main frame in Figure 516.

NACELLE INLETS

The nacelle inlets consist of an aluminum framework, a fiber glass skin, and foam filler material. The aluminum framework has four longitudinal beams which were attached to the mounting surface on the main frame with aluminum angles.

The urethane foam was poured around the aluminum structure, then shaped to the required contours. The fiber glass was formed around the foam after shaping. Wall static pressure taps were installed as the fiber glass was applied.

Three interchangeable nacelle inlets were used. They were designated Type 1, Type 2, and Type 3, with design critical Mach numbers of 0.8, 0.7, and 0.55, respectively. Figure 520 shows the dimensional details of the inlets.

NACELLE AFTERBODIES

Three interchangeable nacelle afterbodies were used during the test. The external contour is a metal spinning of .050-inch-thick AISI 1020 steel. The internal contour on the turbine side of the fan is a spinning of .050-inch-thick 321 stainless steel. A spinning of .050-inch-thick 1020 steel is used as the internal contour on the cold side of the fan. The internal and external skins are fastened to a structural framework consisting of longitudinal stringers contoured to fit the skins and circular rings to provide rigidity. The internal skin on the turbine exhaust side of the fan is fastened to the framework with shoulder bolts and a series of slotted holes to allow for thermal growth. This skin will move relative to the framework and external skin. The entire internal skin is insulated with a 1-inch-thick mineral wool blanket. Three primary longitudinal stringers were used to attach the afterbody to the mounting surface on the main frame. Wall static pressure taps were installed in the external skin during fabrication.

Overlapping strips and nichrome were used to provide a gas seal between the fan rear frame and the front lip of the nacelle afterbody. This same arrangement was used at the slots where the centerbody support struts come through the inner skin.

Figures 521, 522, and 523 show dimensional details of the afterbodies. The external contour is a segment of a circular arc which ends in a boattail angle of 12 degrees, 14.5 degrees, and 10 degrees for Type 1, Type 2, and Type 3, respectively. The internal contours are formed of transition

curves to match the plugs and form a continuously converging flow area which terminates at the required exit diameter.

CENTERBODY PLUGS

The centerbody plugs determine the nozzle exit area when used with a particular afterbody. The contour is shaped to provide a smooth transition from the fan exit area to the required nozzle exit area. All the plugs terminate in a cone of 25 degrees included angle. See Figure 524 for dimensional details.

The plugs were made by pouring urethane foam around an aluminum framework. The foam was shaped to the desired contour and was used as a mandrel for application of the fiber glass skin. Wall static pressure taps were installed in the fiber glass skin.

For assembly purposes, the aft conical section of the plug is removable. The forward structure consists of $\frac{1}{4}$ -inch-thick aluminum plates fastened in a "cross" arrangement. Angles attached to the forward end of these crossed plates are drilled to match the bolt pattern on the support ring. Four radial struts attach the support ring to the main frame.

The forward end of the plug's fiber glass skin slipped over the support ring to match the fan rear frame's hub. When the canister spacers were used, it was necessary to use an aluminum cover to provide a smooth flow path between the plug and the fan. Figure 517 shows a completed plug.

FLOW SPLITTER

To measure fan performance, it is necessary to measure turbine exhaust gas pressure and temperature before the gas mixes with fan exhaust flow. To prevent mixing and to provide support for measuring probes, a sheet metal divider was located directly aft of the fan rear frame box section which separates the fan and the turbine. Circumferentially, the flow splitter spans the active arc of the turbine.

ENGINE INLET AND COWLING

Figure 525 gives dimensional details of the engine inlet. The external contour ends in a 22-inch-diameter circular section. The engine cowl is a 22-inch-diameter cylinder which runs the length of the cruise fan installation, except as modified for fan nacelle fairings.

The engine inlet is formed of a steel cylinder, which forms the internal flow path, load-carrying longitudinal gussets, a circular mounting plate, foam filler material, and fiber glass skin for the external contour. Wall static pressure taps are installed on both the internal and the external walls.

The engine cowling is made of .063-inch-thick 1020 steel rolled into 22-inch-diameter cylinders. These cylinders are made in two halves which meet at a point approximately $3\frac{1}{2}$ inches below the nacelle center line. The cowling is made in several sections to allow access to the engine as desired.

At the aft end of the engine cowling, the outer wall of the oil tank forms the external surface for the lower half. Just aft of the oil tank is a silicone fabric seal which separates the load cell mounted cowling from the sting mounted cowling. A sheet metal cone makes the transition from the Teflon seal to the sting. This cone is mounted directly on the sting.

NACELLE FAIRINGS

The sections of engine cowling which blend with the nacelle inlets are used to support the inlet fairings. The fiber glass fairings are permanently attached to the cowling and one cowling section is available for each inlet.

The afterbody fairing is formed of sheet metal and is bolted directly to both the afterbody and the engine cowling. The afterbody fairing and the inlet fairing meet at the axial station of the fan rotor center line.

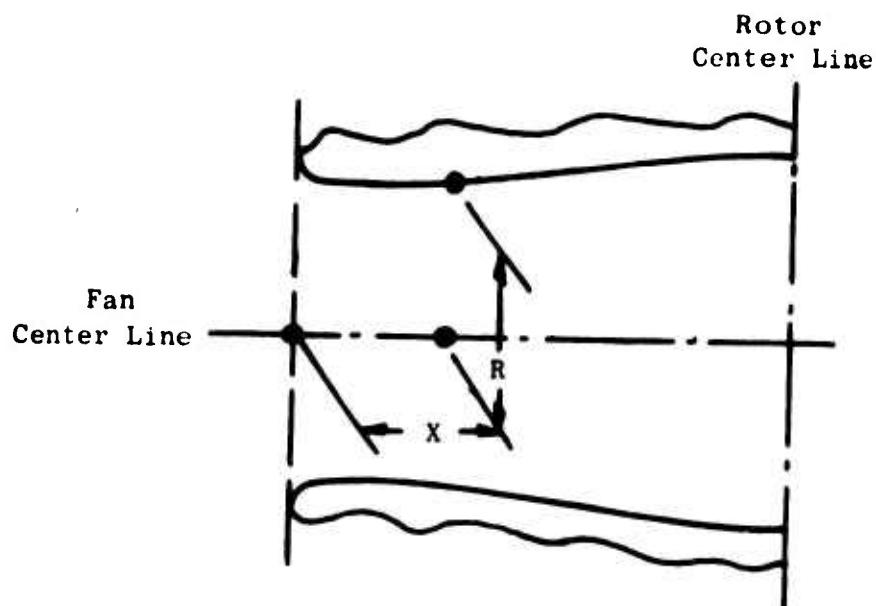
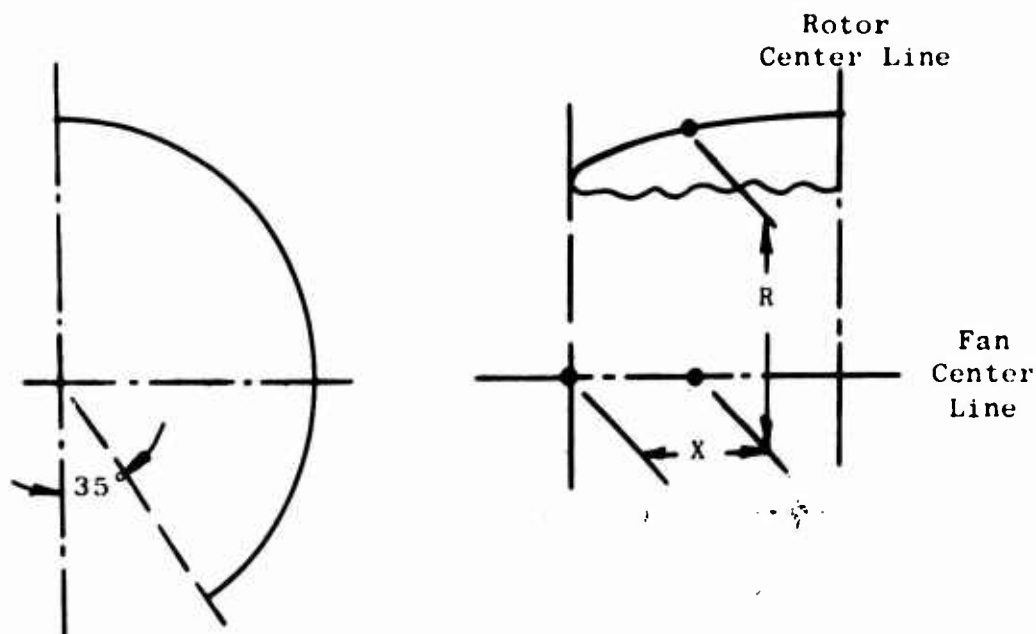


TABLE I
MODEL COORDINATES, INLET COWL INTERNAL SURFACE

Inlet 1		Inlet 2		Inlet 3	
X (inches)	R (inches)	X (inches)	R (inches)	X (inches)	R (inches)
0.0	16.23	0.0	18.17	0.0	20.40
0.50	15.385	0.27	17.44	0.18	19.76
0.98	15.055	0.54	17.16	0.36	19.47
1.47	14.84	0.81	16.95	0.72	19.12
2.94	14.48	1.62	16.52	1.08	18.88
4.76	14.33	2.43	16.27	1.80	18.53
7.35	14.33	4.26	16.09	3.60	18.09
14.70	14.60	8.10	16.36	4.70	18.00
24.50	15.40	13.50	17.15	6.00	18.00
36.75	17.34	20.25	17.96	8.72	18.00
45.72	18.00	23.72	18.00	12.00	18.00
49.00	18.00	27.00	18.00	-	-



(Coordinates applicable ± 145 degrees from vertical; remaining 35 degrees of contour is shown in Table X)

TABLE II
MODEL COORDINATES, INLET COWL EXTERNAL SURFACE

Inlet 1		Inlet 2		Inlet 3	
X (inches)	R (inches)	X (inches)	R (inches)	X (inches)	R (inches)
0.0	16.23	0.0	18.17	0.0	20.40
0.36	16.995	0.20	18.78	0.12	20.94
0.72	17.315	0.40	19.05	0.24	21.21
1.08	17.575	0.60	19.27	0.36	21.40
1.47	17.820	0.81	19.47	0.72	21.98
2.94	18.59	1.62	20.05	1.08	22.25
4.49	19.20	2.43	20.53	1.80	22.84
7.35	20.22	4.05	21.27	3.60	23.86
14.70	21.91	8.10	22.62	6.00	24.66
24.50	23.55	13.50	23.82	9.00	24.98
36.75	24.72	20.25	24.73	11.40	25.00
46.55	24.96	25.65	24.98	12.00	25.00
49.00	25.00	27.00	25.00	-	-

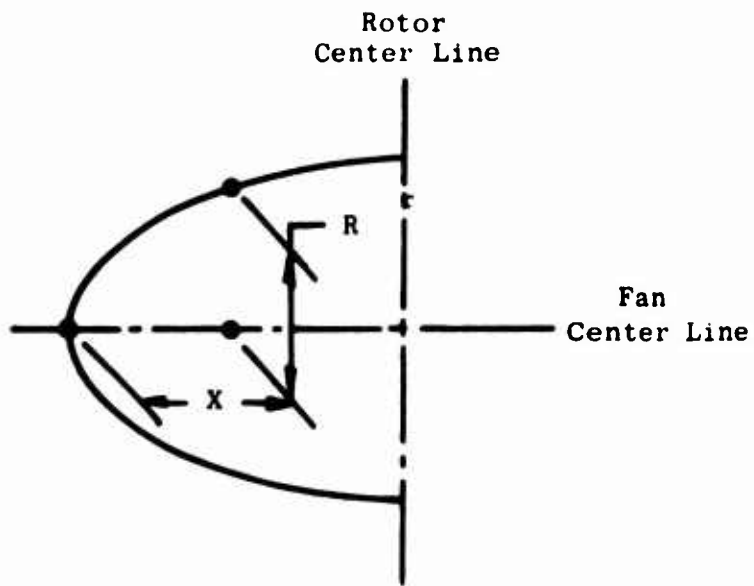
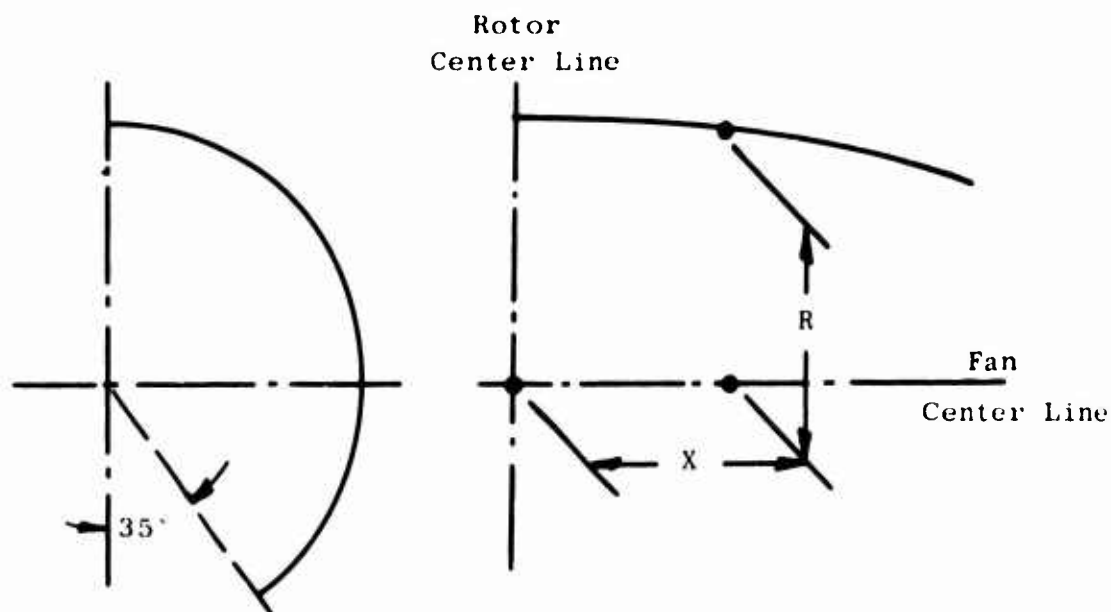


TABLE III
MODEL COORDINATES, FAN BULETNOSE

X (inches)	R (inches)
0.0	0.0
0.46	1.78
0.92	2.34
1.39	2.88
2.31	3.77
4.60	5.16
7.68	6.44
11.53	7.61
14.60	8.0 ^P
16.35	8.10



(Coordinates applicable \pm 145 degrees from vertical; remaining 35 degrees of contour is shown in Table X1)

TABLE IV
MODEL COORDINATES, AFTERBODY OUTER CONTOUR

Afterbody 1		Afterbody 2		Afterbody 4	
X (inches)	R (inches)	X (inches)	R (inches)	X (inches)	R (inches)
0.0	25.00	0.0	25.00	0.0	25.00
5.99	24.92	4.27	24.91	4.27	24.99
11.98	24.71	8.54	24.76	8.54	24.98
20.97	24.12	14.95	24.35	14.95	24.91
29.95	23.24	21.35	23.69	21.35	24.60
41.93	21.58	29.89	22.47	29.89	23.92
45.61	20.94	38.43	20.78	35.00	23.37
53.10	19.47	43.70	19.50	43.7	22.06
54.11	19.30	44.74	19.30	44.7	21.90

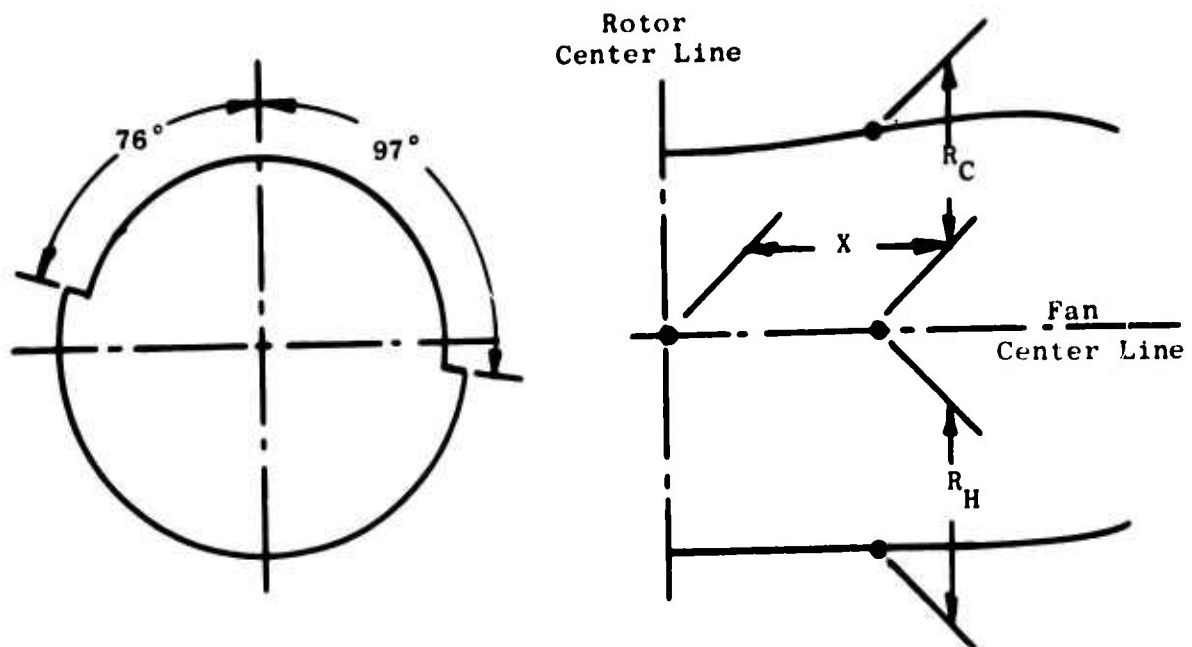


TABLE V
MODEL COORDINATES, NOZZLE OUTER SHROUD

Afterbody 1		
X (inches)	R_C (inches)	R_H (inches)
0.0	18.00	20.82
10.00	18.00	20.82
21.50	18.00	20.82
27.40	18.73	20.82
33.40	19.56	20.82
38.40	19.56	20.82
43.35	20.82	20.82
45.60	20.72	20.72
48.10	20.44	20.44
50.60	19.96	19.96
53.10	19.42	19.42
54.11	19.20	19.20

TABLE V (Continued)
MODEL COORDINATES, NOZZLE OUTER SHROUD

Afterbody 2		
X (inches)	R _C (inches)	R _H (inches)
0.0	18.00	20.82
5.00	18.00	20.82
12.10	18.00	20.82
18.00	18.73	20.82
24.00	19.56	20.82
29.00	20.24	20.82
33.95	20.82	20.82
36.20	20.72	20.72
38.70	20.44	20.44
41.20	19.96	19.96
43.20	19.42	19.42
44.74	19.20	19.20

TABLE V (Continued)
MODEL COORDINATES, NOZZLE OUTER SHROUD

Afterbody 4		
X (inches)	R _C (inches)	R _H (inches)
0.0	18.00	20.82
7.74	18.30	20.82
13.14	19.20	20.82
18.14	20.06	21.12
24.14	21.08	21.62
29.14	21.95	22.20
32.64	22.54	22.56
34.64	22.76	22.76
36.89	22.85	22.85
39.14	22.64	22.64
43.74	21.93	21.93
44.74	21.80	21.80

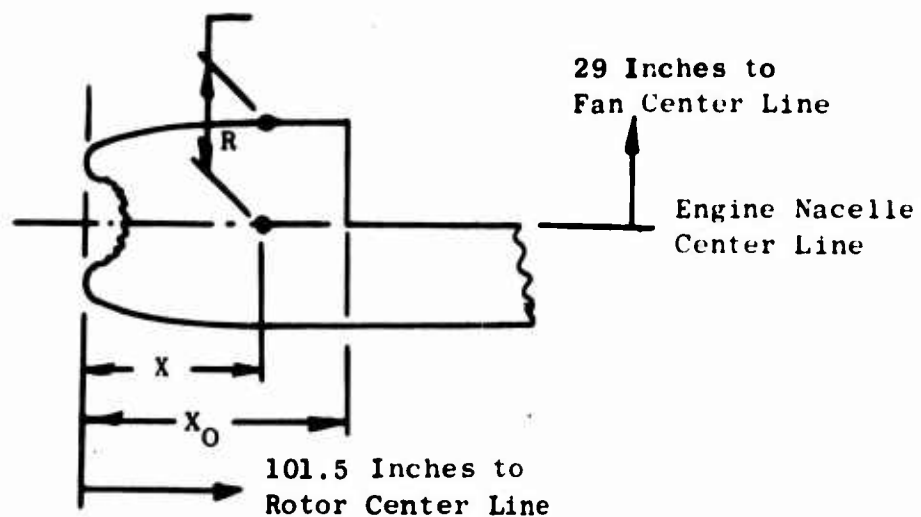


TABLE VI
MODEL COORDINATES, ENGINE COWL OUTER SURFACE

X (inches)	R (inches)
0.0	5.63
1.21	6.95
2.42	7.58
4.85	8.48
9.67	9.64
19.33	10.88
29.00	11.00
167.4	11.00

(From X_0 to end of model, upper 180 degrees of engine cowl is part of engine-fan nacelle fairing. X_0 depends on type of fan inlet as follows:)

TABLE VI (Continued)
MODEL COORDINATES, ENGINE COWL OUTER SURFACE

Fan Inlet Number	X_0 (inches)
1	49.5
2	72.1
3	87.5

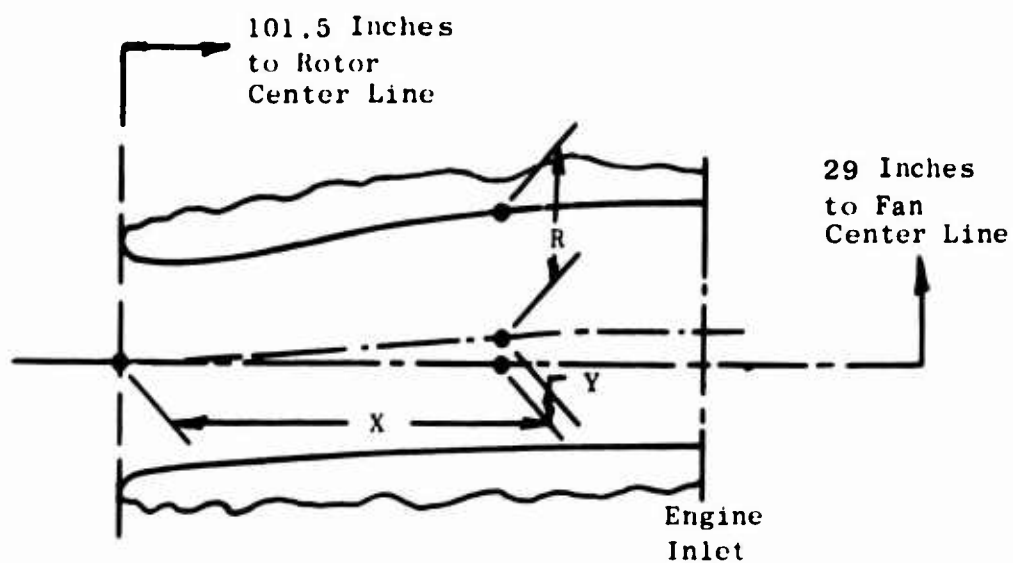


TABLE VII
MODEL COORDINATES, ENGINE INLET INTERNAL SURFACE

X (inches)	Y (inches)	R (inches)
0.0	0.0	5.63
0.4	0.0	5.18
0.8	0.0	5.02
1.25	0.0	4.97
2.40	0.06	4.95
4.85	0.30	5.00
9.65	0.70	5.12
19.30	1.70	5.35
29.20	2.00	5.358

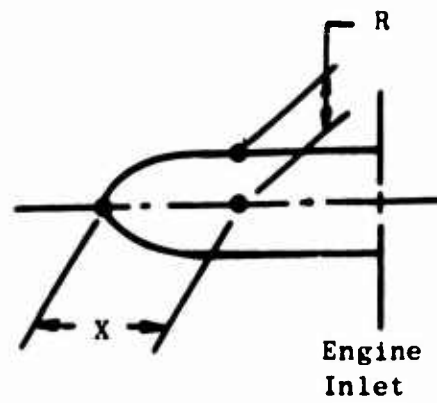


TABLE VIII
MODEL COORDINATES, ENGINE BULLETHNOSE

X (inches)	R (inches)
0	0.0
1	1.50
2	2.00
3	2.30
5	2.50
14	2.50

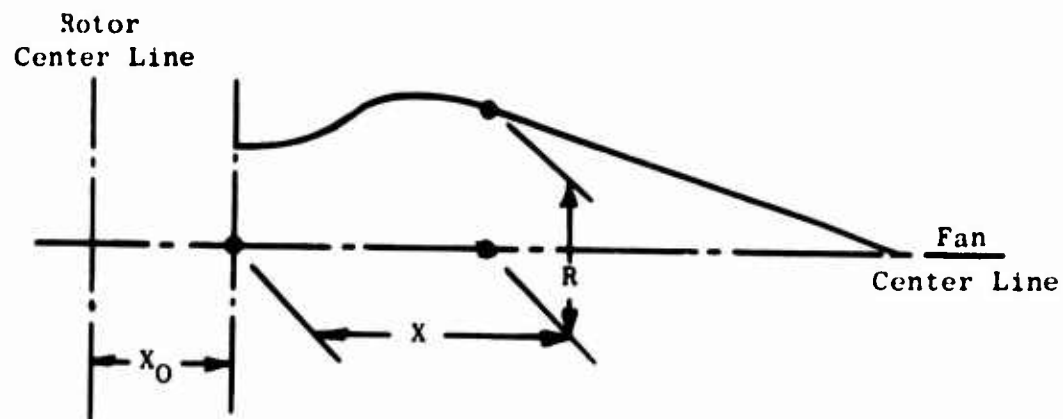


TABLE IX
MODEL COORDINATES, NOZZLE PLUG

Plug 2	
X (inches)	R (inches)
0.00	8.16
5.77	9.49
11.54	11.37
17.31	13.26
23.07	14.94
28.84	14.80
29.80	14.64
30.76	14.46
31.72	14.29
32.68	14.07
33.64	13.85
34.61	13.65
46.15	11.09
57.68	8.53
69.22	5.97
80.76	3.41
96.14	0.00

TABLE IX (Continued)
MODEL COORDINATES, NOZZLE PLUG

Plug 3	
X (inches)	R (inches)
0.00	8.16
6.14	9.74
12.27	11.93
18.41	14.15
24.55	16.02
30.68	15.76
31.70	15.58
32.72	15.37
33.74	15.13
34.77	14.96
35.79	14.74
36.82	14.51
49.09	11.80
61.37	9.07
73.64	6.34
85.92	3.61
102.28	0.00

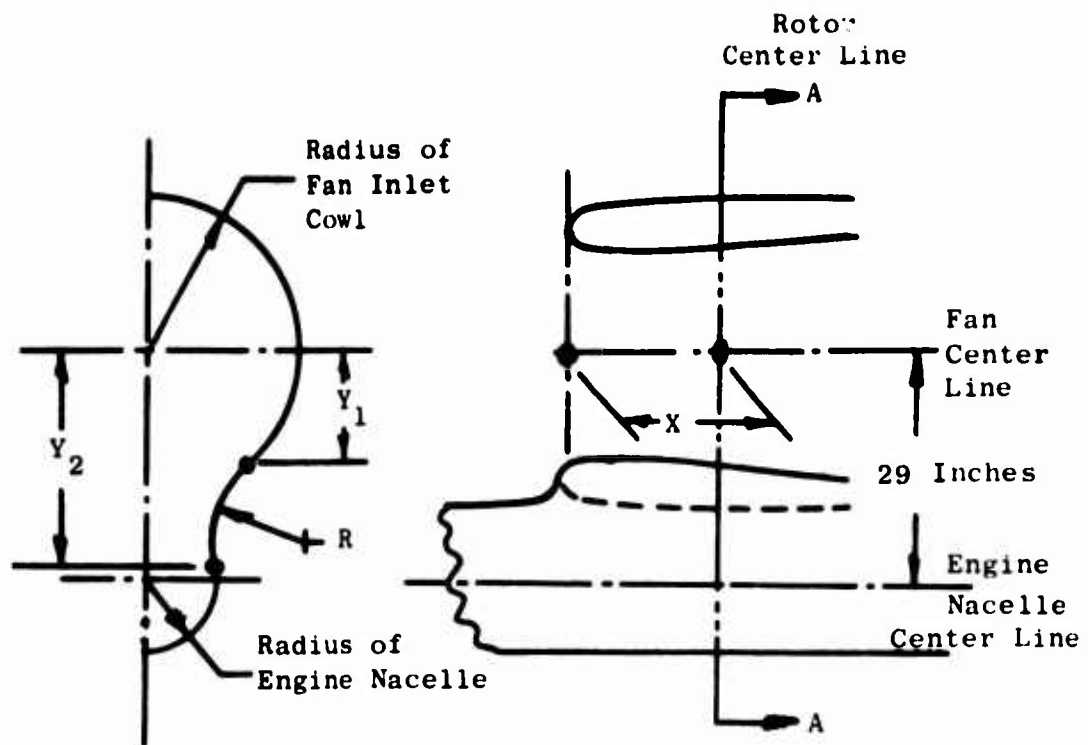
TABLE IX (Continued)
MODEL COORDINATES, NOZZLE PLUG

Plug 4	
X (inches)	R (inches)
0.00	8.16
7.43	9.20
14.90	11.62
22.30	14.12
29.73	16.63
37.18	18.55
38.42	18.61
39.66	18.55
40.90	18.39
42.14	18.14
43.37	17.86
44.60	17.59
59.50	14.39
74.35	10.99
89.20	7.69
104.00	4.41
123.90	0.00

TABLE IX (Continued)
MODEL COORDINATES, NOZZLE PLUG

(X_0 distance is dependent on afterbody-plug combination as follows:)

Plug	Afterbody	X_0 (inches)
2	1	20.33
2	2	10.96
3	1	20.33
3	2	10.96
3	4	10.96
4	4	3.24



(Radius of fairing intersects engine and fan nacelle radii at points Y_1 and Y_2)

TABLE X
MODEL COORDINATES, FAN INLET TO ENGINE NACELLE FAIRING

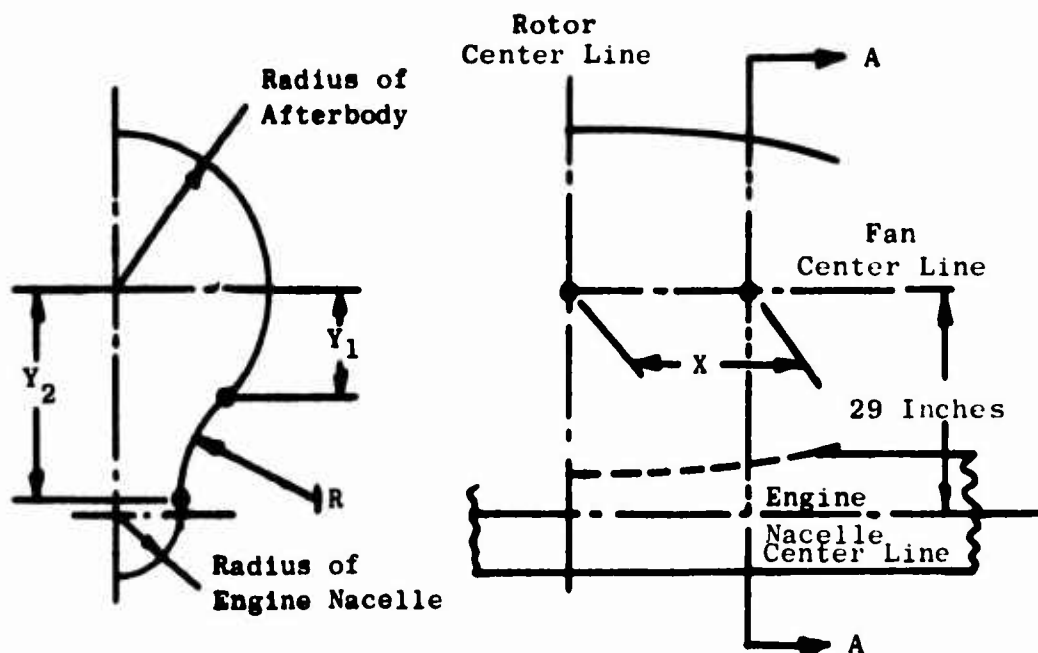
Inlet 1			
X (inches)	Y_1 (inches)	Y_2 (inches)	R (inches)
0.0	16.23	18.00	1.80
1.5	15.08	19.65	2.65
2.9	16.20	20.45	2.70
4.4	16.70	21.05	2.70
7.4	17.10	21.50	2.80
14.7	17.65	22.50	3.30
24.5	18.50	24.50	4.78
36.8	19.40	26.60	7.90
46.6	20.50	28.00	8.20
49.0	20.65	28.10	8.50

TABLE X (Continued)
MODEL COORDINATES, FAN INLET TO ENGINE NACELLE FAIRING

Inlet 2			
X (inches)	Y ₁ (inches)	Y ₂ (inches)	R (inches)
0.00	18.00	18.00	0.0
0.80	16.75	21.00	2.60
1.65	16.90	22.35	3.60
2.45	17.25	22.70	3.86
4.05	17.55	23.15	4.08
8.10	18.05	23.85	4.46
13.50	18.85	25.35	5.64
20.30	19.50	26.85	7.22
25.65	20.25	28.00	7.90
27.00	20.65	28.10	8.50

TABLE X (Continued)
MODEL COORDINATES, FAN INLET TO ENGINE NACELLE FAIRING

Inlet 3			
X (inches)	Y ₁ (inches)	Y ₂ (inches)	R (inches)
0.00	18.00	18.00	0.0
0.35	18.95	22.60	2.46
0.70	19.20	23.20	2.80
1.08	19.40	23.60	3.10
1.78	19.80	24.25	3.44
3.60	20.10	26.05	5.40
6.00	20.20	27.60	7.78
9.00	20.50	27.90	8.10
11.35	20.55	27.95	8.30
12.00	20.65	28.10	8.50



(Radius of fairing intersects afterbody and engine nacelle radii at points Y_1 and Y_2)

TABLE XI
MODEL COORDINATES, AFTERBODY TO ENGINE NACELLE FAIRING

Afterbody 1			
X (inches)	Y_1 (inches)	Y_2 (inches)	R (inches)
0.0	20.65	28.10	8.5
6.0	20.45	28.00	8.3
12.0	20.25	27.90	8.2
21.0	19.75	26.80	7.0
30.0	19.60	26.00	6.0
41.9	19.45	22.70	2.5
45.6	19.35	21.10	1.1
54.11	19.30	19.30	-

TABLE XI (Continued)
MODEL COORDINATES, AFTERBODY TO ENGINE NACELLE FAIRING

Afterbody 2			
X (inches)	Y ₁ (inches)	Y ₂ (inches)	R (inches)
0.0	20.65	28.10	8.5
4.30	20.40	28.65	8.3
8.55	20.25	28.10	8.1
14.95	20.00	27.50	8.0
21.35	19.35	24.30	5.3
29.90	19.30	23.05	4.3
38.40	19.30	21.25	1.3
44.74	19.30	19.30	-

TABLE XI (Continued)
MODEL COORDINATES, AFTERBODY TO ENGINE NACELLE FAIRING

Afterbody 4			
X (inches)	Y ₁ (inches)	Y ₂ (inches)	R (inches)
0.0	20.65	28.10	8.5
4.30	20.60	28.05	8.5
8.60	20.55	28.00	8.5
15.00	20.50	27.95	8.5
21.40	20.75	27.3	6.0
29.90	21.15	24.6	2.2
38.45	21.35	23.15	1.1
44.74	21.90	21.90	0.0

TABLE XII
SURFACE PRESSURE INSTRUMENTATION LOCATION, INLET COWL INTERNAL SURFACE

Inlet 1								
X (inches)	R (inches)	Instrumentation Plane						
		T	U	V	W	X	Y	
0.0	16.23	498	131	132	133	134	135	Leading Edge
0.50	15.385	180	-	-	-	-	-	
0.98	15.055	181	-	-	-	-	-	
1.47	14.84	136	137	138	139	140	-	
2.94	14.48	141	142	143	144	145	146	
4.76	14.33	147	148	149	150	151	-	Throat
7.35	14.33	152	153	154	155	156	157	
14.70	14.60	158	159	160	161	162	-	
24.50	15.40	163	164	165	166	167	168	
36.75	17.34	169	170	171	172	173	-	
45.72	18.00	174	175	176	177	178	179	Fan Inlet

TABLE XII (Continued)
SURFACE PRESSURE INSTRUMENTATION LOCATION, INLET COWL INTERNAL SURFACE

Inlet 2								
X (inches)	R (inches)	Instrumentation Plane						
		T	U	V	W	X	Y	
0.0	18.17	498	-	132	-	134	-	Leading Edge
0.27	17.44	180	-	-	-	-	-	
0.54	17.16	181	-	-	-	-	-	
0.81	16.95	136	-	138	-	140	-	
1.62	16.52	141	-	143	-	145	-	
2.43	16.27	147	-	149	-	151	-	
4.26	16.09	152	-	154	-	156	-	Throat
8.10	16.36	158	-	160	-	162	-	
13.50	17.15	163	-	165	-	167	-	
20.25	17.96	169	-	171	-	173	-	
23.72	18.00	174	175	176	177	178	179	Fan Inlet

TABLE XII (Continued)
SURFACE PRESSURE INSTRUMENTATION LOCATION, INLET COWL INTERNAL SURFACE

Inlet 3								
X (inches)	R (inches)	Instrumentation Plane						
		T	U	V	W	X	Y	
0.0	20.40	498	-	132	134	-	-	Leading Edge
0.18	19.76	180	-	-	-	-	-	
0.36	19.47	136	-	138	140	-	-	
0.72	19.12	141	-	143	145	-	-	
1.08	18.88	147	-	149	151	-	-	
1.80	18.53	152	-	154	156	-	-	Throat
3.60	18.09	158	-	160	162	-	-	
4.70	18.00	153	-	158	157	-	-	
6.00	18.00	163	-	165	167	-	-	
8.72	18.00	174	175	176	177	178	179	

TABLE XIII
SURFACE PRESSURE INSTRUMENTATION LOCATION, INLET COWL EXTERNAL SURFACE

Inlet 1								
X (inches)	R (inches)	Instrumentation Plane						
		A	B	C	D	E	Z	
0.36	16.995	495	-	-	-	-	-	Max. Diameter
0.72	17.315	496	-	-	-	-	-	
1.08	17.575	497	-	-	-	-	-	
1.47	17.820	182	183	184	185	186	187	
2.94	18.59	188	189	190	191	192	-	
4.49	19.20	193	194	195	196	197	198	
7.35	20.22	199	200	201	202	203	-	
14.70	21.91	204	205	206	207	208	209	
24.50	23.55	210	211	212	213	214	-	
36.75	24.72	215	216	217	218	219	220	
46.55	24.96	221	222	223	224	225	-	
49.00	25.00	226	227	228	229	230	231	

TABLE XIII (Continued)
SURFACE PRESSURE INSTRUMENTATION LOCATION, INLET COWL EXTERNAL SURFACE

Inlet 2								
X (inches)	R (inches)	Instrumentation Plane						
		A	B	C	D	E	Z	
0.12	20.94	495	-	-	-	-	-	
0.24	21.21	496	-	-	-	-	-	
0.36	21.40	182	-	184	185	186	-	
0.72	21.98	188	-	190	191	192	-	
1.08	22.25	193	-	195	196	197	-	
1.80	22.84	199	-	201	202	203	-	
3.60	23.86	204	-	206	207	208	-	
6.00	24.66	210	-	212	213	214	-	
9.00	24.98	215	-	217	218	219	-	
11.40	25.00	221	-	223	224	225	-	
12.00	25.00	226	227	228	229	230	231	Max. Diameter

TABLE XIII (Continued)
SURFACE PRESSURE INSTRUMENTATION LOCATION, INLET COWL EXTERNAL SURFACE

Inlet 3								
X (inches)	R (inches)	Instrumentation Plane						
		A	B	C	D	E	Z	
0.12	20.94	495	-	-	-	-	-	
0.24	21.21	496	-	-	-	-	-	
0.36	21.40	182	-	184	185	186	-	
0.72	21.98	188	-	190	191	192	-	
1.08	22.25	193	-	195	196	197	-	
1.80	22.84	199	-	201	202	203	-	
3.60	23.86	204	-	206	207	208	-	
6.00	24.66	210	-	212	213	214	-	
9.00	24.98	215	-	217	218	219	-	
11.40	25.00	221	-	223	224	225	-	
12.00	25.00	226	227	228	229	230	231	Max. Diameter

TABLE XIV
SURFACE PRESSURE INSTRUMENTATION LOCATION, FAN BULLETNODE

X (inches)	R (inches)	Instrumentation Plane		
		V	Y	
0.0	0.0	125	-	Leading Edge
0.46	1.78	101	103	
0.92	2.34	104	106	
1.39	2.88	107	109	
2.31	3.77	110	112	
4.60	5.16	113	115	
7.68	6.44	116	118	
11.53	7.61	119	121	
14.60	8.08	122	124	

TABLE XV
SURFACE PRESSURE INSTRUMENTATION LOCATION, AFTERBODY OUTER CONTOUR

Afterbody 1								
X (inches)	R (inches)	Instrumentation Plane					Z	
		A	B	C	D	E		
0.0	25.00	226	227	228	229	230	231	Max. Diameter
5.99	24.92	232	-	234	235	236	-	
11.98	24.71	237	-	239	240	241	242	
20.97	24.12	243	-	245	246	247	-	
29.95	23.24	248	-	250	251	252	253	
41.93	21.58	254	-	256	257	258	-	
45.61	20.94	259	-	261	262	263	-	
53.10	19.47	588	-	589	590	-	587	

TABLE XV (Continued)
SURFACE PRESSURE INSTRUMENTATION LOCATION, AFTERBODY OUTER CONTOUR

Afterbody 2								
X (inches)	R (inches)	Instrumentation Plane						
		A	B	C	D	E	Z	
0.0	25.00	226	227	228	229	230	231	Max. Diameter
4.27	24.91	232	233	234	235	236	-	
8.54	24.76	237	238	239	240	241	242	
14.95	24.35	243	244	245	246	247	-	
21.35	23.69	248	249	250	251	252	253	
29.89	22.47	254	255	256	257	258	-	
38.43	20.78	259	260	261	262	263	-	
43.70	19.50	588	-	589	590	587	-	

TABLE XV (Continued)
SURFACE PRESSURE INSTRUMENTATION LOCATION, AFTERBODY OUTER CONTOUR

Afterbody 4								
X (inches)	R (inches)	Instrumentation Plane						
		A	B	C	D	E	Z	
0.0	25.00	226	227	228	229	230	231	Max. Diameter
4.27	24.99	232	233	234	235	236	-	
8.54	24.98	237	238	239	240	241	242	
14.95	24.91	243	244	245	246	247	-	
21.35	24.60	248	249	250	251	252	253	
29.89	23.92	254	255	256	257	258	-	
35.00	23.37	259	260	261	262	263	-	
43.70	22.06	588	-	589	590	-	587	

TABLE XVI
SURFACE PRESSURE INSTRUMENTATION LOCATION, NOZZLE OUTER SHROUD

Afterbody 1				
X (inches)	Instrumentation Plane			
	R (inches)	T	R (inches)	X
10.00	18.00	591	-	-
21.50	18.00	592	20.82	102
27.40	18.73	105	20.82	108
33.40	19.56	111	20.82	114
38.40	20.24	117	20.82	120
43.35	20.82	123	20.82	313
45.60	20.72	324	20.72	335
48.10	20.44	347	20.44	348
50.60	19.96	354	19.96	360
53.10	19.42	371	19.42	382

TABLE XVI (Continued)
SURFACE PRESSURE INSTRUMENTATION LOCATION, NOZZLE OUTER SHROUD

Afterbody 2				
X (inches)	Instrumentation Plane			
	R (inches)	T	R (inches)	X
5.00	18.00	591	-	-
12.10	18.00	592	20.82	102
18.00	18.73	105	20.82	108
24.00	19.56	111	20.82	114
29.00	20.24	117	20.82	120
33.95	20.82	123	20.82	313
36.20	20.72	324	20.72	335
38.70	20.44	347	20.44	348
41.20	19.96	354	19.96	360
43.70	19.42	371	19.42	382

TABLE XVI (Continued)
SURFACE PRESSURE INSTRUMENTATION LOCATION, NOZZLE OUTER SHROUD

Afterbody 4				
X (inches)	Instrumentation Plane			
	R (inches)	T	R (inches)	X
7.74	18.30	591	-	-
13.14	19.20	592	20.82	102
18.14	20.06	105	21.12	108
24.14	21.08	111	21.62	114
29.14	21.95	117	22.20	120
32.64	22.54	123	22.56	313
34.64	22.76	324	22.76	335
36.89	22.85	347	22.85	348
39.14	22.64	354	22.64	360
43.74	21.93	371	21.93	382

TABLE XVII
SURFACE PRESSURE INSTRUMENTATION LOCATION, ENGINE NACELLE OUTER CONTOUR

X (inches)	R (inches)	Instrumentation Plane					
		F	G	H	I	J	
0.0	5.63	308	309	310	311	312	Leading Edge
1.21	6.95	349	350	351	352	353	
2.42	7.58	355	356	357	358	359	
4.85	8.48	361	362	363	364	365	
9.67	9.64	366	367	368	369	370	
19.33	10.88	372	373	374	375	376	
29.00	11.00	377	378	379	380	381	
34.00	11.00	383	-	-	384	385	
49.00	11.00	386	-	-	387	388	
64.00	11.00	389	-	-	390	391	
79.00	11.00	392	-	-	393	394	
94.00	11.00	-	-	-	395	396	
109.00	11.00	-	-	-	397	398	
124.00	11.00	-	-	-	399	400	
139.00	11.00	-	-	-	401	402	
154.00	11.00	-	-	-	403	404	Aft Edge of Model

TABLE XVIII
SURFACE PRESSURE INSTRUMENTATION LOCATION, ENGINE NACELLE INNER CONTOUR

X (inches)	R (inches)	Instrumentation Plane					
		L	M	N	O	P	
1.21	4.96	314	315	316	317	318	Engine Inlet
2.42	4.97	319	320	321	322	323	
4.85	5.00	325	326	327	328	329	
9.67	5.12	330	331	332	333	334	
19.33	5.35	336	337	338	339	340	
29.00	5.35	341	342	343	344	345	

TABLE XIX
SURFACE PRESSURE INSTRUMENTATION LOCATION, PLUG CONTOUR

Plug 2					
X (inches)	R (inches)	Instrumentation Plane			
		T	V	X	
0.60	8.16	265	-	266	
5.77	9.49	267	-	268	
11.54	11.39	269	-	270	
17.31	13.26	271	-	272	
23.07	14.94	273	-	274	
28.84	14.80	275	276	277	
29.80	14.64	278	279	280	
30.76	14.46	281	282	283	
31.72	14.29	284	285	286	
32.68	14.07	287	288	289	
33.64	13.85	290	291	292	
34.61	13.65	293	294	295	
46.15	11.09	296	297	298	
57.68	8.53	299	300	301	
69.22	5.97	302	303	304	
80.76	3.41	305	306	307	
96.14	0.00	-	264	-	
Note: Distance from rotor center line is $(X + X_0)$ where X_0 is given in Table IX for each plug-afterbody combination.					

TABLE XIX (Continued)
SURFACE PRESSURE INSTRUMENTATION LOCATION, PLUG CONTOUR

Plug 3					
X (inches)	R (inches)	Instrumentation Plane			
		T	V	X	
0.60	8.16	265	-	266	
6.14	9.74	267	-	268	
12.27	11.93	269	-	270	
18.41	14.15	271	-	272	
24.55	16.02	273	-	274	
30.68	15.76	275	276	277	
31.70	15.58	278	279	280	
32.72	15.37	281	282	283	
33.74	15.13	284	285	286	
34.77	14.96	287	288	289	
35.79	14.74	290	291	292	
36.82	14.51	293	294	295	
49.09	11.80	296	297	298	
61.37	9.07	299	300	301	
73.64	6.34	302	303	304	
85.92	3.61	305	306	307	
102.28	0.00	-	264	-	
Note: Distance from rotor center line is $(X + X_0)$ where X_0 is given in Table IX for each plug-afterbody combination.					

TABLE XIX (Continued)
SURFACE PRESSURE INSTRUMENTATION LOCATION, PLUG CONTOUR

Plug 4					
X (inches)	R (inches)	Instrumentation Plane			
		T	V	X	
0.60	8.16	265	-	266	
7.43	9.20	267	-	268	
14.90	11.62	269	-	270	
22.30	14.12	271	-	272	
29.73	16.63	273	-	274	
37.18	18.55	275	276	278	
38.42	18.61	279	280	281	
39.66	18.55	282	283	284	
40.90	18.39	285	286	287	
42.14	18.14	288	289	290	
43.37	17.86	291	292	293	
44.60	17.59	294	295	296	
59.50	14.39	297	298	299	
74.35	10.99	300	301	302	
89.20	7.69	303	304	305	
104.00	4.41	306	307	308	
123.90	0.00	-	264	-	
Note: Distance from rotor center line is $(X + X_0)$ where X_0 is given in Table IX for each plug-afterbody combination.					

TABLE XX
GAS STREAM PRESSURE INSTRUMENTATION LOCATION - STATION 2.0

R (inches)	Instrumentation Plane					
	L'		N'		P'	
	Total Press.	Static Press.	Total Press.	Static Press.	Total Press.	Static Press.
5.228	411	-	418	-	425	-
4.988	412	-	419	-	426	-
4.598	413	432	420	435	427	438
4.038	414	433	421	436	428	439
3.328	415	434	422	437	429	440
2.878	416	-	423	-	430	-
2.618	417	-	424	-	431	-
Engine Compressor Inlet - Station 2.0 (77.45 inches forward of rotor center line). Hub Radius = 2.50 inches Tip Radius = 5.358 inches						

TABLE XX (Continued)
GAS STREAM PRESSURE INSTRUMENTATION LOCATION - STATION 5.1

R (inches)	Instrumentation Plane	
	L Total Press.	P Total Press.
2.185	407	410
3.785	406	409
4.885	405	408
Engine Turbine Discharge - Station 5.1. Radius = 5.30 inches		

TABLE XX (Continued)
GAS STREAM PRESSURE INSTRUMENTATION LOCATION - STATION 5.6

Plane	
V '	543
W	544
W '	545
X	546
X '	547
A '	548
A ' '	549
Y	550
<p>Fan Turbine Discharge - Station 5.6 (12.12 inches aft of rotor center line).</p> <p>Probes located on radius of 19.85 inches</p> <p>Hub Radius = 18.96 inches</p> <p>Tip Radius = 20.82 inches</p>	

TABLE XX (Continued)
GAS STREAM PRESSURE INSTRUMENTATION LOCATION - STATION 10.0

Radius (inches)			Instrumentation Plane							
Inlet 1	Inlet 2	Inlet 3	U		W		A'		B'	
			Total Press.	Static Press.	Total Press.	Static Press.	Total Press.	Static Press.	Total Press.	Static Press.
17.64	17.60	18.12	-	-	499	-	503	-	491	-
17.44	17.40	17.92	-	-	500	-	504	-	492	-
17.26	17.22	17.74	-	-	501	-	505	-	493	-
17.07	17.03	17.55	-	-	502	-	506	-	494	-
16.31	16.31	16.31	441	465	447	471	453	477	459	483
15.09	15.09	15.09	442	466	448	472	454	478	460	484
13.78	13.78	13.78	443	467	449	473	455	479	461	485
12.32	12.32	12.32	444	468	450	474	456	480	462	486
10.67	10.67	10.67	445	469	451	475	457	481	463	487
8.72	8.72	8.72	446	470	452	476	458	482	464	488
6.87	6.87	6.87	126	-	-	-	-	-	-	-
6.69	6.69	6.69	127	-	-	-	-	-	-	-
6.52	6.52	6.52	128	-	-	-	-	-	-	-
6.34	6.34	6.34	129	-	-	-	-	-	-	-
Fan Rotor Inlet - Station 10.0 (9.25 inches forward of rotor center line).										
Hub Radius			Inlet 1	Inlet 2	Inlet 3					
			6.22	6.22	6.22					
Tip Radius			17.76	17.72	18.24					

TABLE XX (Continued)
GAS STREAM PRESSURE INSTRUMENTATION LOCATION - STATION 10.6

R (inches)	Instrumentation Plane				
	U'	W'	A'	B'	
17.69	561	567	573	579	
16.44	562	568	574	580	
15.00	563	569	575	581	
13.50	564	570	576	582	
11.75	565	571	577	583	
9.26	566	572	578	584	
Fan Rotor Discharge - Station 10.6 (2 inches aft of rotor center line).					
Hub Radius = 8.10 inches					
Tip Radius = 18.00 inches					

TABLE XX (Continued)
GAS STREAM PRESSURE INSTRUMENTATION LOCATION - STATION 11.0

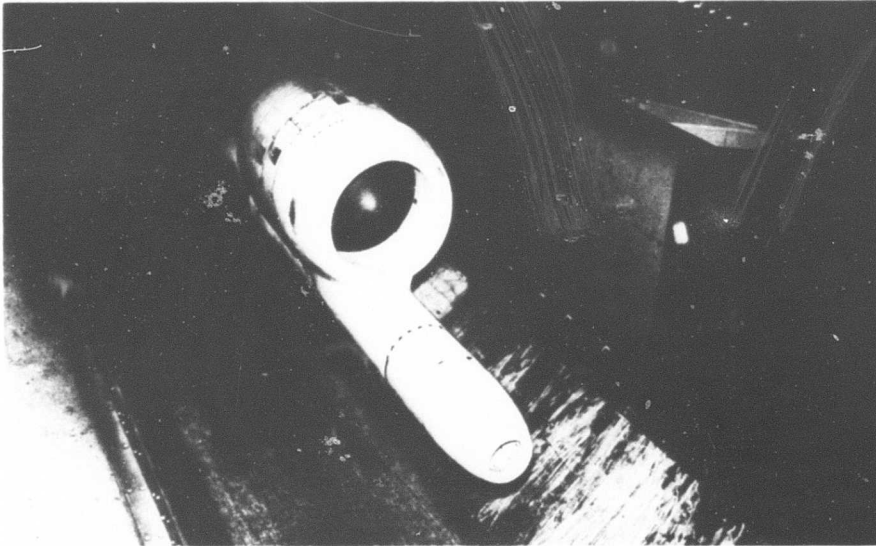
Configuration						Instrumentation Plane			
X-1-2	X-1-3	X-2-2	X-2-3	X-4-3	X-4-4	U'	W'	A'	B'
		Radius (inches)							
17.88	17.88	17.88	17.88	18.91	18.91	-	539	-	531
17.68	17.68	17.68	17.68	18.53	18.71	-	540	-	532
17.50	17.50	17.50	17.50	18.34	18.53	-	541	-	533
17.31	17.31	17.31	17.31	17.41	18.34	-	542	-	534
16.75	16.75	16.62	16.62	16.47	17.41	507	513	519	525
15.56	15.56	15.41	15.42	15.28	16.47	508	514	520	526
14.32	14.32	14.15	14.15	14.05	15.25	509	515	521	527
12.82	12.82	12.67	12.66	12.54	13.96	510	516	522	528
11.83	11.83	11.15	11.13	11.03	12.40	511	517	523	529
9.19	9.19	8.98	8.95	8.96	10.84	512	518	524	530
8.87	8.87	8.96	9.00	9.00	11.38	-	535	-	-
8.69	8.69	8.77	8.81	8.81	11.19	-	536	-	-
8.48	8.48	8.60	8.63	8.63	11.01	-	537	-	-
8.28	8.28	8.39	8.43	8.43	10.81	-	538	-	-
8.16	8.16	8.27	8.31	8.31	9.69	Hub Radius			
18.00	18.00	18.00	18.00	19.03	19.03	Tip Radius			
Fan Stage Discharge - Station 11.0 (12.1 inches aft of rotor center line).									

TABLE XX (Continued)
GAS STREAM PRESSURE INSTRUMENTATION LOCATION - STATION 14

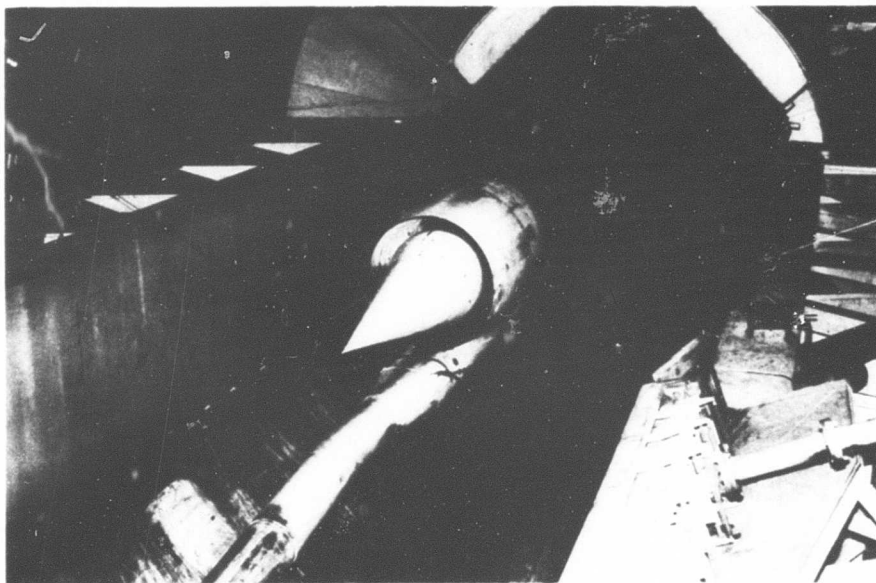
Instrumentation Plane	
F	549
G	550
H	551
I	552
J	553
J	554
K	555
K	556
Model Base at Sting Support - Station 14.0 (65.9 inches aft of rotor center line).	

TABLE XXI
SUMMARY OF TEST POINTS DURING NOISE STUDIES - MODEL 3

Point No.	Mach No. M_0	Fan Speed (rpm)	Blade Tip Mach No. (Rotational)	Fan Face Mach No. M_0	Blade Passing Frequency (cps)
1	0.30	1900	0.283	0.216	1140
2	0.40	2450	0.347	0.285	1470
3	0.50	2950	0.414	0.344	1770
4	0.60	3410	0.477	0.394	2045
5	0.70	3760	0.519	0.423	2255
6	0.80	4050	0.550	0.444	2430
7	0.30	1920	0.283	0.215	1152
8	0.30	2000	0.294	0.217	1200
Fan - X376 Cruise Fan Blade Tip Diameter - 36.0 inches Rotor Hub Diameter - 16.1 inches Number of Blades - 36					



a. Front View of Model 3



b. Rear View of Model 3

Figure 1. Typical Model Mounted in Test Section of Langley 16-Foot Tunnel.

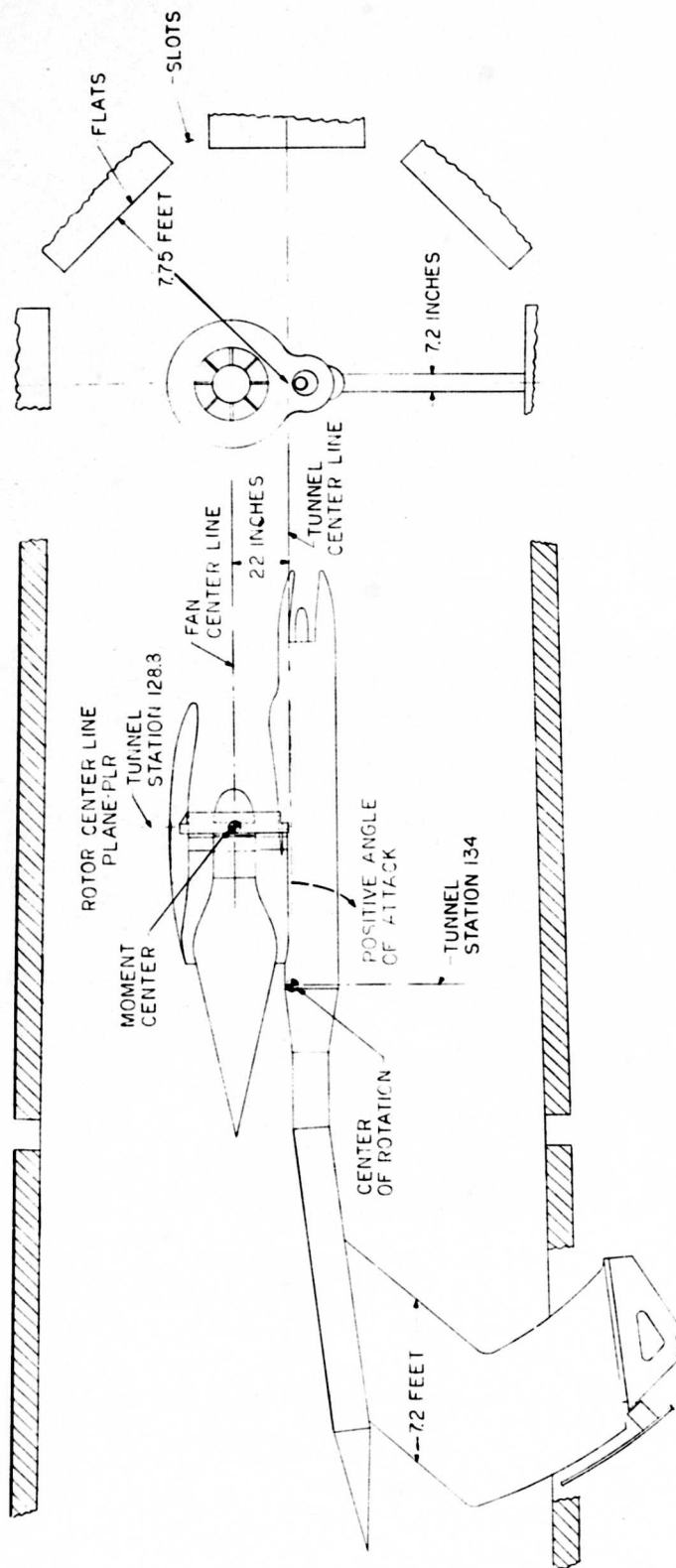


Figure 2. Installation Drawing of Model in Wind Tunnel.

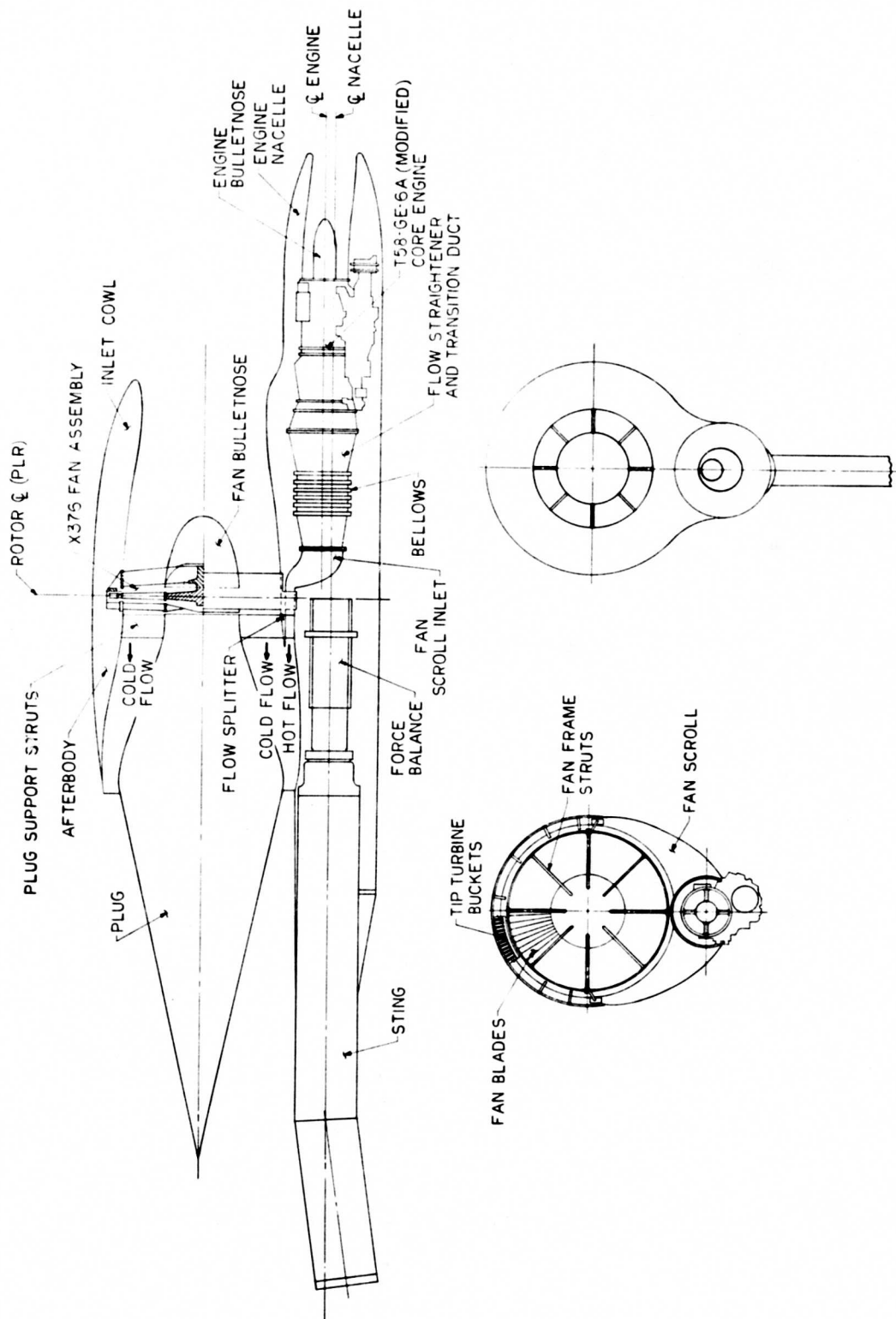


Figure 3. Cruise Fan Model Nomenclature.

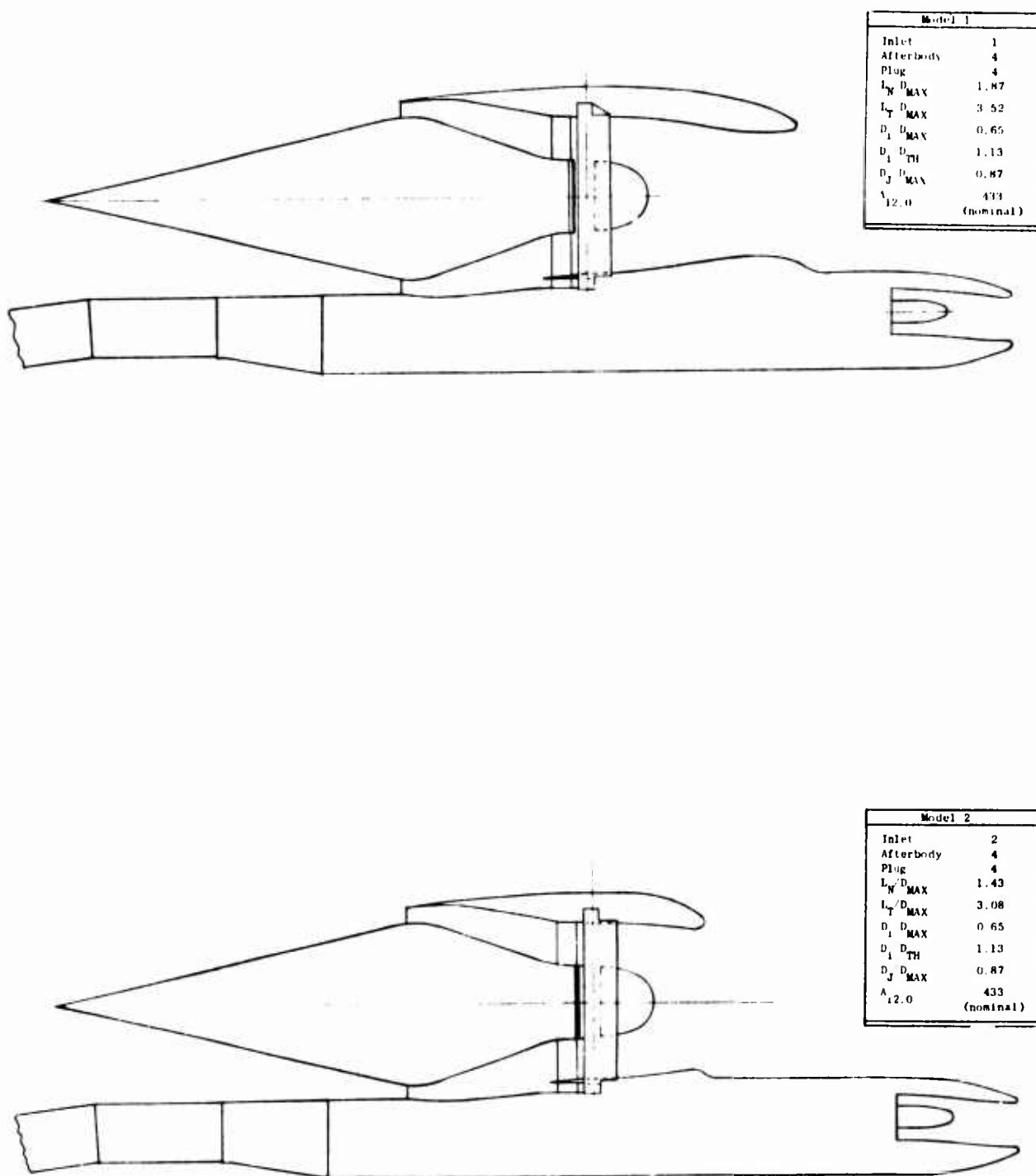


Figure 4. Geometry and Dimensional Data for Models 1 and 2.

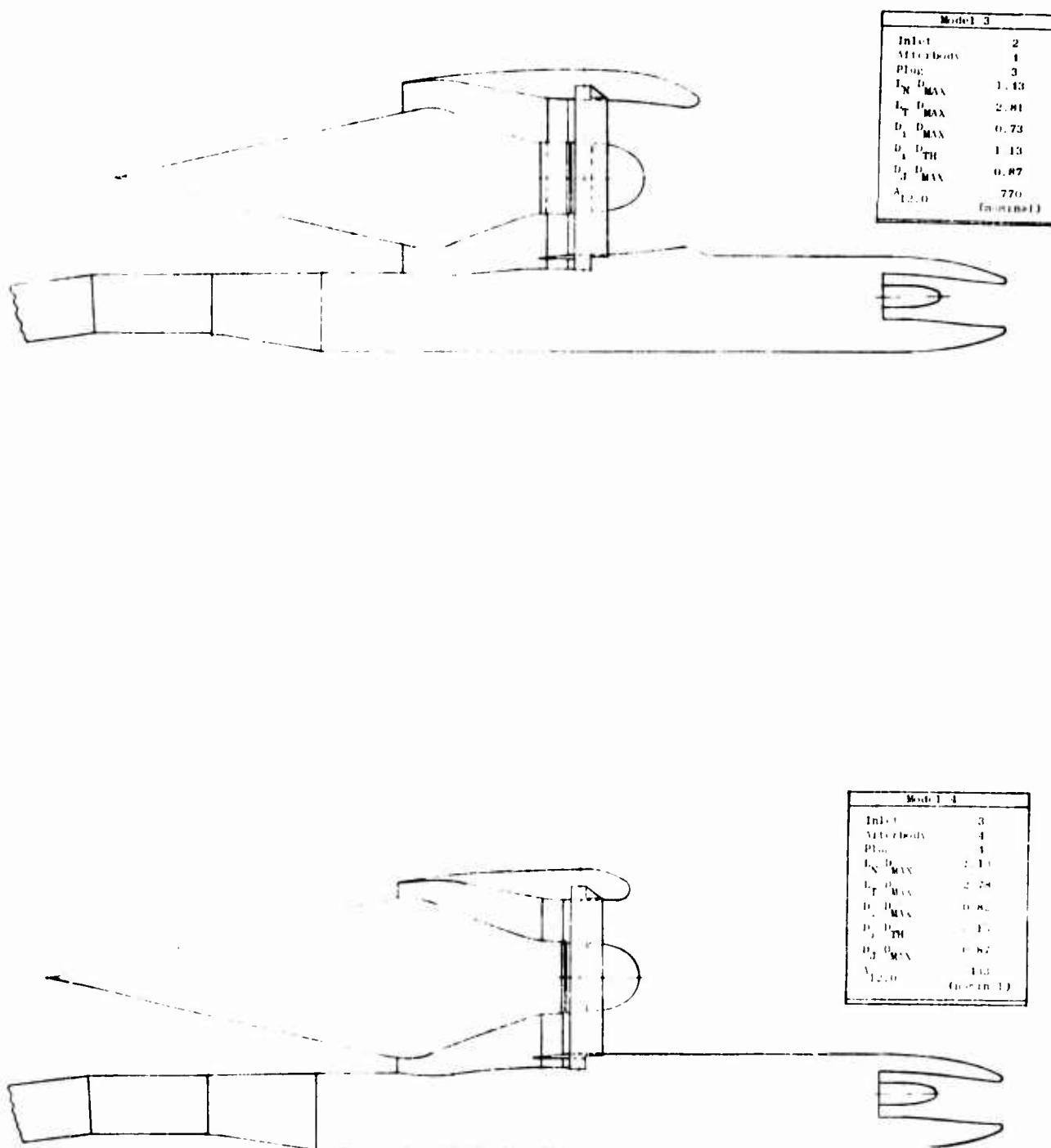


Figure 5. Geometry and Dimensional Data for Models 3 and 4.

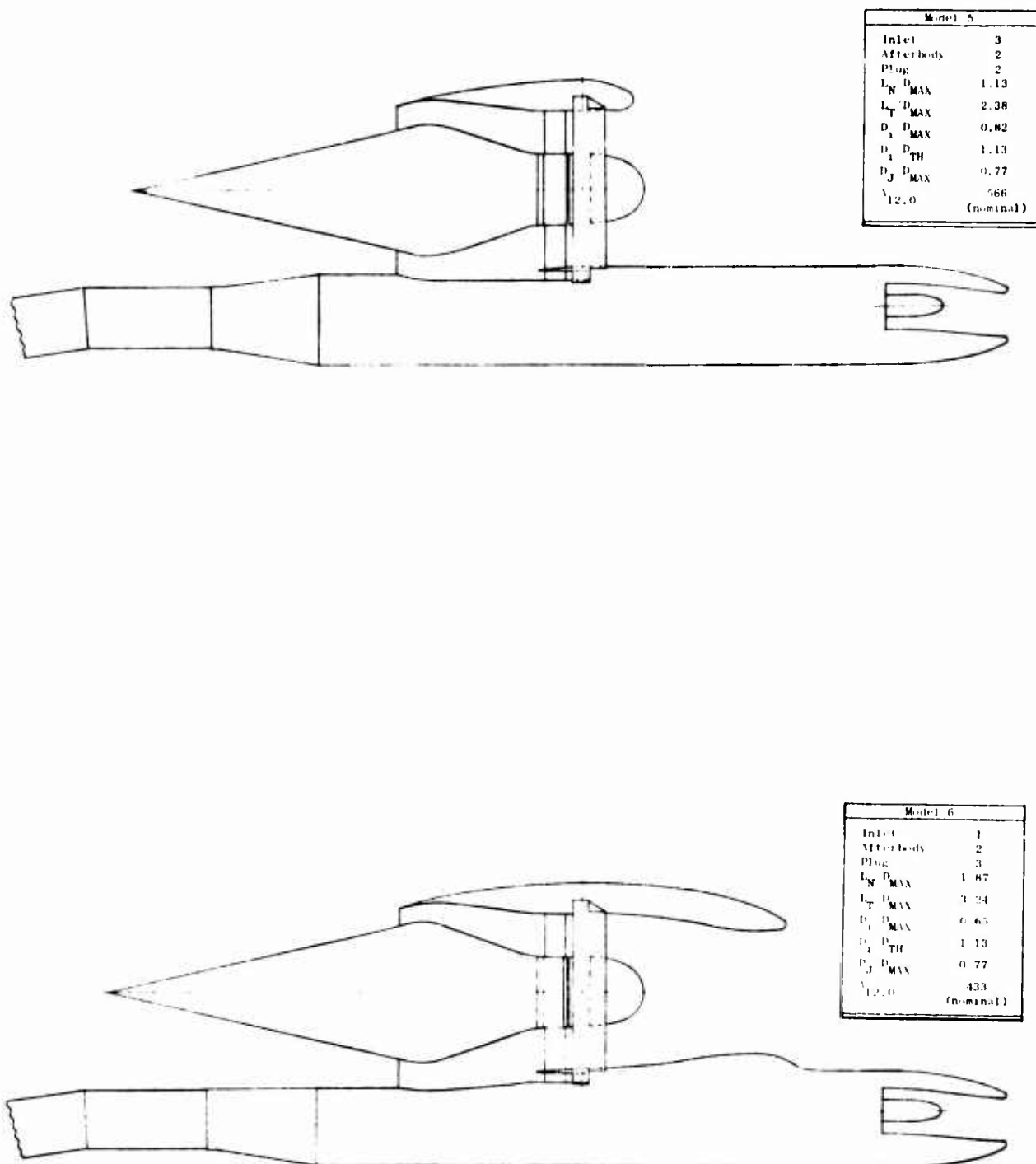


Figure 6. Geometry and Dimensional Data for Models 5 and 6.

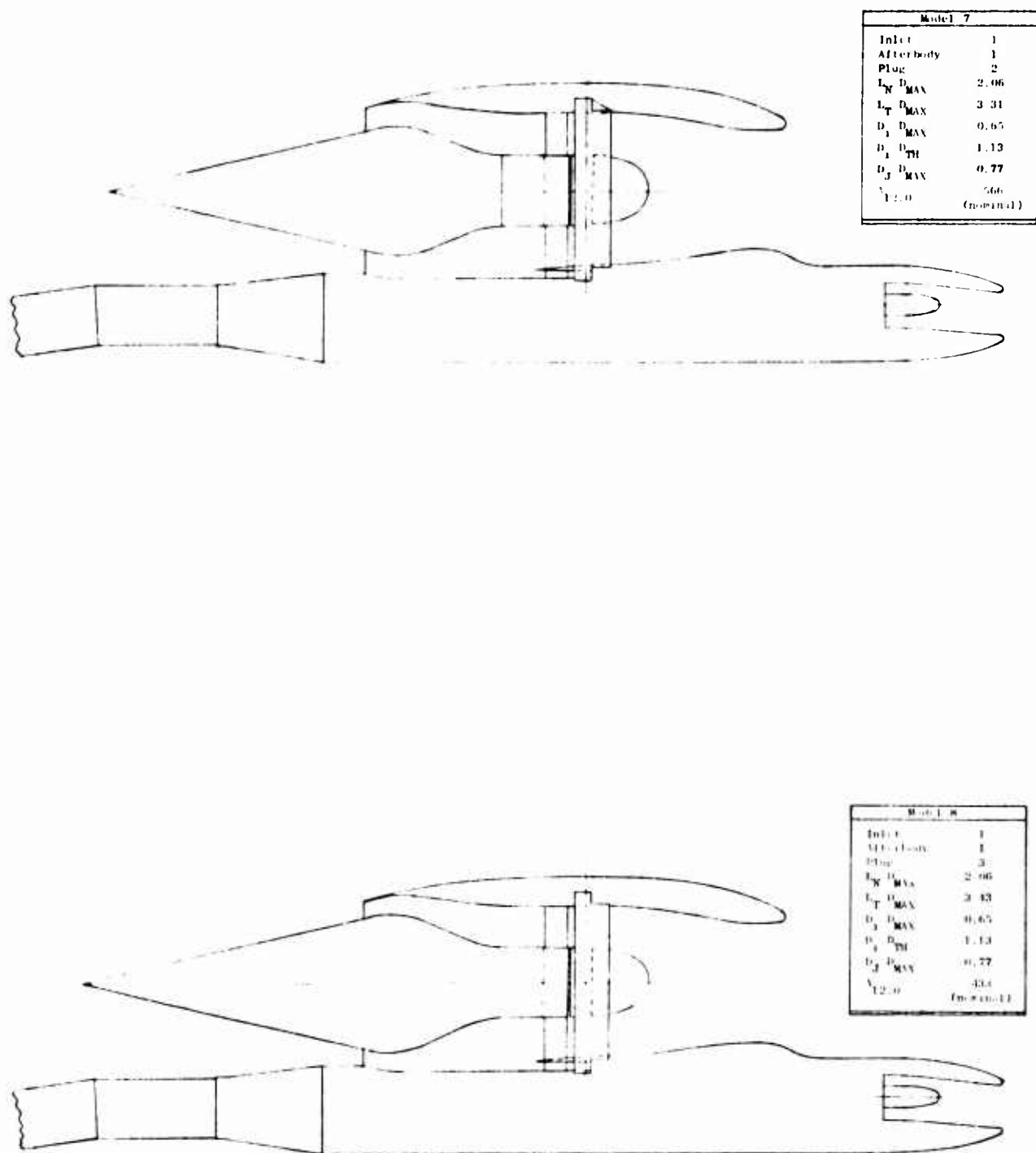


Figure 7. Geometry and Dimensional Data for Models 7 and 8.

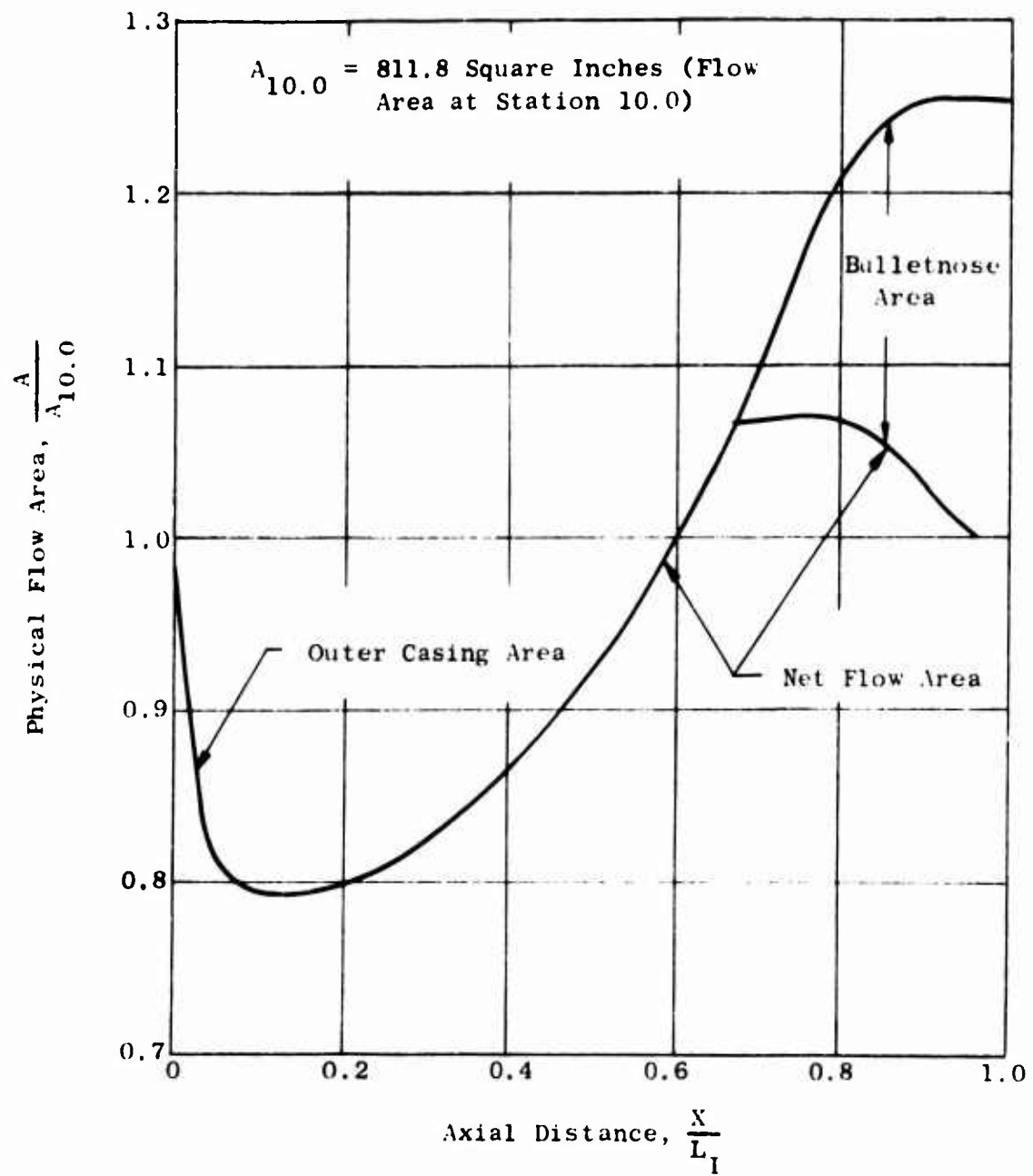


Figure 8. Internal Area Distribution - Inlet 1.

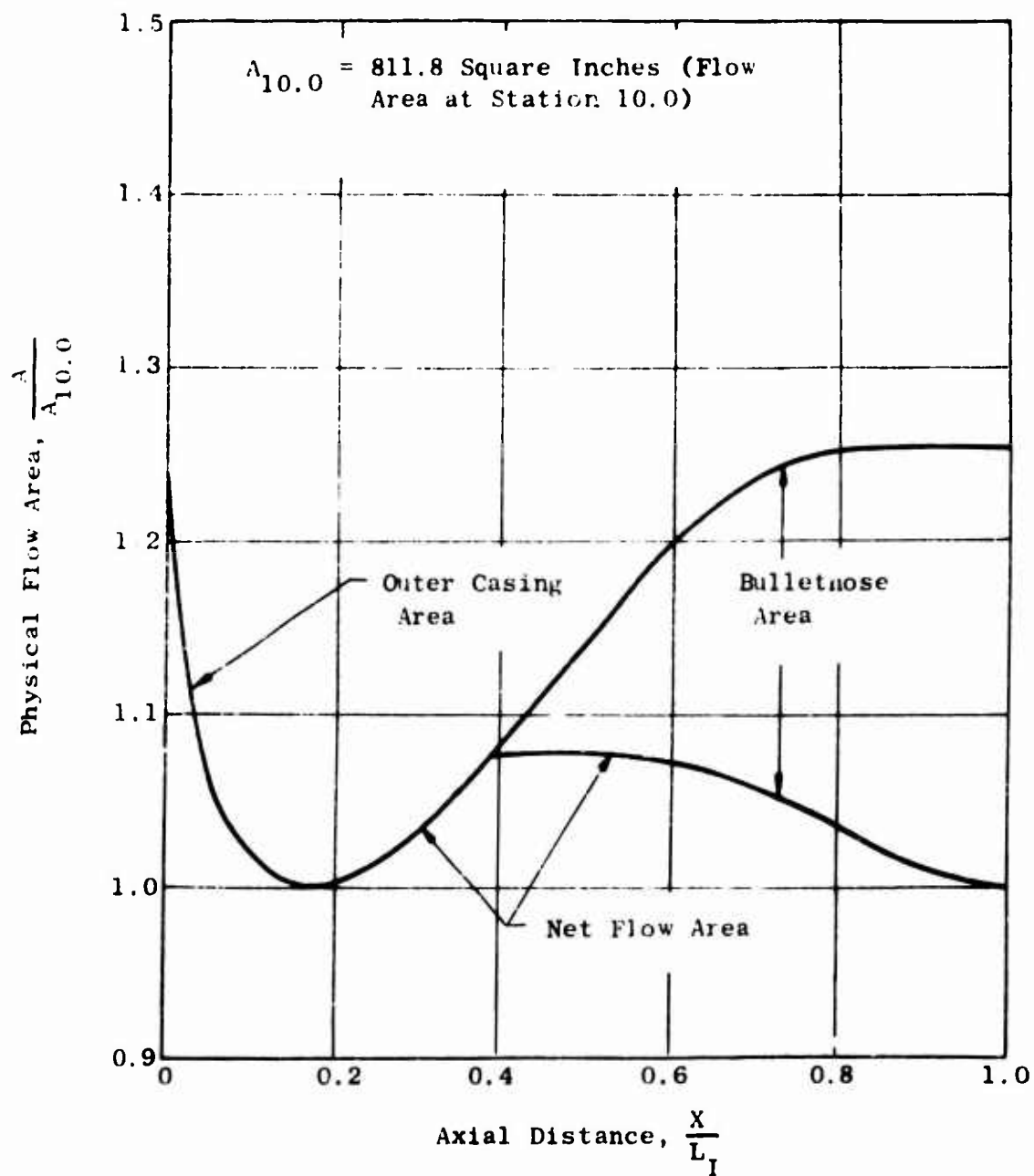


Figure 9. Internal Area Distribution - Inlet 2.

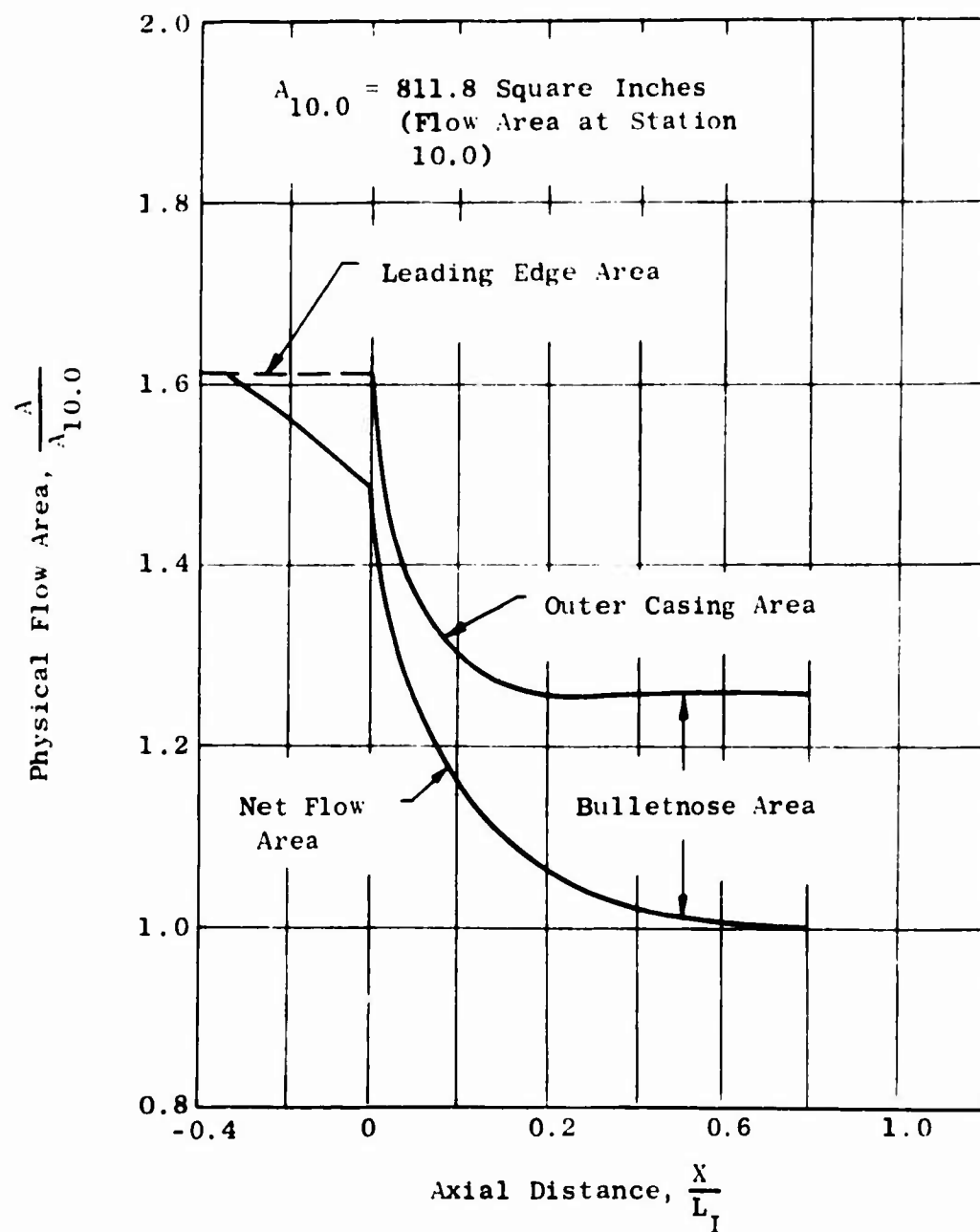


Figure 10. Internal Area Distribution - Inlet 3.

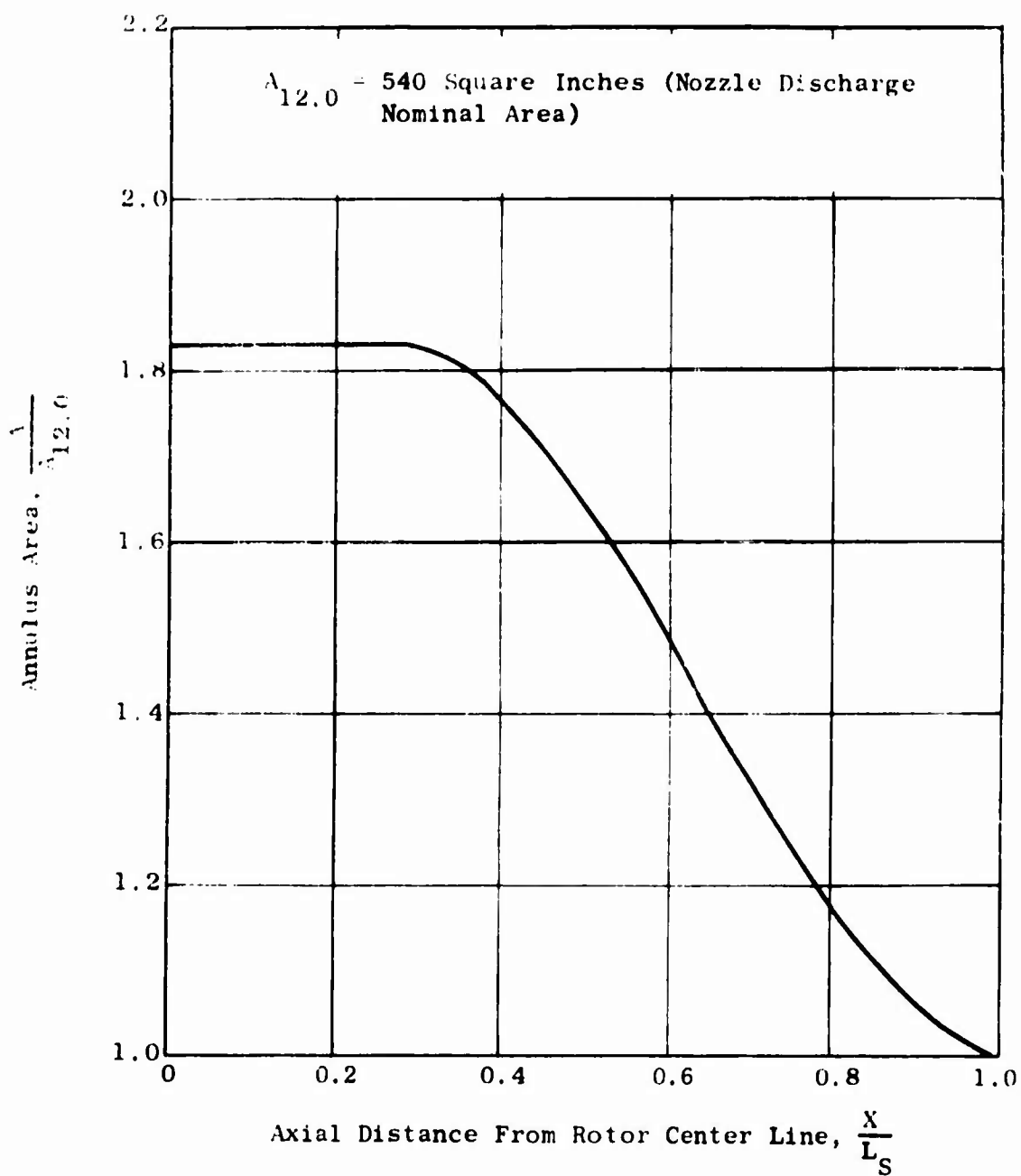


Figure 11. Nozzle Area Distribution for Model Using Afterbody 1 and Plug 2.

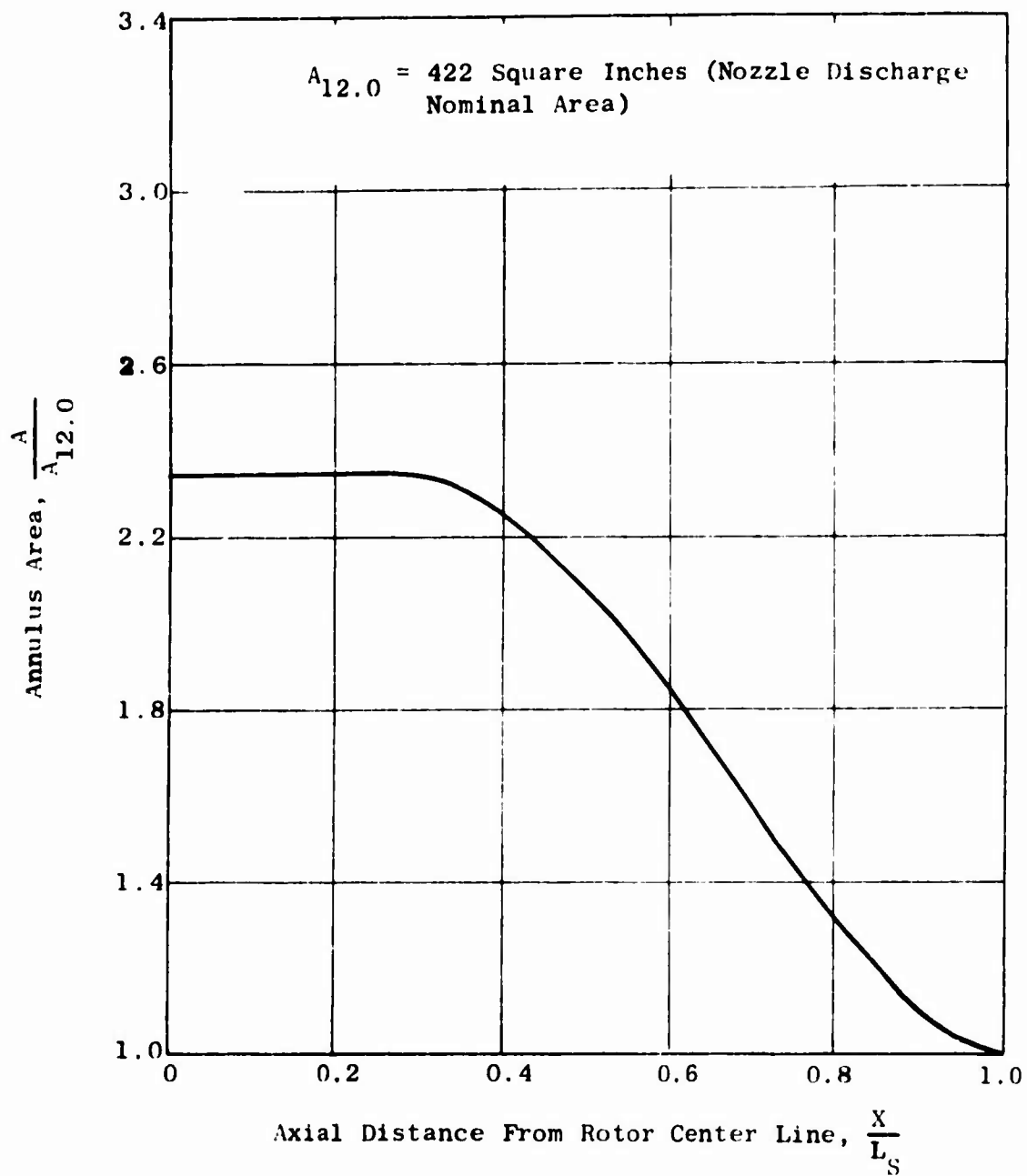


Figure 12. Nozzle Area Distribution for Model Using Afterbody 1 and Plug 3.

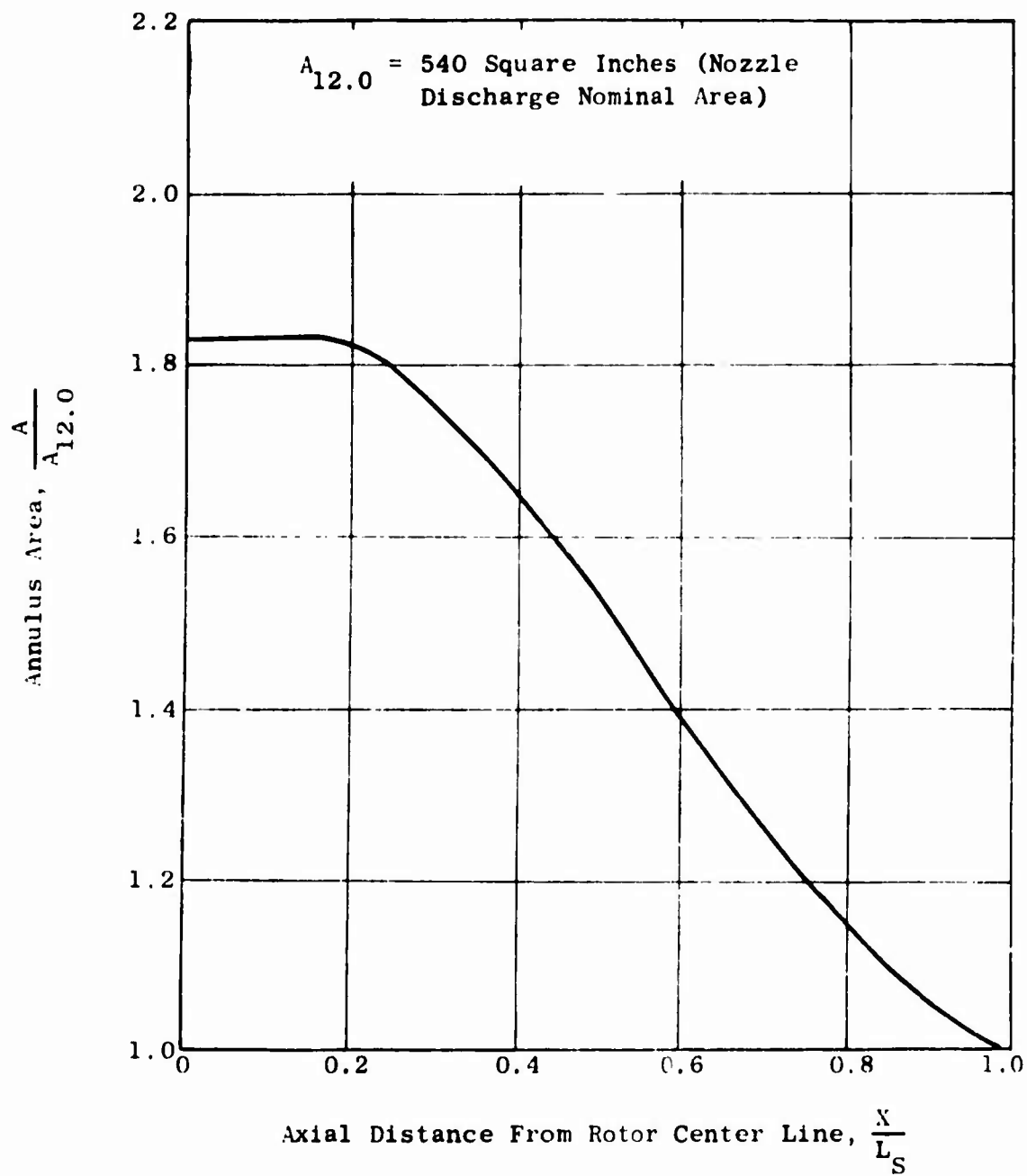


Figure 13. Nozzle Area Distribution for Model Using Afterbody 2 and Plug 2.

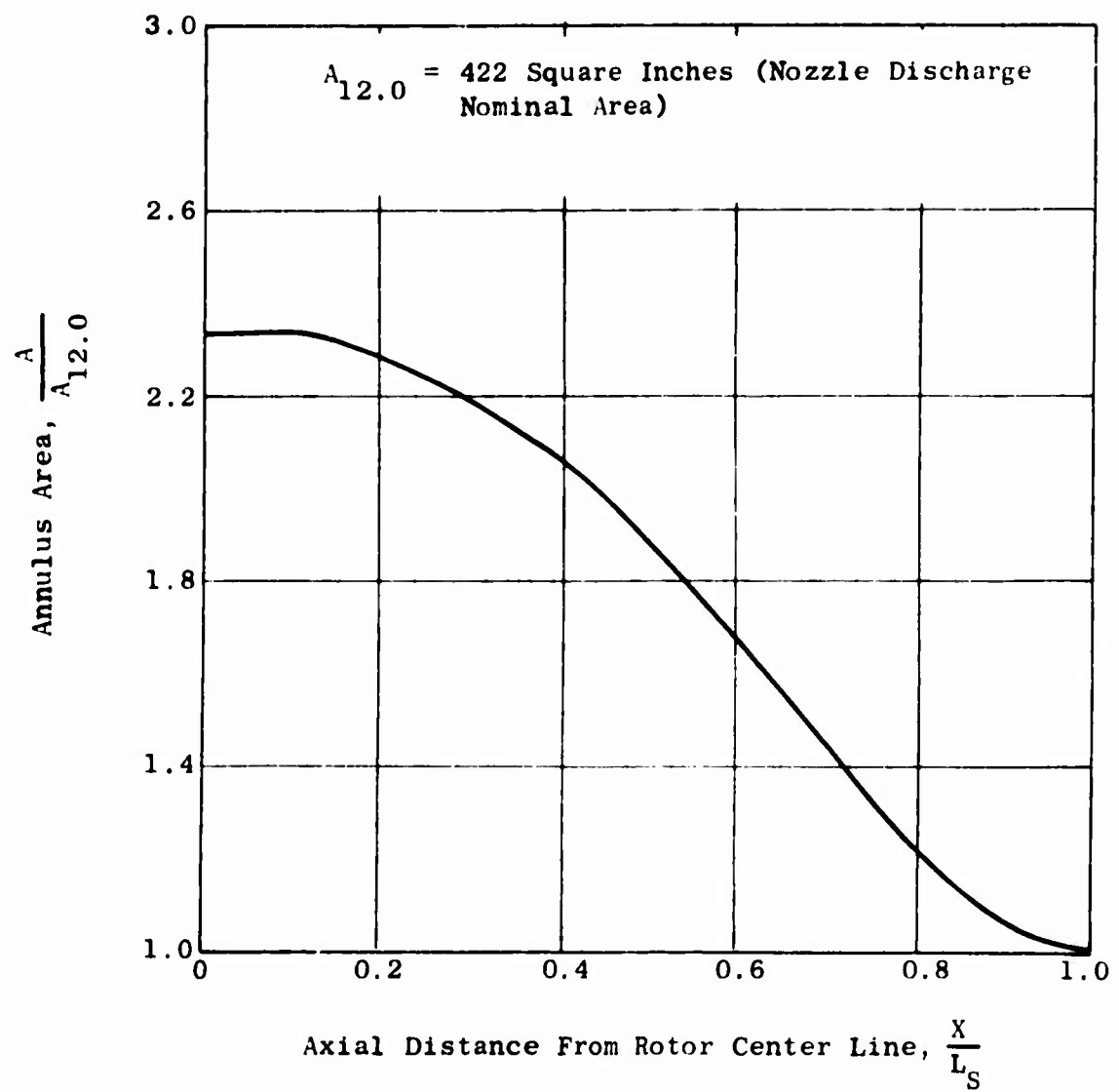


Figure 14. Nozzle Area Distribution for Model Using Afterbody 2 and Plug 3.

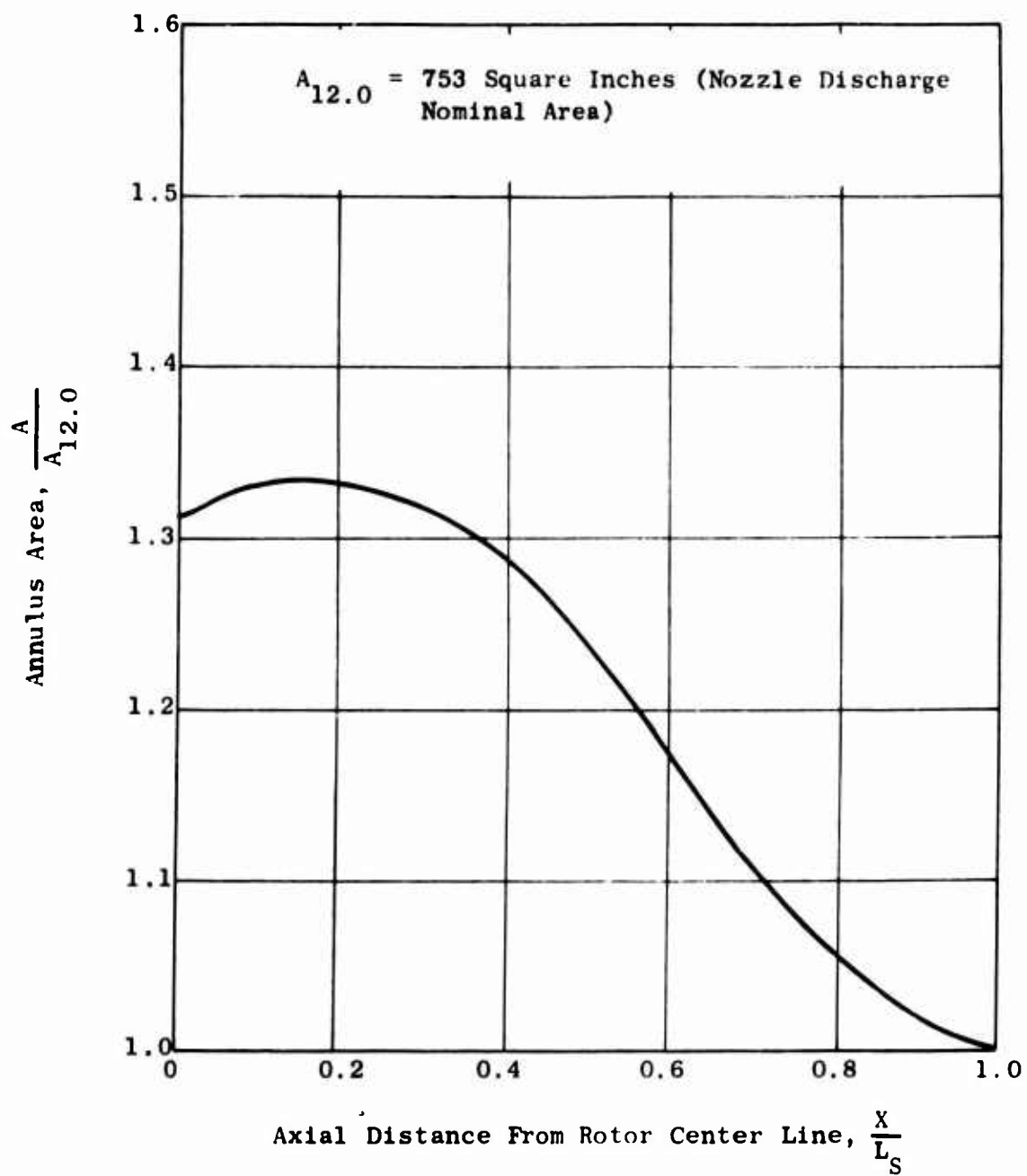


Figure 15. Nozzle Area Distribution for Model Using Afterbody 4 and Plug 3.

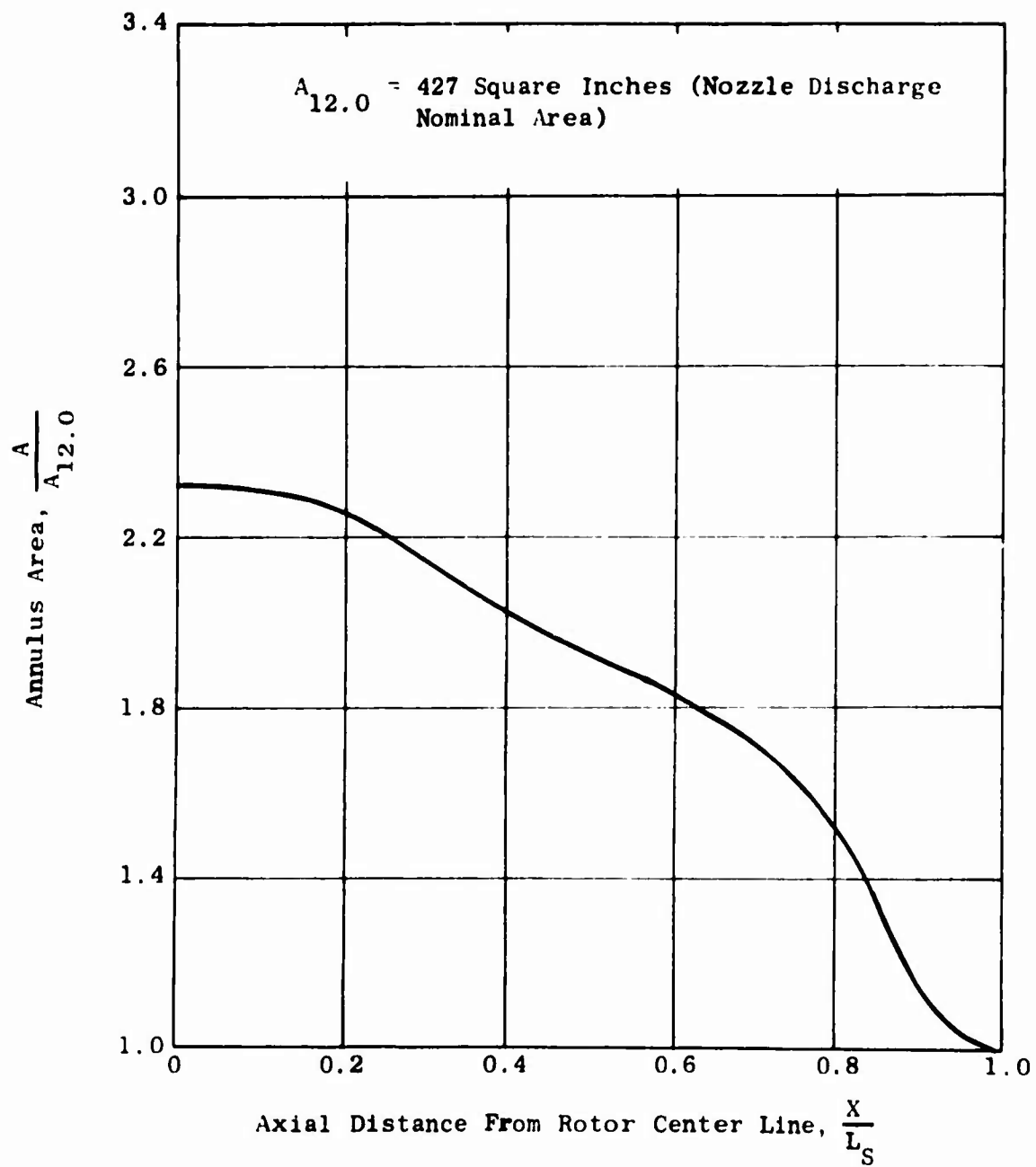


Figure 16. Nozzle Area Distribution for Model Using Afterbody 4 and Plug 4.

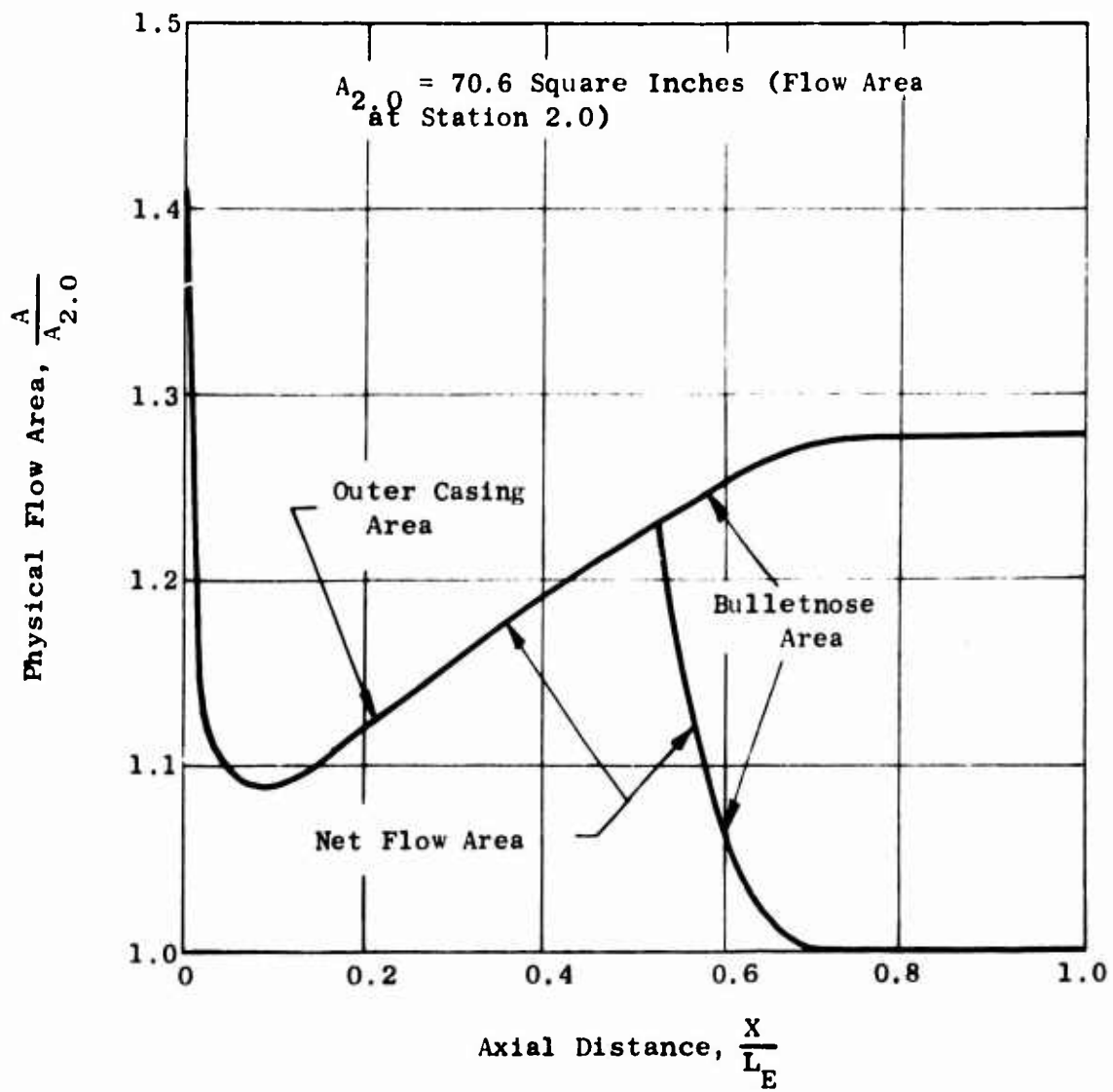
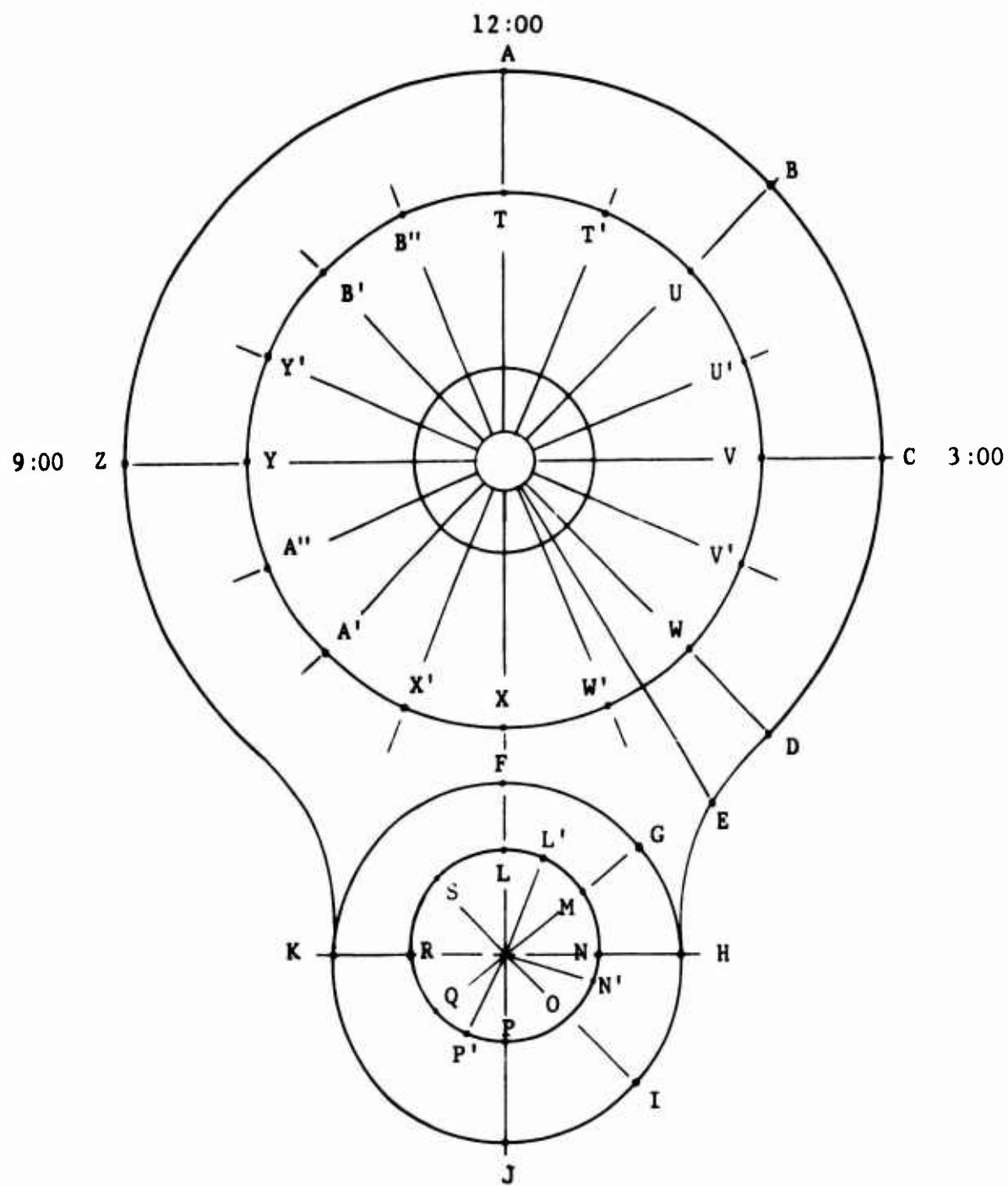


Figure 17. Internal Area Distribution for Engine Inlet.



(Forward Looking Aft)

	ϕ		ϕ		ϕ		ϕ		ϕ
A	0	U	45	A'	225	H	90	N'	112.5
B	45	U'	67.5	A''	247.5	I	135	O	135
C	90	V	90	Y	270	J	180	P	180
D	137	V'	112.5	Y'	292.5	K	270	P'	202.5
E	150	W	137	B'	315	L	0	Q	225
Z	270	W'	157.5	B''	337.5	L'	22.5	R	270
T	0	X	180	F	0	M	45	S	315
T'	22.5	X'	202.5	G	45	N	90		

Figure 18. Instrumentation Plane Nomenclature.

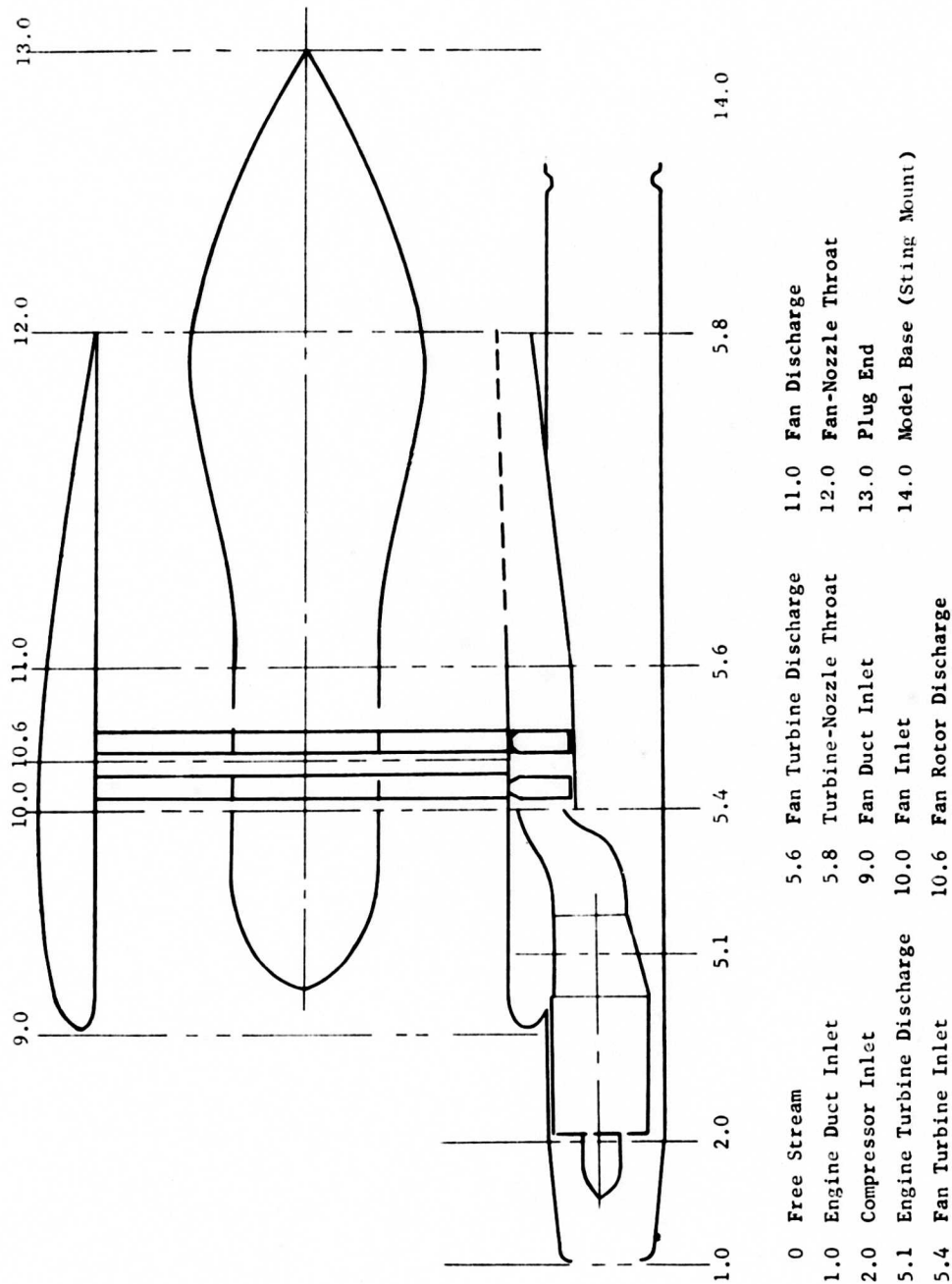


Figure 19. Model Axial Plane Notation.

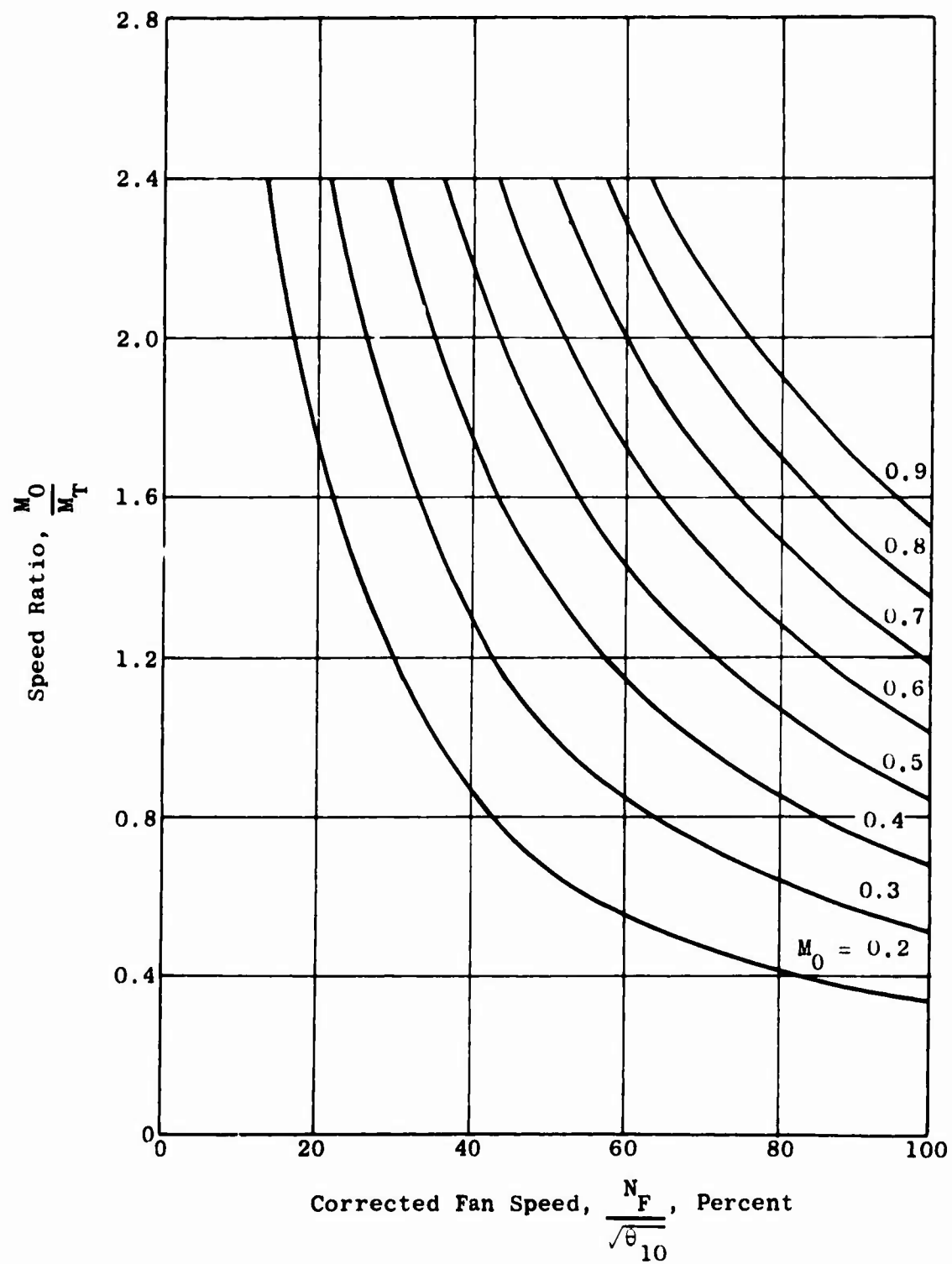


Figure 20. Variation of Speed Ratio Parameter with Mach Number and Corrected Fan Speed.

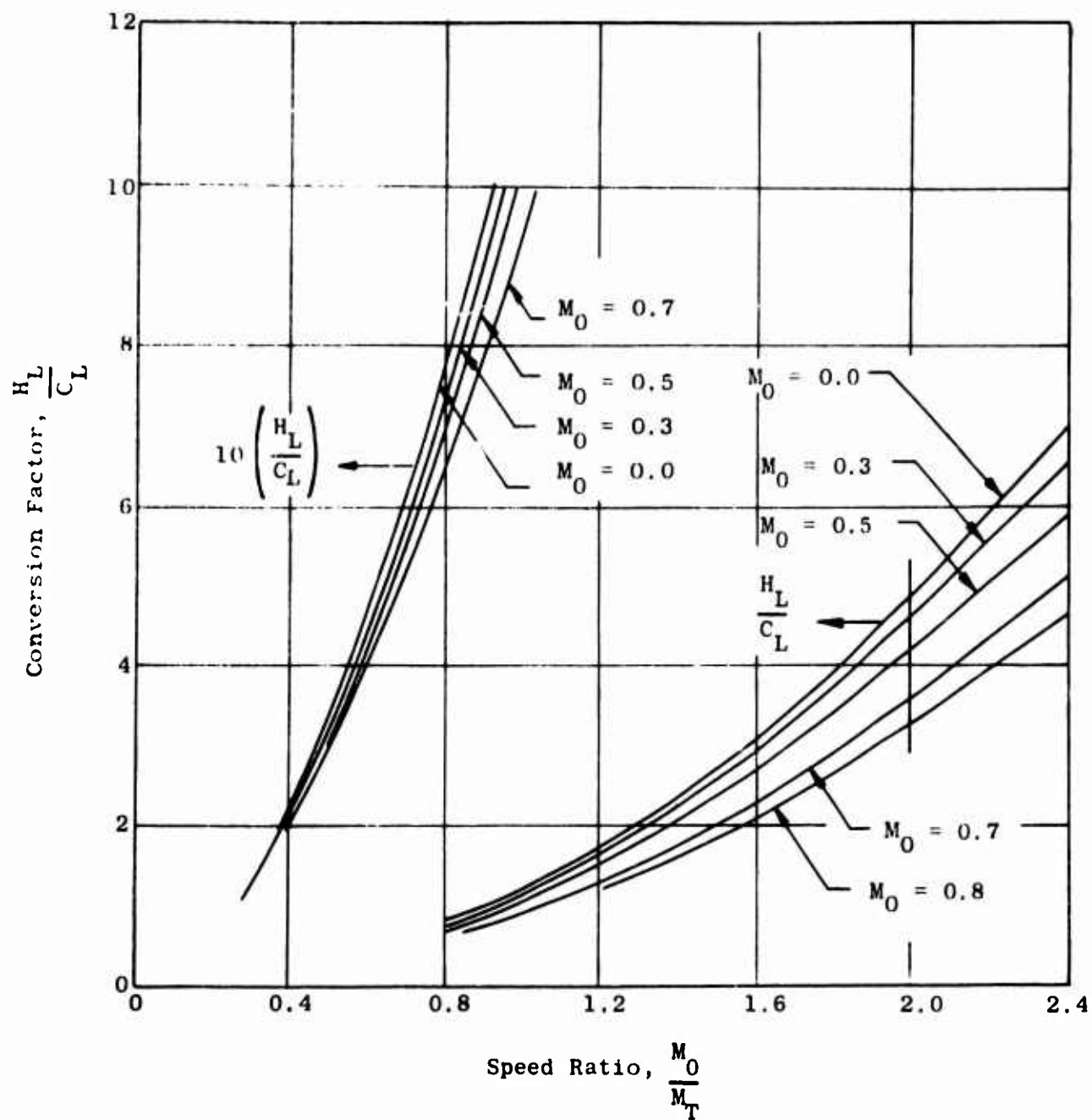


Figure 21. Relationship of Fan and Conventional Coefficients.

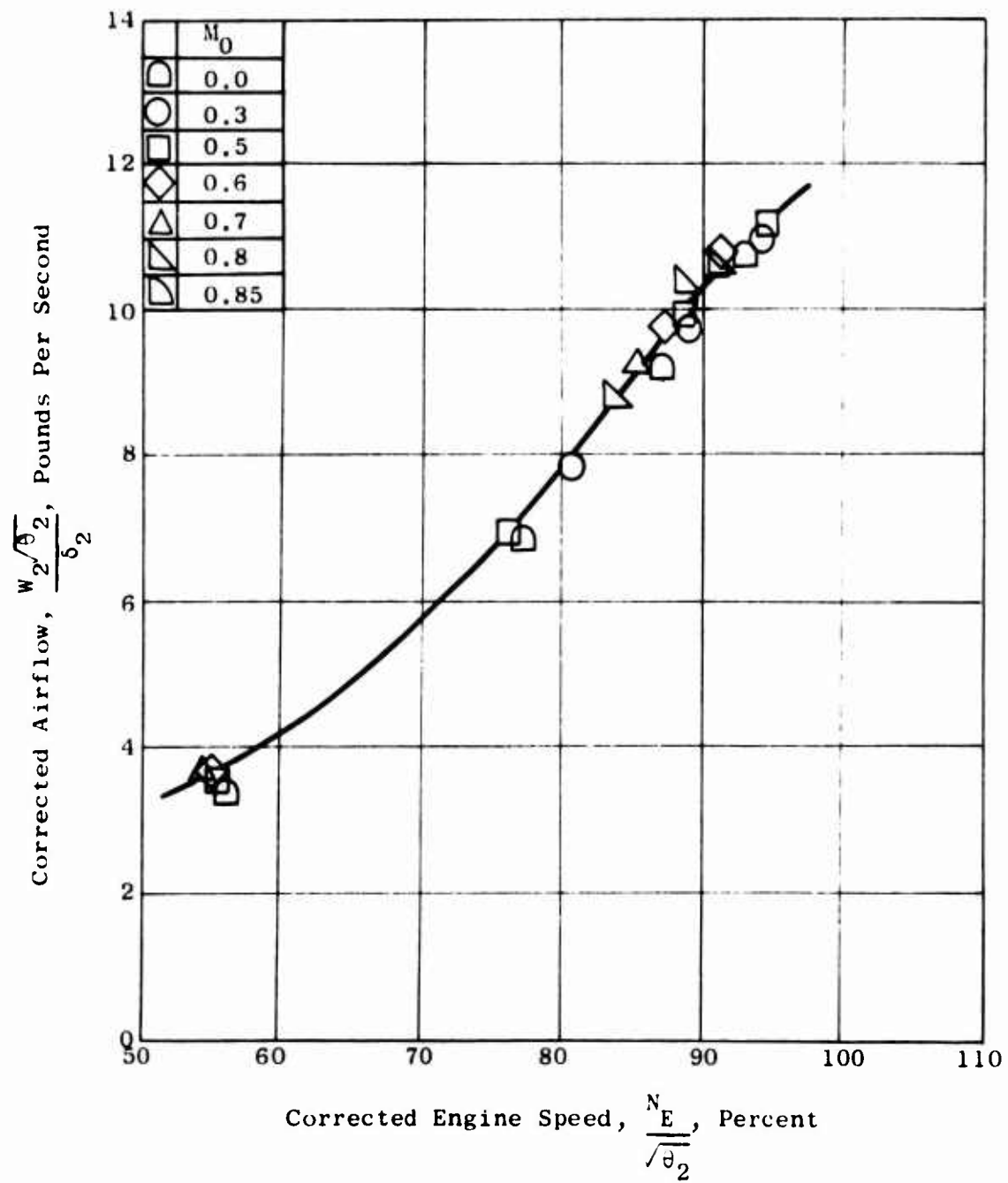


Figure 22. Engine Airflow Characteristics - Model 1.

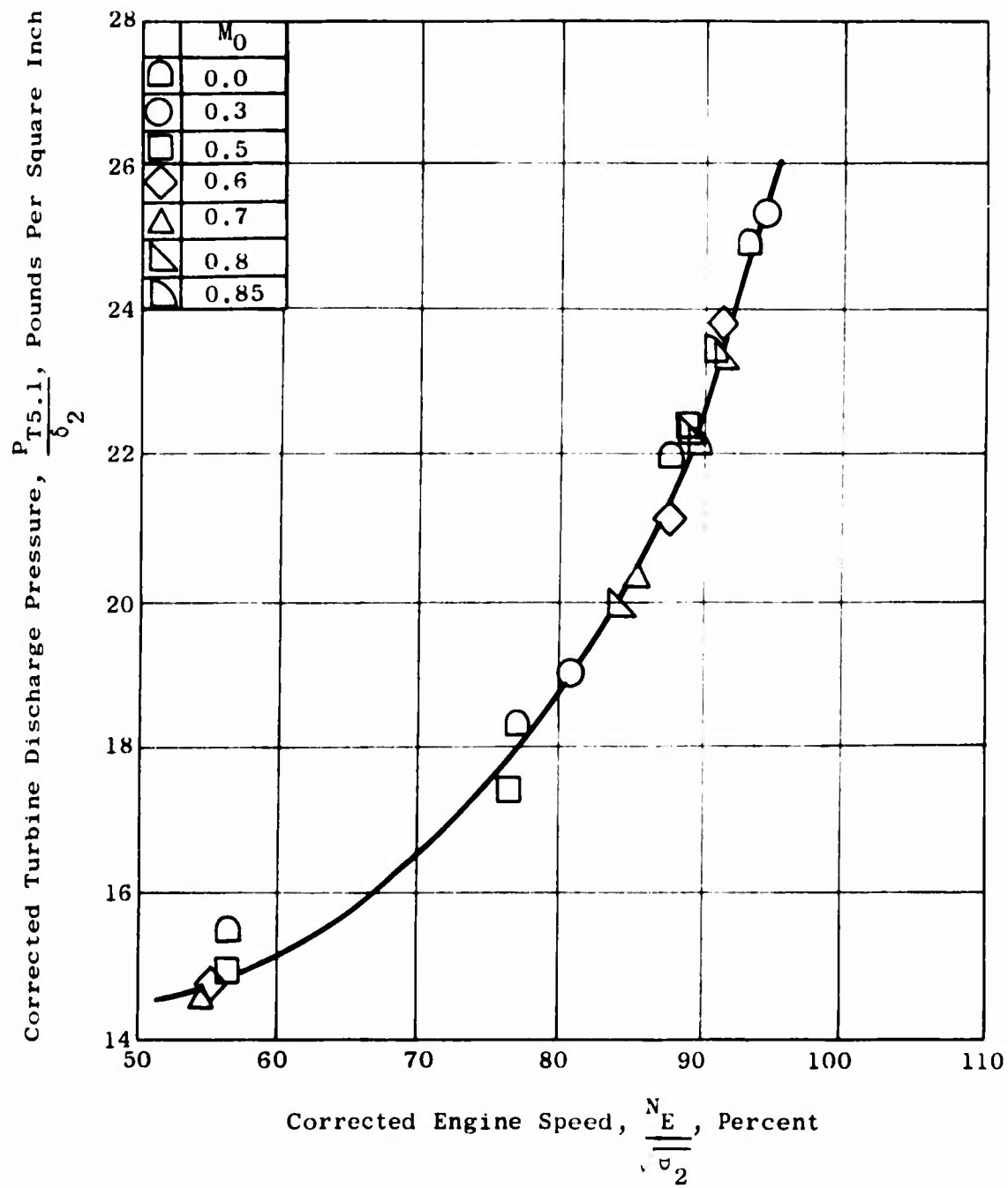


Figure 23. Engine Turbine Discharge Total Pressure - Model 1.

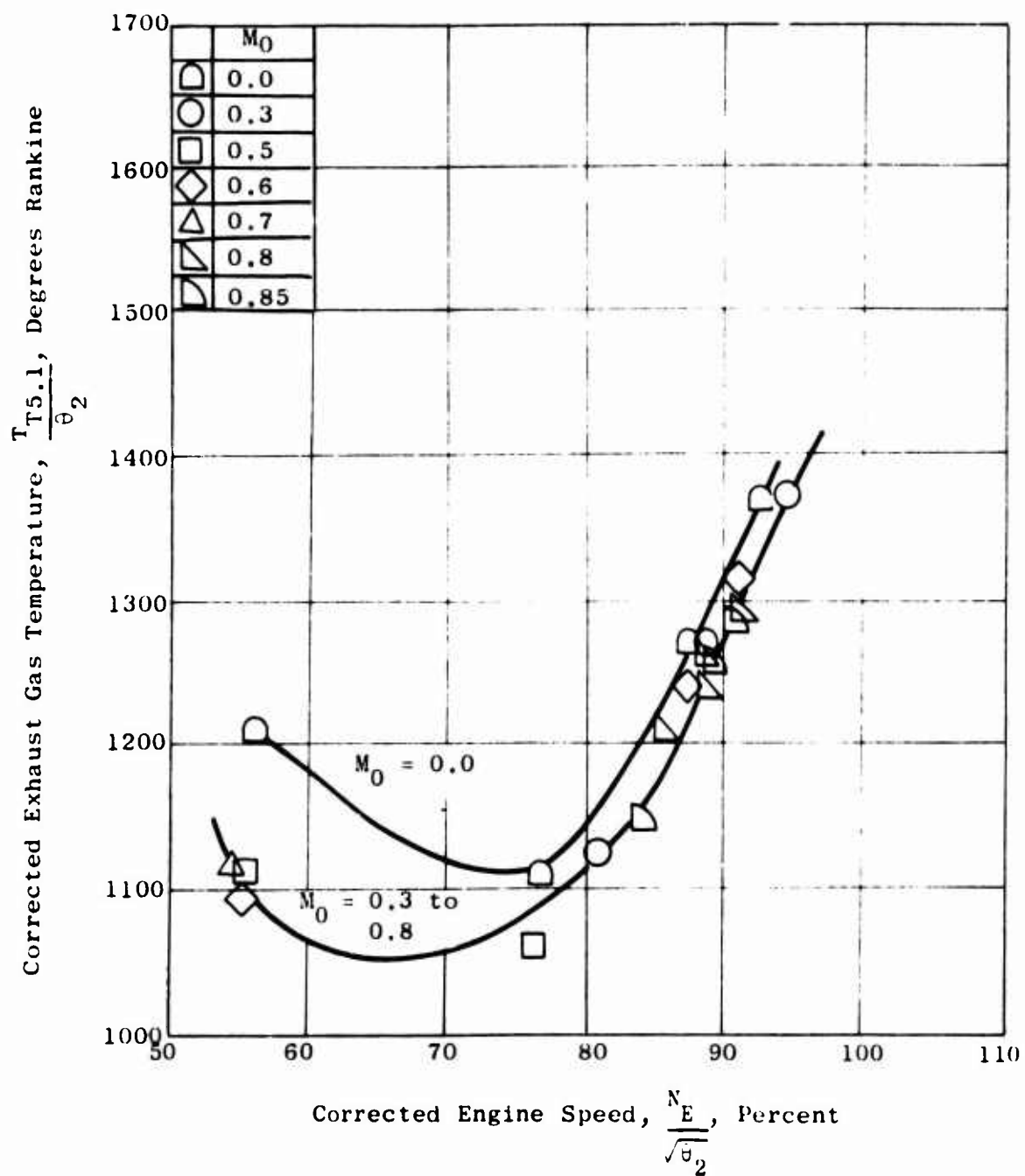


Figure 24. Engine Exhaust Gas Temperature - Model 1.

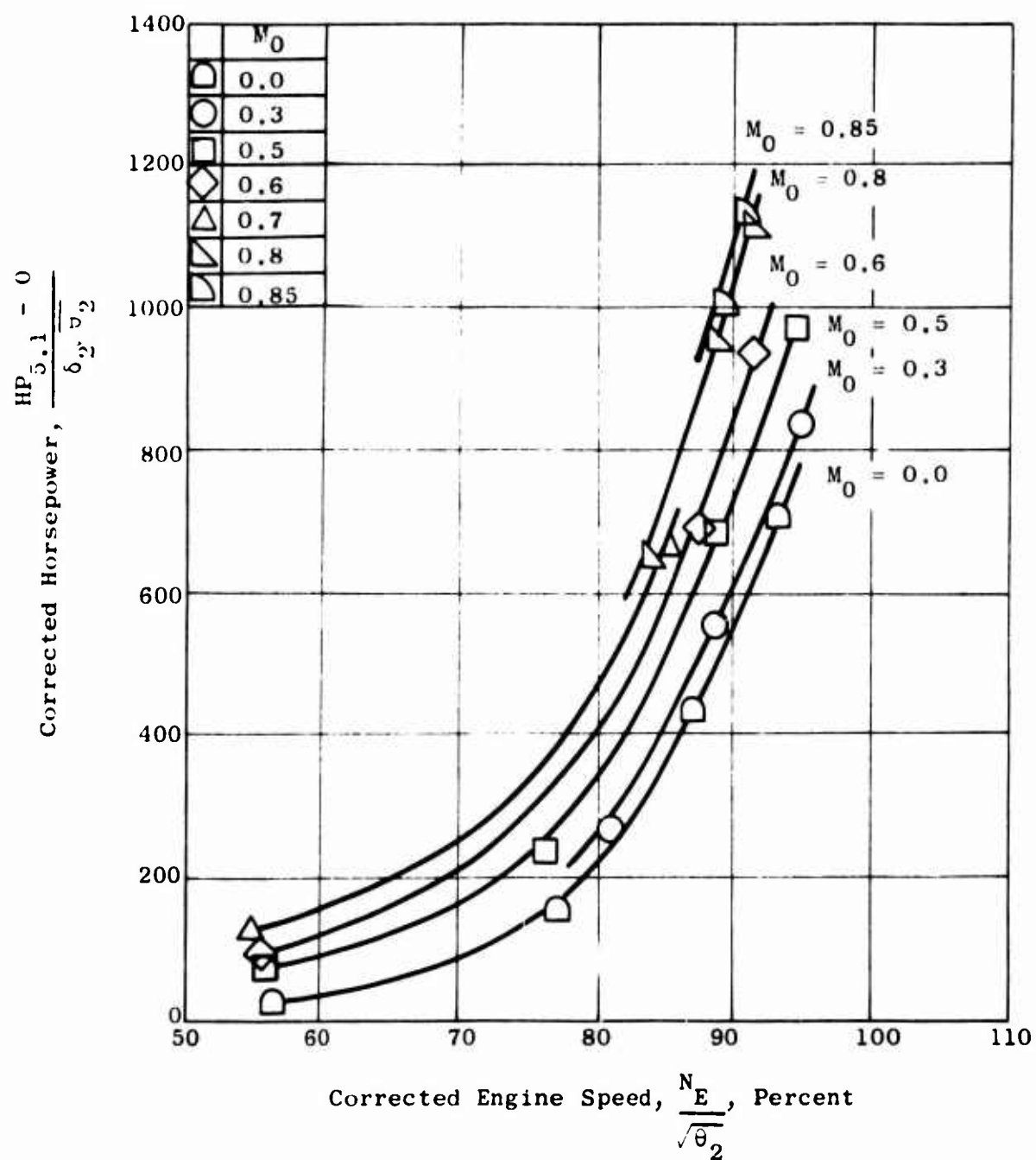


Figure 25. Engine Ideal Gas Horsepower Characteristics - Model 1.

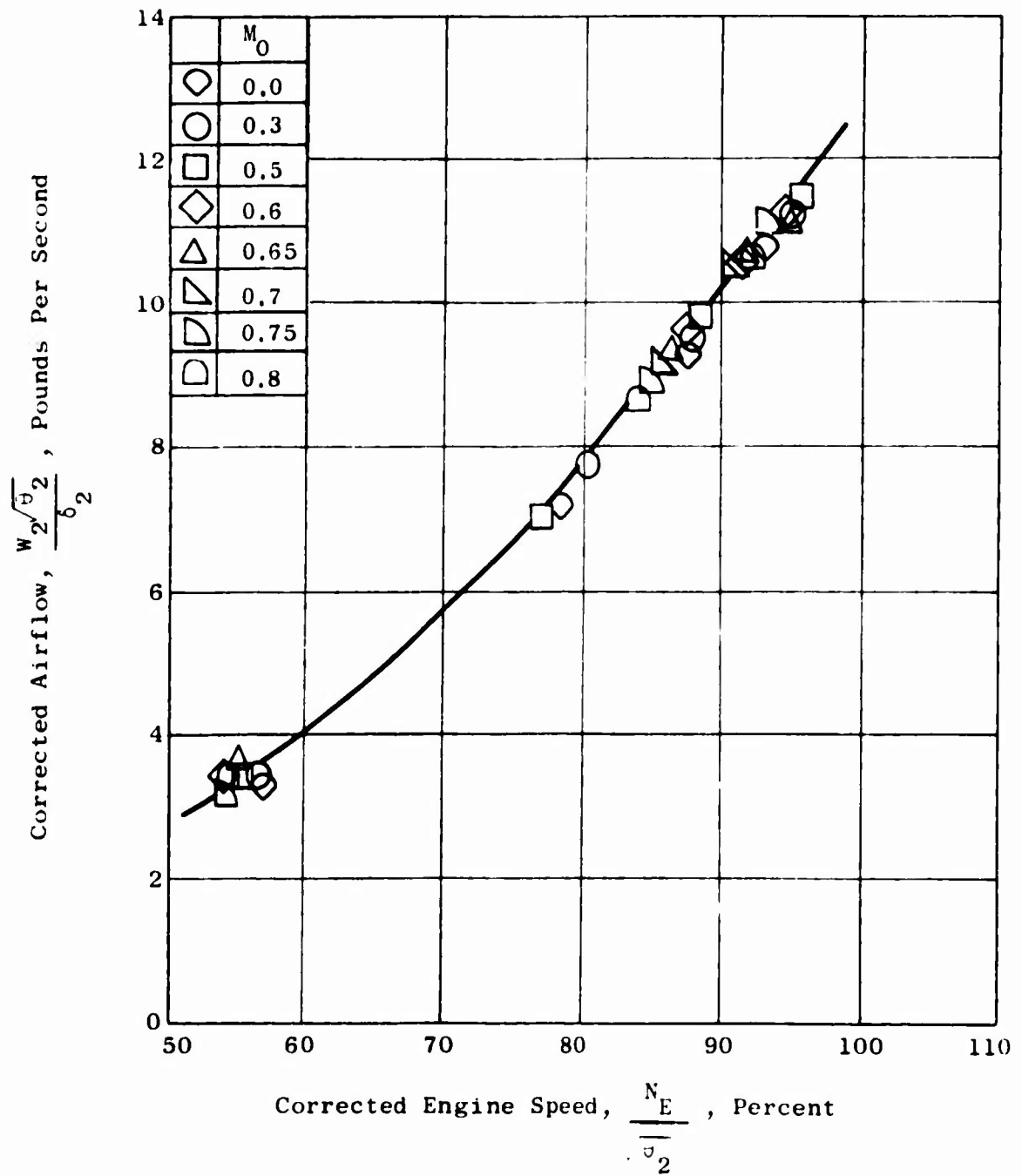


Figure 26. Engine Airflow Characteristics - Model 2.

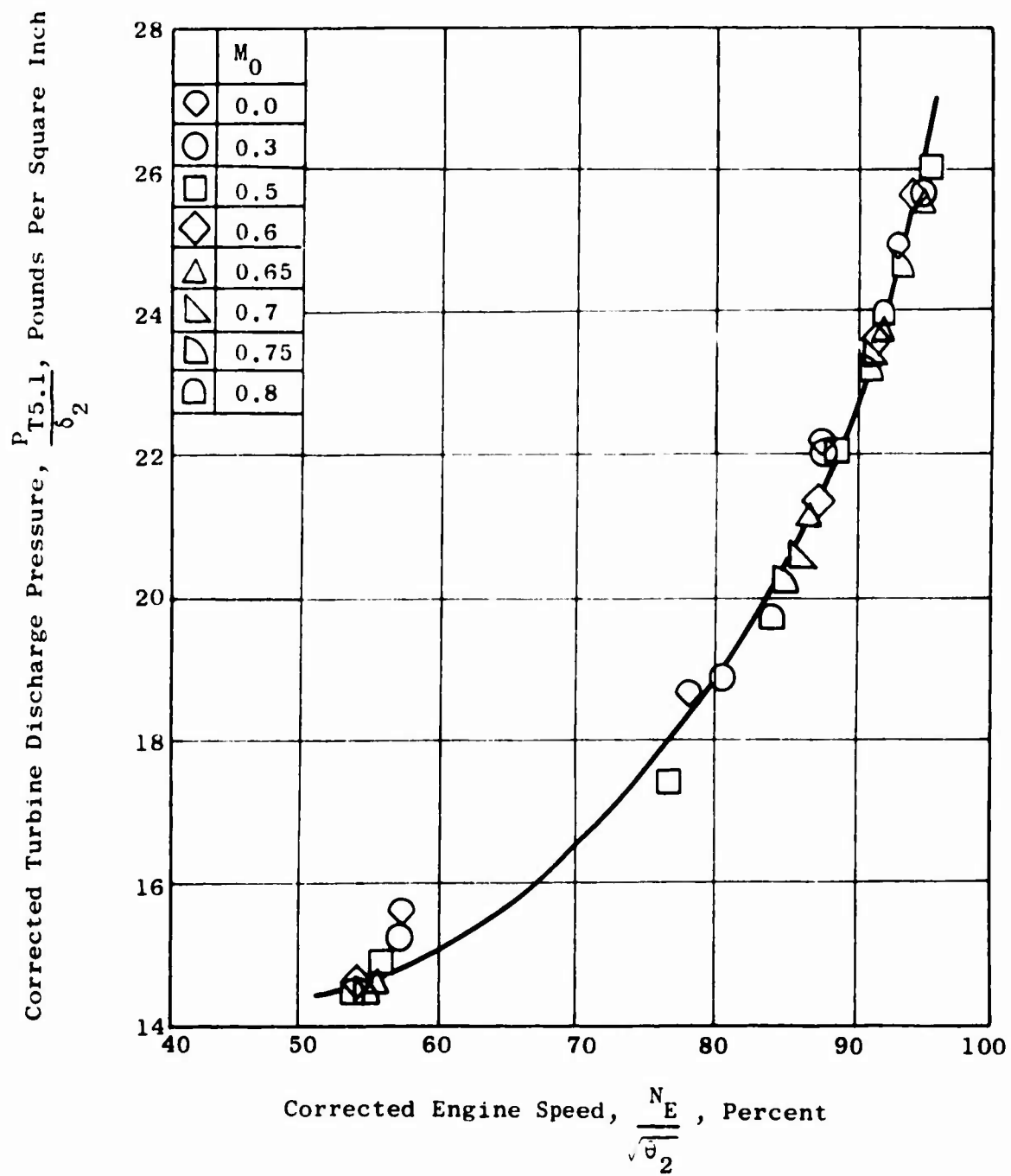


Figure 27. Engine Turbine Discharge Total Pressure - Model 2.

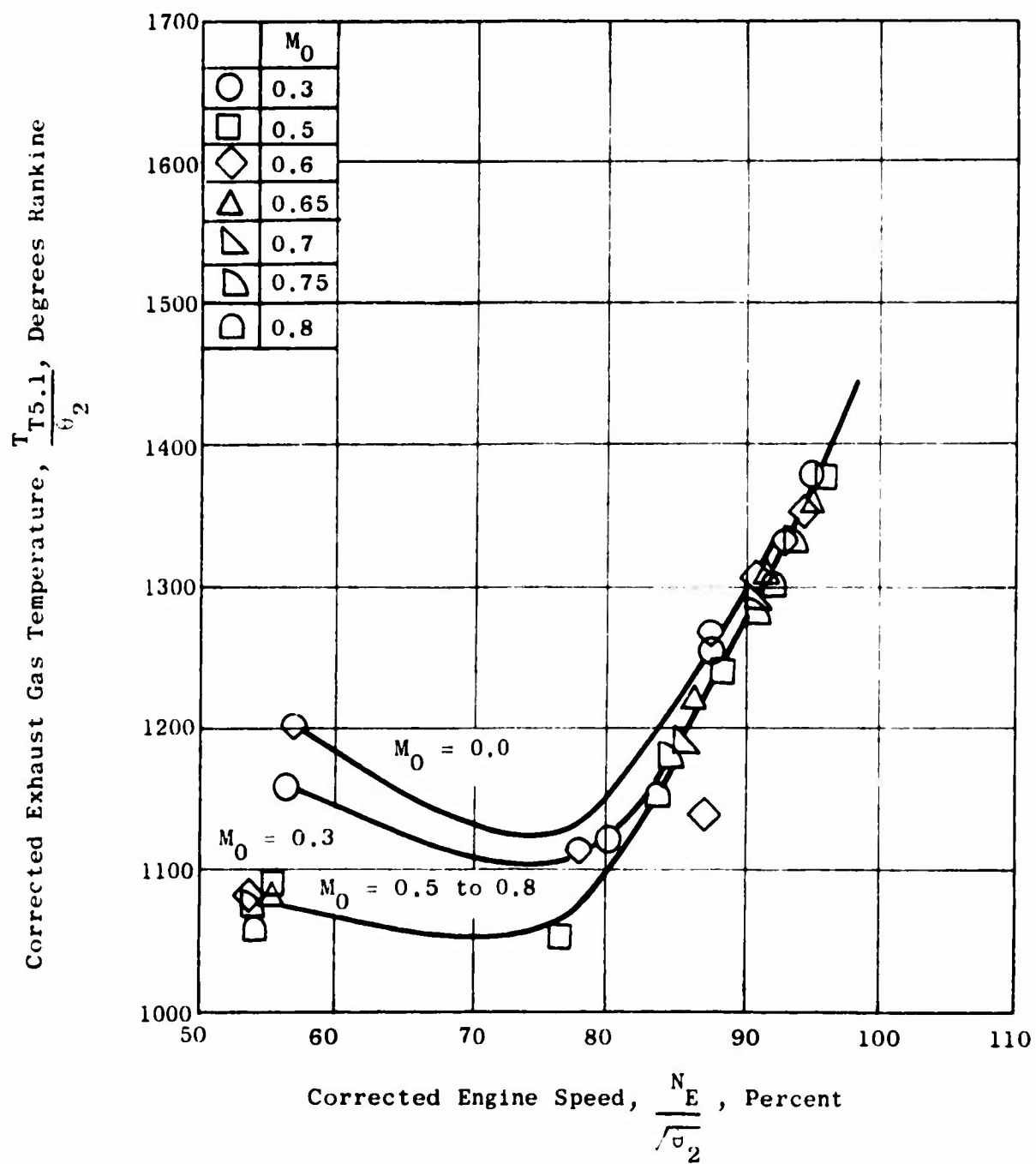


Figure 28. Engine Exhaust Gas Temperature - Model 2.

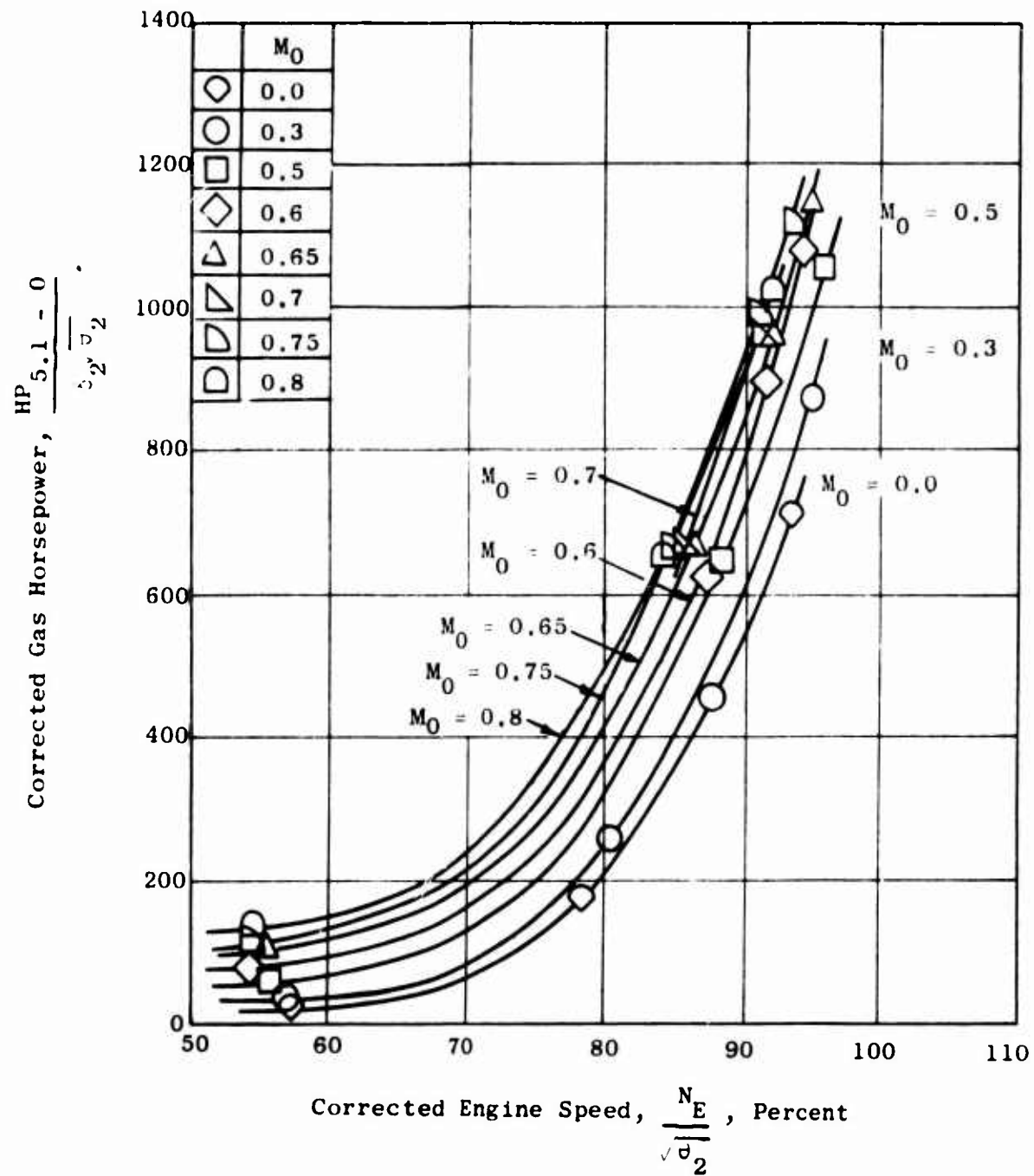


Figure 29. Engine Ideal Gas Horsepower Characteristics - Model 2.

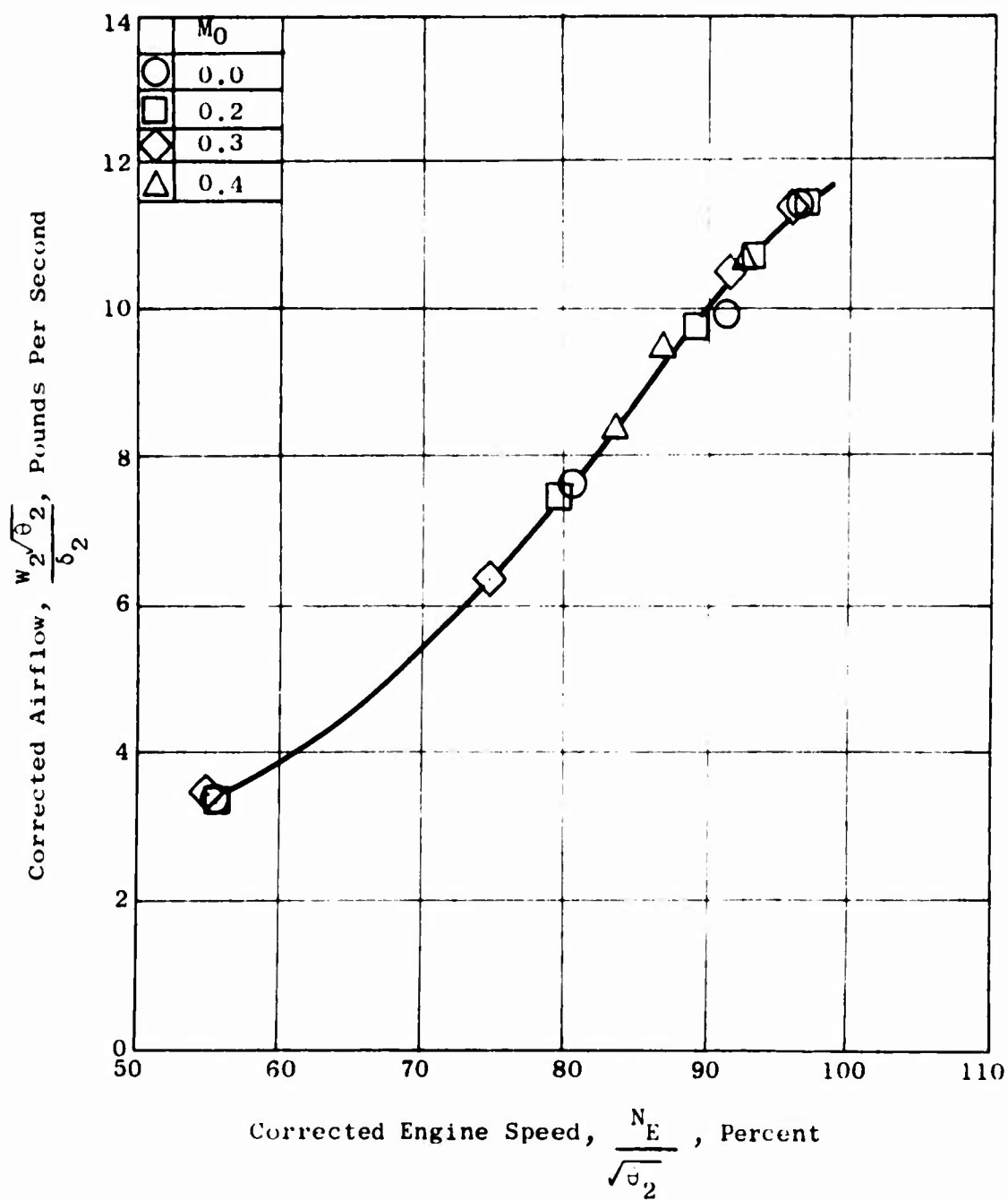


Figure 30. Engine Airflow Characteristics - Model 3.

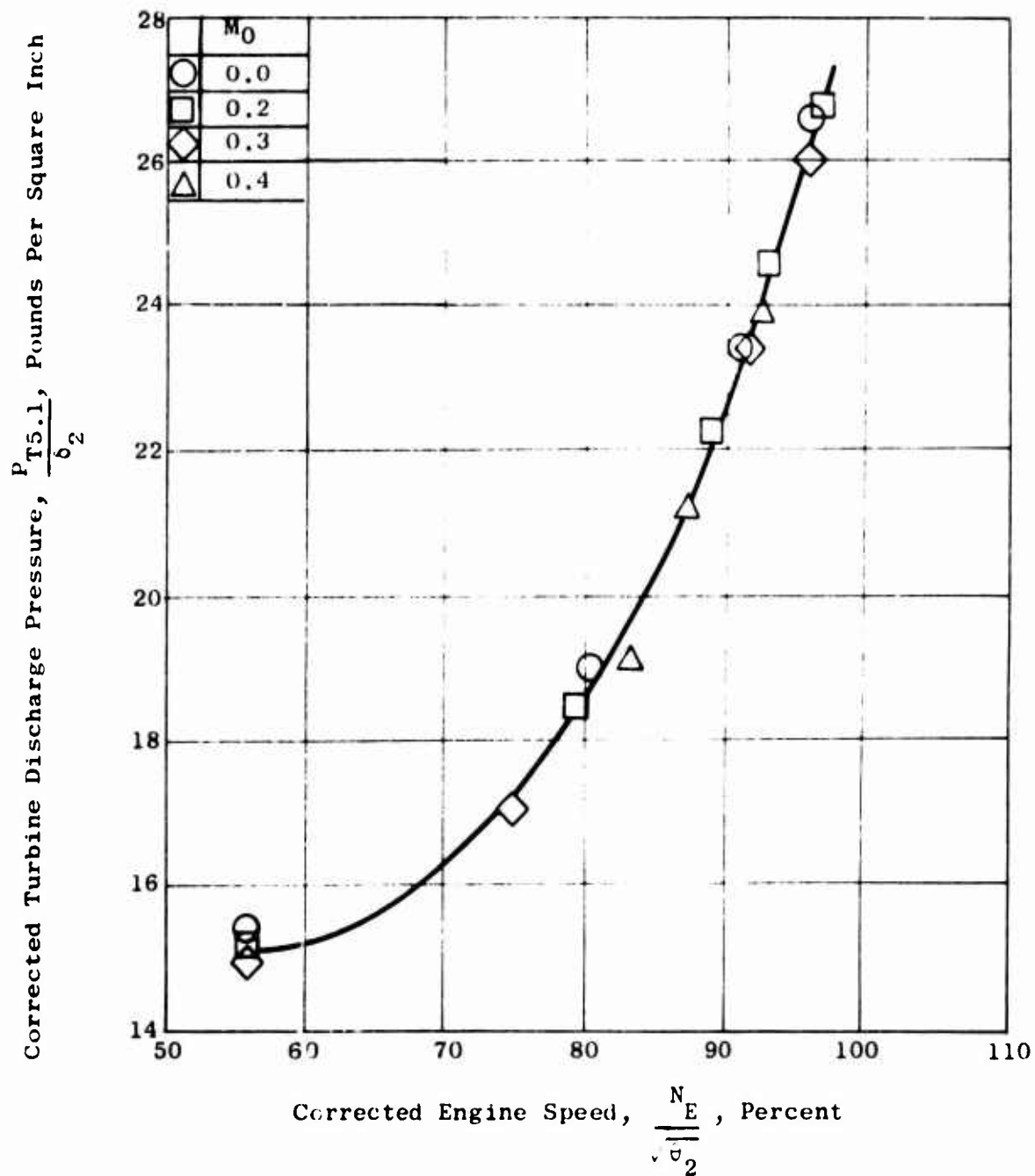


Figure 31. Engine Turbine Discharge Total Pressure - Model 3.

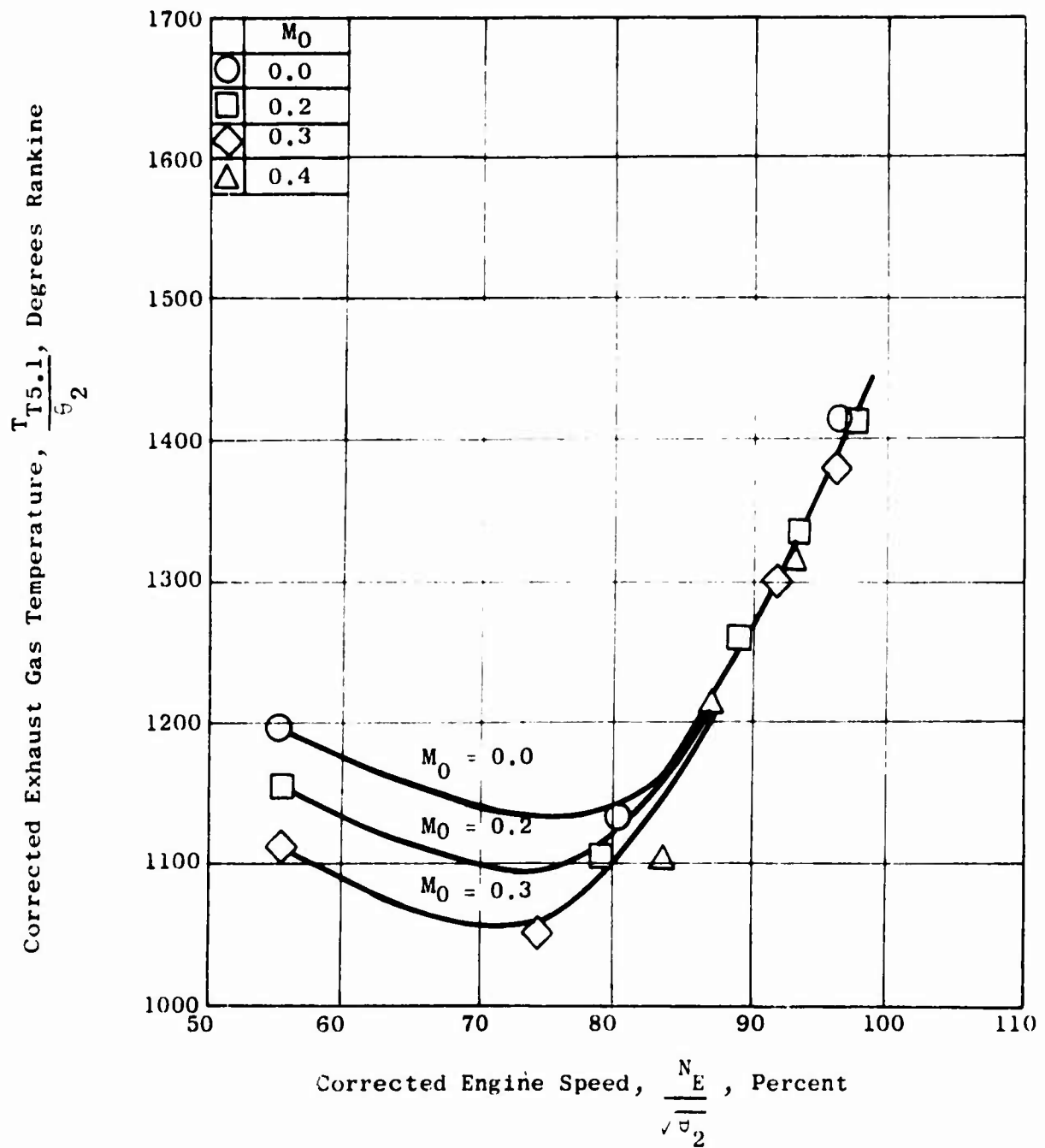


Figure 32. Engine Exhaust Gas Temperature - Model 3.

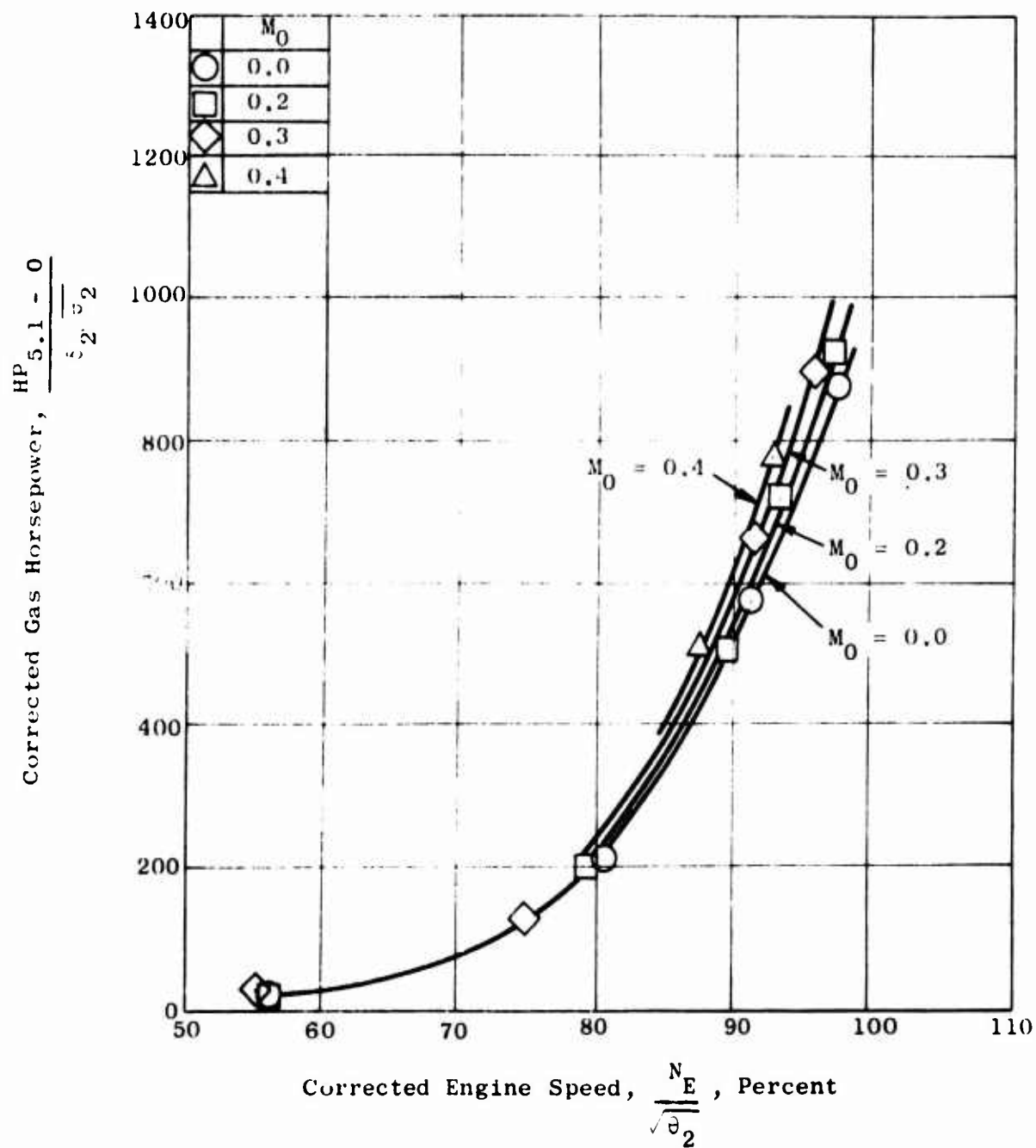


Figure 33. Engine Ideal Gas Horsepower Characteristics - Model 3.

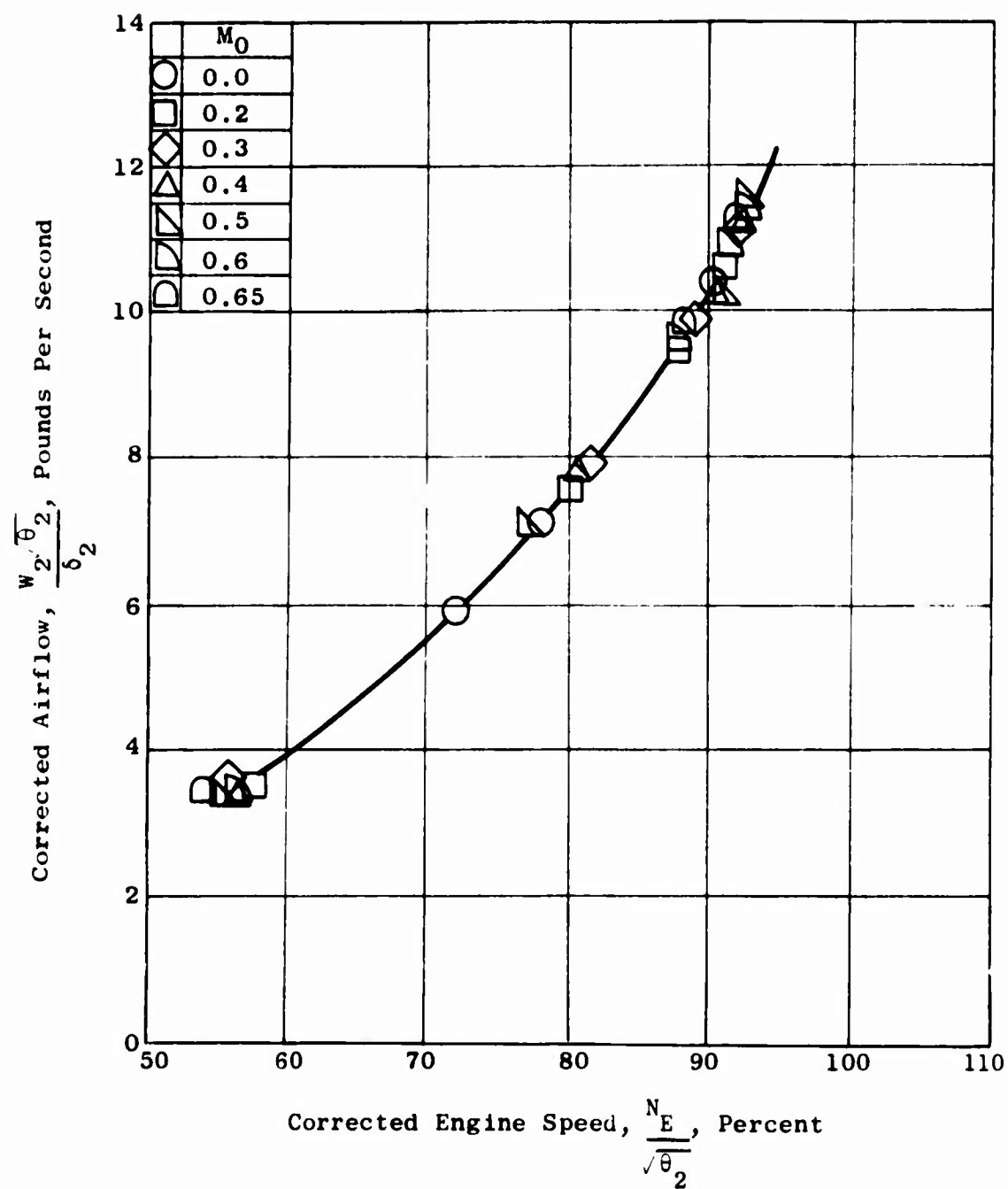


Figure 34. Engine Airflow Characteristics - Model 4.

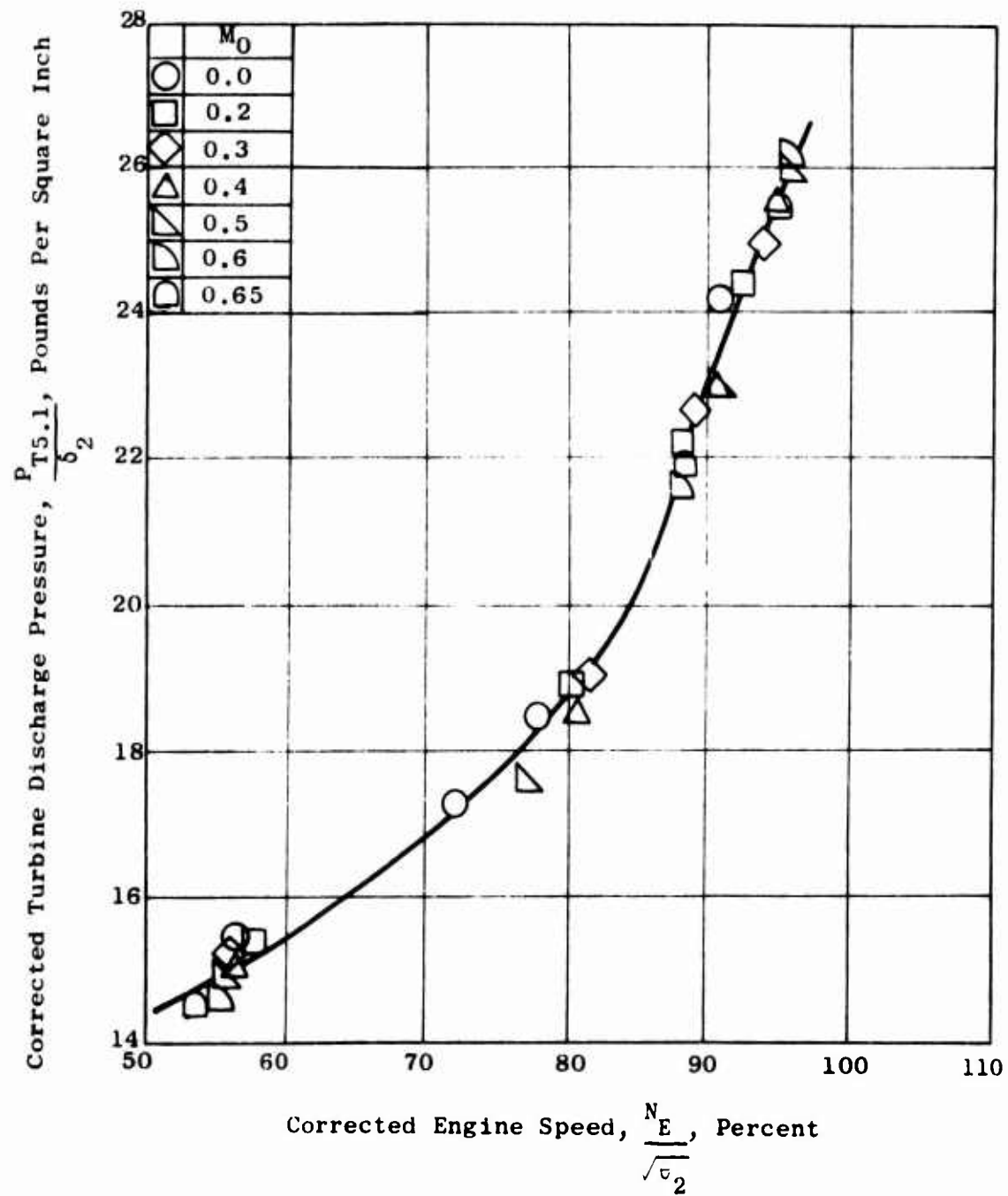


Figure 35. Engine Turbine Discharge Total Pressure - Model 4.

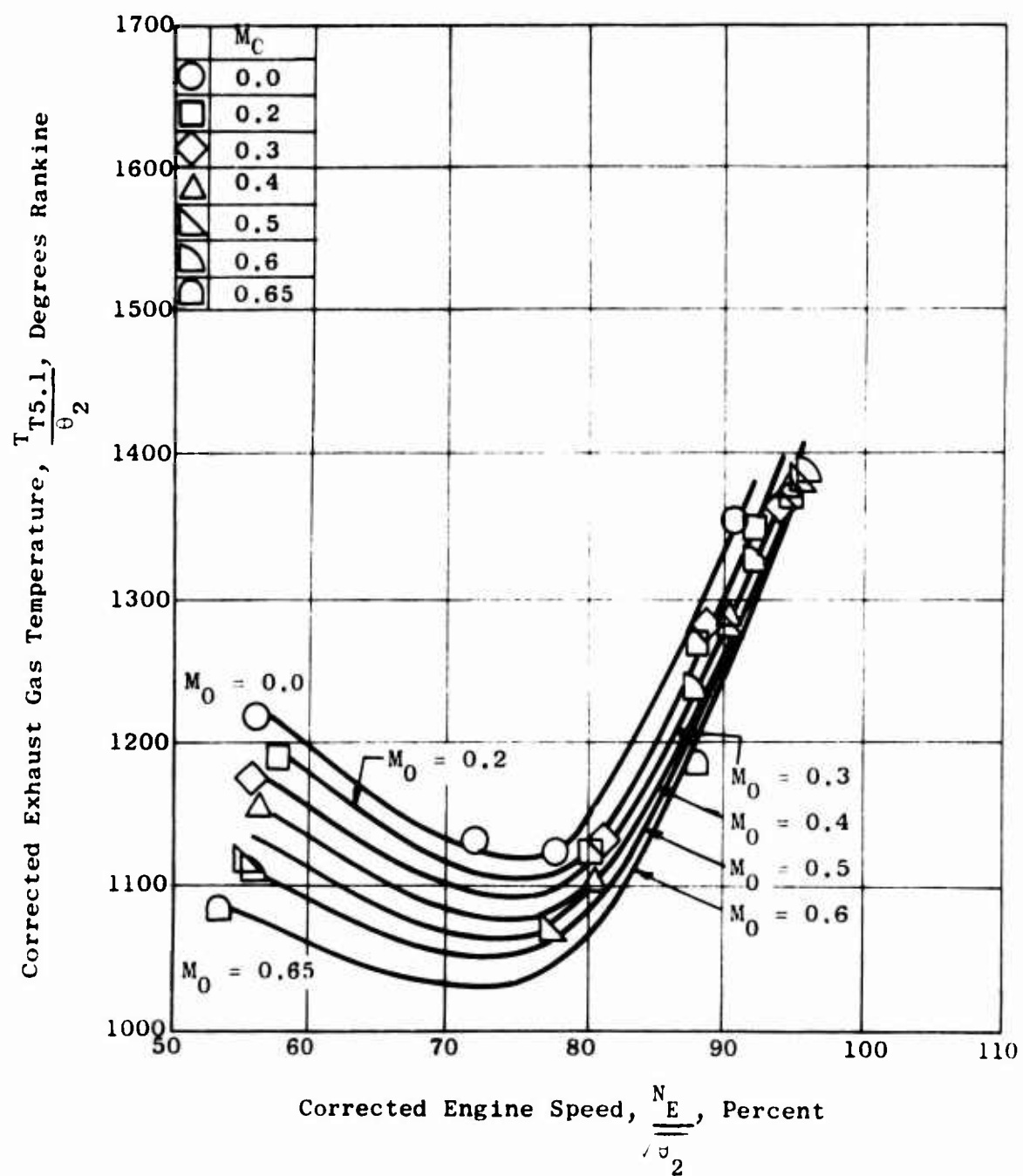


Figure 36. Engine Exhaust Gas Temperature - Model 4.

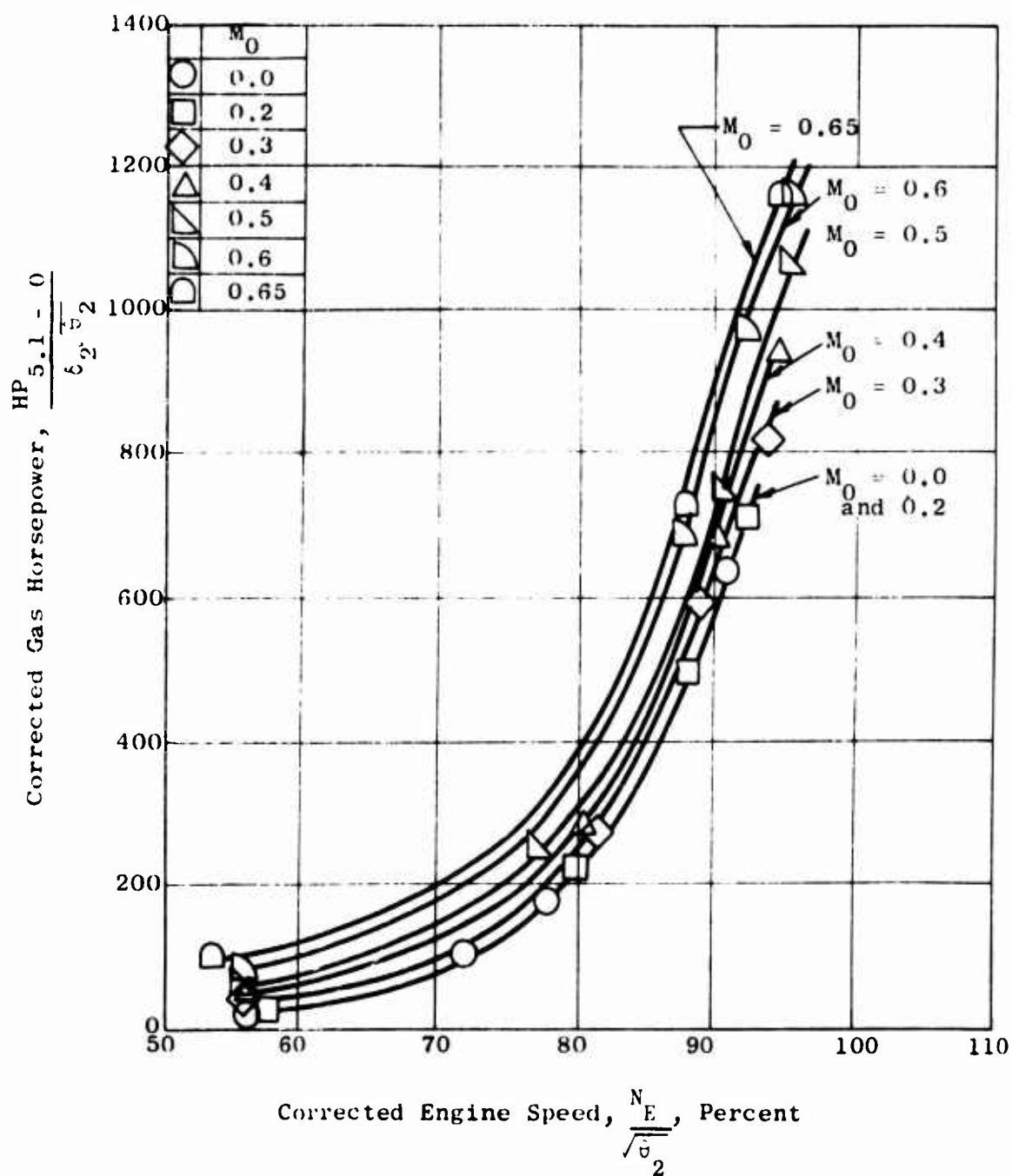


Figure 37. Engine Ideal Gas Horsepower Characteristics - Model 4.

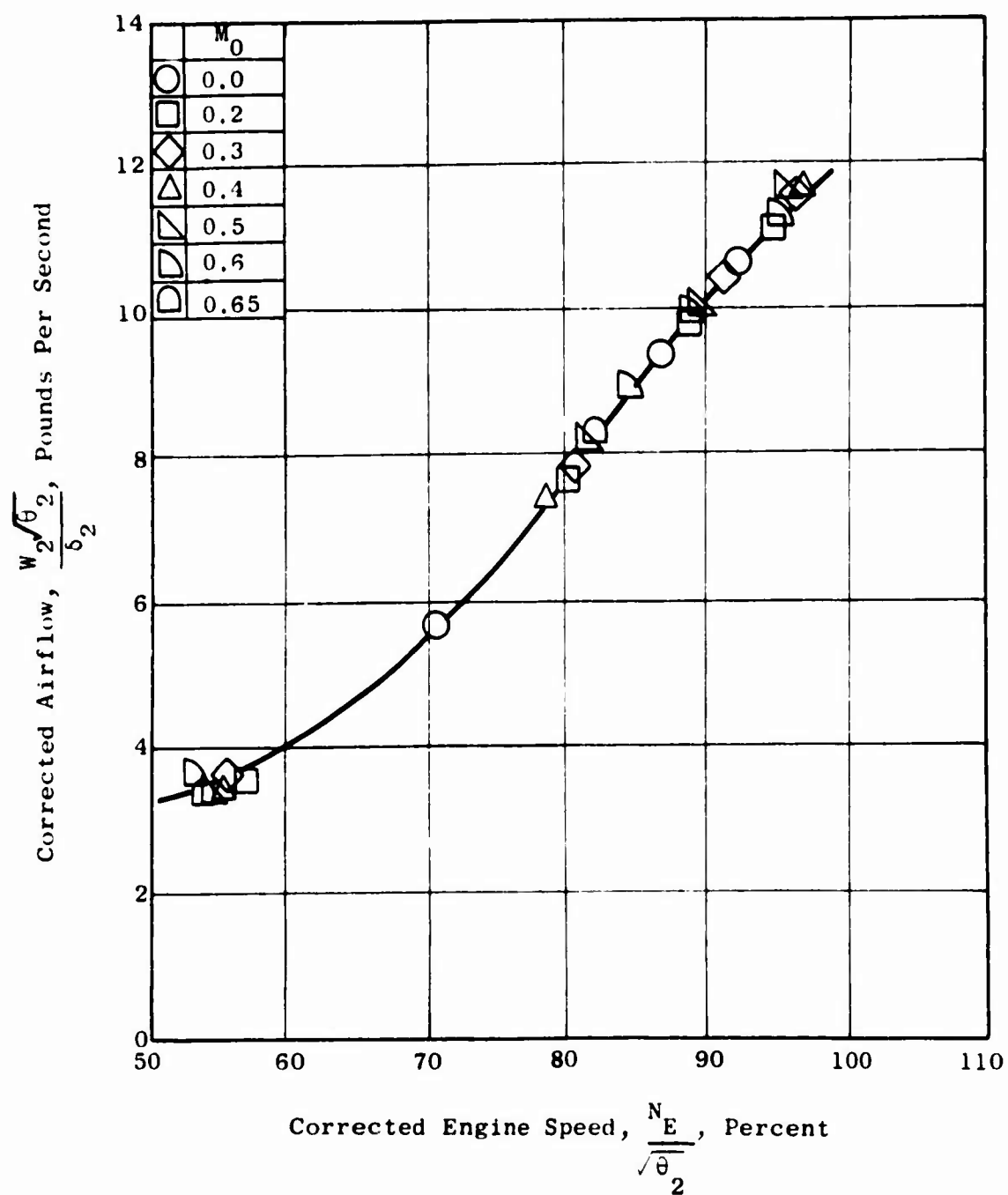


Figure 38. Engine Airflow Characteristics - Model 5.

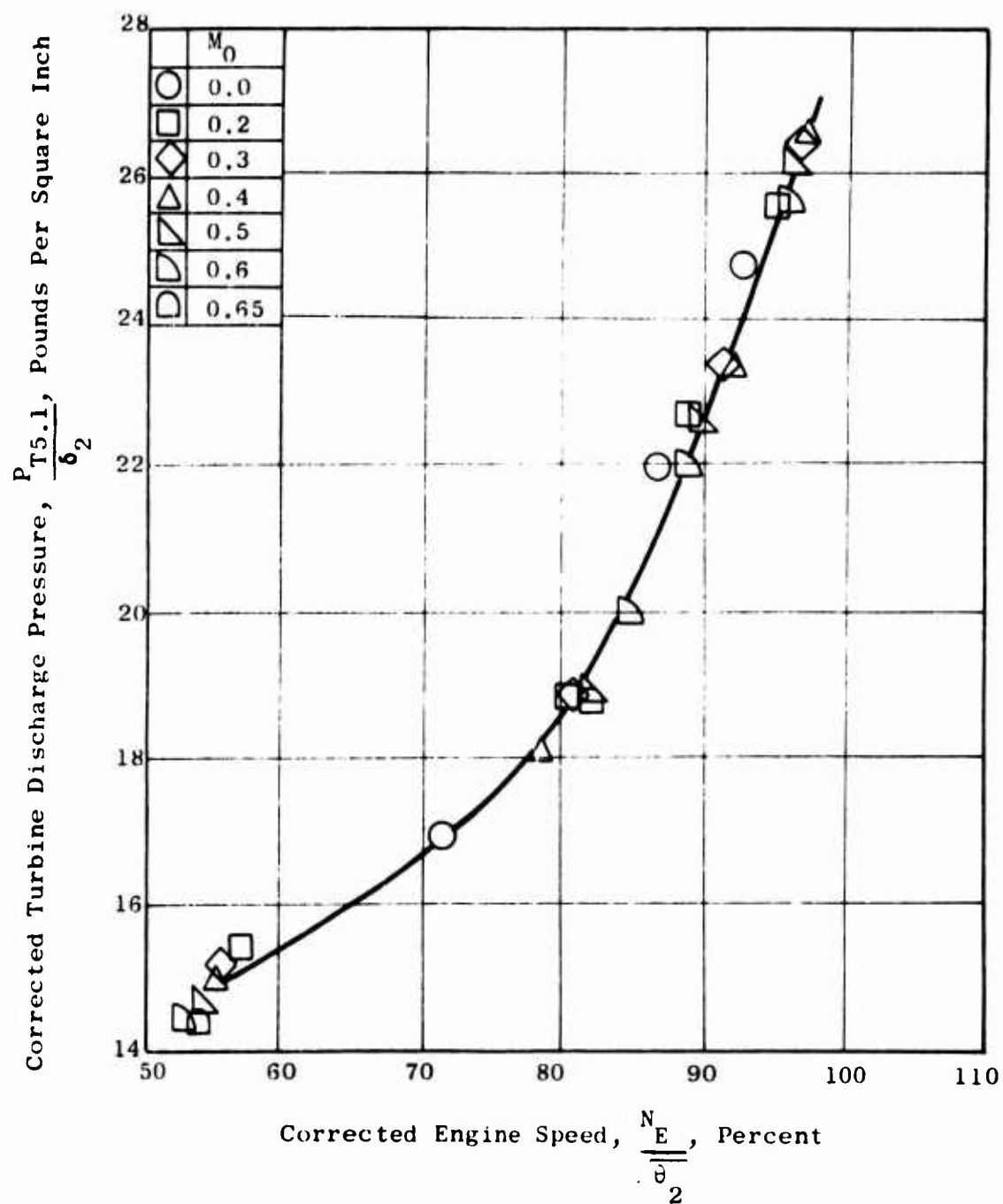


Figure 39. Engine Turbine Discharge Total Pressure - Model 5.

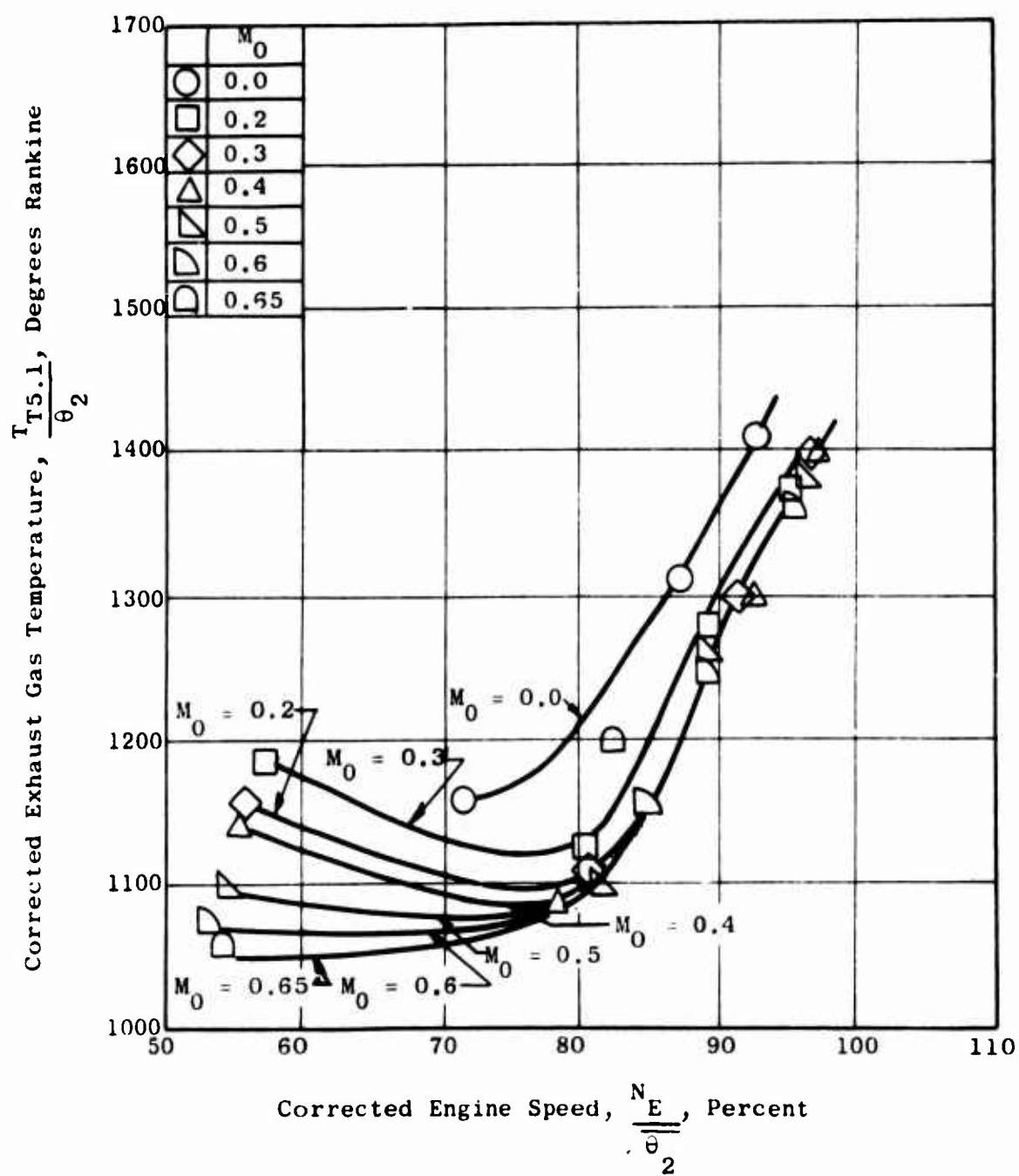


Figure 40. Engine Exhaust Gas Temperature - Model 5.

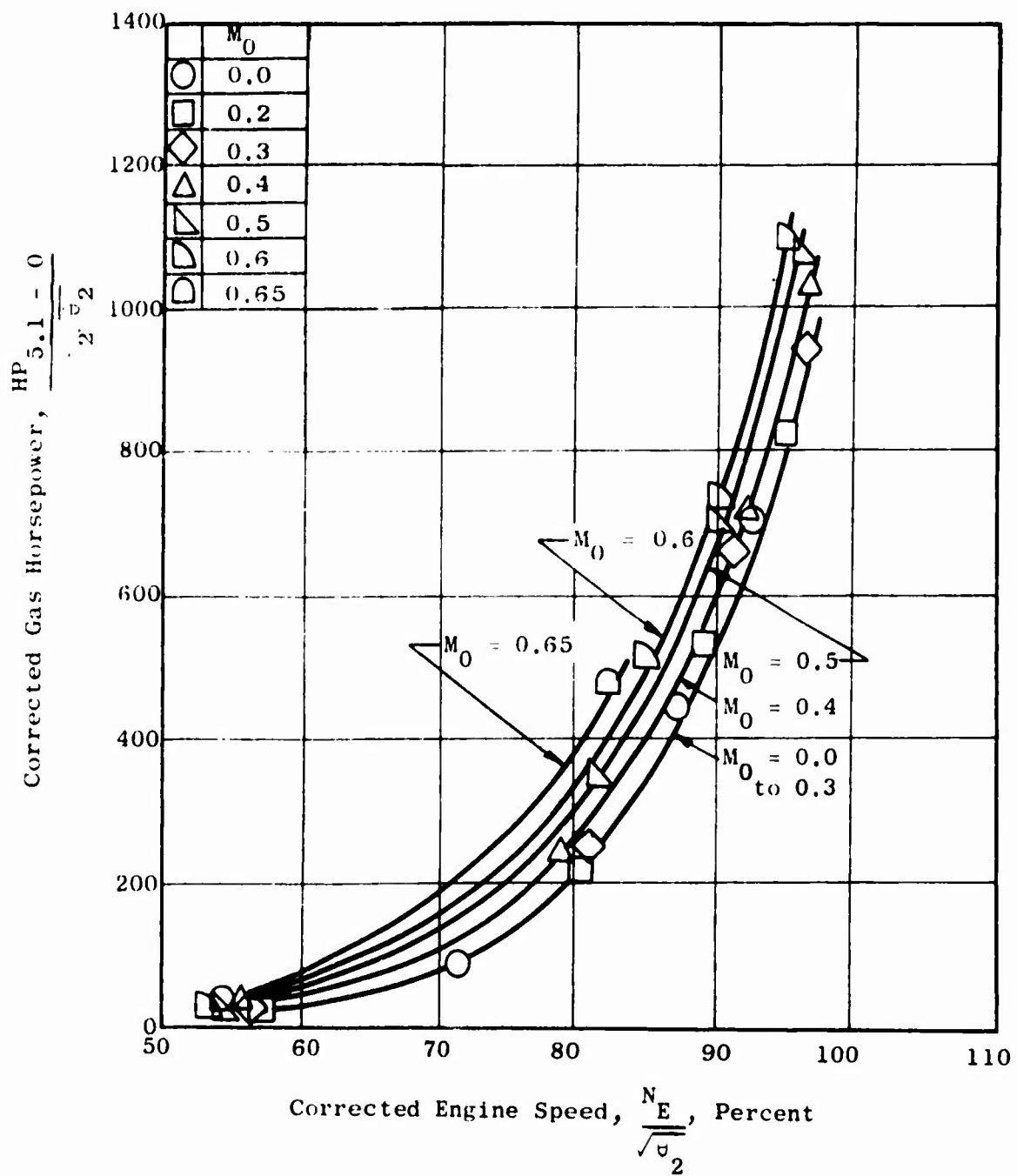


Figure 41. Engine Ideal Gas Horsepower Characteristics - Model 5.

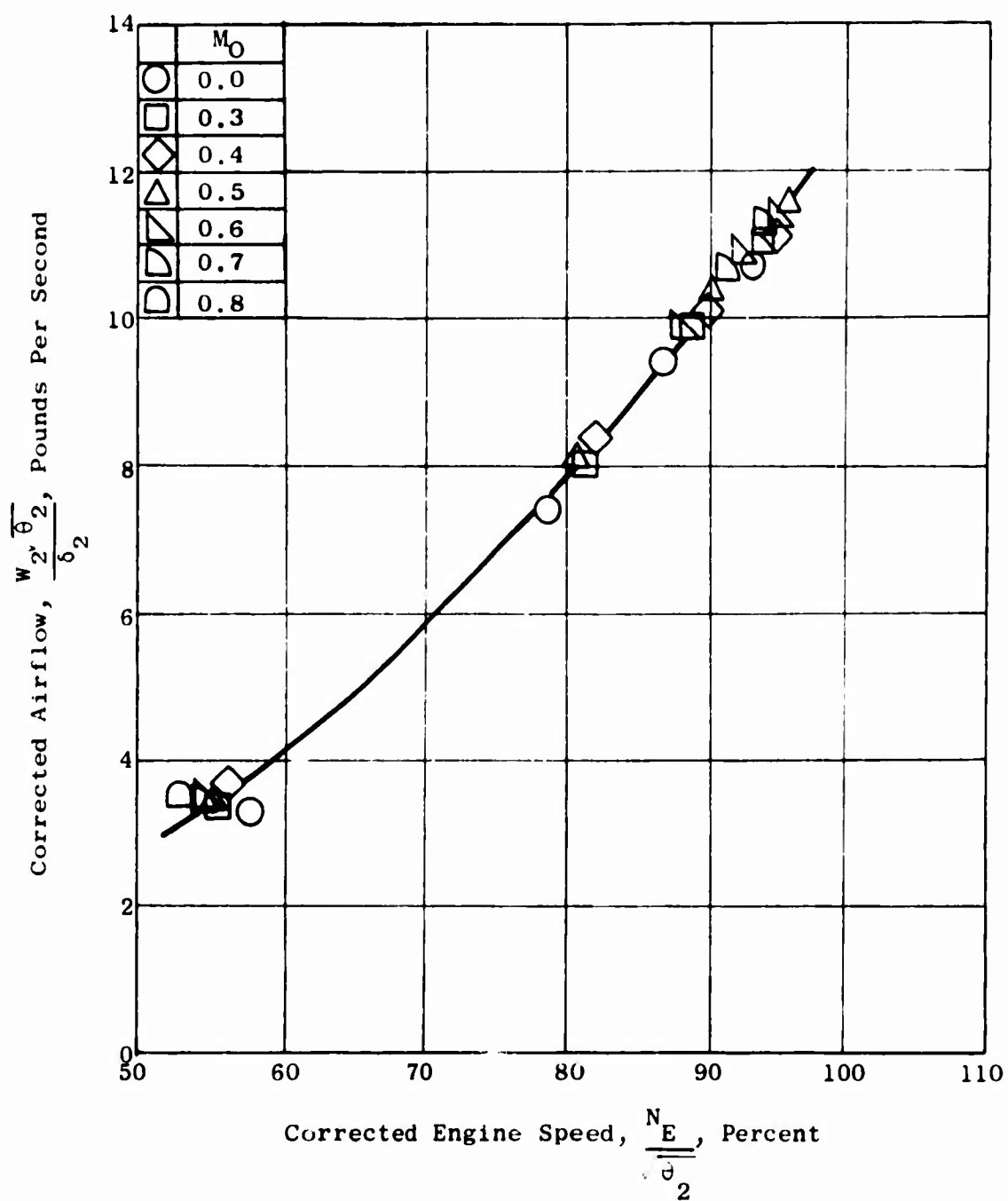


Figure 42. Engine Airflow Characteristics - Model 6.

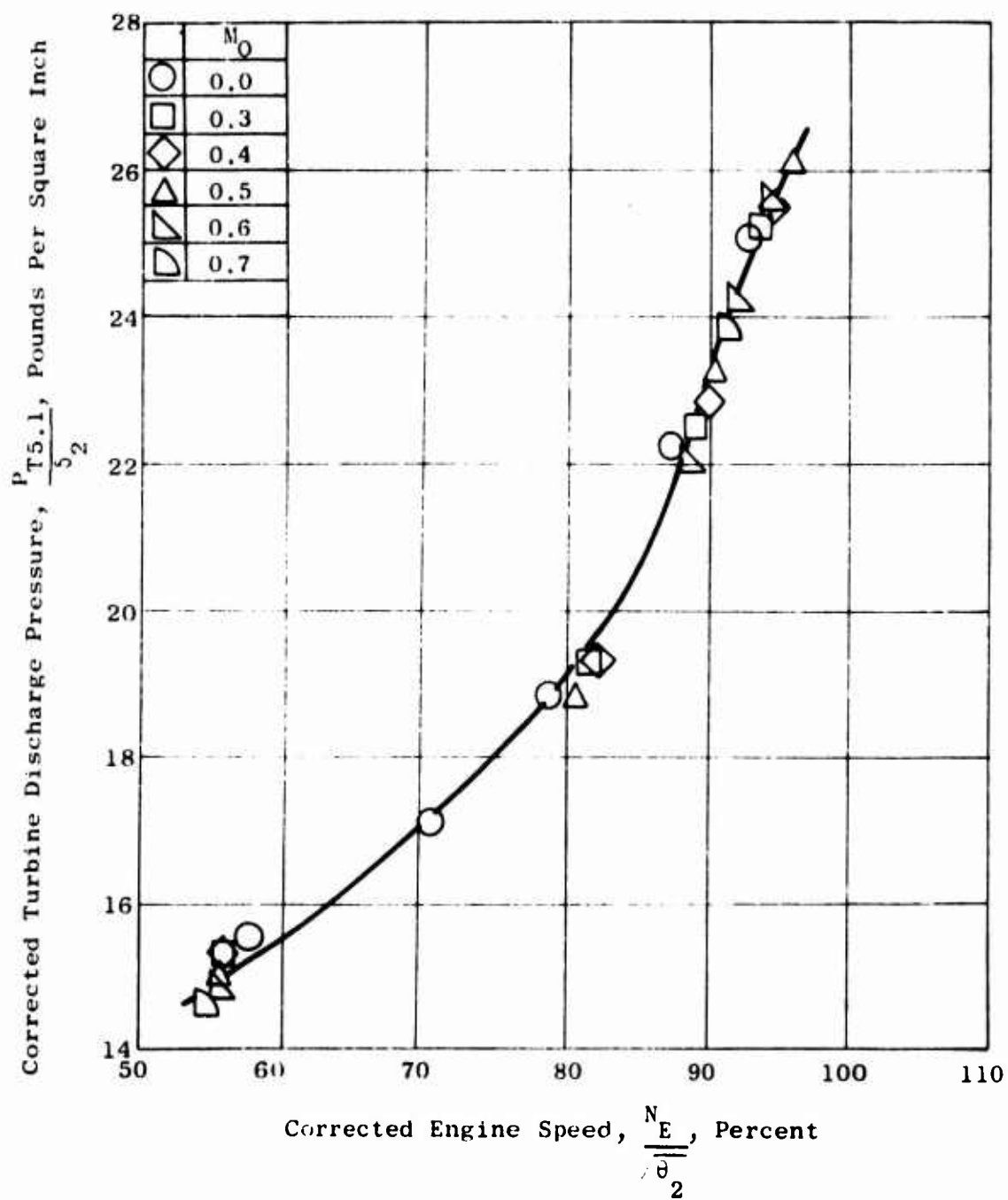


Figure 43. Engine Turbine Discharge Total Pressure - Model 6.

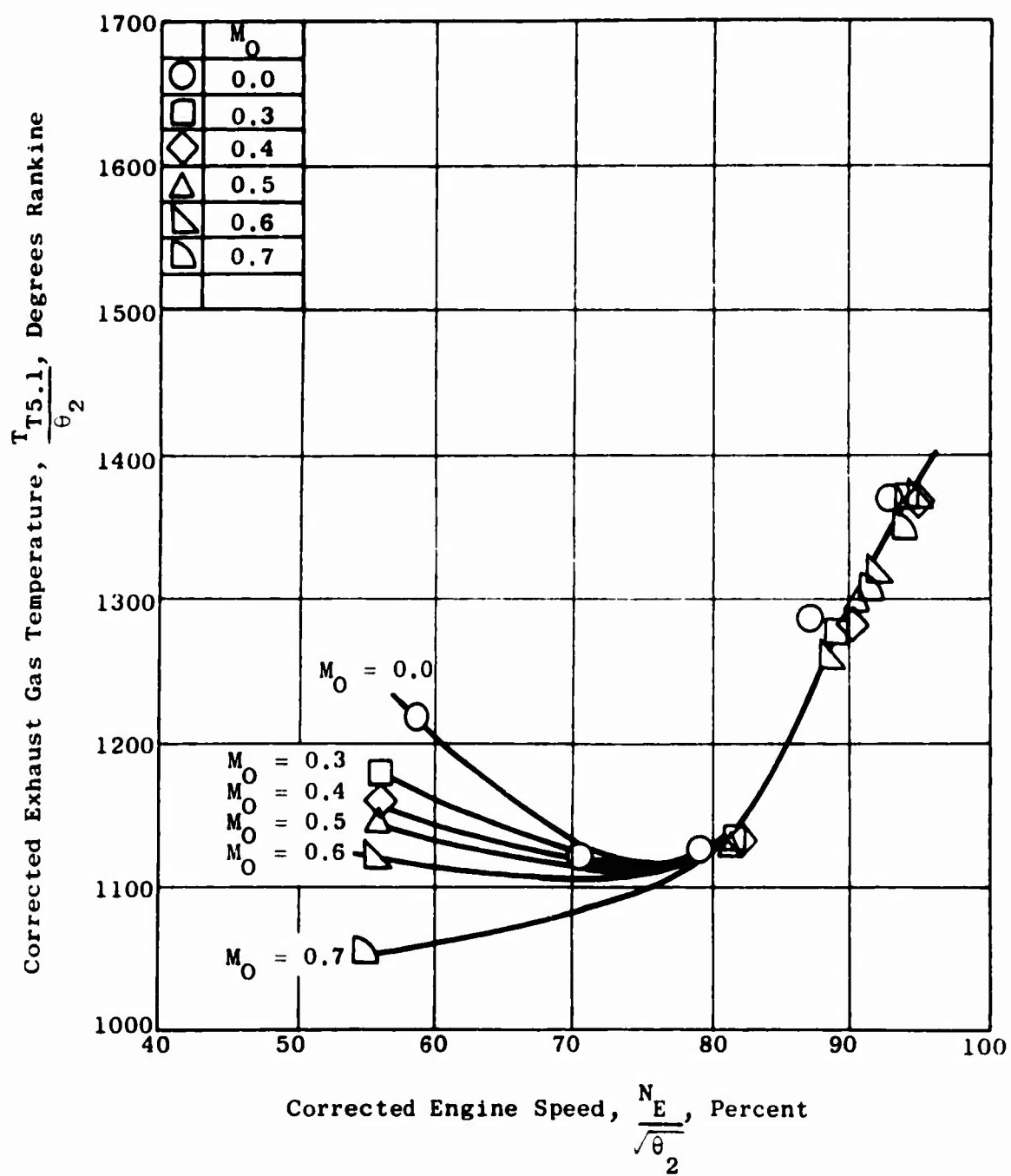


Figure 44. Engine Exhaust Gas Temperature - Model 6.

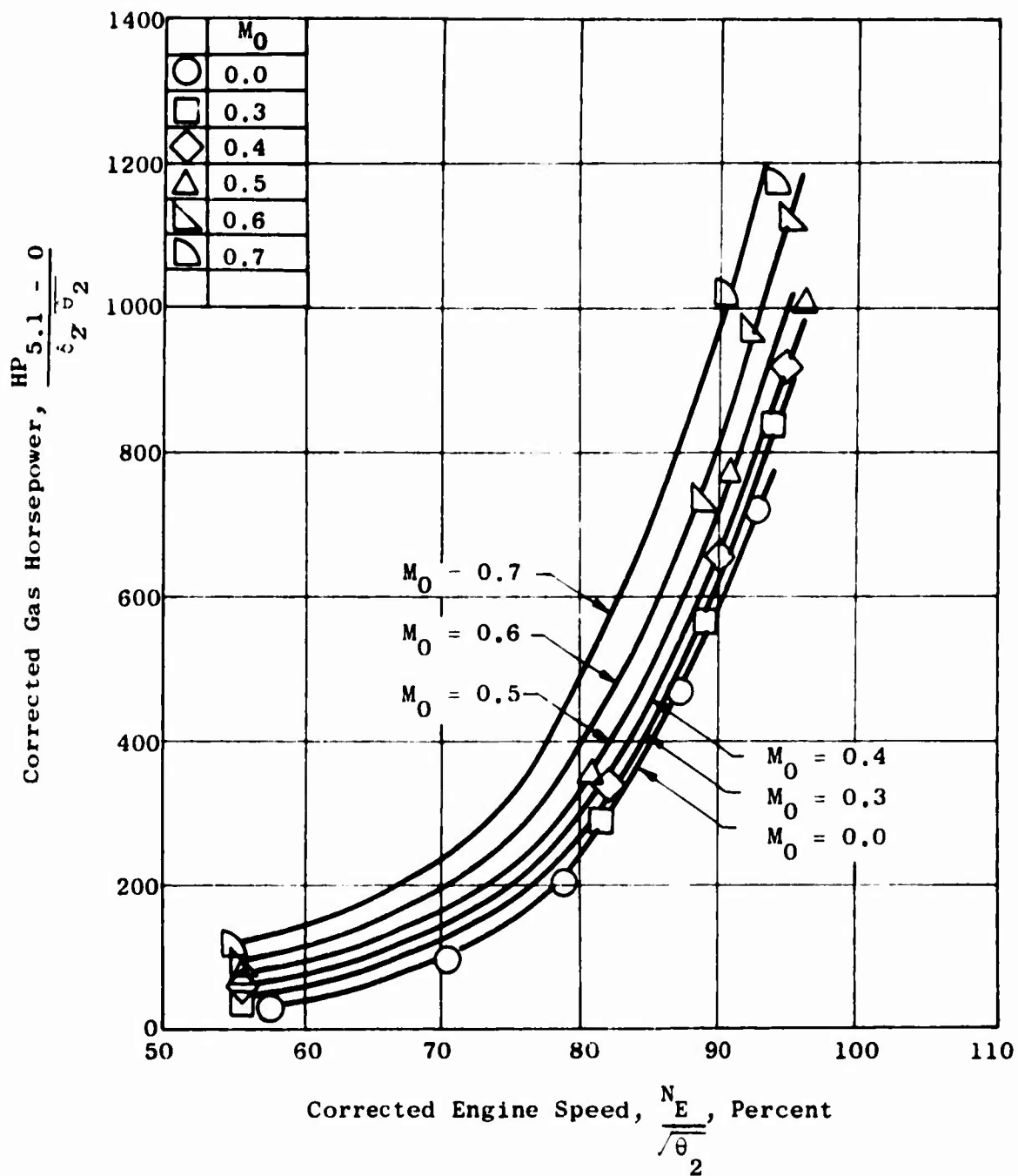


Figure 45. Engine Ideal Gas Horsepower Characteristics - Model 6.

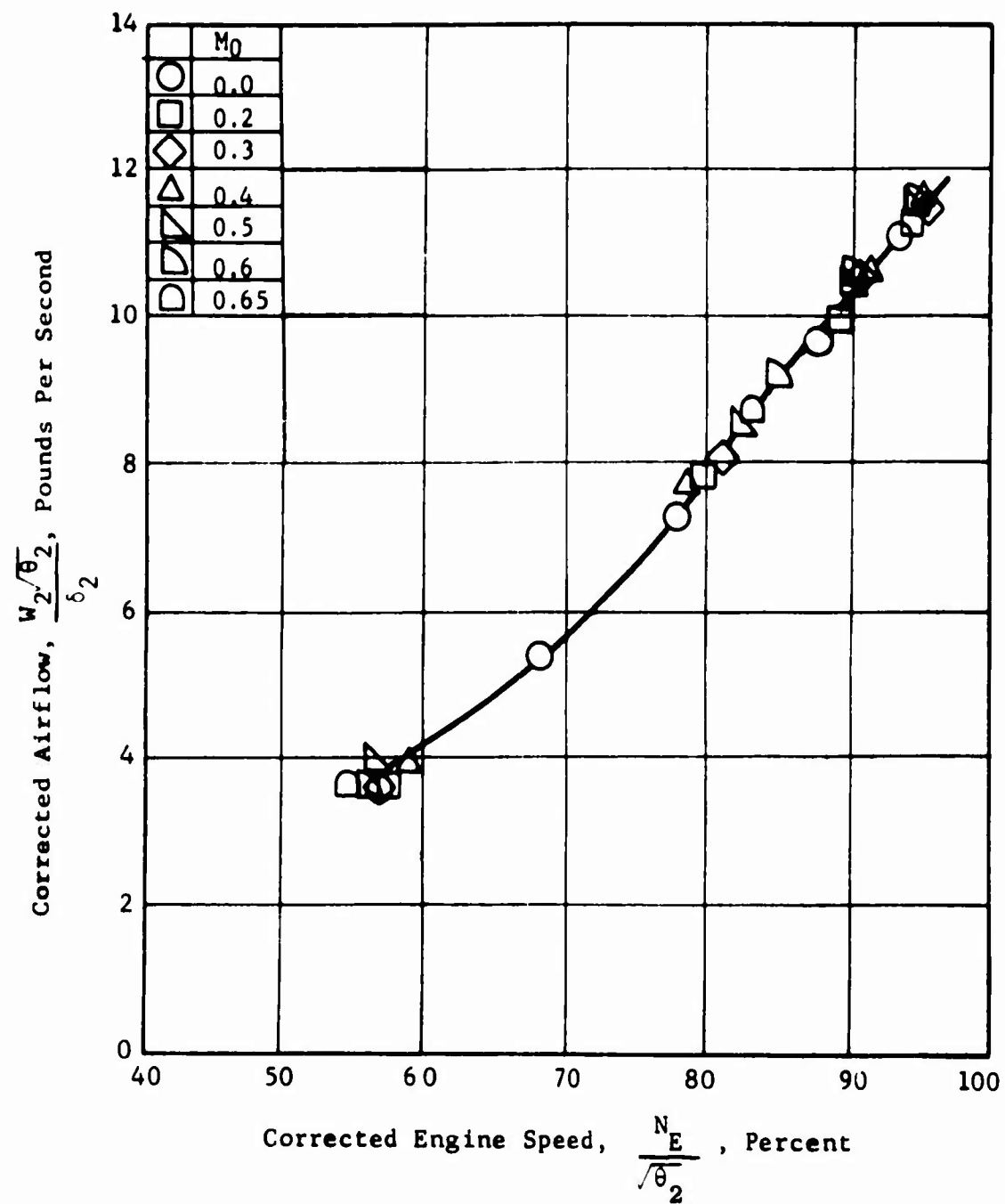


Figure 46. Engine Airflow Characteristics - Model 7.

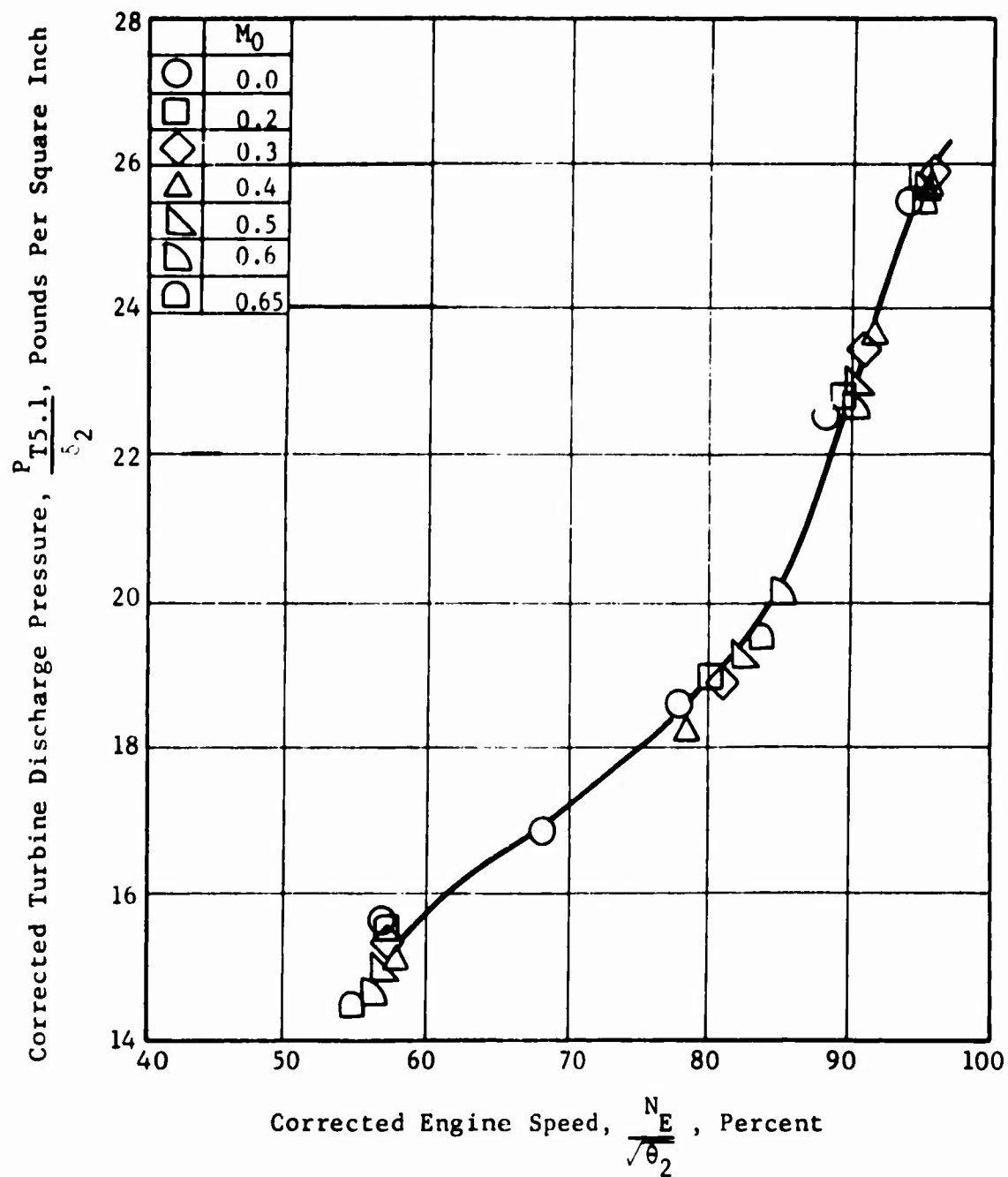


Figure 47. Engine Turbine Discharge Total Pressure - Model 7.

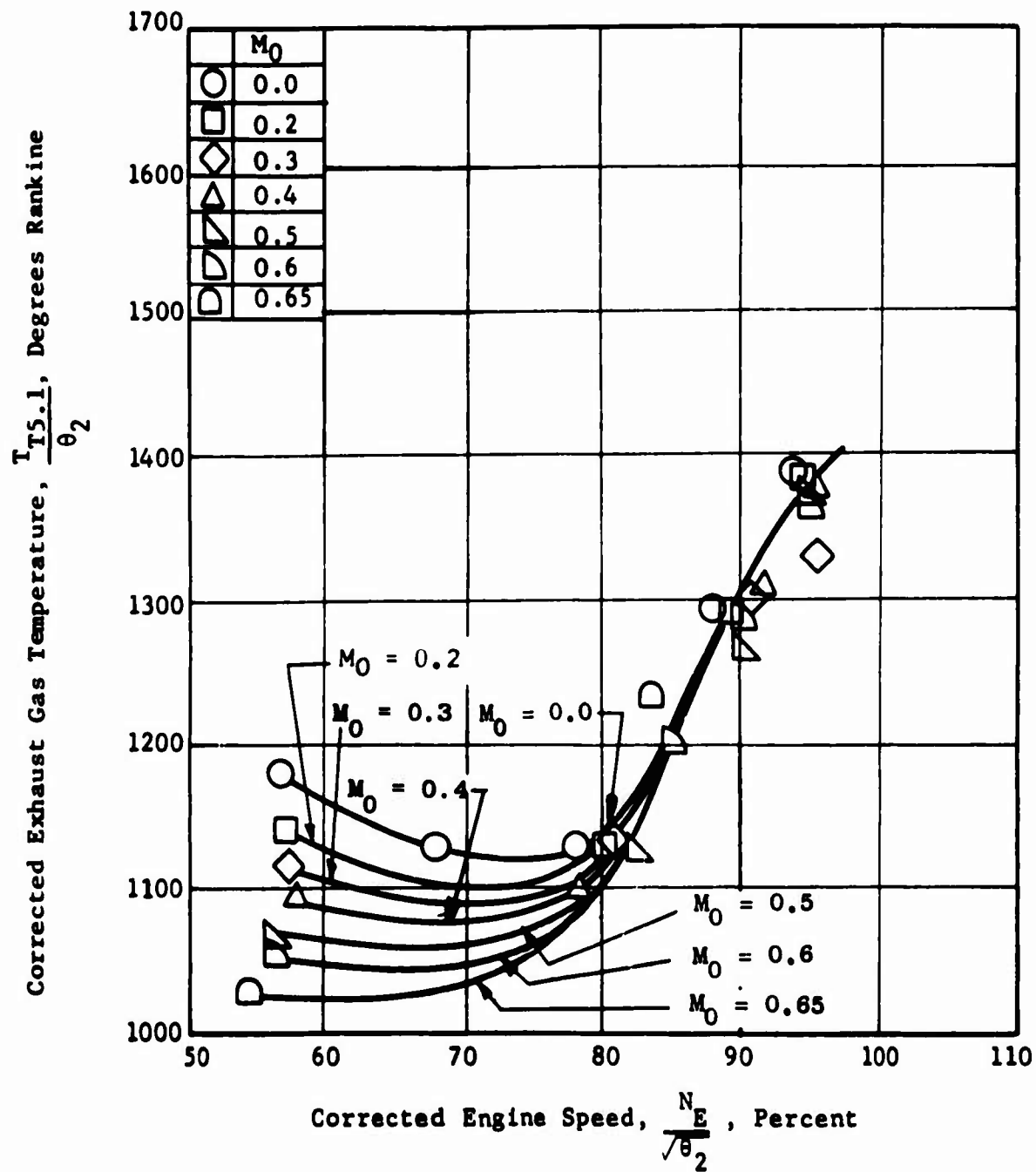


Figure 48. Engine Exhaust Gas Temperature - Model 7.

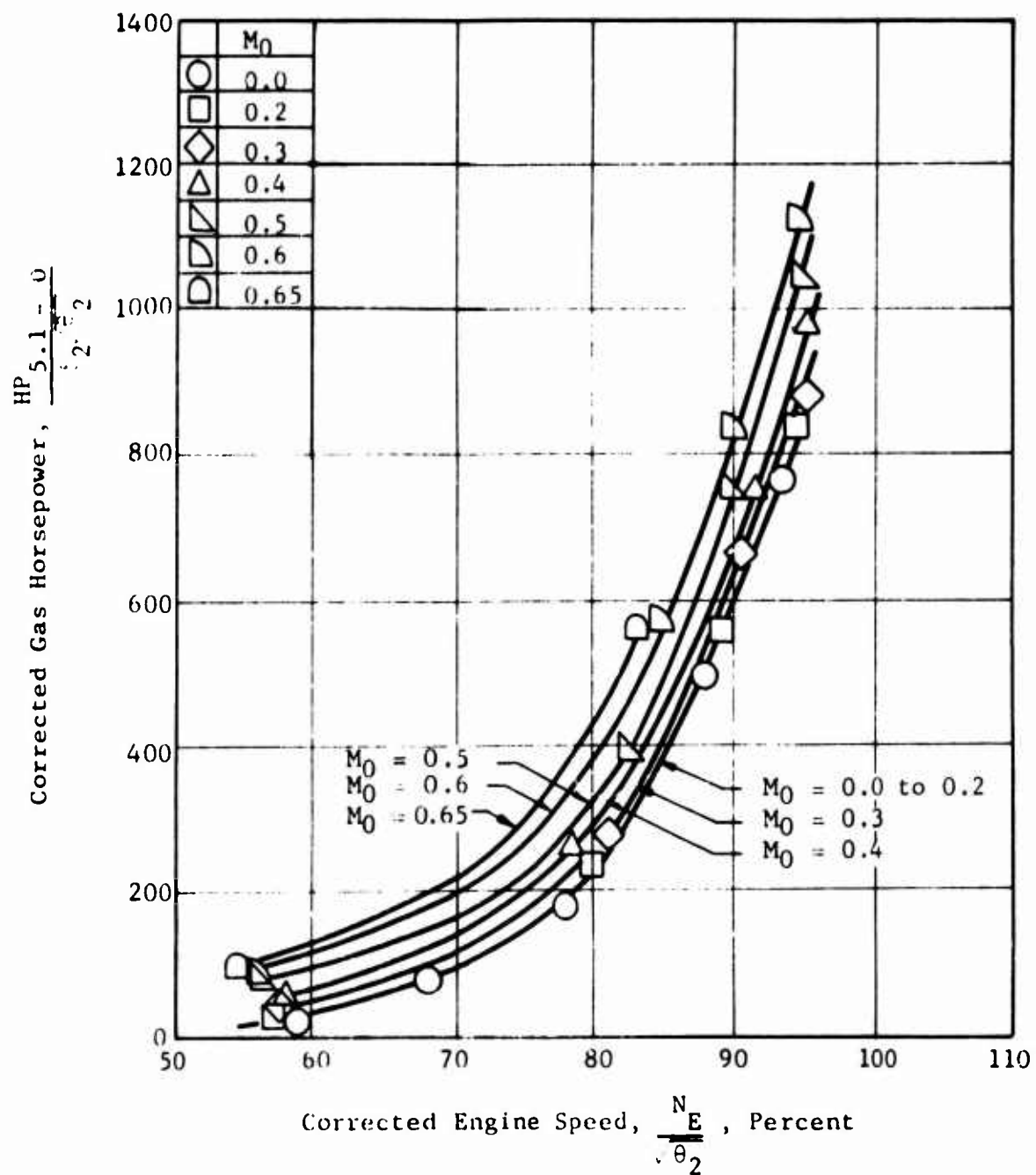


Figure 49. Engine Ideal Gas Horsepower Characteristics - Model 7.

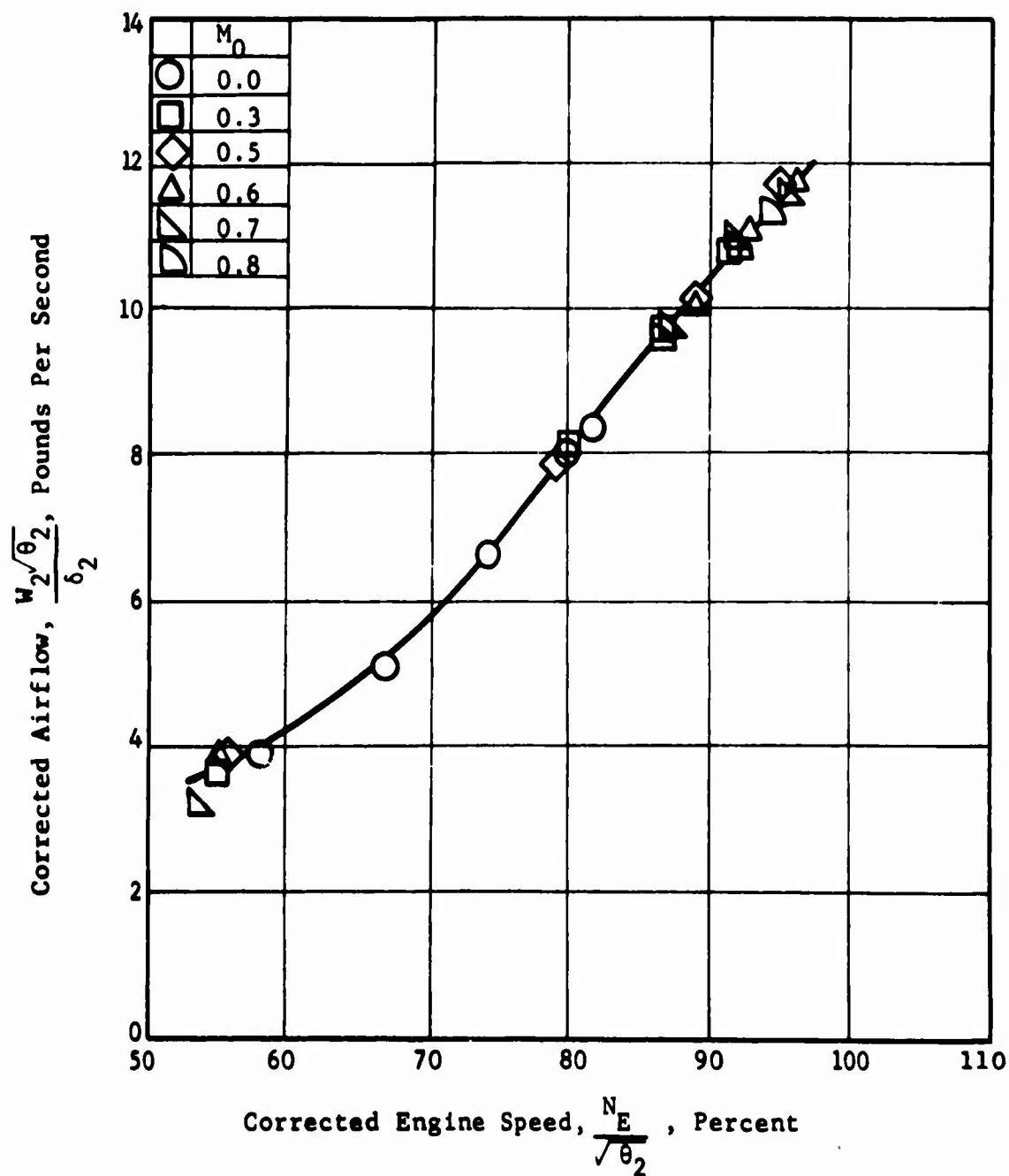


Figure 50. Engine Airflow Characteristics - Model 8.

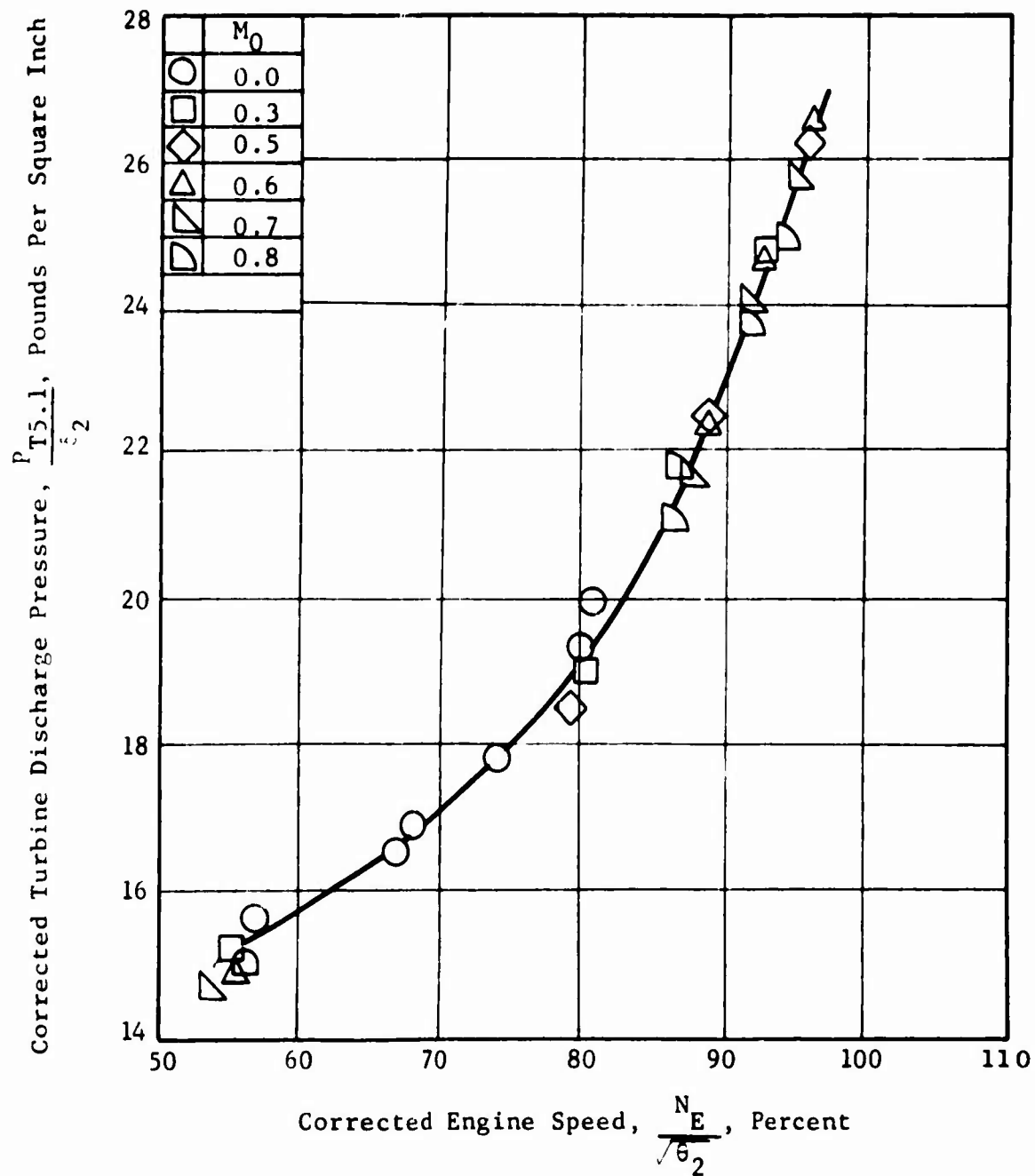


Figure 51. Engine Turbine Discharge Total Pressure - Model 8.

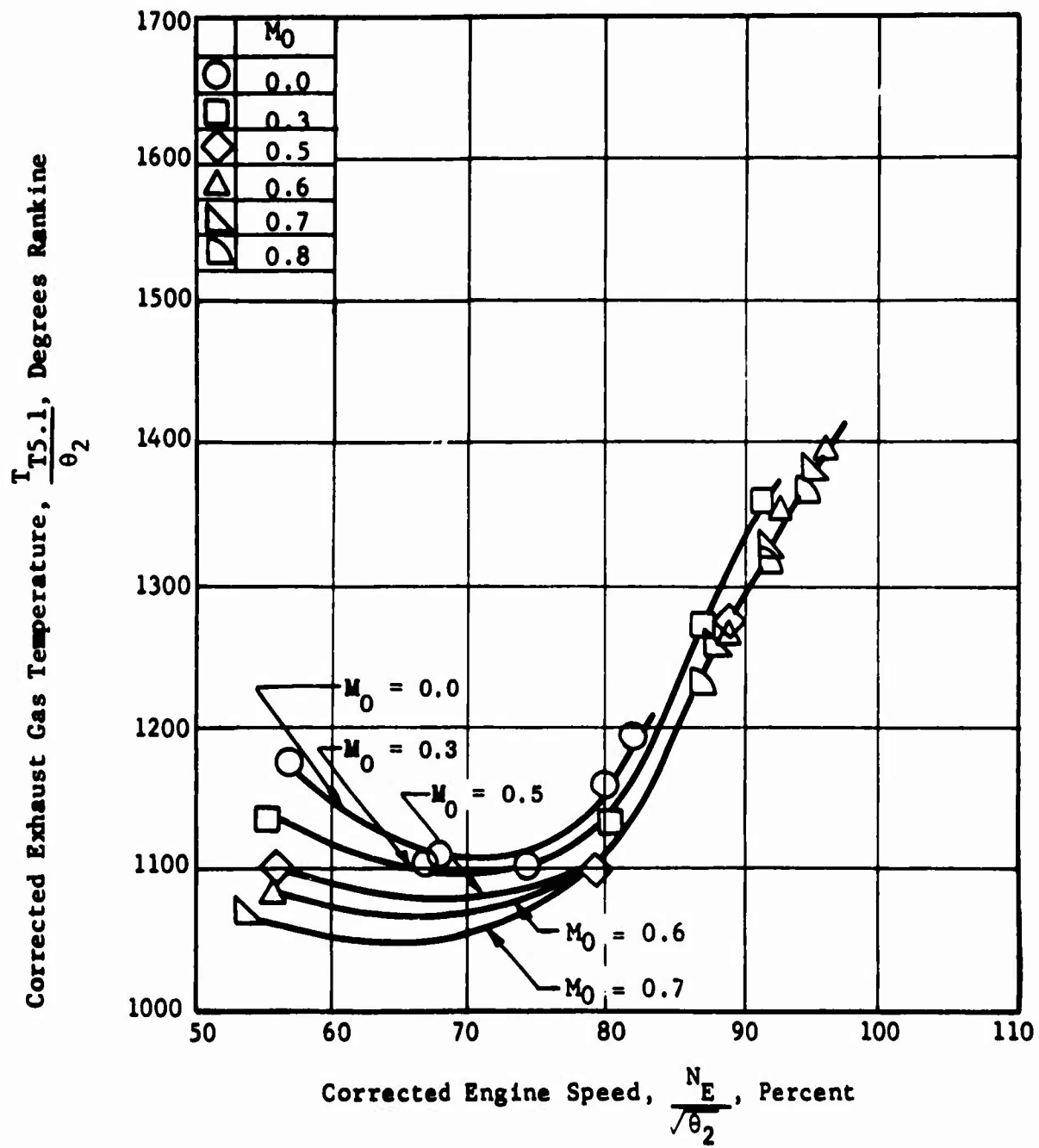


Figure 52. Engine Exhaust Gas Temperature - Model 8.

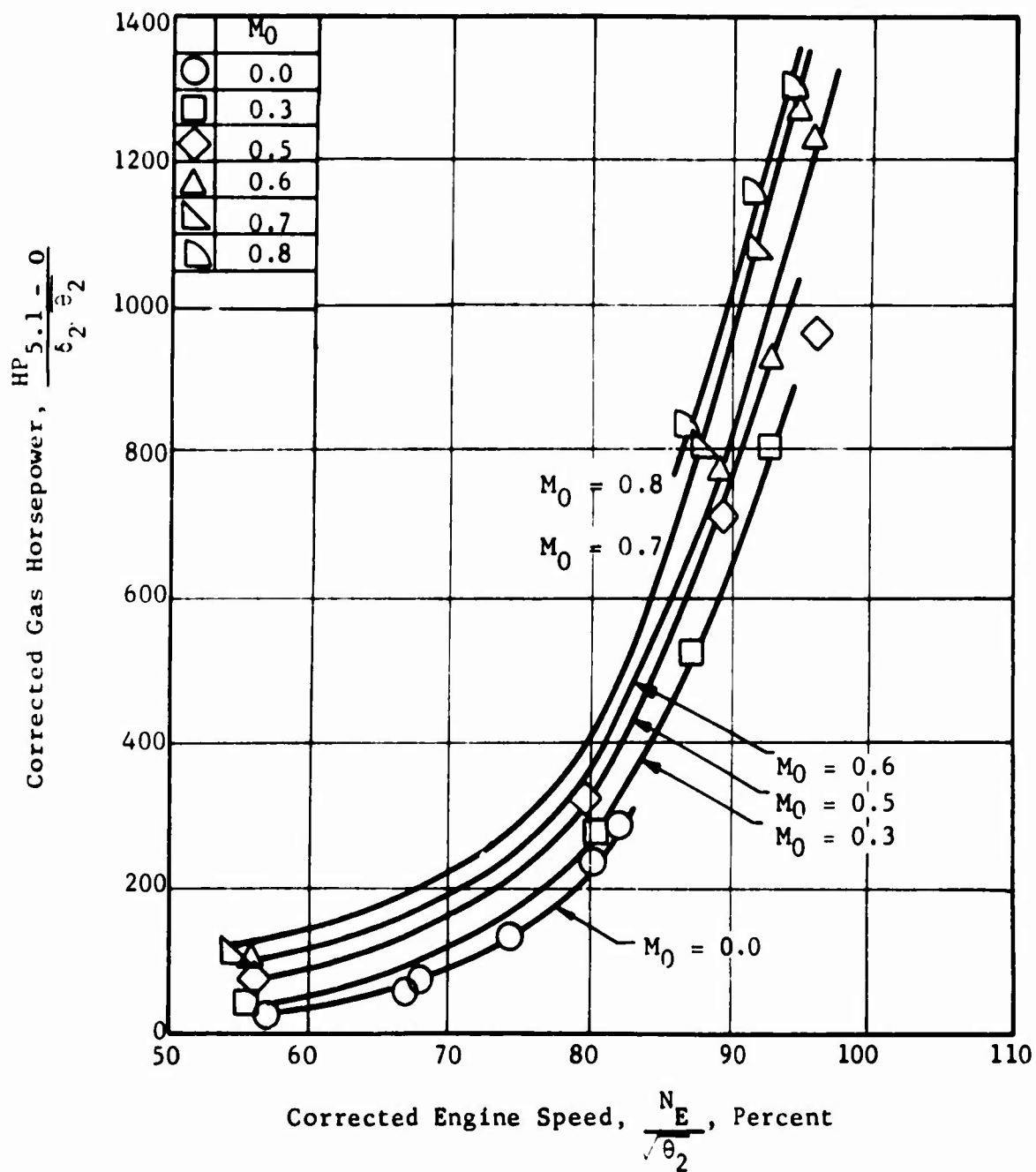


Figure 53. Engine Ideal Gas Horsepower Characteristics - Model 8.

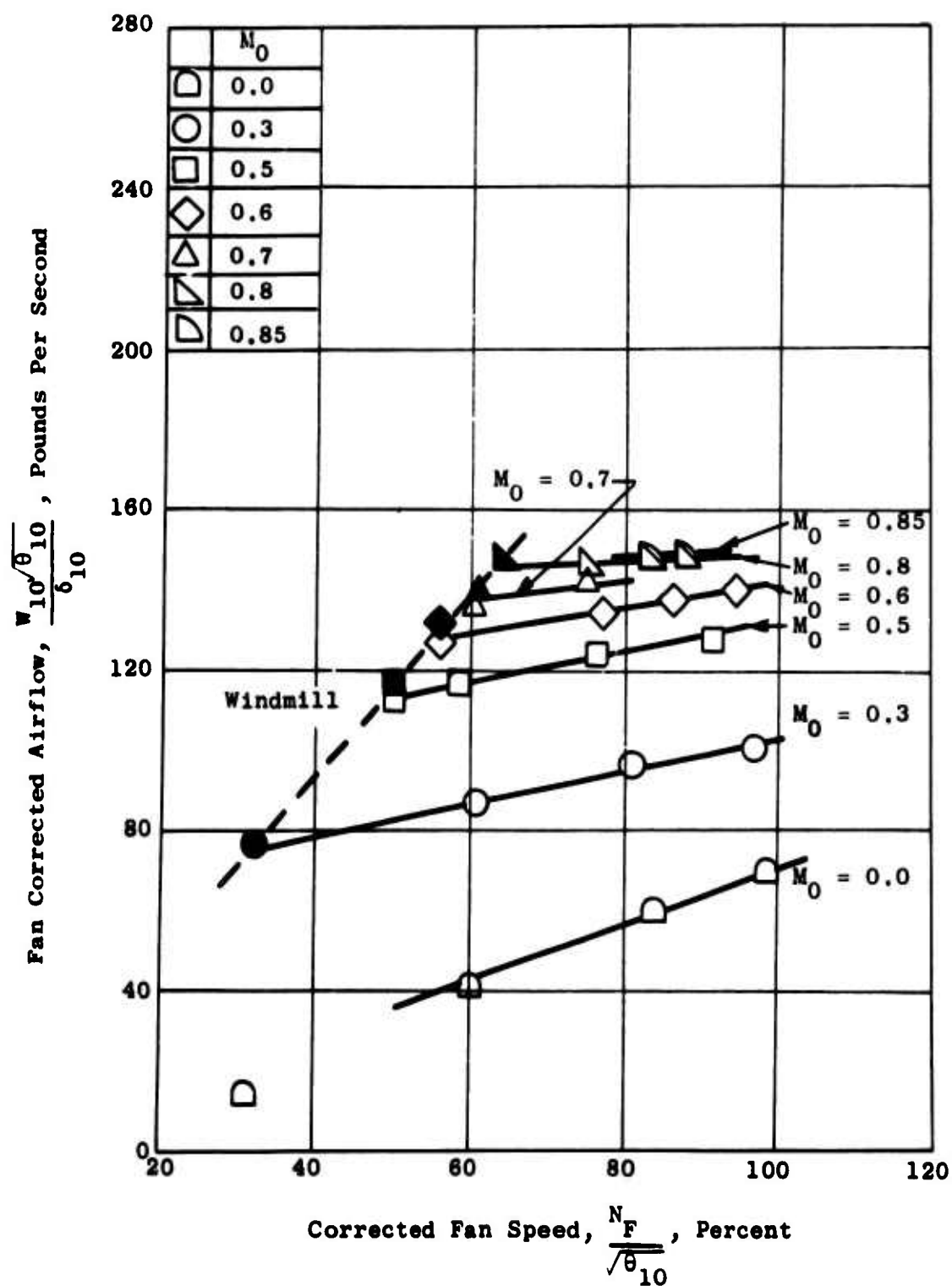


Figure 54. Fan Airflow Characteristics - Model 1.

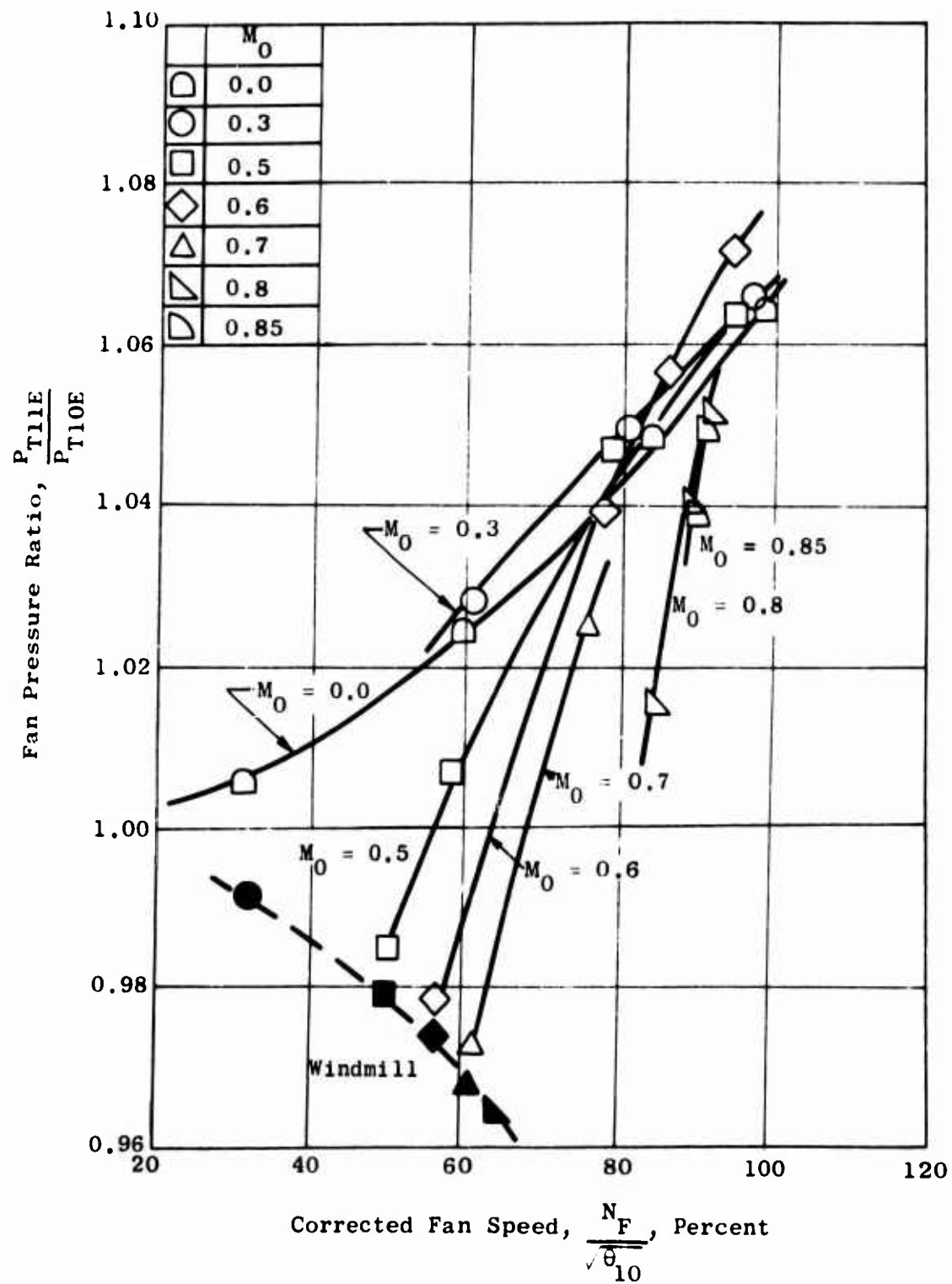


Figure 55. Fan Total Pressure Ratio - Model 1.

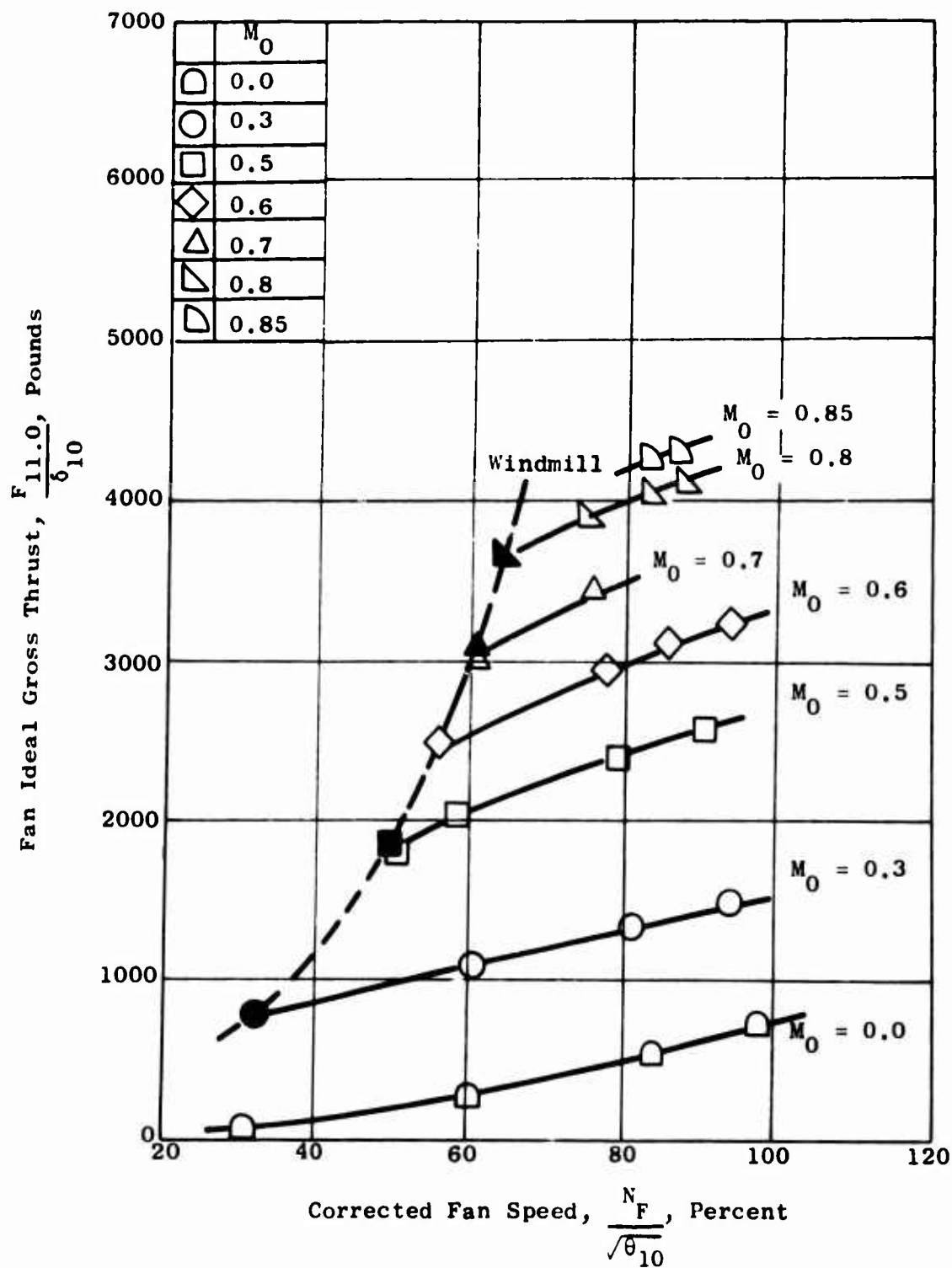


Figure 56. Fan Stream Ideal Gross Thrust - Model 1.

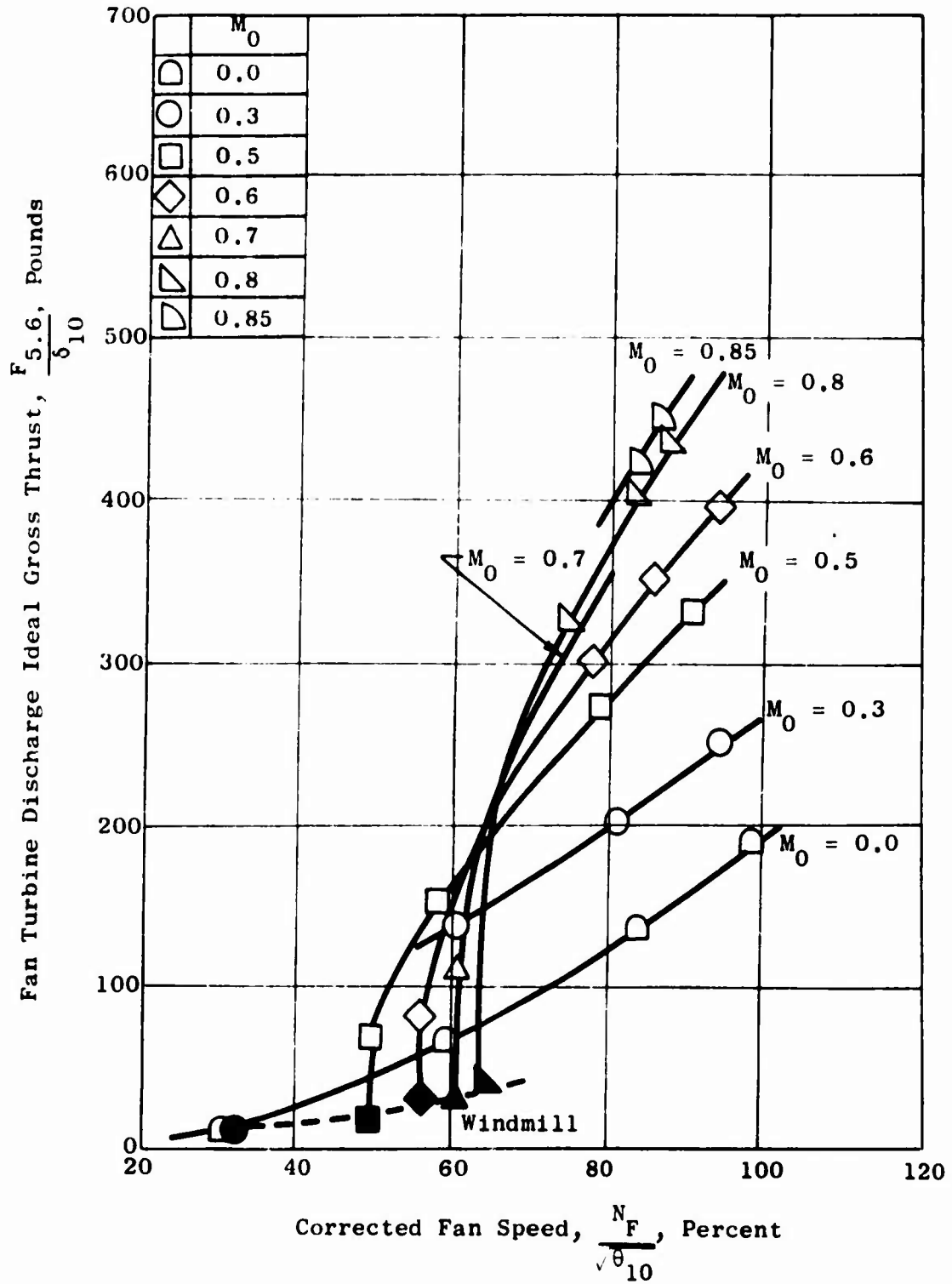


Figure 57. Fan Turbine Residual Ideal Gross Thrust - Model 1.

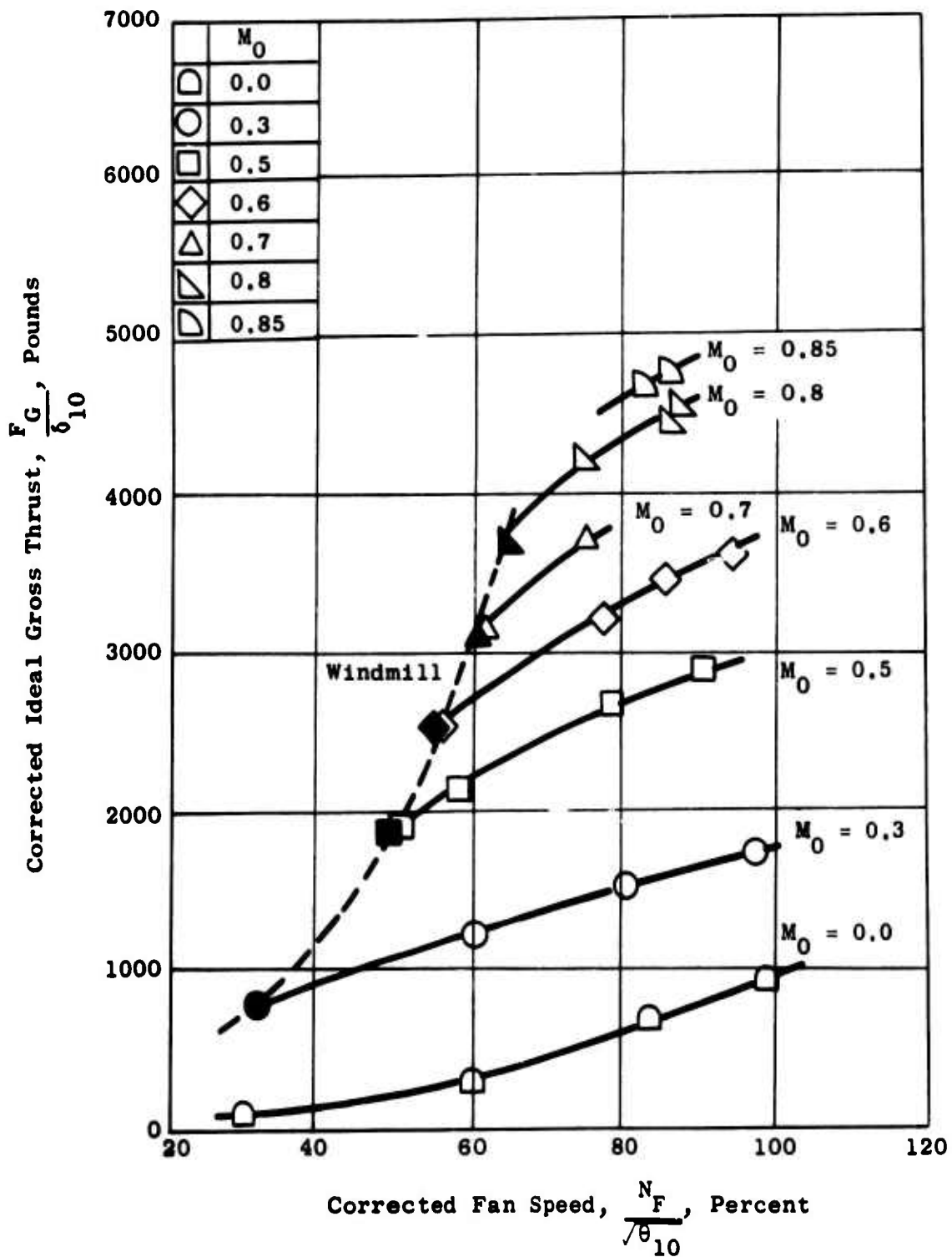


Figure 58. Fan System Ideal Gross Thrust - Model 1.

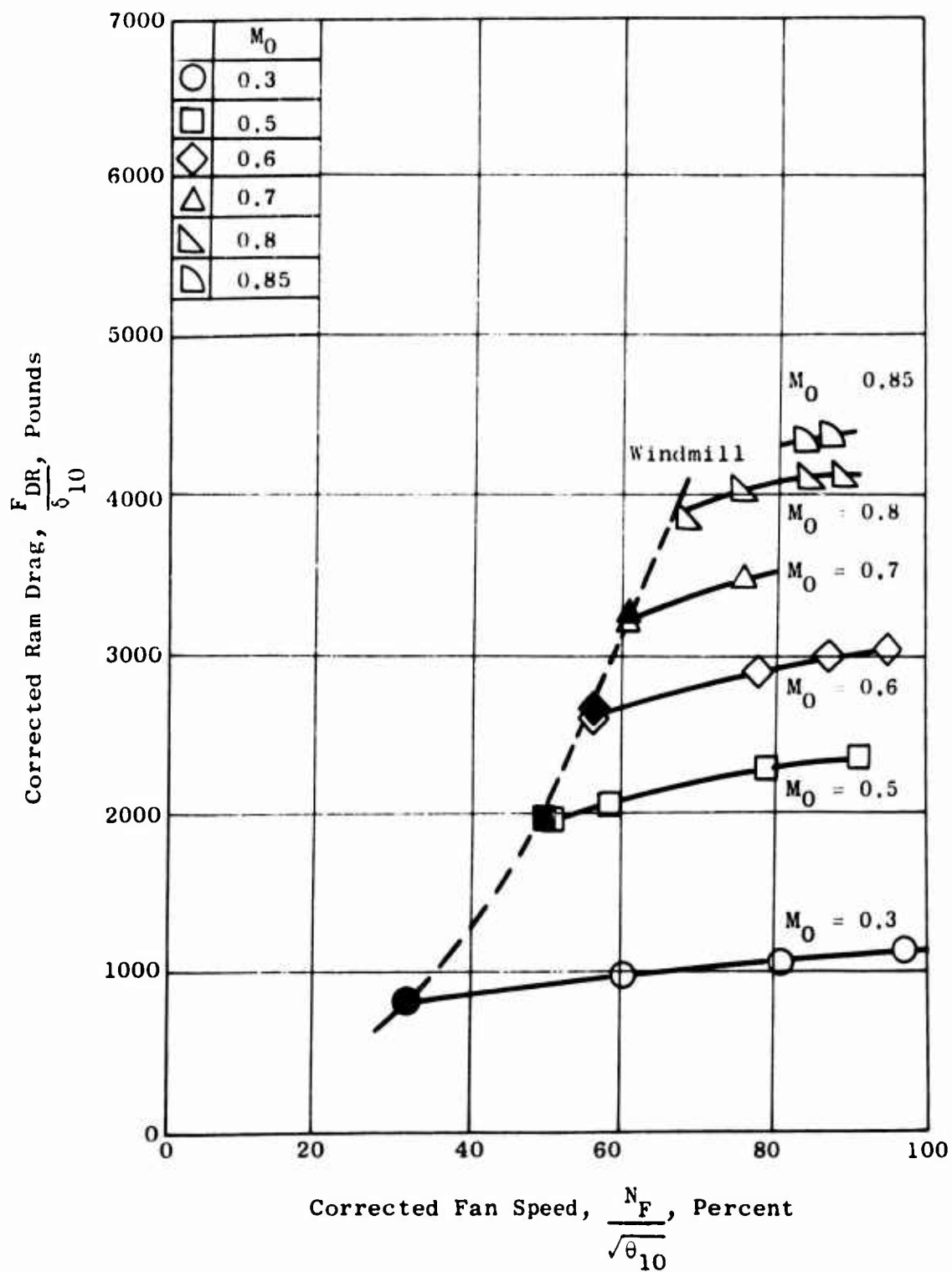


Figure 59. Total Ram Drag - Model 1.

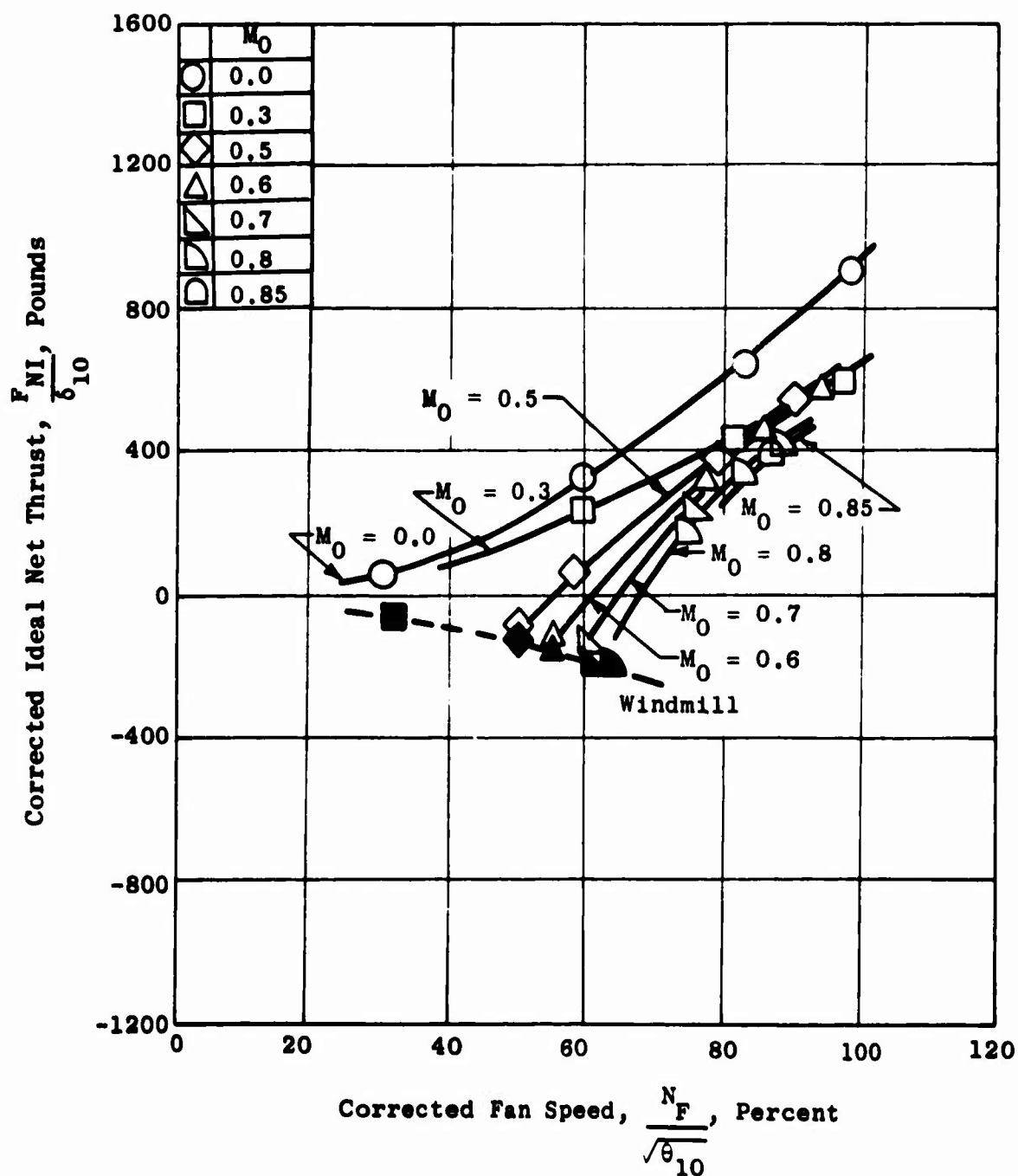


Figure 60. Fan System Ideal Net Thrust - Model 1.

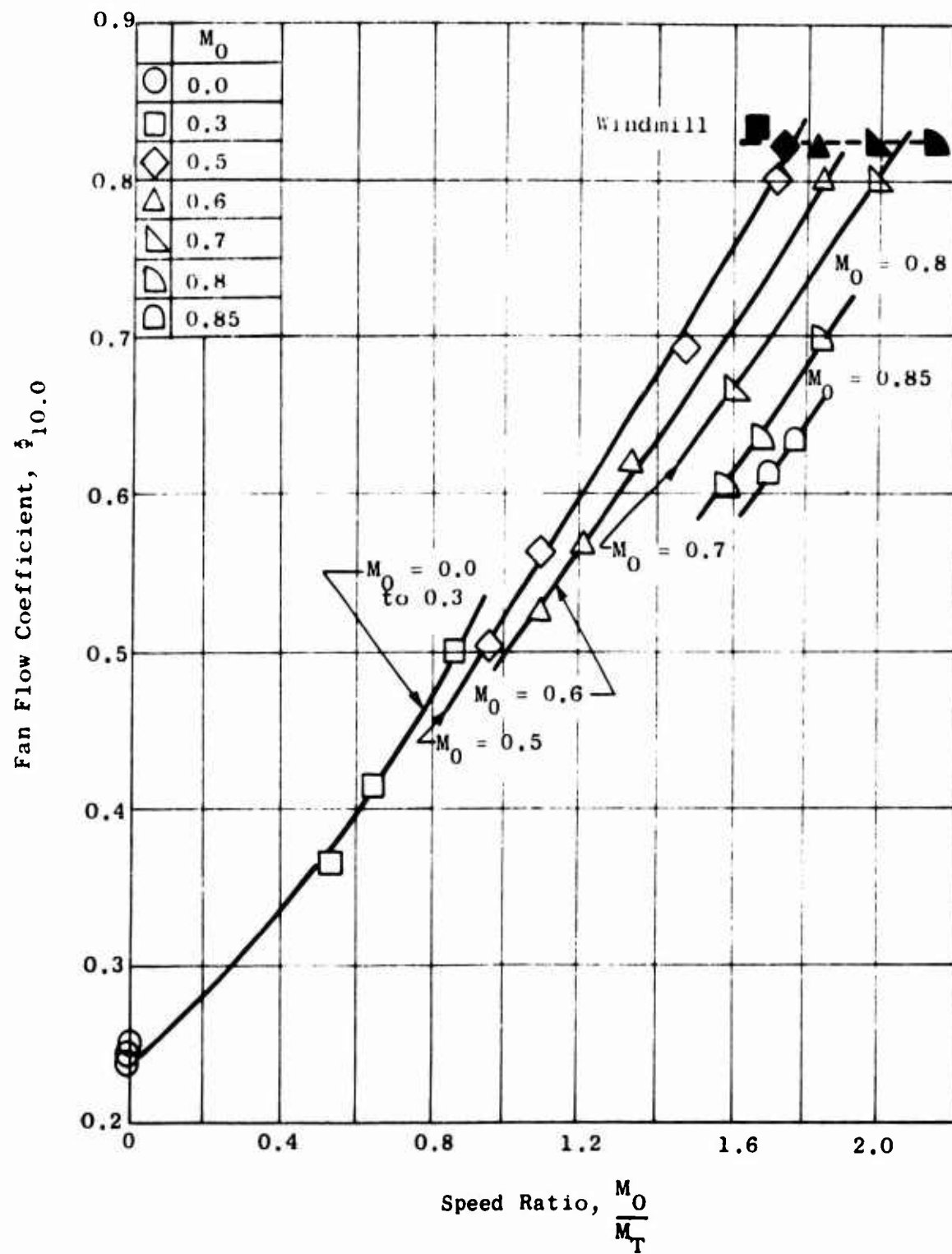


Figure 61. Fan Flow Function Characteristics - Model 1.

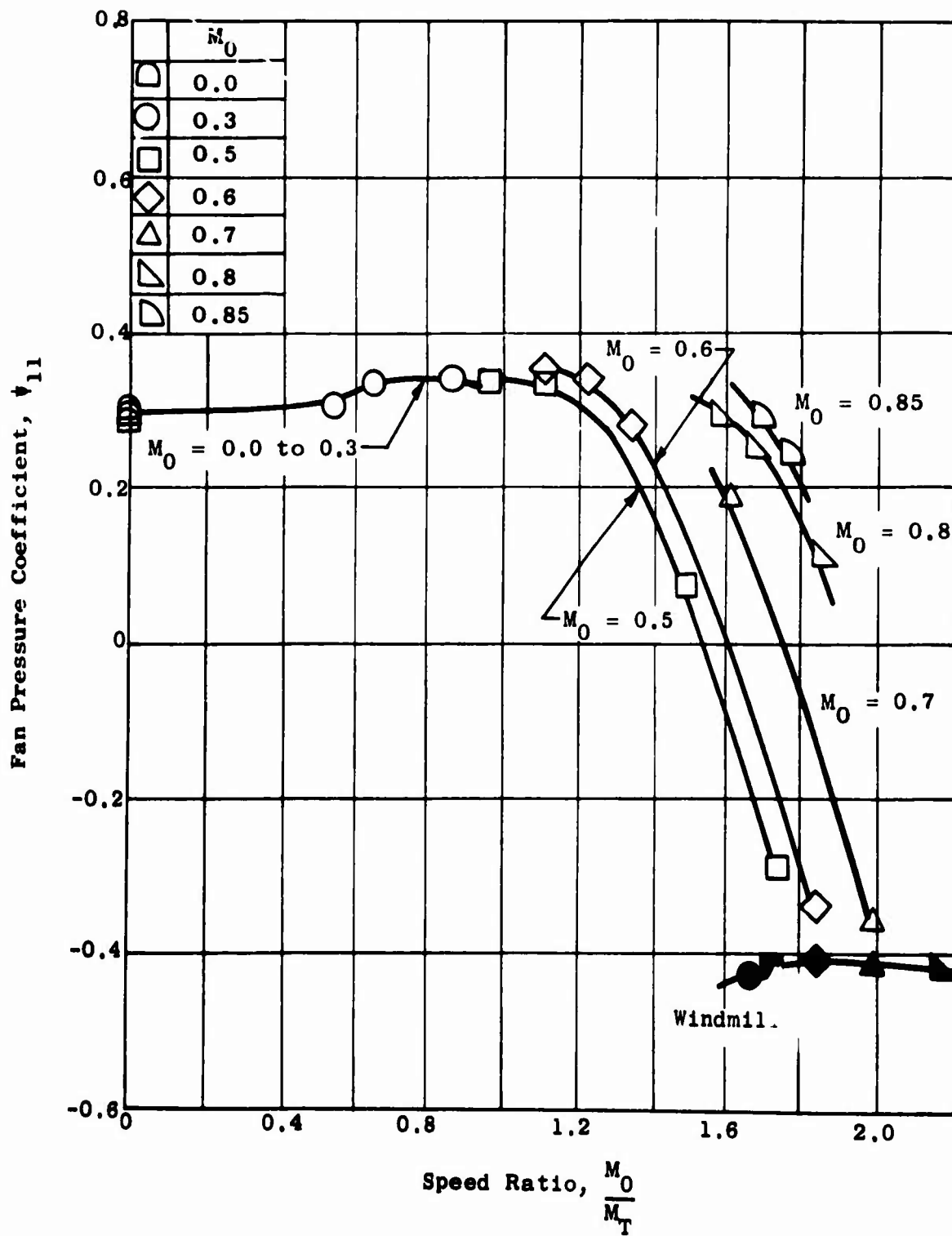


Figure 62. Fan Pressure Coefficient Characteristics - Model 1.

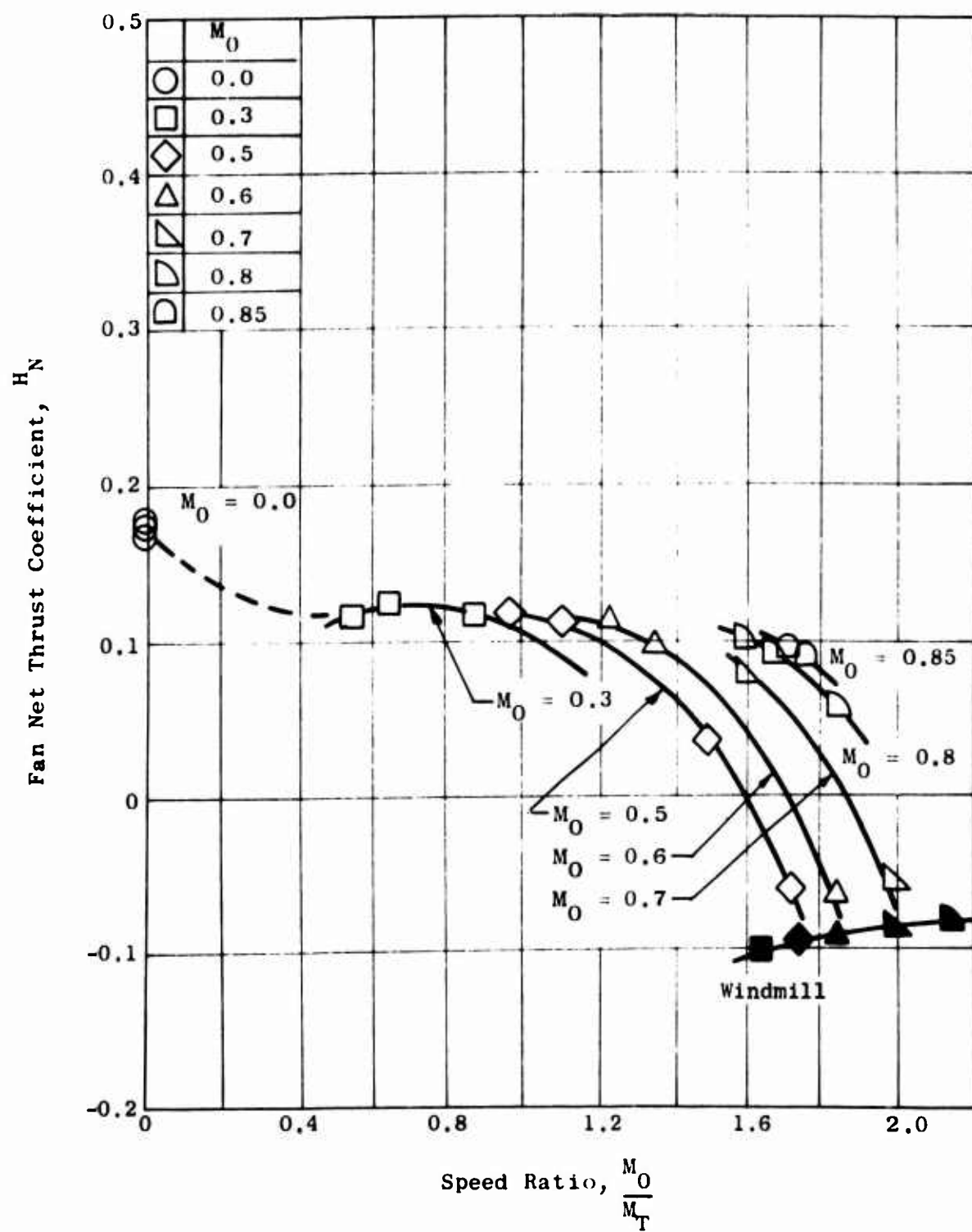


Figure 63. Fan Ideal Net Thrust Coefficient - Model 1.

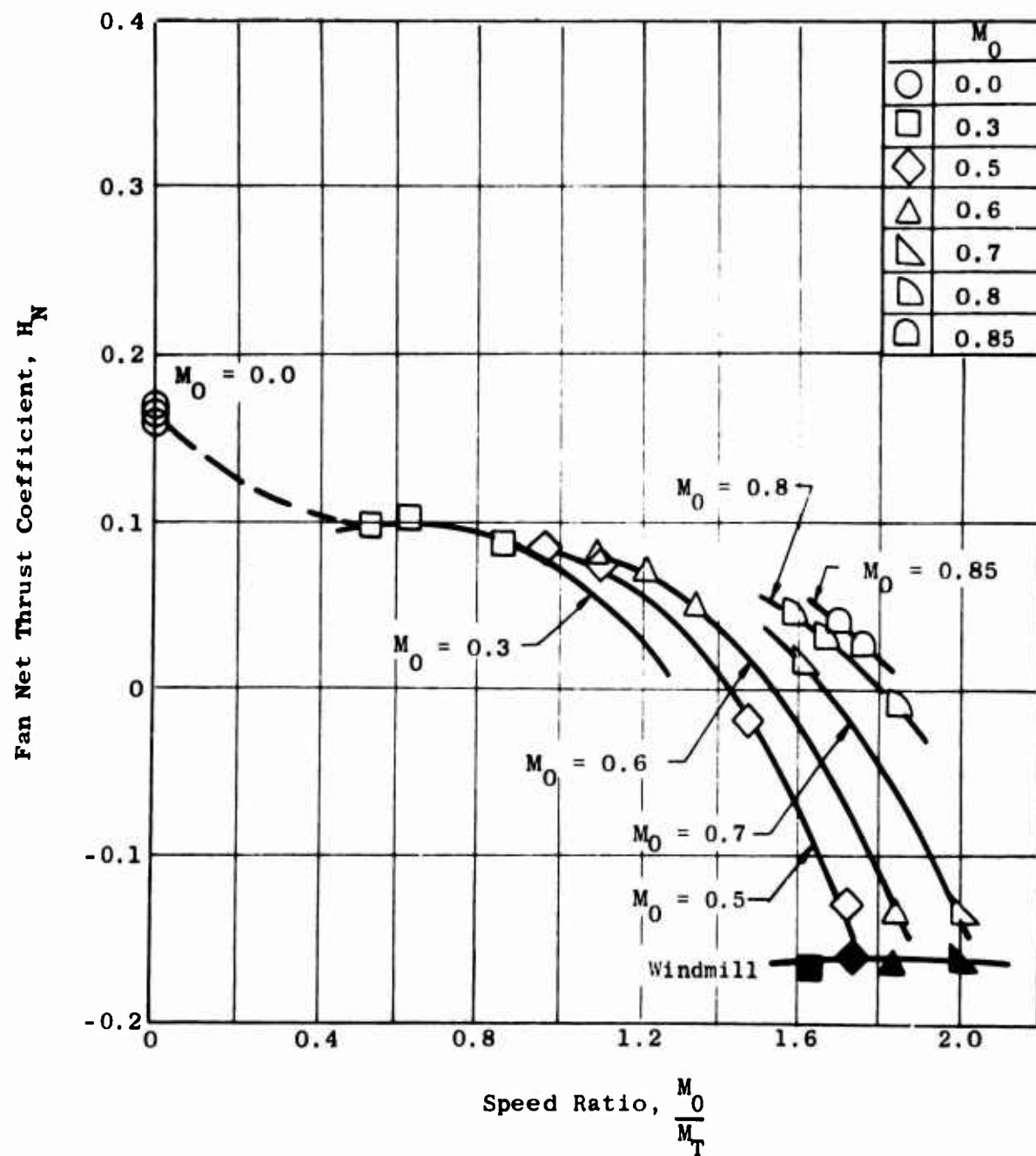


Figure 64. Fan Net Thrust Coefficient with a Nozzle Coefficient of 0.95 - Model 1.

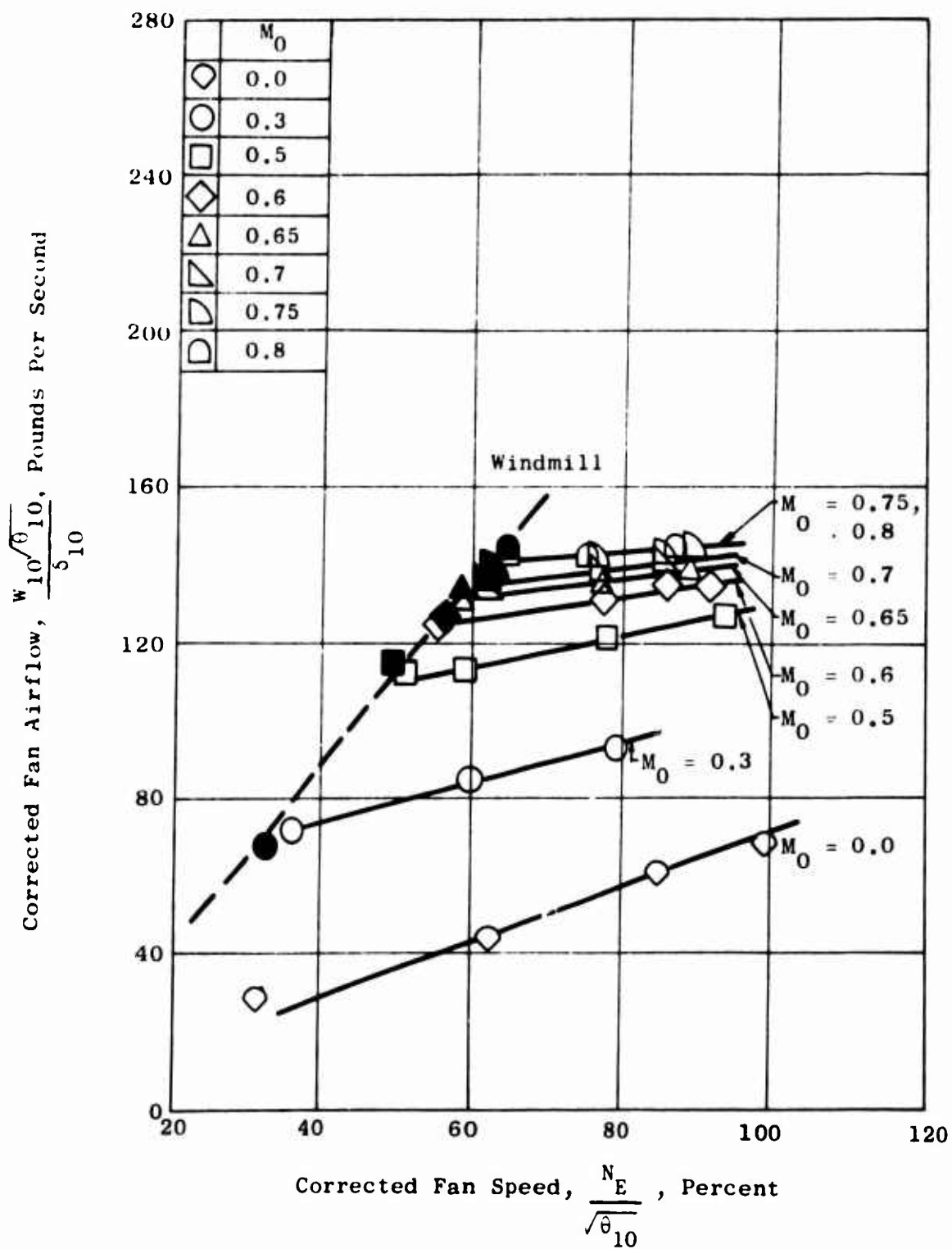


Figure 65. Fan Airflow Characteristics - Model 2.

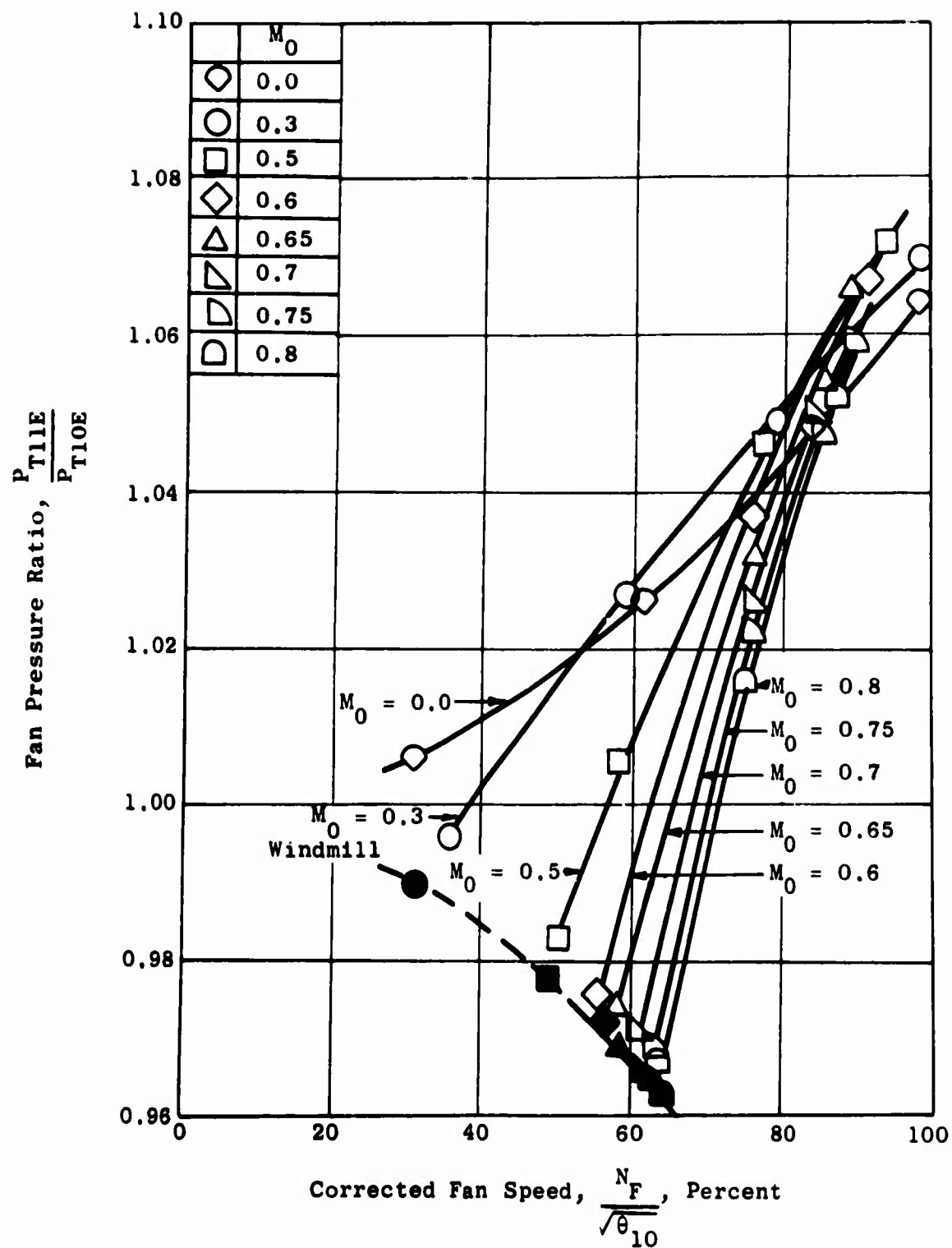


Figure 66. Fan Total Pressure Ratio - Model 2.

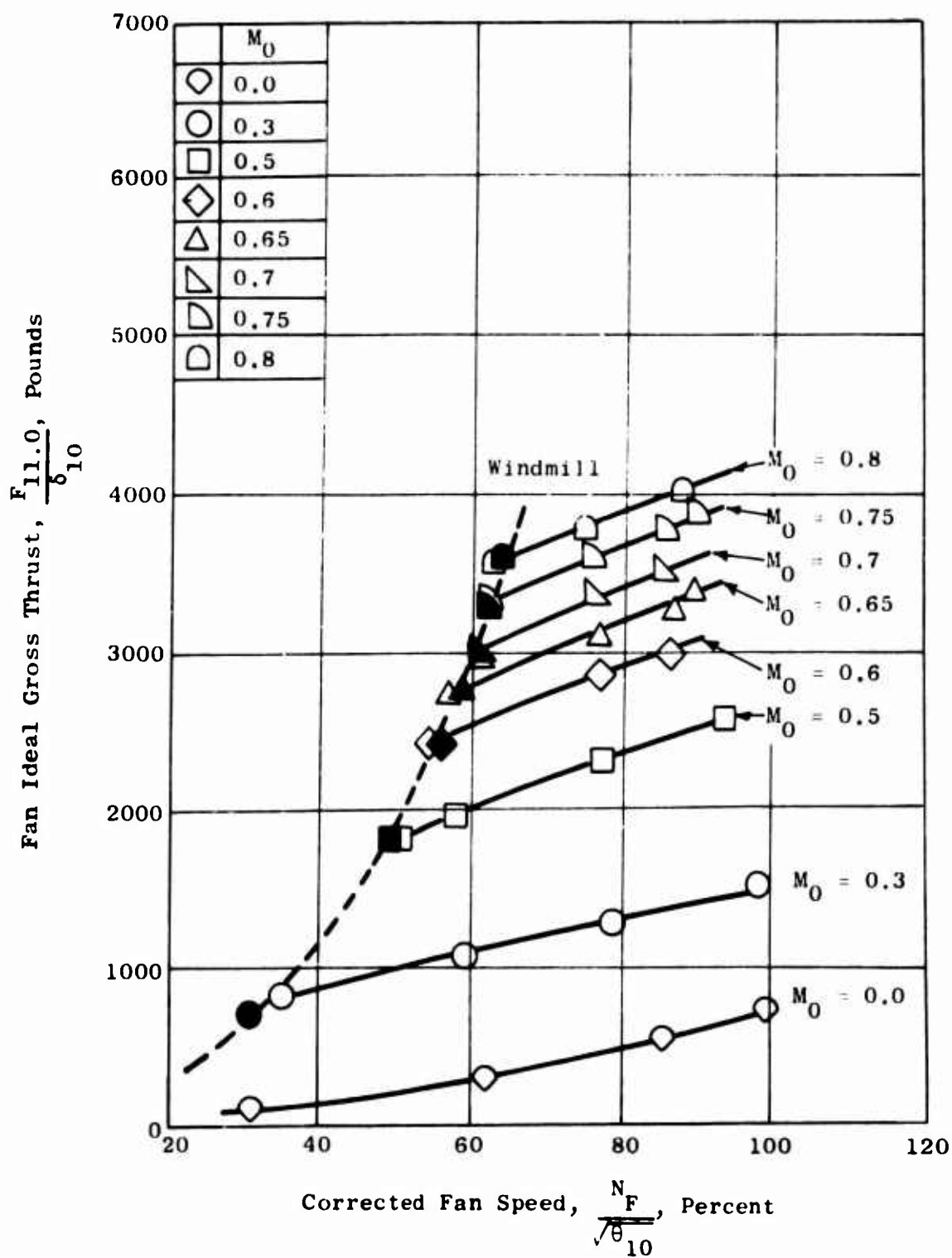


Figure 67. Fan Stream Ideal Gross Thrust - Model 2.

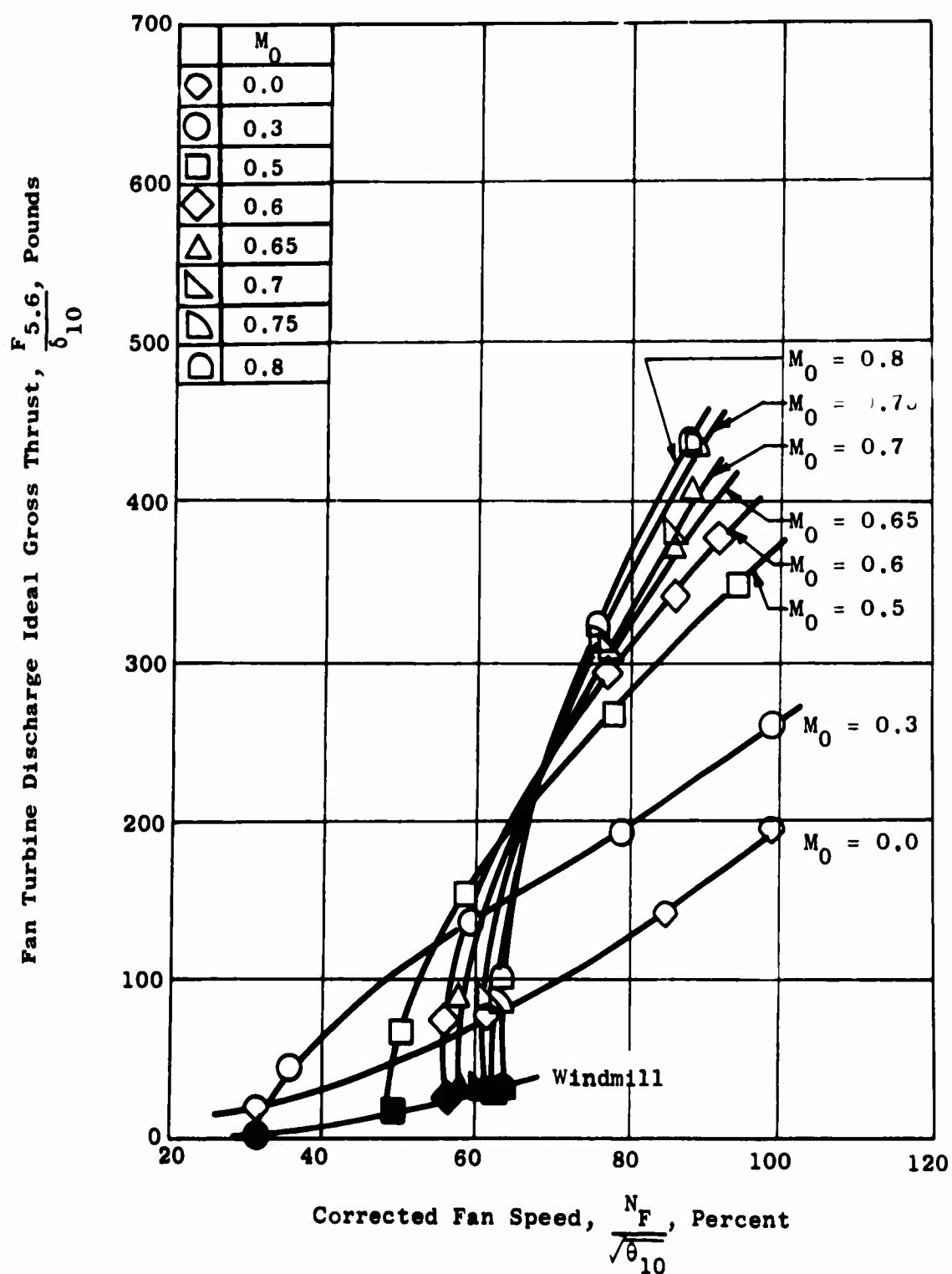


Figure 68. Fan Turbine Residual Ideal Gross Thrust - Model 2.

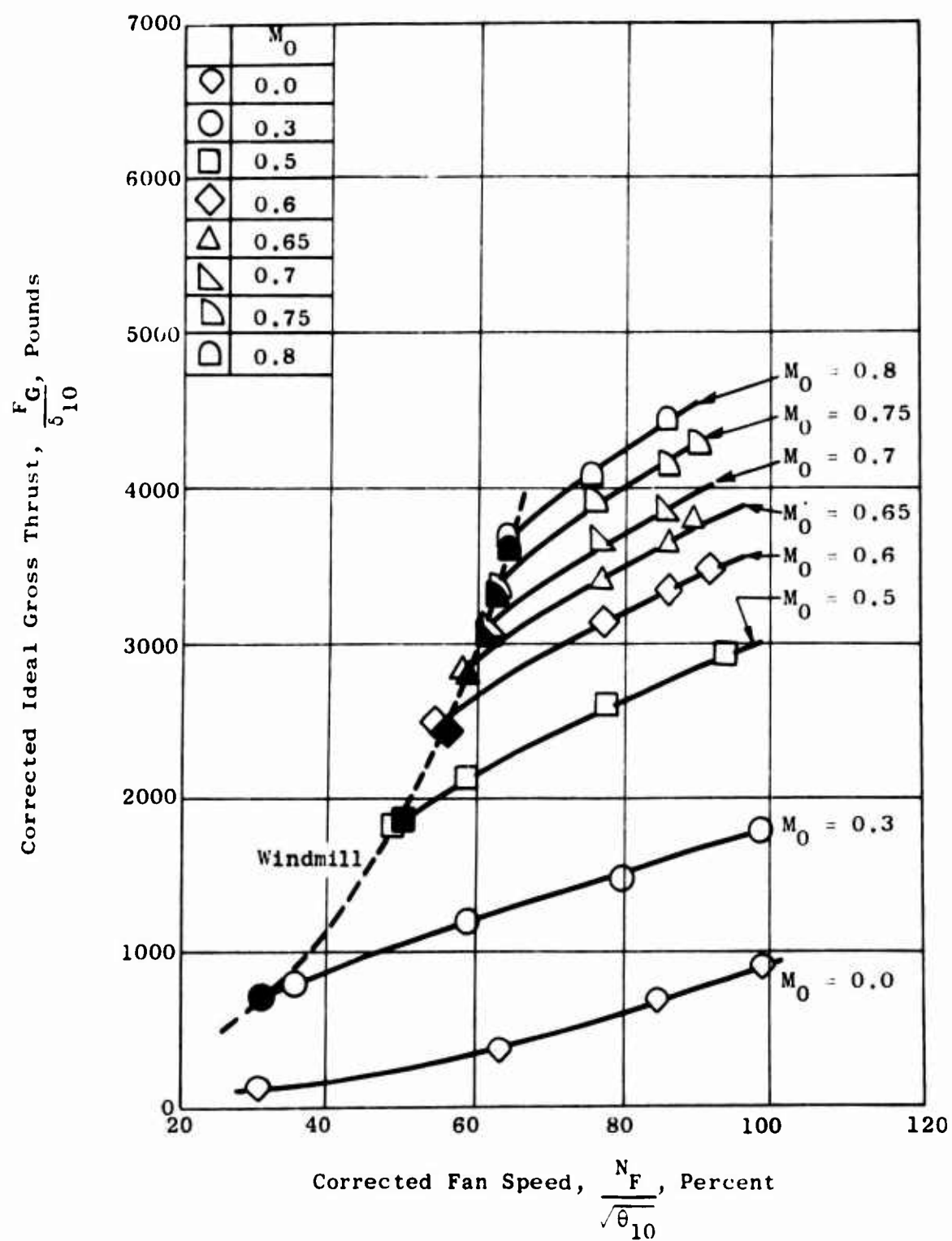


Figure 69. Fan System Ideal Gross Thrust - Model 2.

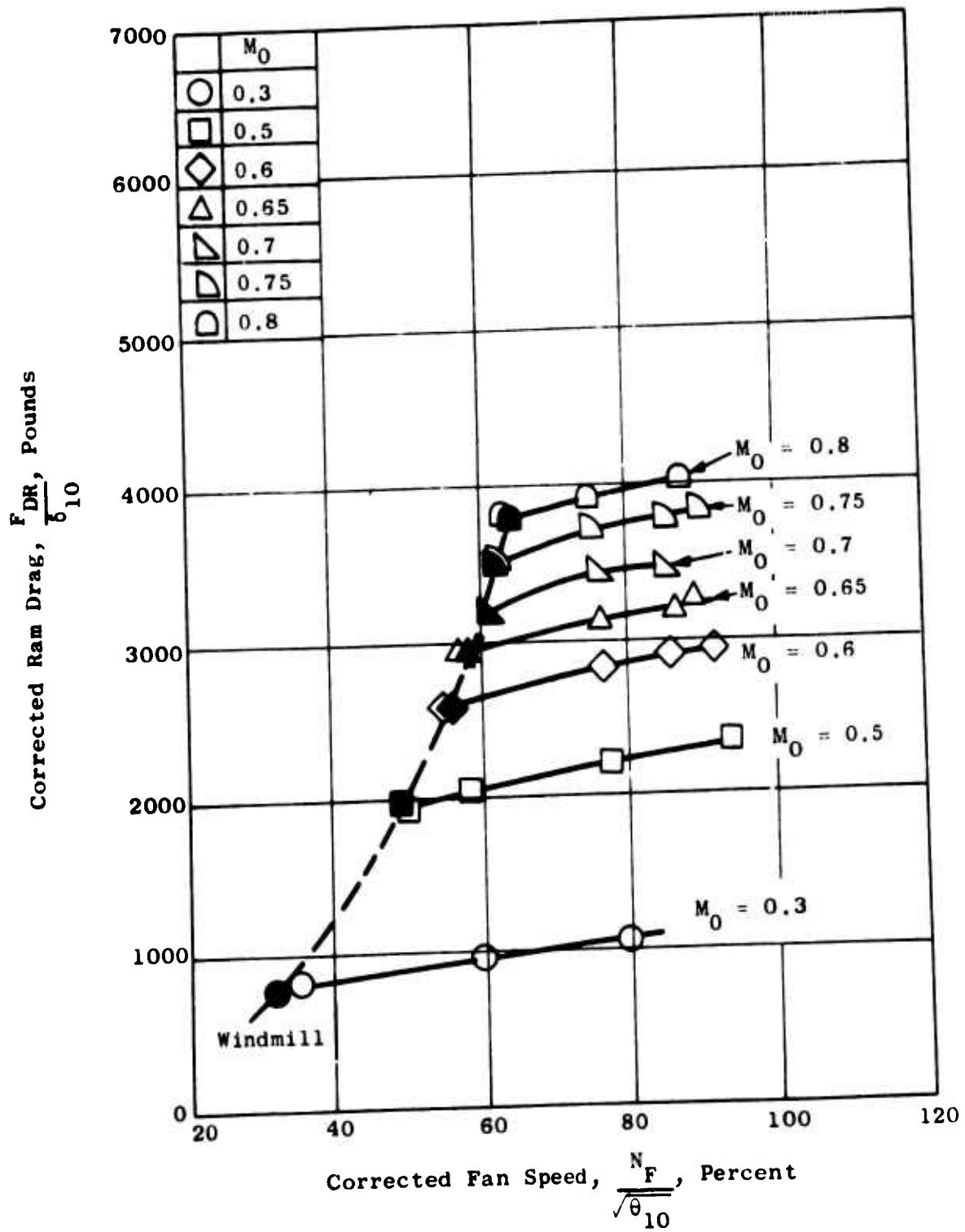


Figure 70. Total Ram Drag - Model 2.

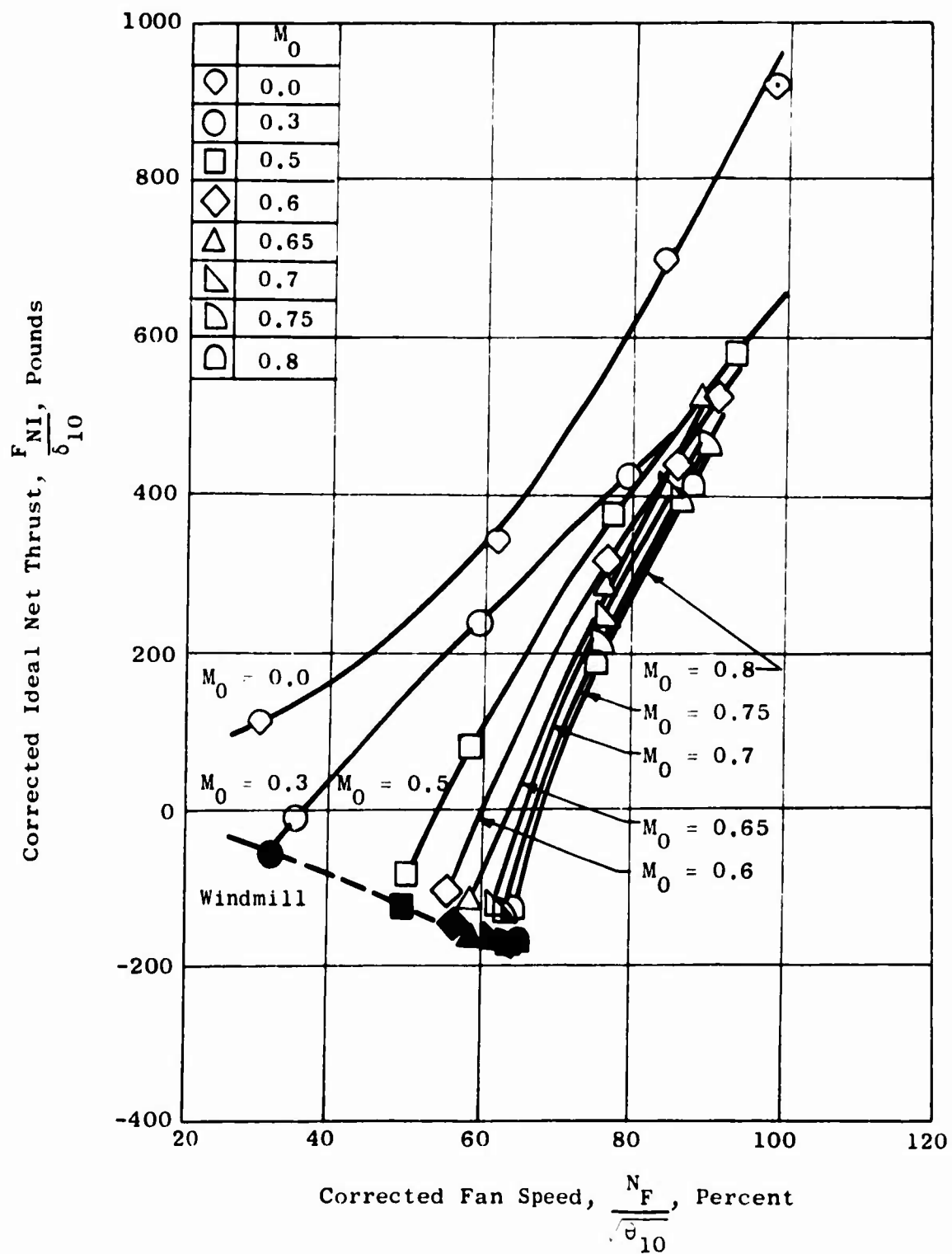


Figure 71. Fan System Ideal Net Thrust - Model 2.

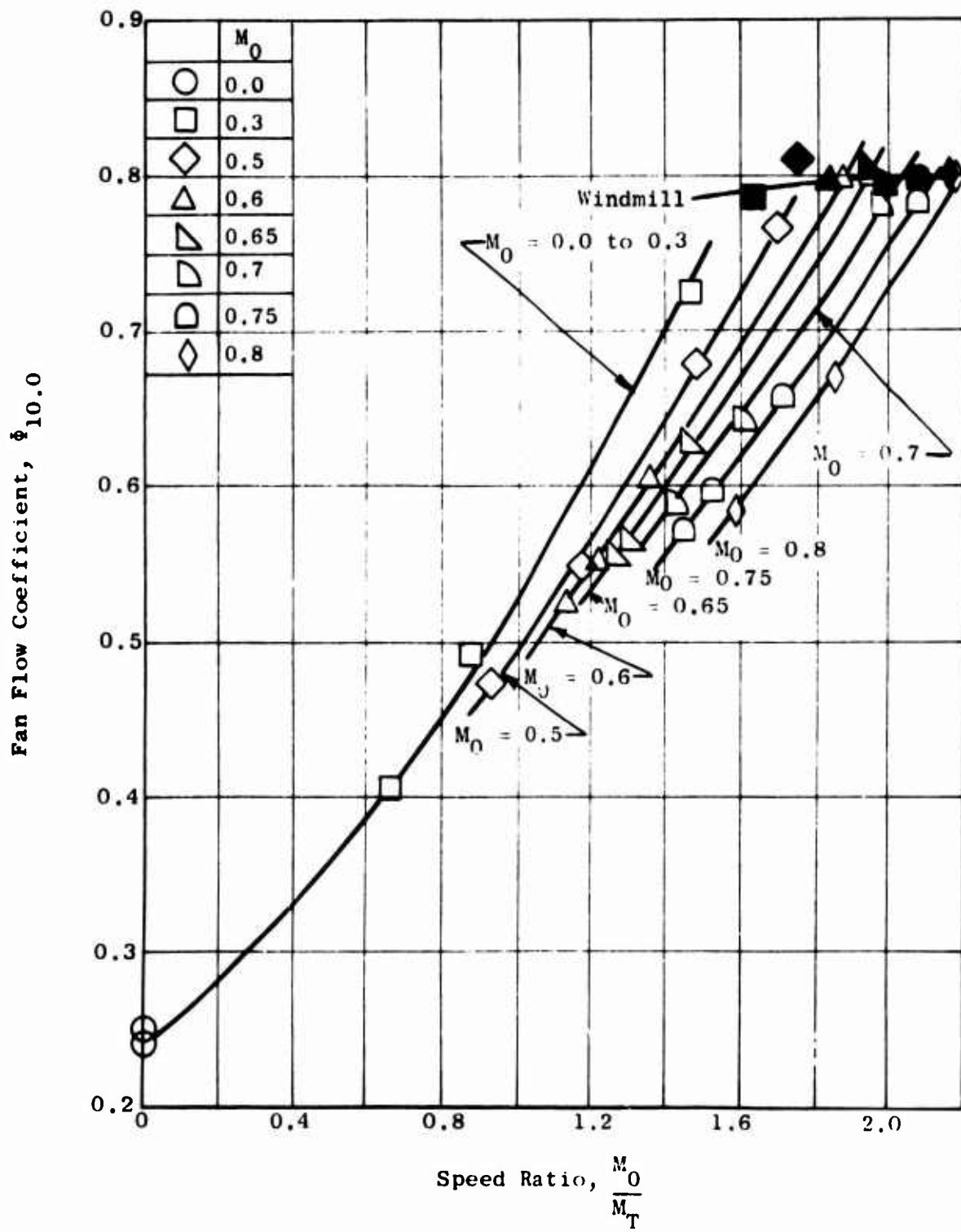


Figure 72. Fan Flow Function Characteristics - Model 2.

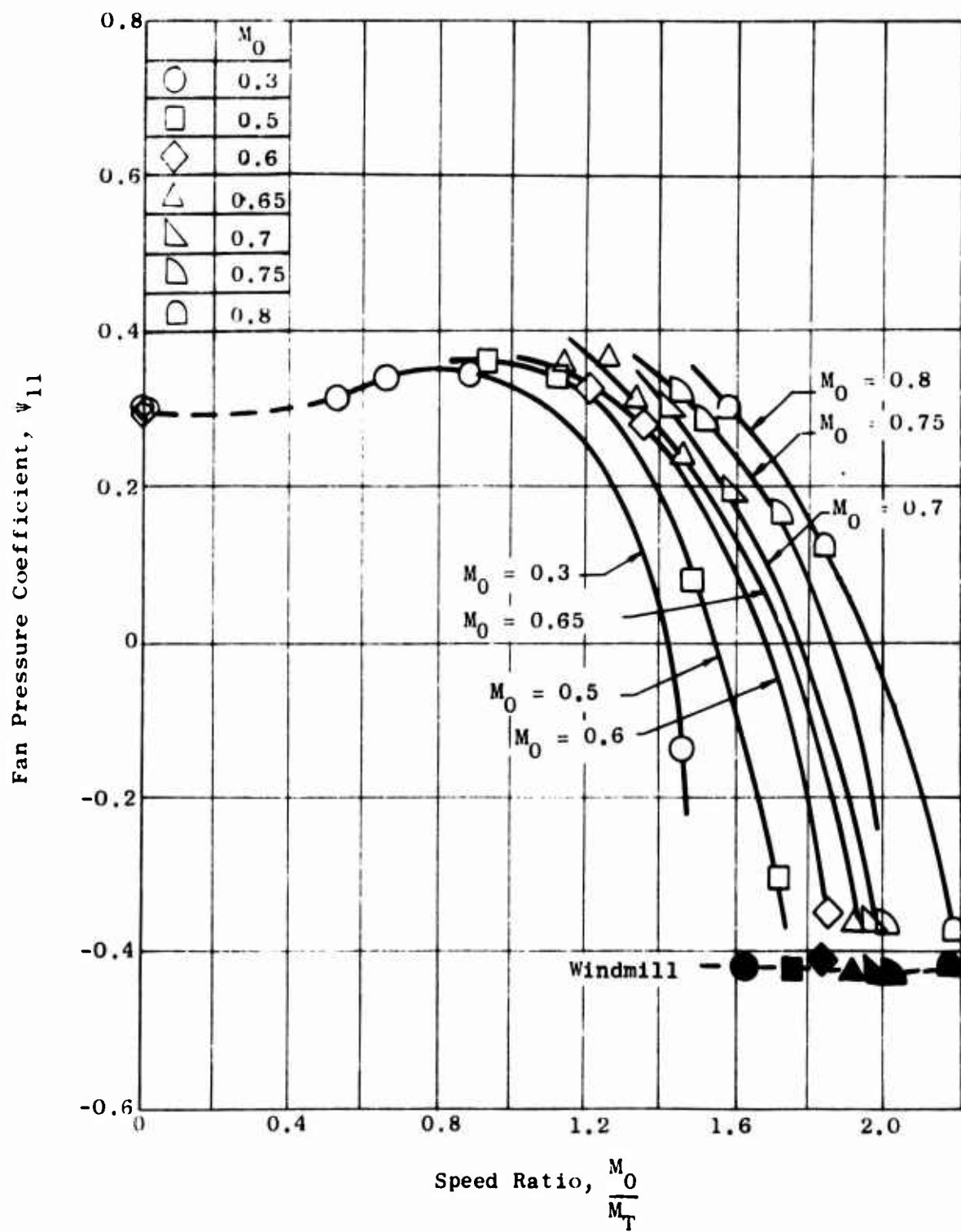


Figure 73. Fan Pressure Coefficient Characteristics - Model 2.

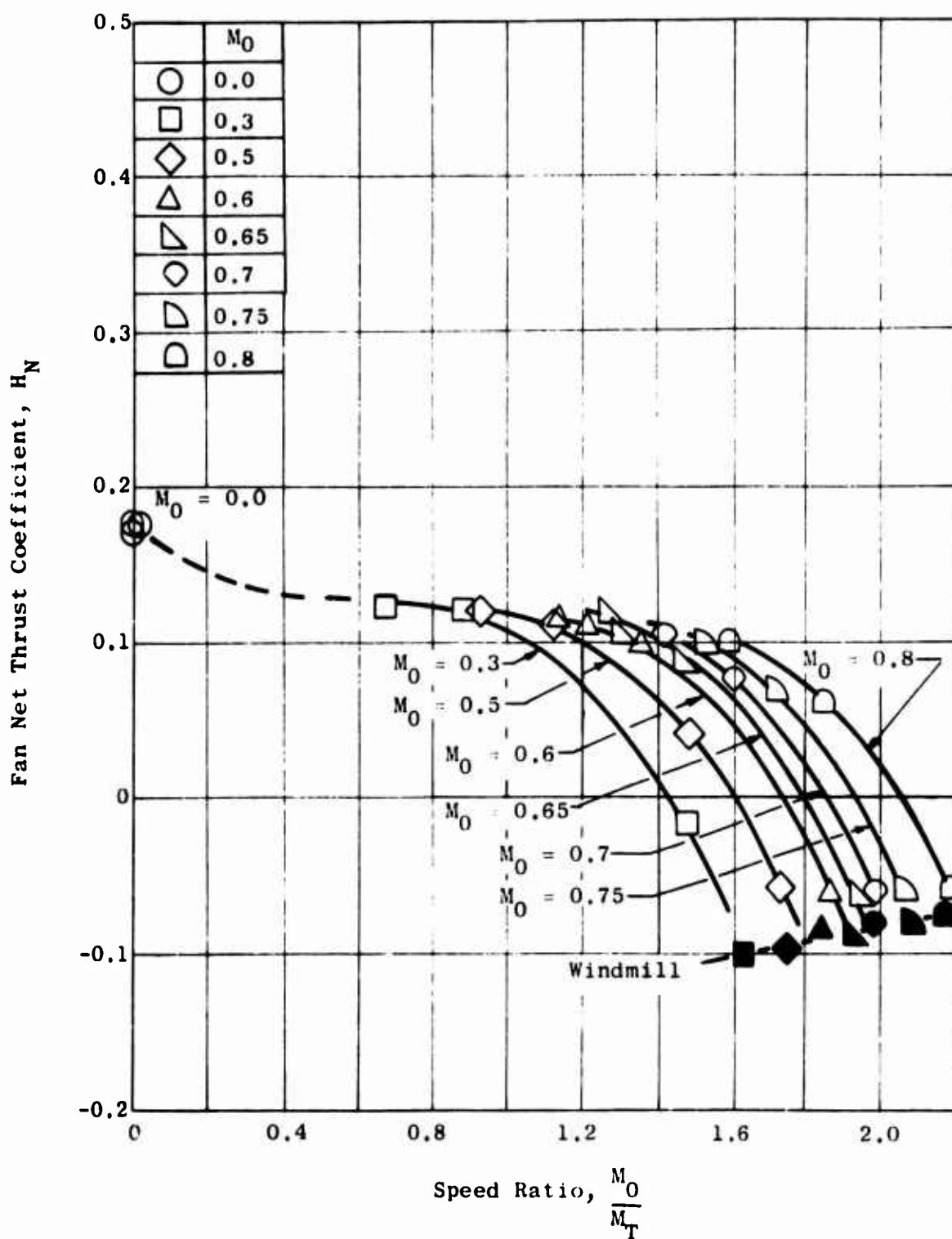


Figure 74. Fan Ideal Net Thrust Coefficient - Model 2.

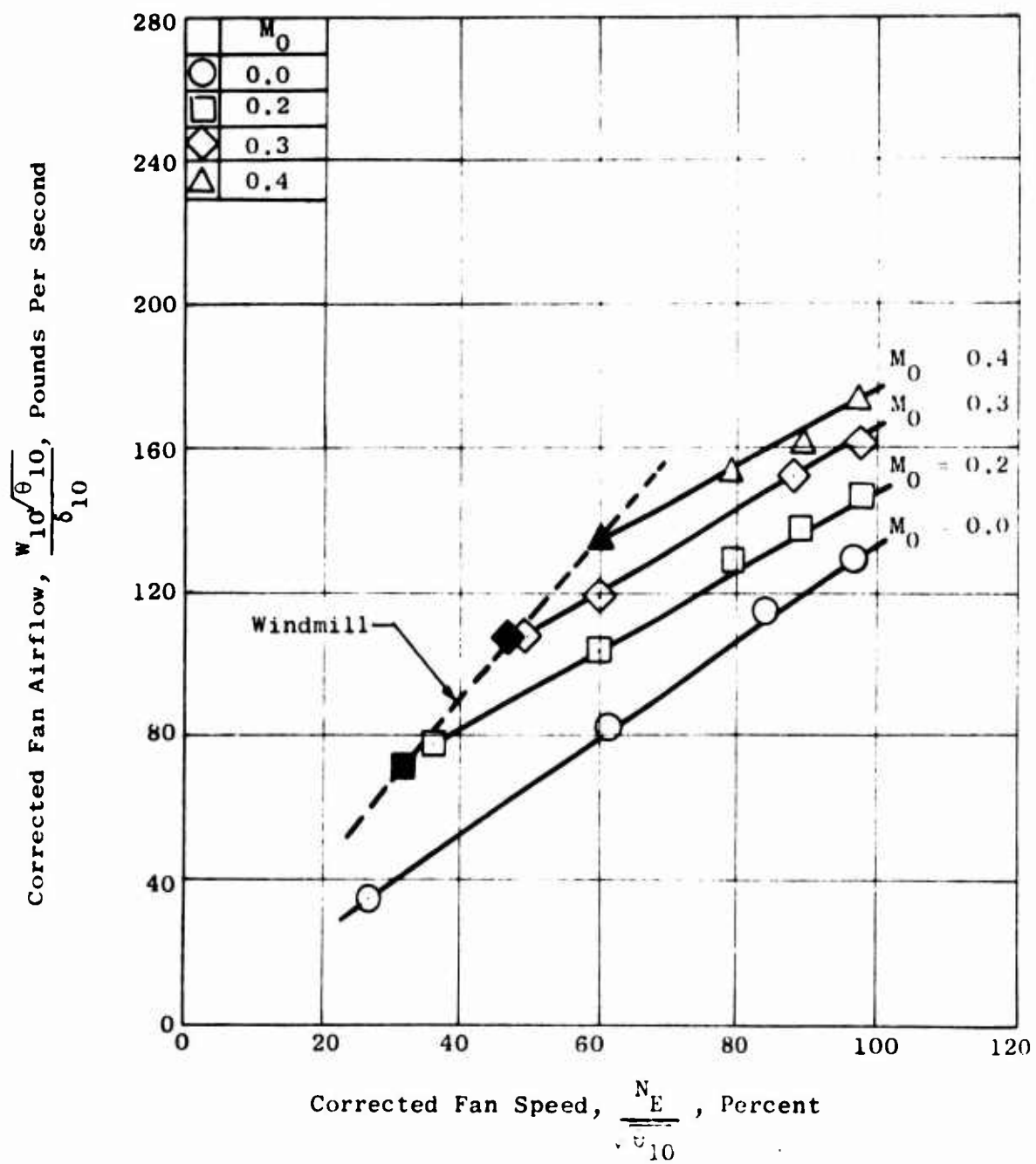


Figure 76. Fan Airflow Characteristics - Model 3.

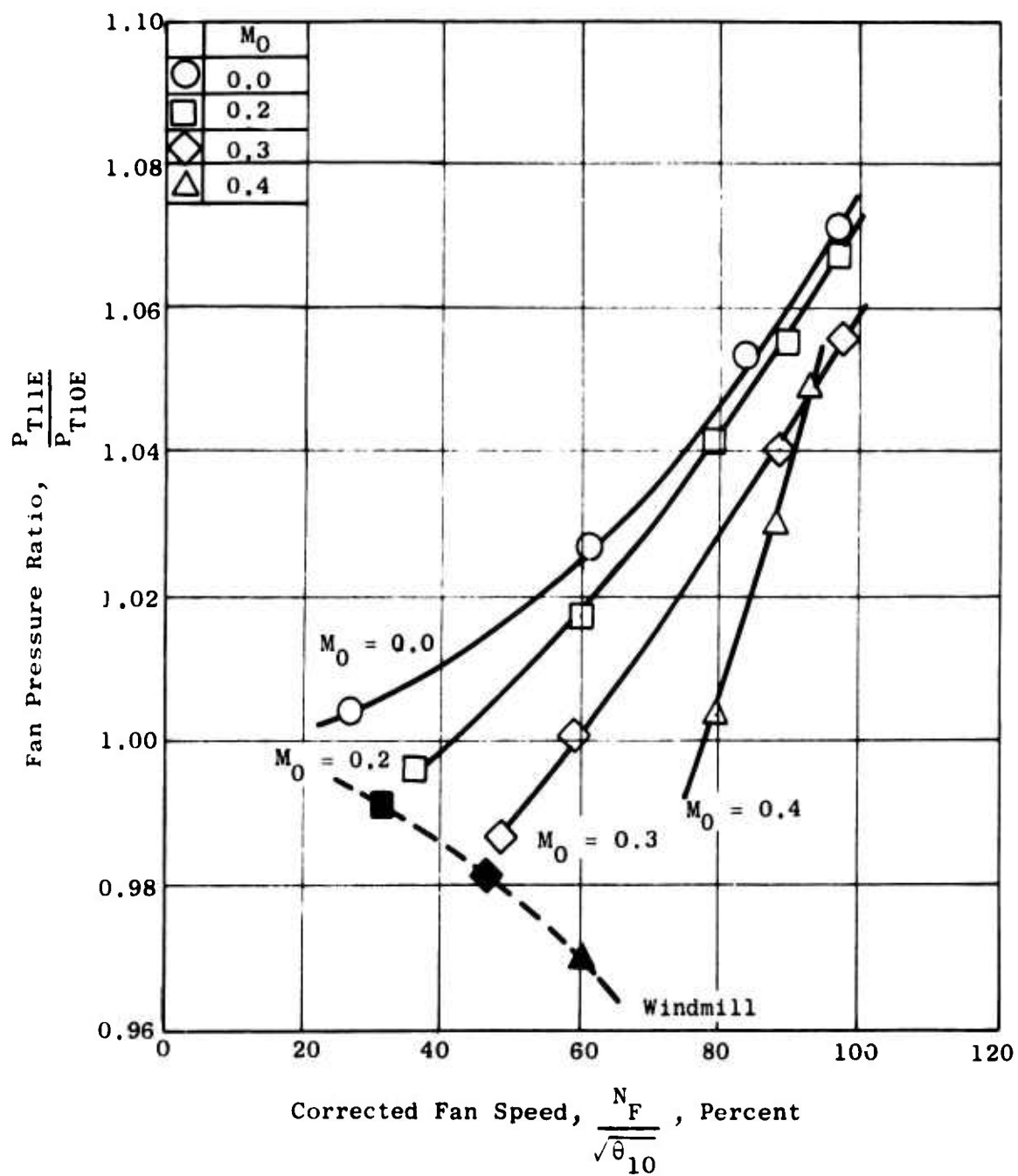


Figure 77. Fan Total Pressure Ratio - Model 3.

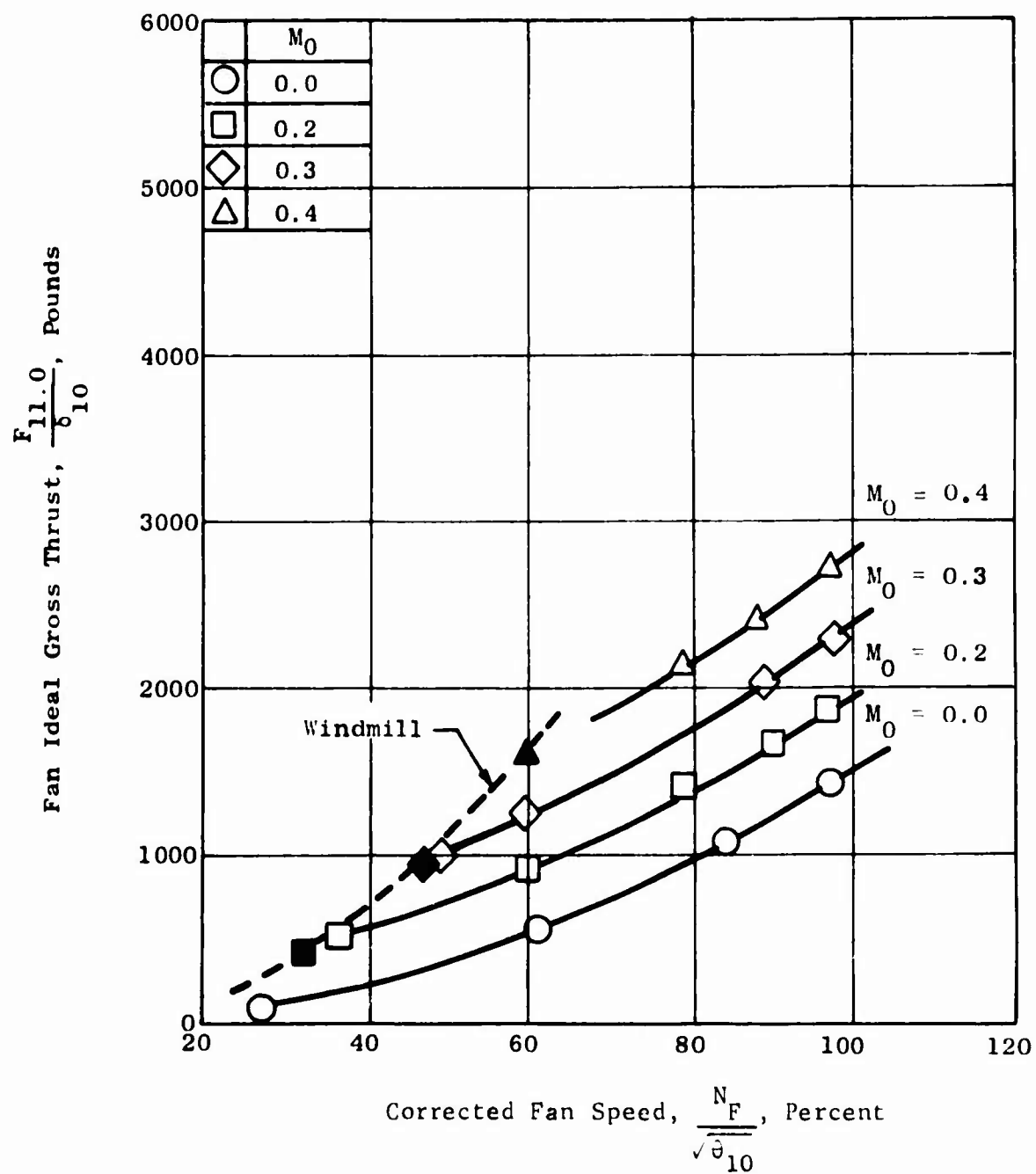


Figure 78. Fan System Ideal Gross Thrust - Model 3.

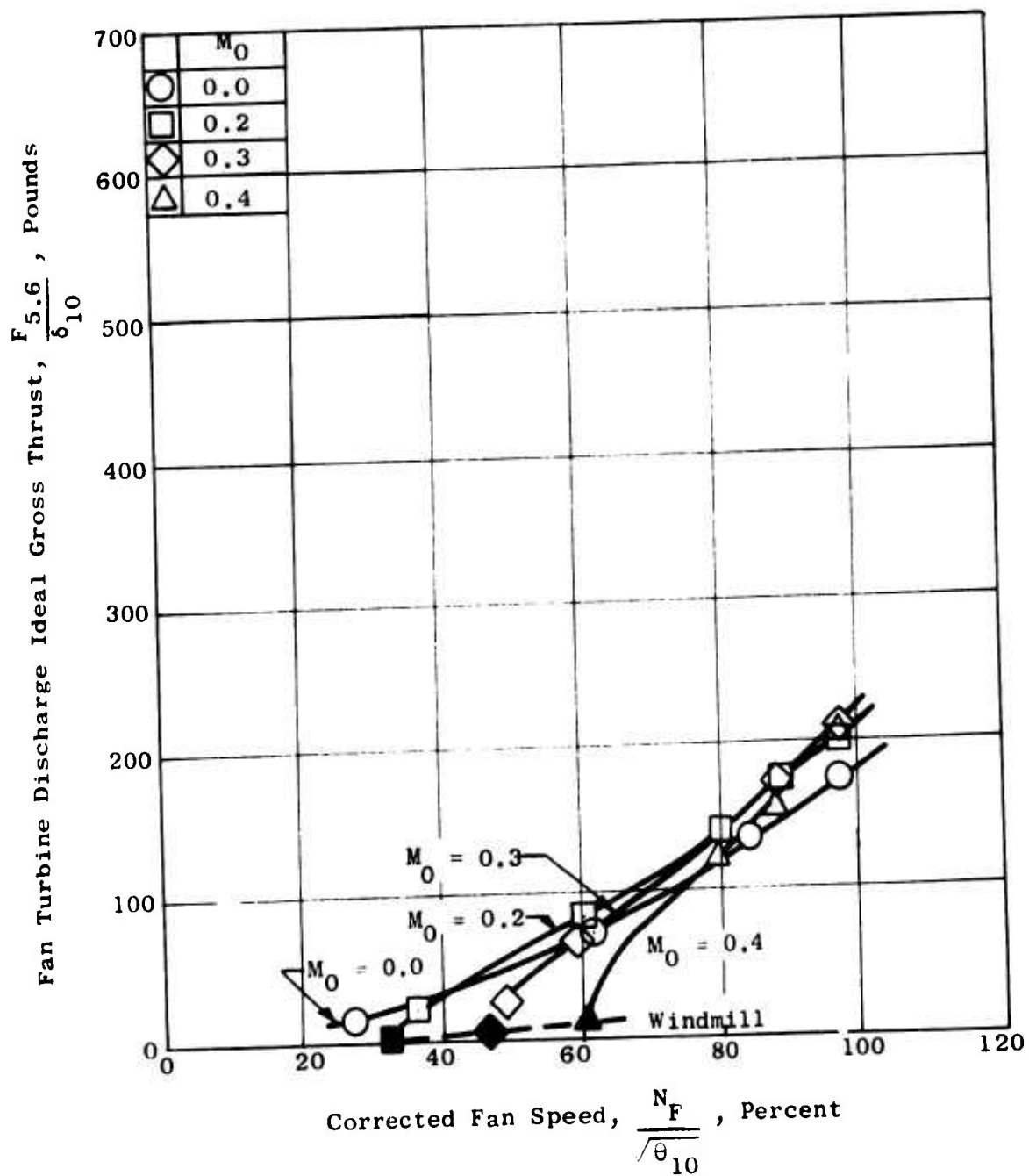


Figure 79. Fan Turbine Residual Ideal Gross Thrust - Model 3.

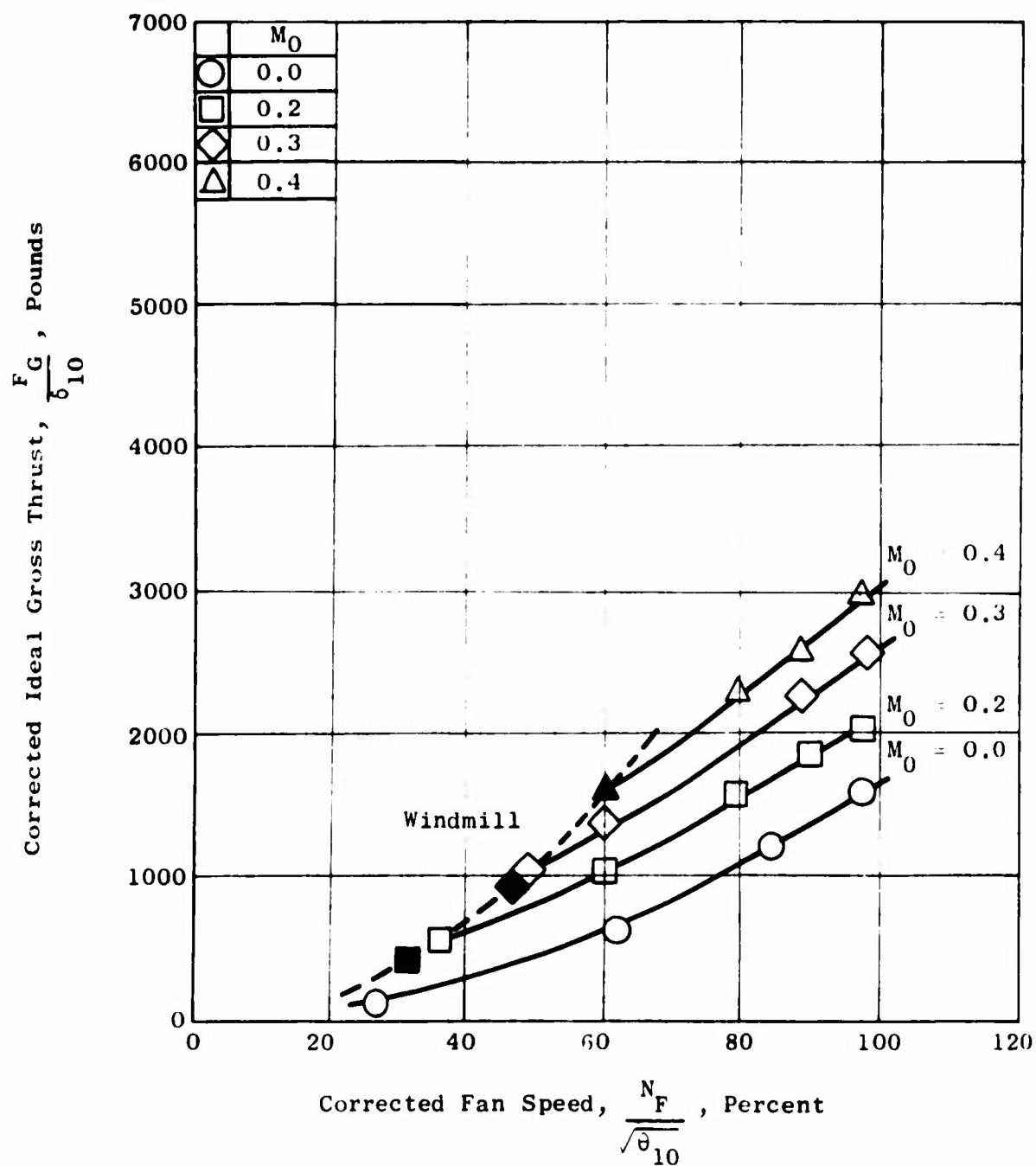


Figure 80. Fan System Ideal Gross Thrust - Model 3.

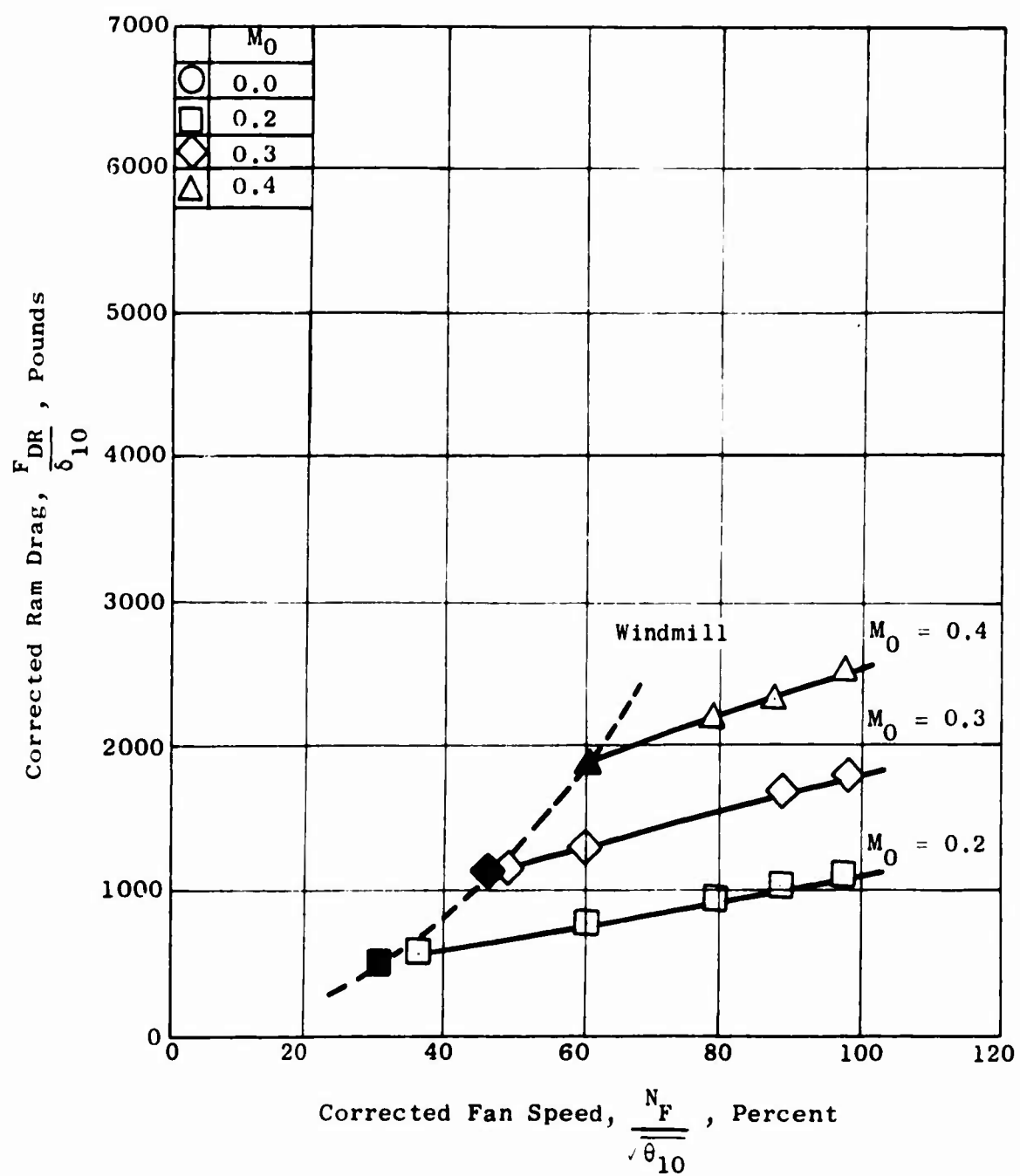


Figure 81. Total Ram Drag - Model 3.

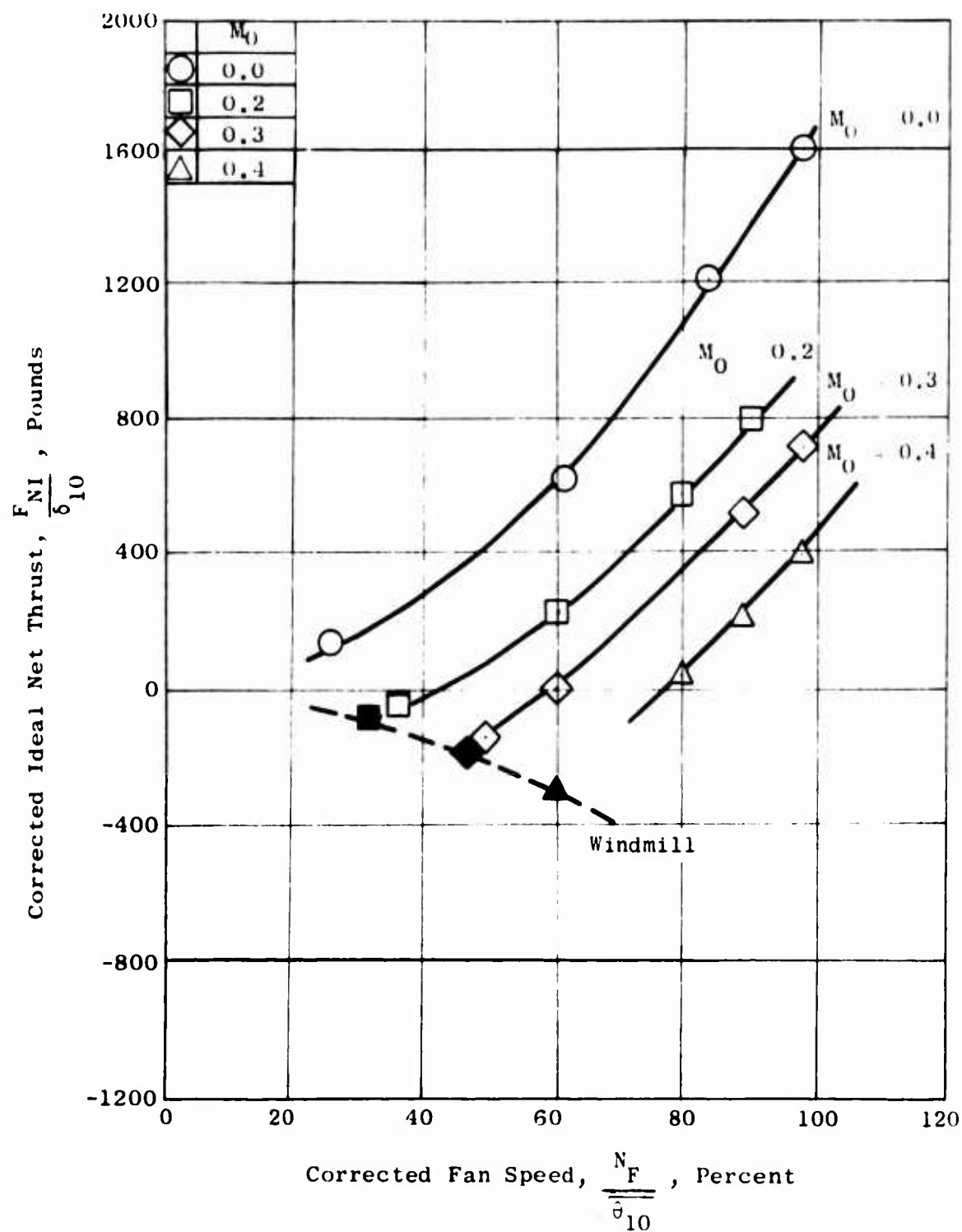


Figure 82. Fan System Ideal Net Thrust - Model 3.

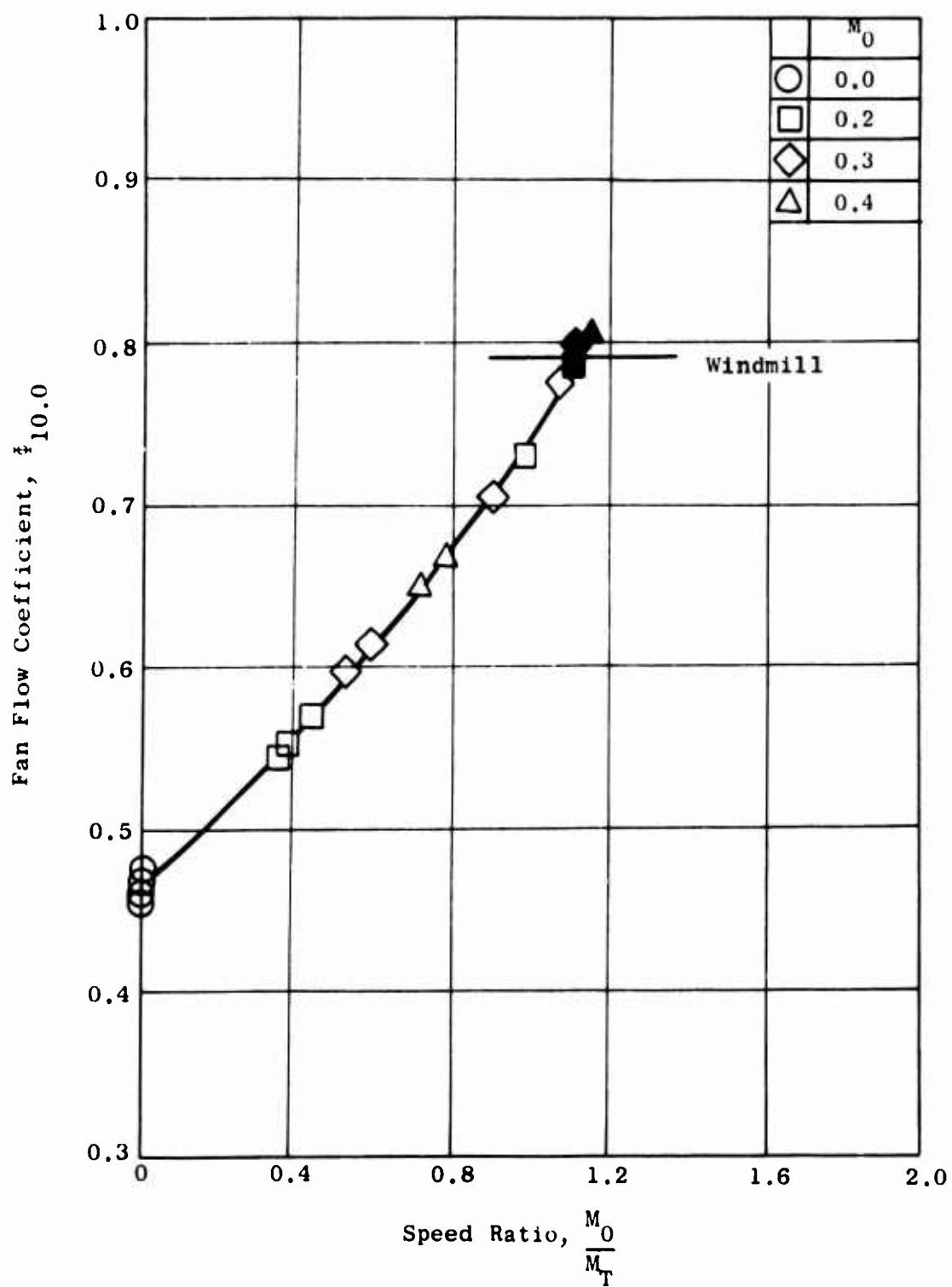


Figure 83. Fan Flow Coefficient Characteristics - Model 3.

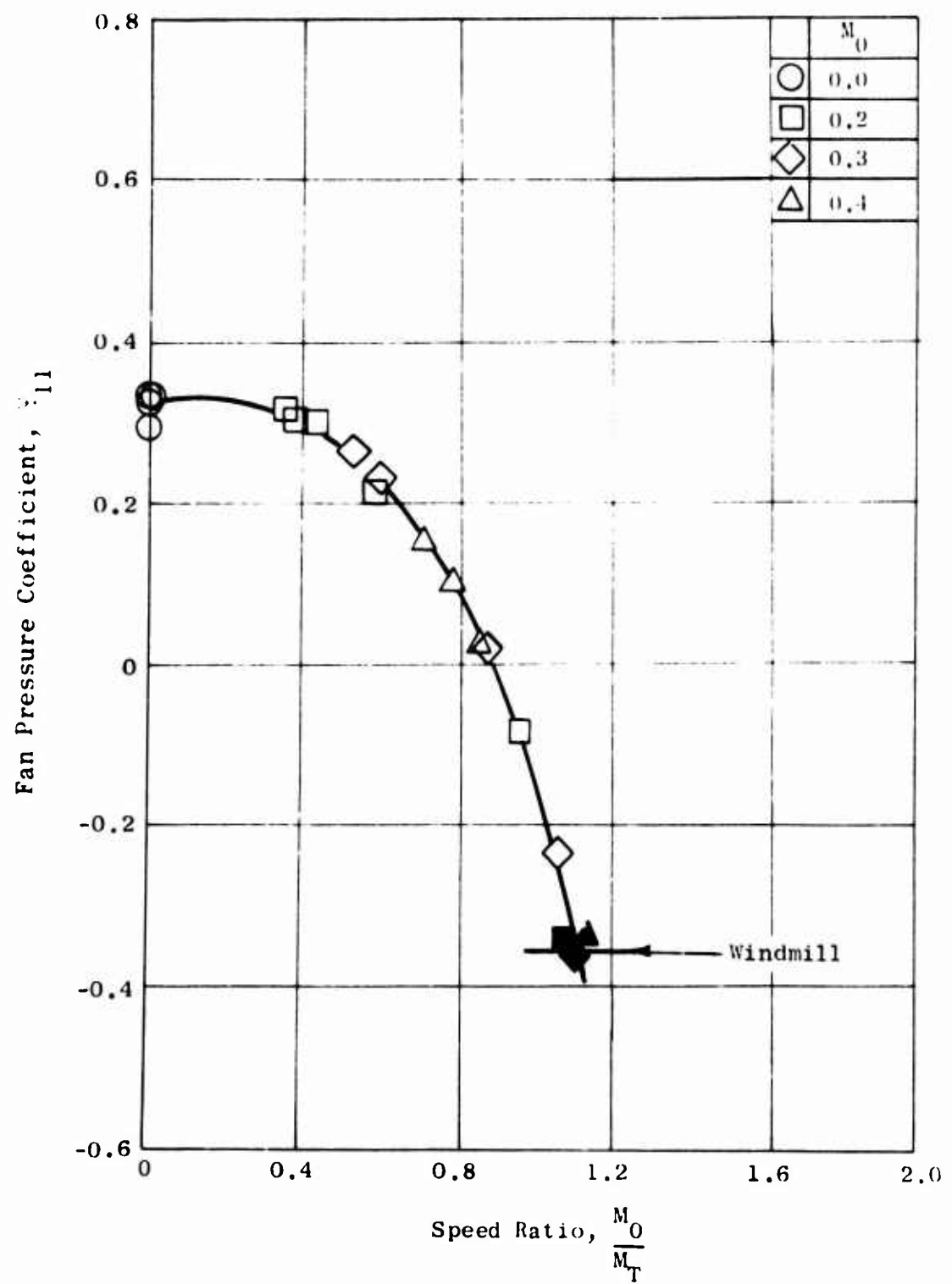


Figure 84. Fan Pressure Coefficient Characteristics - Model 3.

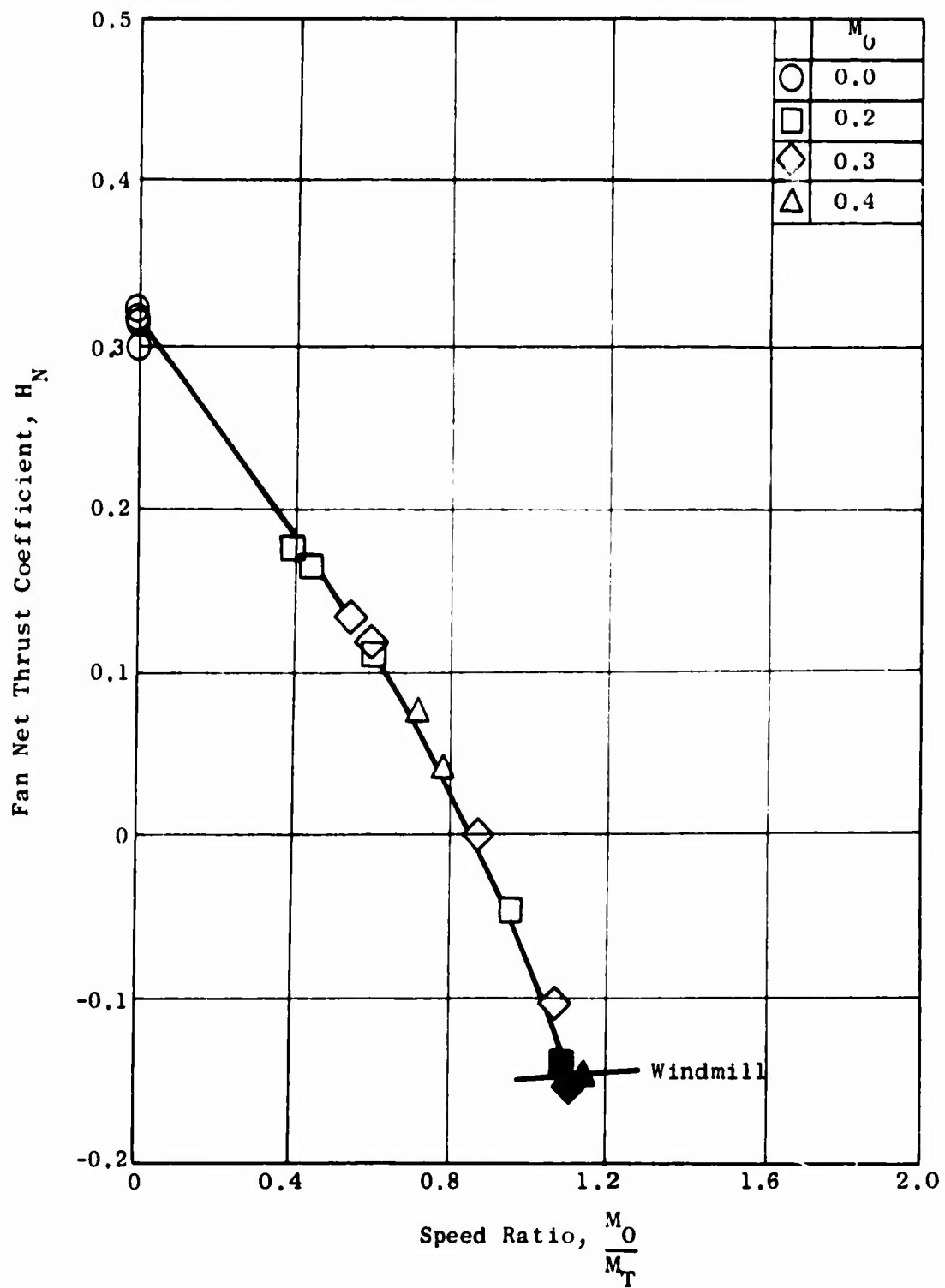


Figure 85. Fan Ideal Net Thrust Coefficient - Model 3.

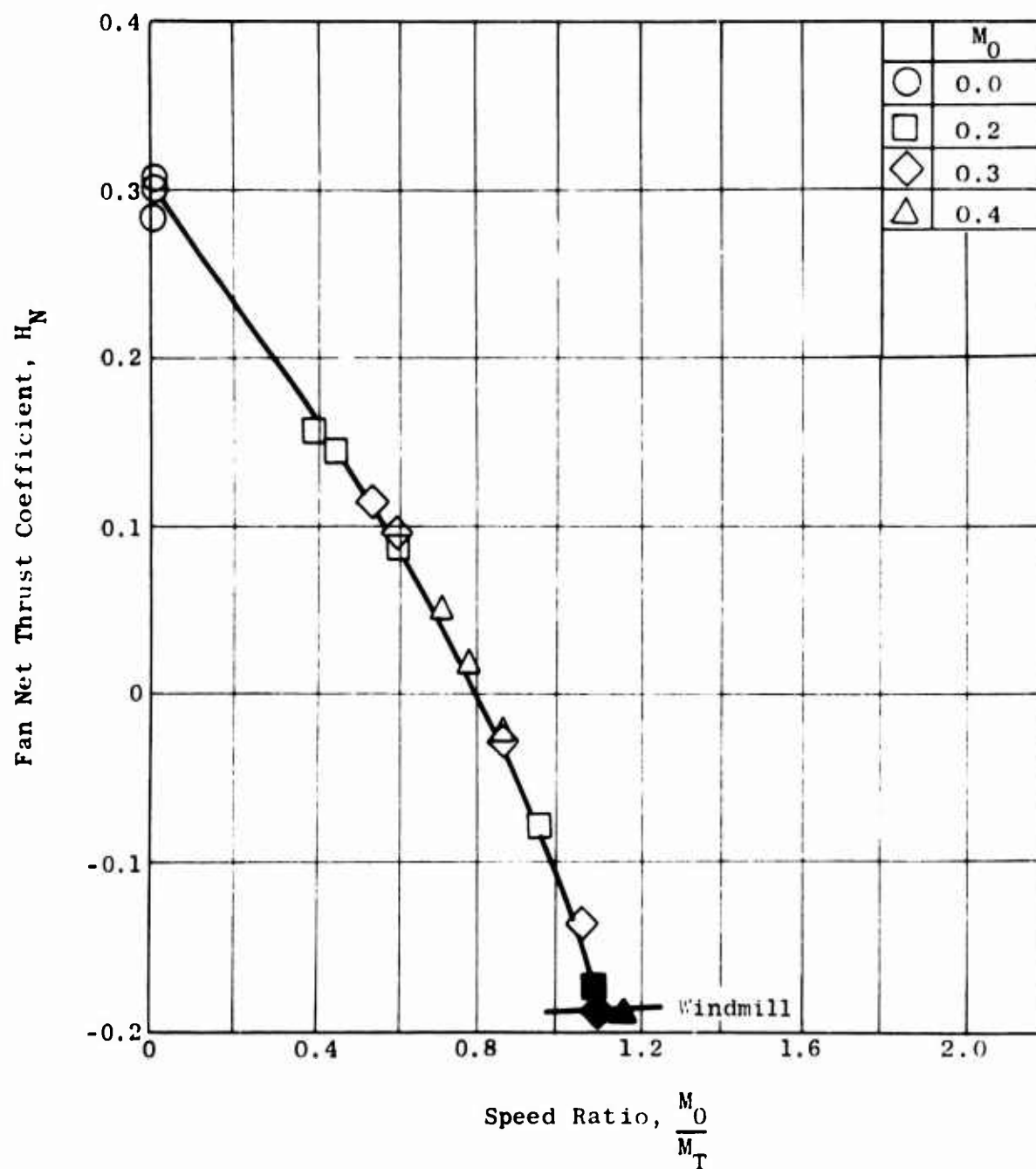


Figure 86. Fan Net Thrust Coefficient with a Nozzle Coefficient of 0.95 - Model 3.

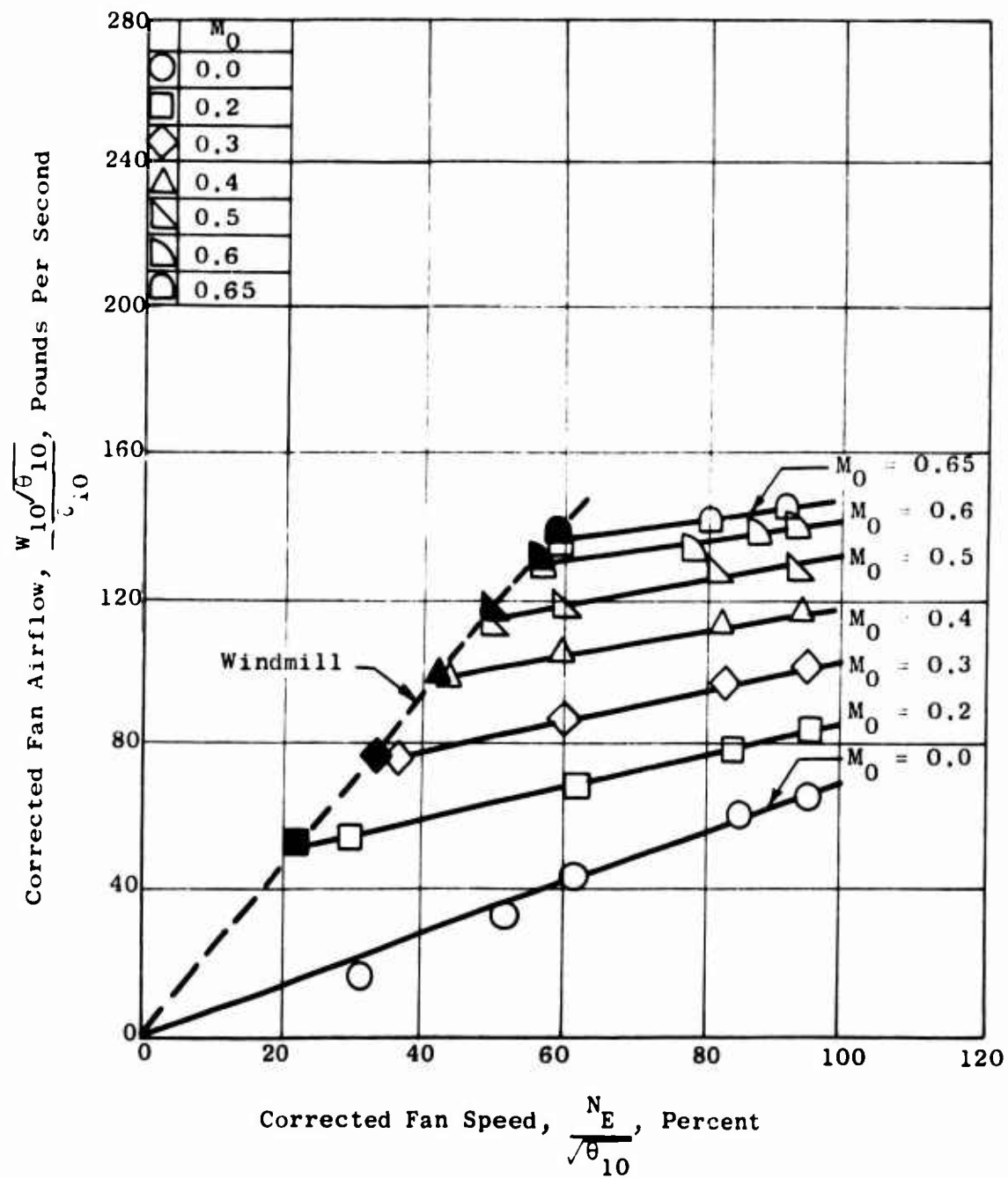


Figure 87. Fan Airflow Characteristics - Model 4.

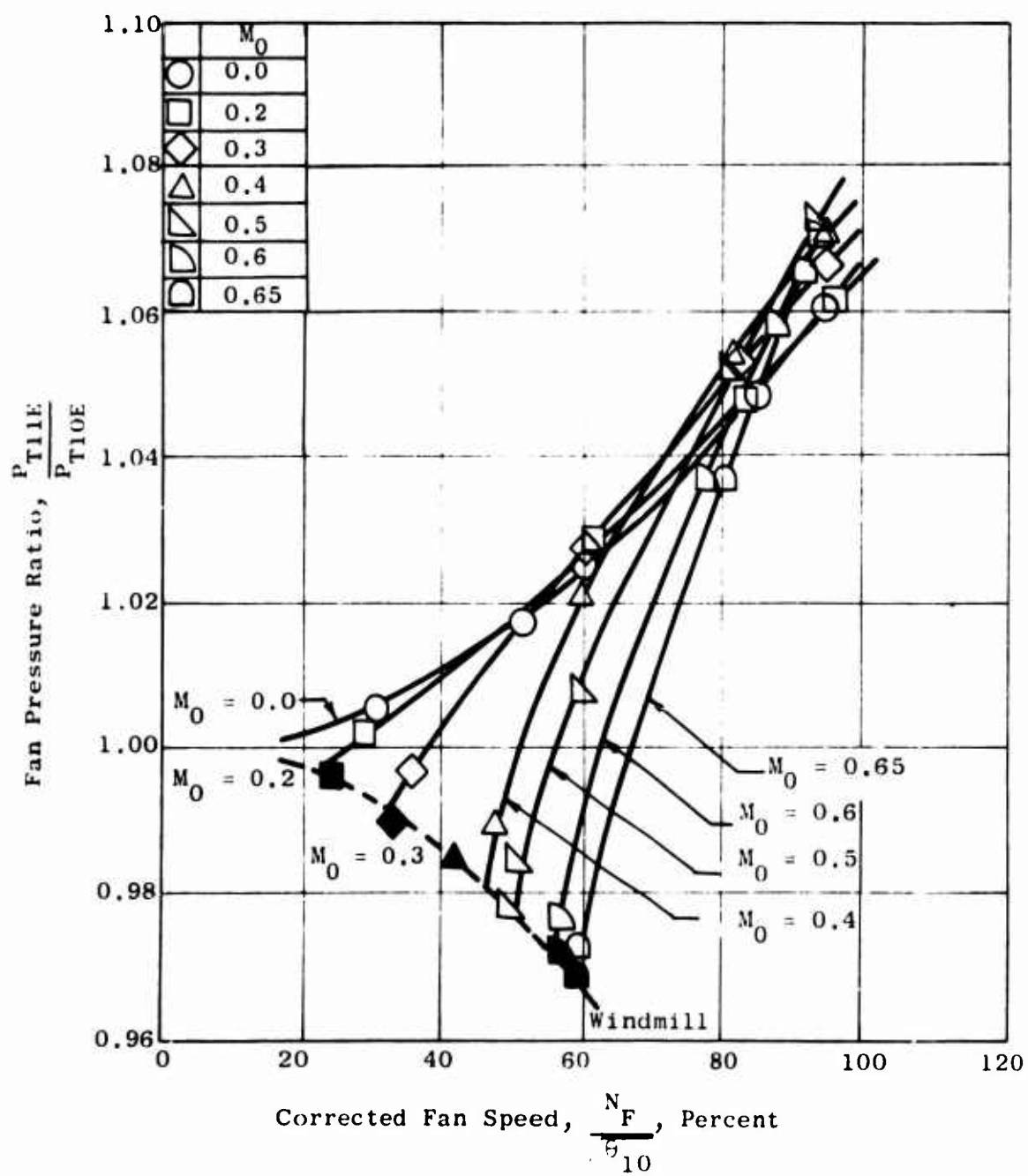


Figure 88. Fan Total Pressure Ratio - Model 4.

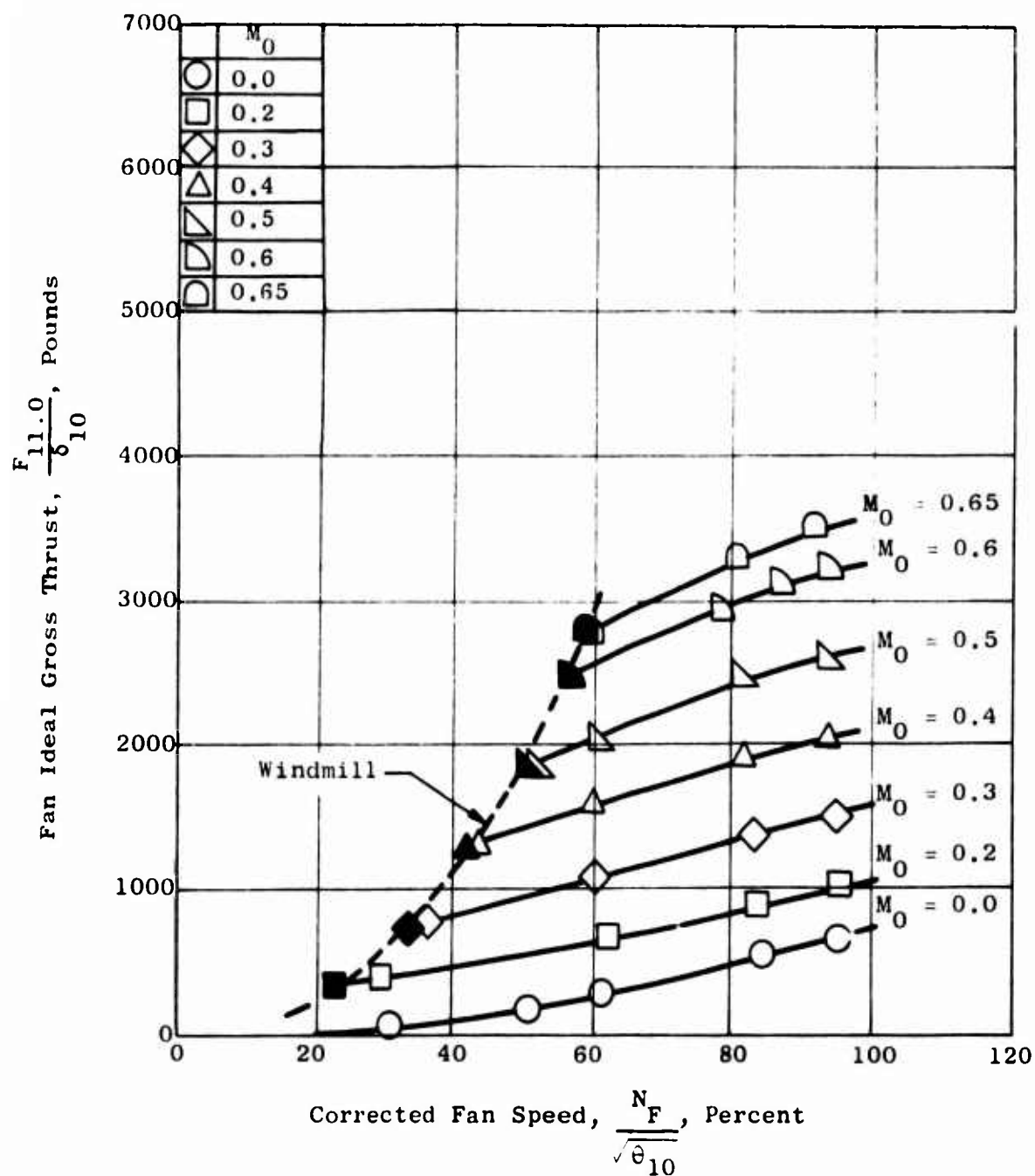


Figure 89. Fan Stream Ideal Gross Thrust - Model 4.

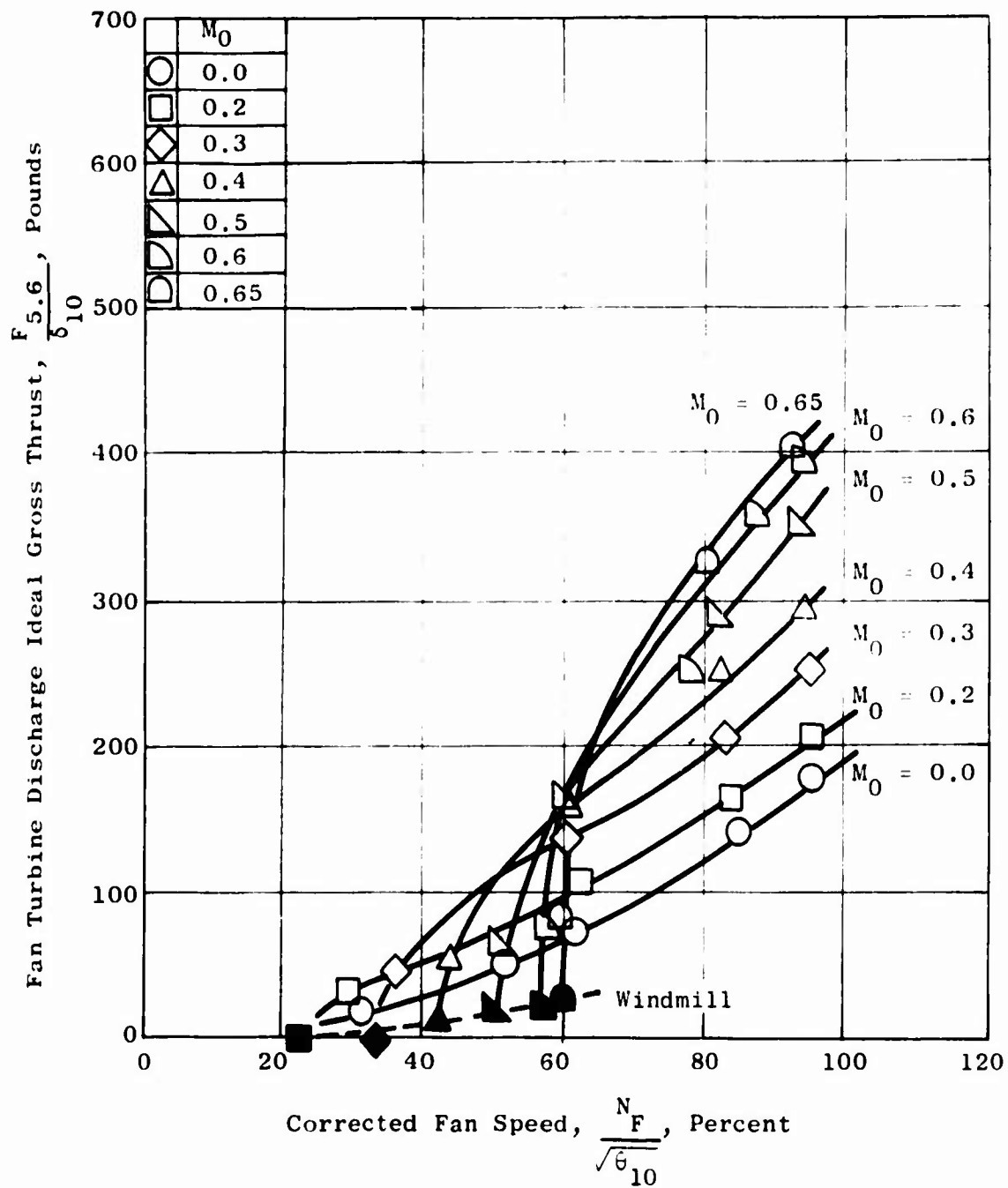


Figure 90. Fan Turbine Residual Ideal Gross Thrust - Model 4.

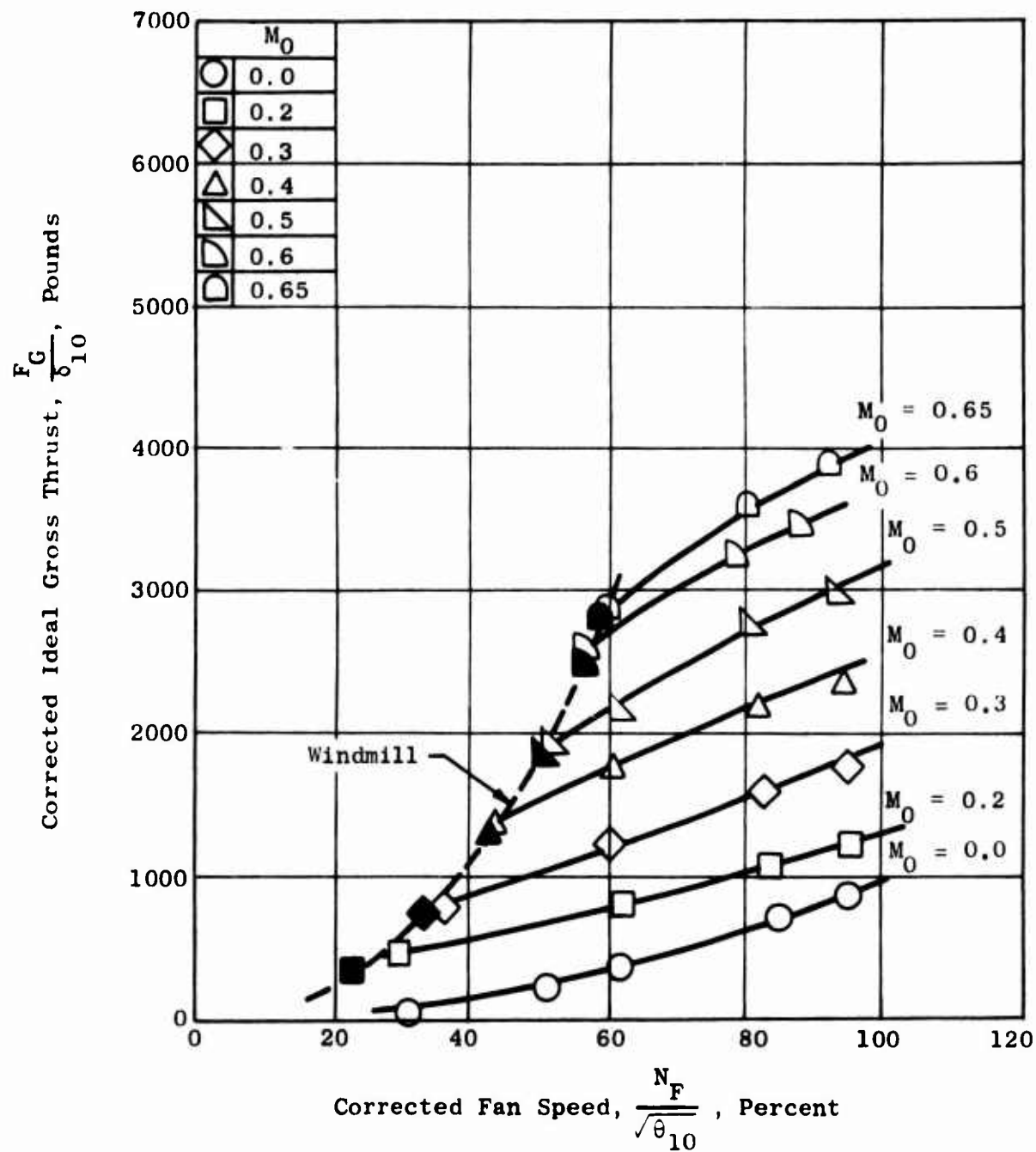


Figure 91. Fan System Ideal Gross Thrust - Model 4.

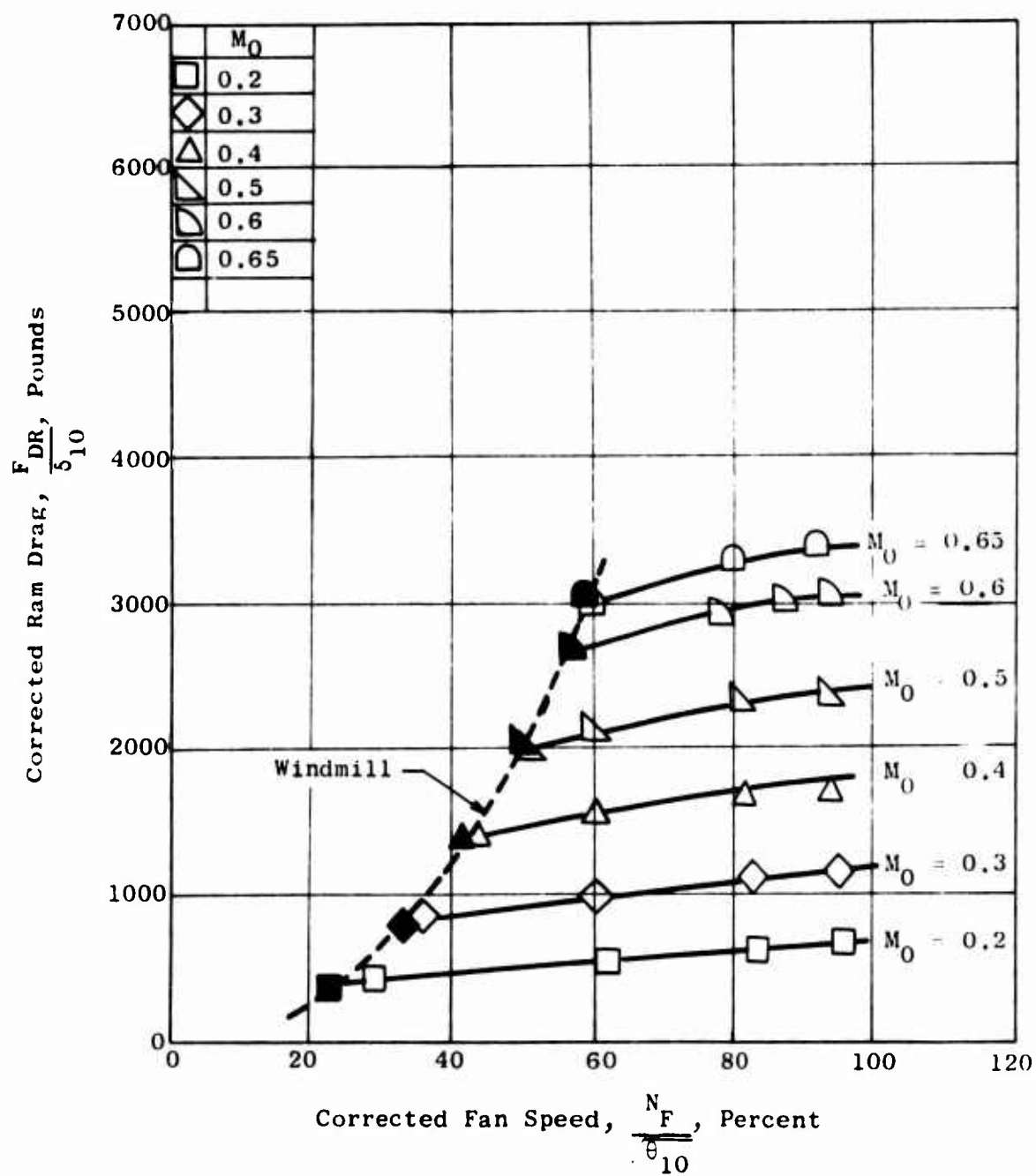


Figure 92. Total Ram Drag - Model 4.

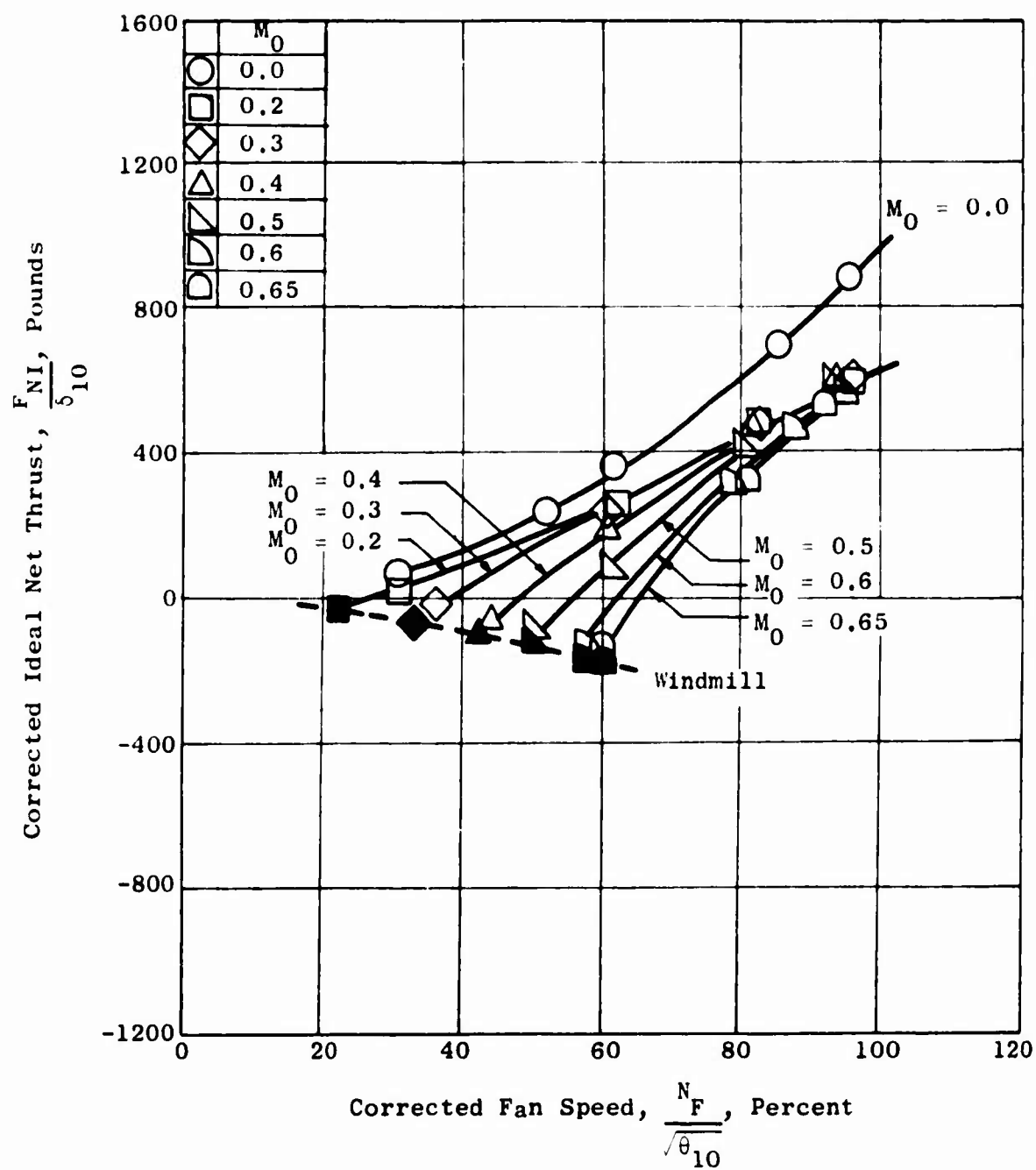


Figure 93. Fan System Ideal Net Thrust - Model 4.

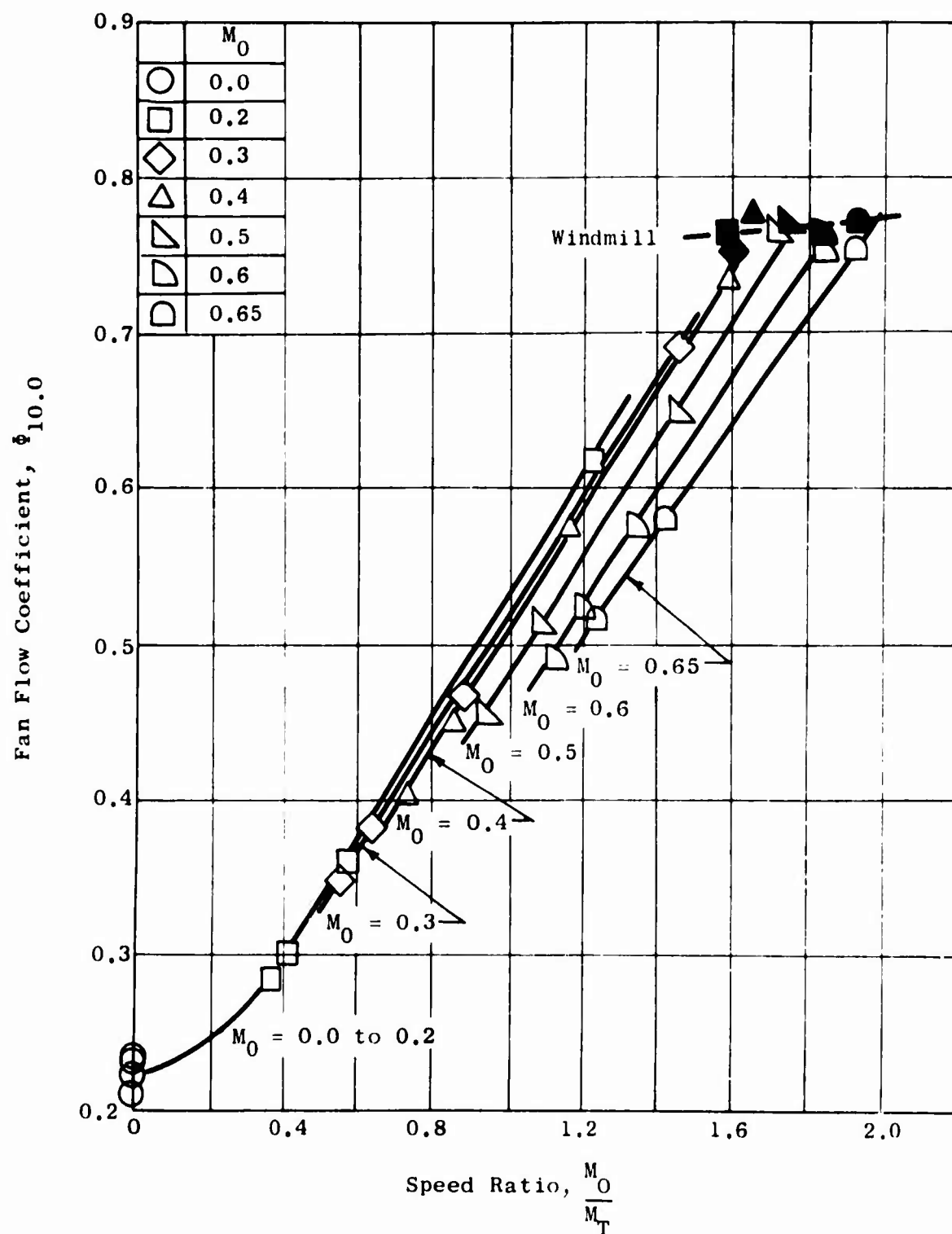


Figure 94. Fan Flow Coefficient Characteristics - Model 4.

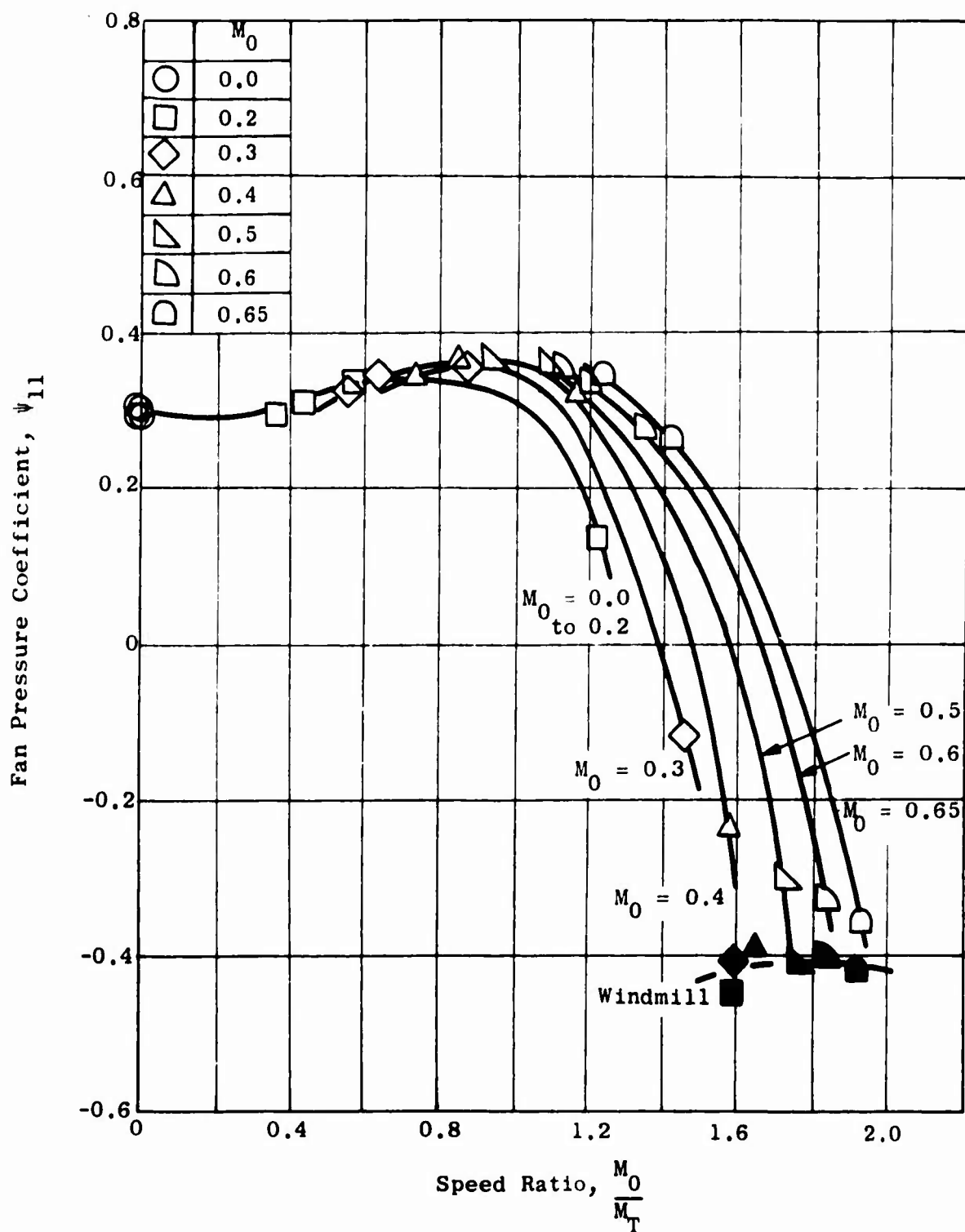


Figure 95. Fan Pressure Coefficient Characteristics - Model 4.

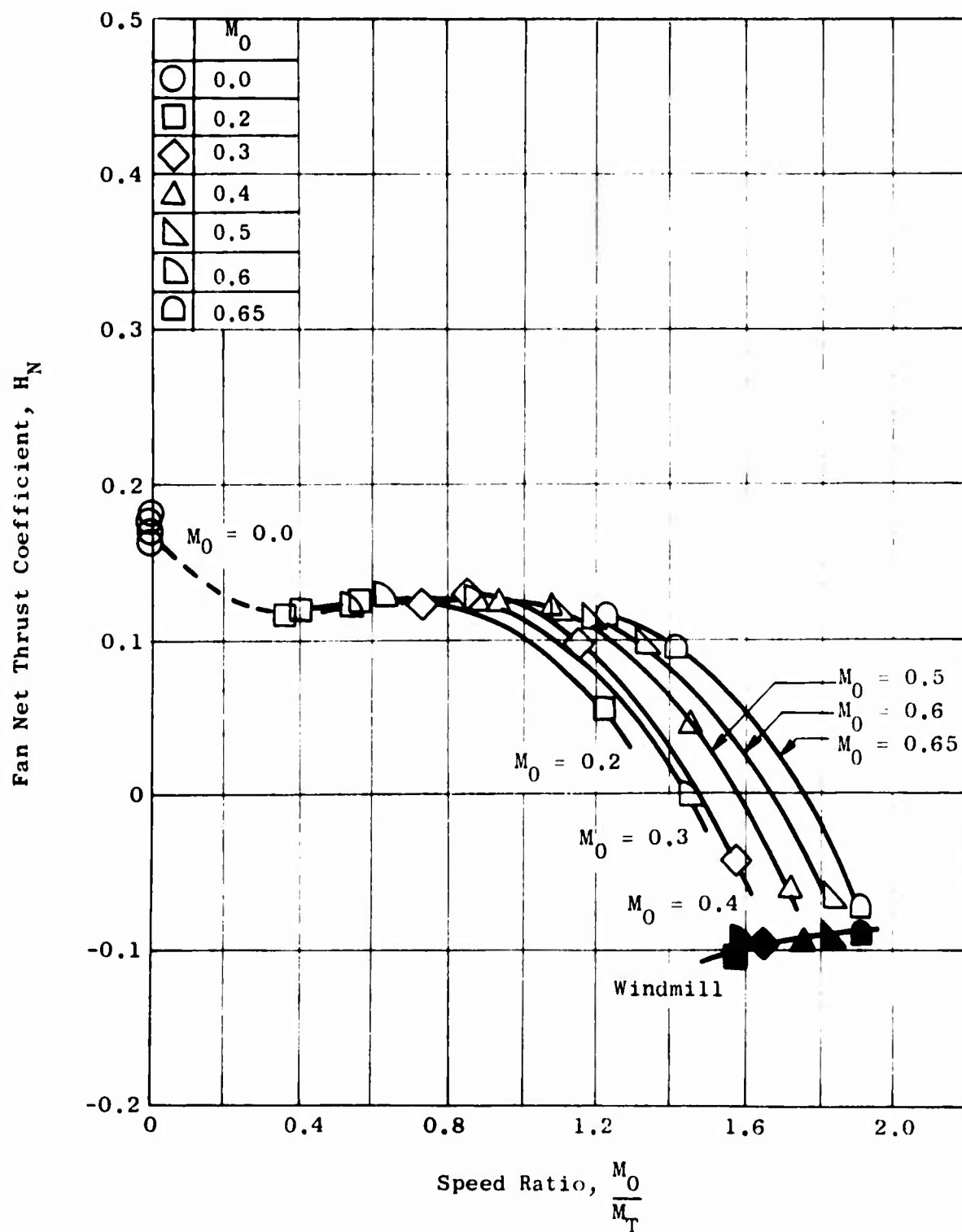


Figure 96. Fan Ideal Net Thrust Coefficient - Model 4.

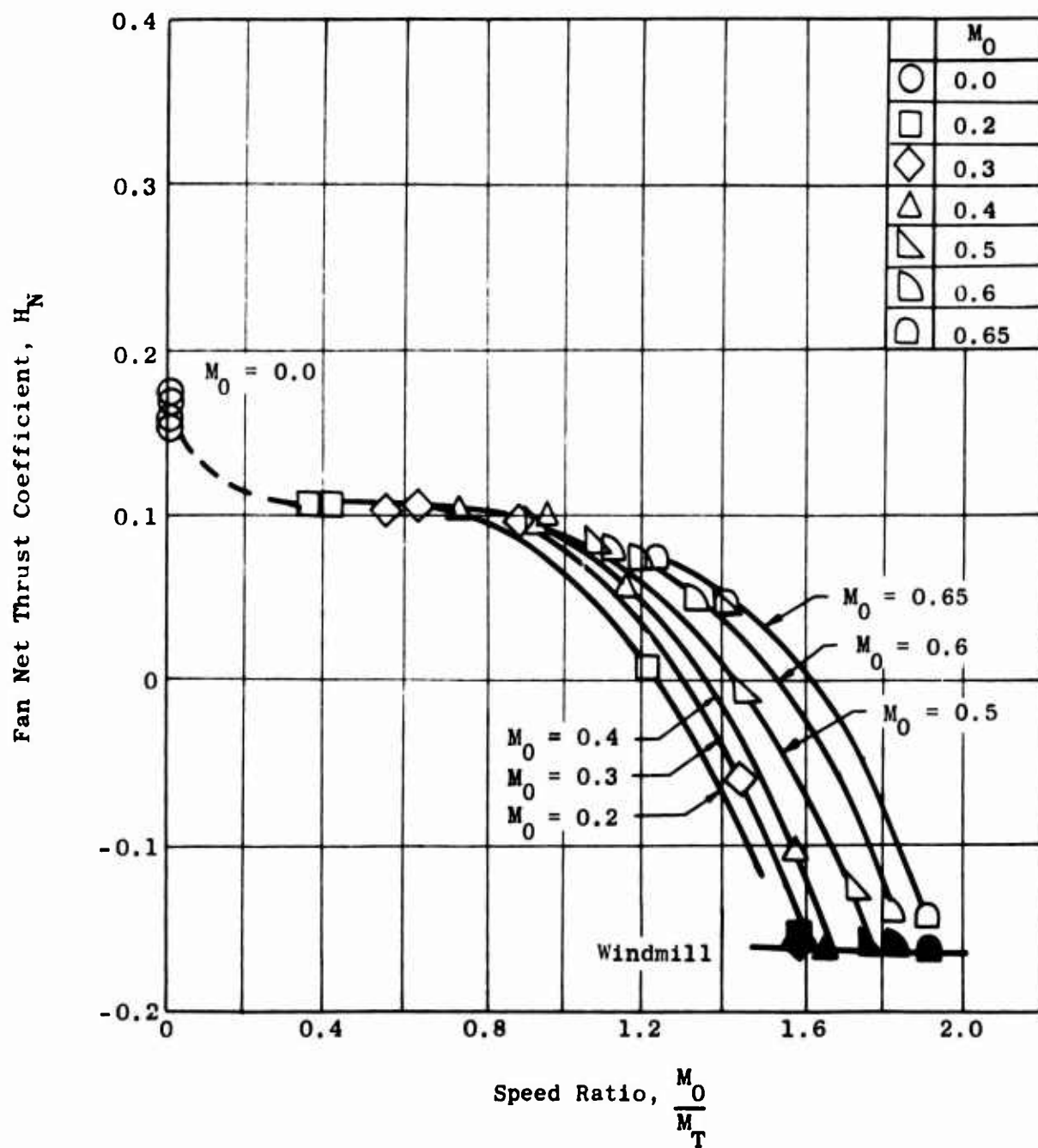


Figure 97. Fan Net Thrust Coefficient with a Nozzle Coefficient of 0.95 - Model 4.

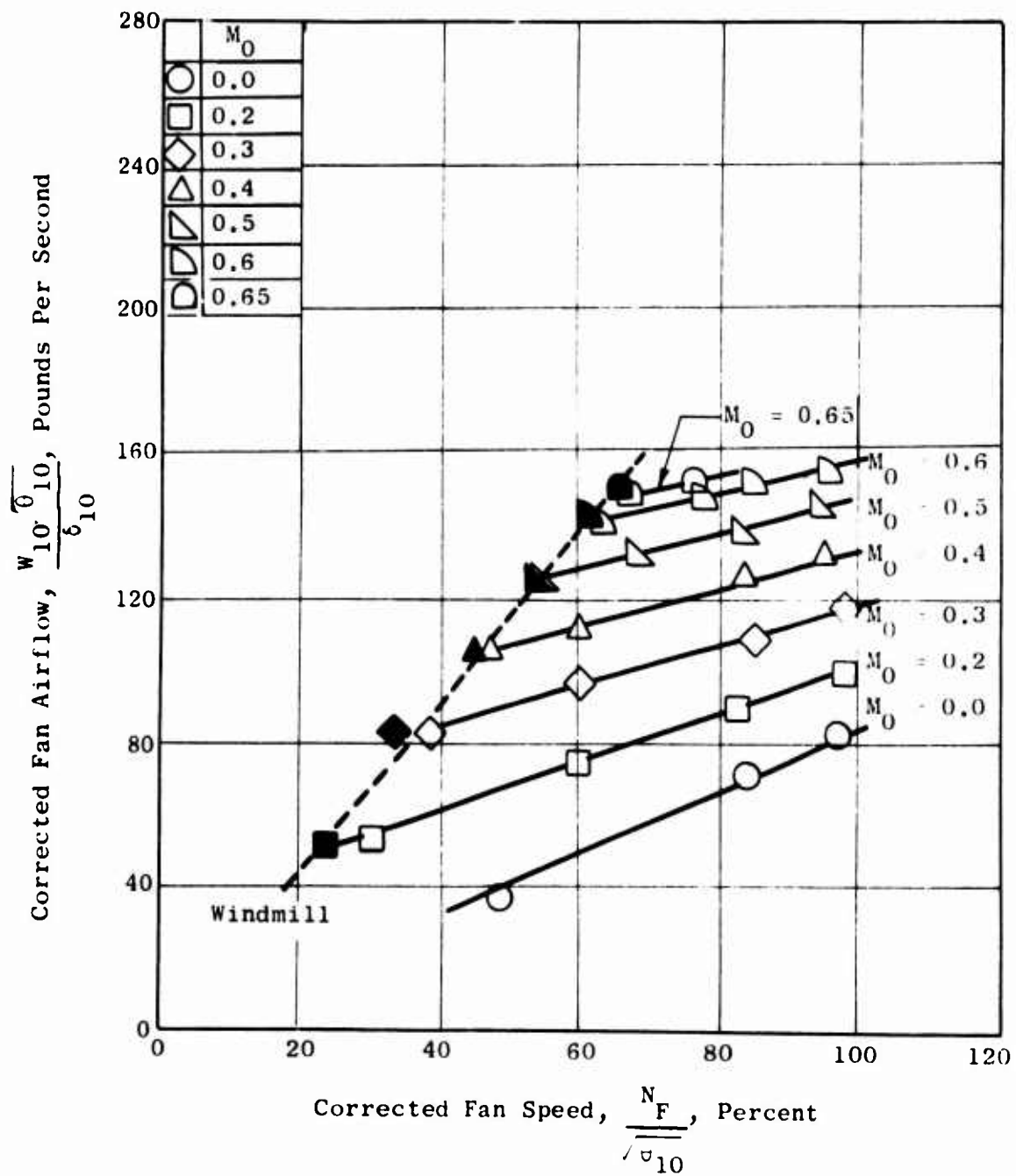


Figure 98. Fan Airflow Characteristics - Model 5.

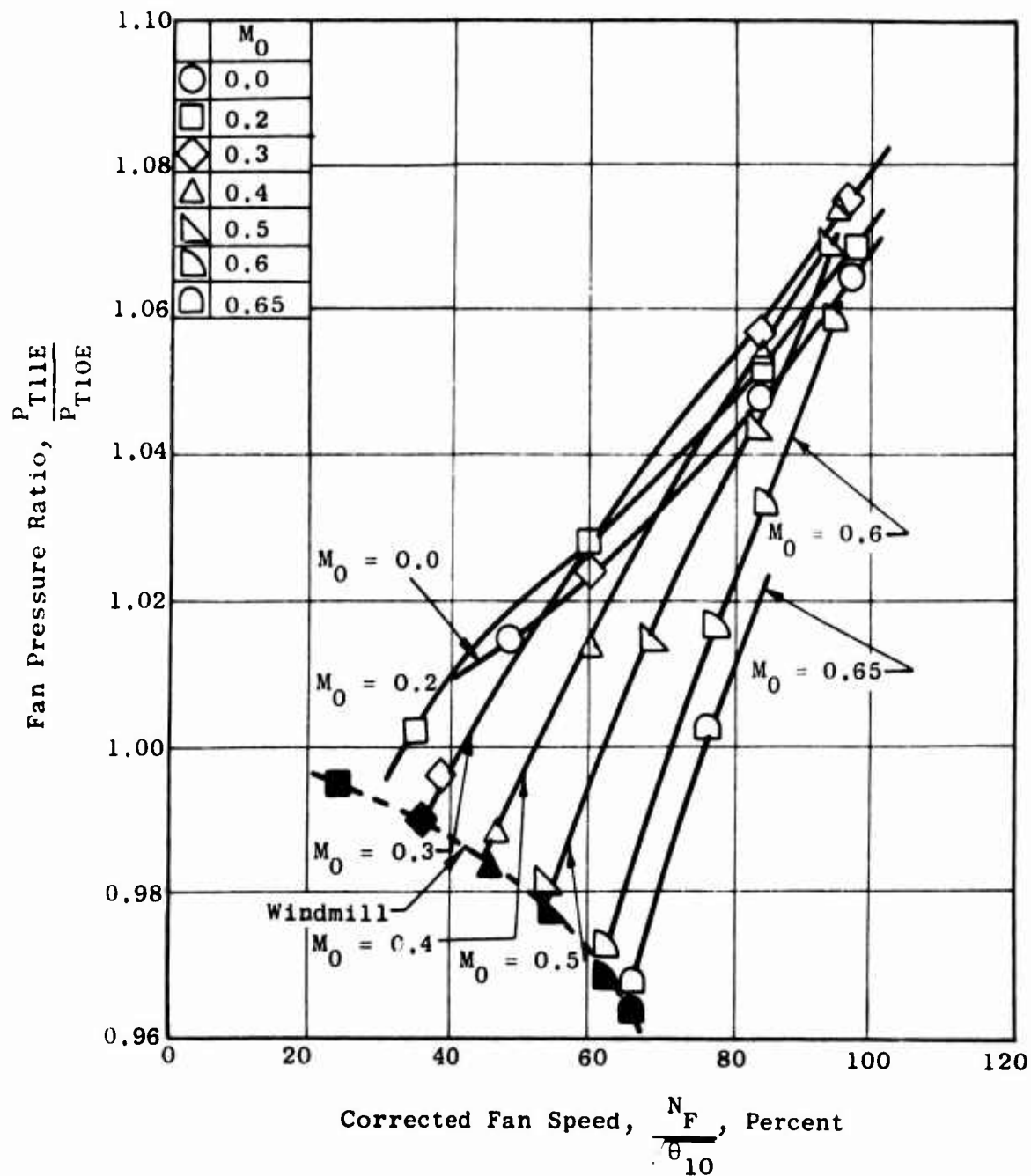


Figure 99. Fan Total Pressure Ratio - Model 5.

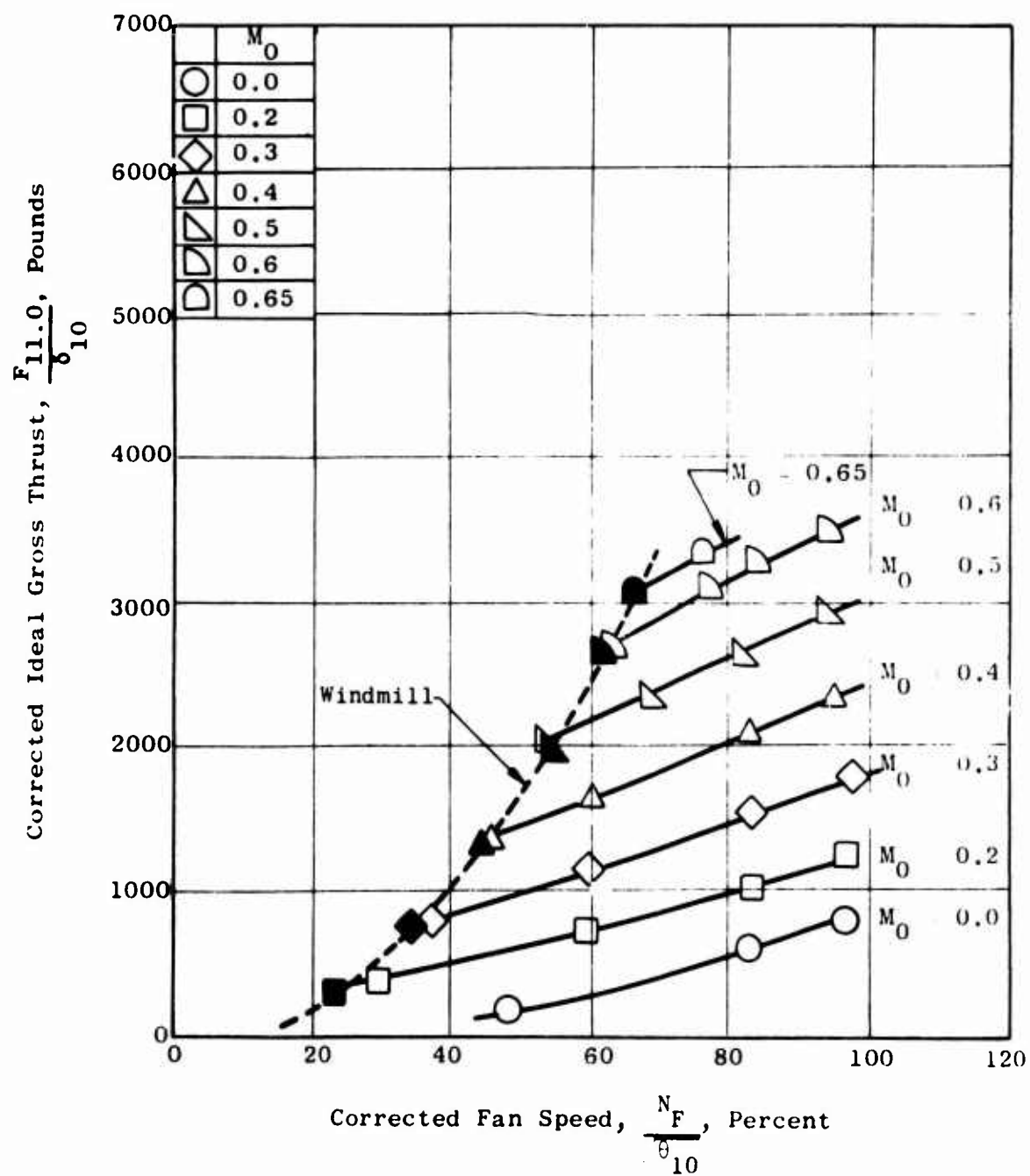


Figure 100. Fan Stream Ideal Gross Thrust - Model 3.

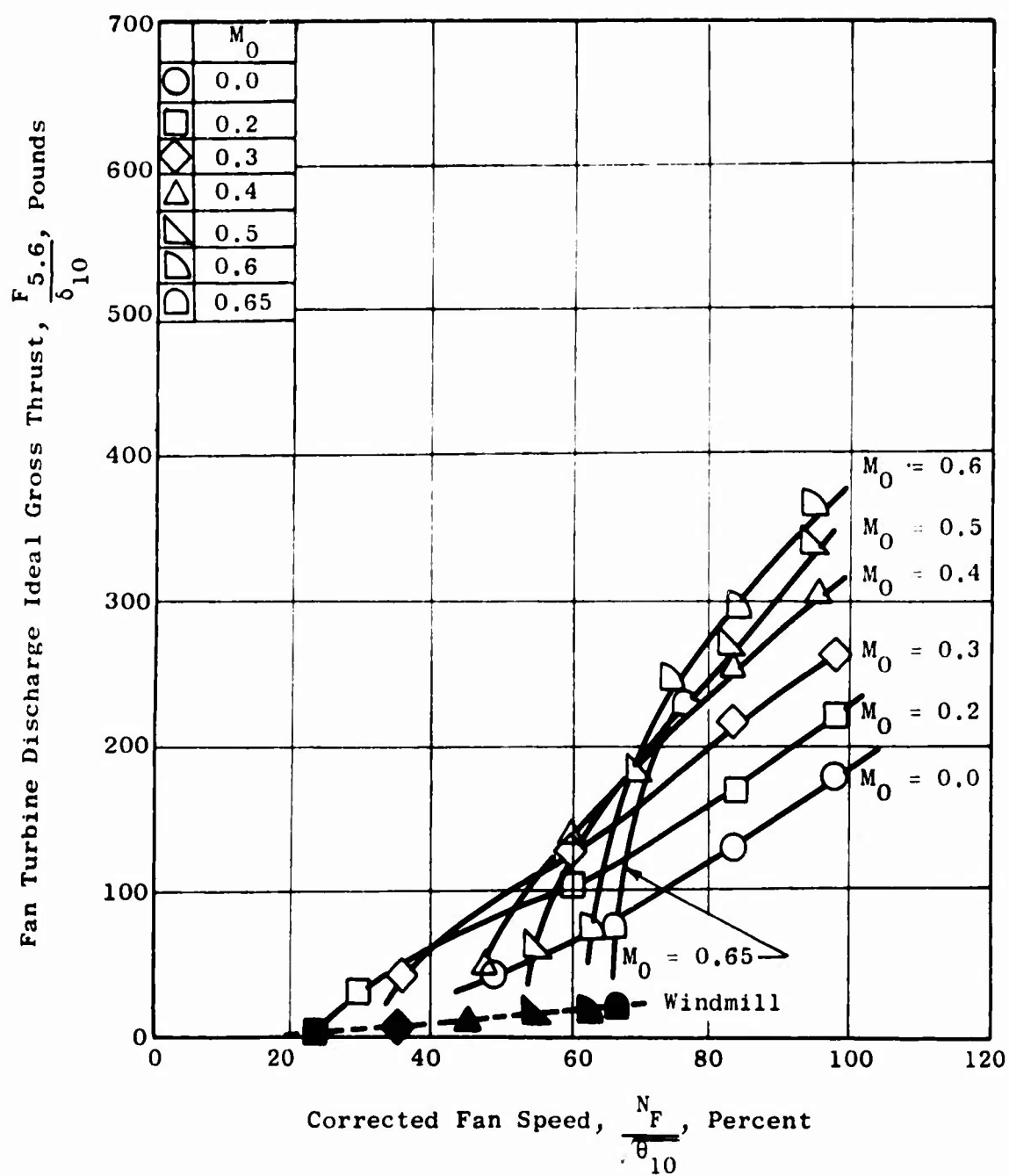


Figure 101. Fan Turbine Residual Ideal Gross Thrust - Model 5.

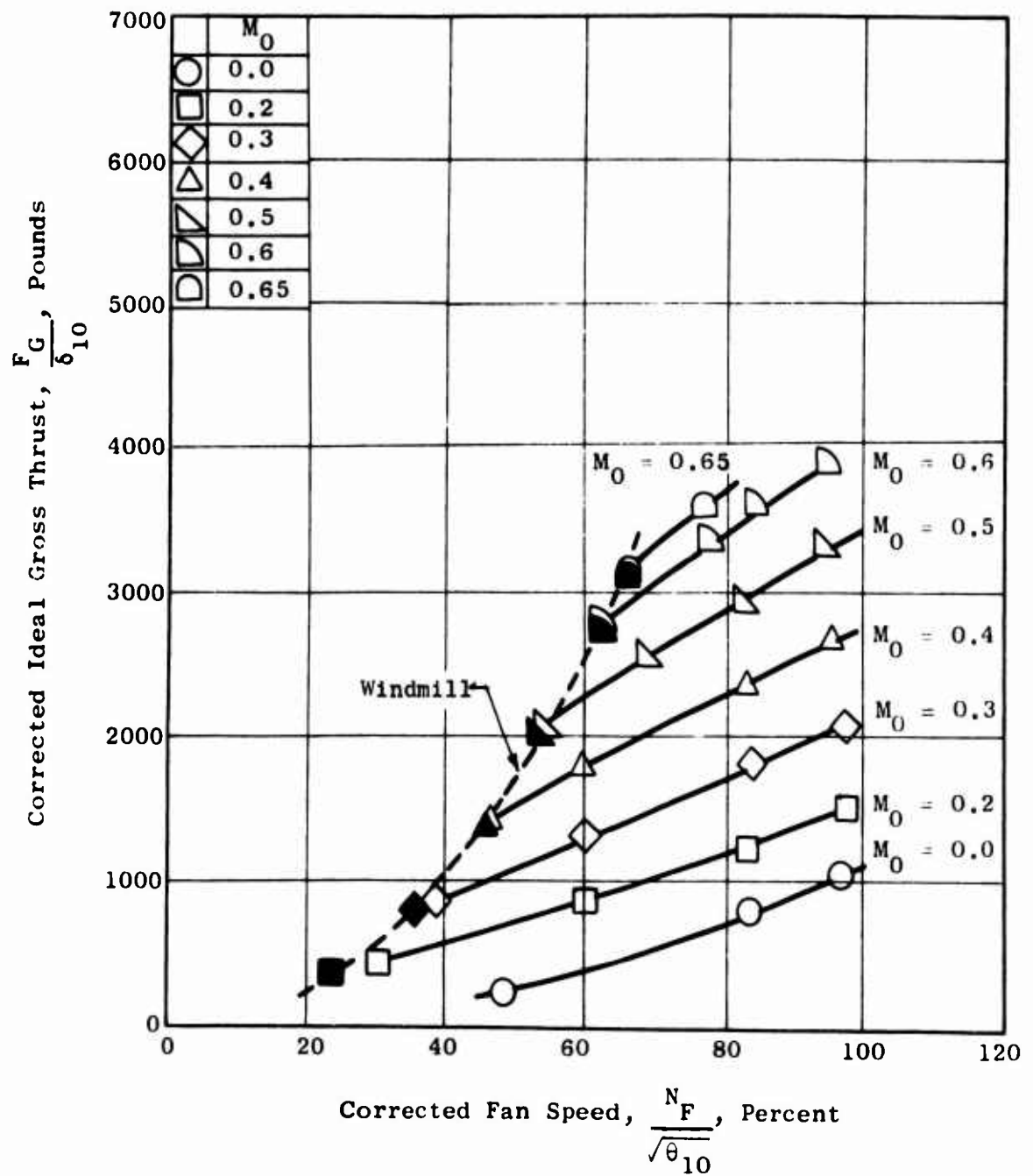


Figure 102. Fan System Ideal Gross Thrust - Model 5.

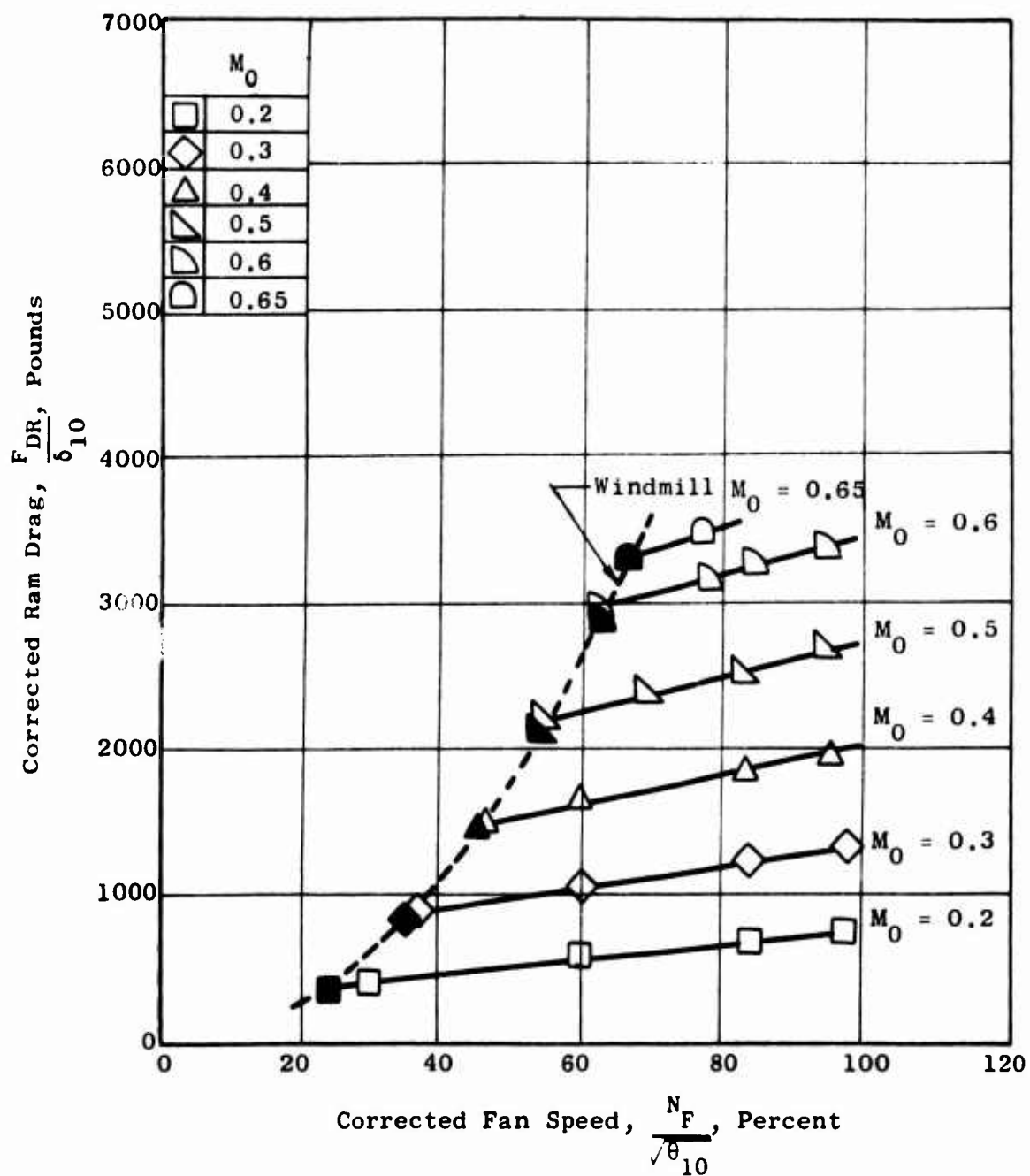


Figure 103. Total Ram Drag - Model 5.

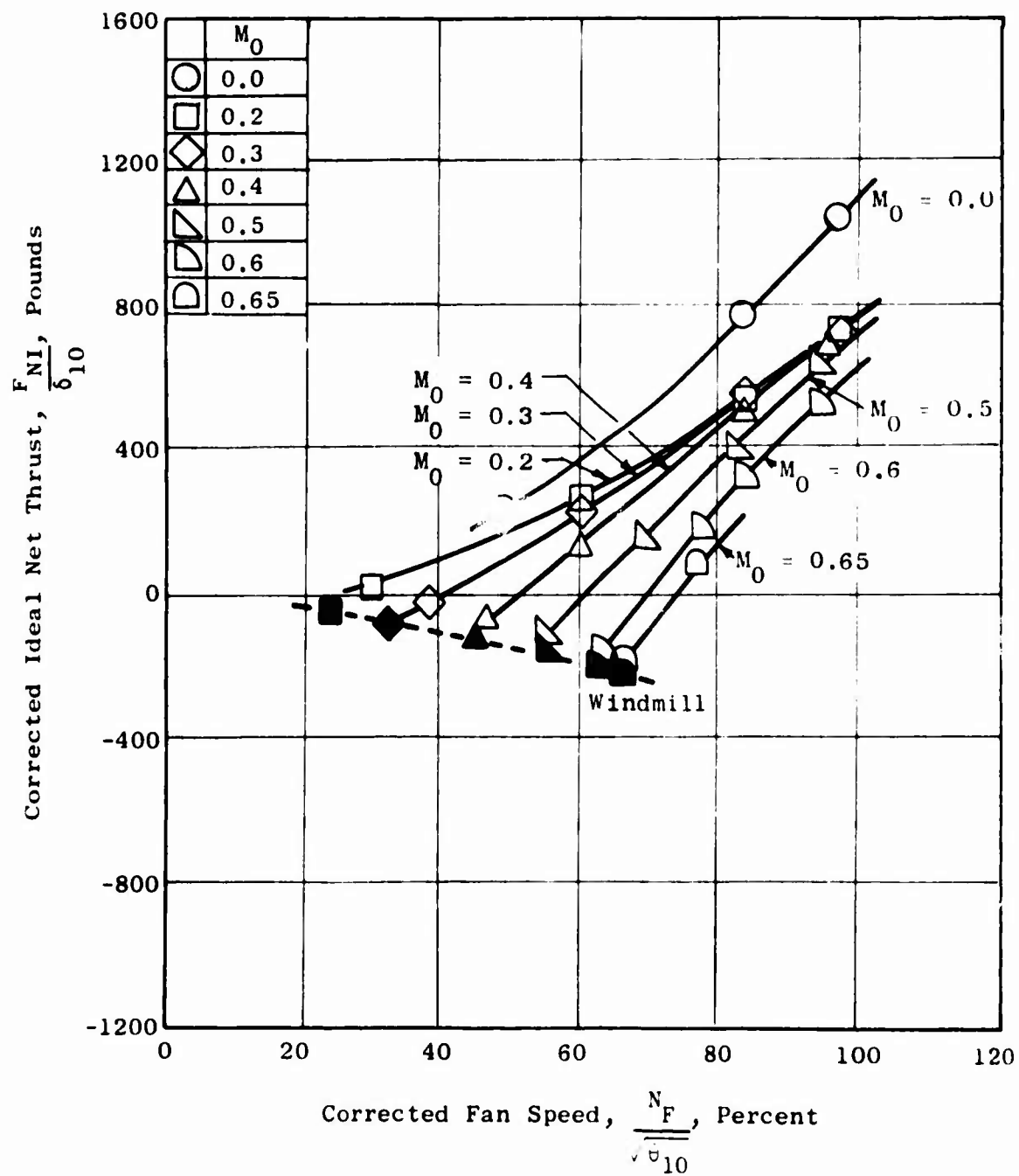


Figure 104. Fan System Ideal Net Thrust - Model 5.

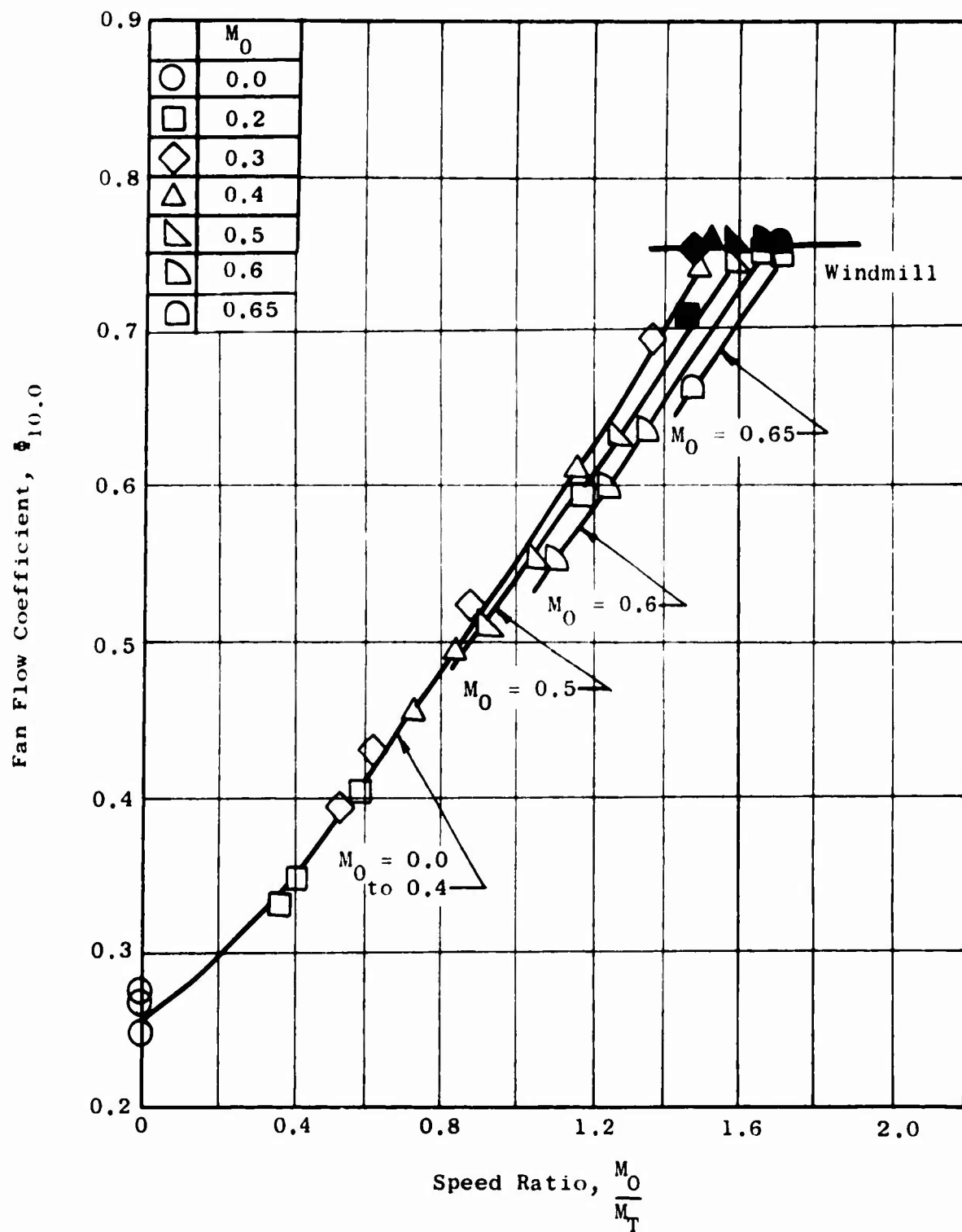


Figure 105. Fan Flow Coefficient Characteristics - Model 5.

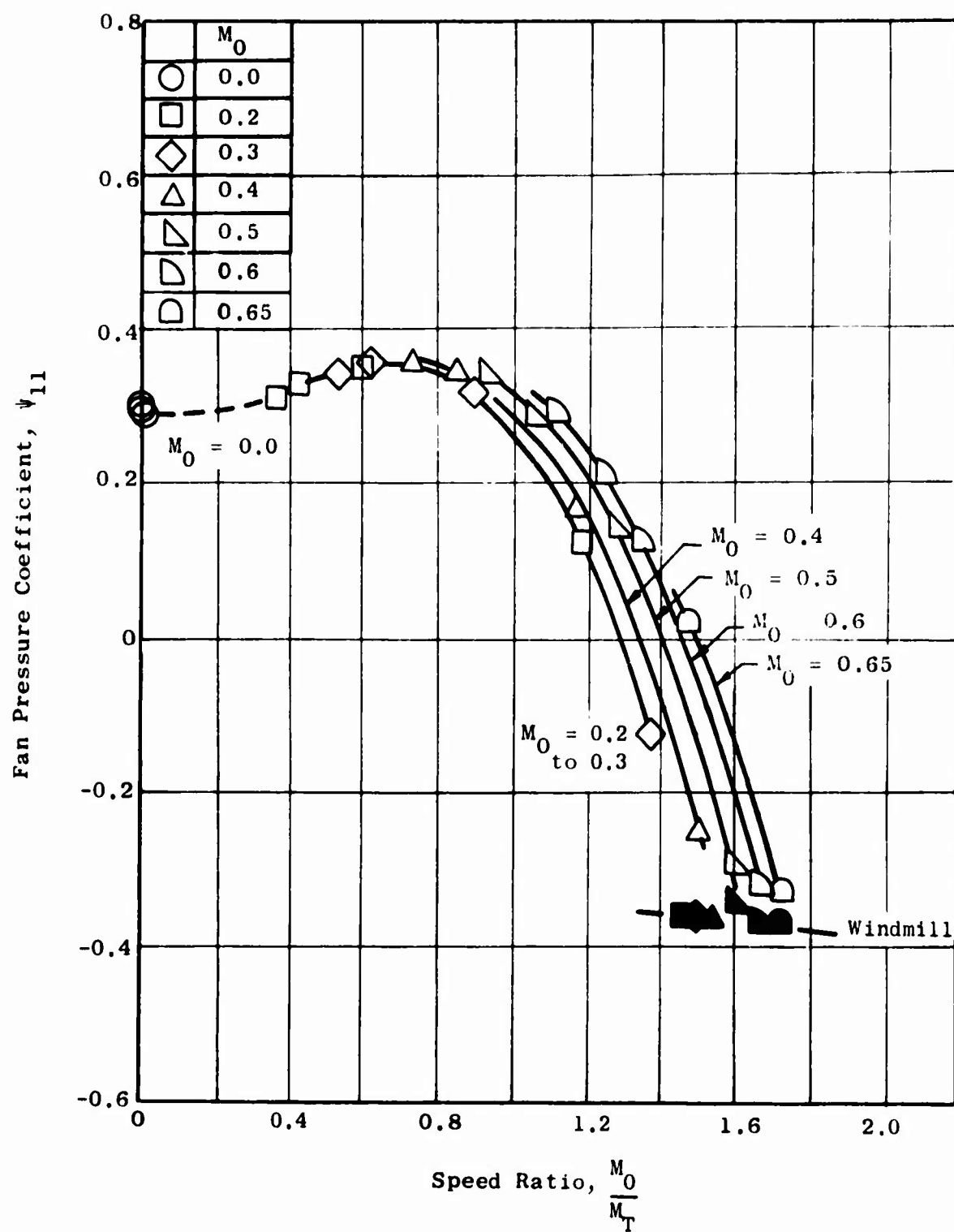


Figure 106. Fan Pressure Coefficient Characteristics - Model 5.

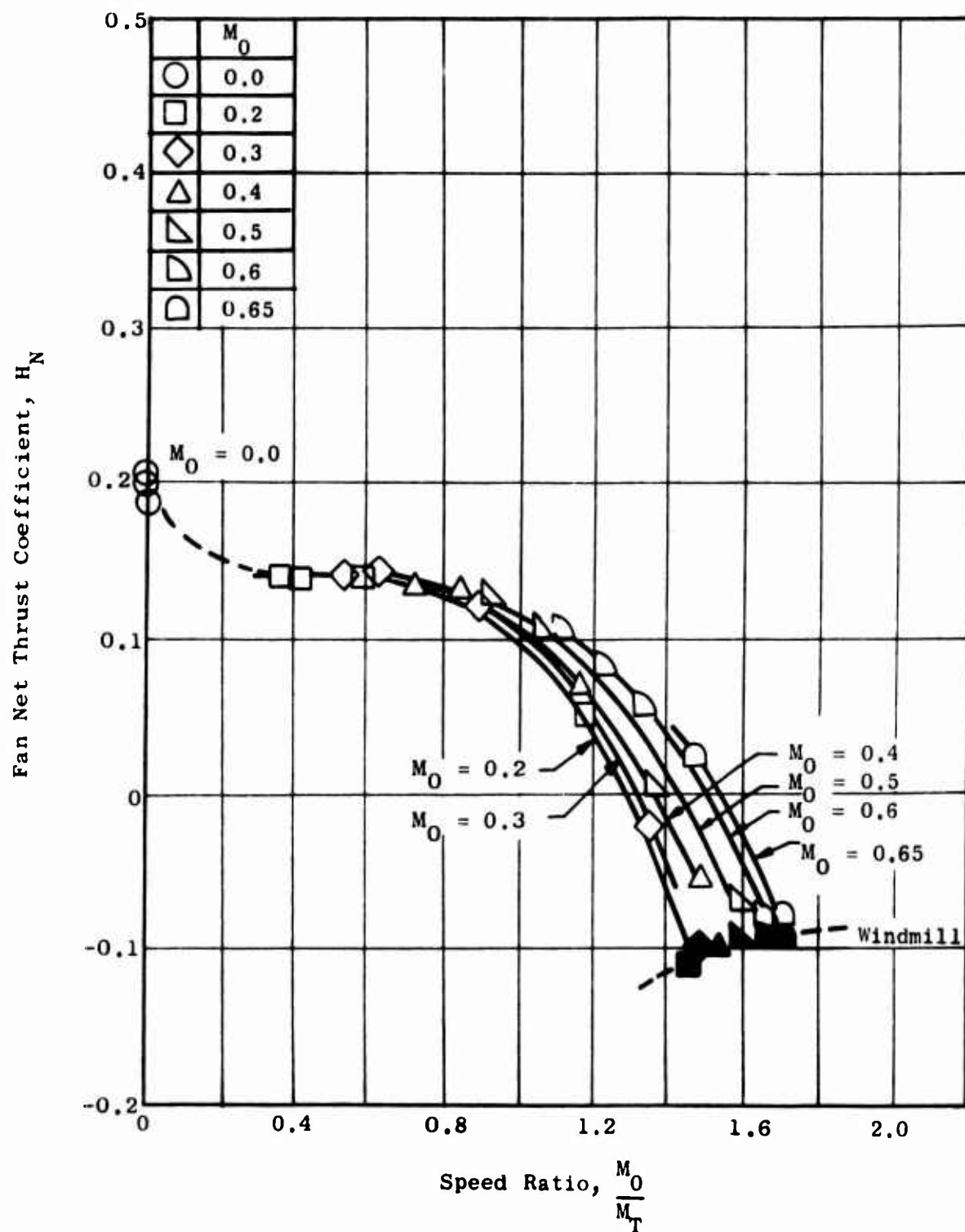


Figure 107. Fan Ideal Net Thrust Coefficient - Model 5.

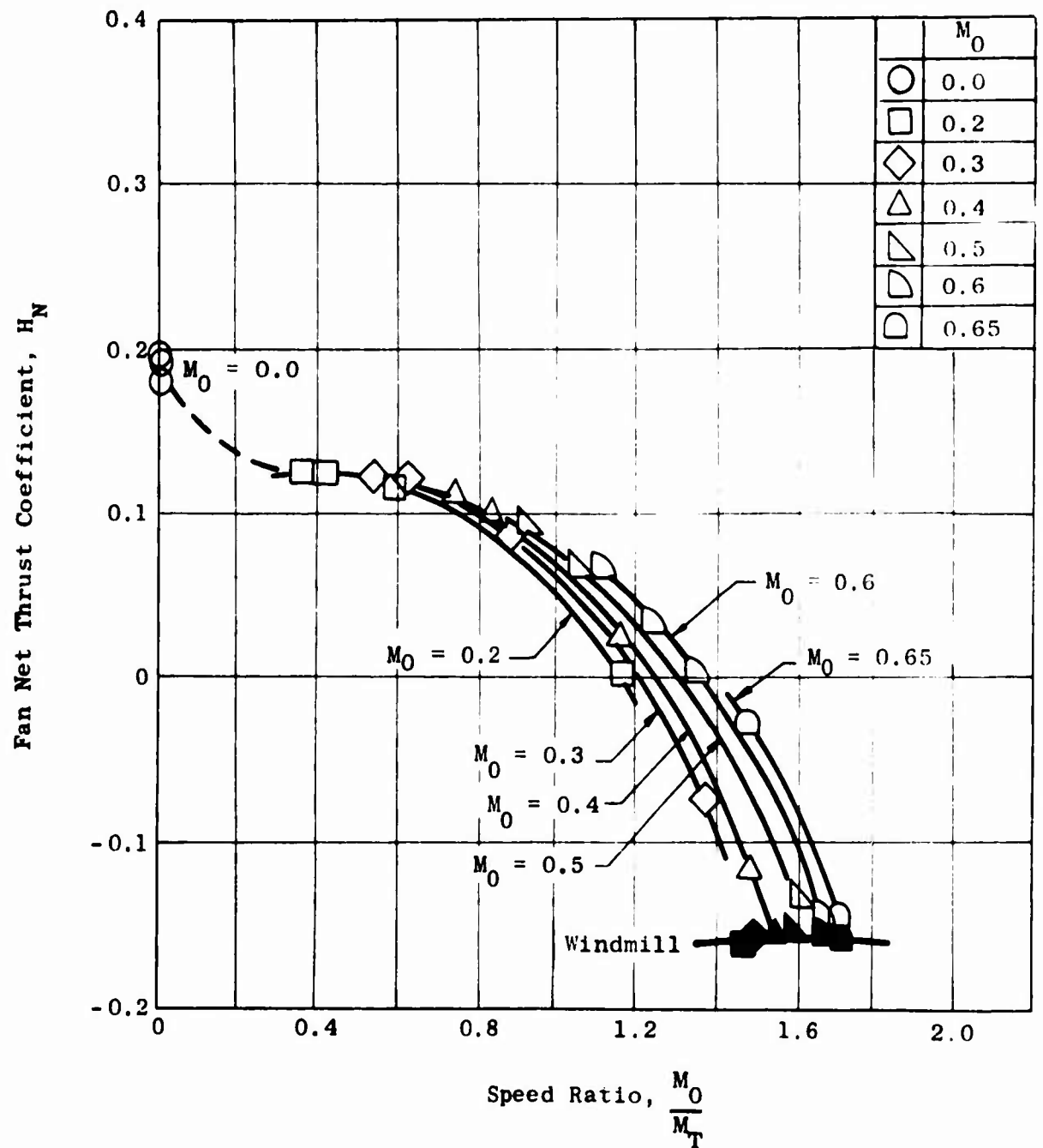


Figure 108. Fan Net Thrust Coefficient with a Nozzle Coefficient of 0.95 - Model 5.

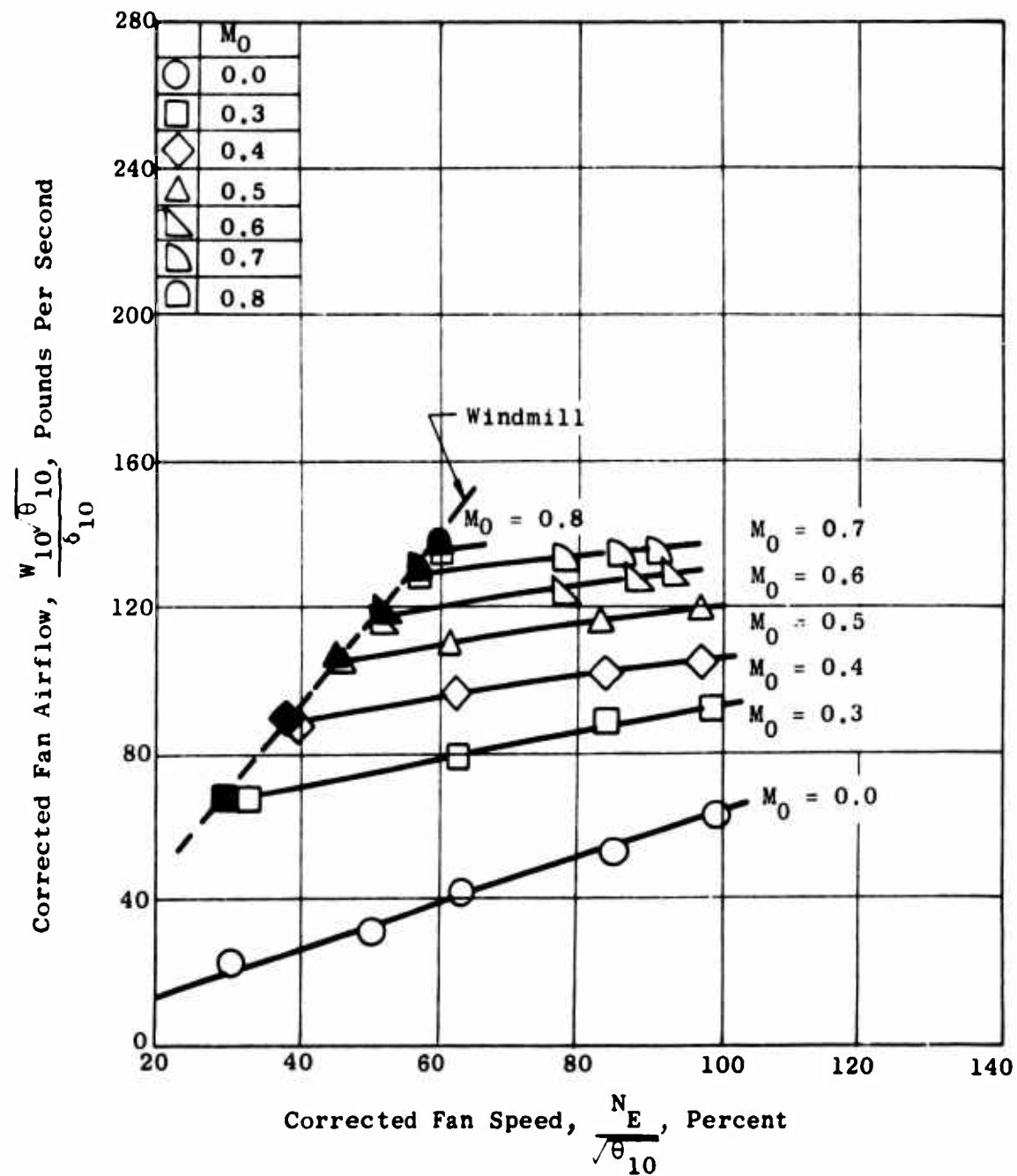


Figure 109. Fan Airflow Characteristics - Model 6.

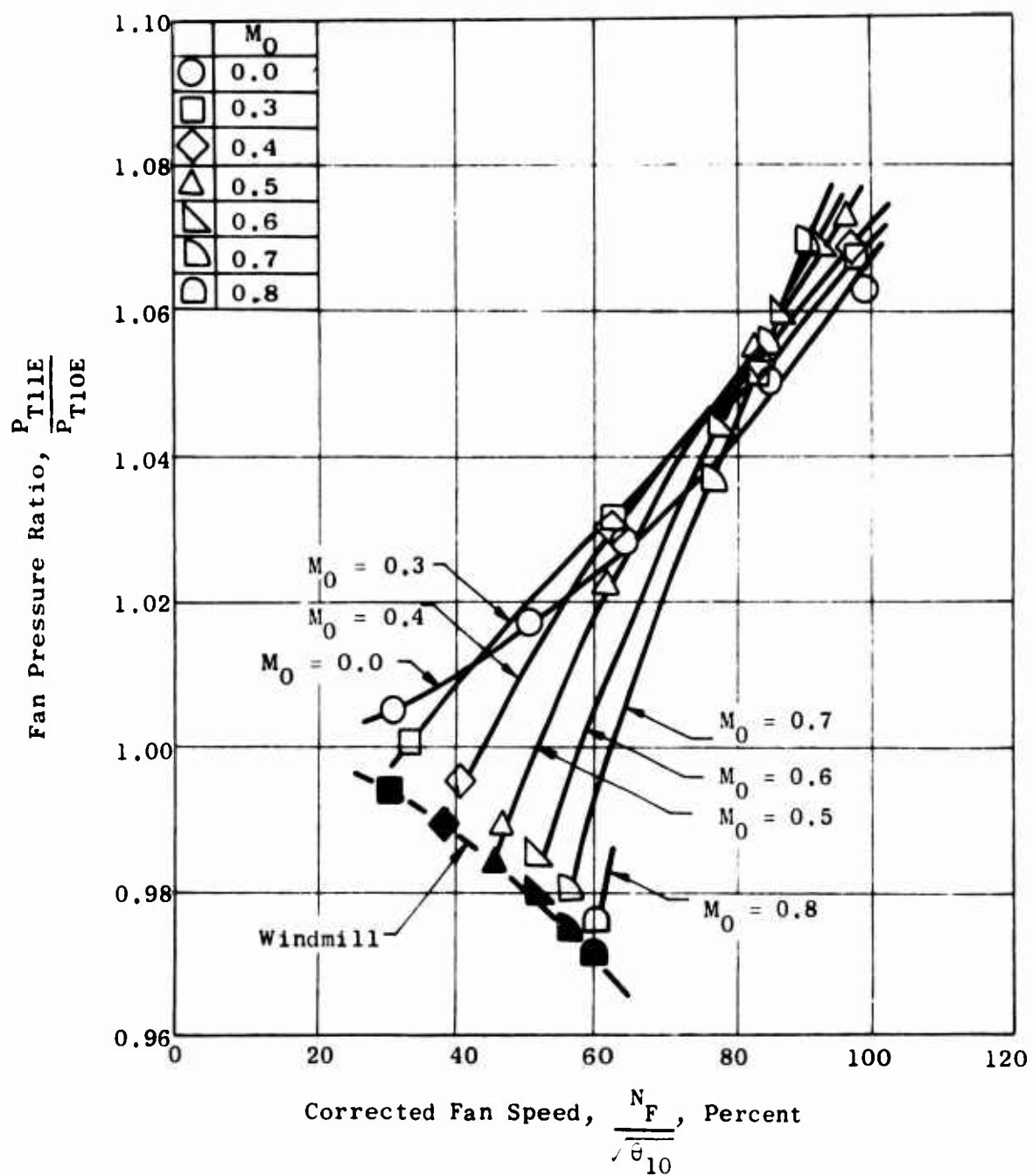


Figure 110. Fan Total Pressure Ratio - Model 6.

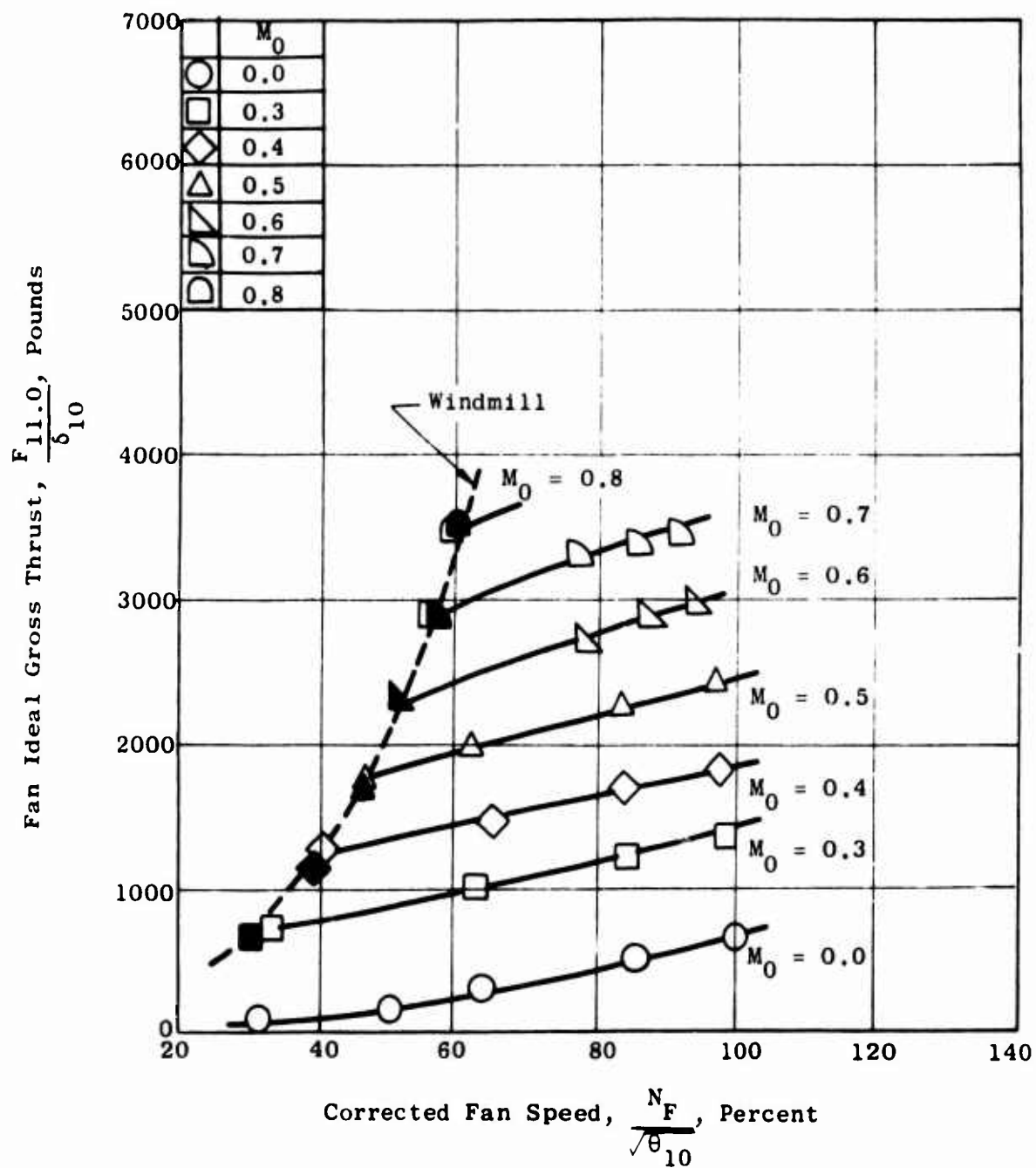


Figure 111. Fan Stream Ideal Gross Thrust - Model 6.

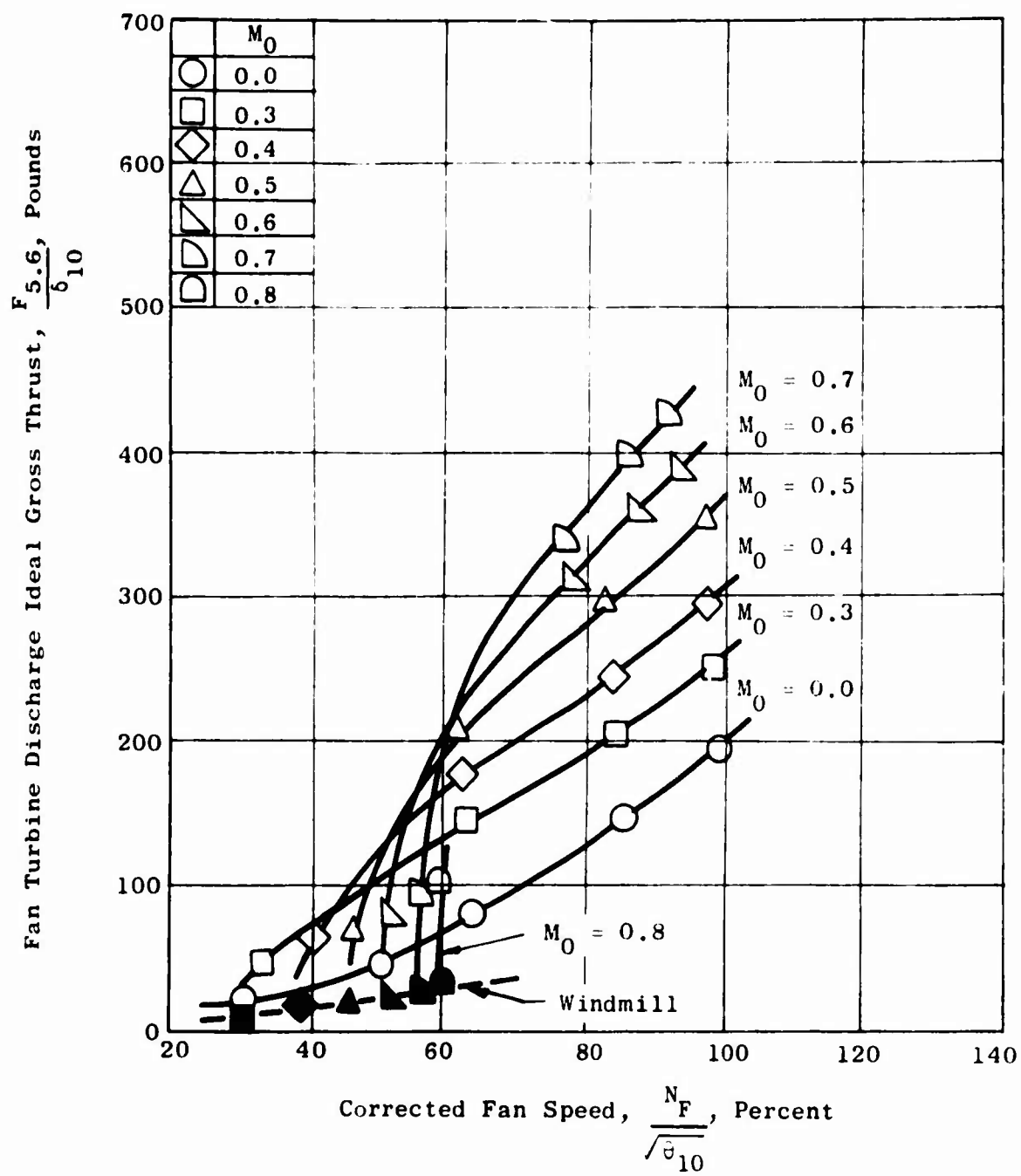


Figure 112. Fan Turbine Residual Ideal Gross Thrust - Model 6.

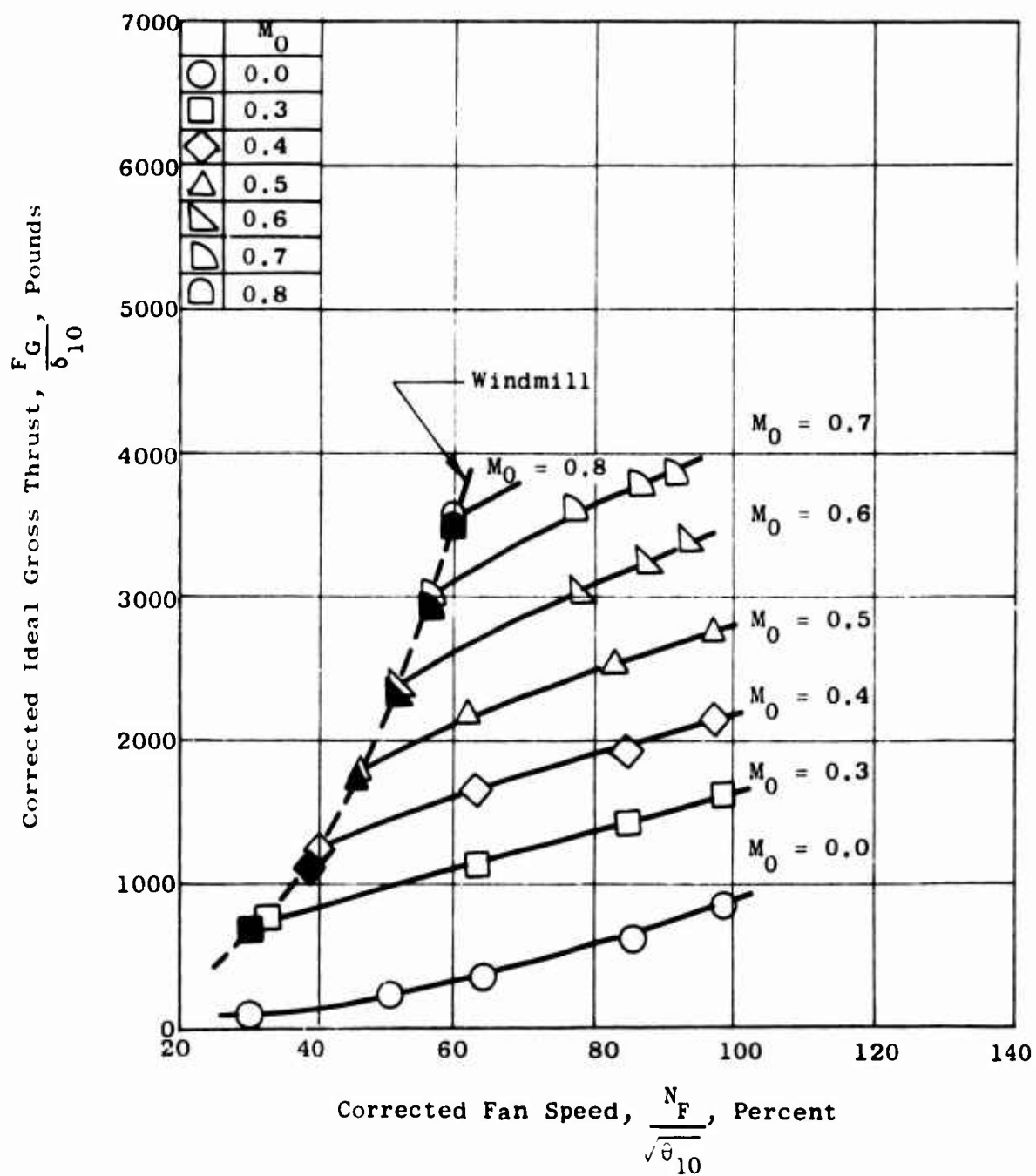


Figure 113. Fan System Ideal Gross Thrust - Model 6.

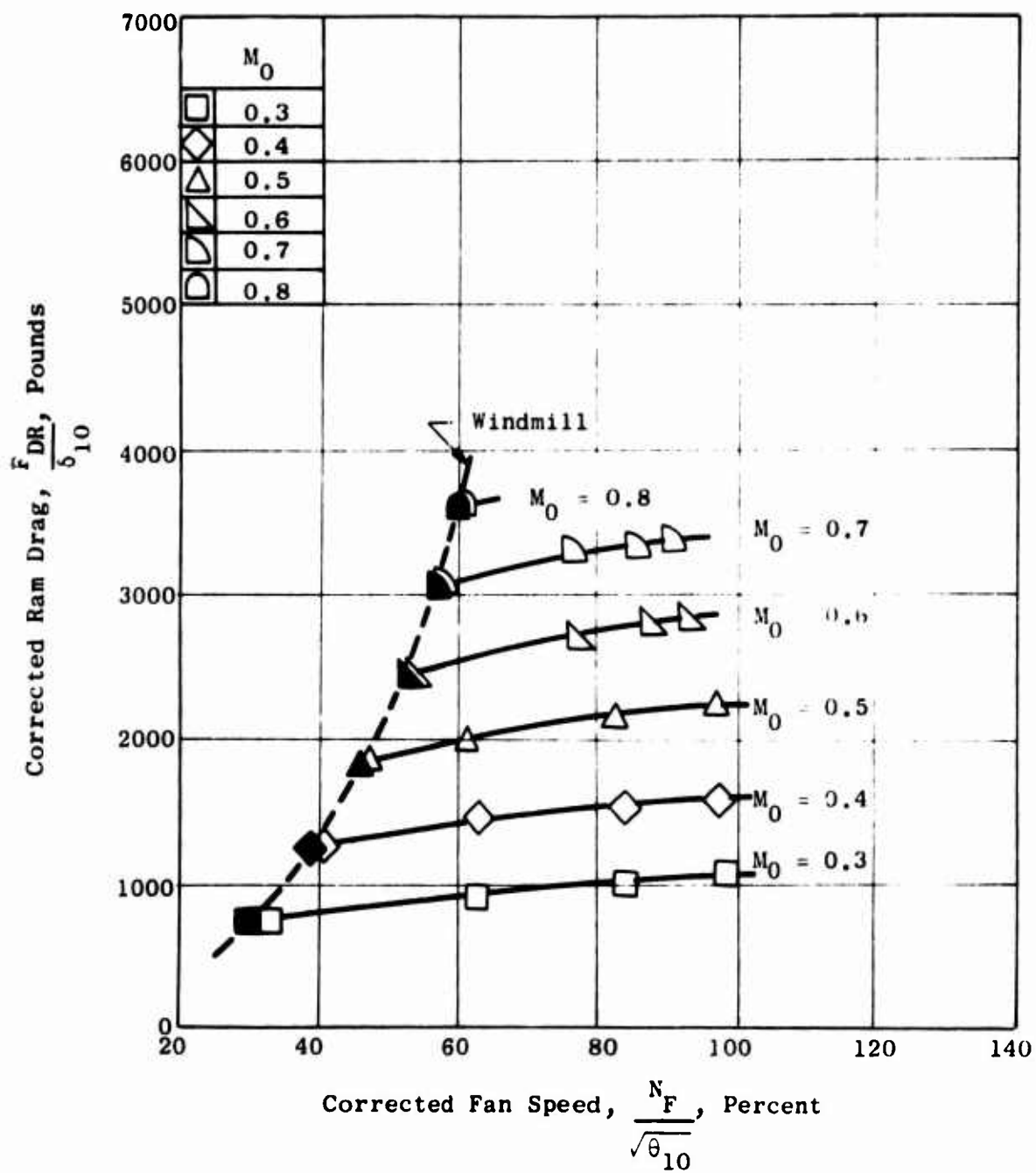


Figure 114. Total Ram Drag - Model 6.

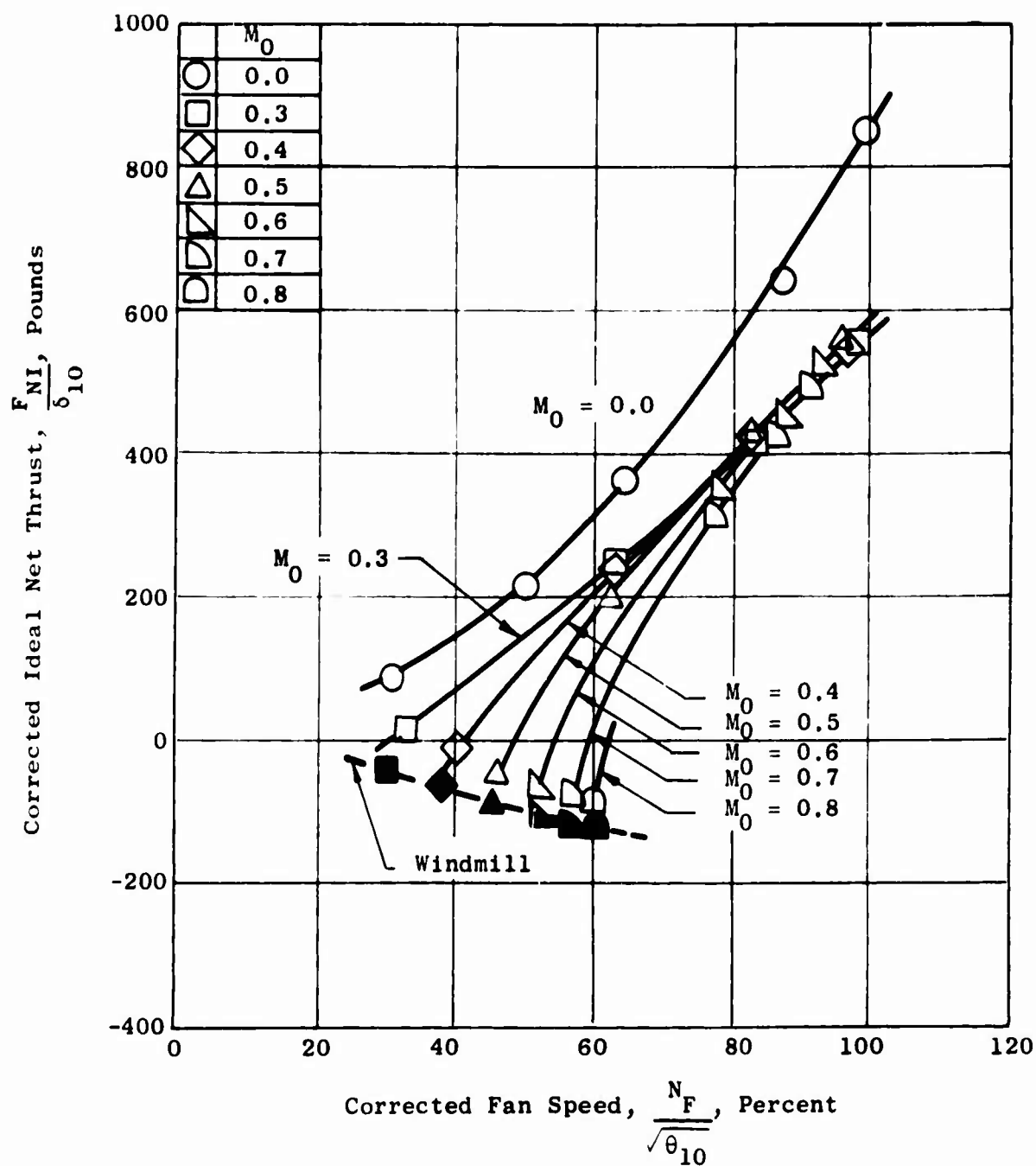


Figure 115. Fan System Ideal Net Thrust - Model 6.

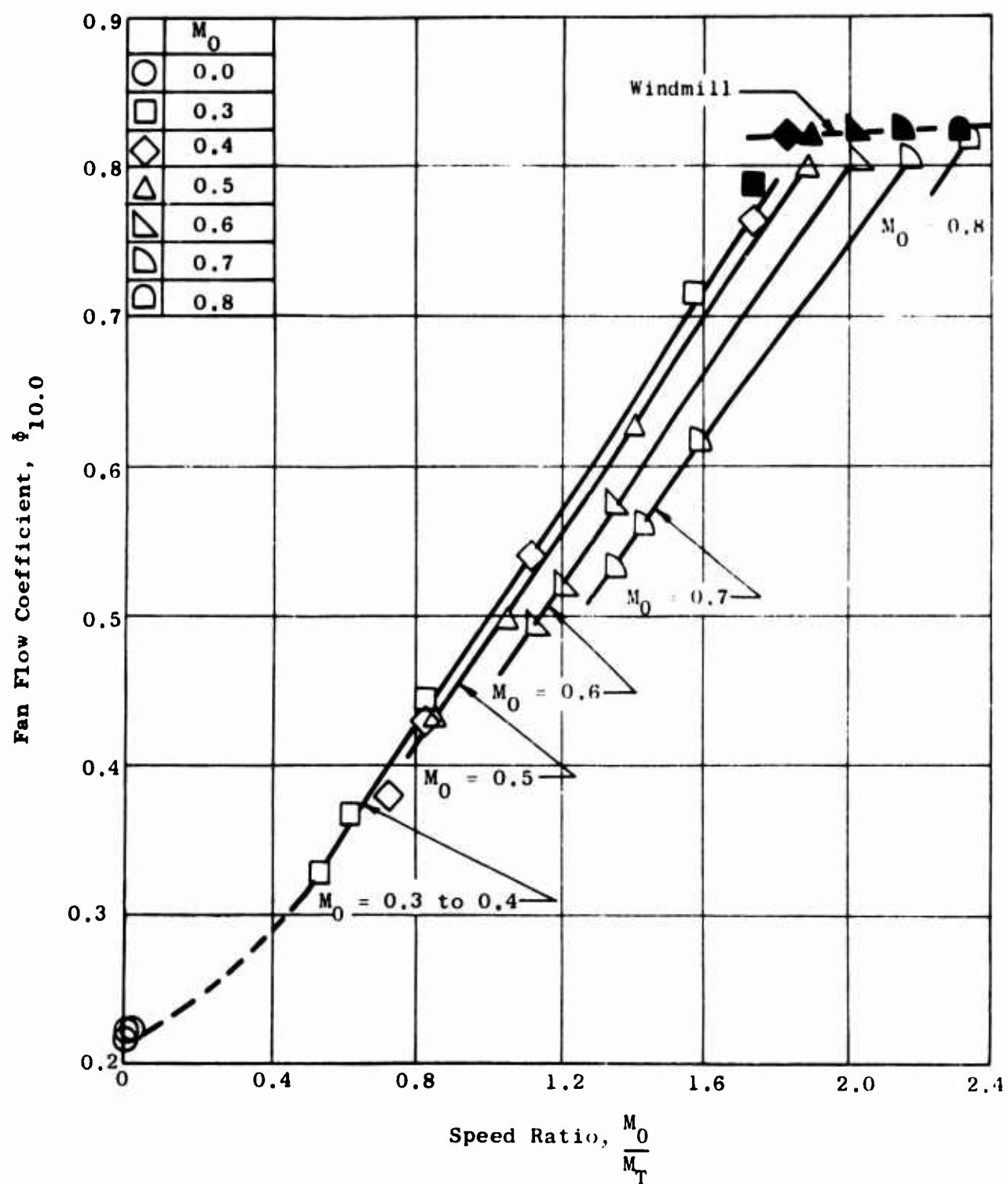


Figure 116. Fan Flow Function Characteristics - Model 6.

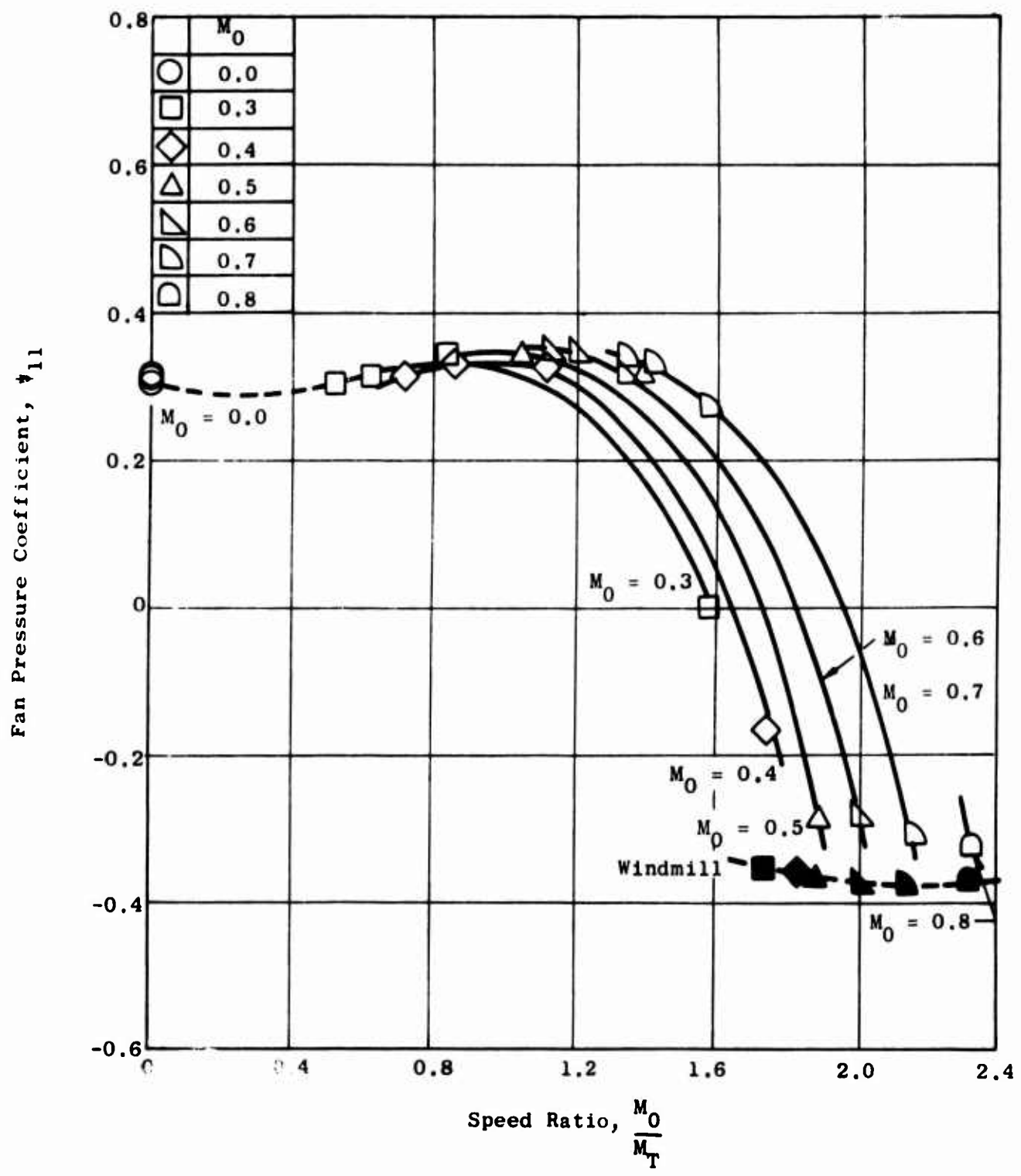


Figure 117. Fan Pressure Coefficient Characteristics - Model 6.

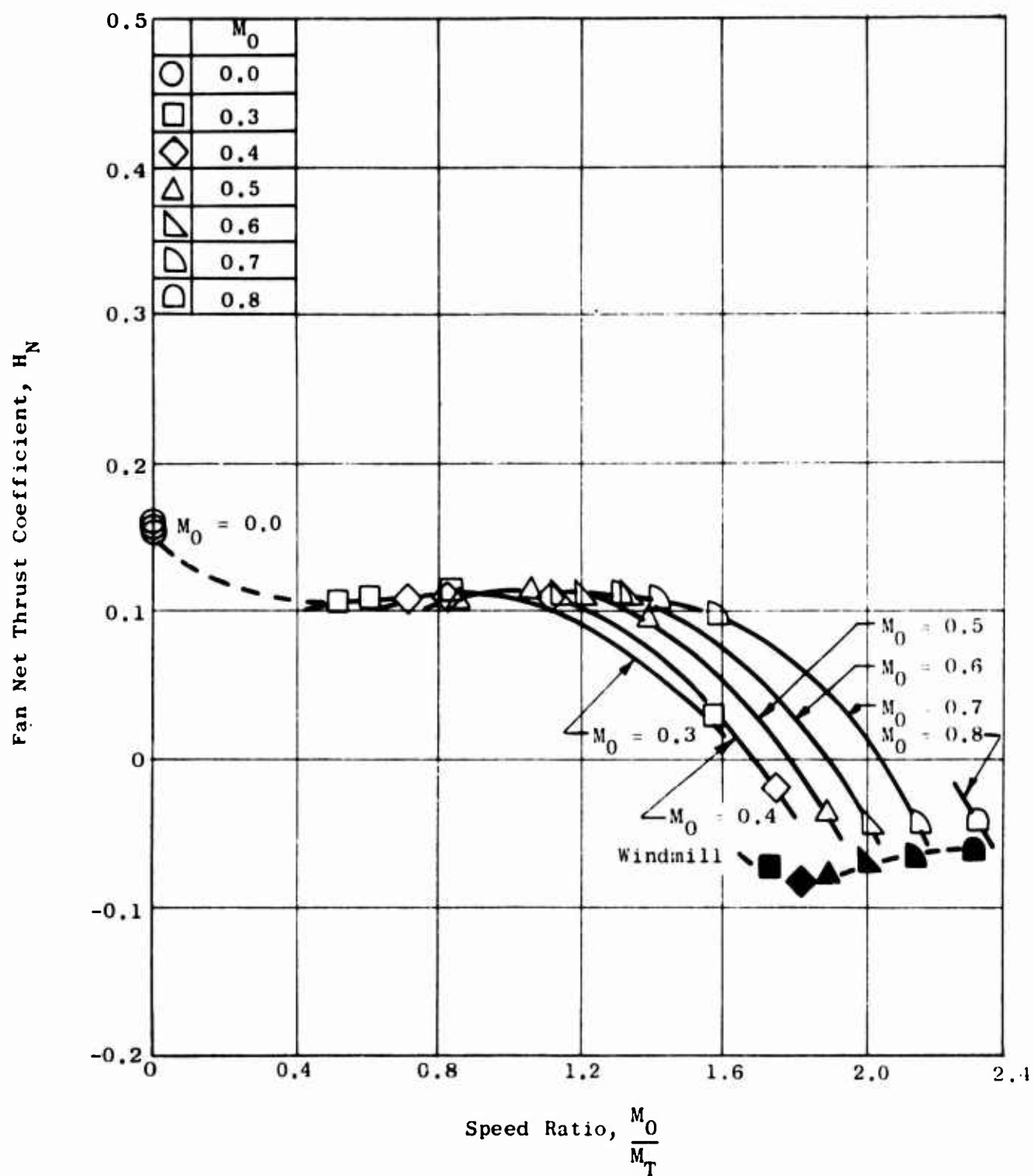


Figure 118. Fan Ideal Net Thrust Coefficient - Model 6.

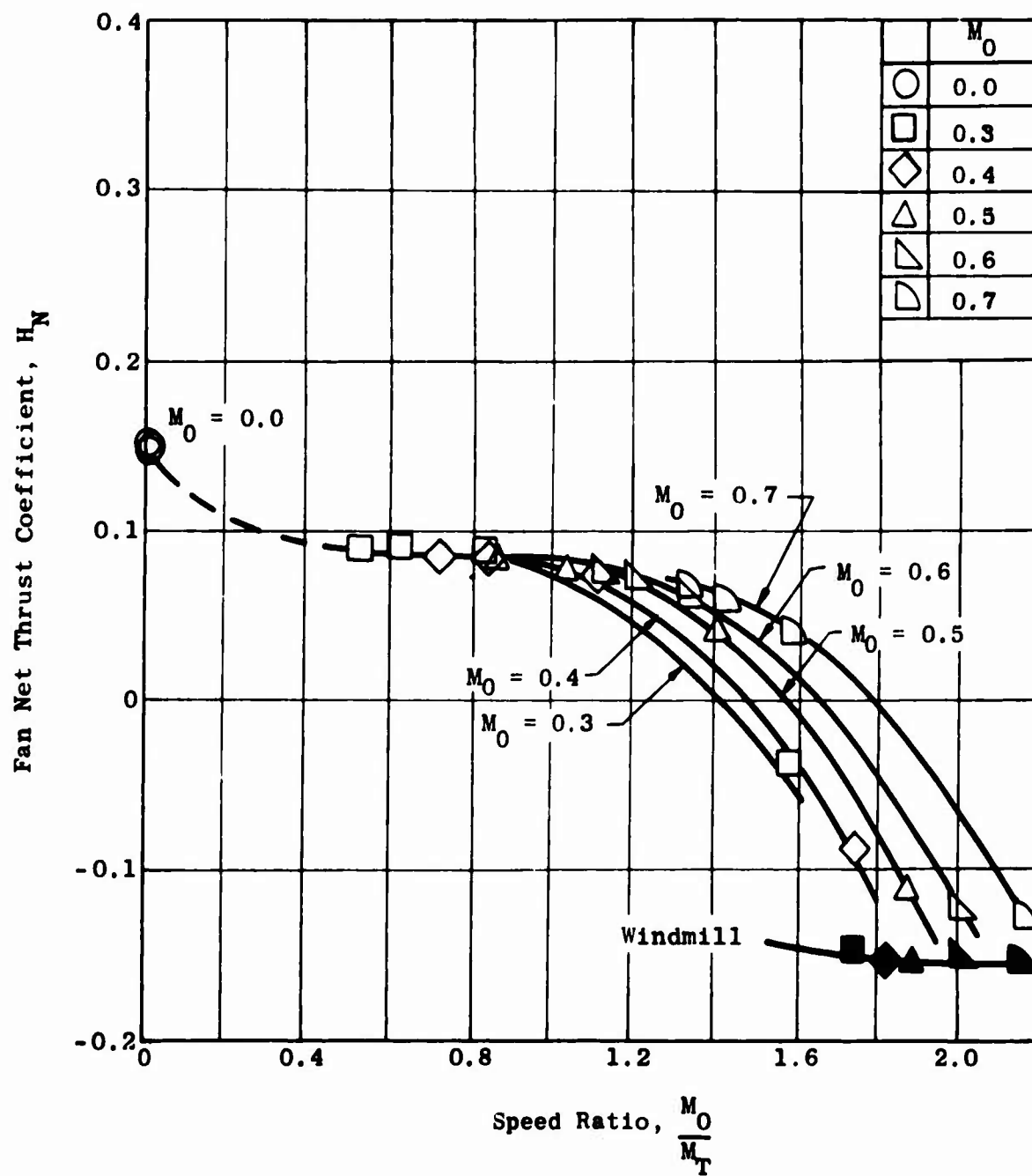


Figure 119. Fan Net Thrust Coefficient with a Nozzle Coefficient of 0.95 - Model 6.

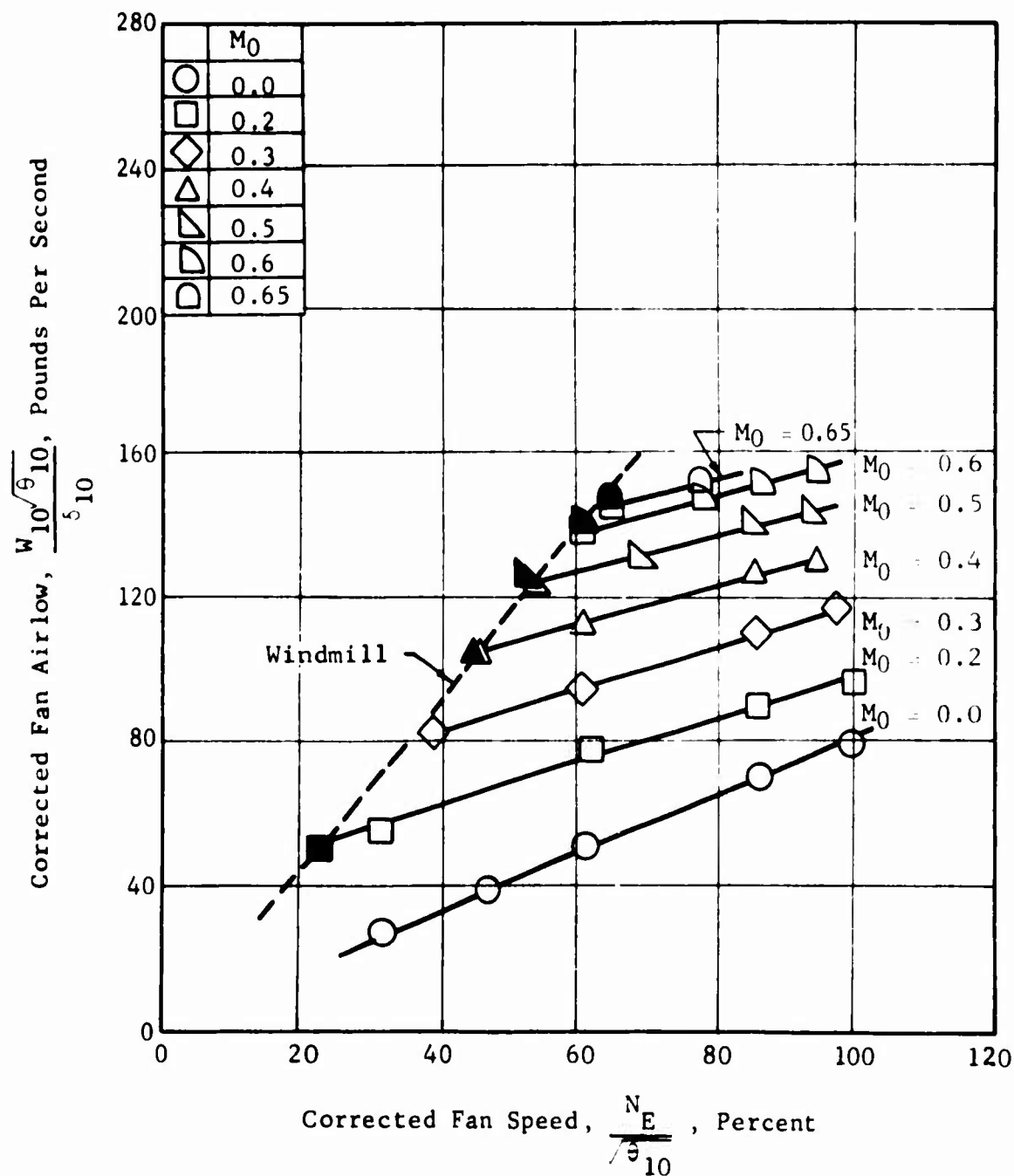


Figure 120. Fan Airflow Characteristics - Model 7.

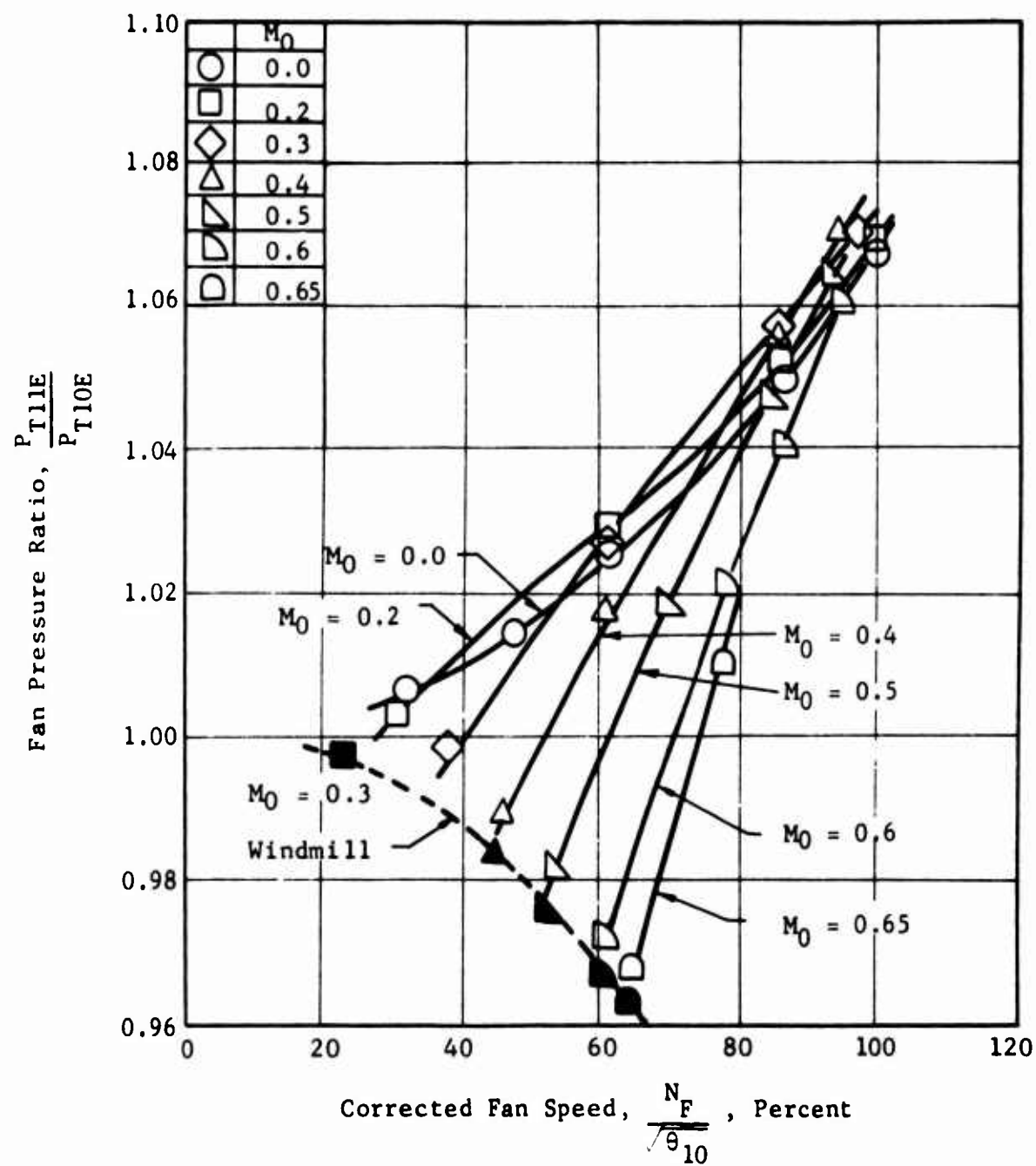


Figure 121. Fan Total Pressure Ratio - Model 7.

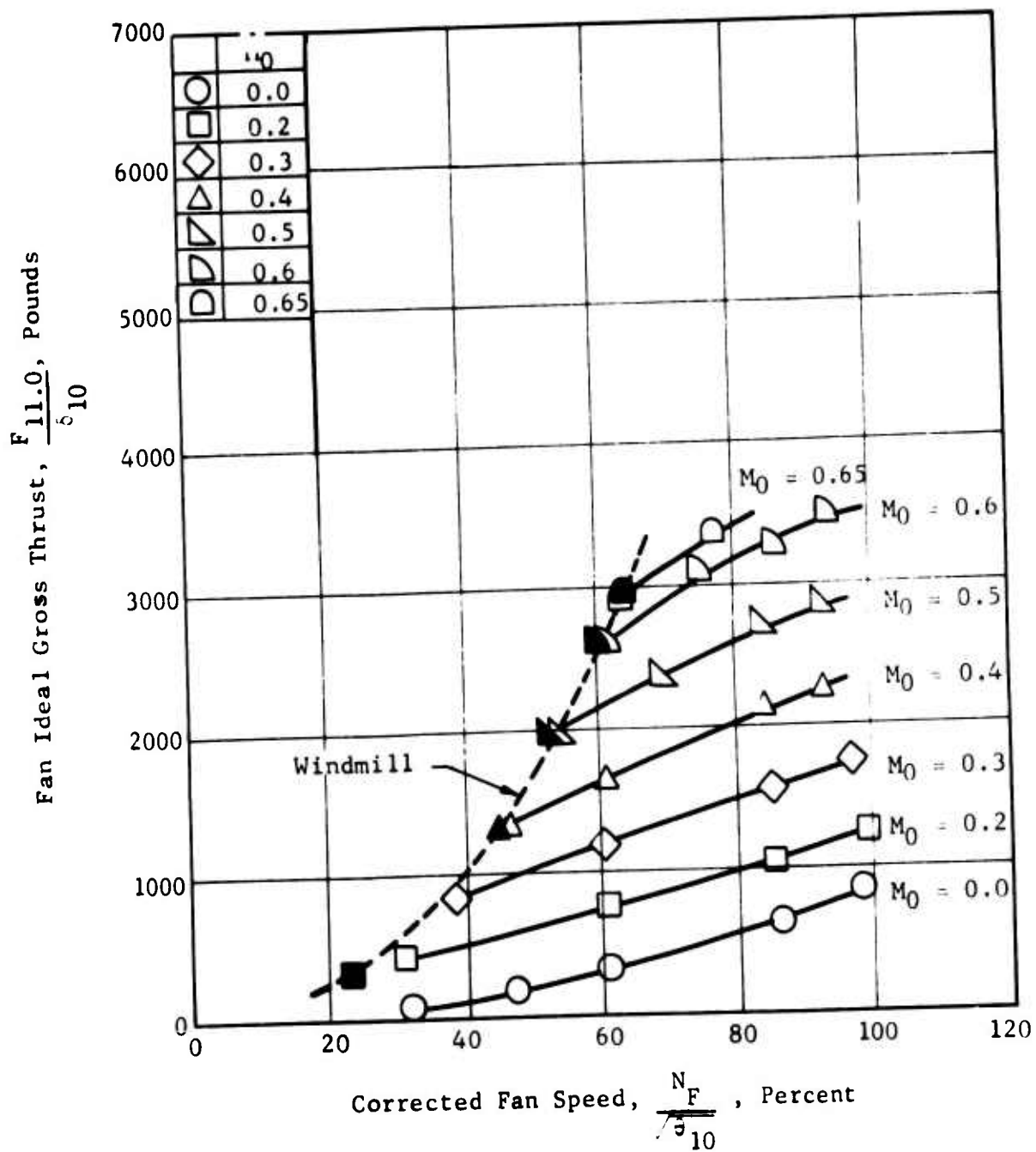


Figure 122. Fan Stream Ideal Gross Thrust - Model 7.

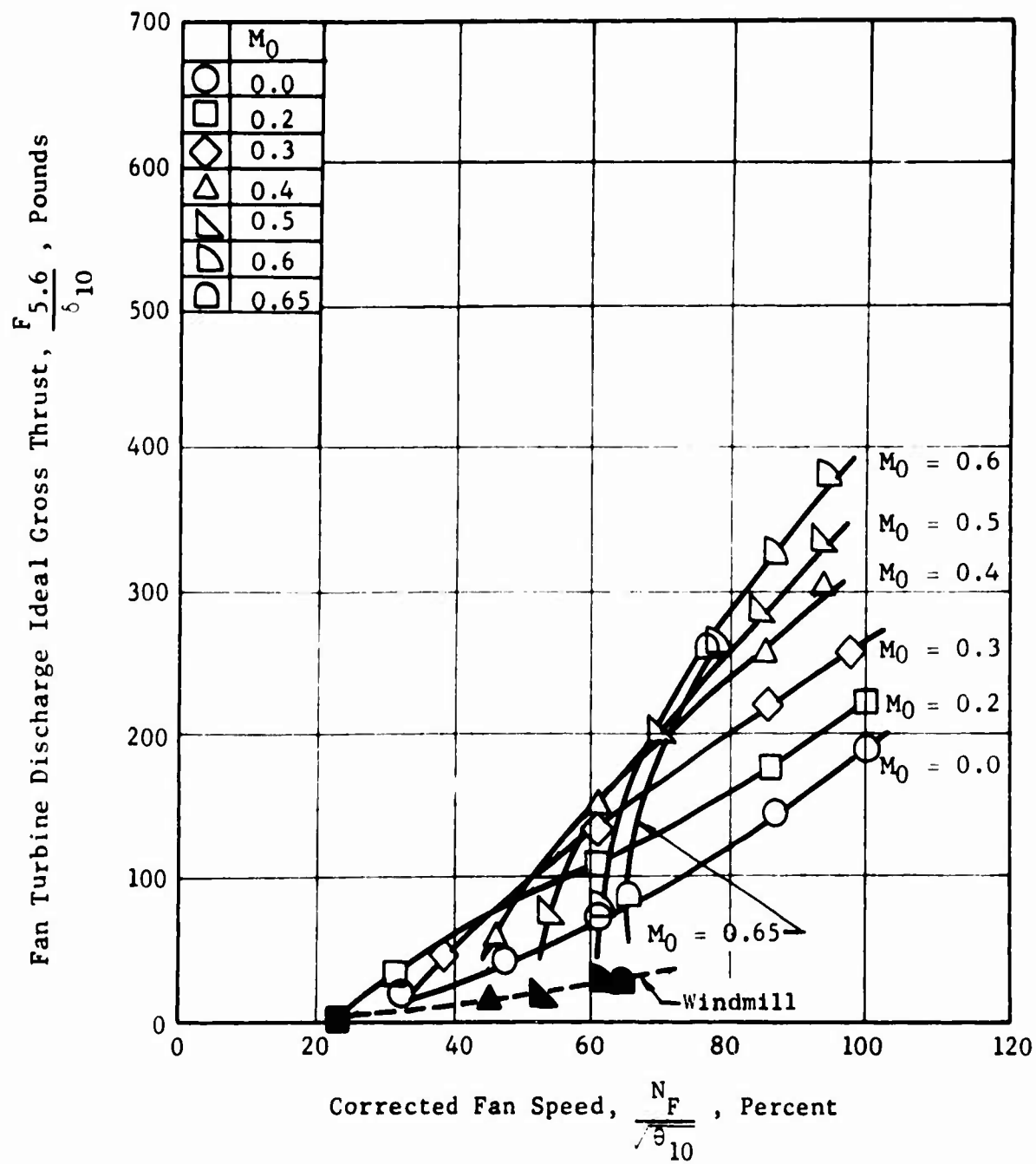


Figure 123. Fan Turbine Residual Ideal Gross Thrust - Model 7.

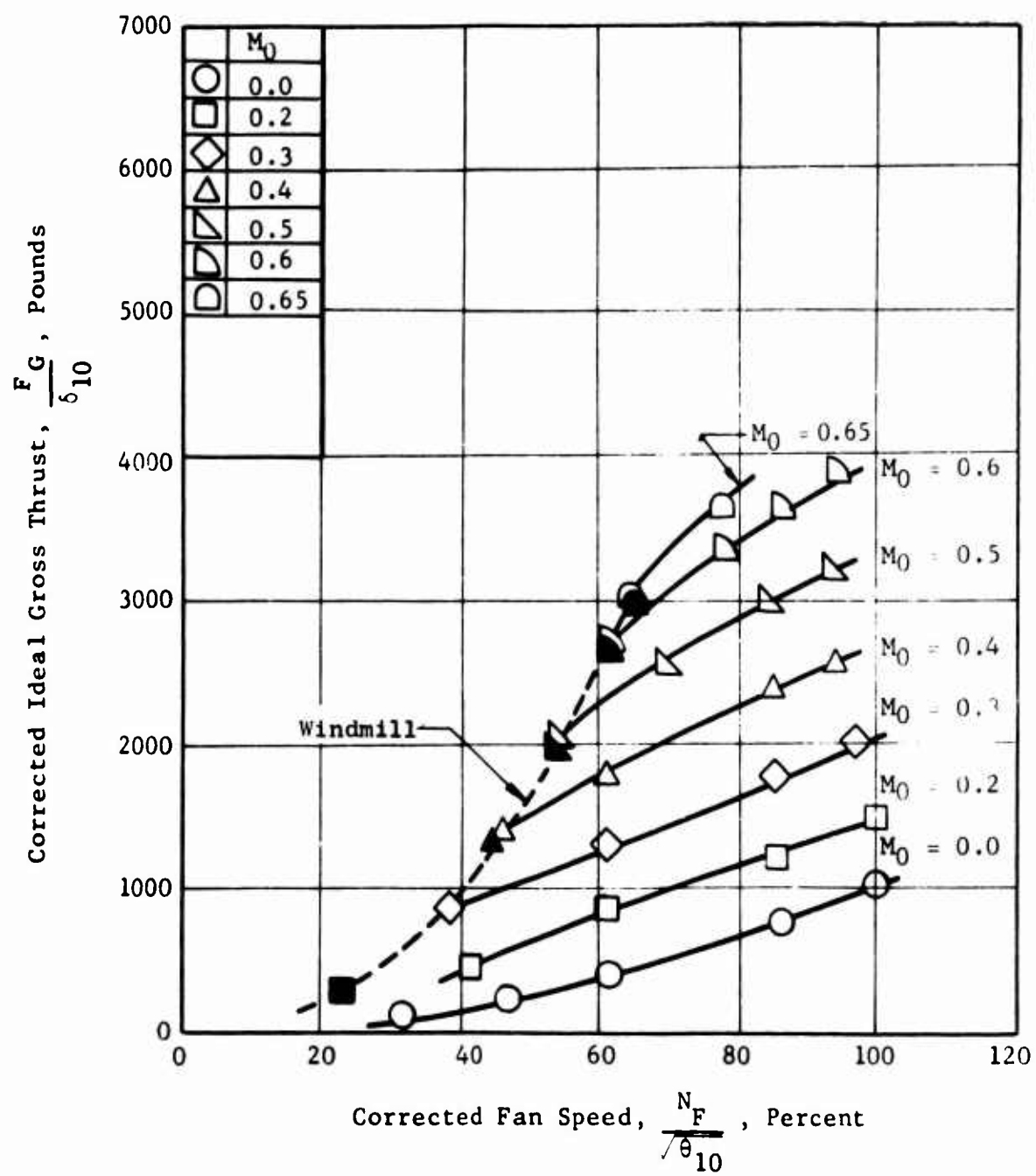


Figure 124. Fan System Ideal Gross Thrust - Model 7.

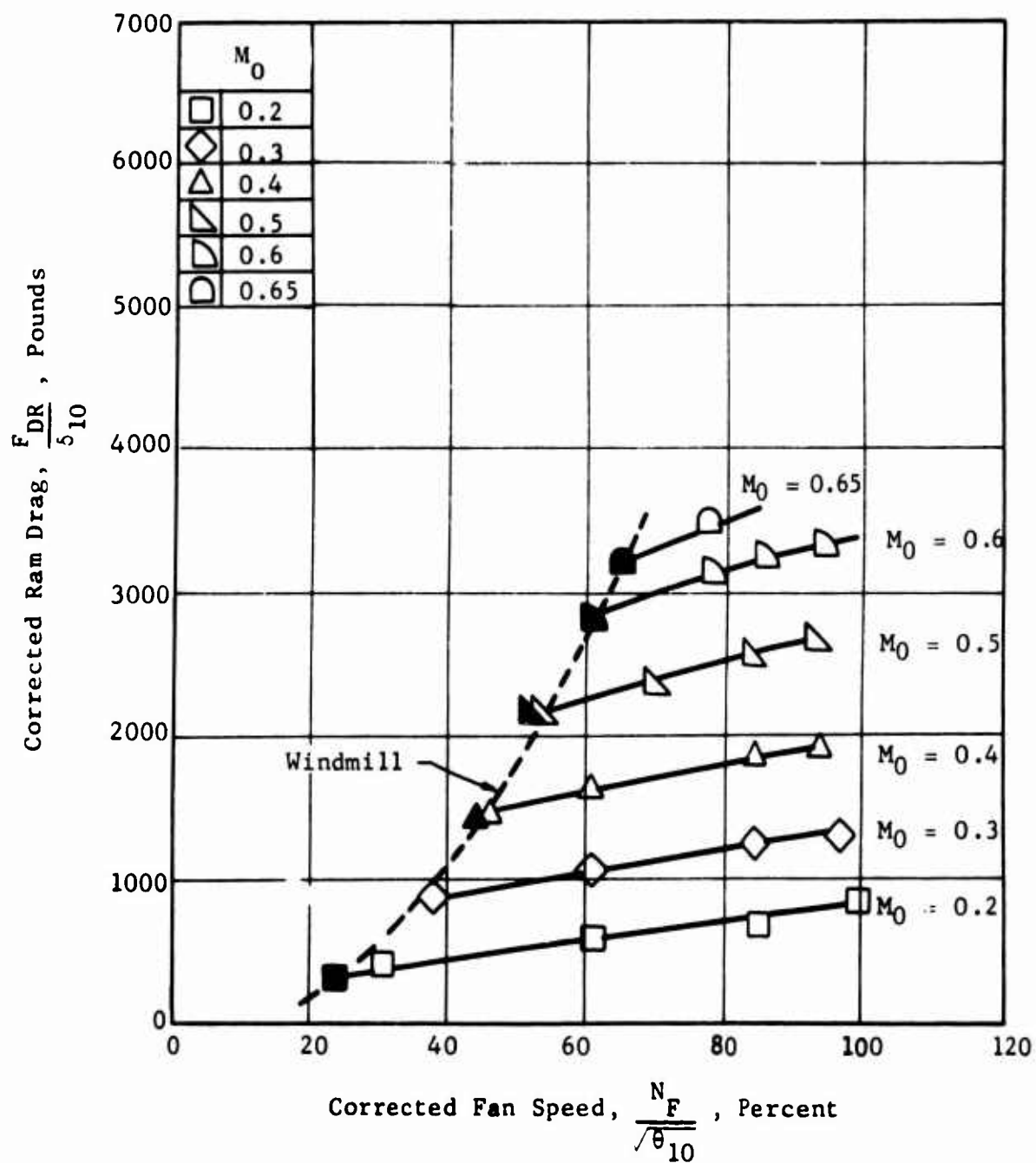


Figure 125. Total Ram Drag - Model 7.

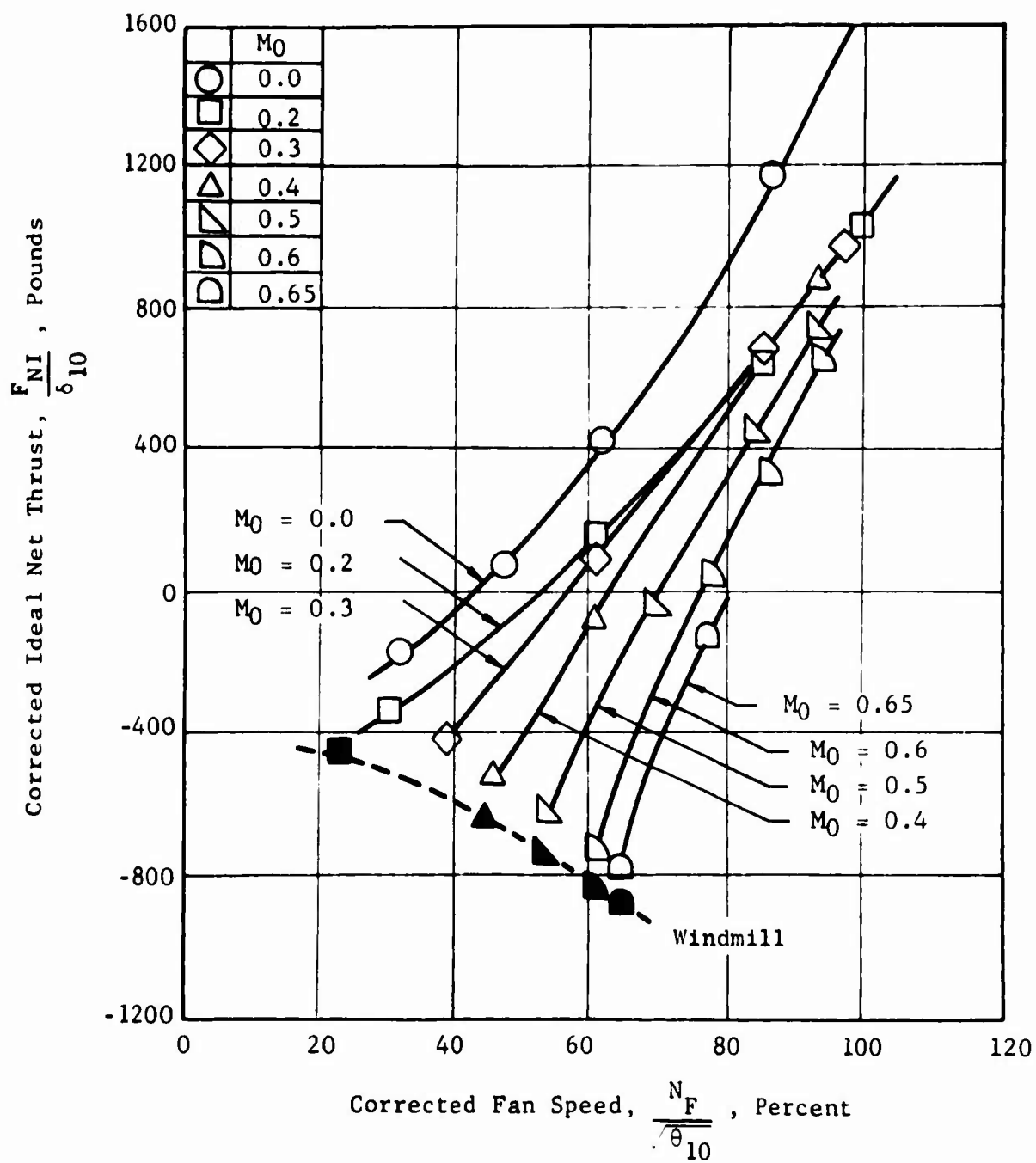


Figure 126. Fan System Ideal Net Thrust - Model 7.

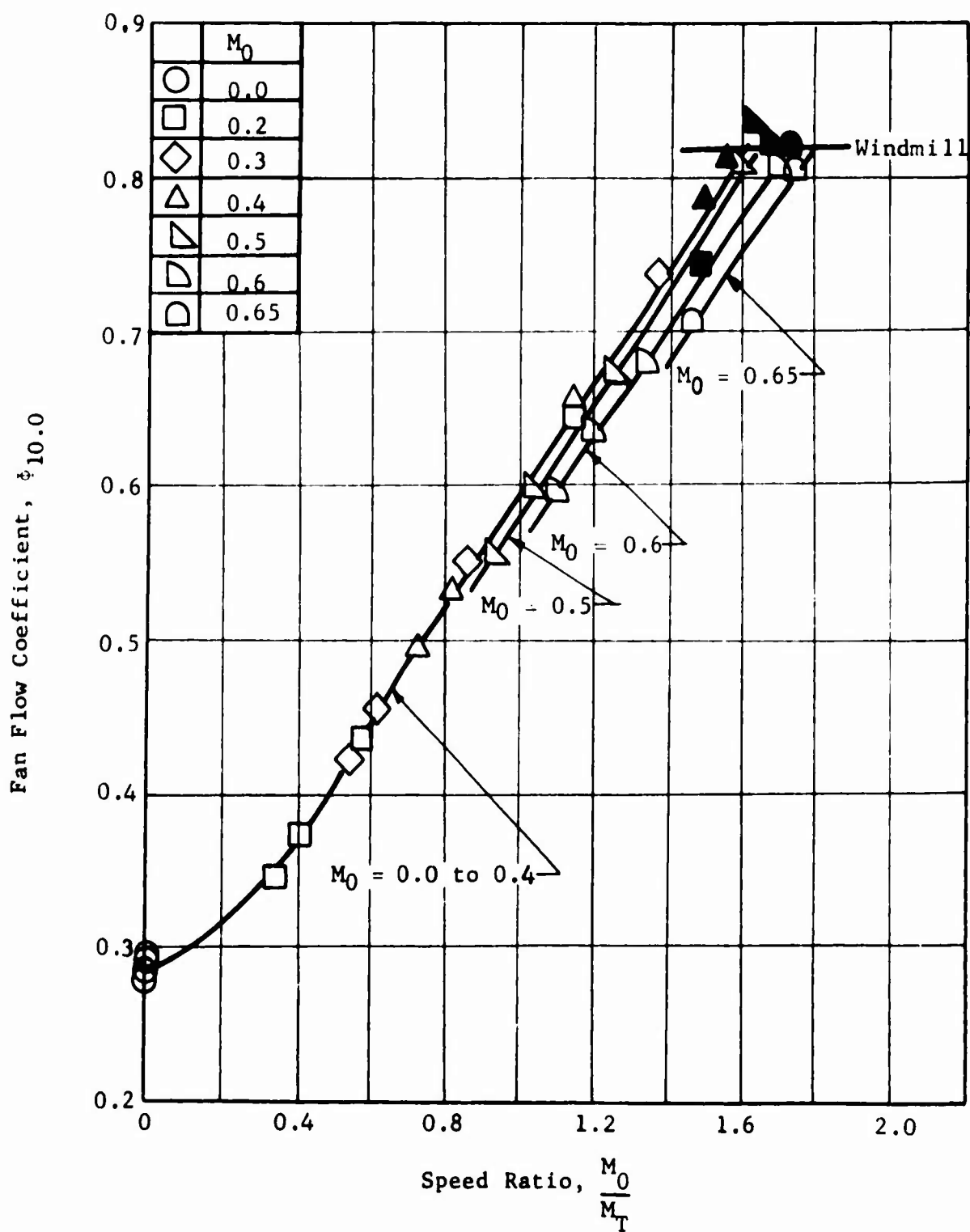


Figure 127. Fan Flow Function Characteristics - Model 7.

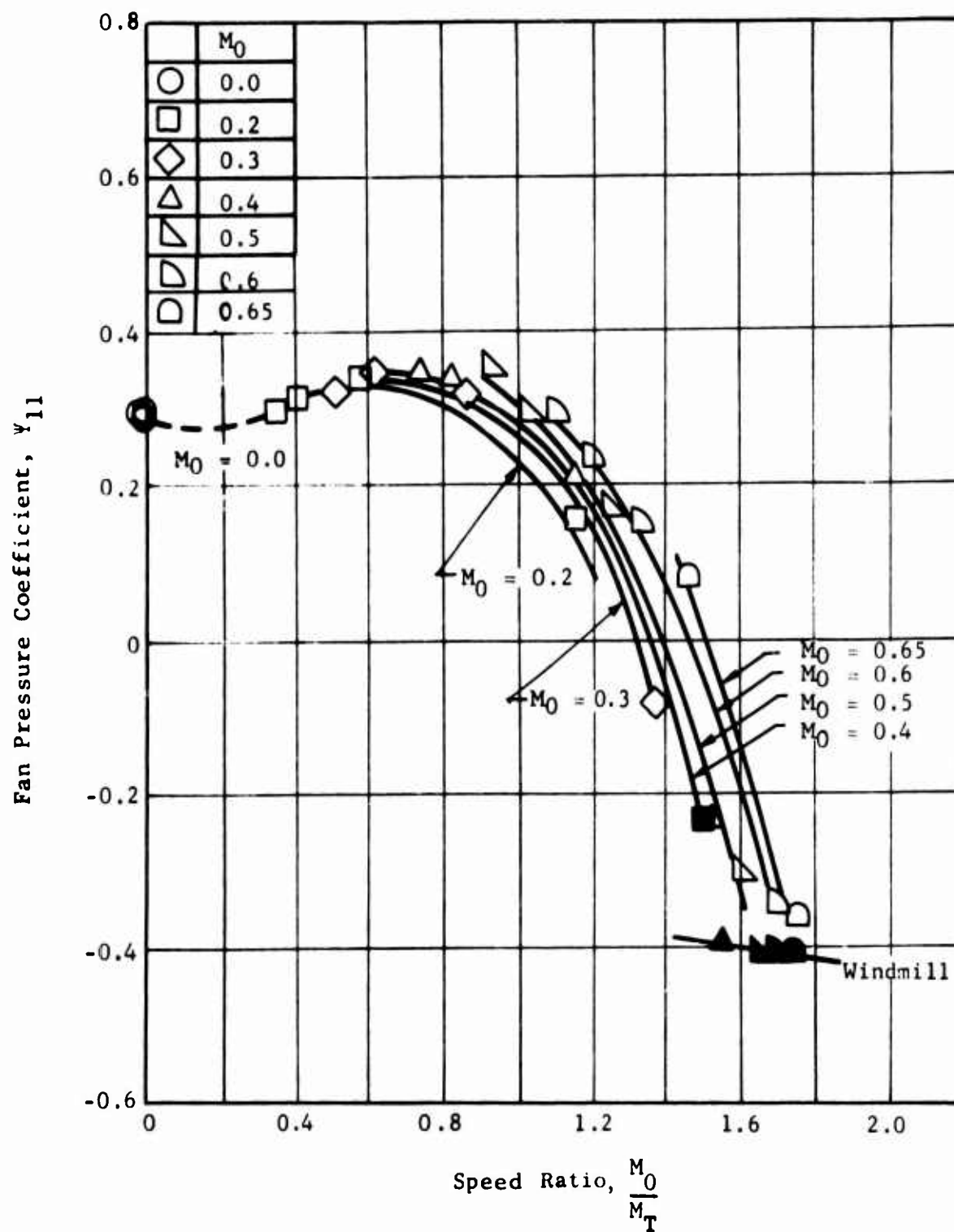


Figure 128. Fan Pressure Coefficient Characteristics - Model 7.

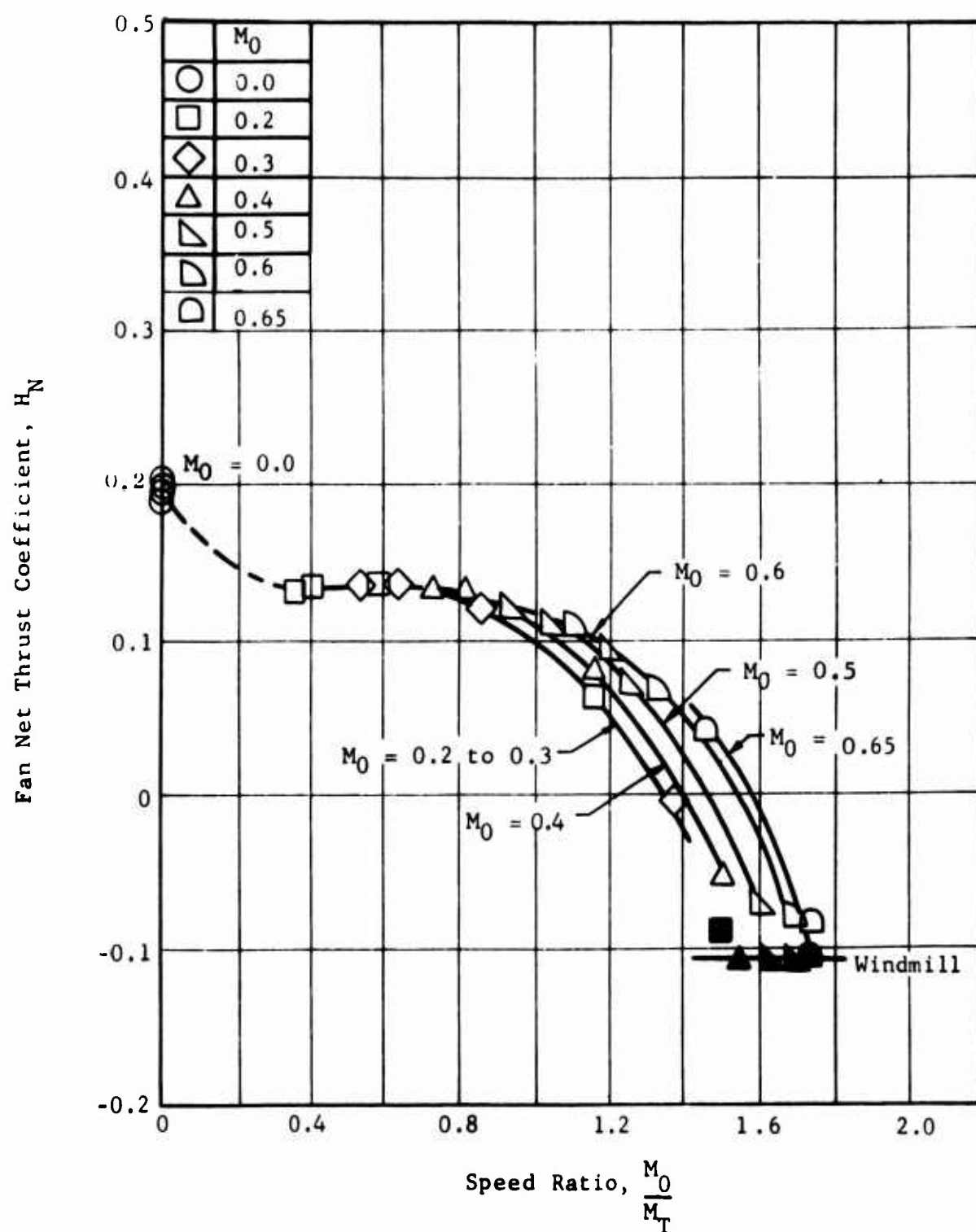


Figure 129. Fan Ideal Net Thrust Coefficient - Model 7.

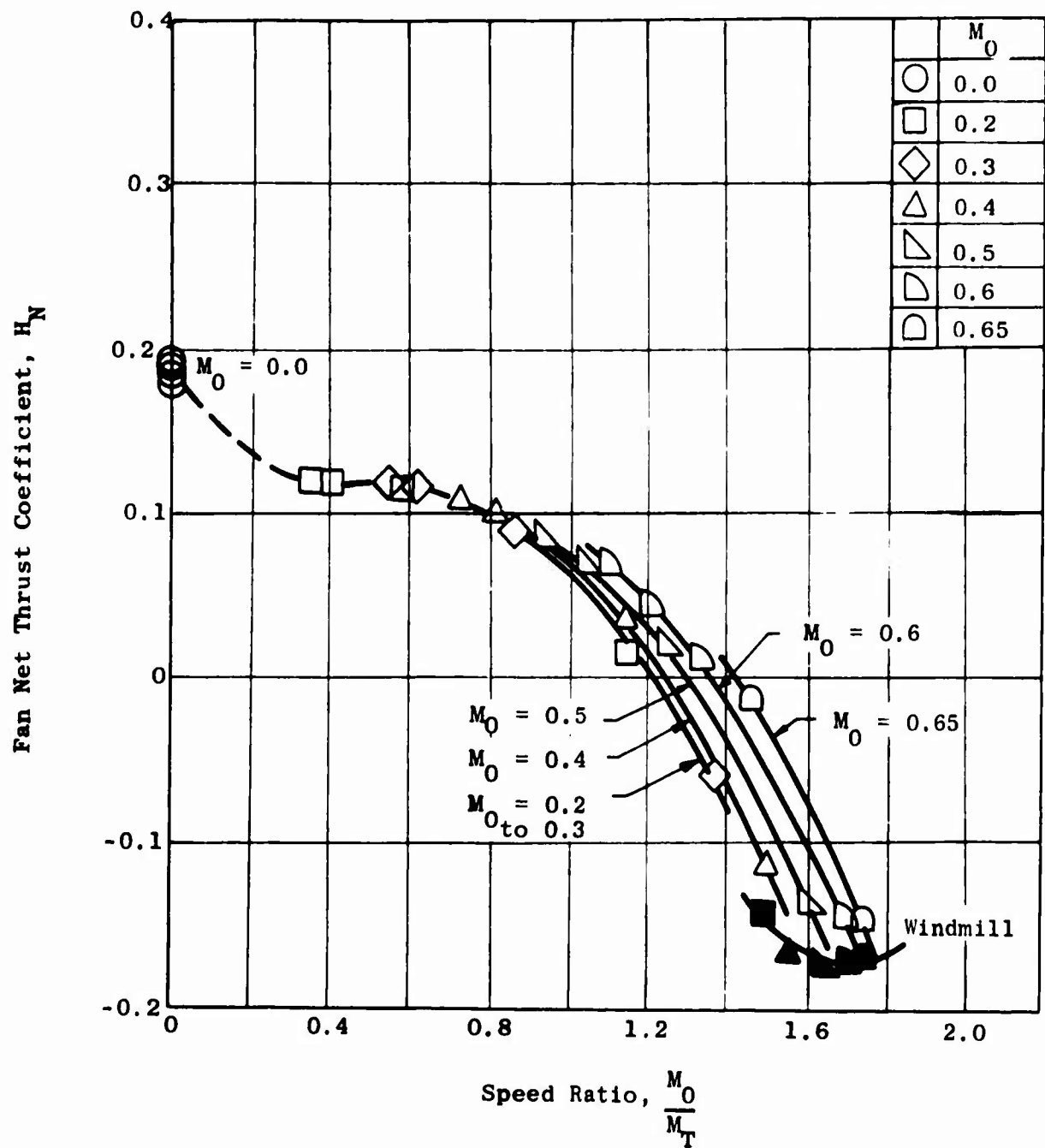


Figure 130. Fan Net Thrust Coefficient with a Nozzle Coefficient of 0.95 - Model 7.

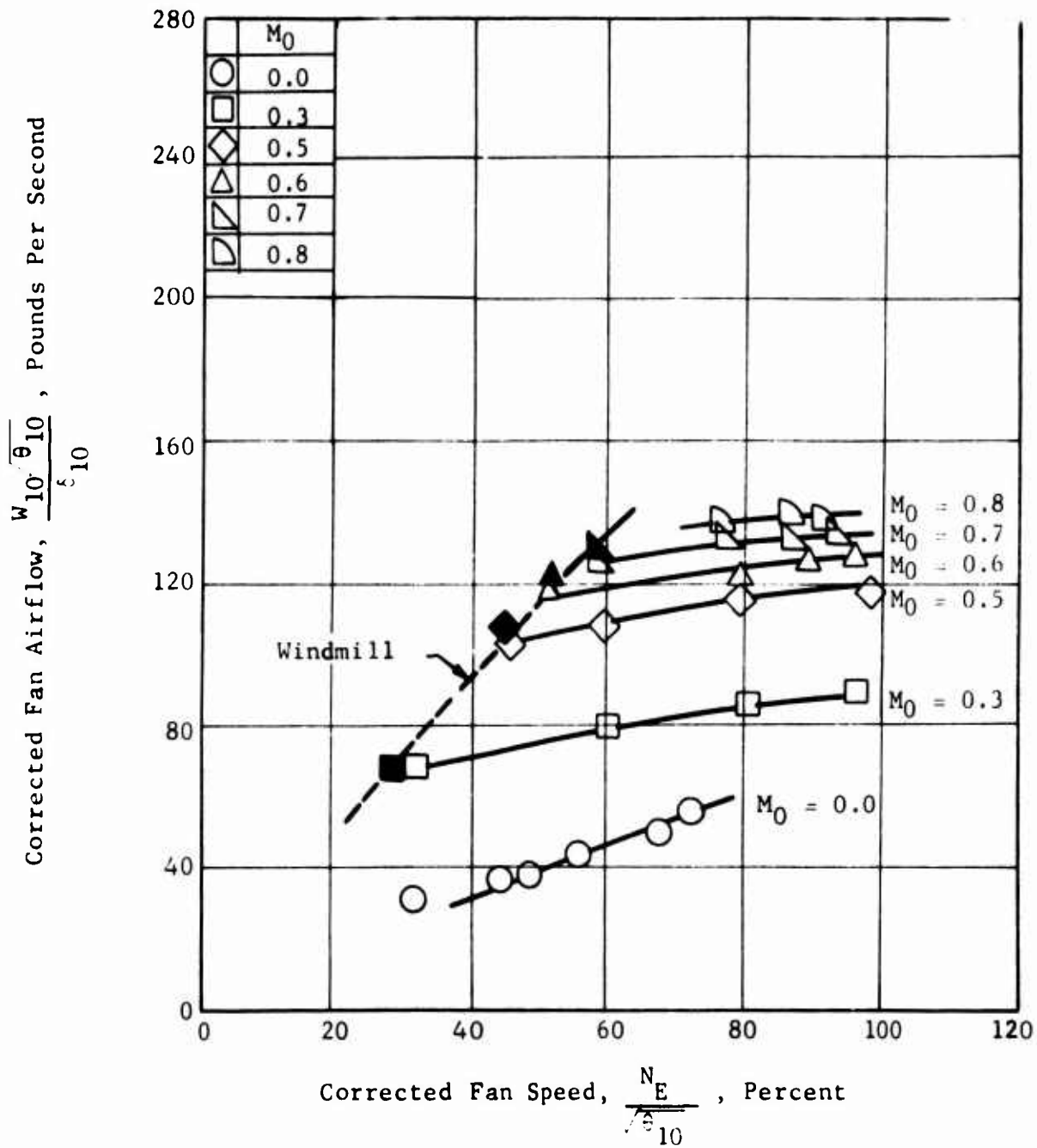


Figure 131. Fan Airflow Characteristics - Model 8.

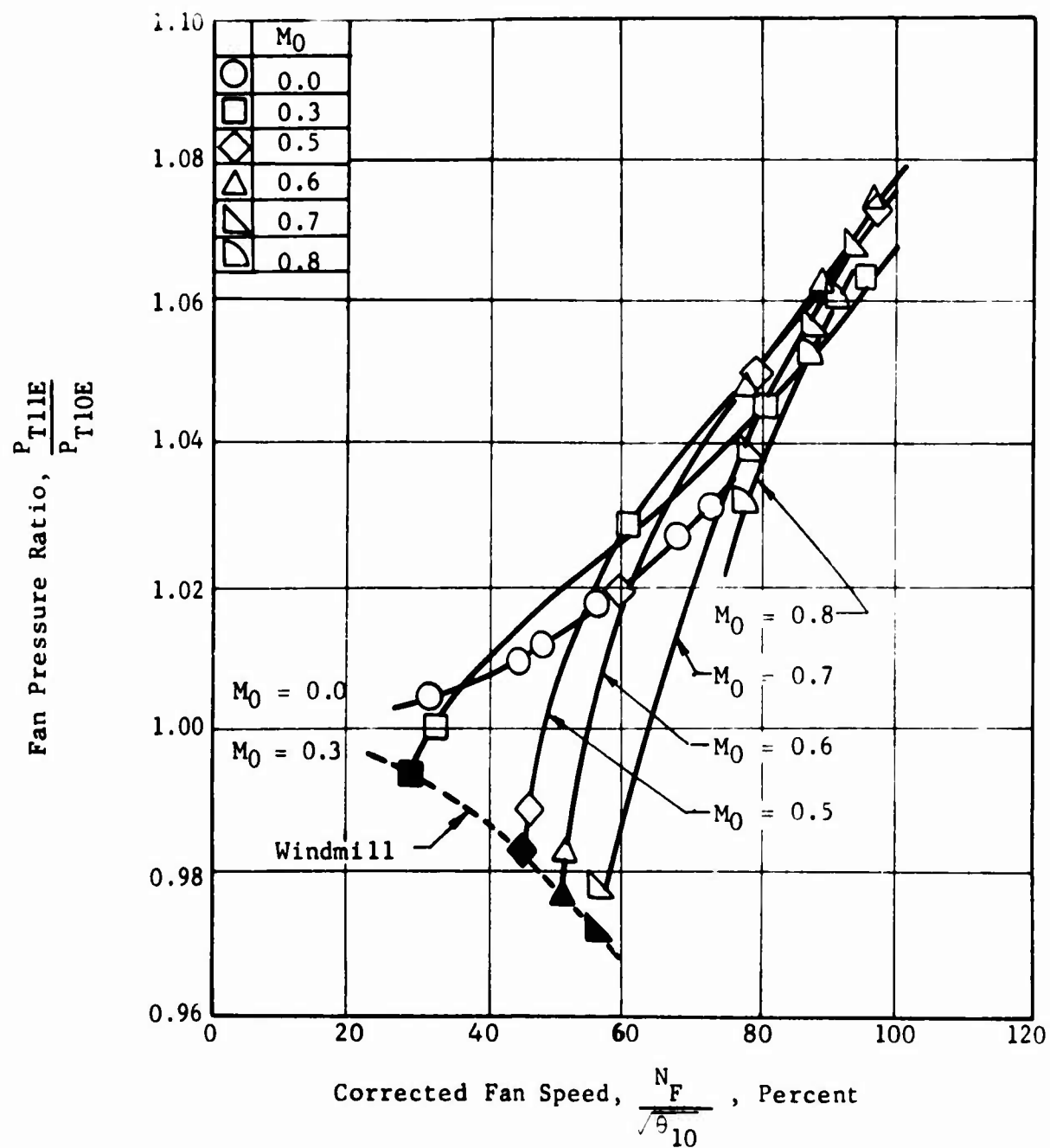


Figure 132. Fan Total Pressure Ratio - Model 8.

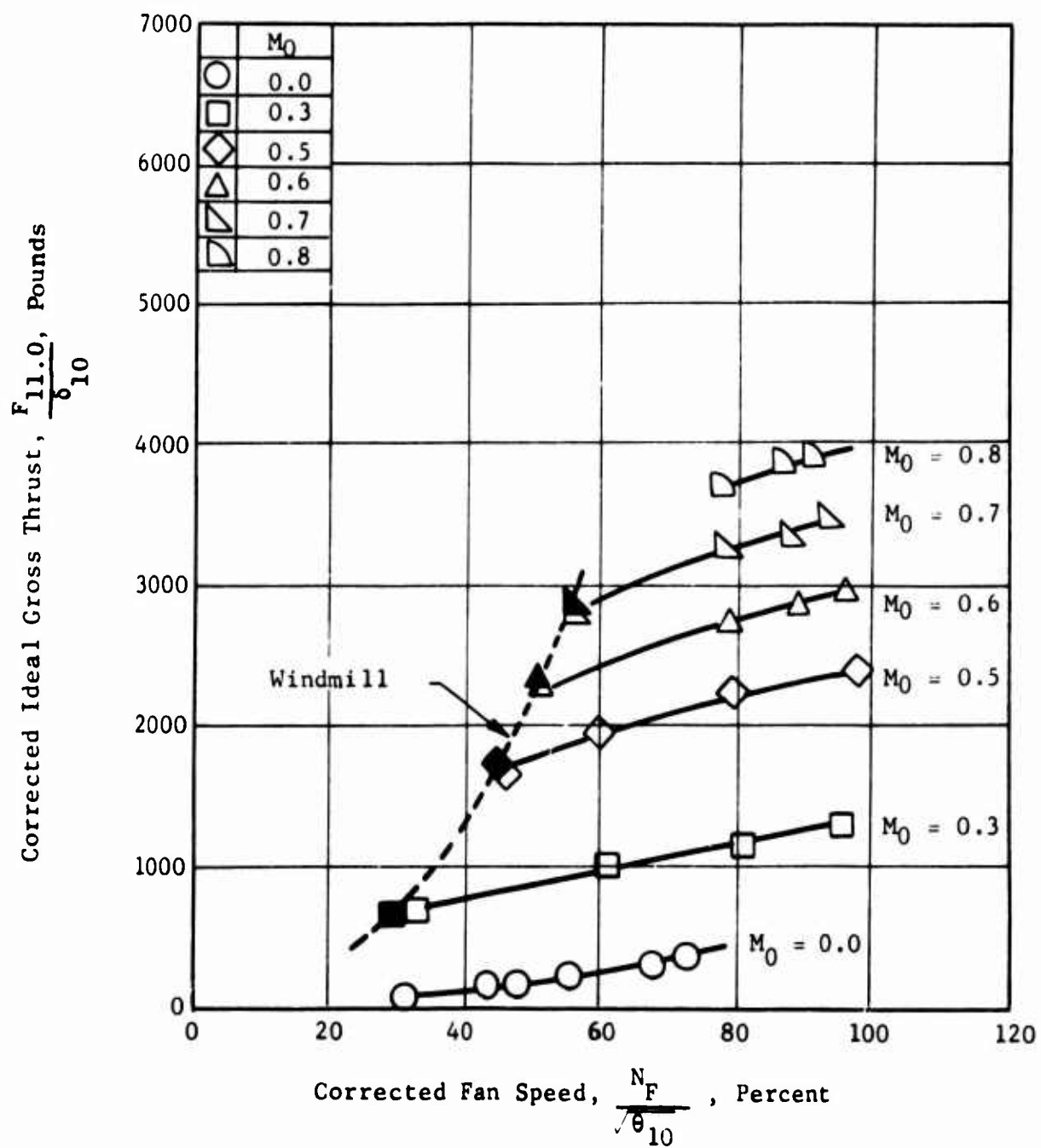


Figure 133. Fan Stream Ideal Gross Thrust - Model 8.

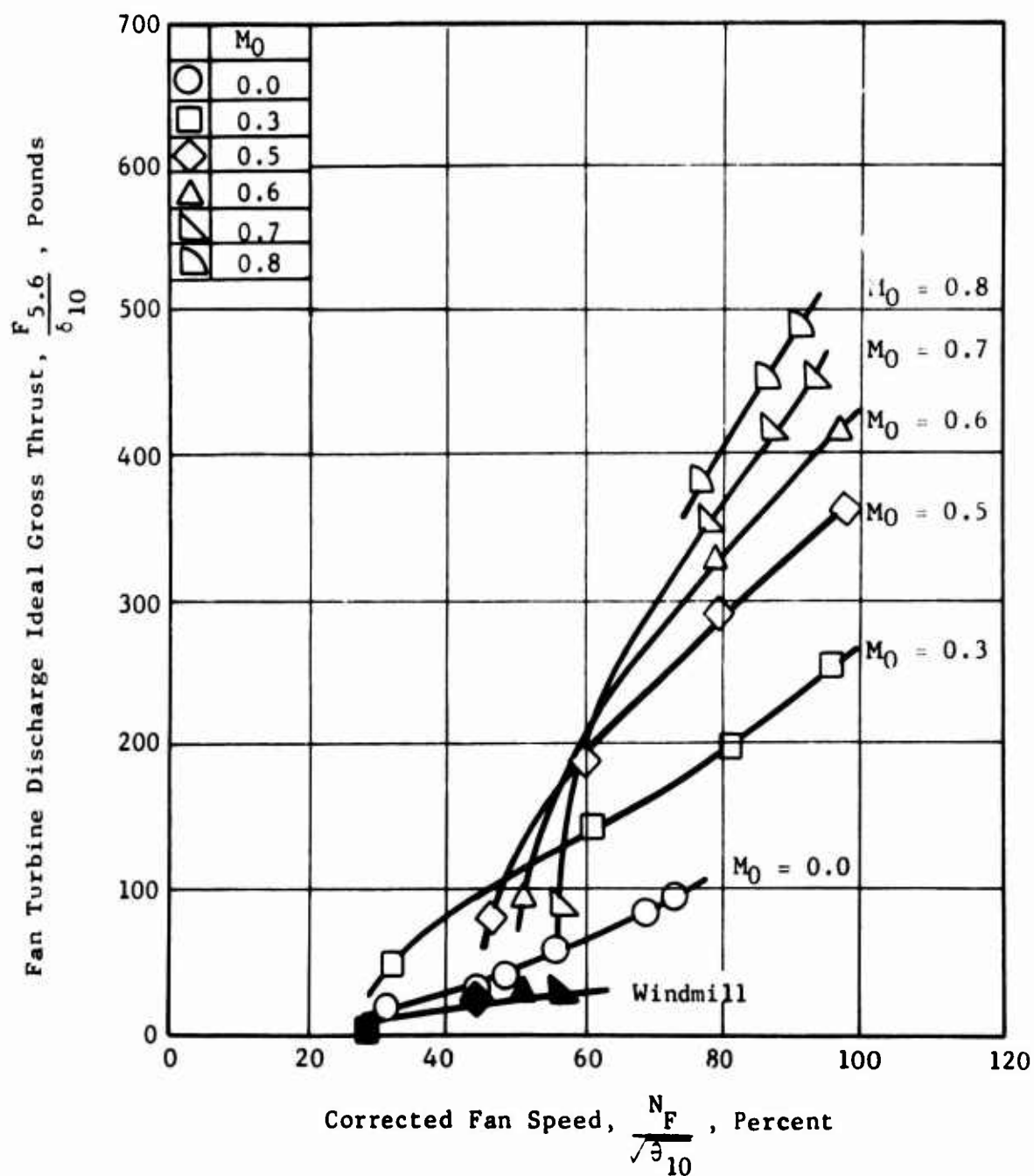


Figure 134. Fan Turbine Residual Ideal Gross Thrust - Model 8.

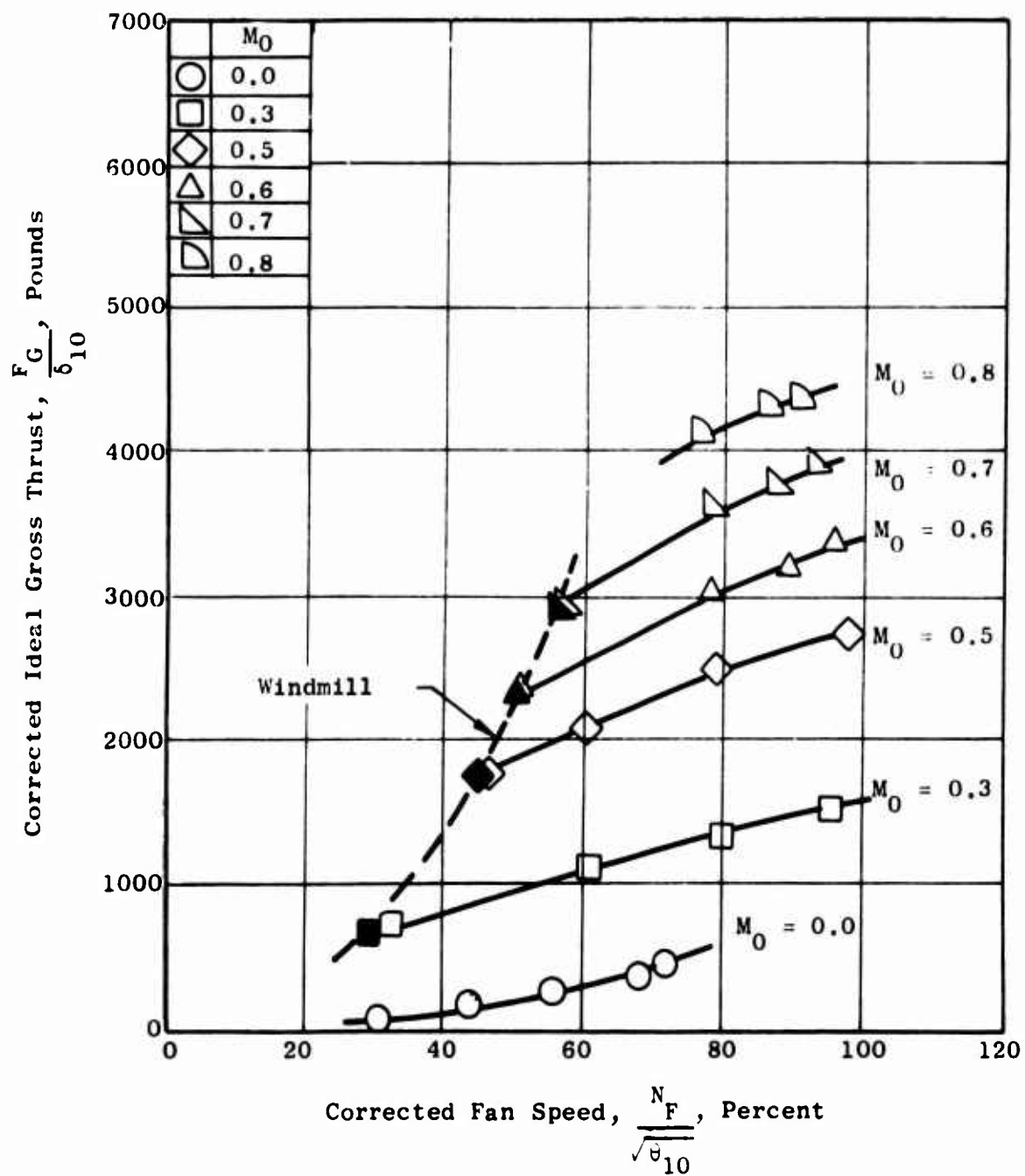


Figure 135. Fan System Ideal Gross Thrust - Model 8.

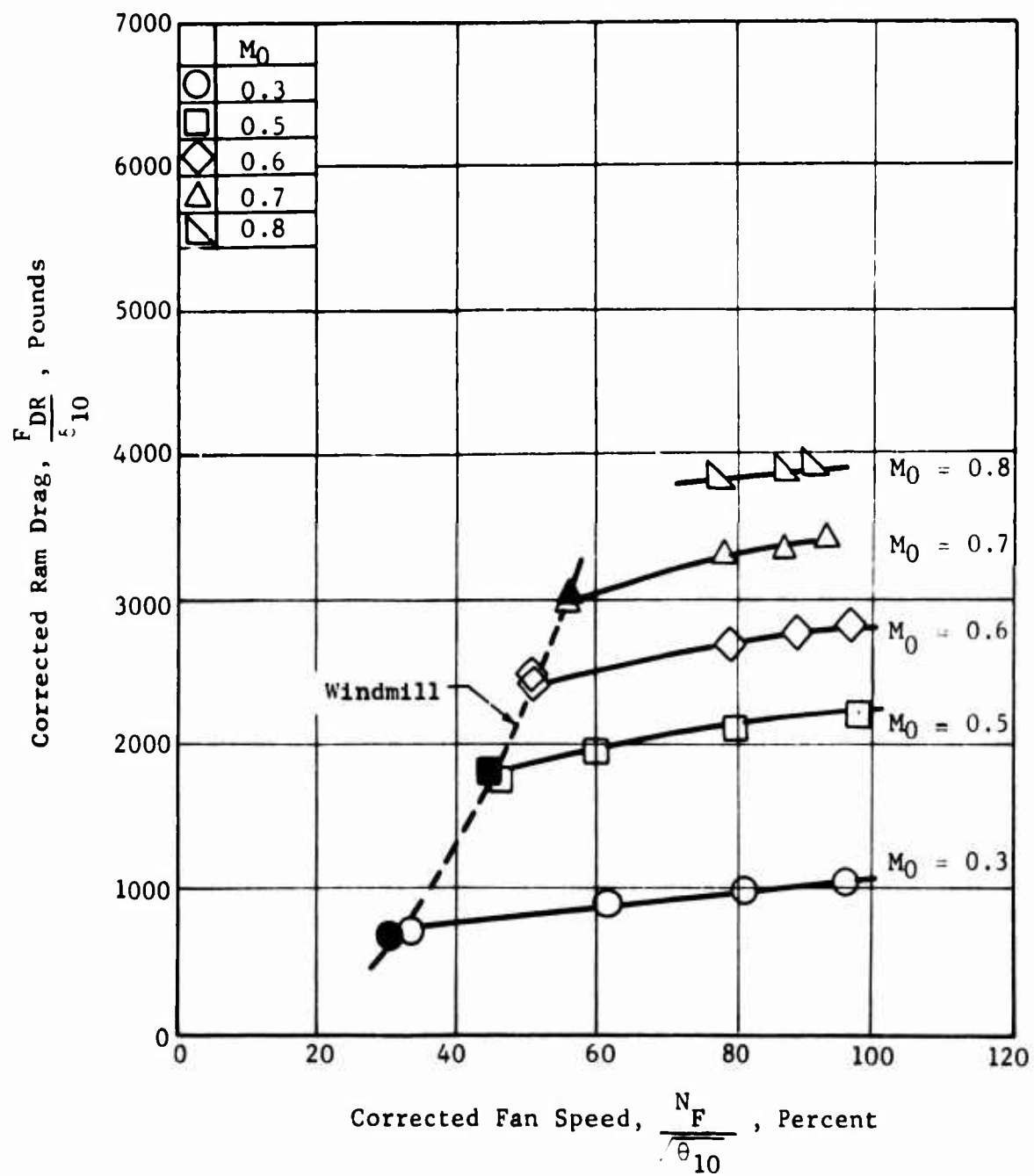


Figure 136. Total Ram Drag - Model 8.

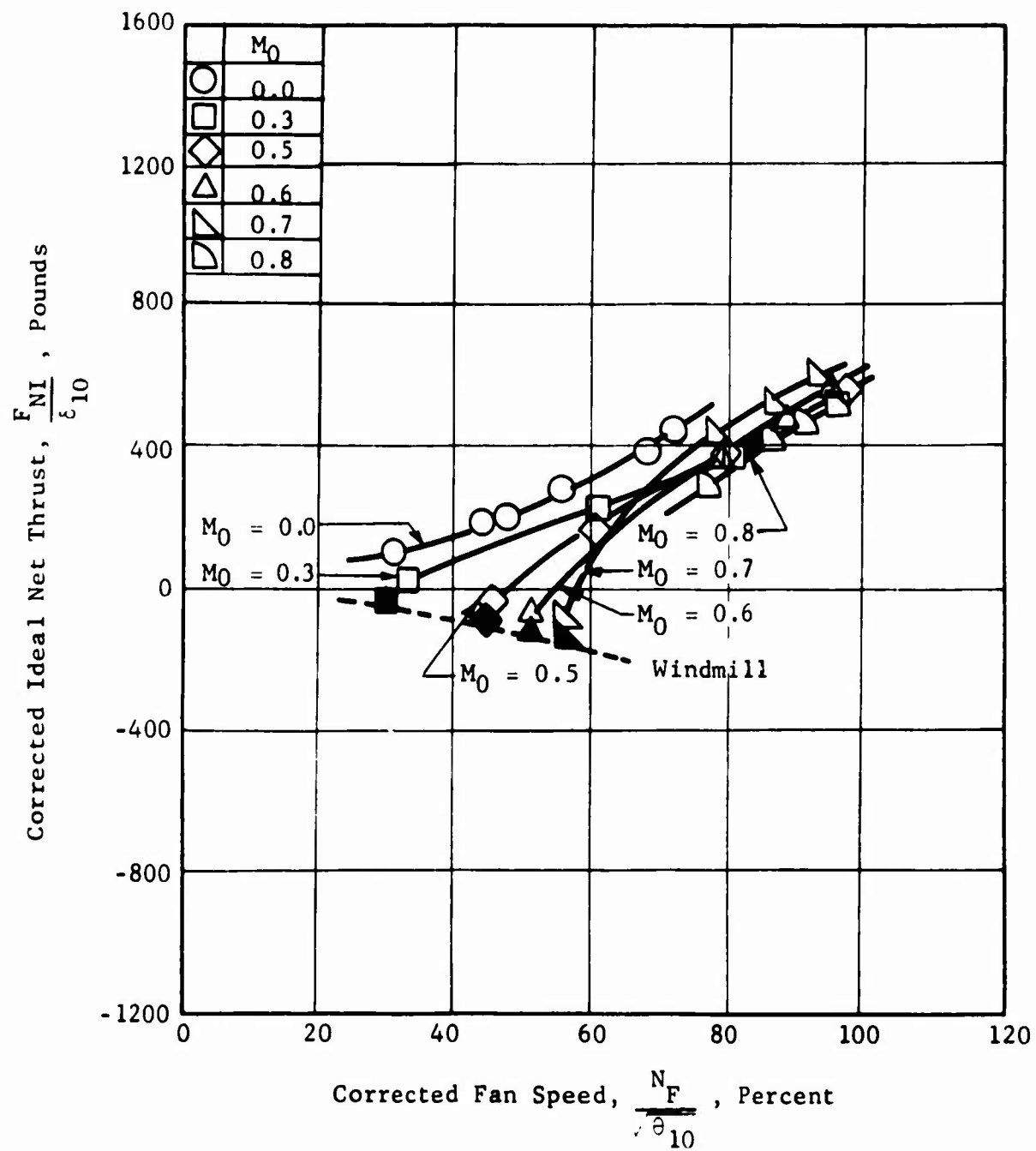


Figure 137. Fan System Ideal Net Thrust - Model 8.

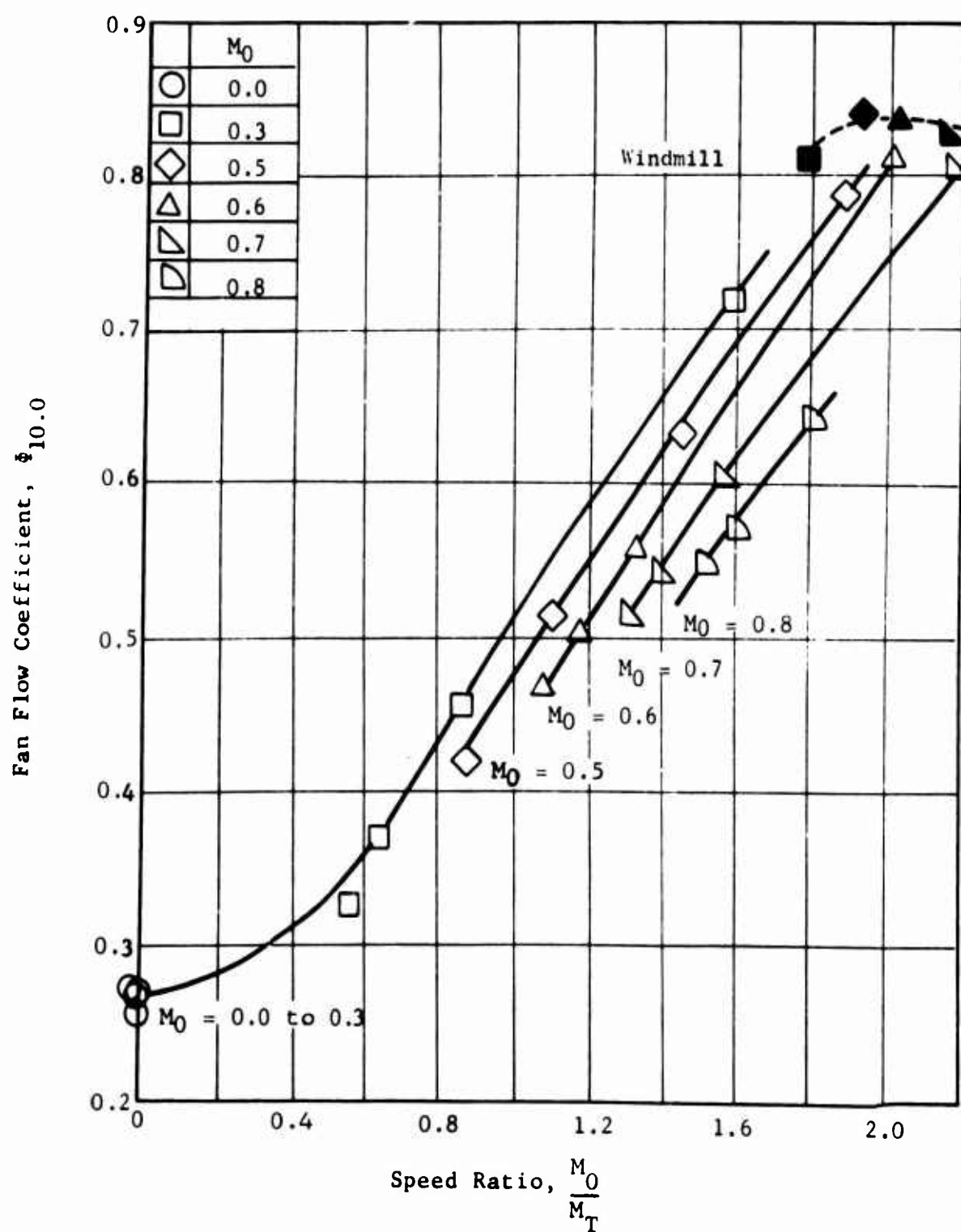


Figure 138. Fan Flow Function Characteristics - Model 8.

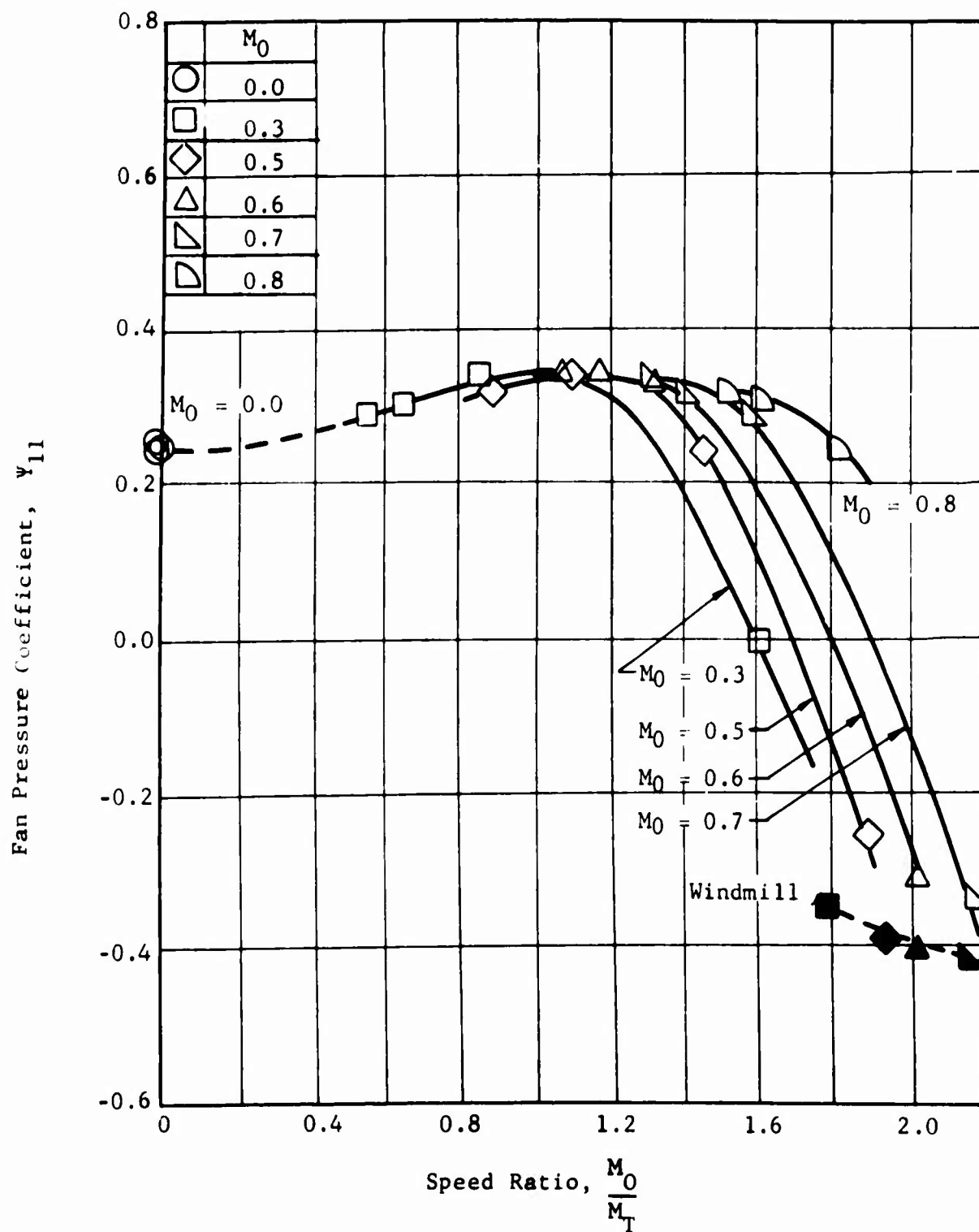


Figure 139. Fan Pressure Coefficient Characteristics - Model 8.

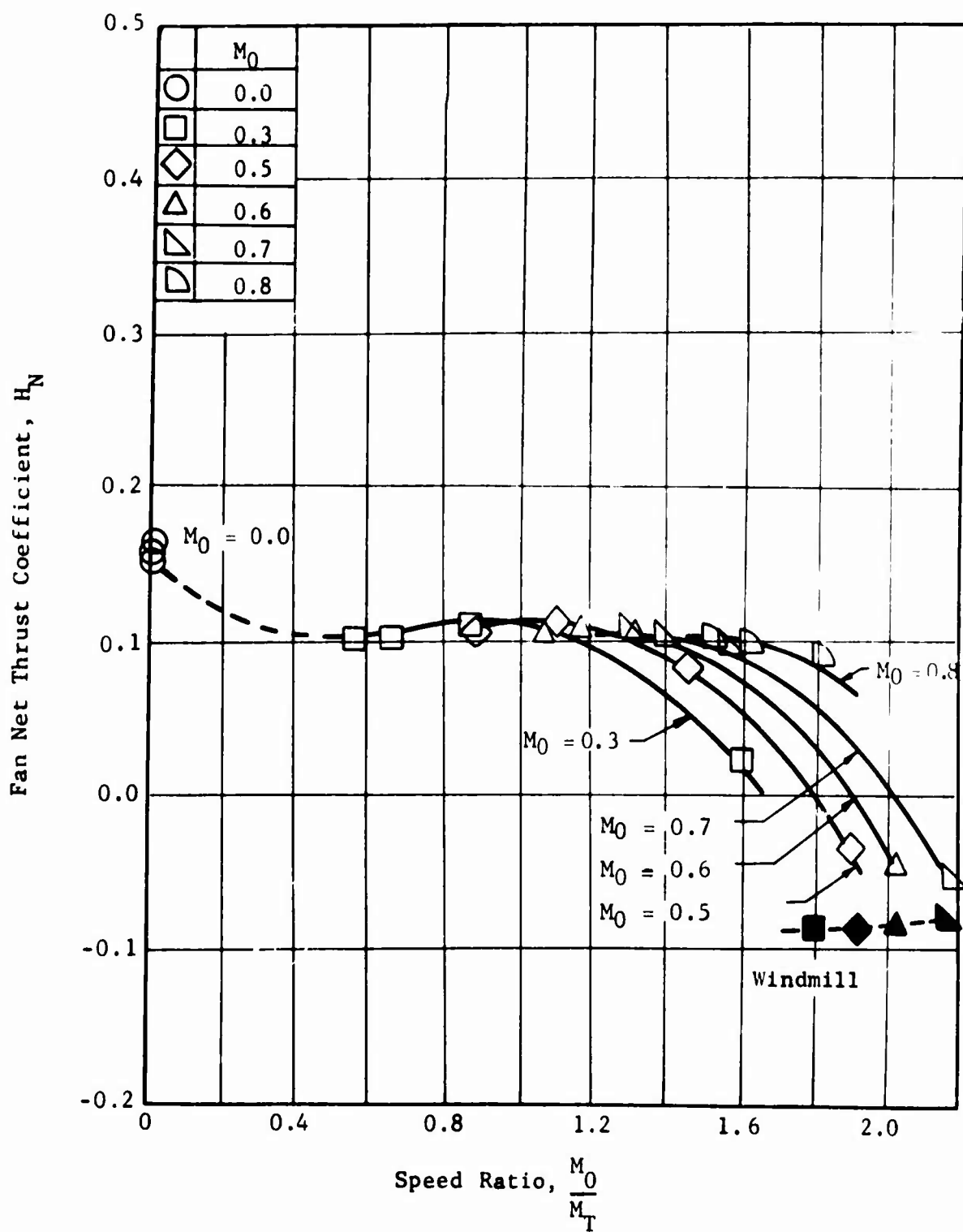


Figure 140. Fan Ideal Net Thrust Coefficient - Model 8.

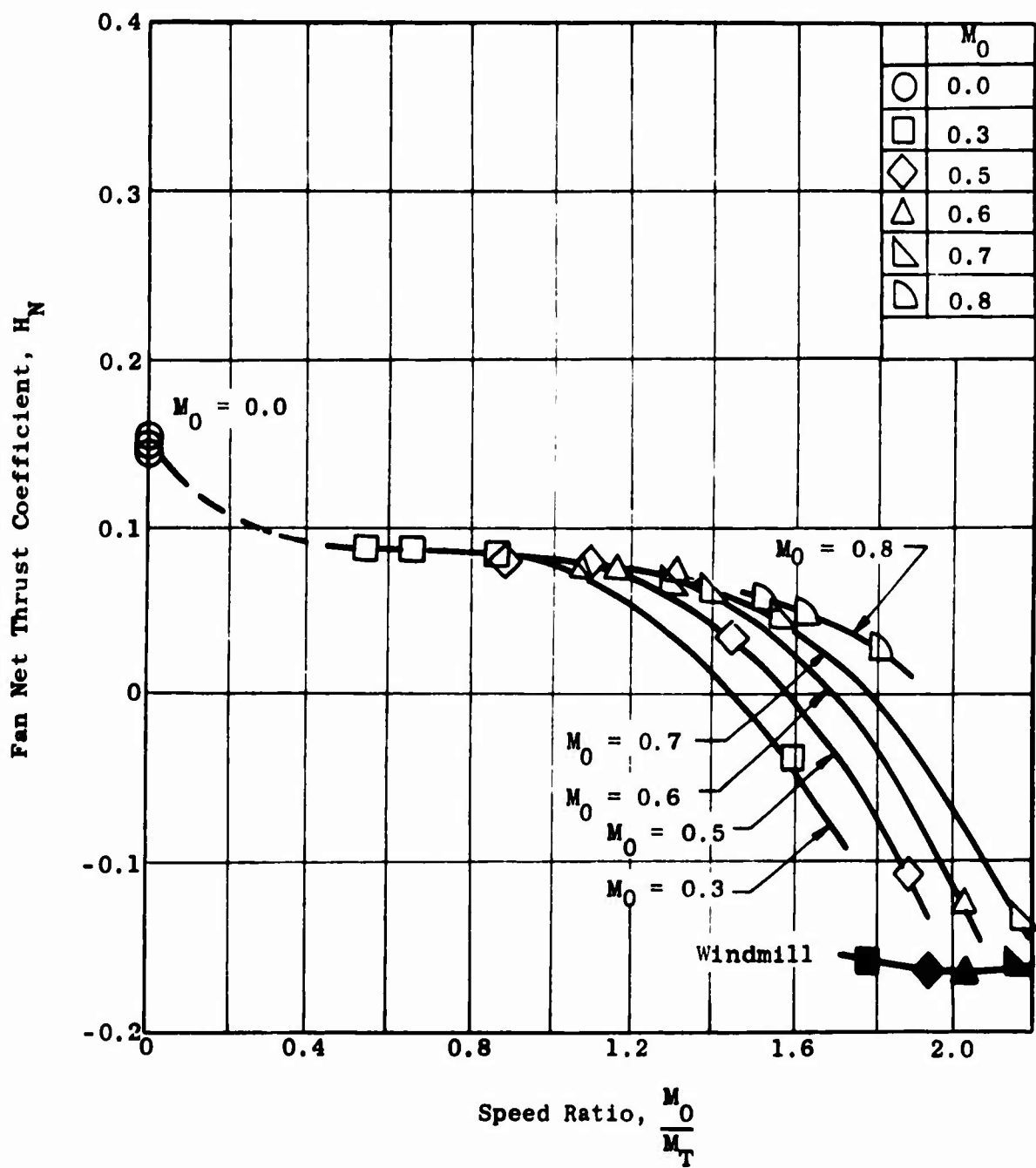


Figure 141. Fan Net Thrust Coefficient with a Nozzle Coefficient of 0.95 - Model 8.

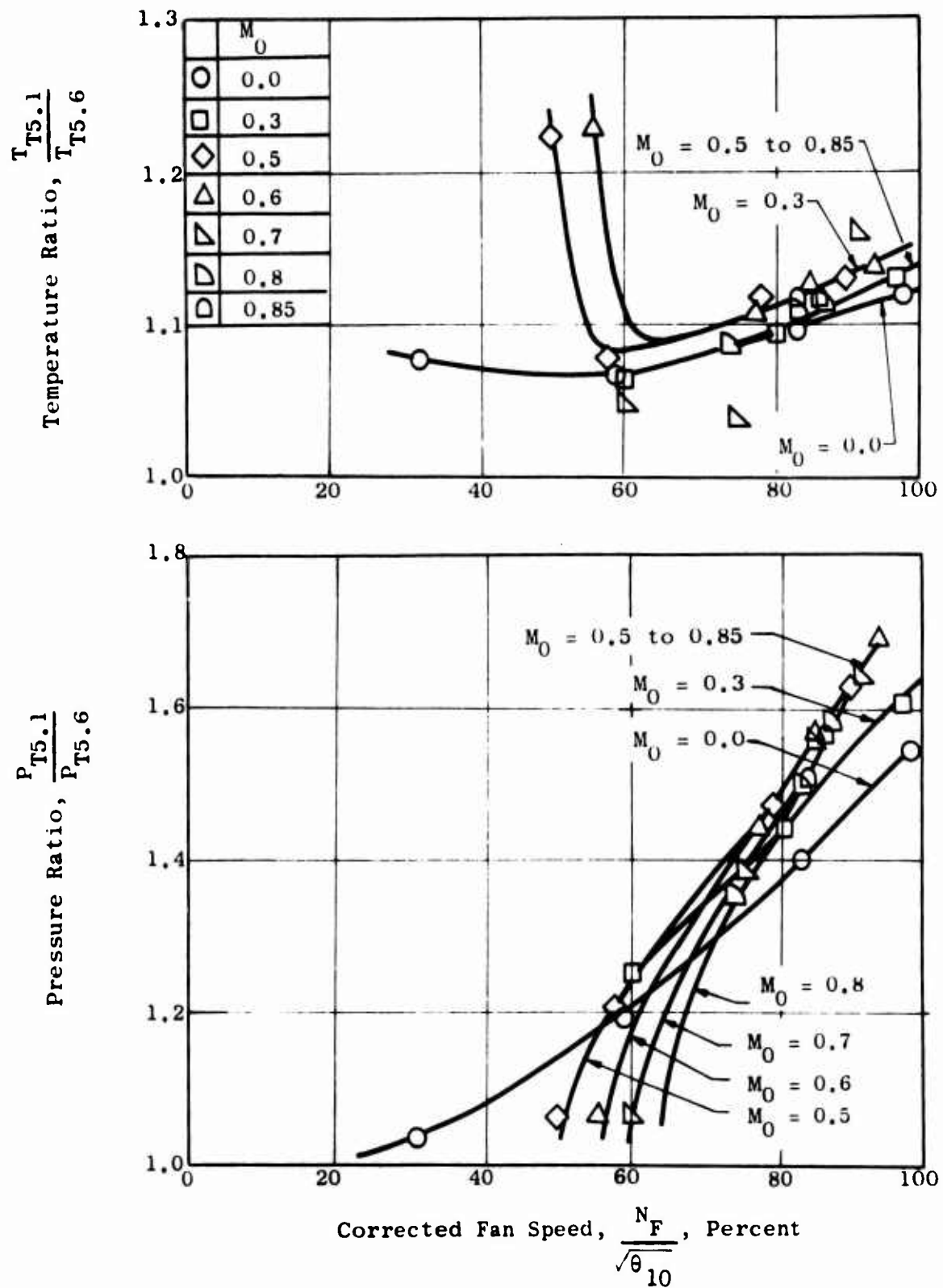


Figure 142. Fan Turbine Pressure and Temperature Ratios - Model 1.

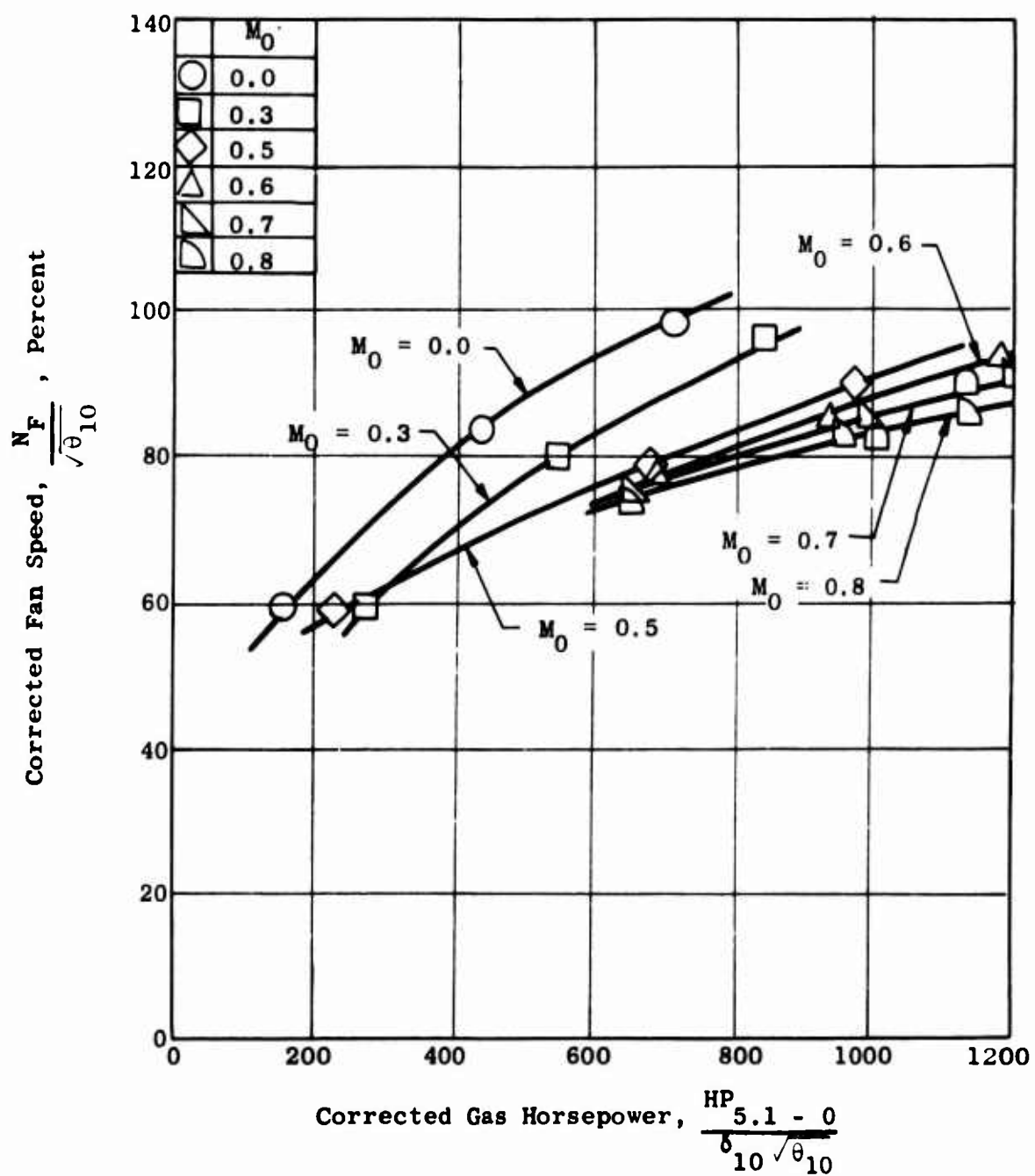


Figure 143. Fan Speed - Horsepower Characteristics - Model 1.

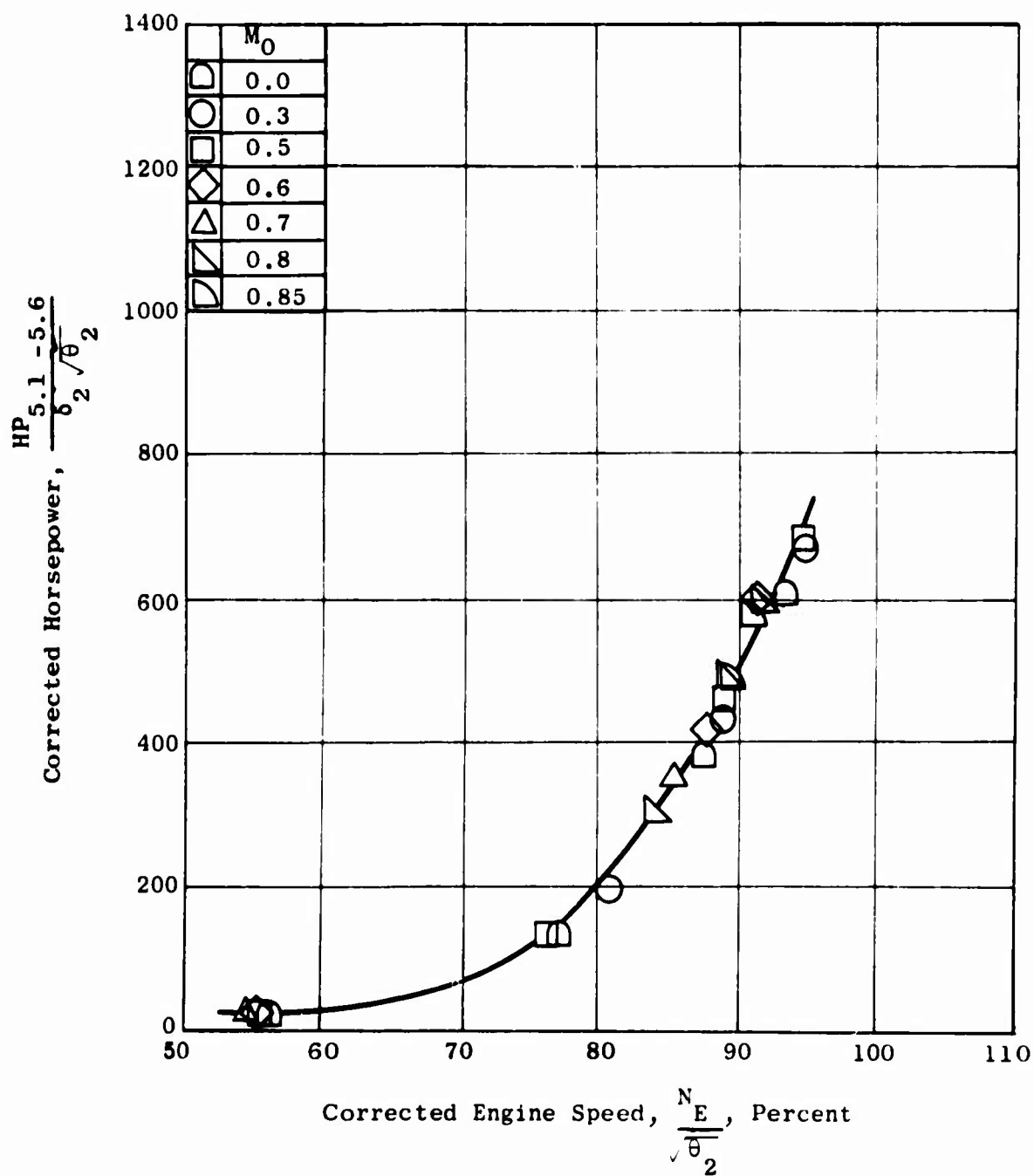


Figure 144. Engine Horsepower Absorbed by Fan Turbine - Model 1.

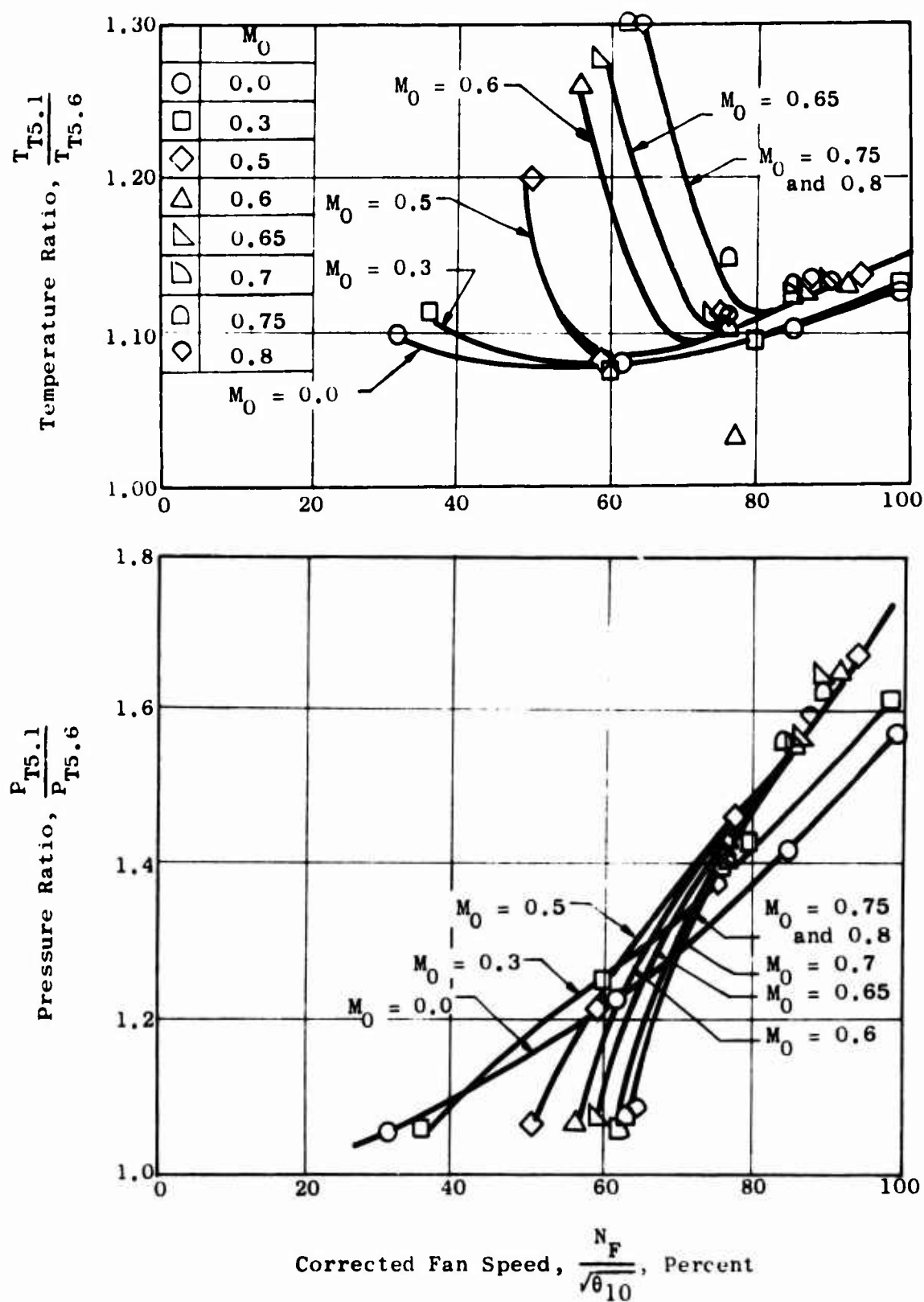


Figure 145. Fan Turbine Pressure and Temperature Ratios - Model 2.

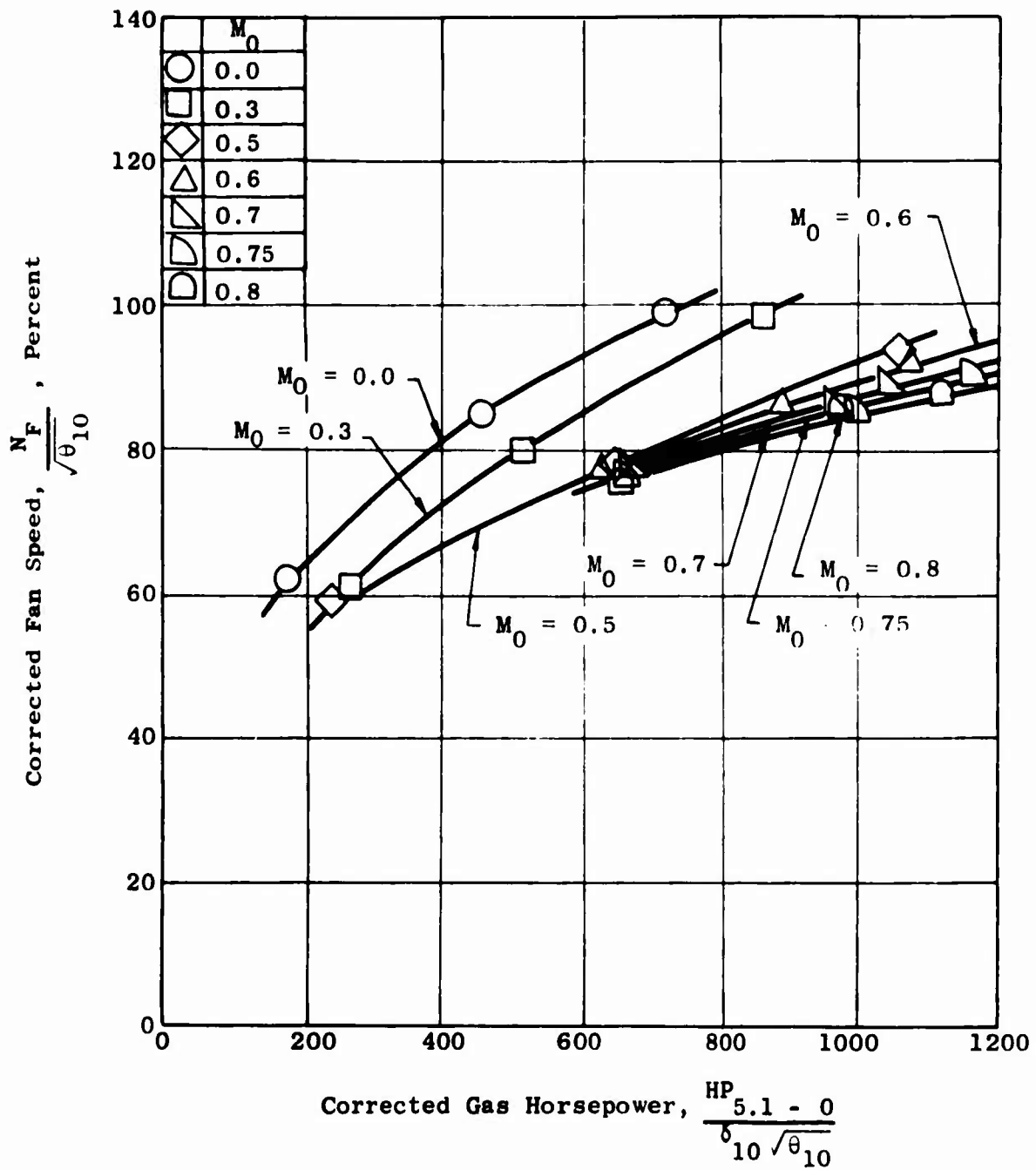


Figure 146. Fan Speed - Horsepower Characteristics - Model 2.

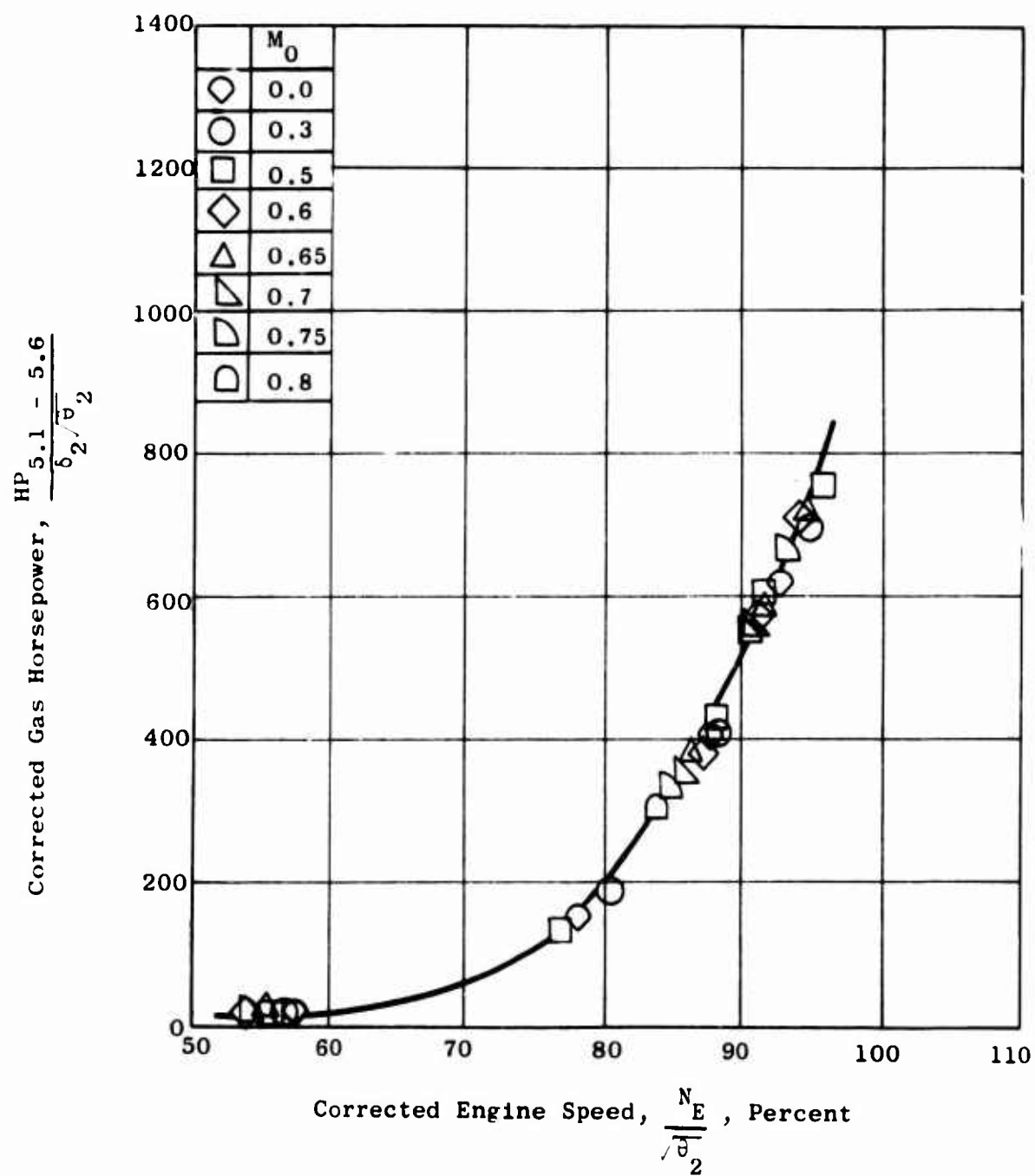


Figure 147. Engine Horsepower Absorbed by Fan Turbine - Model 2.

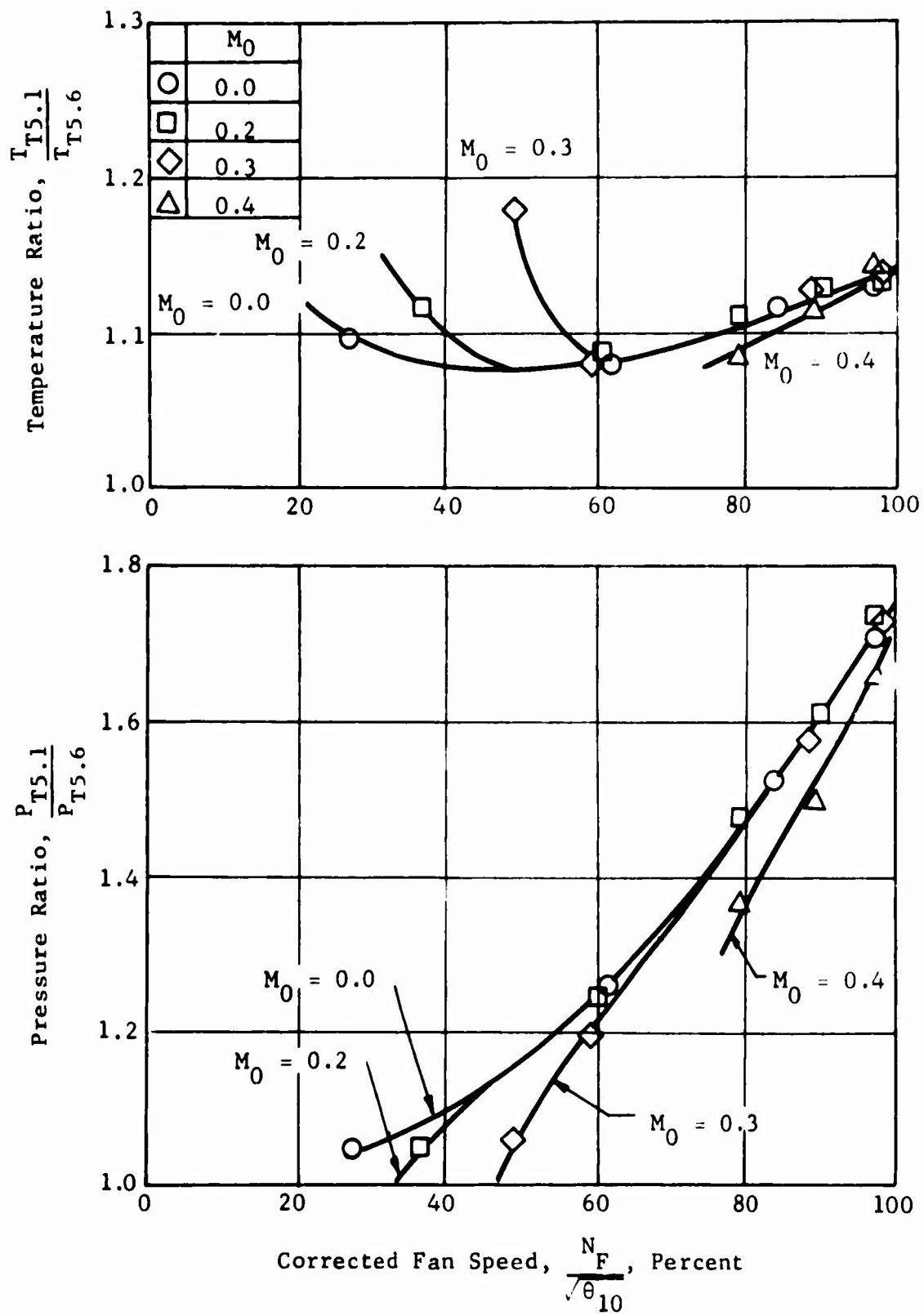


Figure 148. Fan Turbine Pressure and Temperature Ratios - Model 3.

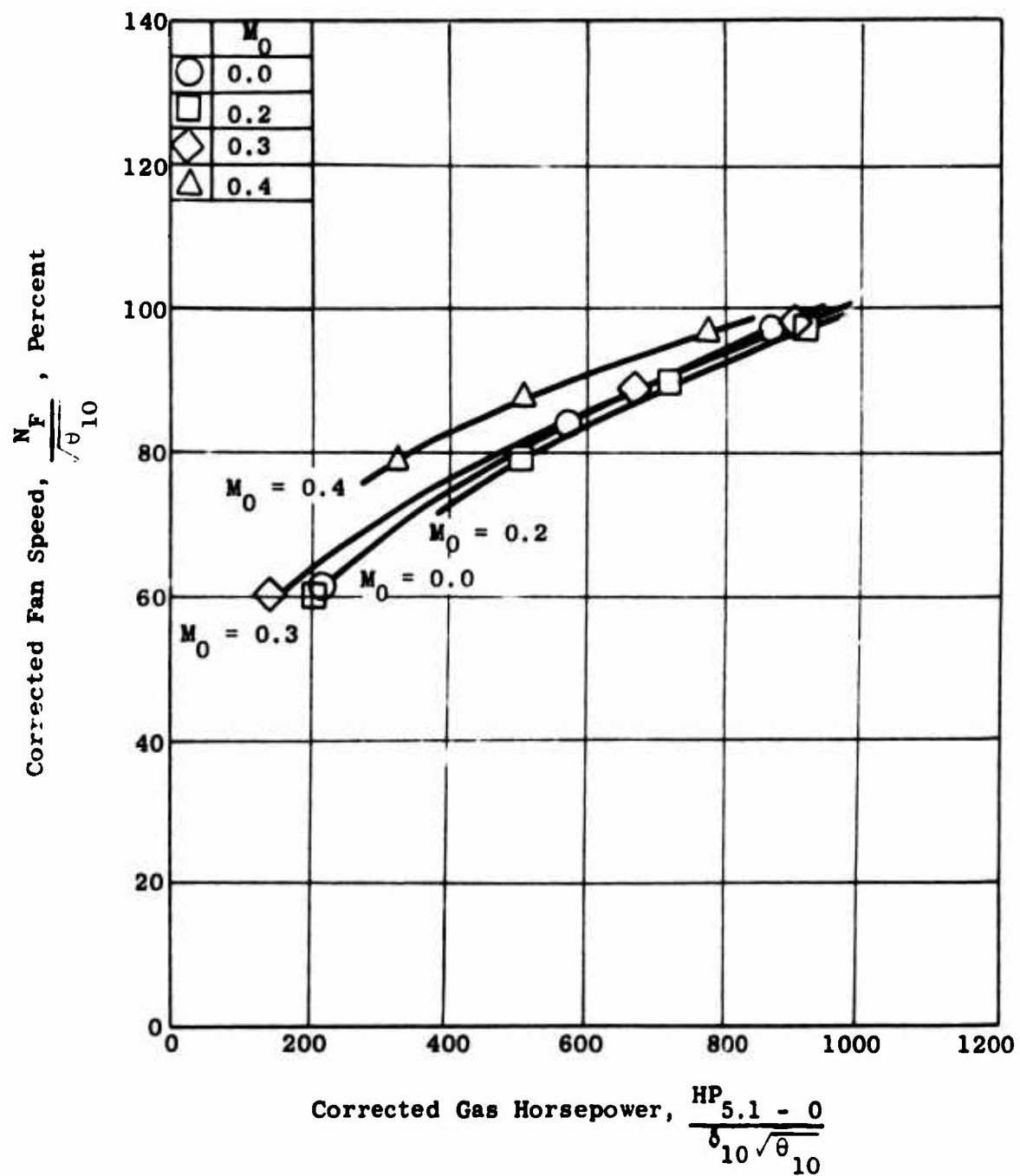


Figure 149. Fan Speed - Horsepower Characteristics - Model 3.

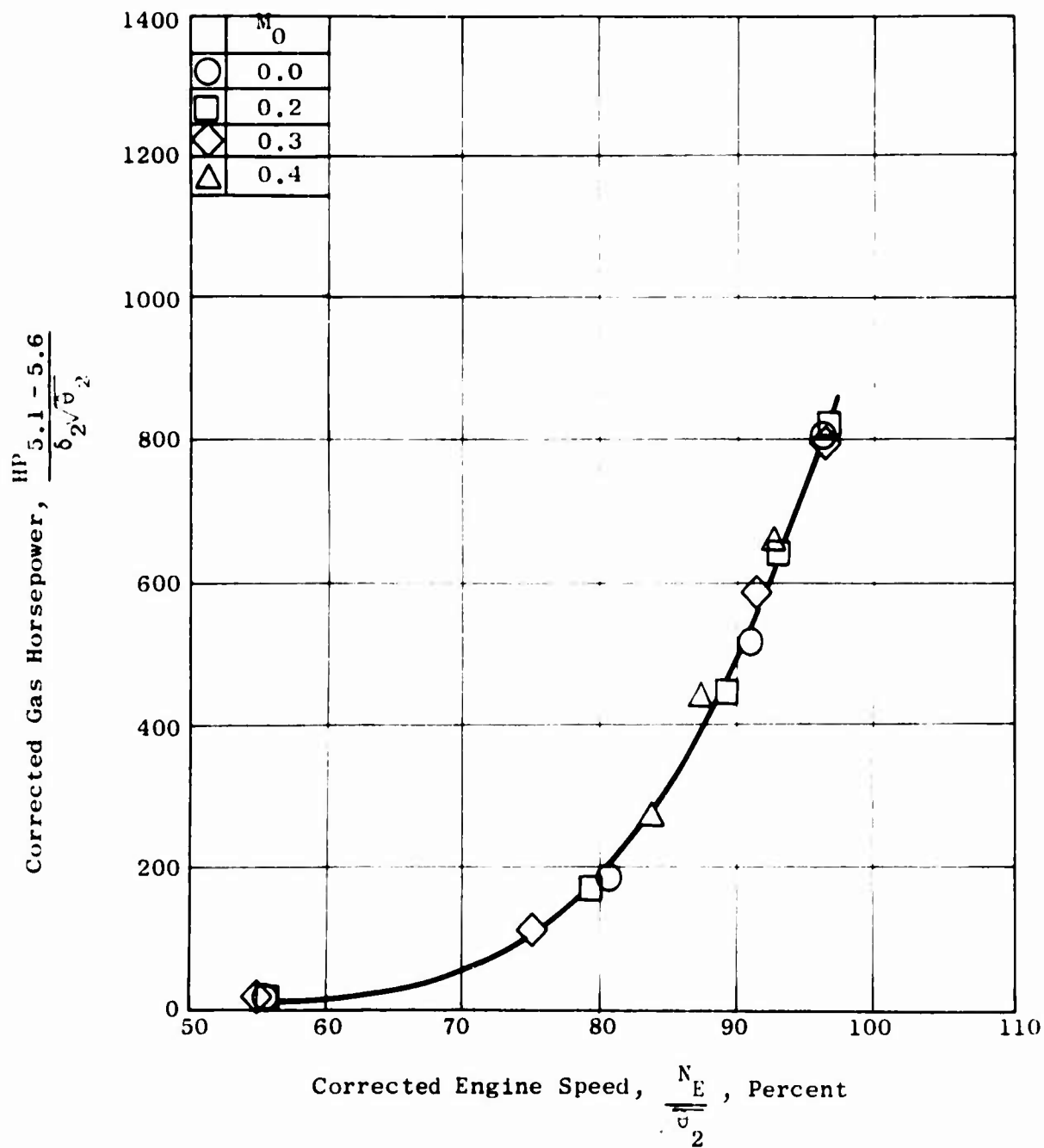


Figure 150. Engine Horsepower Absorbed by Fan Turbine - Model 3.

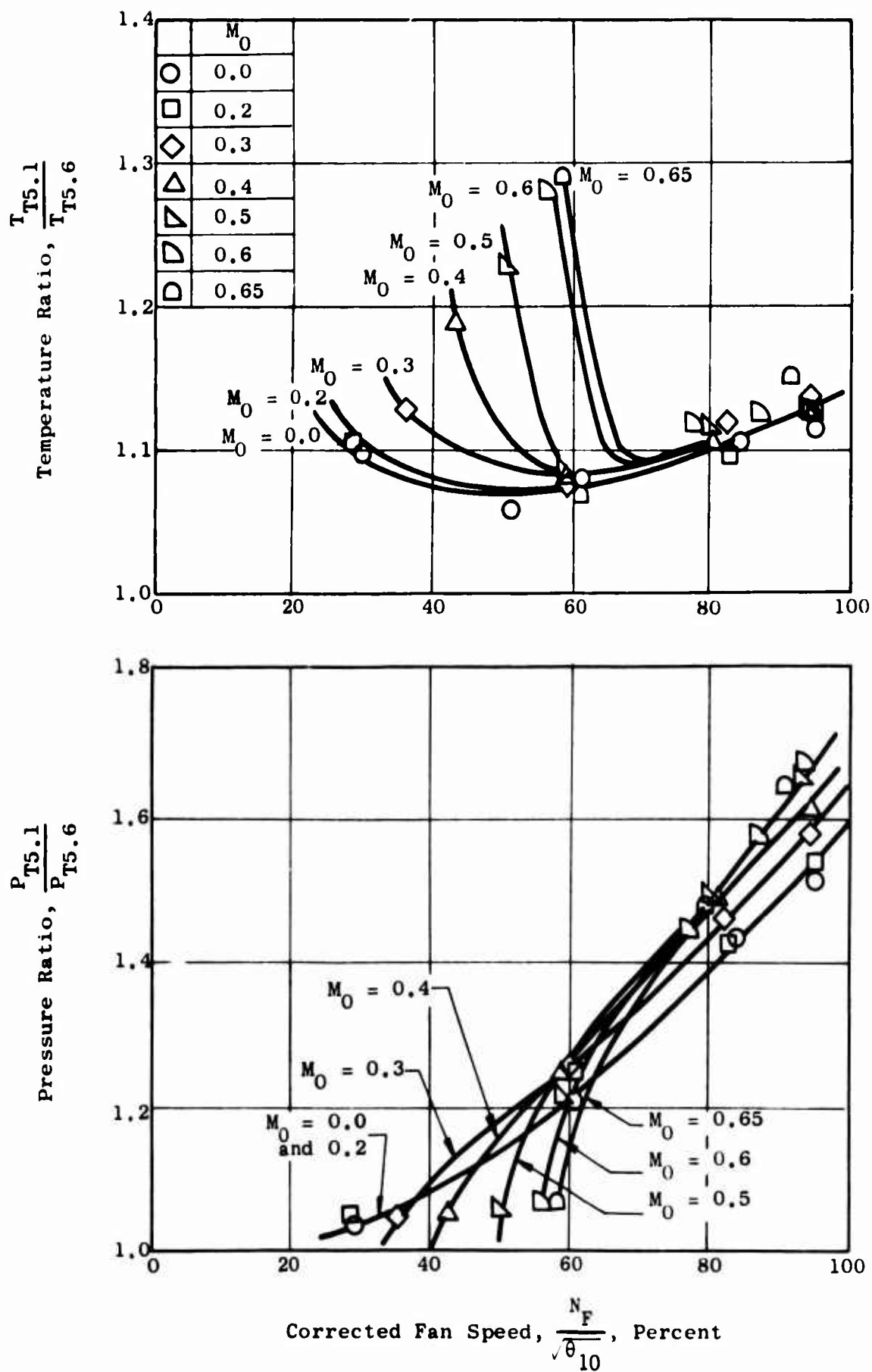


Figure 151. Fan Turbine Pressure and Temperature Ratios - Model 4.

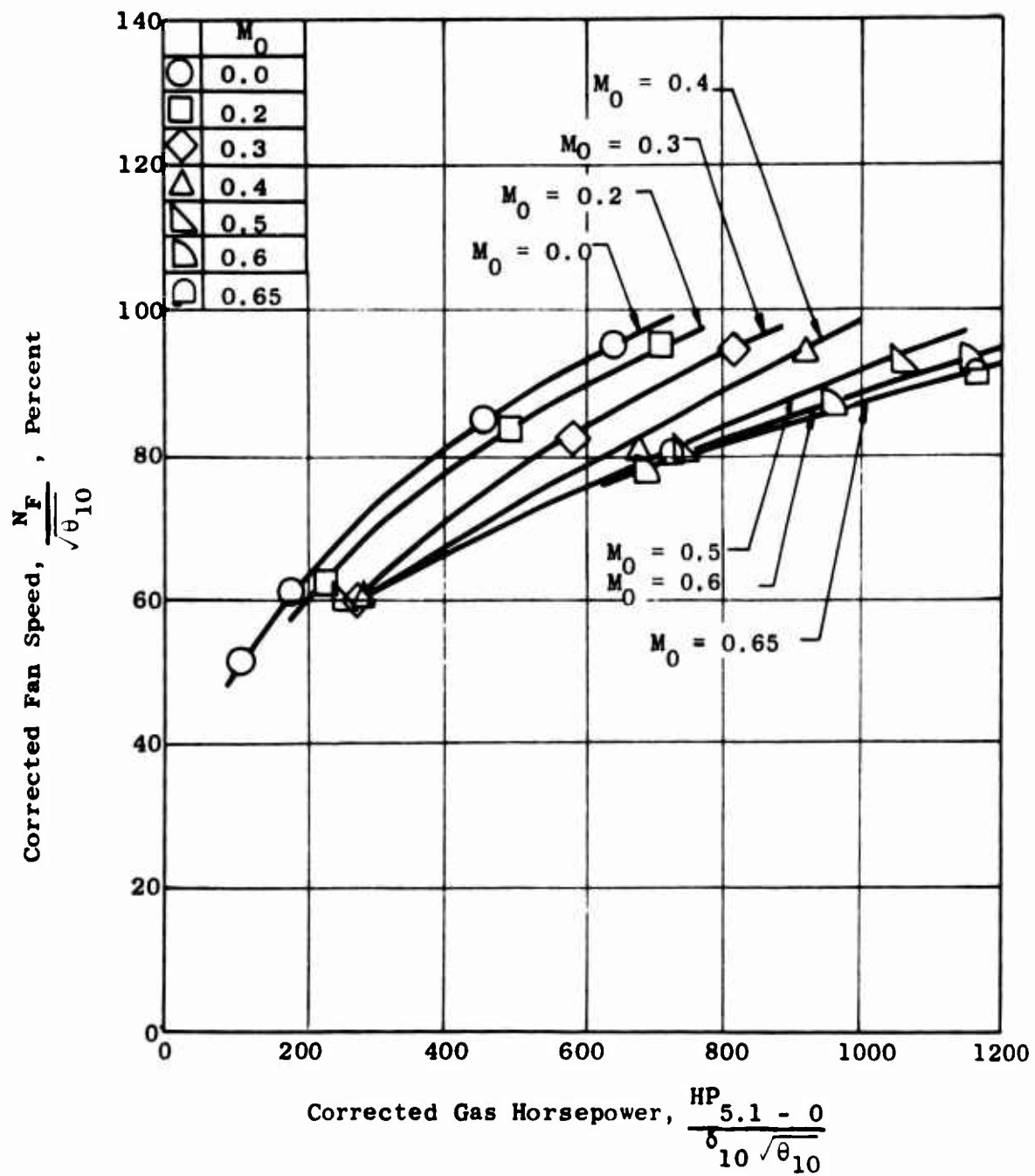


Figure 152. Fan Speed - Horsepower Characteristics - Model 4.

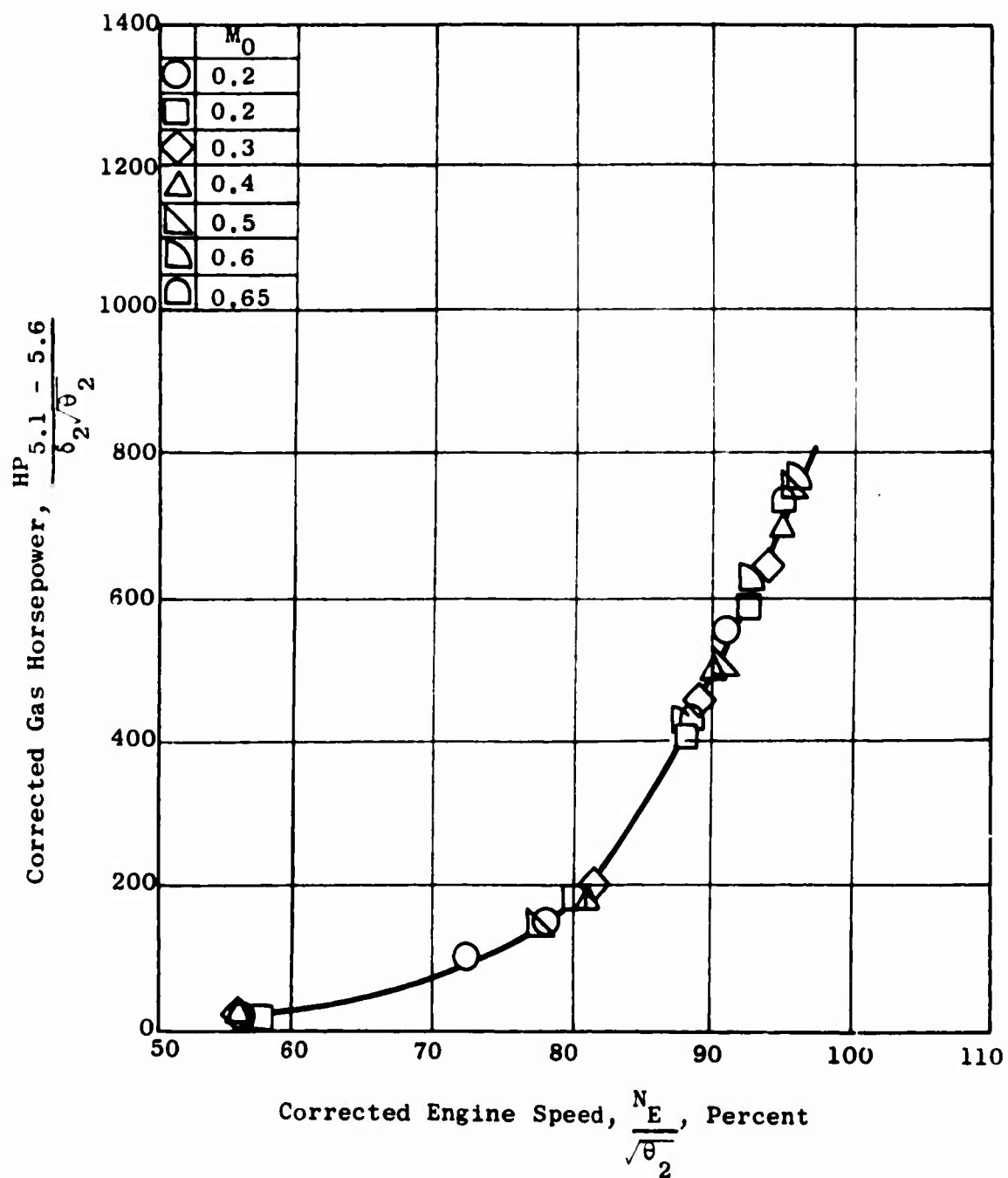


Figure 153. Engine Horsepower Absorbed by Fan Turbine - Model 4.

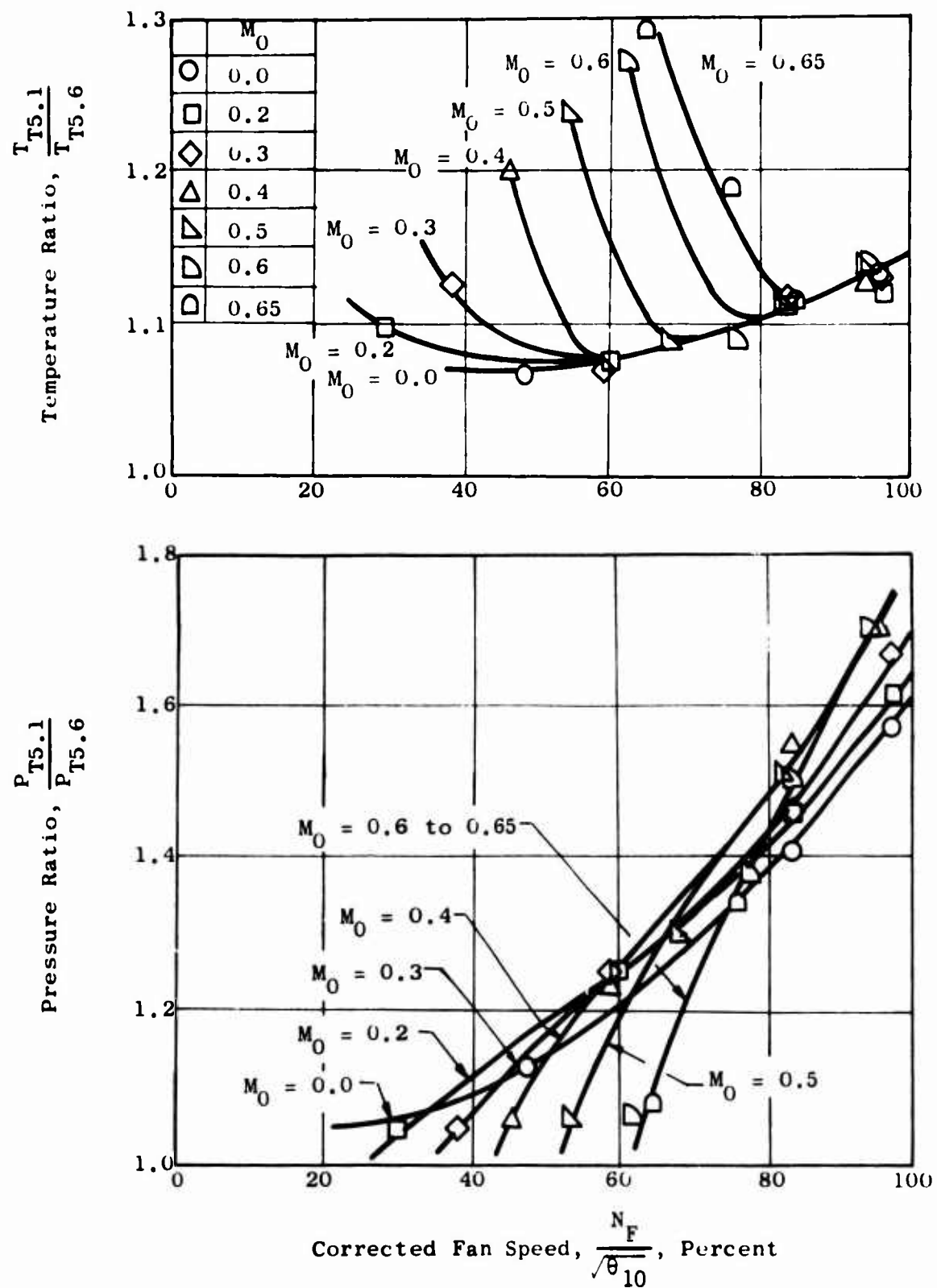


Figure 154. Fan Turbine Pressure and Temperature Ratios - Model 5.

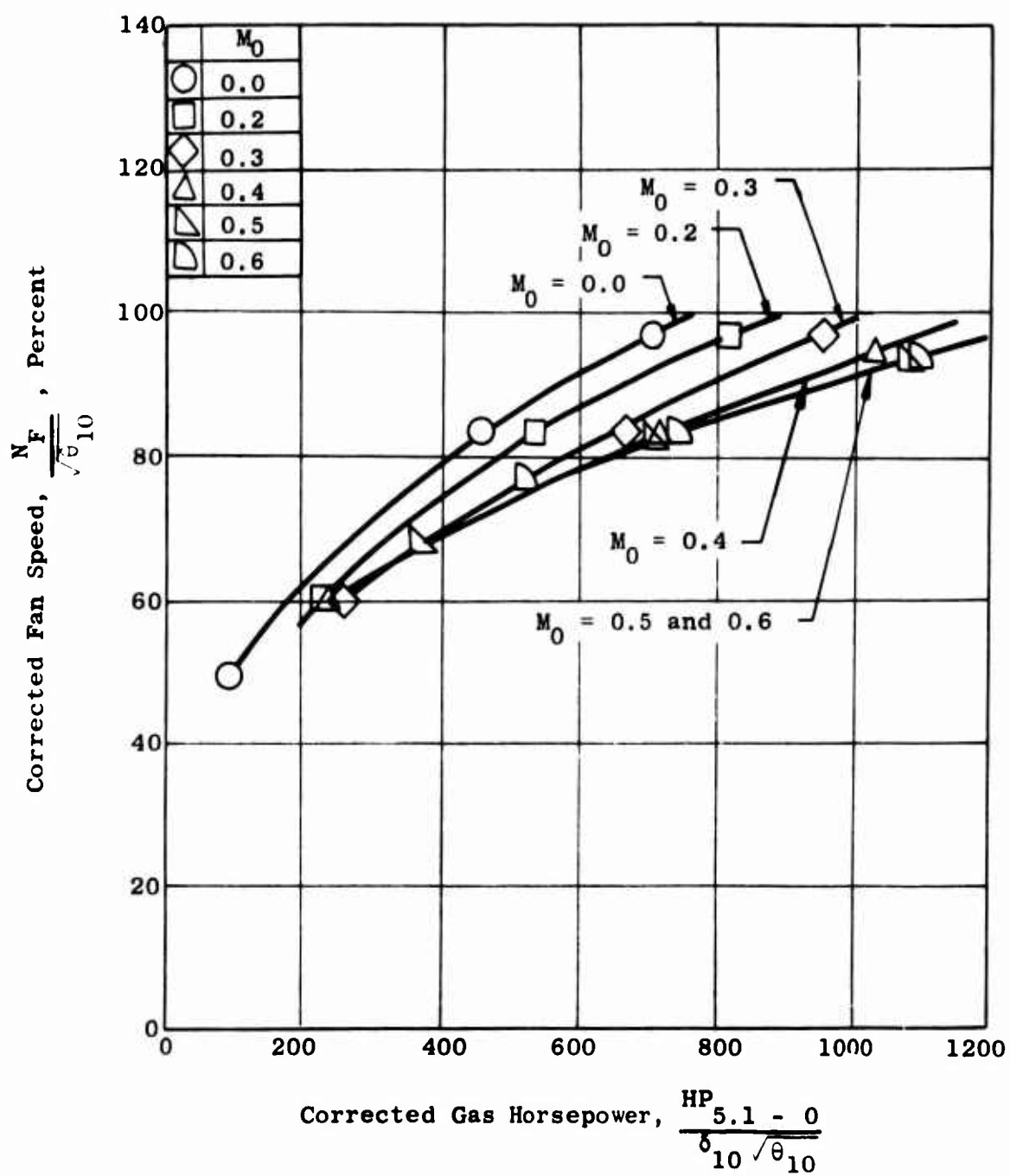


Figure 155. Fan Speed - Horsepower Characteristics - Model 5.

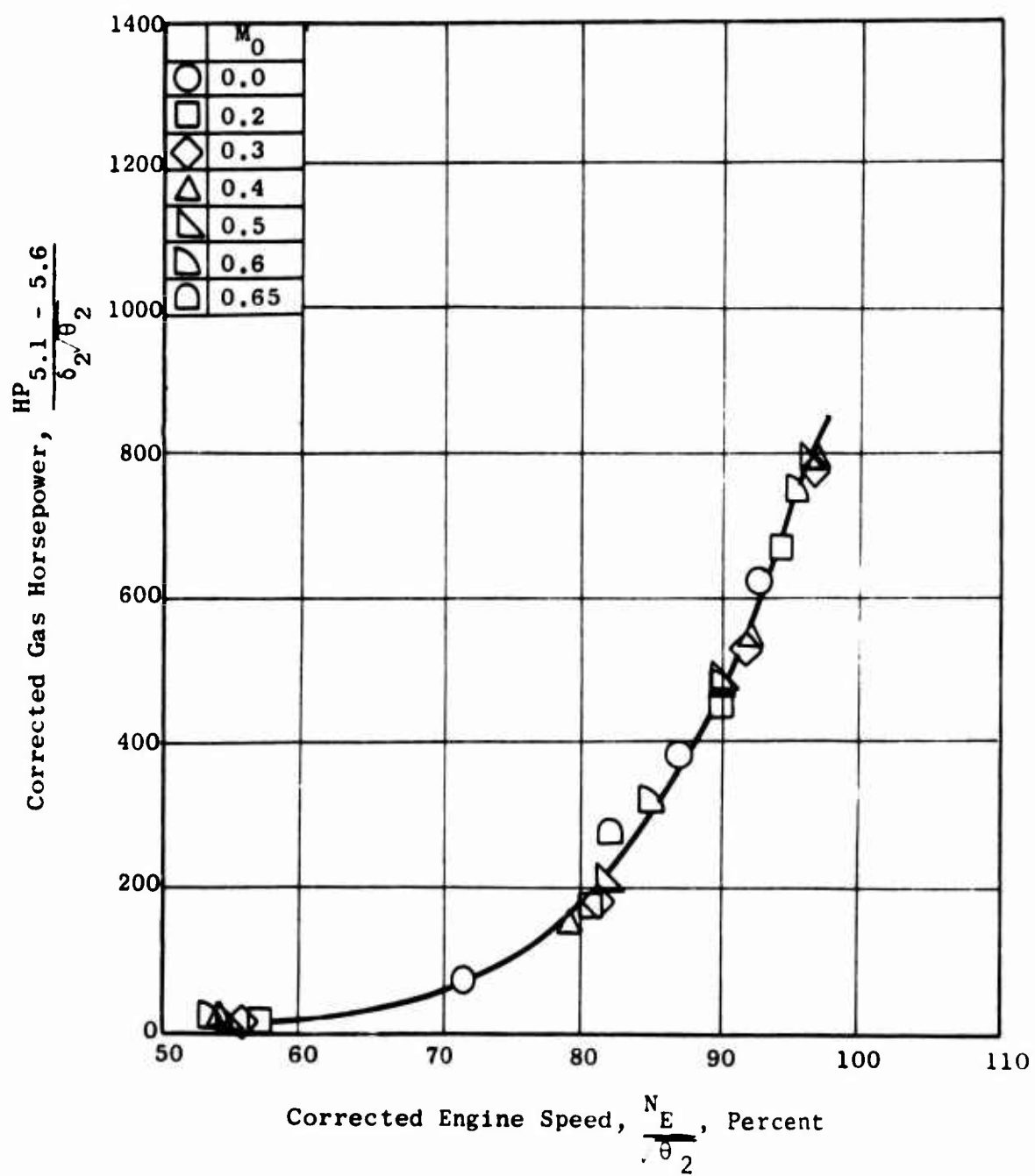
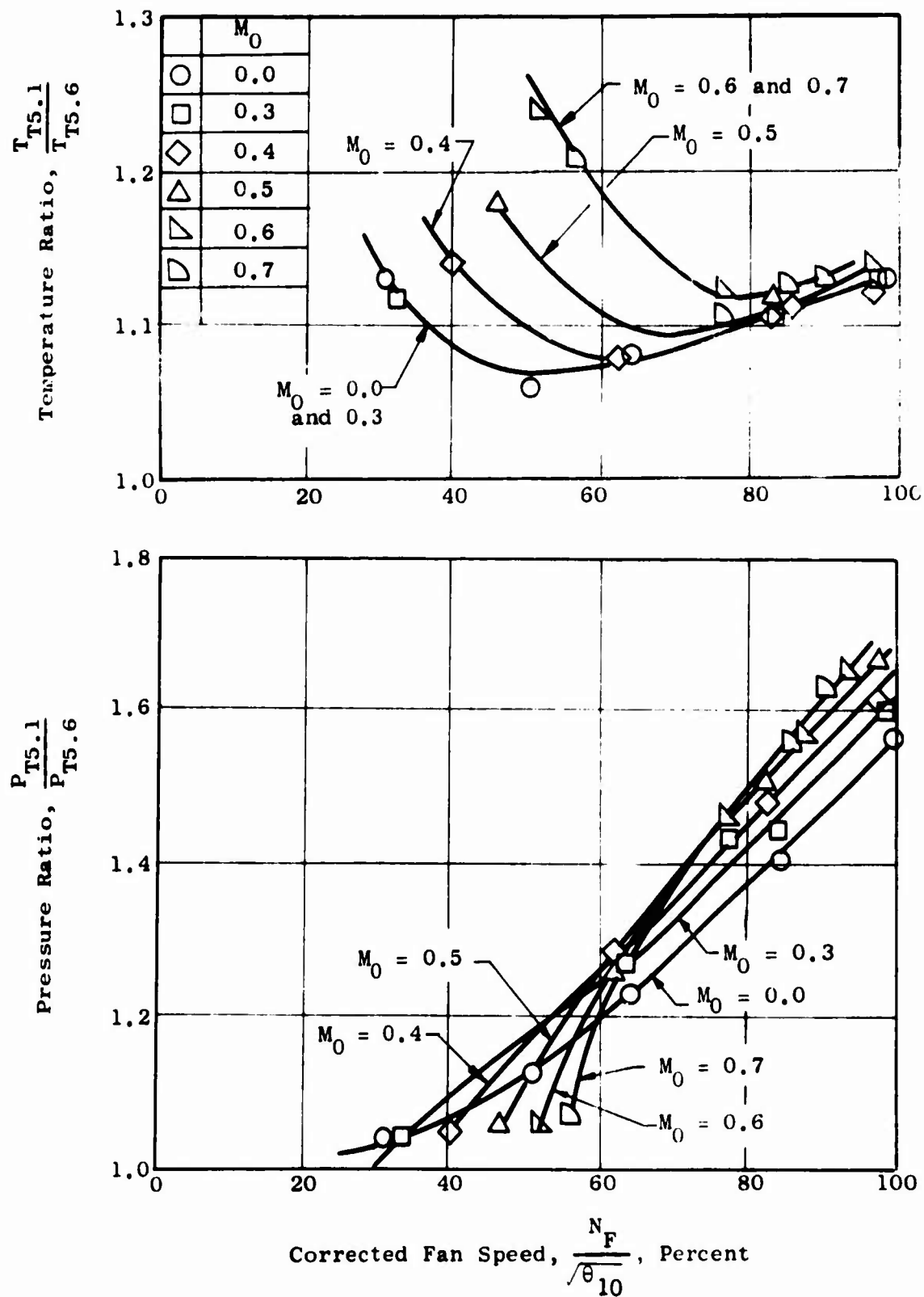


Figure 156. Engine Horsepower Absorbed by Fan Turbine - Model 5.



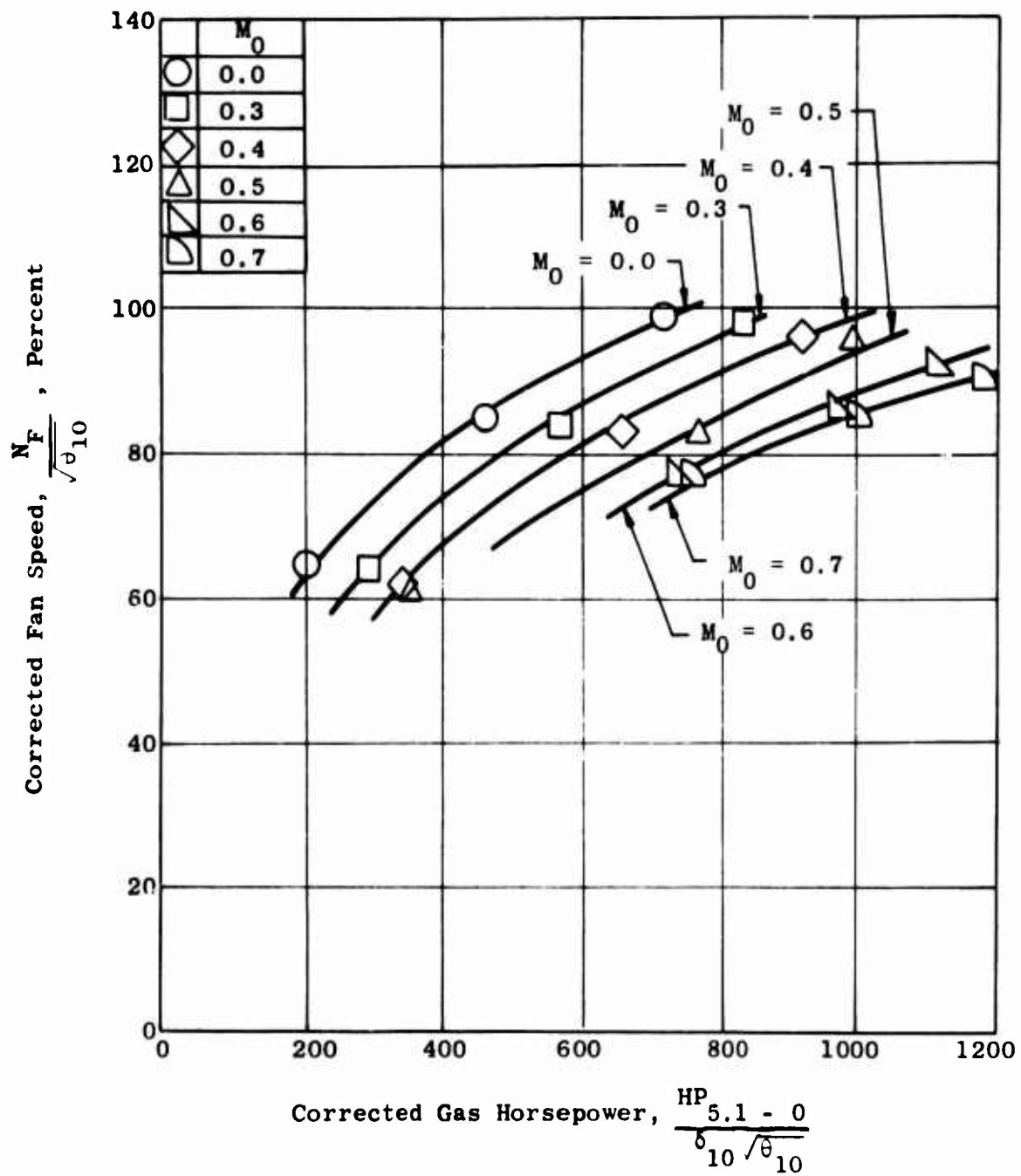


Figure 158. Fan Speed - Horsepower Characteristics - Model 6.

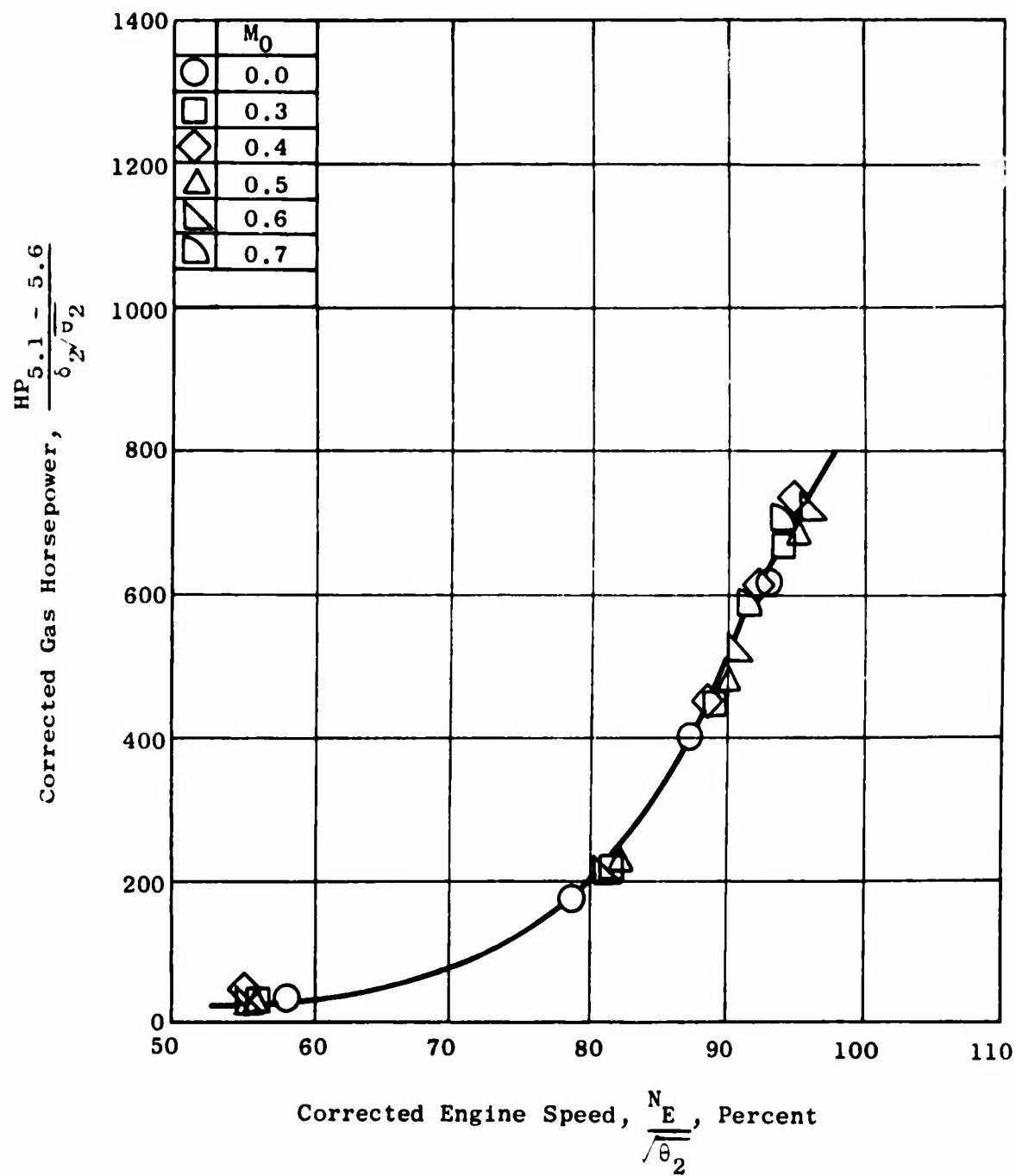


Figure 159. Engine Horsepower Absorbed by Fan Turbine - Model 6.

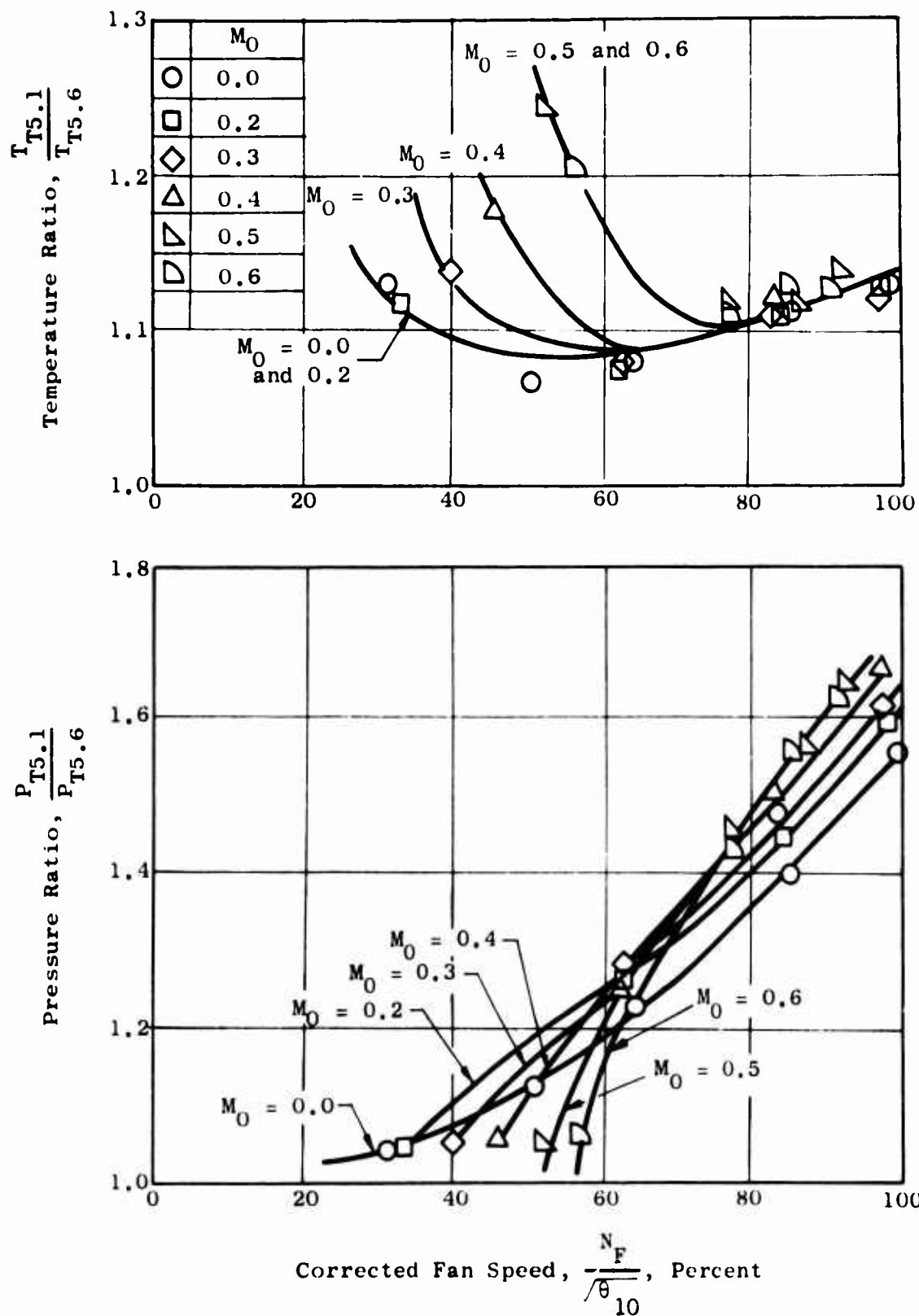


Figure 160. Fan Turbine Pressure and Temperature Ratios - Model 7.

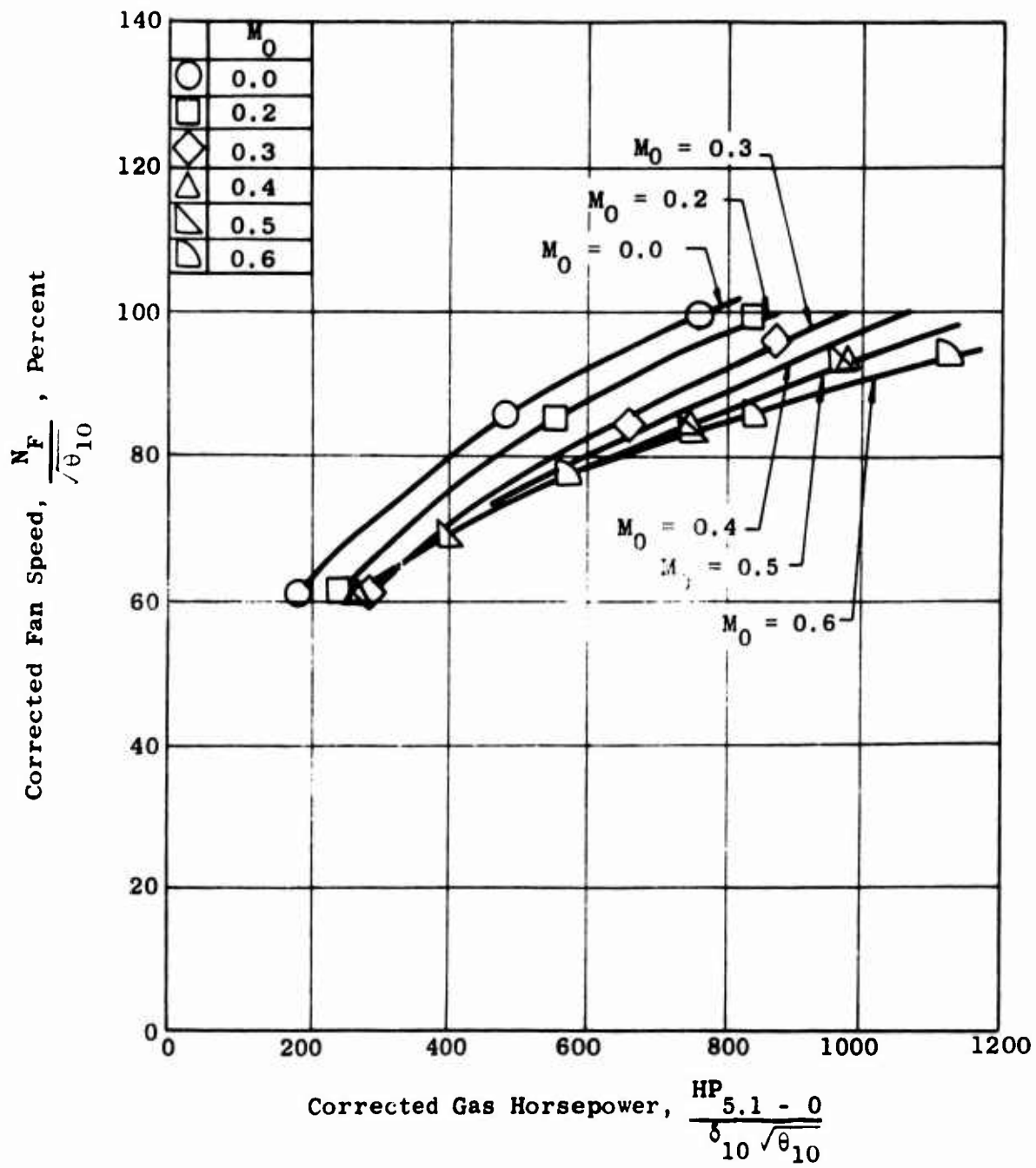


Figure 161. Fan Speed - Horsepower Characteristics - Model 7.

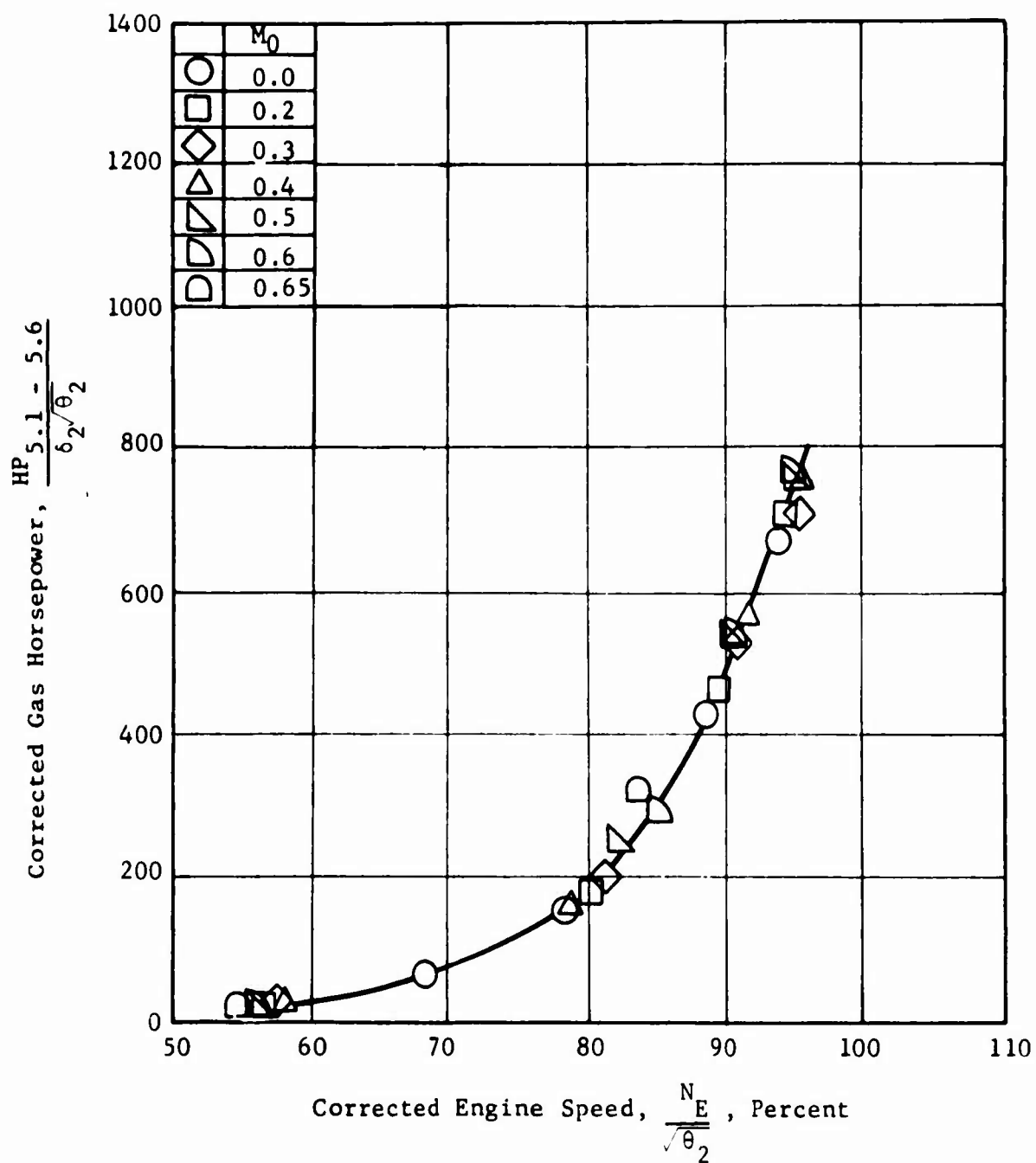


Figure 162. Engine Horsepower Absorbed by Fan Turbine - Model 7.

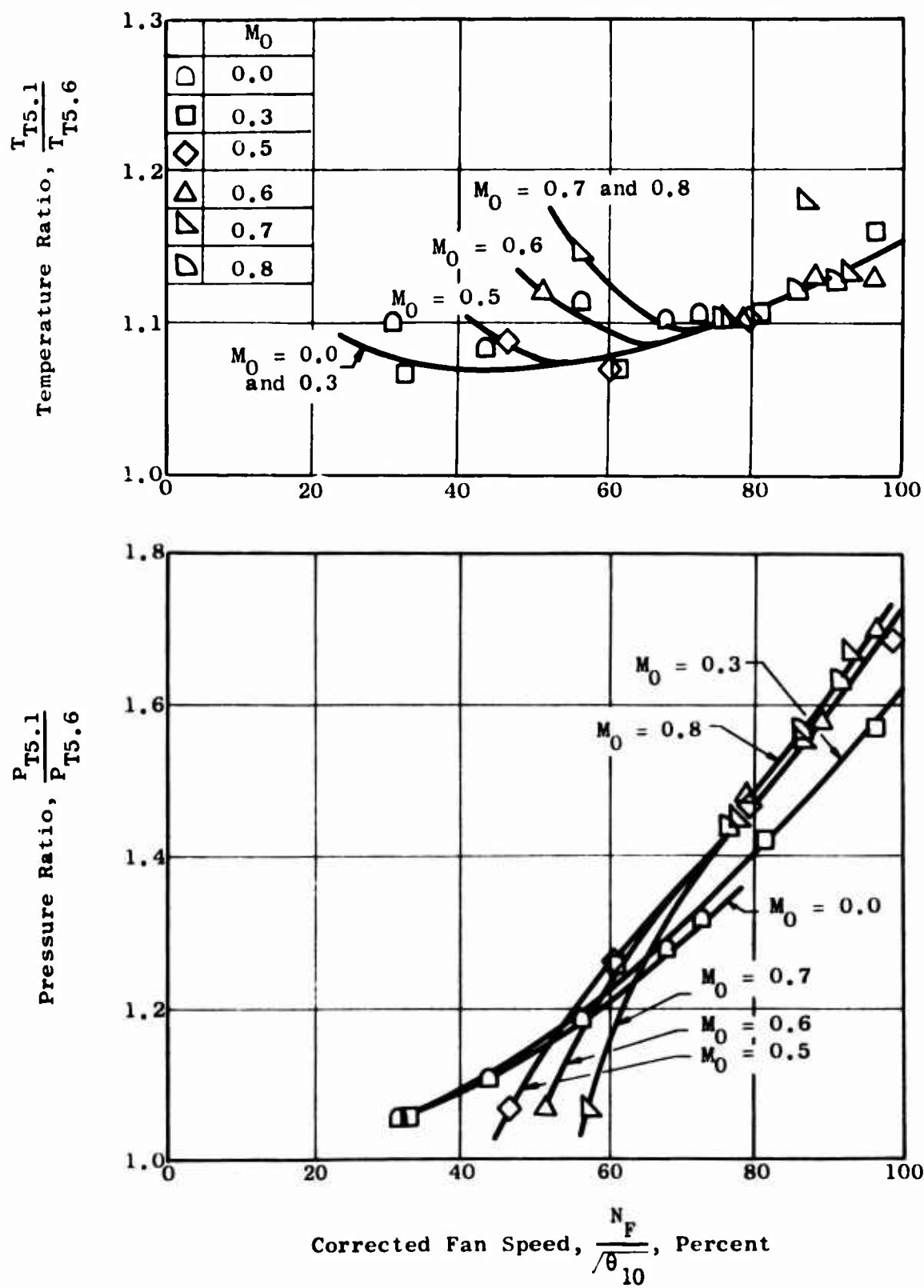


Figure 163. Fan Turbine Pressure and Temperature Ratios - Model 8.

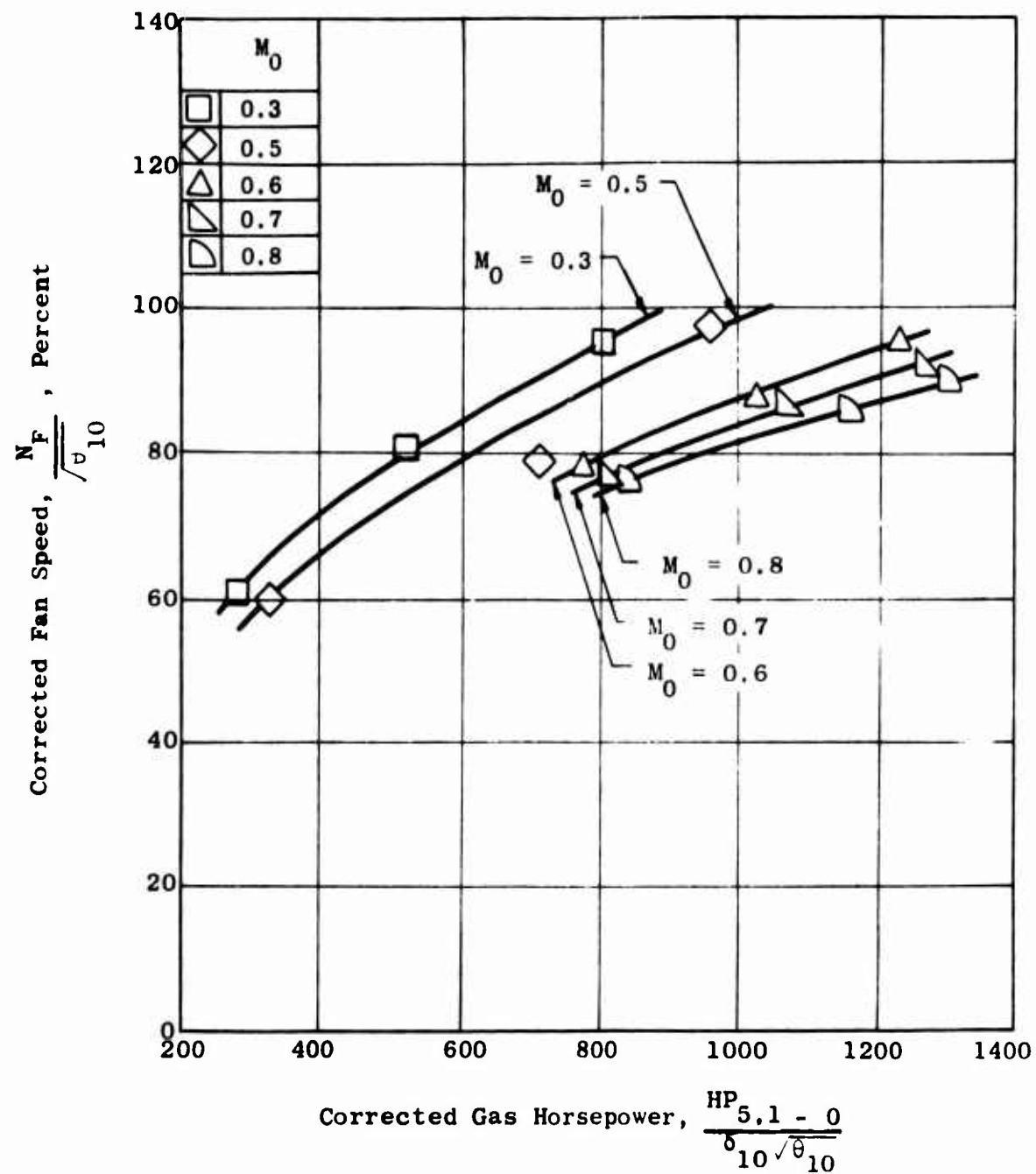


Figure 164. Fan Speed - Horsepower Characteristics - Model 8.

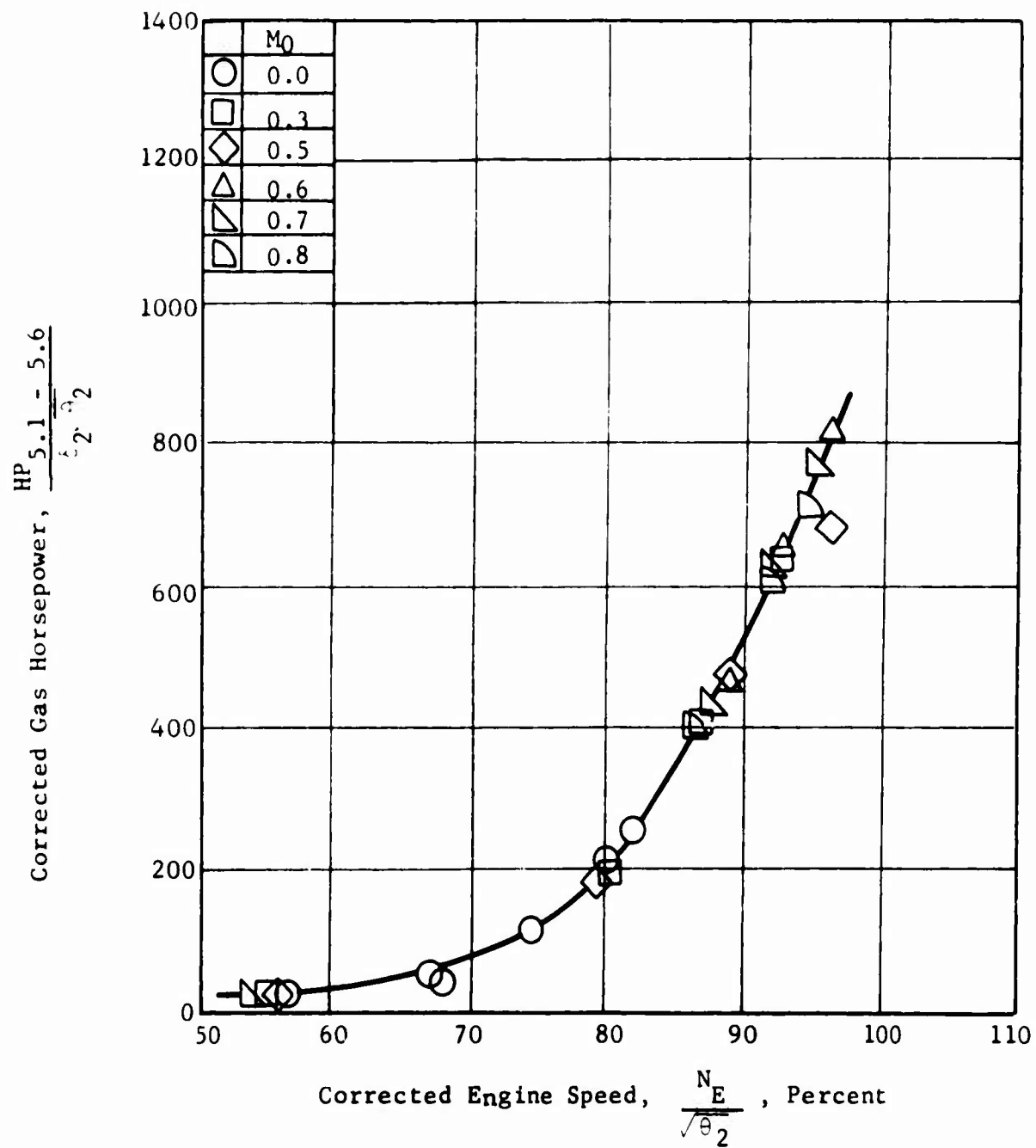


Figure 165. Engine Horsepower Absorbed by Fan Turbine - Model 8.

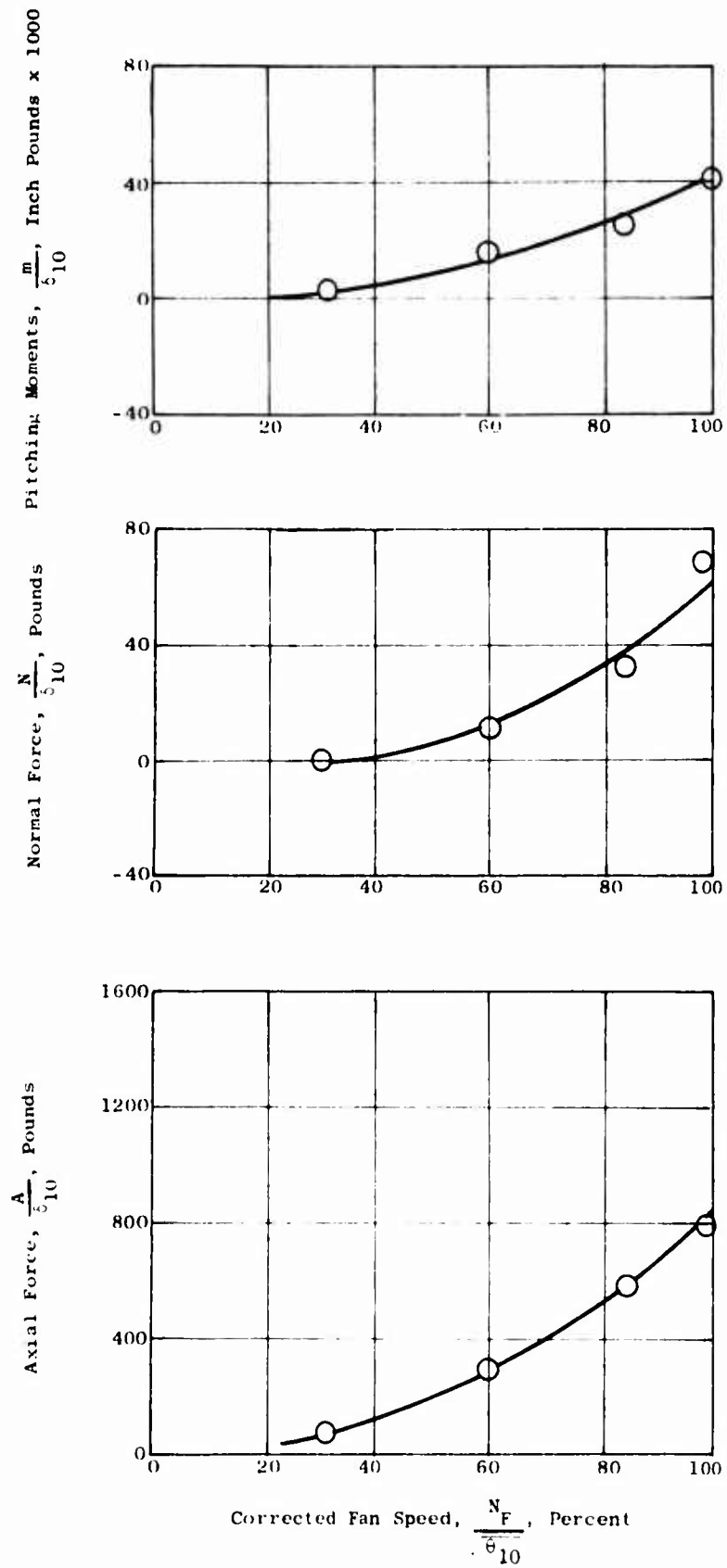


Figure 166. Static Forces from Balance Measurements - Model 1.

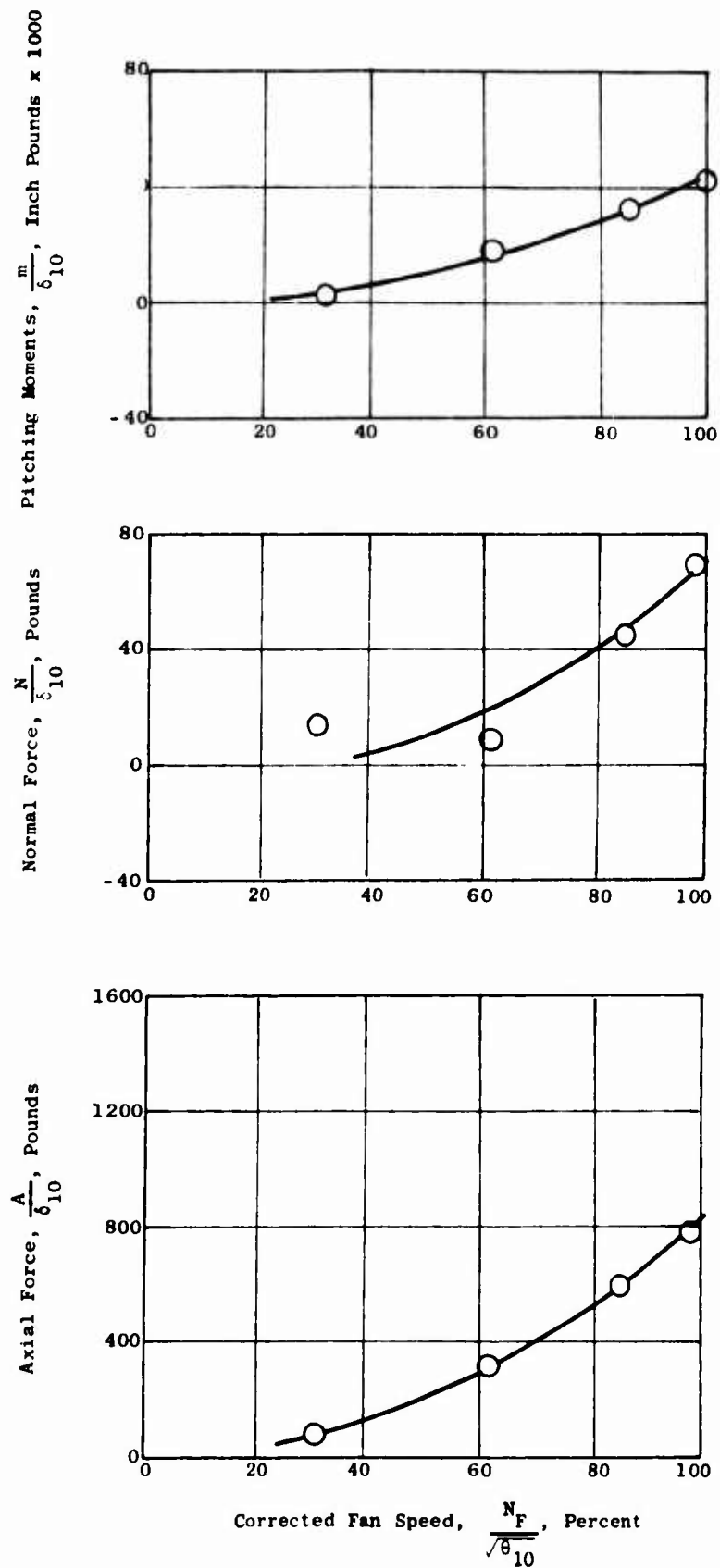


Figure 167. Static Forces from Balance Measurements - Model 2.

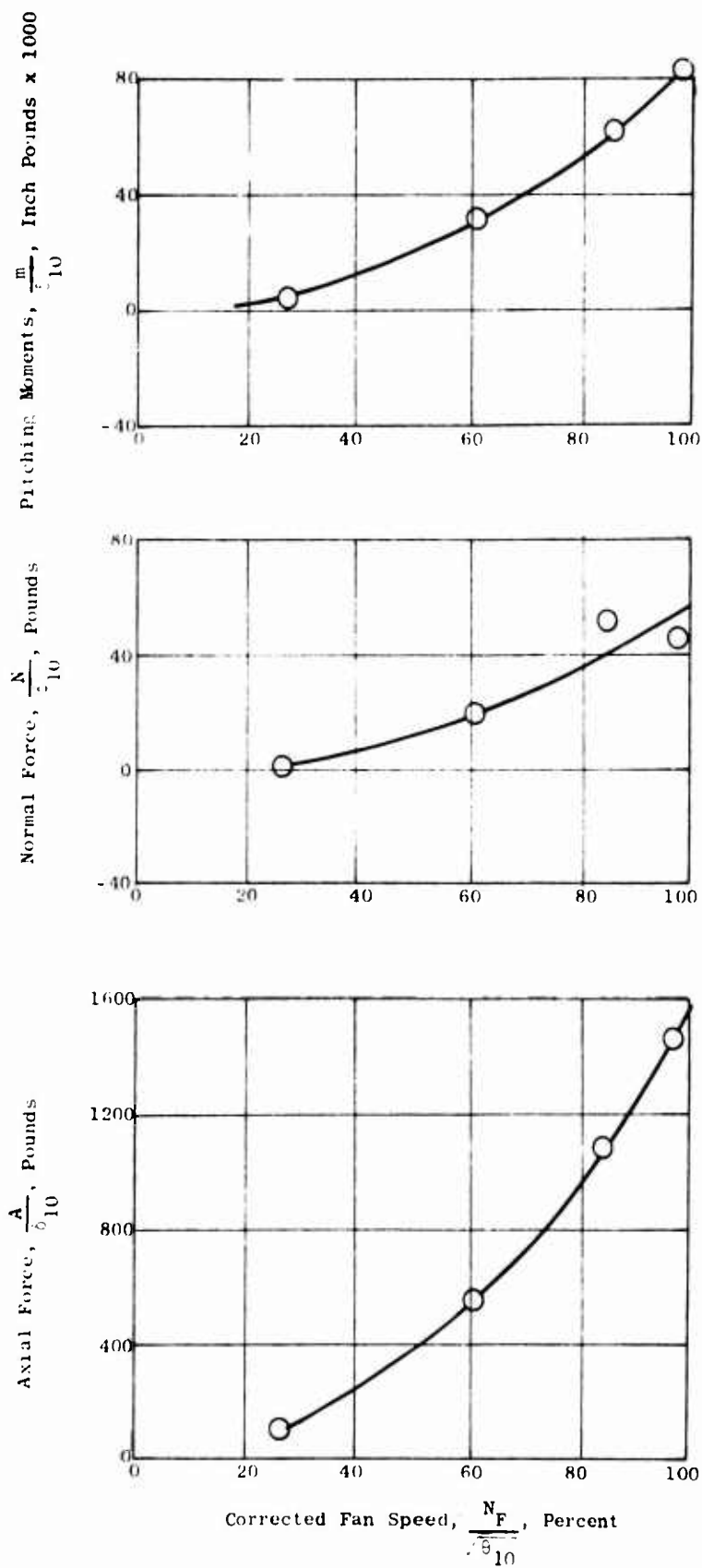


Figure 168. Static Forces from Balance Measurements - Model 3.

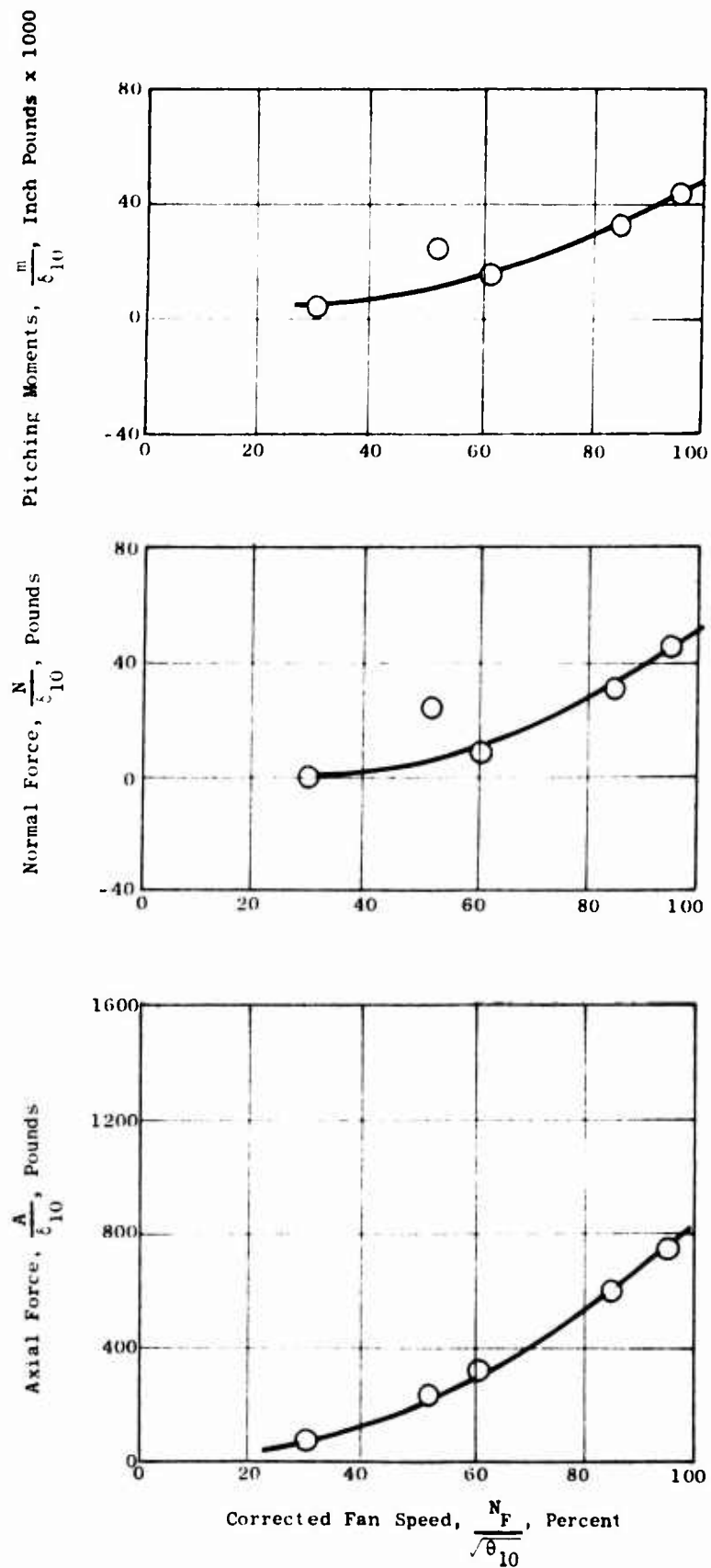


Figure 169. Static Forces from Balance Measurements - Model 4.

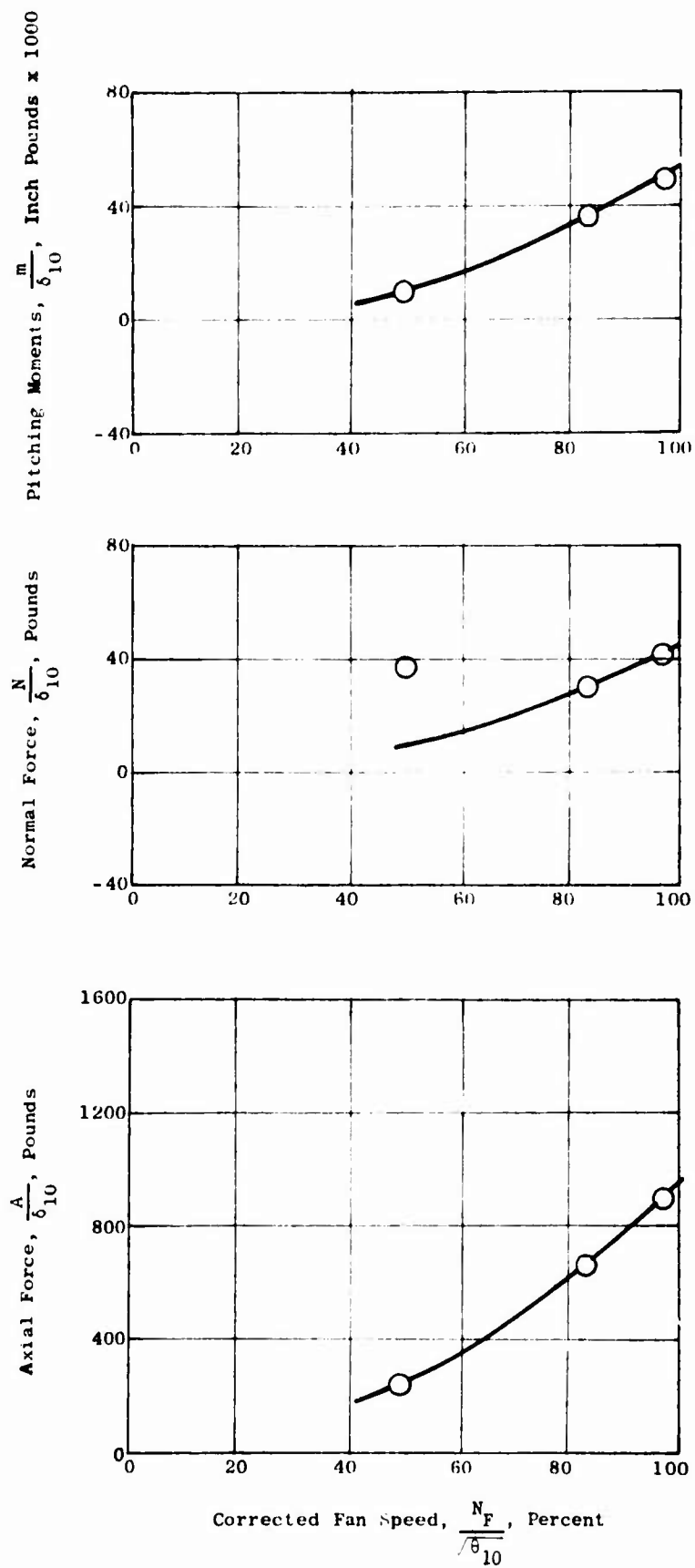


Figure 170. Static Forces from Balance Measurements - Model 5.

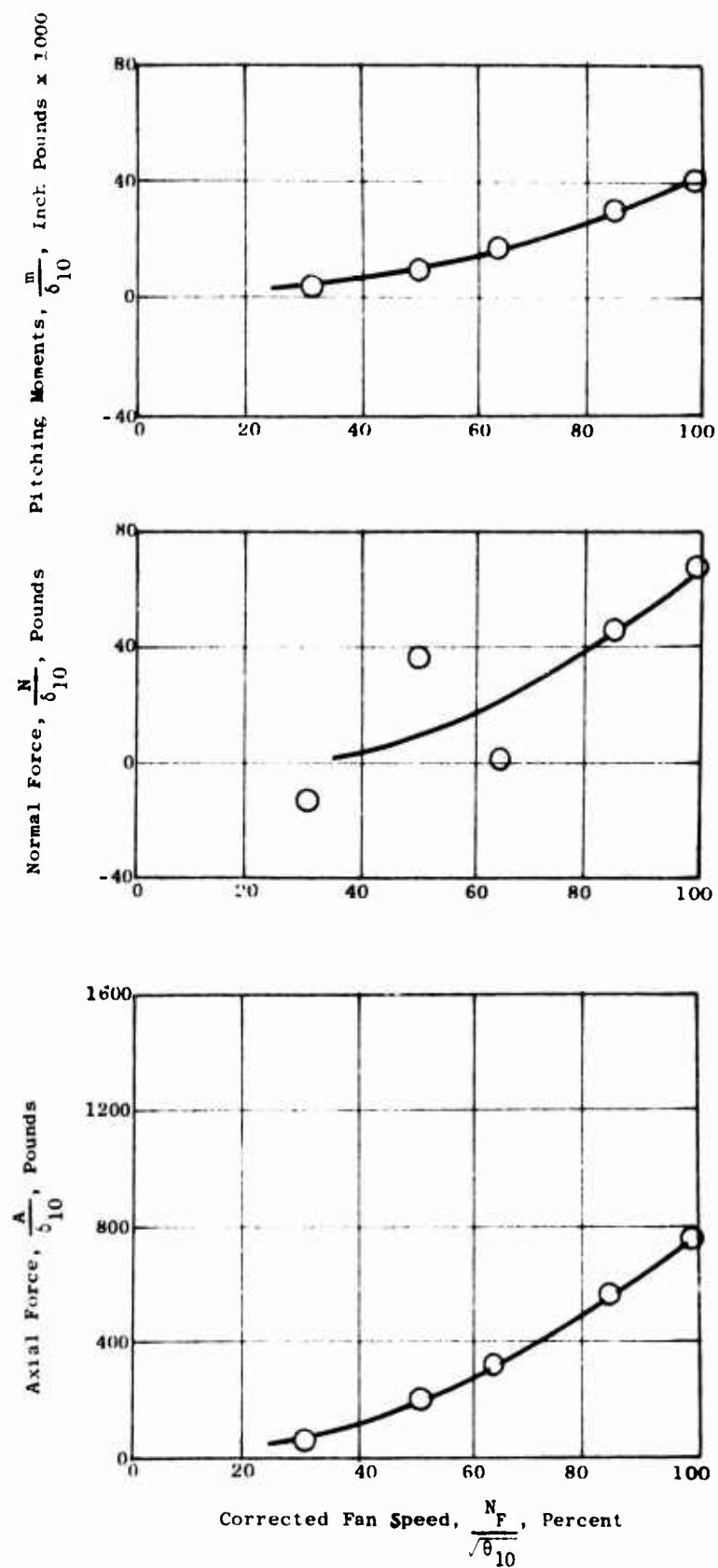


Figure 171. Static Forces from Balance Measurements - Model 6.

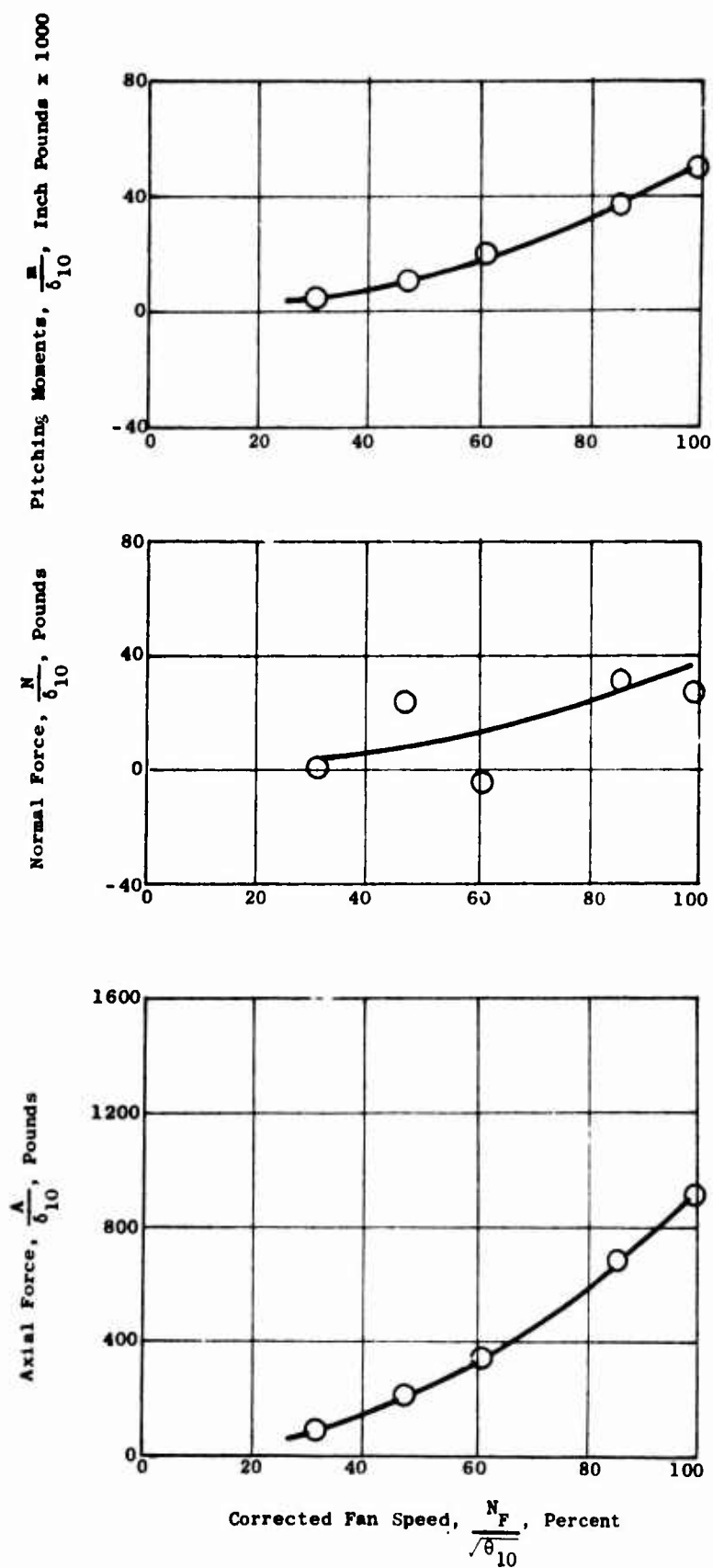


Figure 172. Static Forces from Balance Measurements - Model 7.

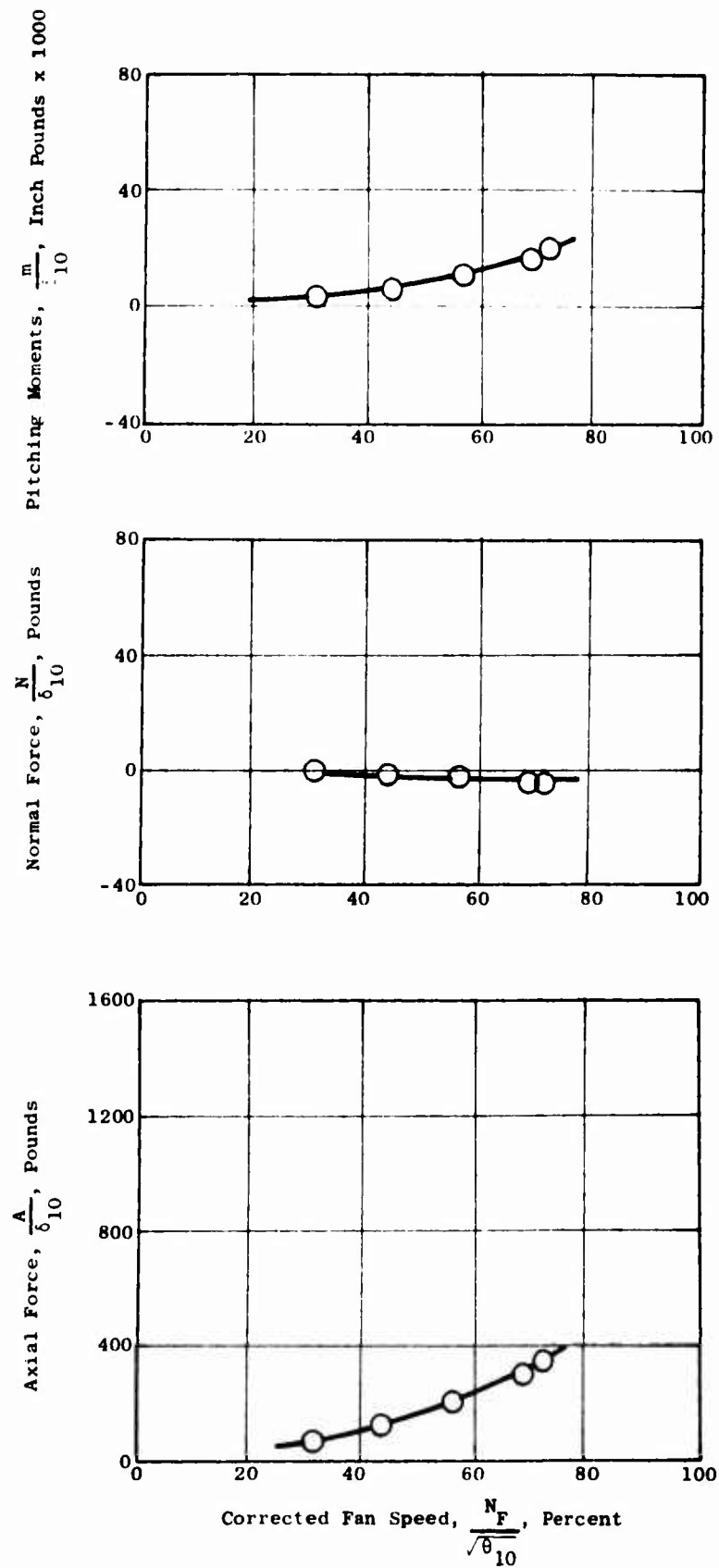


Figure 173. Static Forces from Balance Measurements - Model 8.

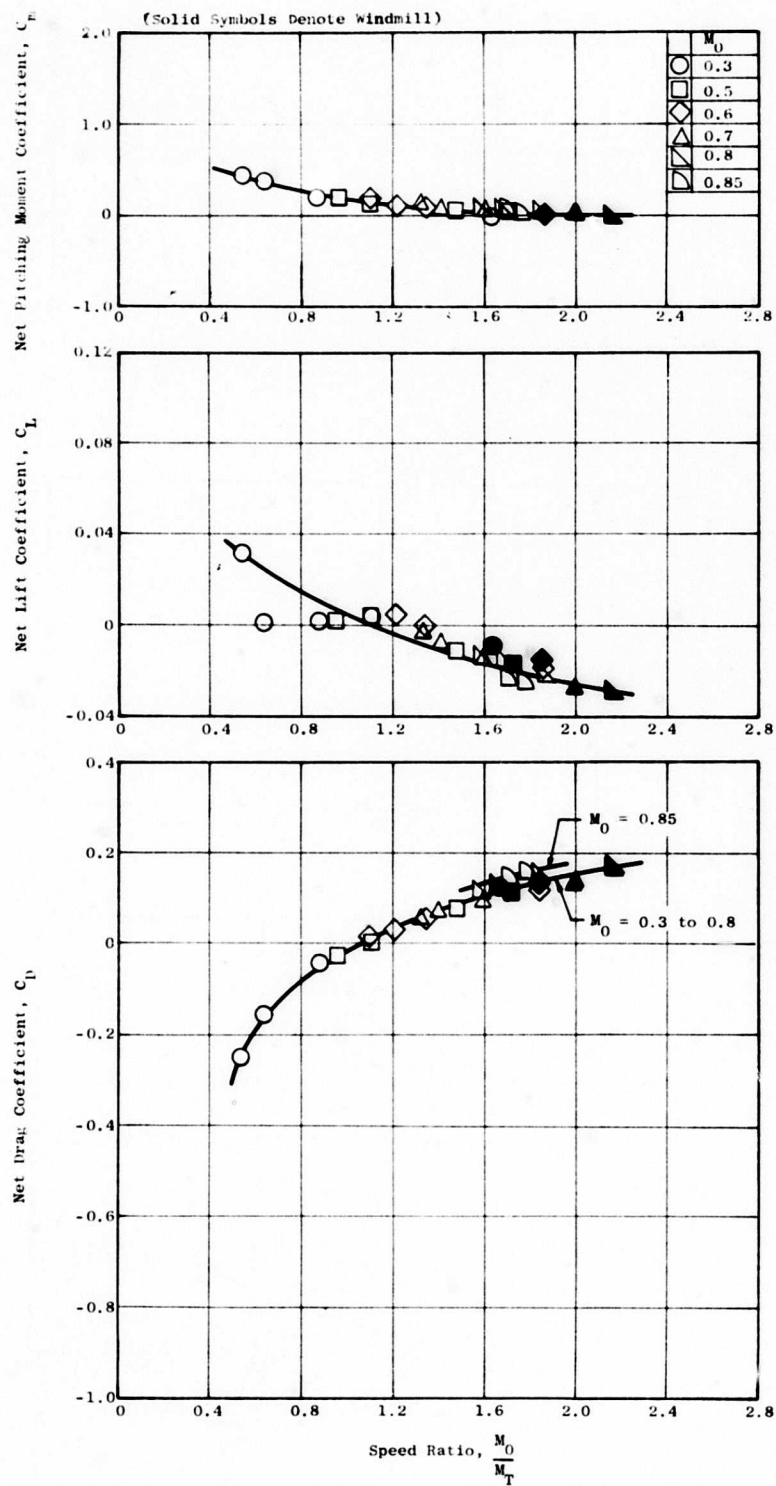


Figure 174. Variation of Net System Forces with Speed Based on Force Measurements - Model 1.

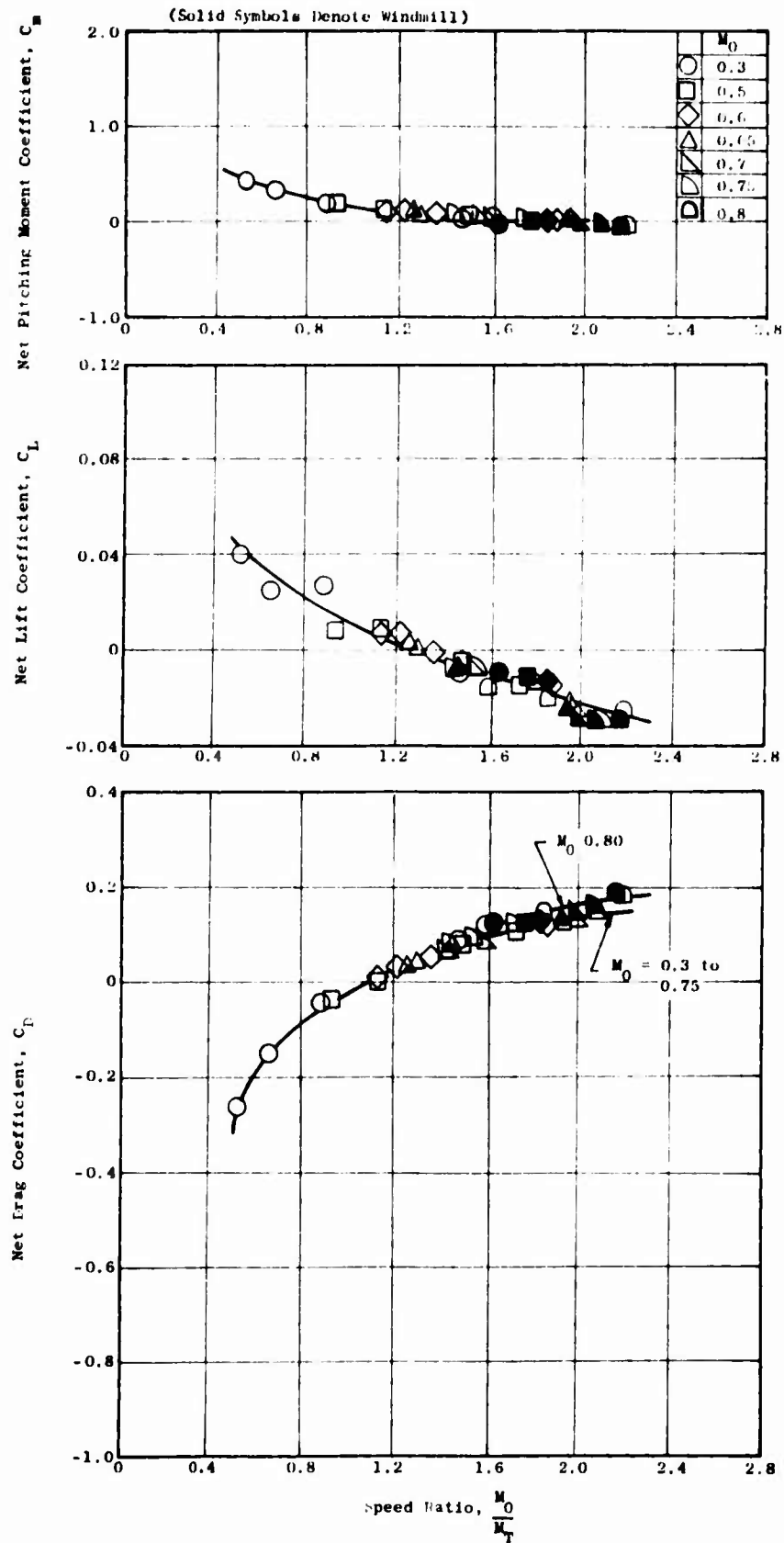


Figure 175. Variation of Net System Forces with Speed Based on Force Measurements - Model 2.

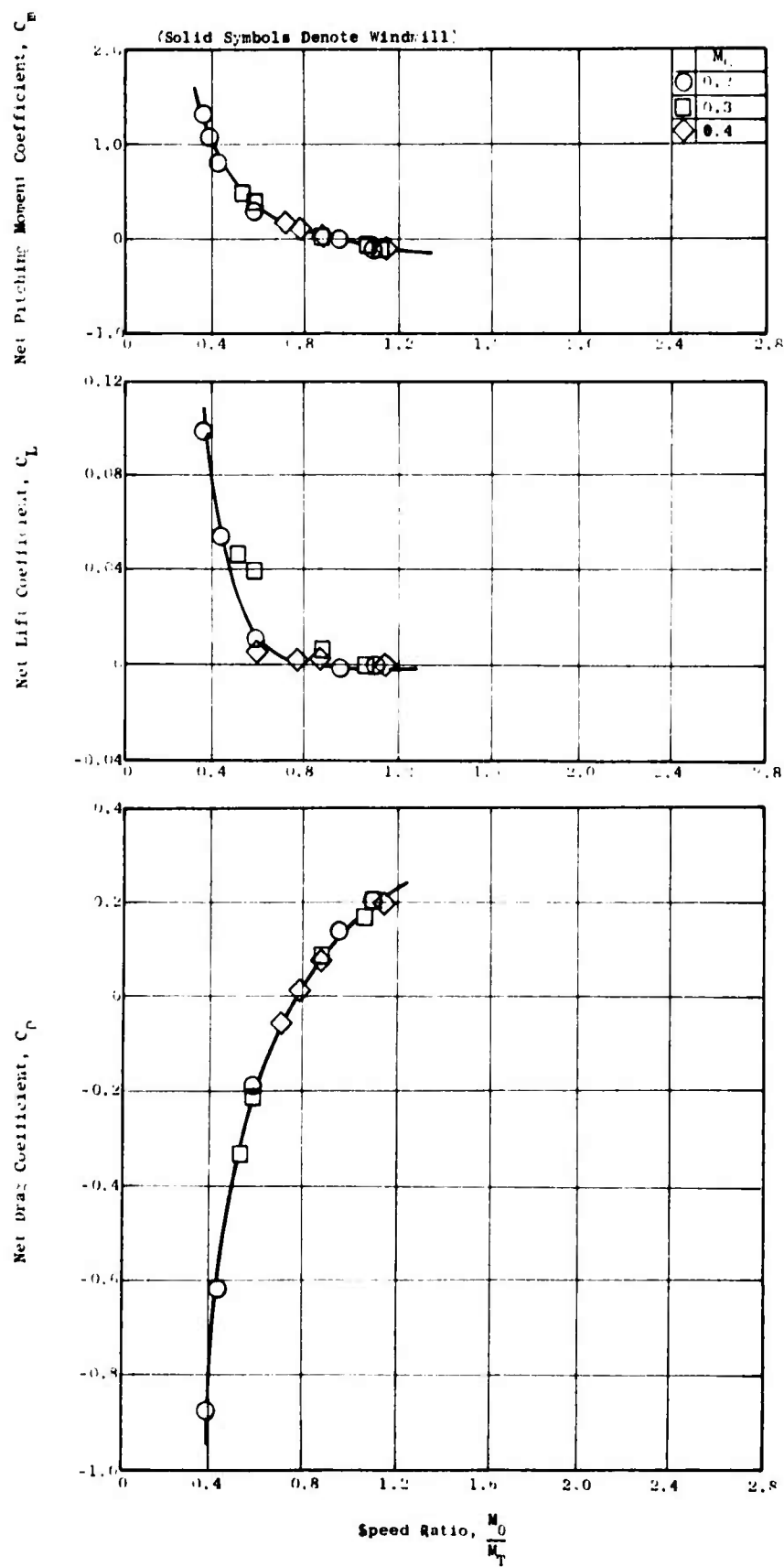


Figure 176. Variation of Net System Forces with Speed Based on Force Measurements - Model 3.

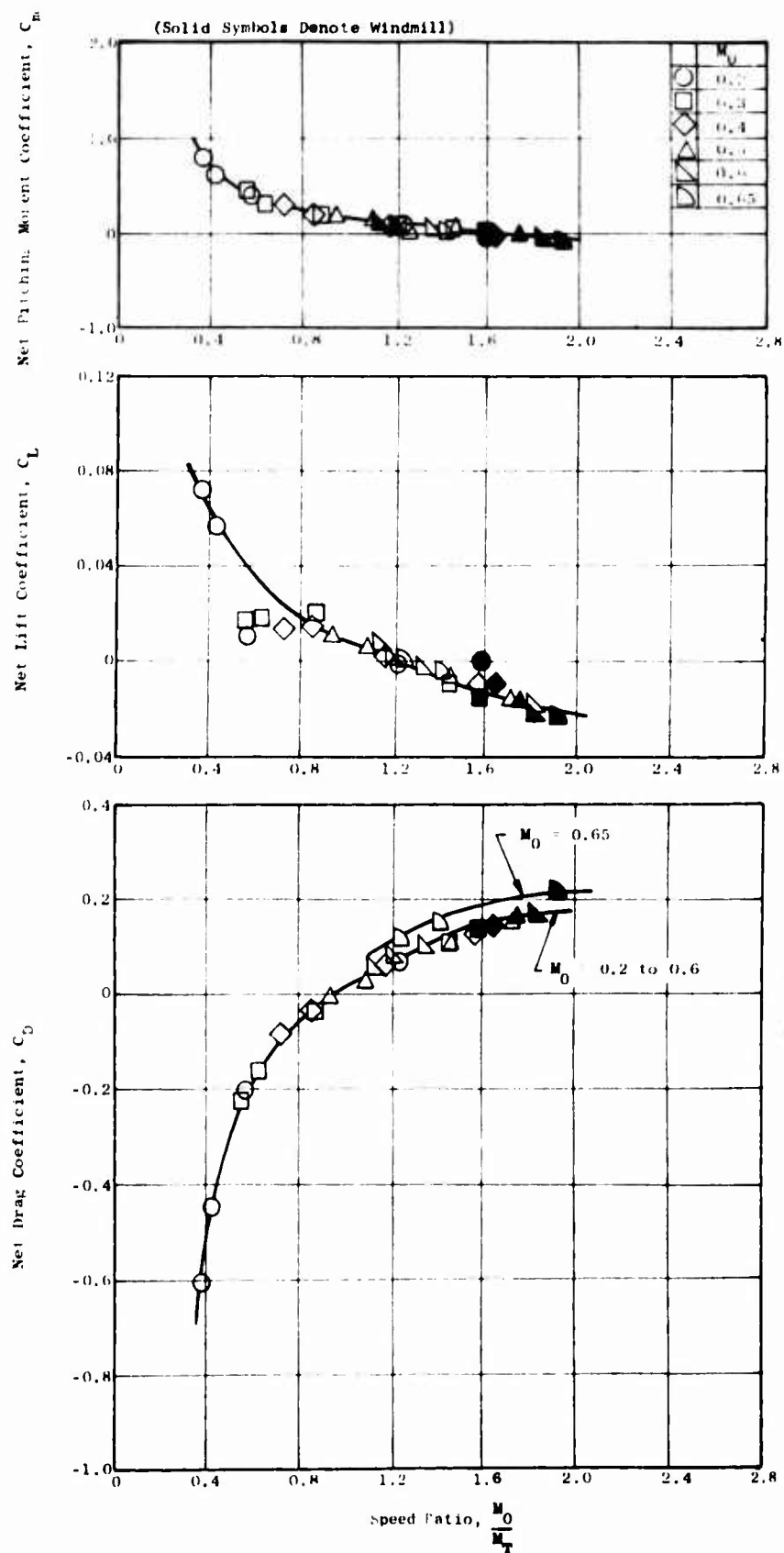


Figure 177. Variation of Net System Forces with Speed Based on Force Measurements - Model 4.

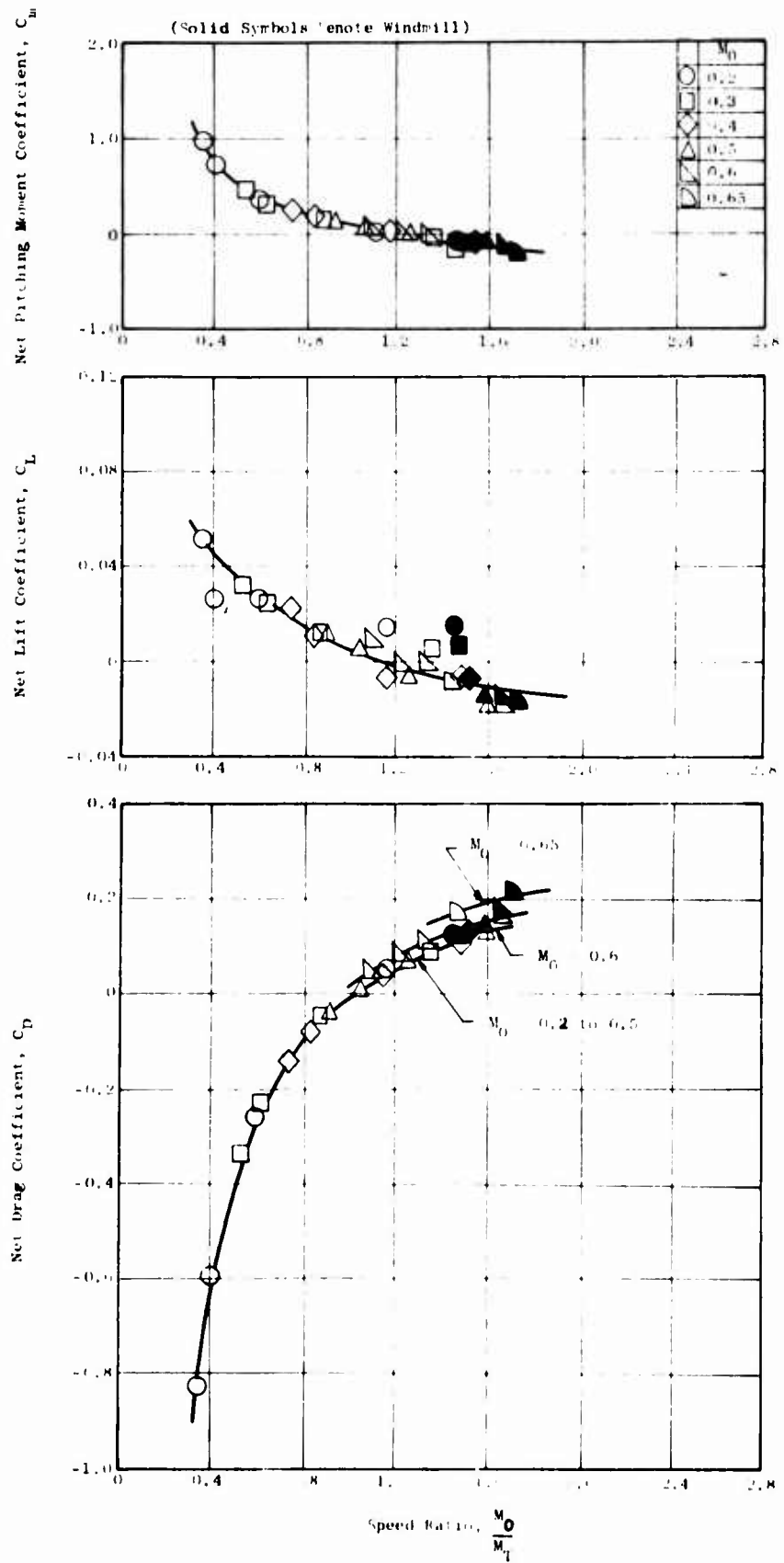


Figure 178. Variation of Net System Forces with Speed Based on Force Measurements - Model 5.

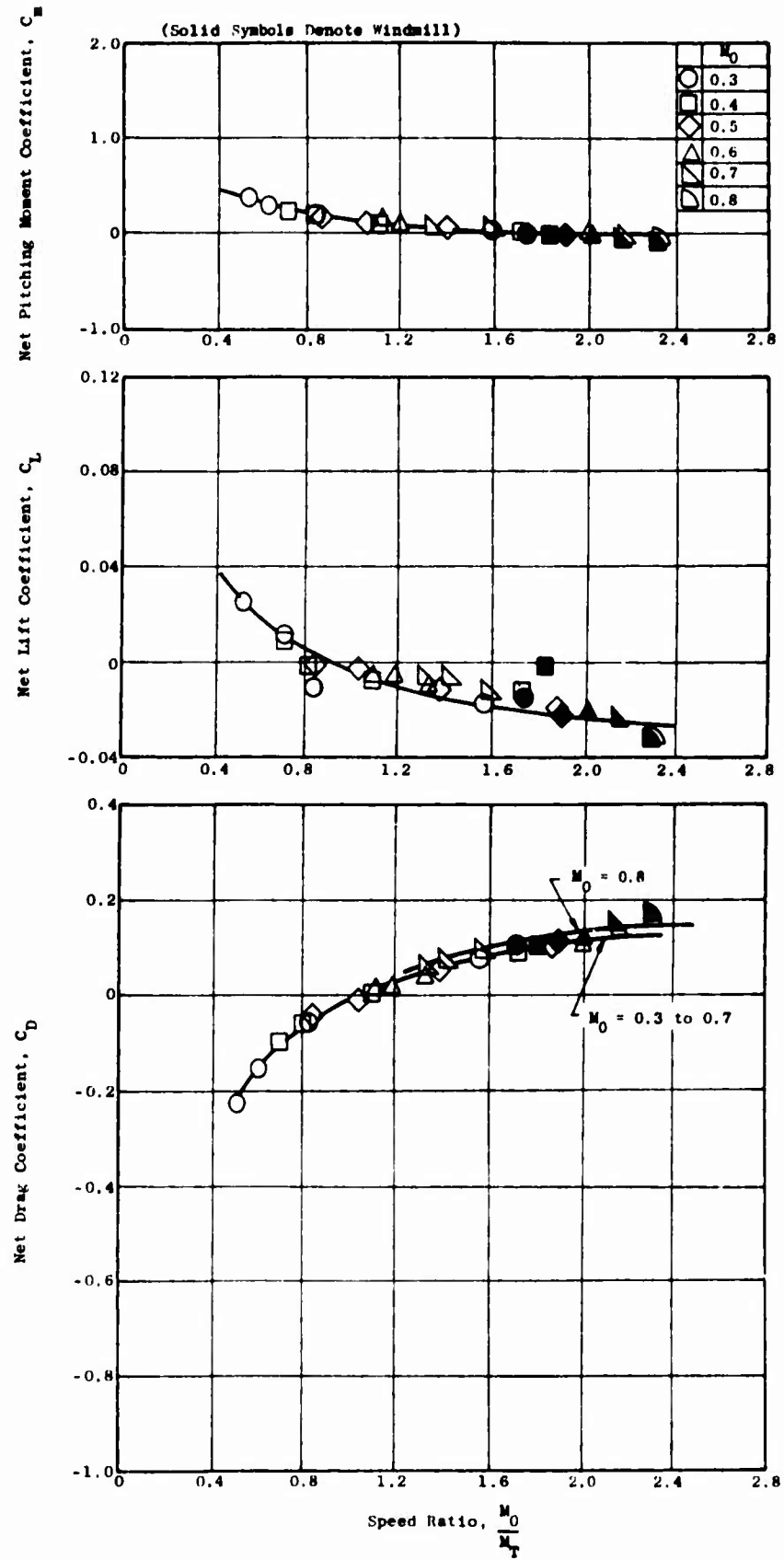


Figure 179. Variation of Net System Forces with Speed Based on Force Measurements - Model 6.

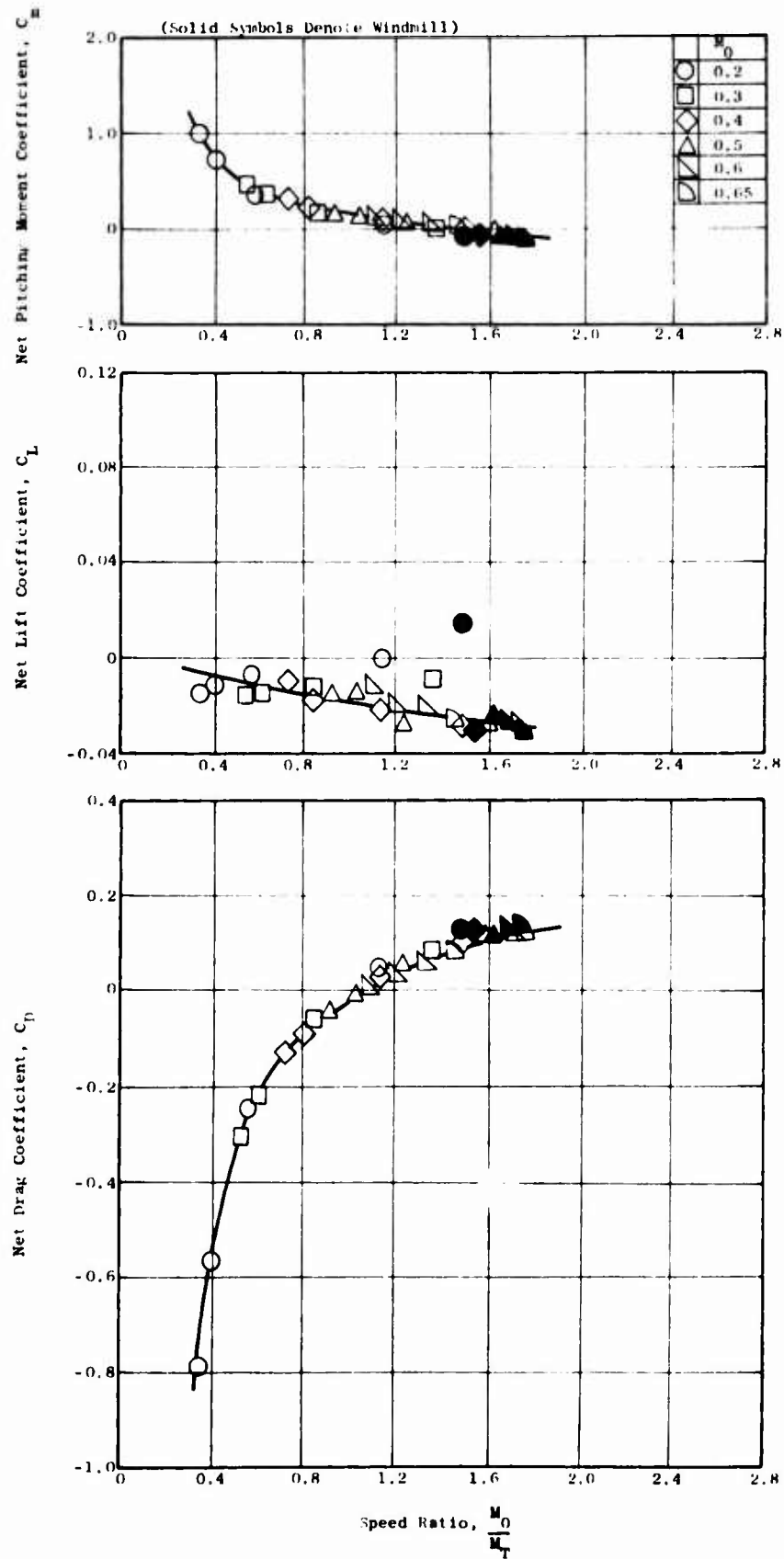


Figure 180. Variation of Net System Forces with Speed Based on Force Measurements - Model 7.

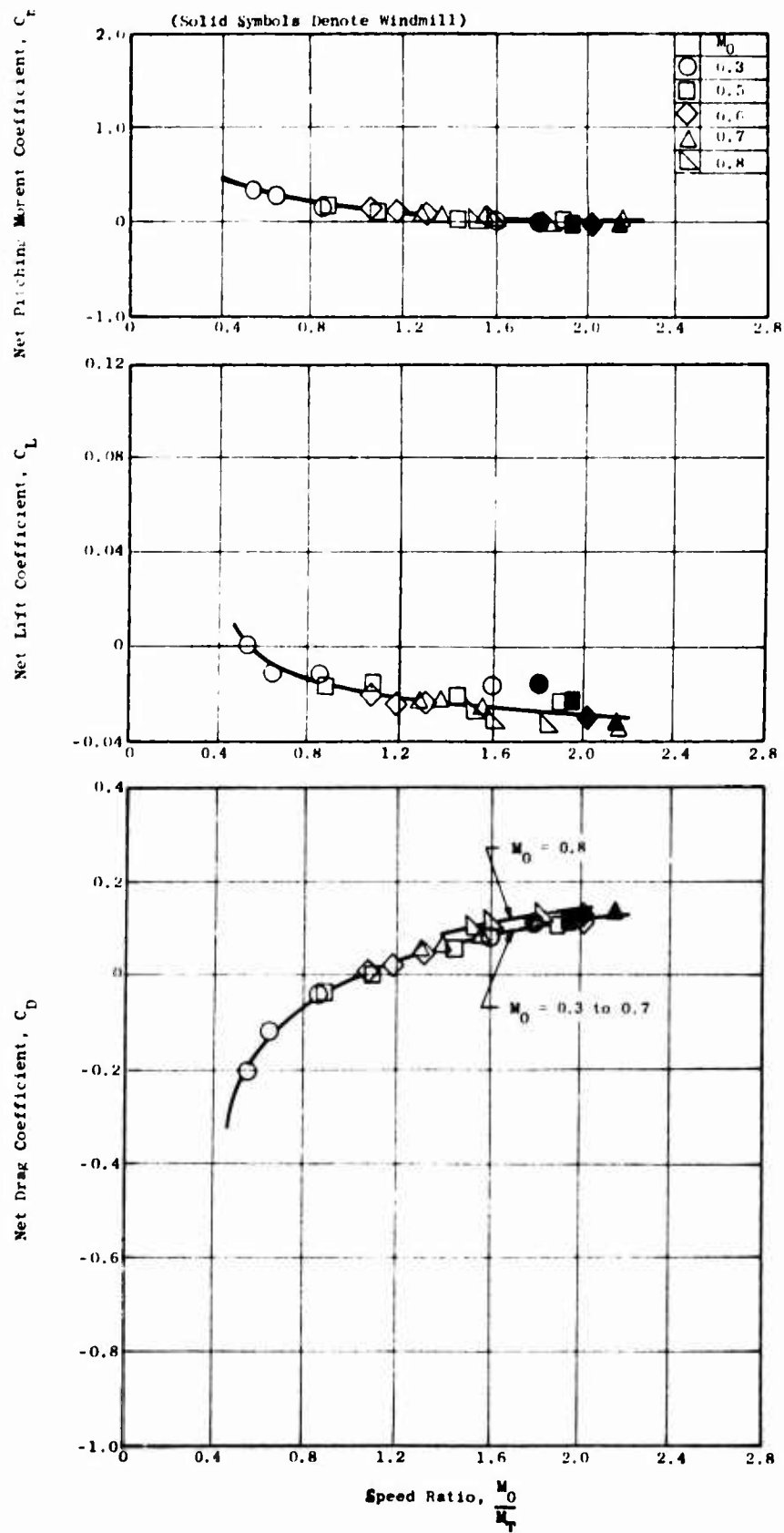


Figure 181. Variation of Net System Forces with Speed Based on Force Measurements - Model 8.

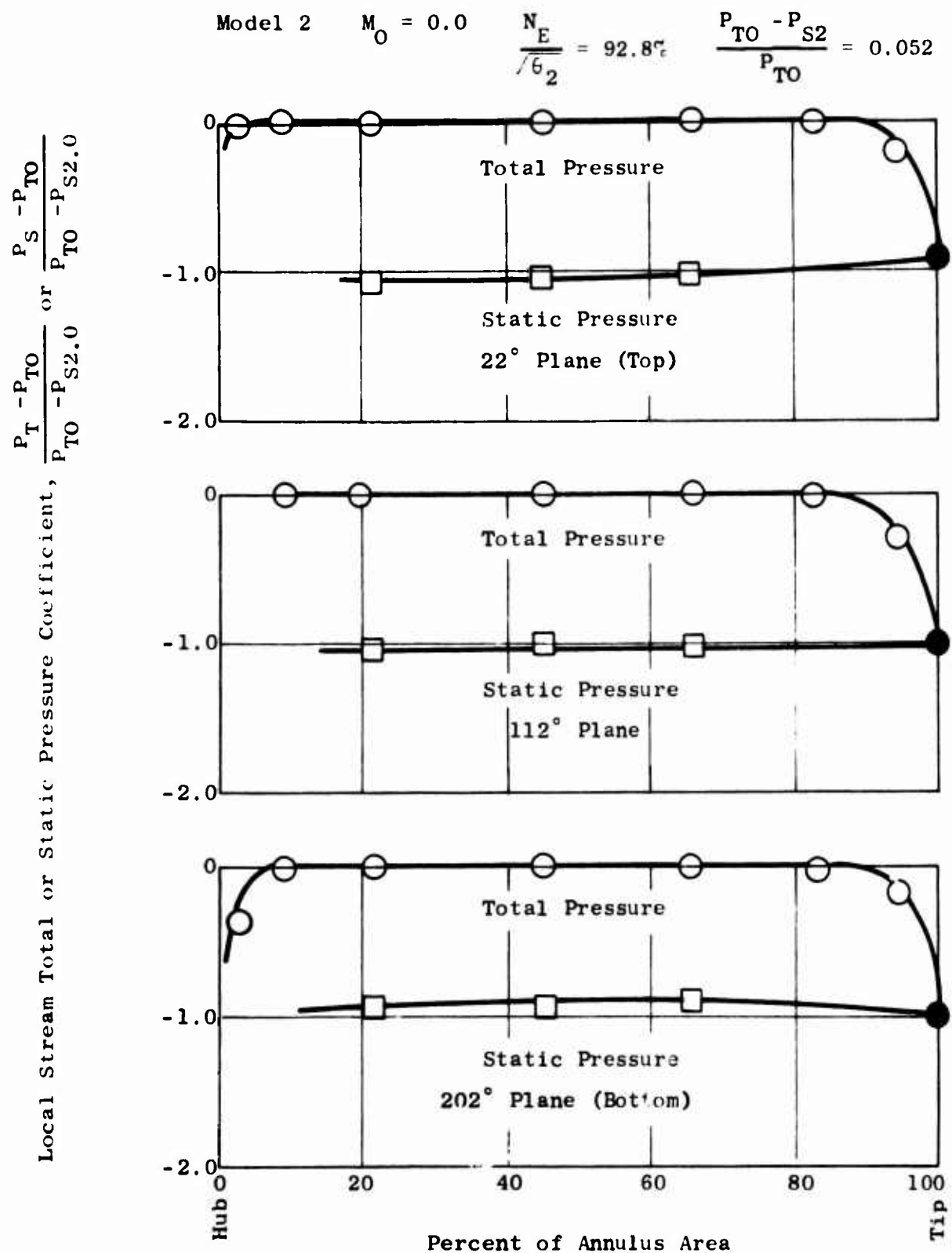


Figure 182. Typical Engine Inlet Stream Pressure Distributions at Station 2.0.

Model 2 $M_0 = 0.30$ $\frac{N_E}{\sqrt{\theta_2}} = 95.0\%$ $\frac{P_{TO} - P_{S2}}{P_{TO}} = 0.056$

Local Stream Total or Static Pressure Coefficient, $\frac{P_T - P_{TO}}{P_{TO} - P_{S2.0}}$ or $\frac{P_S - P_{TO}}{P_{TO} - P_{S2.0}}$

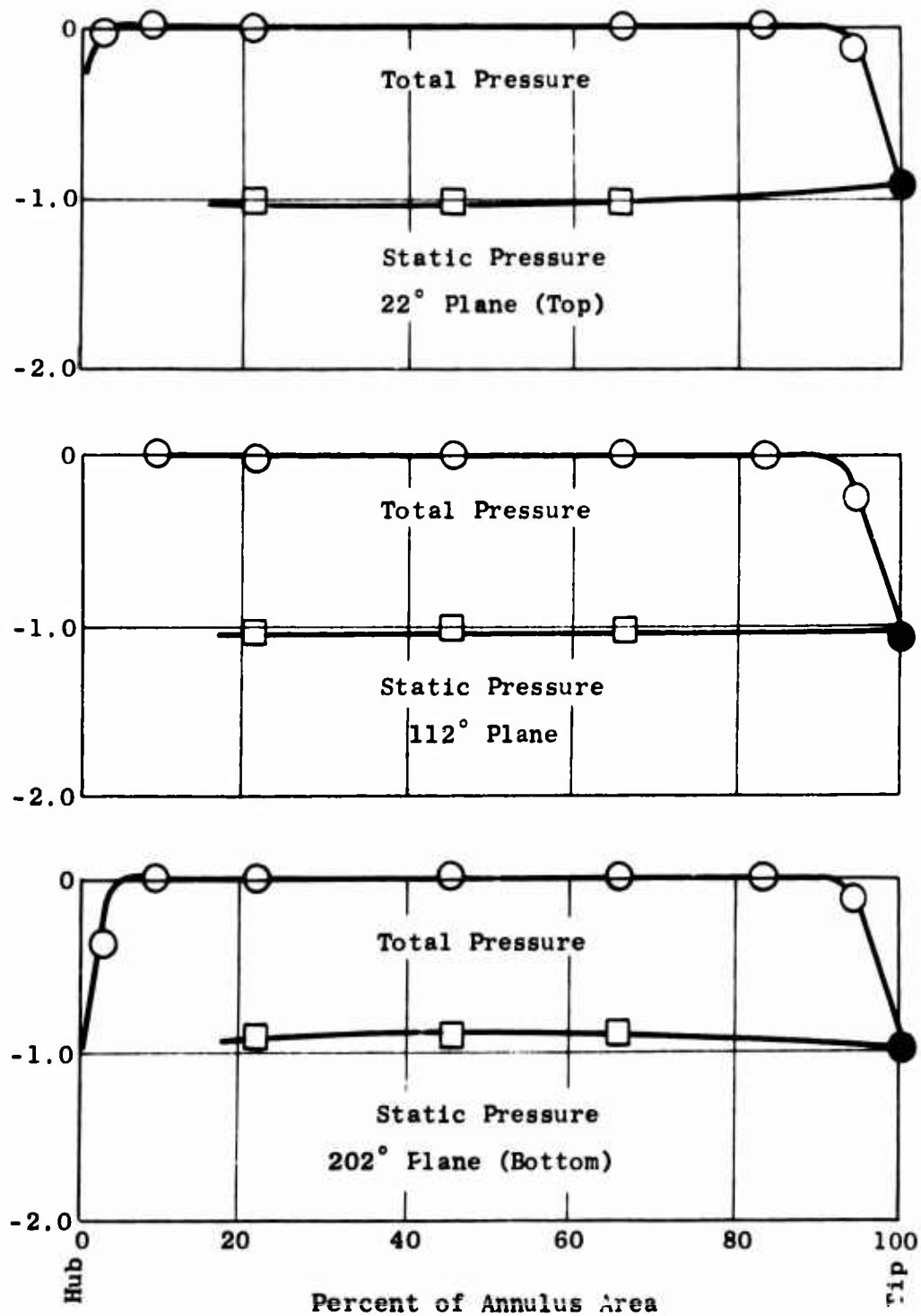
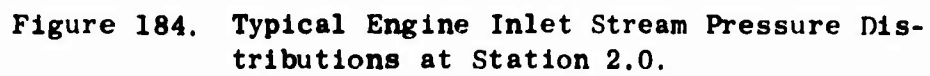
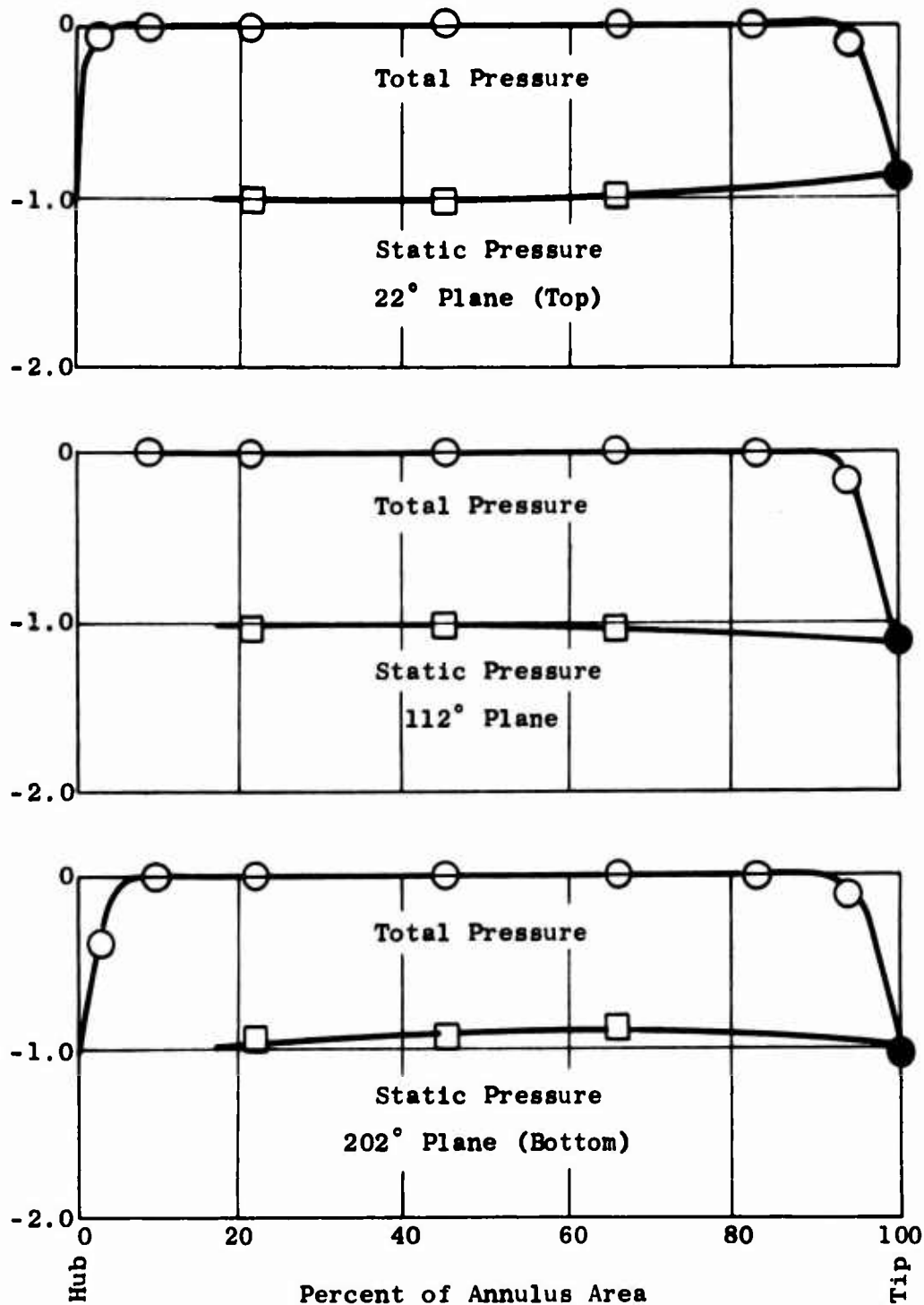


Figure 183. Typical Engine Inlet Stream Pressure Distributions at Station 2.0.

Local Stream Total or Static Pressure Coefficient, $\frac{P_T - P_{TO}}{P_{TO} - P_{S2.0}}$ or $\frac{P_S - P_{TO}}{P_{TO} - P_{S2.0}}$



$$\text{Local Stream Total or Static Pressure Coefficient, } \frac{P_T - P_{TO}}{P_{TO} - P_{S2.0}} \text{ or } \frac{P_S - P_{TO}}{P_{TO} - P_{S2.0}}$$


291

Model 2 $M_0 = 0.80$ $\frac{N_E}{\sqrt{\theta_2}} = 92.0\%$ $\frac{P_{TO} - P_{S2}}{P_{TO}} = 0.052$

Local Stream Total or Static Pressure Coefficient, $\frac{P_T - P_{TO}}{P_{TO} - P_{S2.0}}$ or $\frac{P_S - P_{TO}}{P_{TO} - P_{S2.0}}$

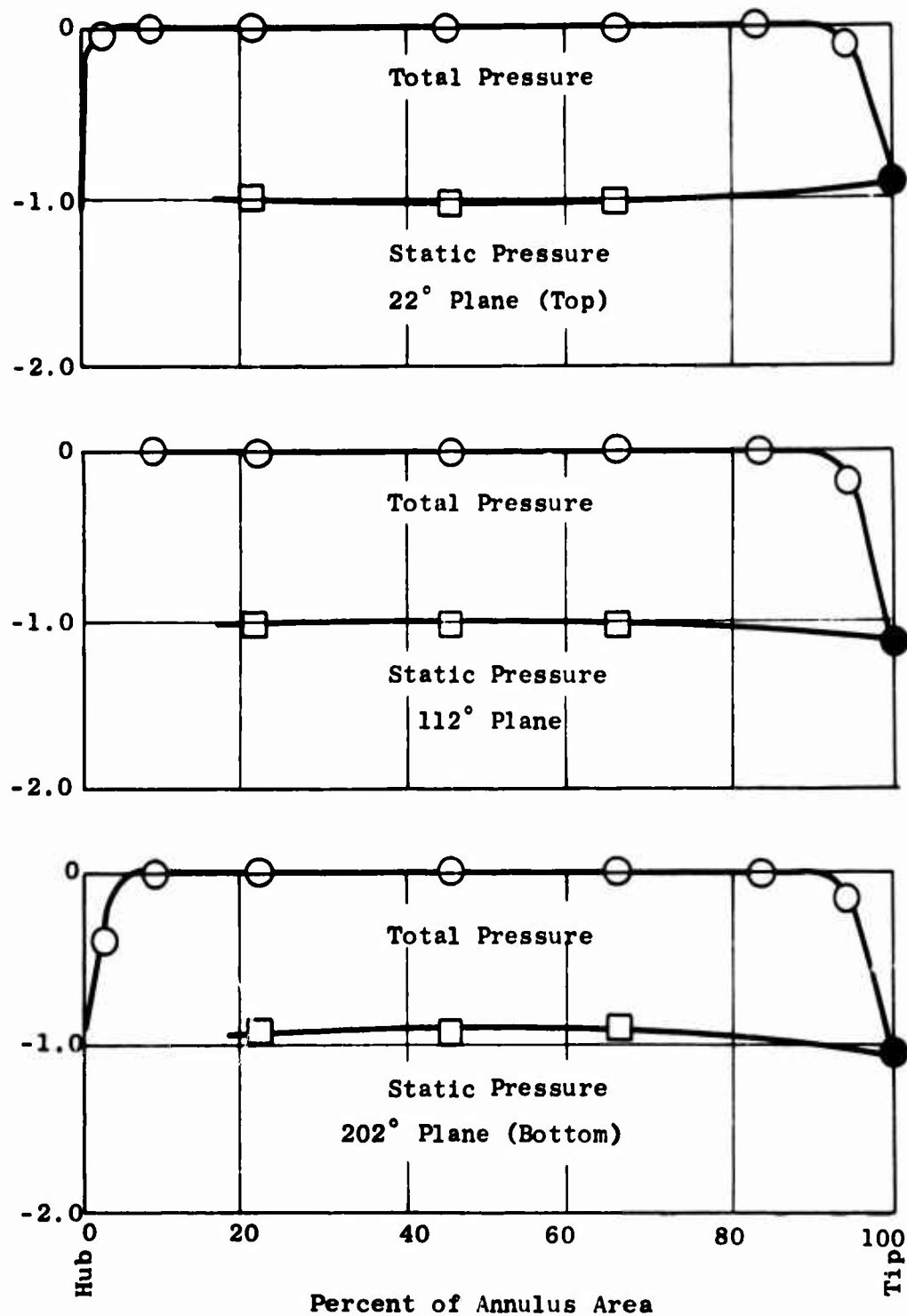


Figure 186. Typical Engine Inlet Stream Pressure Distributions at Station 2.0.

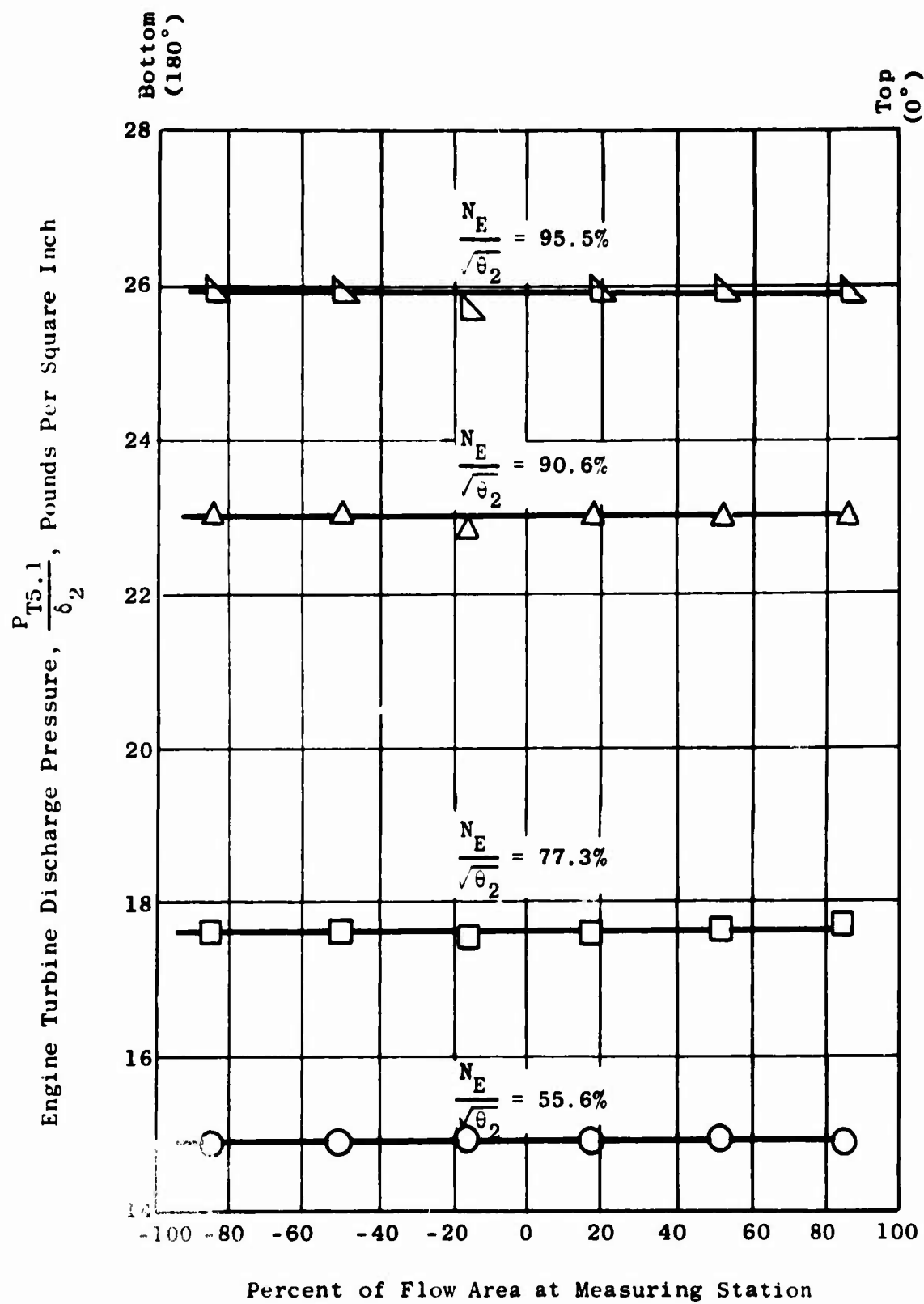


Figure 187. Typical Engine Discharge Total Pressure Distributions - Model 3, $M_0 = 0.50$.

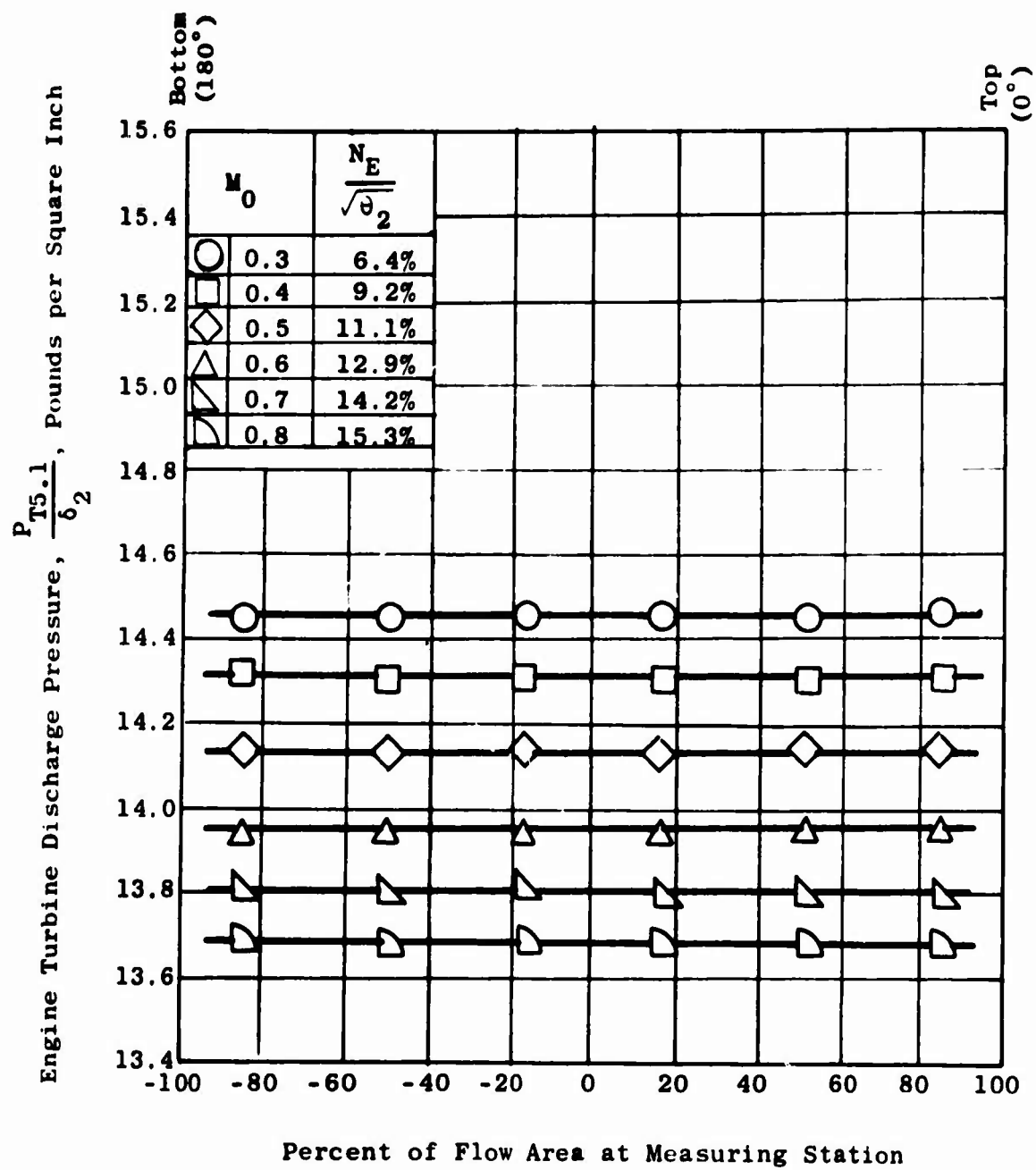


Figure 188. Typical Engine Discharge Total Pressure Distributions During Windmill - Model 6.

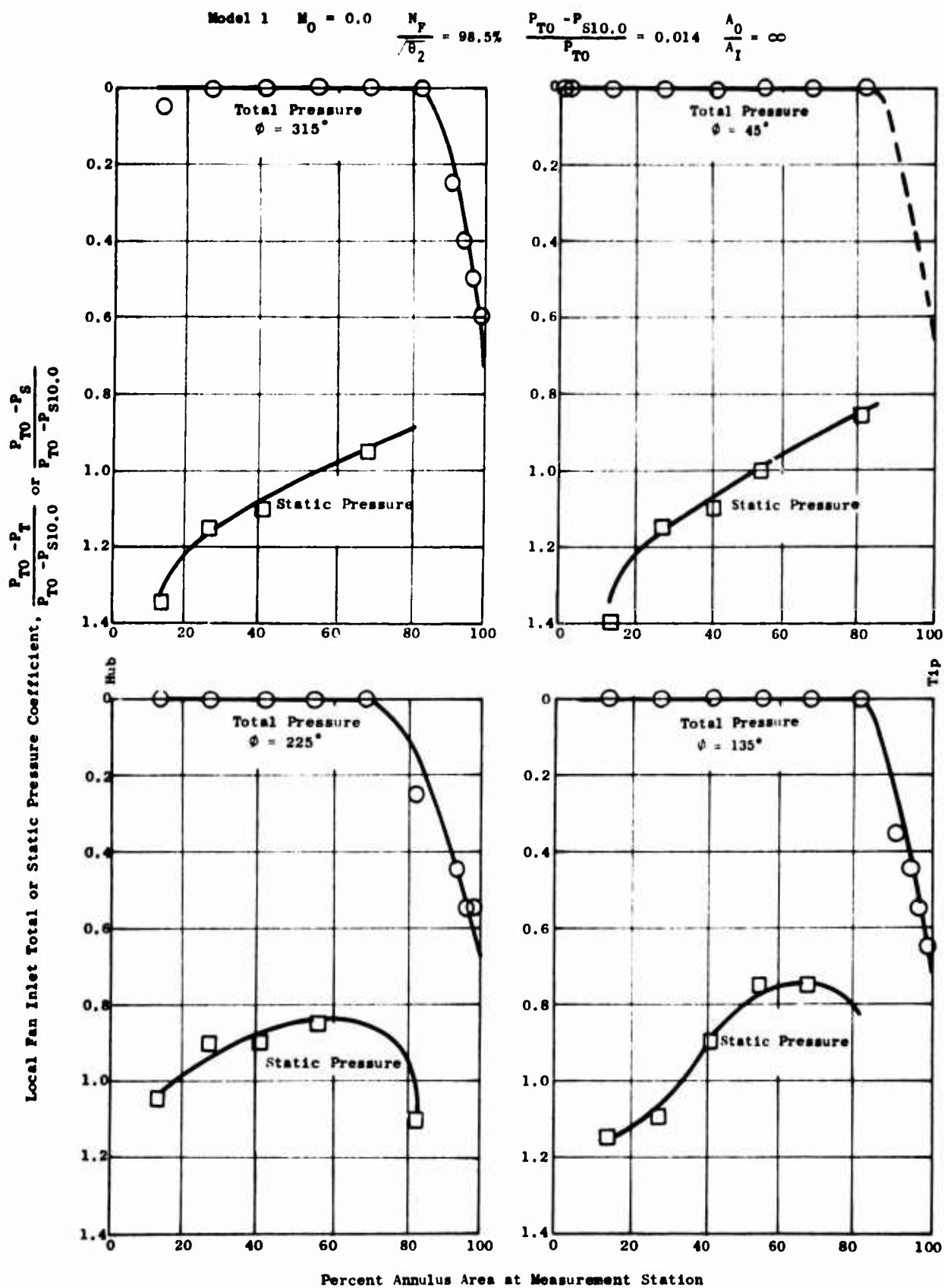


Figure 189. Fan Rotor Inlet Pressure Distributions - Model 1, $M_0 = 0.0$.

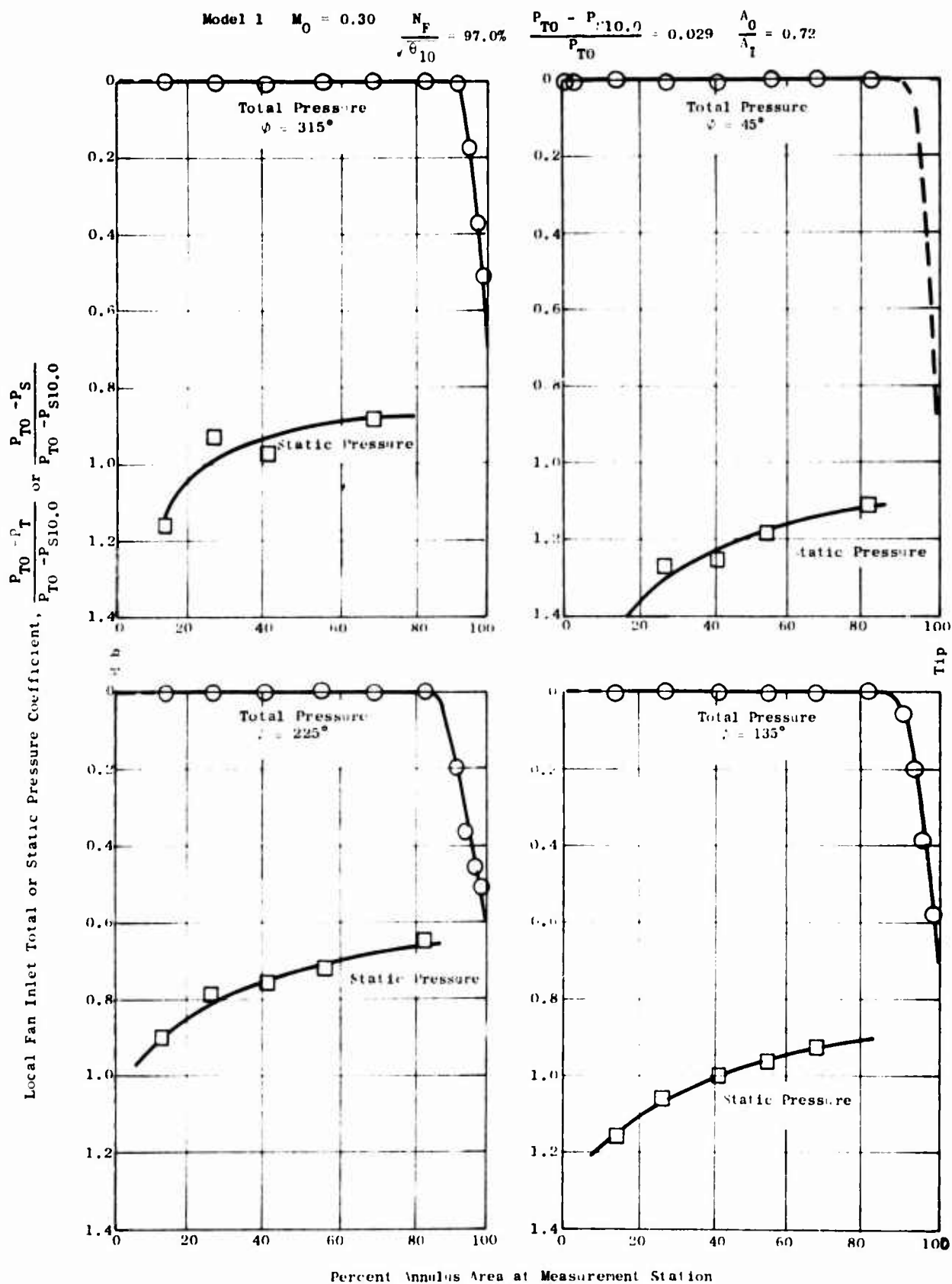


Figure 190. Fan Rotor Inlet Pressure Distributions - Model 1, $M_0 = 0.3$.

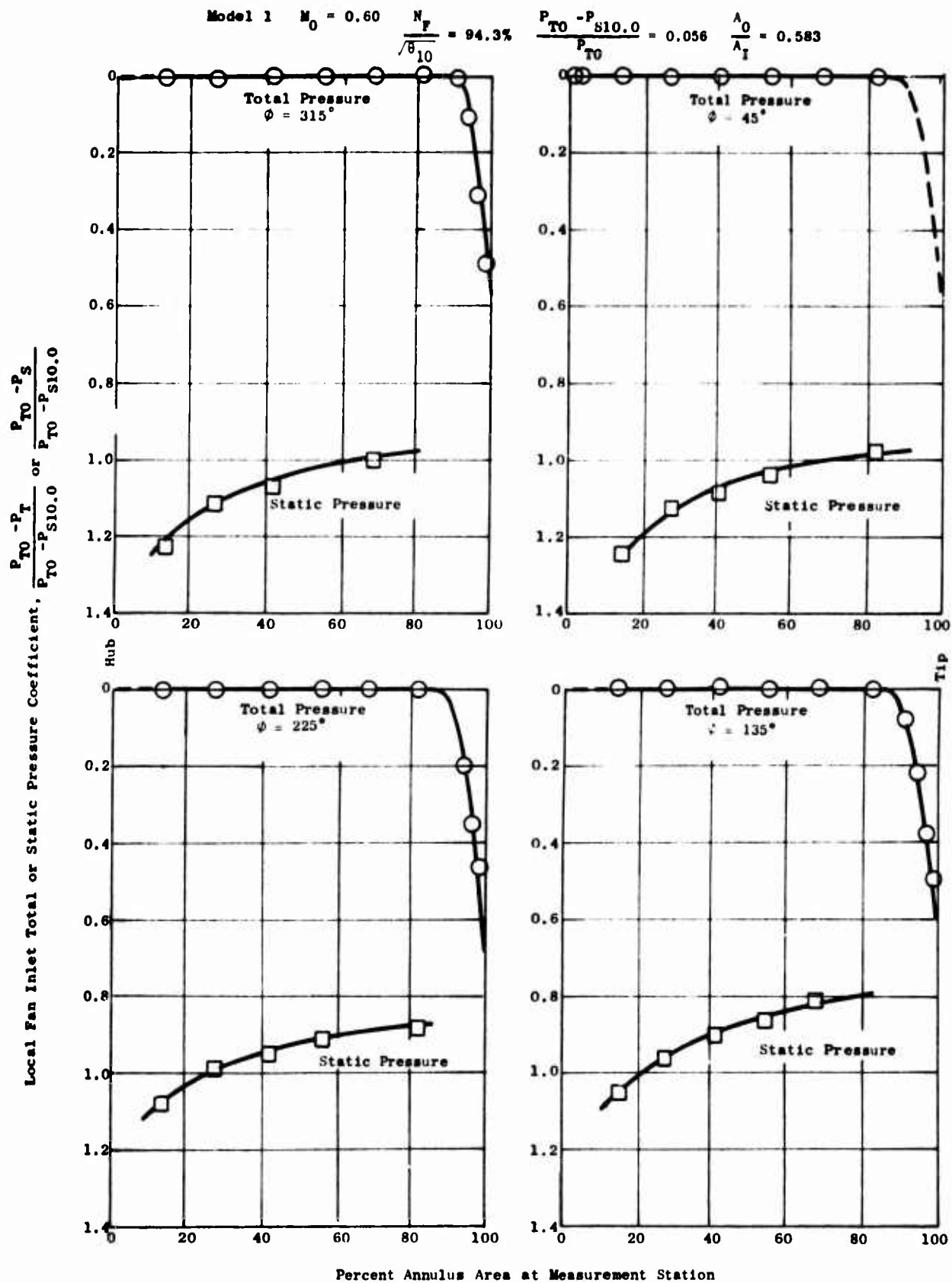


Figure 191. Fan Rotor Inlet Pressure Distributions - Model 1, $M_0 = 0.6$.

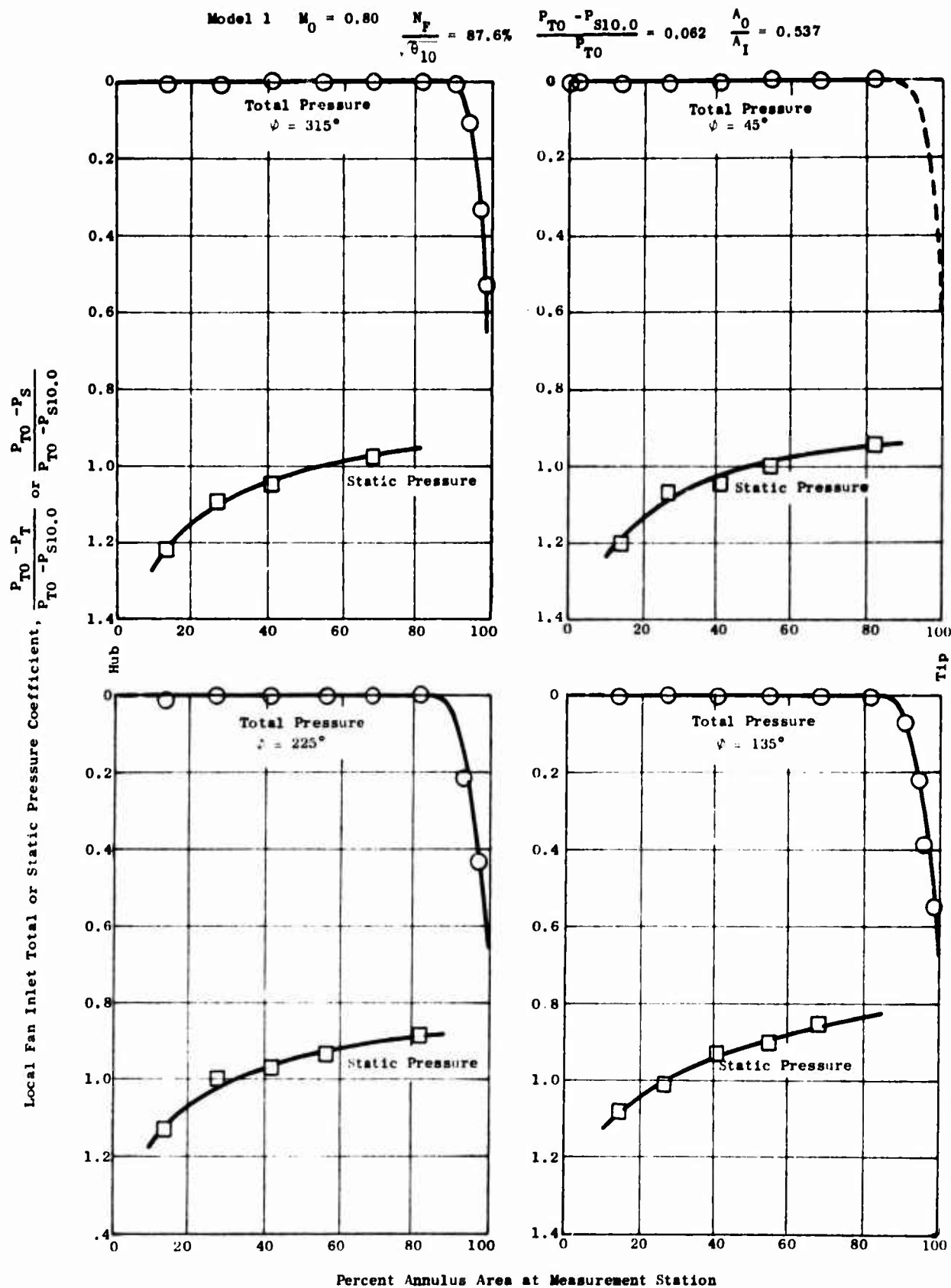


Figure 192. Fan Rotor Inlet Pressure Distributions - Model 1, $M_0 = 0.8$.

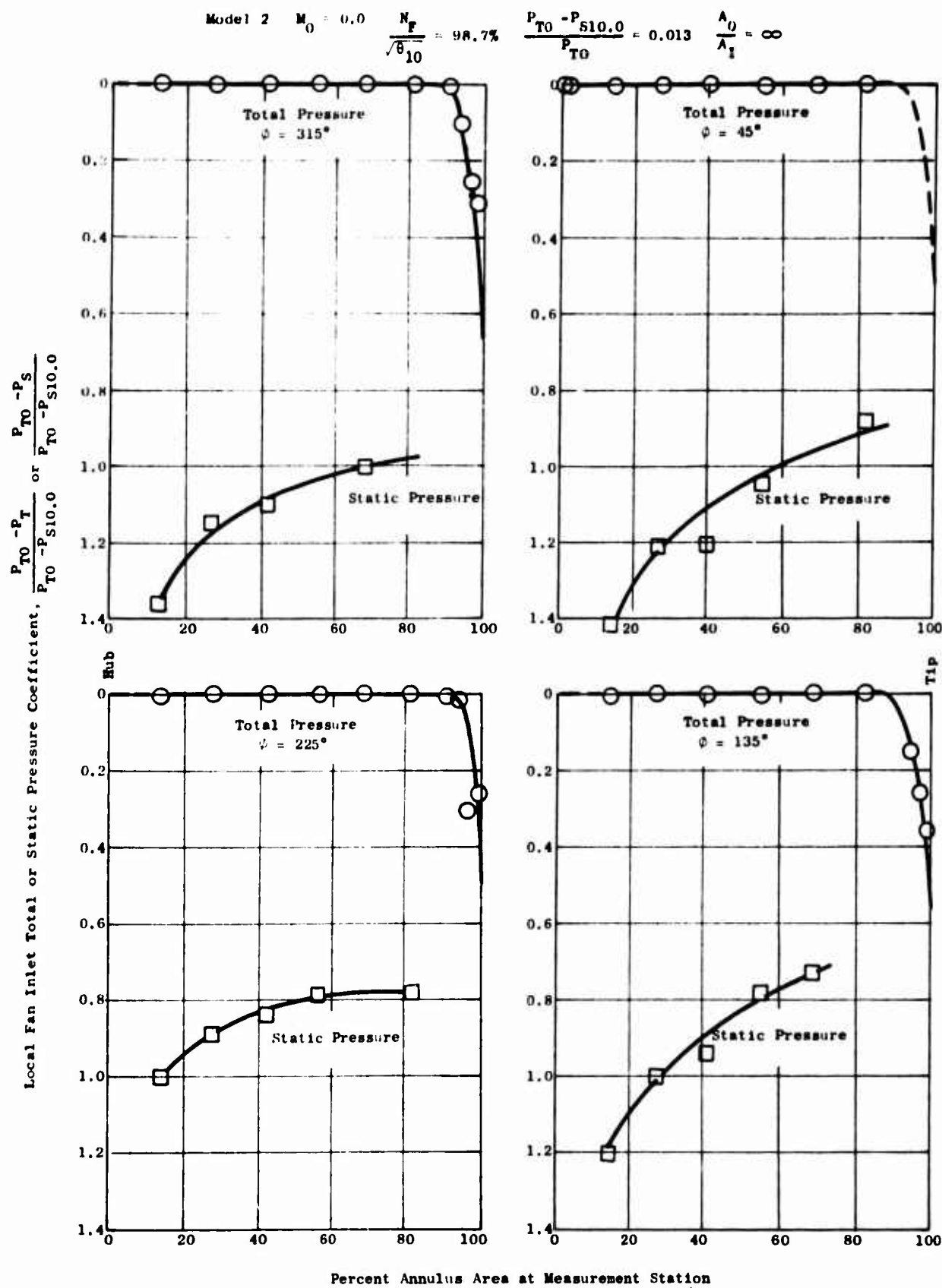


Figure 193. Fan Rotor Inlet Pressure Distributions - Model 2, $M_0 = 0.0$.

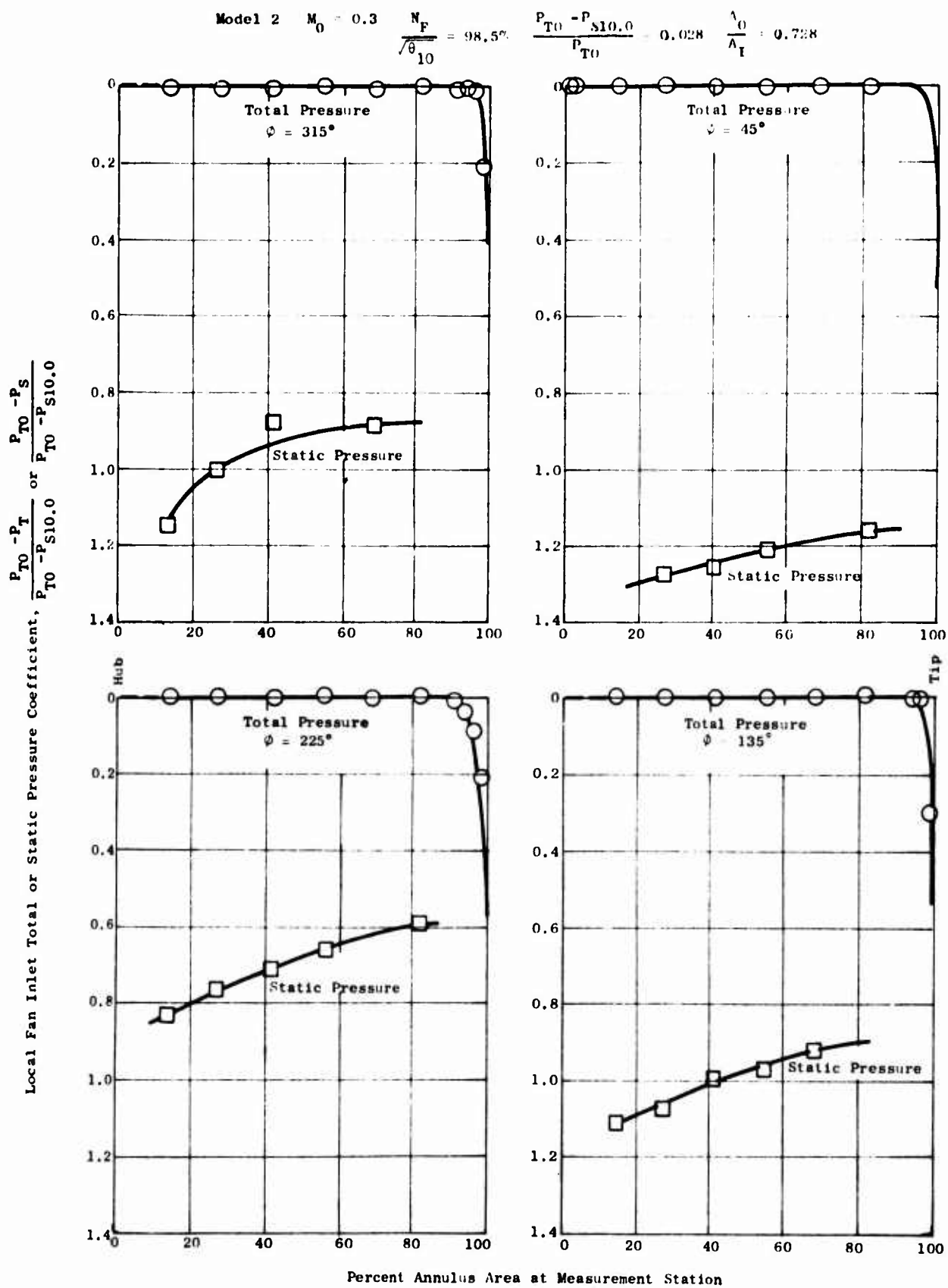


Figure 194. Fan Rotor Inlet Pressure Distributions - Model 2, $M_0 = 0.3$.

Model 2 $M_0 = 0.6$ $\frac{N_F}{\theta_{10}} = 91.5\%$ $\frac{P_{T0} - P_{S10.0}}{P_{T0}} = 0.052$ $\frac{\lambda_0}{\lambda_1} = 0.563$

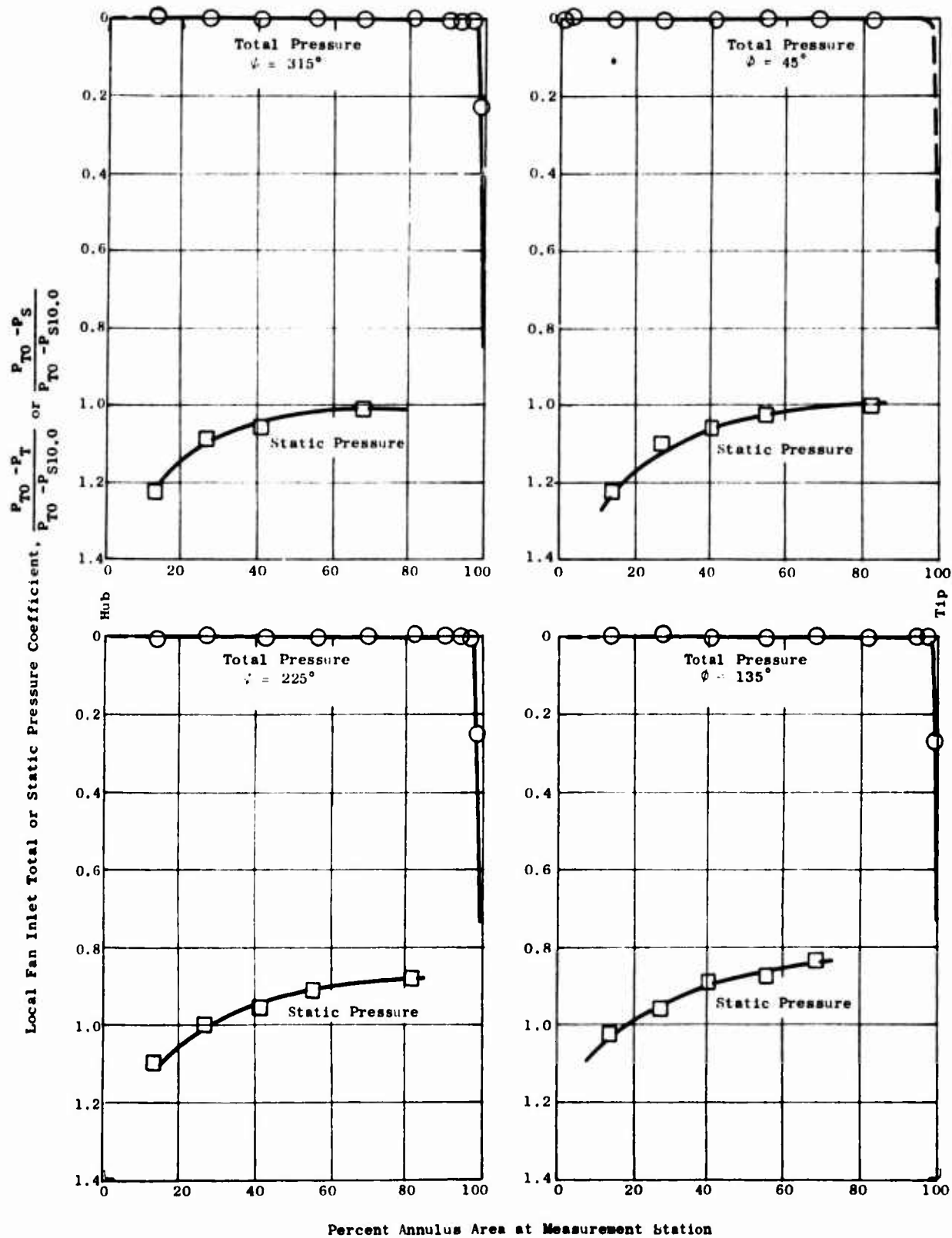


Figure 195. Fan Rotor Inlet Pressure Distributions - Model 2, $M_0 = 0.6$.

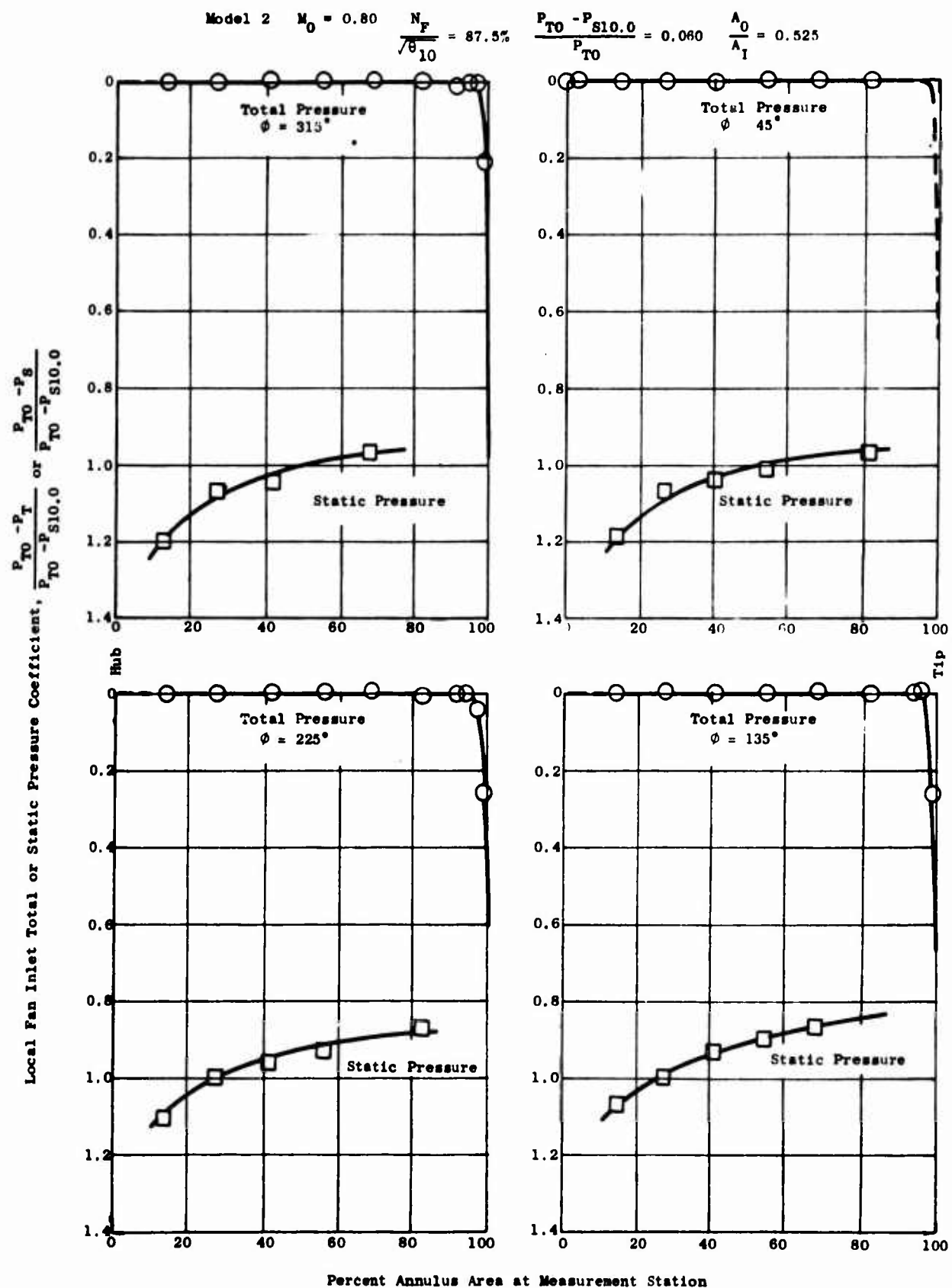


Figure 196. Fan Rotor Inlet Pressure Distributions - Model 2, $M_0 = 0.8$.

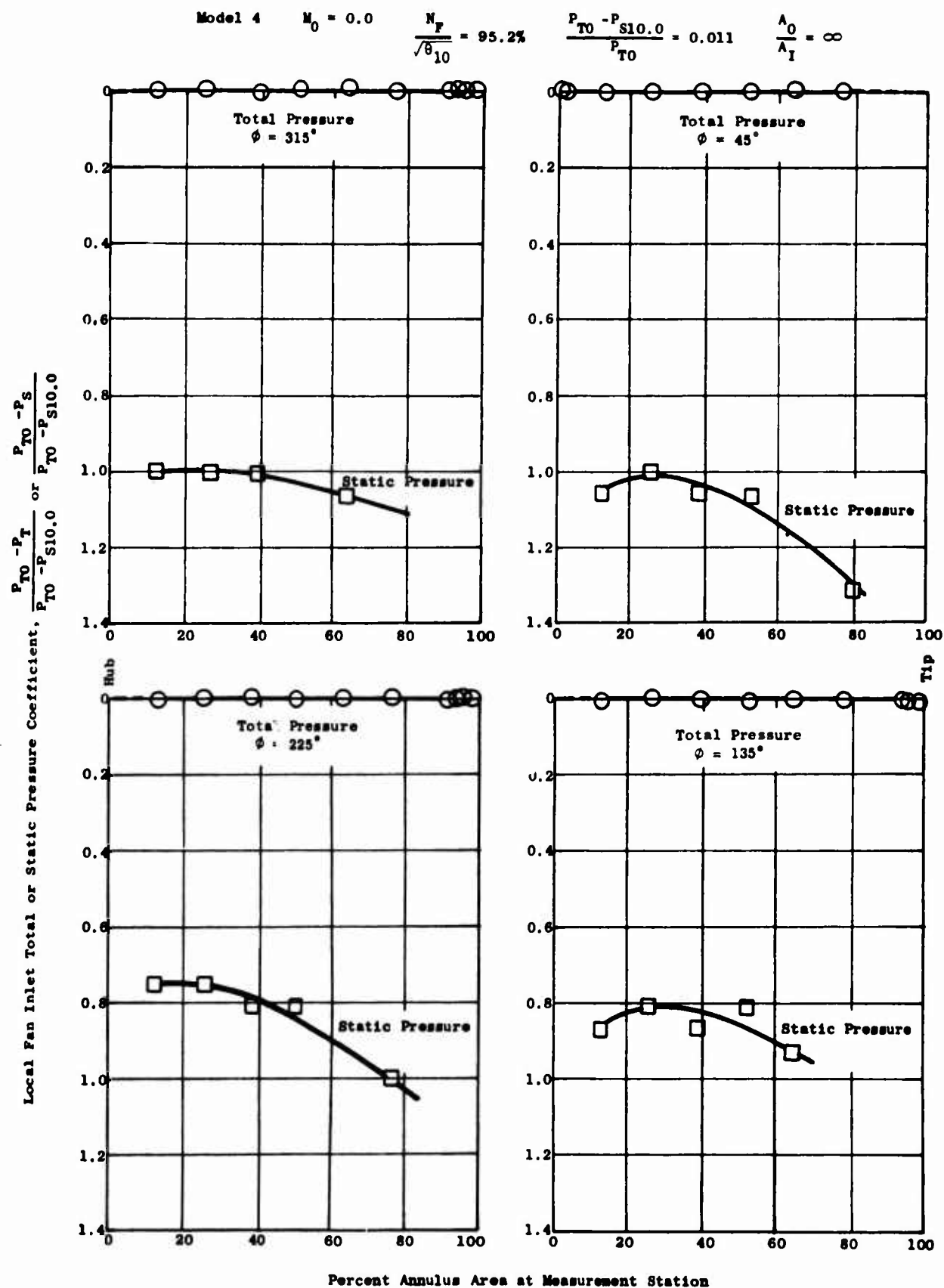


Figure 197. Fan Rotor Inlet Pressure Distributions - Model 4, $M_0 = 0.0$.

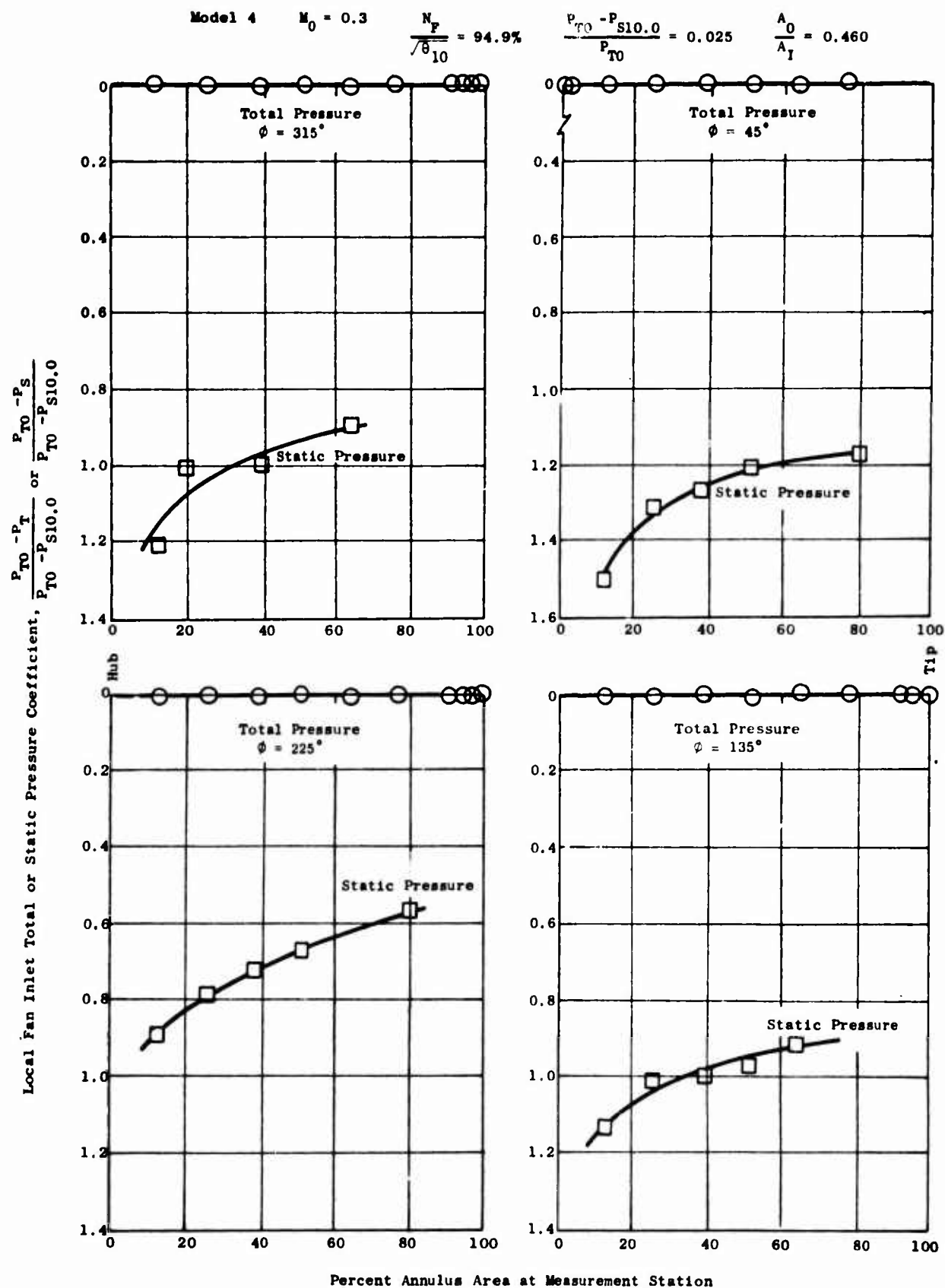


Figure 198. Fan Rotor Inlet Pressure Distributions - Model 4, $M_0 = 0.3$.

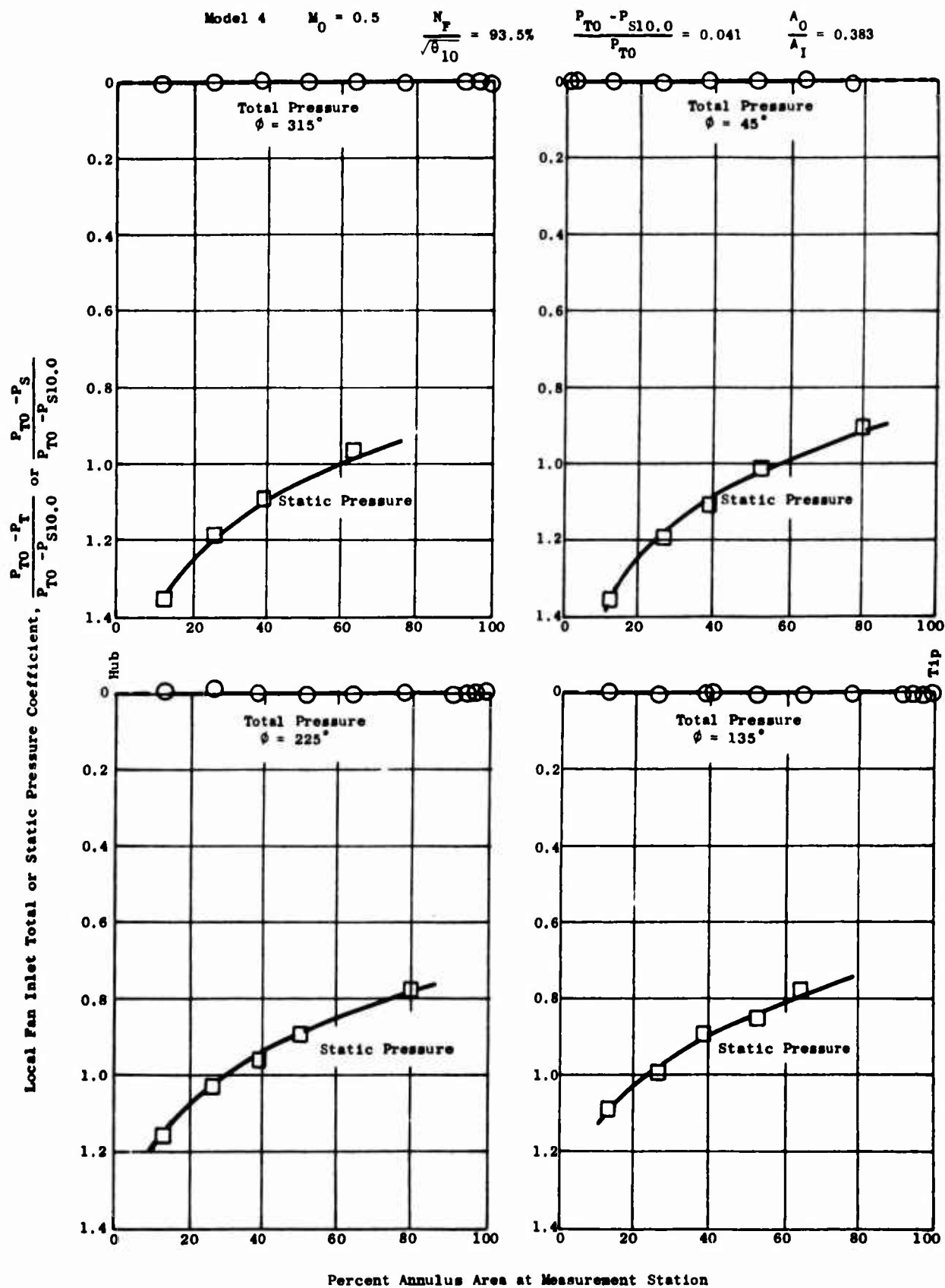


Figure 199. Fan Rotor Inlet Pressure Distributions - Model 4, $M_0 = 0.5$.

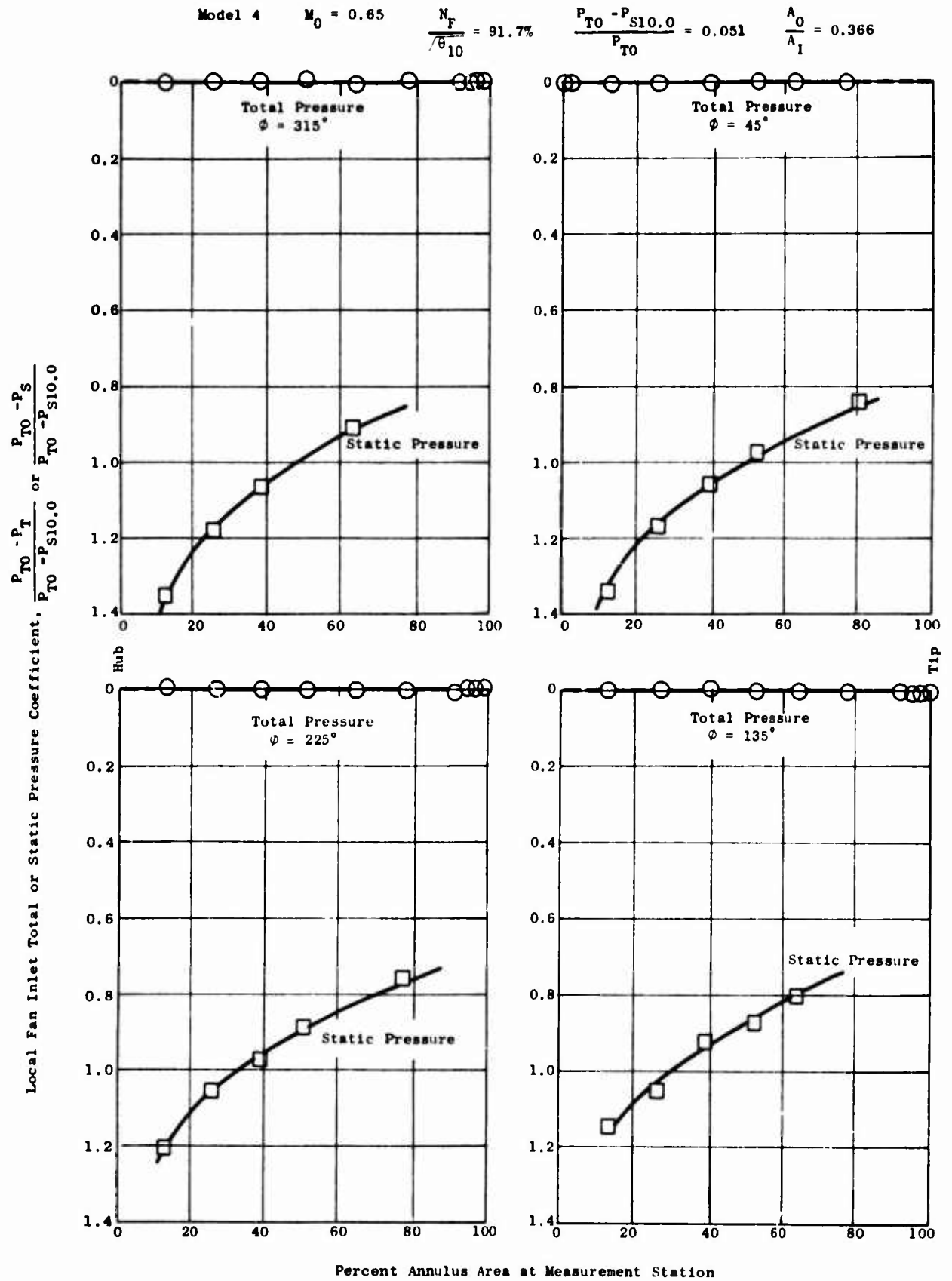


Figure 200. Fan Rotor Inlet Pressure Distributions - Model 4, $M_0 = 0.65$.

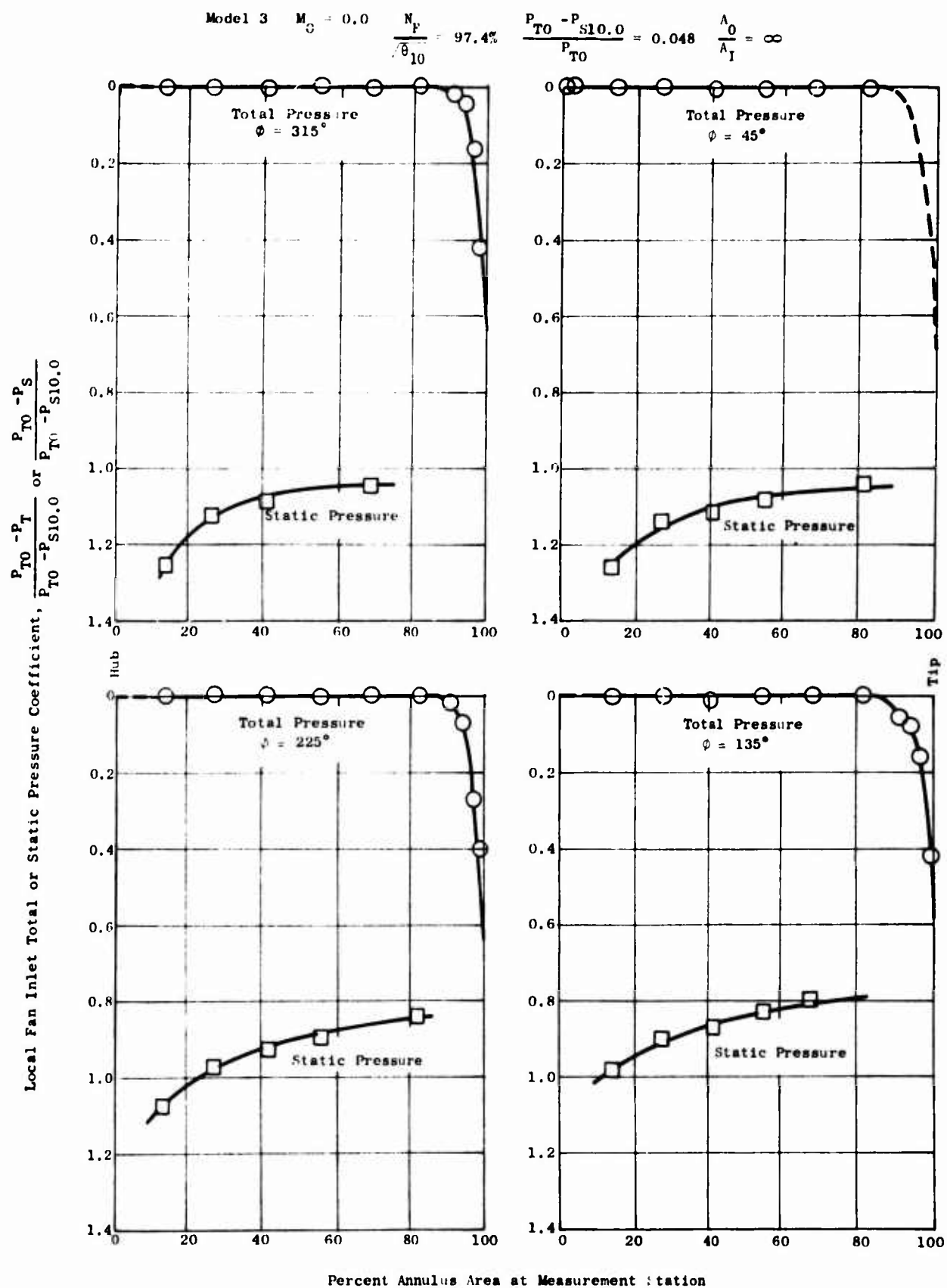


Figure 201. Fan Rotor Inlet Pressure Distributions - Model 3, $M_0 = 0.0$.

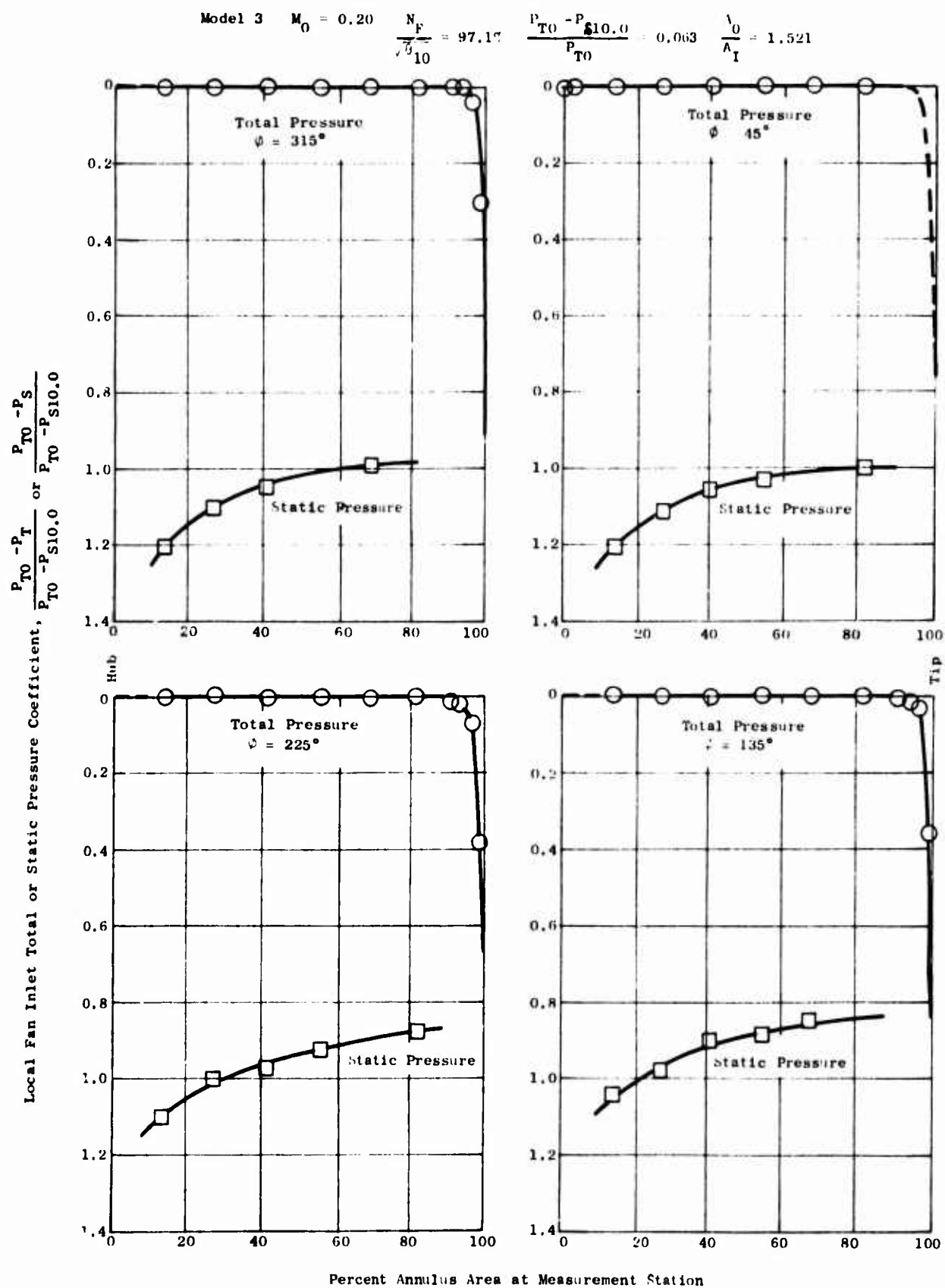


Figure 202. Fan Rotor Inlet Pressure Distributions - Model 3, $M_0 = 0.2$.

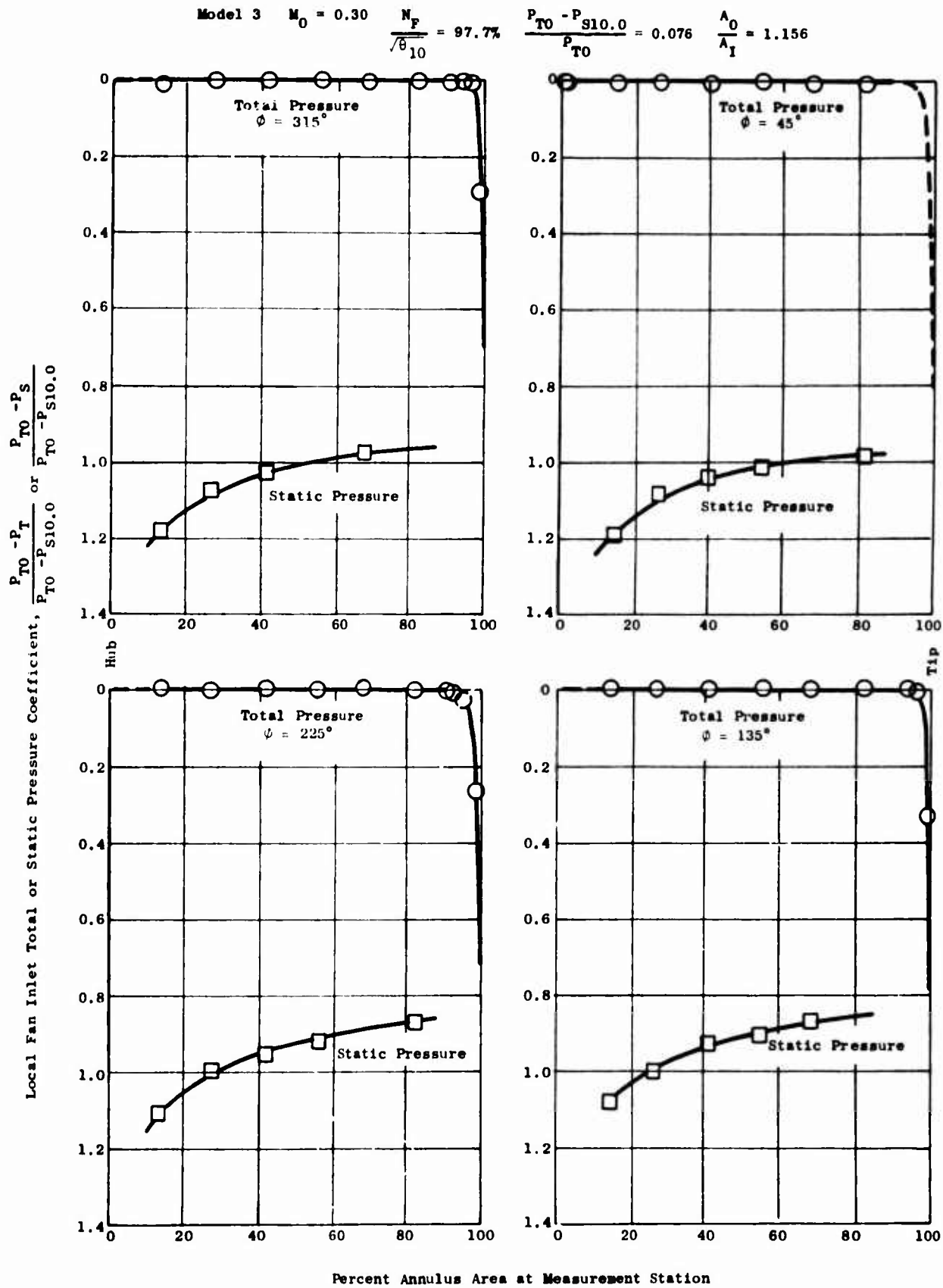


Figure 203. Fan Rotor Inlet Pressure Distributions - Model 3, $M_0 = 0.3$.

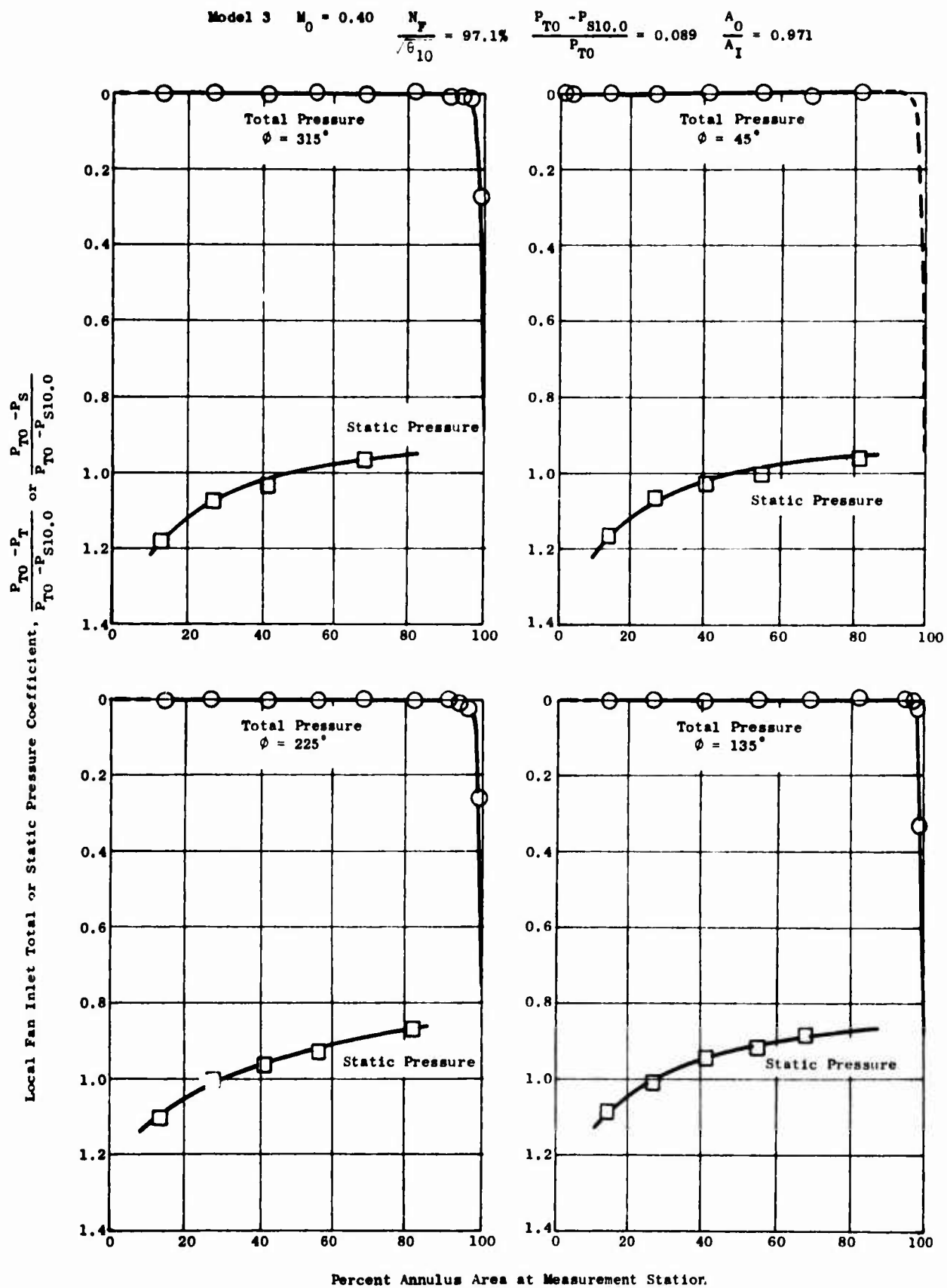


Figure 204. Fan Rotor Inlet Pressure Distributions - Model 3, $M_0 = 0.4$.

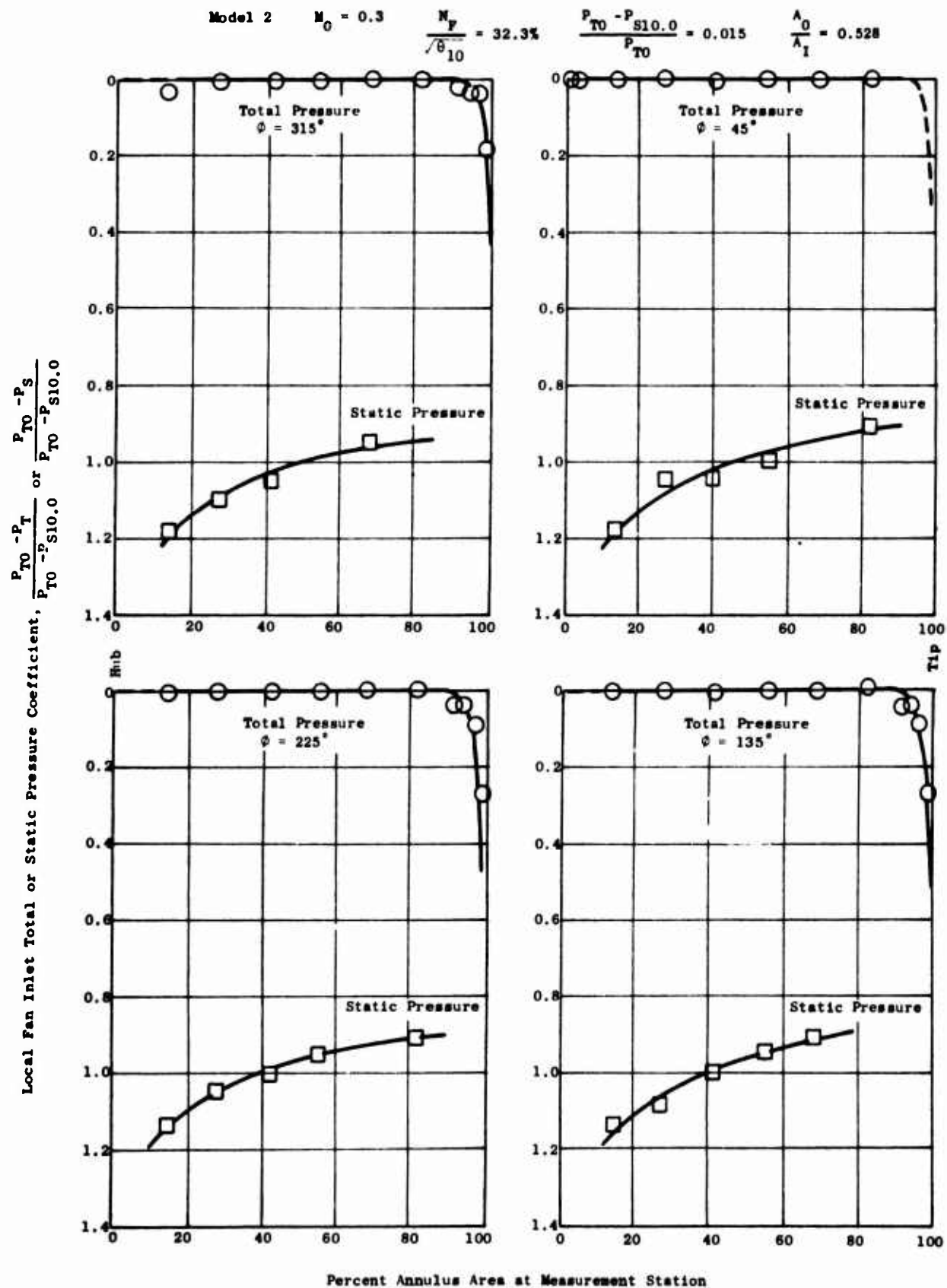


Figure 205. Fan Rotor Inlet Pressure Distributions During Windmilling - $M_0 = 0.3$.

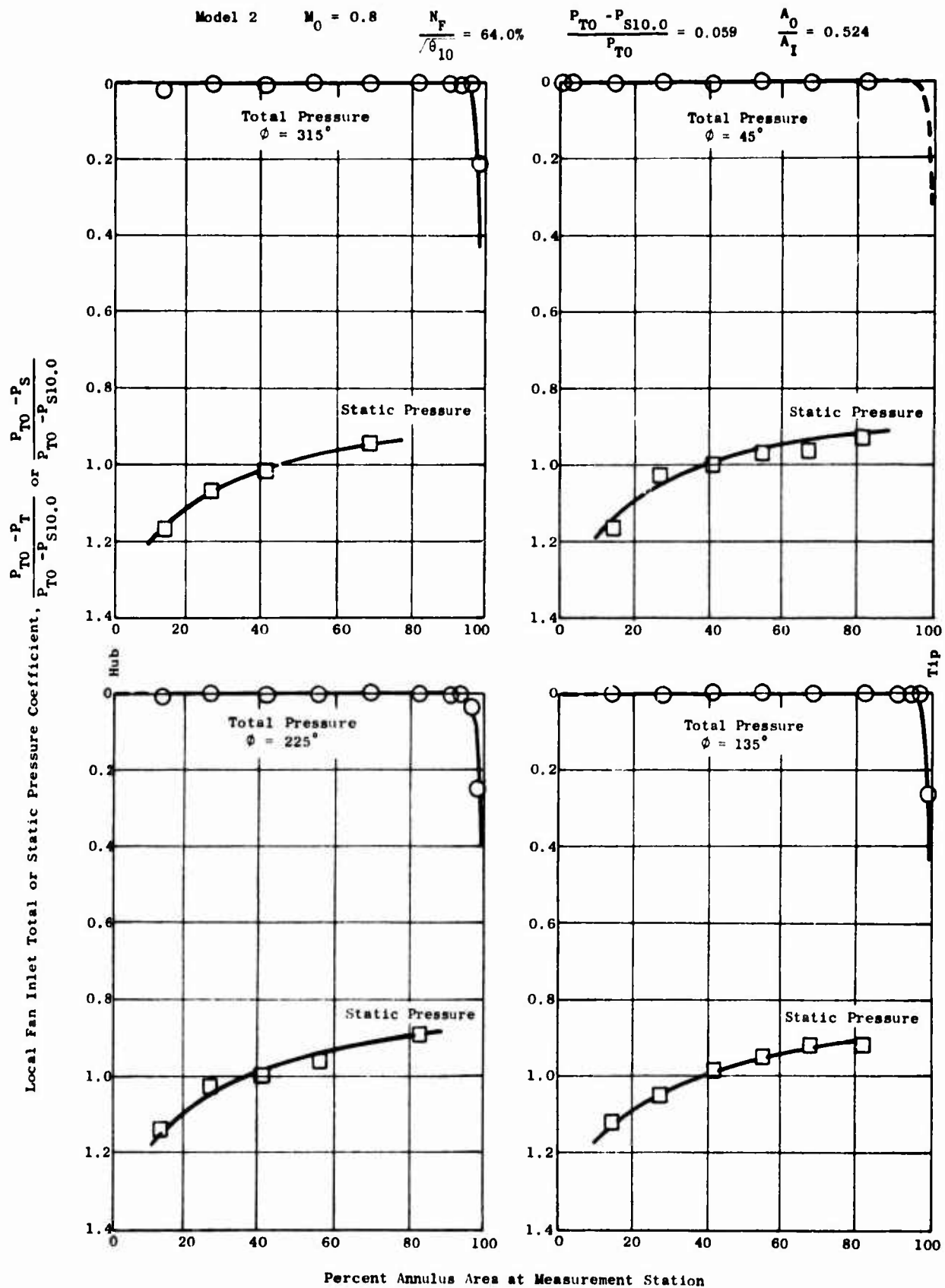


Figure 206. Fan Rotor Inlet Pressure Distributions During Windmilling - $M_0 = 0.8$.

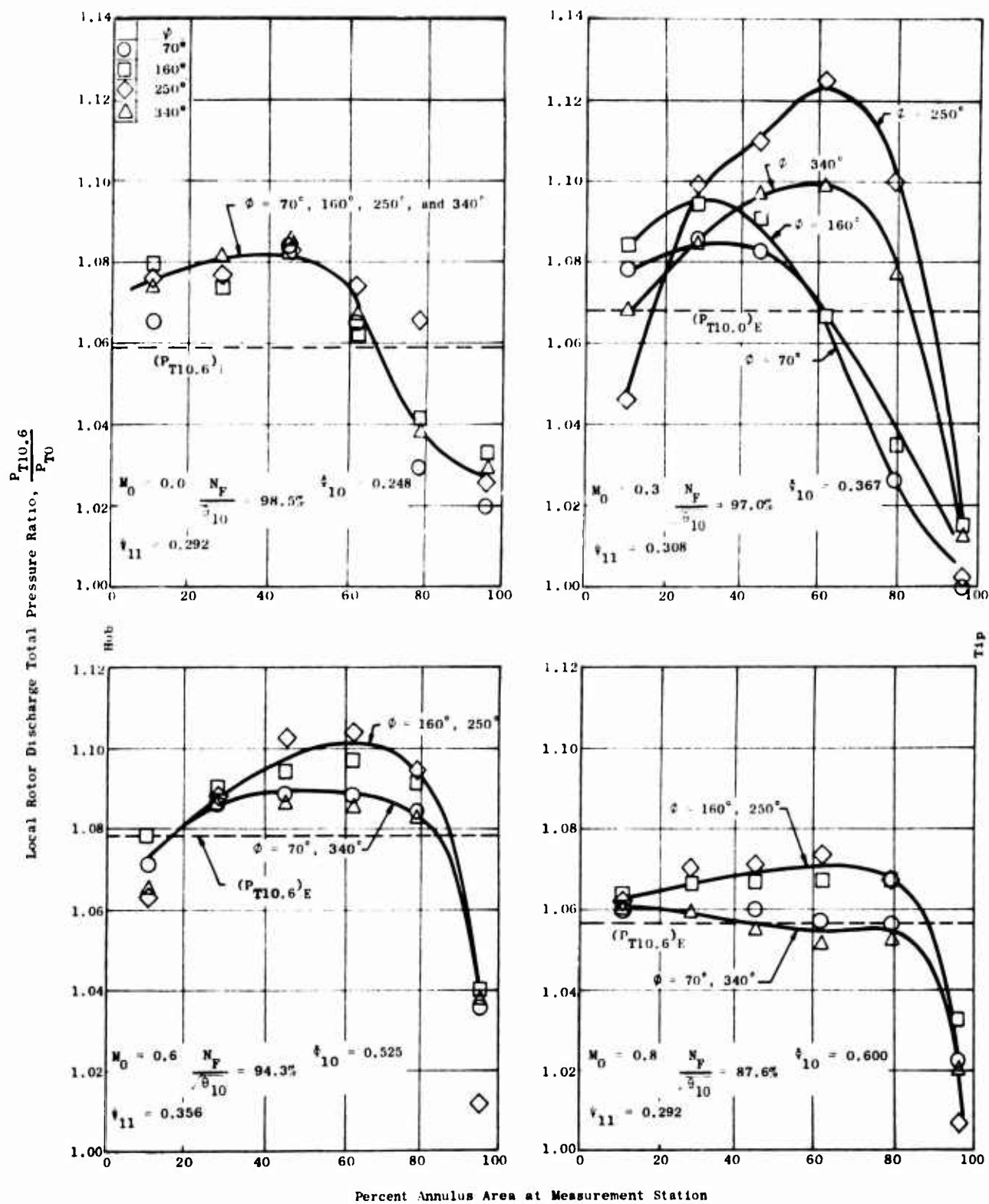


Figure 207. Fan Rotor Discharge Total Pressure Distributions - Model 1.

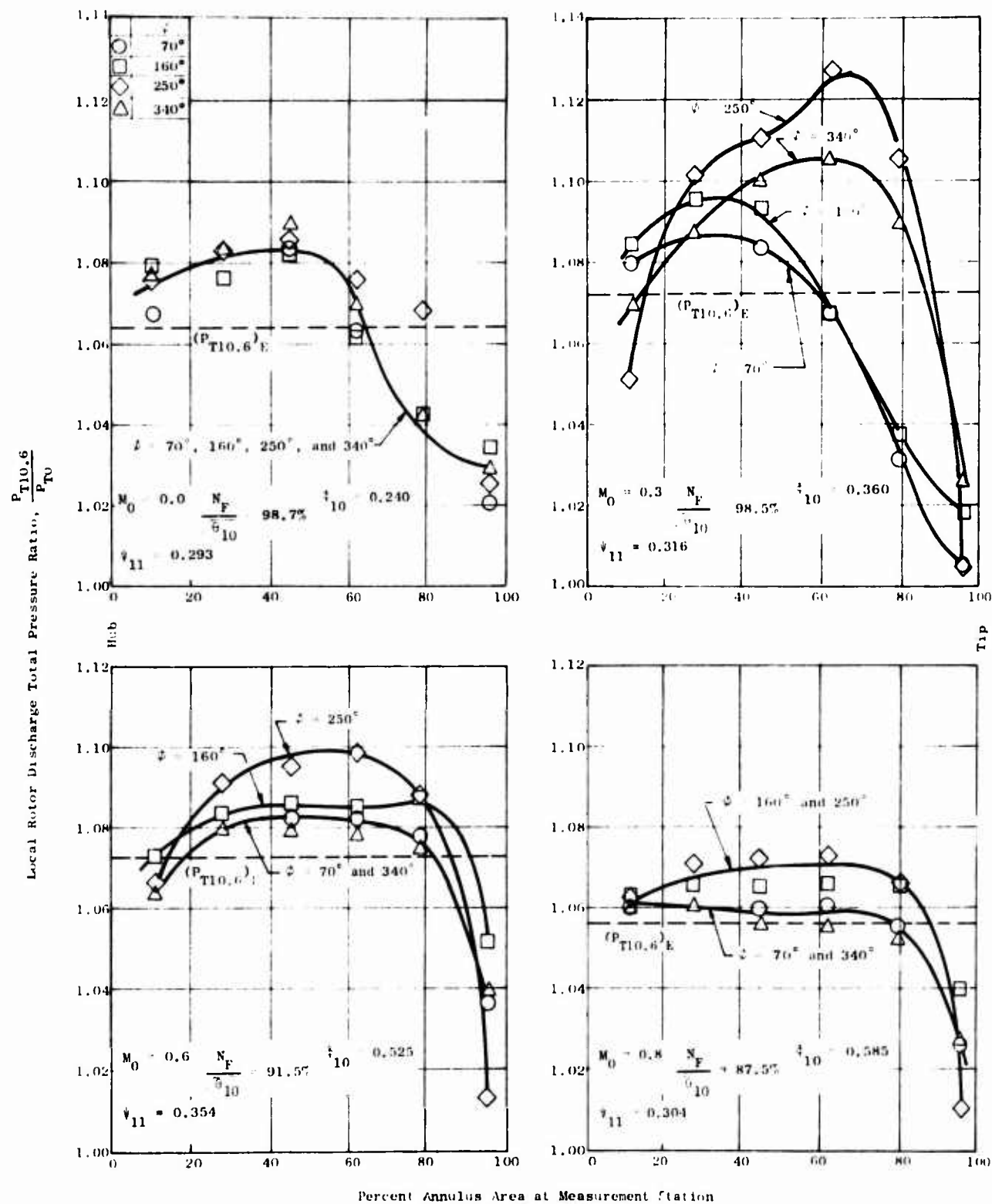


Figure 208. Fan Rotor Discharge Total Pressure Distributions - Model 2.

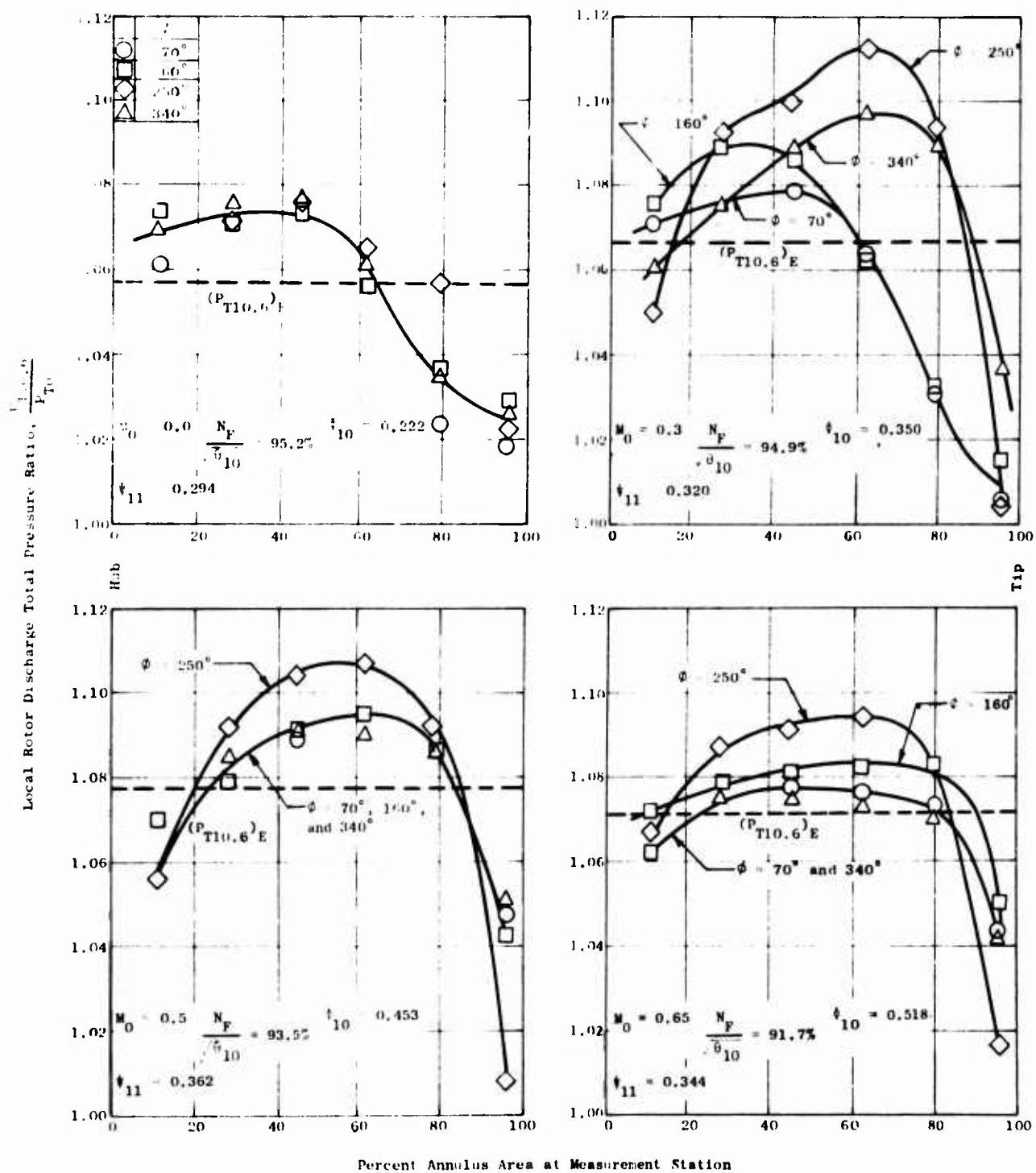


Figure 209. Fan Rotor Discharge Total Pressure Distributions - Model 4.

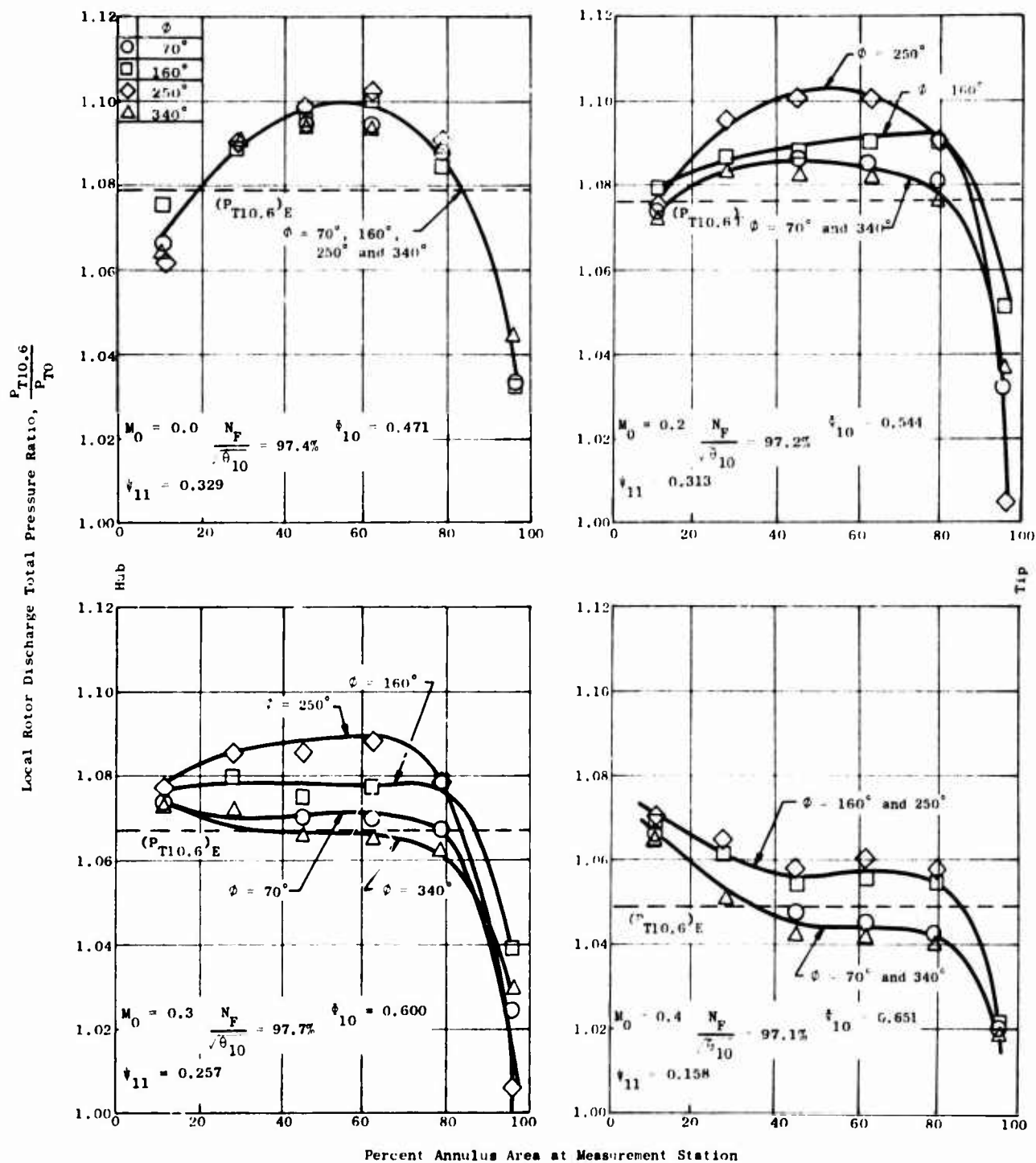


Figure 210. Fan Rotor Discharge Total Pressure Distributions - Model 3.

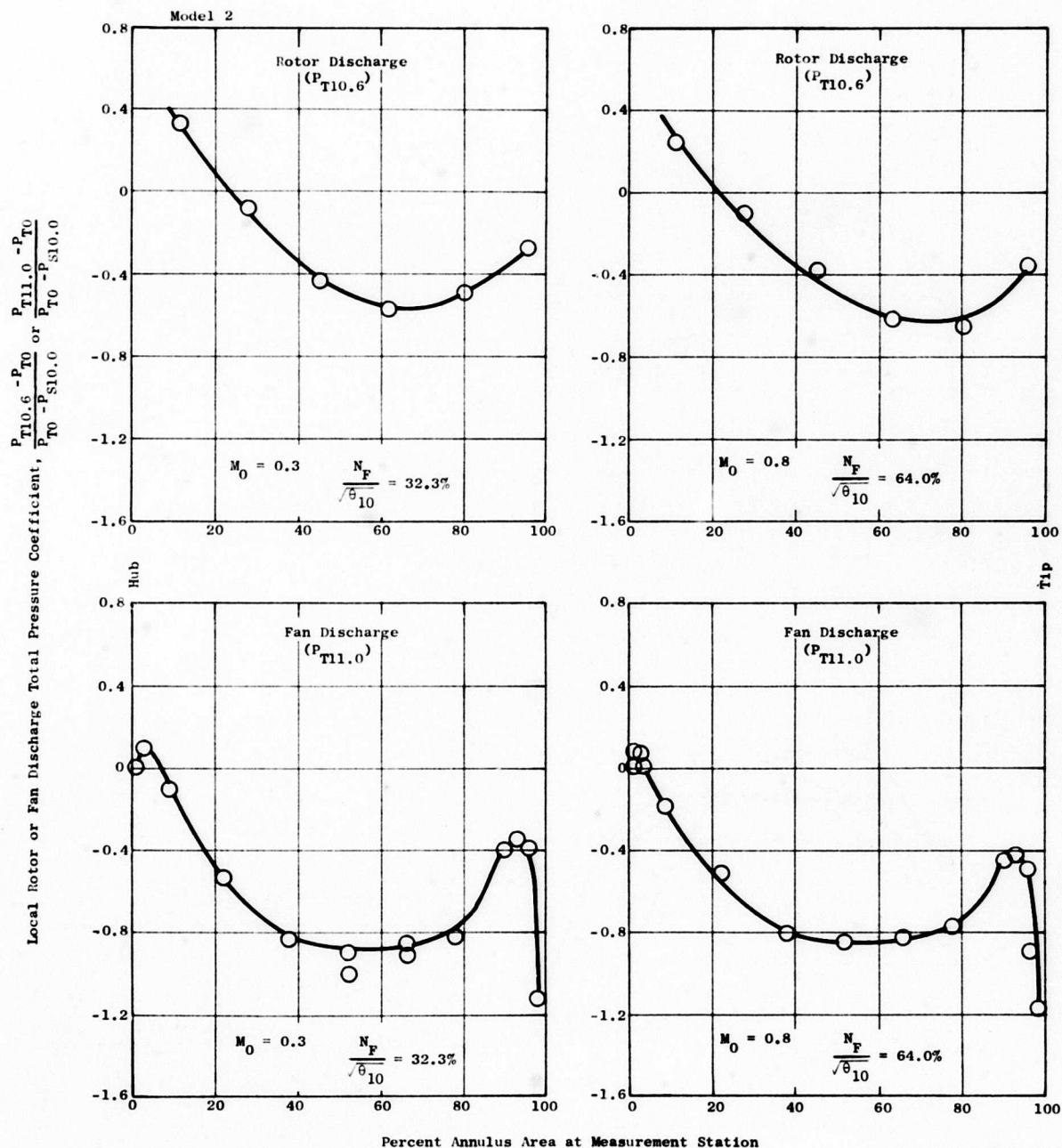


Figure 211. Fan Discharge Total Pressure Distributions During Wind-milling.

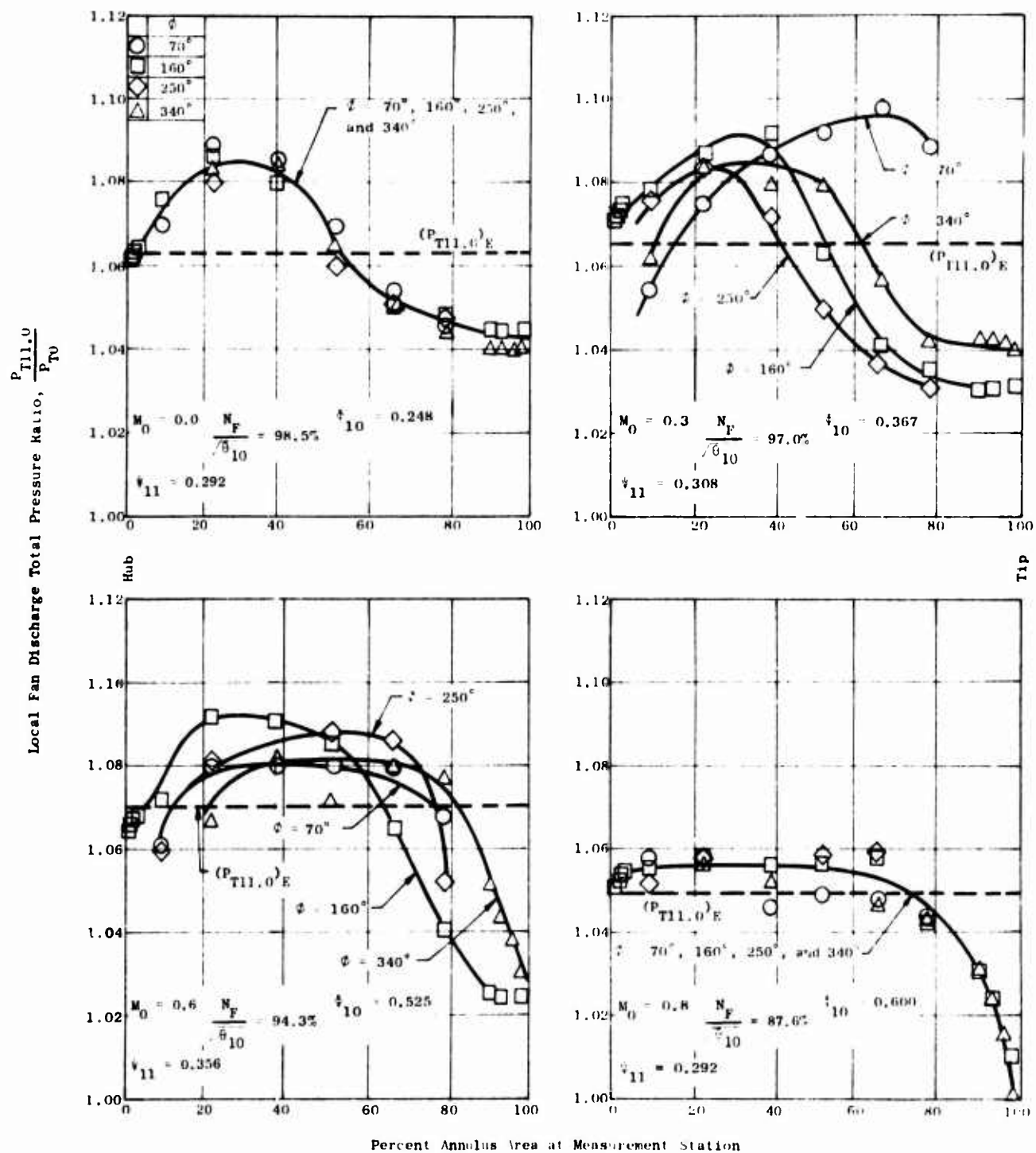


Figure 212. Fan Discharge Total Pressure Distributions - Model 1.

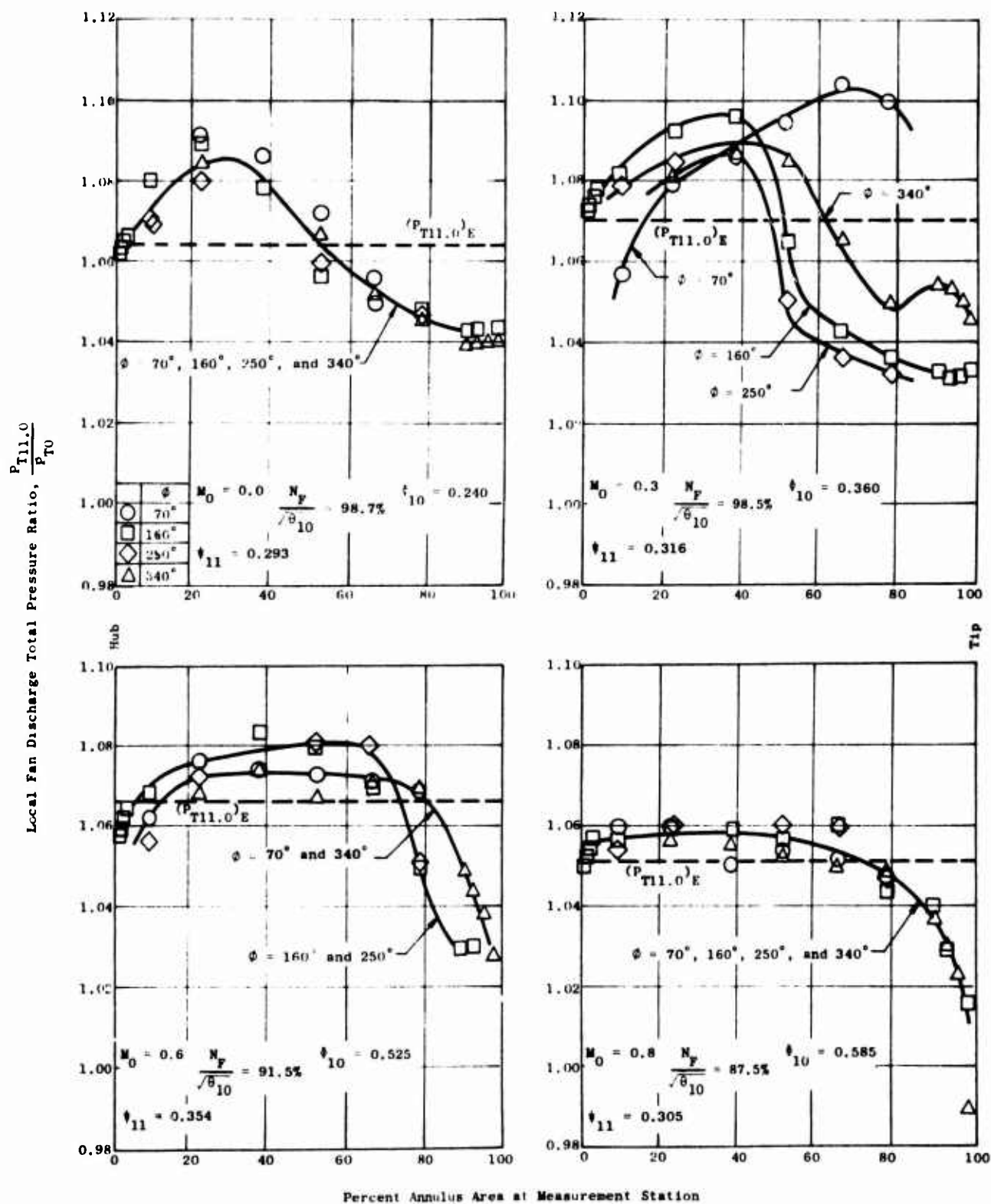


Figure 213. Fan Discharge Total Pressure Distributions - Model 2.

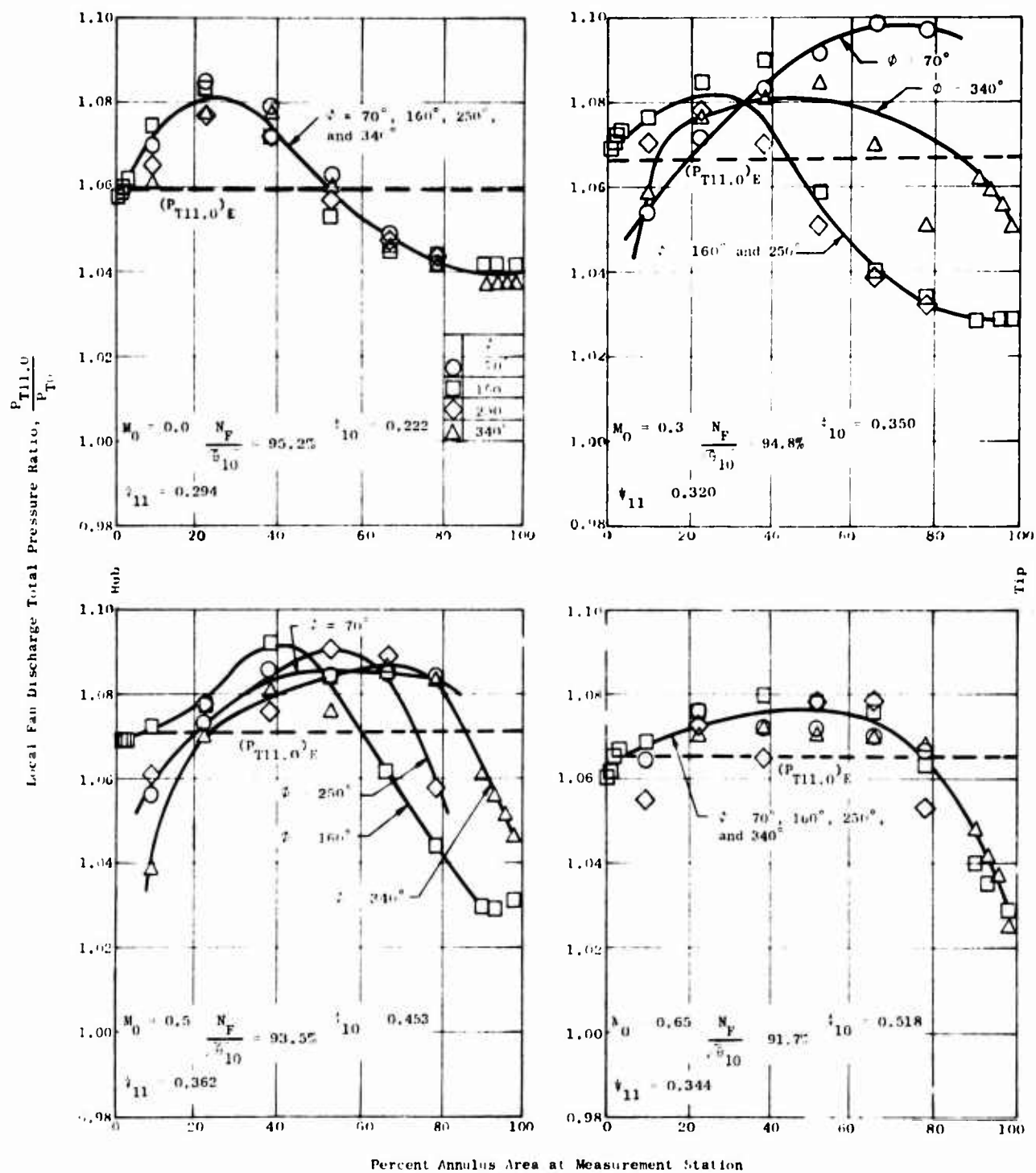


Figure 214. Fan Discharge Total Pressure Distributions - Model 4.

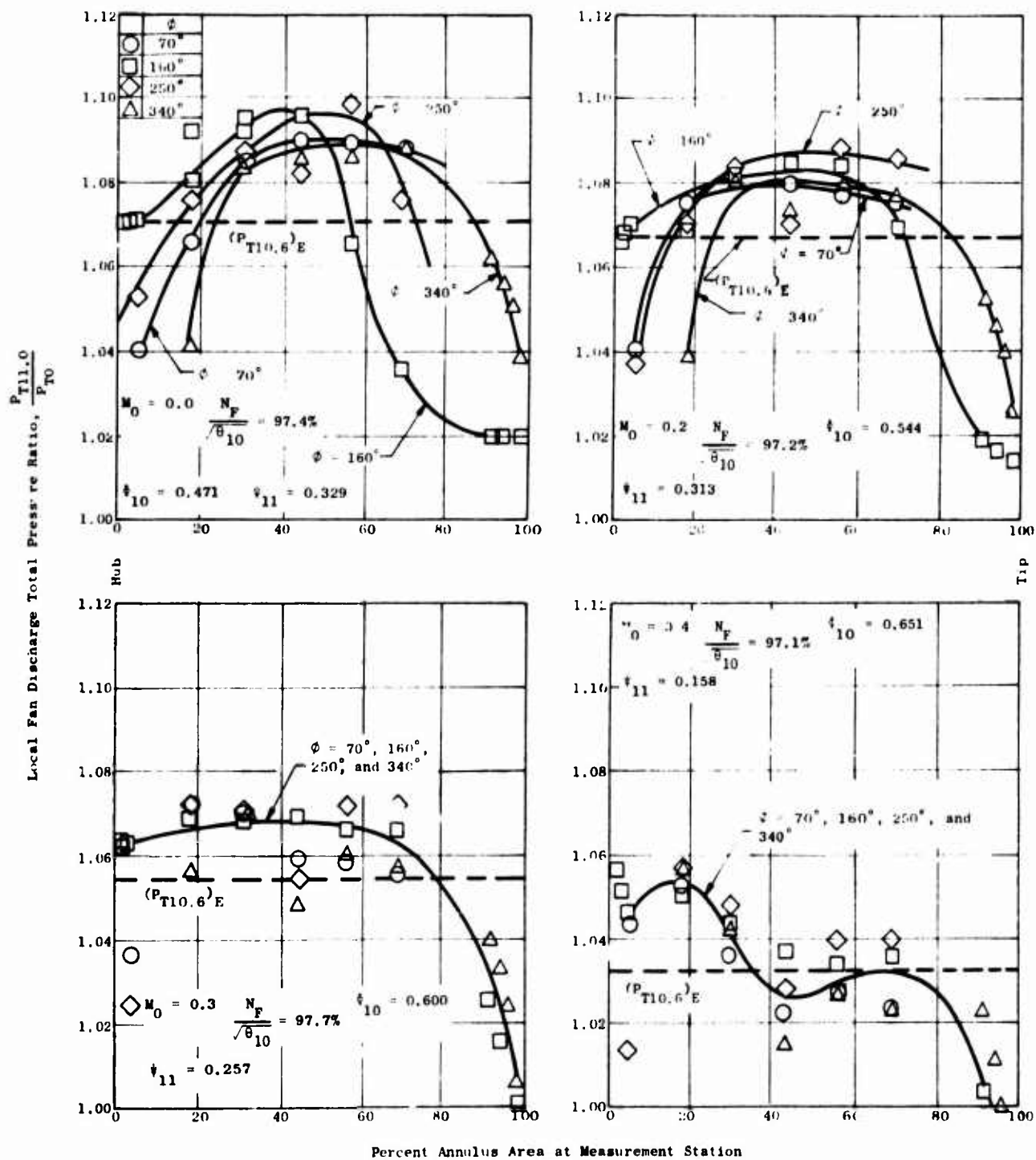


Figure 215. Fan Discharge Total Pressure Distributions - Model 3.

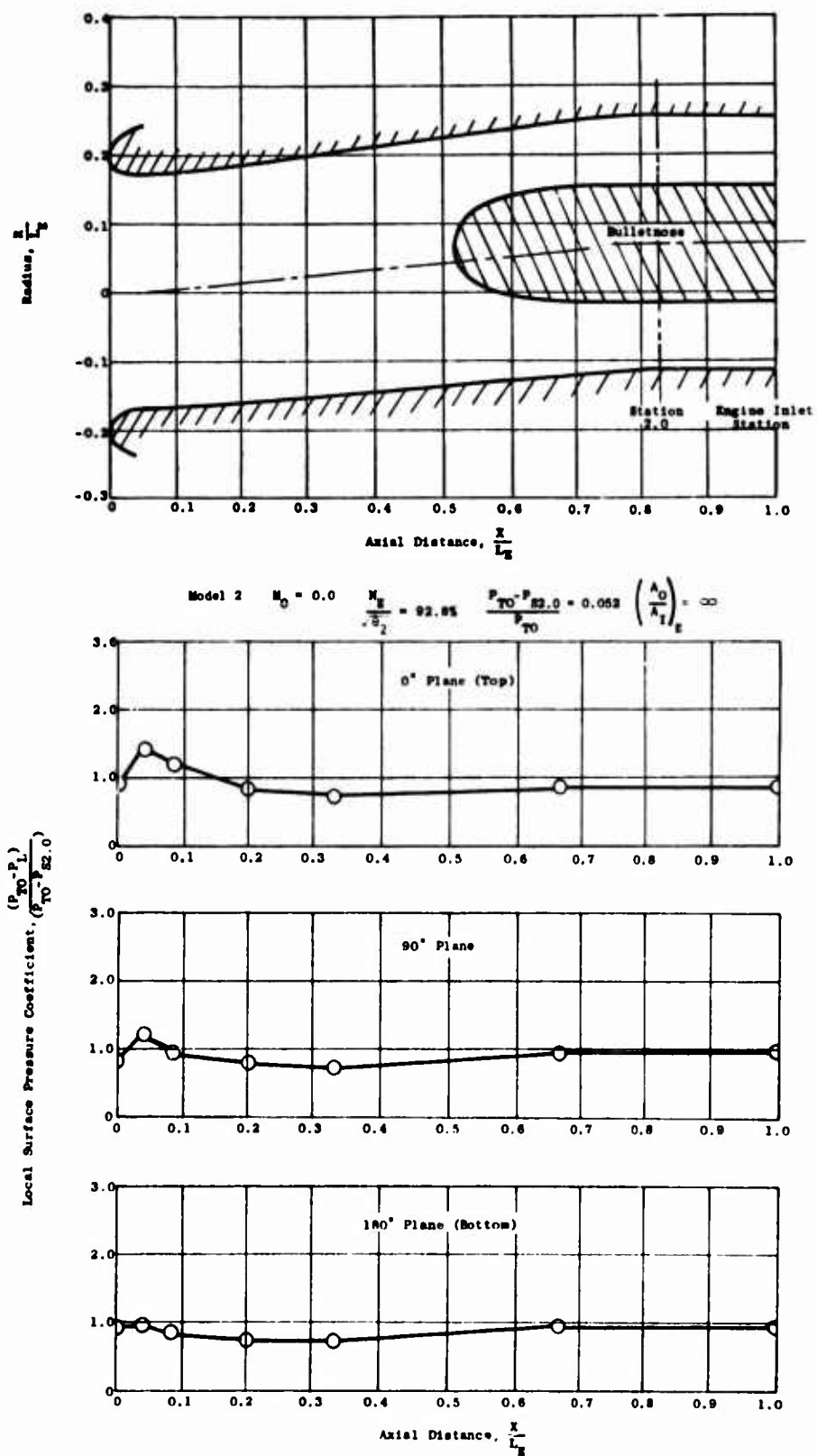


Figure 216. Typical Engine Inlet Internal Pressure Distributions -
 $M_0 = 0.0$, $N_E = 92.8\%$.
 $\frac{N_E}{\sqrt{\theta_2}}$

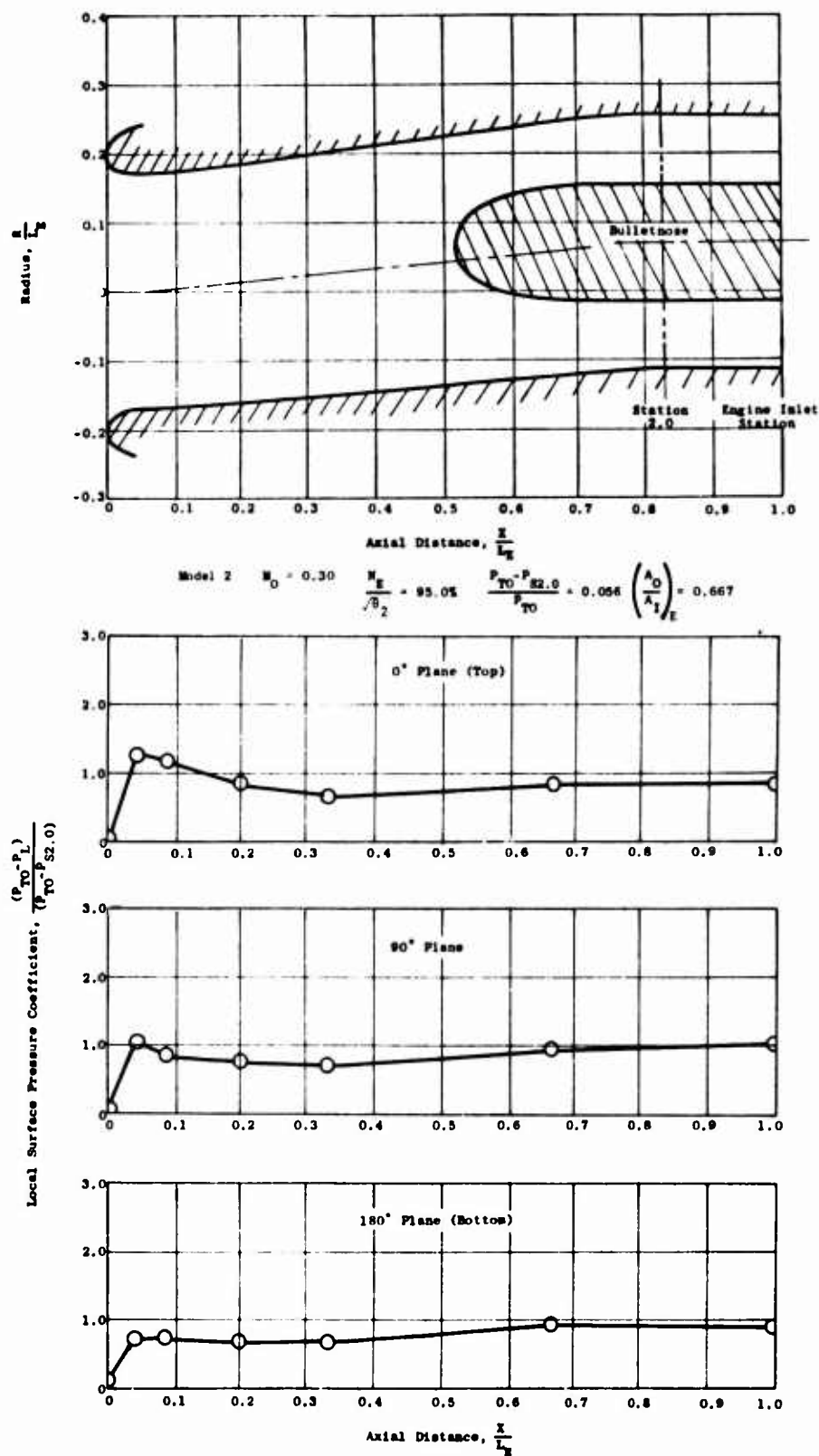


Figure 217. Typical Engine Inlet Internal Pressure Distributions - $M_0 = 0.3$, $N_E = 95.0\%$.

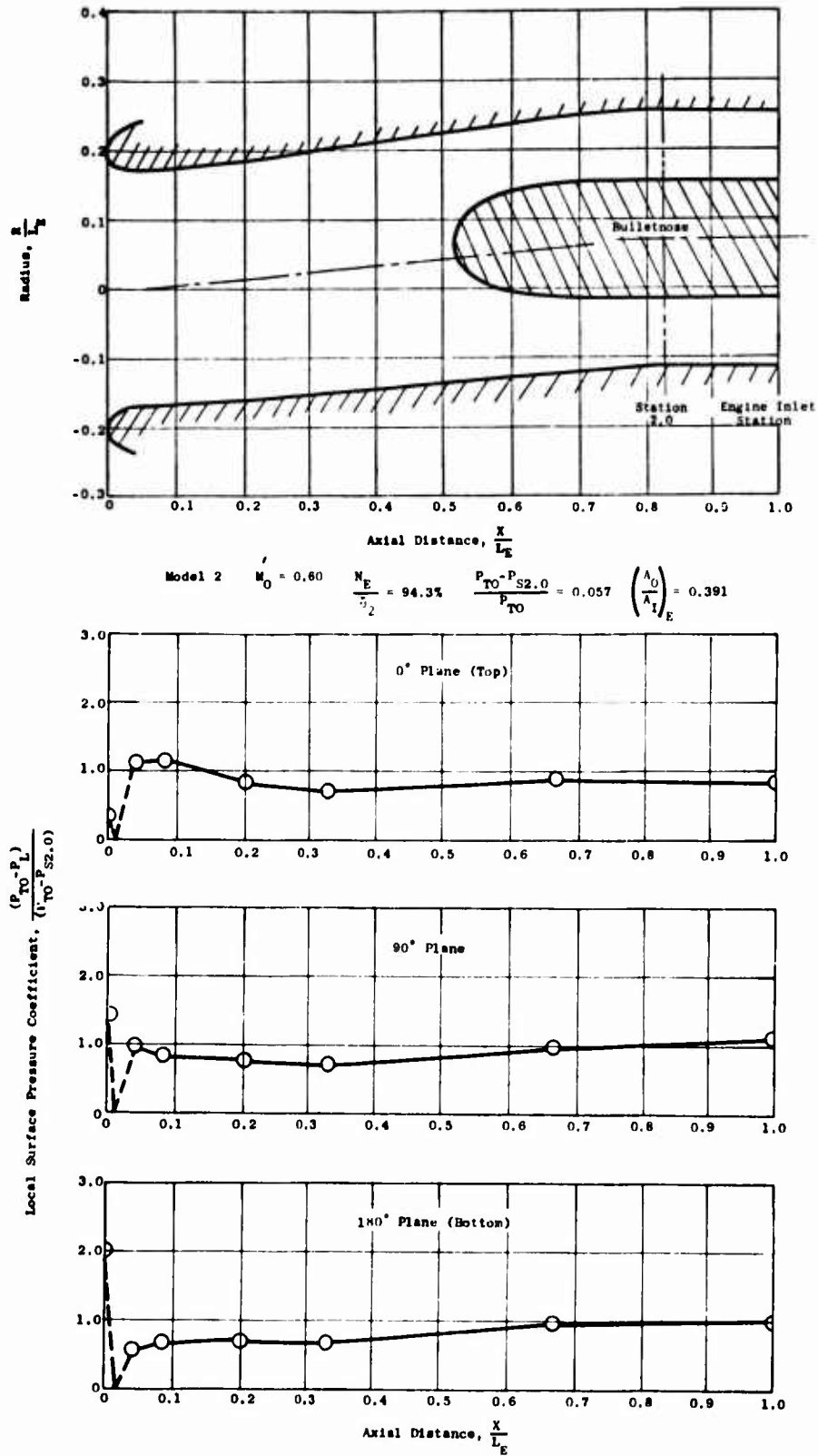


Figure 218. Typical Engine Inlet Internal Pressure Distributions - $M_0 = 0.6$, $N_E = 94.3\%$.

$$\sqrt{\theta_2}$$

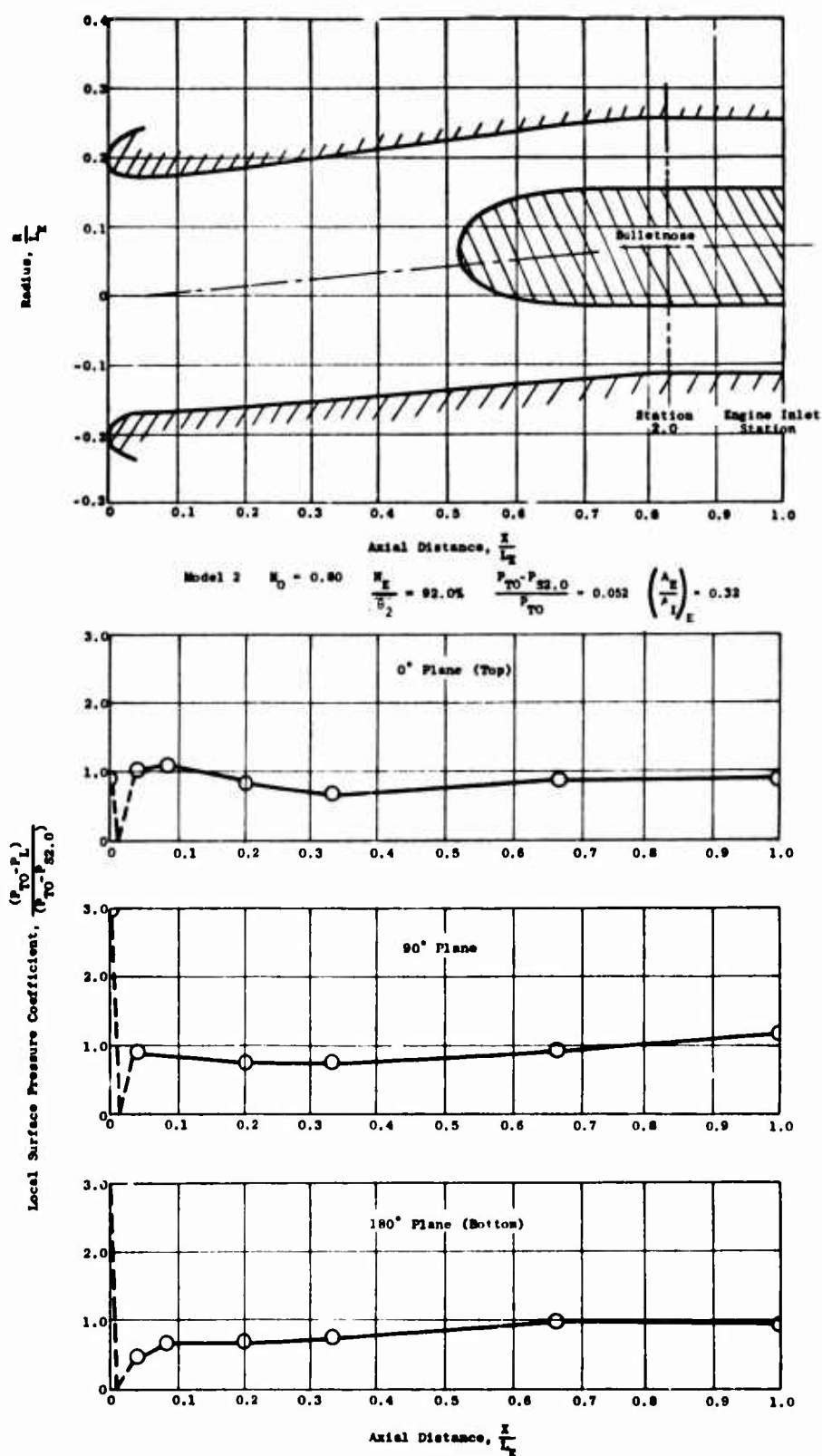


Figure 219. Typical Engine Inlet Internal Pressure Distributions - $M_0 = 0.8$, $N_E = 92.0\%$.

$\sqrt{\theta_2}$

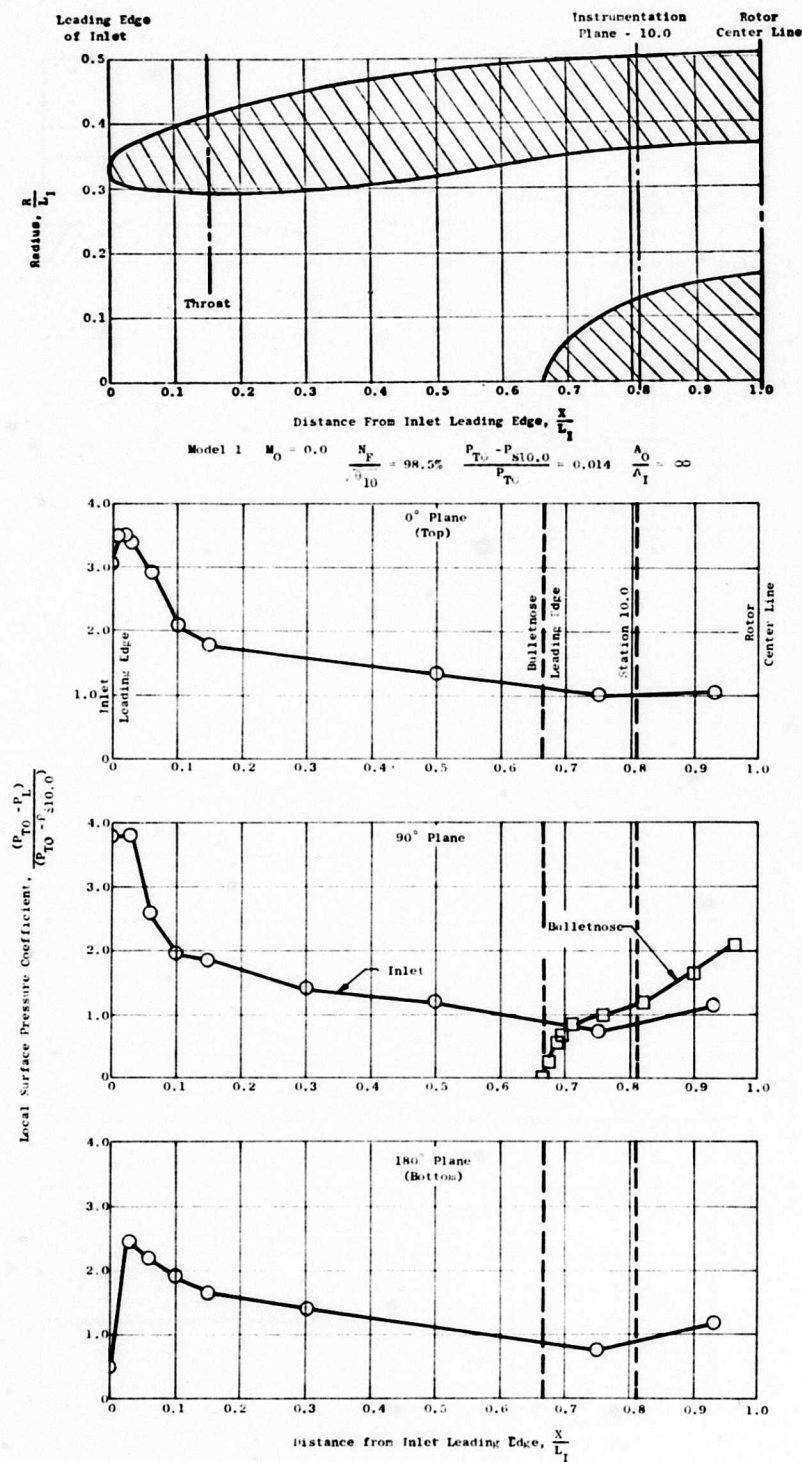


Figure 220. Typical Fan Inlet Internal Pressure Distributions for Inlet 1 - $M_0 = 0.0$, $N_F = 98.5\%$.

$$\sqrt{\theta_{10}}$$

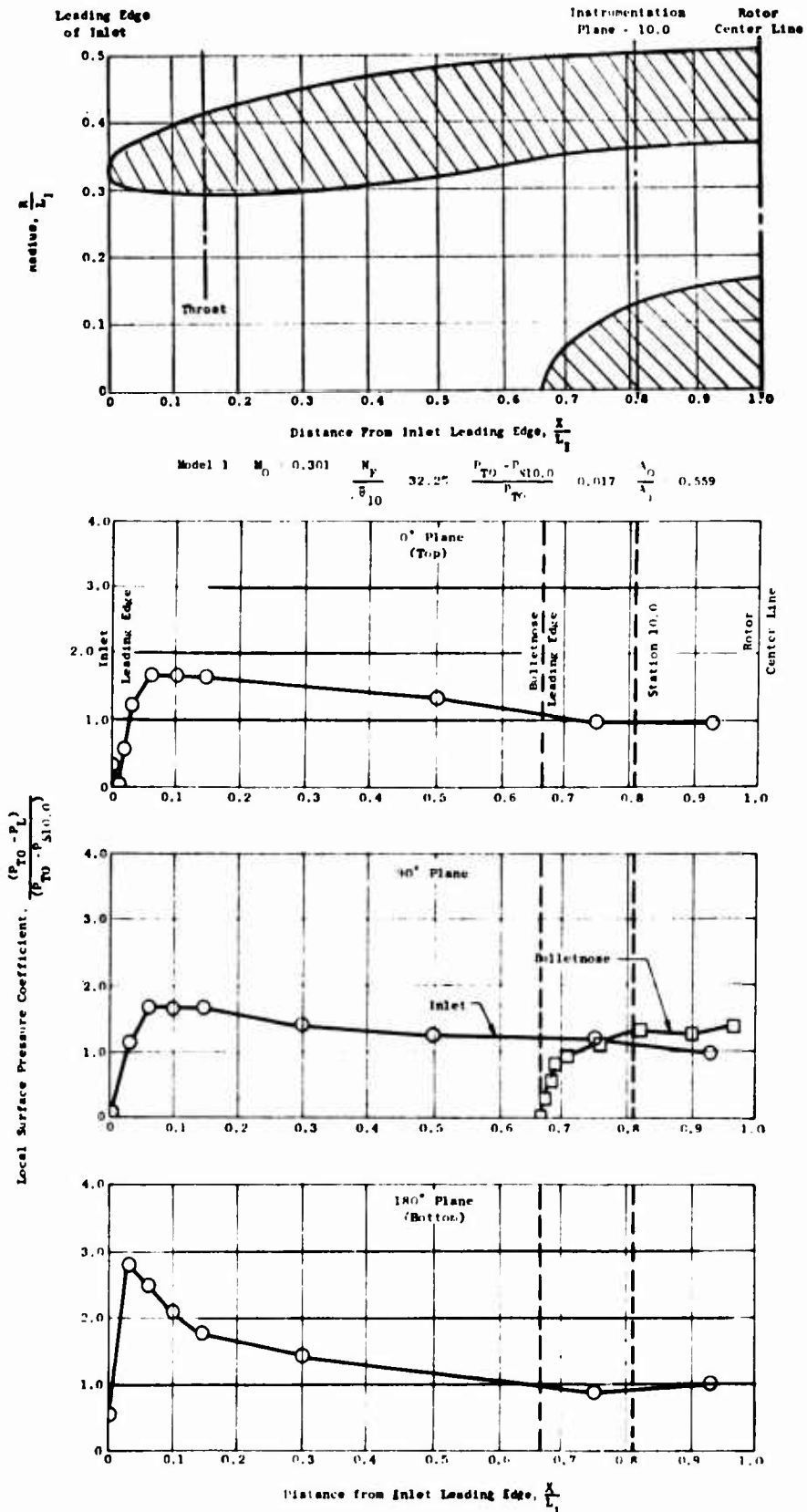


Figure 221. Typical Fan Inlet Internal Pressure Distributions for Inlet 1 - $M_0 = 0.3$, $N_F = 32.2\%$ (Windmill).

$$\sqrt{\theta_{10}}$$

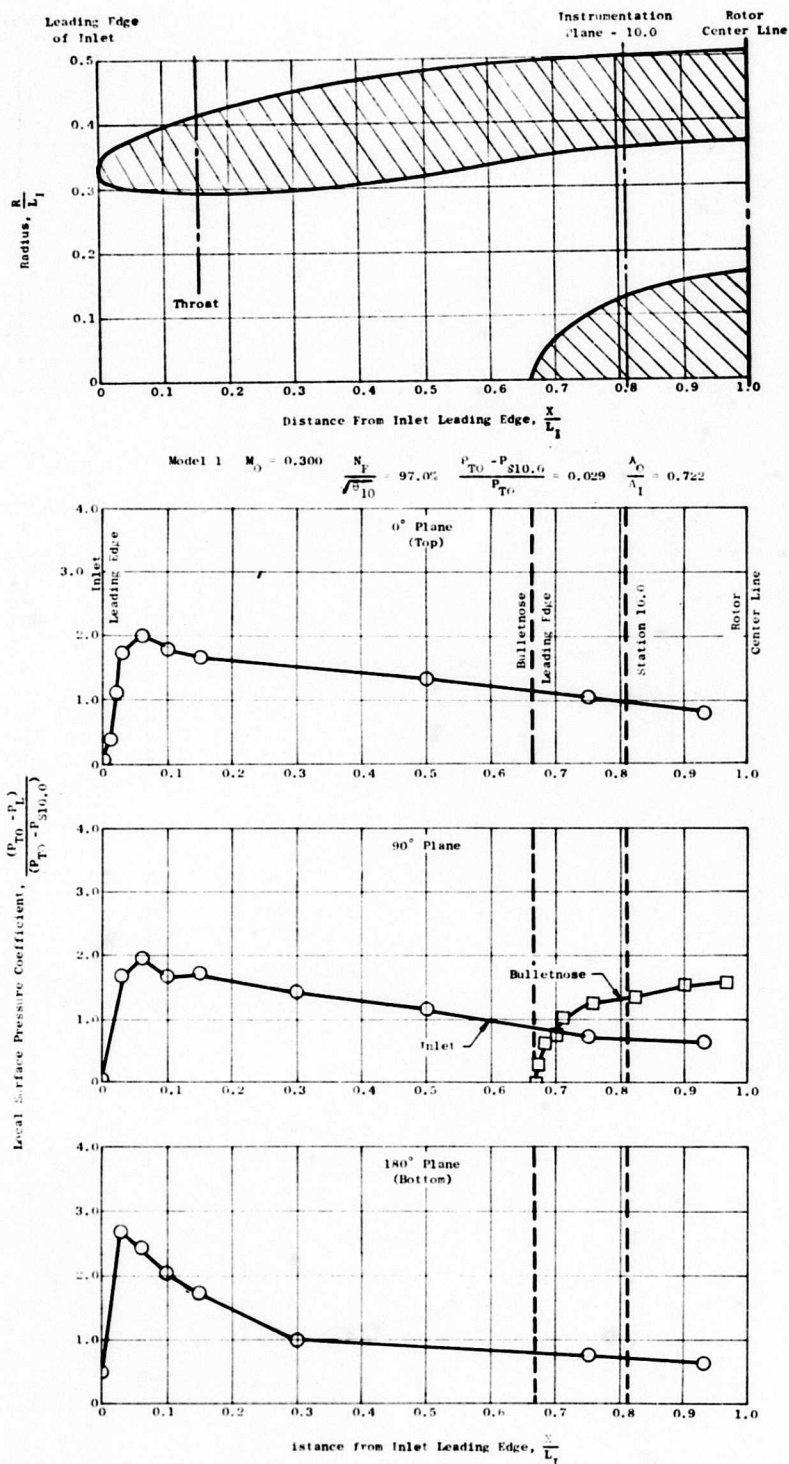


Figure 222. Typical Fan Inlet Internal Pressure Distributions for Inlet 1 - $M_0 = 0.3$, $N_F = 97.0\%$.

$$\sqrt{\theta_{10}}$$

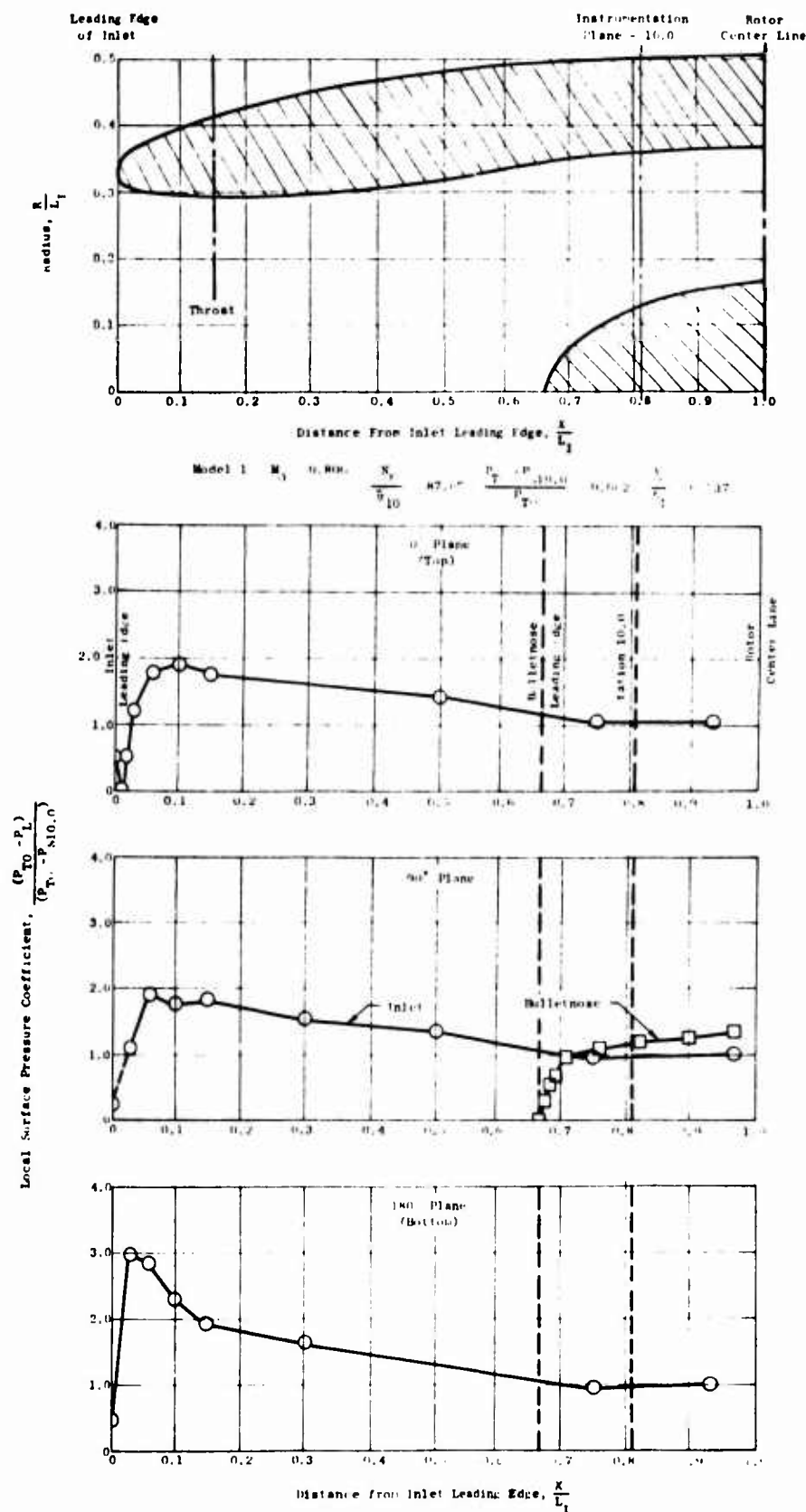


Figure 223. Typical Fan Inlet Internal Pressure Distributions for Inlet 1 - $M_0 = 0.8$, $N_F = 64.2\%$ (Windmill).

$$\sqrt{\theta_{10}}$$

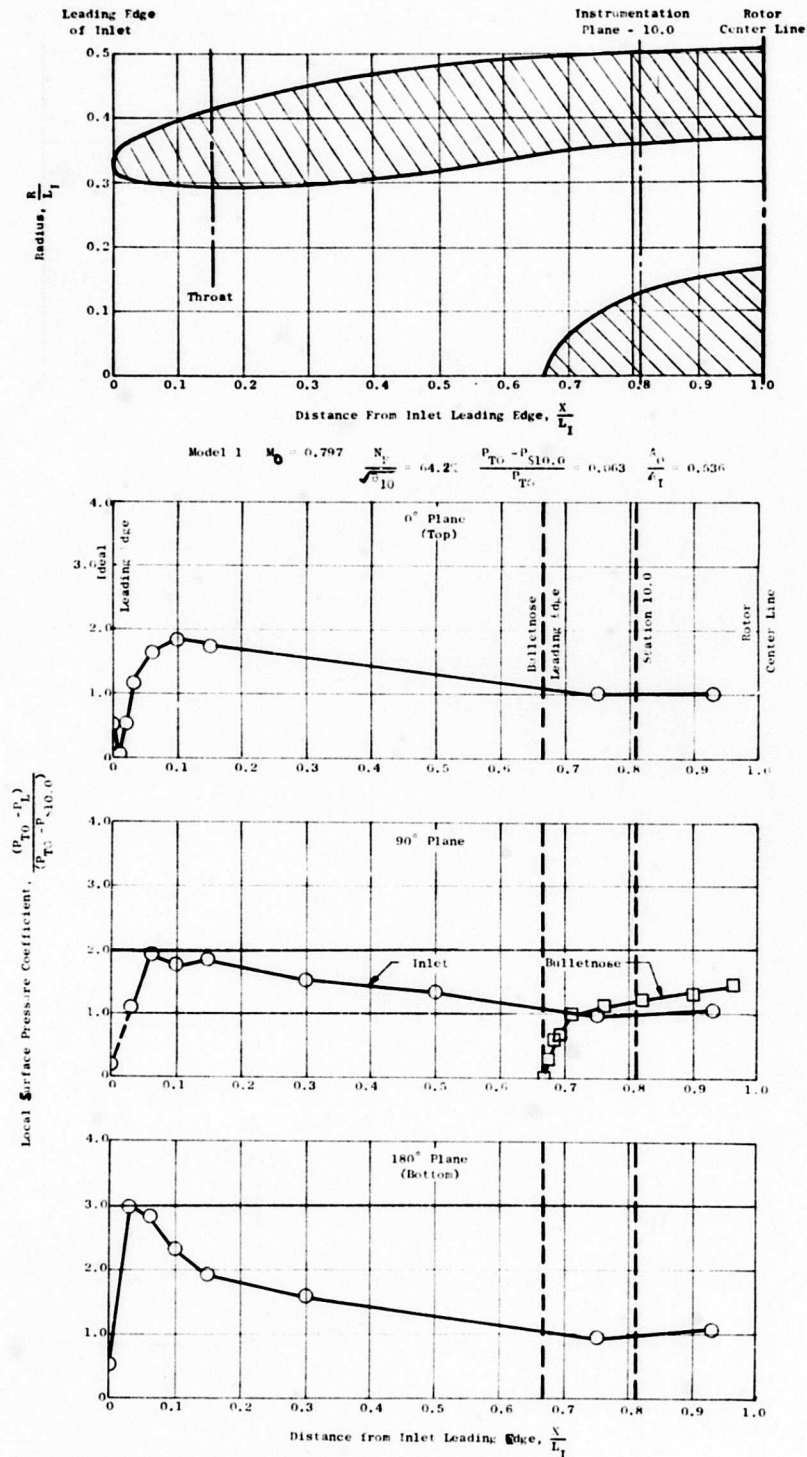


Figure 224. Typical Fan Inlet Internal Pressure Distributions for Inlet 1 - $M_0 = 0.8$, $N_F = 87.6\%$.

$$\sqrt{\theta_{10}}$$

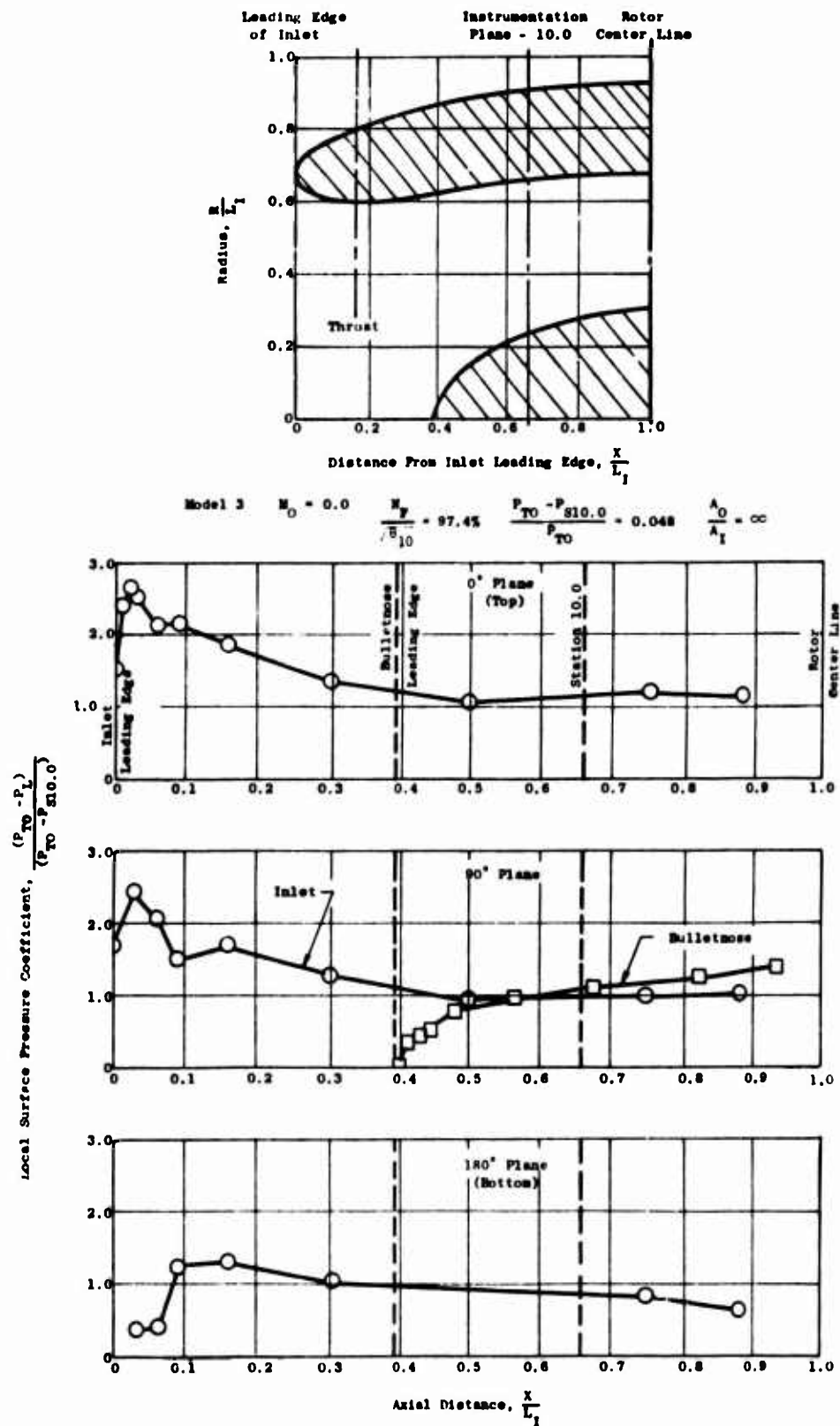


Figure 225. Typical Fan Inlet Internal Pressure Distributions for Inlet 2 - $M_0 = 0.0$, $N_F = 97.4\%$.

$$\frac{N_F}{\sqrt{\theta_{10}}}$$

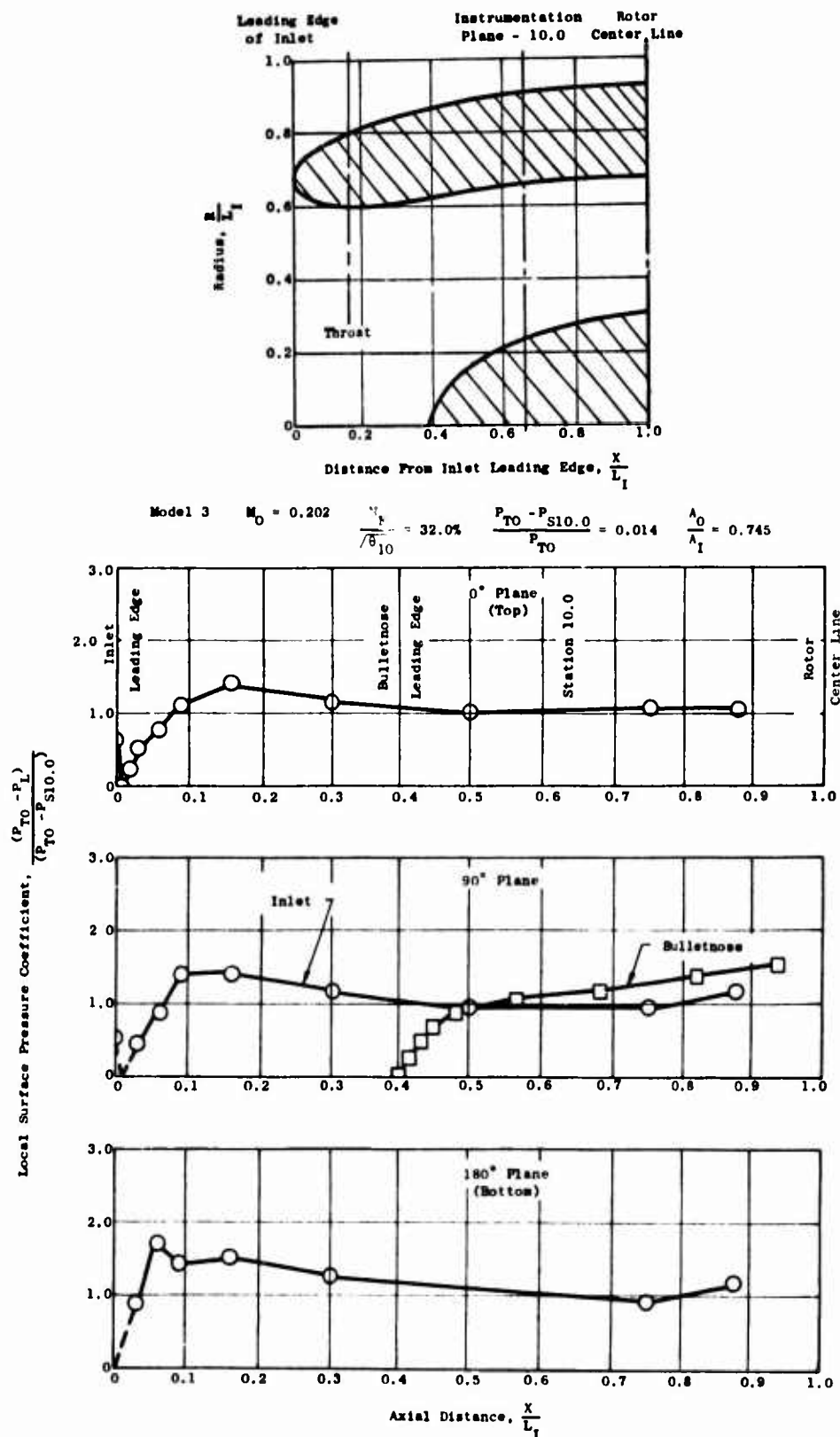


Figure 226. Typical Fan Inlet Internal Pressure Distributions for Inlet 2 - $M_0 = 0.2$, $N_F = 32.0\%$ (Windmill).

$$\frac{\sqrt{\theta}}{\theta_{10}}$$

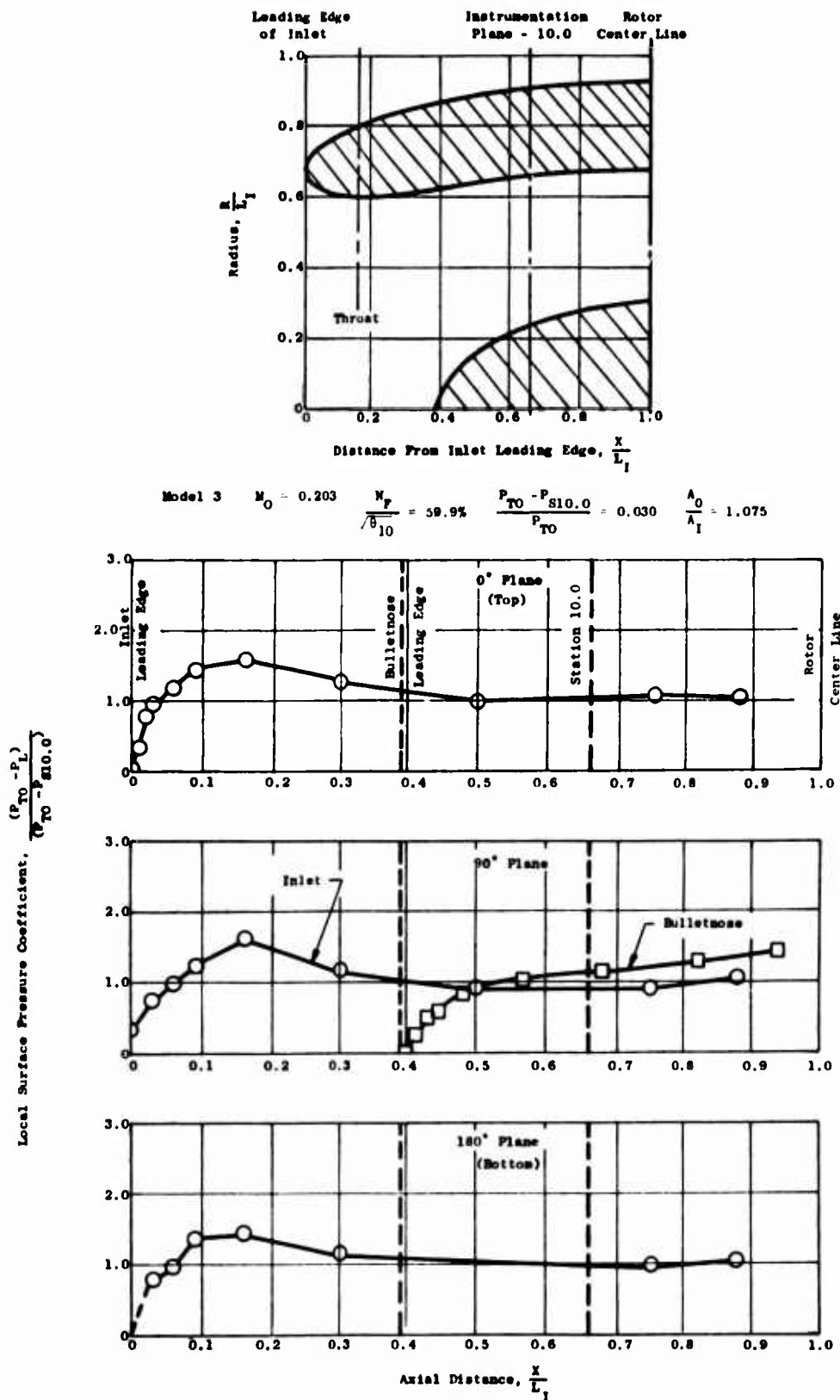


Figure 227. Typical Fan Inlet Internal Pressure Distributions for Inlet 2 - $M_0 = 0.2$, $N_F = 59.9\%$.

$$\sqrt{\theta}_{10}$$

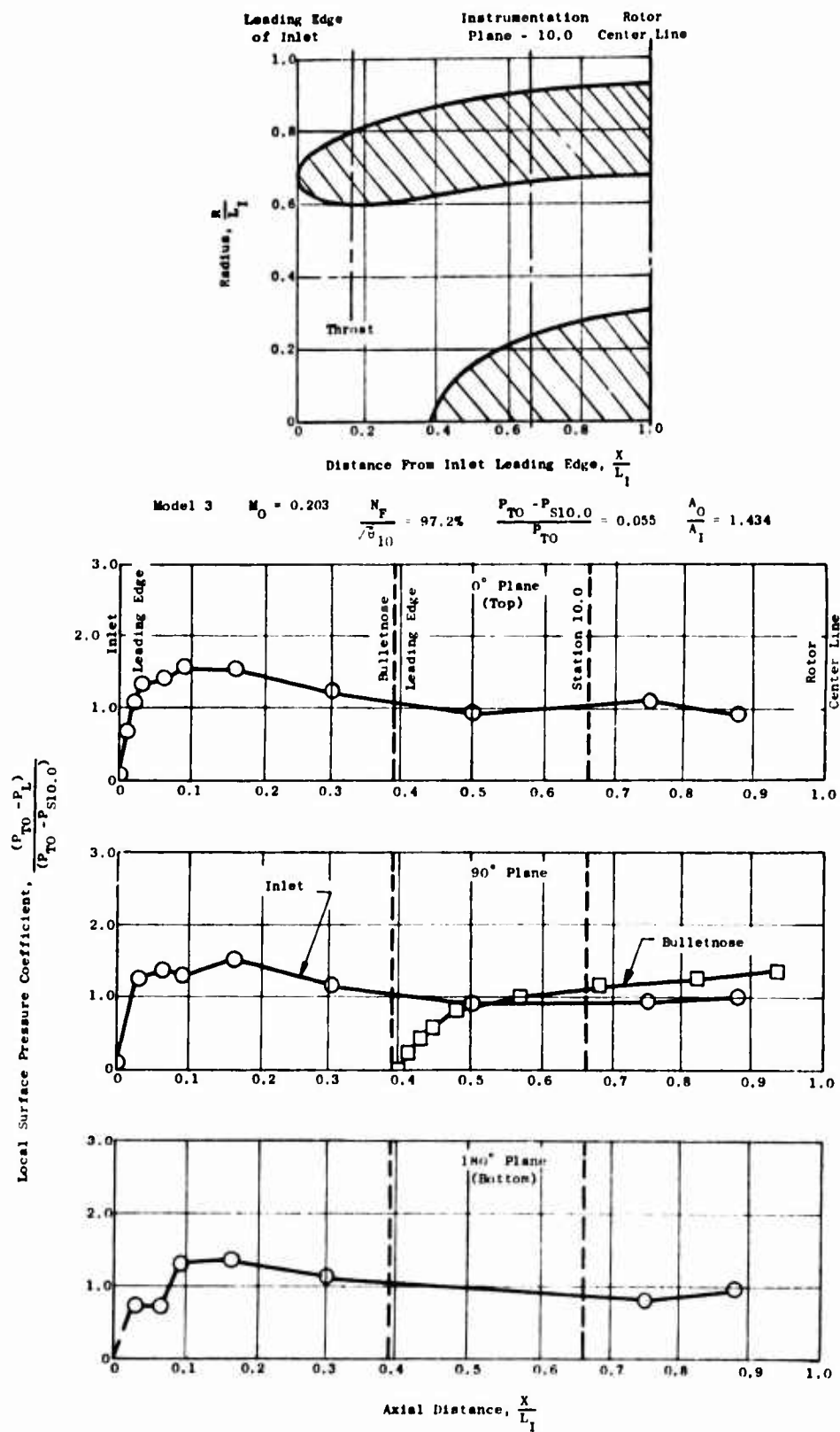


Figure 228. Typical Fan Inlet Internal Pressure Distributions for Inlet 2 - $M_0 = 0.2$, $N_F = 97.2\%$.

$$\frac{N_F}{\sqrt{\theta_{10}}}$$

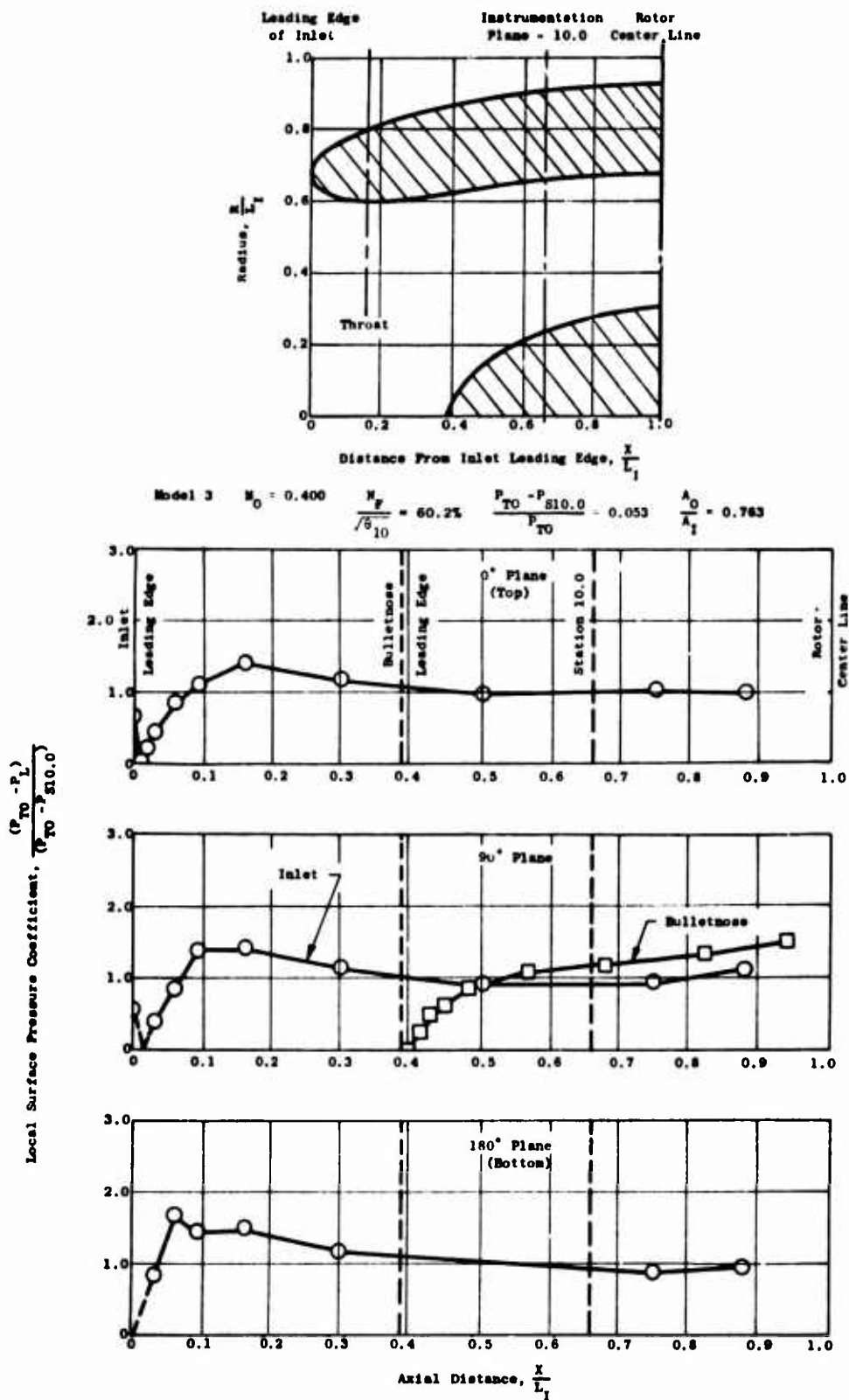


Figure 229. Typical Fan Inlet Internal Pressure Distributions for Inlet 2 - $M_0 = 0.4$, $N_F = 60.2\%$ (Windmill).

$$\sqrt{\theta}_{10}$$

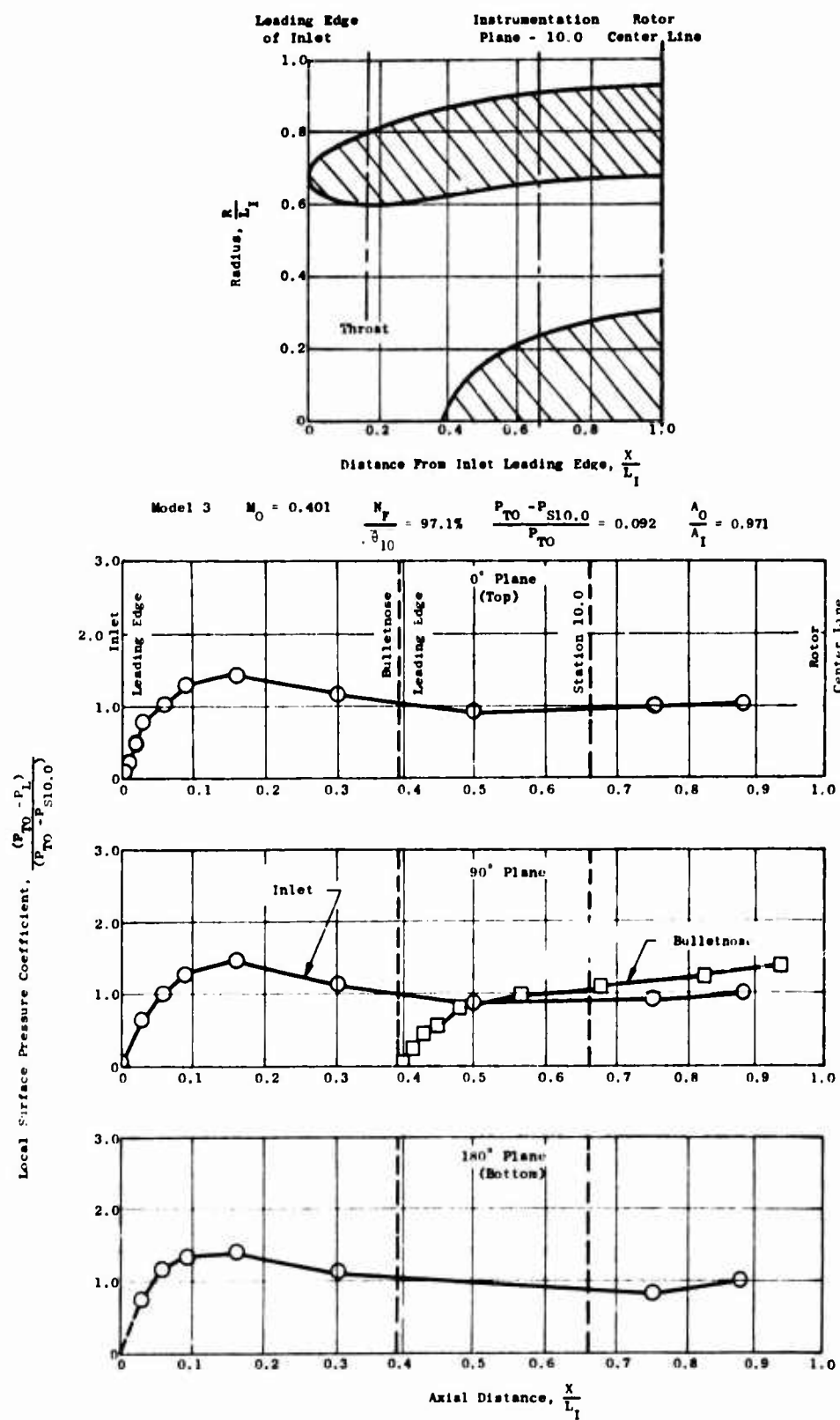


Figure 230. Typical Fan Inlet Internal Pressure Distributions for Inlet 2 - $M_0 = 0.4$, $N_F = 97.1\%$.

$\sqrt{\theta_{10}}$

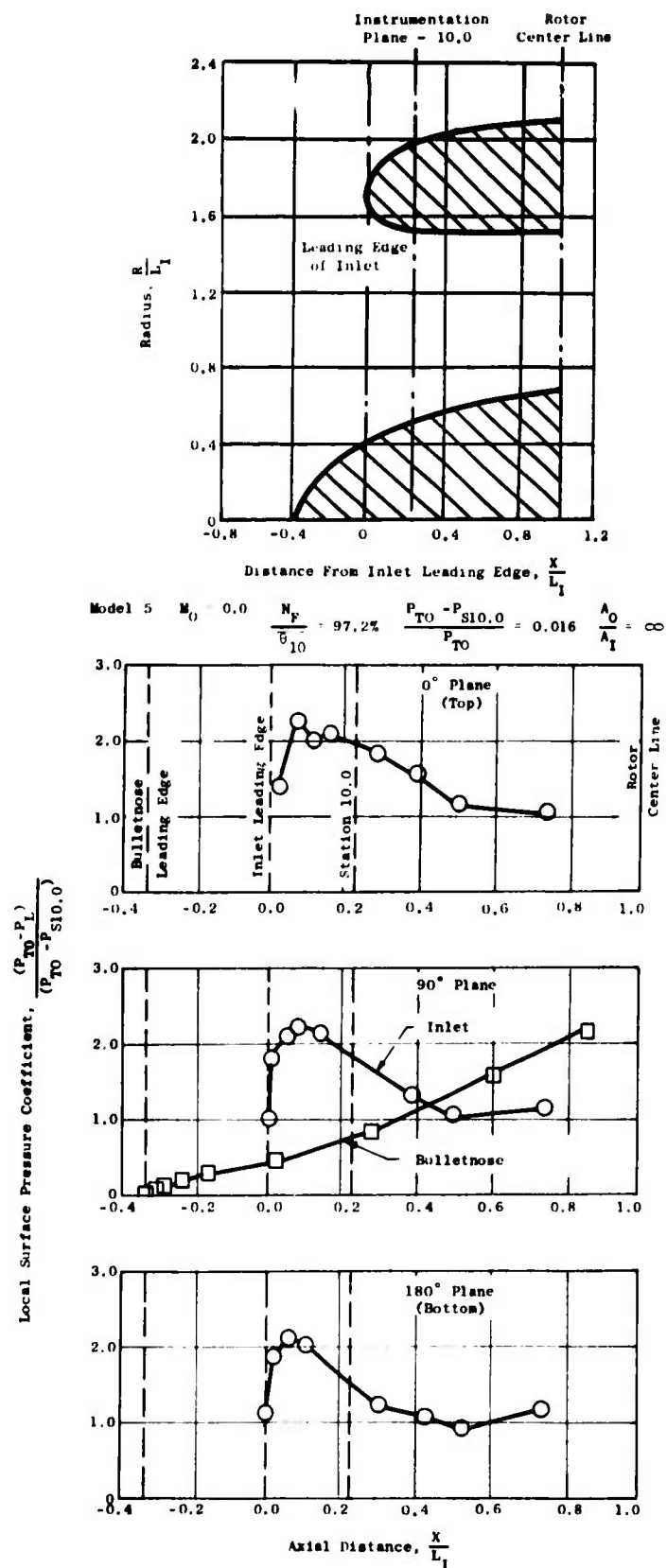


Figure 231. Typical Fan Inlet Internal Pressure Distributions for Inlet 3 - $M_0 = 0.0$, $N_F = 97.2\%$.

$$\sqrt{\theta_{10}}$$

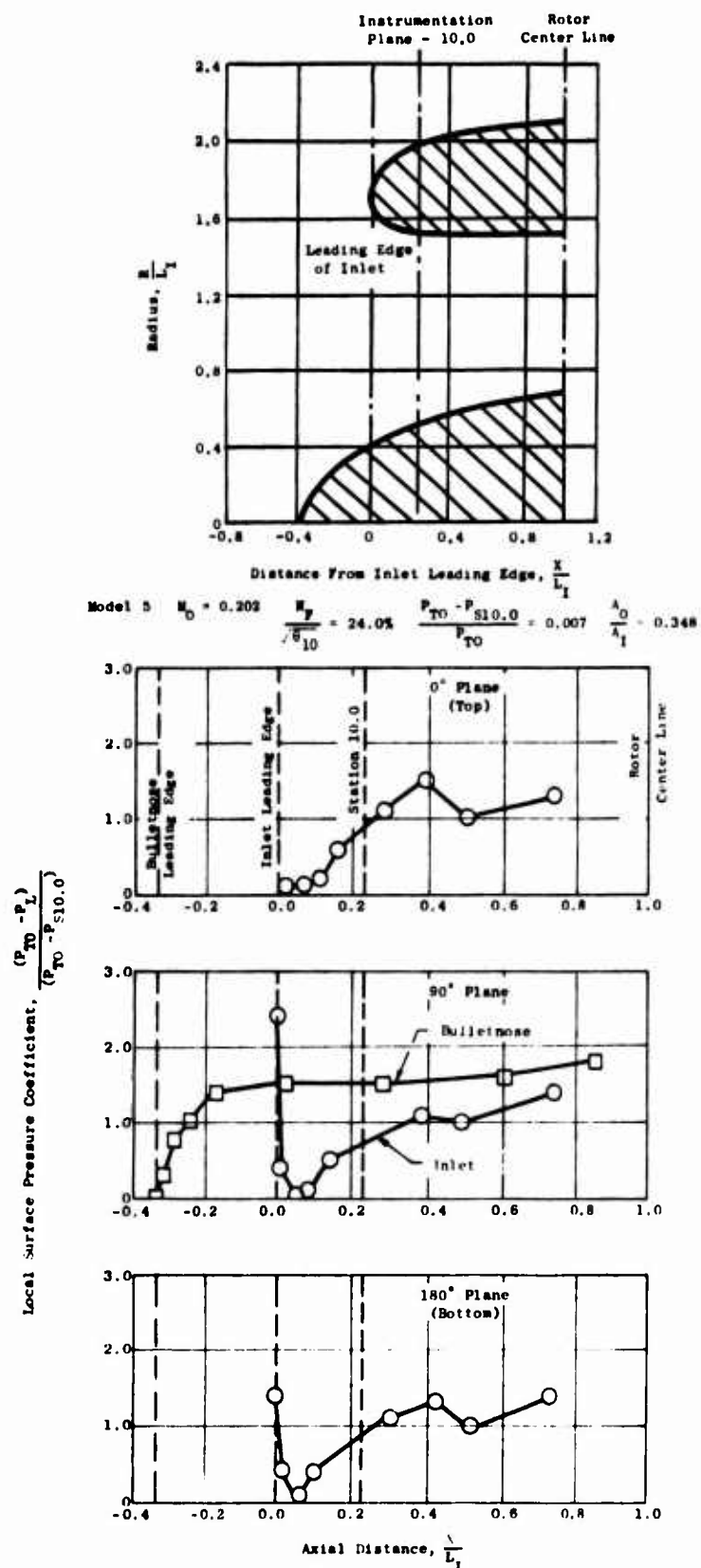


Figure 232. Typical Fan Inlet Internal Pressure Distributions for Inlet 3 - $M_0 = 0.2$, $N_F = 24.0\%$ (Windmill).

$$\frac{N_F}{\sqrt{\theta}_{10}}$$

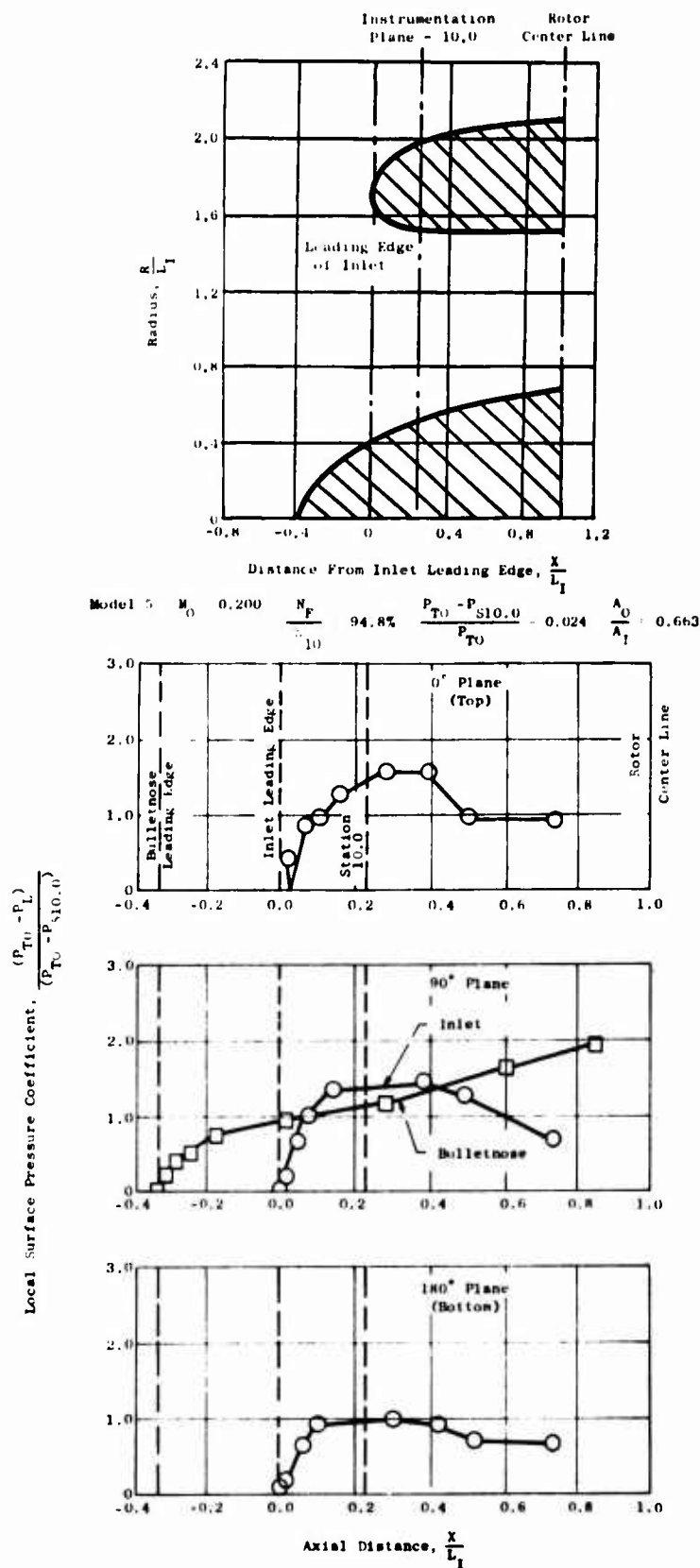


Figure 233. Typical Fan Inlet Internal Pressure Distributions for Inlet 3 - $M_0 = 0.2$, $N_F = 94.8\%$.

$\sqrt{\theta_{10}}$

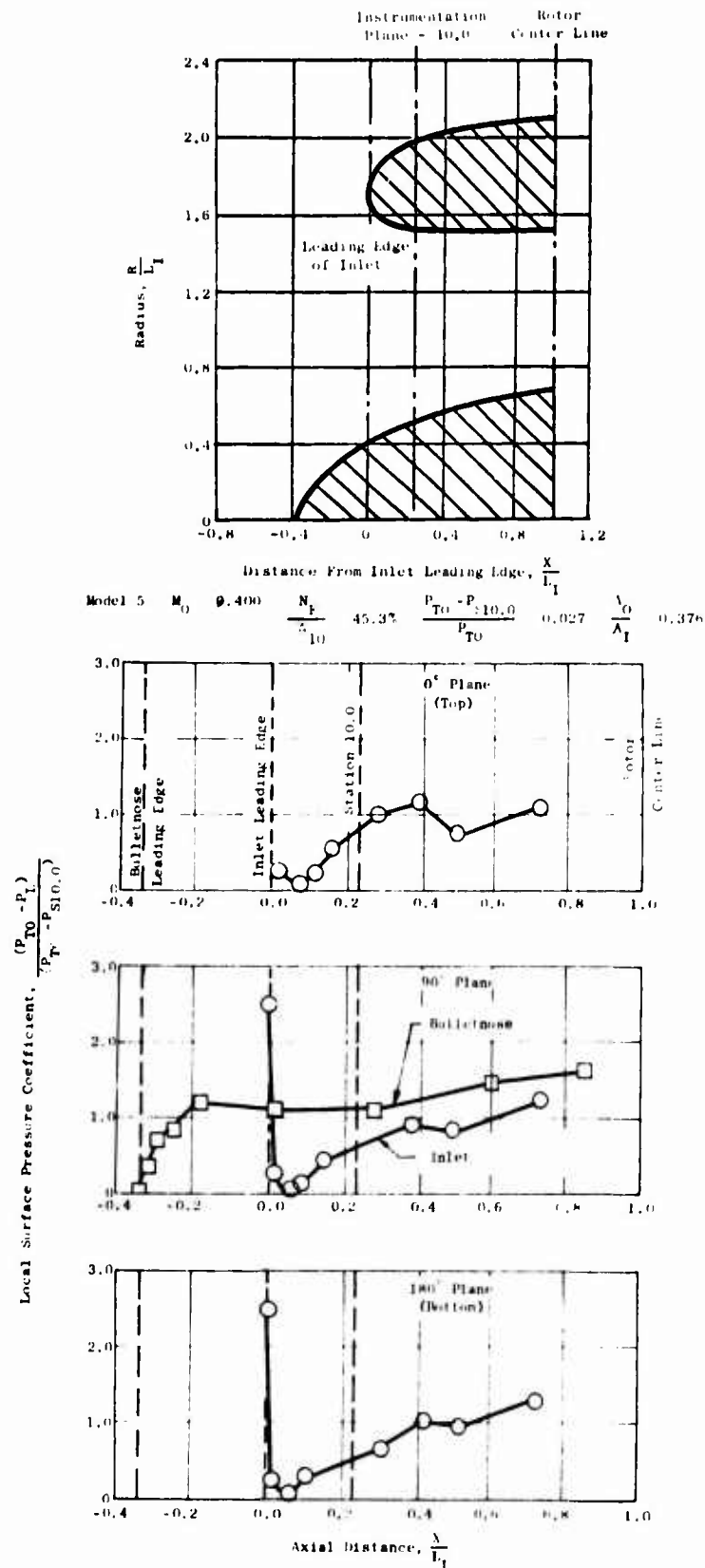


Figure 234. Typical Fan Inlet Internal Pressure Distributions for Inlet 3 - $M_0 = 0.4$, $N_F = 45.3\%$ (Windmill).

$$\sqrt{\theta_{10}}$$

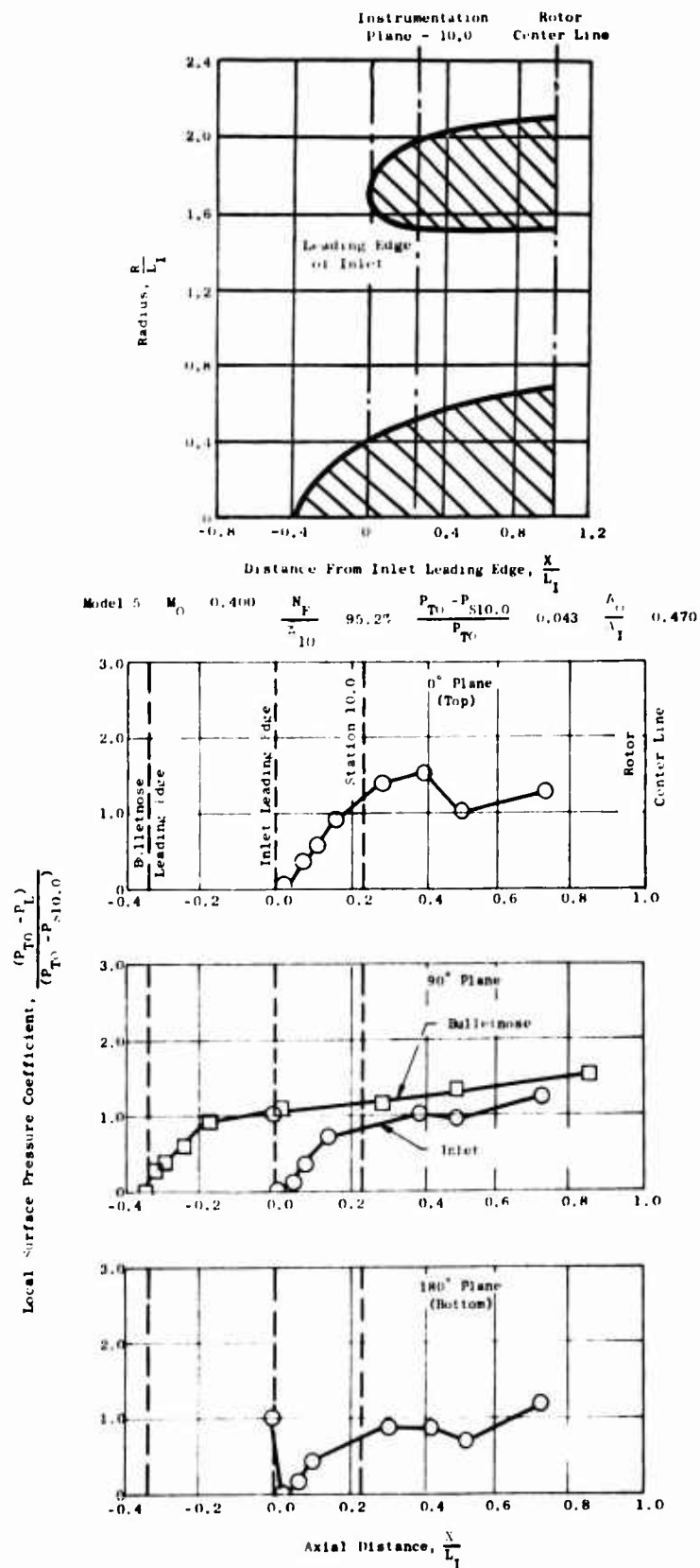


Figure 235. Typical Fan Inlet Internal Pressure Distributions for Inlet 3 - $M_0 = 0.4$, $N_F = 95.2\%$.

$$\sqrt{\theta_{10}}$$

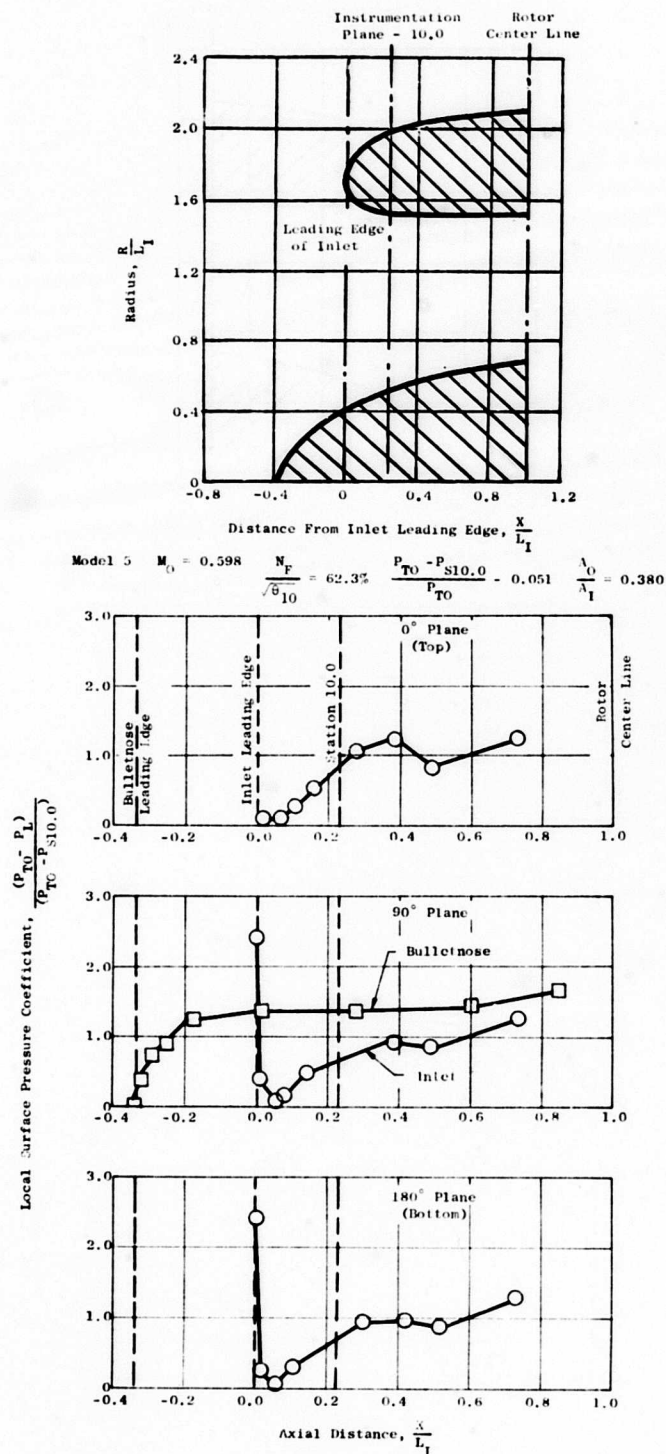


Figure 236. Typical Fan Inlet Internal Pressure Distributions for Inlet 3 - $M_0 = 0.6$, $N_F = 62.3\%$ (Windmill).

$$\sqrt{\theta_{10}}$$

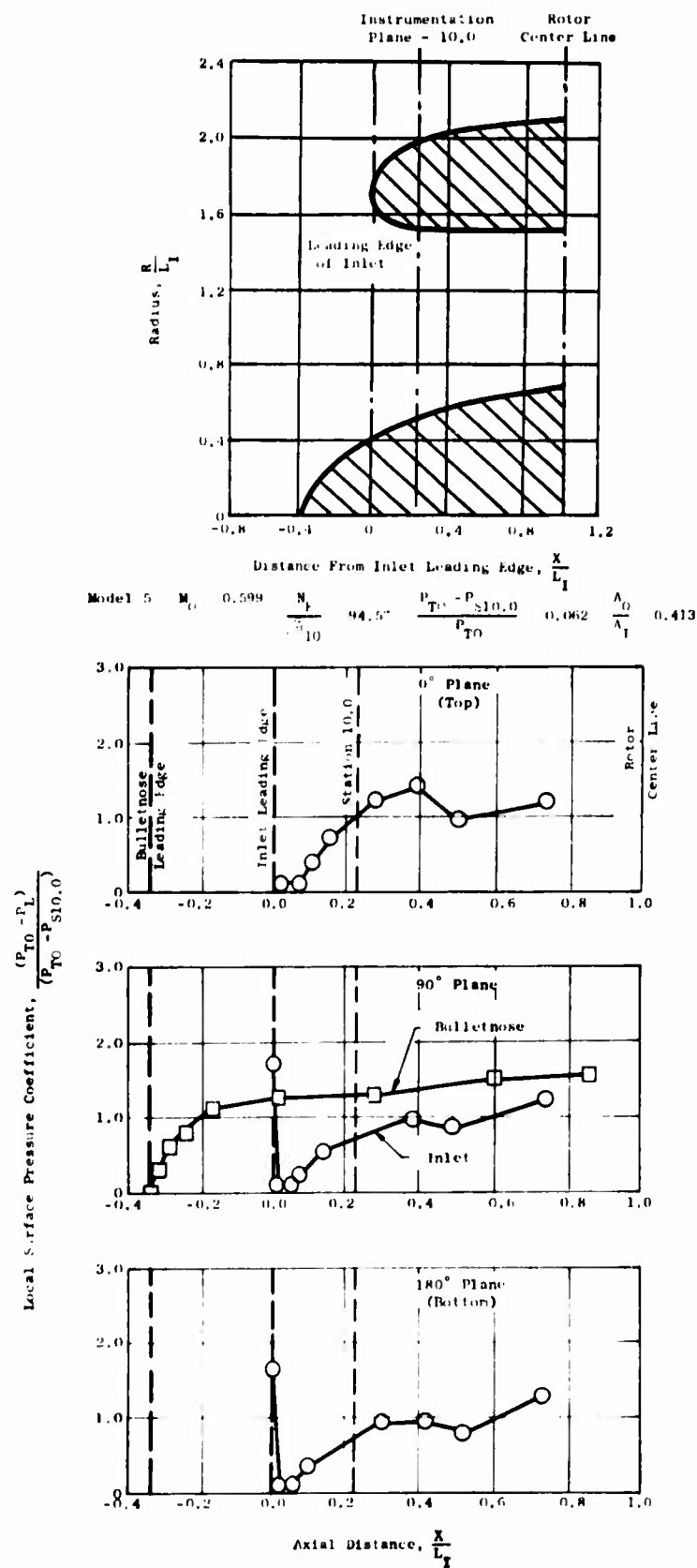


Figure 237. Typical Fan Inlet Internal Pressure Distributions for Inlet 3 - $M_0 = 0.6$, $N_F = 94.5\%$.

$$\sqrt{\theta_{10}}$$

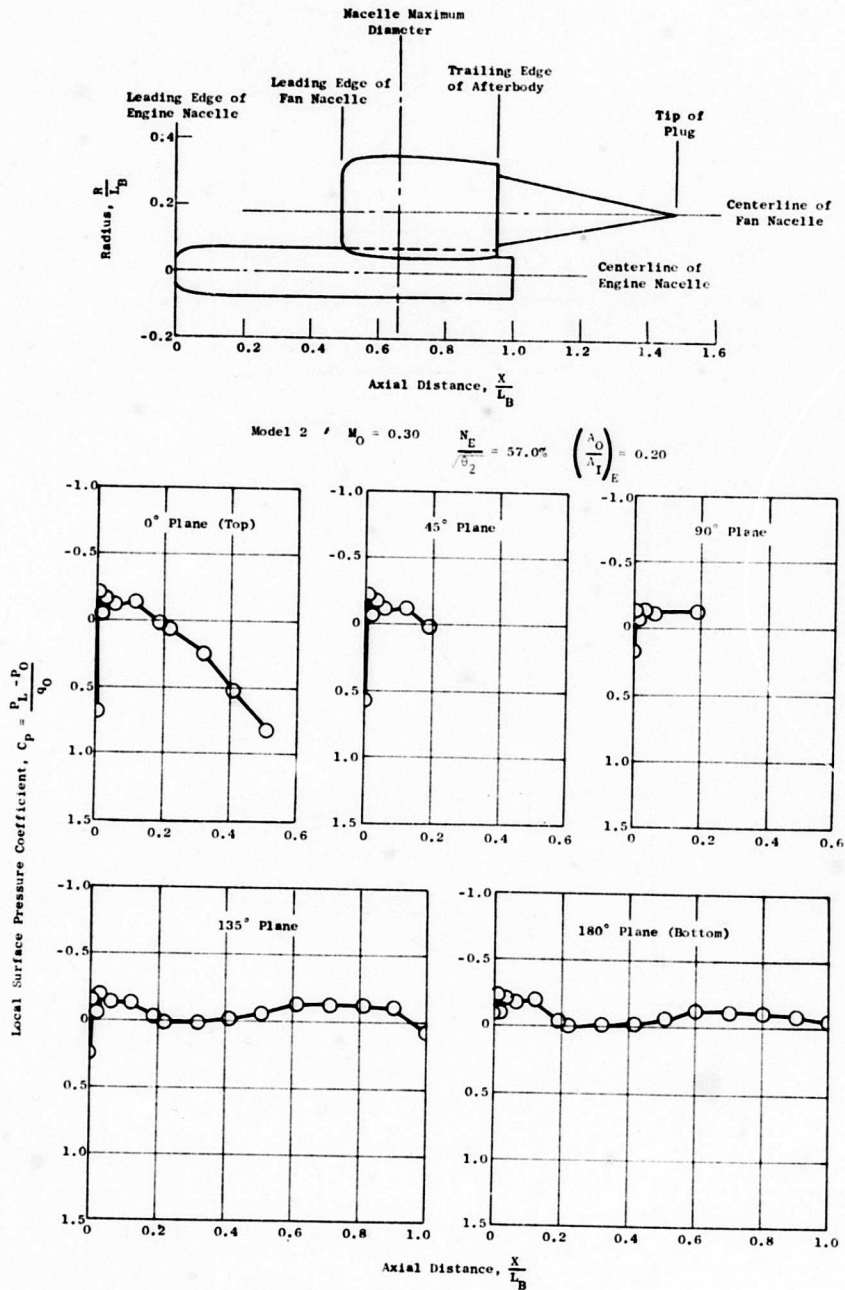


Figure 238. Typical Engine Nacelle Pressure Distributions - $M_0 = 0.3$,
 $\frac{N_E}{\theta_2} = 57.0\%$.

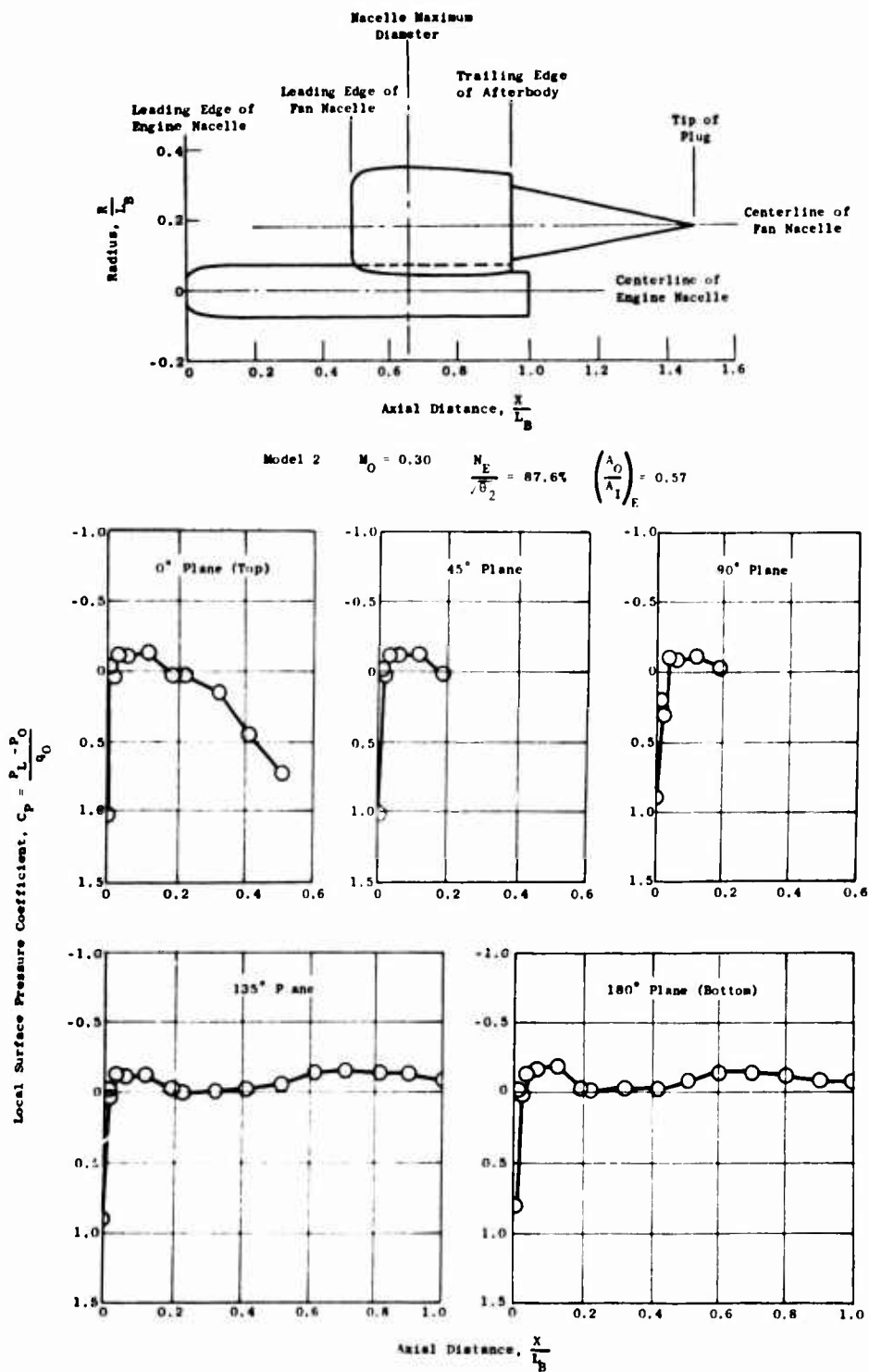


Figure 239. Typical Engine Nacelle Pressure Distributions - $M_0 = 0.3$,
 $\frac{N_E}{\sqrt{\theta_2}} = 87.6\%$.

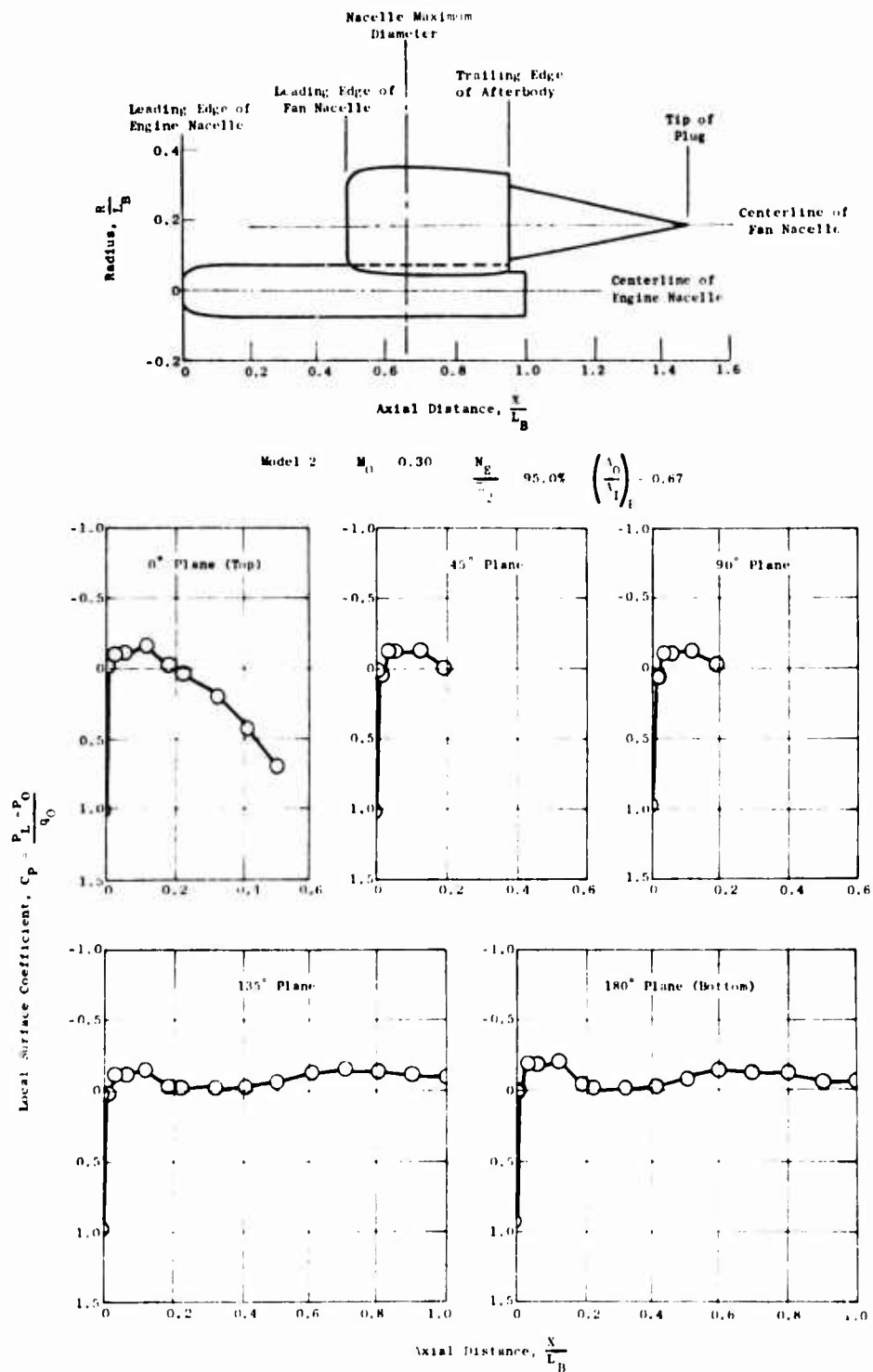


Figure 240. Typical Engine Nacelle Pressure Distributions - $M_0 = 0.3$, $N_E = 95.0\%$, $\sqrt{\theta_2}$

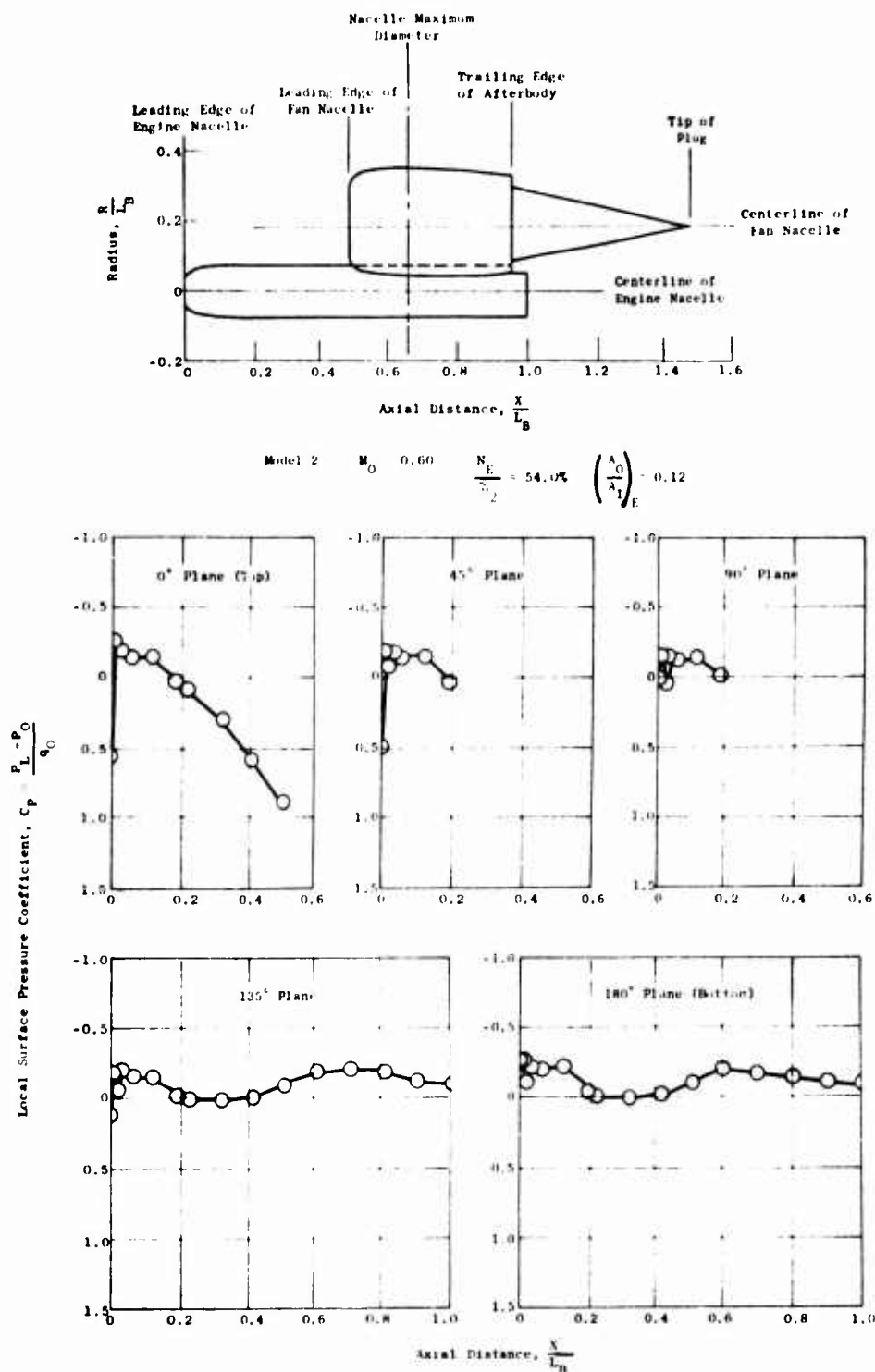


Figure 241. Typical Engine Nacelle Pressure Distributions - $M_0 = 0.6$,
 $\frac{N_E}{\sqrt{\theta_2}} = 54.0\%$.

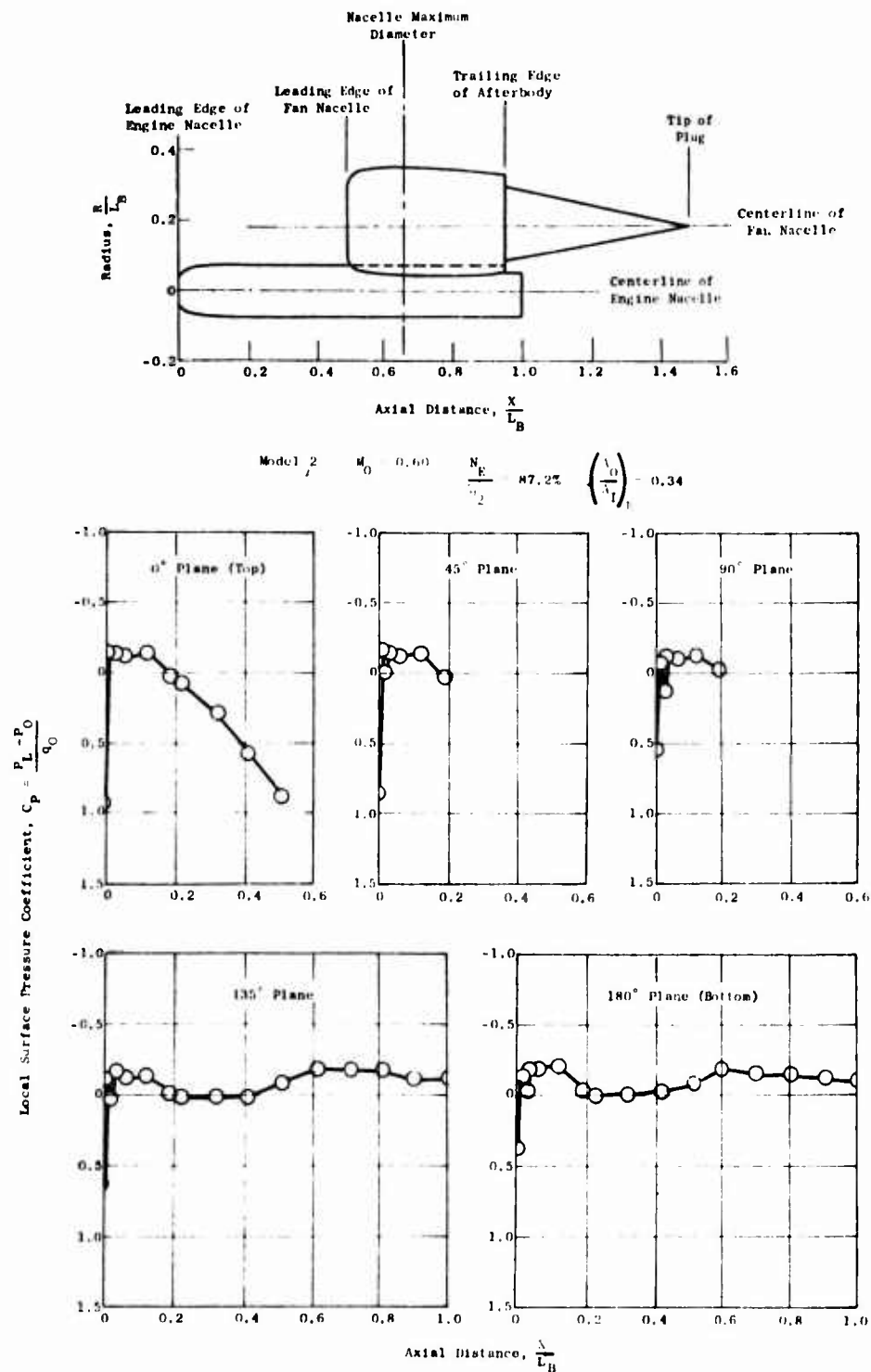


Figure 242. Typical Engine Nacelle Pressure Distributions - $M_0 = 0.6$,
 $\frac{N_E}{\sqrt{\theta_2}} = 87.2\%$.

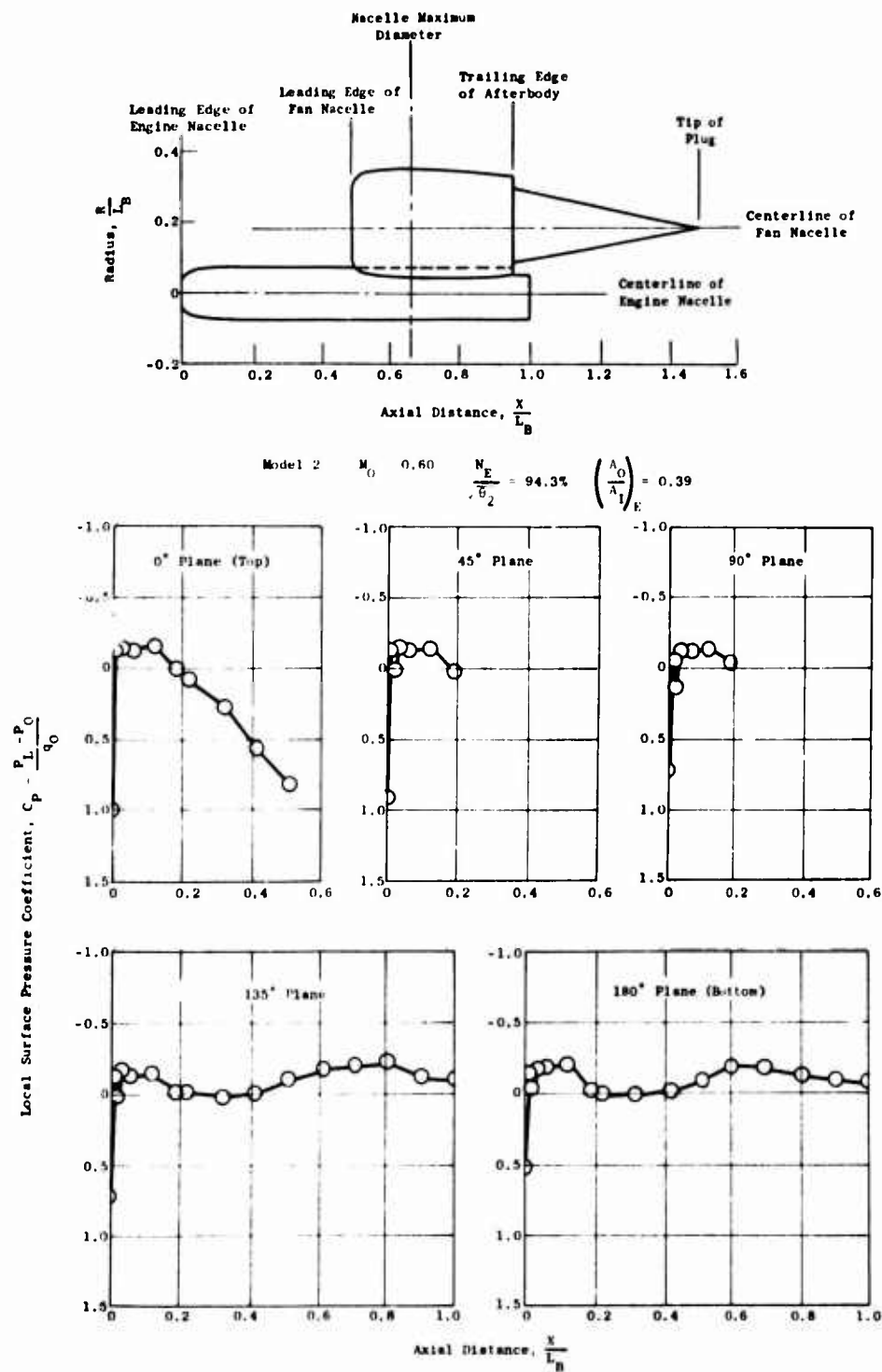


Figure 243. Typical Engine Nacelle Pressure Distributions - $M_0 = 0.6$, $\frac{N_E}{\sqrt{\theta_2}} = 94.3\%$.

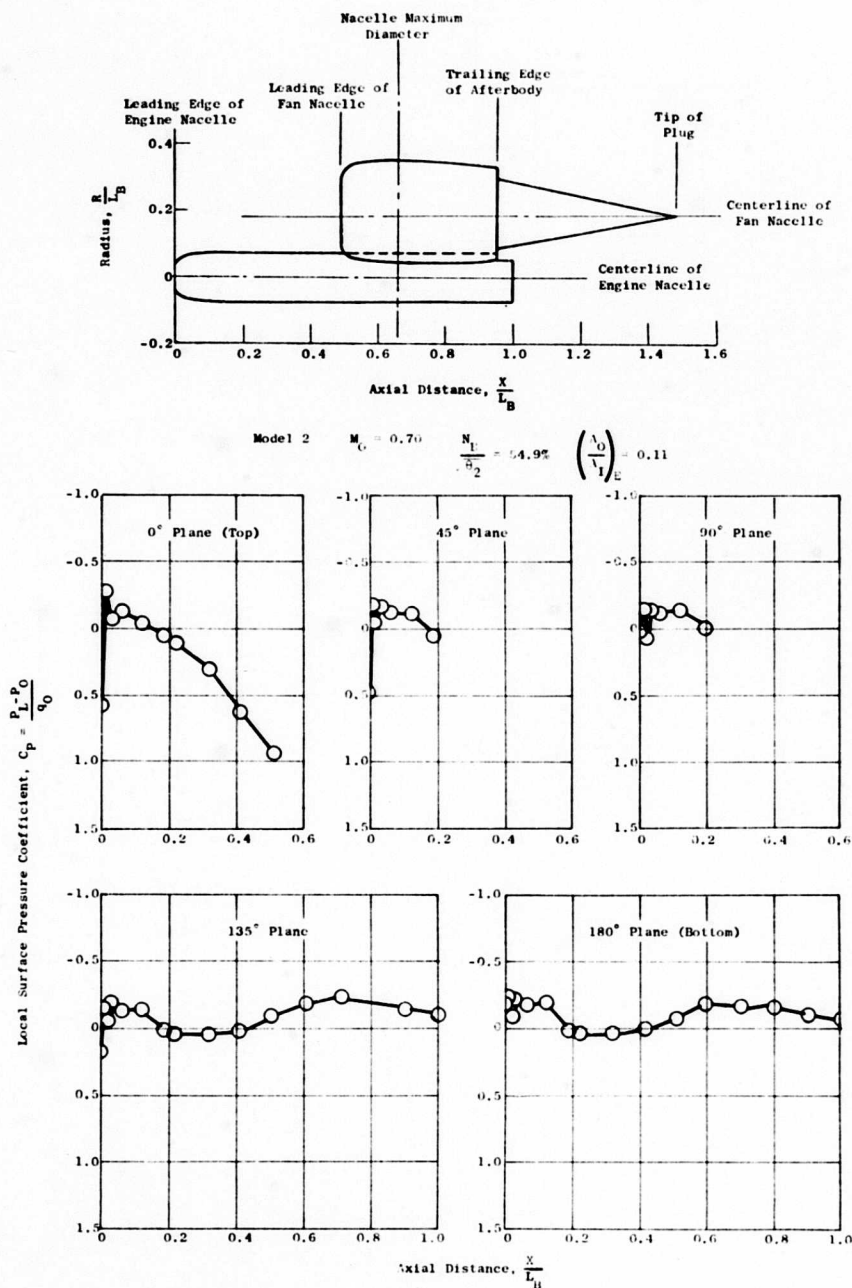


Figure 244. Typical Engine Nacelle Pressure Distributions - $M_0 = 0.7$, $N_E = 54.9\%$.

$\sqrt{\theta_2}$

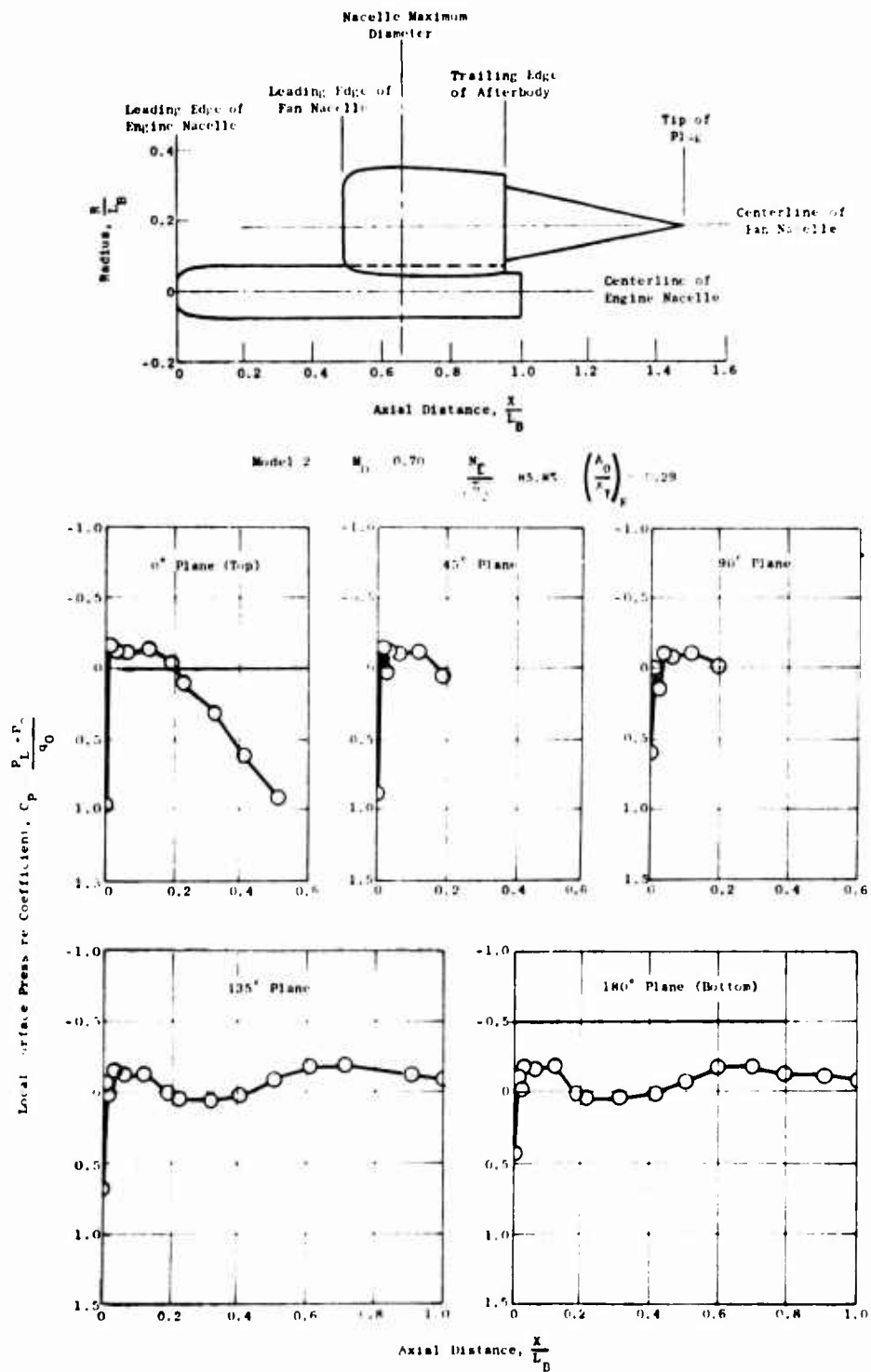


Figure 245. Typical Engine Nacelle Pressure Distributions - $M_0 = 0.7$,
 $N_E = 85.8\%$,
 $\sqrt{\theta_2}$

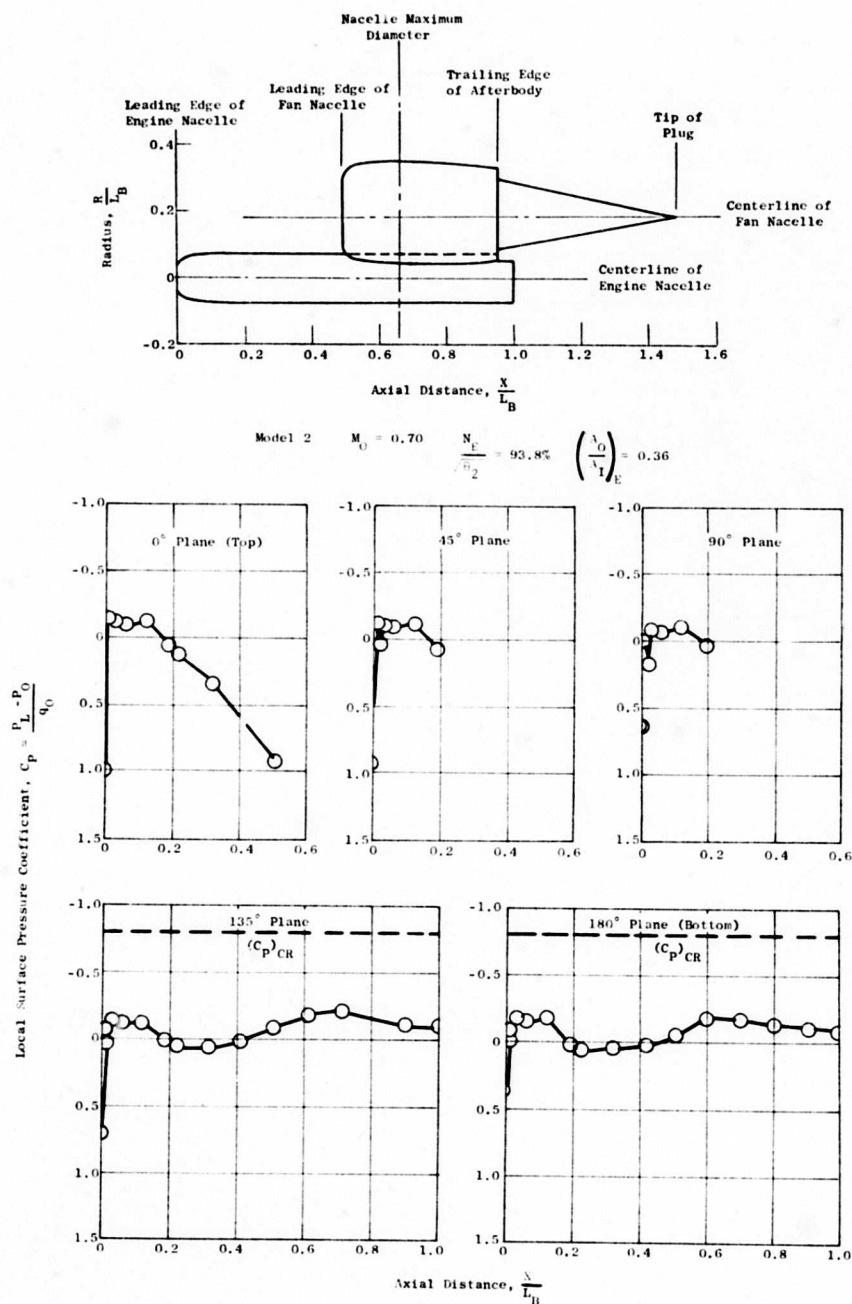


Figure 246. Typical Engine Nacelle Pressure Distributions - $M_0 = 0.7$, $\frac{N_E}{\sqrt{\theta_2}} = 93.8\%$.

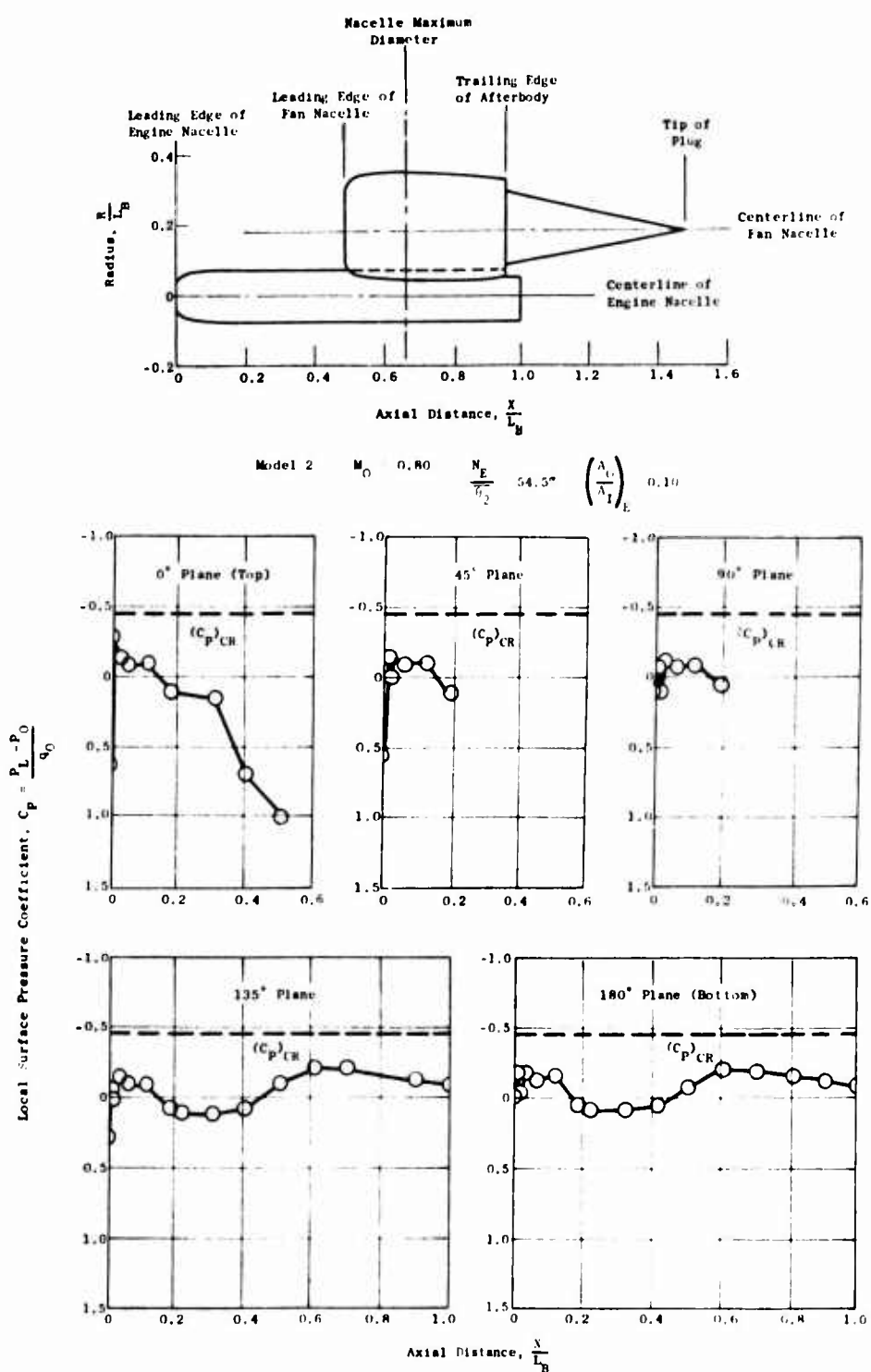


Figure 247. Typical Engine Nacelle Pressure Distributions - $M_0 = 0.8$, $\frac{N_E}{\sqrt{\theta_2}} = 54.5\%$.

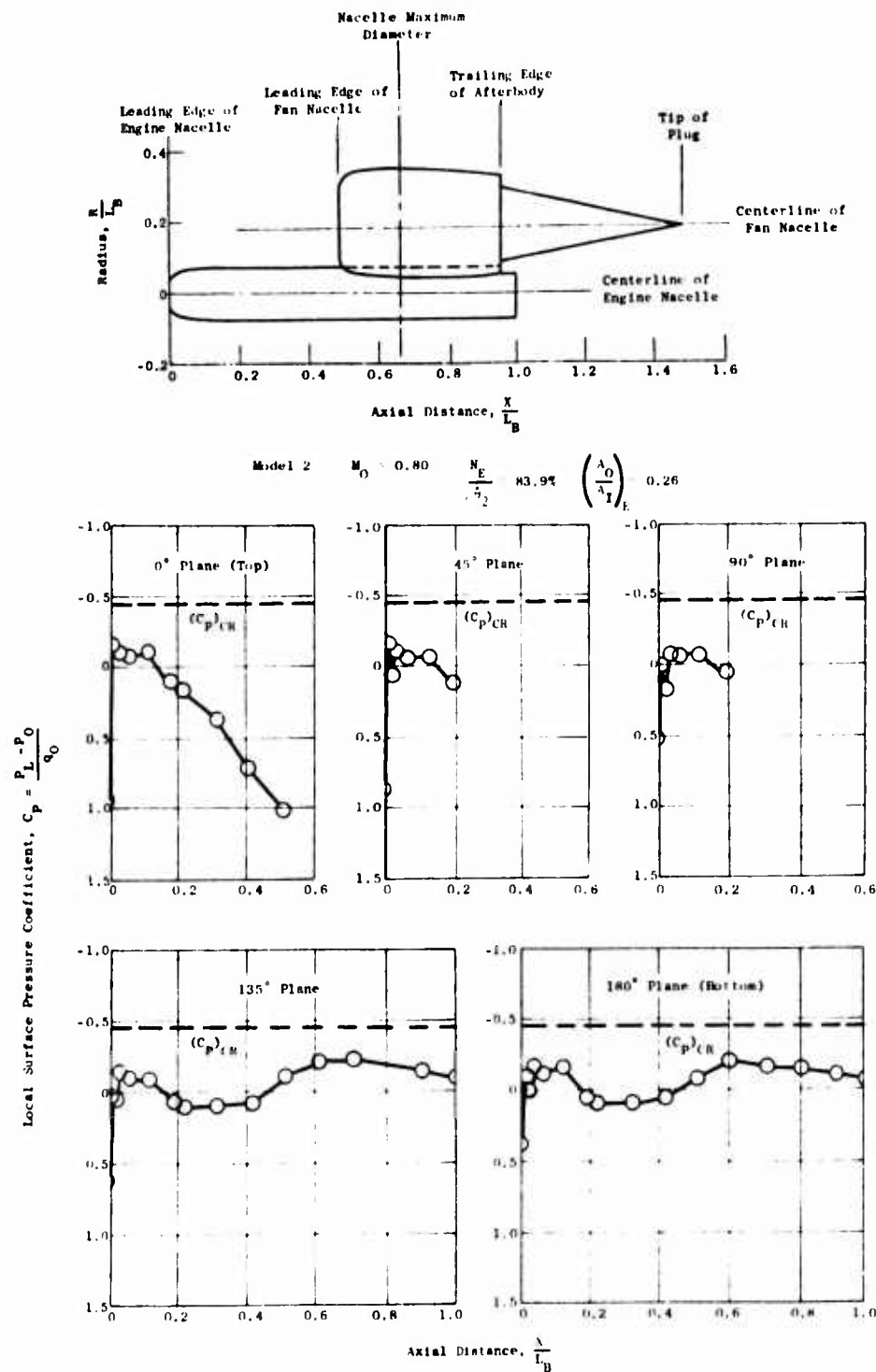
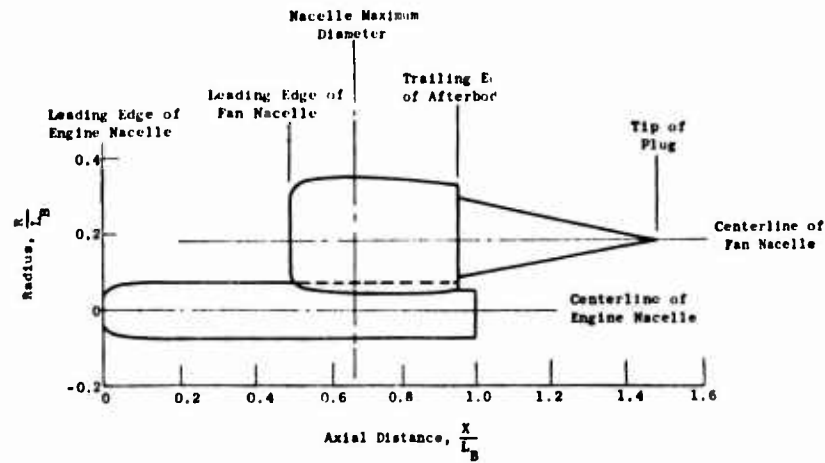


Figure 248. Typical Engine Nacelle Pressure Distributions - $M_0 = 0.8$,
 $\frac{N_E}{\sqrt{\theta_2}} = 83.9\%$



Model 2 $M_0 = 0.80$ $\frac{N_E}{\sqrt{\theta_2}} = 92.0\%$ $\left(\frac{A_0}{A_1}\right)_E = 0.32$

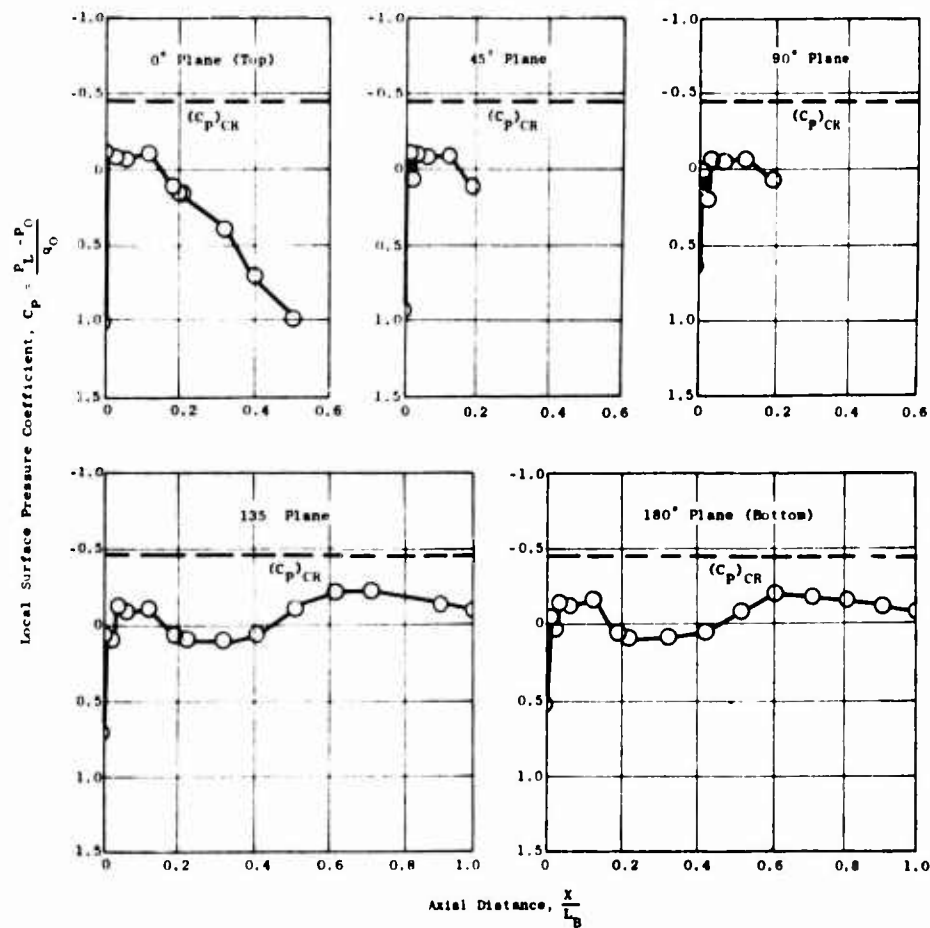


Figure 249. Typical Engine Nacelle Pressure Distributions - $M_0 = 0.8$,
 $\frac{N_E}{\sqrt{\theta_2}} = 92.0\%$.

$$M_0 = 0.301$$

$$\frac{N_F}{\sqrt{\theta_{10}}} = 32.2\% \text{ (Windmill)}$$

$$\frac{A_0}{A_1} = 0.559$$

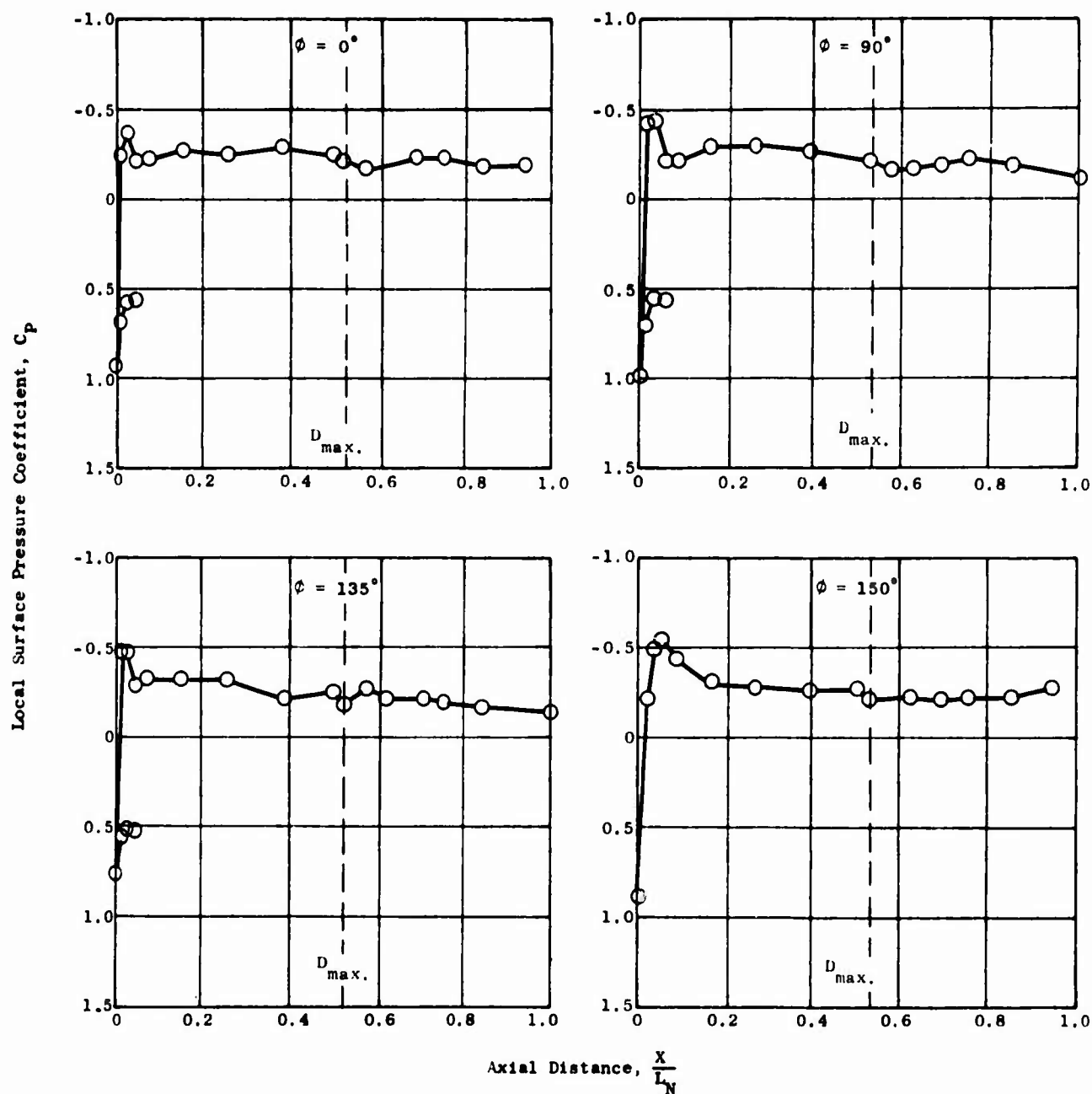


Figure 250. Nacelle External Pressure Distributions - Model 1, $M_0 = 0.301$, $N_F = 32.2\%$ (Windmill).

$$M_0 = 0.300$$

$$\frac{N_F}{\sqrt{\theta_{10}}} = 97.0\%$$

$$\frac{A_0}{A_1} = 0.722$$

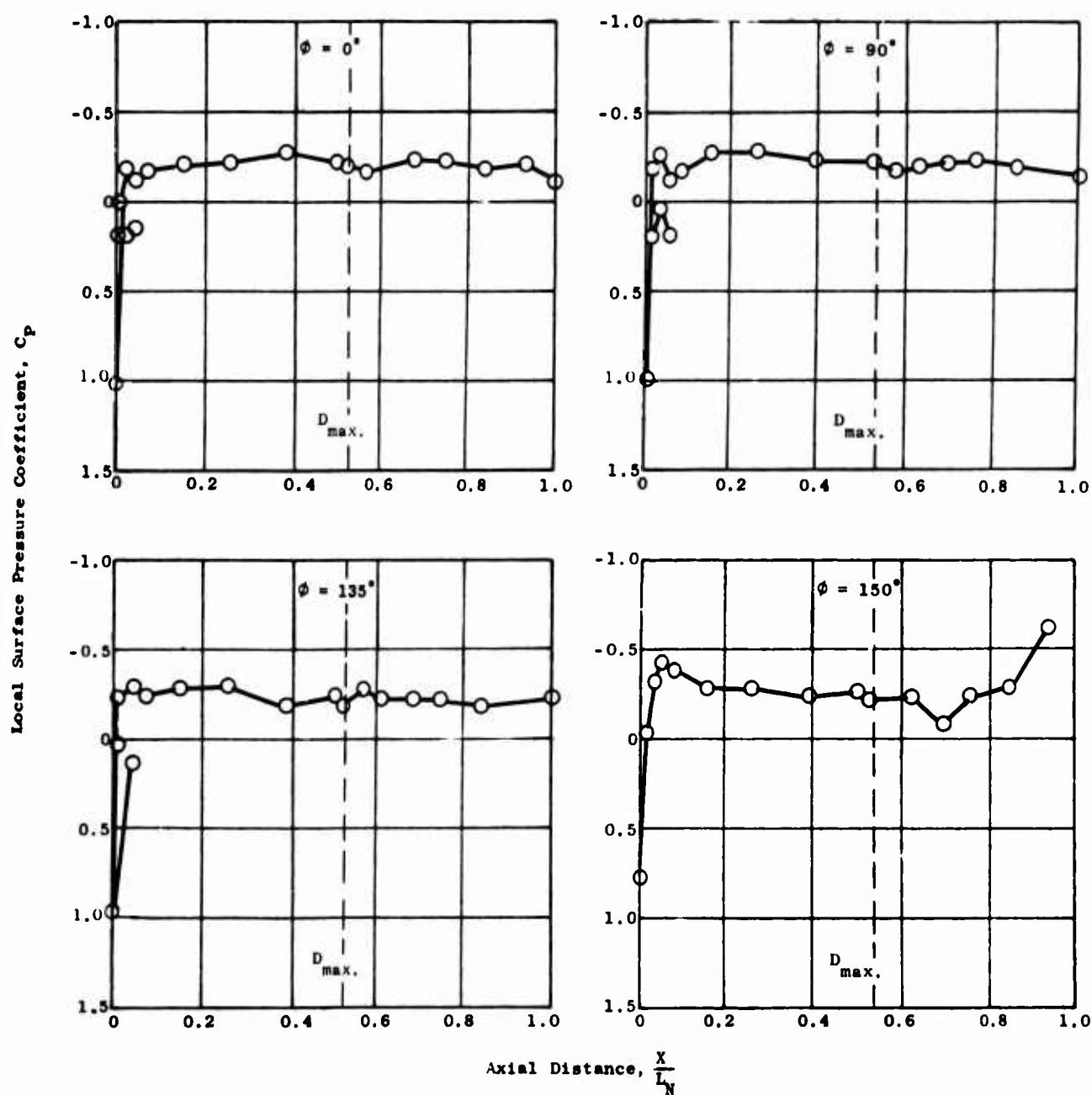


Figure 251. Nacelle External Pressure Distributions - Model 1, $M_0 = 0.300$, $N_F = 97.0\%$.

$$\frac{N_F}{\sqrt{\theta_{10}}}$$

$$M_0 = 0.601$$

$$\frac{N_F}{\sqrt{\theta_{10}}} = 56.4\%$$

$$\frac{A_0}{A_I} = 0.546$$

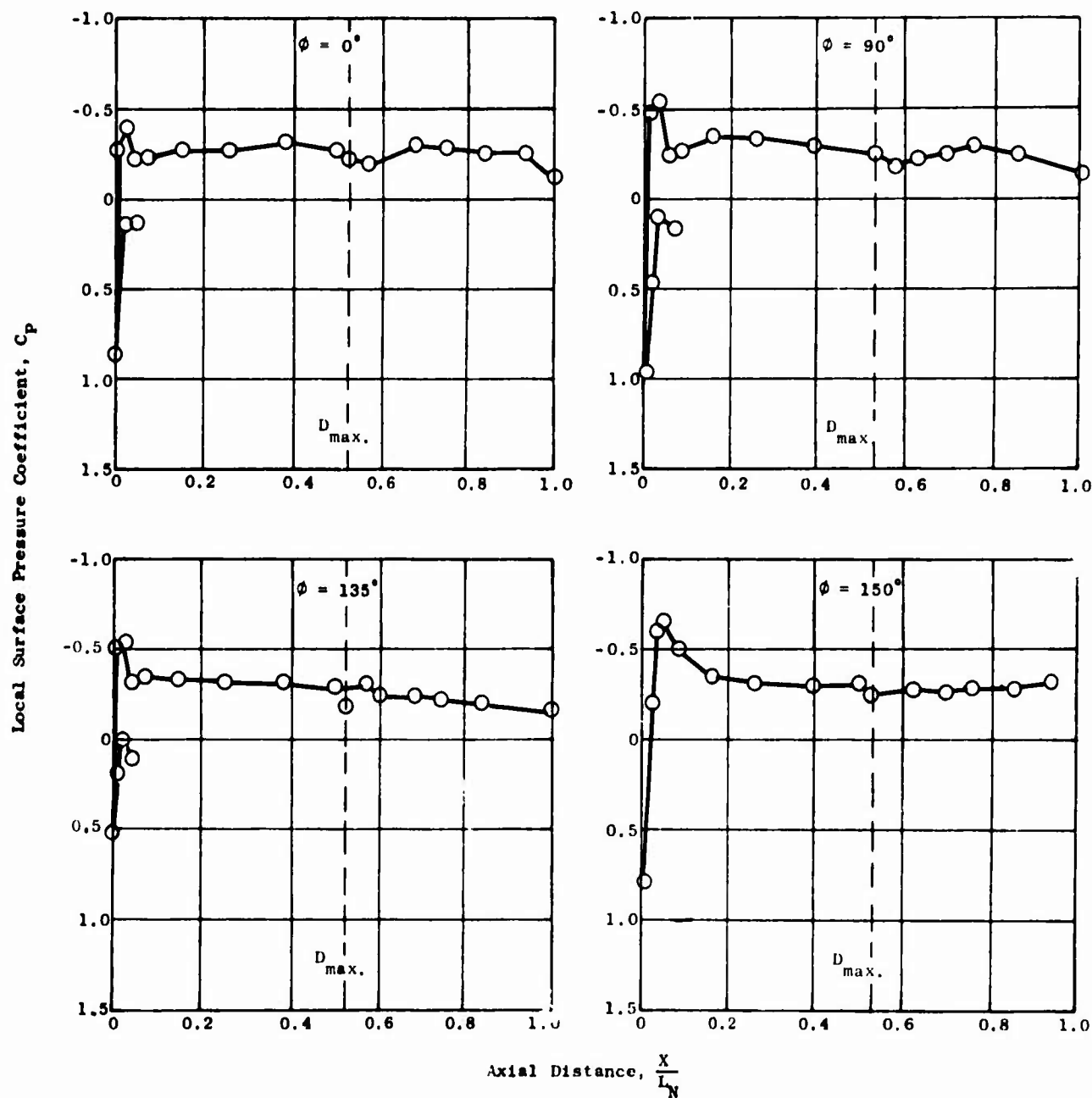


Figure 252. Nacelle External Pressure Distributions - Model 1, $M_0 = 0.601$, $N_F = 56.4\%$.

$$\sqrt{\theta_{10}}$$

$$M_0 = 0.600$$

$$\frac{N_F}{\sqrt{\theta_{10}}} = 94.2\%$$

$$\frac{A_0}{A_1} = 0.583$$

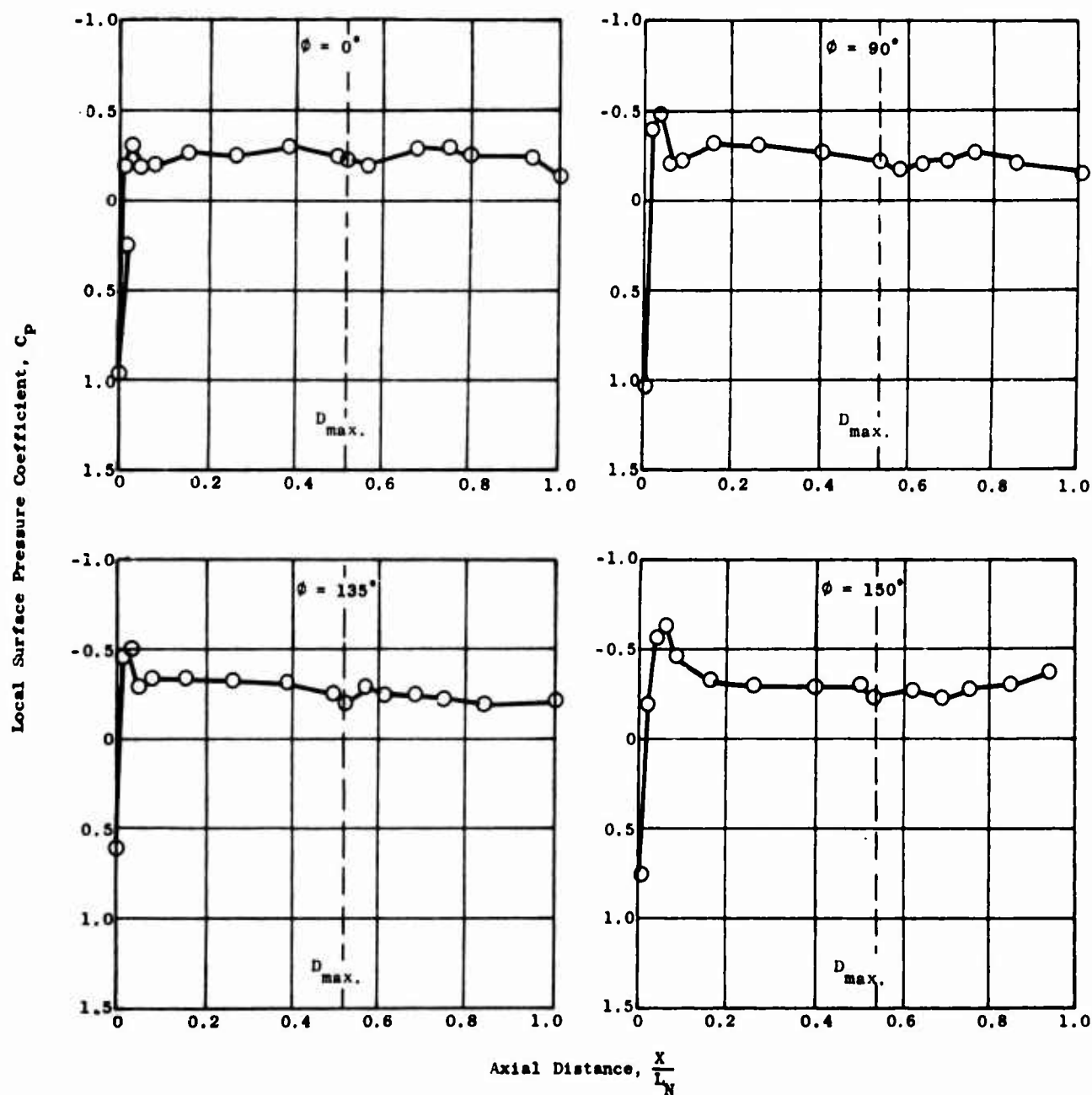


Figure 253. Nacelle External Pressure Distributions - Model 1, $M_0 = 0.600$, $N_F = 94.2\%$.

$$\sqrt{\theta_{10}}$$

$$M_0 = 0.797 \quad \frac{N_F}{\sqrt{\theta_{10}}} = 64.2\% \quad \frac{A_0}{A_I} = 0.337$$

(Windmill)

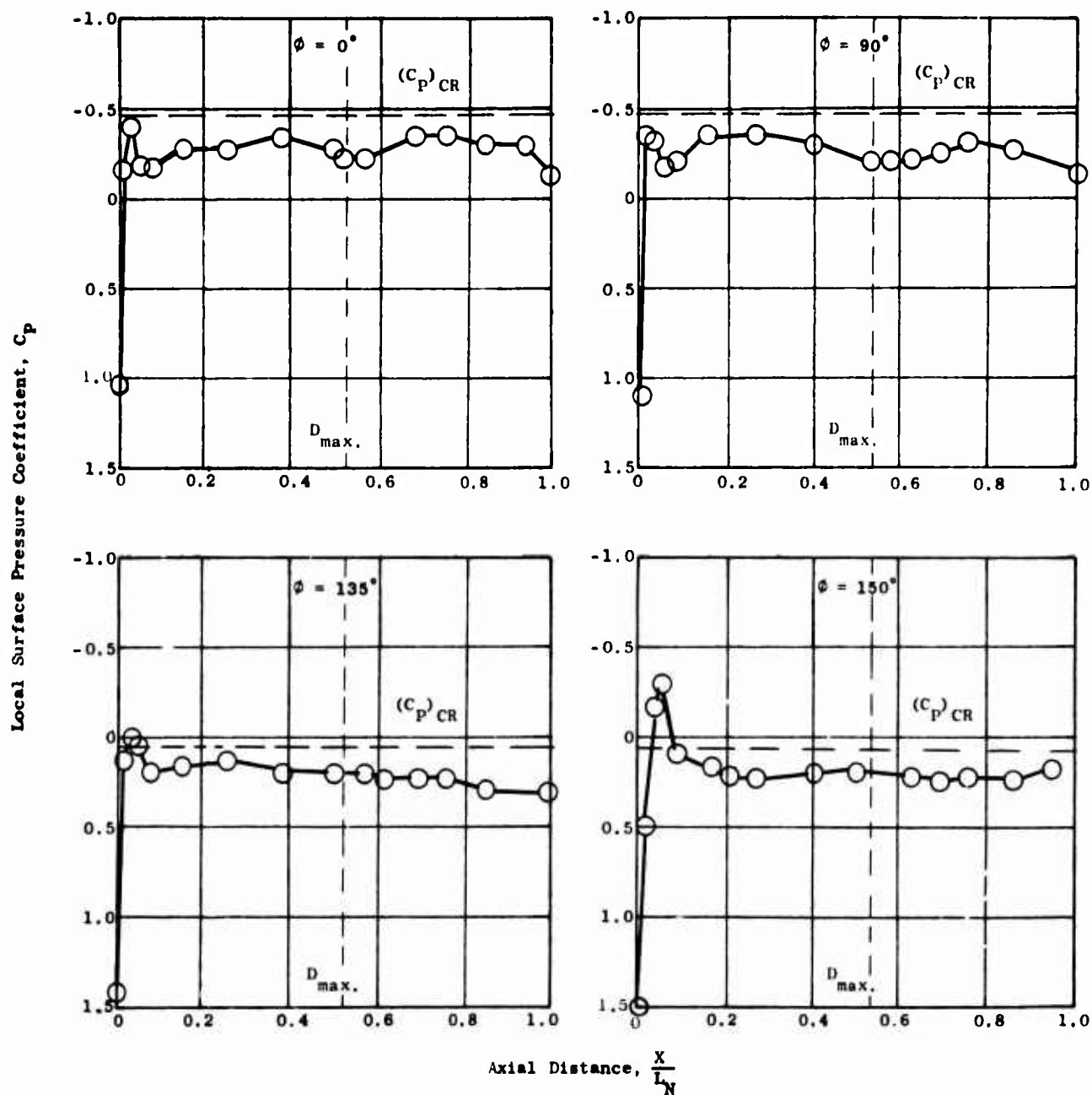


Figure 254. Nacelle External Pressure Distributions - Model 1, $M_0 = 0.797$, $N_F = 64.2\%$ (Windmill).

$$\sqrt{\theta_{10}}$$

$$M_0 = 0.800$$

$$\frac{N_F}{\sqrt{\theta_{10}}} = 87.6\%$$

$$\frac{A_0}{A_1} = 0.537$$

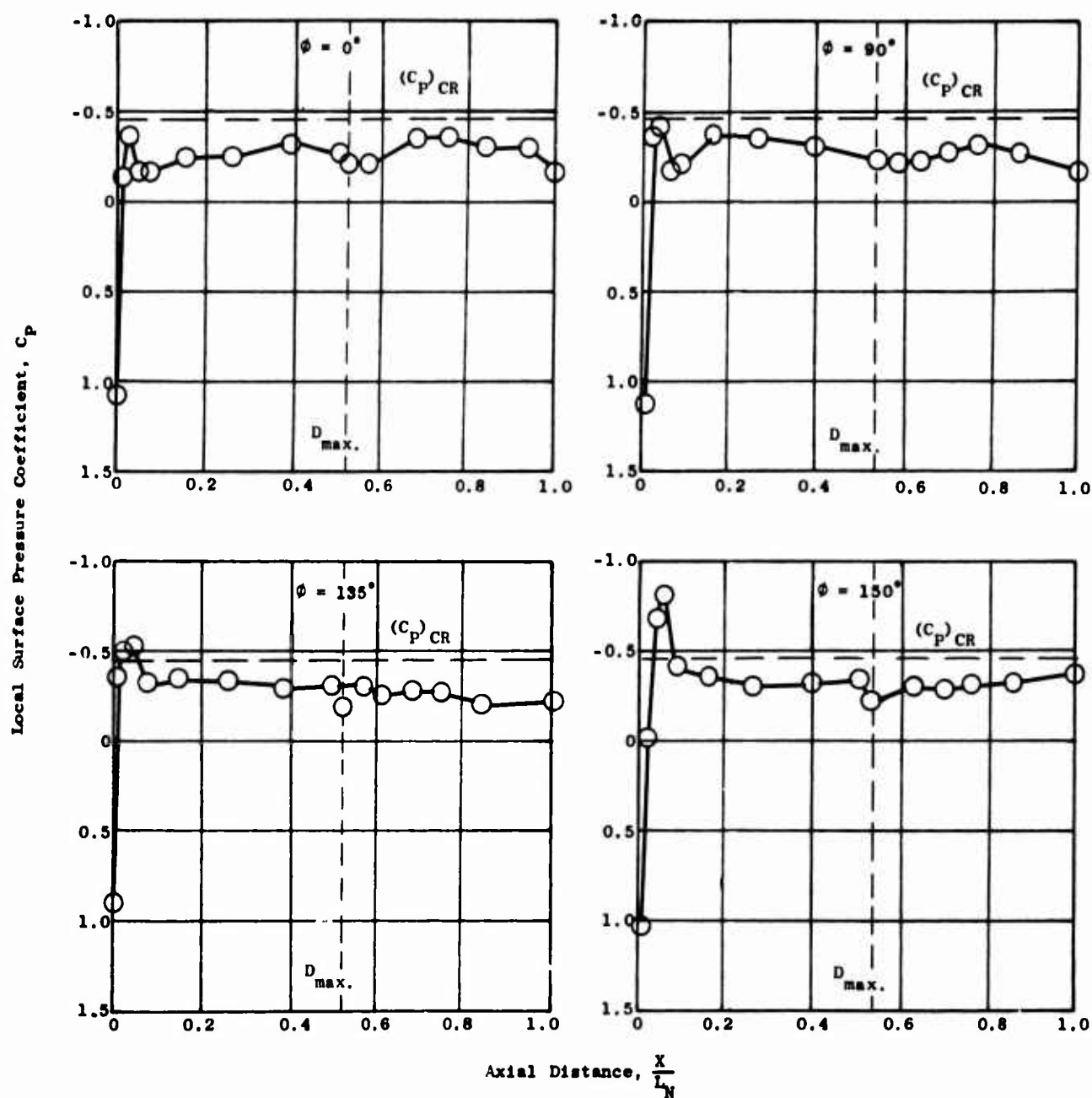


Figure 255. Nacelle External Pressure Distributions - Model 1, $M_0 = 0.800$, $\frac{N_F}{\sqrt{\theta_{10}}} = 87.6\%$.

$$\frac{N_F}{\sqrt{\theta_{10}}}$$

$$M_0 = 0.301$$

$$\frac{N_F}{\sqrt{\theta_{10}} \text{ (Windmill)}} = 32.3\%$$

$$\frac{A_0}{A_1} = 0.528$$

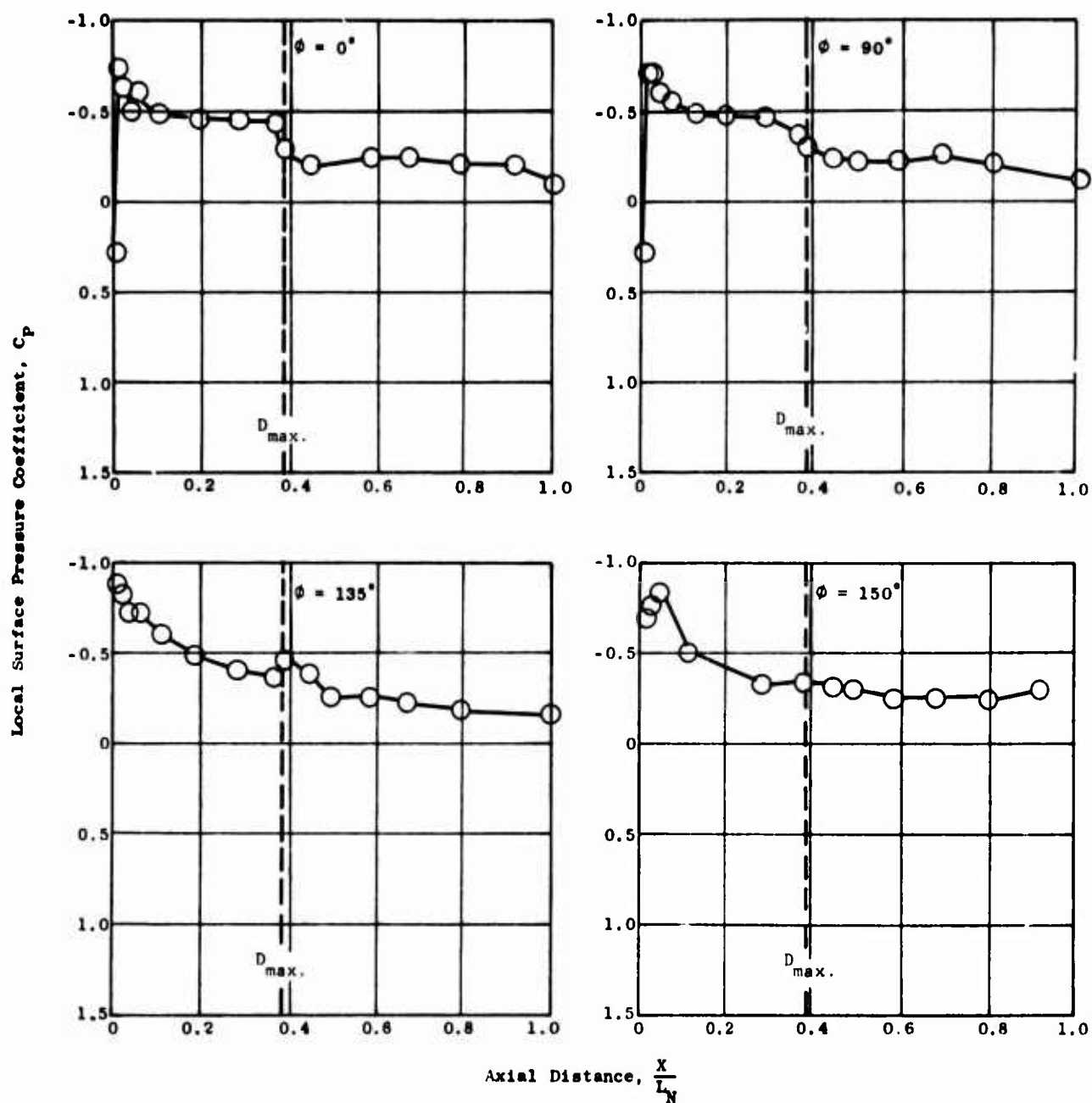


Figure 256. Nacelle External Pressure Distributions - Model 2, $M_0 = 0.301$, $N_F = 32.3\%$ (Windmill).
 $\sqrt{\theta_{10}}$

$$M_0 = 0.300$$

$$\frac{N_F}{\sqrt{\theta_{10}}} = 98.4\%$$

$$\frac{A_0}{A_1} = 0.728$$

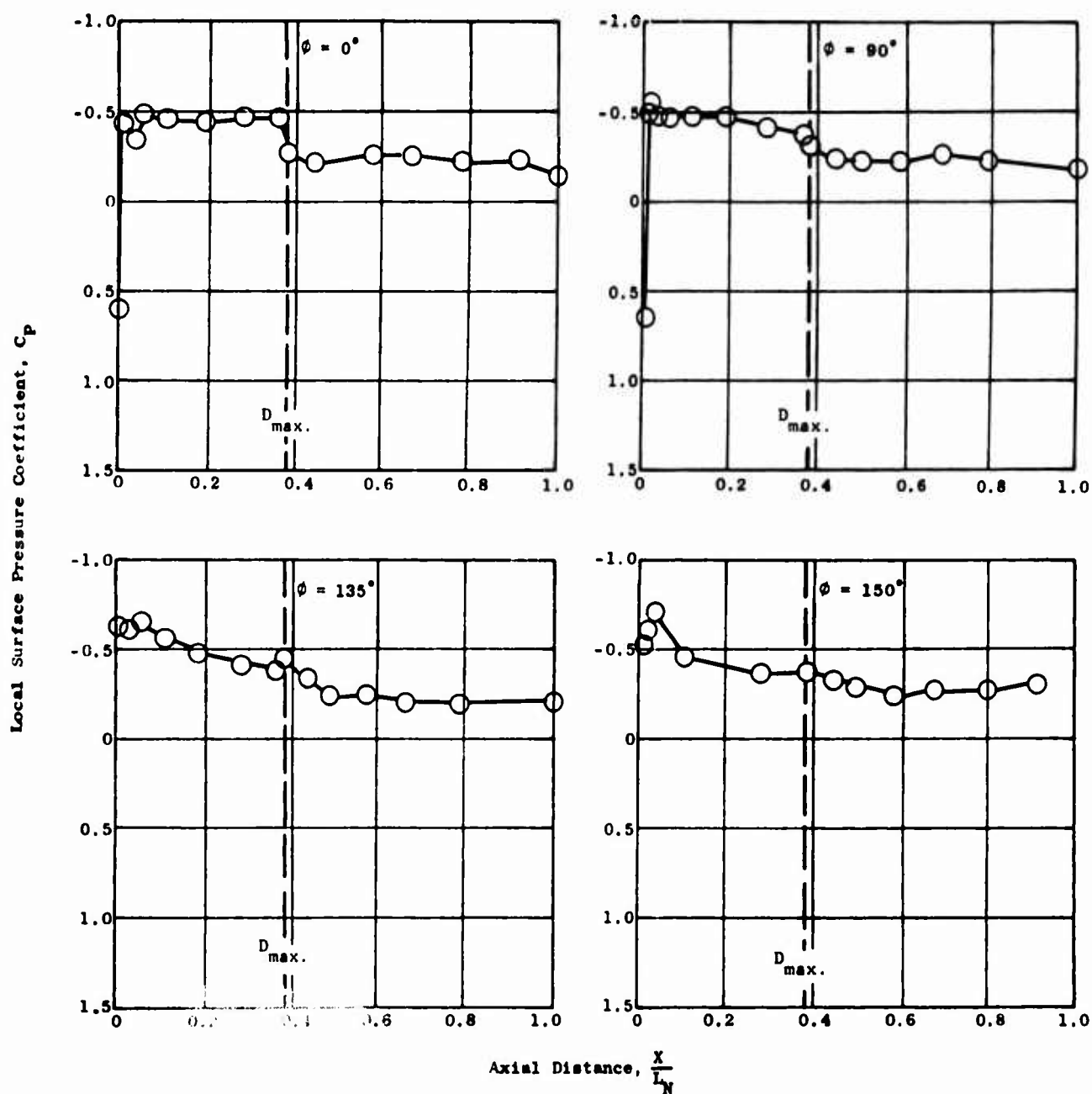


Figure 257. Nacelle External Pressure Distributions - Model 2, $M_0 = 0.300$, $N_F = 98.4\%$.

$$\frac{N_F}{\sqrt{\theta_{10}}}$$

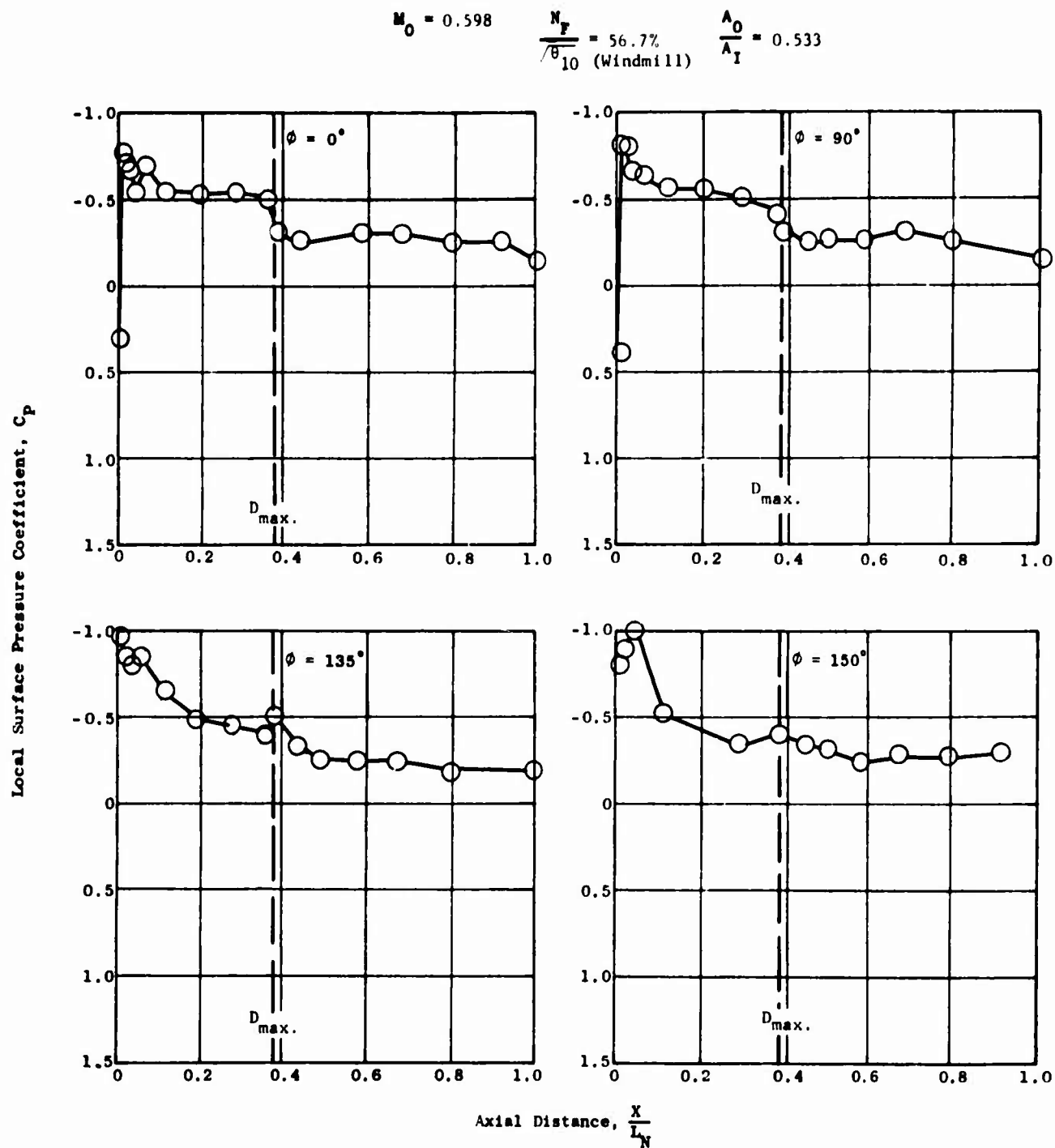


Figure 258. Nacelle External Pressure Distributions - Model 2, $M_0 = 0.598$, $\frac{N_F}{\sqrt{\theta_{10}}} = 56.7\%$ (Windmill).

$$M_0 = 0.599$$

$$\frac{N_F}{\sqrt{\theta_{10}}} = 91.5\%$$

$$\frac{A_0}{A_I} = 0.563$$

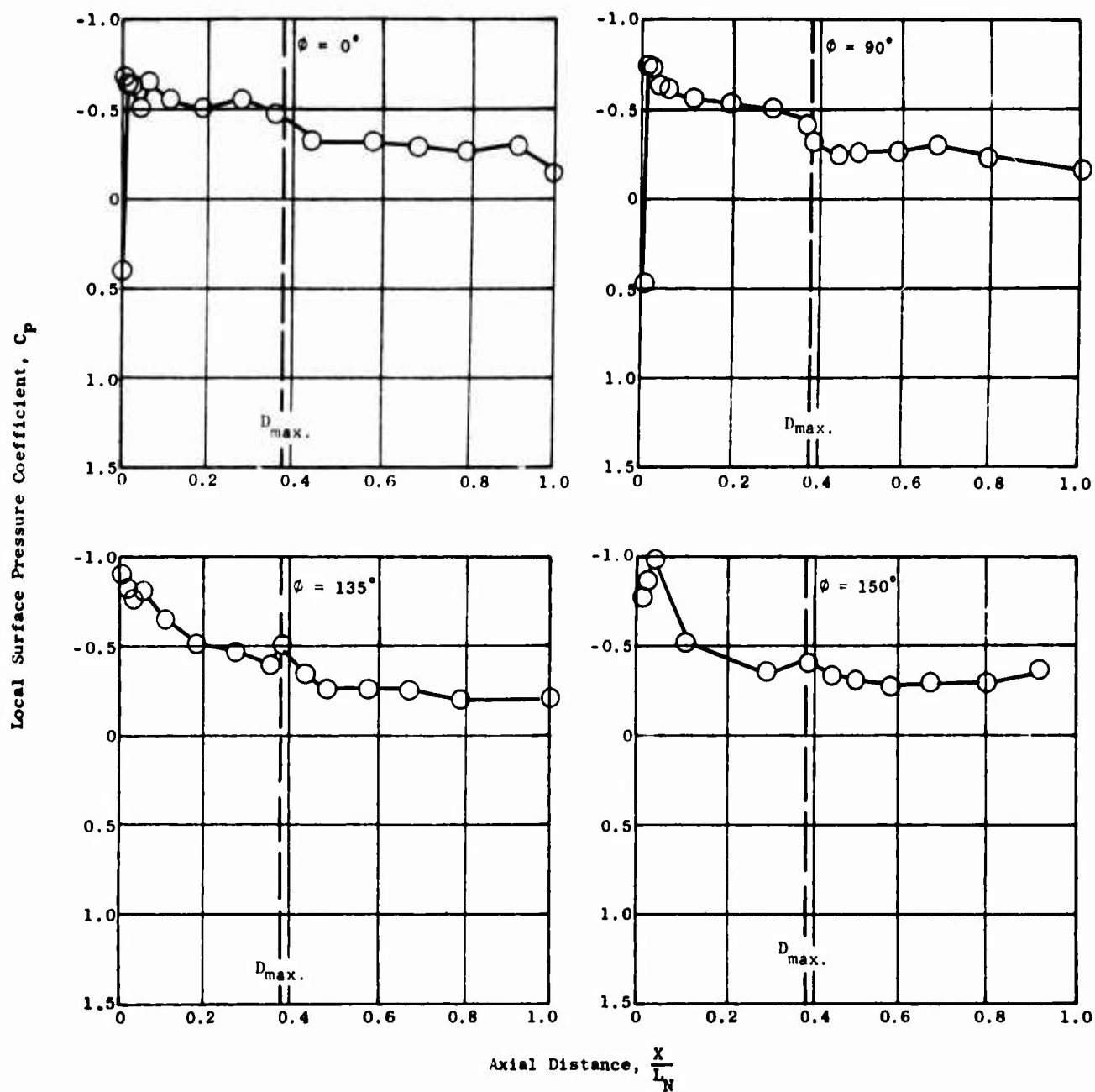


Figure 259. Nacelle External Pressure Distributions - Model 2, $M_0 = 0.599$, $N_F = 91.5\%$.

$$\sqrt{\theta_{10}}$$

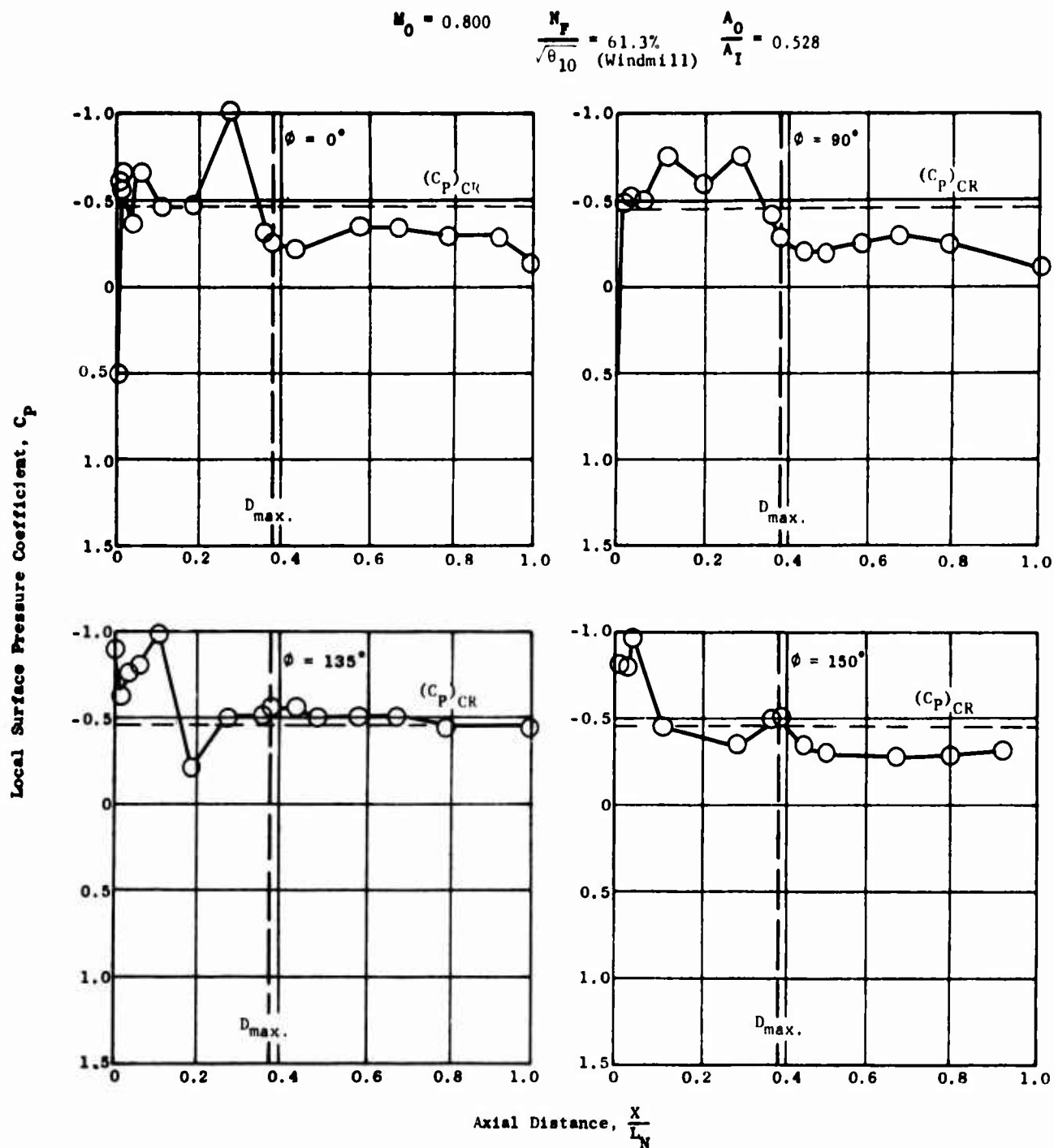


Figure 260. Nacelle External Pressure Distributions - Model 2, $M_0 = 0.800$, $\frac{N_F}{\sqrt{\theta_{10}}} = 61.3\%$ (Windmill).

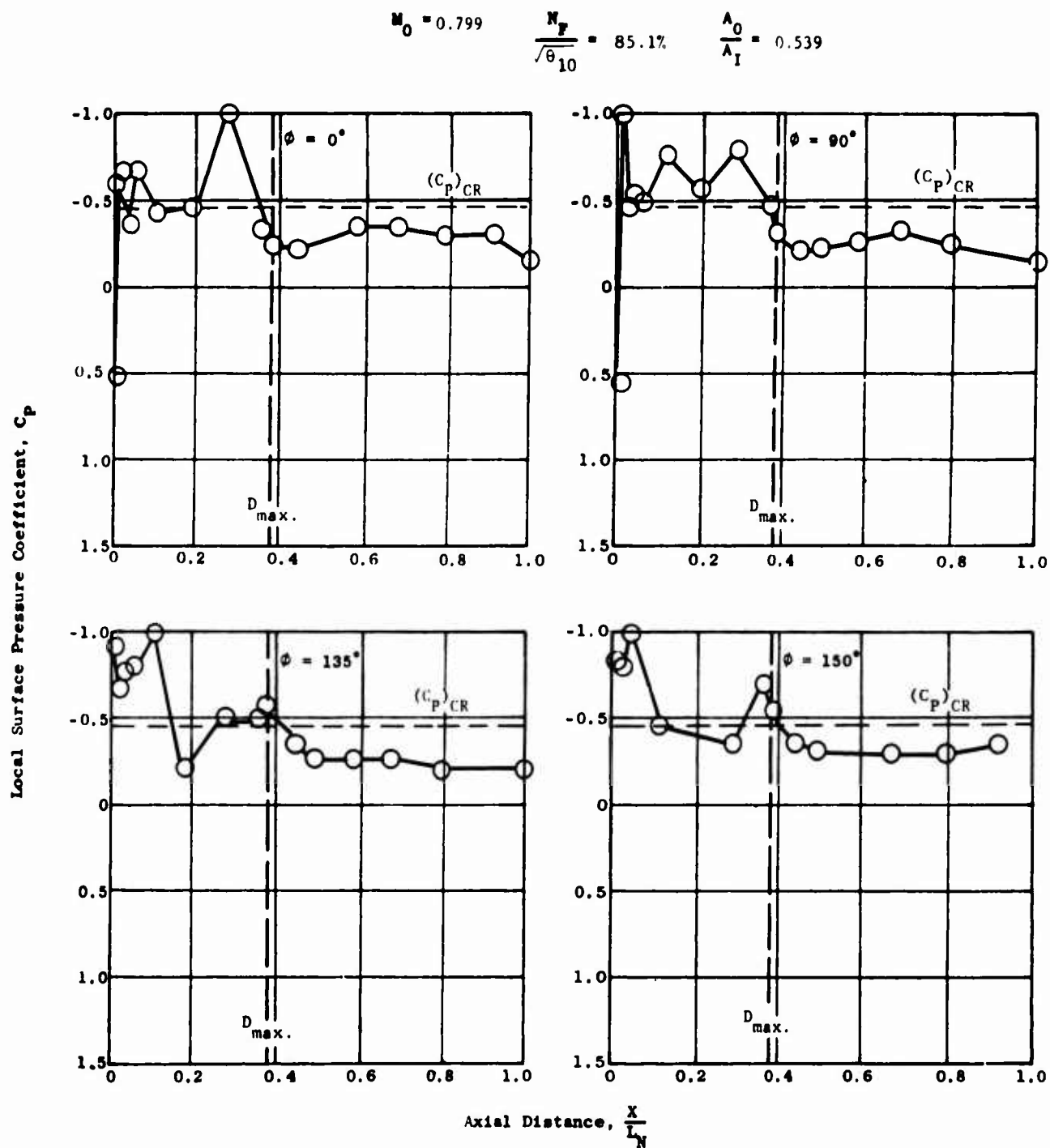


Figure 261. Nacelle External Pressure Distributions - Model 2, $M_0 = 0.799$, $\frac{N_F}{\sqrt{\theta_{10}}} = 85.1\%$.

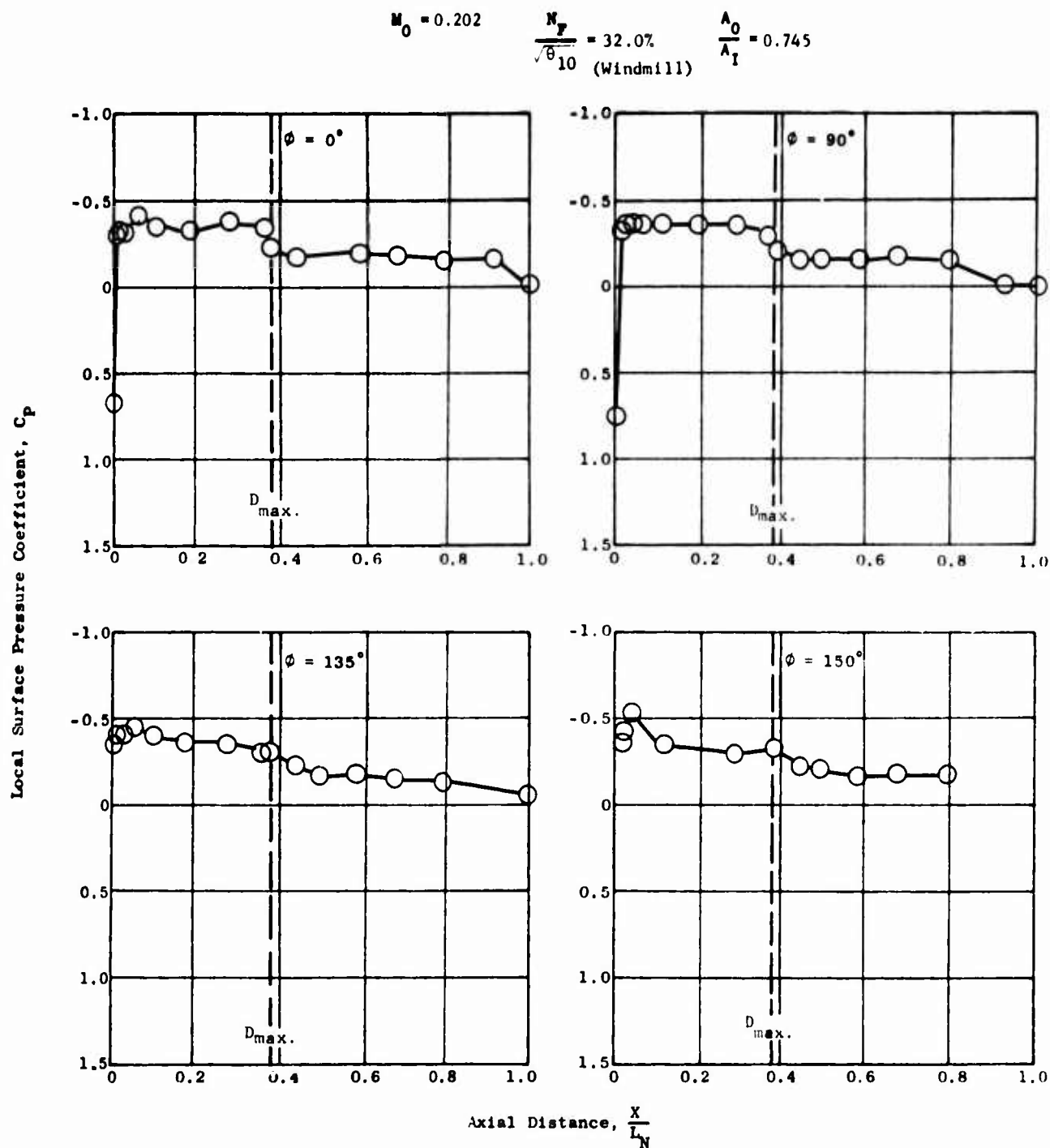


Figure 262. Nacelle External Pressure Distributions - Model 3, $M_0 = 0.202$, $N_F = 32.0\%$ (Windmill).

$\sqrt{\theta_{10}}$

$$M_0 = 0.202$$

$$\frac{N_F}{\sqrt{\theta_{10}}} = 97.2\%$$

$$\frac{A_0}{A_I} = 1.521$$

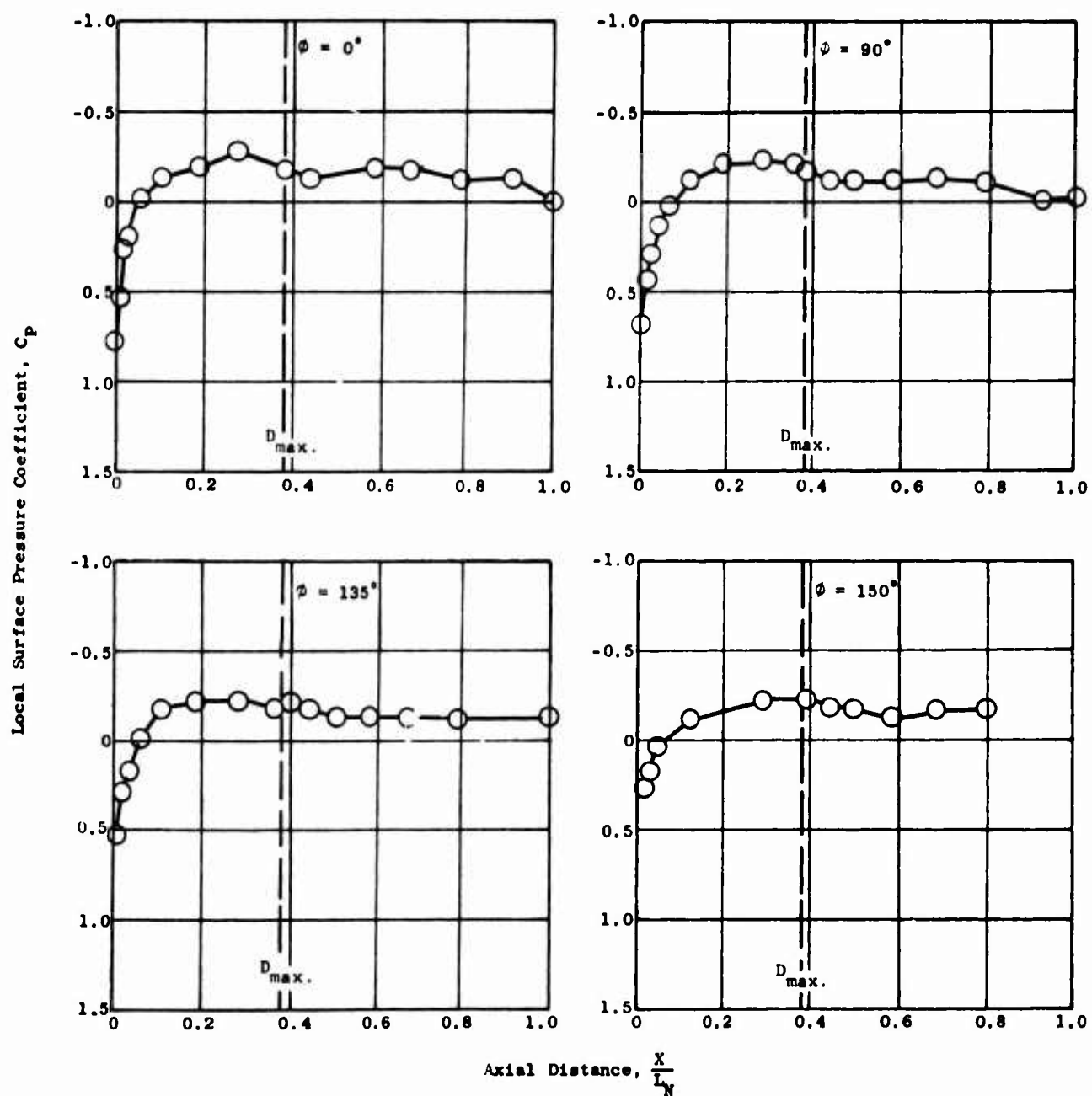


Figure 263. Nacelle External Pressure Distributions - Model 3, $M_0 = 0.202$, $\frac{N_F}{\sqrt{\theta_{10}}} = 97.2\%$.

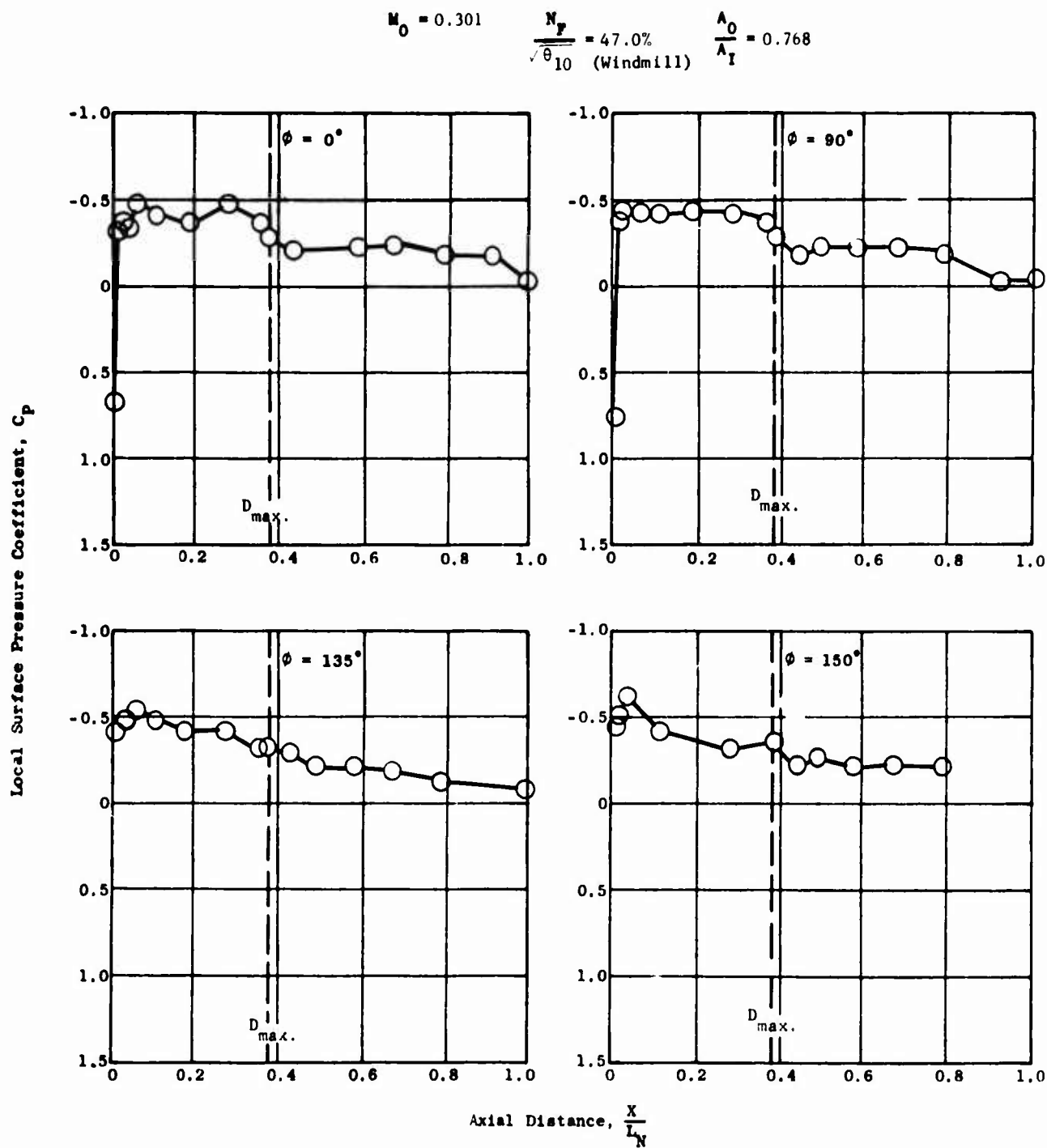


Figure 264. Nacelle External Pressure Distributions - Model 3, $M_0 = 0.301$, $\frac{N_F}{\sqrt{\theta_{10}}} = 47.0\%$ (Windmill).

$$M_0 = 0.301$$

$$\frac{N_F}{\sqrt{\theta_{10}}} = 97.7\%$$

$$\frac{A_0}{A_I} = 1.156$$

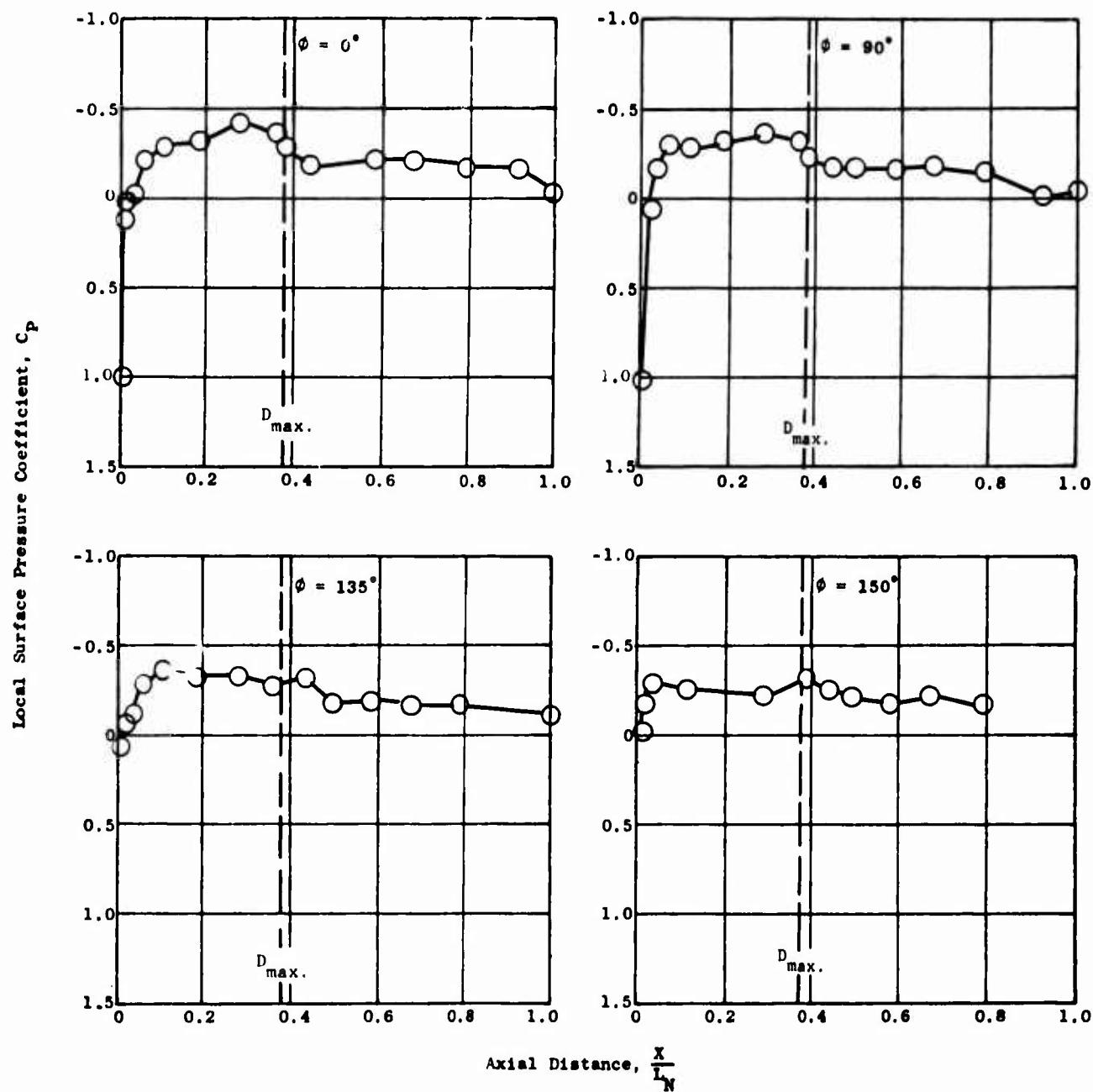


Figure 265. Nacelle External Pressure Distributions - Model 3, $M_0 = 0.301$, $\frac{N_F}{\sqrt{\theta_{10}}} = 97.7\%$.

$$M_0 = 0.400$$

$$\frac{N_F}{\sqrt{\theta}_{10}} = 60.2\% \text{ (Windmill)}$$

$$\frac{A_0}{A_I} = 0.763$$

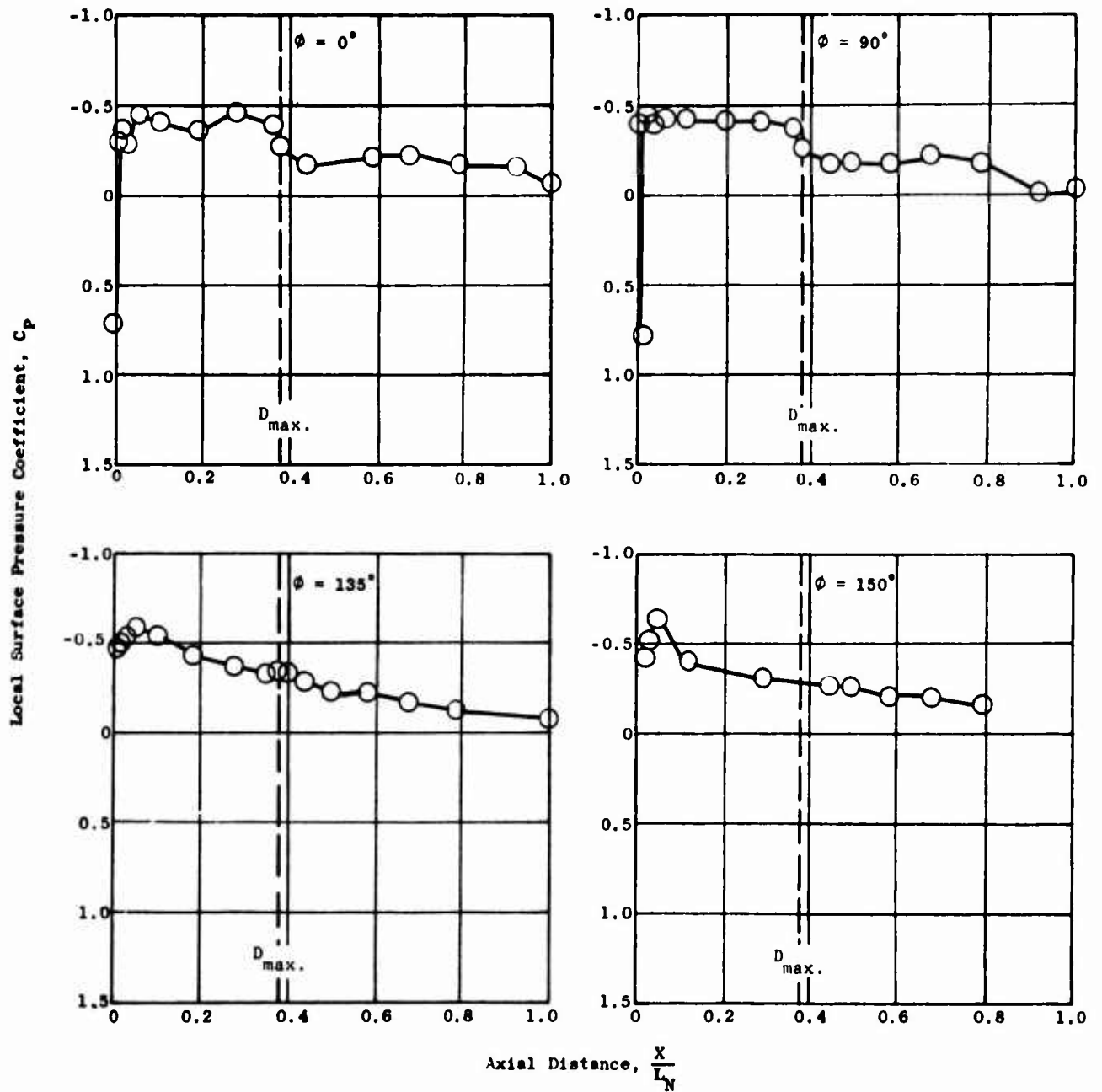


Figure 266. Nacelle External Pressure Distributions - Model 3, $M_0 = 0.400$, $N_F = 60.2\%$ (Windmill).
 $\sqrt{\theta}_{10}$

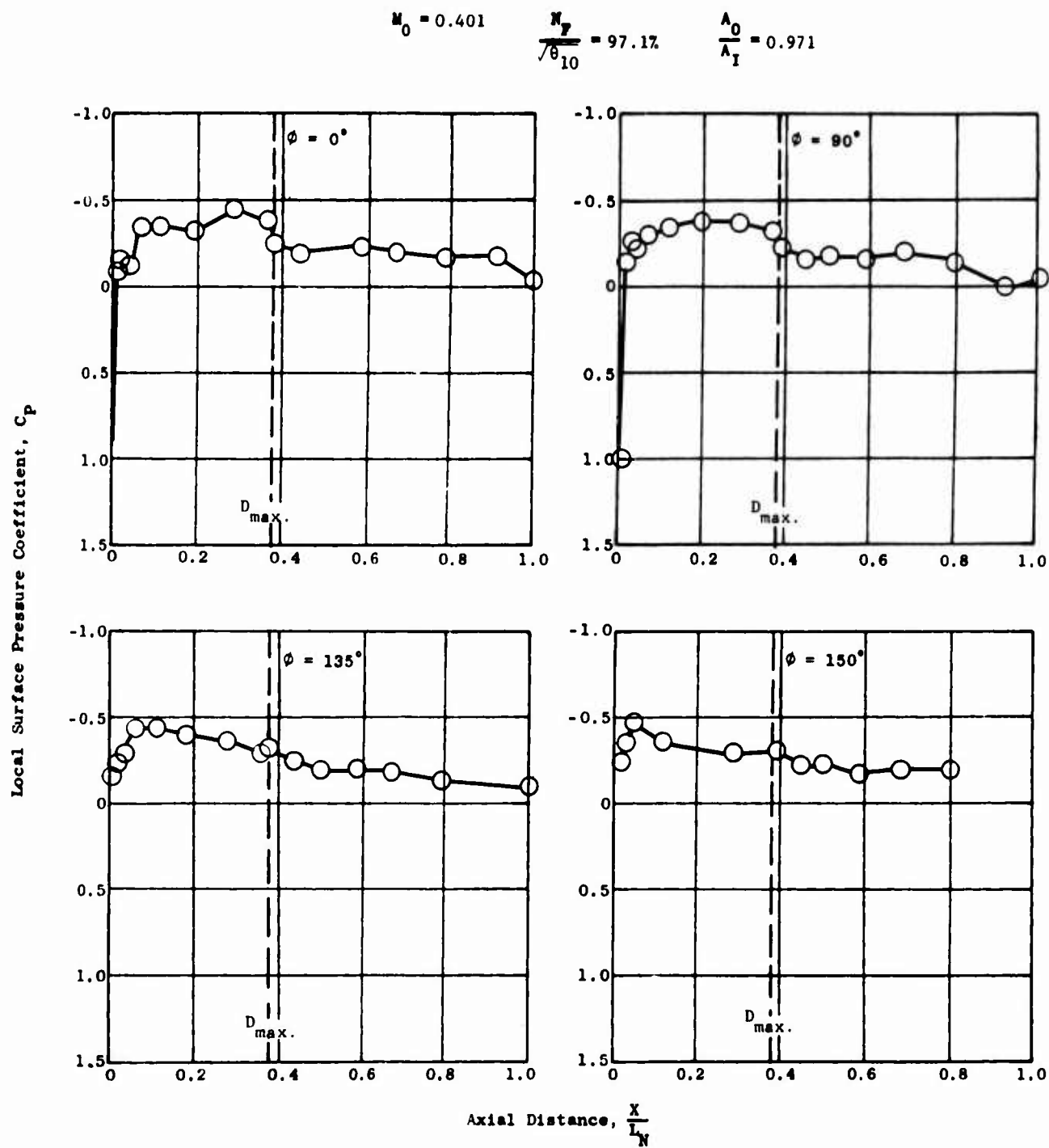


Figure 267. Nacelle External Pressure Distributions - Model 3, $M_0 = 0.401$, $N_F = 97.1\%$.

$$M_0 = 0.203$$

$$\frac{N_F}{\sqrt{\theta_{10}}} = 22.3\% \text{ (Windmill)}$$

$$\frac{A_0}{A_I} = 0.346$$

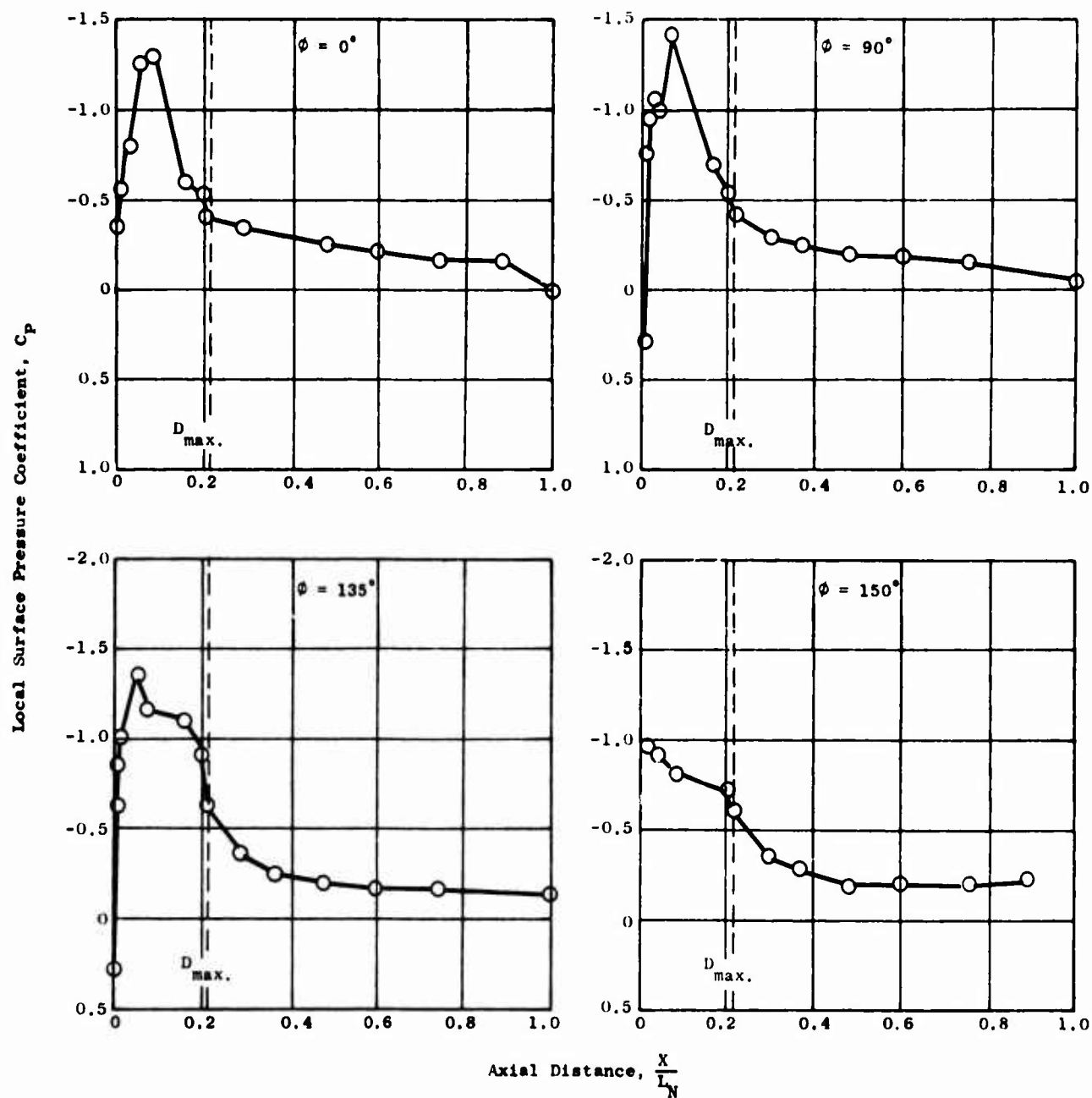


Figure 268. Nacelle External Pressure Distributions - Model 4, $M_0 = 0.203$, $\frac{N_F}{\sqrt{\theta_{10}}} = 22.3\%$ (Windmill).

$$M_0 = 0.202$$

$$\frac{N_F}{\sqrt{\theta_{10}}} = 95.3\%$$

$$\frac{A_0}{A_1} = 0.555$$

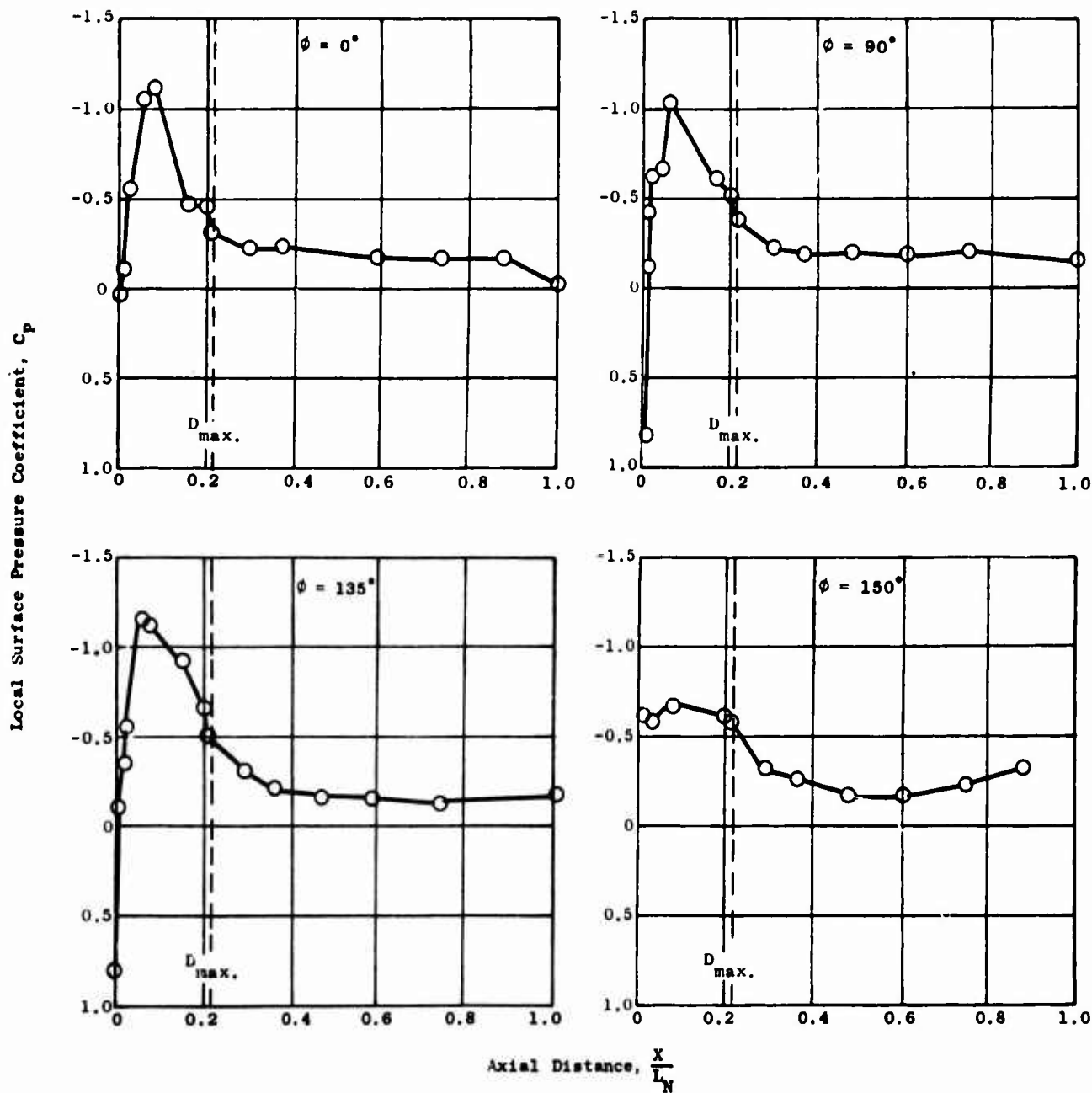


Figure 269. Nacelle External Pressure Distributions - Model 4, $M_0 = 0.202$, $\frac{N_F}{\sqrt{\theta_{10}}} = 95.3\%$.

$$\sqrt{\theta_{10}}$$

$$M_0 = 0.501$$

$$\frac{N_F}{\sqrt{\theta_{10}}} = 49.9\% \text{ (Windmill)}$$

$$\frac{A_0}{A_1} = 0.350$$

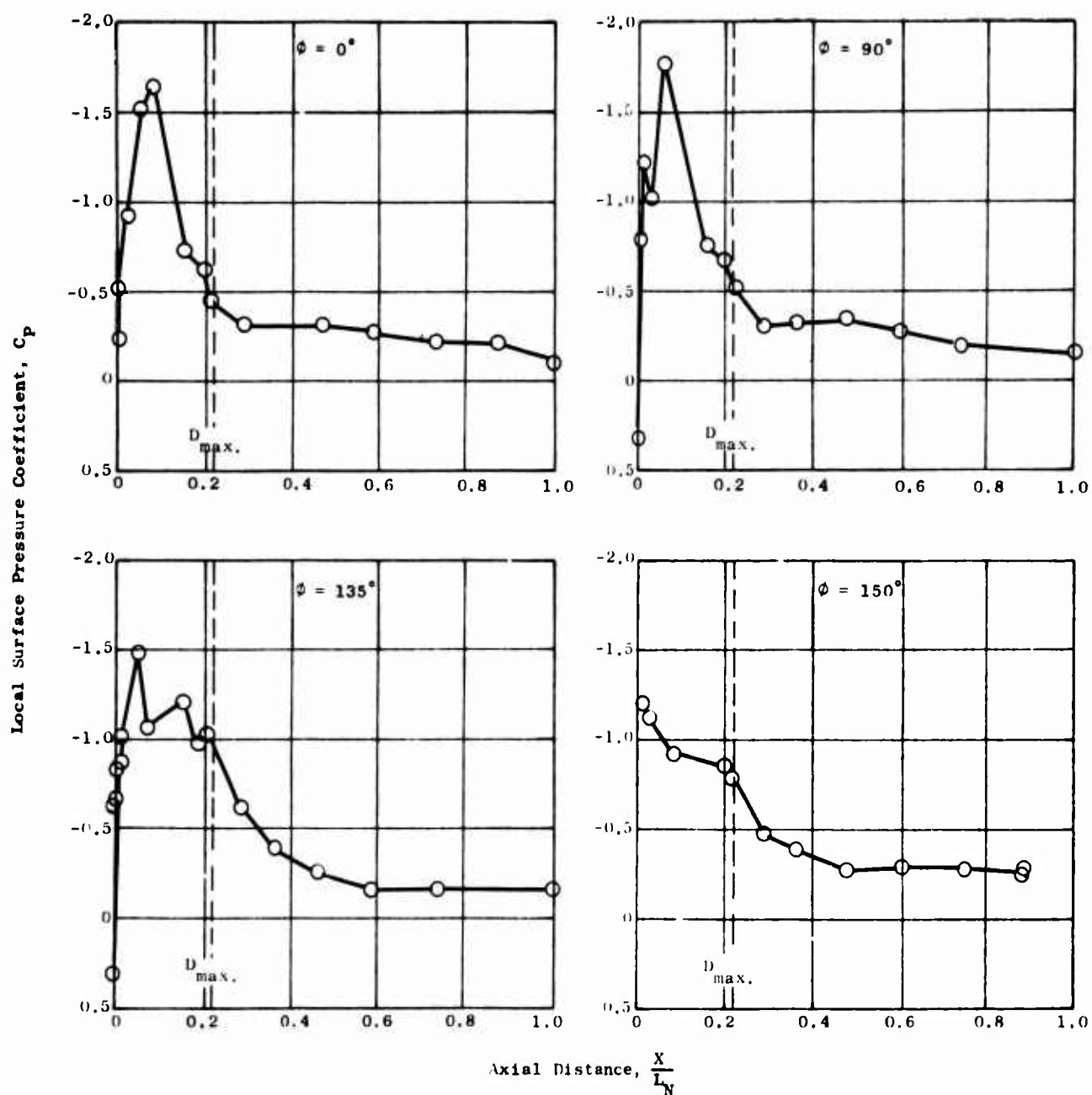


Figure 270. Nacelle External Pressure Distributions - Model 4, $M_0 = 0.501$, $\frac{N_F}{\sqrt{\theta_{10}}} = 49.9\%$ (Windmill).

$$M_0 = 0.500 \quad \frac{N_F}{\sqrt{\theta}_{10}} = 93.5\% \quad \frac{A_0}{A_I} = 0.383$$

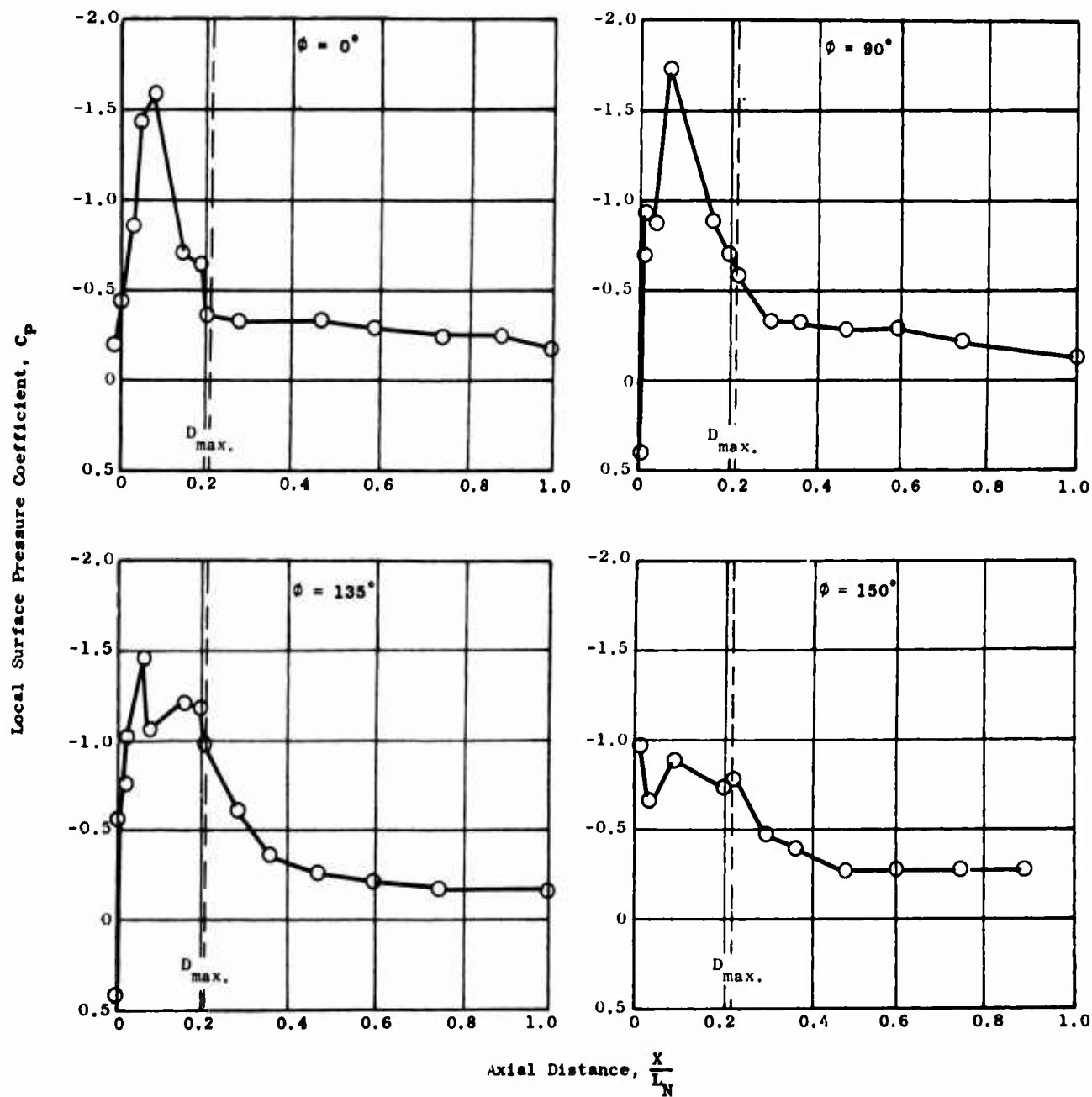


Figure 271. Nacelle External Pressure Distributions - Model 4, $M_0 = 0.500$, $\frac{N_F}{\sqrt{\theta}_{10}} = 93.5\%$.

$$M_0 = 0.649$$

$$\frac{N_F}{\sqrt{\theta}_{10}} = 58.8\% \text{ (Windmill)}$$

$$\frac{A_0}{A_I} = 0.351$$

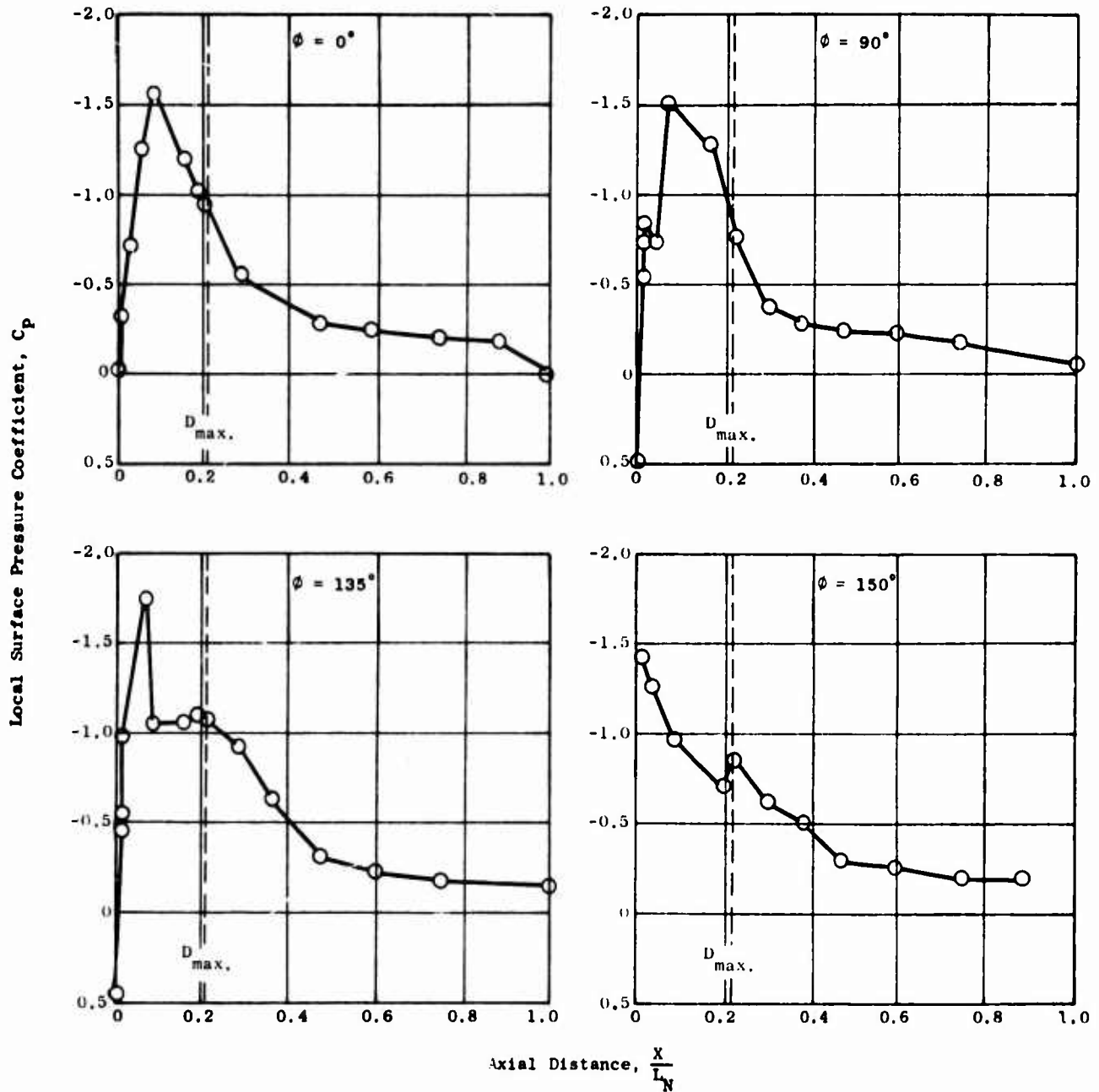


Figure 272. Nacelle External Pressure Distributions - Model 4, $M_0 = 0.649$, $N_F = 58.8\%$ (Windmill).

$$\frac{N_F}{\sqrt{\theta}_{10}}$$

$$M_0 = 0.650$$

$$\frac{N_F}{\sqrt{\theta_{10}}} = 91.7\%$$

$$\frac{A_0}{A_1} = 0.360$$

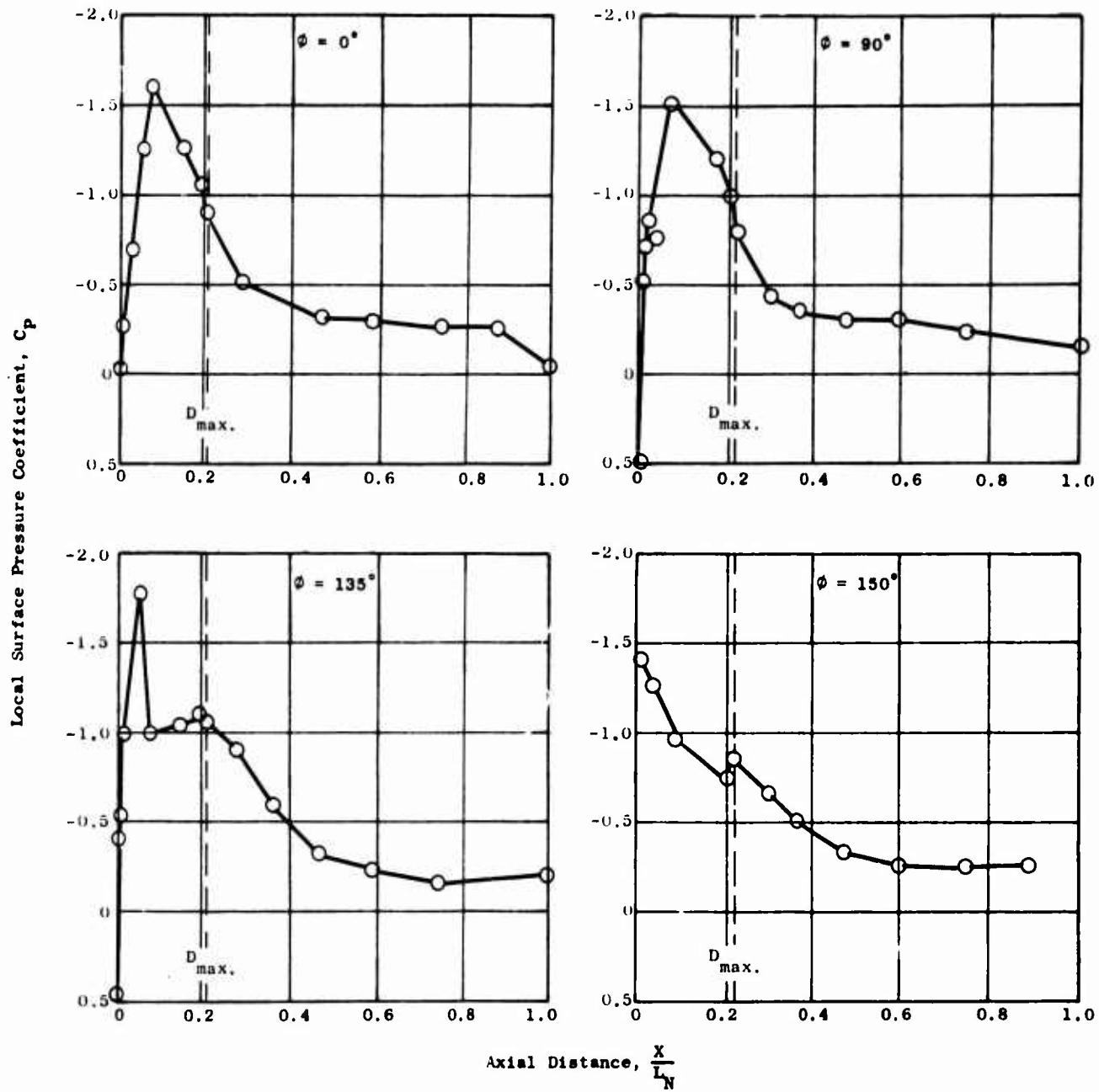


Figure 273. Nacelle External Pressure Distributions - Model 4, $M_0 = 0.650$, $N_F = 91.7\%$.

$$M_0 = 0.202$$

$$\frac{N_F}{\sqrt{\theta_{10}}} = 24.0\% \quad (\text{Windmill})$$

$$\frac{A_0}{A_I} = 0.348$$

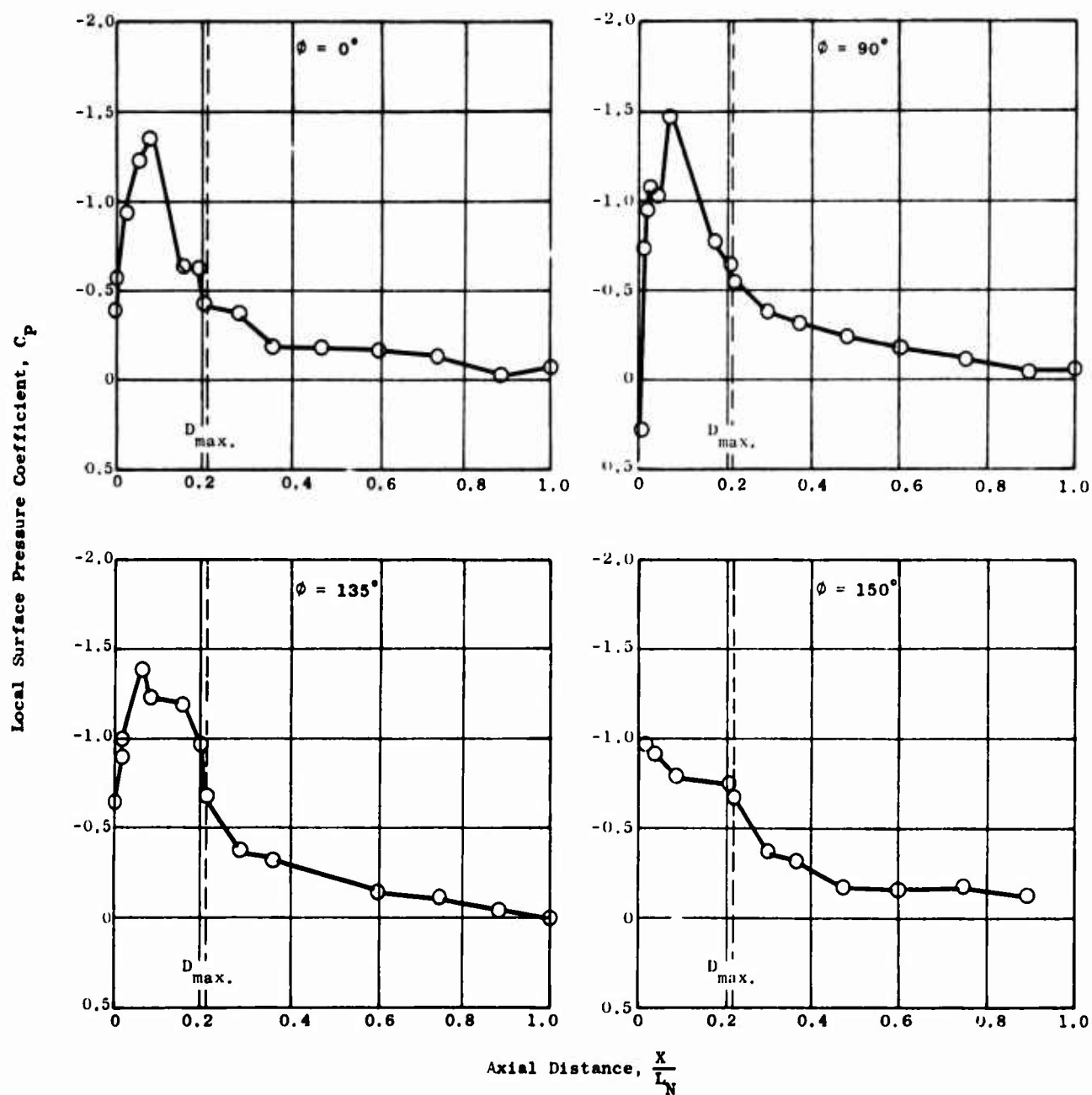


Figure 274. Nacelle External Pressure Distributions - Model 5, $M_0 = 0.202$, $\frac{N_F}{\sqrt{\theta_{10}}} = 24.0\%$ (Windmill).

$$M_0 = 0.200 \quad \frac{N_F}{\sqrt{\theta_{10}}} = 97.8\% \quad \frac{A_0}{A_1} = 0.663$$

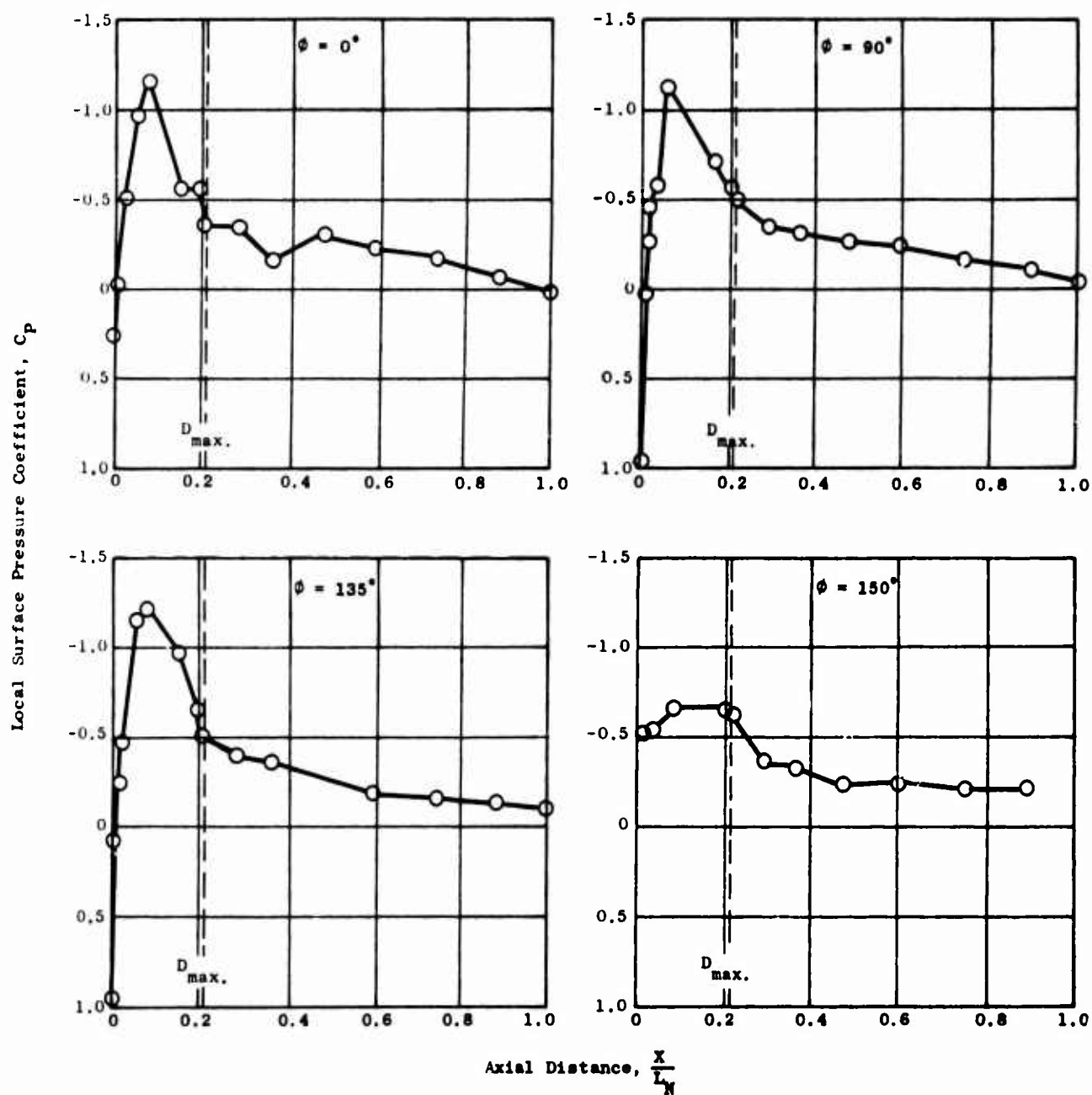


Figure 275. Nacelle External Pressure Distributions - Model 5, $M_0 = 0.200$, $N_F = 97.8\%$.

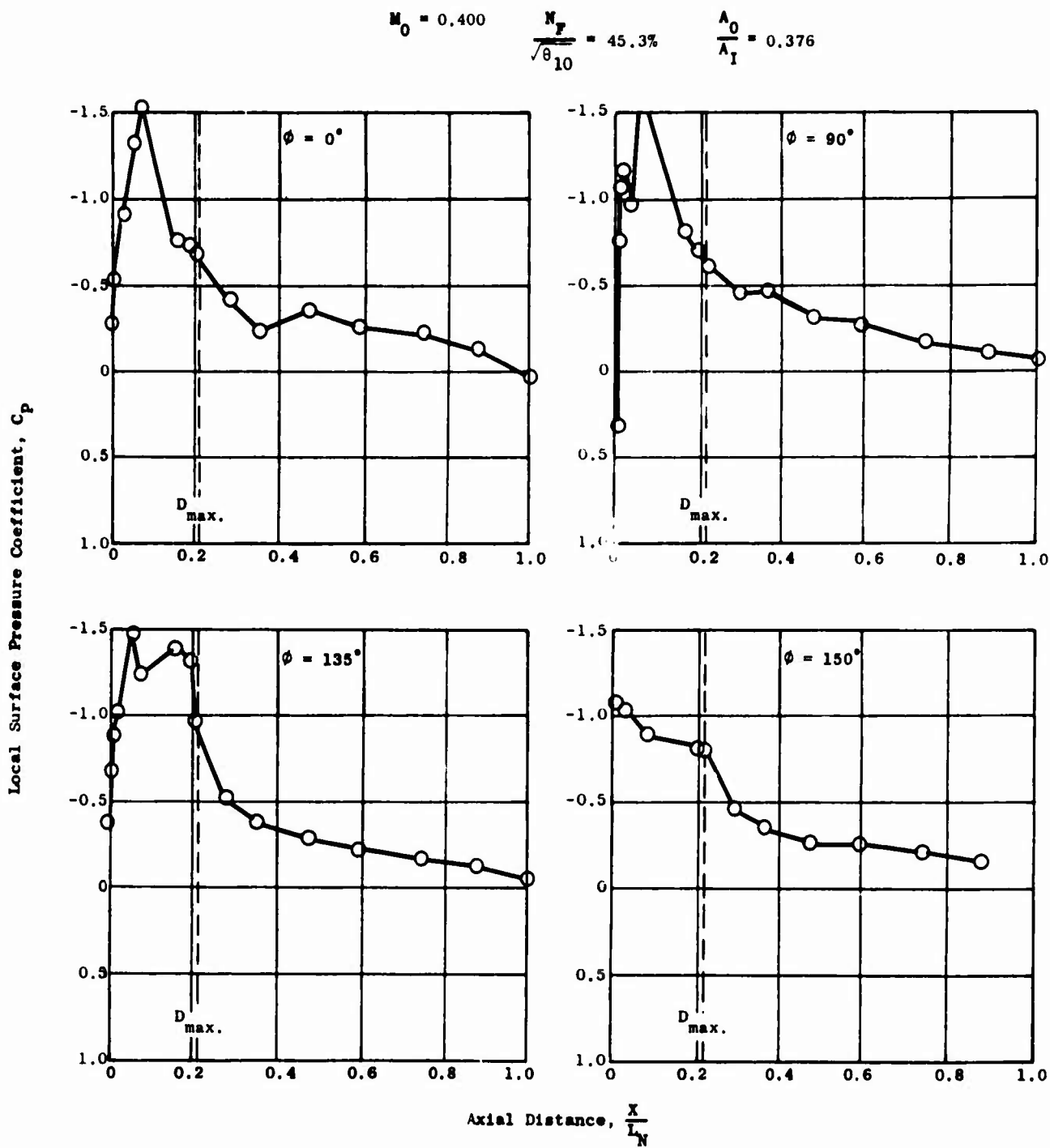


Figure 276. Nacelle External Pressure Distributions - Model 5, $M_0 = 0.400$, $N_F = 45.3\%$ (Windmill).

$$M_0 = 0.400 \quad \frac{N_F}{\sqrt{\theta_{10}}} = 95.2\% \quad \frac{A_0}{A_1} = 0.470$$

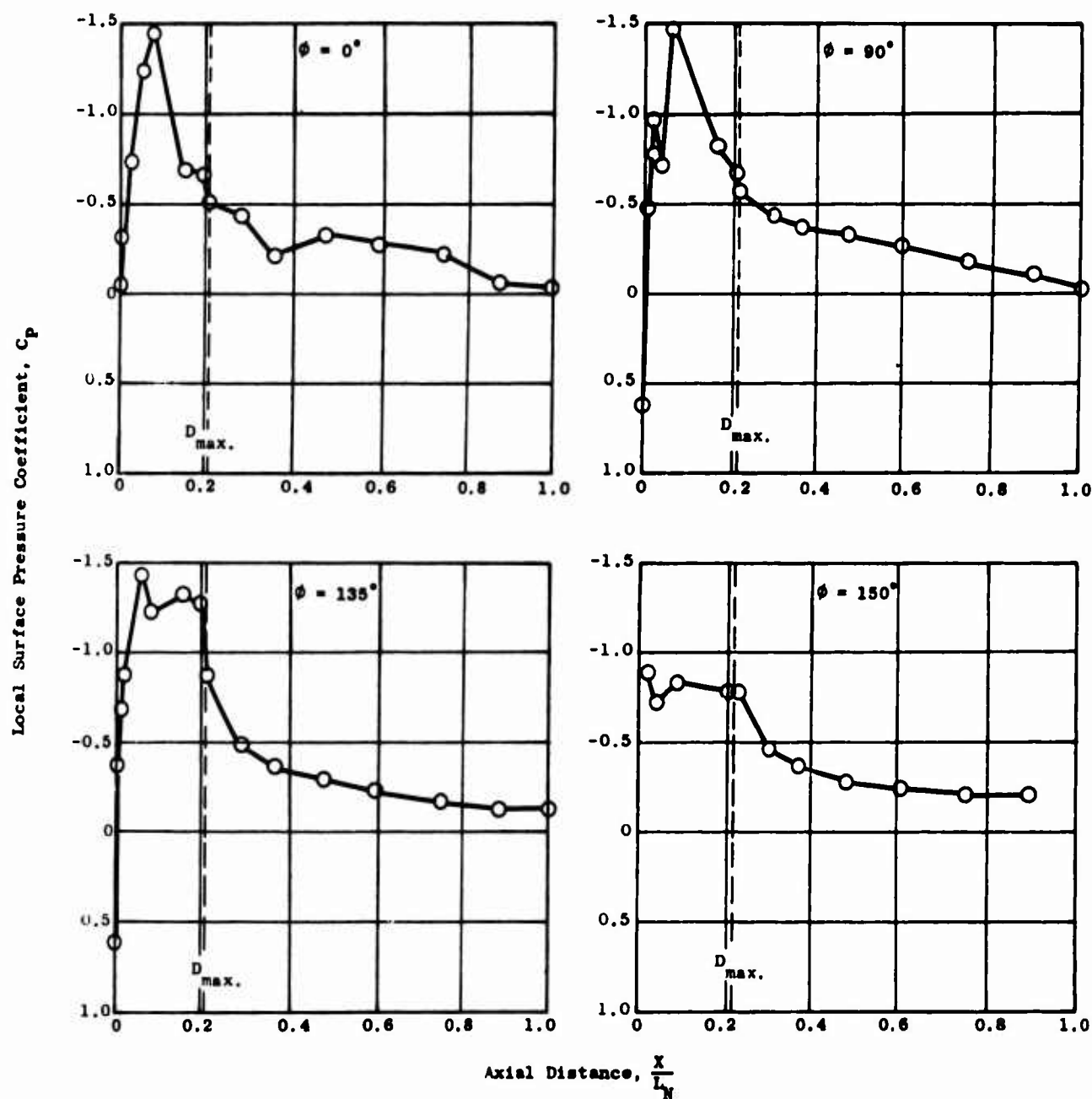


Figure 277. Nacelle External Pressure Distributions - Model 5, $M_0 = 0.400$, $N_F = 95.2\%$.

$$M_0 = 0.650$$

$$\frac{N_F}{\sqrt{\theta_{10}}} = 65.8\%$$

$$\frac{A_0}{A_1} = 0.413$$

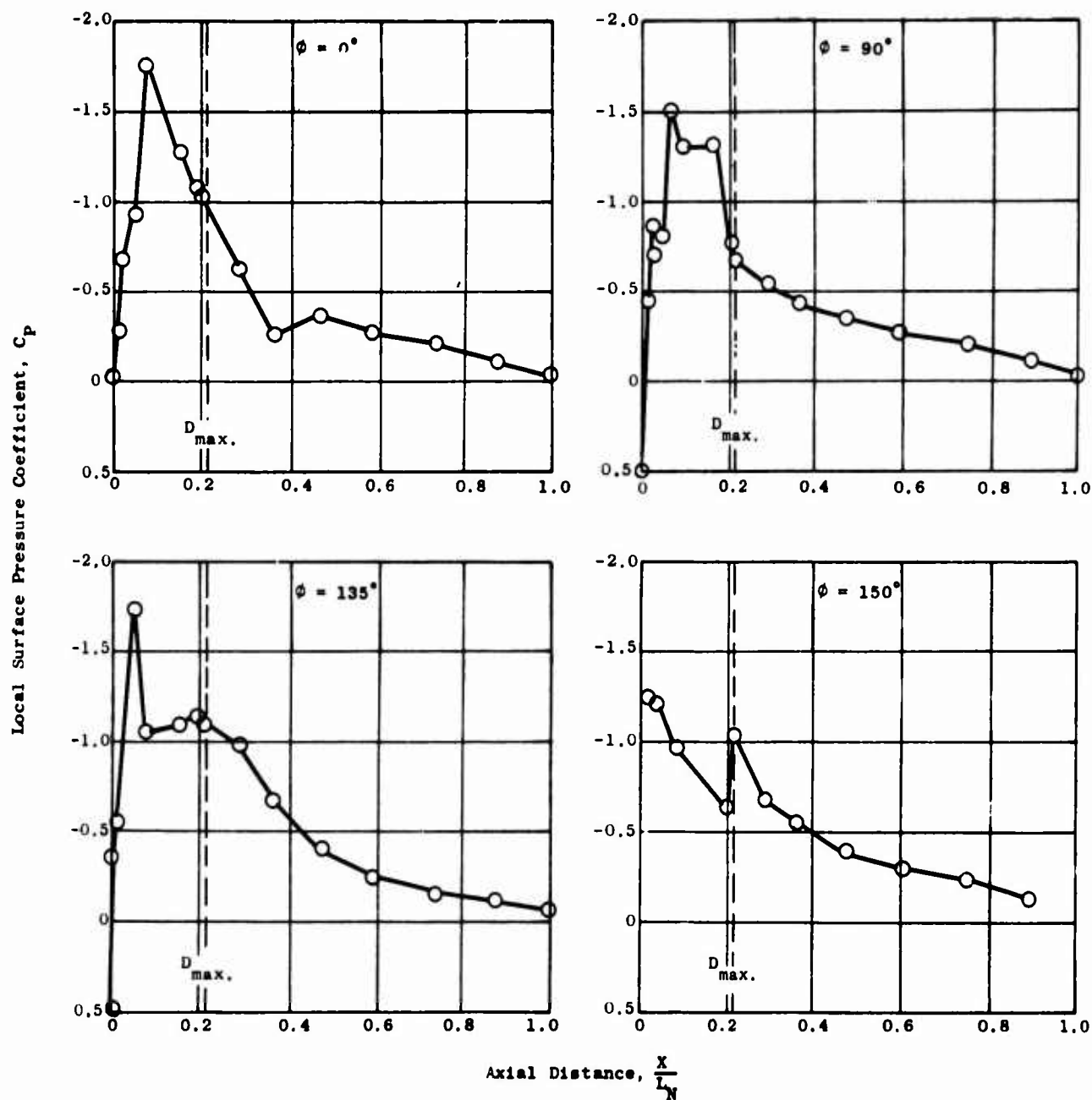


Figure 278. Nacelle External Pressure Distributions - Model 5, $M_0 = 0.650$, $N_F = 65.9\%$ (Windmill).
 $\frac{N_F}{\sqrt{\theta_{10}}}$

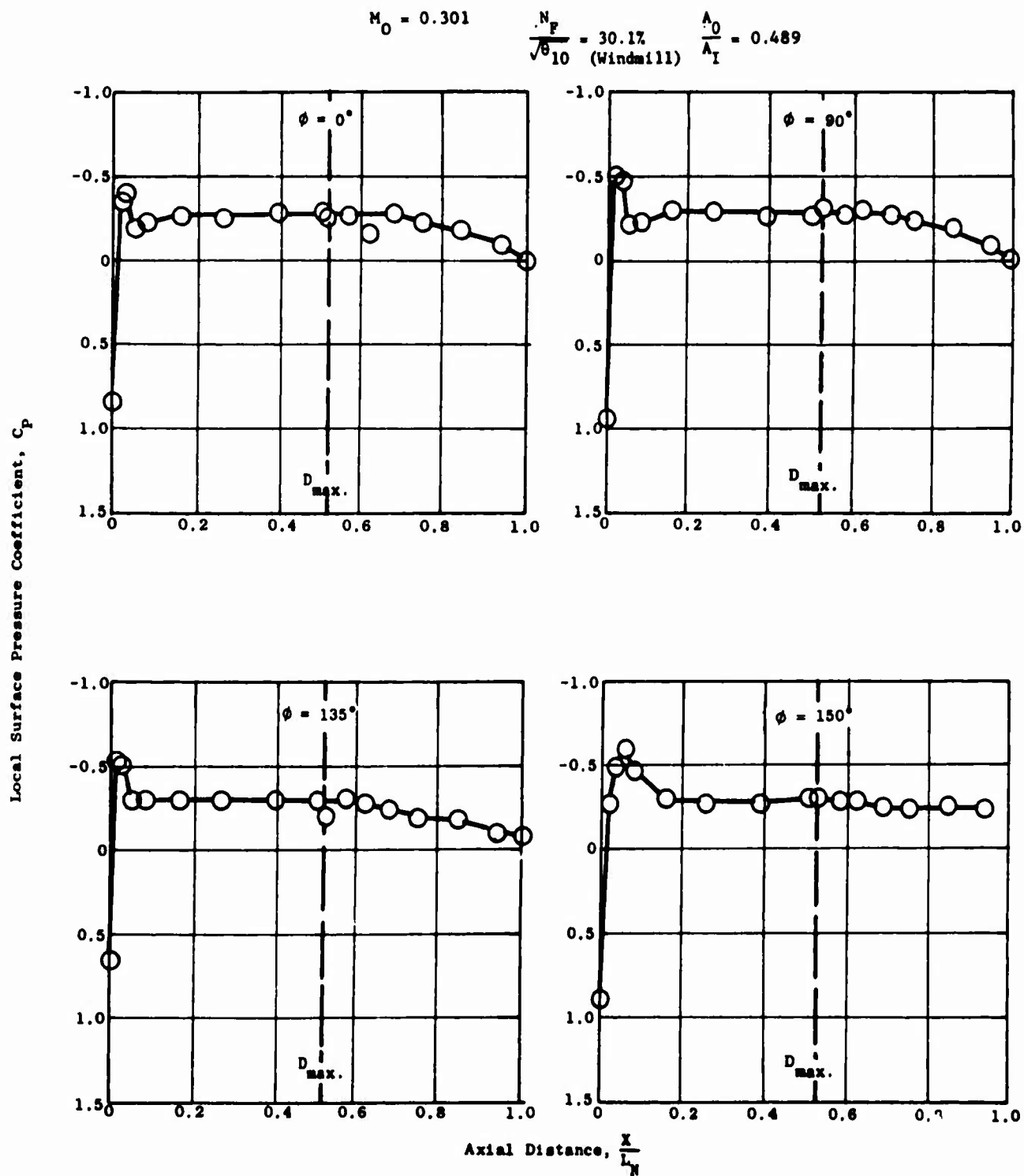


Figure 279. Nacelle External Pressure Distributions - Model 6, $M_0 = 0.301$, $N_F = 30.1\%$ (Windmill).

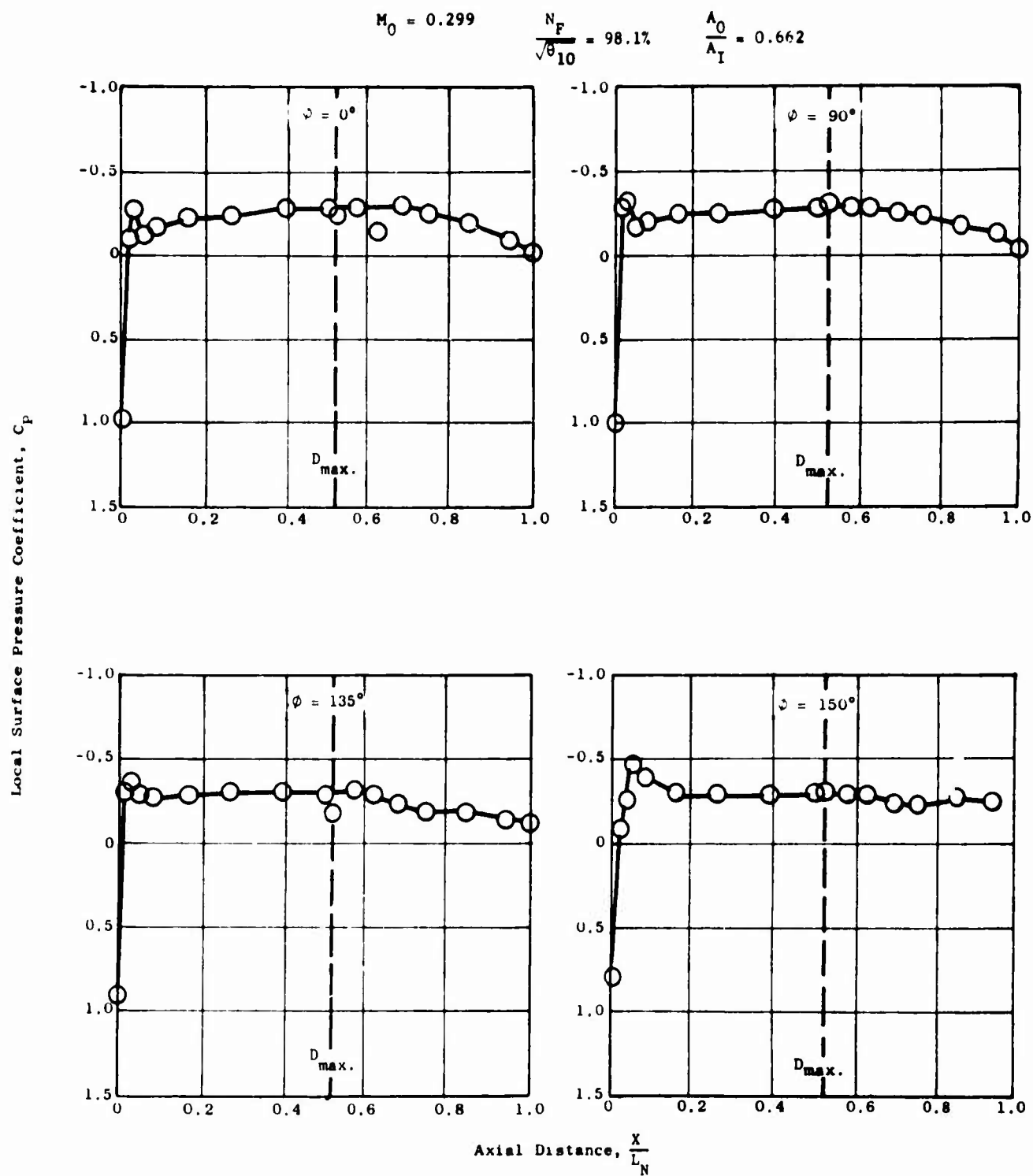


Figure 280. Nacelle External Pressure Distributions - Model 6, $M_0 = 0.299$, $N_F = 98.1\%$.

$\frac{A_0}{A_I} = 0.662$

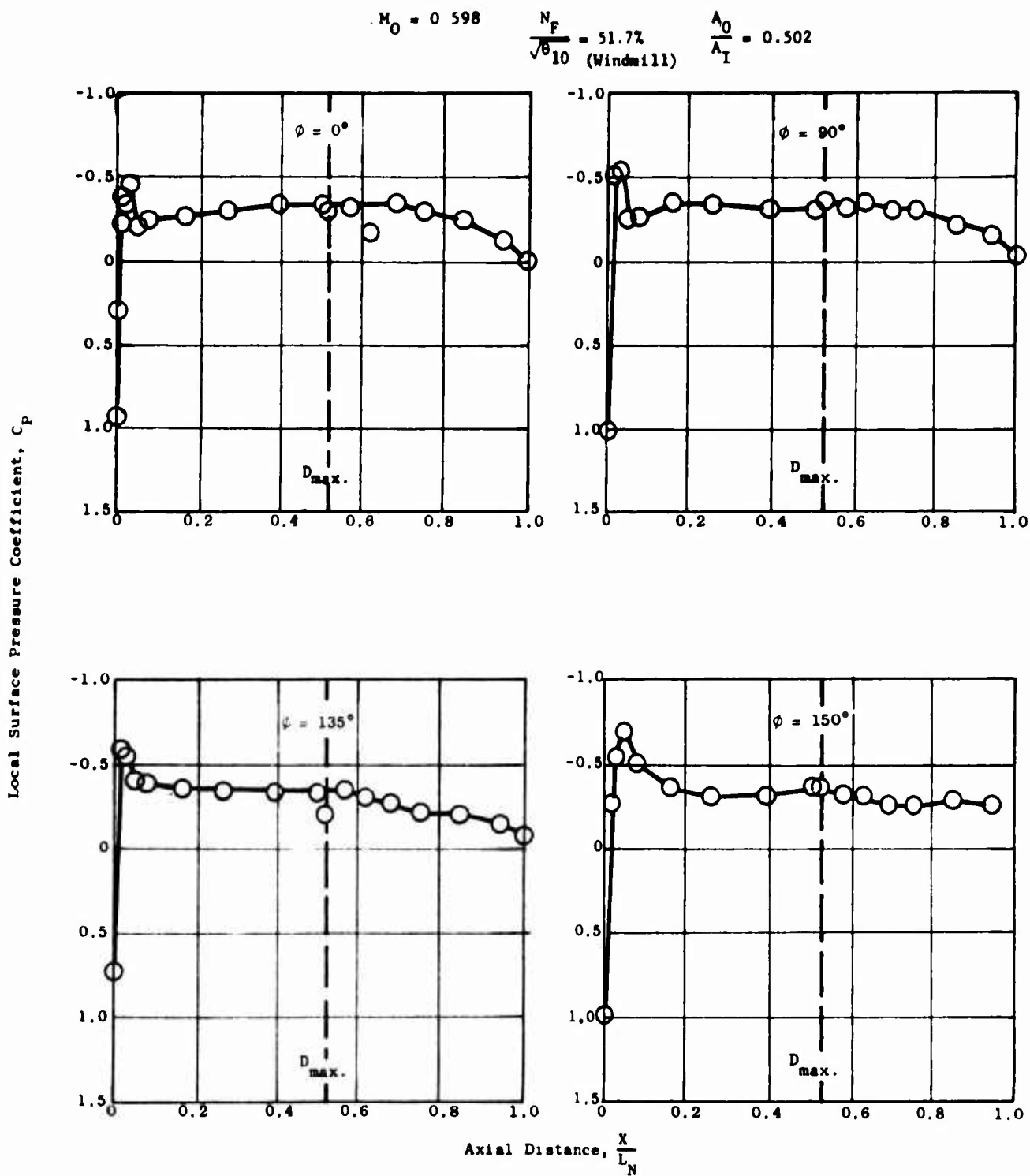


Figure 281. Nacelle External Pressure Distributions - Model 6, $M_0 = 0.598$, $\frac{N_F}{\sqrt{\theta_{10}}} = 51.7\%$ (Windmill).

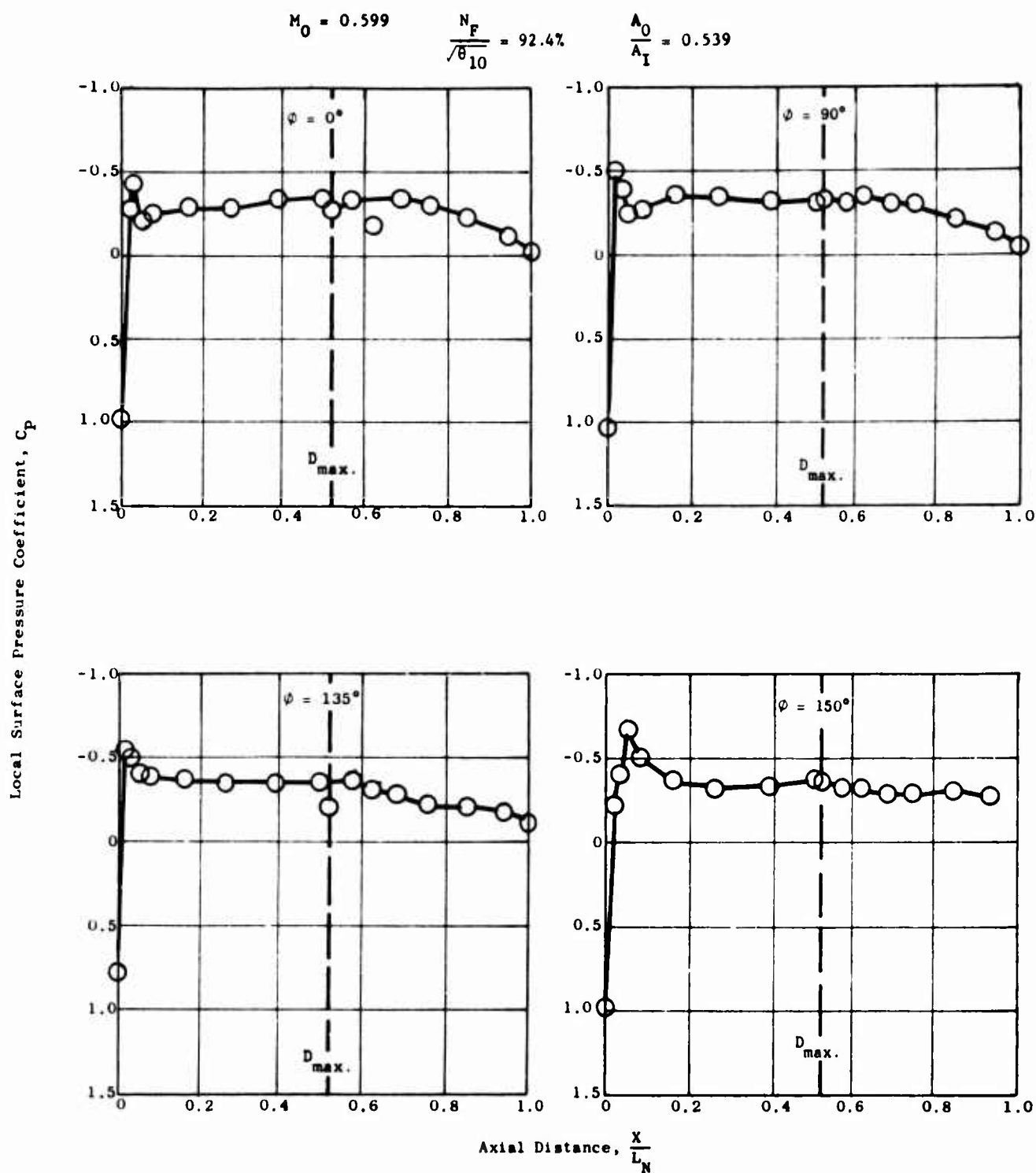


Figure 282. Nacelle External Pressure Distributions - Model 6, $M_0 = 0.599$, $\frac{N_F}{\sqrt{\theta_{10}}} = 92.4\%$.

$$M_0 = 0.800$$

$$\frac{N_F}{\sqrt{\theta_{10}}} = 59.9\% \text{ (Windmill)}$$

$$\frac{A_0}{A_I} = 0.502$$

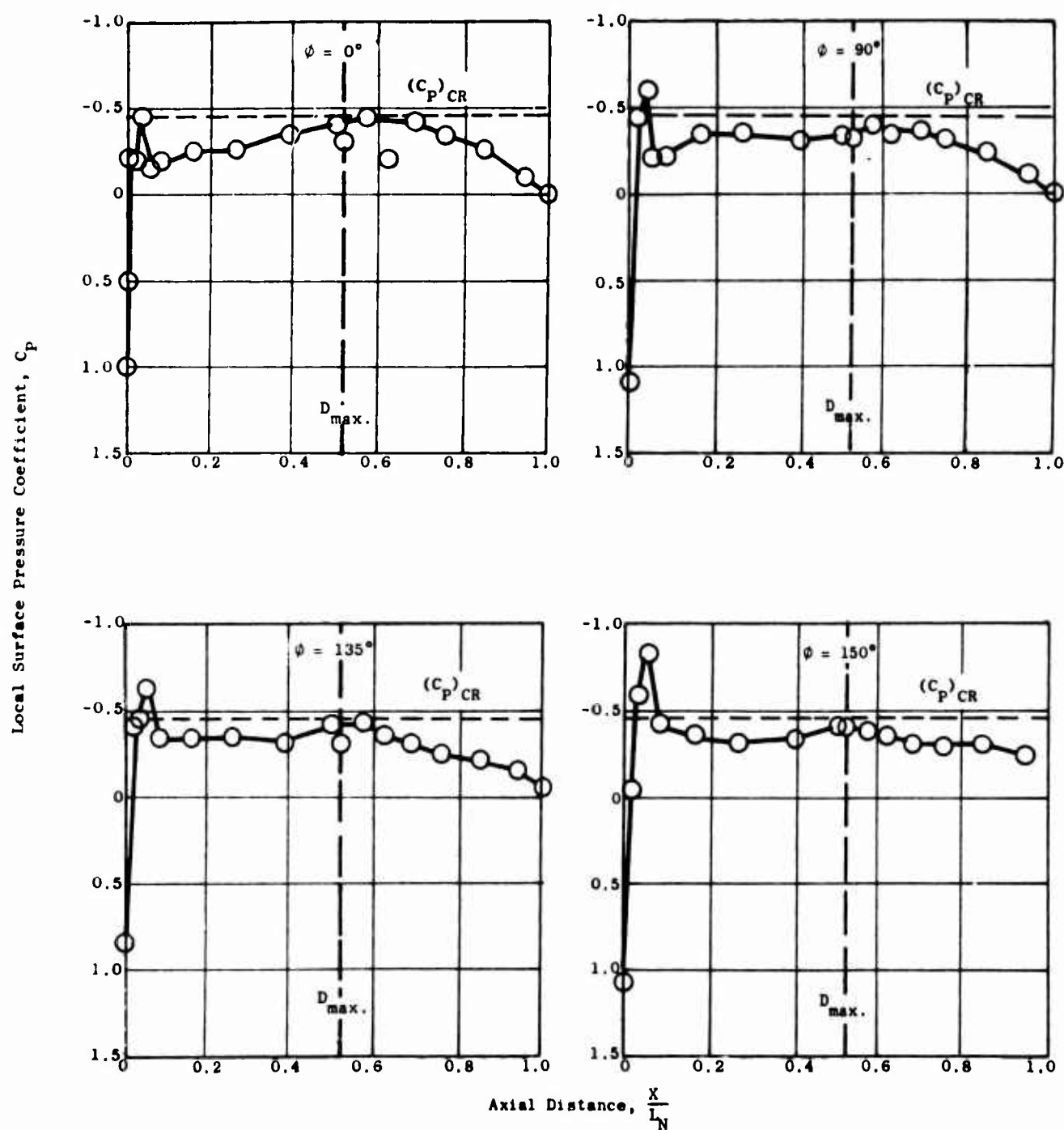


Figure 283. Nacelle External Pressure Distributions - Model 6, $M_0 = 0.800$, $N_F = 59.9\%$ (Windmill).

$$\frac{N_F}{\sqrt{\theta_{10}}}$$

$$M_0 = 0.200$$

$$\frac{N_F}{\sqrt{\theta_{10}}} = 23.2\% \text{ (Windmill)}$$

$$\frac{A_0}{A_I} = 0.519$$

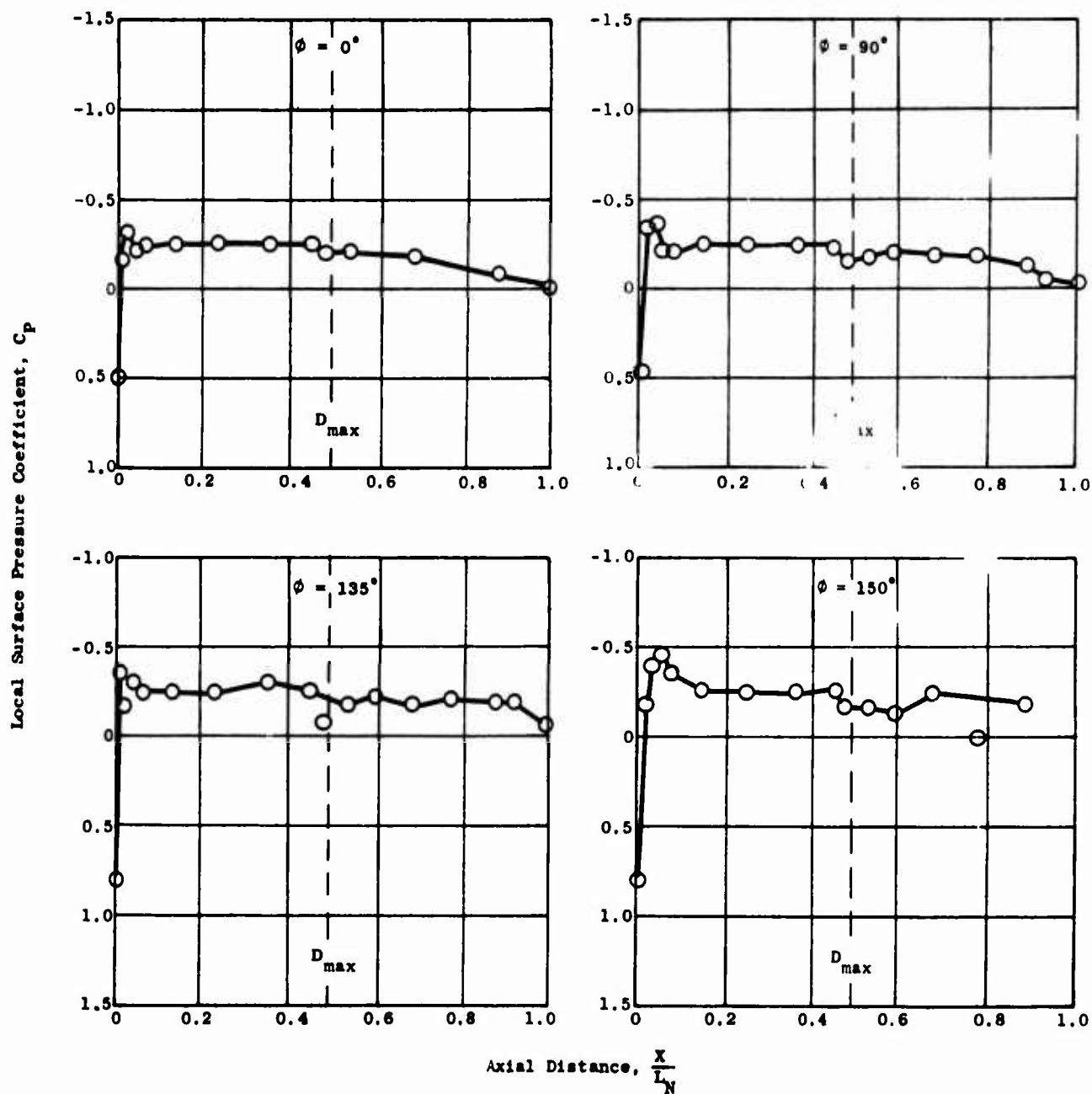


Figure 284. Nacelle External Pressure Distributions - Model 7, $M_0 = 0.200$, $N_F/\sqrt{\theta_{10}} = 23.2\%$ (Windmill).

$$M_0 = 0.202 \quad \frac{N_F}{\sqrt{\theta_{10}}} = 99.6\% \quad \frac{A_0}{A_1} = 1.013$$

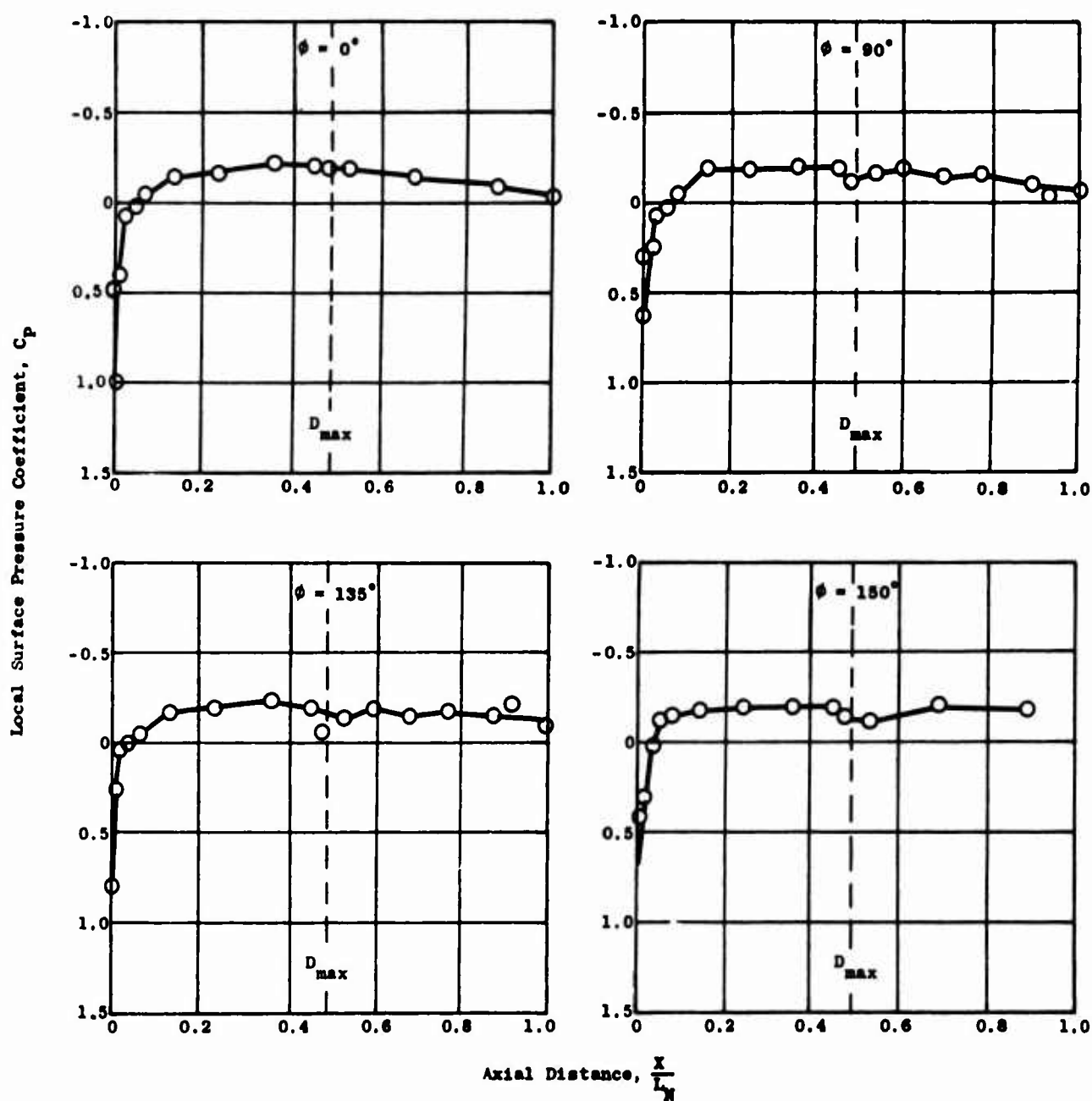


Figure 285. Nacelle External Pressure Distributions - Model 7, $M_0 = 0.202$, $N_F = 99.6\%$.

$$\frac{N_F}{\sqrt{\theta_{10}}}$$

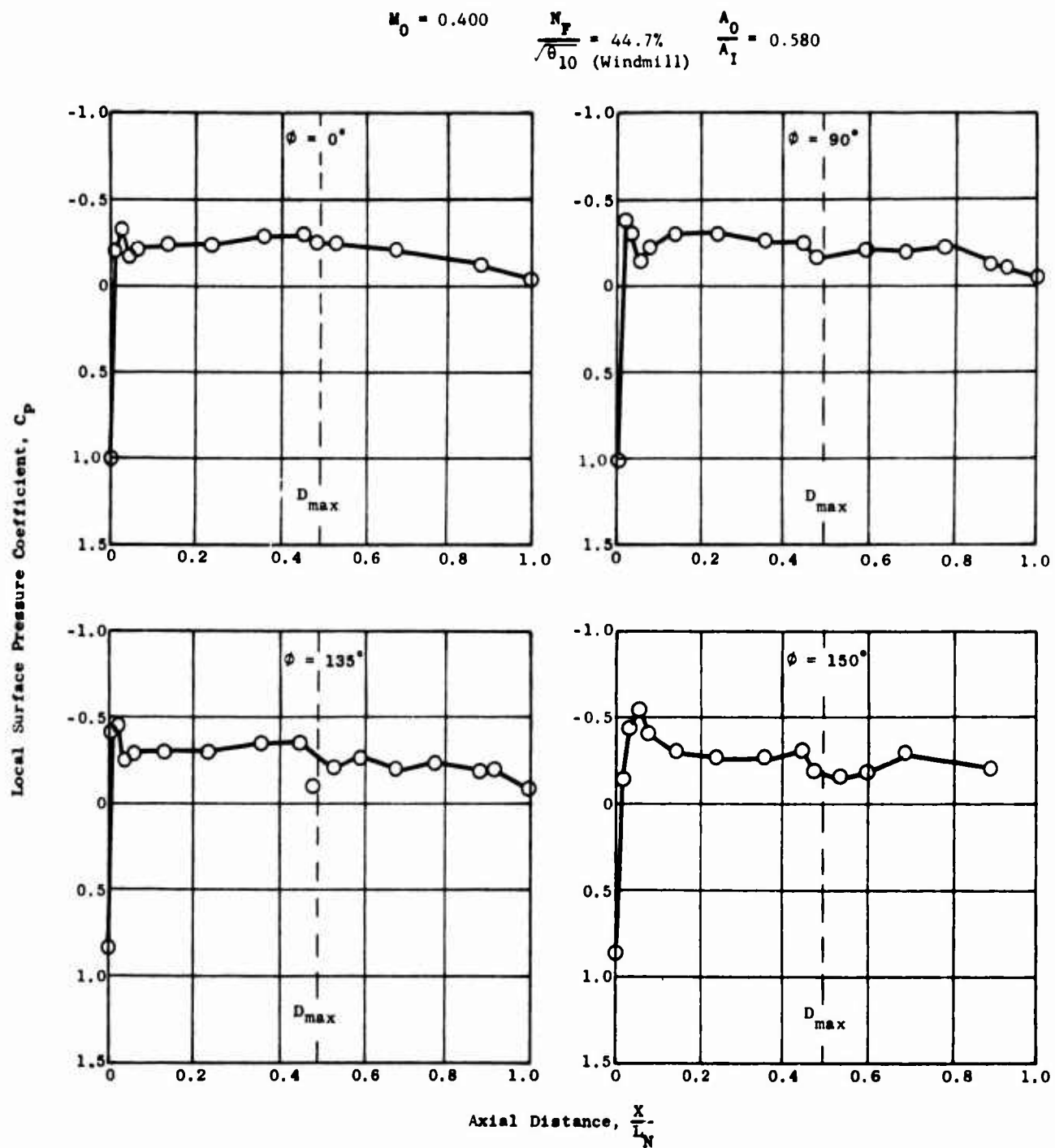


Figure 286. Nacelle External Pressure Distributions - Model 7, $M_0 = 0.400$, $\frac{N_F}{\sqrt{\theta_{10}}} = 44.7\%$ (Windmill).

$$M_0 = 0.400 \quad \frac{N_F}{\sqrt{\theta_{10}}} = 93.3\% \quad \frac{A_0}{A_1} = 0.725$$

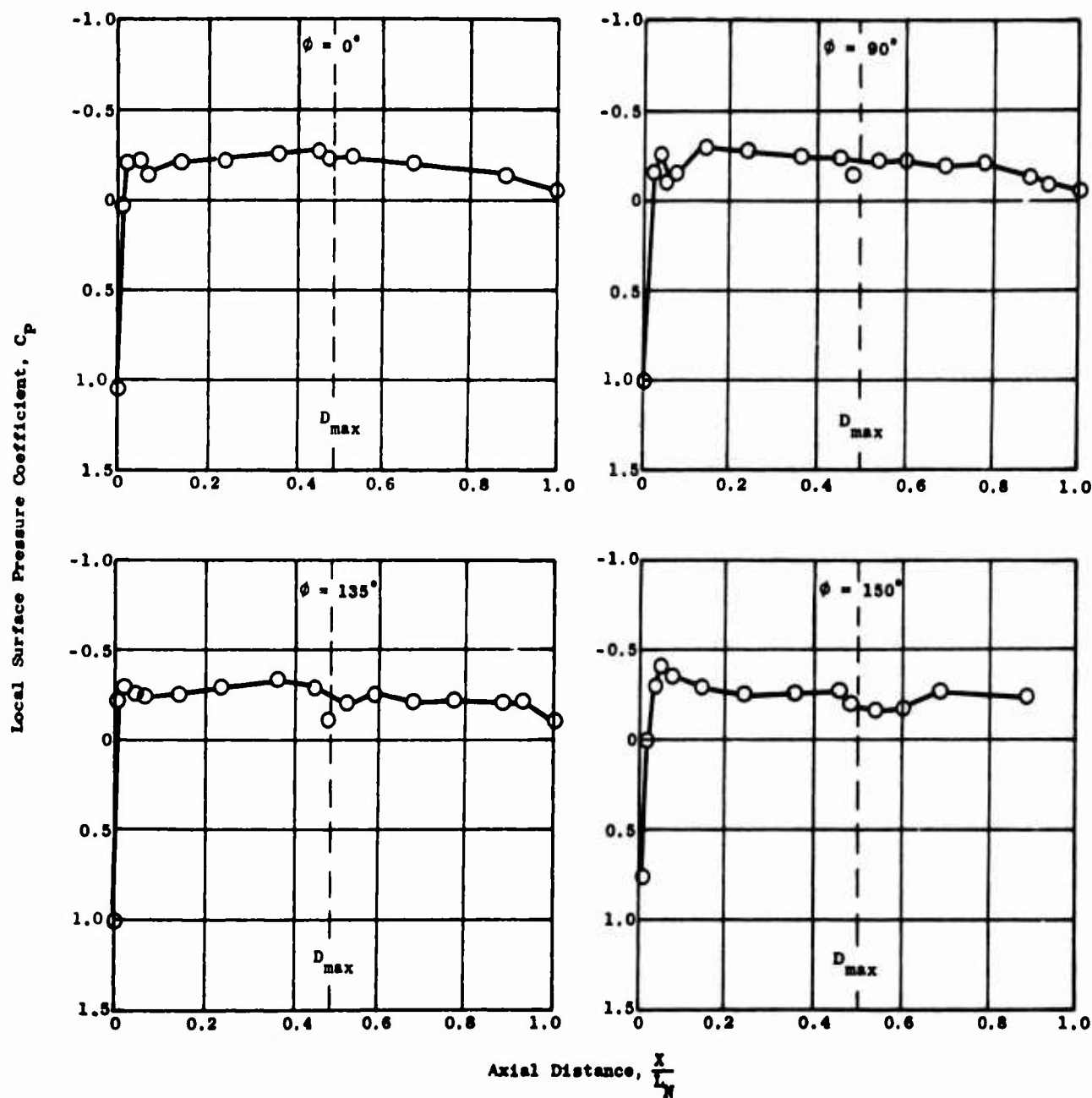


Figure 287. Nacelle External Pressure Distributions - Model 7, $M_0 = 0.400$, $N_F = 93.3\%$.

$$\frac{N_F}{\sqrt{\theta_{10}}}$$

$$M_0 = 0.649$$

$$\frac{N_F}{\sqrt{\theta_{10}}} = 64.6\% \text{ (Windmill)}$$

$$\frac{A_0}{A_I} = 0.587$$

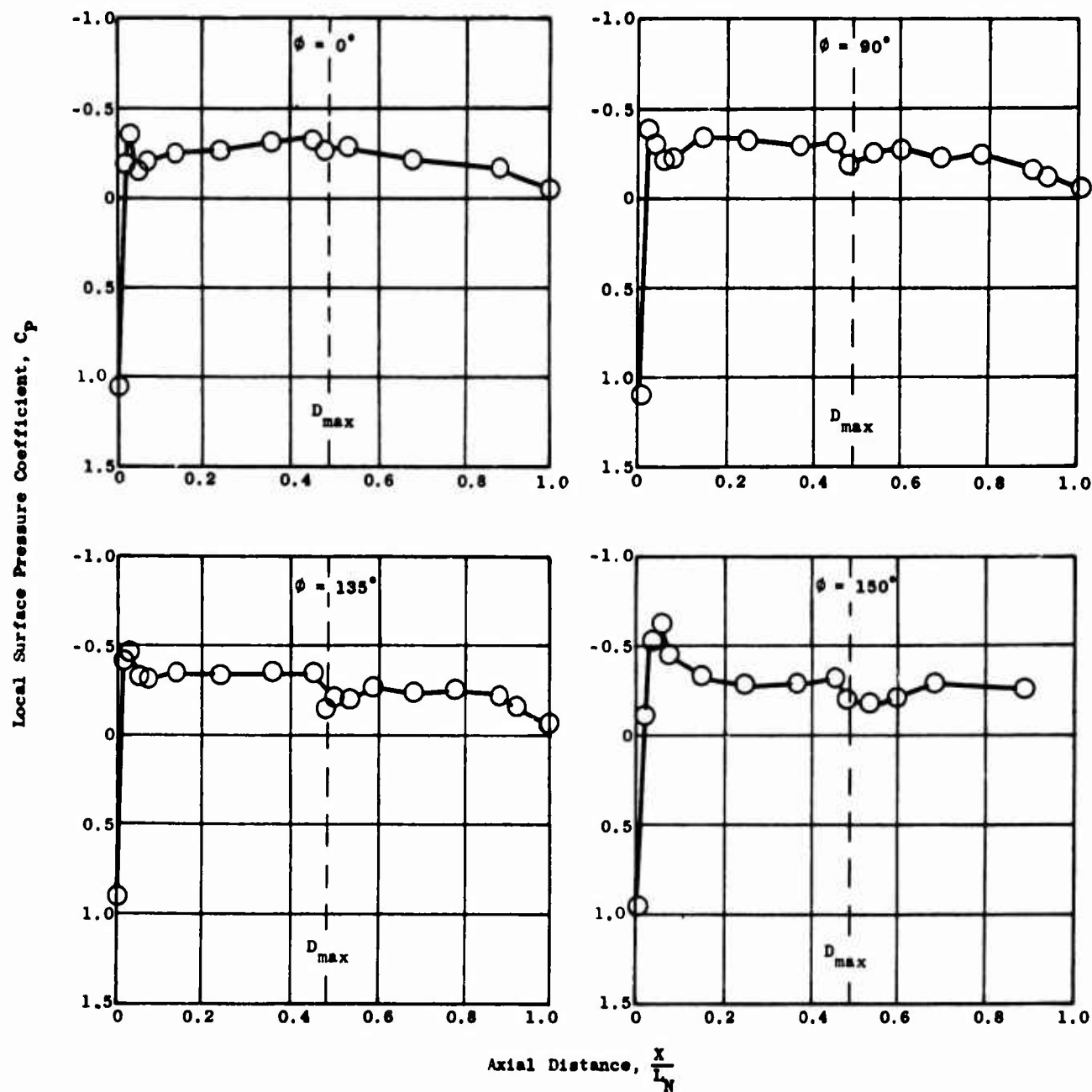


Figure 288. Nacelle External Pressure Distributions - Model 7, $M_0 = 0.649$, $N_F = 64.6\%$ (Windmill).
 $\frac{N_F}{\sqrt{\theta_{10}}}$

$$M_0 = 0.301 \quad \frac{N_F}{\sqrt{\theta_{10}}} = 29.3\% \quad \frac{A_0}{A_1} = 0.490$$

(Windmill)

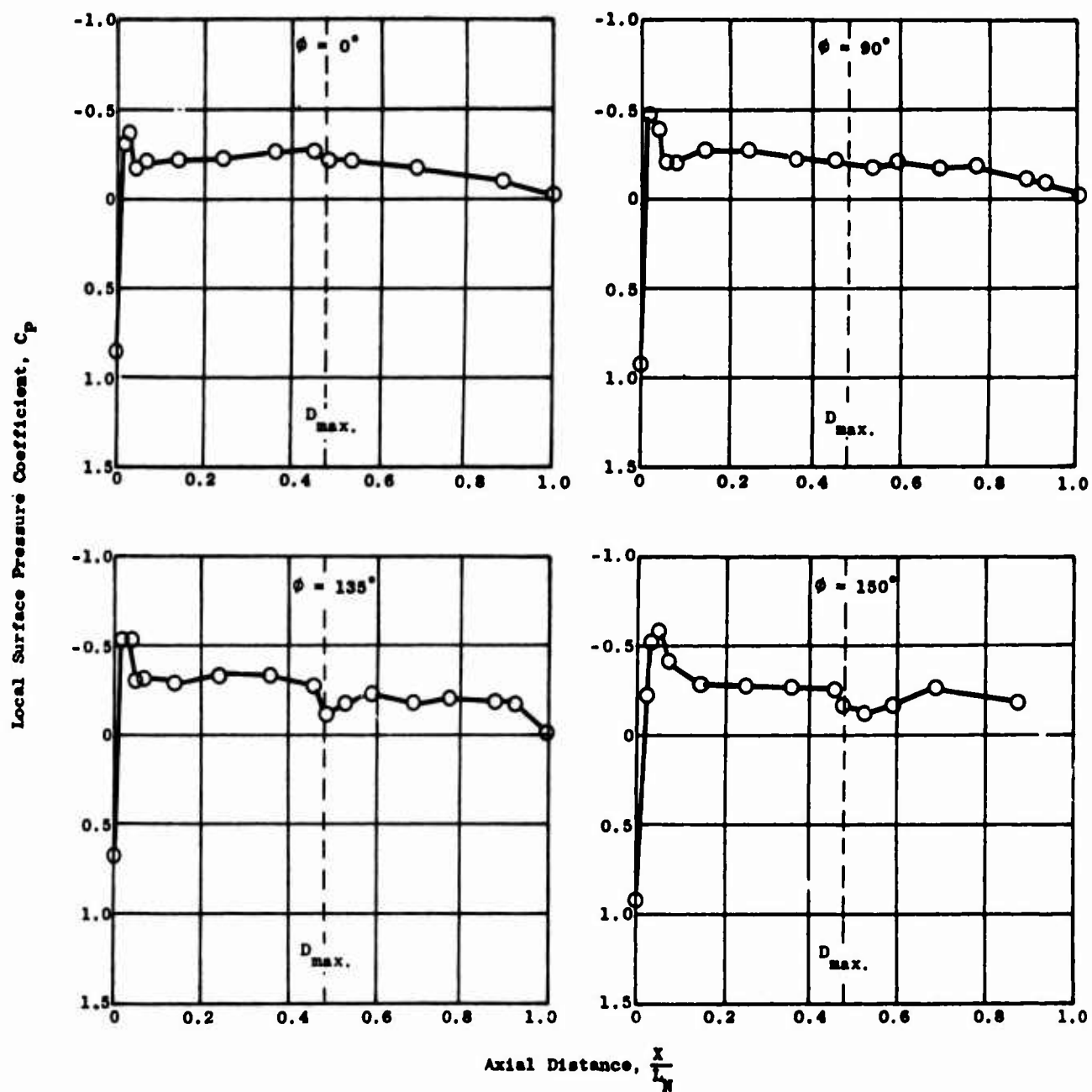


Figure 289. Nacelle External Pressure Distributions - Model 8, $M_0 = 0.301$, $N_F = 29.3\%$ (Windmill).

$$\frac{N_F}{\sqrt{\theta_{10}}}$$

$$M_0 = 0.301$$

$$\frac{N_F}{\sqrt{\theta_{10}}} = 95.8\%$$

$$\frac{A_0}{A_1} = 0.634$$

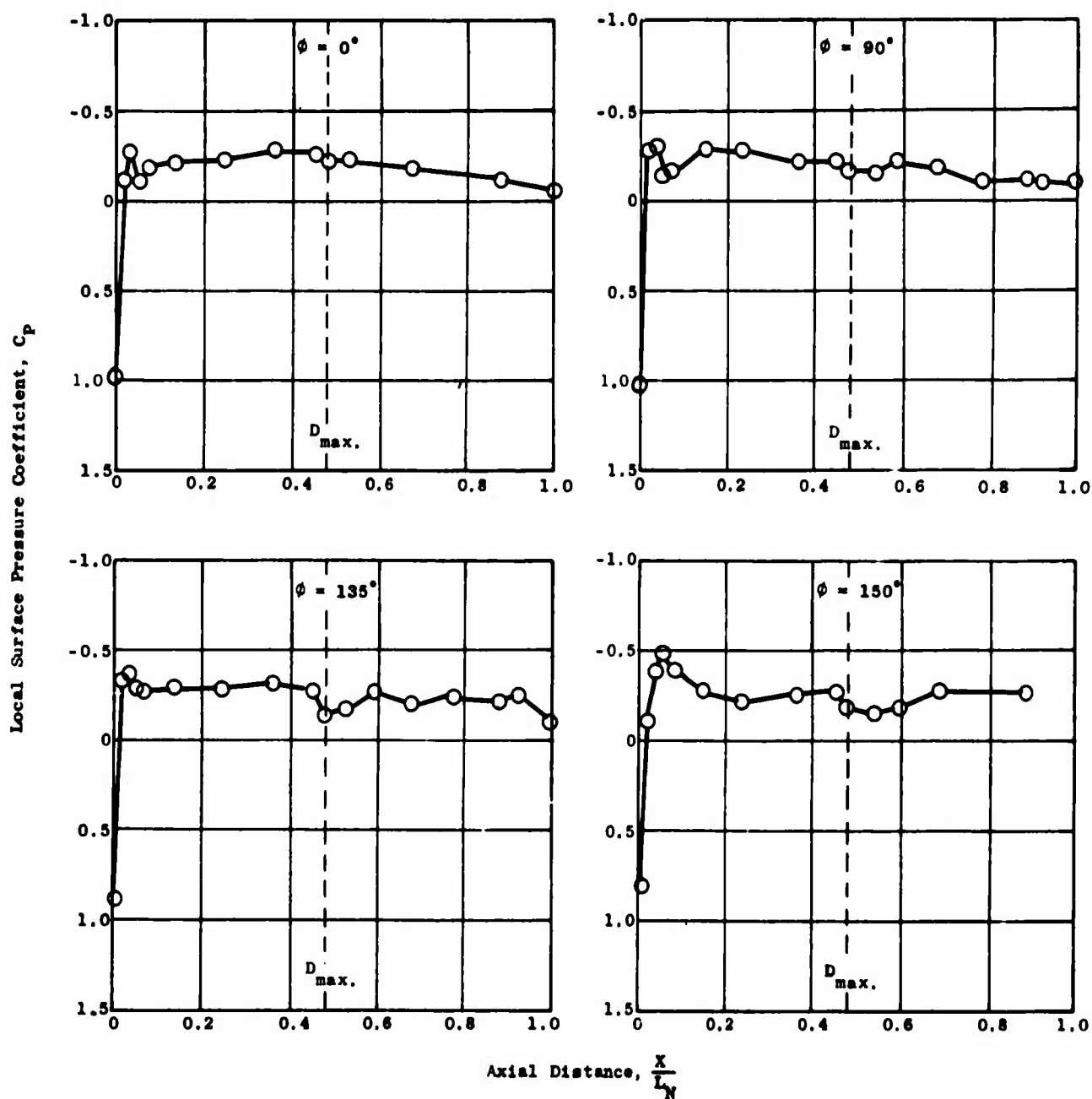


Figure 290. Nacelle External Pressure Distributions - Model 8, $M_0 = 0.301$, $N_F = 95.8\%$.

$$M_0 = 0.500 \quad \frac{N_F}{\sqrt{\theta_{10}}} = 44.8\% \quad \frac{A_0}{A_I} = 0.505$$

(Windmill)

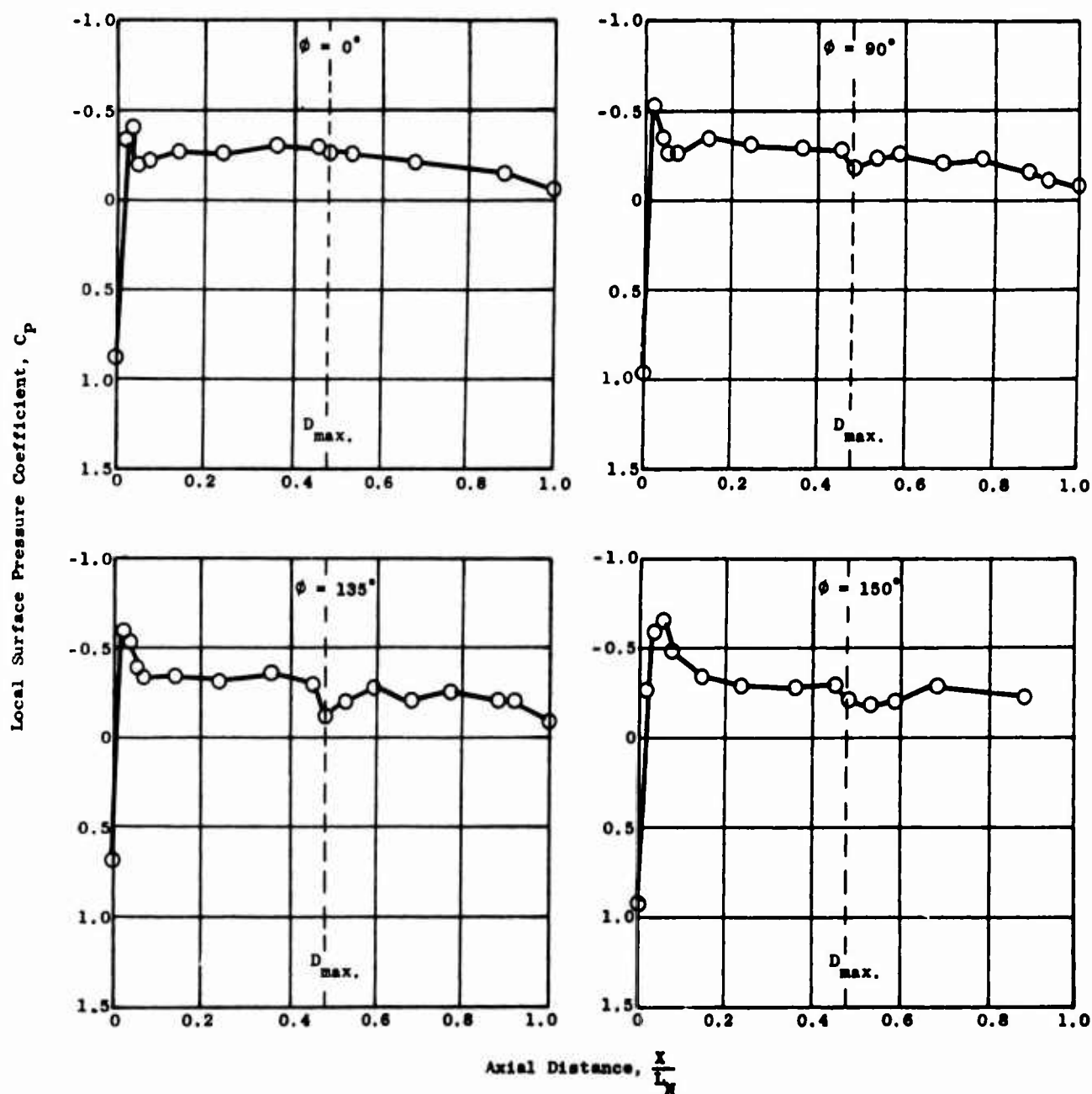


Figure 291. Nacelle External Pressure Distributions - Model 8, $M_0 = 0.500$, $N_F = 44.8\%$ (Windmill).

$\frac{N_F}{\sqrt{\theta_{10}}}$

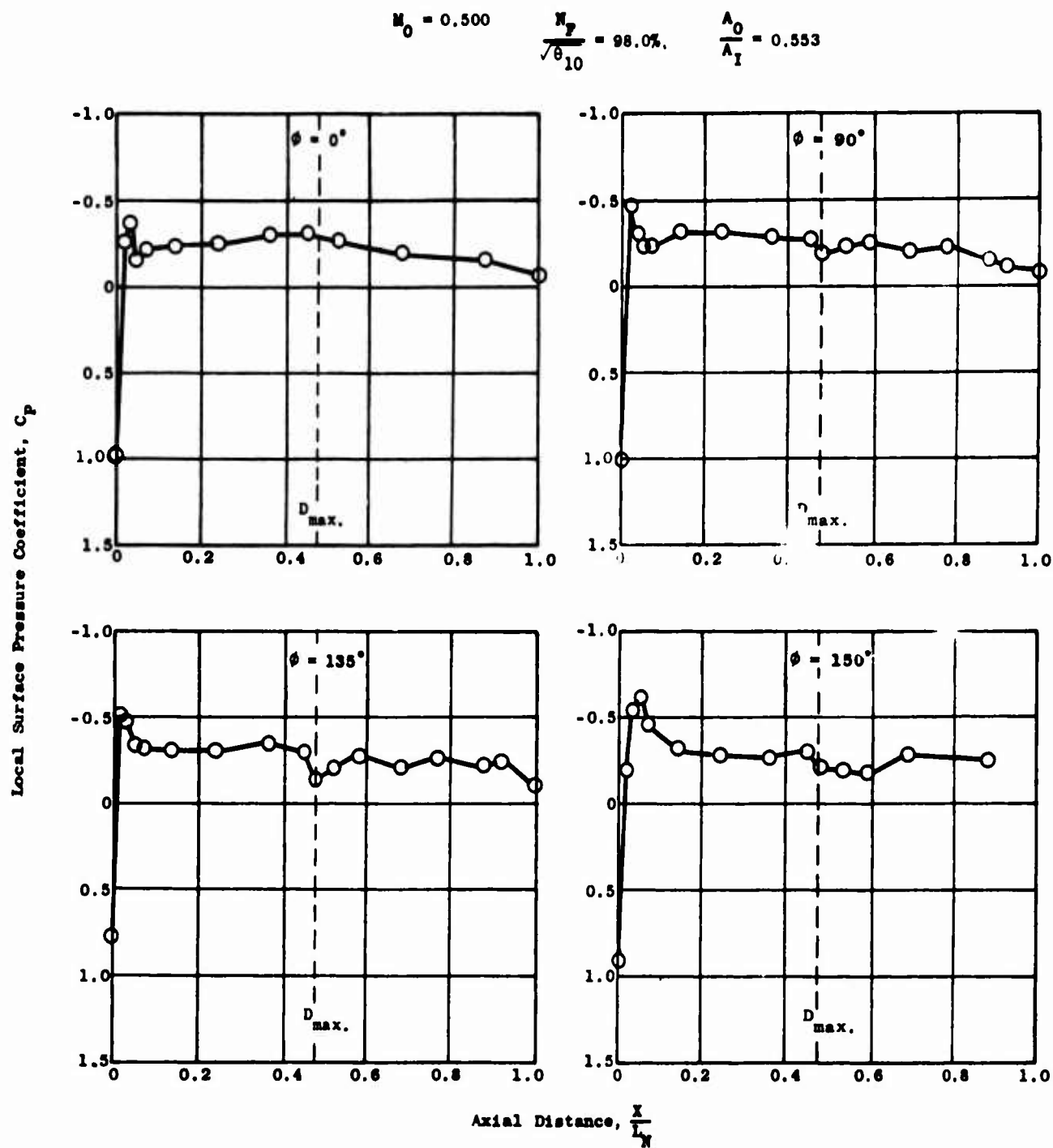


Figure 292. Nacelle External Pressure Distributions - Model 8, $M_0 = 0.500$, $\frac{N_F}{\sqrt{\theta_{10}}} = 98.0\%$.

$$M_0 = 0.699 \quad \frac{N_F}{\sqrt{\theta_{10}}} = 56.0\% \quad \frac{A_0}{A_1} = 1.346$$

(Windmill)

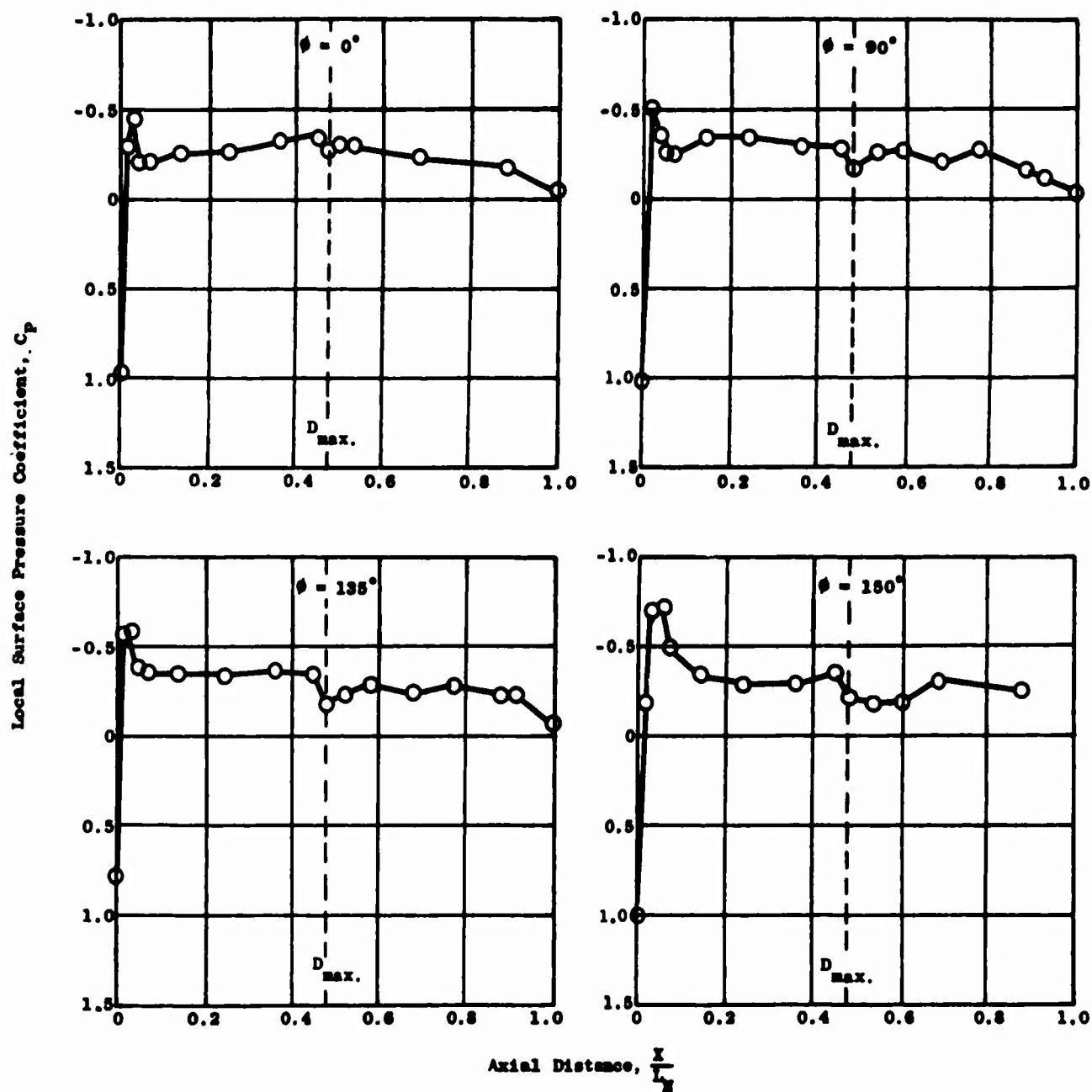


Figure 293. Nacelle External Pressure Distributions - Model 8, $M_0 = 0.699$, $N_F = 56.0\%$ (Windmill).

$$\sqrt{\theta_{10}}$$

$$M_0 = 0.699$$

$$\frac{N_F}{\sqrt{\theta_{10}}} = 93.0\%$$

$$\frac{A_0}{A_1} = 0.520$$

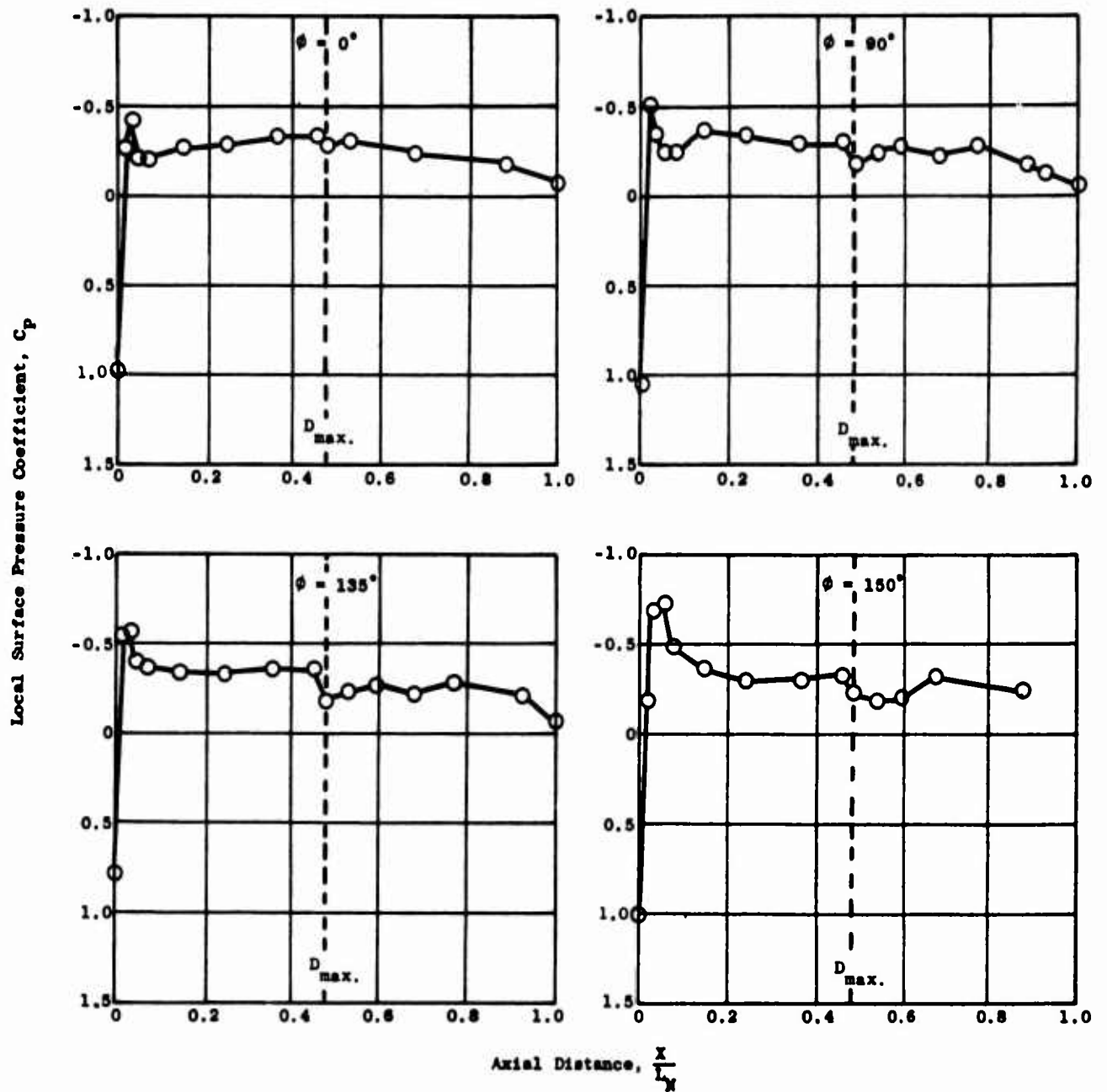
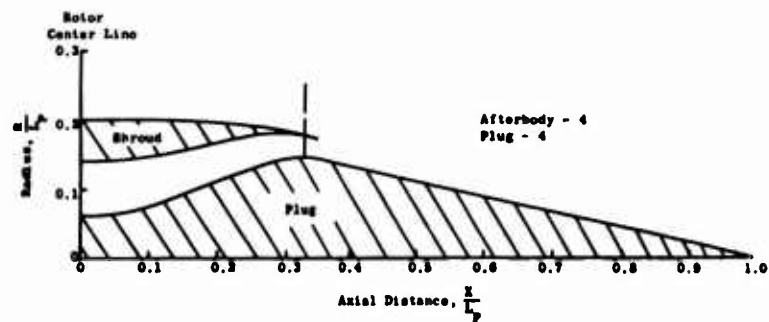


Figure 294. Nacelle External Pressure Distributions - Model 8, $M_0 = 0.699$, $N_F = 93.0\%$.

$$\frac{N_F}{\sqrt{\theta_{10}}}$$



$$M_0 = 0.301 \quad \frac{N_F}{\sqrt{\theta_{10}}} = 32.2\% \quad \frac{(P_{T11.0})_S}{P_0} = 1.064$$

(Windmill)

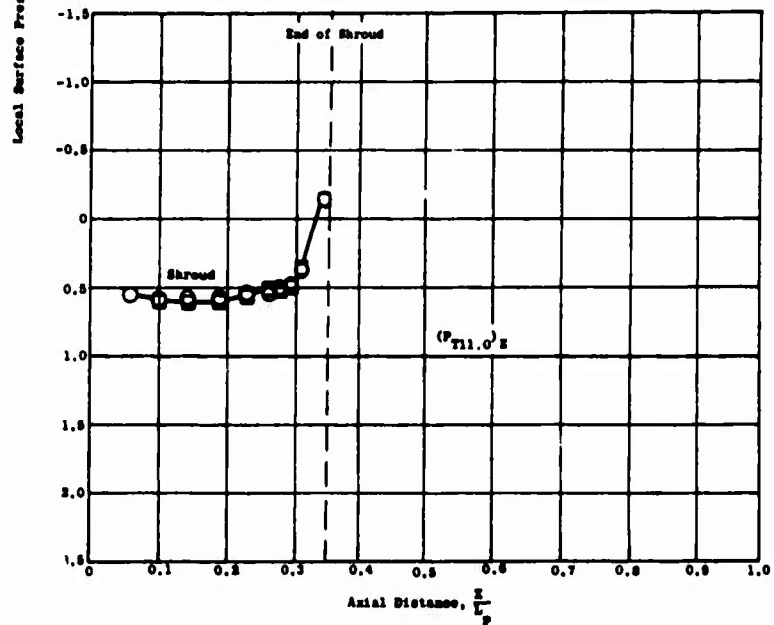
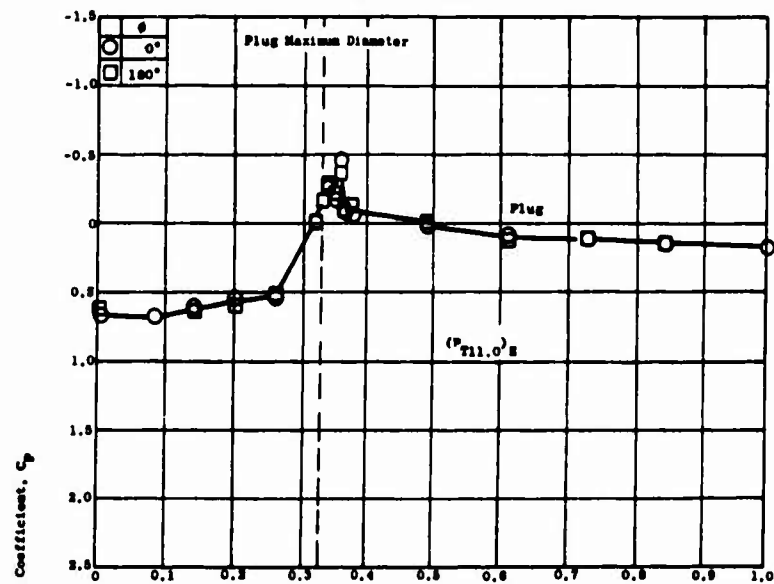


Figure 295. Nozzle Pressure Distribution - Model 1, $M_0 = 0.301$,
 $N_F = 32.2\%$ (Windmill).
 $\sqrt{\theta_{10}}$

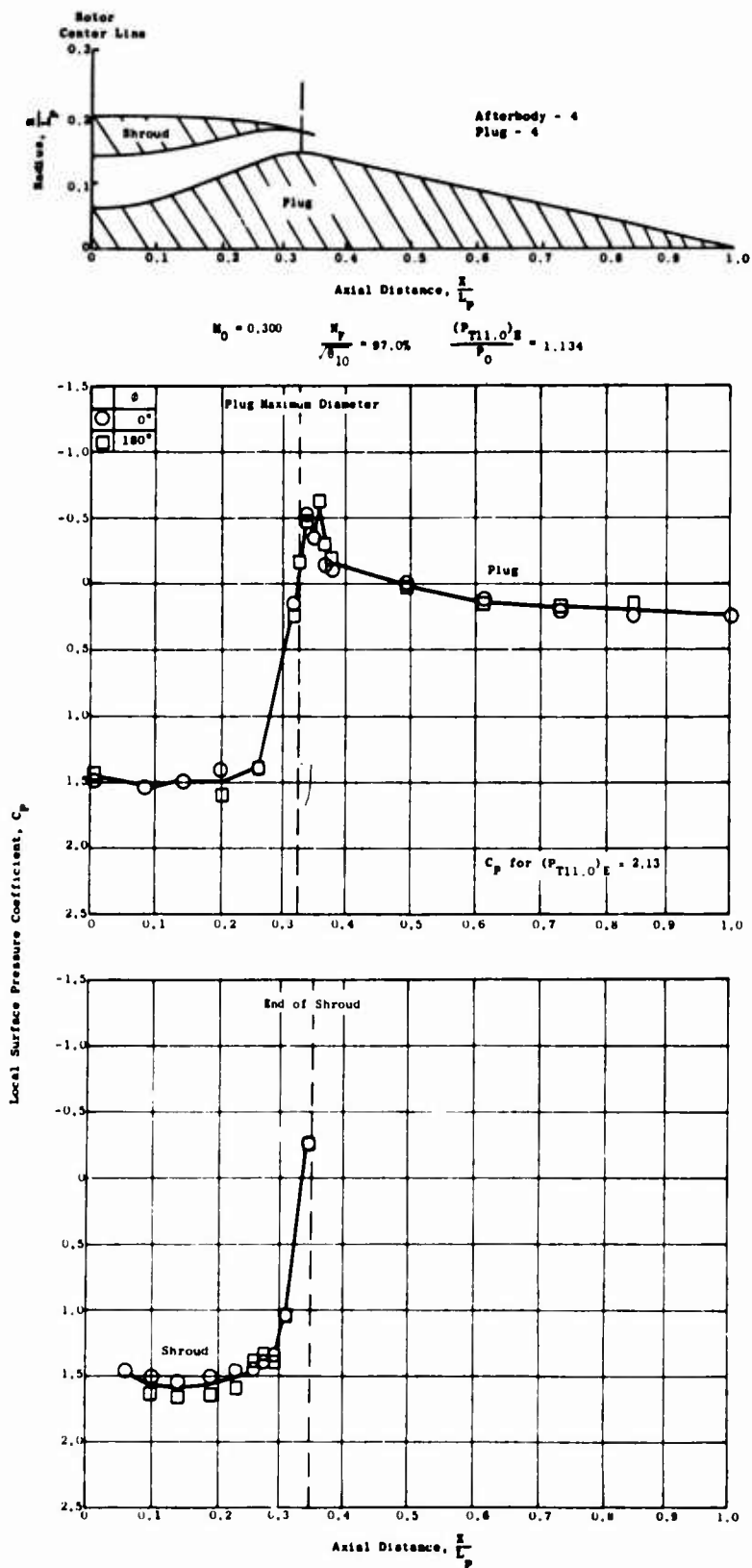


Figure 296. Nozzle Pressure Distribution - Model 1, $M_0 = 0.300$,
 $N_F = 97.0\%$.

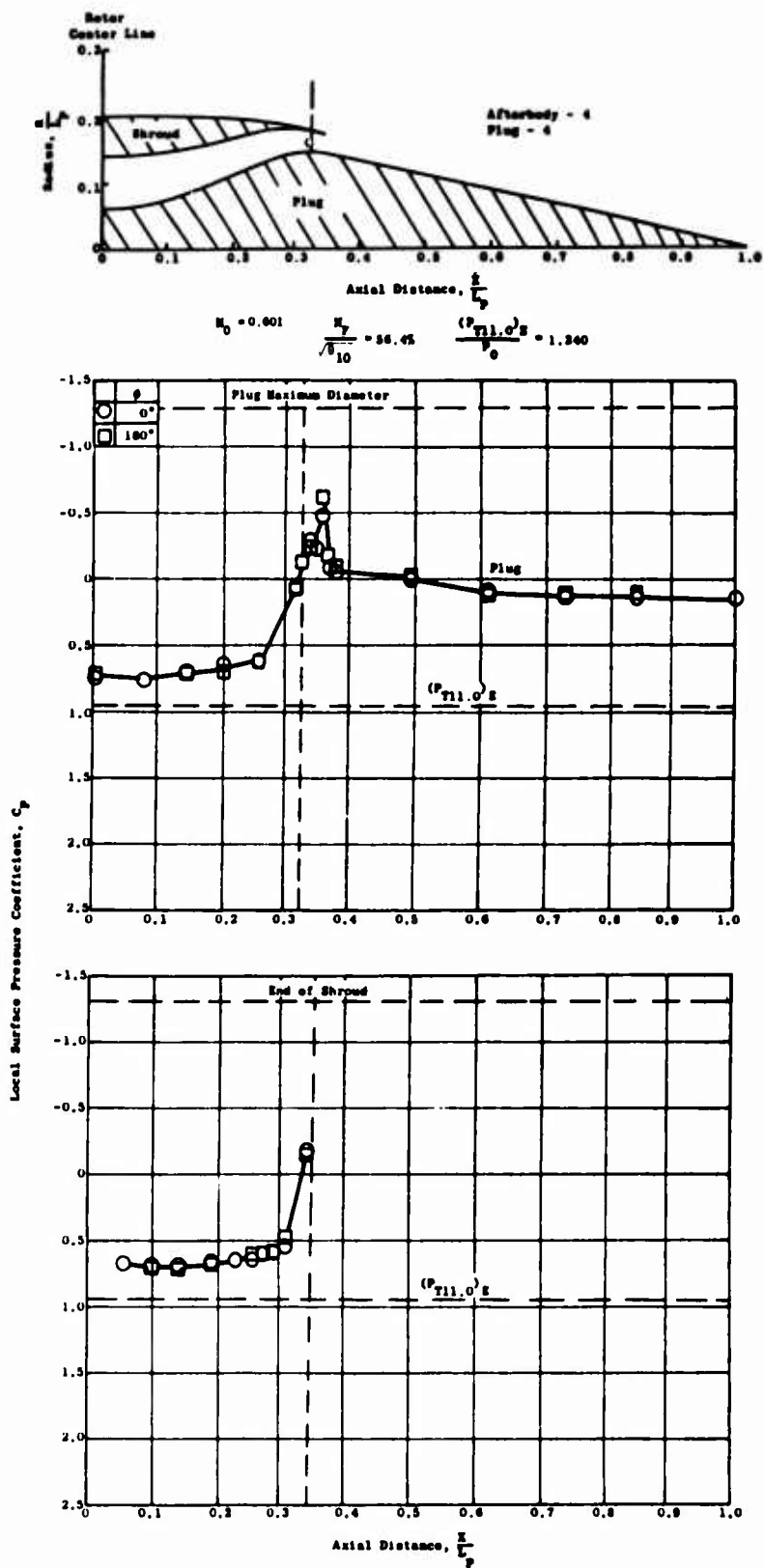


Figure 297. Nozzle Pressure Distribution - Model 1, $M_0 = 0.601$,
 $N_F = 56.4\%$.
 $\frac{N_F}{\sqrt{\theta_{10}}}$

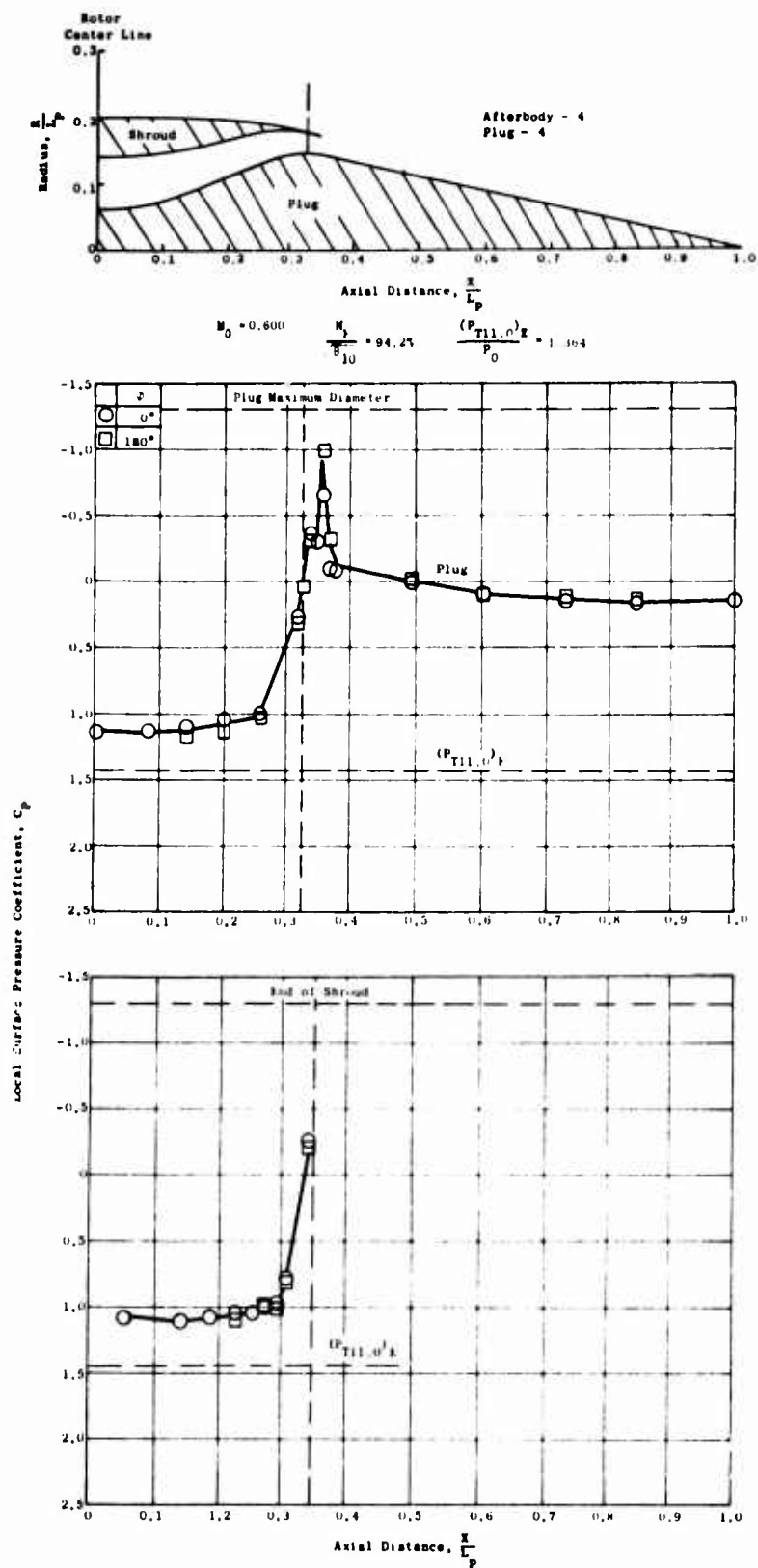


Figure 298. Nozzle Pressure Distribution - Model 1, $M_0 = 0.600$,
 $\frac{N_F}{N_{F0}} = 94.2\%$.

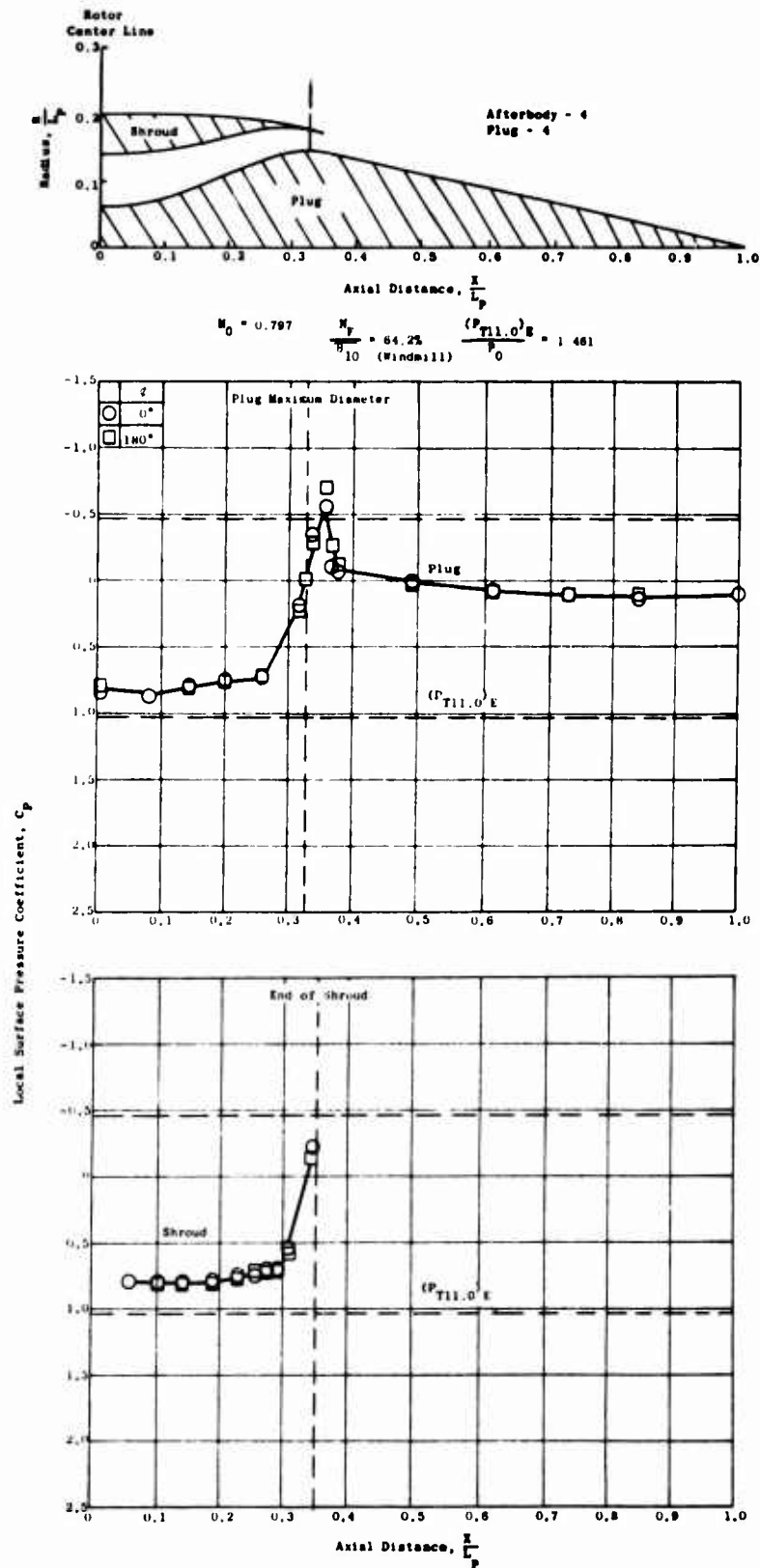


Figure 299. Nozzle Pressure Distribution - Model 1, $M_0 = 0.797$,
 $N_F = 64.2\%$ (Windmill).
 $\sqrt{\theta_{10}}$

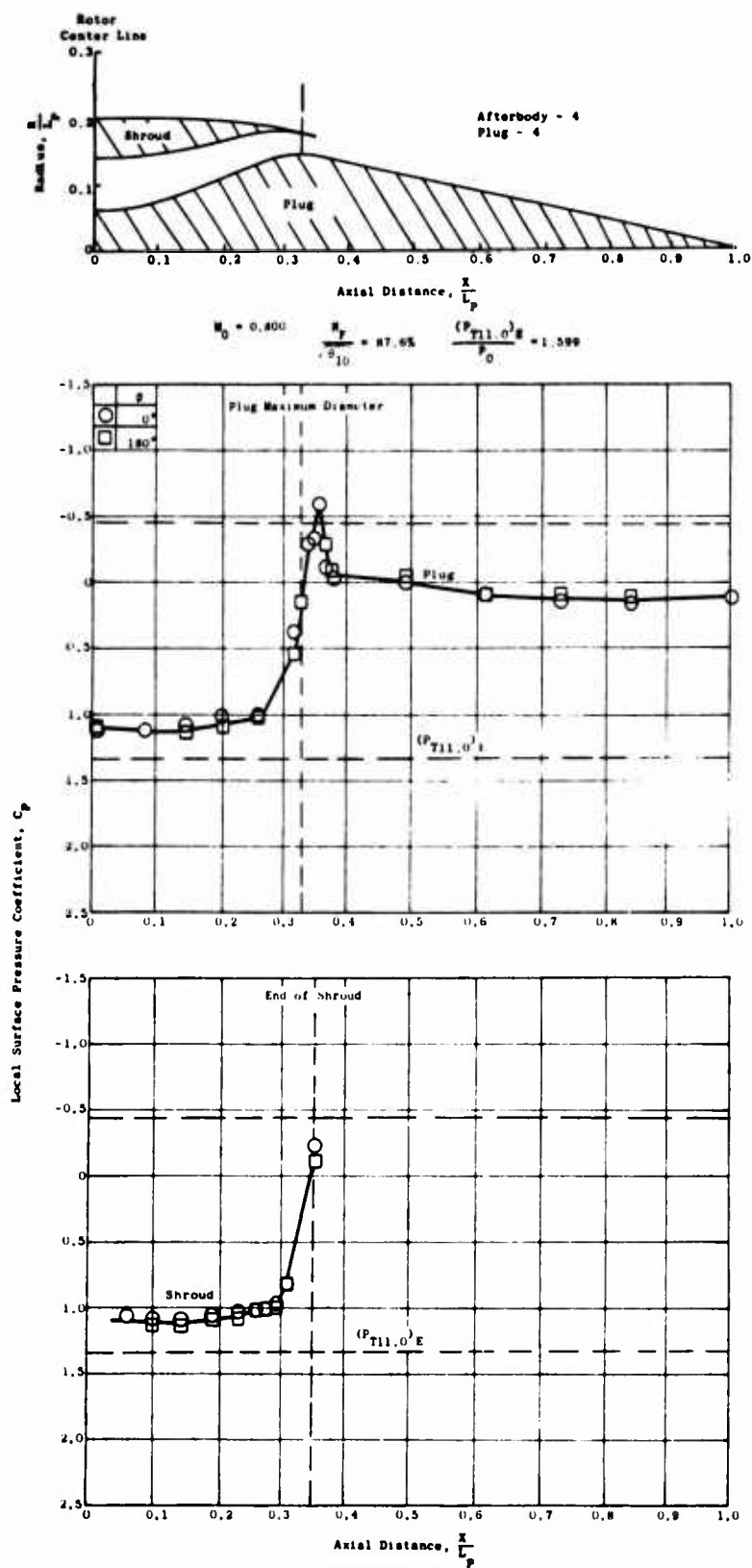


Figure 300. Nozzle Pressure Distribution - Model 1, $M_0 = 0.800$,
 $N_F = 87.6\%$,
 $\sqrt{\theta}_{10}$

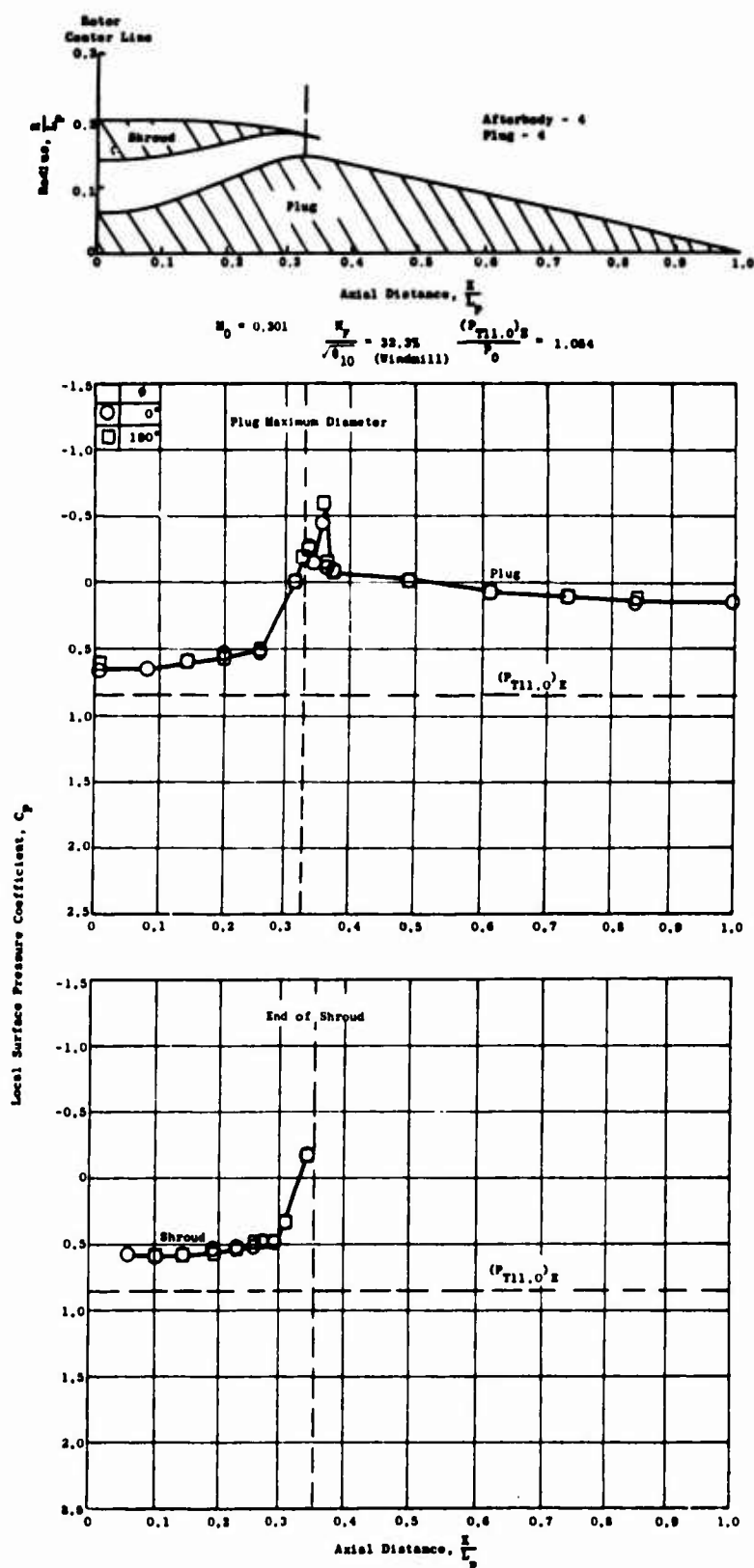


Figure 301. Nozzle Pressure Distribution - Model 2, $M_0 = 0.301$,
 $N_F = 32.3\%$ (Windmill).
 $\sqrt{\theta_{10}}$

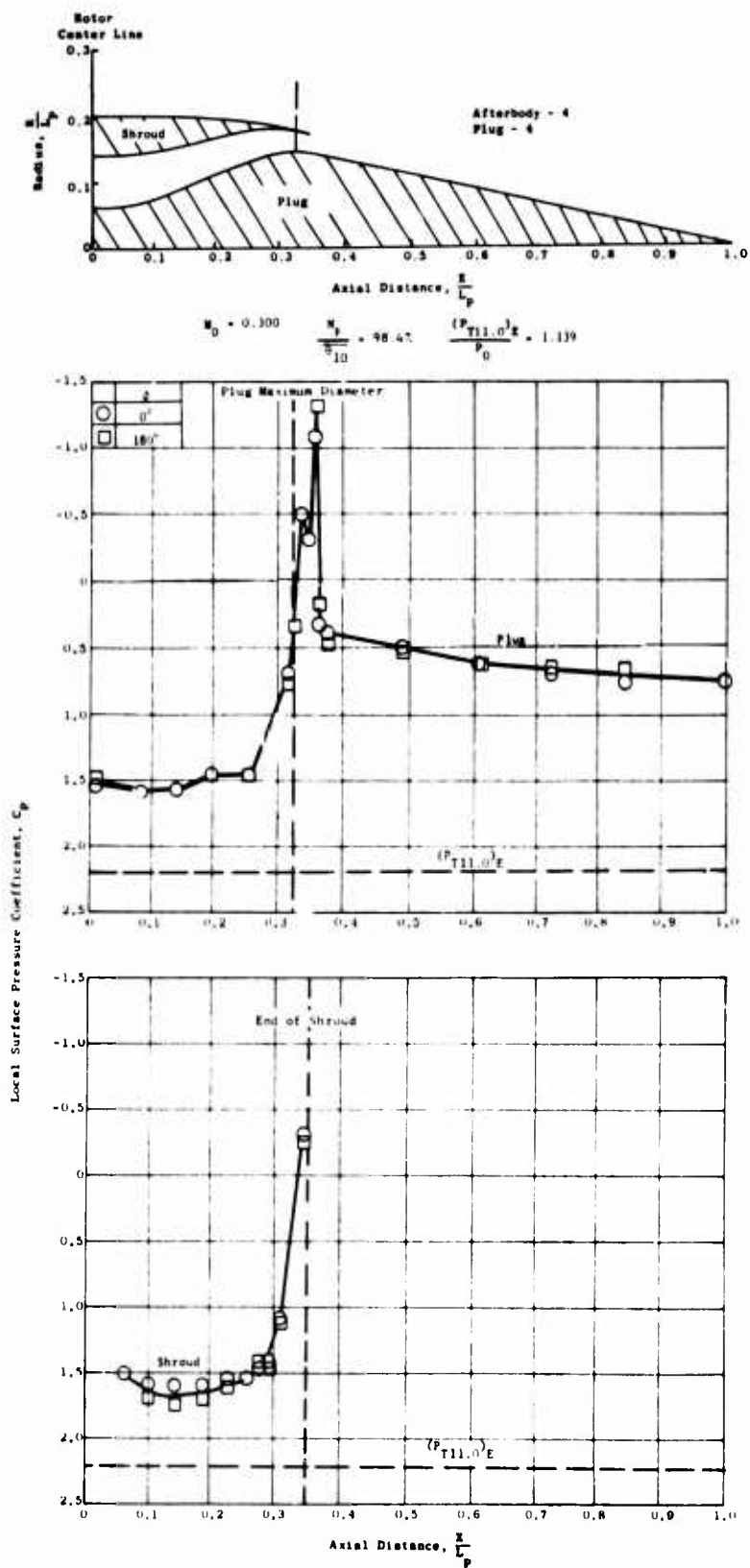


Figure 302. Nozzle Pressure Distribution - Model 2, $M_0 = 0.300$,
 $N_F = 98.4\%$.
 $\sqrt{\theta_{10}}$

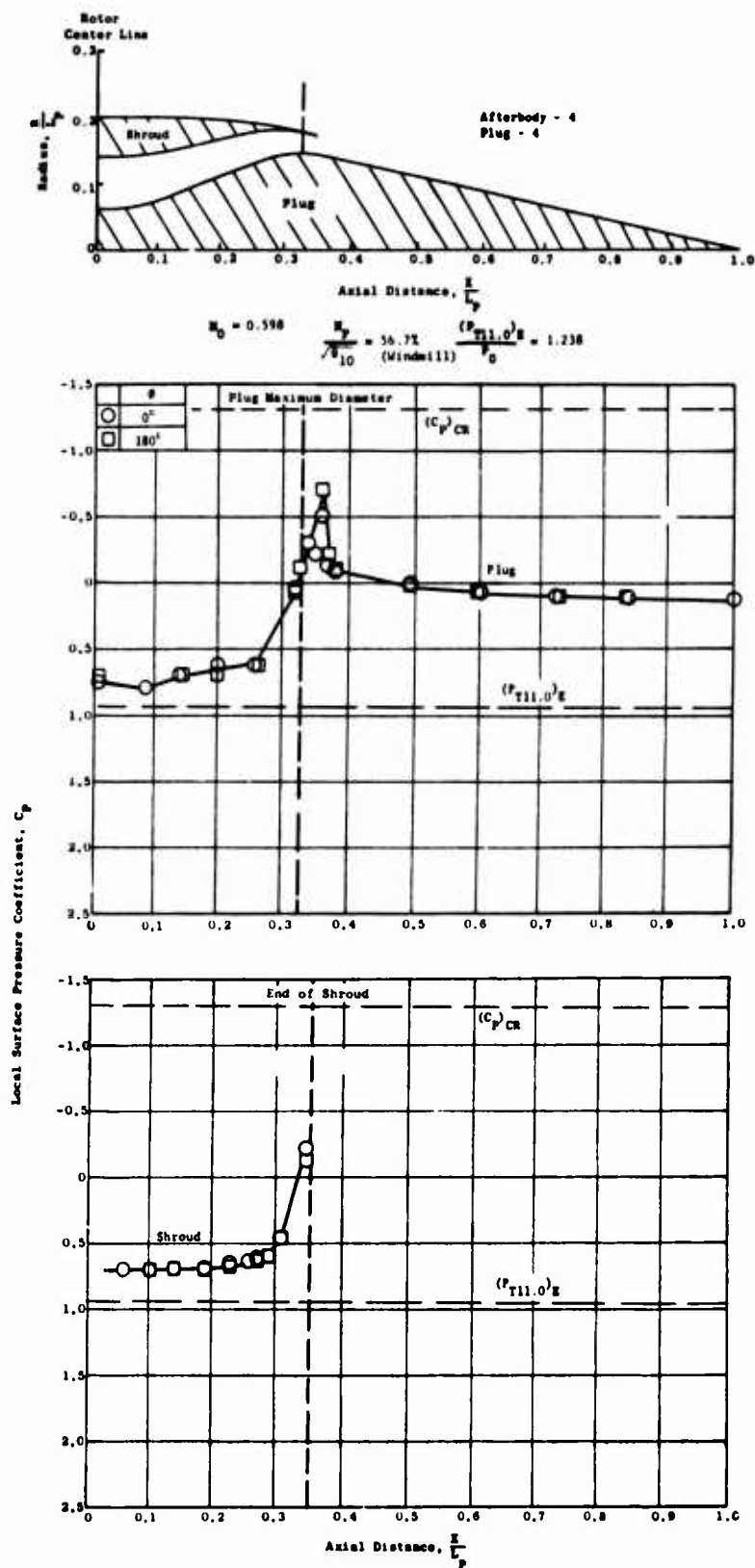


Figure 303. Nozzle Pressure Distribution - Model 2, $M_0 = 0.598$,
 $N_F = 56.7\%$ (Windmill).
 $\sqrt{\theta_{10}}$

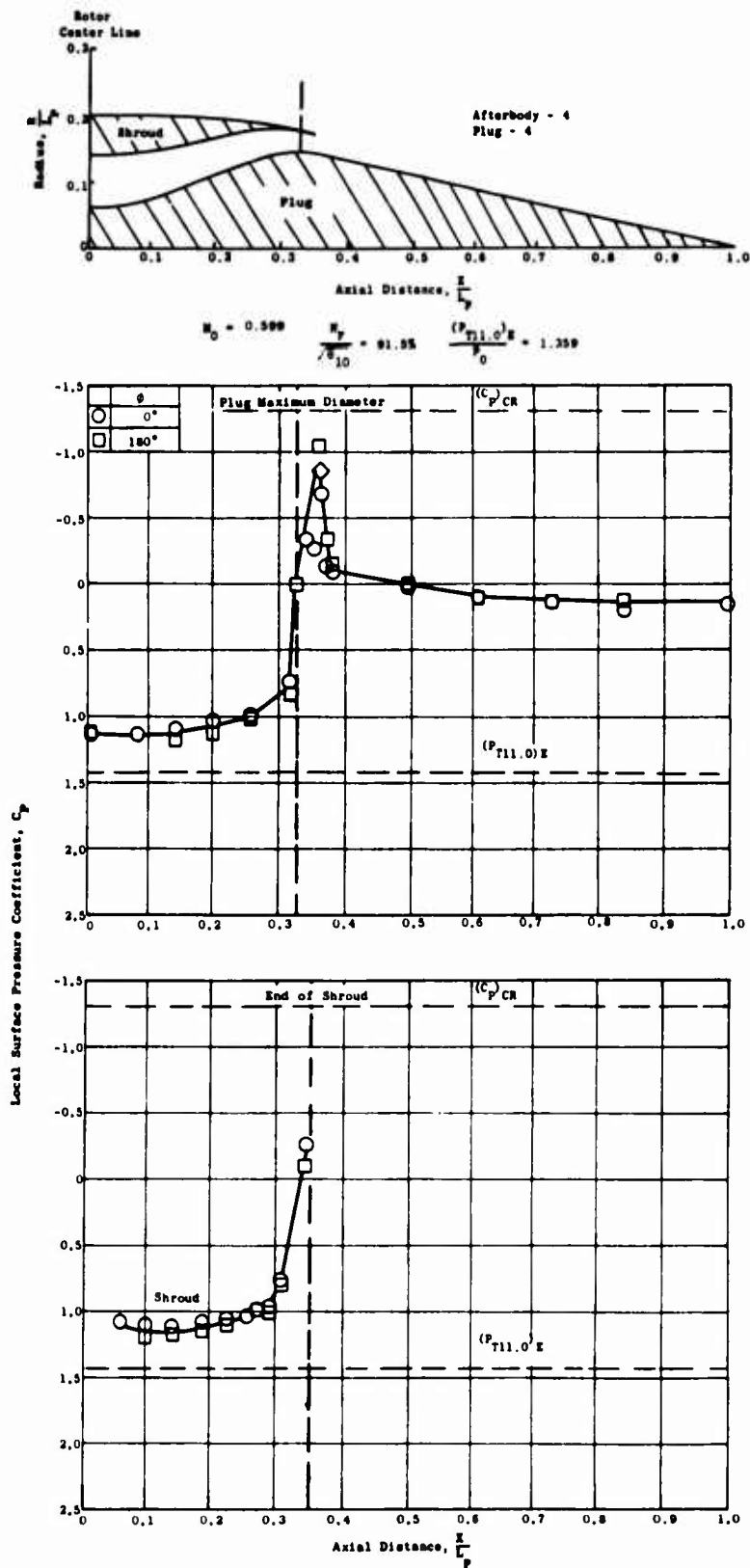


Figure 304. Nozzle Pressure Distribution - Model 2, $M_0 = 0.599$,
 $N_F = 91.5\%$.

$$\sqrt{\theta_{10}}$$

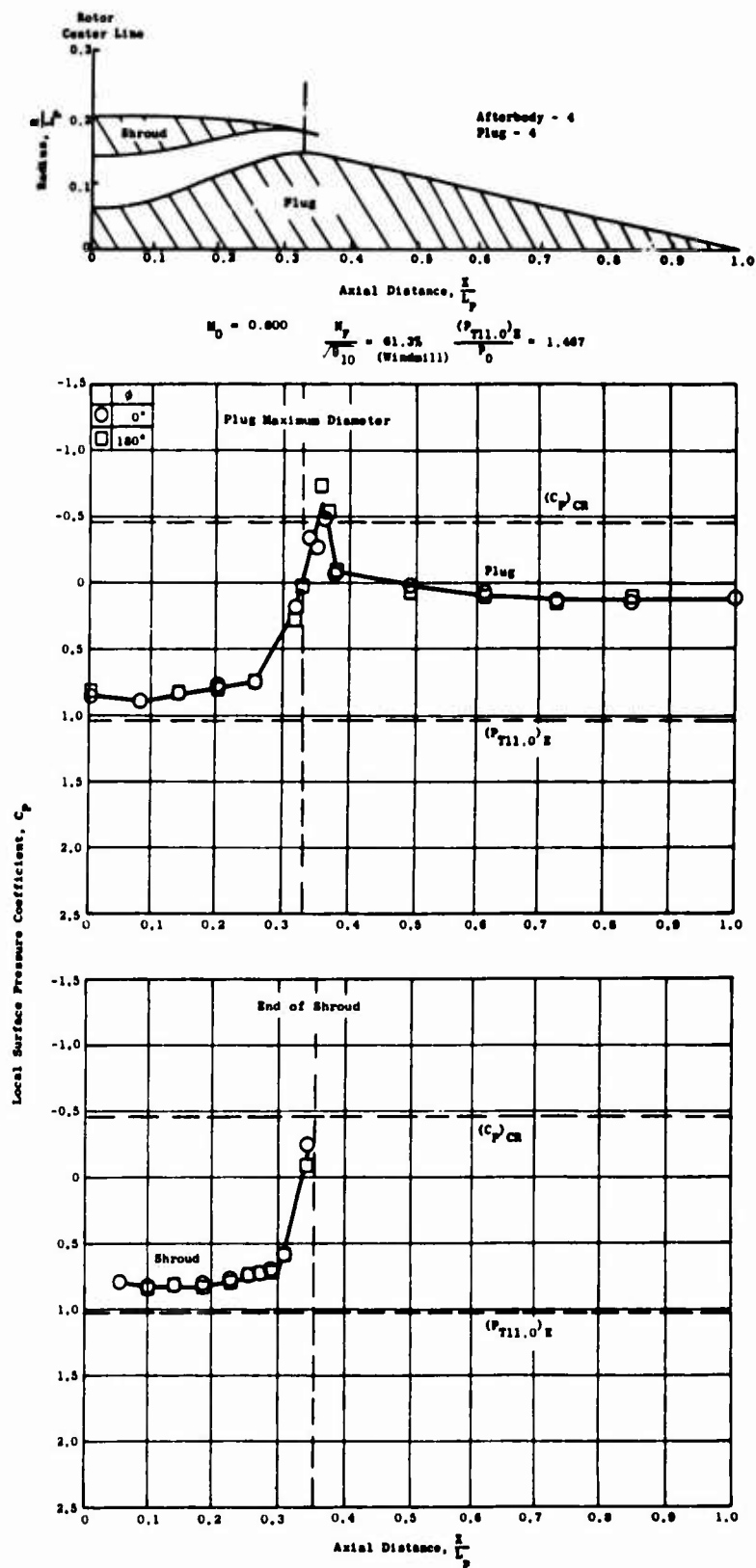


Figure 305. Nozzle Pressure Distribution - Model 2, $M_0 = 0.800$,
 $N_F = 61.3\%$ (Windmill).
 $\frac{N_F}{\sqrt{\theta_{10}}}$

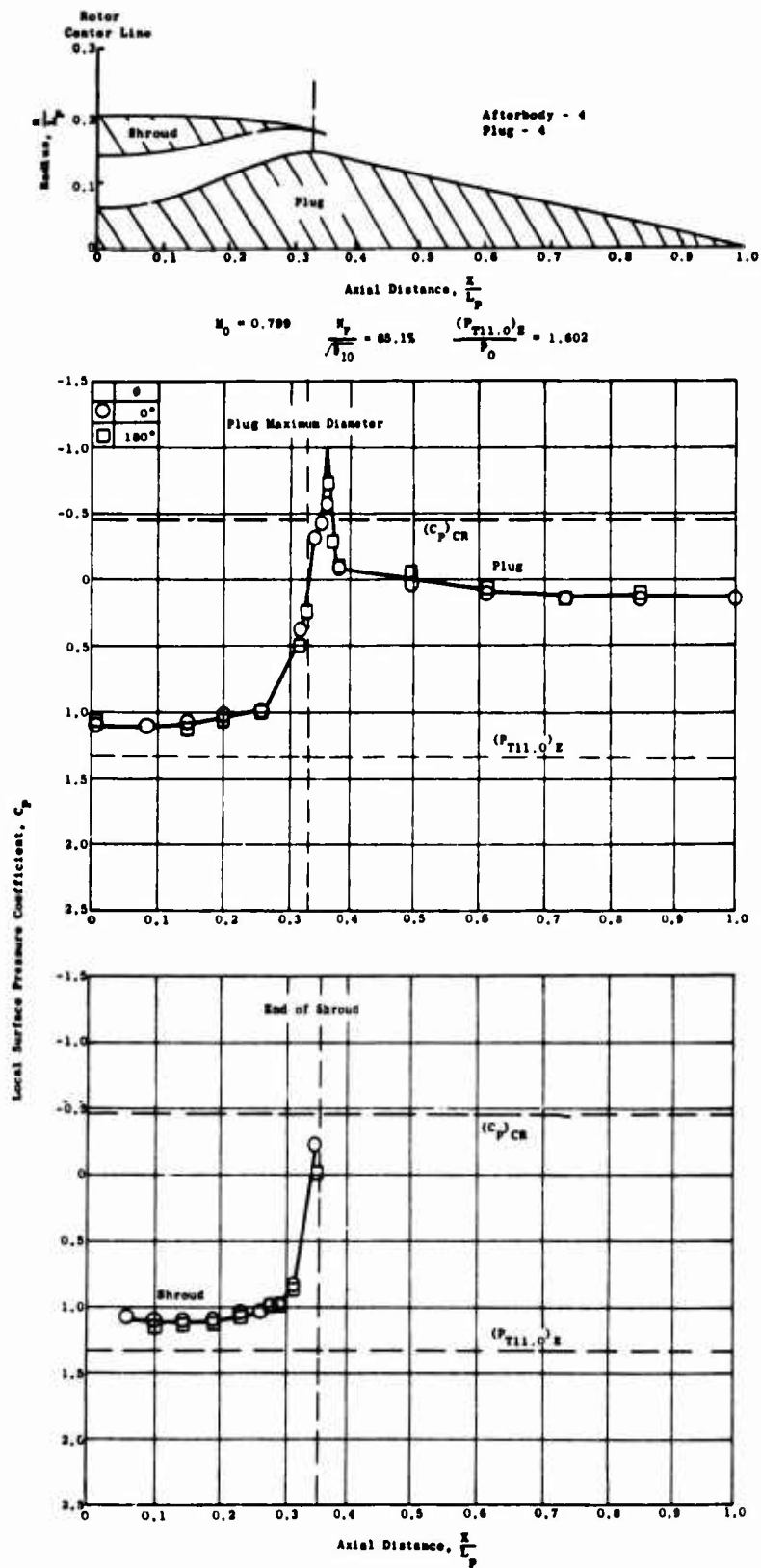
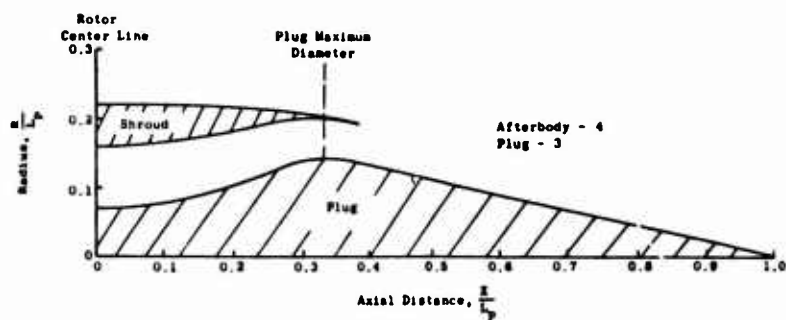


Figure 306. Nozzle Pressure Distribution - Model 2, $M_0 = 0.799$,
 $N_F = 85.1\%$.
 $\sqrt{\theta_{10}}$



$$M_0 = 0.202$$

$$\frac{N_F}{\theta_{10}} = 32.0\% \text{ (Windmill)}$$

$$\frac{(P_{T11.0}) E}{P_0} = 1.020$$

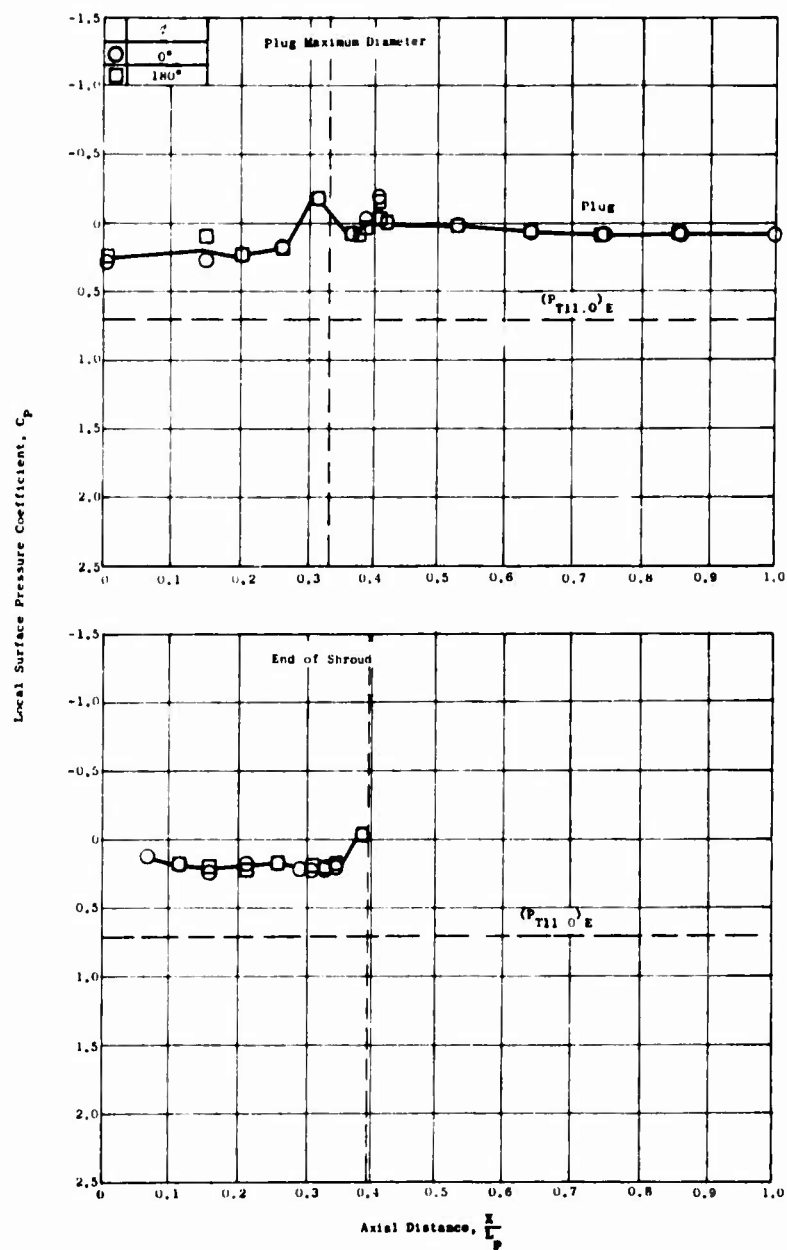


Figure 307. Nozzle Pressure Distribution - Model 3, $M_0 = 0.202$,
 $N_F = 32.0\%$ (Windmill).
 $\sqrt{\theta_{10}}$

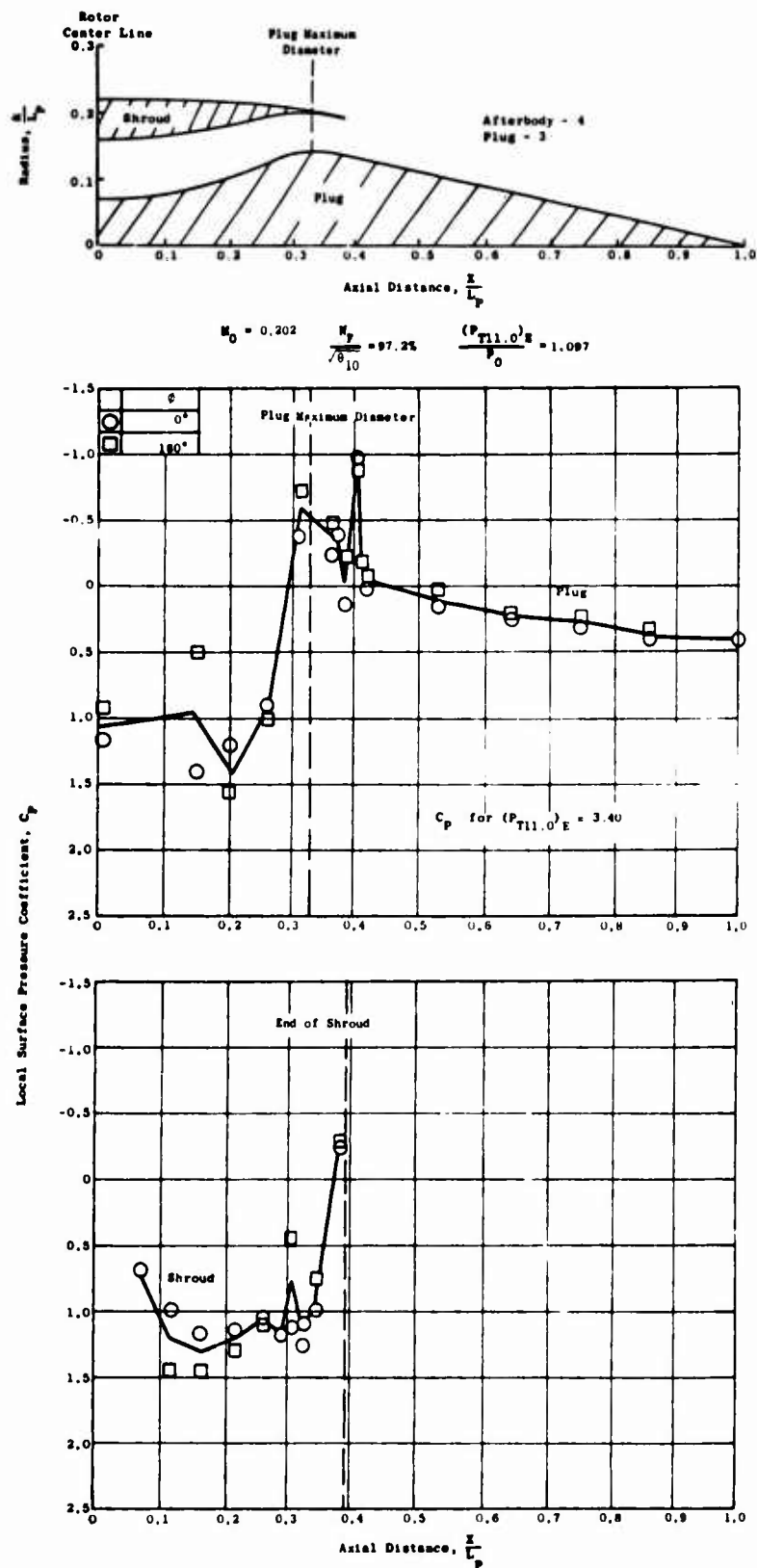


Figure 308. Nozzle Pressure Distribution - Model 3, $M_0 = 0.202$,
 $\frac{N_F}{\sqrt{\theta_{10}}} = 97.2\%$.

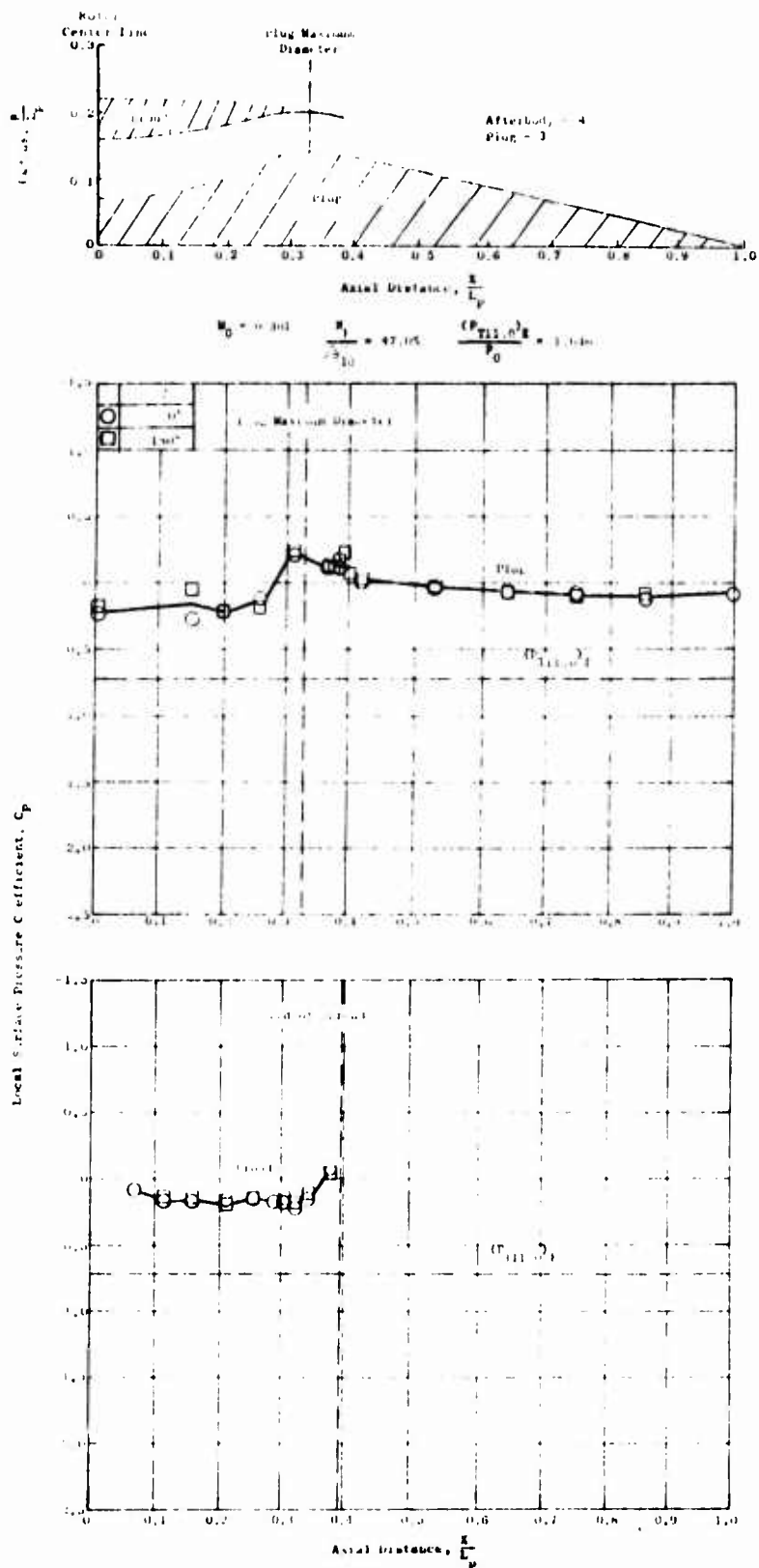
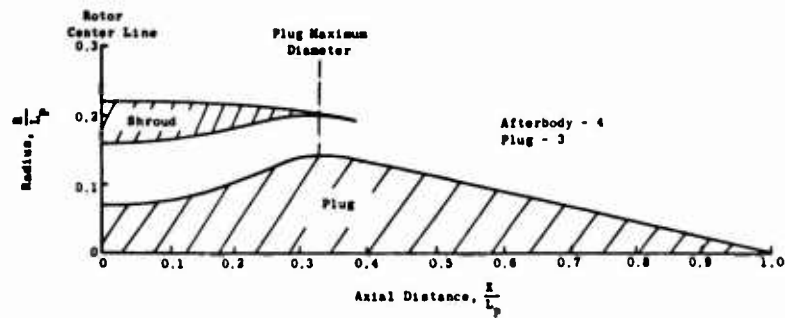


Figure 309. Nozzle Pressure Distribution - Model 3, $M_0 = 0.301$,
 $N_F = 47.0\%$ (Windmill).
 $\sqrt{\theta_{10}}$



$$M_0 = 0.301 \quad \frac{N_F}{\sqrt{\theta_{10}}} = 97.7\% \quad \frac{(P_{T11.0})_E}{P_0} = 1.123$$

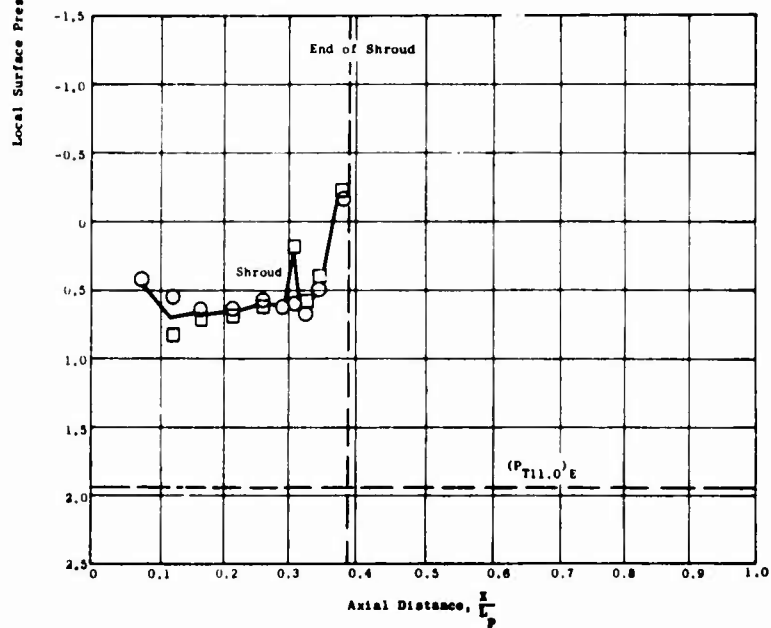
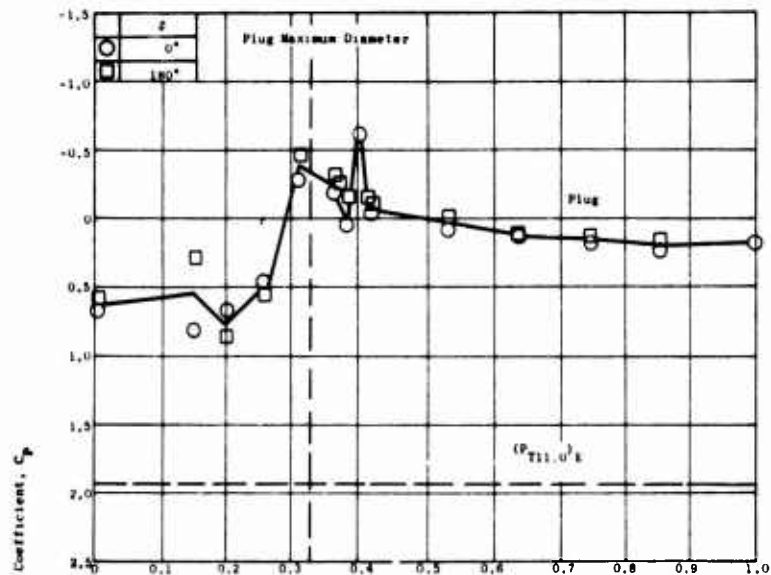


Figure 310. Nozzle Pressure Distribution - Model 3, $M_0 = 0.301$.

$$\frac{N_F}{\sqrt{\theta_{10}}} = 97.7\%$$

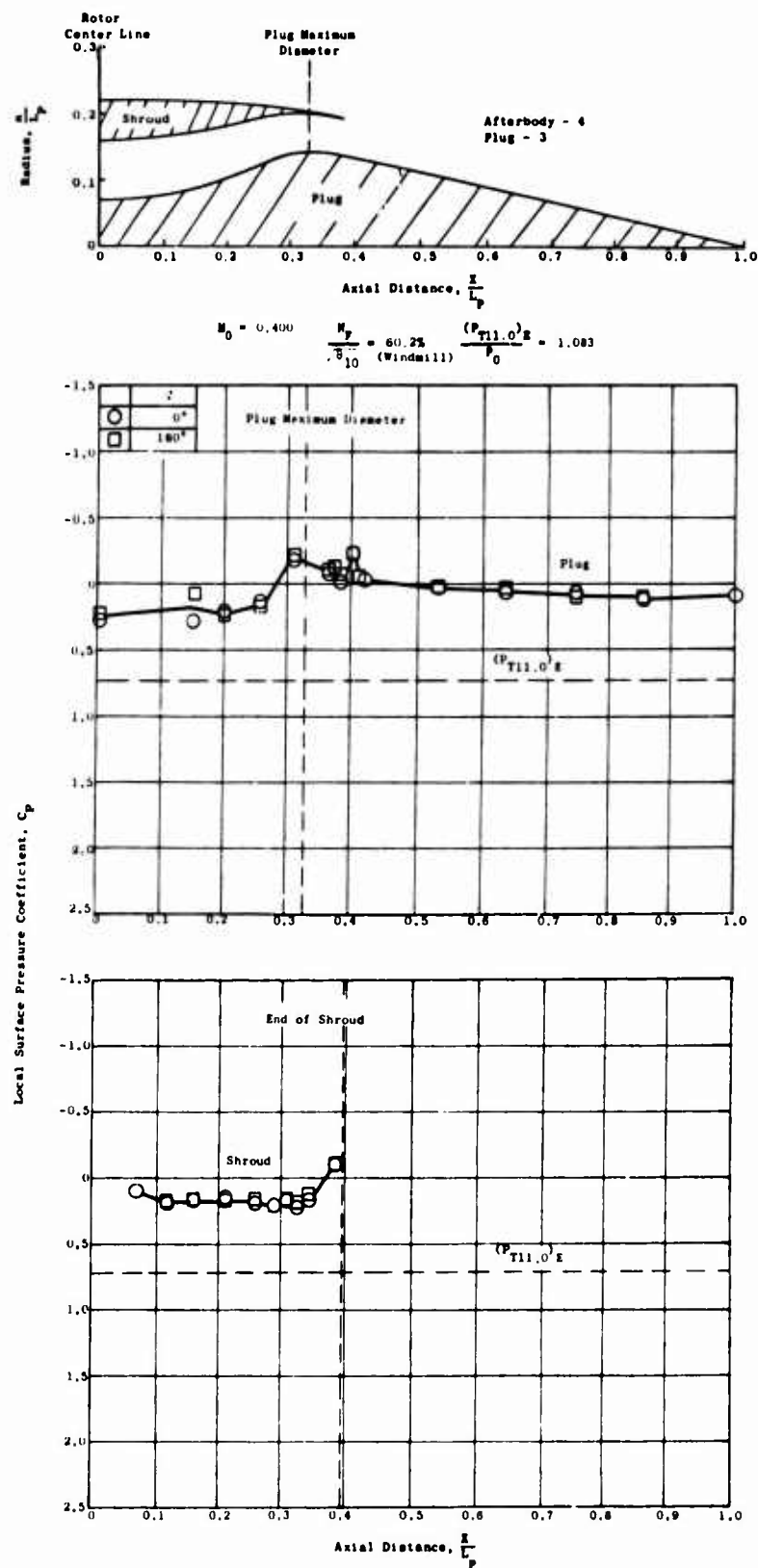


Figure 311. Nozzle Pressure Distribution - Model 3, $M_0 = 0.400$,
 $N_F = 60.2\%$ (Windmill).
 $\sqrt{\theta_{10}}$

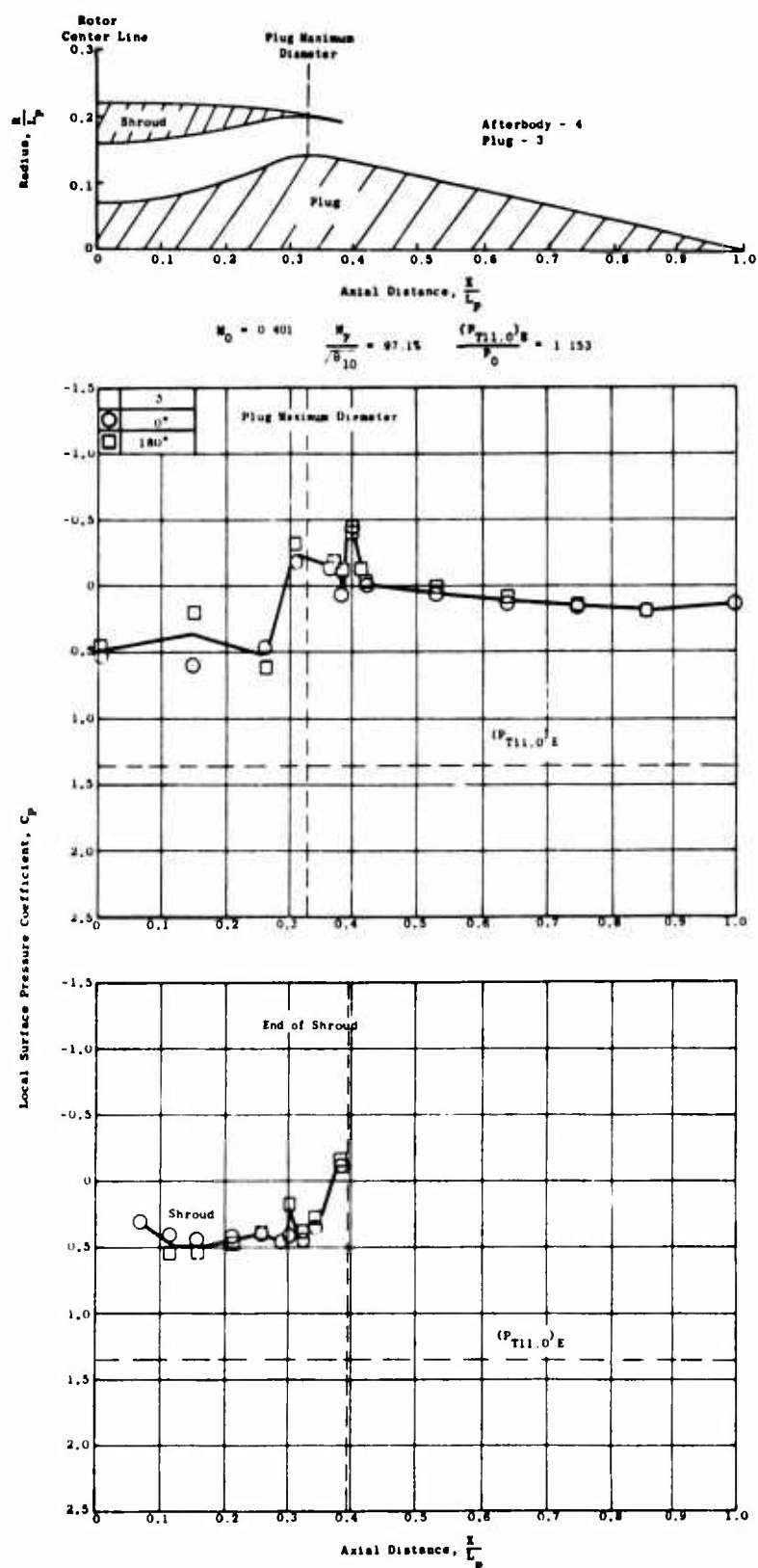


Figure 312. Nozzle Pressure Distribution - Model 3, $M_0 = 0.401$,
 $\frac{M_F}{\sqrt{\theta_{10}}} = 97.1\%$.

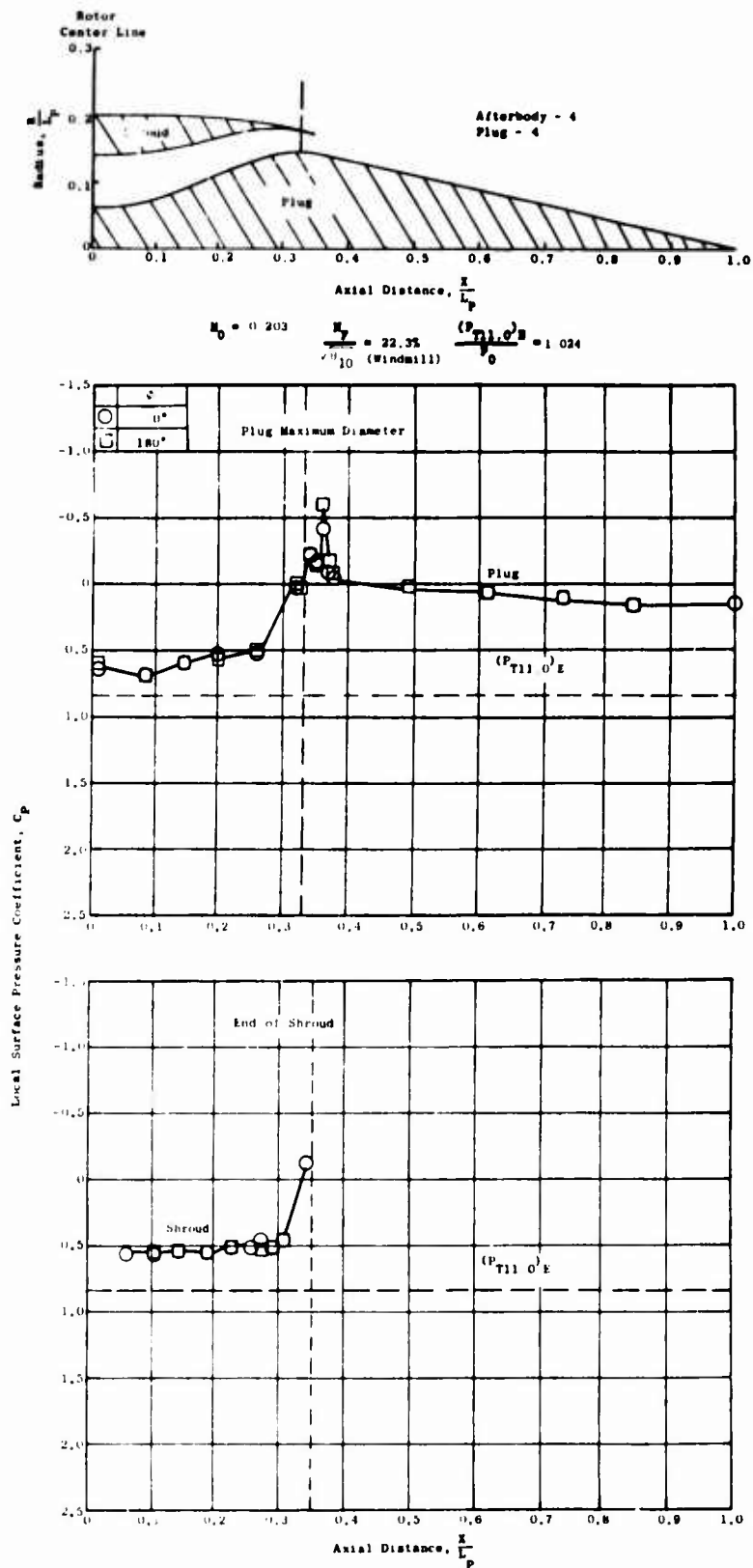


Figure 313. Nozzle Pressure Distribution - Model 4, $M_0 = 0.203$,
 $N_F = 22.3\%$ (Windmill).
 $\sqrt{\theta_{10}}$

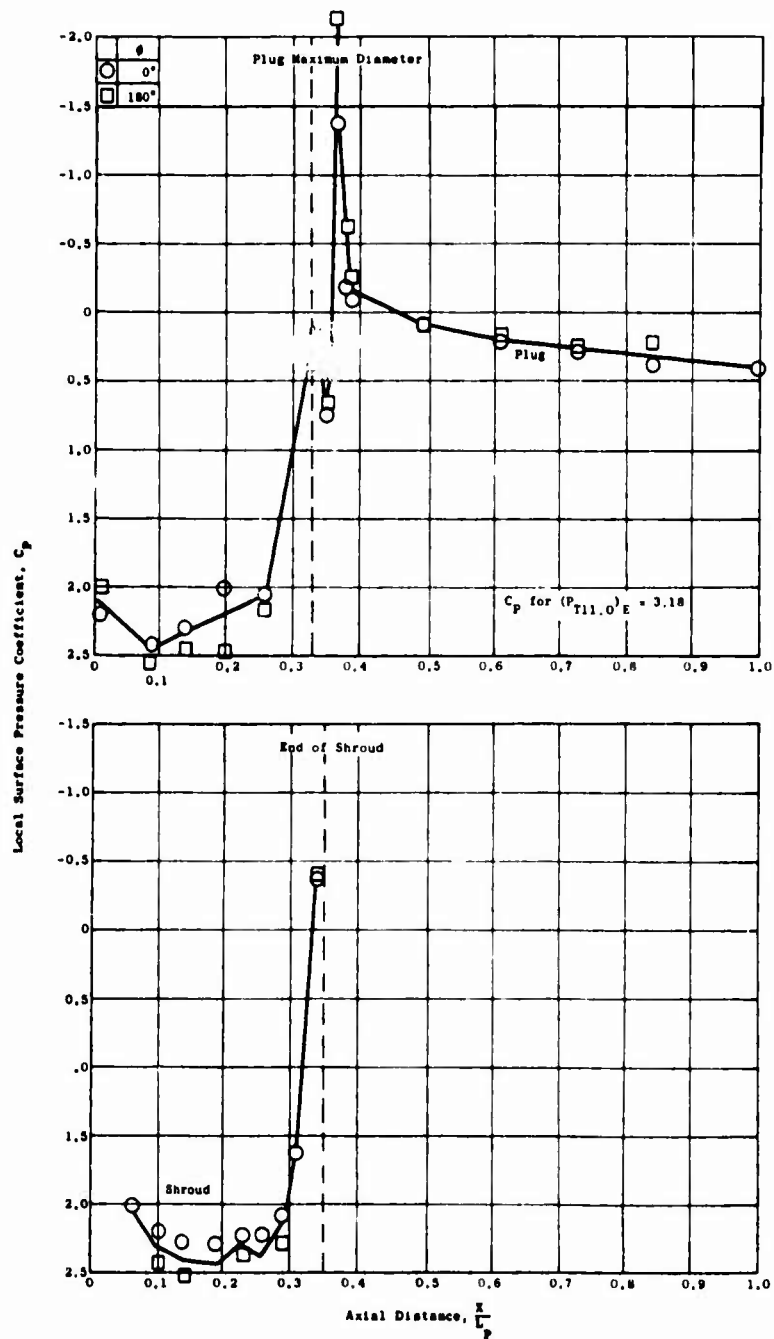
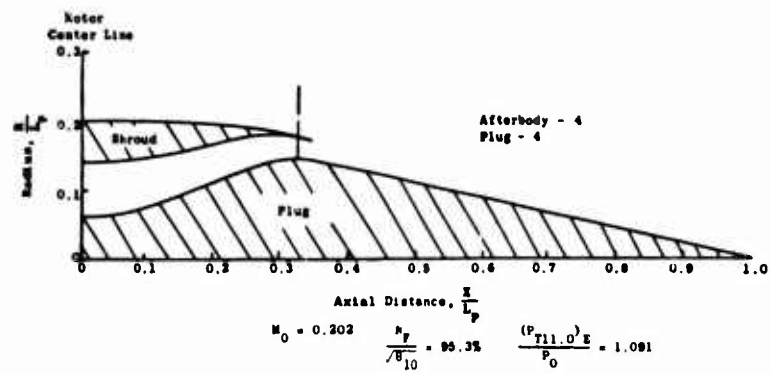


Figure 314. Nozzle Pressure Distribution - Model 4, $M_0 = 0.202$,
 $N_F = 95.3\%$.
 $\frac{N_F}{10}$

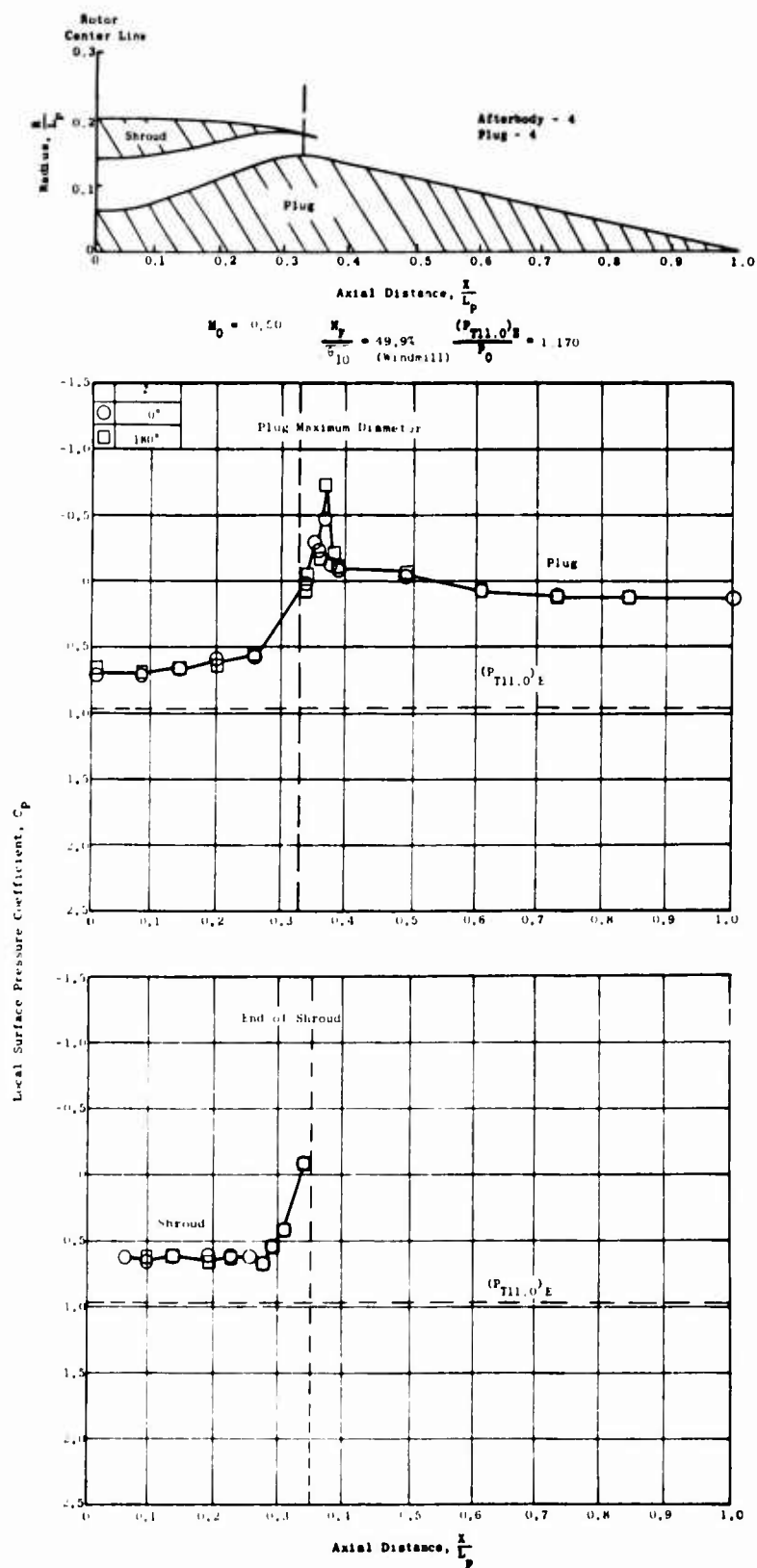


Figure 315. Nozzle Pressure Distribution - Model 4, $M_0 = 0.501$, $N_F = 49.9\%$ (Windmill).

$\sqrt{\theta_{10}}$

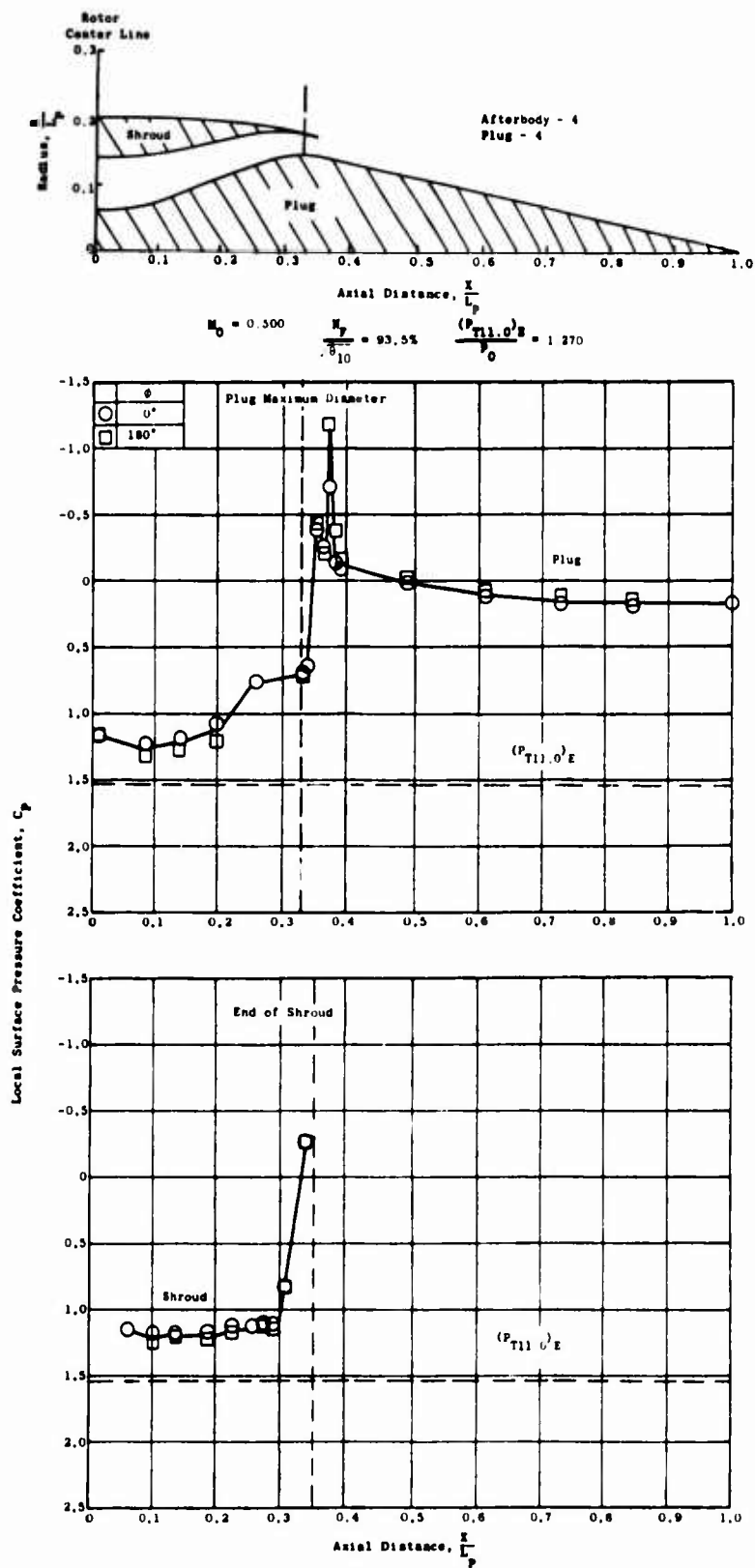
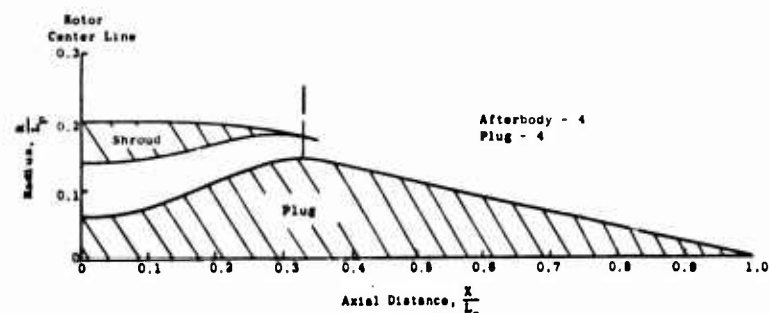


Figure 316. Nozzle Pressure Distribution - Model 4, $M_0 = 0.500$,
 $N_F = 93.5\%$.



$$M_0 = 0.649 \quad \frac{N_F}{\sqrt{\theta_{10}}} = 58.8\% \quad \frac{(P_{T11.0})}{P_0} = 1.285$$

(Windmill)

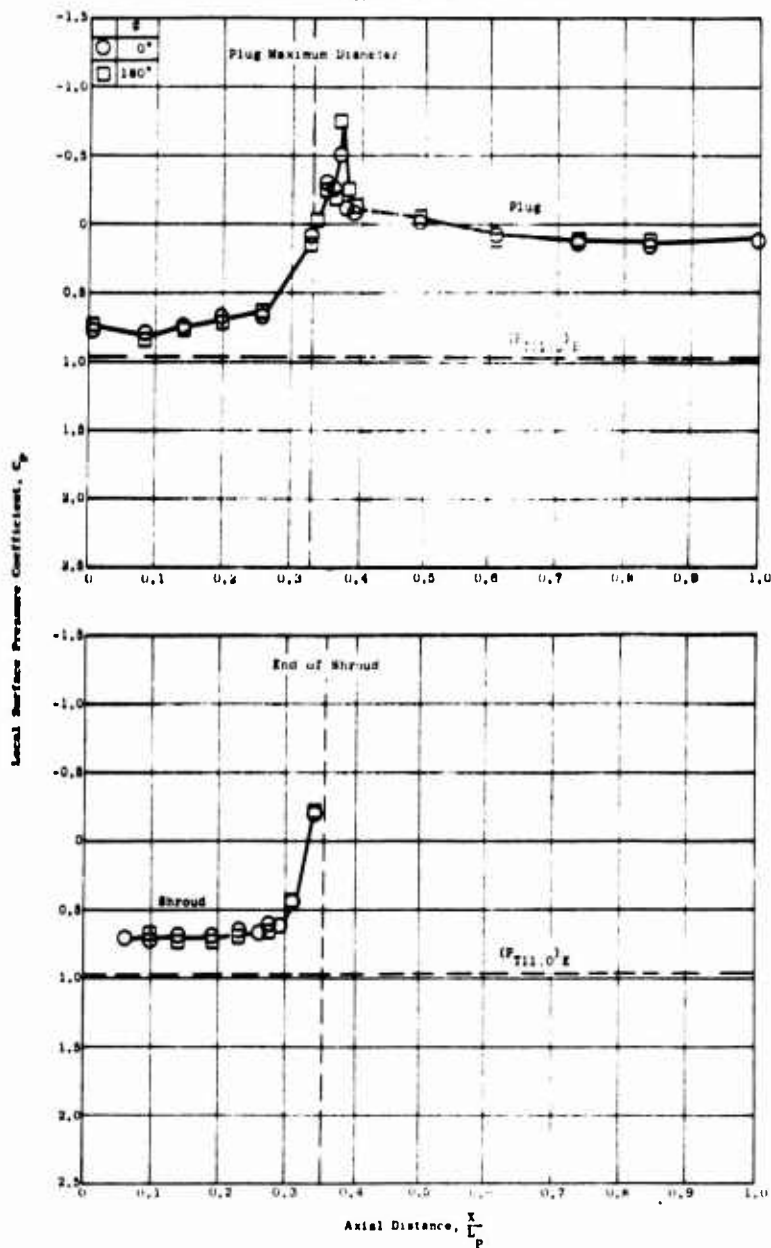


Figure 317. Nozzle Pressure Distribution - Model 4, $M_0 = 0.649$,
 $N_F = 58.8\%$ (Windmill).
 $\sqrt{\theta_{10}}$

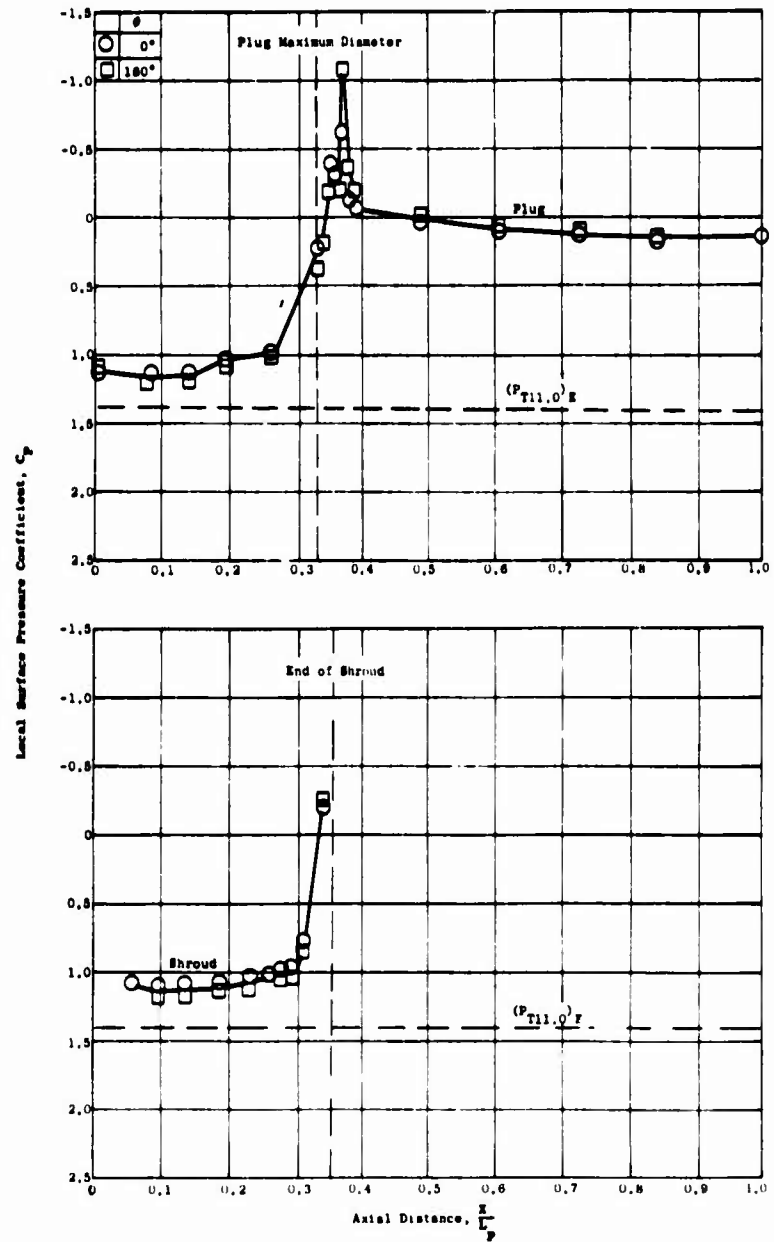
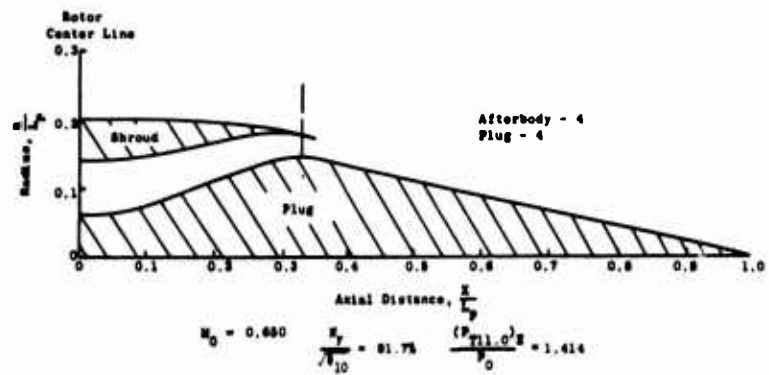


Figure 318. Nozzle Pressure Distribution - Model 4, $M_0 = 0.650$,
 $\frac{N_F}{\sqrt{\theta_{10}}} = 91.7\%$.

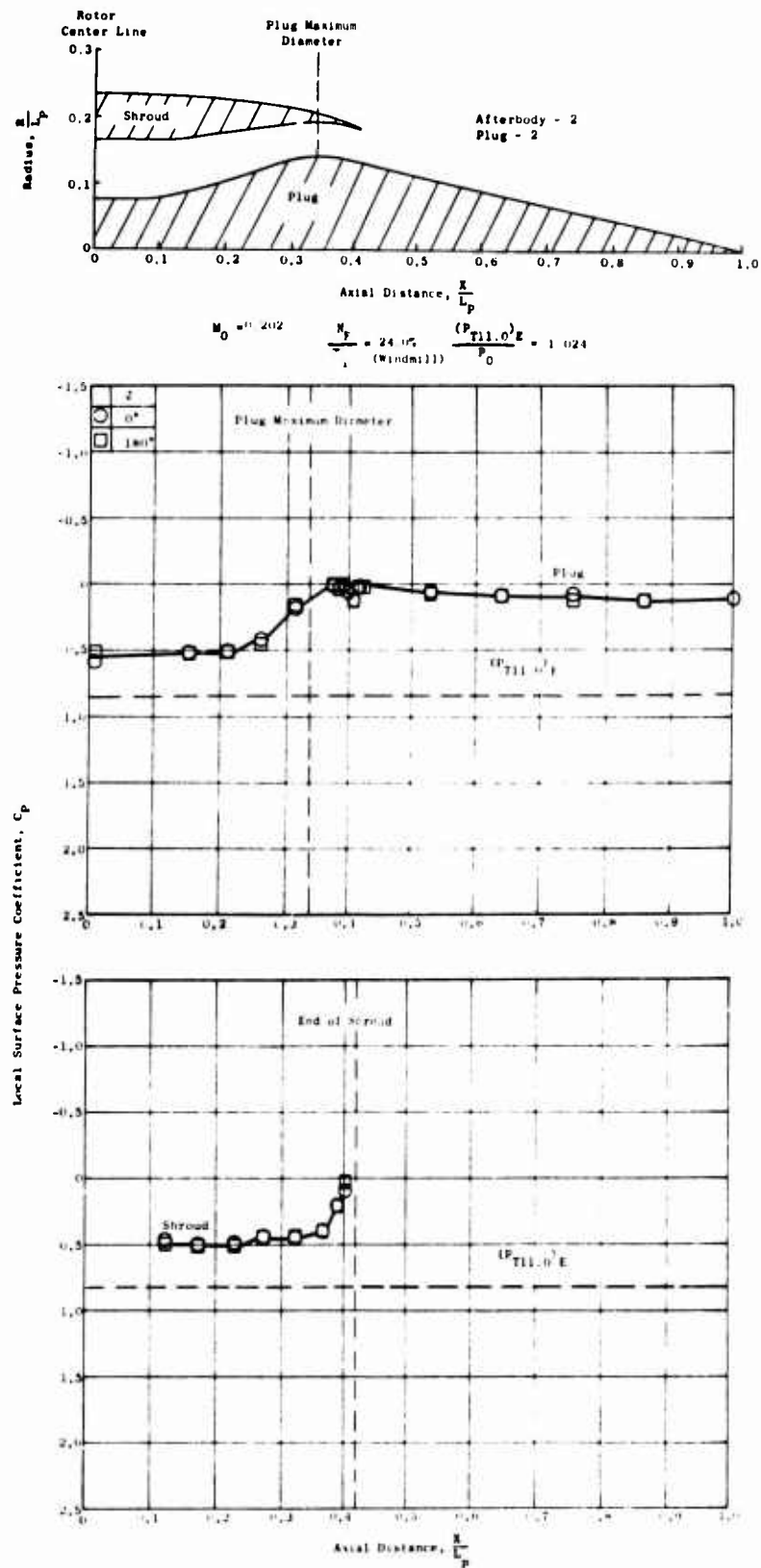


Figure 319. Nozzle Pressure Distribution - Model 5, $M_0 = 0.202$,
 $N_F = 24.0\%$ (Windmill).

$\sqrt{\theta_{10}}$

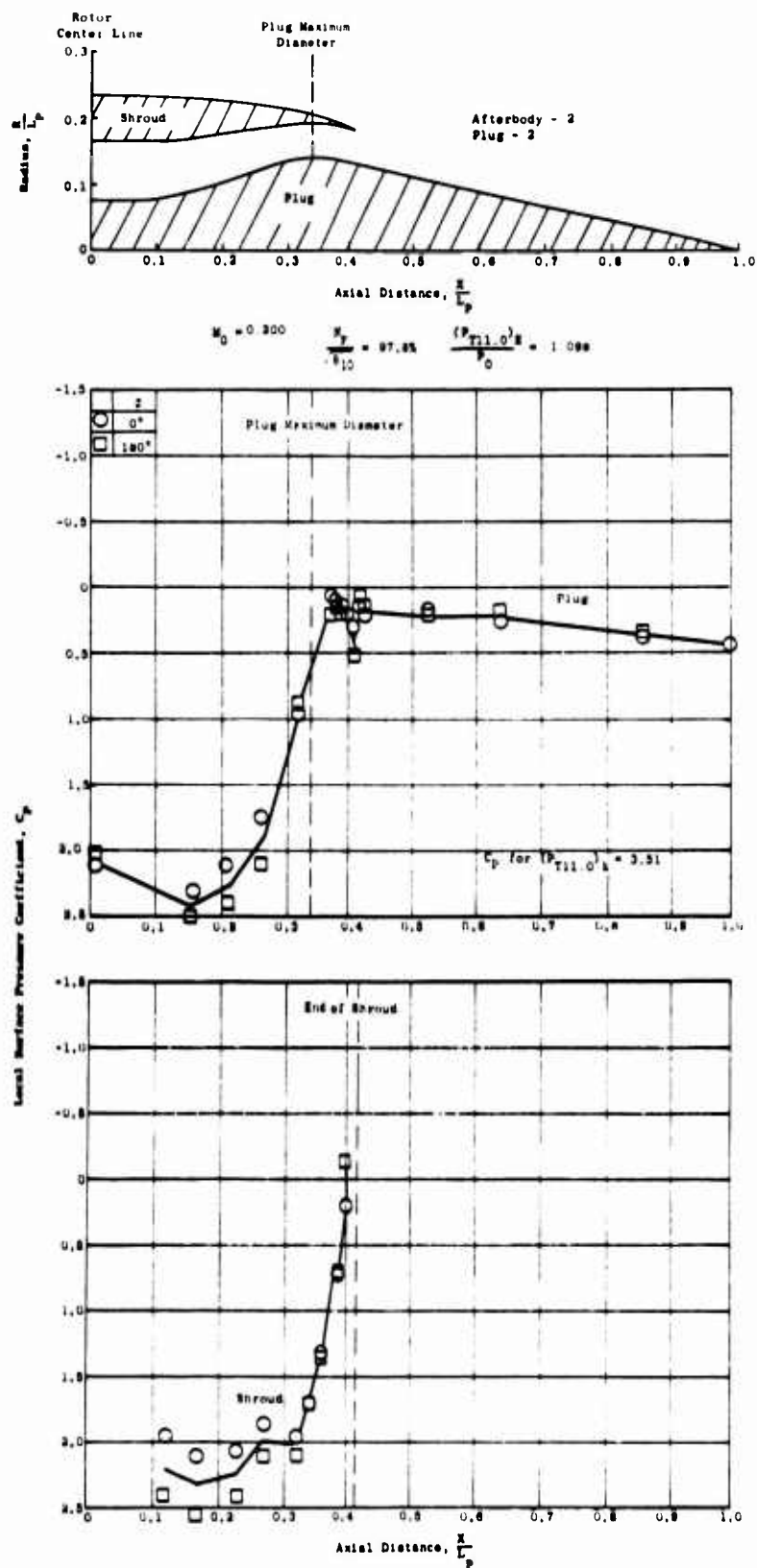


Figure 320. Nozzle Pressure Distribution - Model 5, $M_0 = 0.200$,
 $N_F = 97.8\%$.

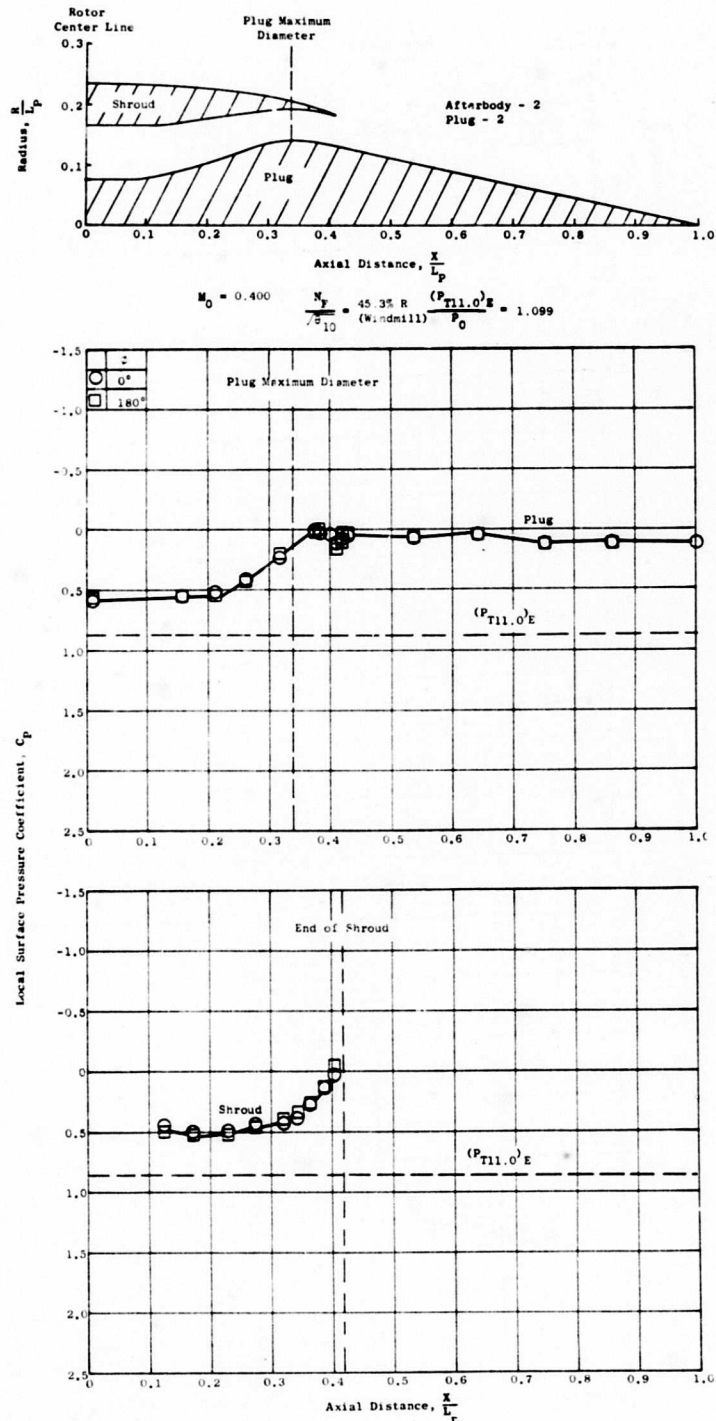


Figure 321. Nozzle Pressure Distribution - Model 5, $M_0 = 0.400$,
 $\frac{N_F}{\sqrt{\theta_{10}}} = 45.3\%$ (Windmill).

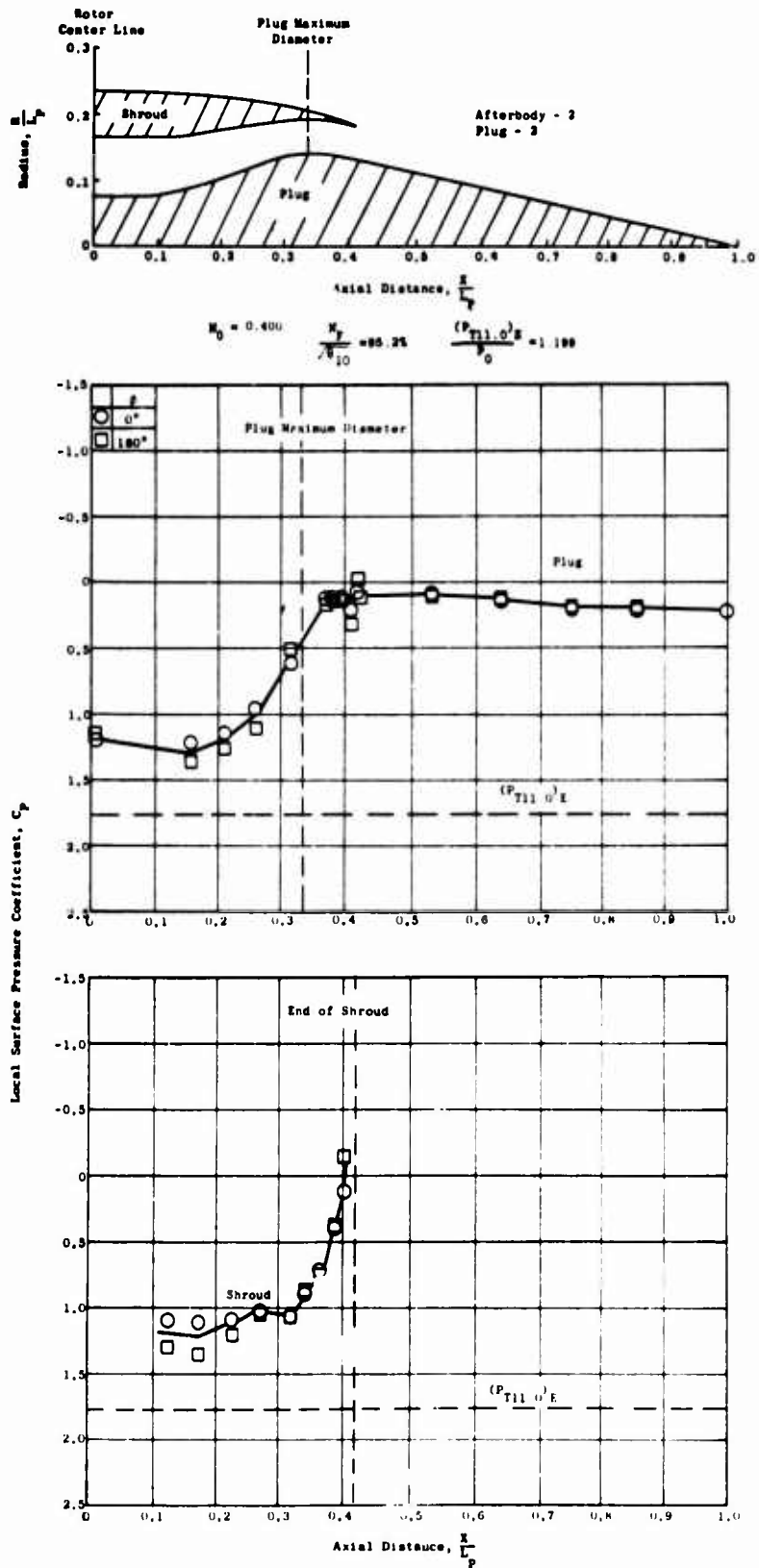


Figure 322. Nozzle Pressure Distribution - Model 5, $M_0 = 0.400$,
 $N_F = 95.2\%$.

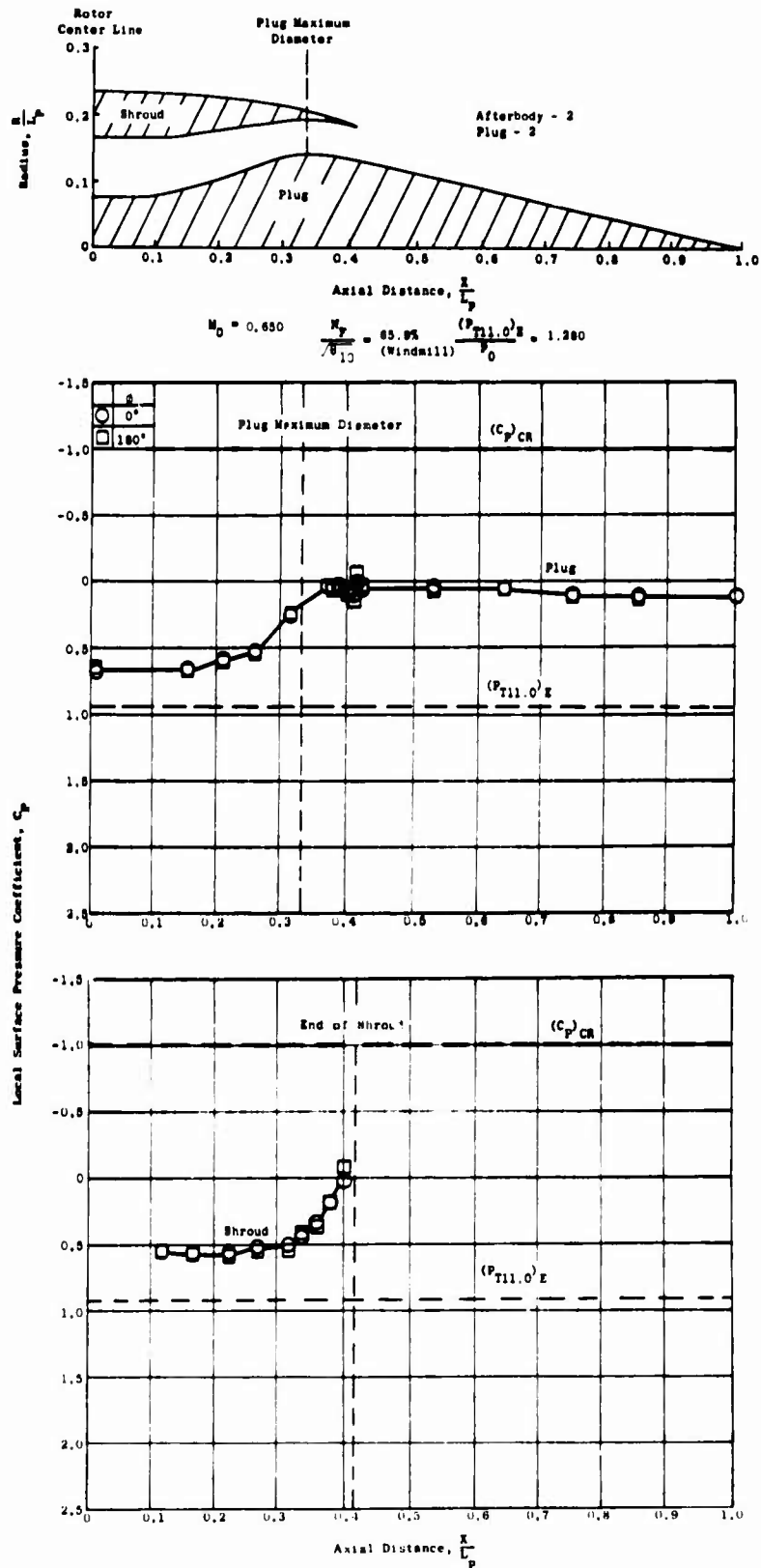


Figure 323. Nozzle Pressure Distribution - Model 5, $M_0 = 0.650$,
 $\frac{N_F}{\sqrt{10}} = 65.9\%$ (Windmill).

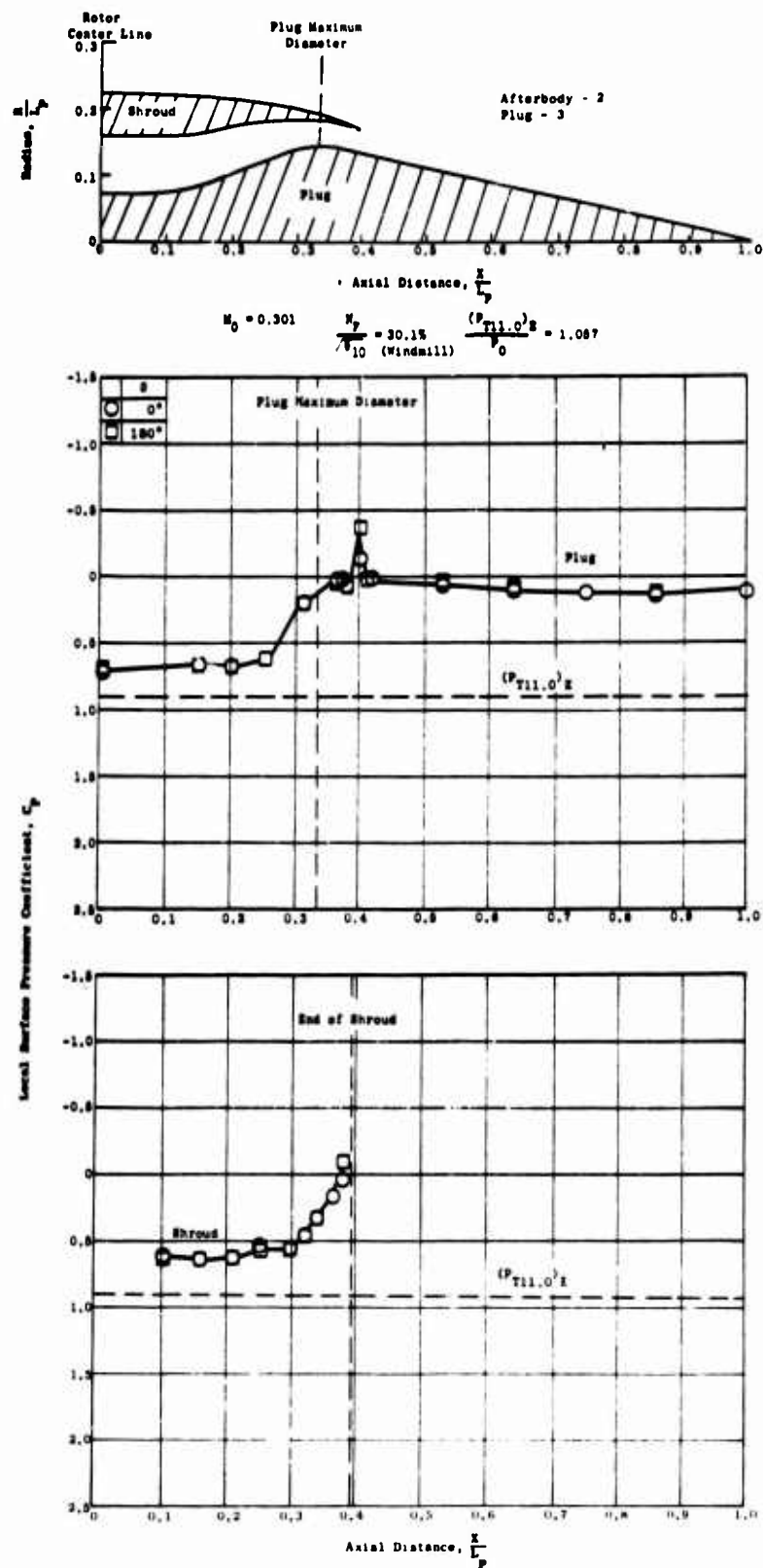


Figure 324. Nozzle Pressure Distribution - Model 6, $M_0 = 0.301$,
 $N_F = 30.1\%$ (Windmill).
 $\sqrt{\theta_{10}}$

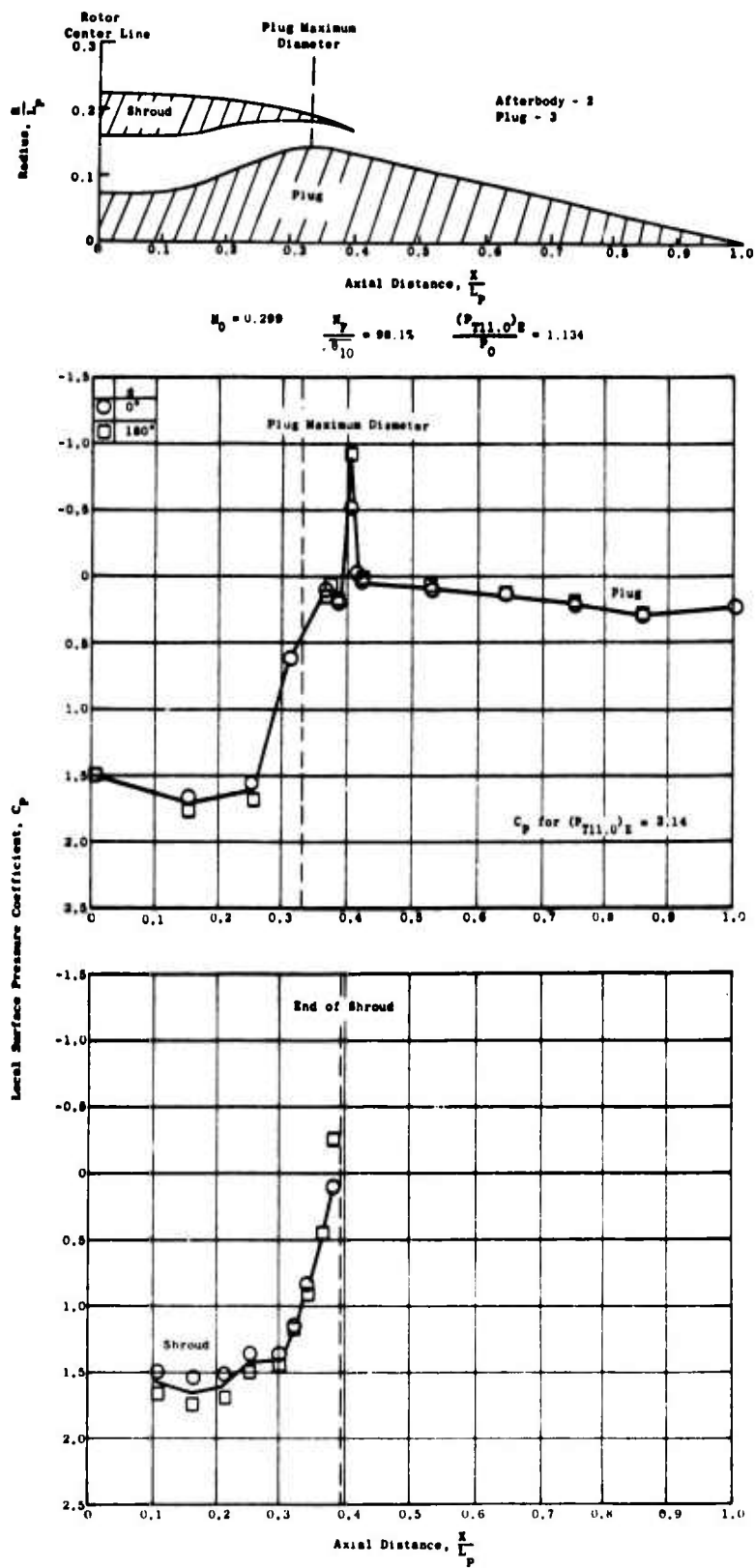


Figure 325. Nozzle Pressure Distribution - Model 6, $M_0 = 0.299$,
 $N_F = 98.1\%$,
 $\sqrt{\theta_{10}}$

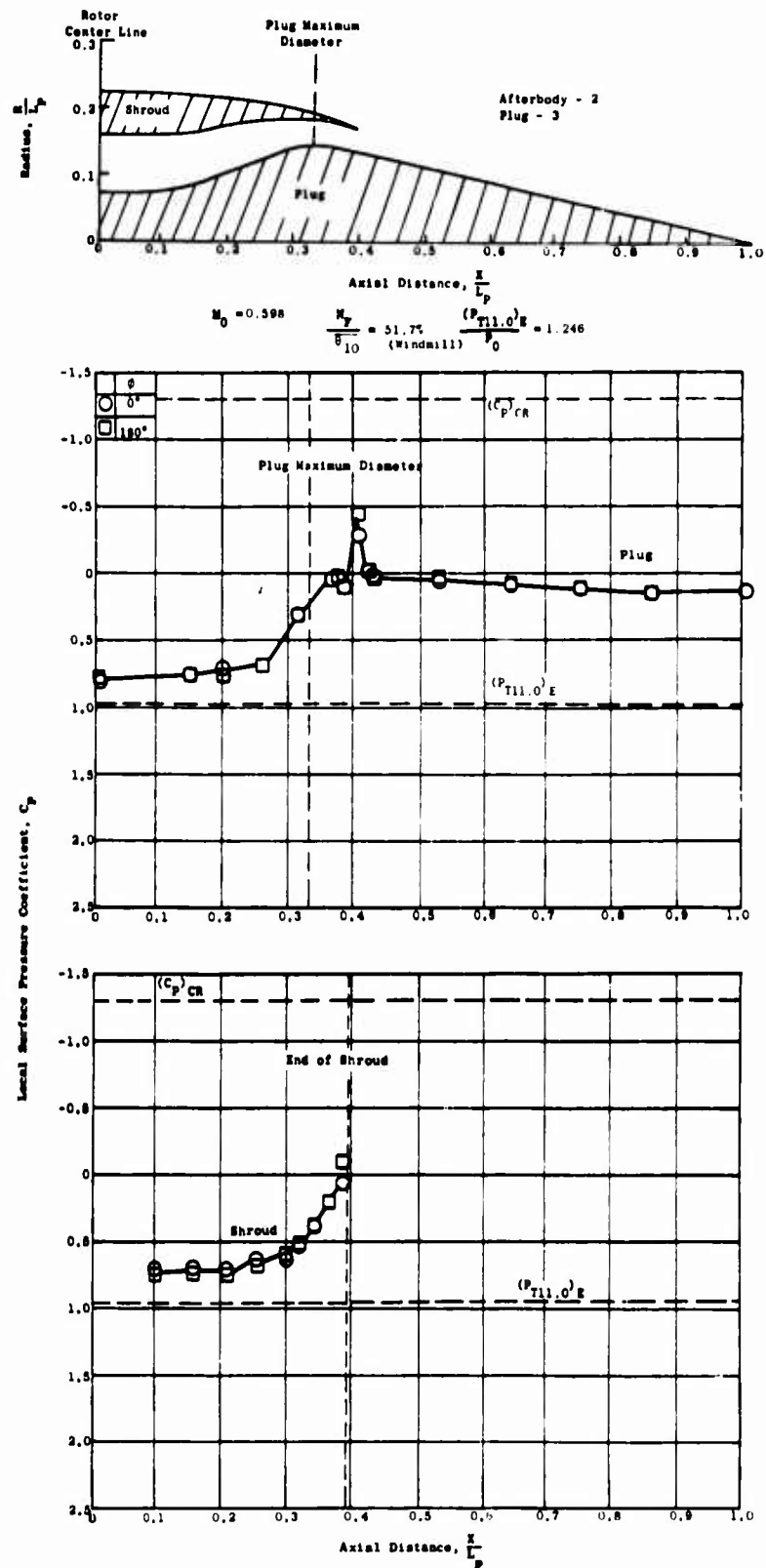


Figure 326. Nozzle Pressure Distribution - Model 6, $M_0 = 0.598$,
 $N_F = 51.6\%$ (Windmill).
 $\sqrt{\theta_{10}}$

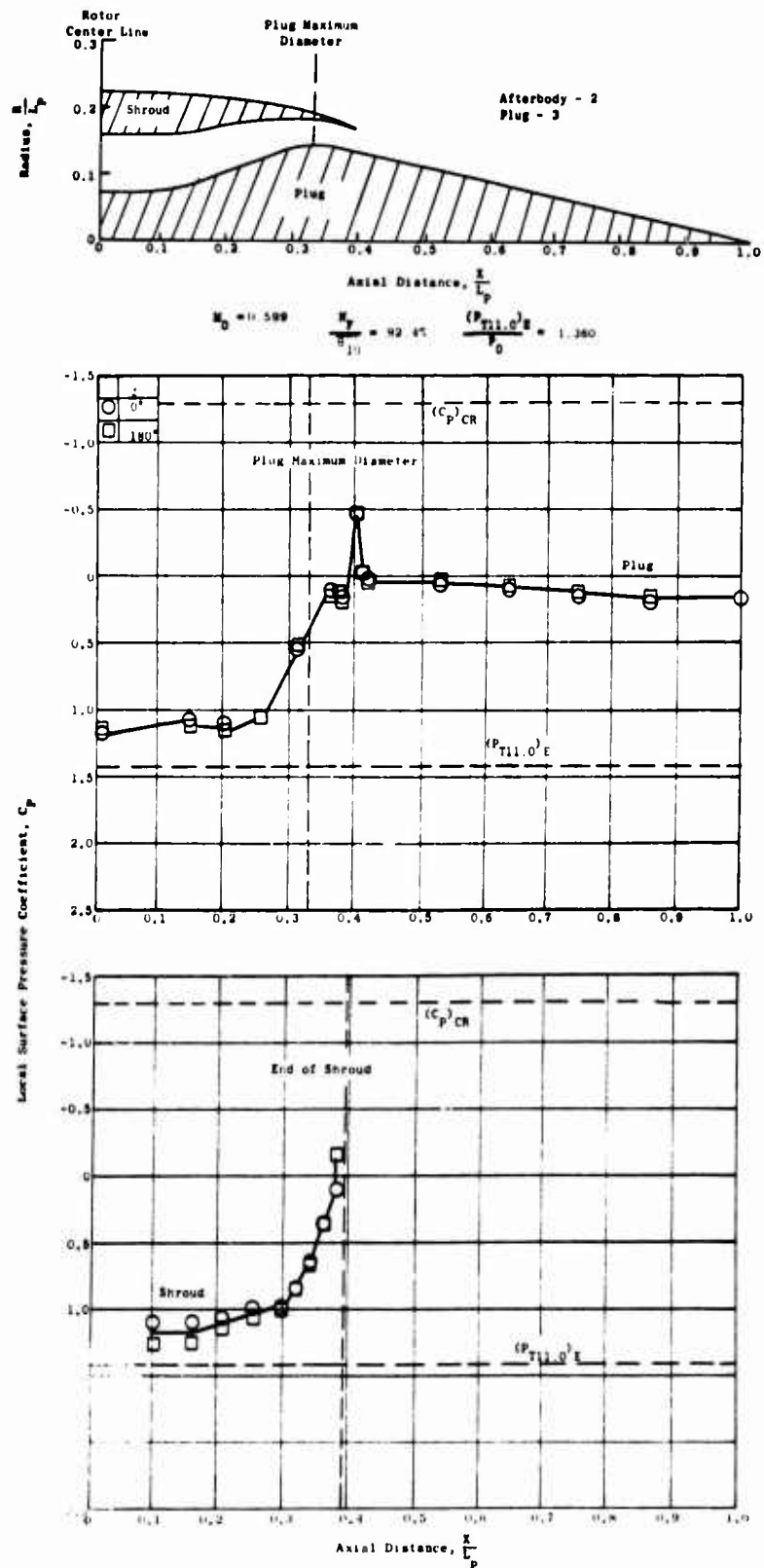


Figure 327. Nozzle Pressure Distribution - Model 6, $M_0 = 0.599$, $N_F = 92.4\%$.

$\sqrt{\theta_{10}}$

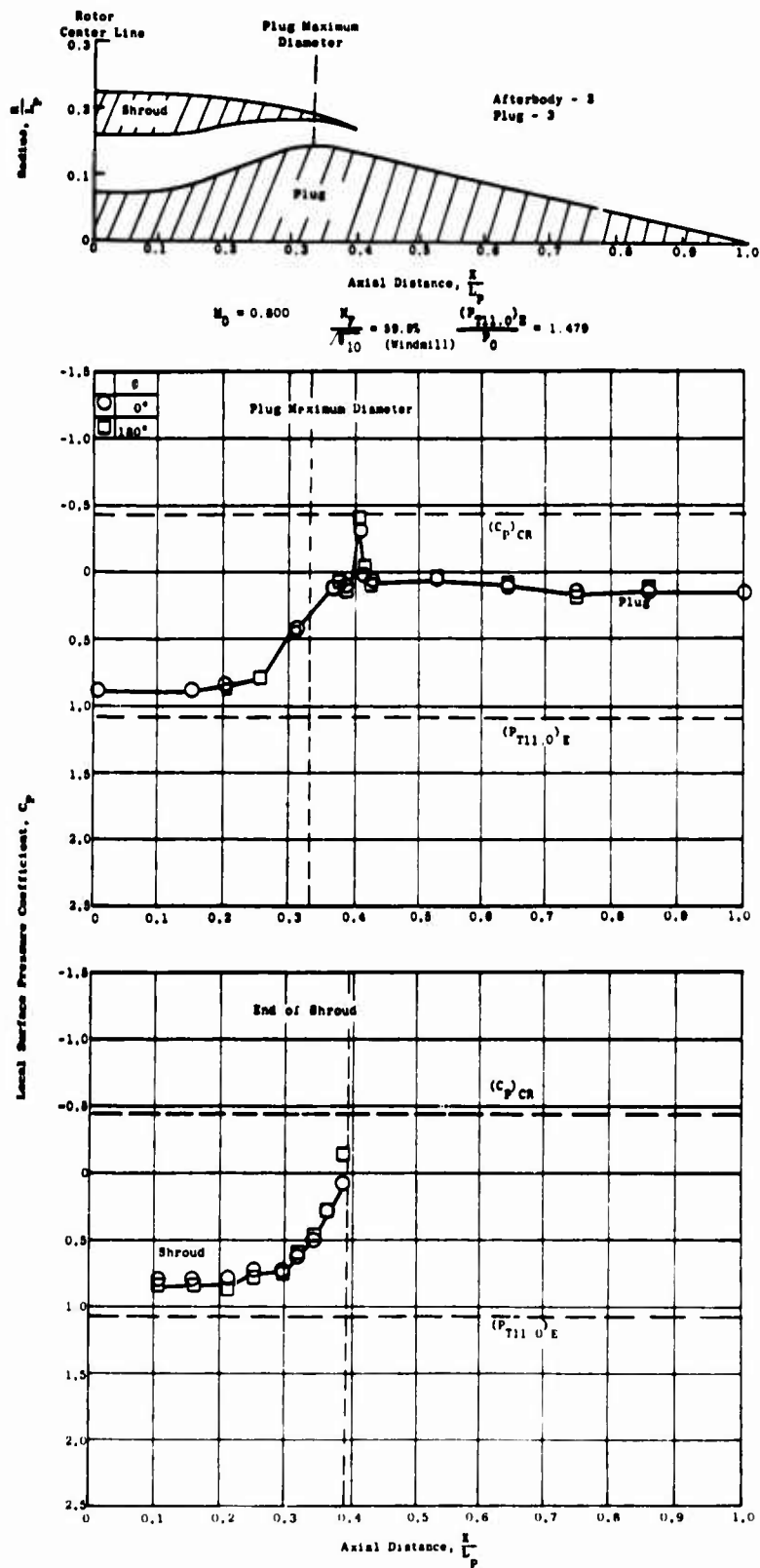


Figure 328. Nozzle Pressure Distribution - Model 6, $M_0 = 0.800$,
 $N_F = 59.9\%$ (Windmill).
 $\sqrt{\theta_{10}}$

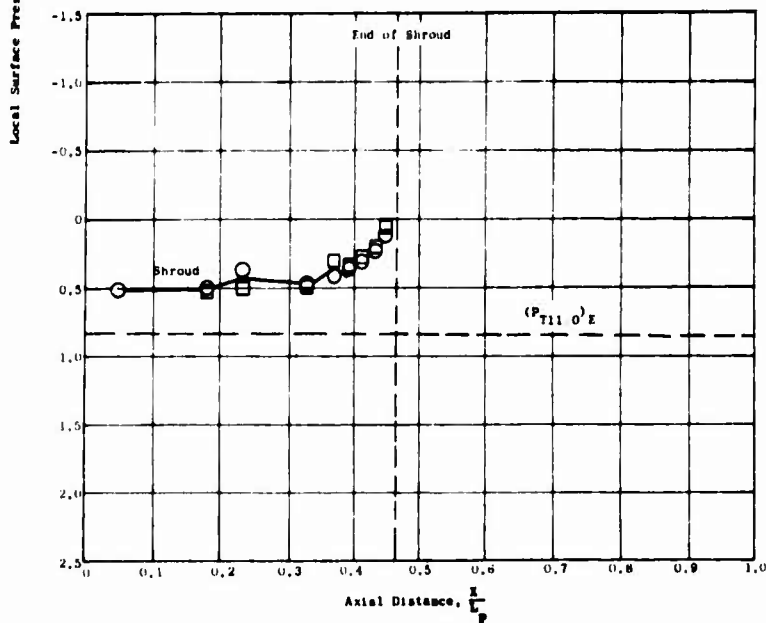
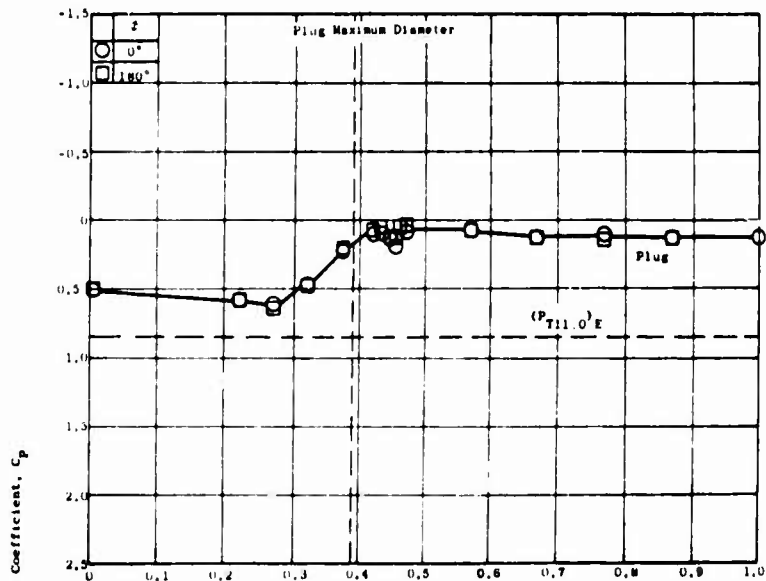
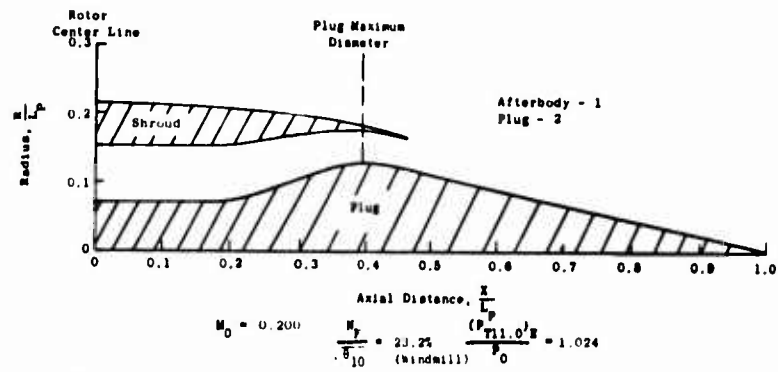


Figure 329. Nozzle Pressure Distribution - Model 7, $M_0 = 0.200$,
 $\frac{N_F}{\sqrt{\theta_{10}}} = 23.2\%$ (Windmill).

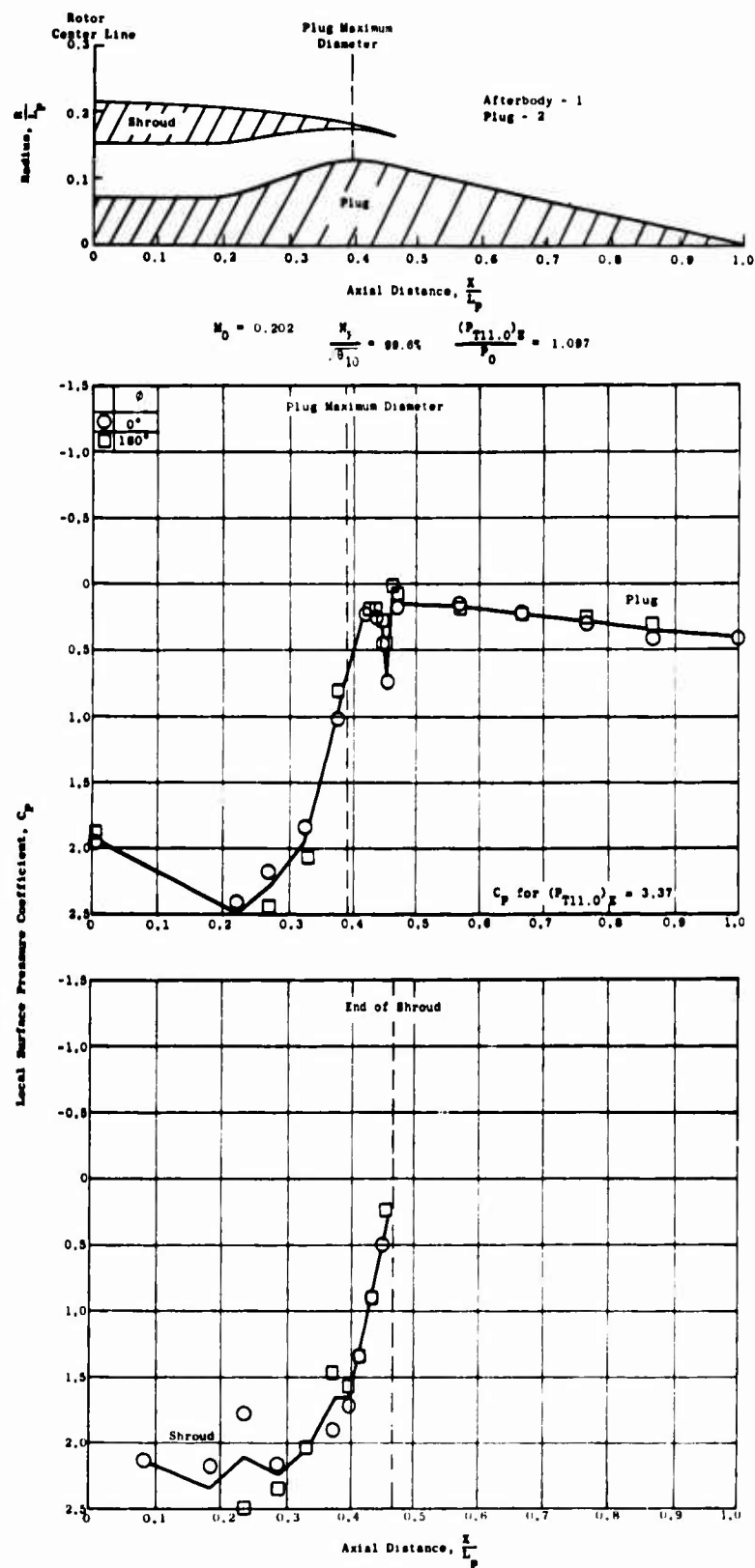


Figure 330. Nozzle Pressure Distribution - Model 7, $M_0 = 0.202$,
 $N_F = 99.6\%$,
 $\sqrt{\theta_{10}}$

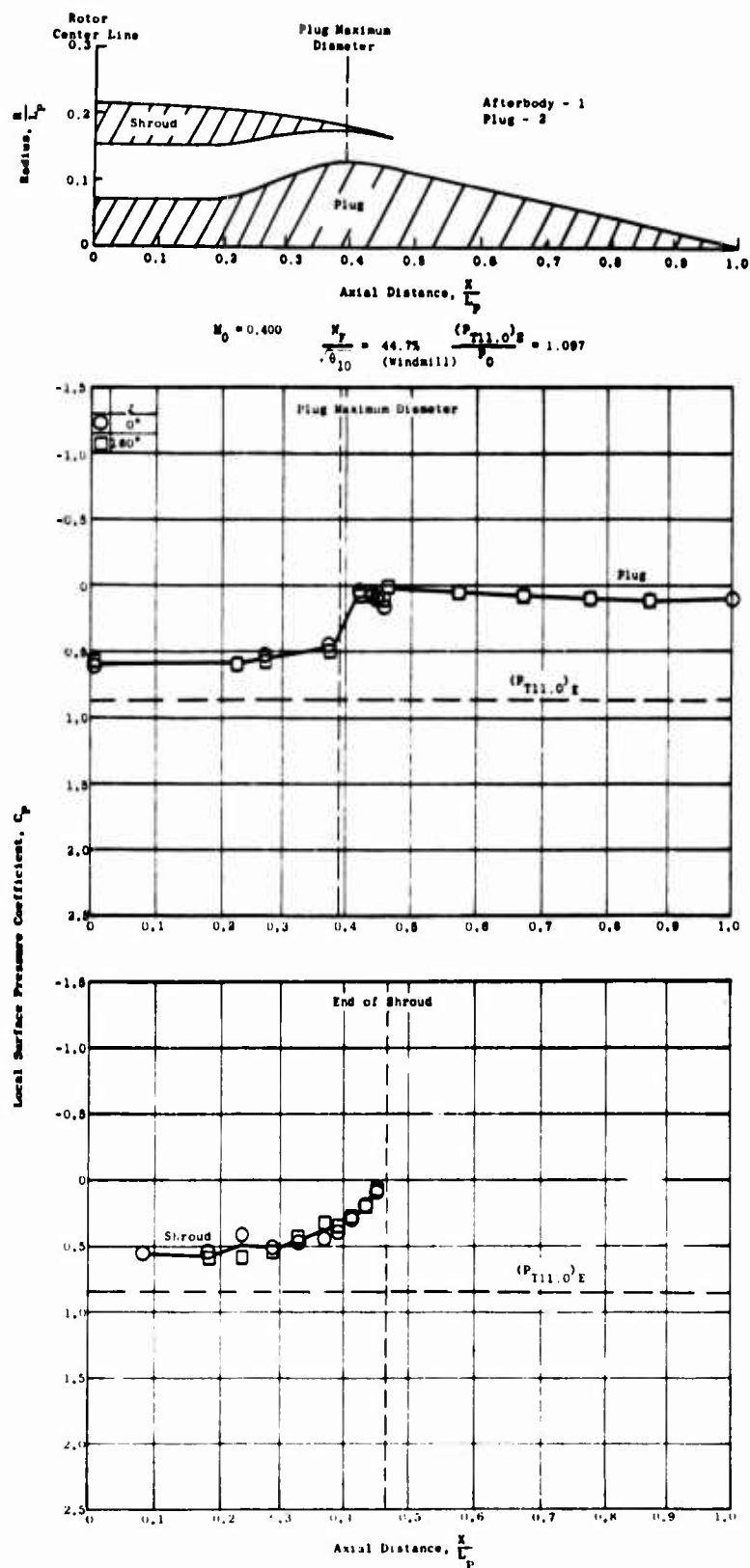


Figure 331. Nozzle Pressure Distribution - Model 7, $M_0 = 0.400$,
 $N_F = 44.7\%$ (Windmill).
 $\frac{(P_{T11.0})/E}{\sqrt{\theta_{10}}}$

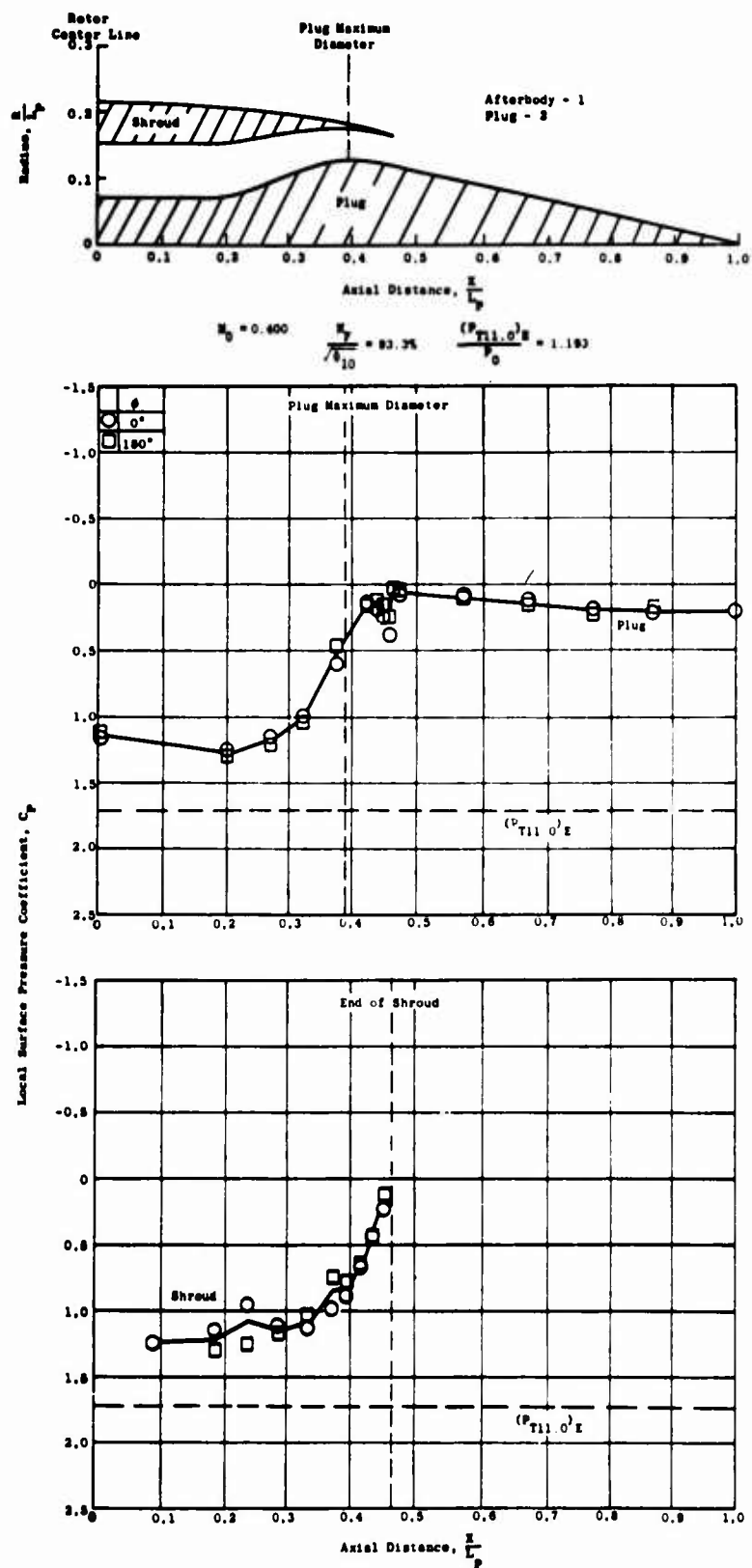


Figure 332. Nozzle Pressure Distribution - Model 7, $M_0 = 0.400$,
 $N_F = 93.3\%$.
 $\frac{N_F}{\sqrt{\theta_{10}}}$

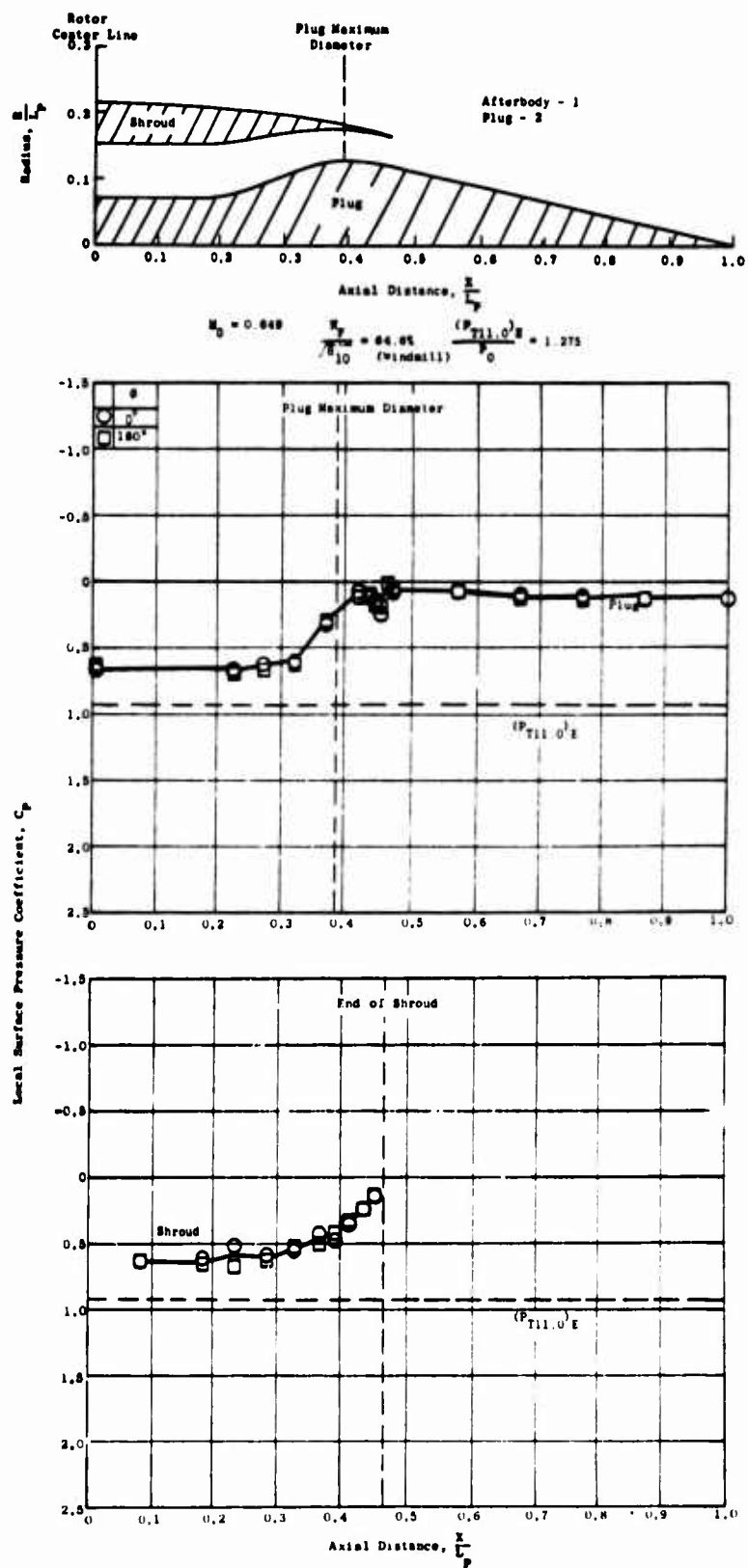
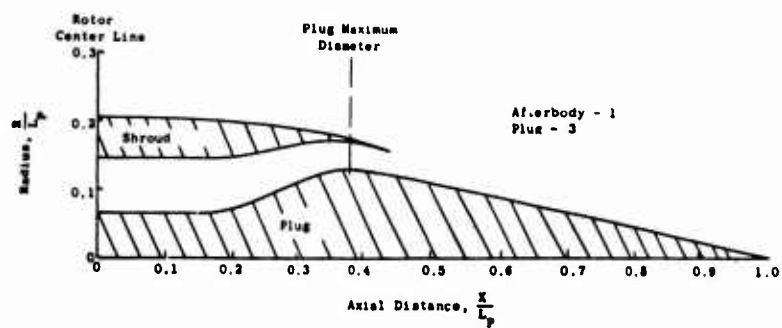


Figure 333. Nozzle Pressure Distribution - Model 7, $M_0 = 0.649$,
 $N_F = 64.6\%$ (Windmill).
 $\sqrt{\theta_{10}}$



$$M_0 = 0.301 \quad \frac{N_F}{\sqrt{\theta_{10}}} = 29.3\% \text{ (Windmill)} \quad \frac{(P_{T11.0})E}{\rho} = 1.097$$

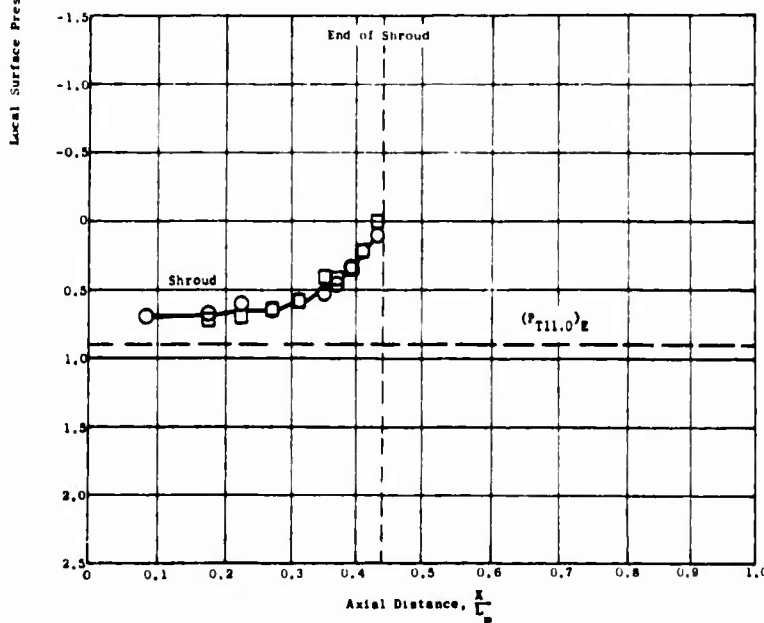
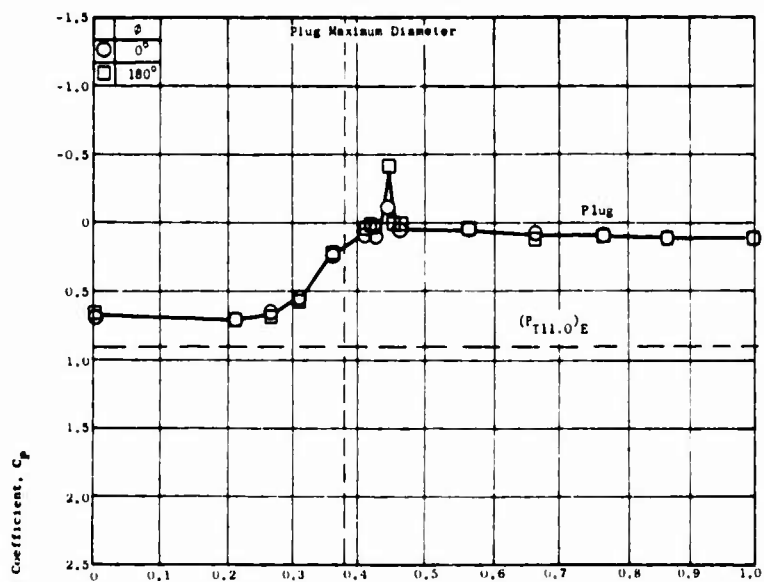


Figure 334. Nozzle Pressure Distribution - Model 8, $M_0 = 0.301$,
 $N_F = 29.3\%$ (Windmill).
 $\sqrt{\theta_{10}}$

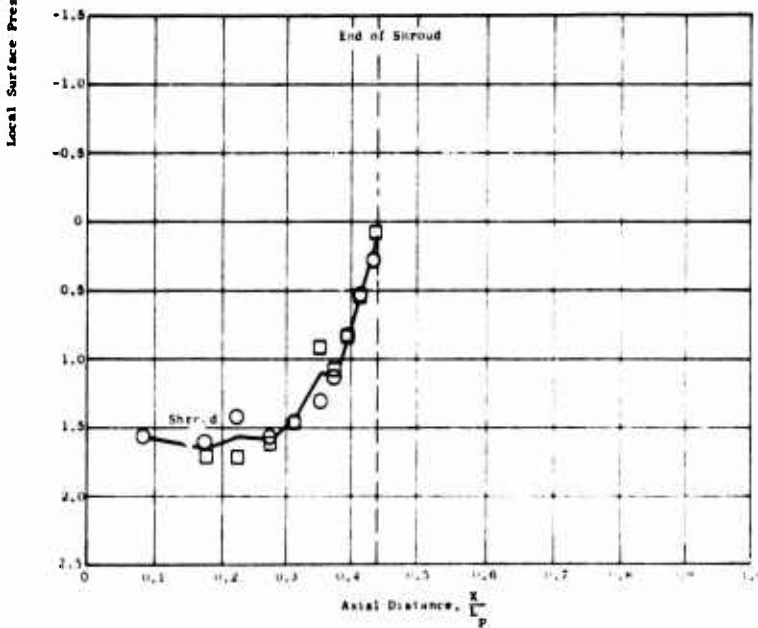
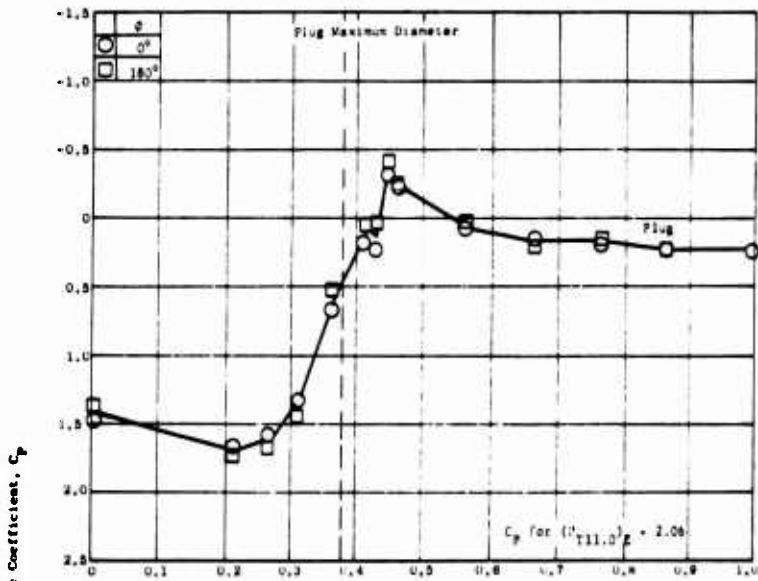
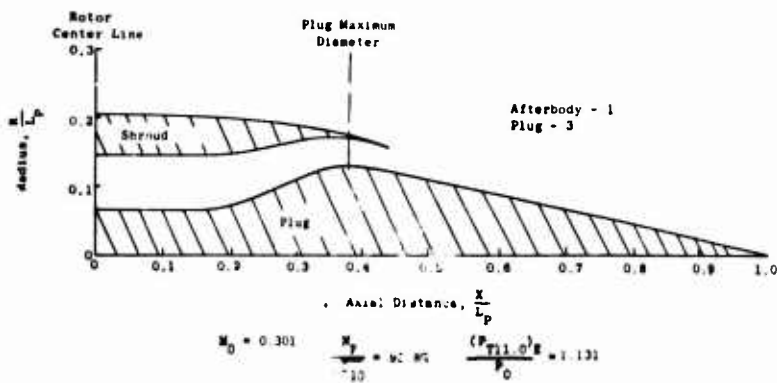


Figure 335. Nozzle Pressure Distribution - Model 8, $M_0 = 0.301$,
 $N_F = 95.8\%$,
 $\sqrt{\theta_{10}}$

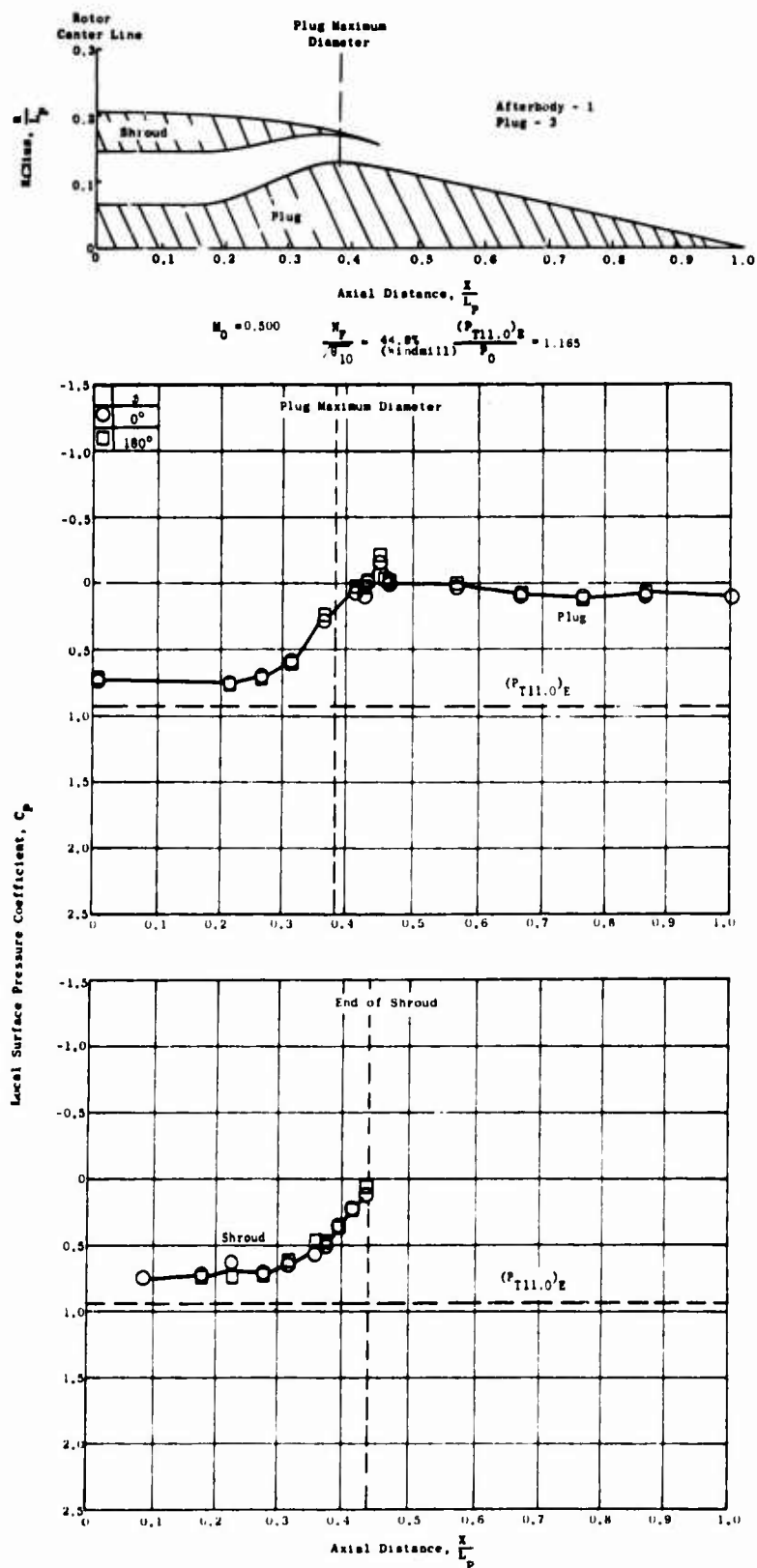


Figure 336. Nozzle Pressure Distribution - Model 8, $M_0 = 0.500$,
 $N_F = 44.8\%$ (Windmill).

$\sqrt{\theta_{10}}$

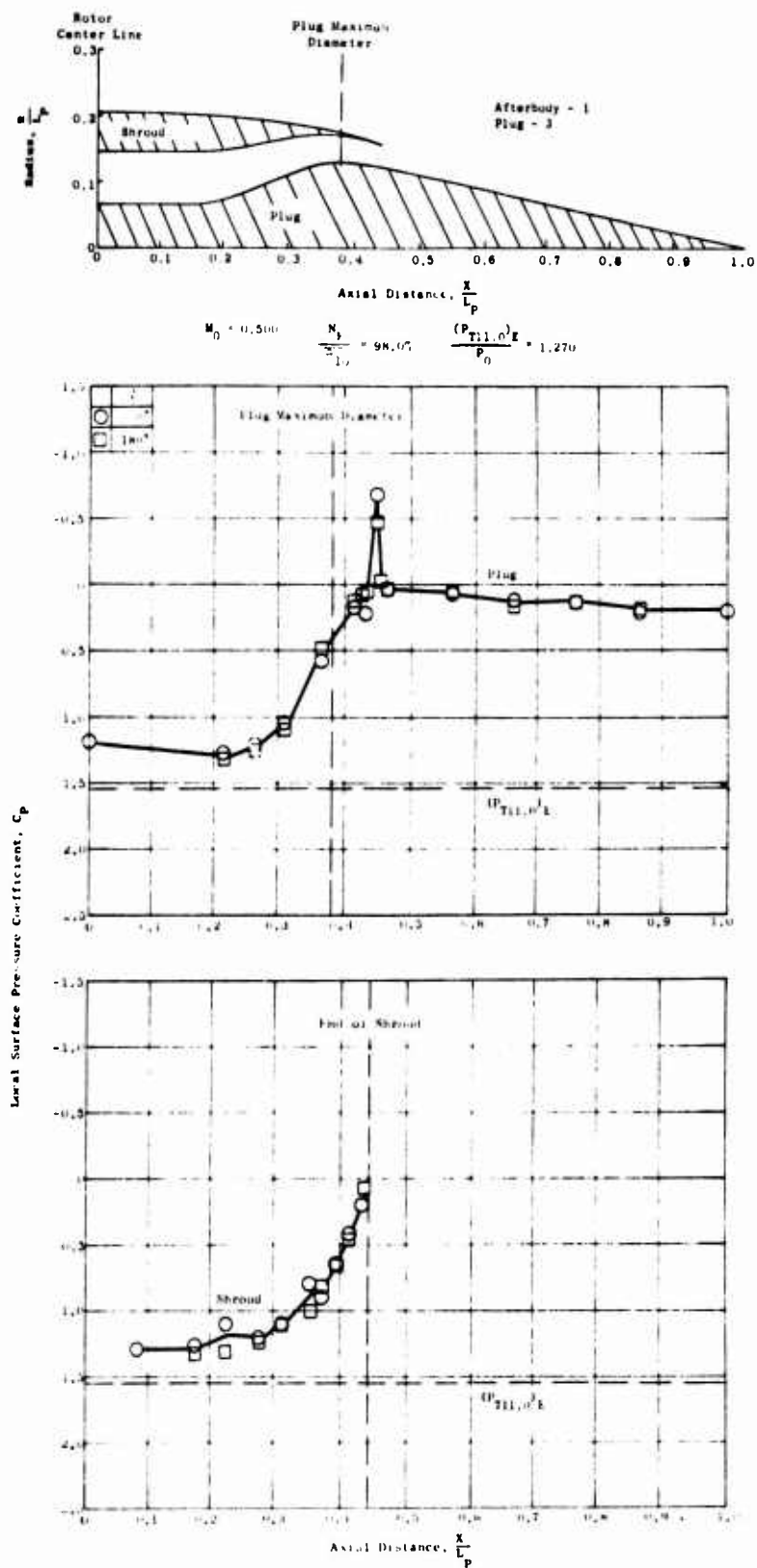
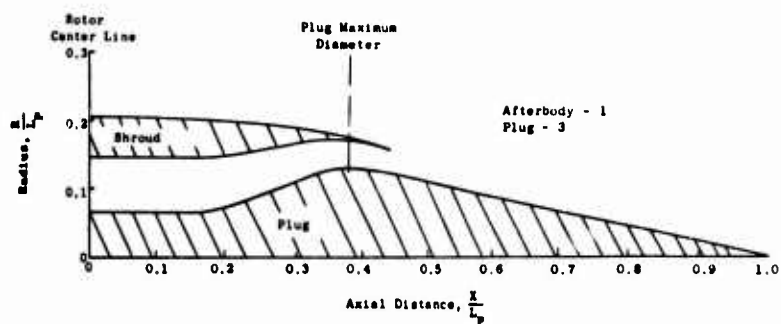


Figure 337. Nozzle Pressure Distribution - Model 8, $M_0 = 0.500$,
 $N_F = 98.0\%$.

$\sqrt{\theta}_{10}$



$$M_0 = 0.699 \quad \frac{N_F}{N_{F10}} = 60.0\% \quad \frac{(P_{T11.0})_E}{P_0} = 1.346$$

(Windmill)

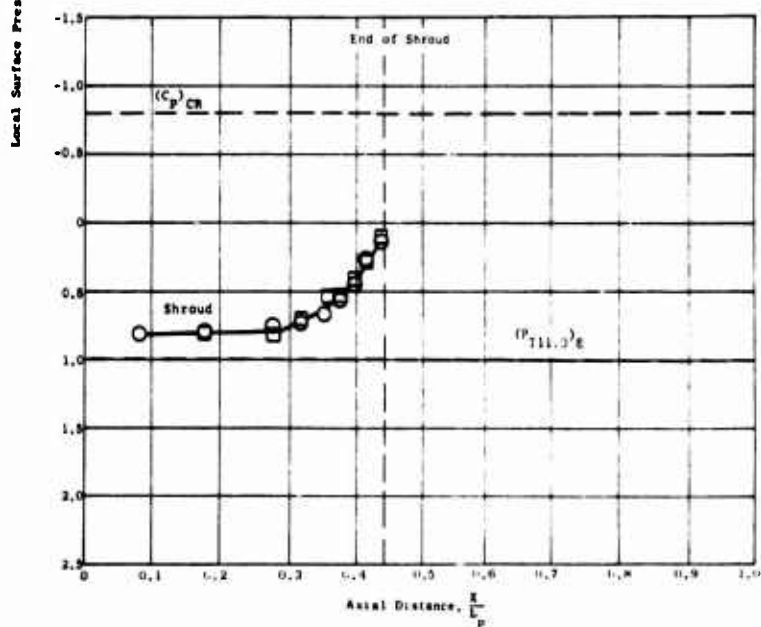
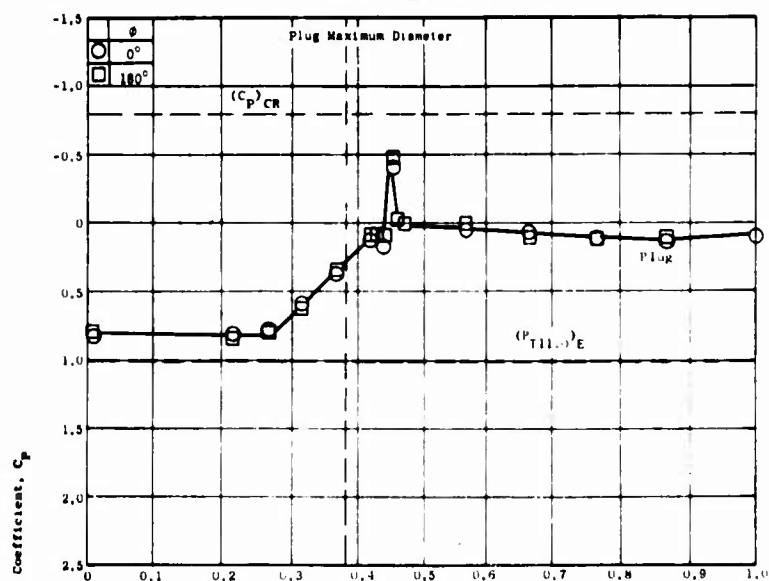


Figure 338. Nozzle Pressure Distribution - Model 8, $M_0 = 0.699$, $N_F = 56.0\%$ (Windmill).

$$\sqrt{\theta_{10}}$$

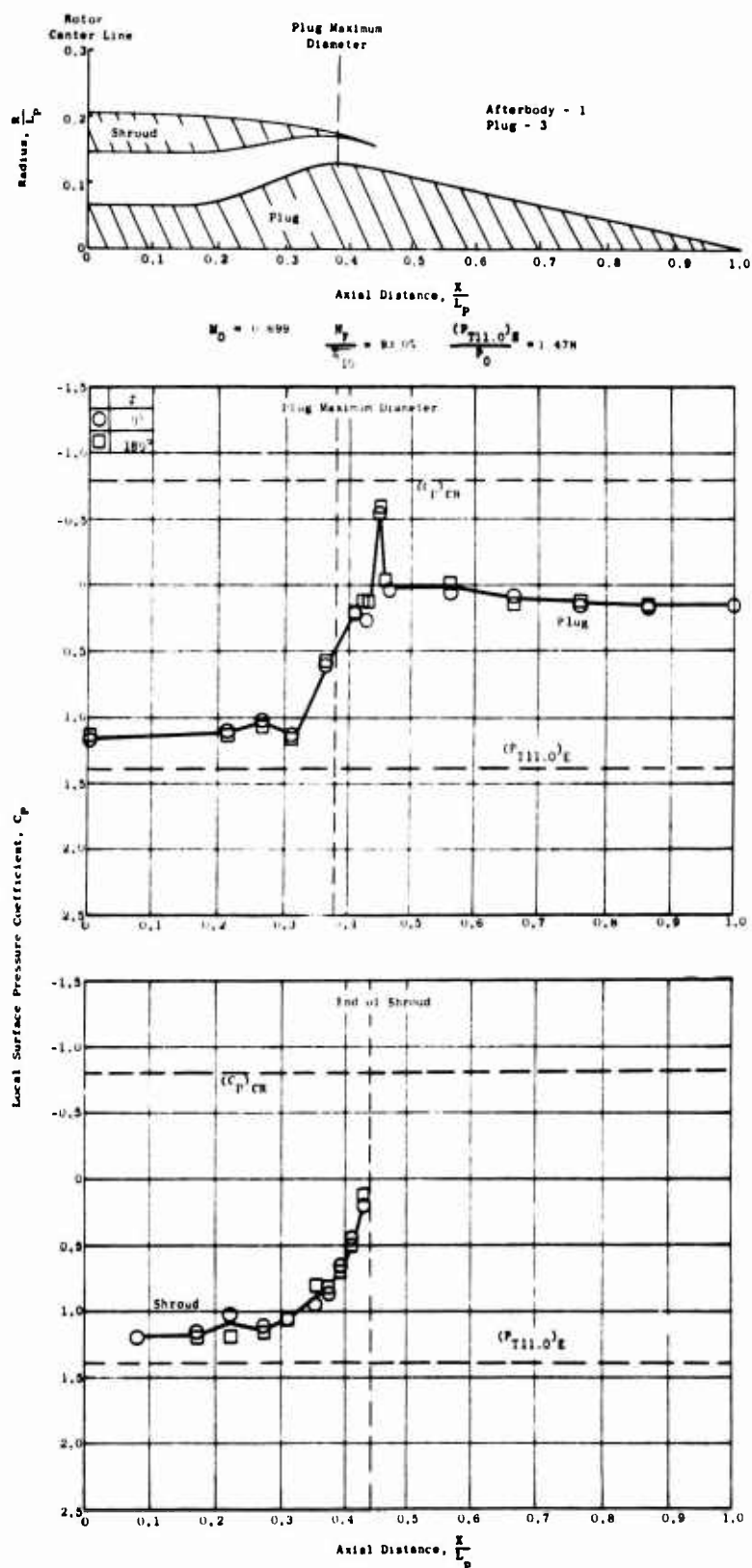


Figure 339. Nozzle Pressure Distribution - Model 8, $M_0 = 0.699$,
 $N_F = 93.0\%$.
 $\sqrt{\theta_{10}}$

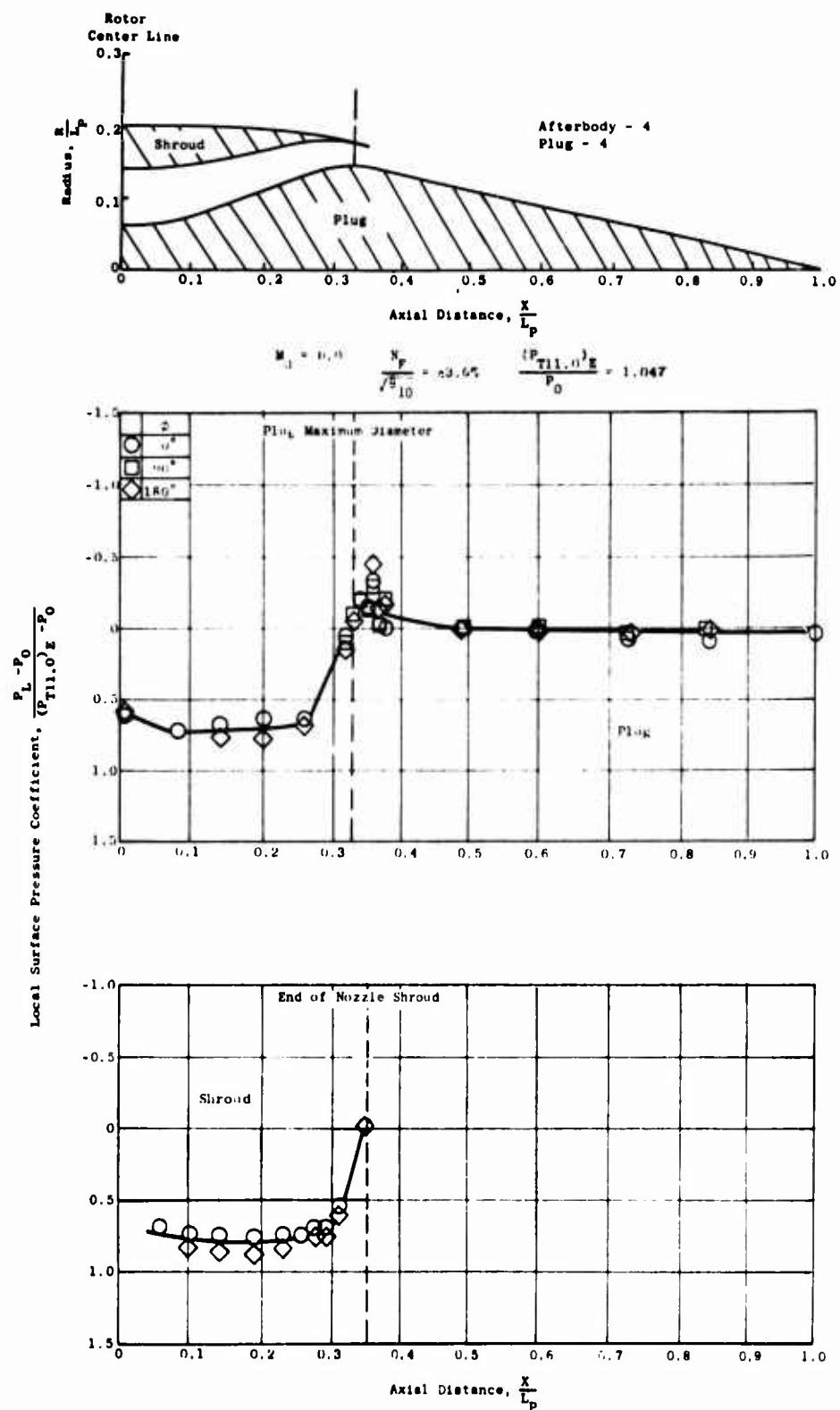


Figure 340. Nozzle Pressure Distribution - Model 1, $M_0 = 0.0$,
 $N_F = 83.6\%$,
 $\frac{\sqrt{\theta}}{10}$

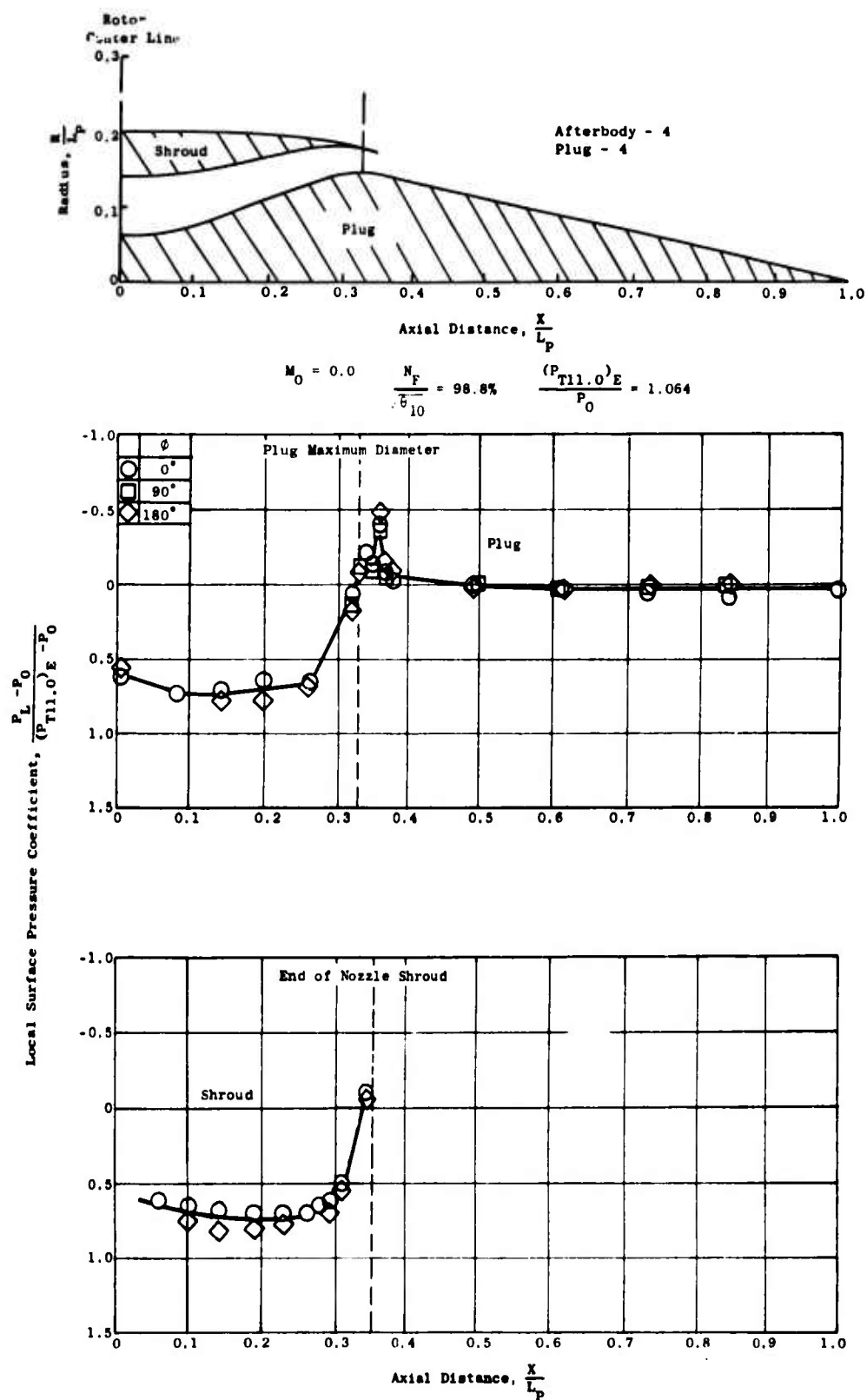


Figure 341. Nozzle Pressure Distribution - Model 2, $M_0 = 0.0$,
 $\frac{N_F}{\sqrt{\theta_{10}}} = 98.8\%$.

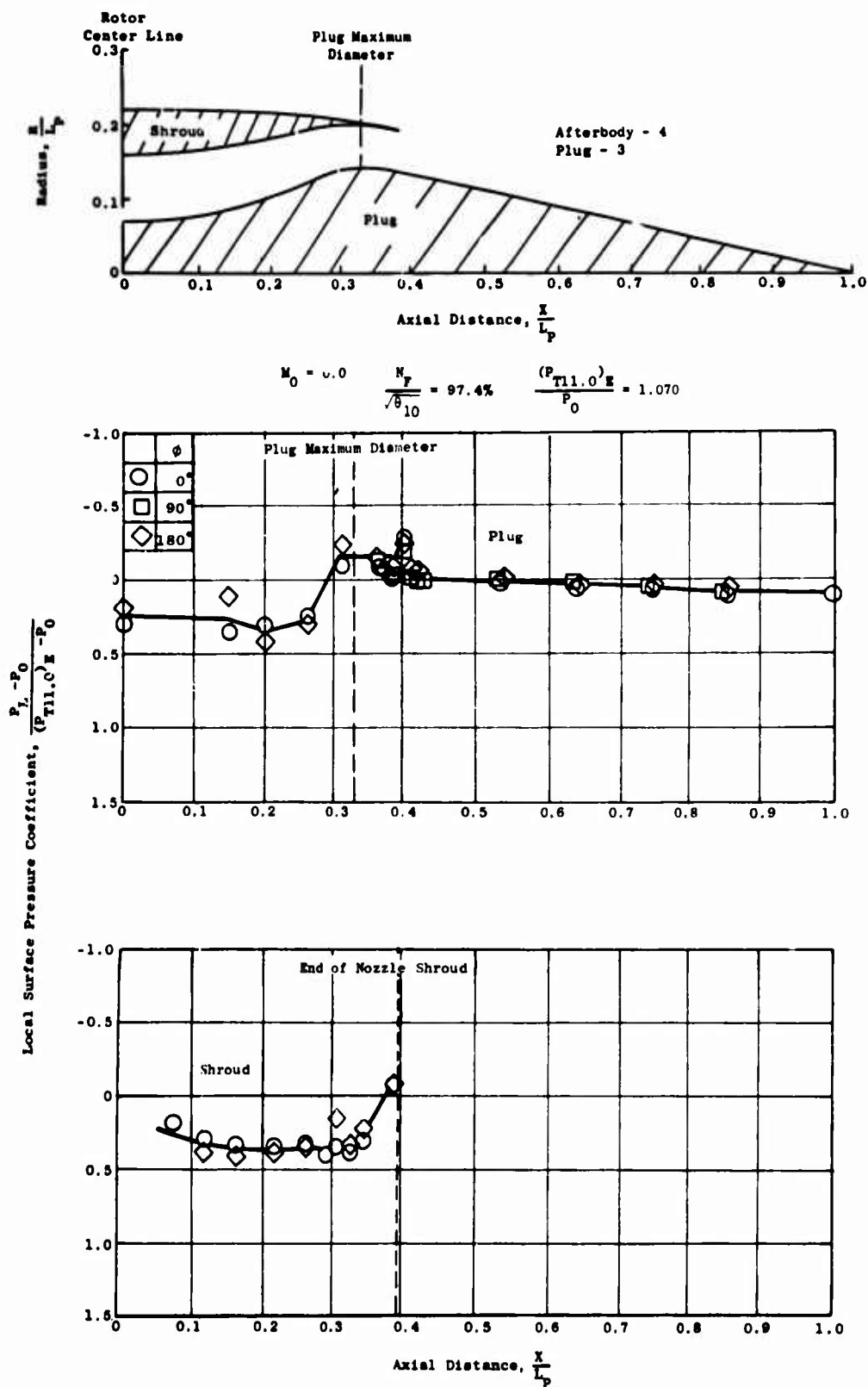


Figure 342. Nozzle Pressure Distribution - Model 3, $M_0 = 0.0$,
 $N_F = 97.4\%$.

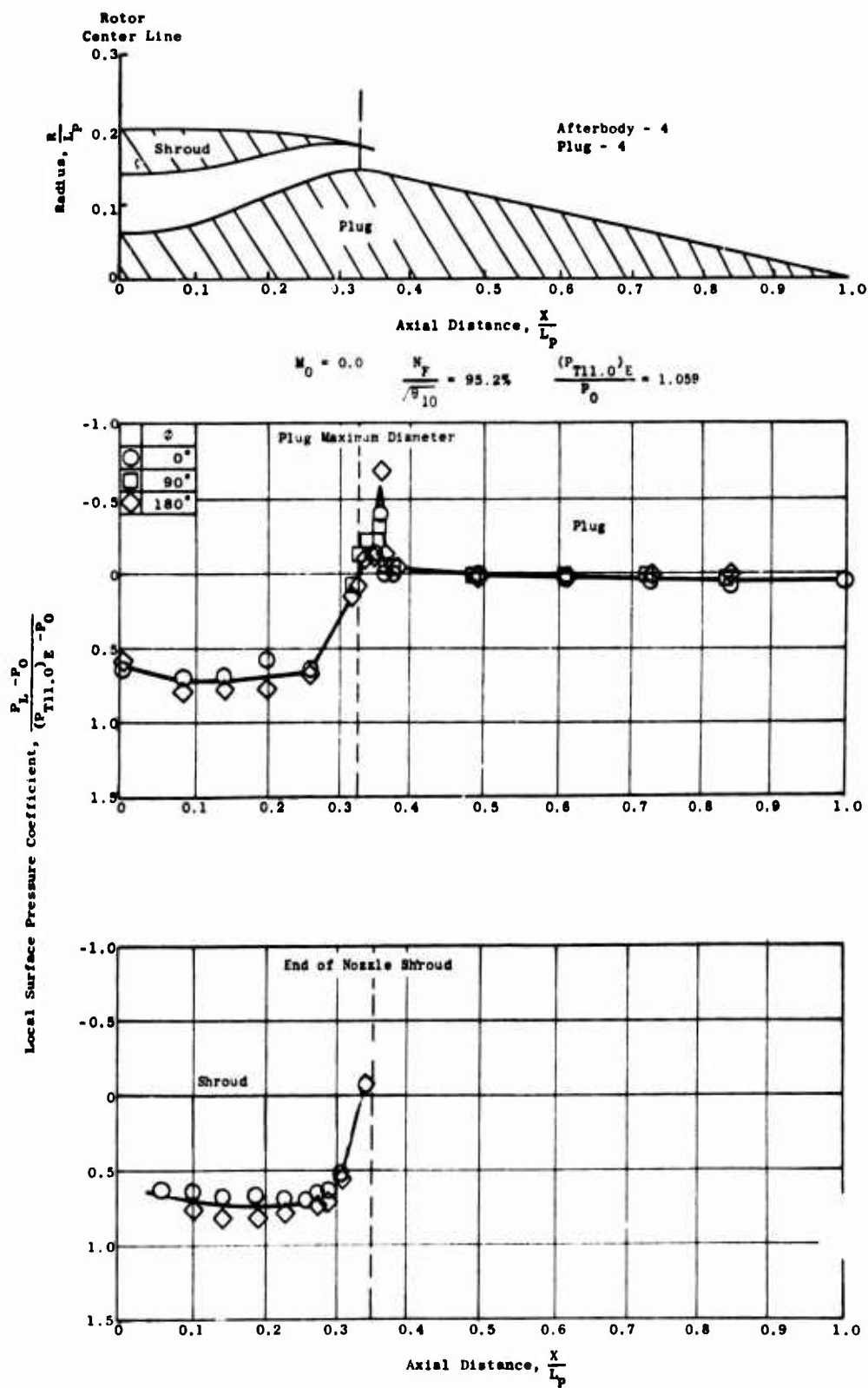


Figure 343. Nozzle Pressure Distribution - Model 4, $M_0 = 0.0$,
 $N_F = 95.2\%$.

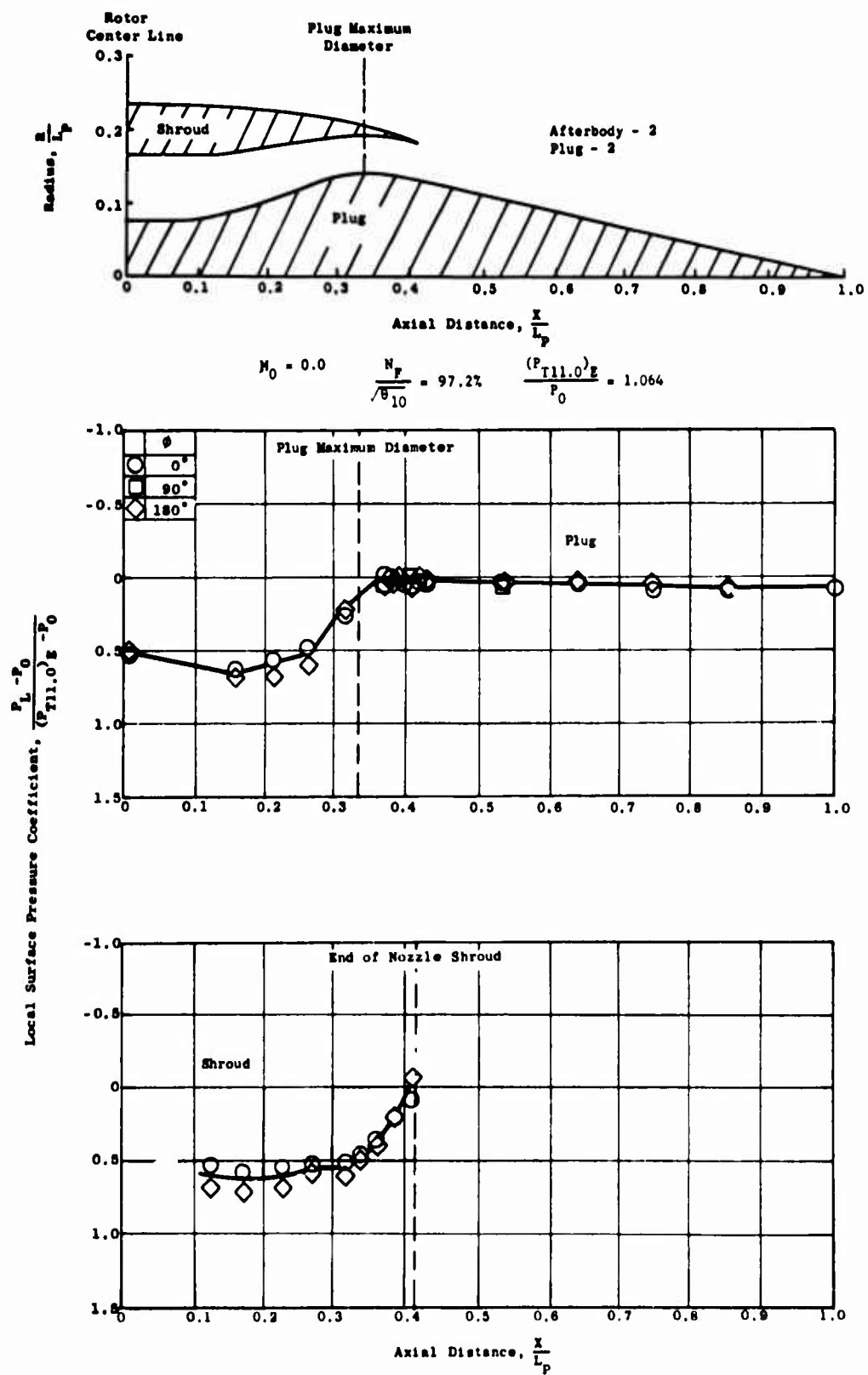


Figure 344. Nozzle Pressure Distribution - Model 5, $M_0 = 0.0$,
 $N_F = 97.2\%$.

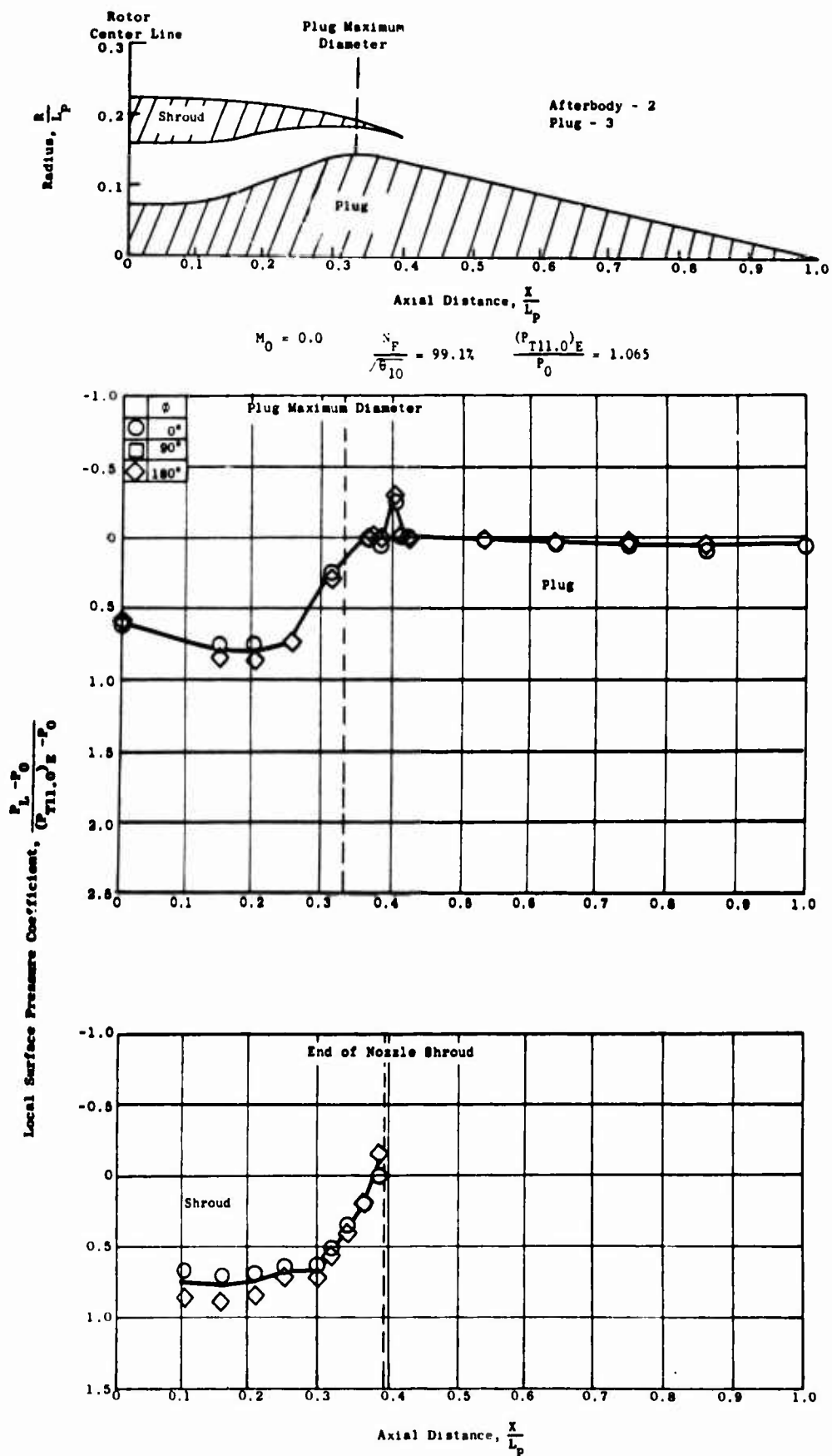


Figure 345. Nozzle Pressure Distribution - Model 6, $M_0 = 0.0$,
 $N_F = 99.1\%$.

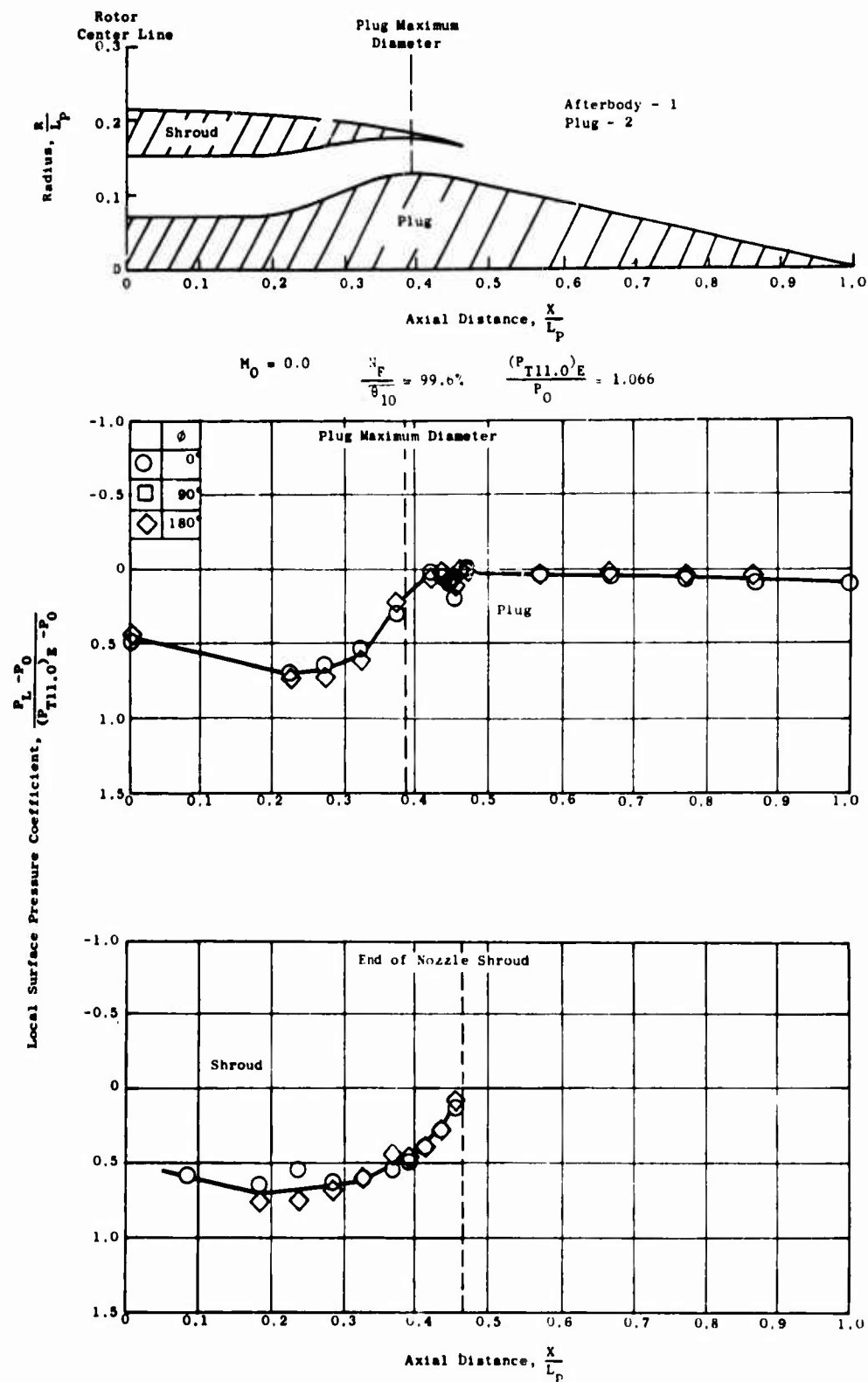
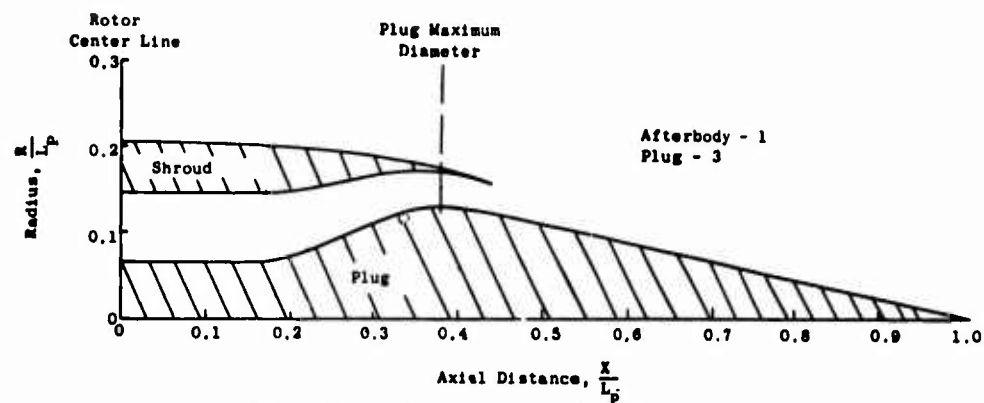


Figure 346. Nozzle Pressure Distribution - Model 7, $M_0 = 0.0$,
 $\frac{N_F}{\theta_{10}} = 99.6\%$.



$$M_0 = 0.0 \quad \frac{N_F}{\sqrt{\theta_{10}}} = 72.7\% \quad \frac{(P_{T11.0})_E}{P_0} = 1.025$$

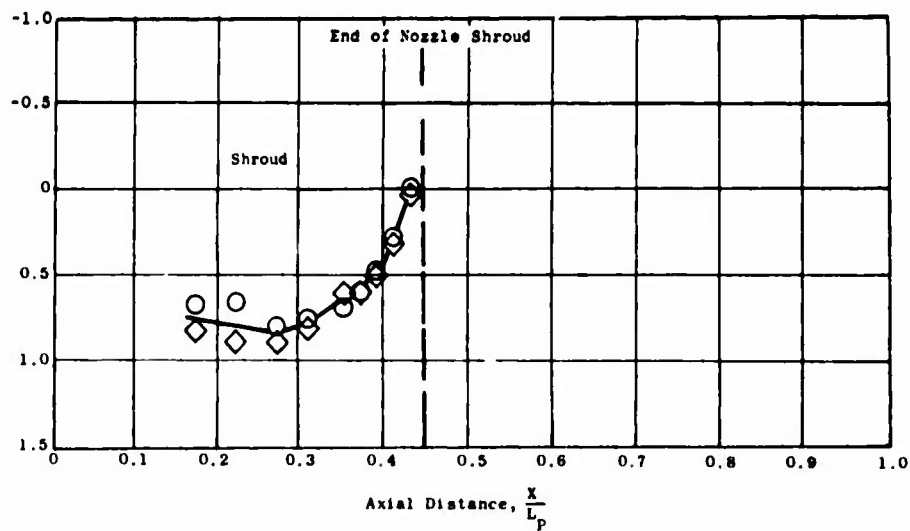
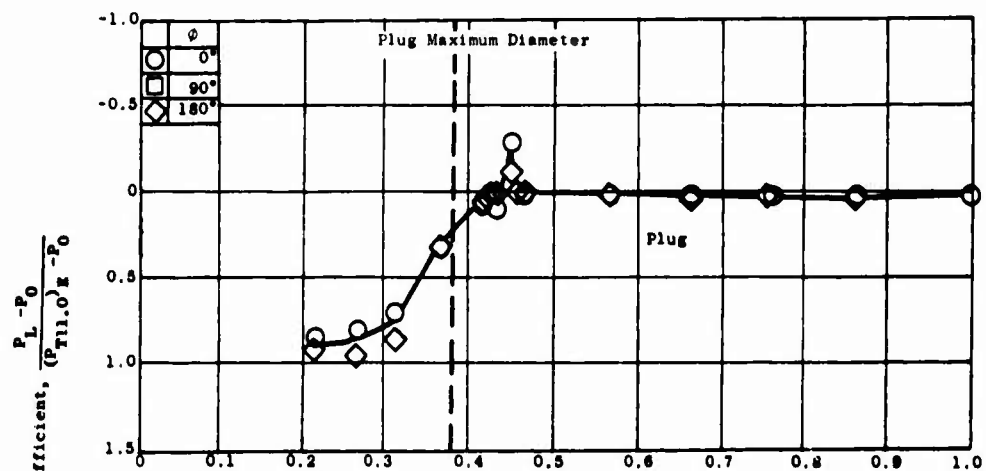


Figure 347. Nozzle Pressure Distribution - Model 8, $M_0 = 0.0$,
 $\frac{N_F}{\sqrt{\theta_{10}}} = 72.7\%$.

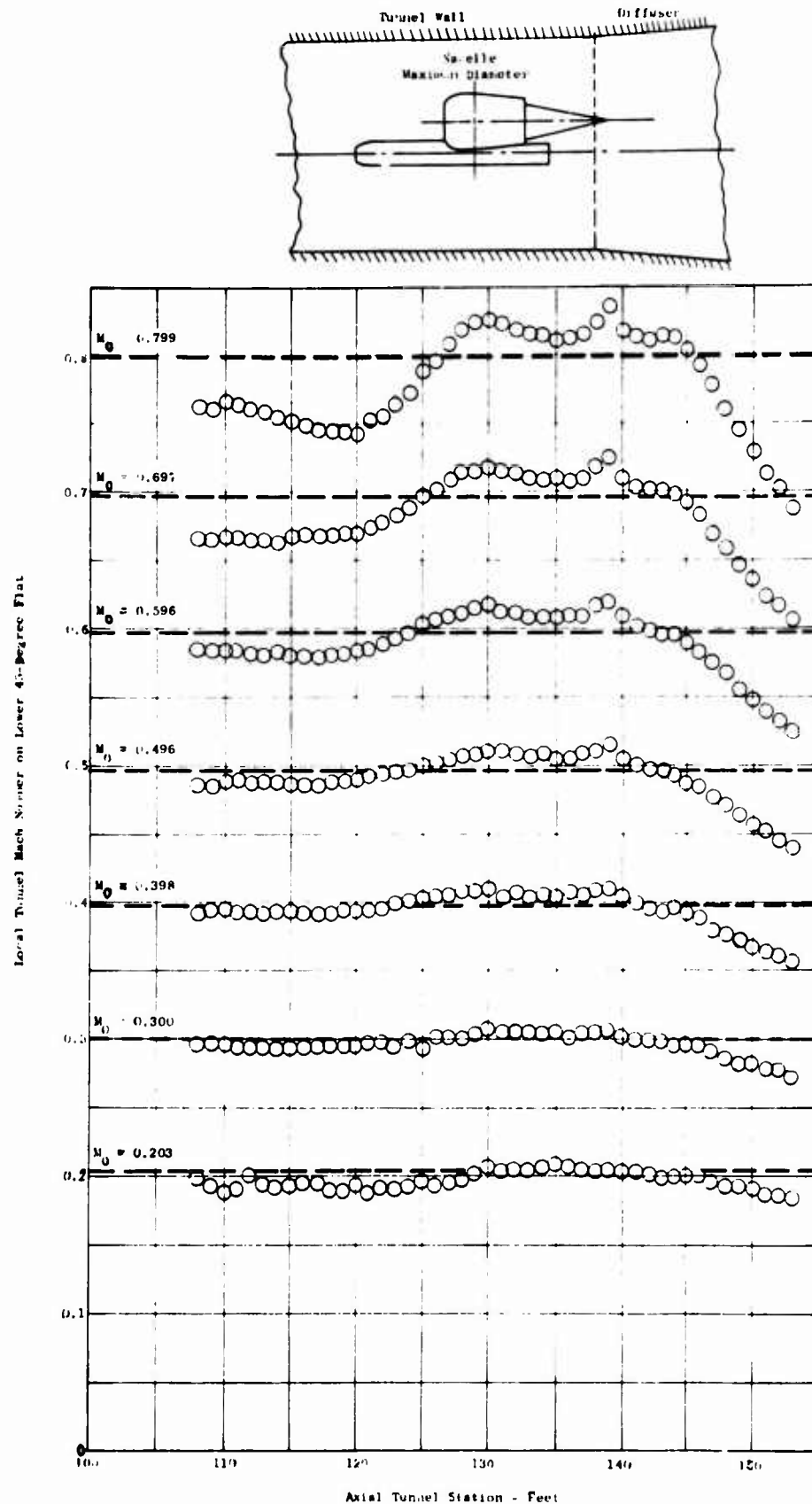


Figure 348. Wind Tunnel Axial Mach Number Distributions.

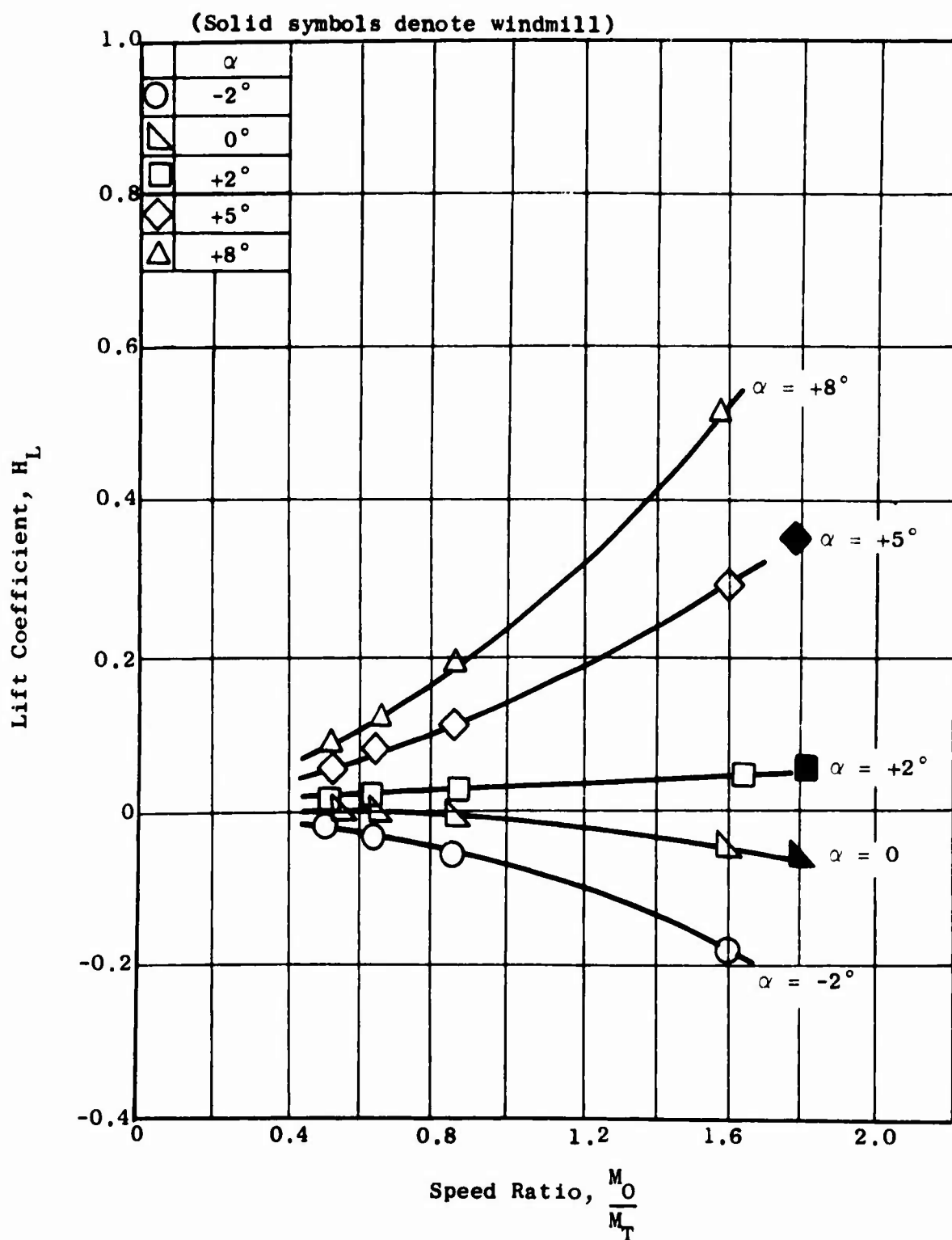


Figure 349. Variation of System Lift with Angle of Attack and Speed, $M_0 = 0.30$ - Model 8.

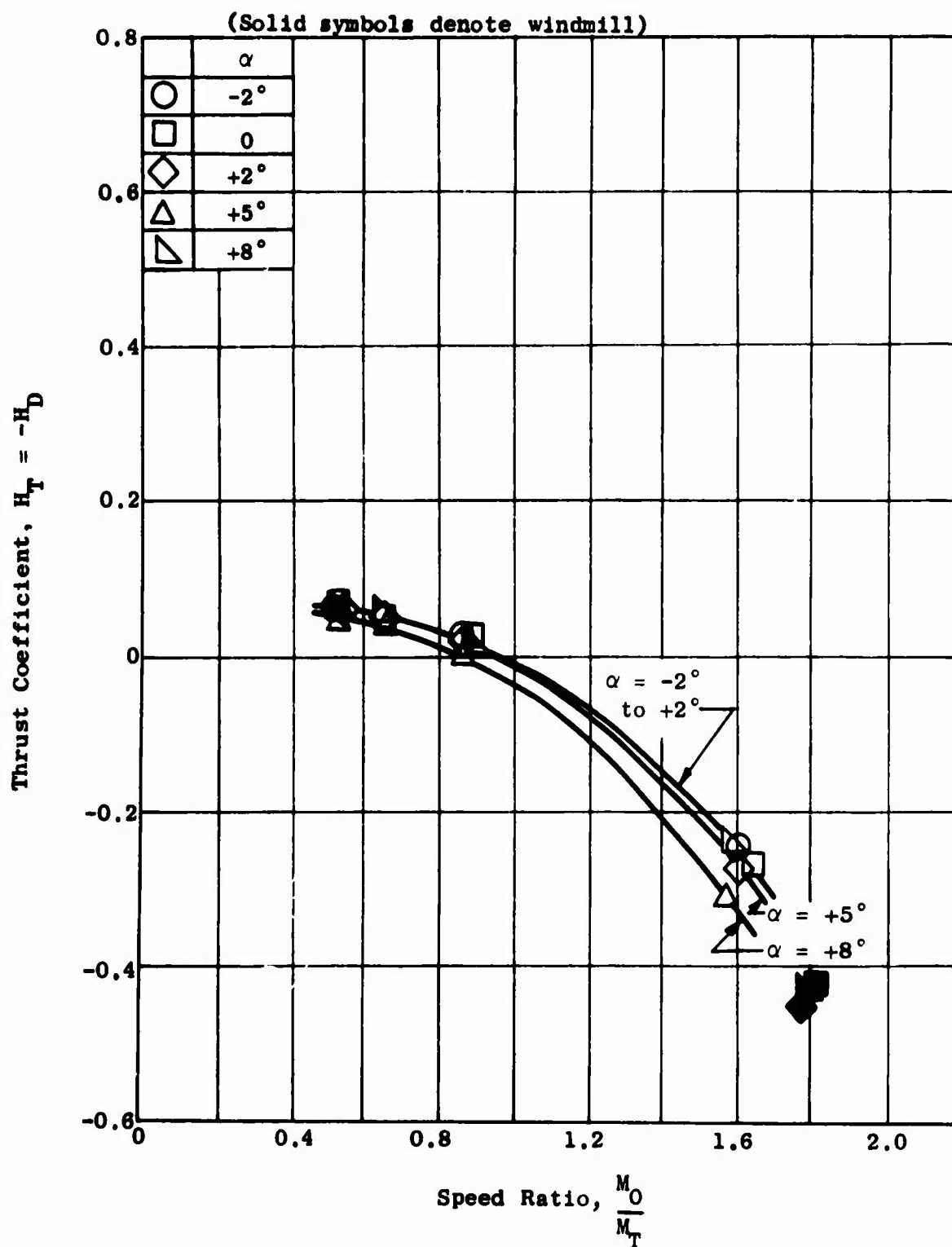


Figure 350. Variation of System Axial Thrust with Angle of Attack and Speed, $M_0 = 0.30$ - Model 8.

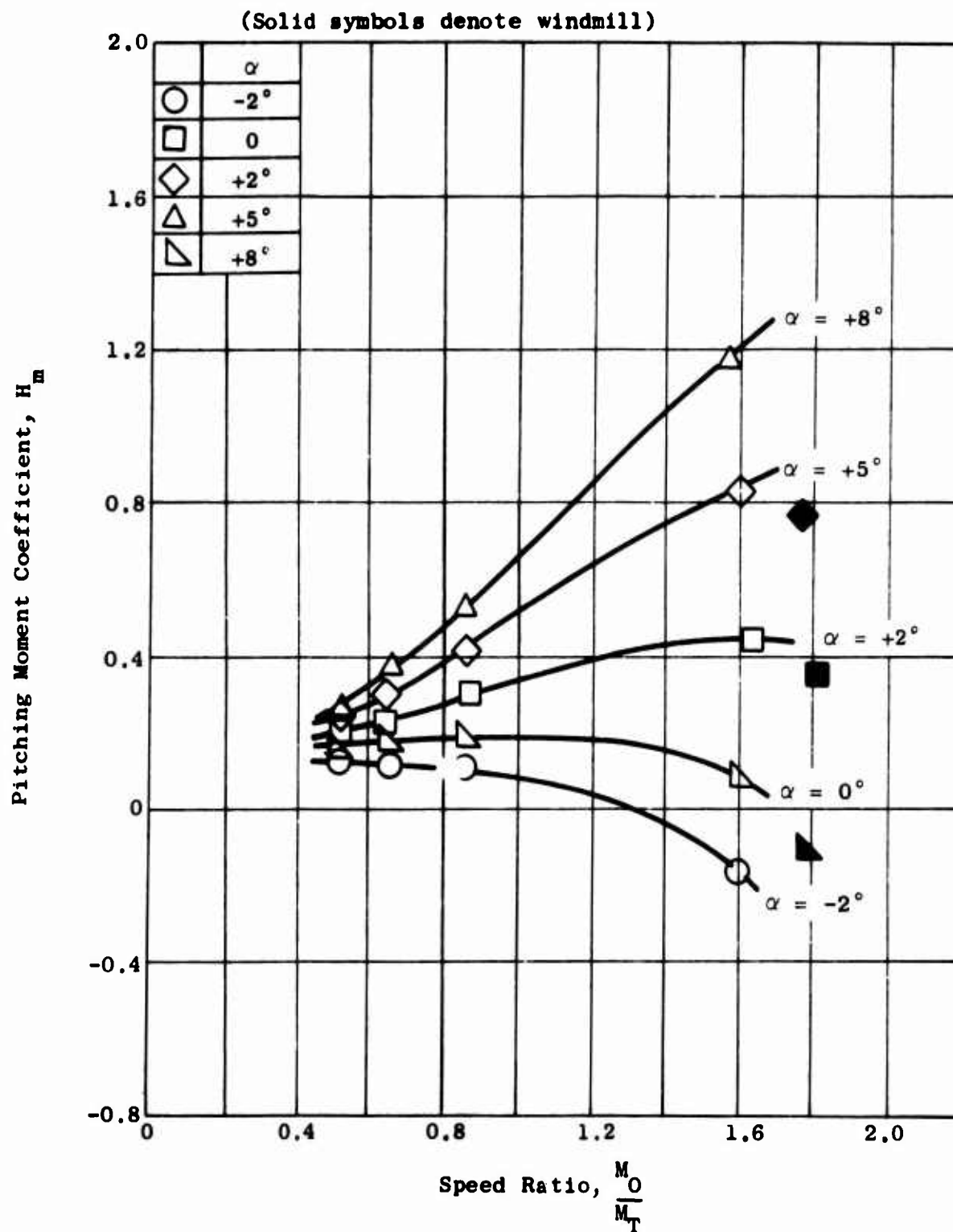


Figure 351. Variation of System Pitching Moment with Angle of Attack and Speed, $M_0 = 0.30$ - Model 8.

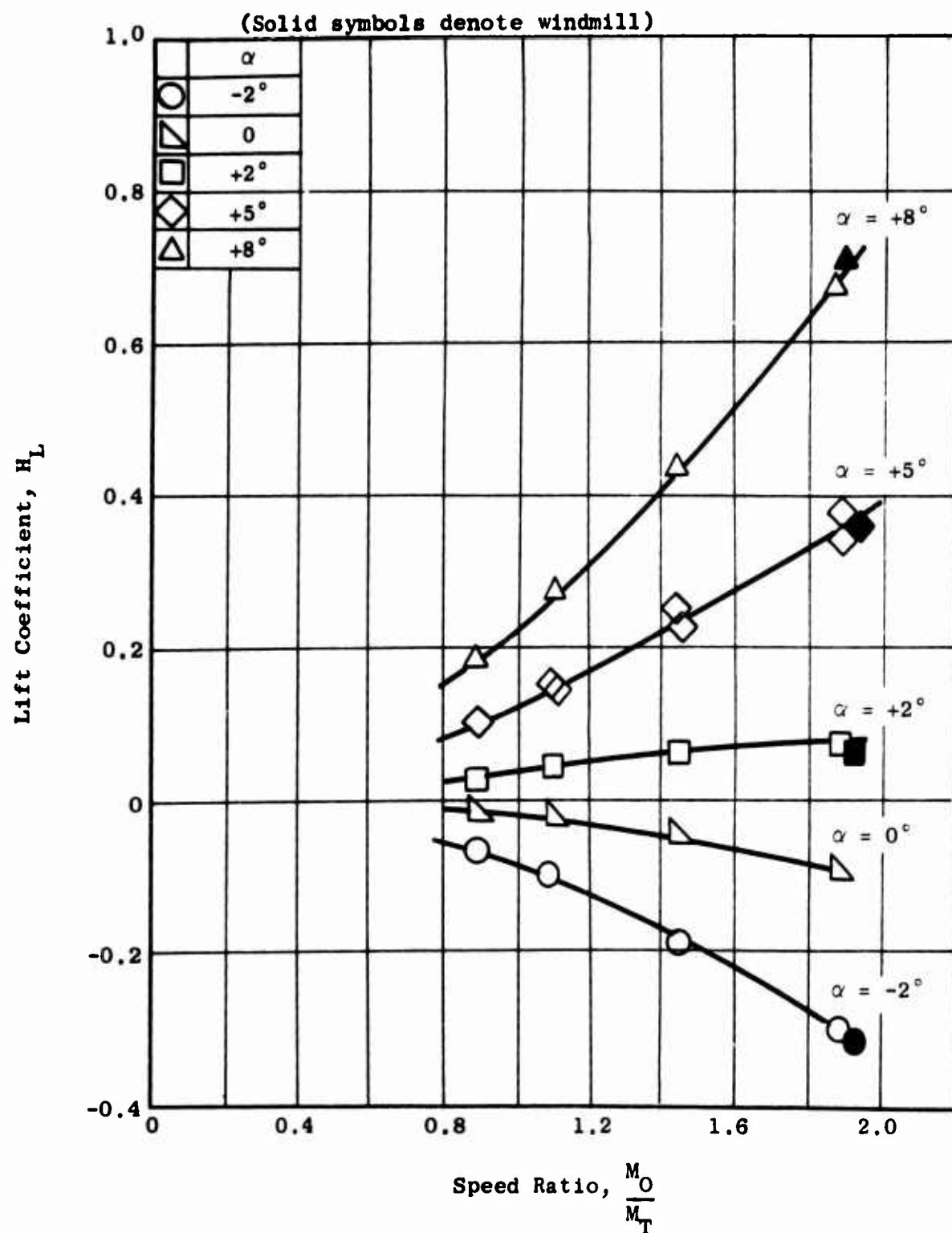


Figure 352. Variation of System Lift with Angle of Attack and Speed, $M_O = 0.50$ - Model 8.

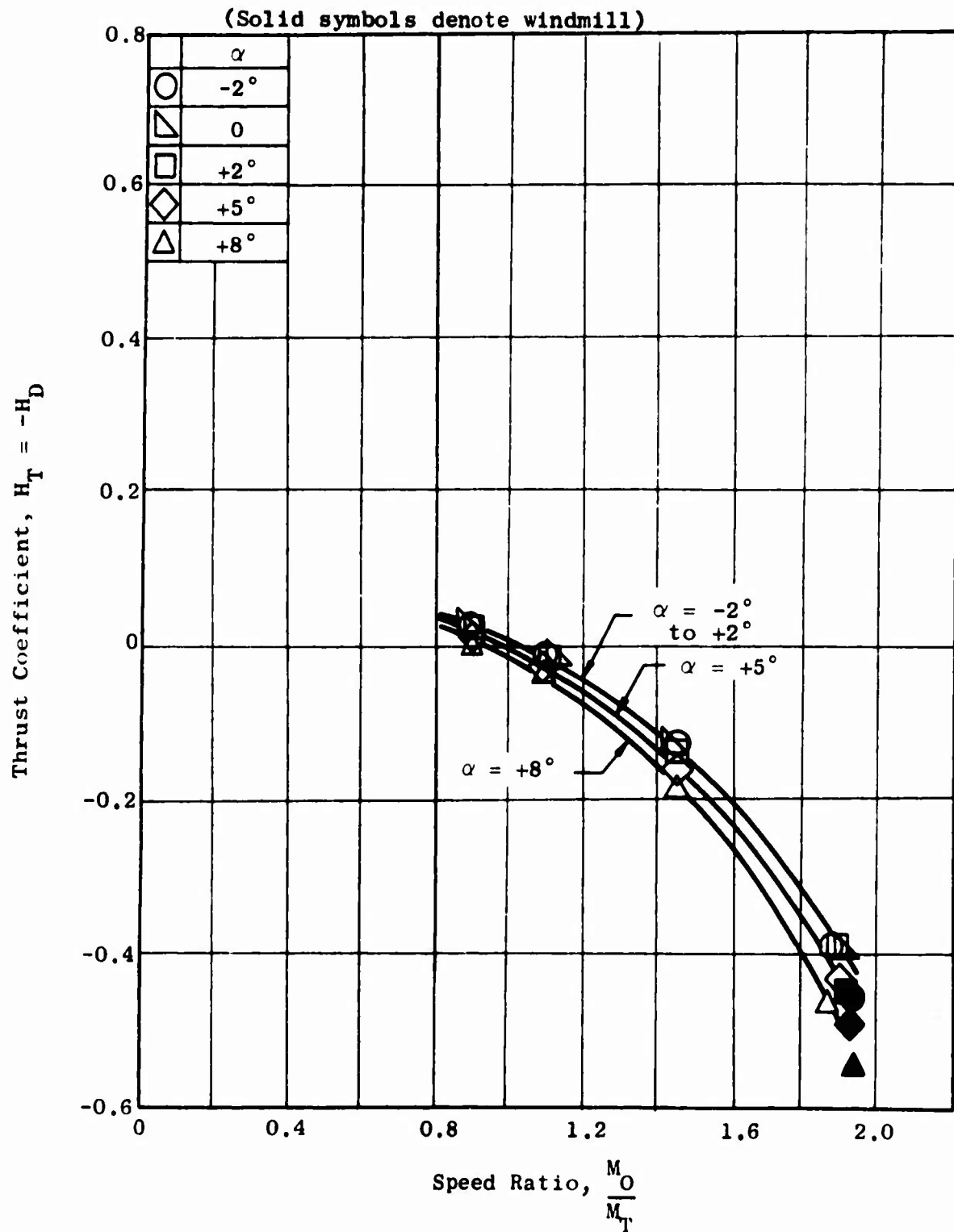


Figure 353. Variation of System Axial Thrust with Angle of Attack and Speed, $M_O = 0.50$ - Model 8.

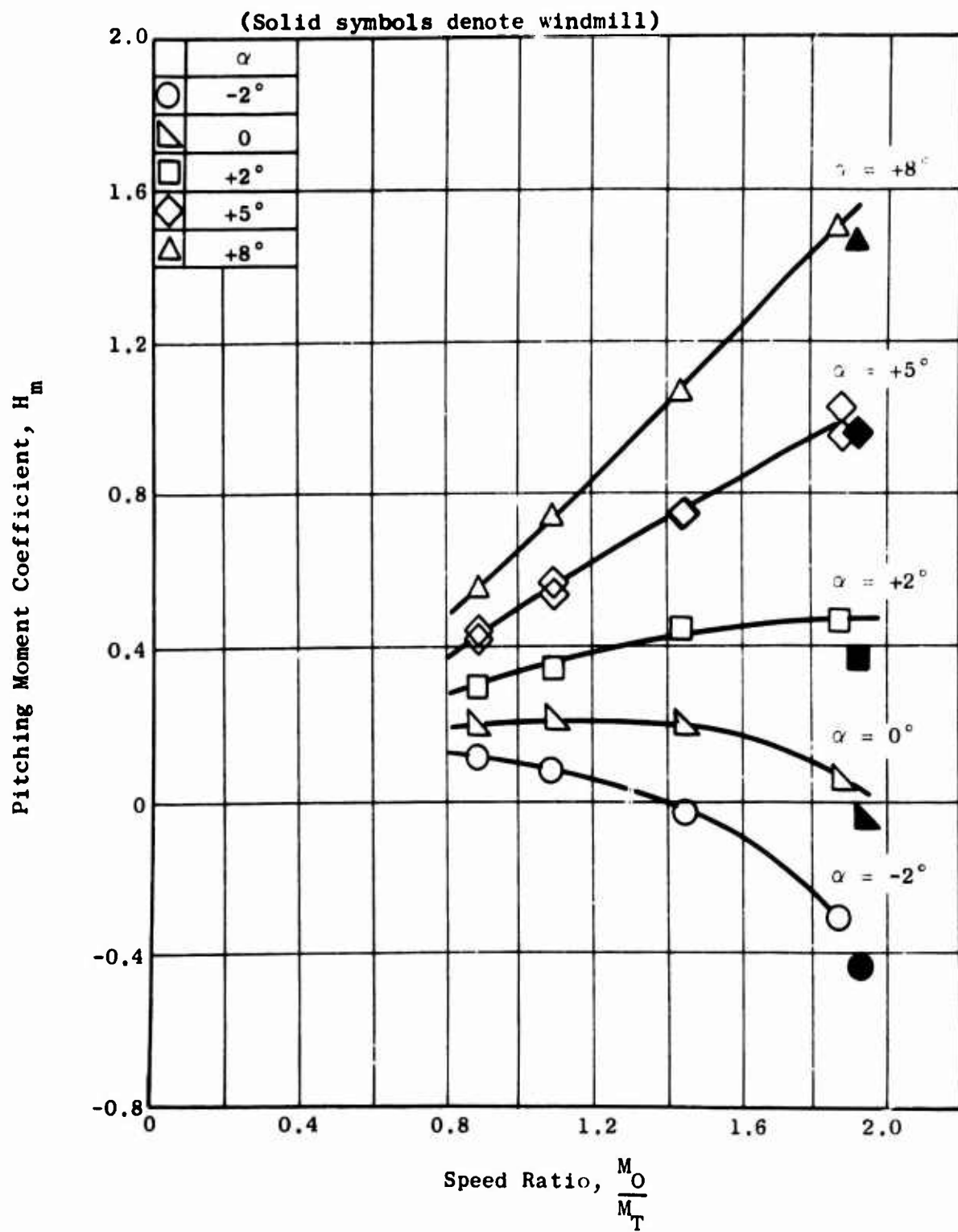


Figure 354. Variation of System Pitching Moment with Angle of Attack and Speed, $M_O = 0.50$ - Model 8.

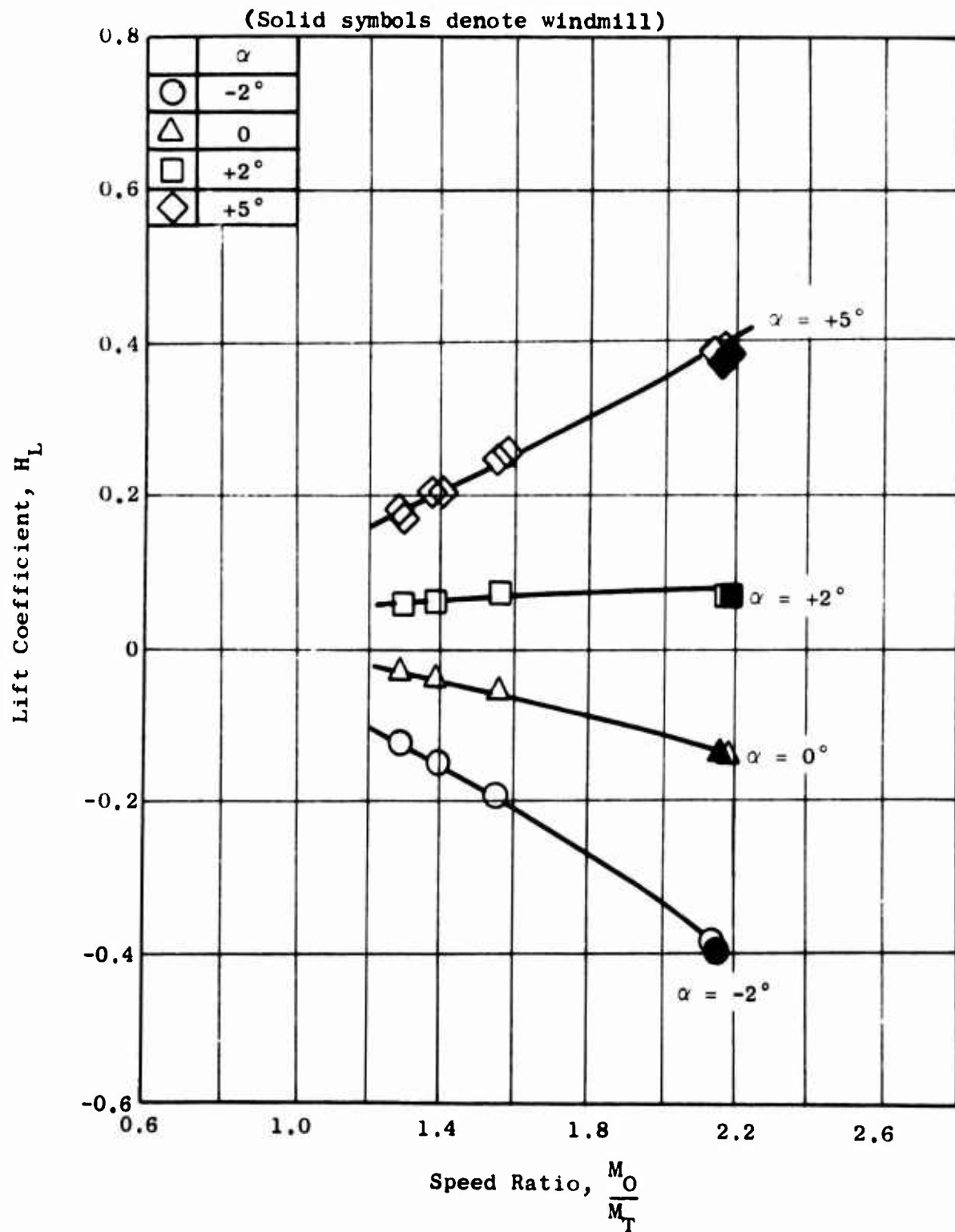


Figure 355. Variation of System Lift with Angle of Attack and Speed, $M_O = 0.70$ - Model 8.

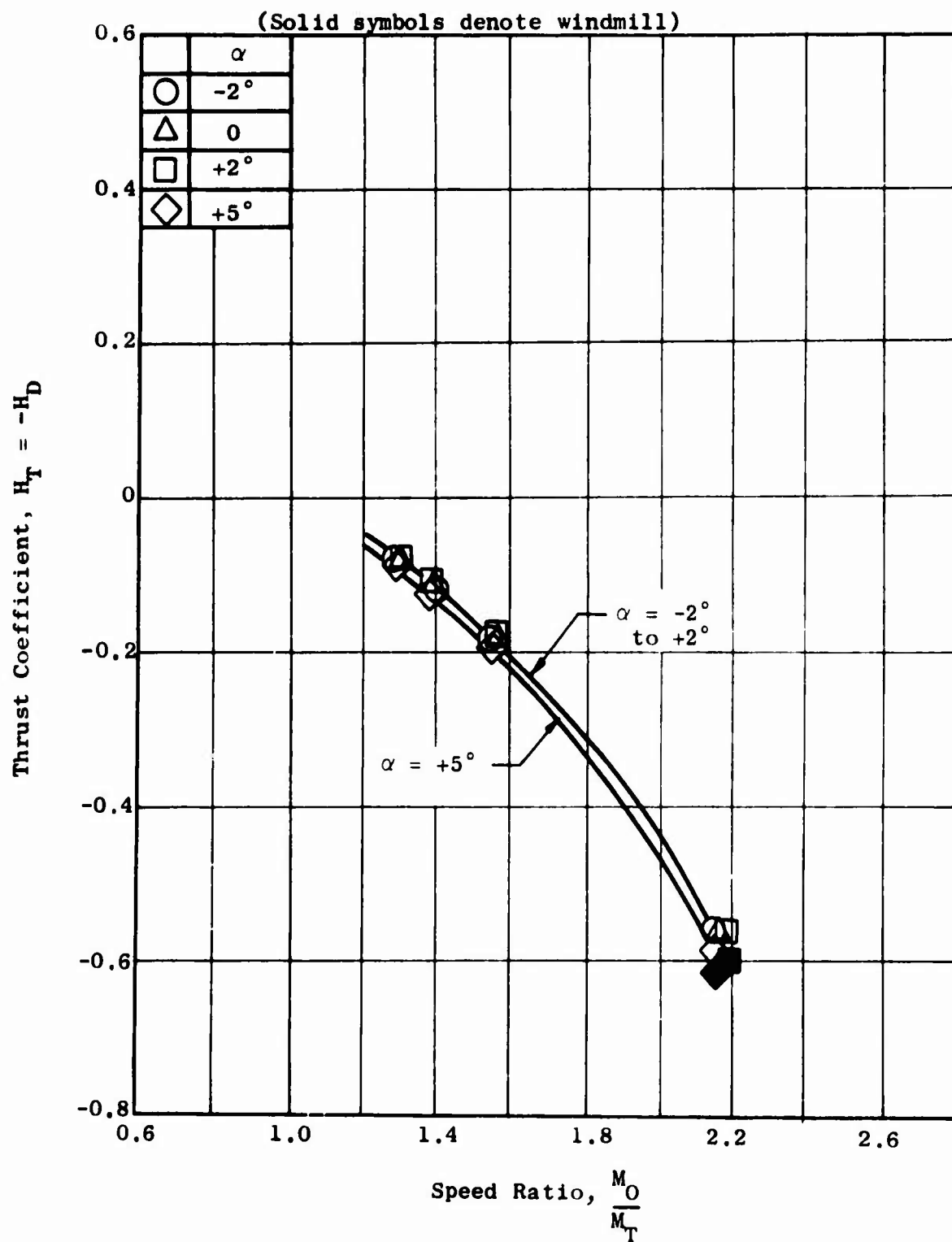


Figure 356. Variation of System Axial Thrust with Angle of Attack and Speed, $M_O = 0.70$ - Model 8.

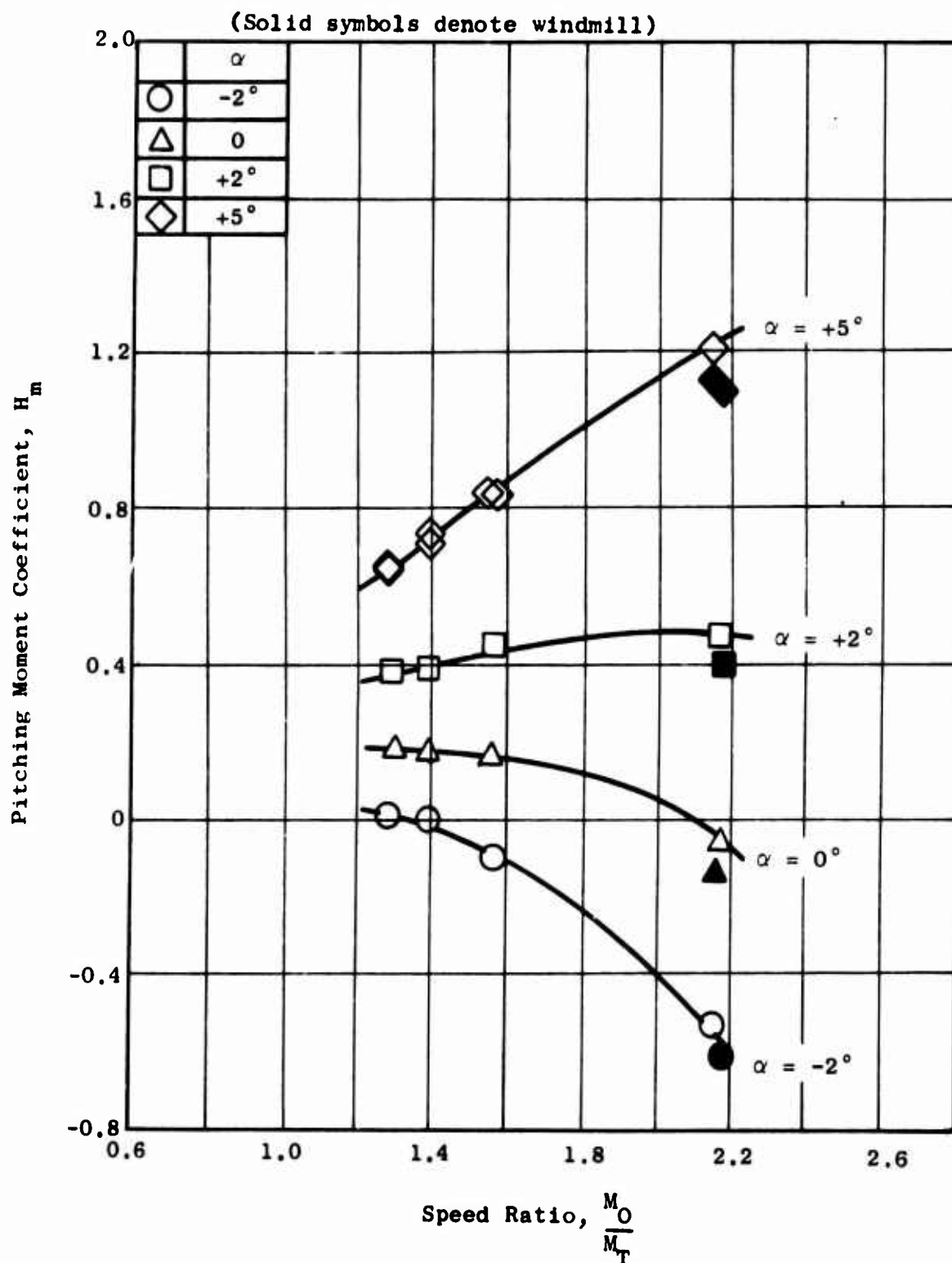


Figure 357. Variation of System Pitching Moment with Angle of Attack and Speed, $M_O = 0.70$ - Model 8.

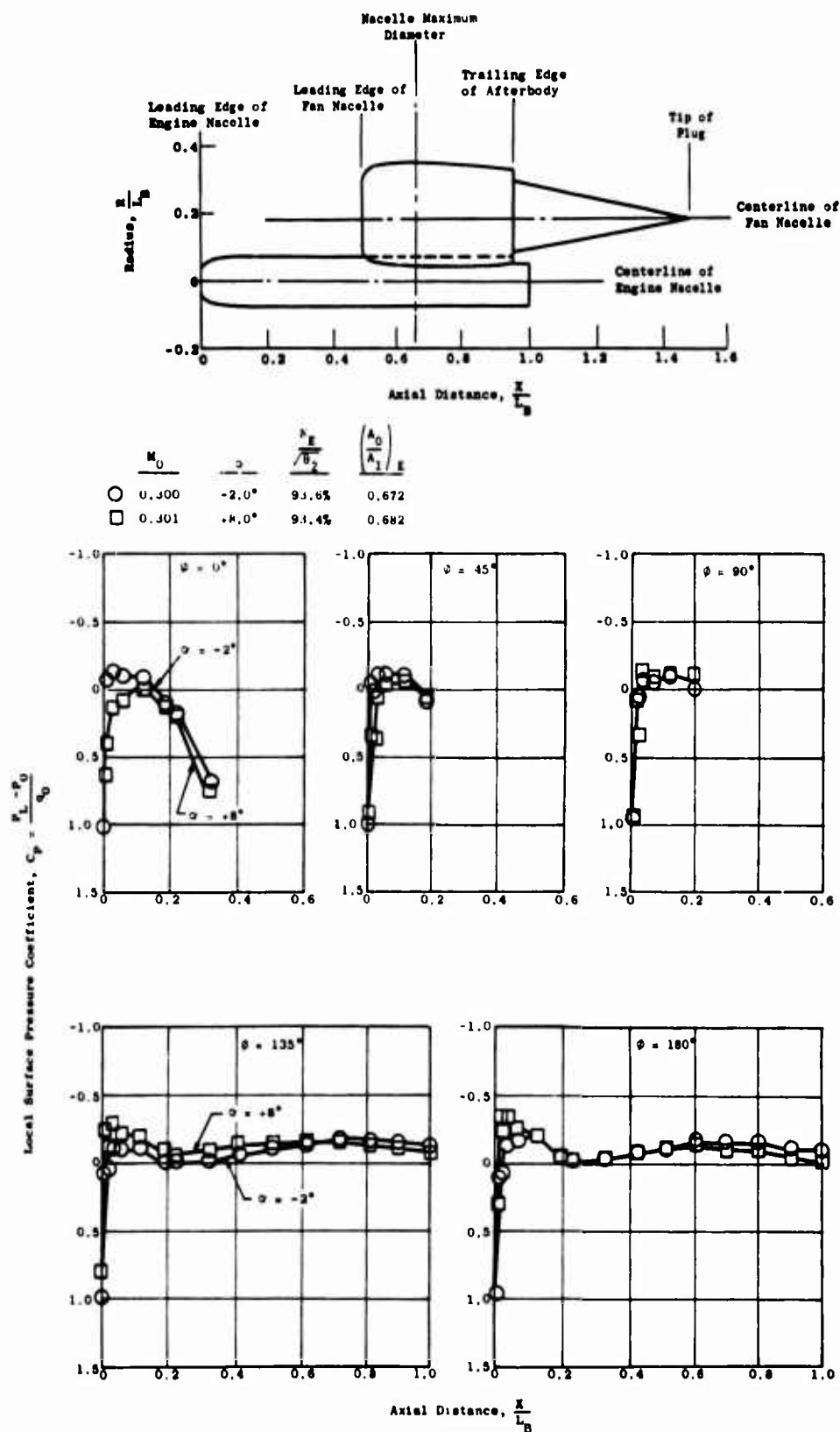
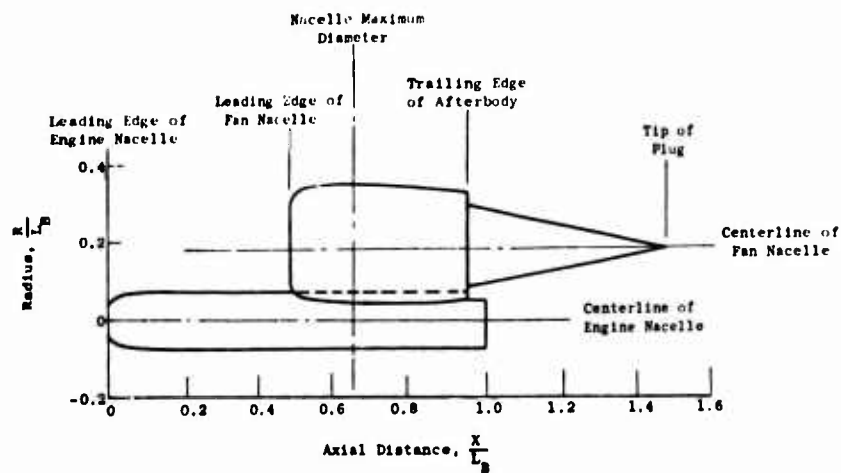


Figure 358. Engine Nacelle Pressure Distributions Showing Effects of Angle of Attack, $M_0 = 0.30$.

Figur



	M_0	α	$\frac{N_F}{\sqrt{S_0}}$	$\left(\frac{A_0}{A_1}\right)_E$
○	0.699	-2.0°	95.0%	0.471
□	0.700	+5.0°	94.9%	0.373

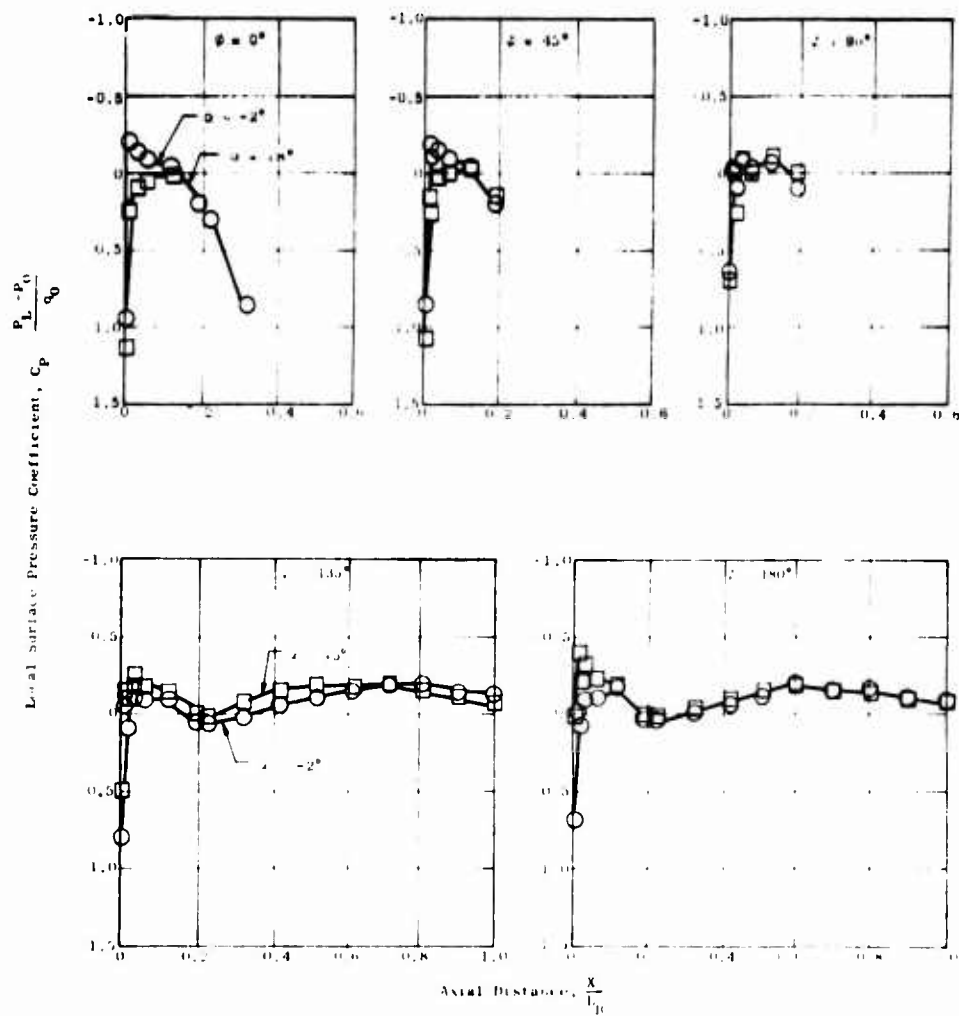


Figure 359. Engine Nacelle Pressure Distributions Showing Effects of Angle of Attack, $M_0 = 0.70$.

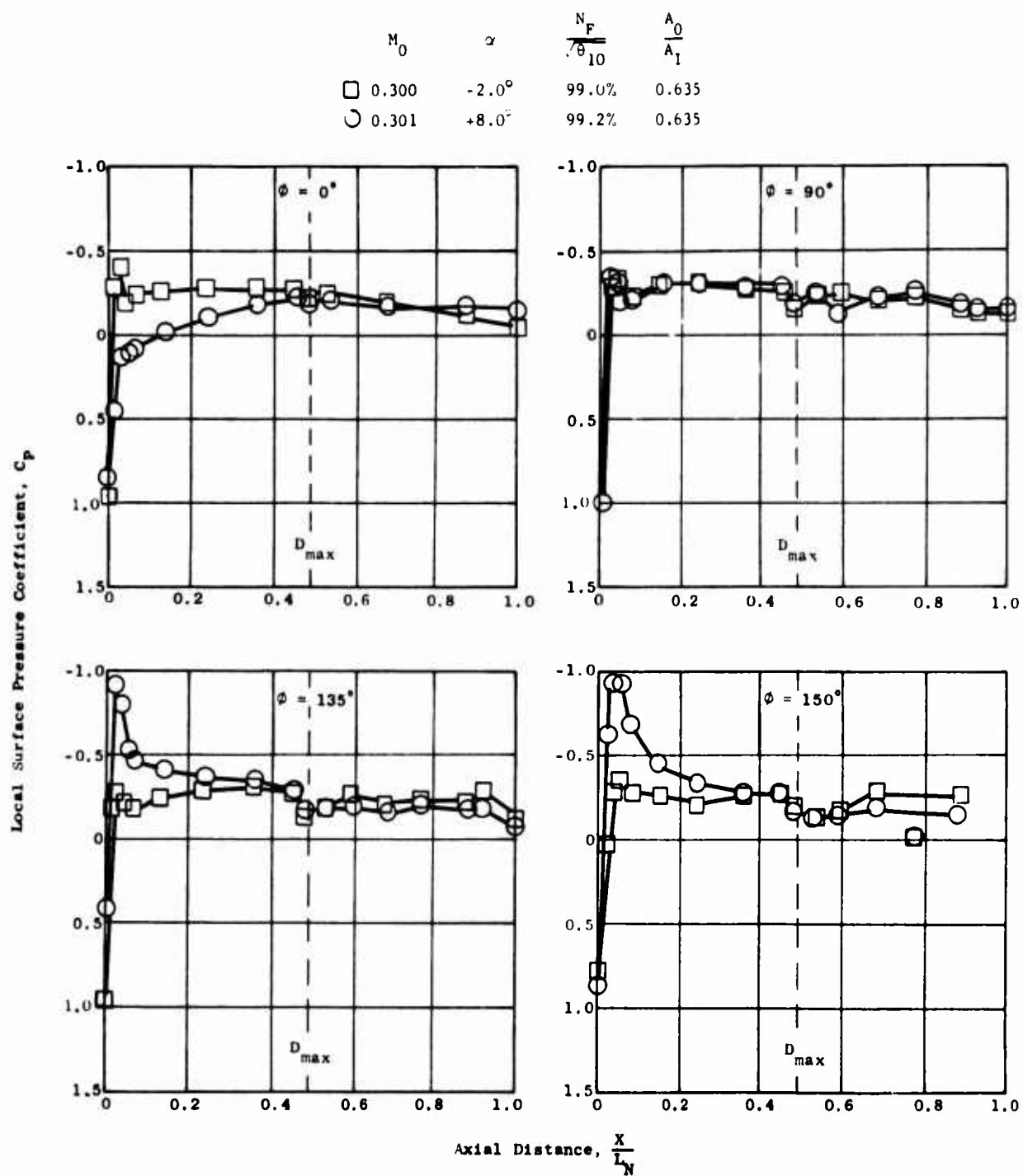


Figure 360. Nacelle External Pressure Distributions Showing Effects of Angle of Attack, $M_0 = 0.30$.

$$M_0 = 0.500$$

$$\frac{N_F}{\theta_{10}} = 44.8\% \quad (\text{Windmill})$$

$$\frac{A_0}{A_I} = 0.505$$

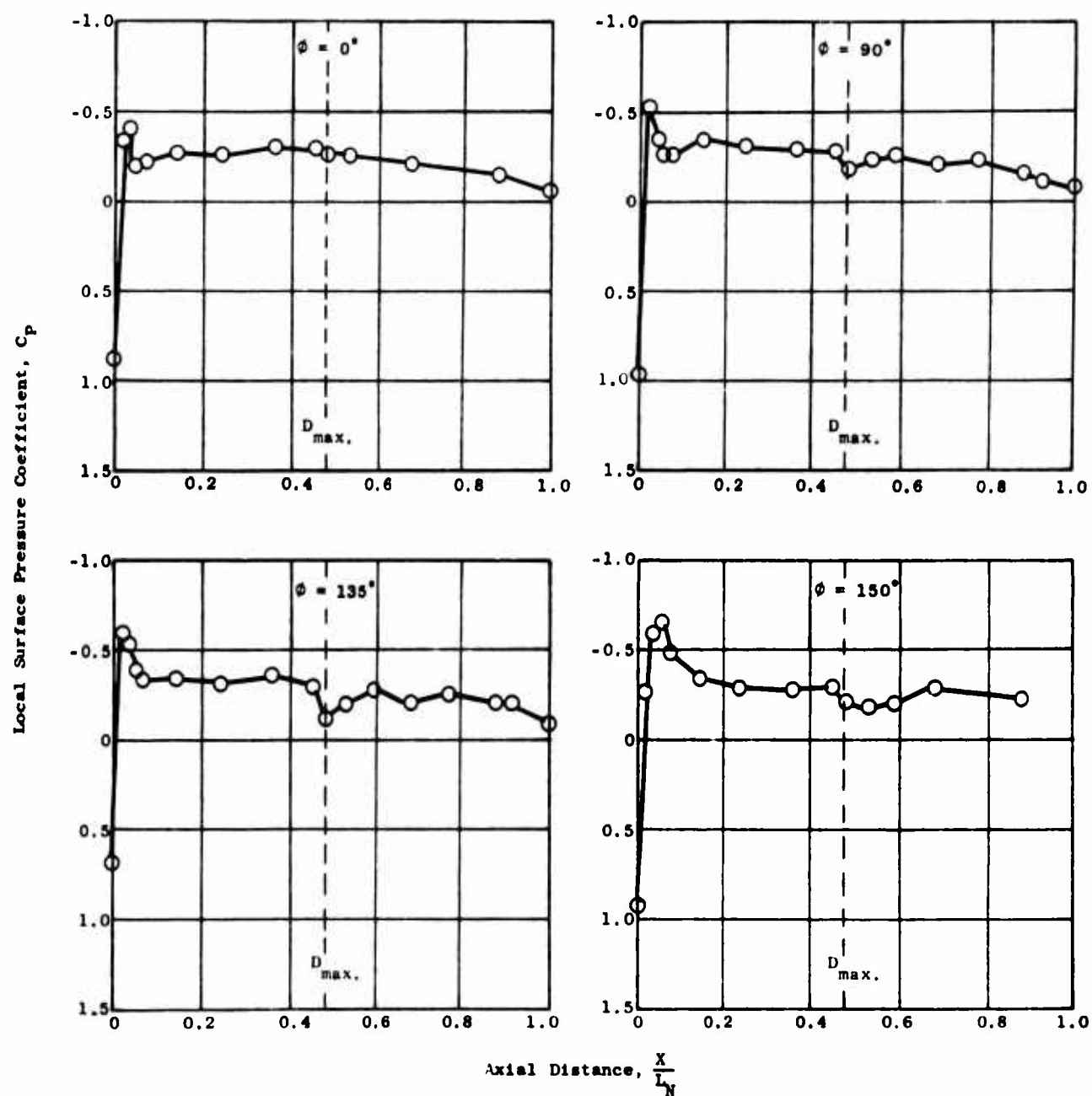


Figure 361. Nacelle External Pressure Distributions Showing Effects of Angle of Attack, $M_0 = 0.70$.

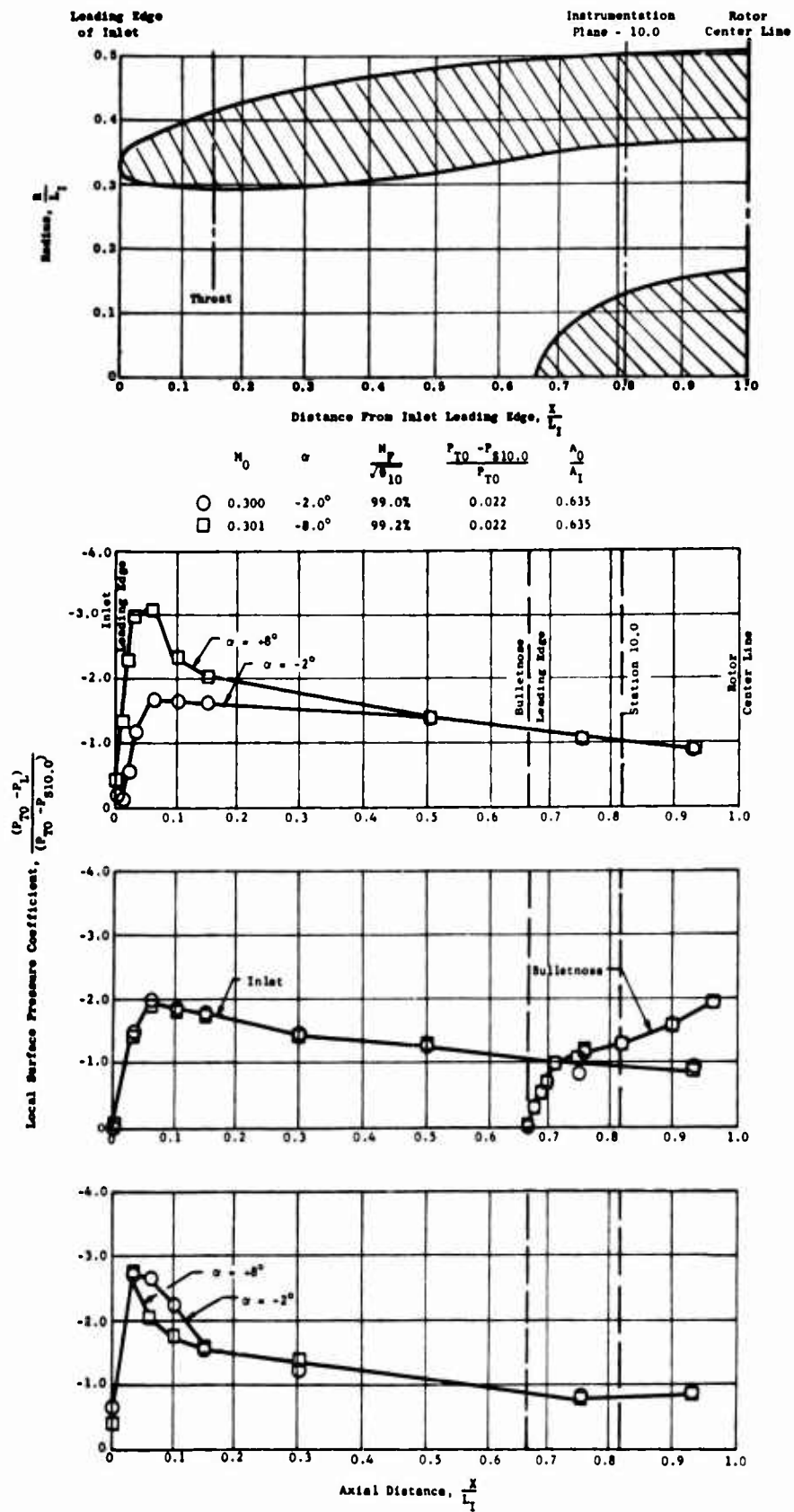


Figure 362. Nacelle Internal Pressure Distributions Showing Effects of Angle of Attack, $M_0 = 0.30$.

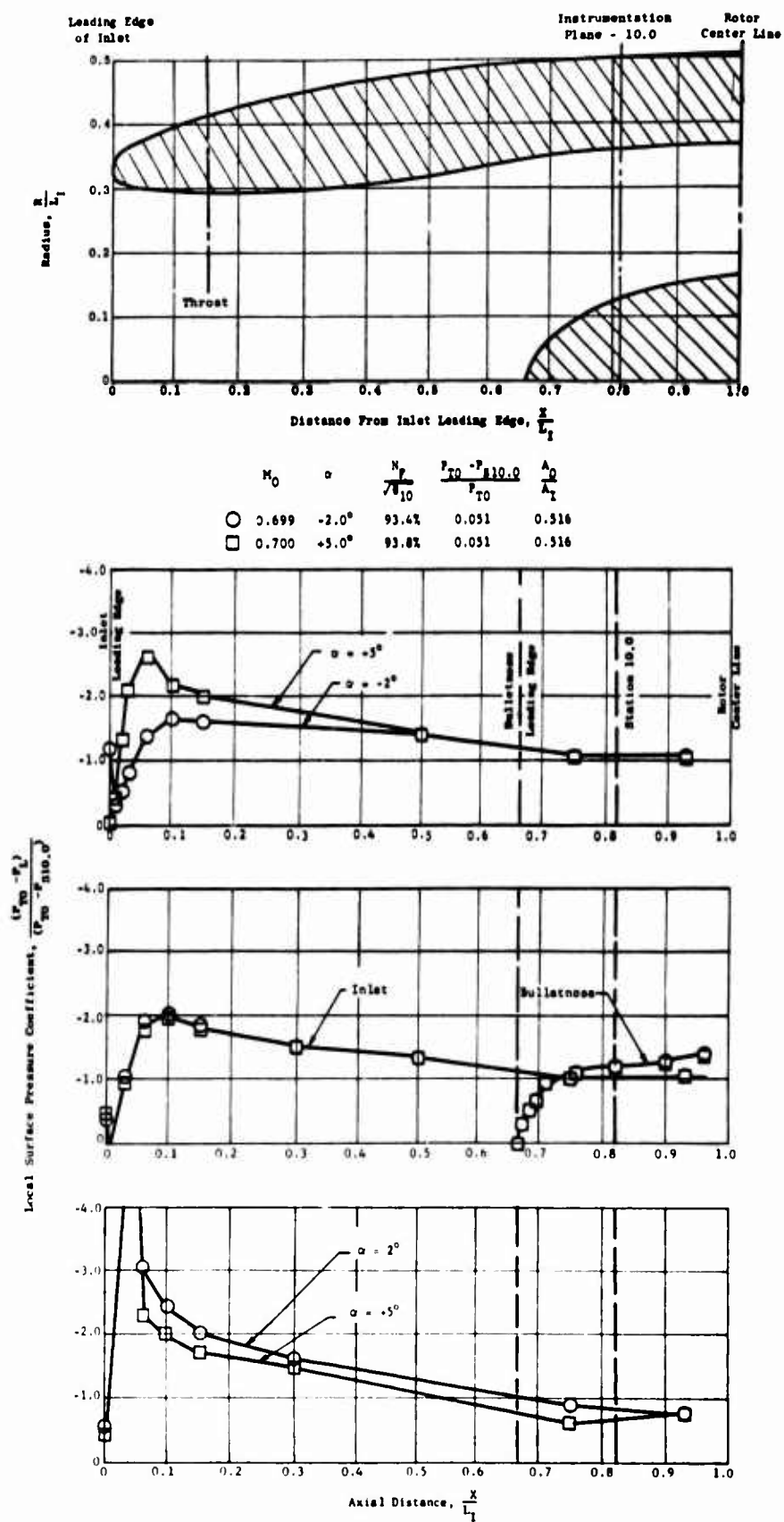


Figure 363. Nacelle Internal Pressure Distributions Showing Effects of Angle of Attack, $M_0 = 0.70$.

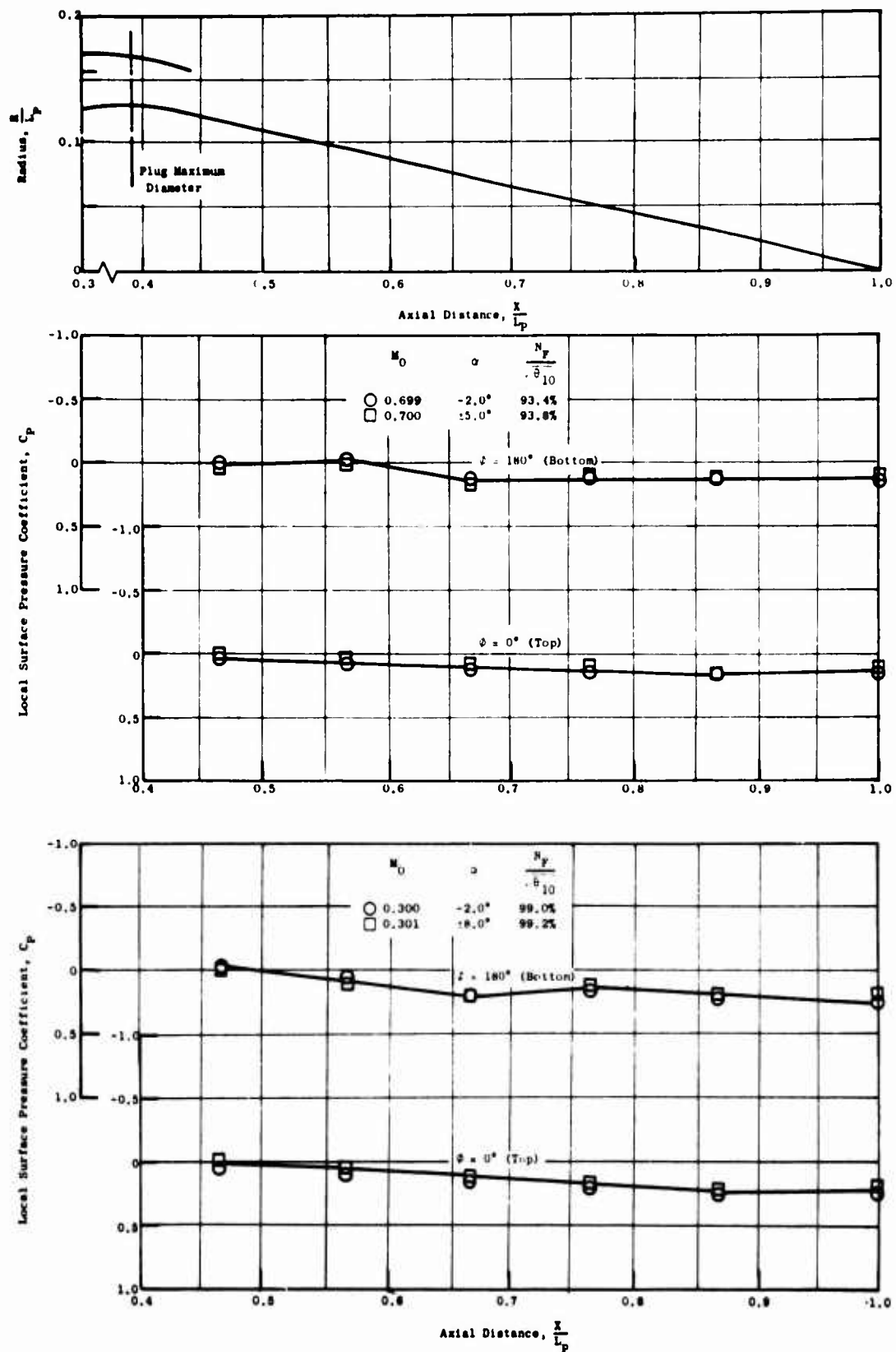


Figure 364. Nozzle Plug Distributions Showing Effects of Angle of Attack, $M_0 = 0.30$ and 0.70 .

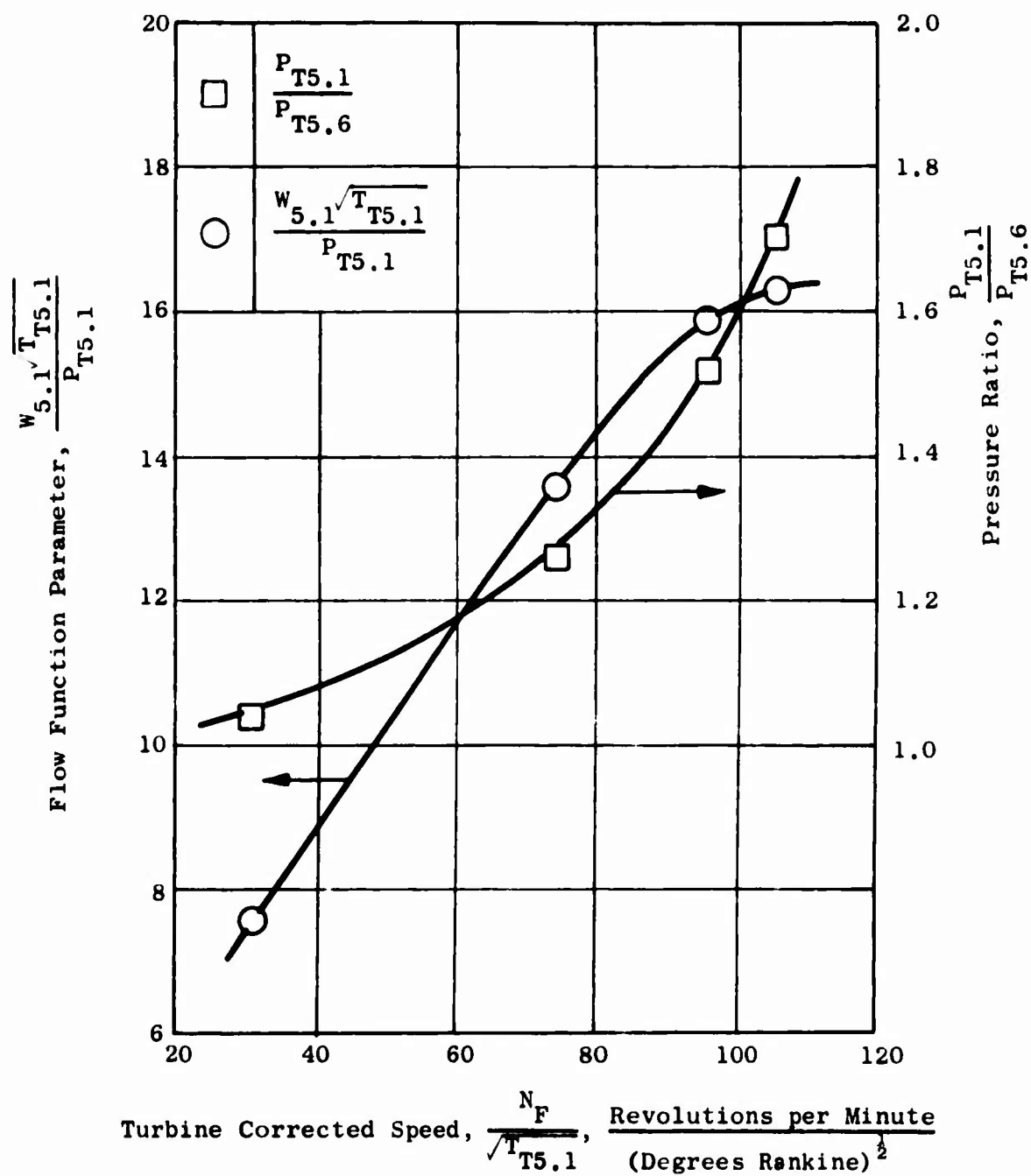


Figure 365. Fan Turbine Operating Characteristics - Model 3,
 $M_0 = 0.0$.

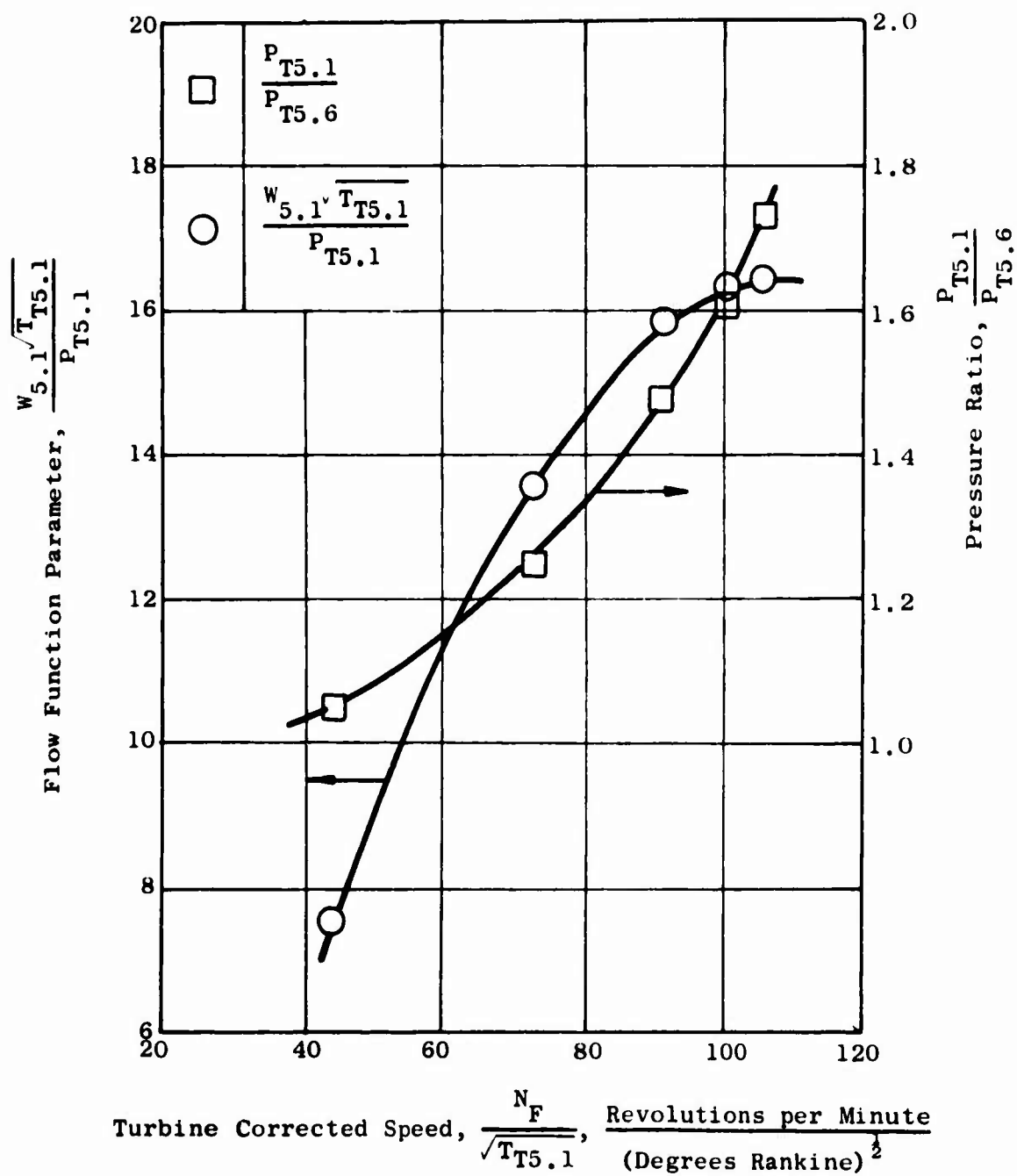


Figure 366. Fan Turbine Operating Characteristics = Model 3,
 $M_0 = 0.2$.

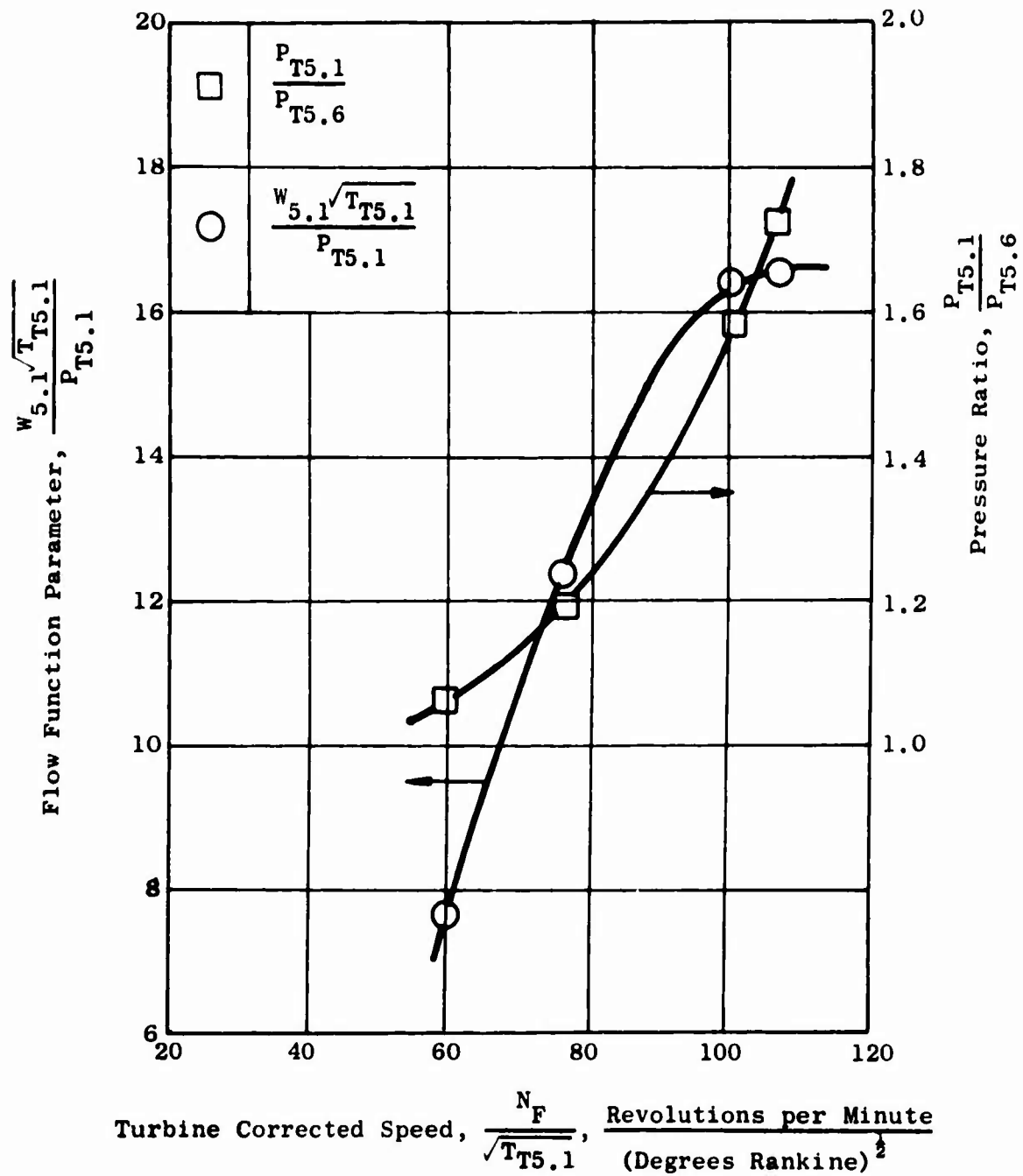


Figure 367. Fan Turbine Operating Characteristics - Model 3,
 $M_0 = 0.3$.

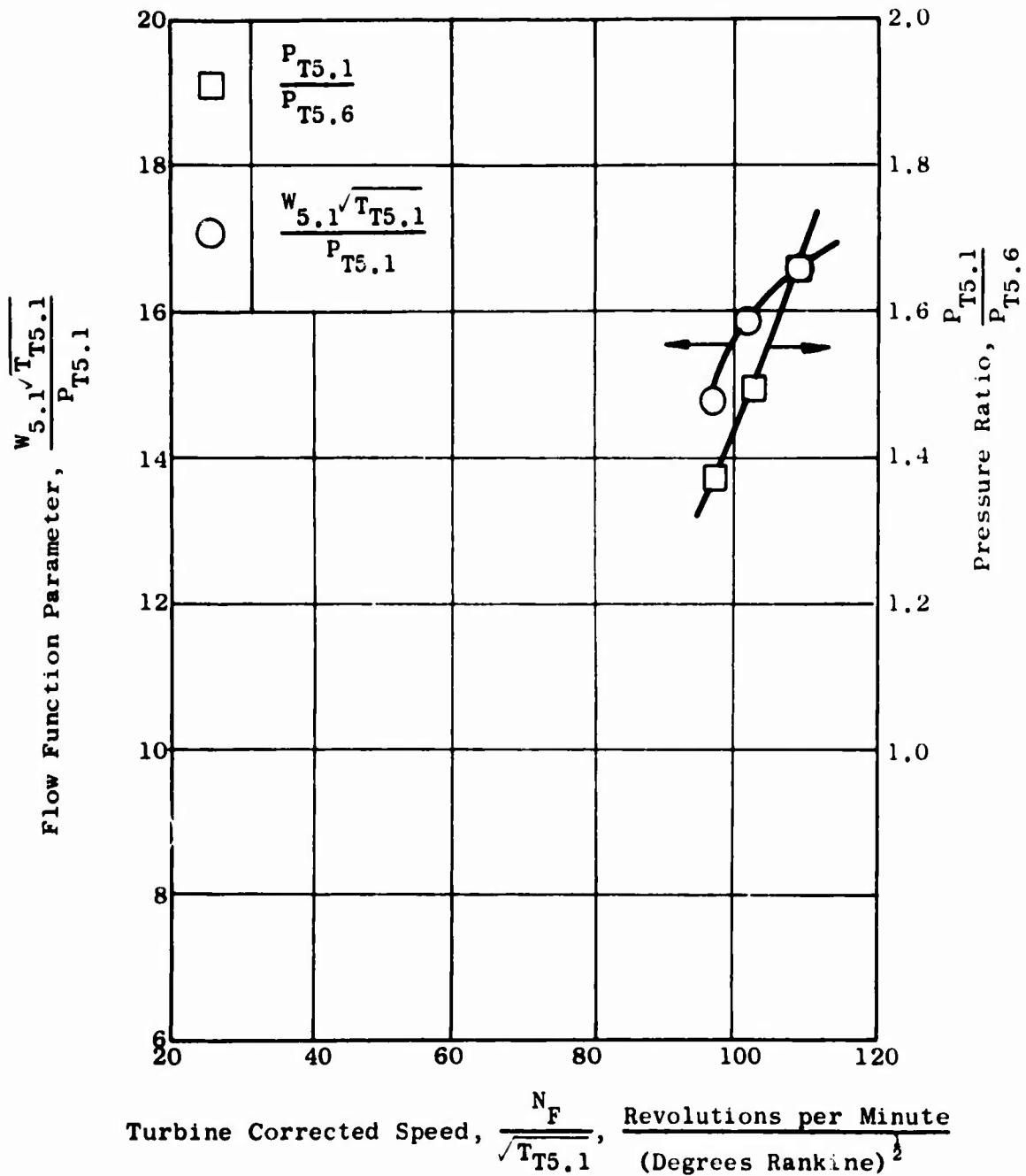


Figure 368. Fan Turbine Operating Characteristics - Model 3,
 $M_0 = 0.4$.

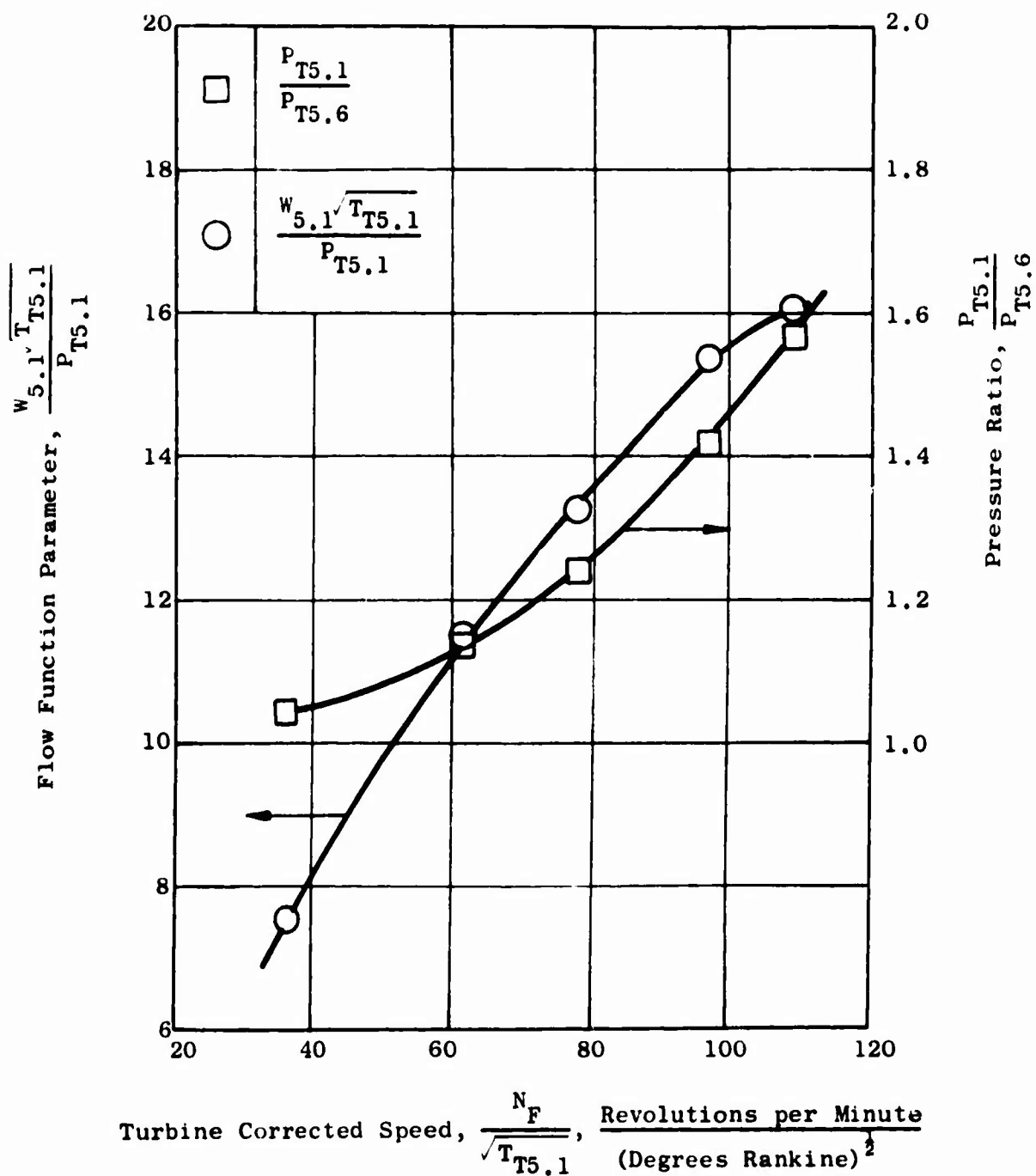


Figure 369. Fan Turbine Operating Characteristics - Model 6,
 $M_0 = 0.0$.

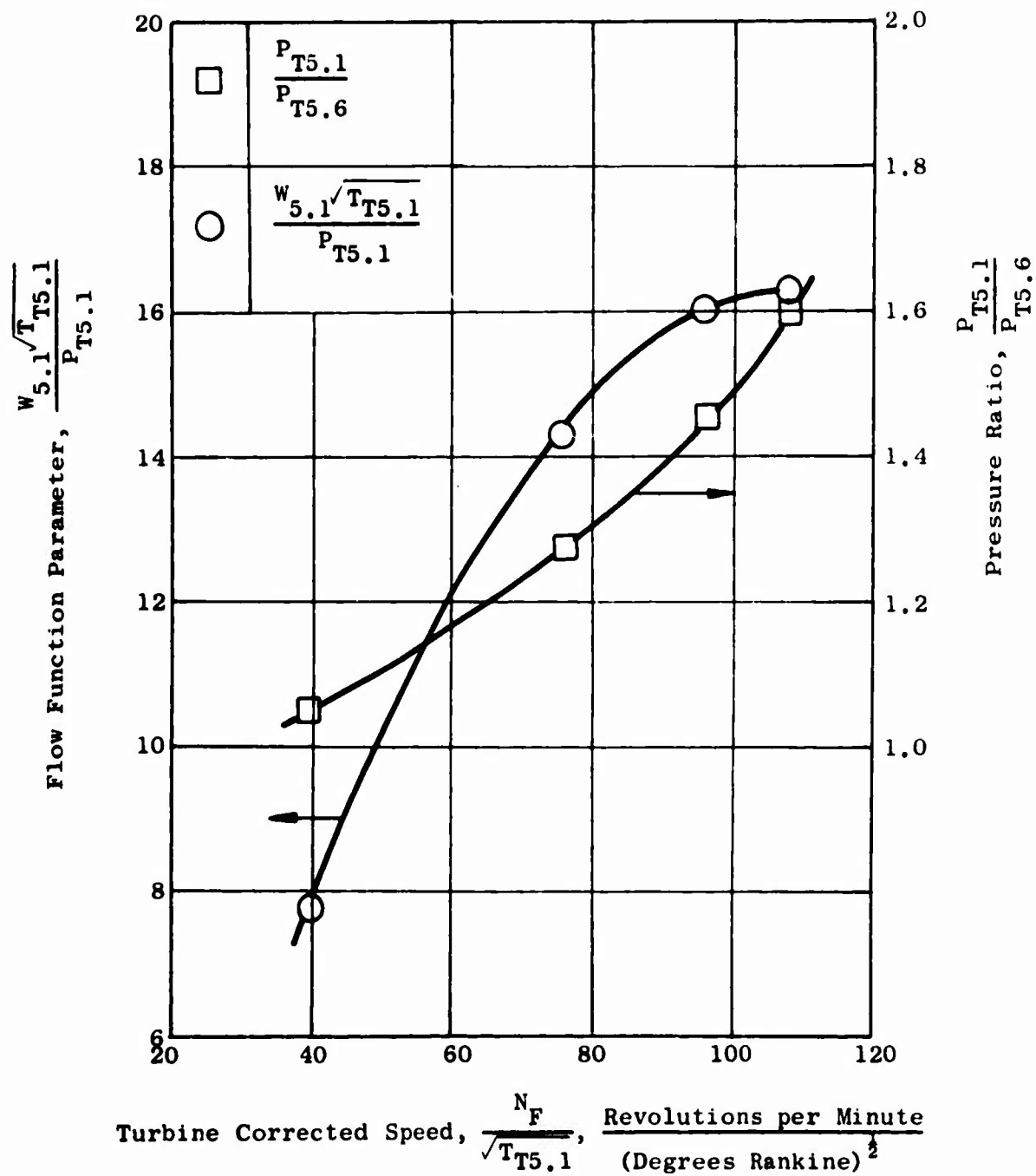


Figure 370. Fan Turbine Operating Characteristics - Model 6,
 $M_0 = 0.3$.

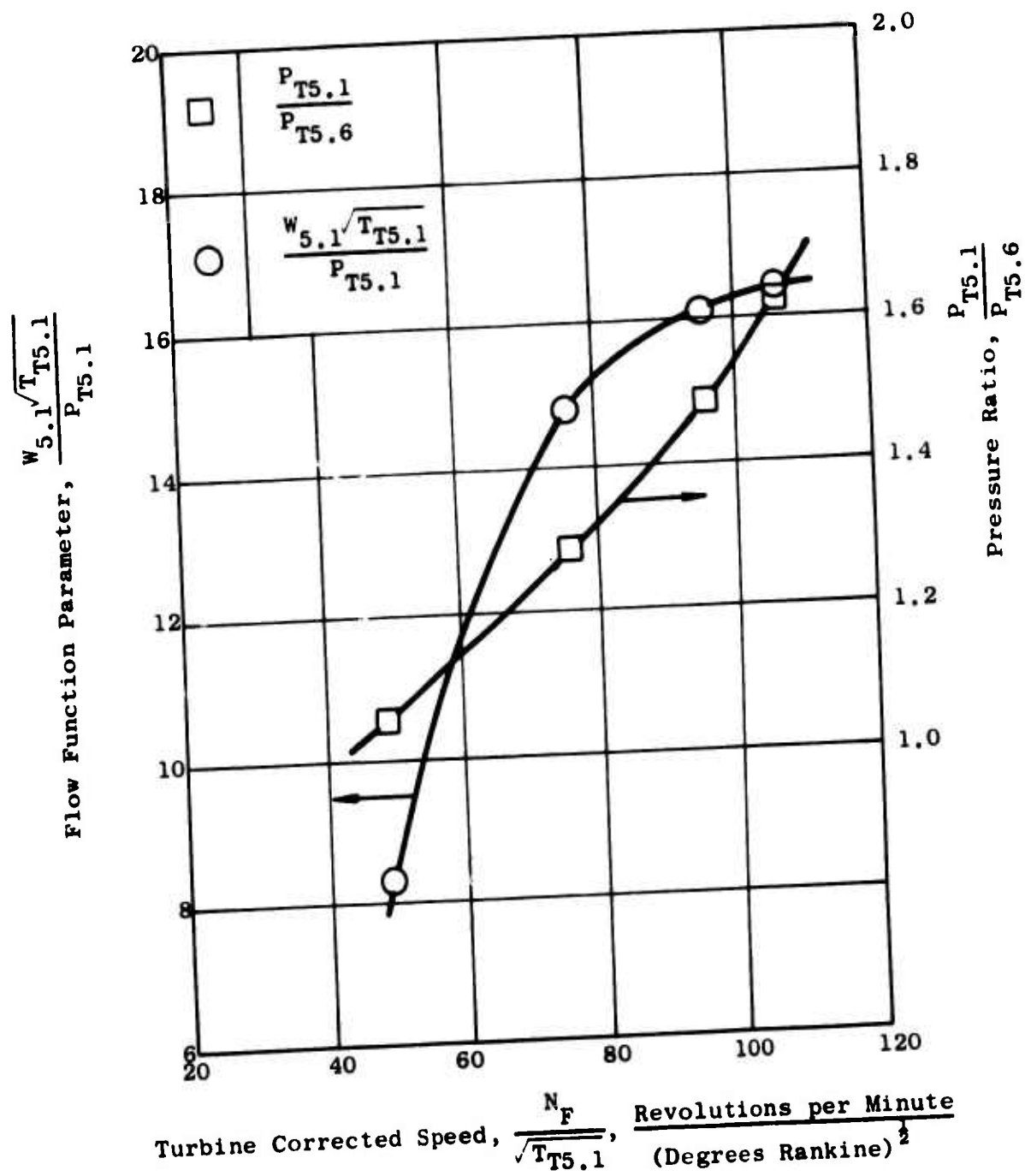


Figure 371. Fan Turbine Operating Characteristics - Model 6,
 $M_0 = 0.4$.

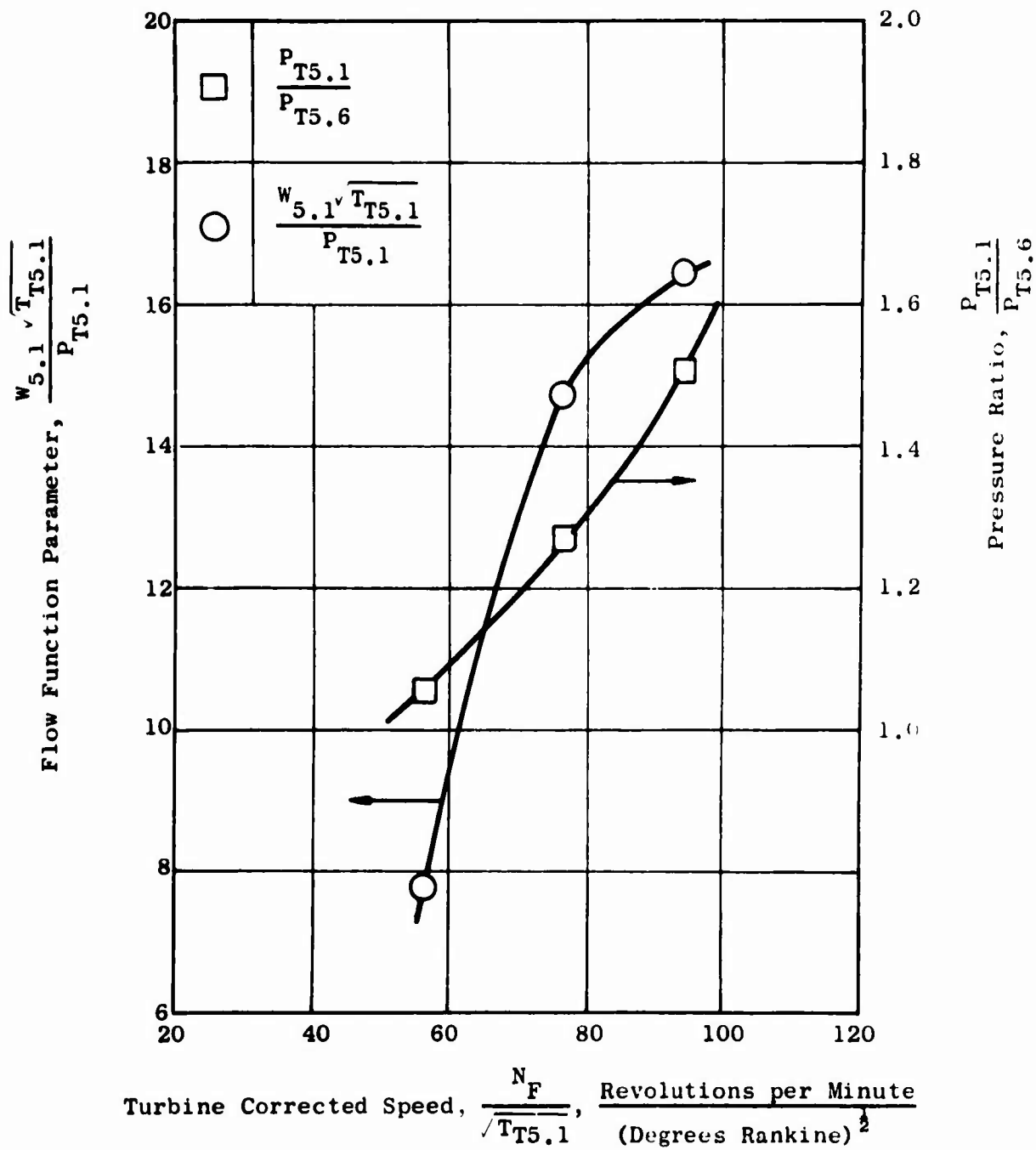


Figure 372. Fan Turbine Operating Characteristics - Model 6,
 $M_0 = 0.5$.

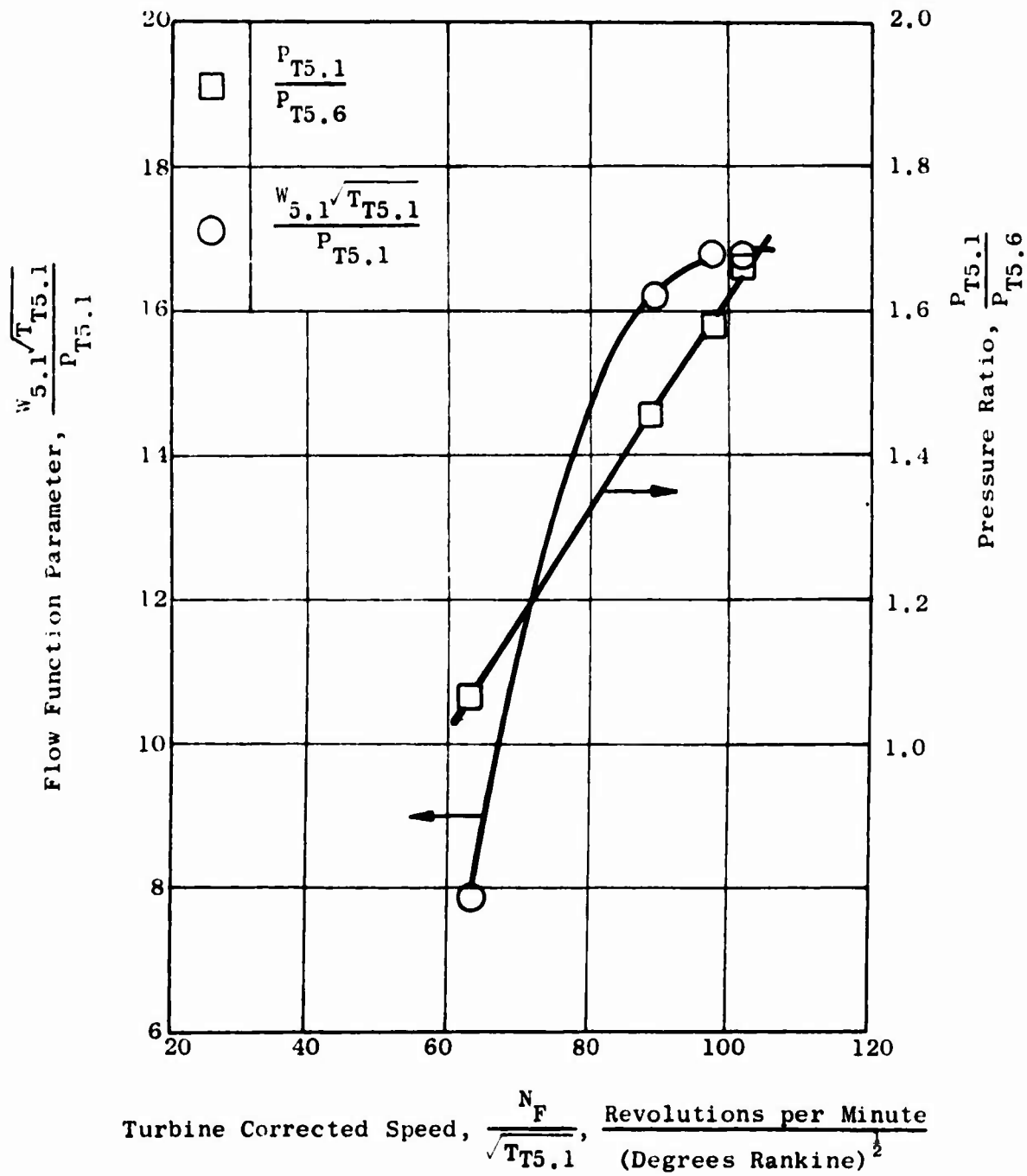


Figure 373. Fan Turbine Operating Characteristics - Model 6,
 $M_0 = 0.6$.

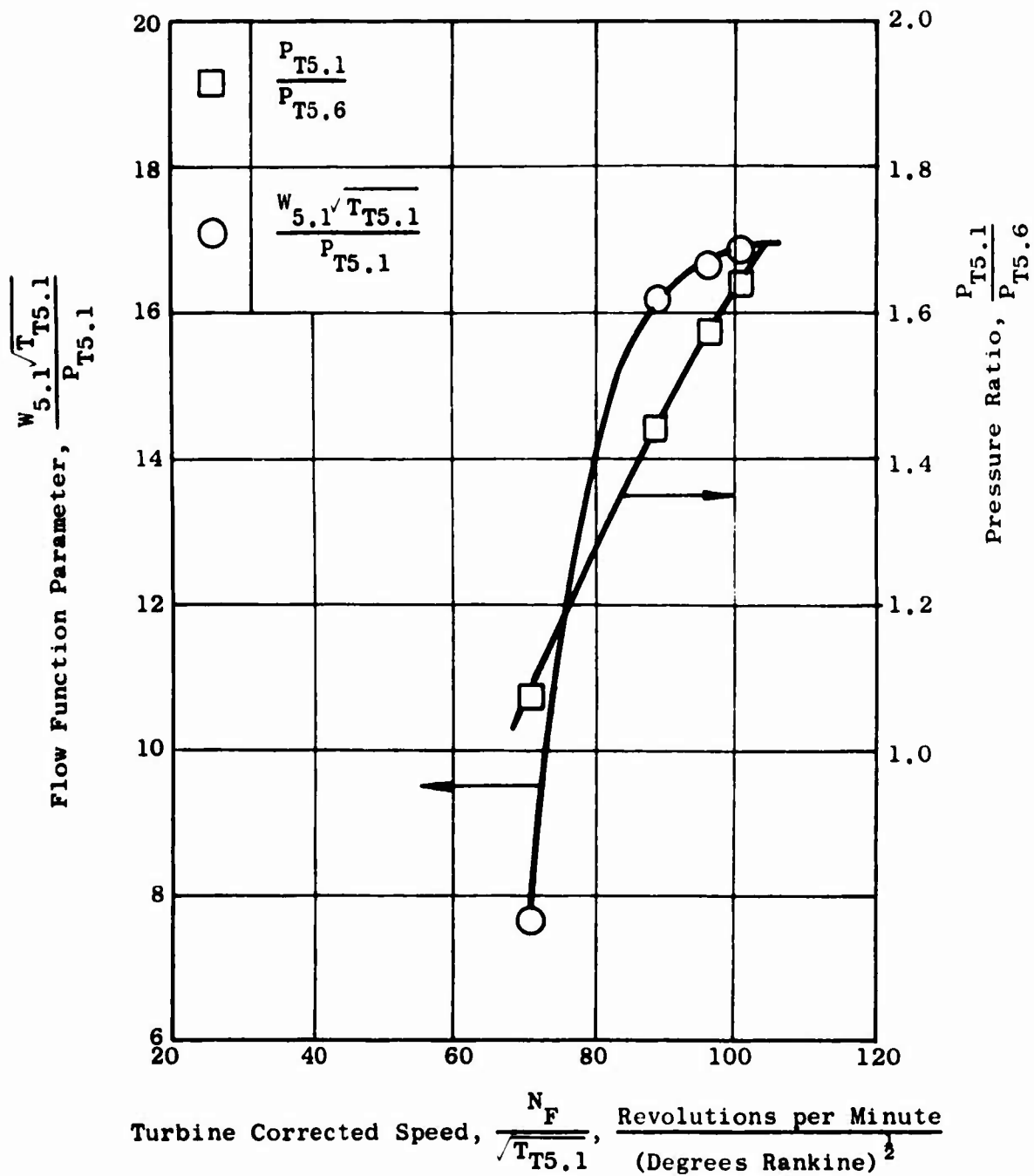


Figure 374. Fan Turbine Operating Characteristics - Model 6, $M_0 = 0.7$.

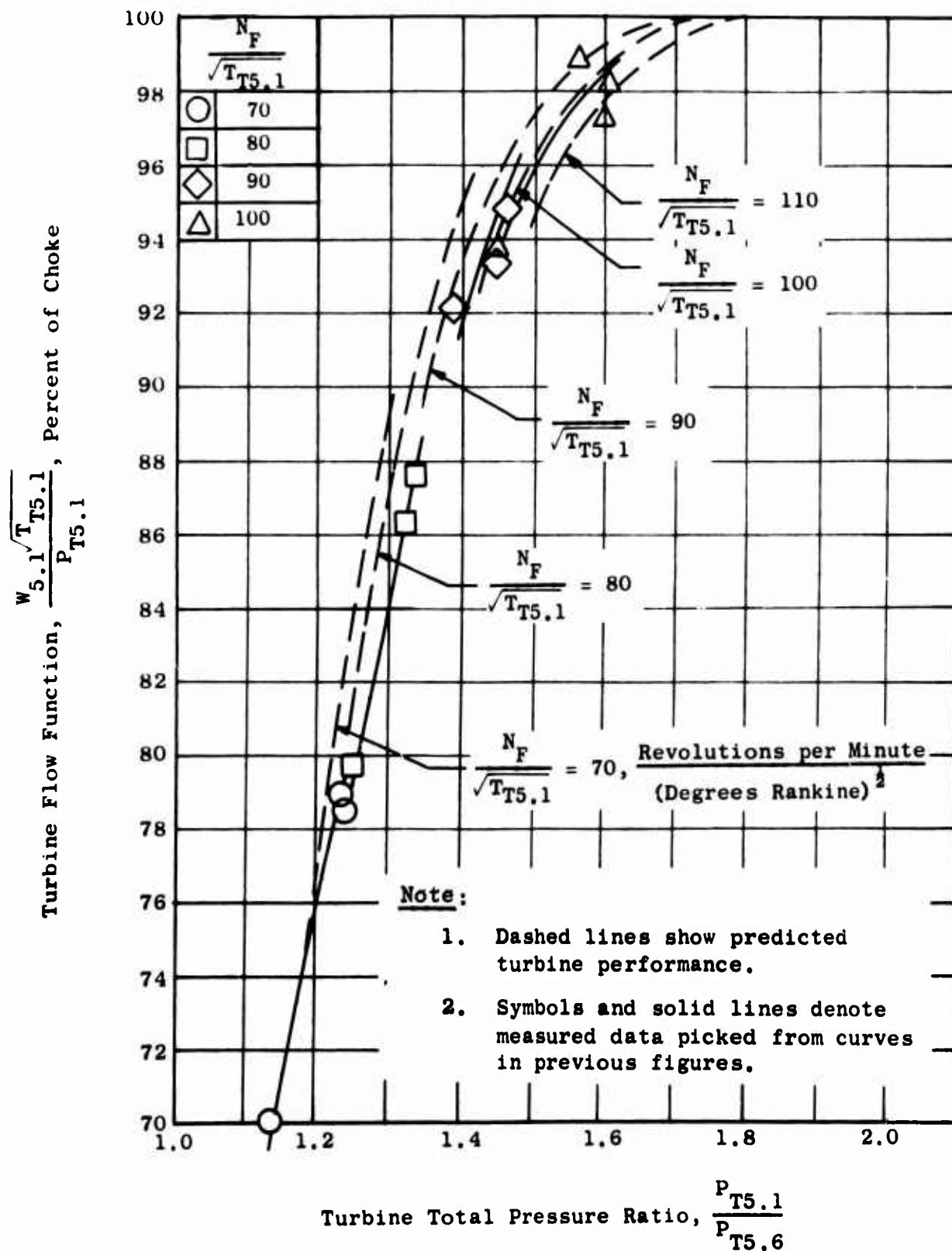


Figure 375. Comparison of Predicted and Measured Fan Turbine Performance - Model 3.

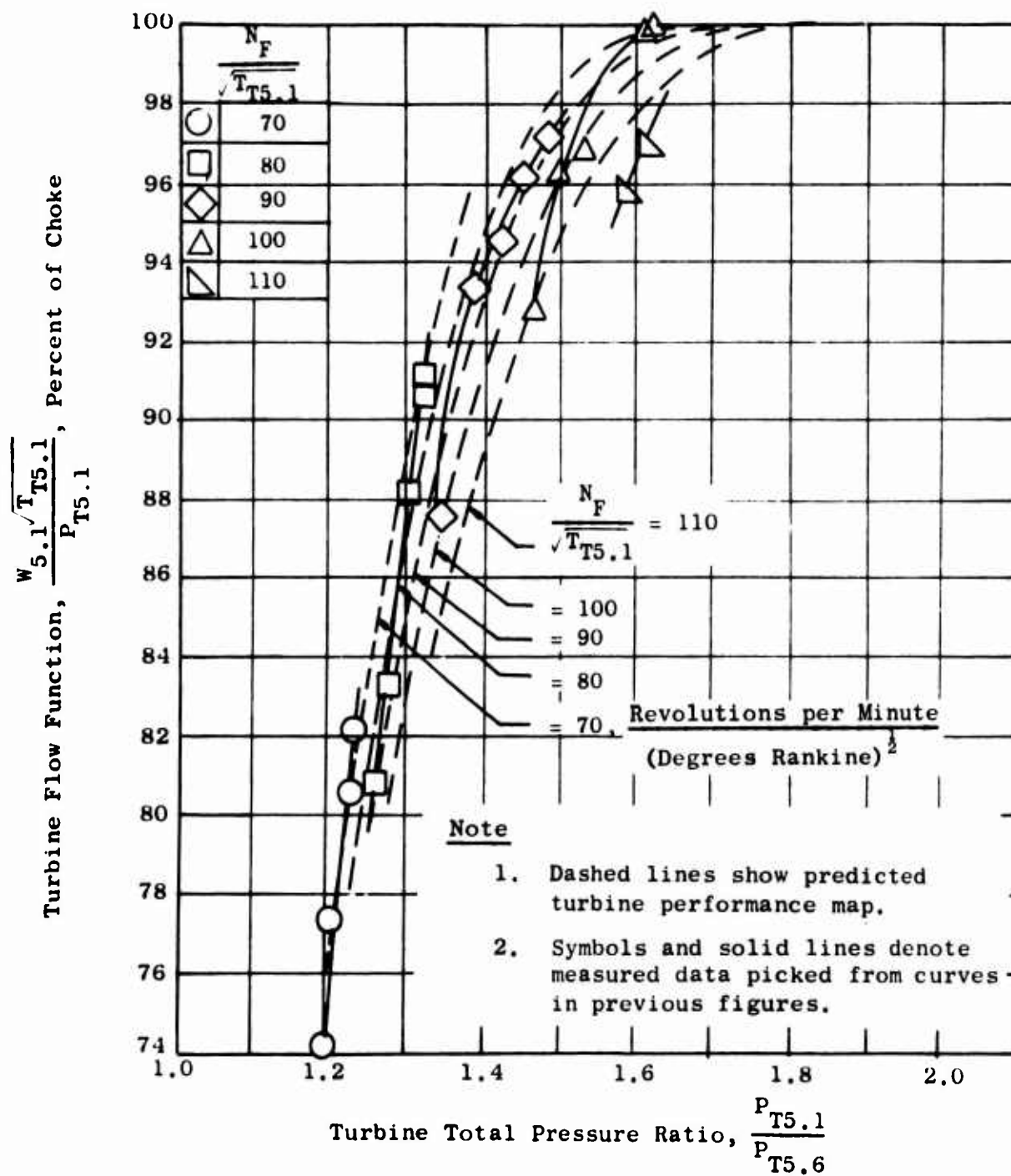


Figure 376. Comparison of Predicted and Measured Fan Turbine Performance - Model 6.

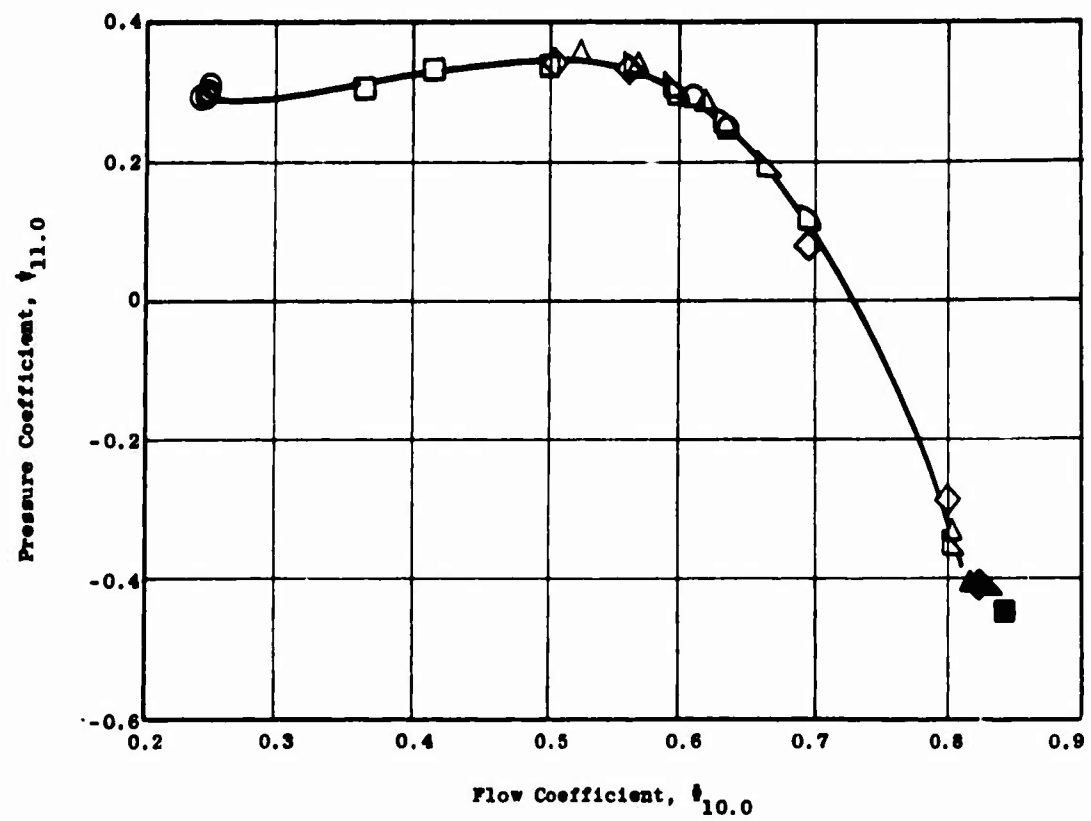
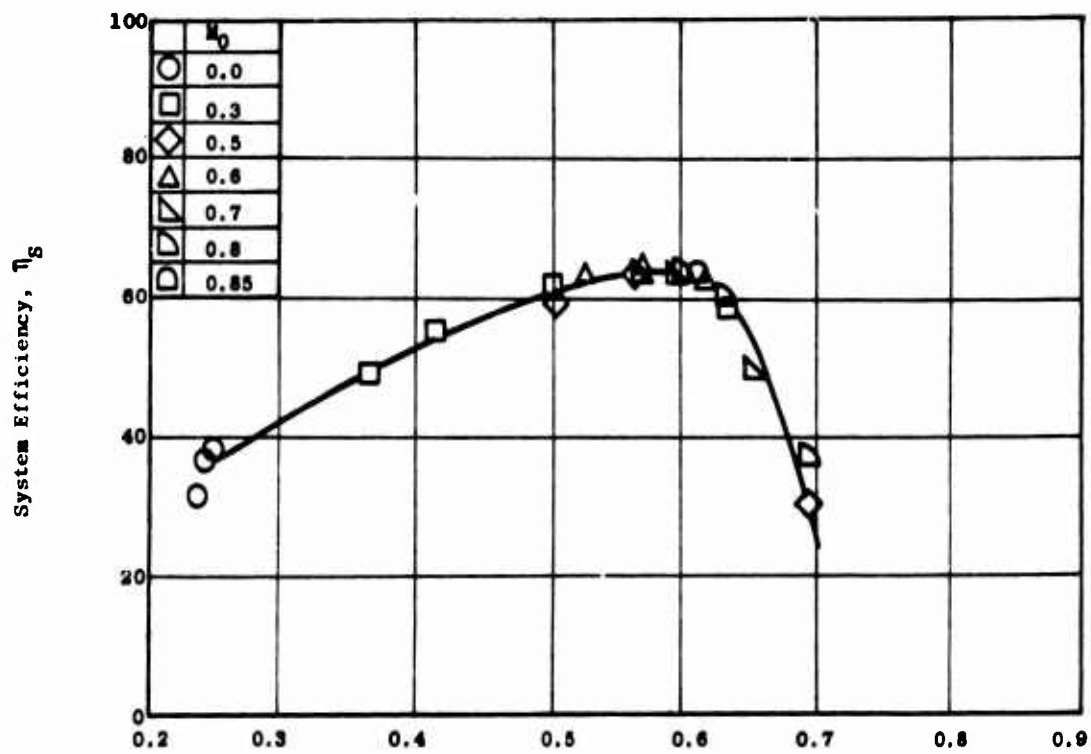


Figure 377. Fan Performance Characteristics - Model 1.

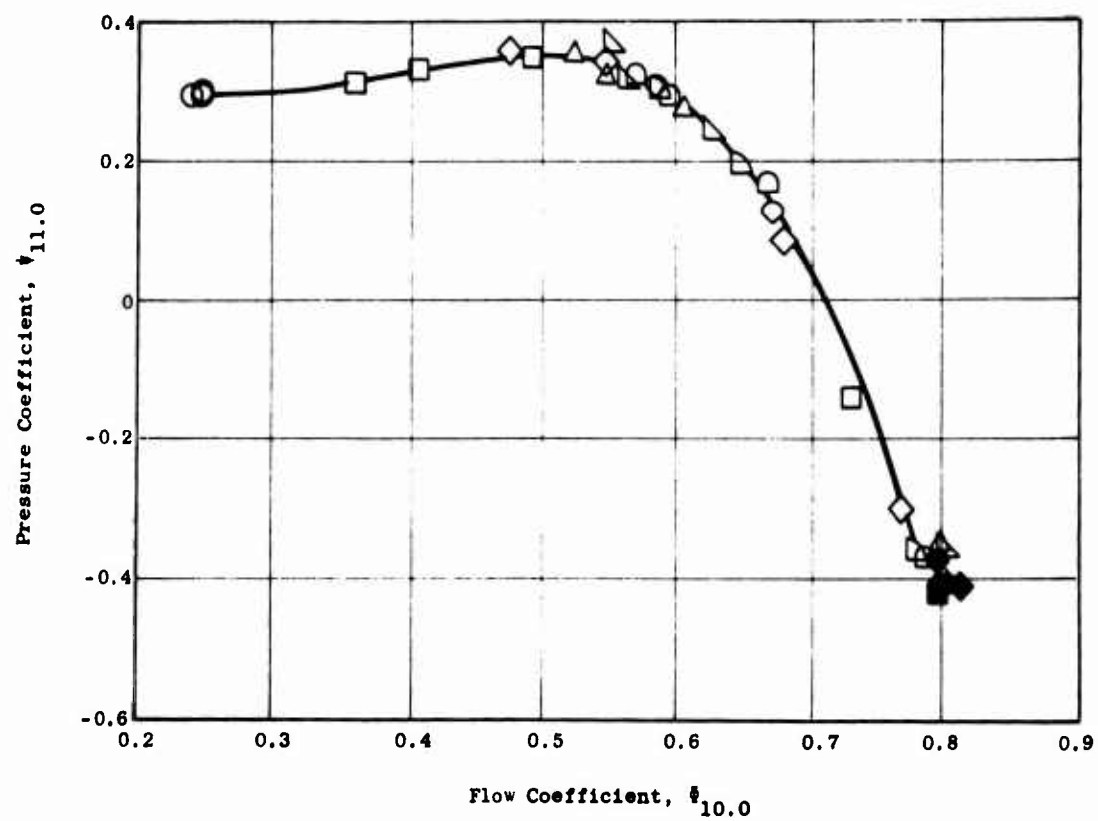
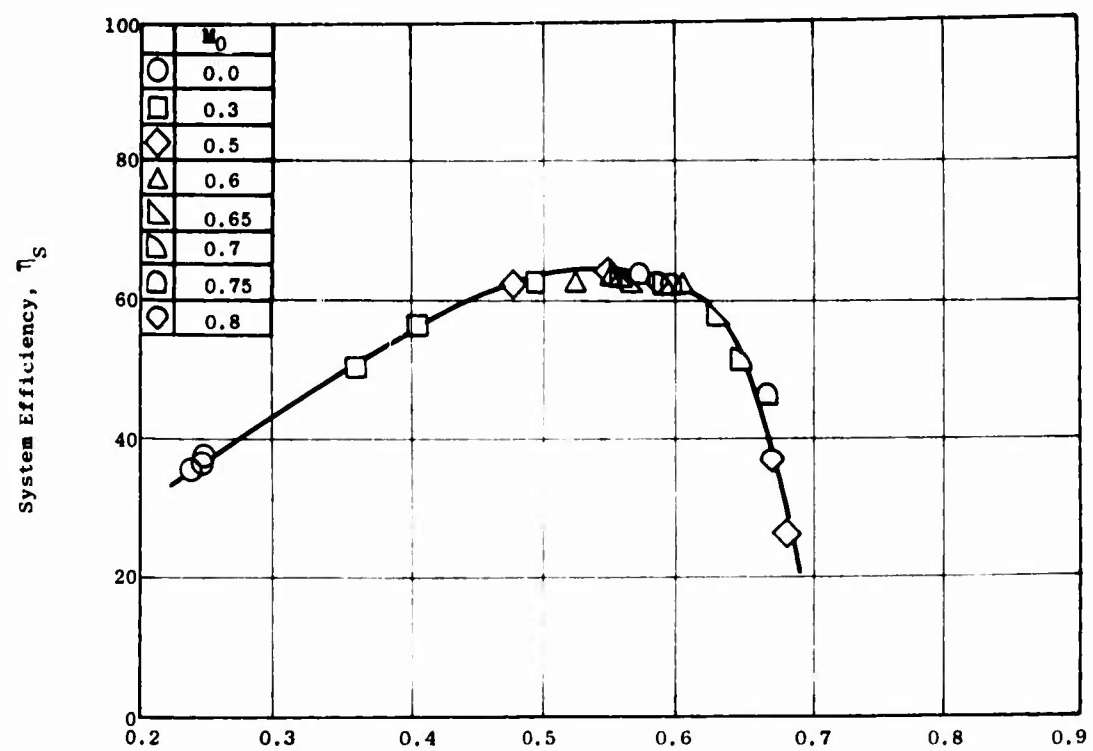


Figure 378. Fan Performance Characteristics - Model 2.

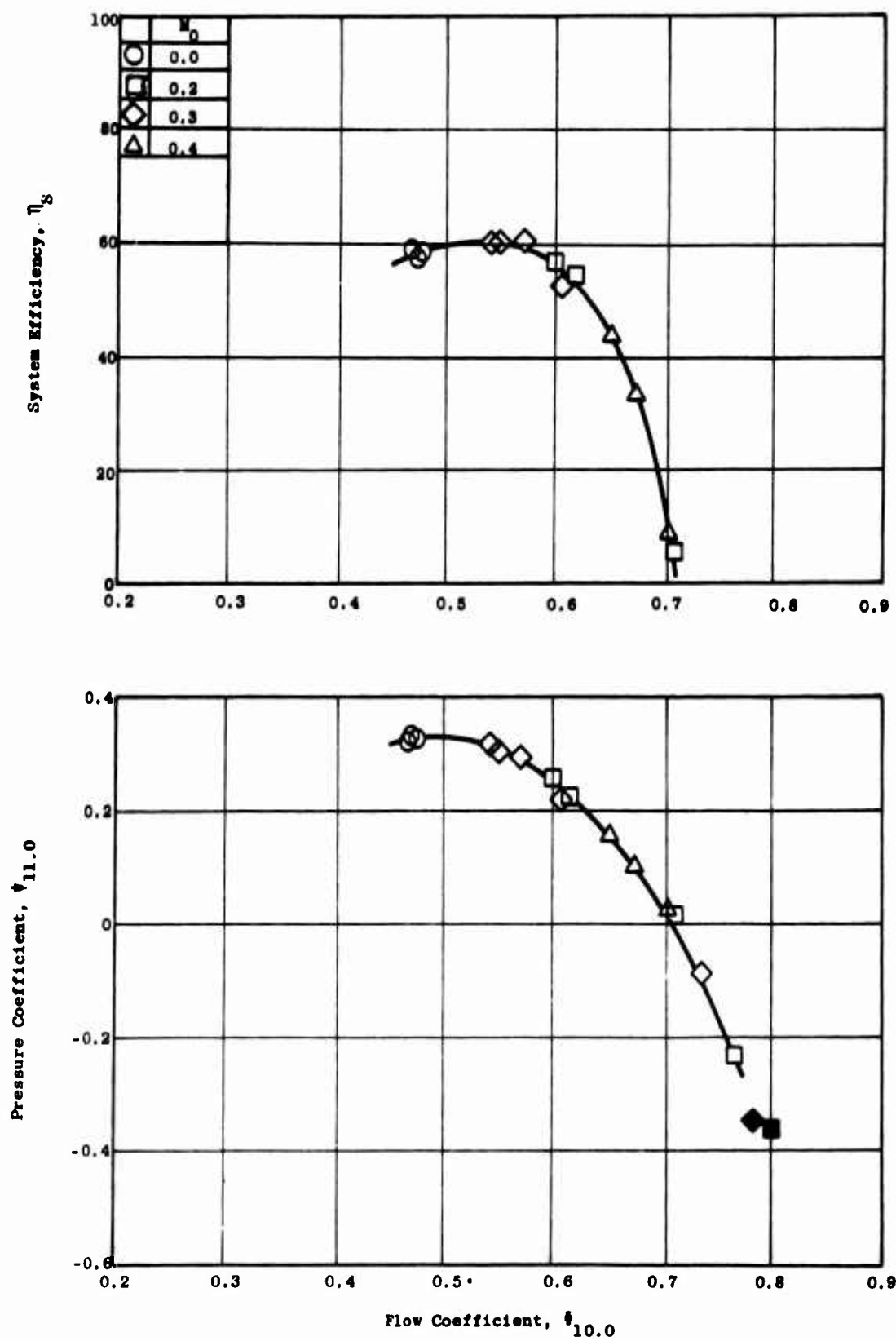


Figure 379. Fan Performance Characteristics - Model 3.

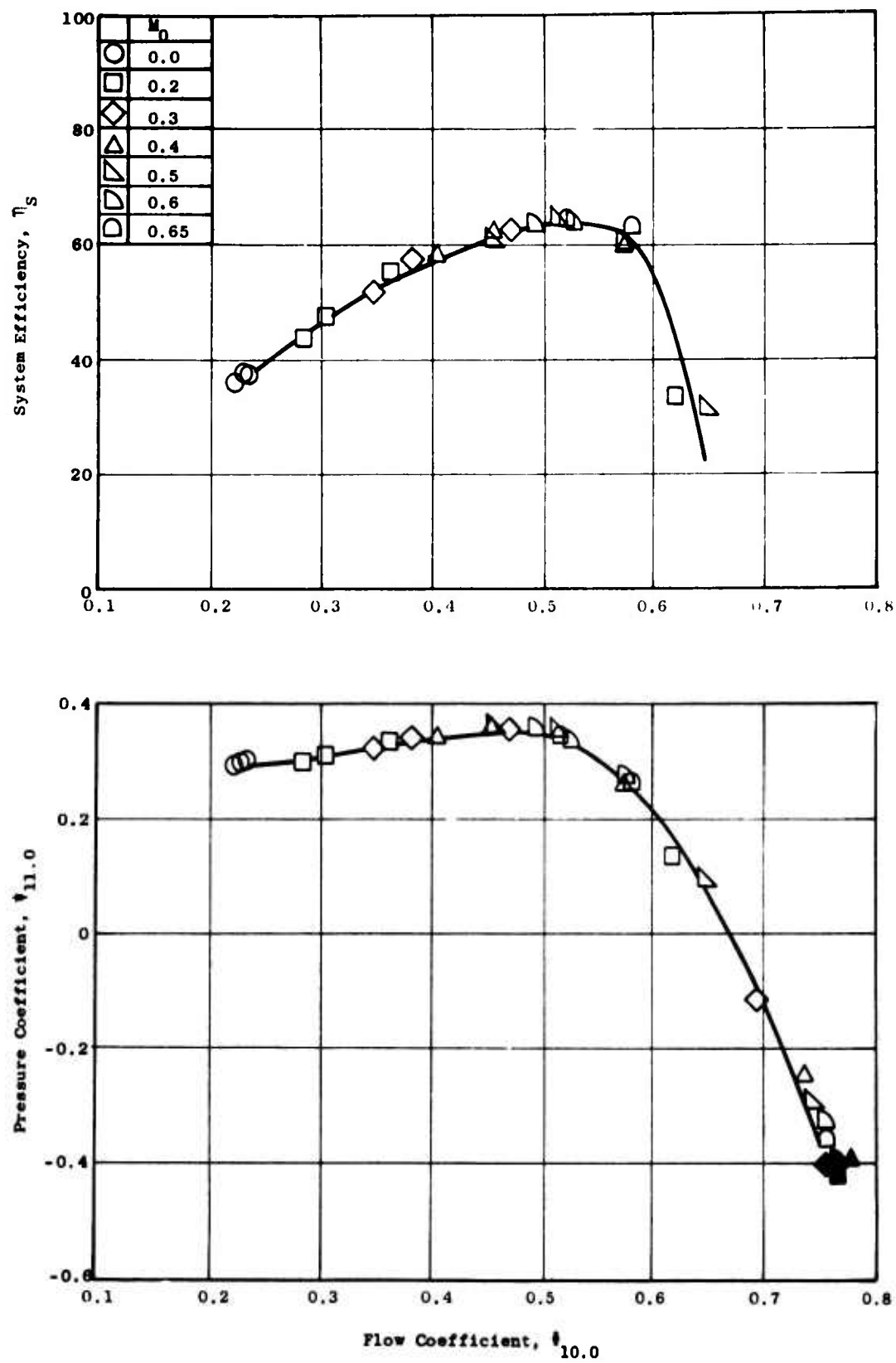


Figure 380. Fan Performance Characteristics - Model 4.

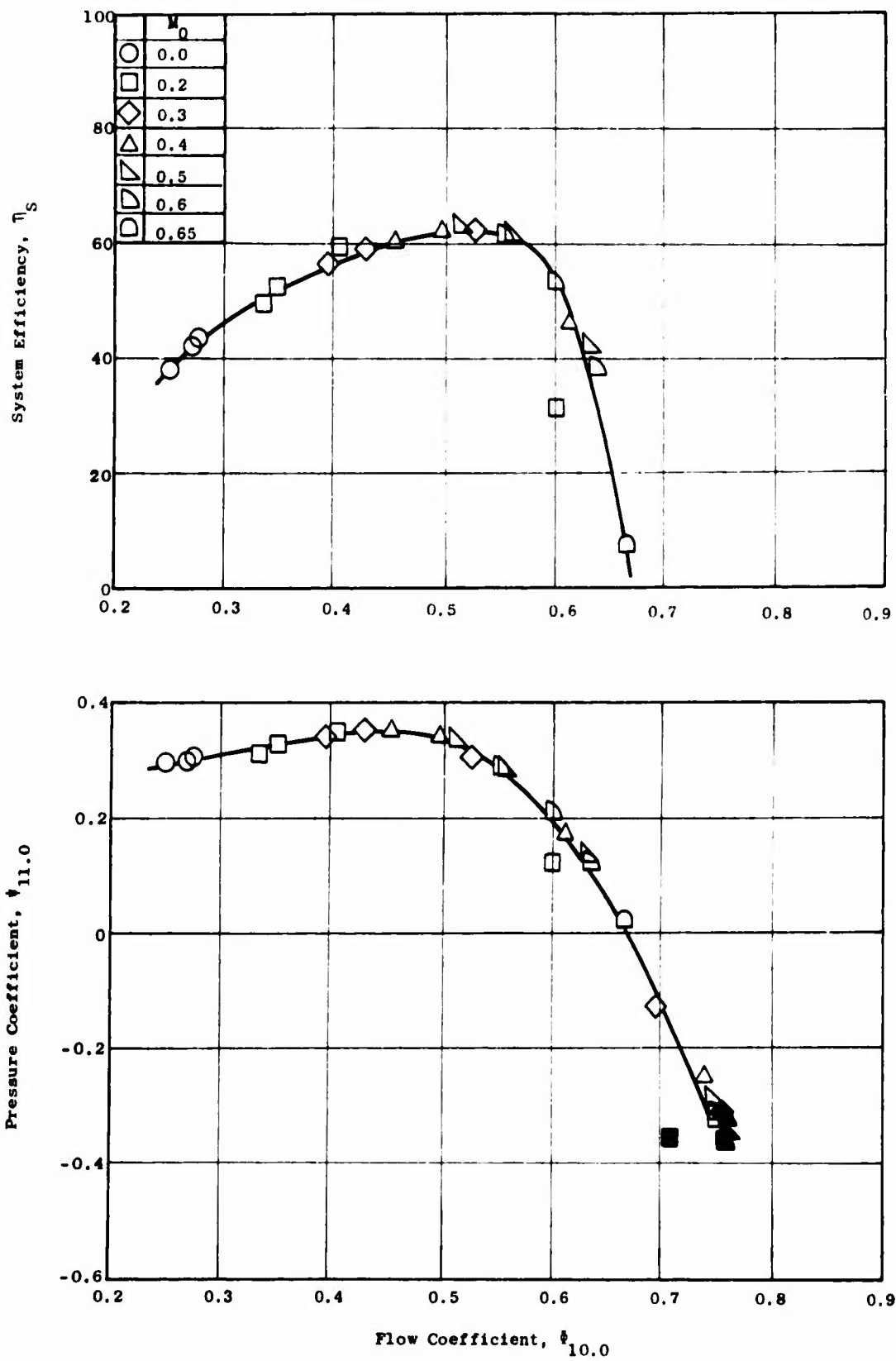


Figure 381. Fan Performance Characteristics - Model 5.

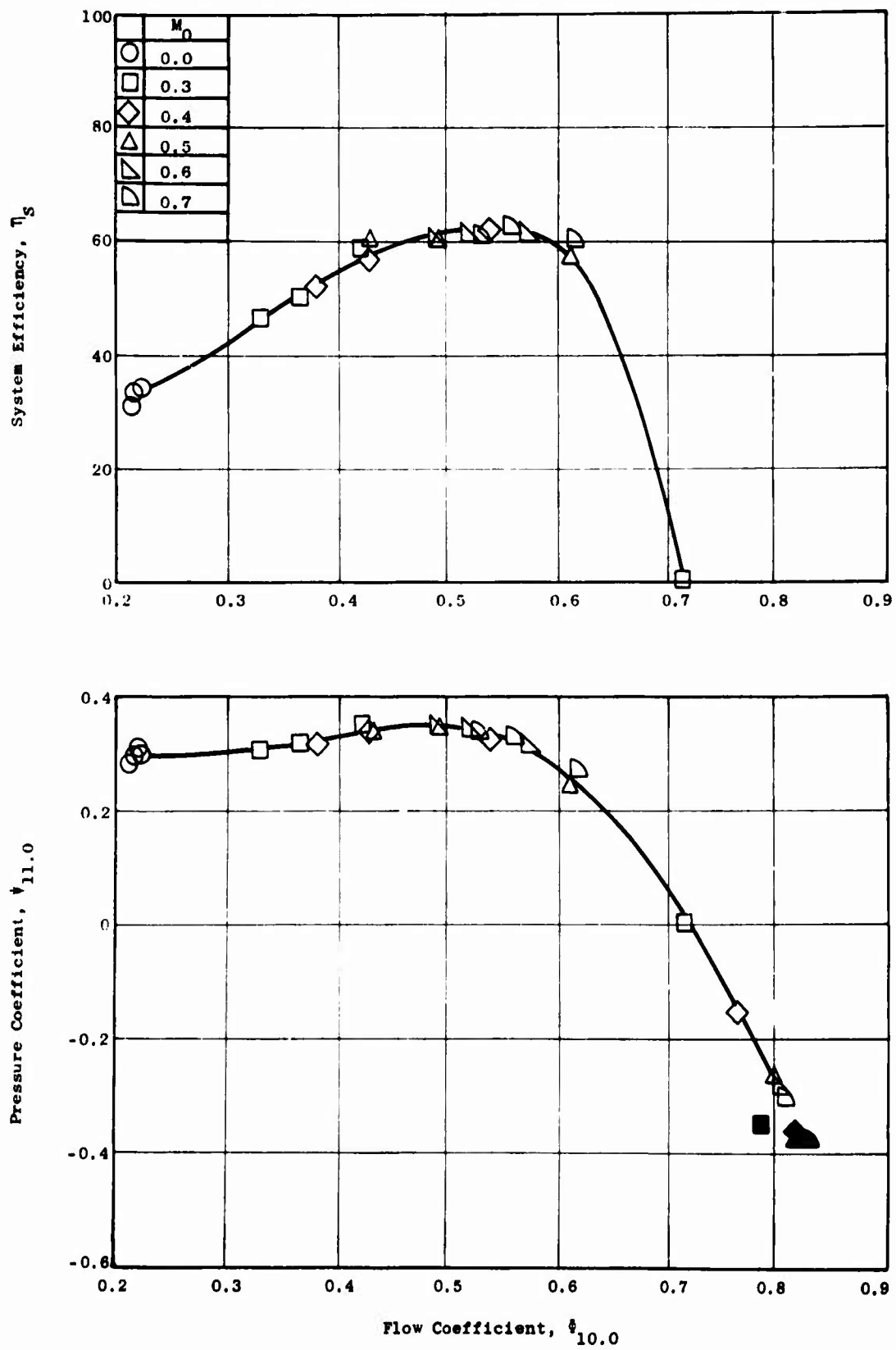


Figure 382. Fan Performance Characteristics - Model 6.

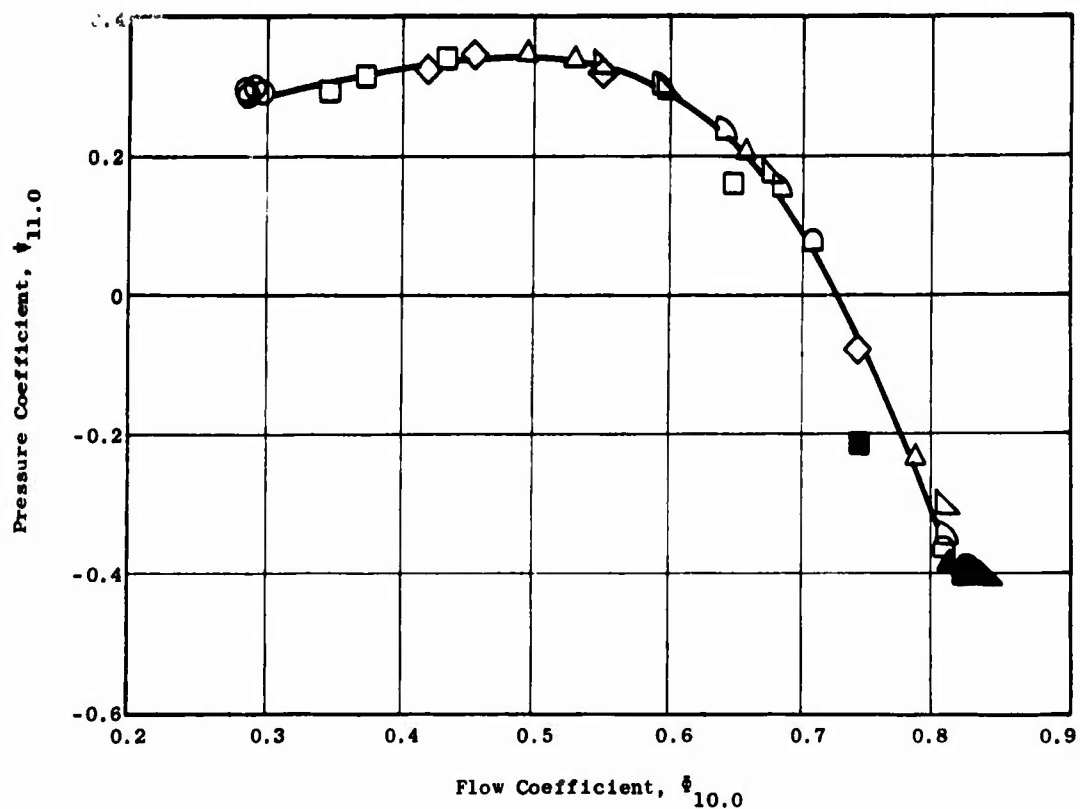
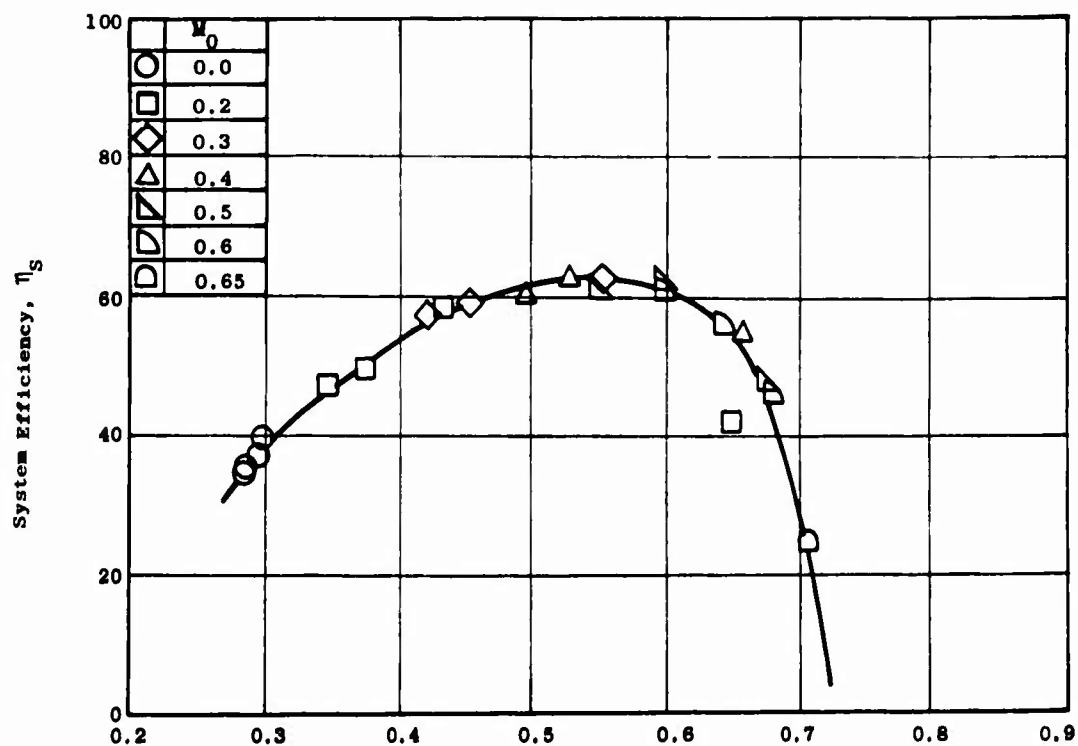


Figure 383. Fan Performance Characteristics - Model 7.

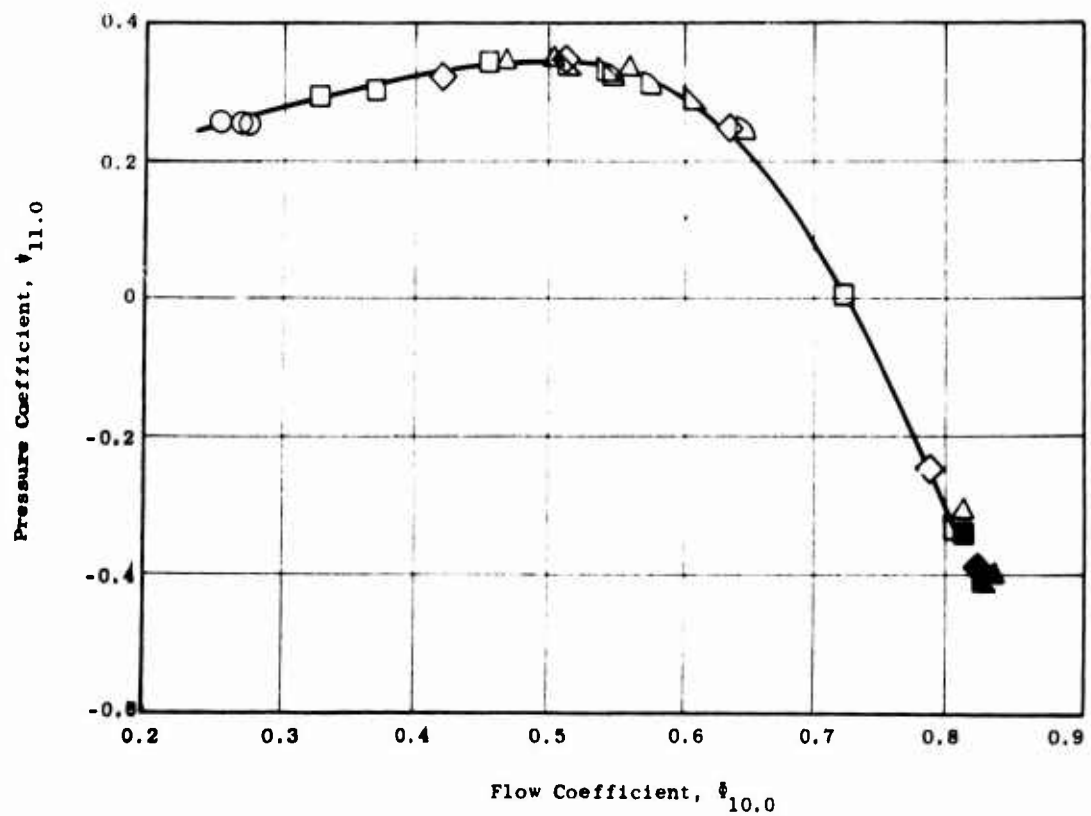
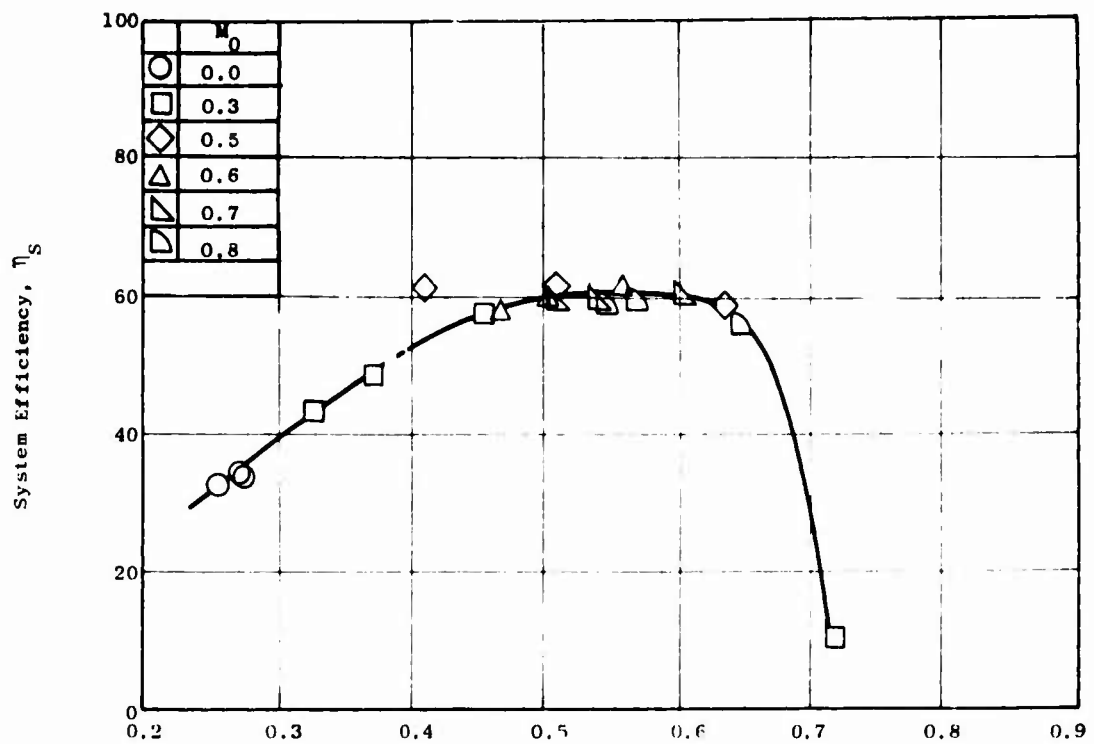


Figure 384. Fan Performance Characteristics - Model 8.

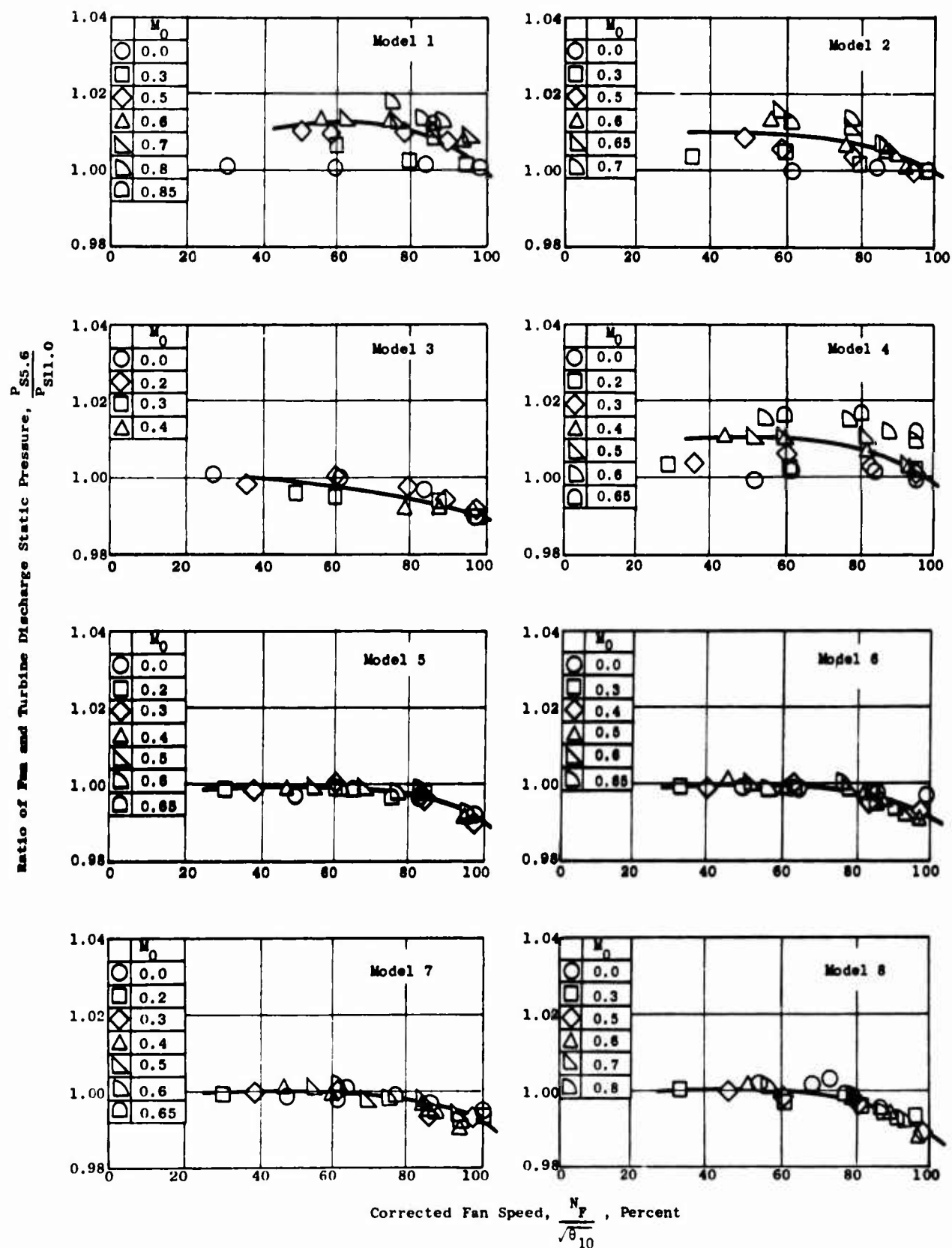


Figure 385. Variation of Fan and Fan Turbine Pressure with Fan Speed for the Eight Models.

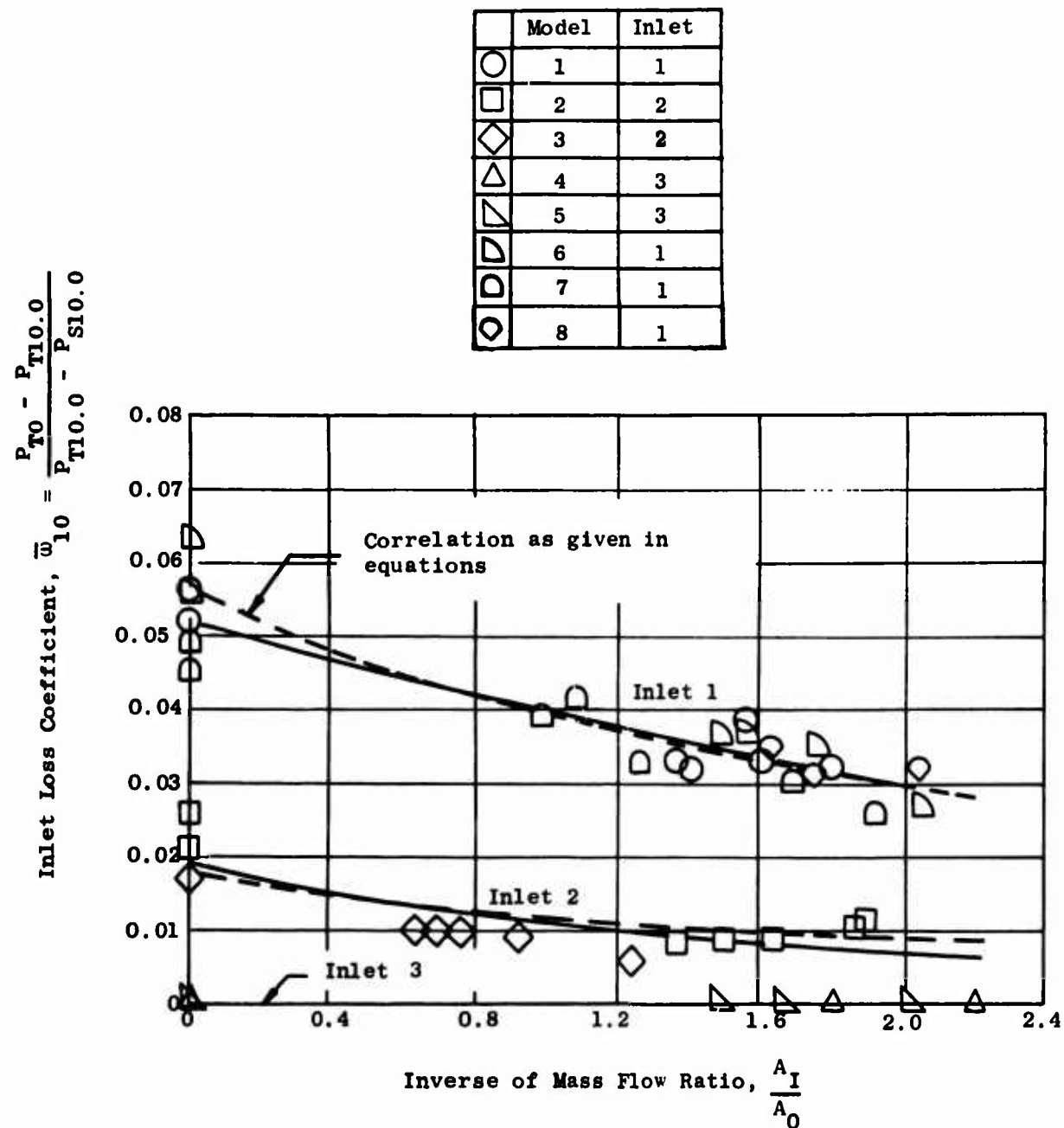


Figure 386. Variation of Fan Inlet Loss Coefficient with Mass Flow Ratio.

Inlet	Length (inches)	Throat Diameter (inches)	A_{10} or A_2 (sq. ft.)	$\frac{A_{10}}{A_{TH}}$ or $\frac{A_2}{A_{TH}}$
1	49.0	28.7	6.04	1.34
2	27.0	32.2	6.01	1.06
3	12.0	36.0	6.41	0.91
Engine	29.0	9.92	0.49	1.10

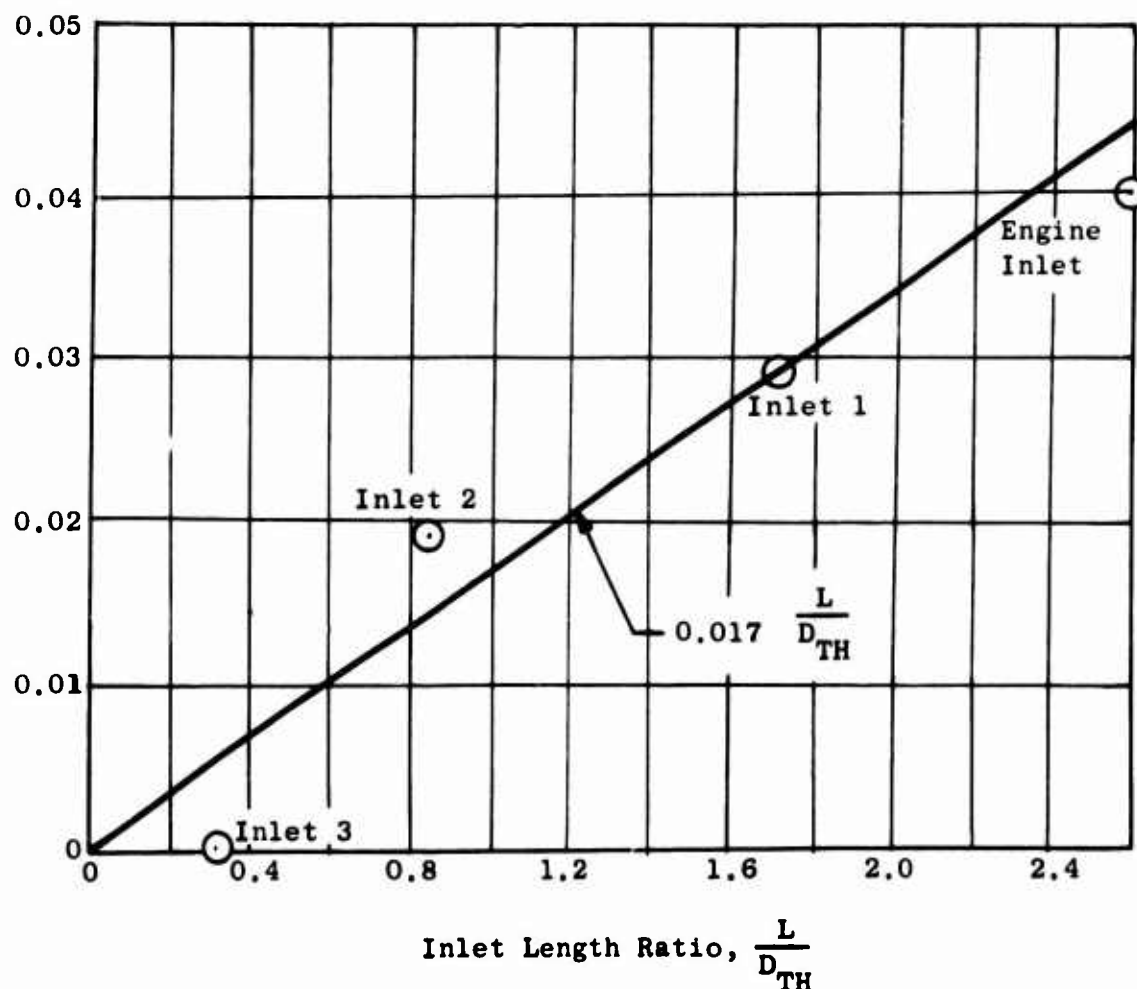


Figure 387. Variation of Static Inlet Loss Coefficient with Inlet Length to Diameter Ratio.

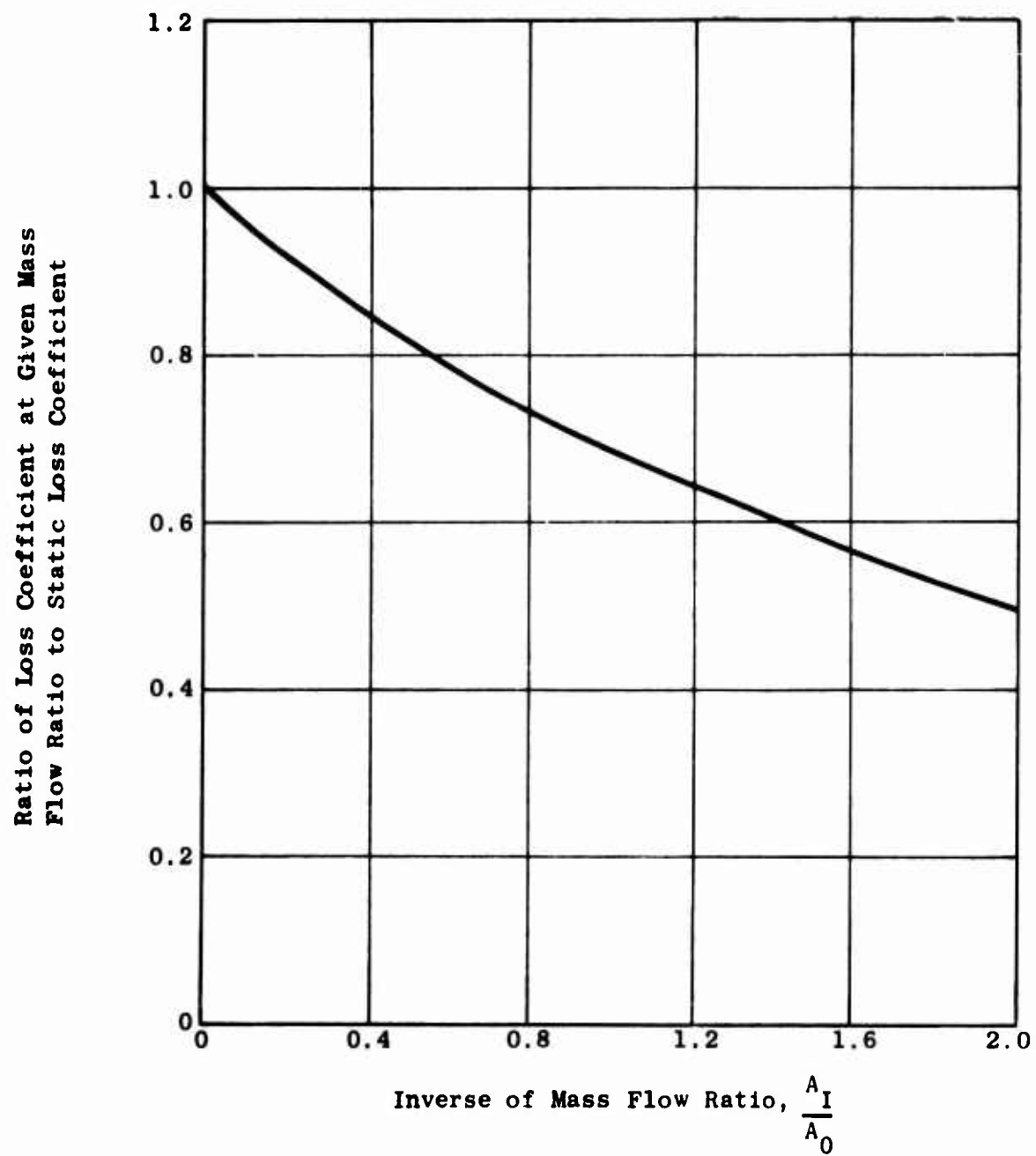


Figure 388. Correlation of Effects of Mass Flow Ratio on Inlet Loss Coefficients.

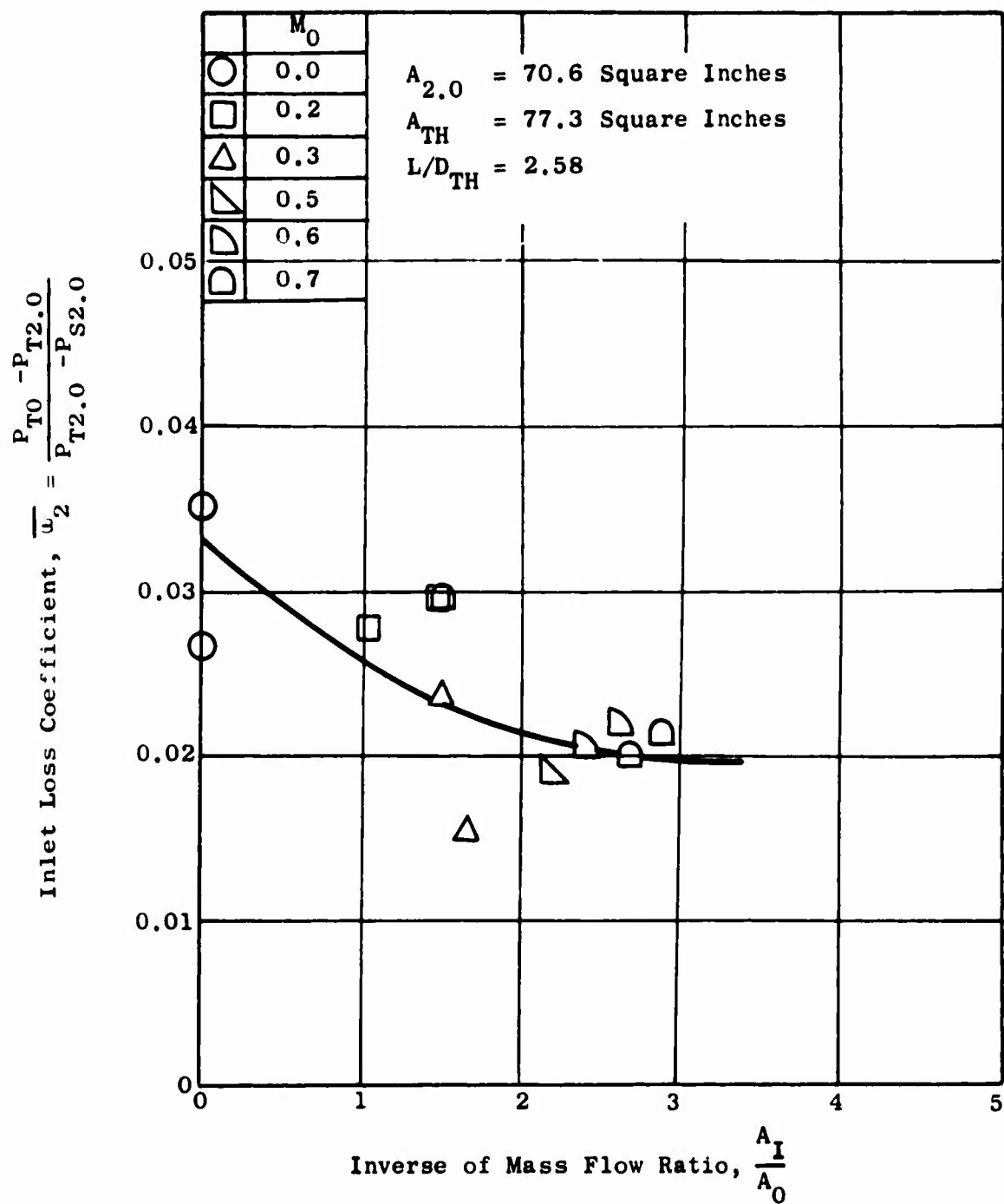


Figure 389. Variation of Engine Inlet Loss Coefficient with Mass Flow Ratio.

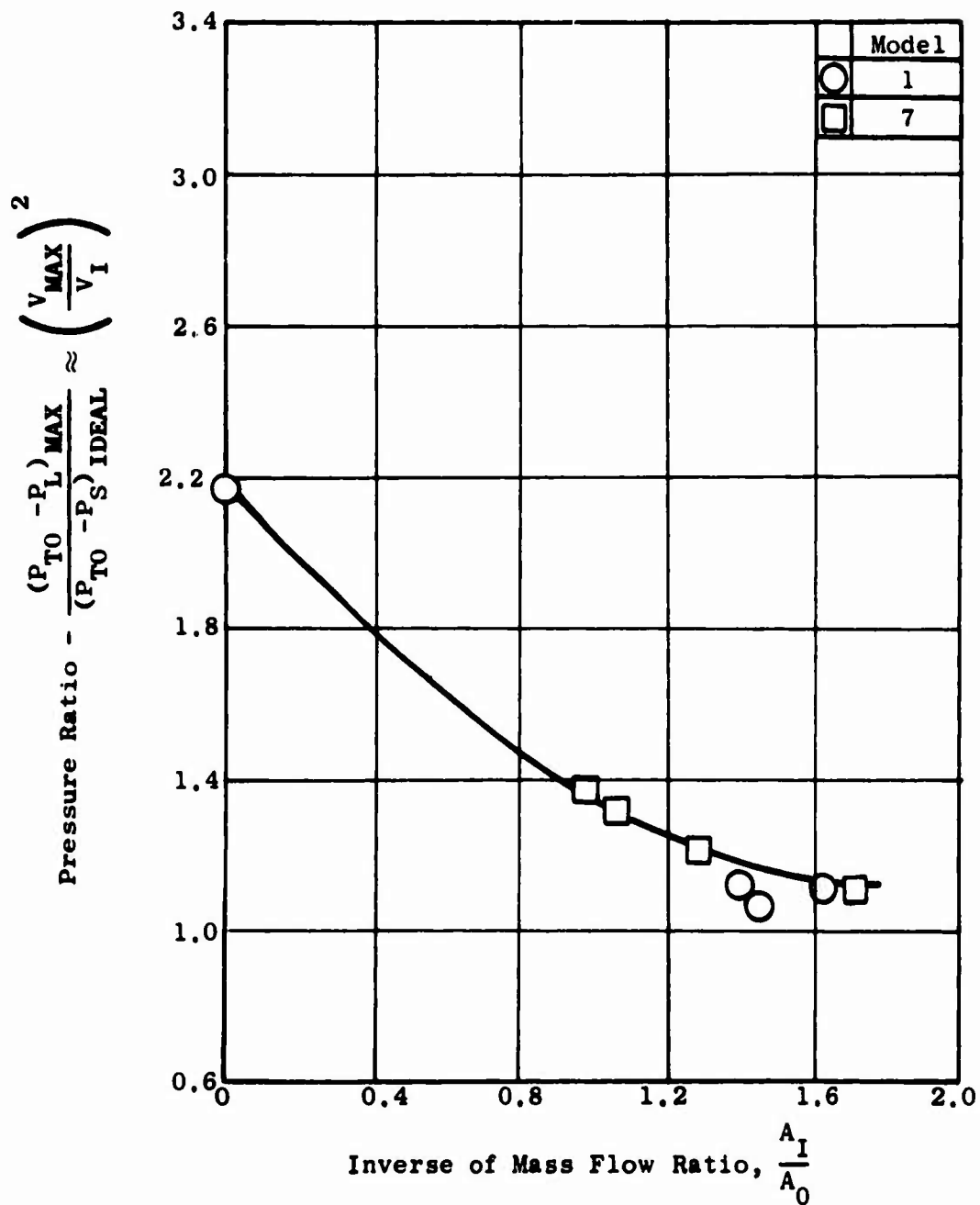


Figure 390. Effects of Mass Flow Ratio on Inlet Maximum Internal Velocity - Inlet 1.

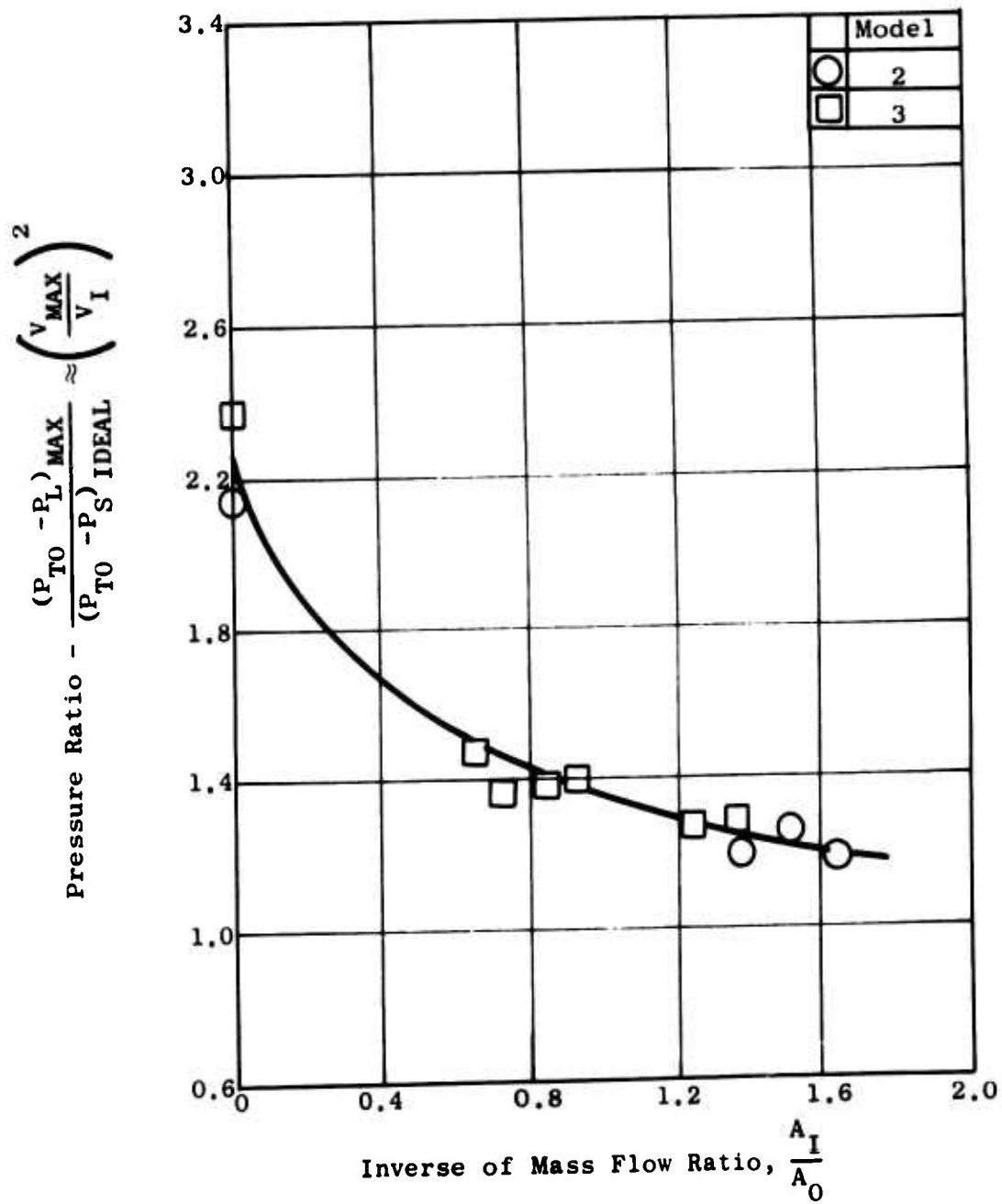


Figure 391. Effects of Mass Flow Ratio on Inlet Maximum Internal Velocity - Inlet 2.

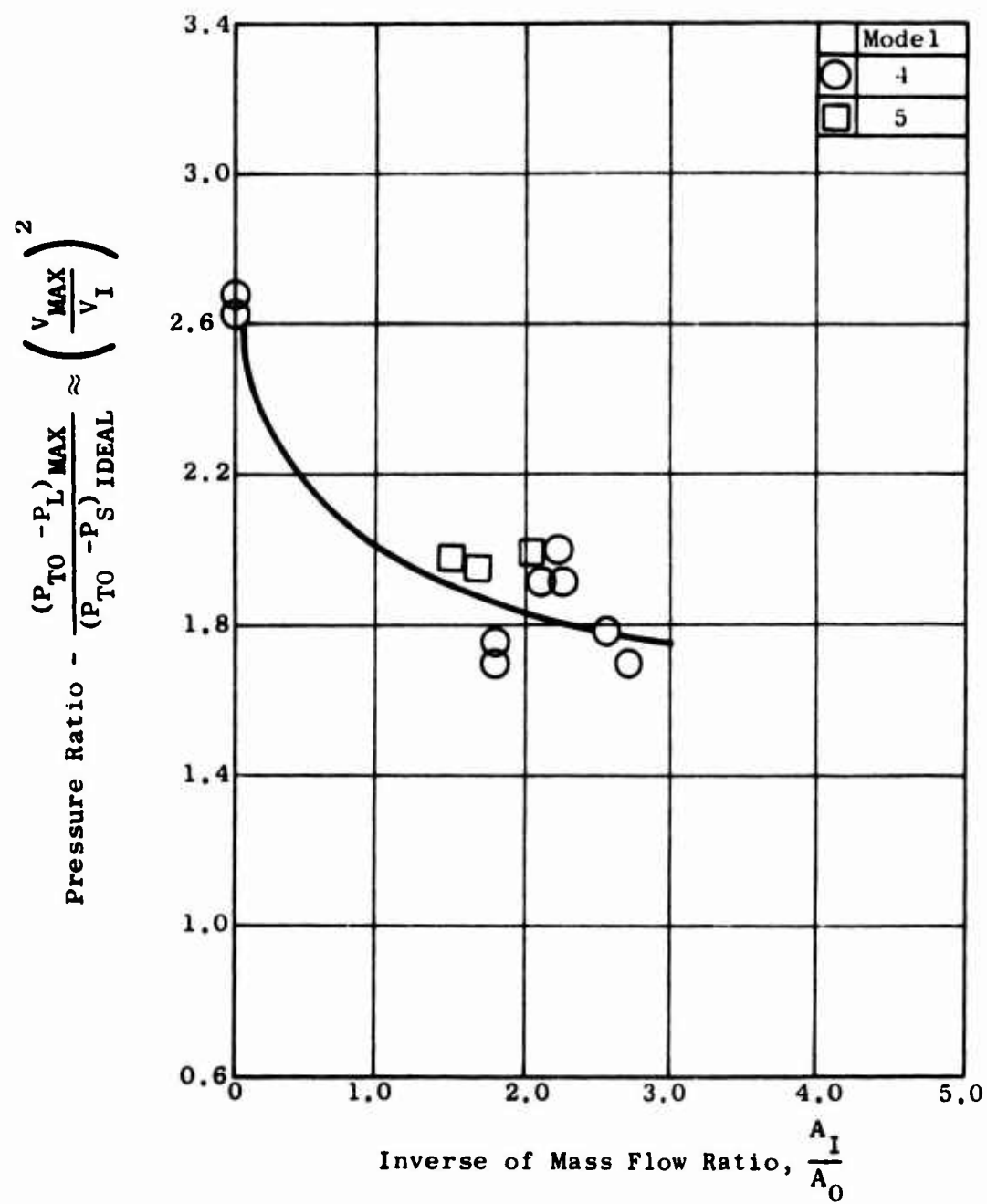


Figure 392. Effects of Mass Flow Ratio on Inlet Maximum Internal Velocity - Inlet 3.

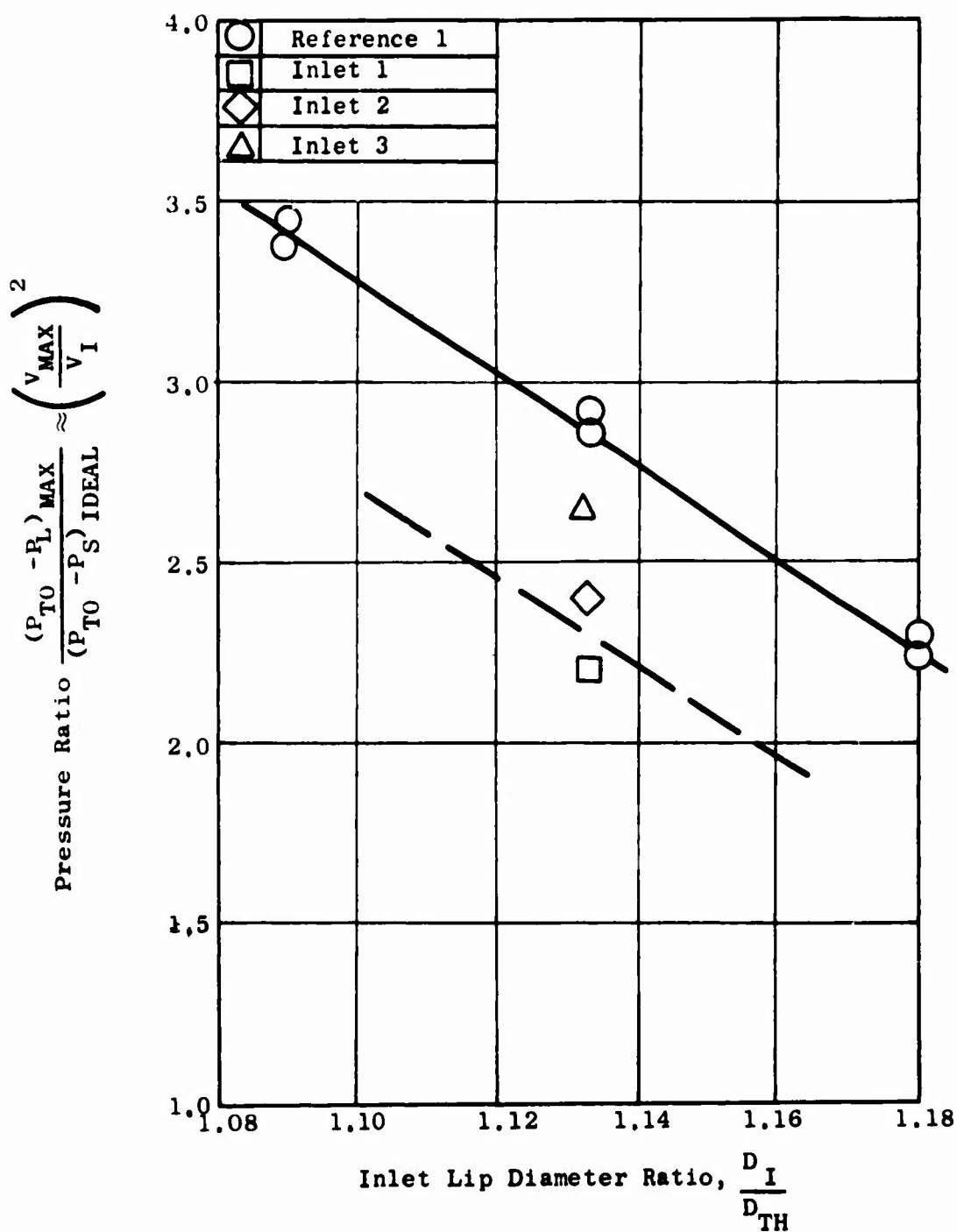


Figure 393. Effects of Inlet Internal Lip Radius on Maximum Surface Velocity at Static ($M_0 = 0.0$) Conditions.

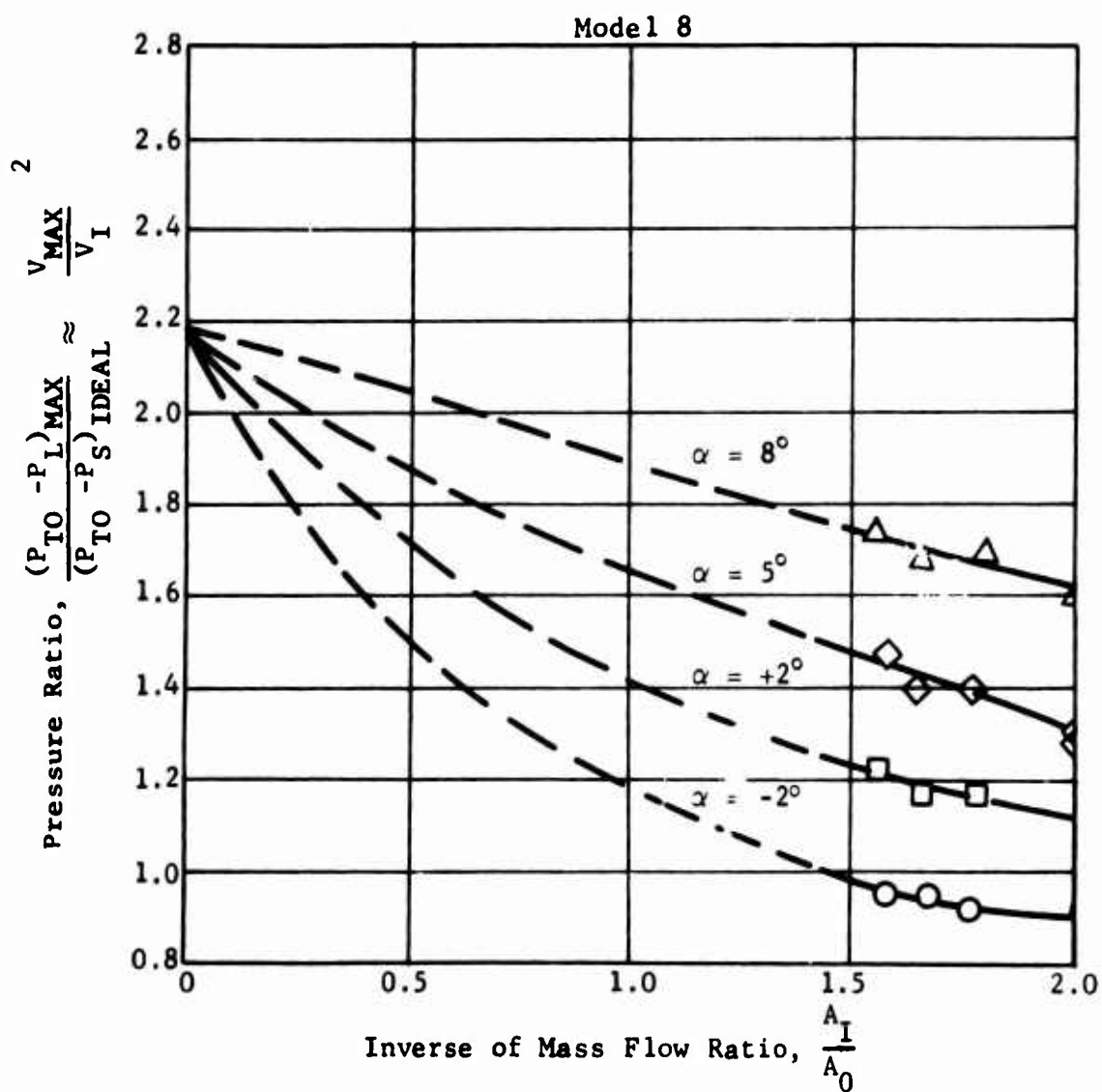


Figure 394. Variation of Inlet Lip Maximum Velocity with Angle of Attack.

Peak Local Pressure Coefficient, $(C_p)_{\text{MIN}}$

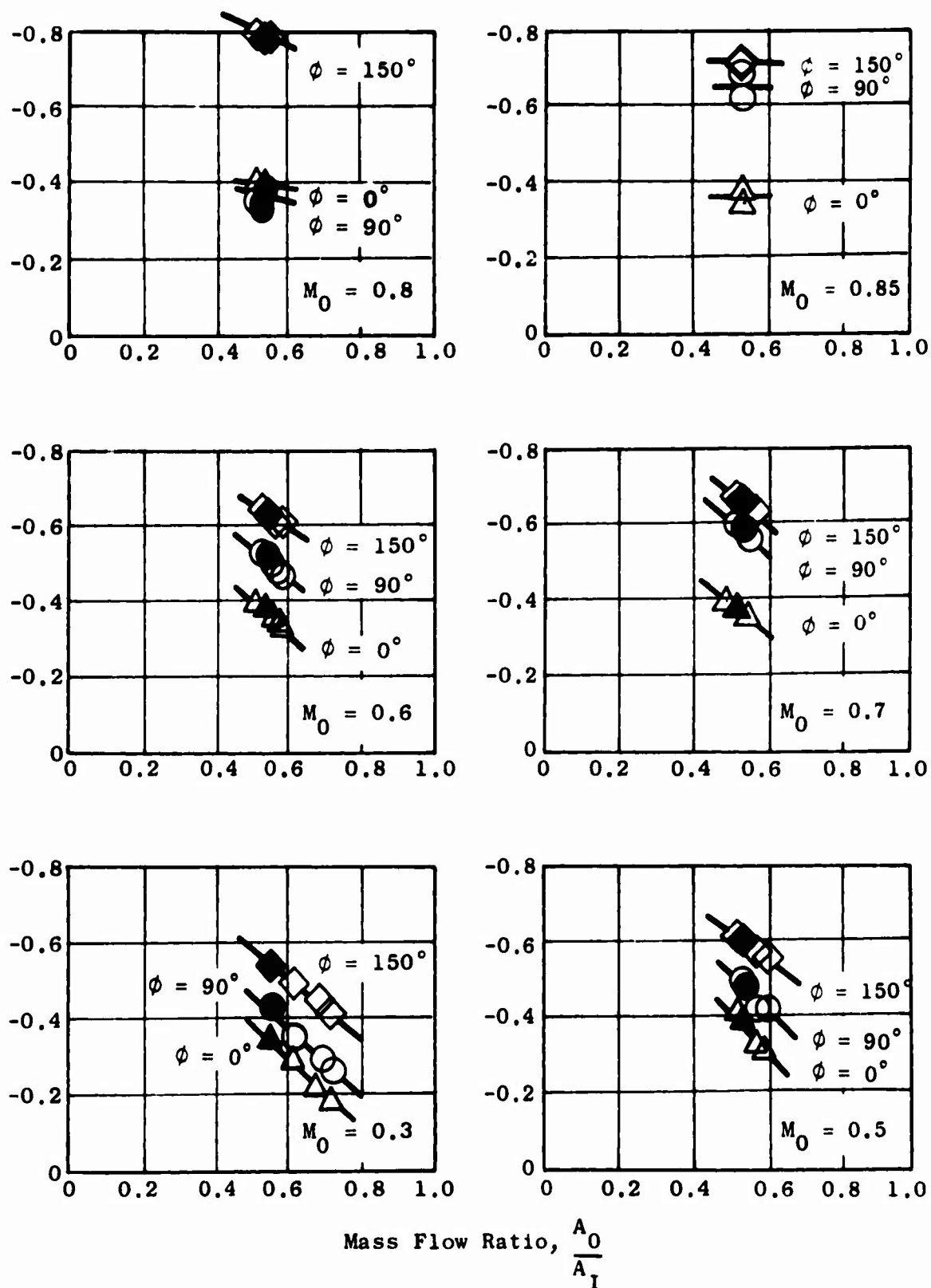


Figure 395. Variation of Peak External Pressure Coefficient with Mach Number and Mass Flow Ratio for Model 1 (Inlet 1).

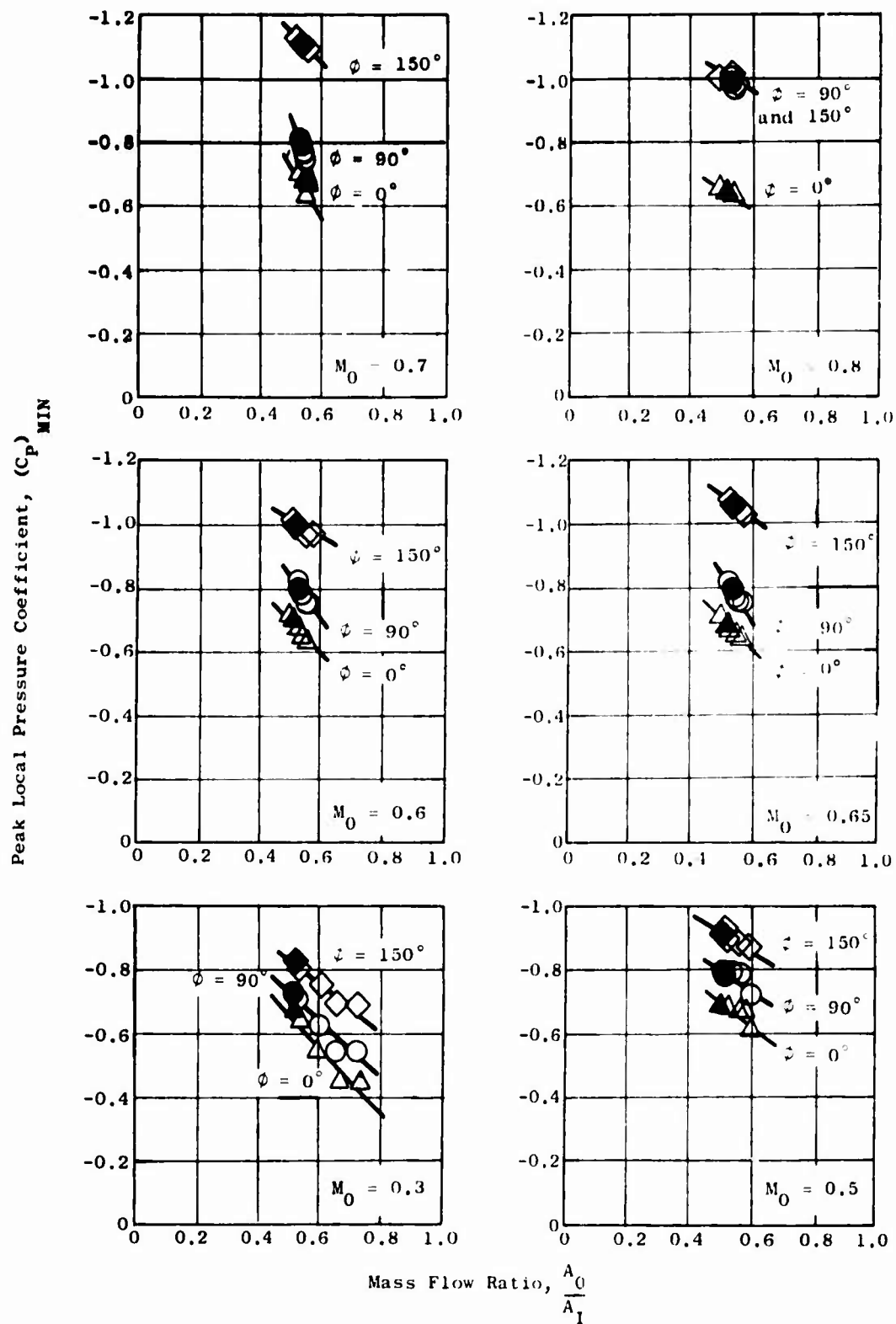
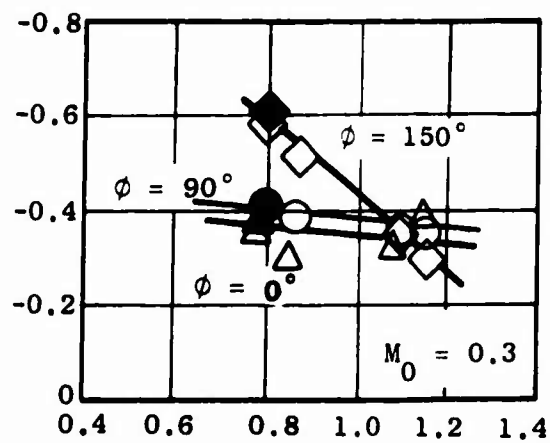
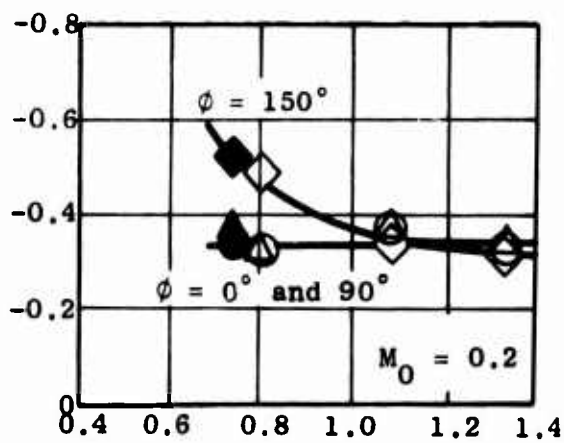
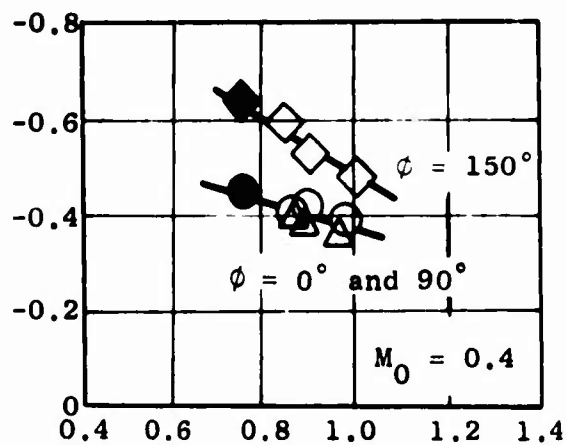


Figure 396. Variation of Peak External Pressure Coefficient with Mach Number and Mass Flow Ratio for Model 2 (Inlet 2).

Peak Local Pressure Coefficient, $(C_p)_{\text{MIN}}$



Mass Flow Ratio, $\frac{A_0}{A_1}$

Figure 397. Variation of Peak External Pressure Coefficient with Mach Number and Mass Flow Ratio for Model 3 (Inlet 2).

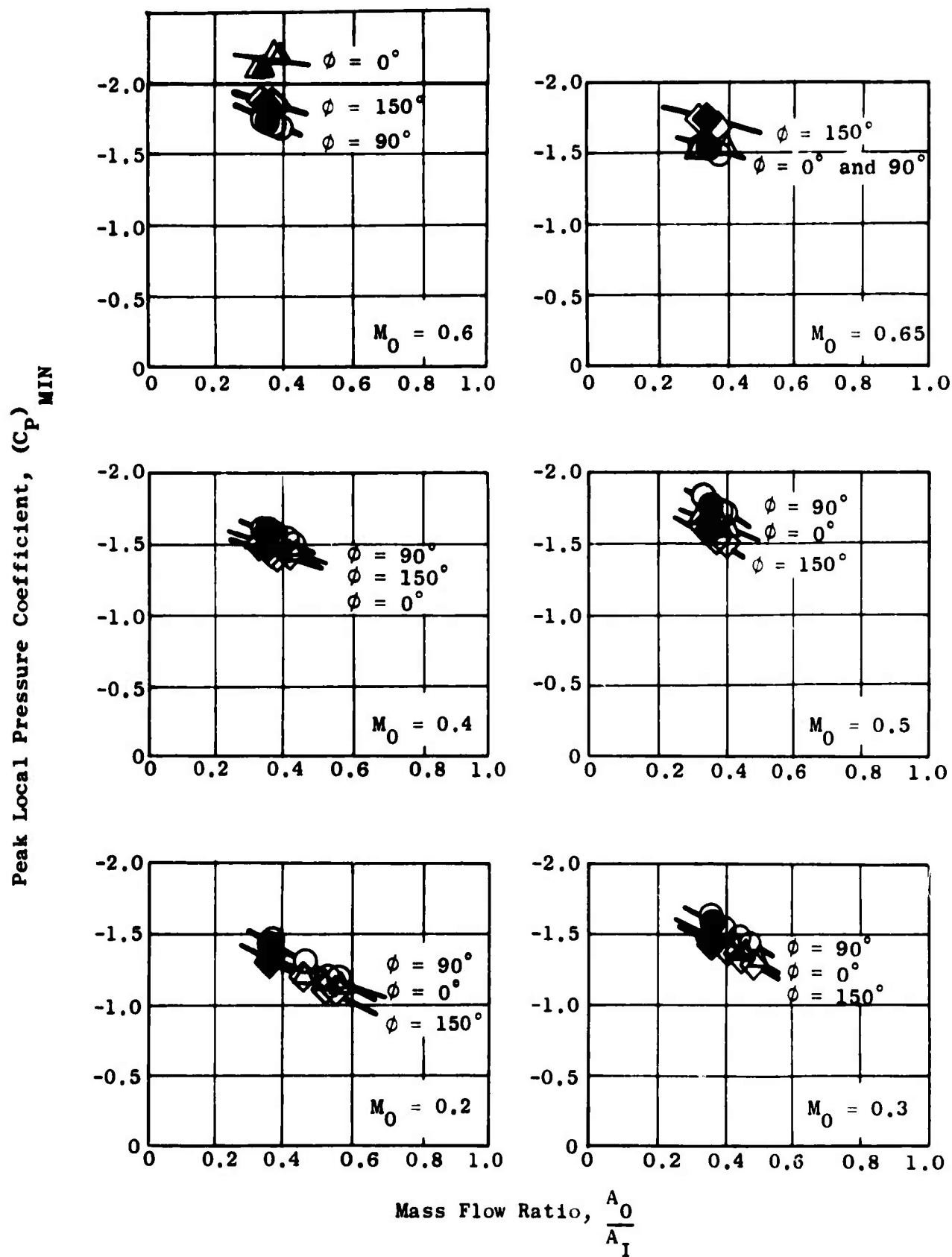


Figure 398. Variation of Peak External Pressure Coefficient with Mach Number and Mass Flow Ratio for Model 4 (Inlet 3).

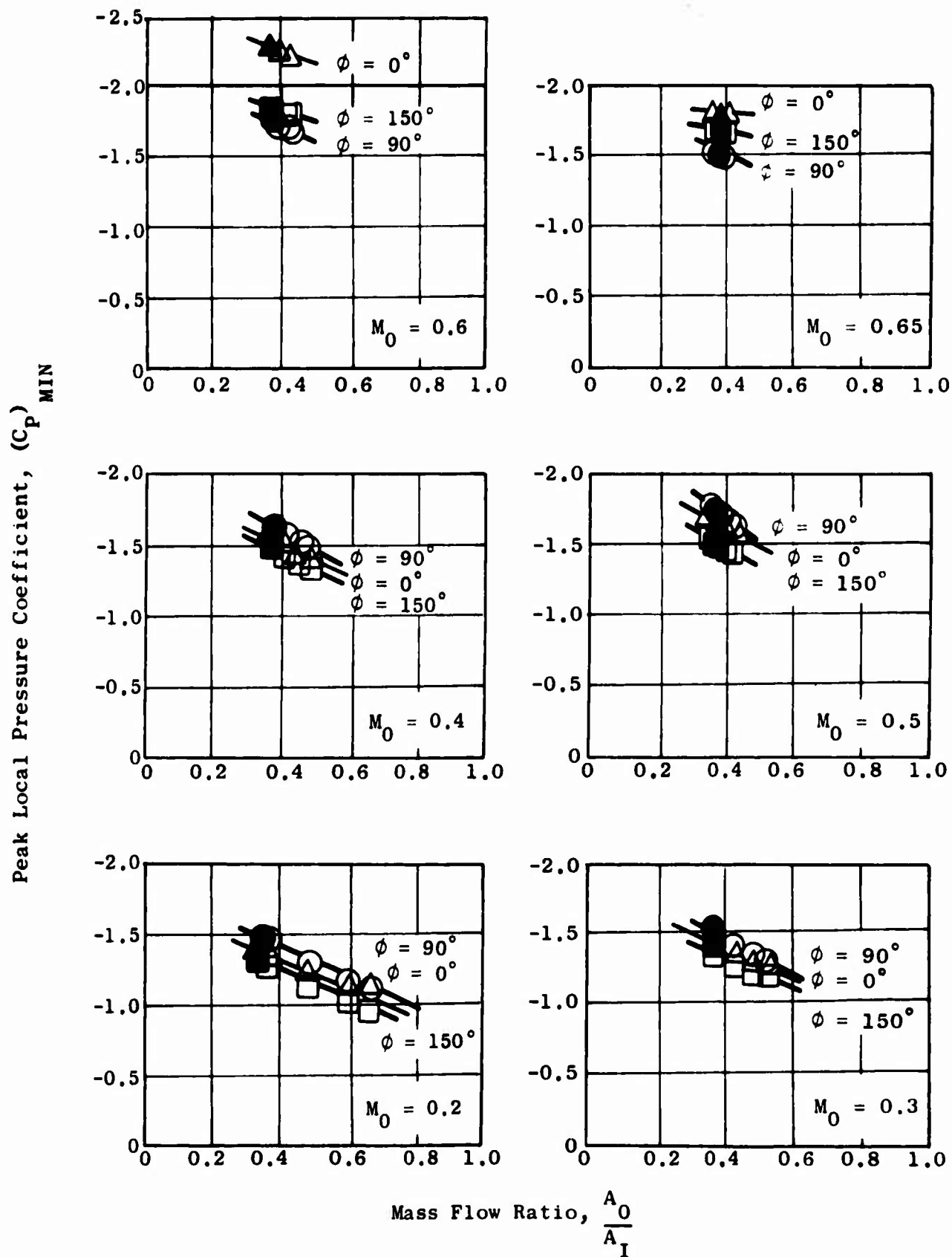


Figure 399. Variation of Peak External Pressure Coefficient with Mach Number and Mass Flow Ratio for Model 5 (Inlet 3).

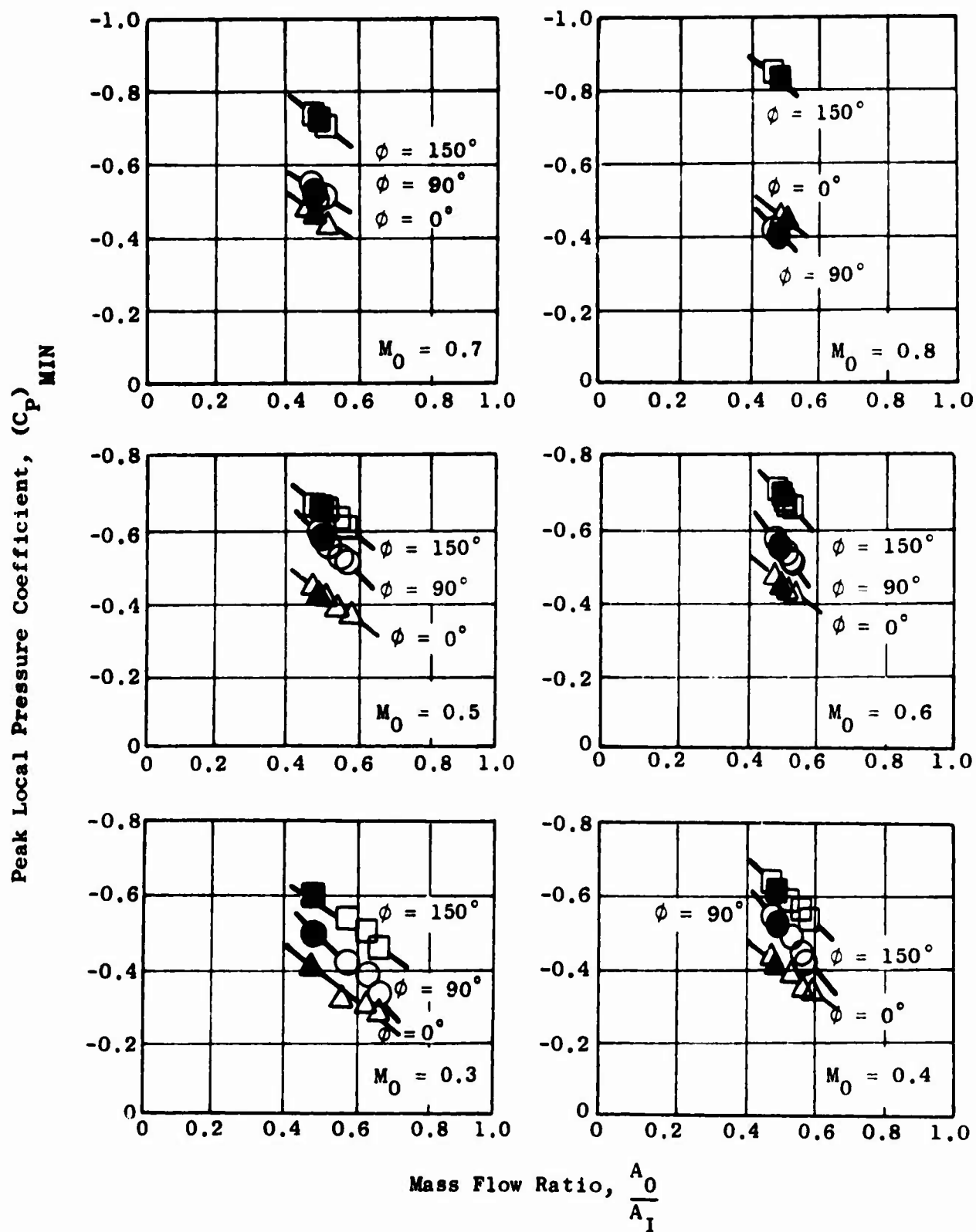


Figure 400. Variation of Peak External Pressure Coefficient with Mach Number and Mass Flow Ratio for Model 6 (Inlet 1).

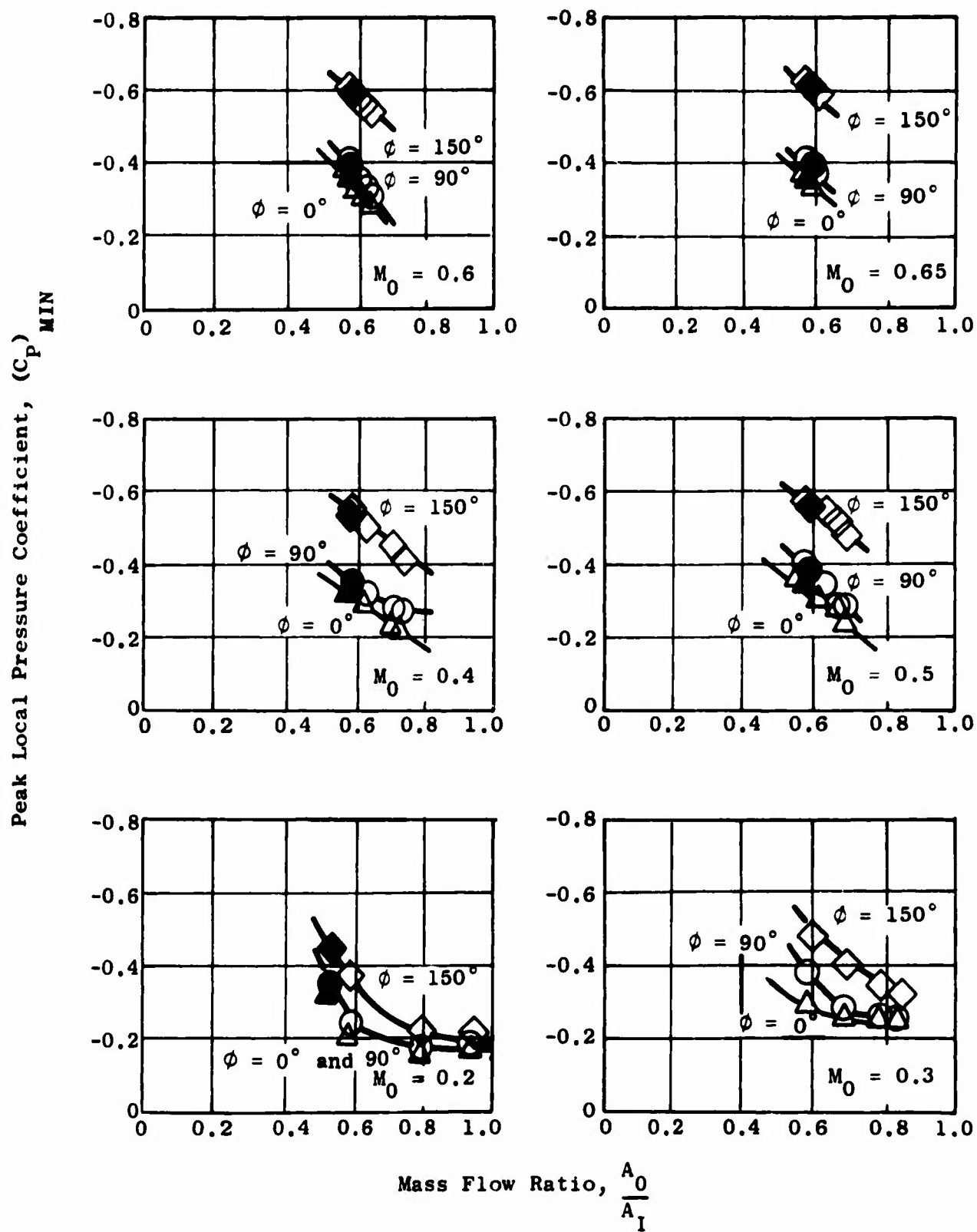


Figure 401. Variation of Peak External Pressure Coefficient with Mach Number and Mass Flow Ratio for Model 7 (Inlet 1).

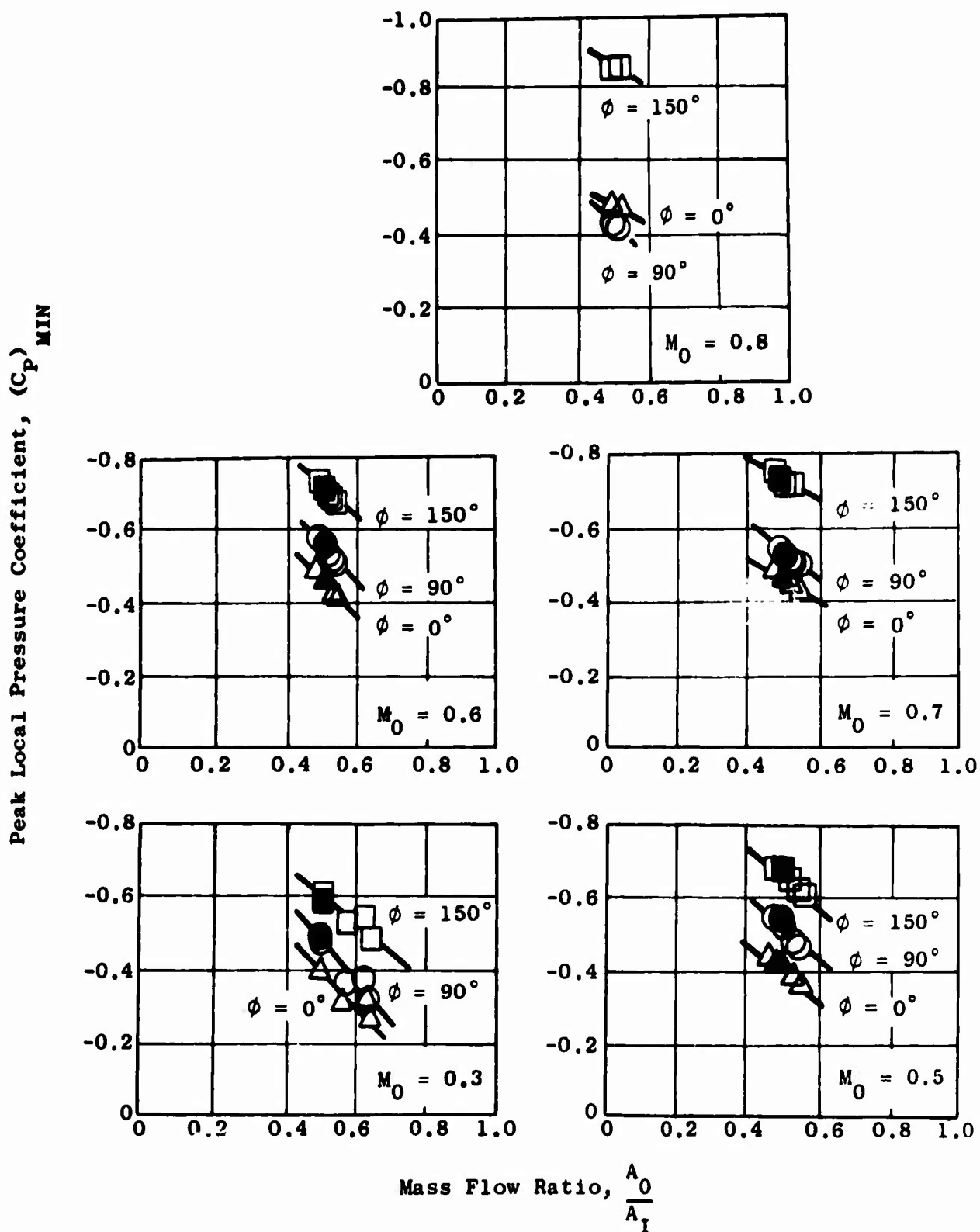


Figure 402. Variation of Peak External Pressure Coefficient with Mach Number and Mass Flow Ratio for Model 8 (Inlet 1).

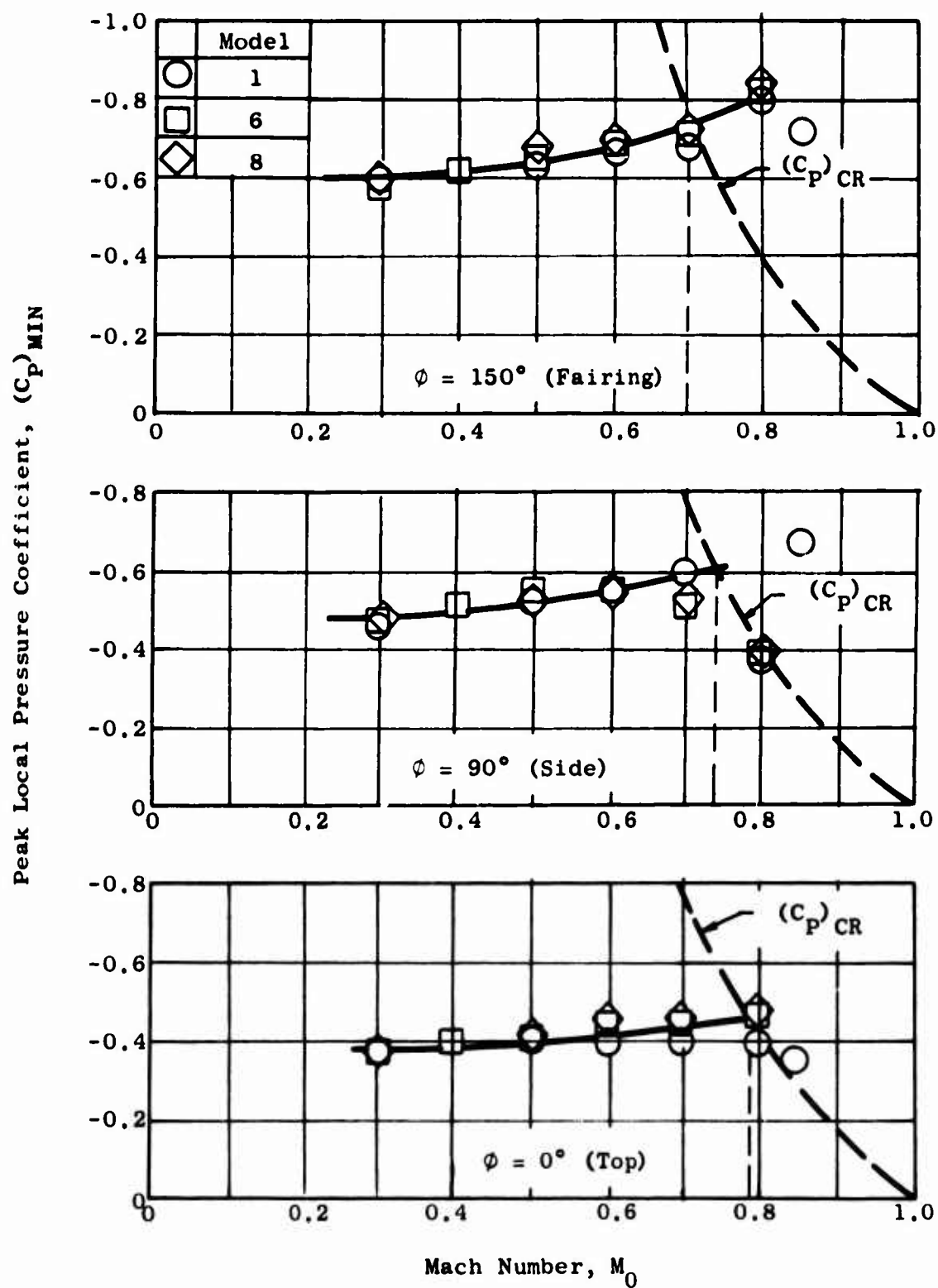


Figure 403. Variation of Peak External Pressure Coefficient with Mach Number for Inlet 1 at a Mass Flow Ratio of 0.5.

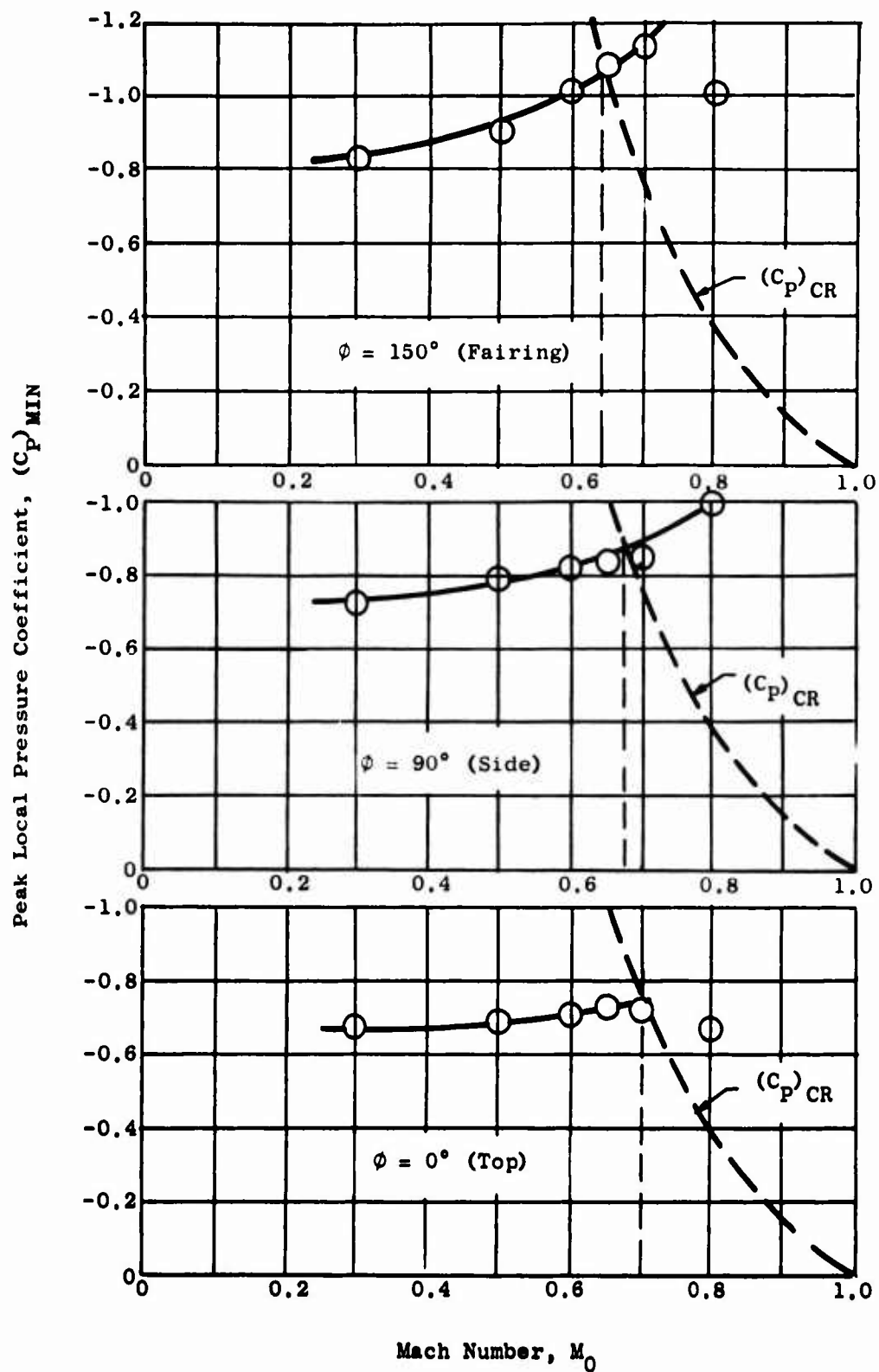


Figure 404. Variation of Peak External Pressure Coefficient with Mach Number for Inlet 2 at a Mass Flow Ratio of 0.50.

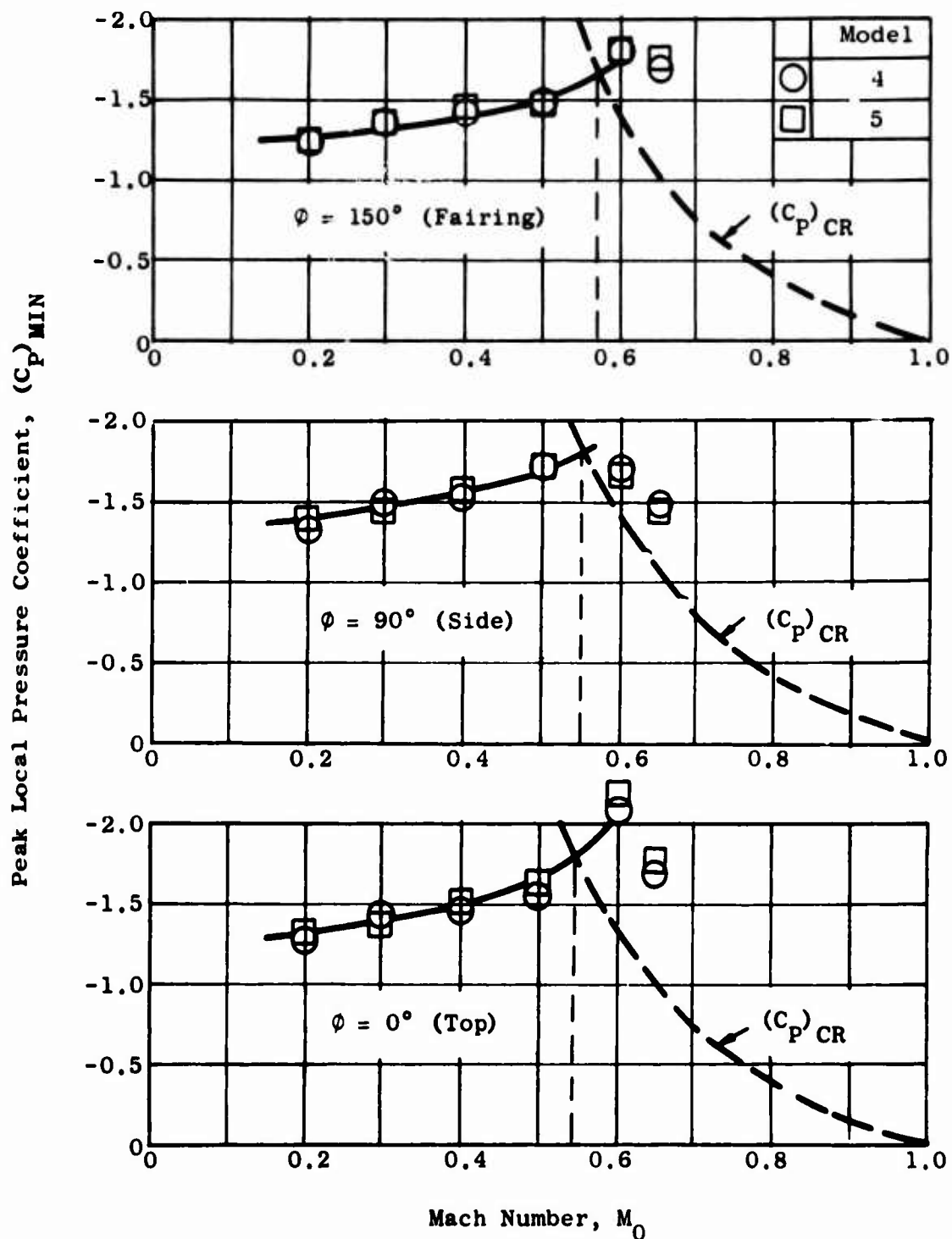


Figure 405. Variation of Peak External Pressure Coefficient with Mach Number for Inlet 3 at a Mass Flow Ratio of 0.4.

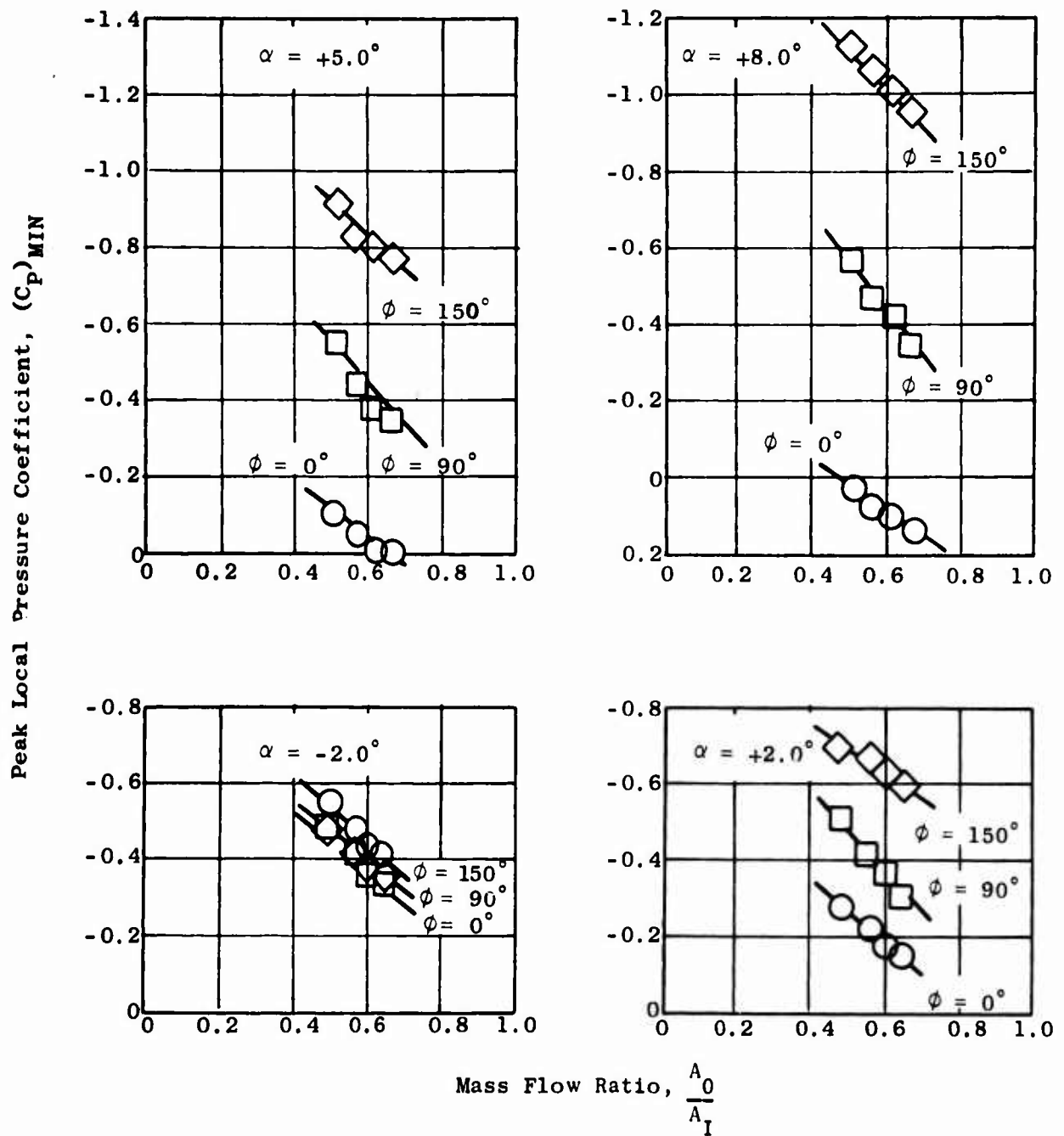


Figure 406. Variation of Peak External Pressure Coefficient on Inlet Leading Edge with Angle of Attack at a Mach Number of 0.30.

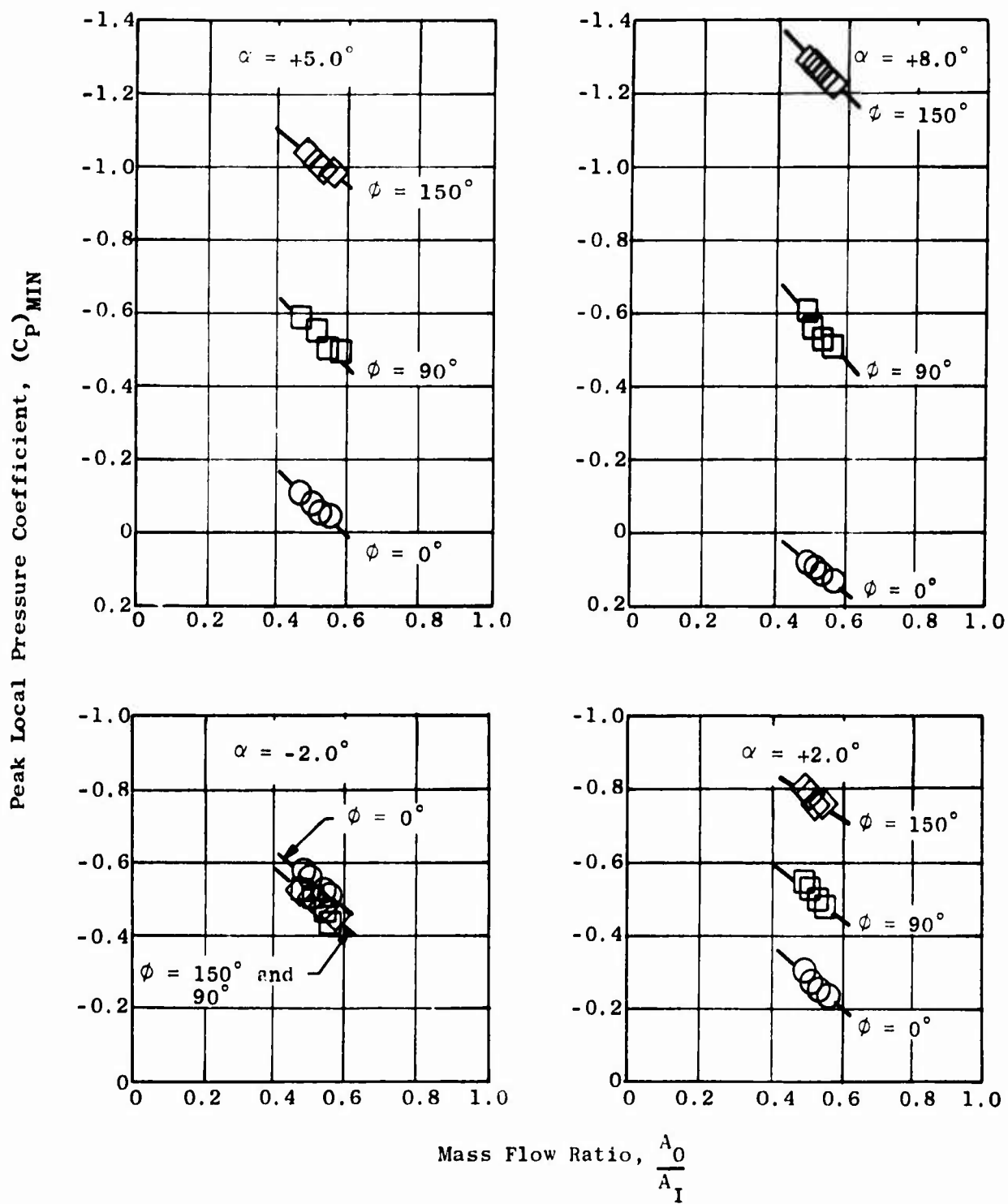


Figure 407. Variation of Peak External Pressure Coefficient on Inlet Leading Edge with Angle of Attack at a Mach Number of 0.50.

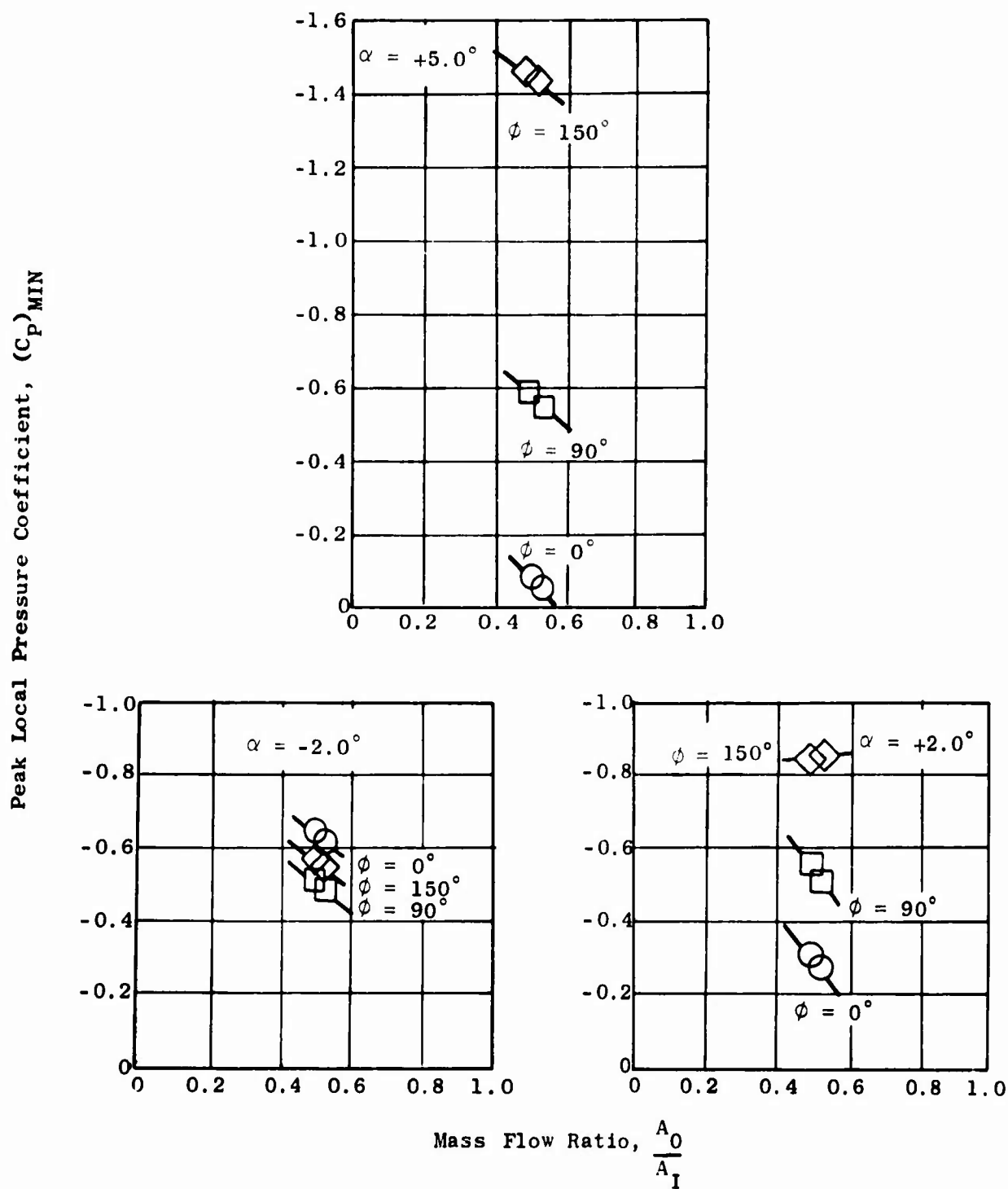


Figure 408. Variation of Peak External Pressure Coefficient on Inlet Leading Edge with Angle of Attack at a Mach Number of 0.70.

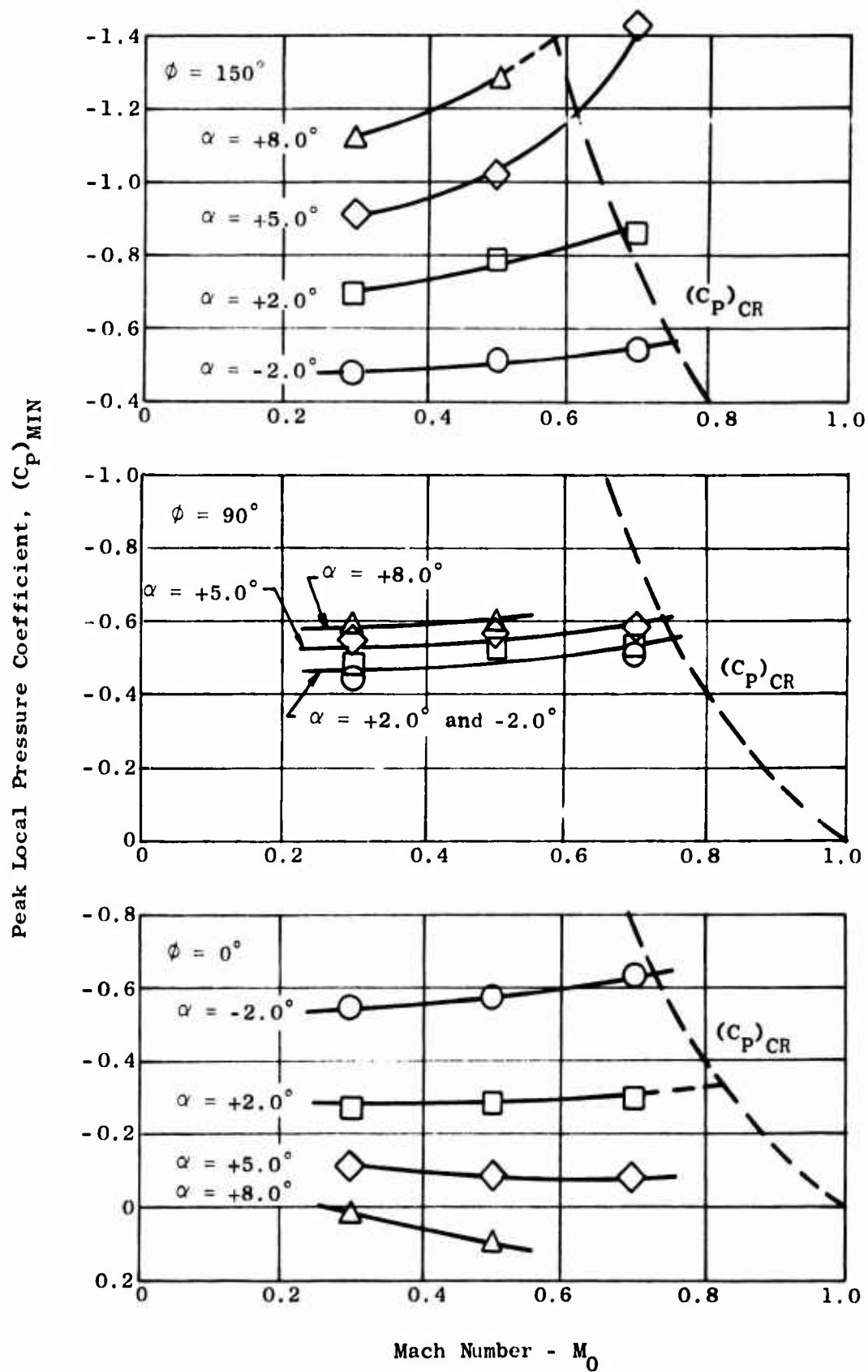


Figure 409. Effects of Angle of Attack on Peak External Pressure Coefficient at a Mass Flow Ratio of 0.50.

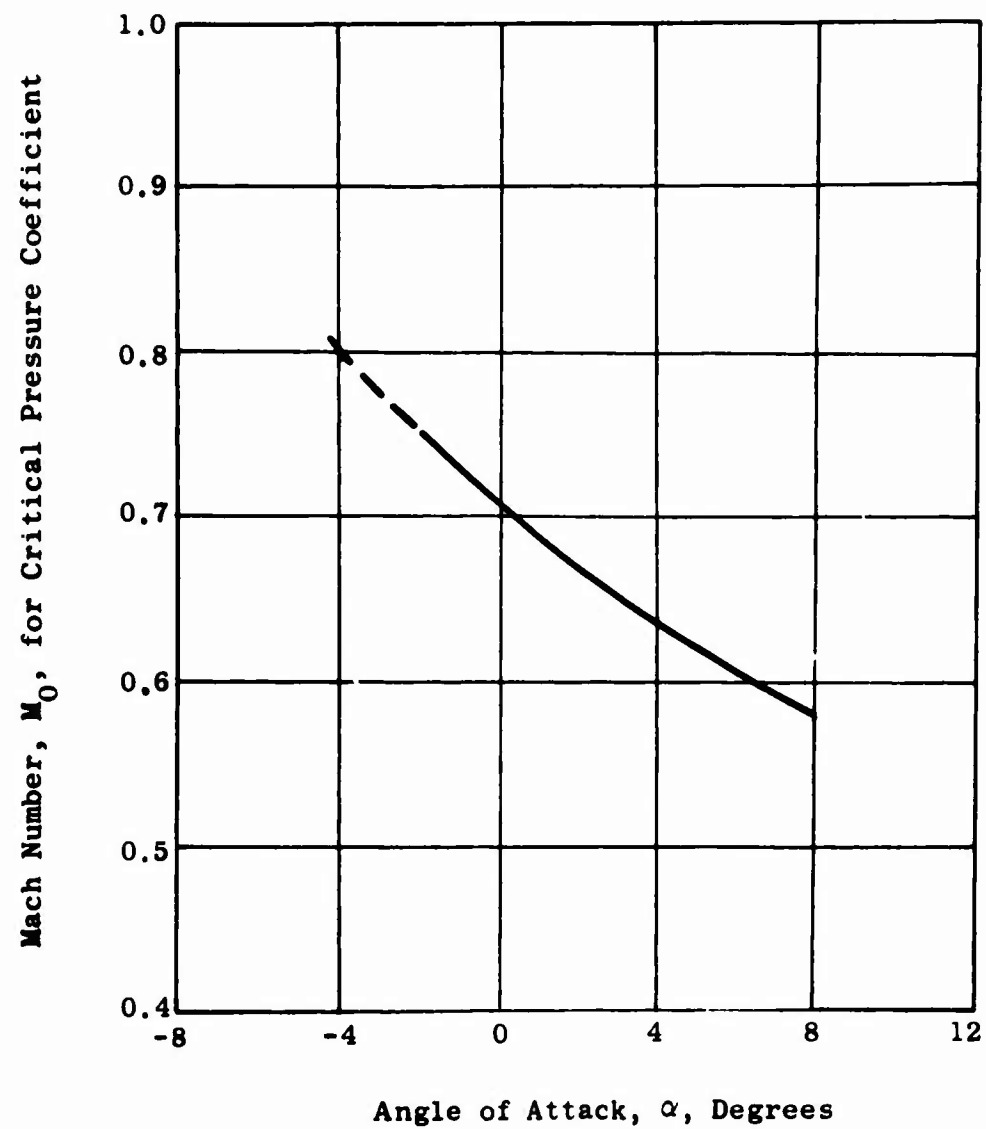


Figure 410. Effects of Angle of Attack on Free-Stream Mach Number for Critical Flow in Area of Fairing - Model 8.

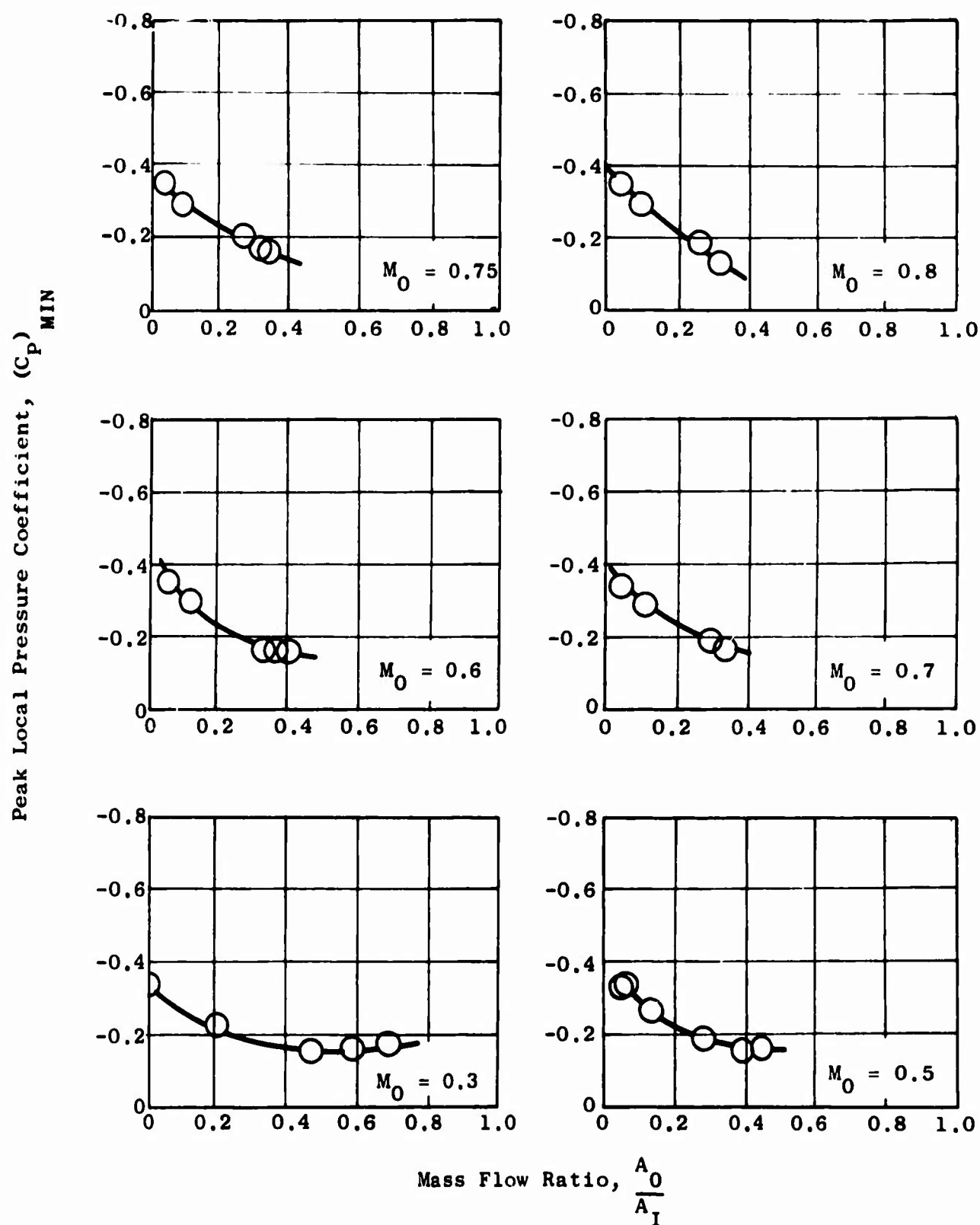


Figure 411. Variation of Peak External Pressure Coefficient with Mach Number and Mass Flow for Engine Nacelle - 0° Plane.

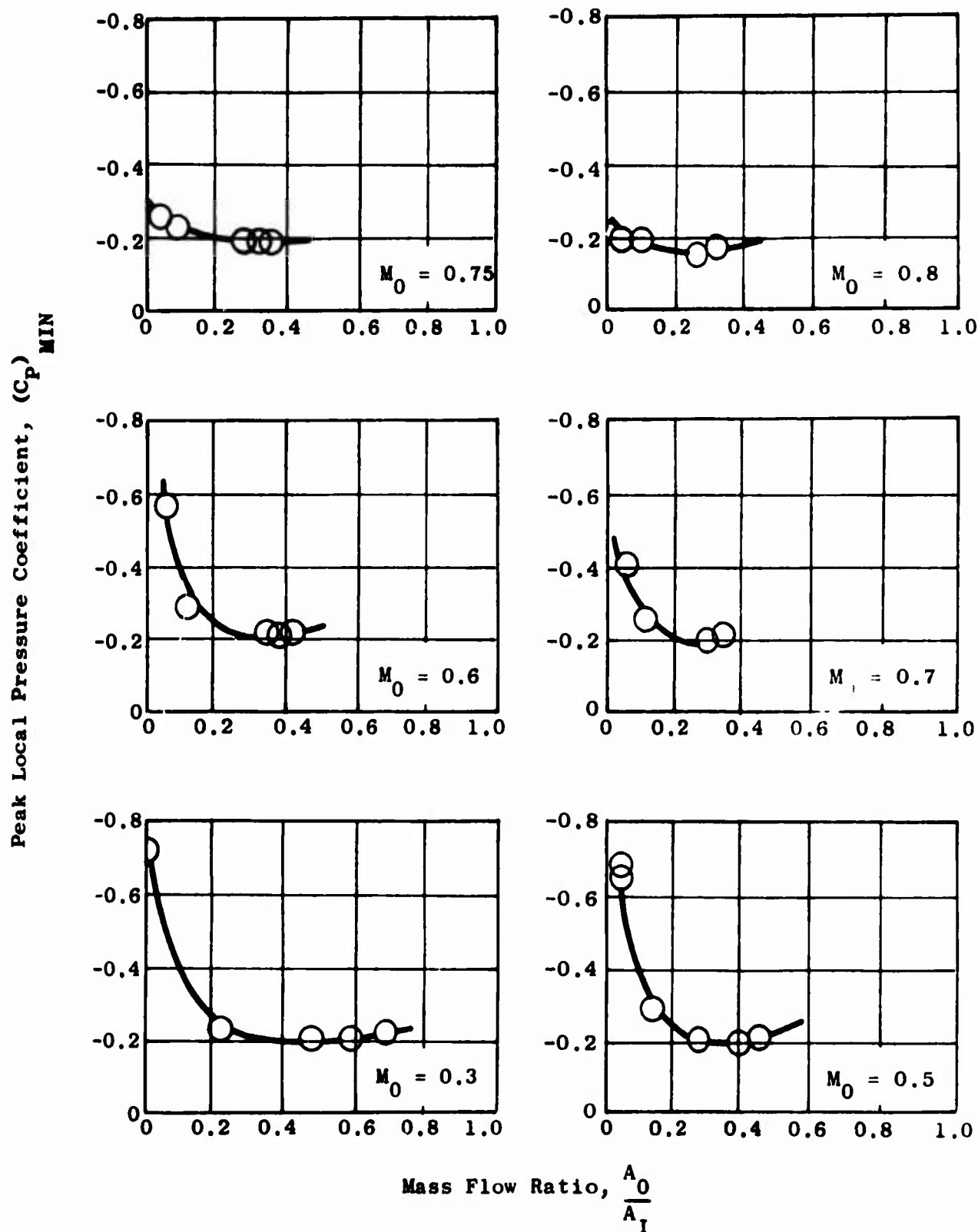


Figure 412. Variation of Peak External Pressure Coefficient with Mach Number and Mass Flow Ratio for Engine Nacelle - 180° Plane.

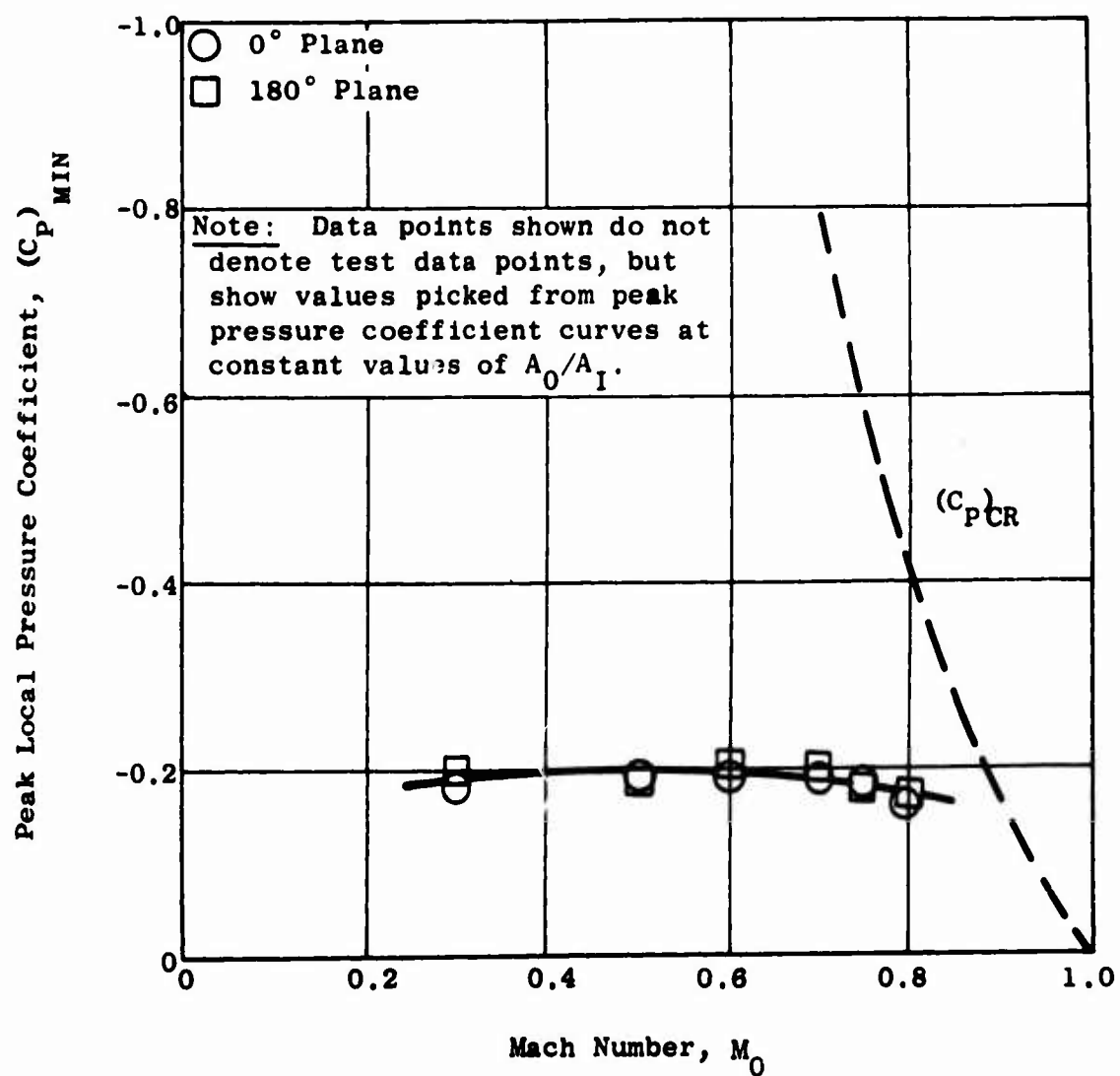


Figure 413. Variation of Engine Nacelle Peak External Pressure Coefficient with Mach Number at a Mass Flow Ratio of 0.32.

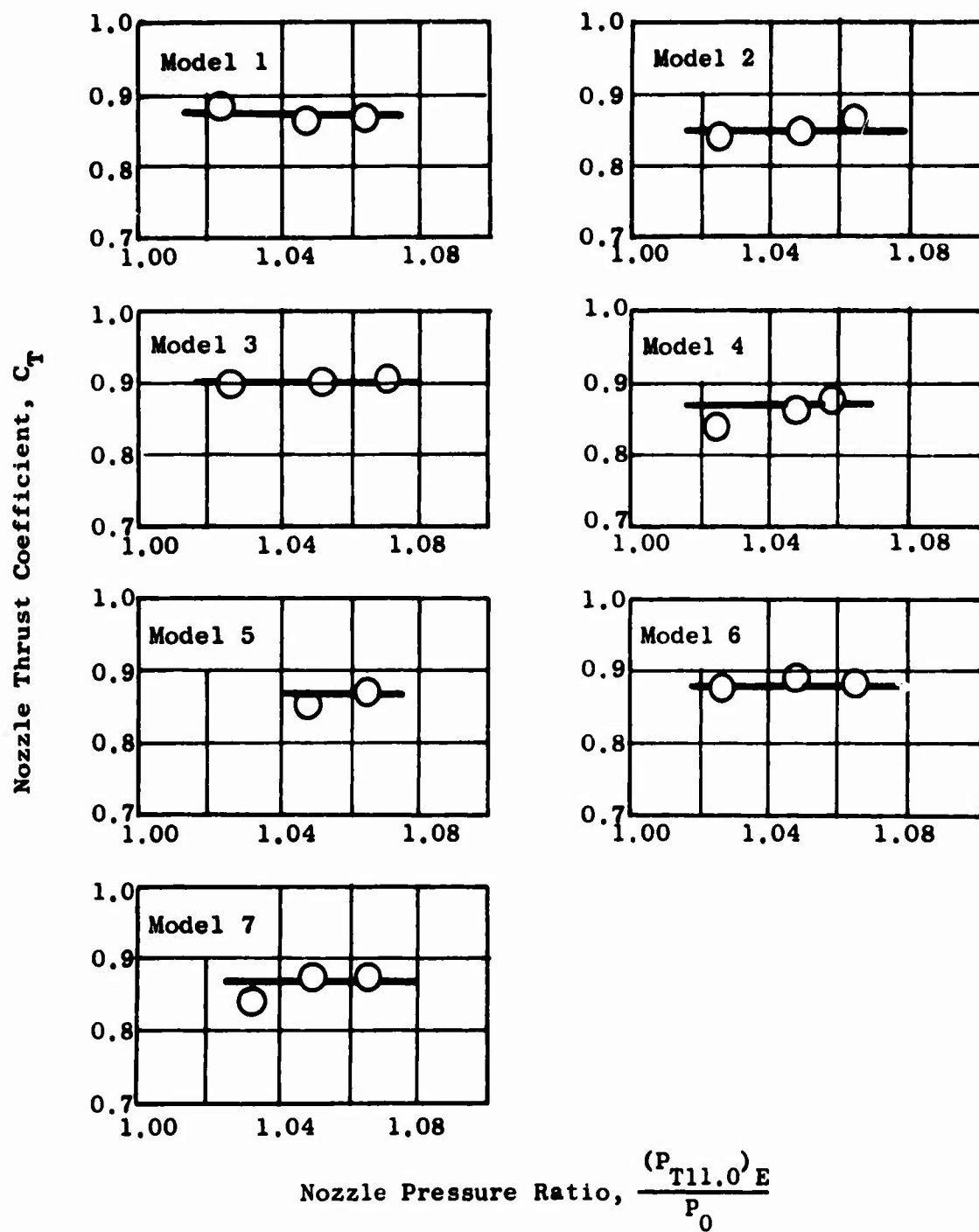


Figure 414. Nozzle Static Thrust Coefficients Based on Force Balance Data.

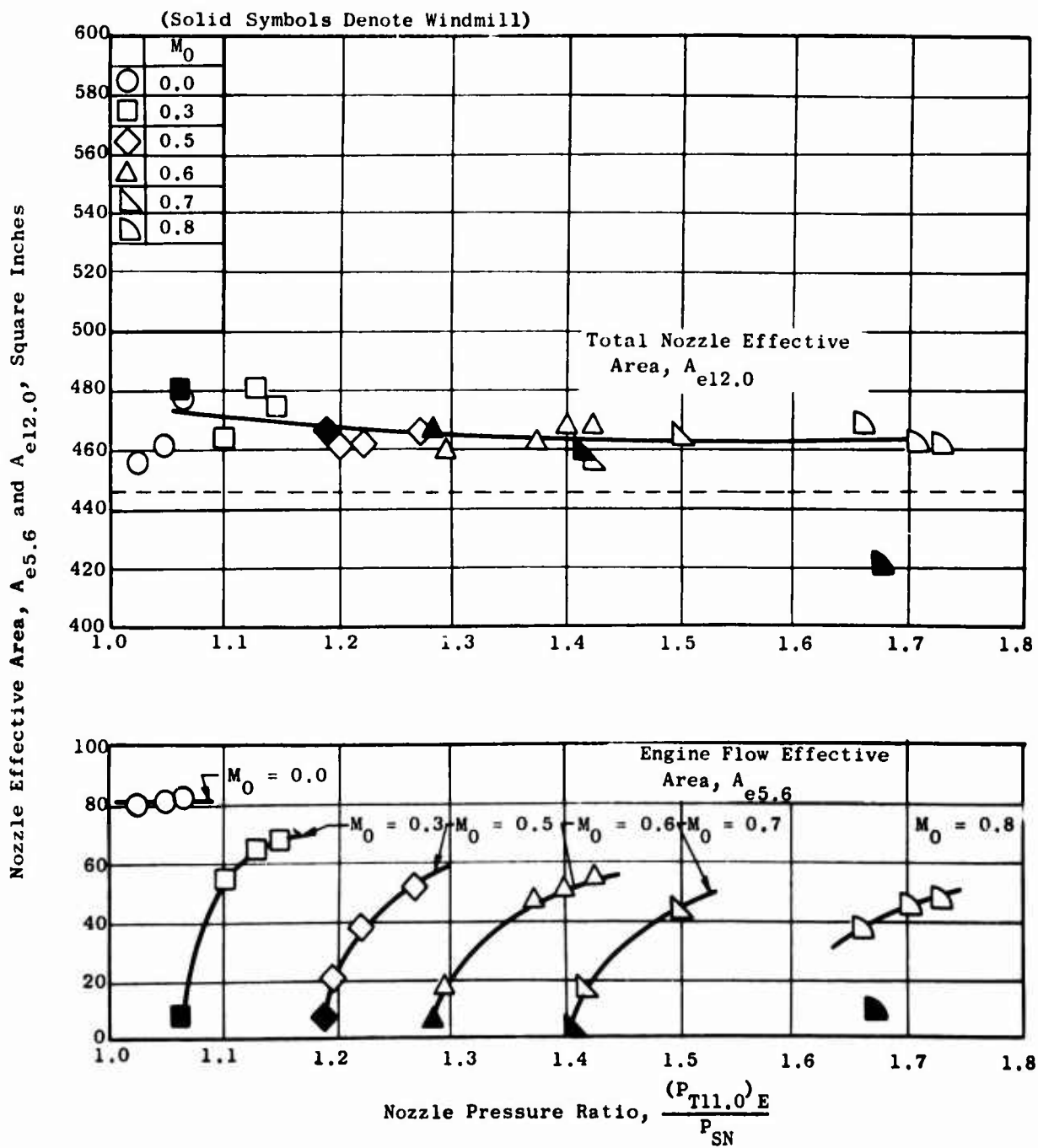


Figure 416. Exhaust Nozzle Effective Area Characteristics - Model 1.

BLANK PAGE

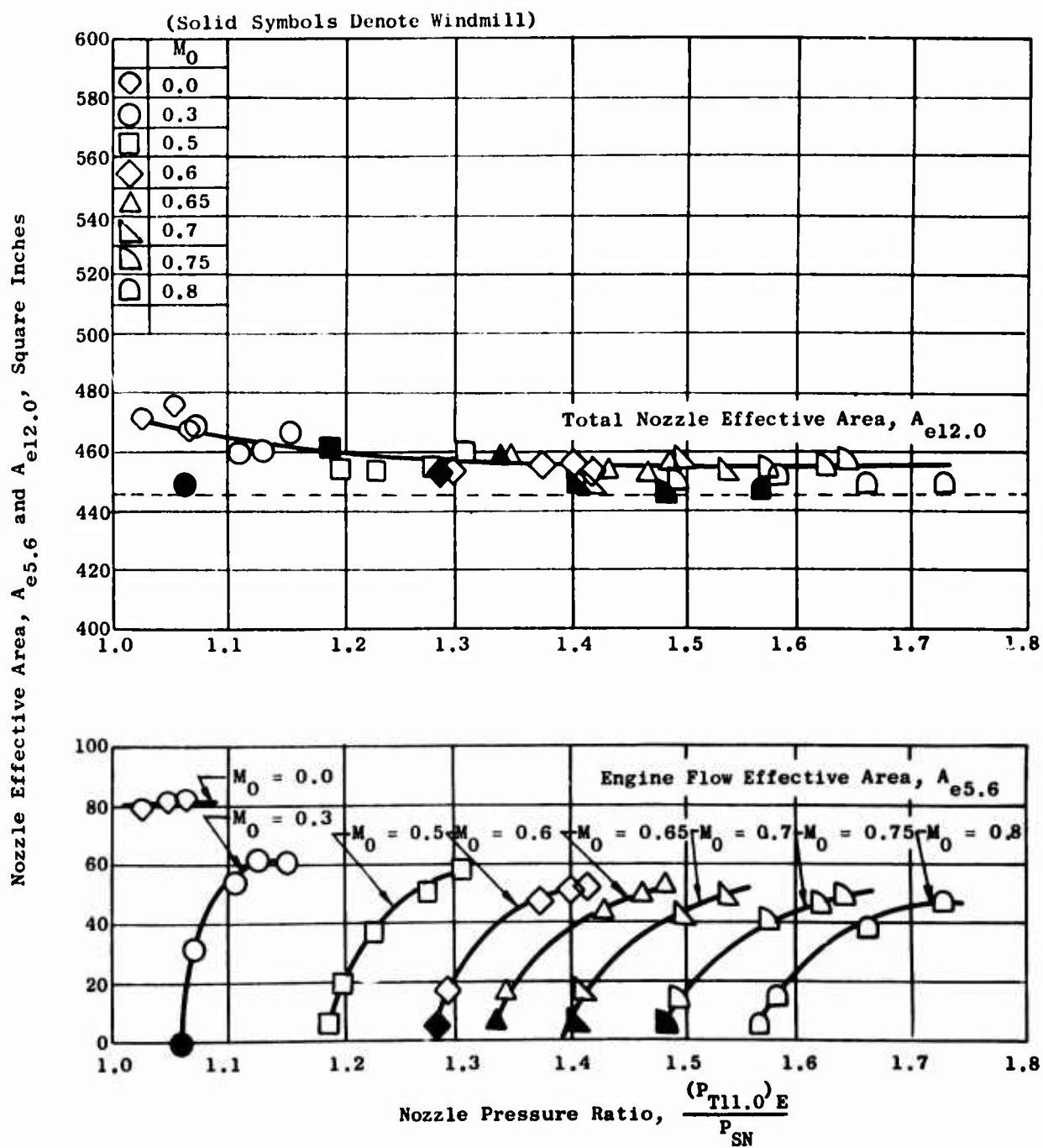


Figure 417. Exhaust Nozzle Effective Area Characteristics - Model 2.

Nozzle Effective Area, $A_{e5.6}$ and $A_{e12.0}$, Square Inches

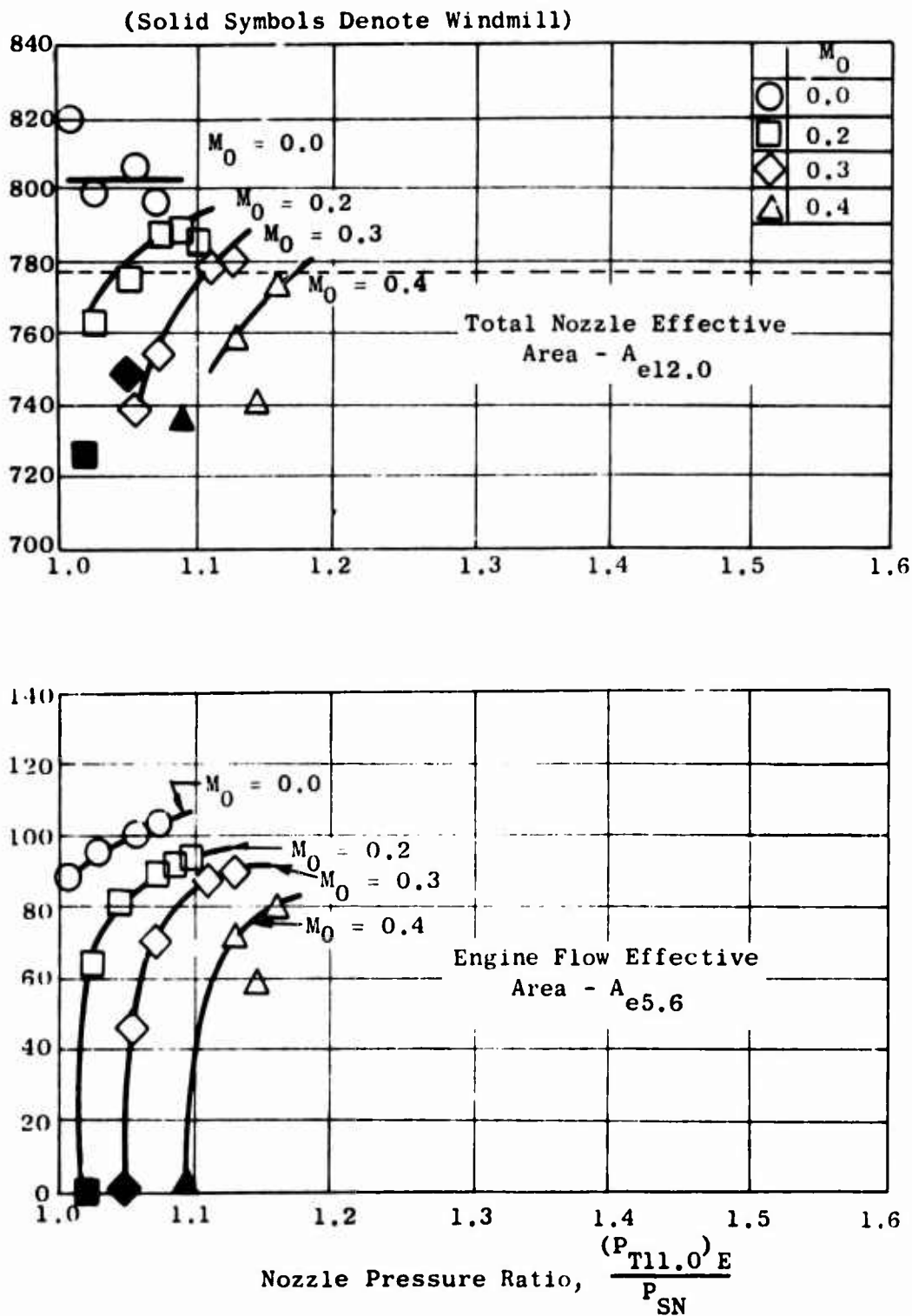


Figure 418. Exhaust Nozzle Effective Area Characteristics - Model 3.

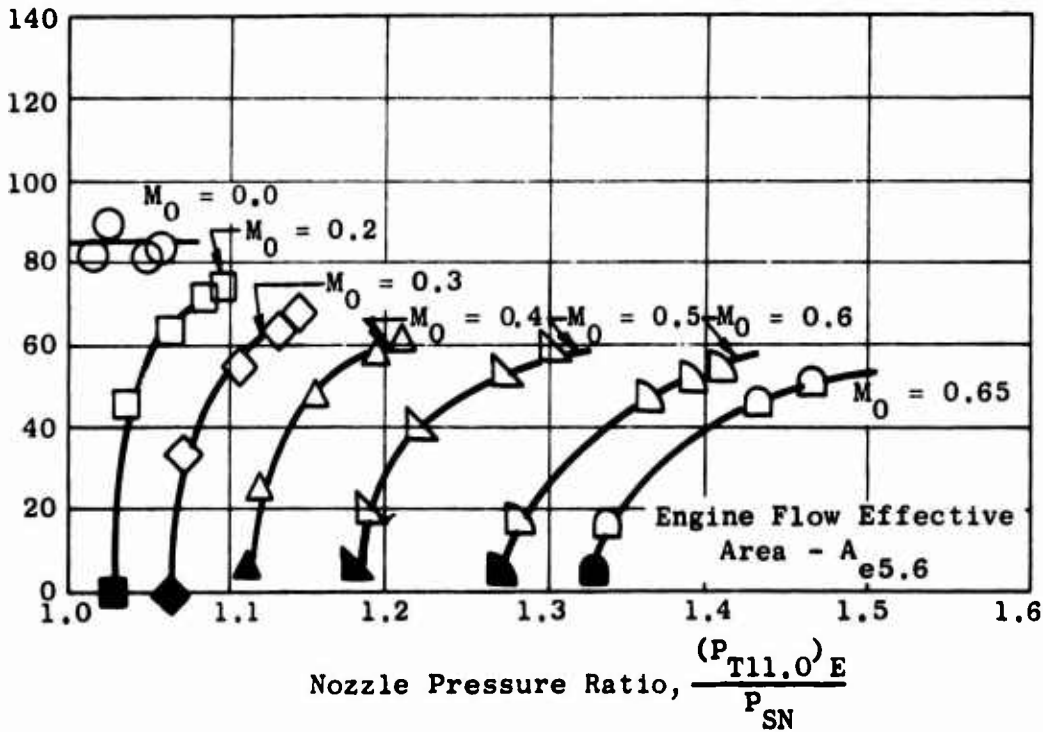
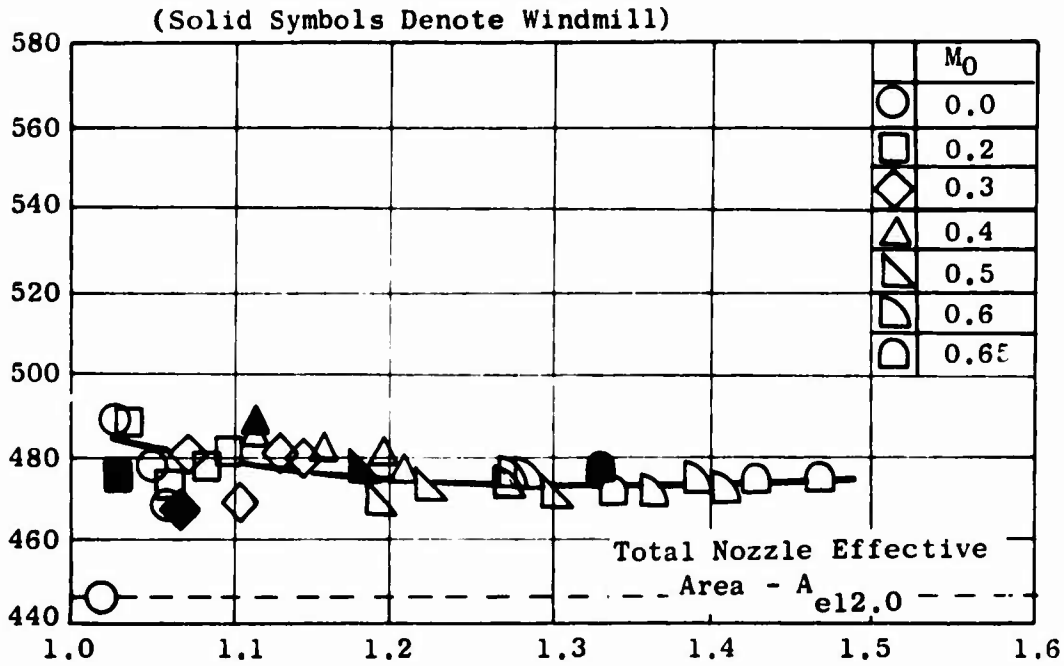


Figure 419. Exhaust Nozzle Effective Area Characteristics - Model 4.

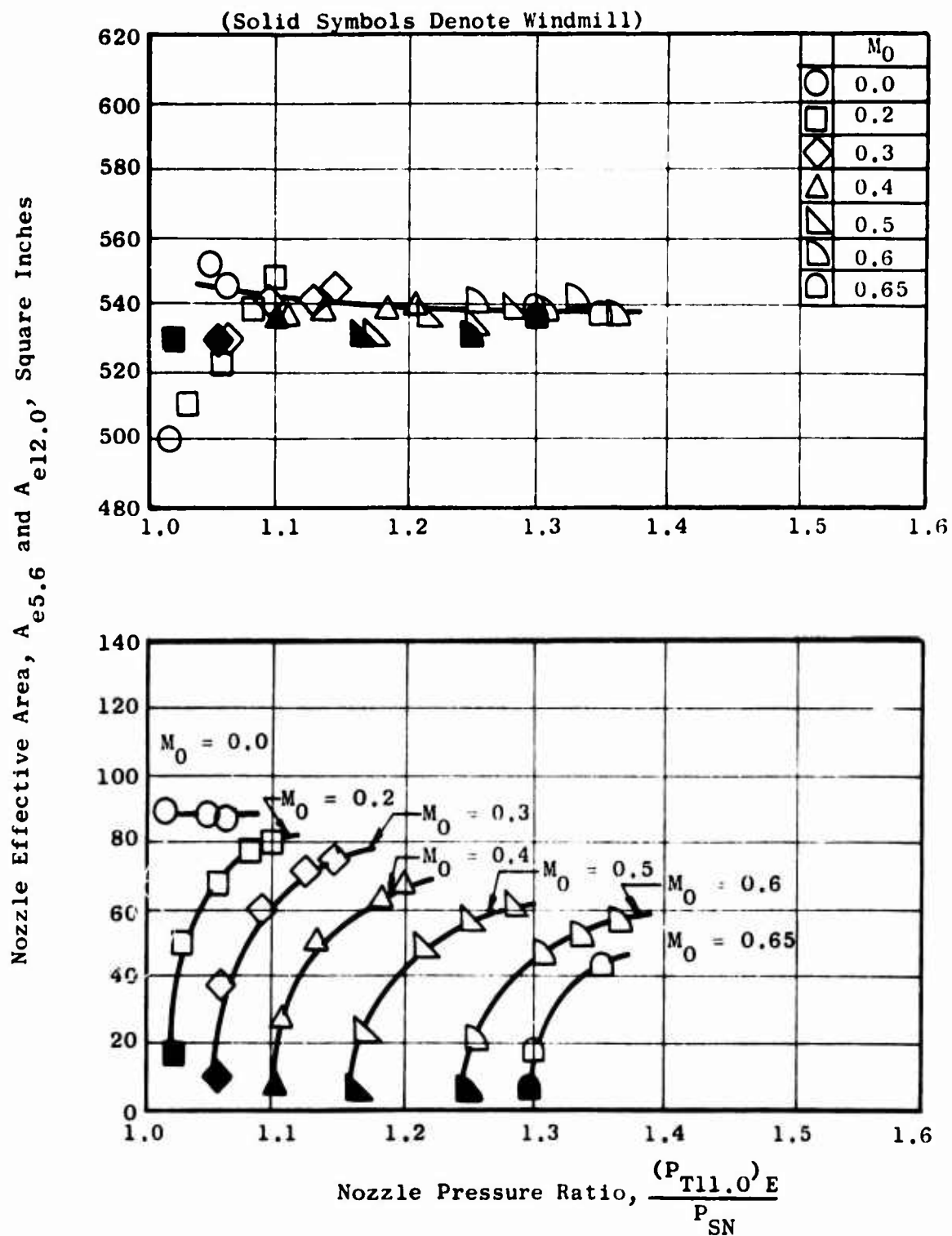


Figure 420. Exhaust Nozzle Effective Area Characteristics - Model 5.

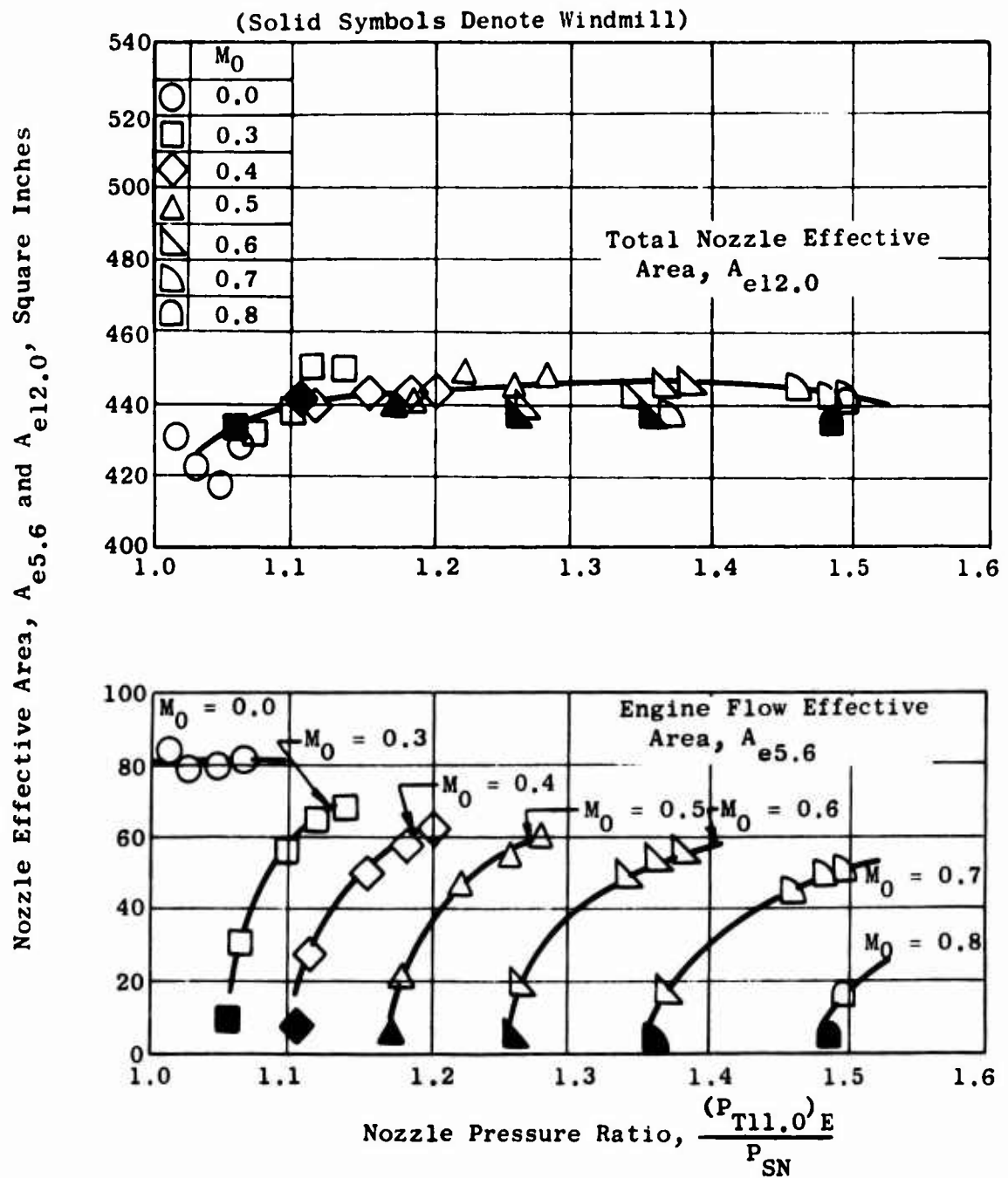


Figure 421. Exhaust Nozzle Effective Area Characteristics - Model 6.

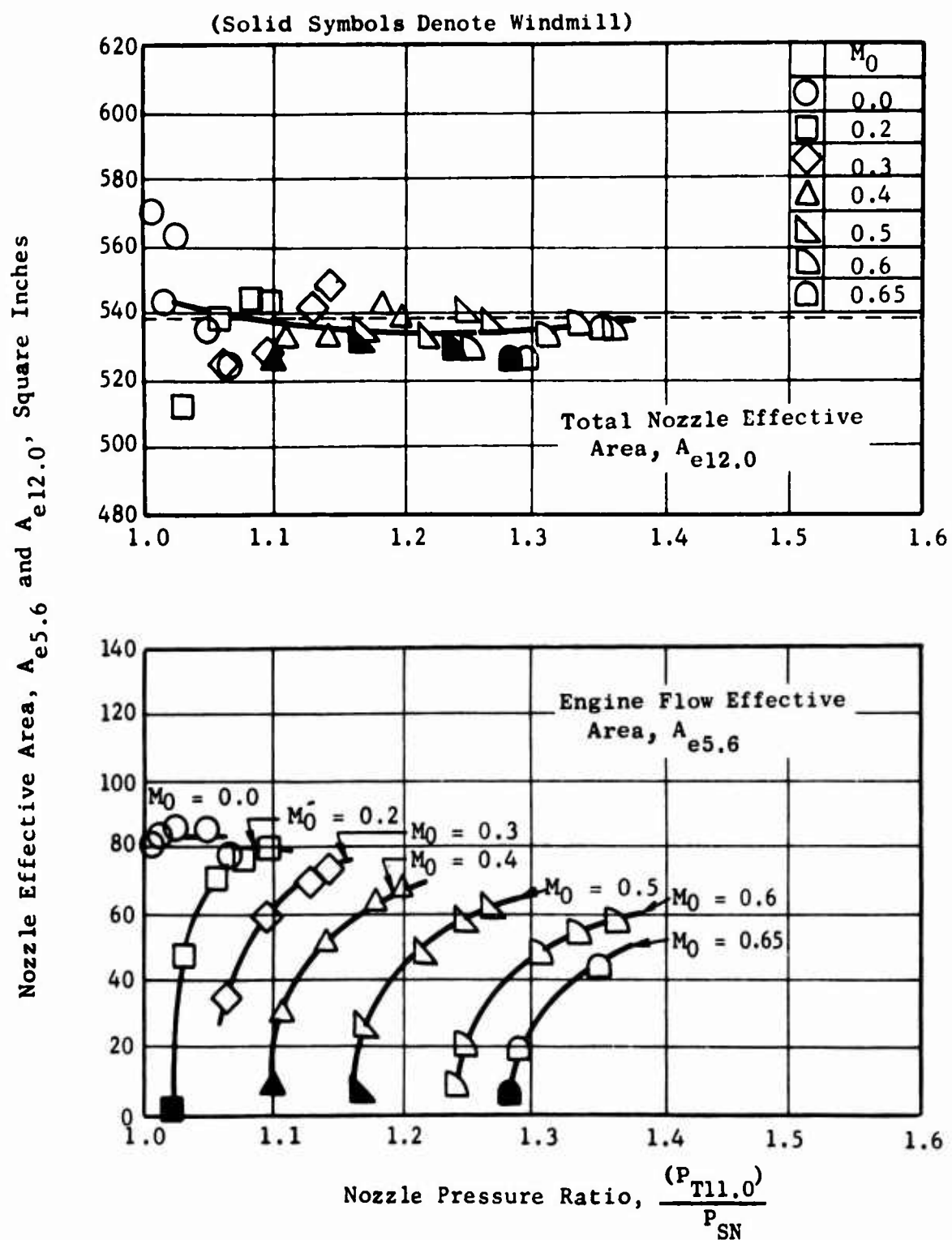


Figure 422. Exhaust Nozzle Effective Area Characteristics - Model 7.

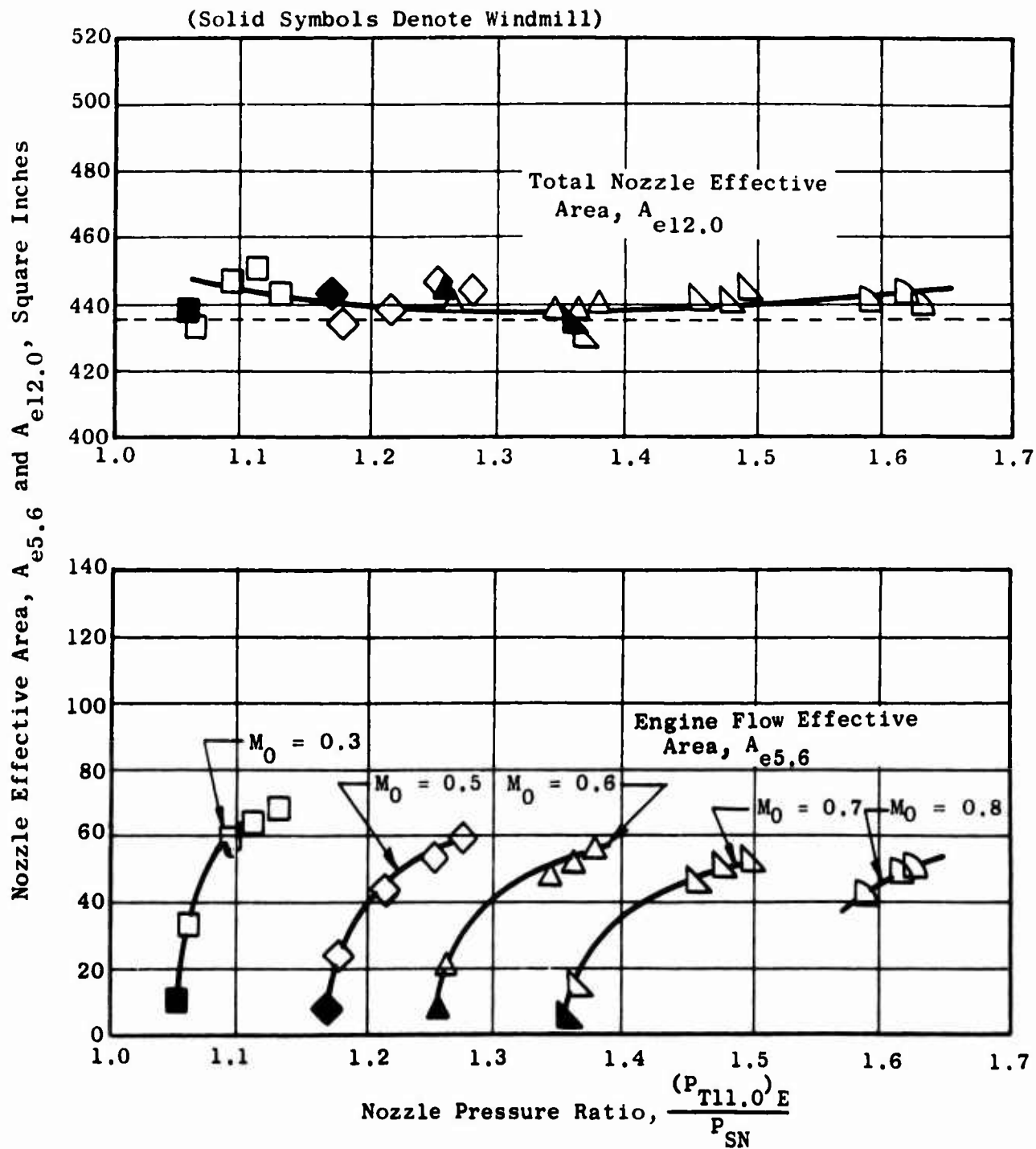


Figure 423. Exhaust Nozzle Effective Area Characteristics - Model 8.

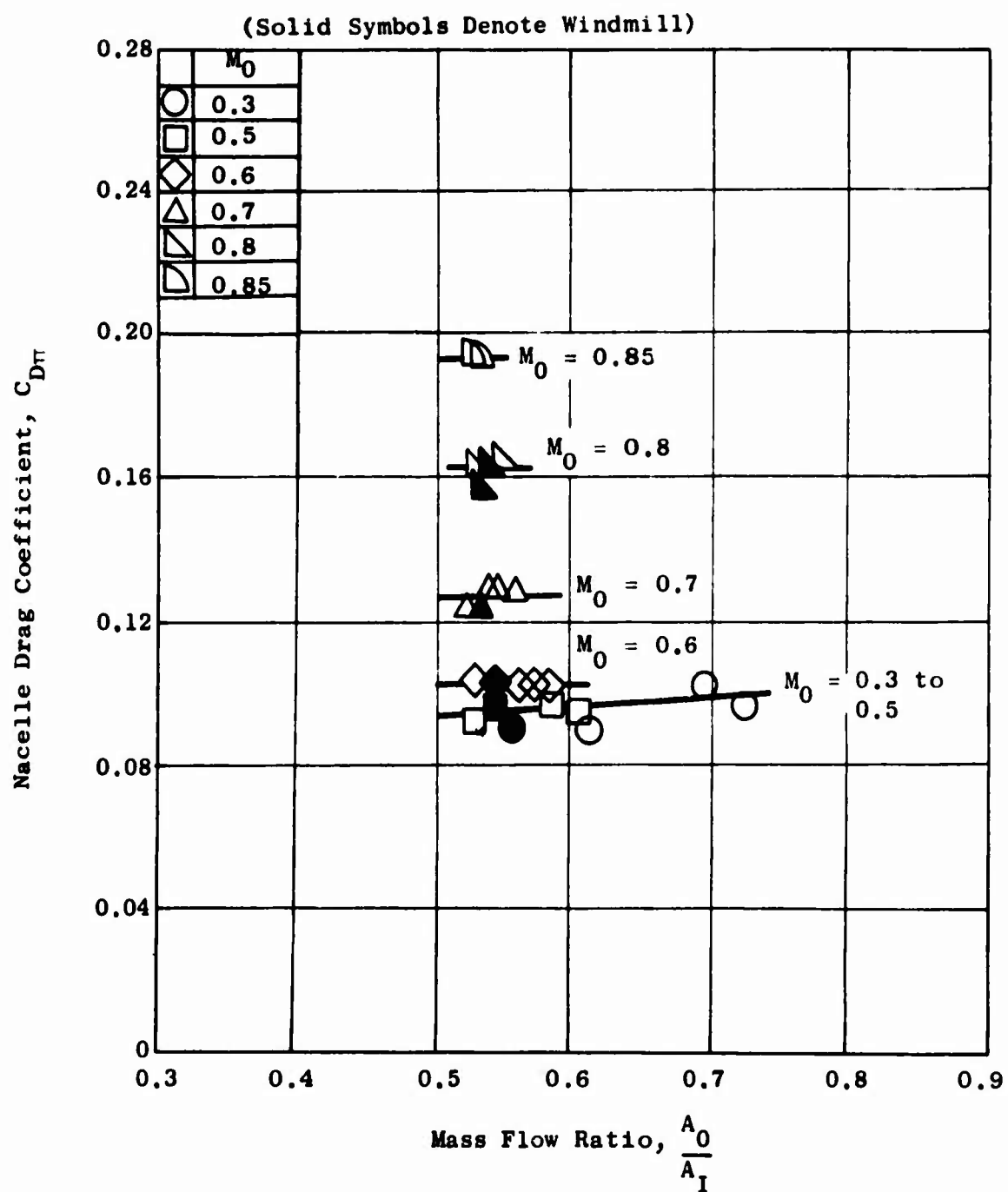


Figure 424. Nacelle Drag Coefficients Based on Force Measurements and an Ideal Exhaust Nozzle - Model 1.

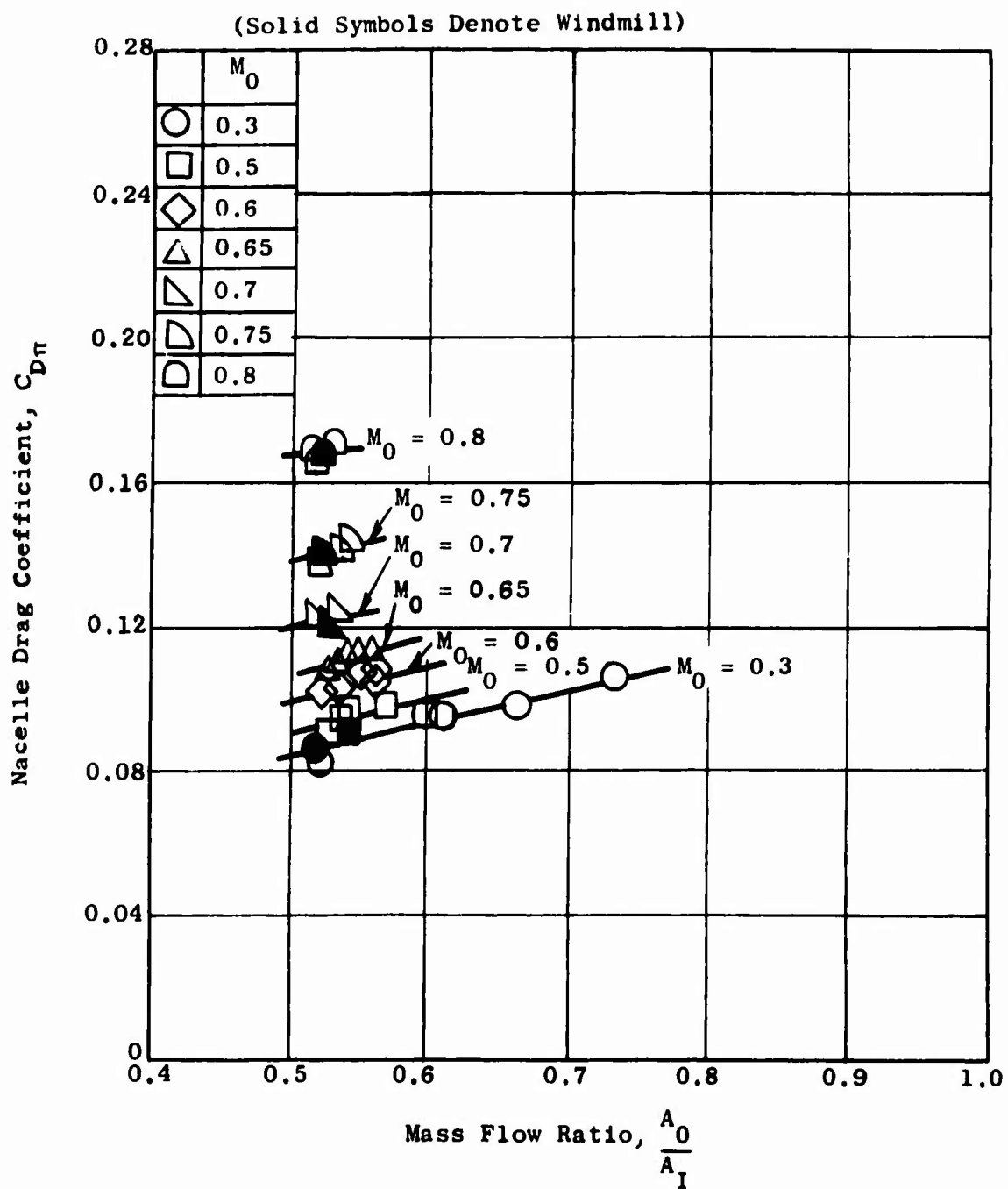


Figure 425. Nacelle Drag Coefficients Based on Force Measurements and an Ideal Exhaust Nozzle - Model 2.

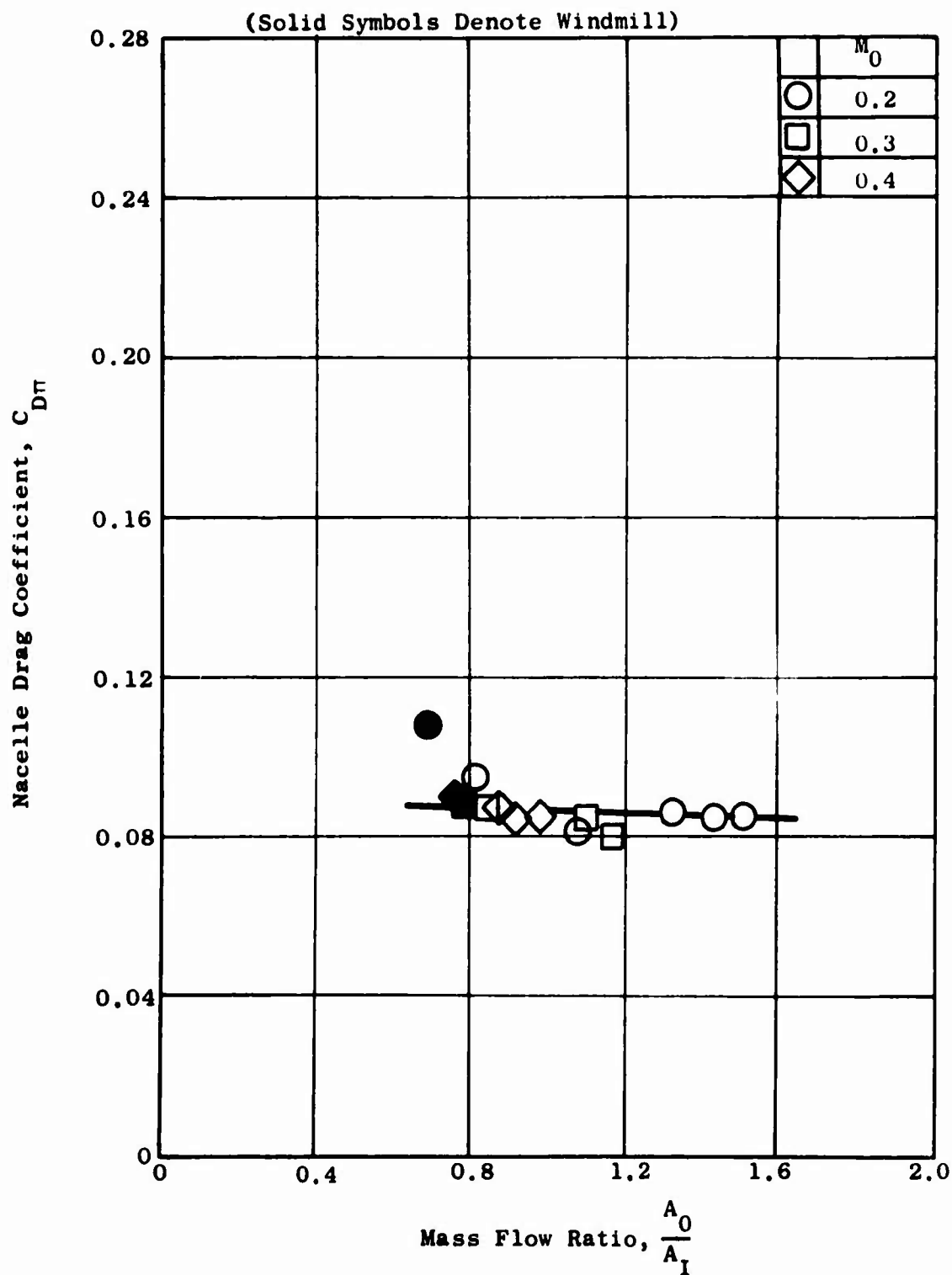


Figure 426. Nacelle Drag Coefficients Based on Force Measurements and an Ideal Exhaust Nozzle - Model 3.

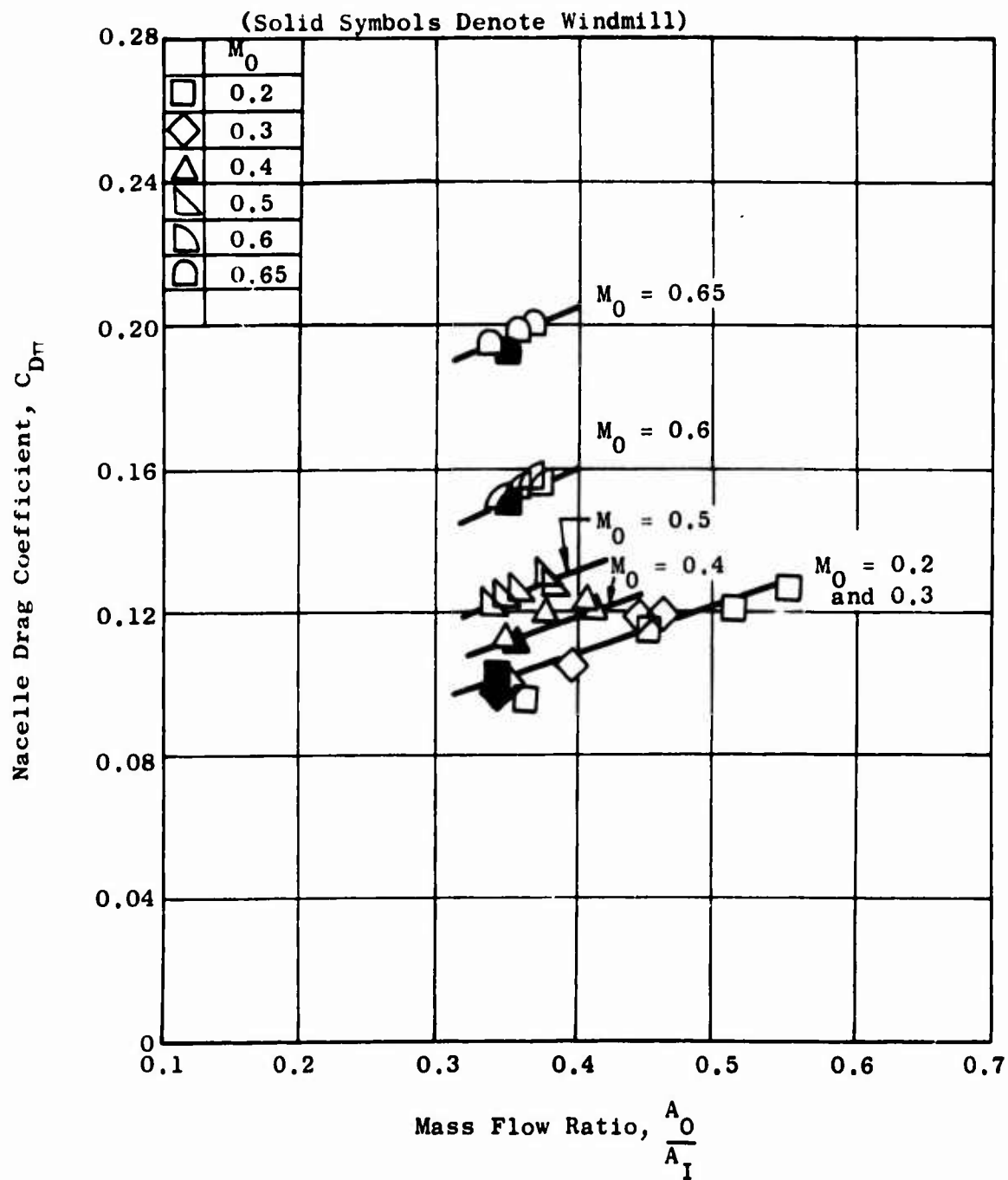


Figure 427. Nacelle Drag Coefficients Based on Force Measurements and an Ideal Exhaust Nozzle - Model 4.

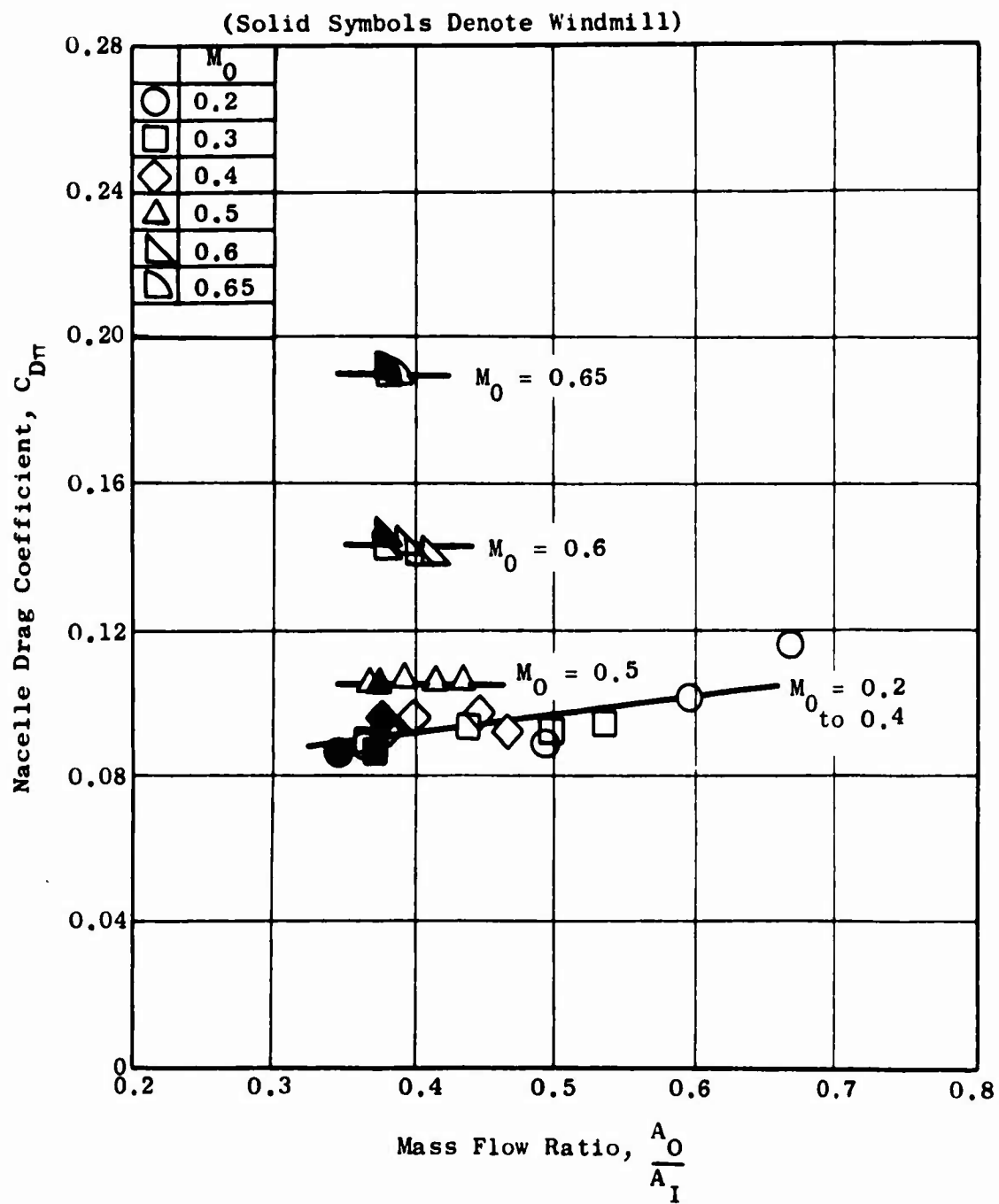


Figure 428. Nacelle Drag Coefficients Based on Force Measurements and an Ideal Exhaust Nozzle - Model 5.

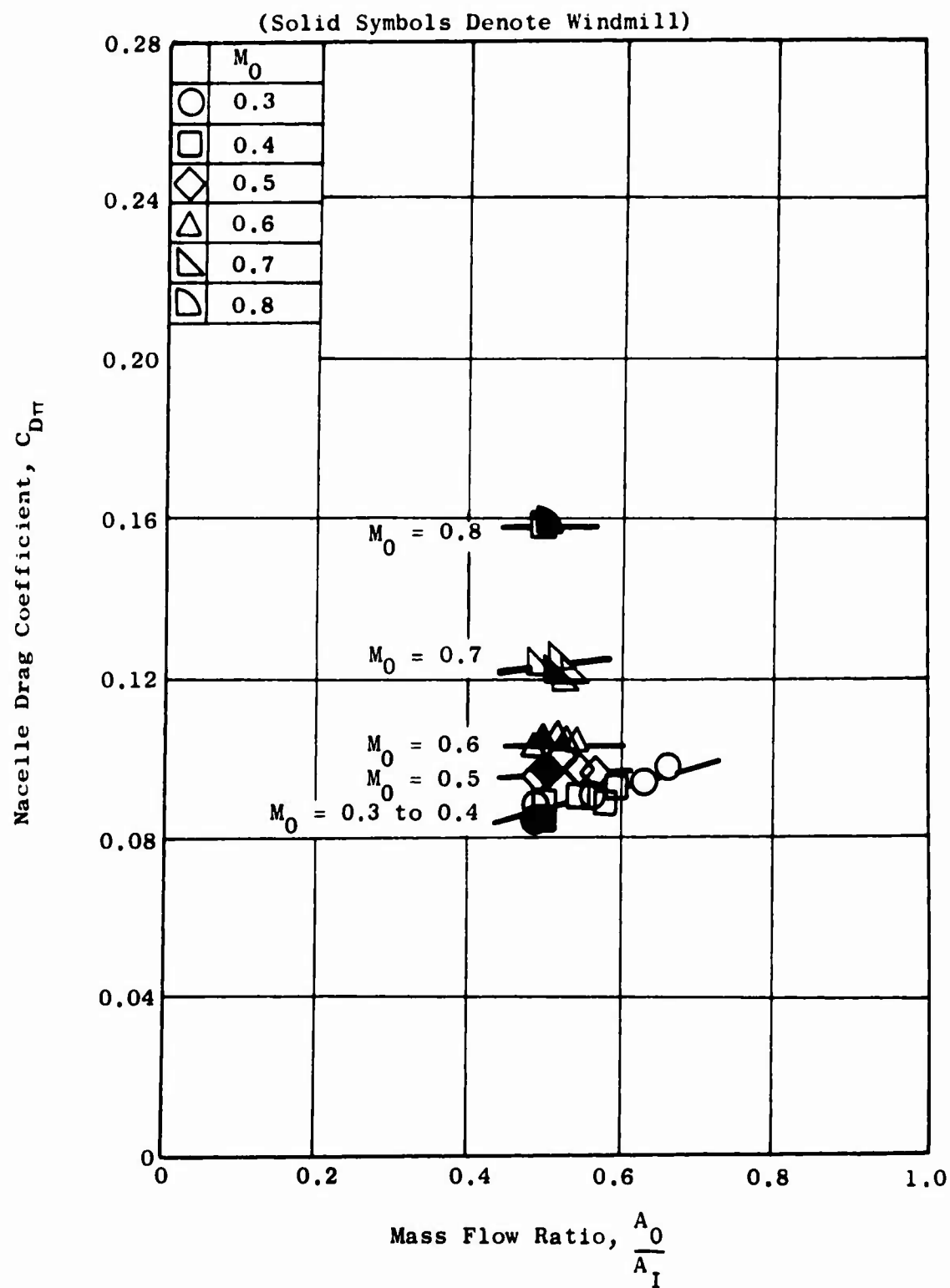


Figure 429. Nacelle Drag Coefficients Based on Force Measurements and an Ideal Exhaust Nozzle - Model 6.

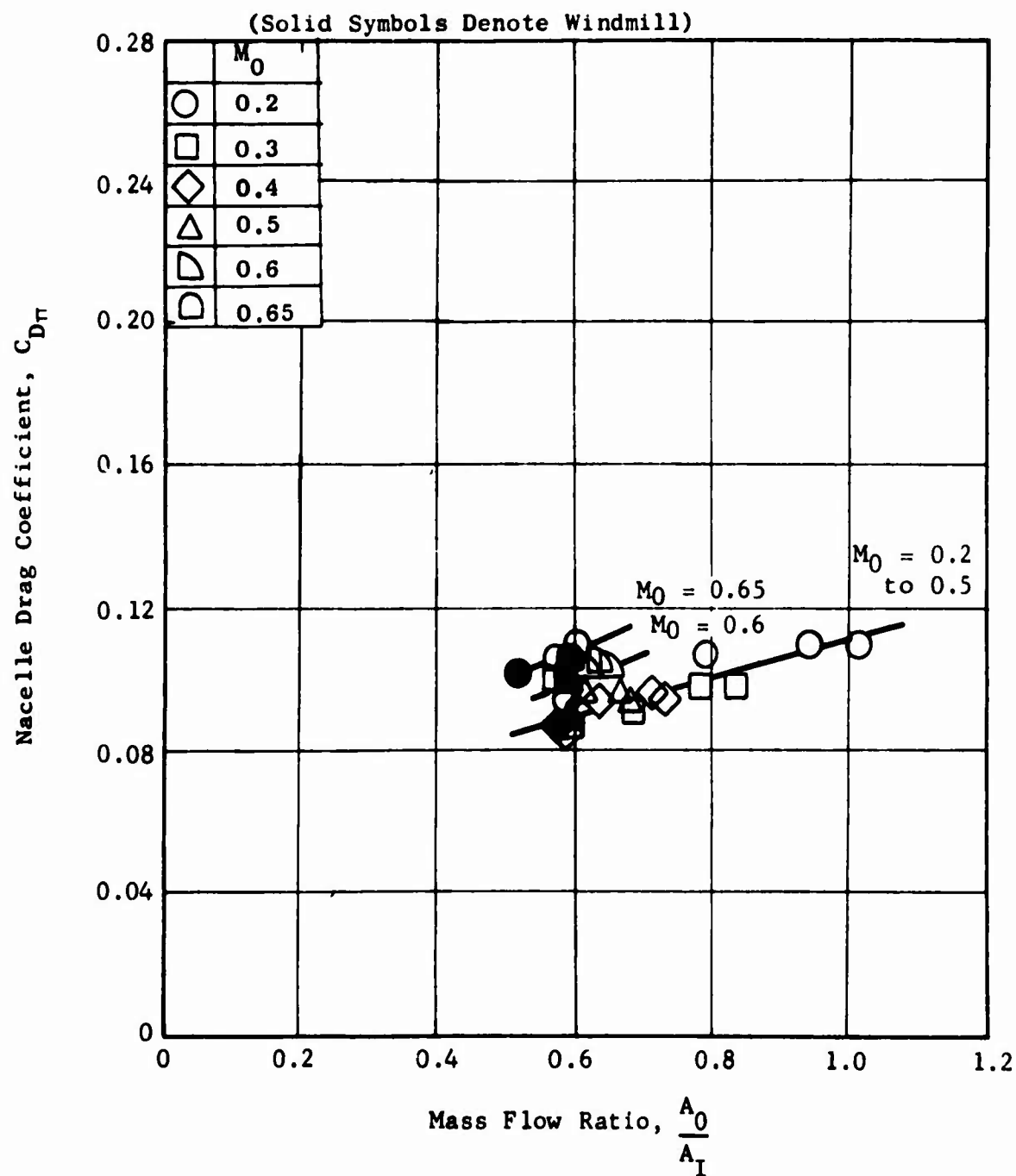


Figure 430. Nacelle Drag Coefficients Based on Force Measurements and an Ideal Exhaust Nozzle - Model 7.

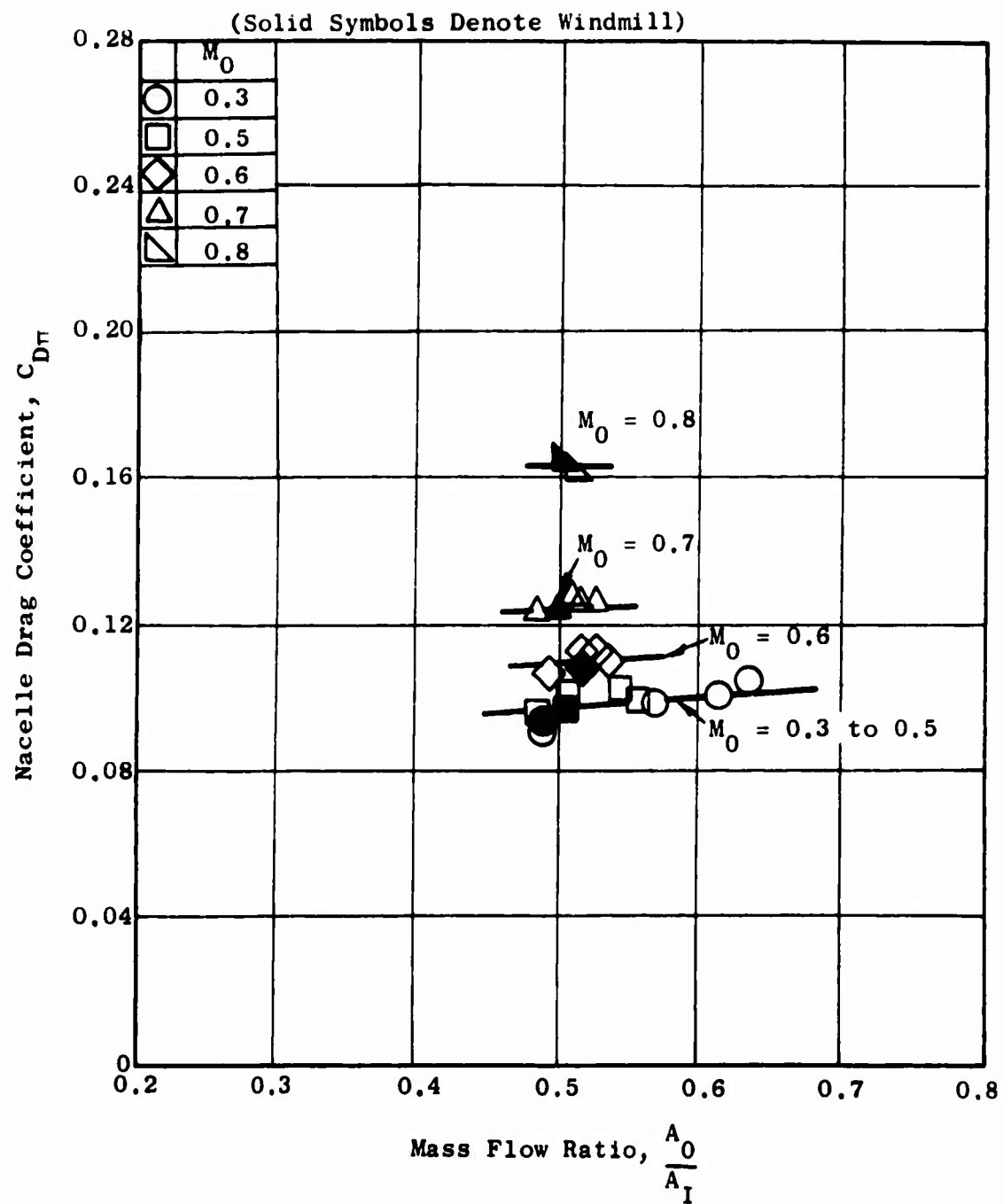


Figure 431. Nacelle Drag Coefficients Based on Force Measurements and an Ideal Exhaust Nozzle - Model 8.

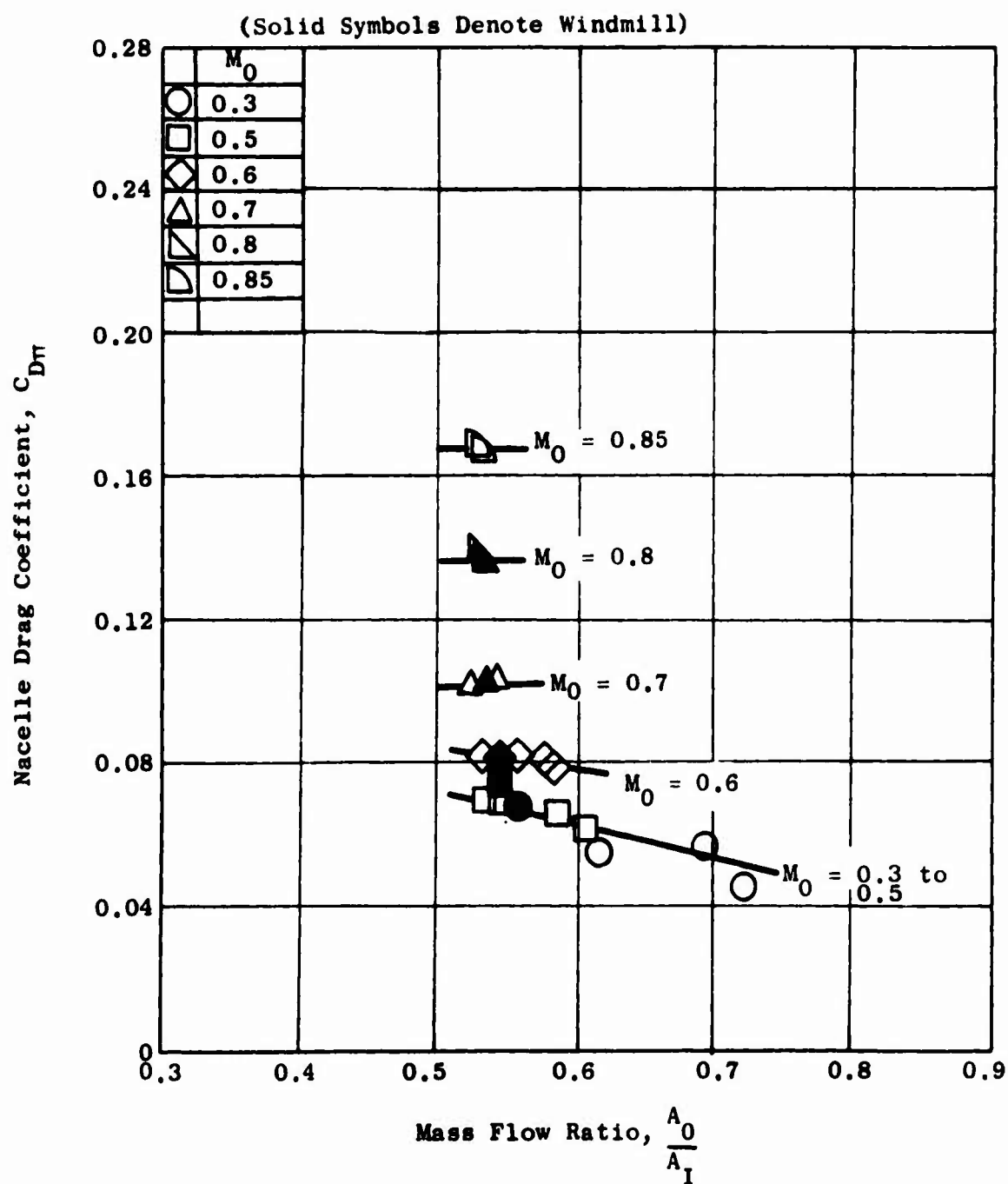


Figure 432. Nacelle Drag Coefficients Based on Force Measurements and a Nozzle with a 0.95 Thrust Coefficient - Model 1.

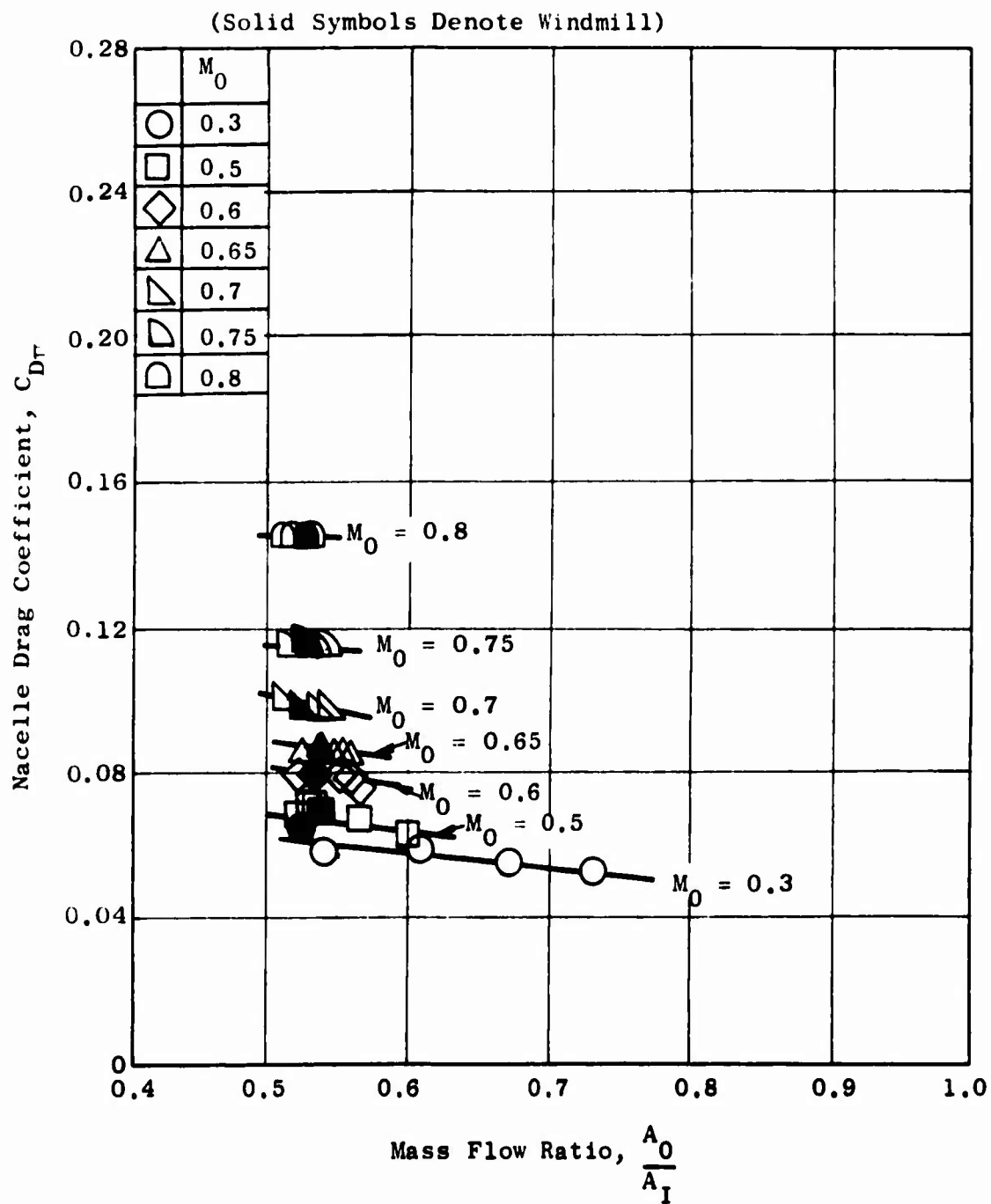


Figure 433. Nacelle Drag Coefficients Based on Force Measurements and a Nozzle with a 0.95 Thrust Coefficient - Model 2.

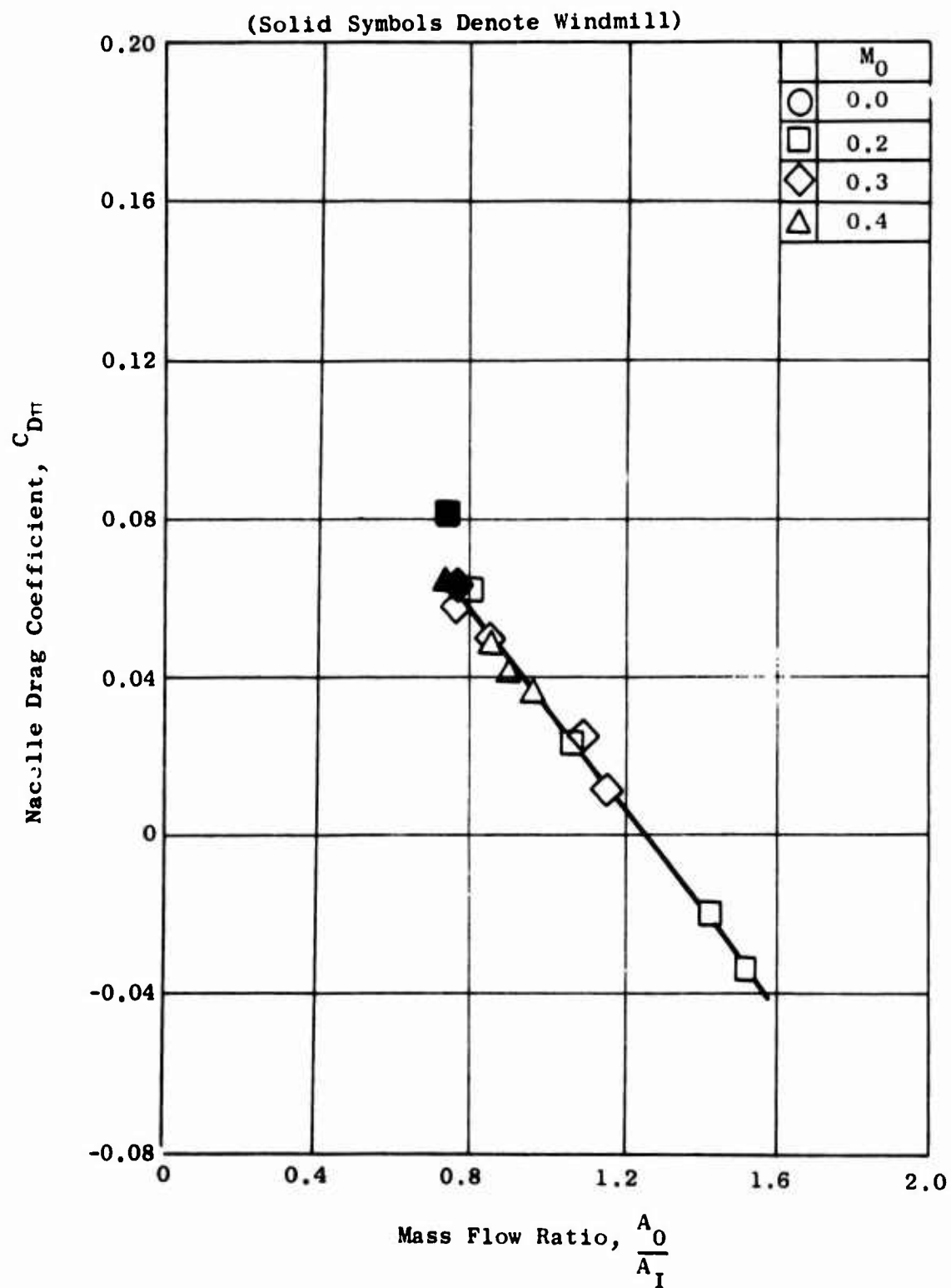


Figure 434. Nacelle Drag Coefficients Based on Force Measurements and a Nozzle with a 0.95 Thrust Coefficient - Model 3.

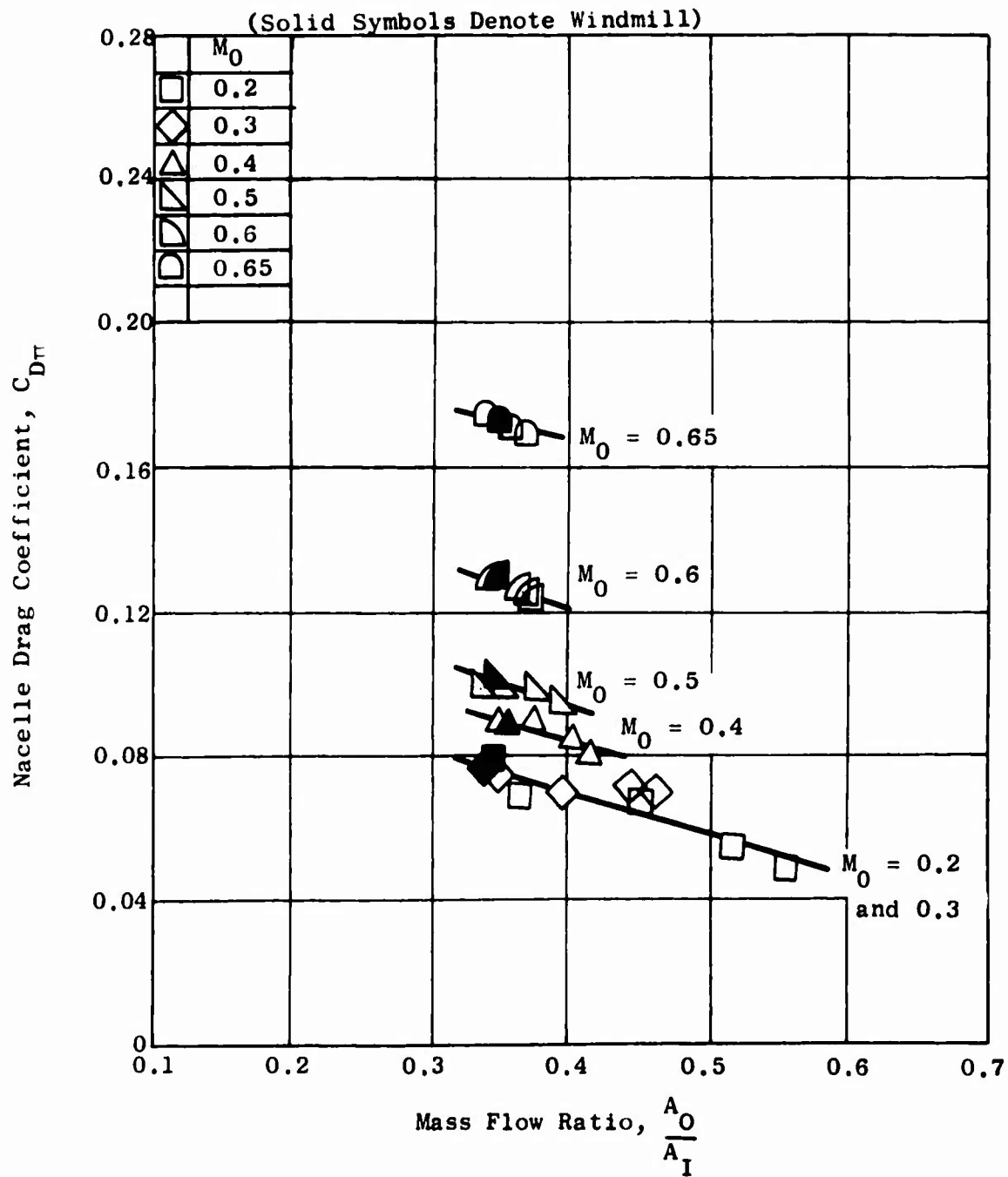
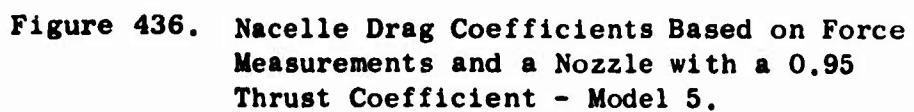


Figure 435. Nacelle Drag Coefficients Based on Force Measurements and a Nozzle with a 0.95 Thrust Coefficient - Model 4.



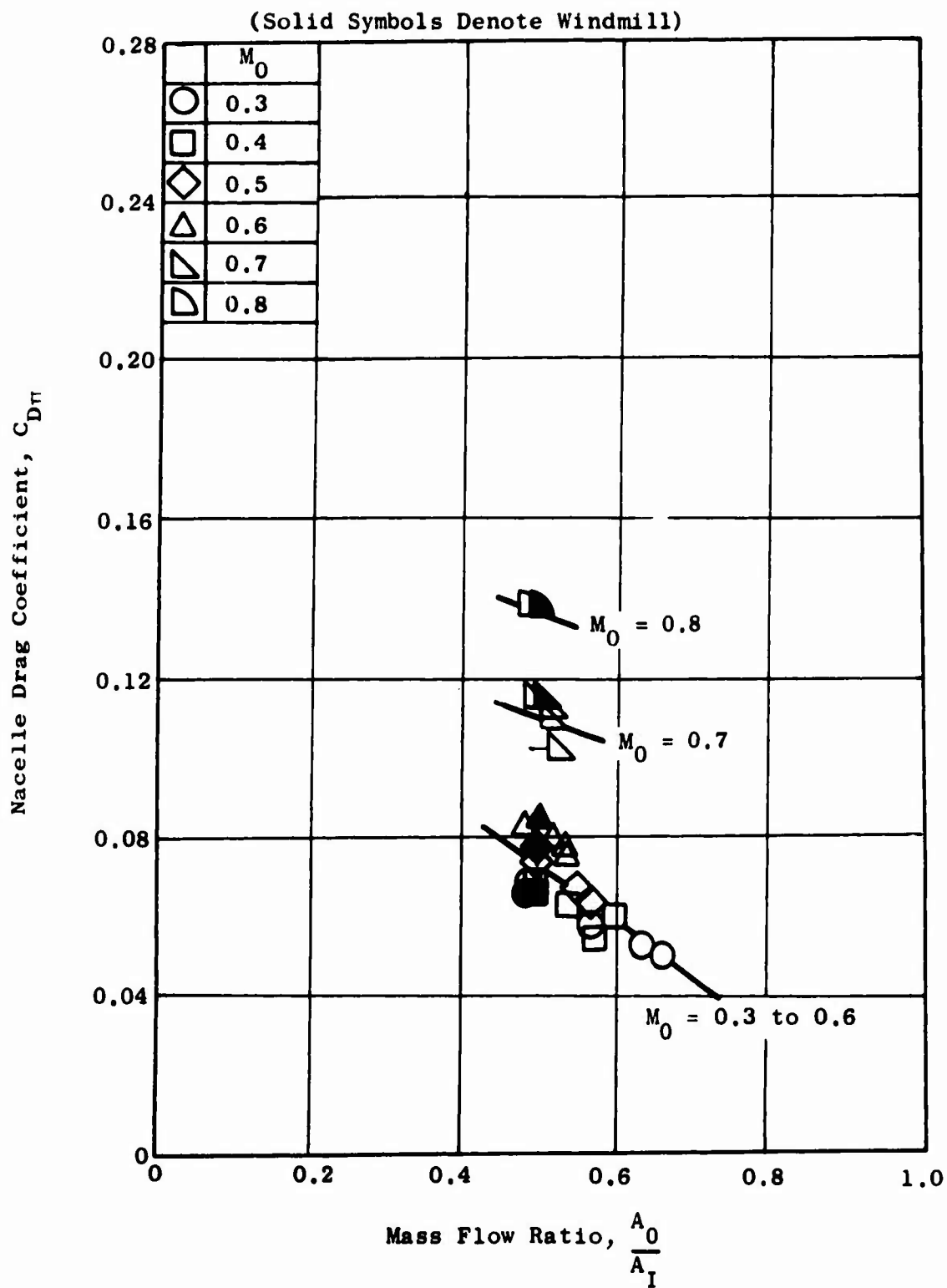


Figure 437. Nacelle Drag Coefficients Based on Force Measurements and a Nozzle with a 0.95 Thrust Coefficient - Model 6.

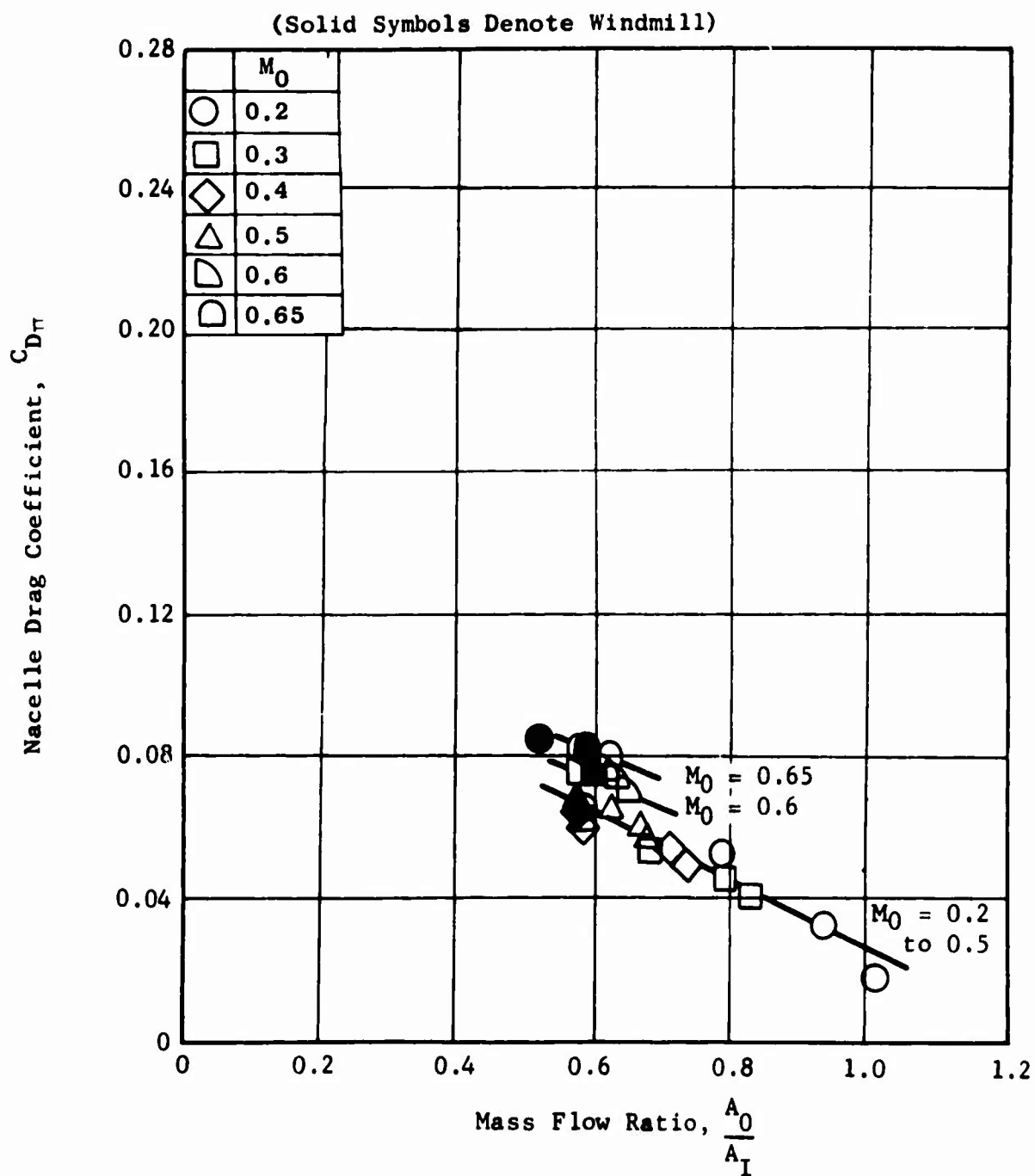


Figure 438. Nacelle Drag Coefficients Based on Force Measurements and a Nozzle with a 0.95 Thrust Coefficient - Model 7.

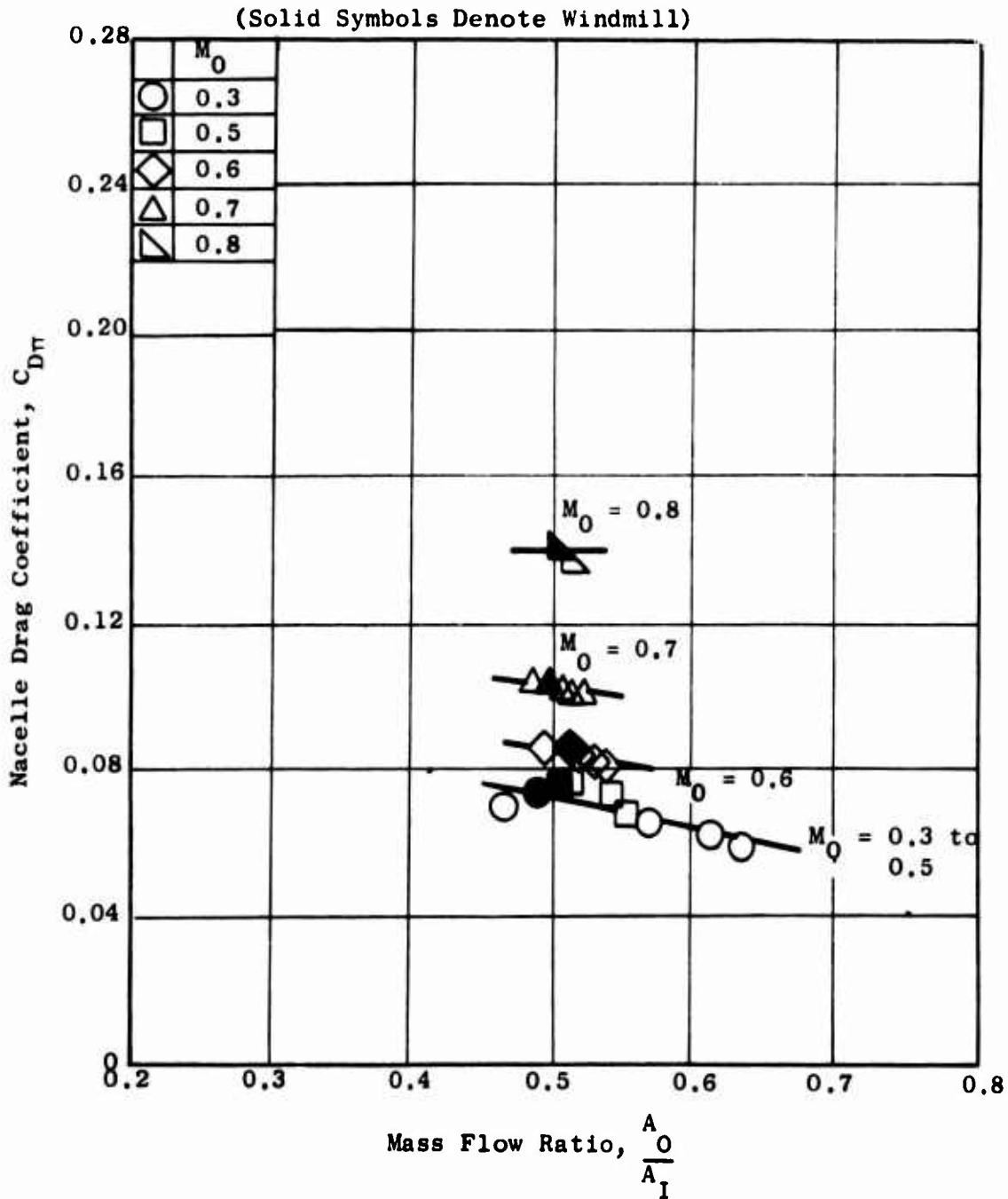


Figure 439. Nacelle Drag Coefficients Based on Force Measurements and a Nozzle with a 0.95 Thrust Coefficient - Model 8.

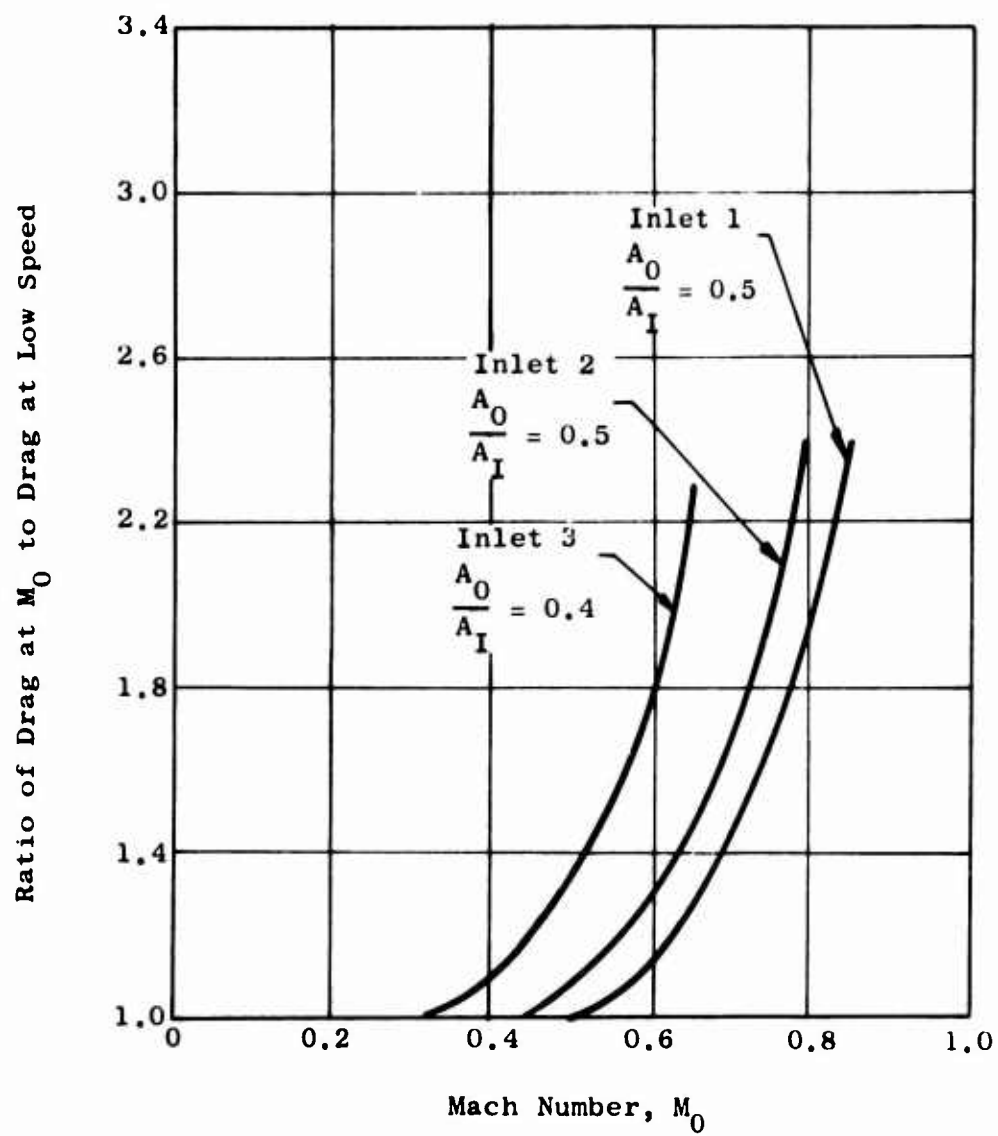


Figure 440. Variation of Drag Coefficient with Mach Number for the Three Inlet Systems.

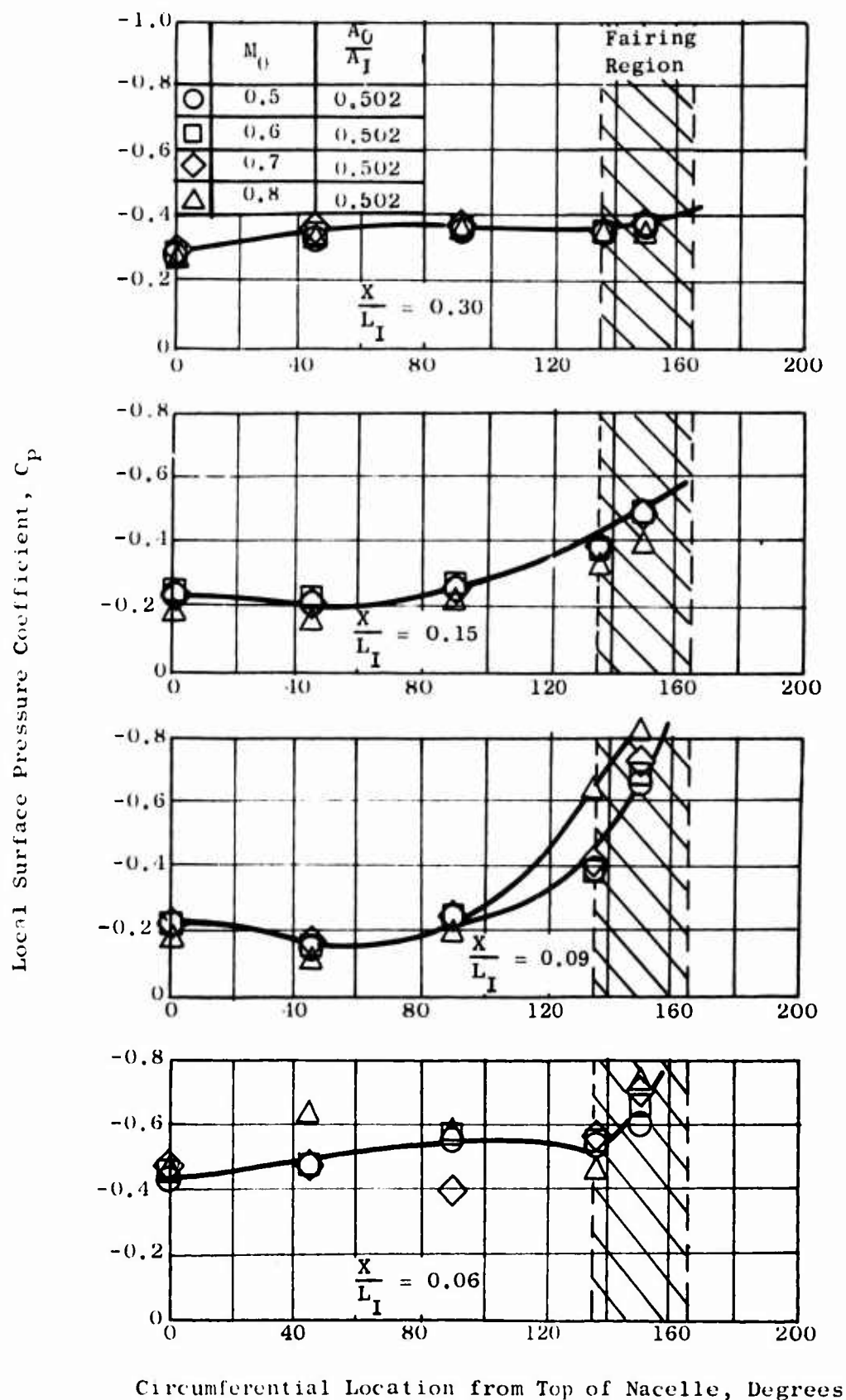


Figure 441. Circumferential Variation of Pressure Coefficient for Model 6 (Inlet 1).

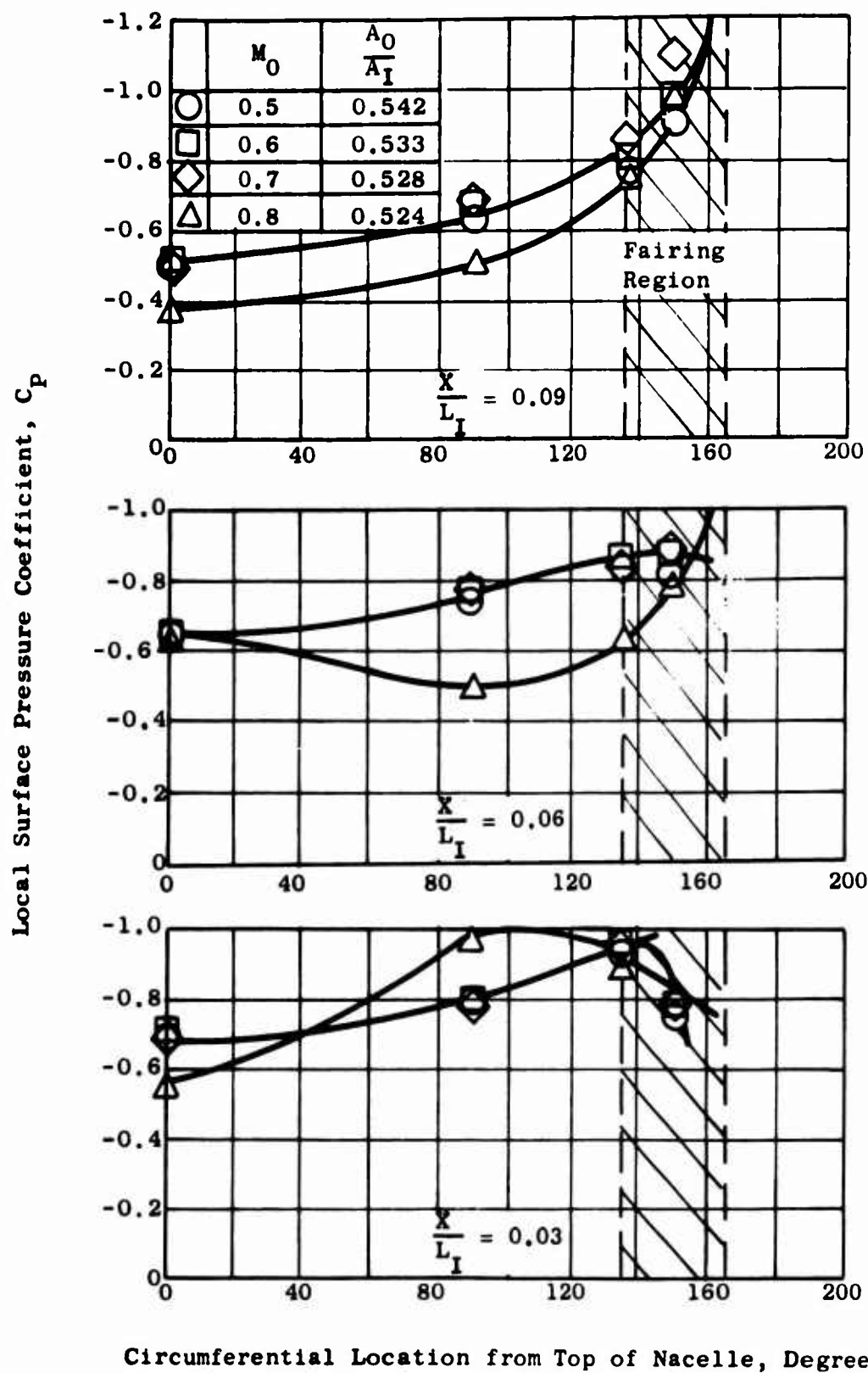


Figure 442. Circumferential Variation of Pressure Coefficient for Model 2 (Inlet 2).

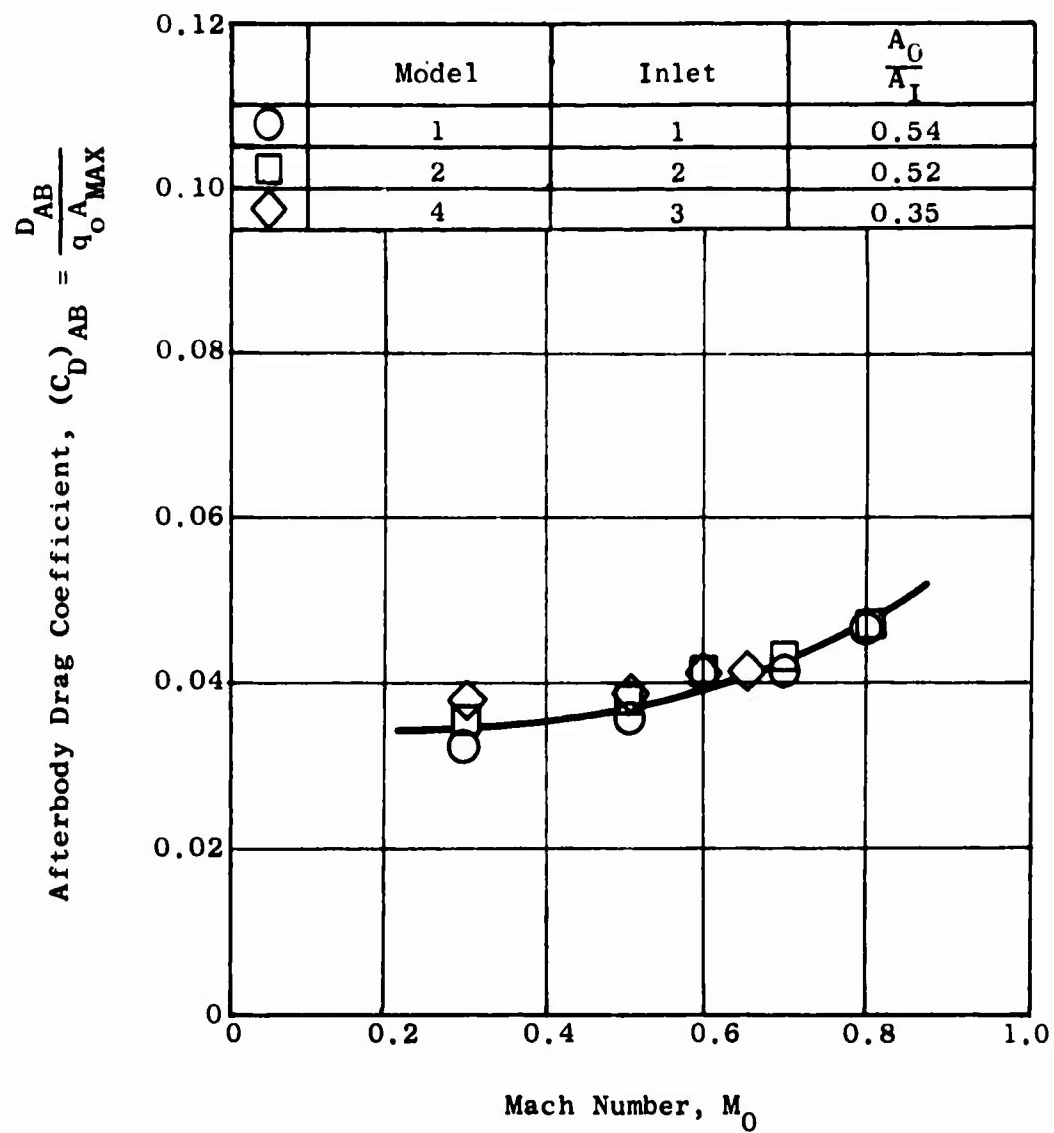


Figure 443. Variation of Afterbody Drag with Mach Number Based on Pressure Integrations.

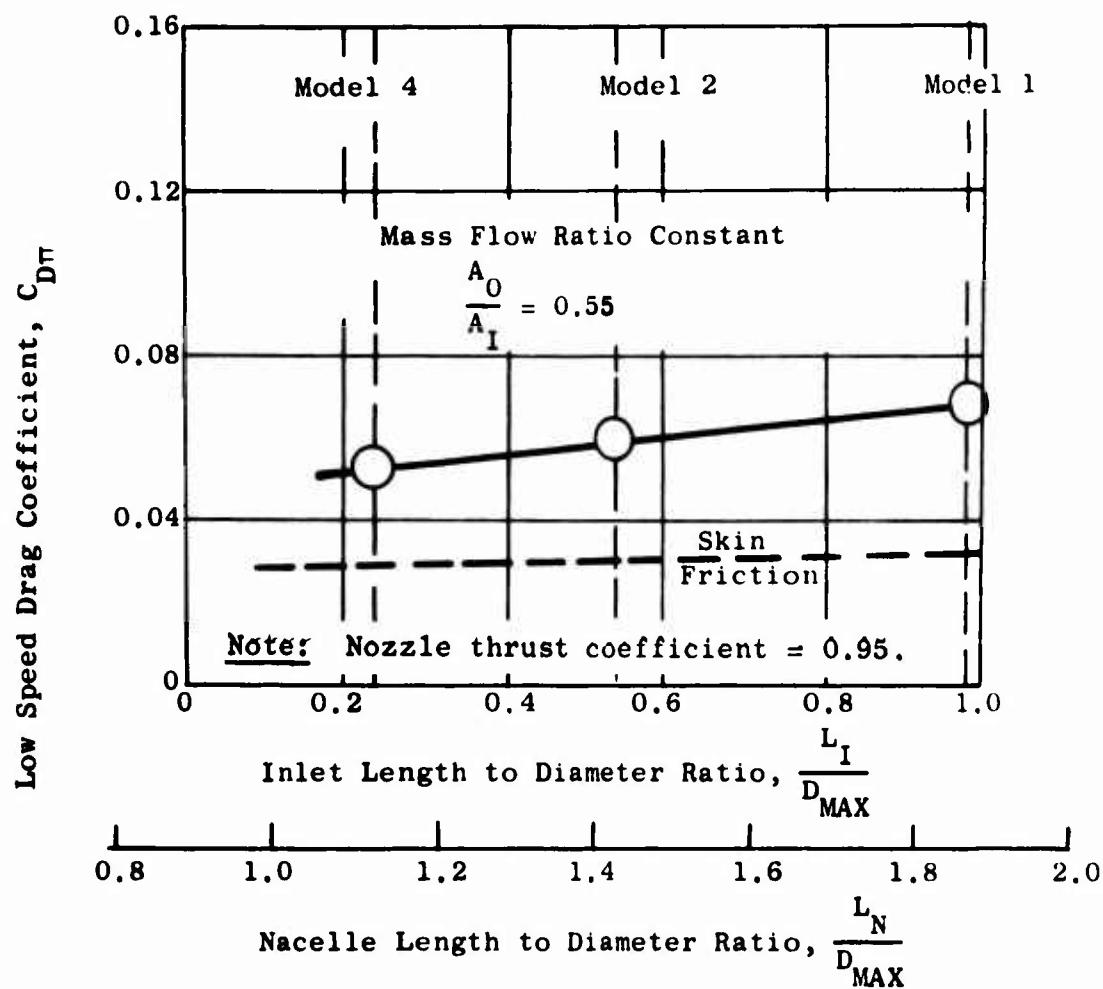


Figure 444. Effects of Inlet Length on Nacelle Drag Coefficients.

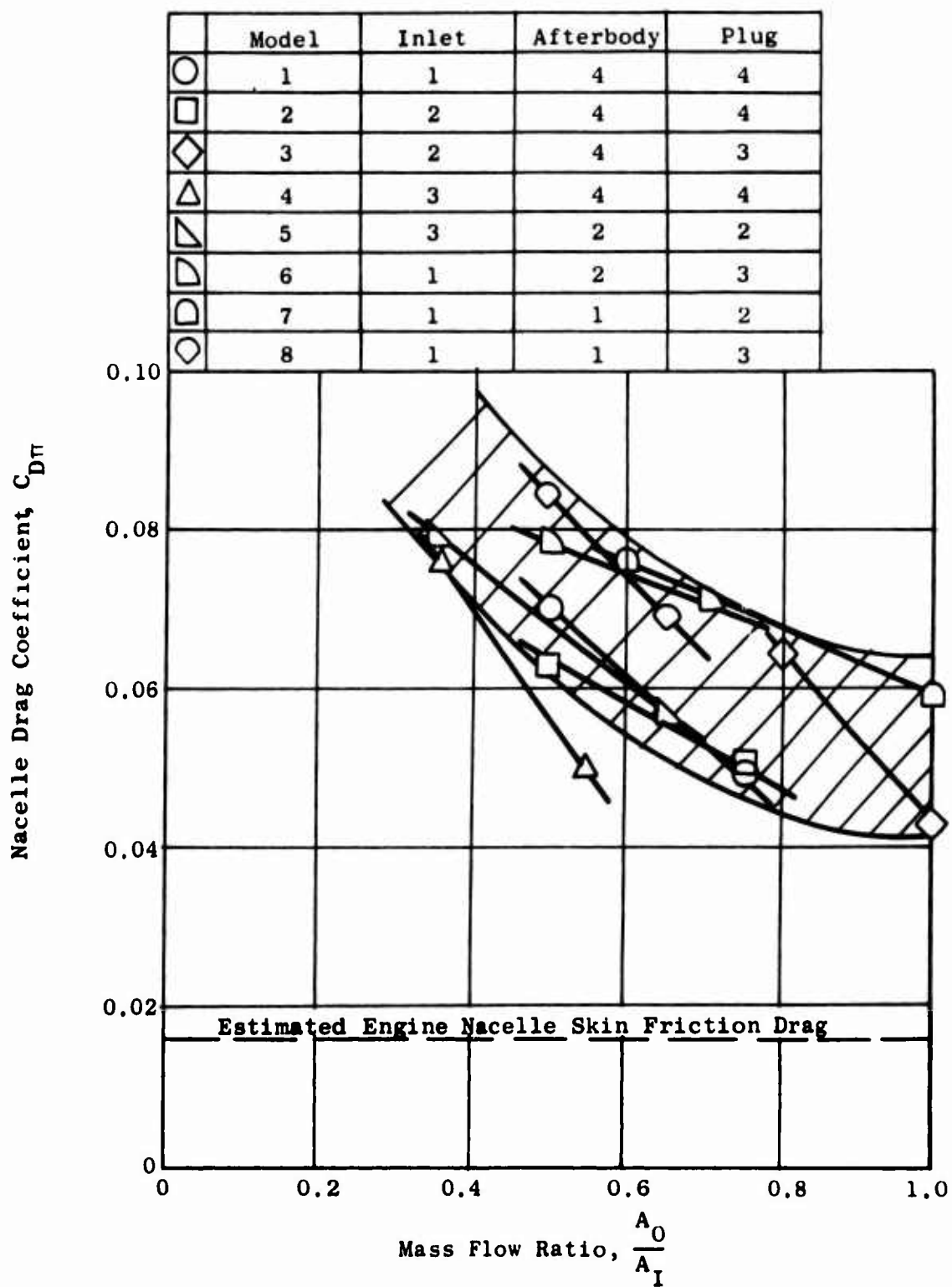


Figure 445. Summary of Nacelle Total Drag Coefficients Based on Balance Measurements.

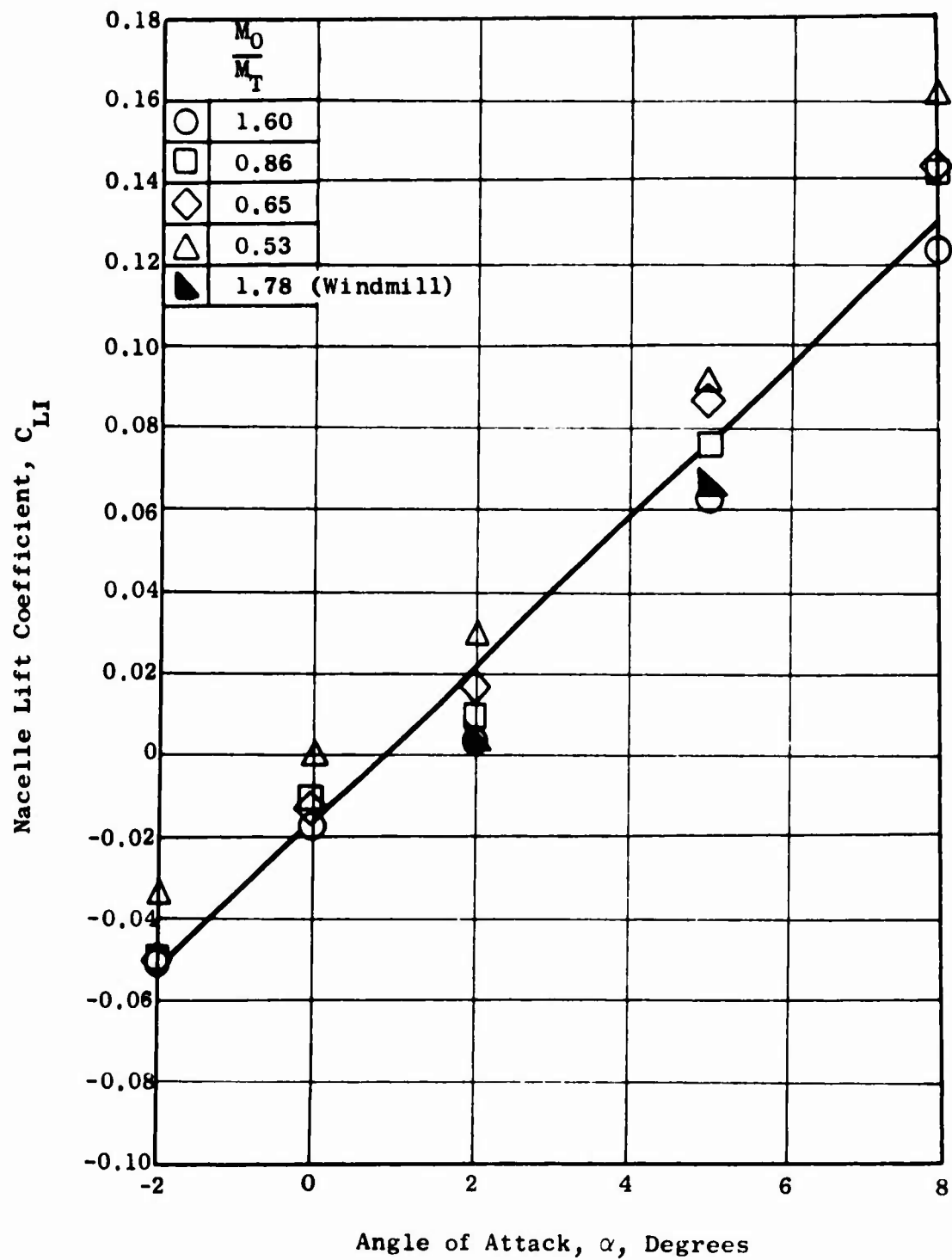


Figure 446. Variation of Nacelle Contribution to Lift with Angle of Attack and Speed, $M_0 = 0.3$.

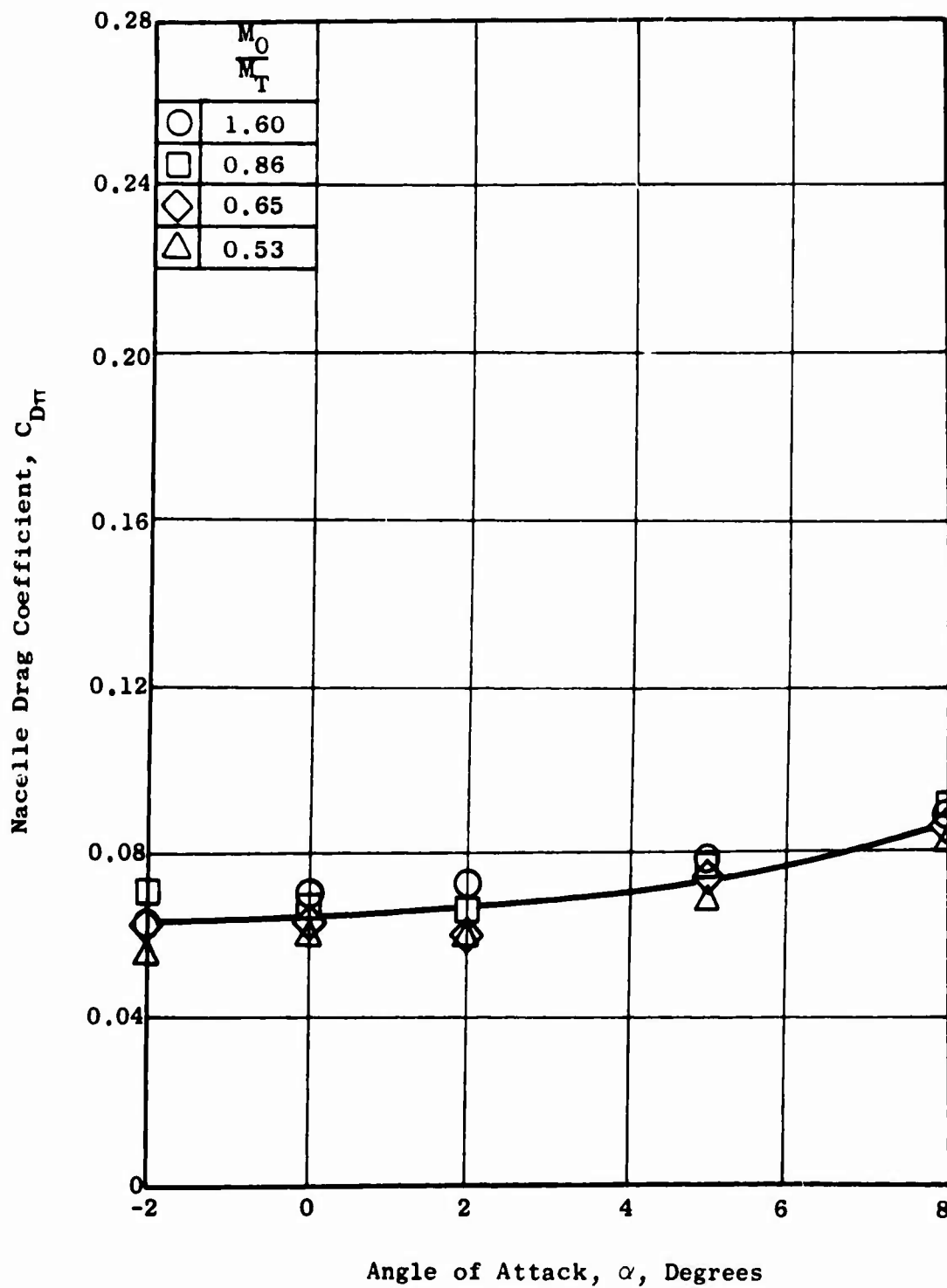


Figure 447. Variation of Nacelle Contribution to Drag with Angle of Attack and Speed, $M_0 = 0.3$.

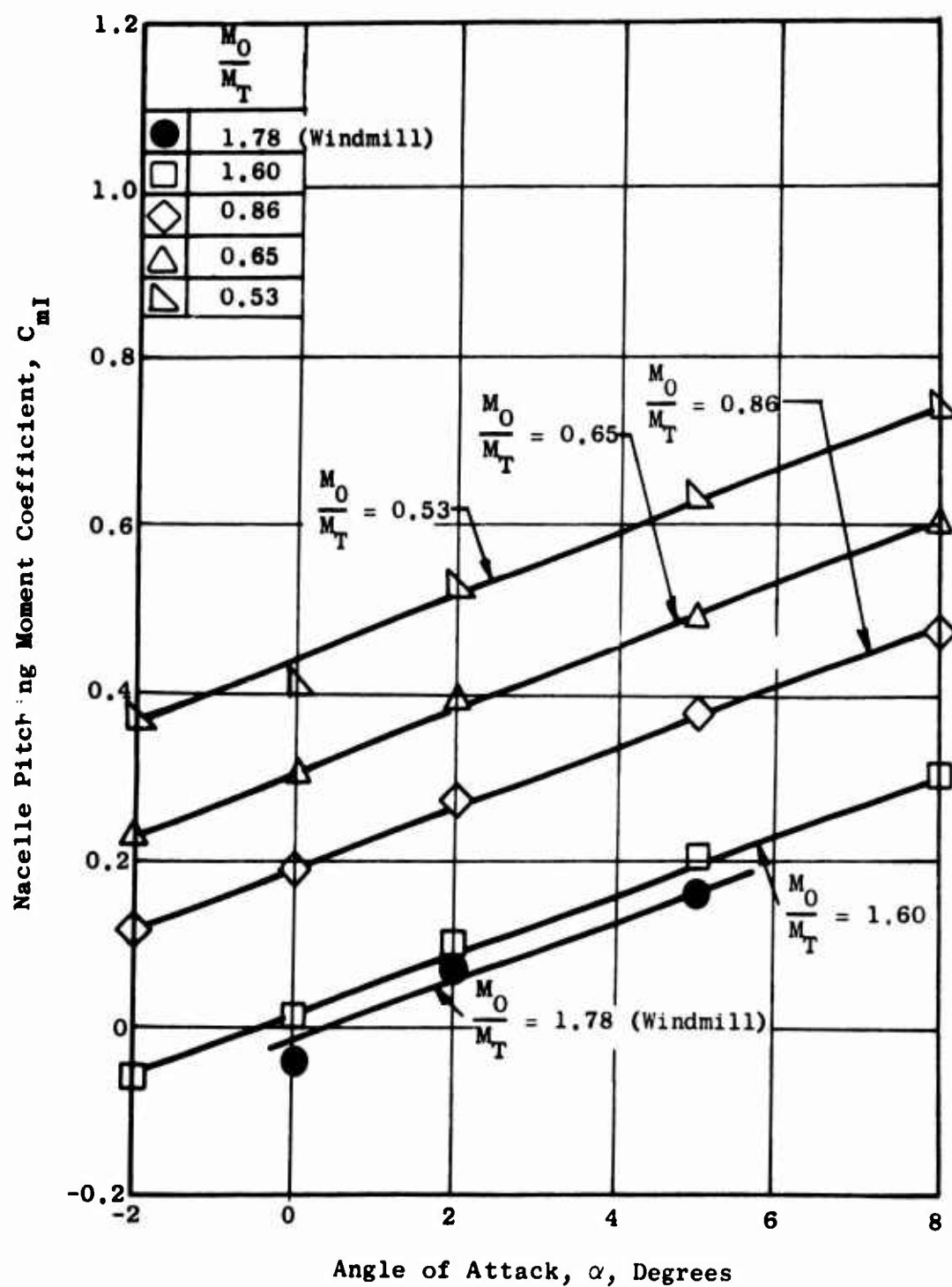


Figure 448. Variation of Nacelle Contribution to Pitching Moment with Angle of Attack and Speed, $M_0 = 0.3$.

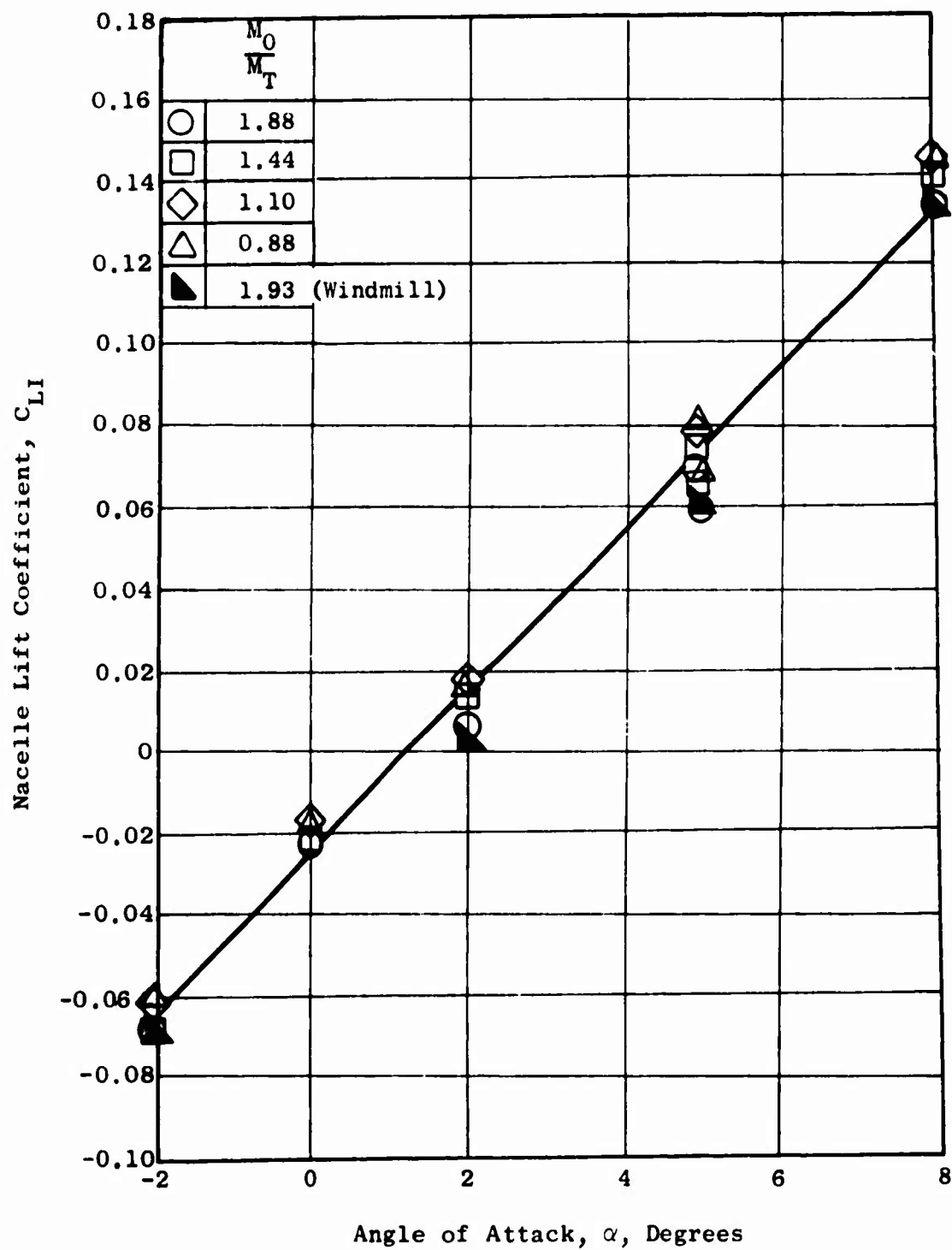


Figure 449. Variation of Nacelle Contribution to Lift with Angle of Attack and Speed, $M_0 = 0.50$.

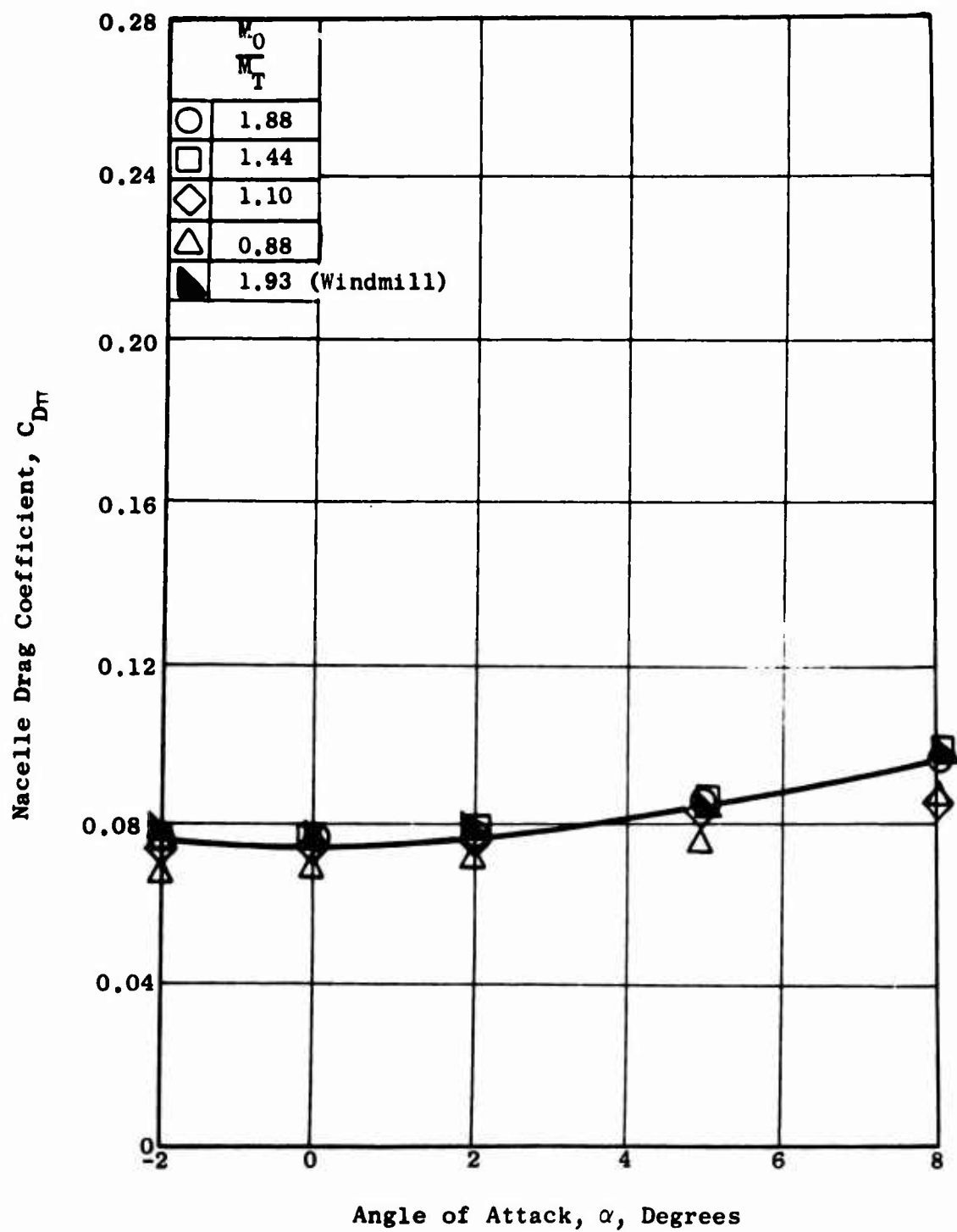


Figure 450. Variation of Nacelle Contribution to Drag with Angle of Attack and Speed, $M_0 = 0.50$.

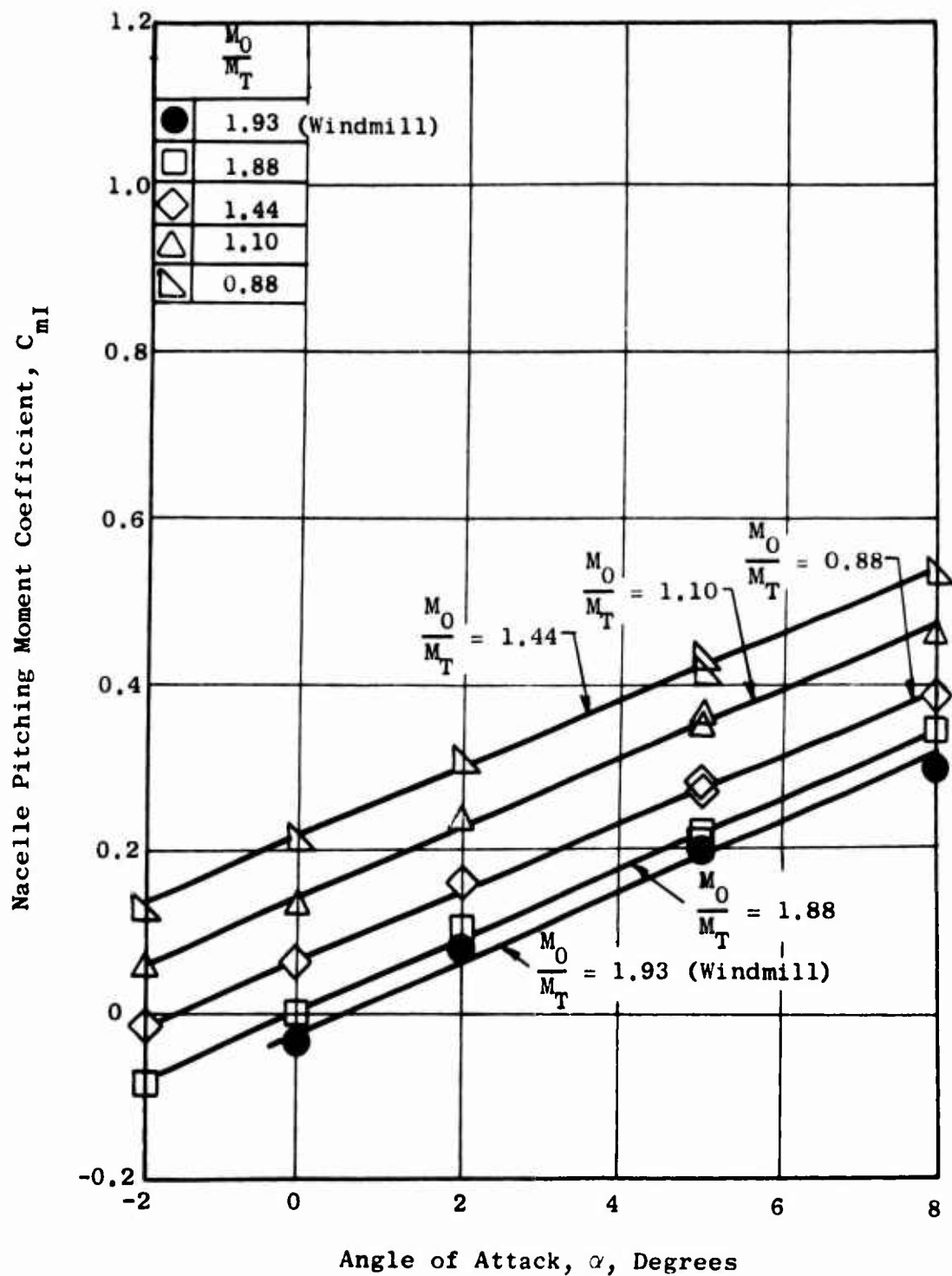


Figure 451. Variation of Nacelle Contribution to Pitching Moment with Angle of Attack and Speed, $M_O = 0.50$.

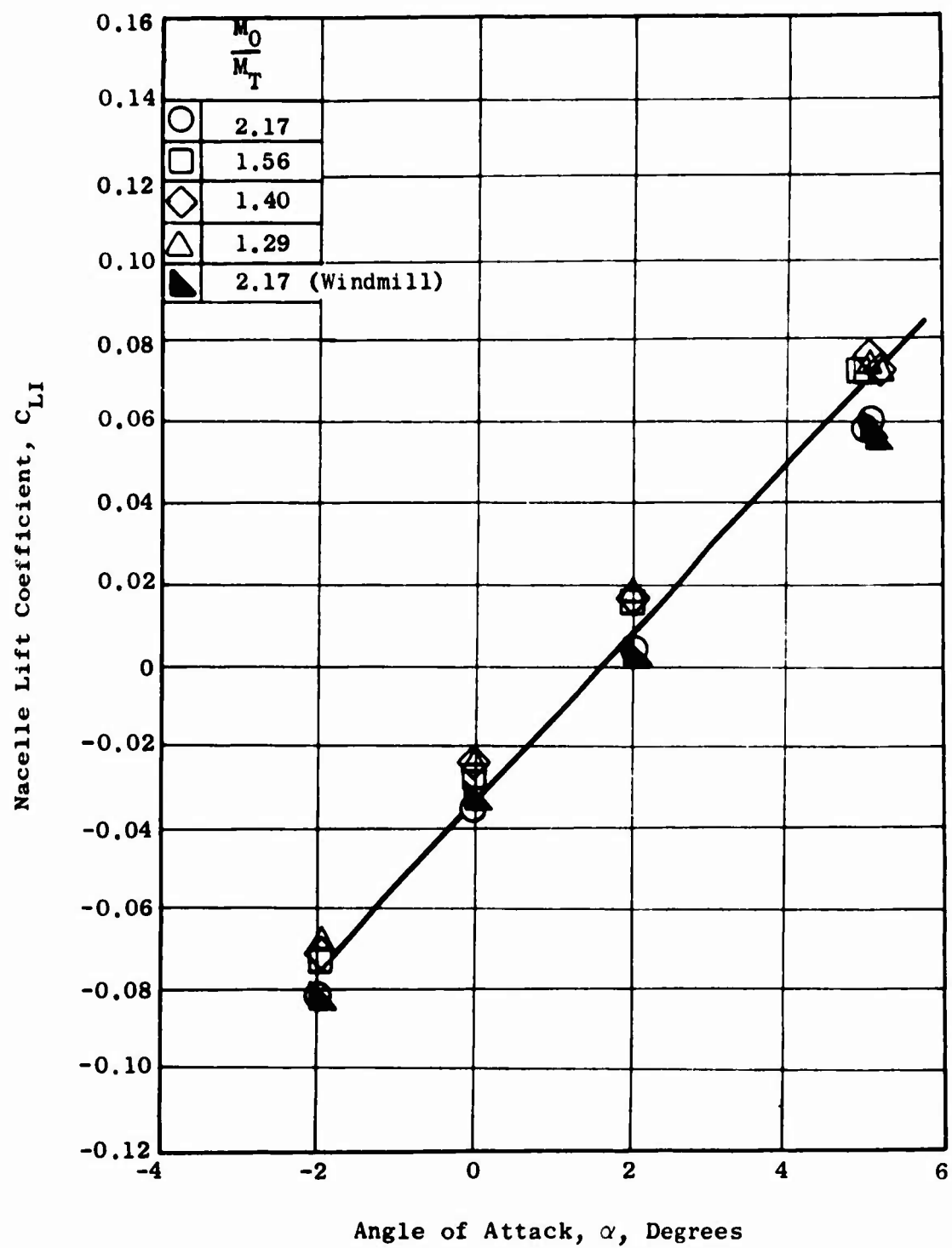


Figure 452. Variation of Nacelle Contribution to Lift with Angle of Attack and Speed, $M_0 = 0.70$.

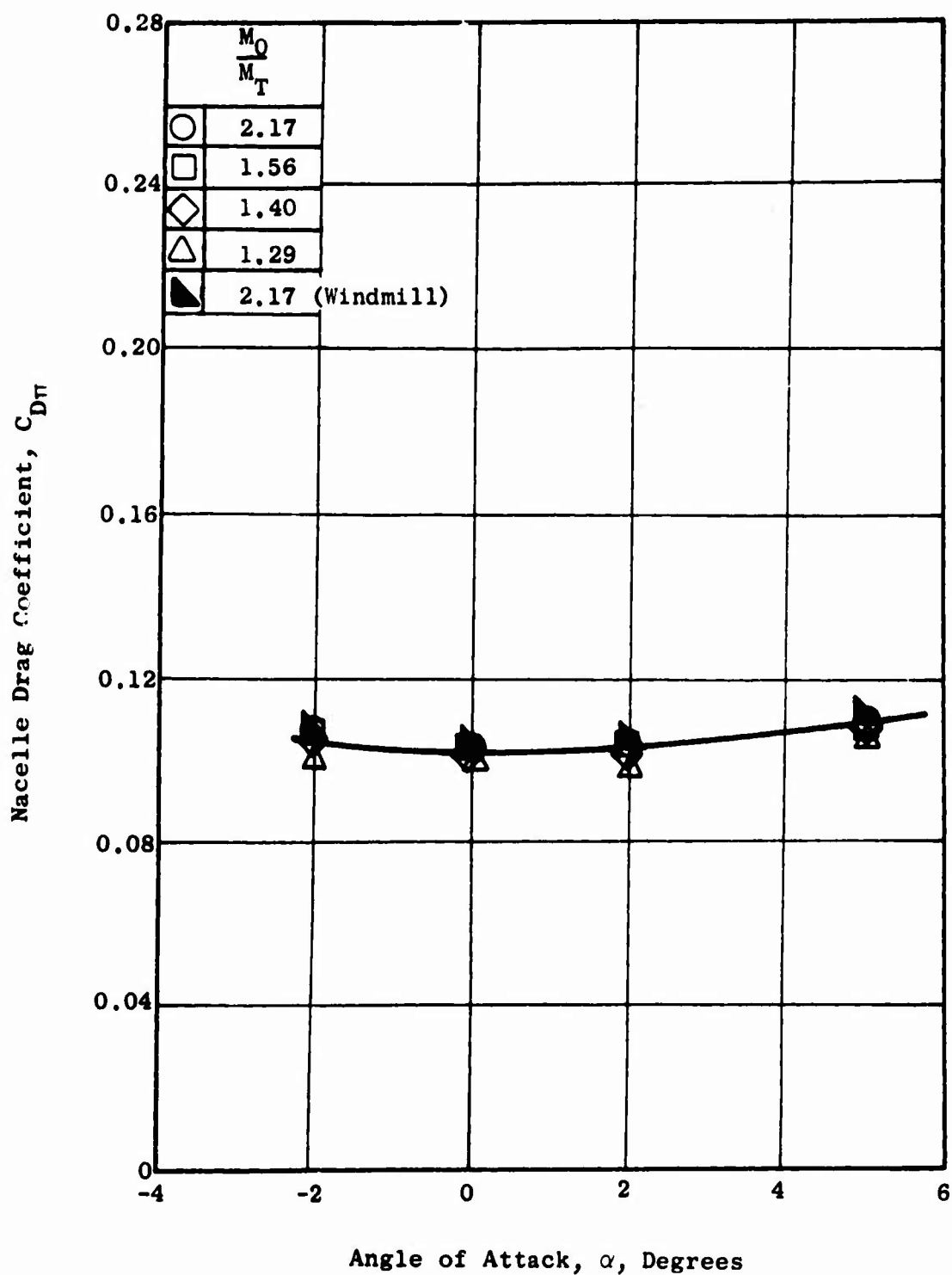


Figure 453. Variation of Nacelle Contribution to Drag with Angle of Attack and Speed, $M_0 = 0.70$.

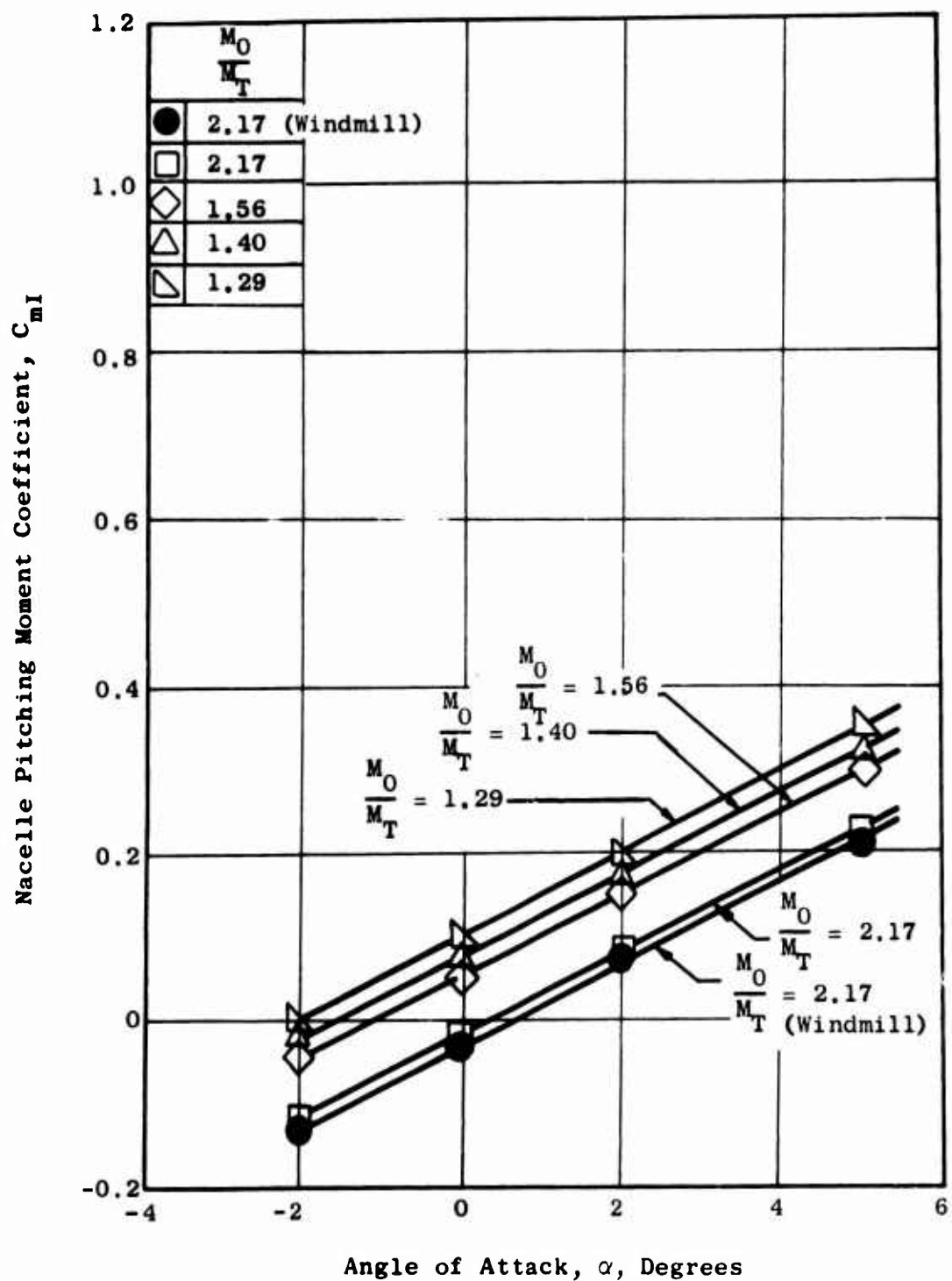


Figure 454. Variation of Nacelle Contribution to Pitching Moment with Angle of Attack and Speed, $M_O = 0.70$.

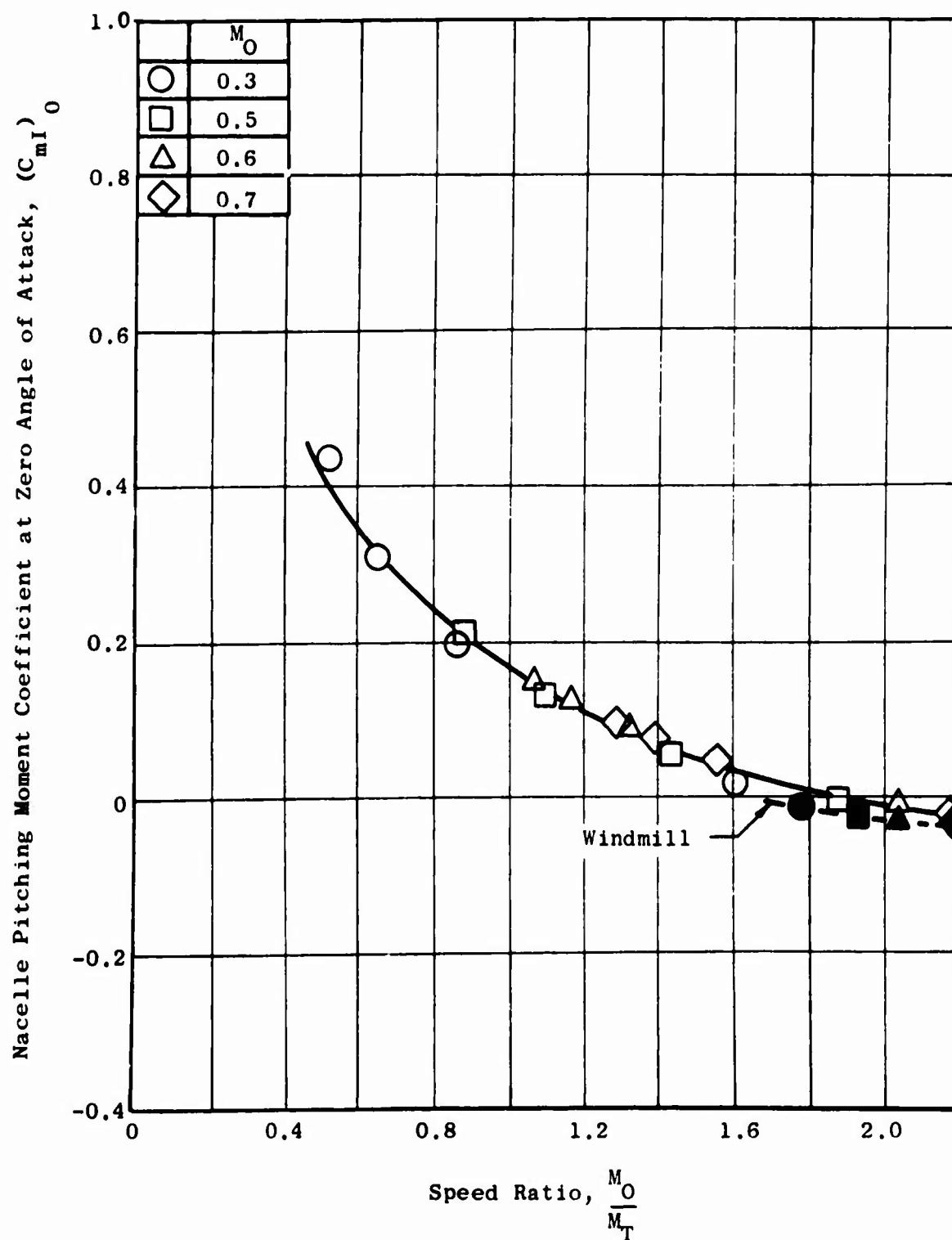


Figure 455. Variation of Nacelle Contribution to Pitching Moments with Speed - No Correction for Fan Thrust Alignment.

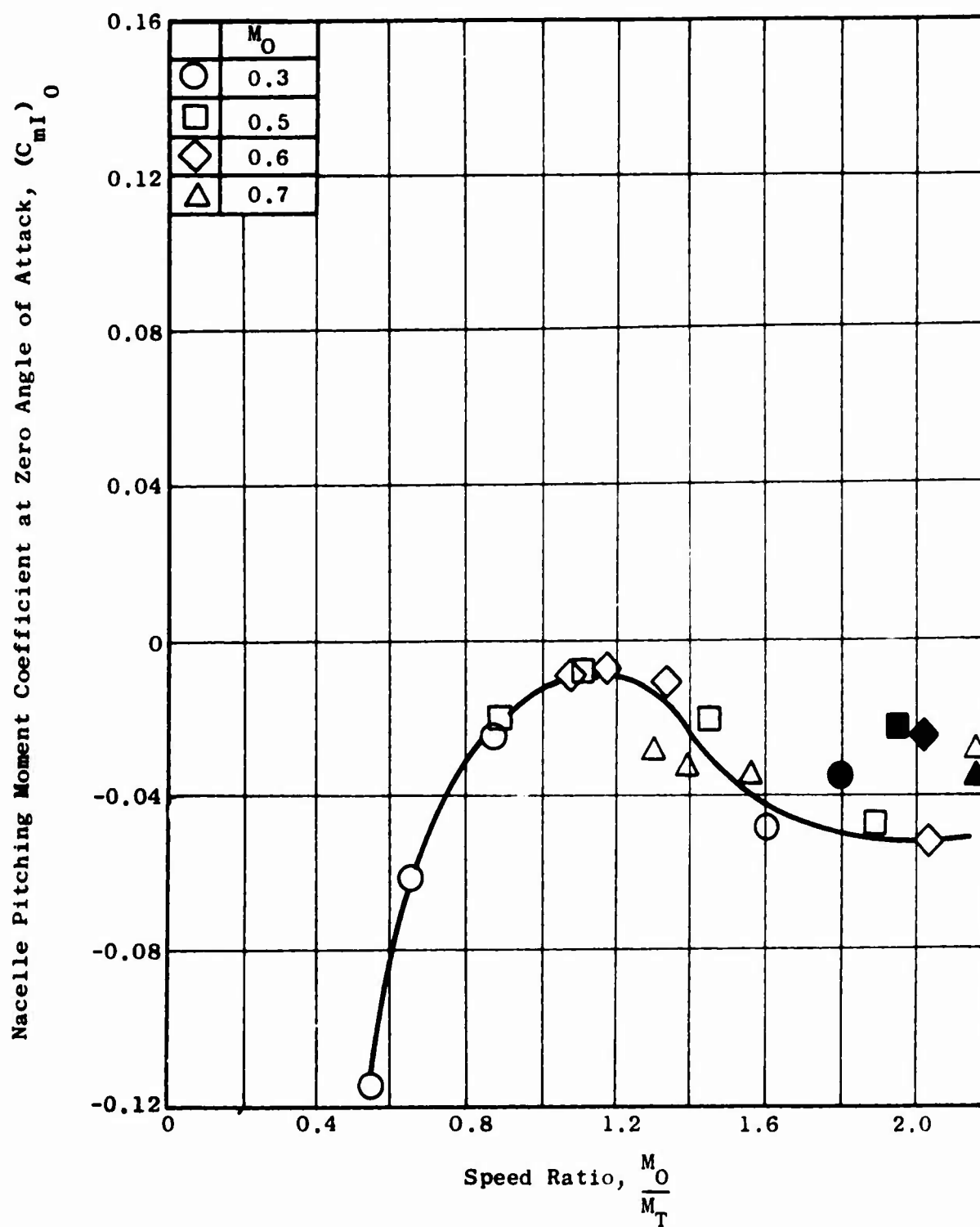


Figure 456. Variation of Nacelle Contribution to Pitching Moments with Speed - Corrected for Static Fan Thrust Alignment.

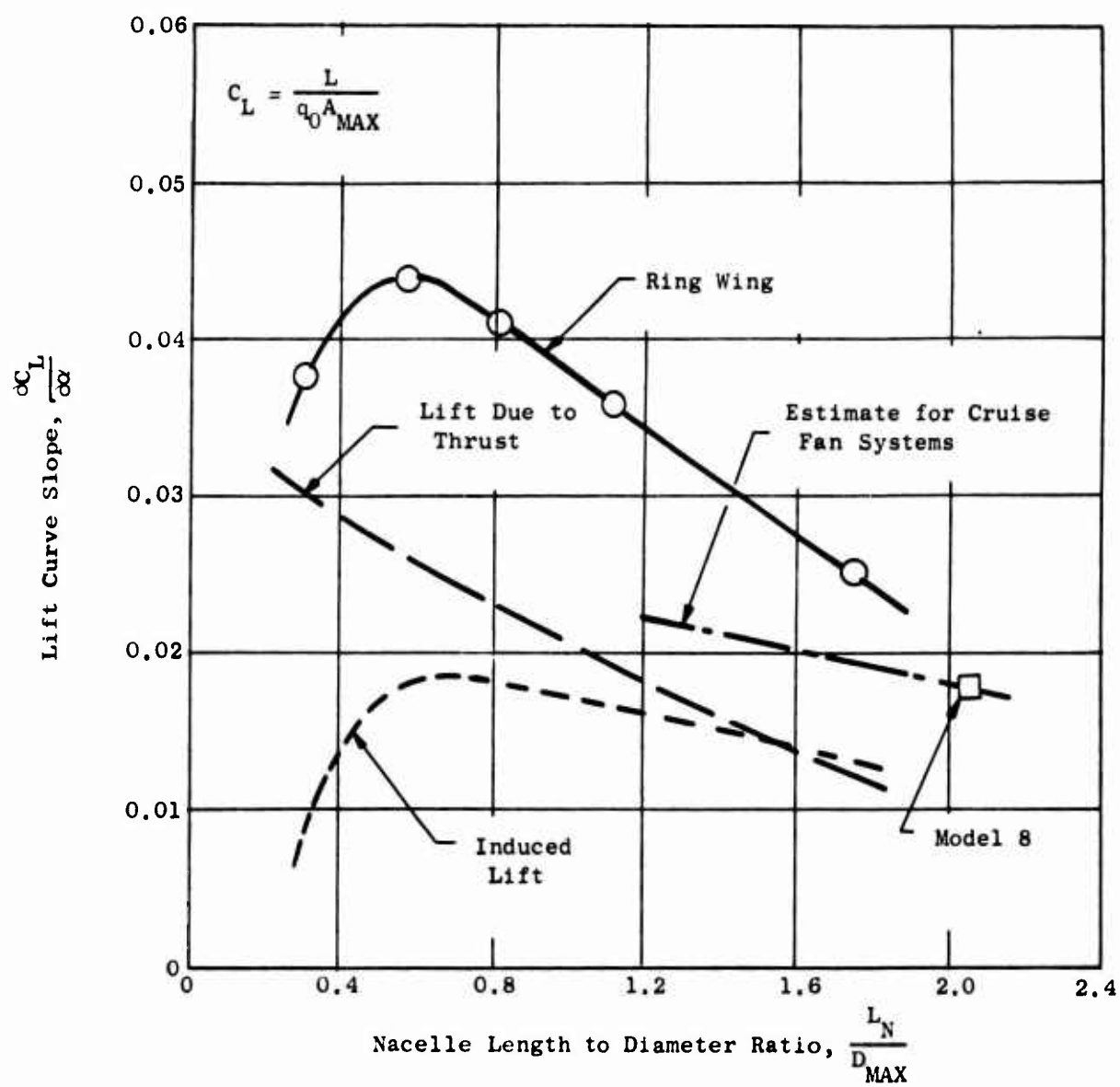


Figure 457. Comparison of Lift Curve Slope of Model 8 and Ring Wing Data.

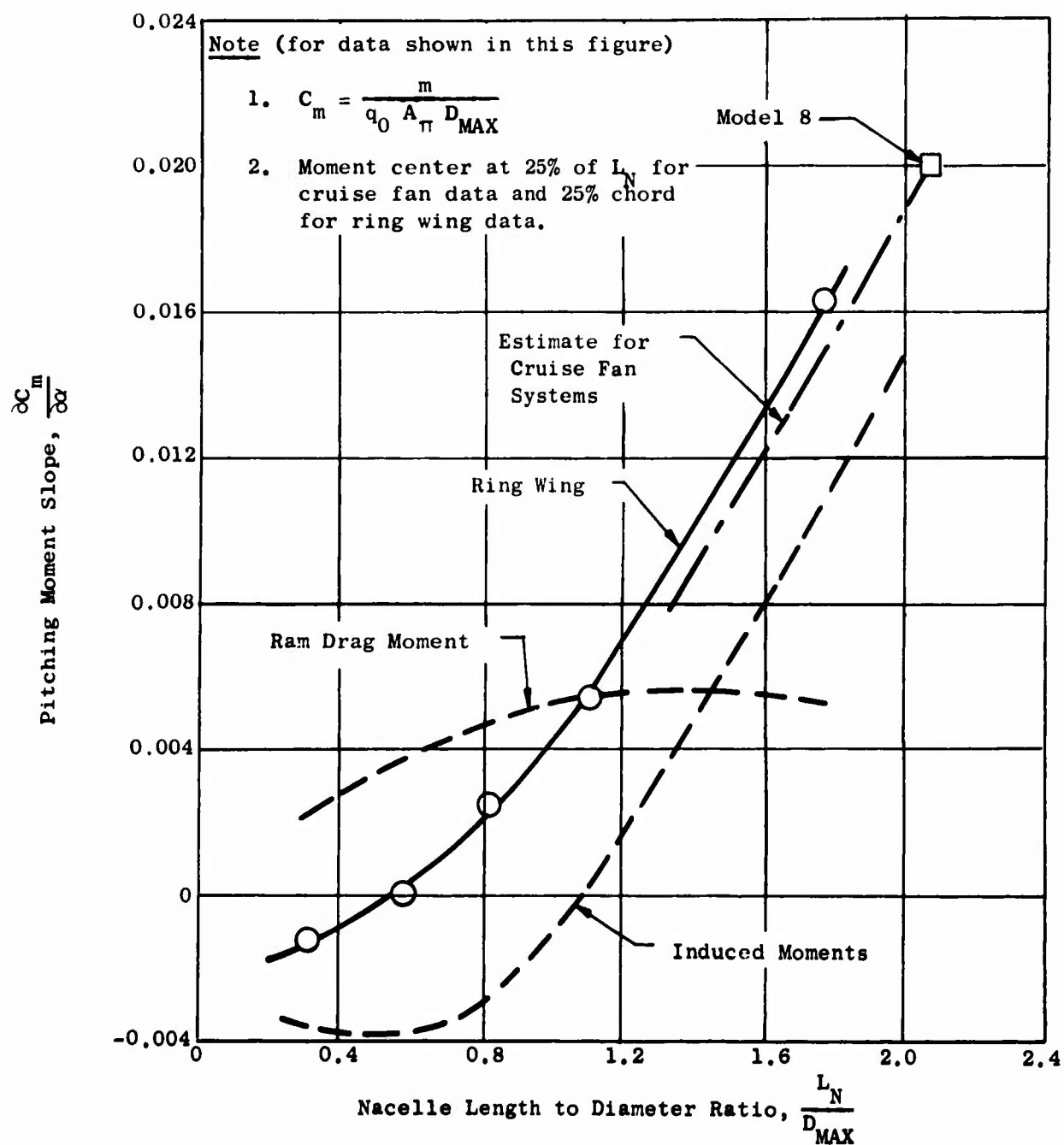


Figure 458. Comparison of Pitching Moment Curve Slope of Model 8 and Ring Wing Data.

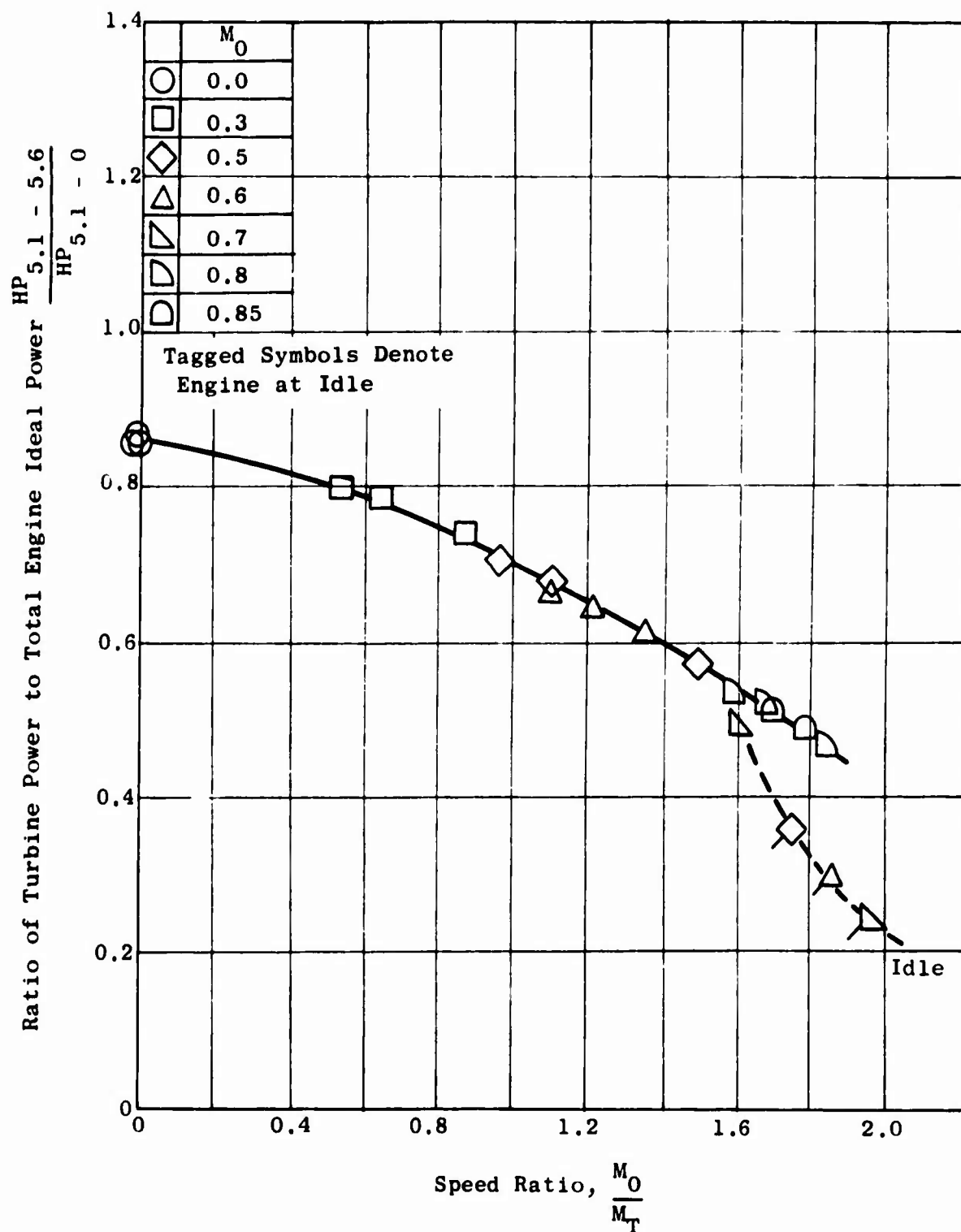


Figure 459. Ratio of Absorbed to Ideal Horsepower - Model 1.

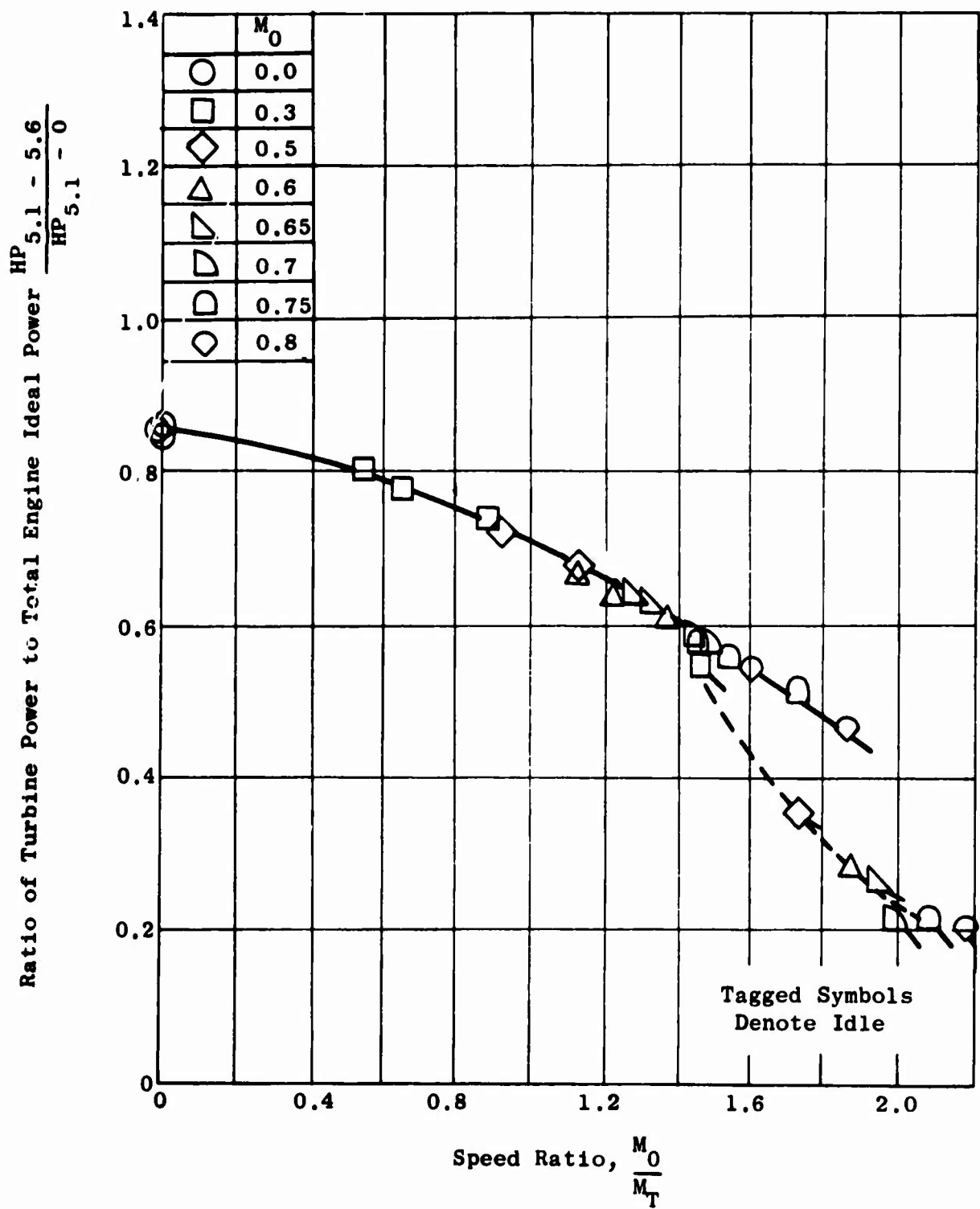


Figure 460. Ratio of Absorbed to Ideal Horsepower - Model 2.

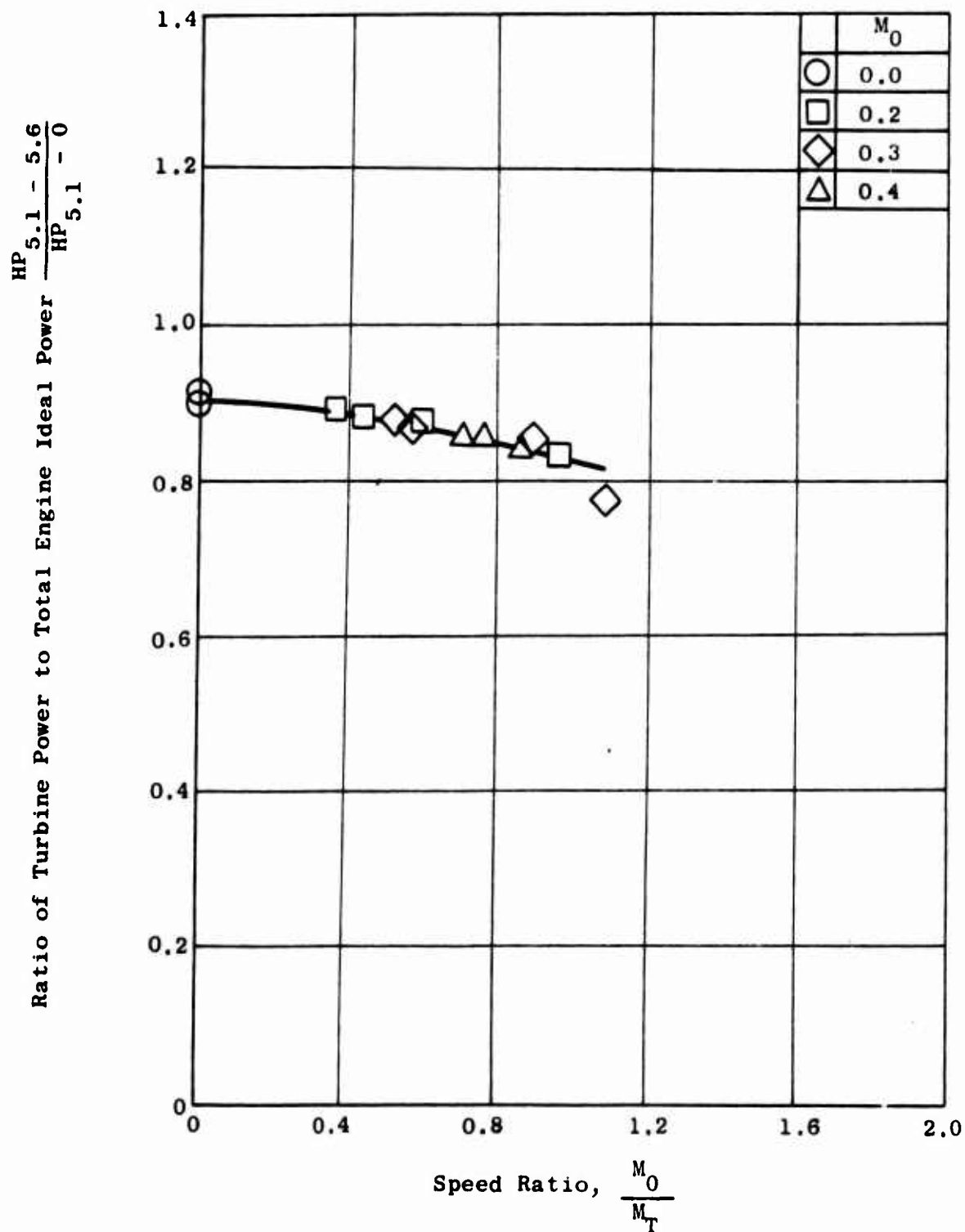


Figure 461. Ratio of Absorbed to Ideal Horsepower - Model 3.

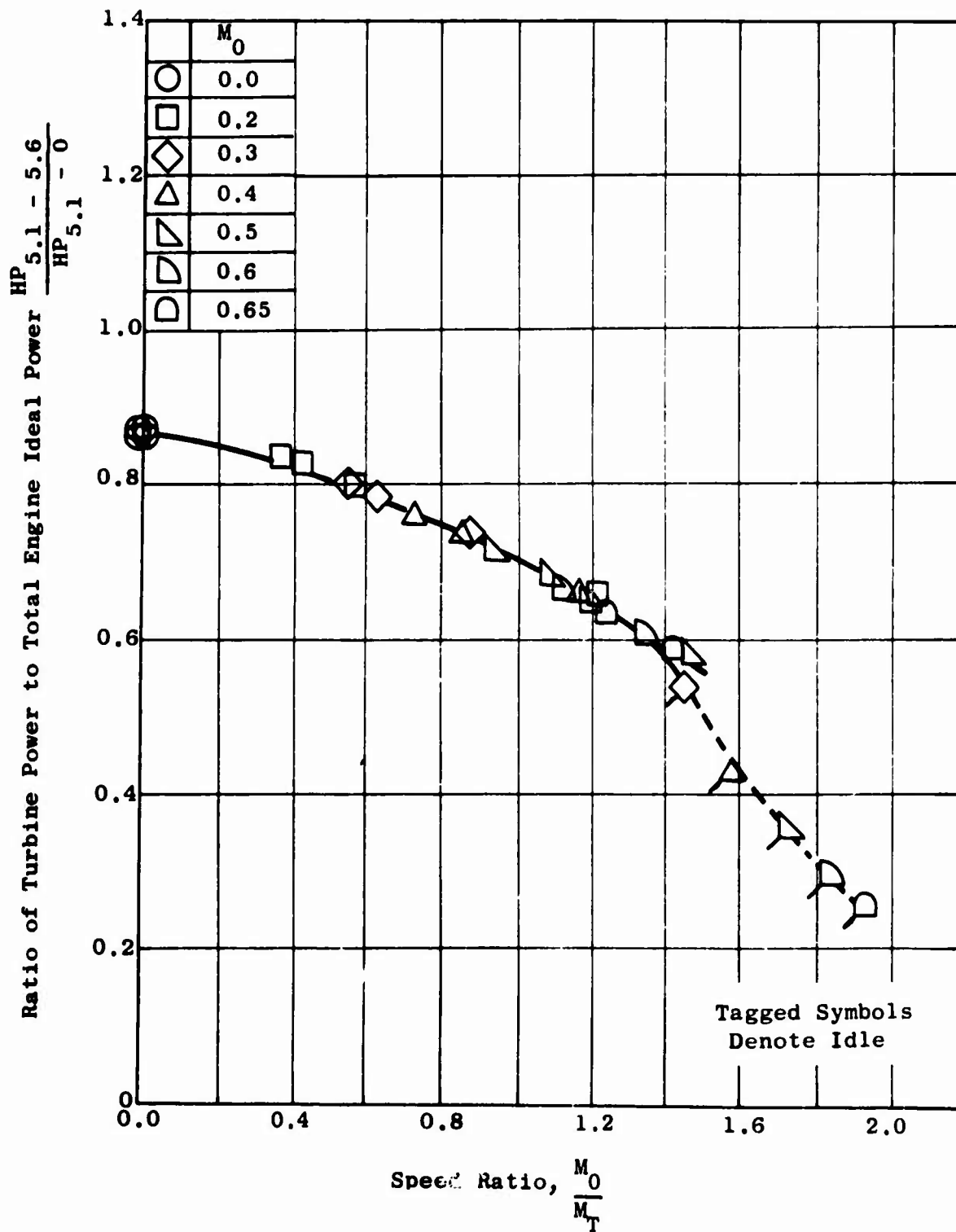


Figure 462. Ratio of Absorbed to Ideal Horsepower - Model 4.

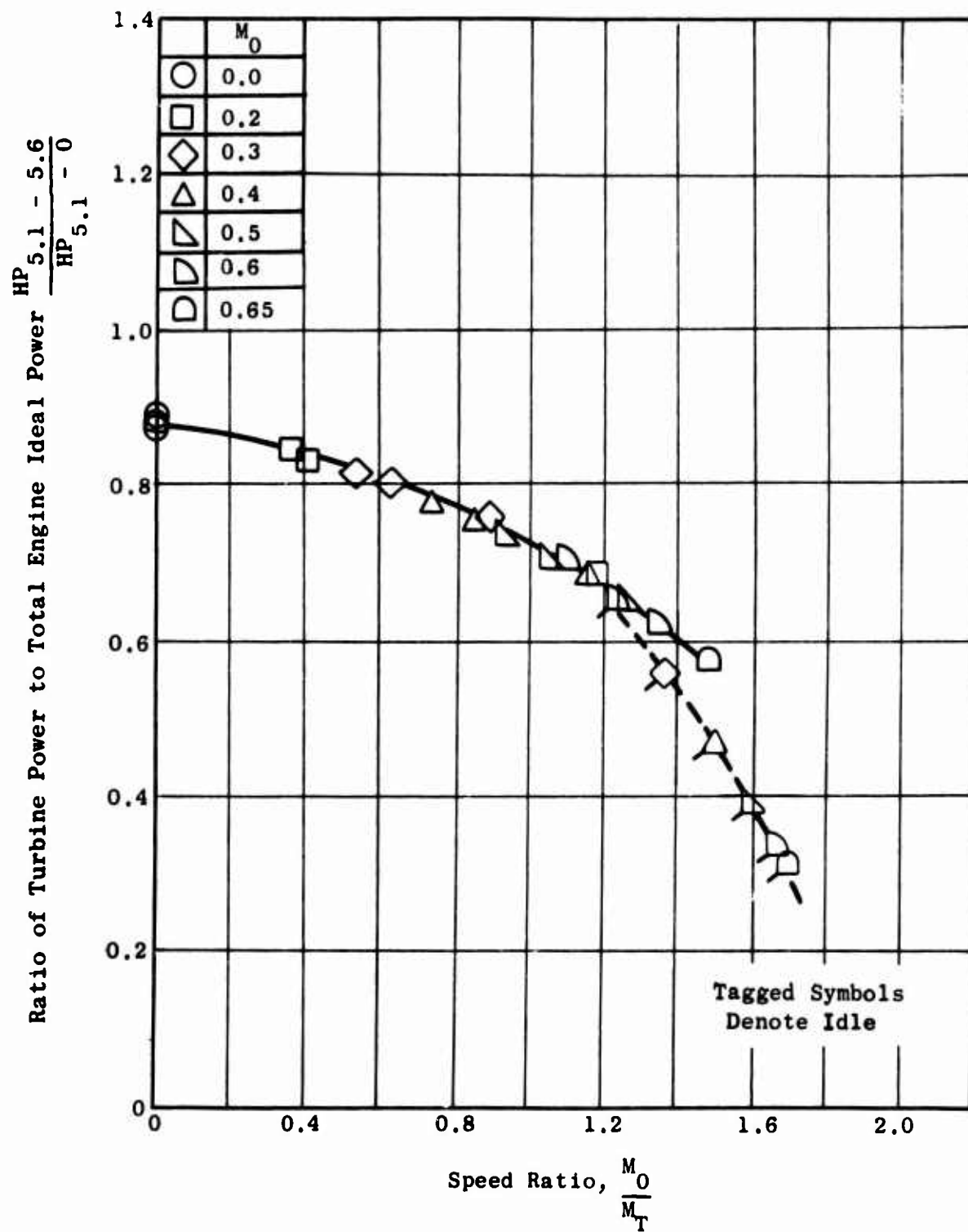


Figure 463. Ratio of Absorbed to Ideal Horsepower - Model 5.

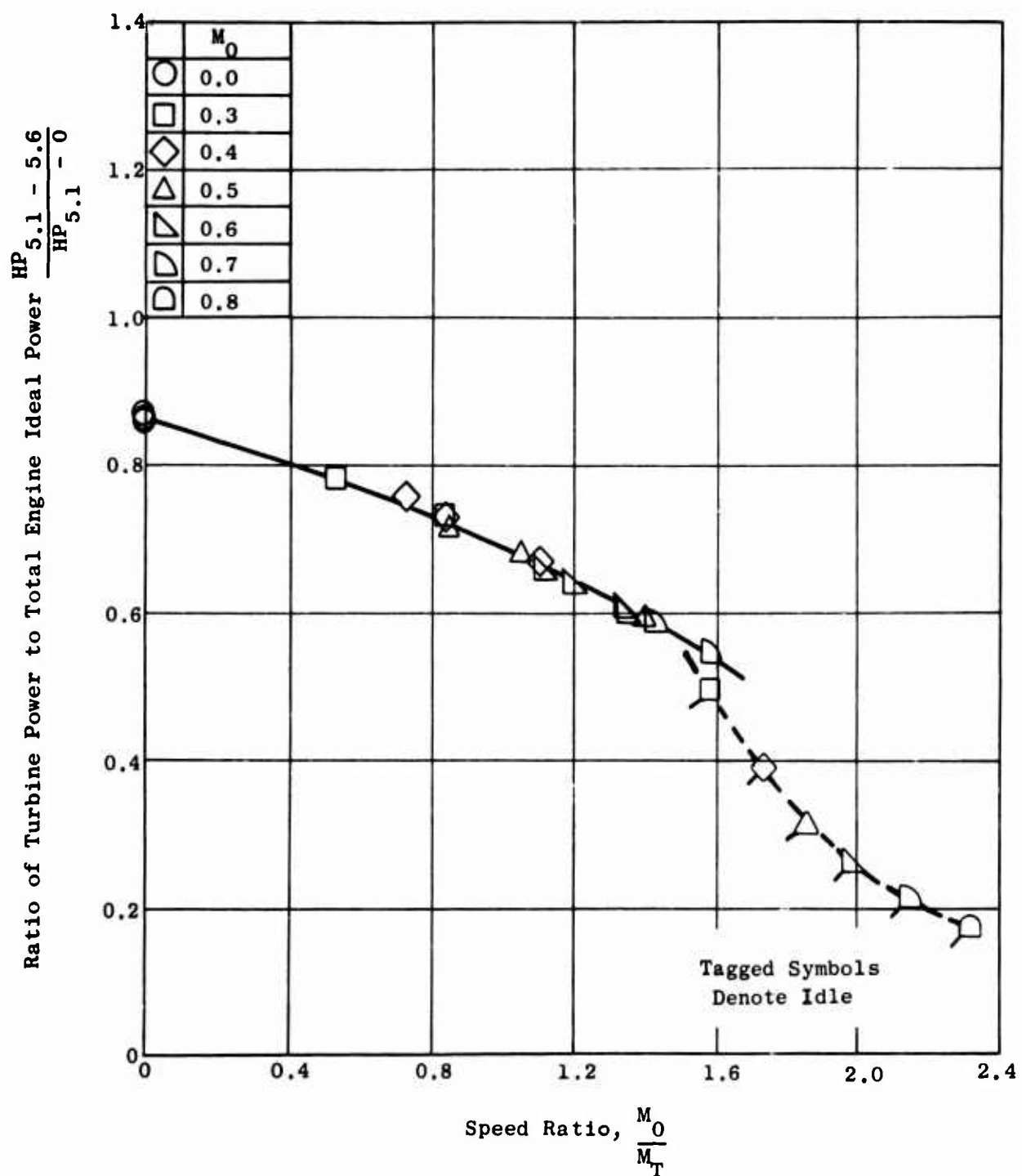


Figure 464. Ratio of Absorbed to Ideal Horsepower - Model 6.

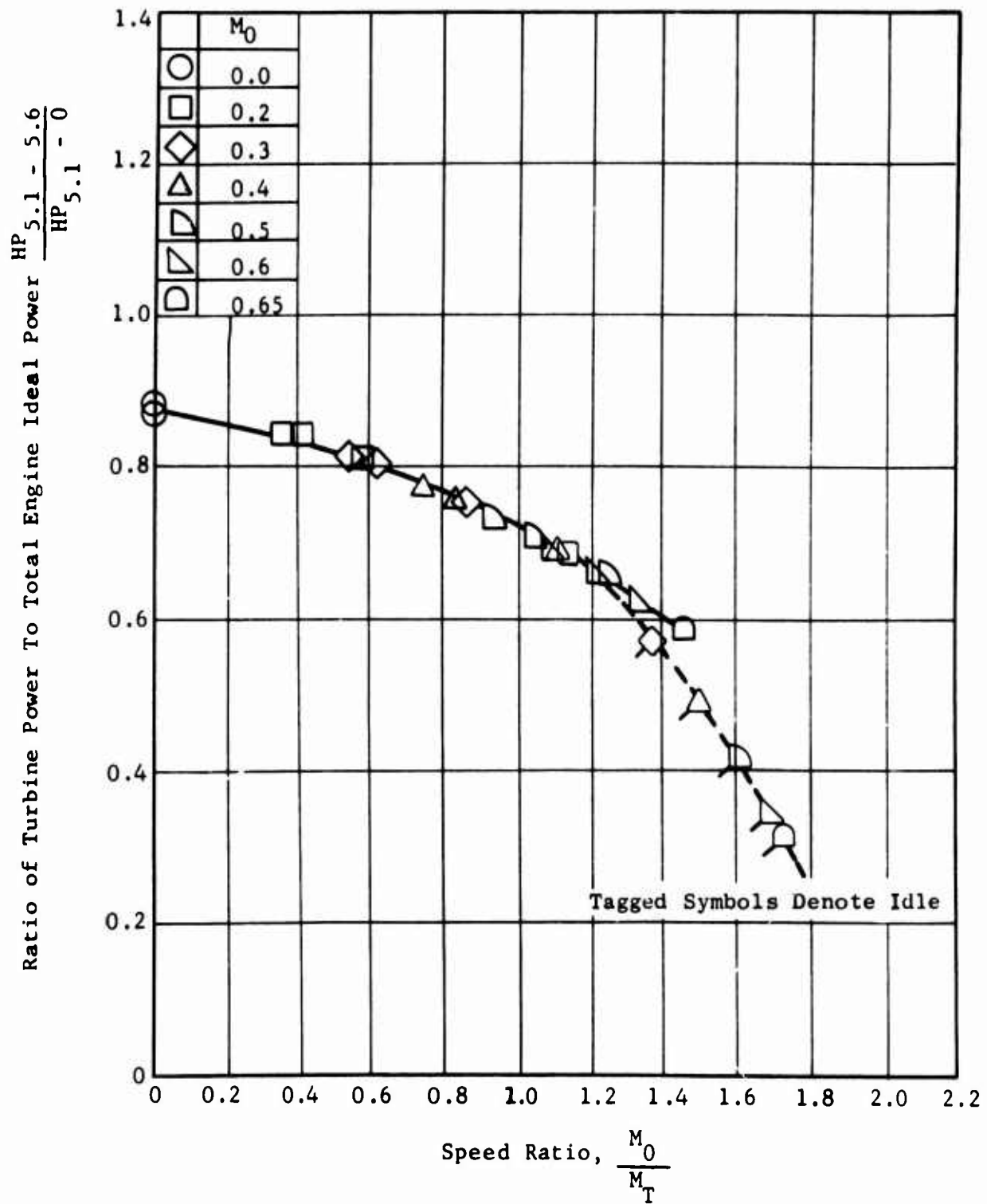


Figure 465. Ratio of Absorbed to Ideal Horsepower - Model 7.

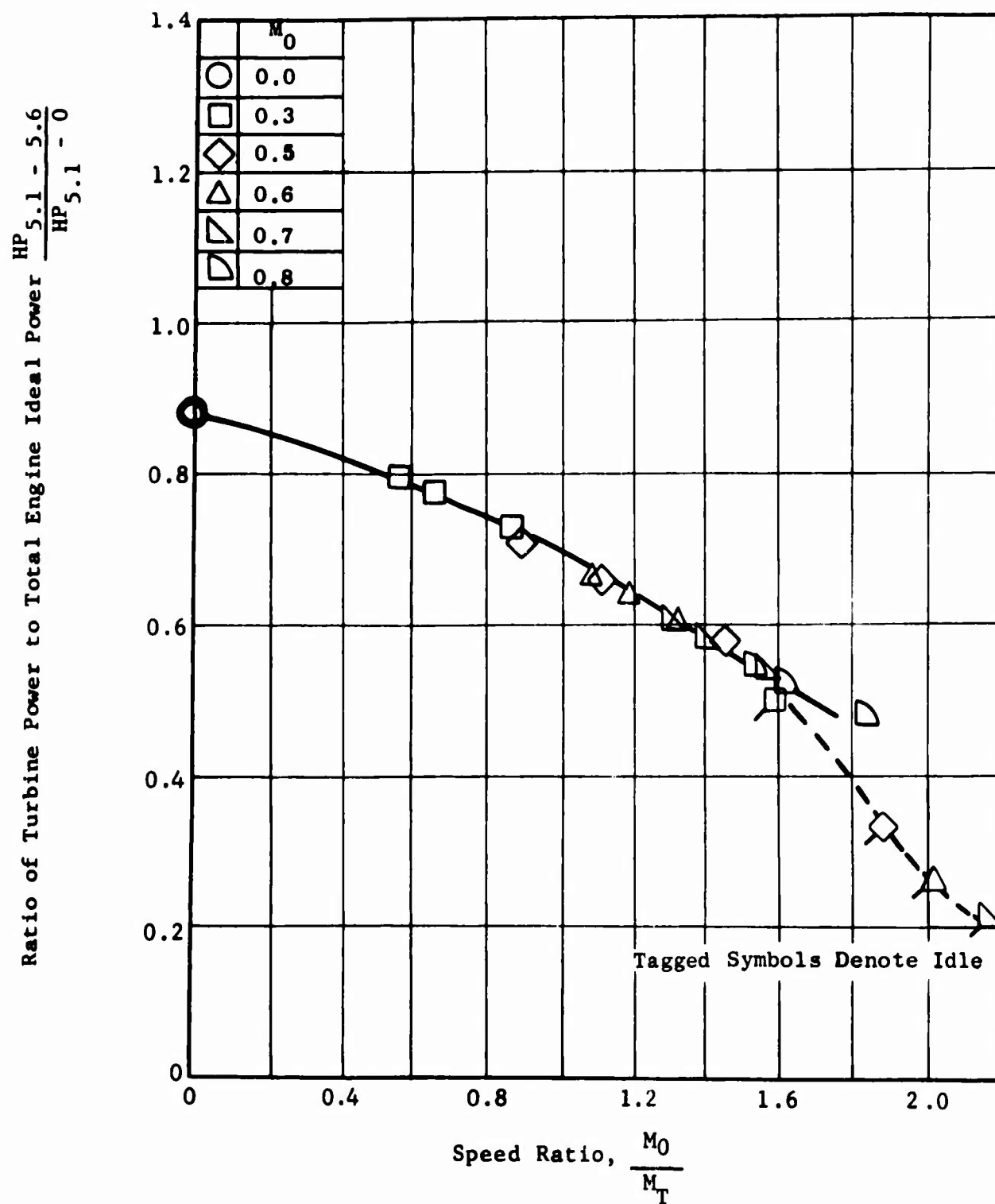


Figure 466. Ratio of Absorbed to Ideal Horsepower - Model 8.

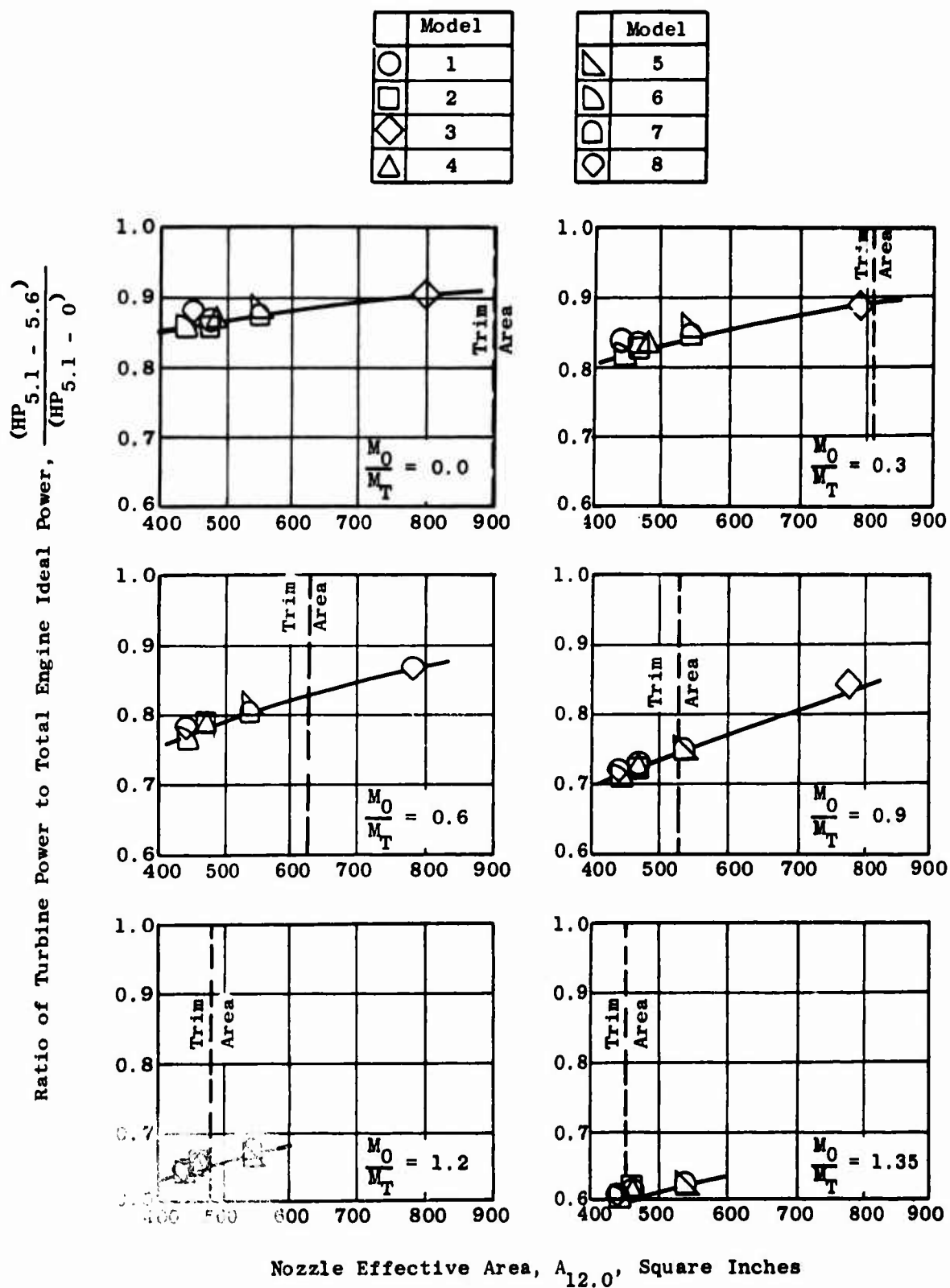


Figure 467. Variation of Horsepower Ratio with Speed and Nozzle Area.

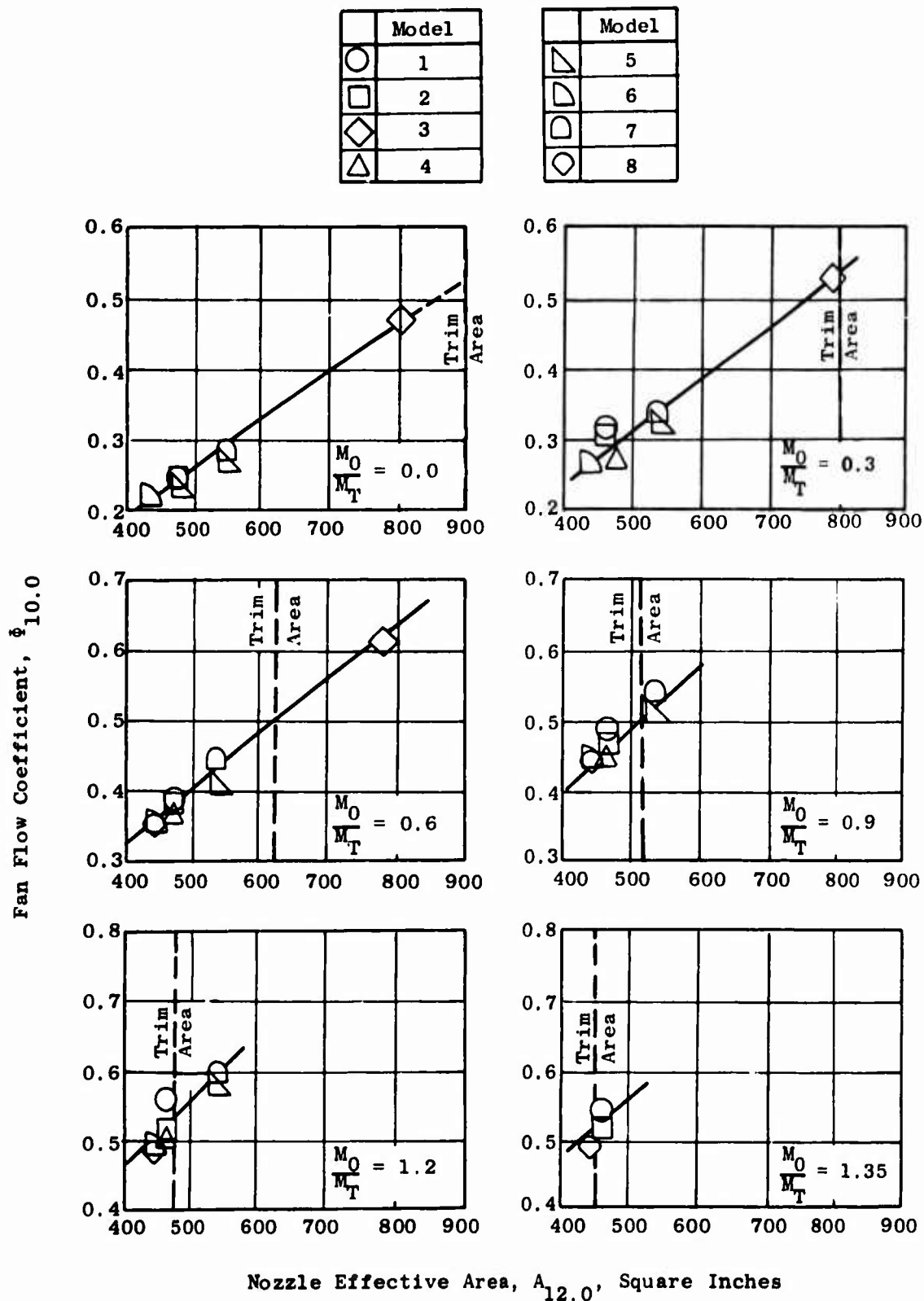
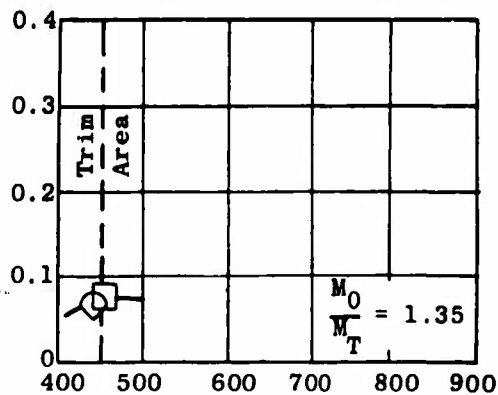
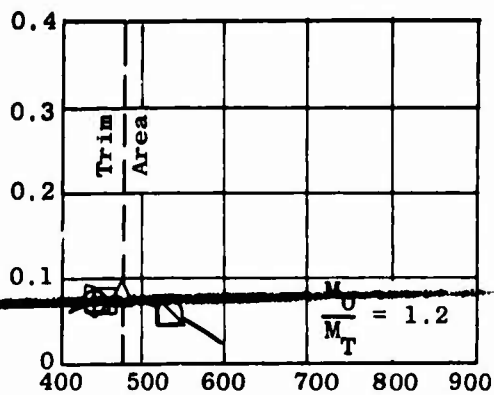
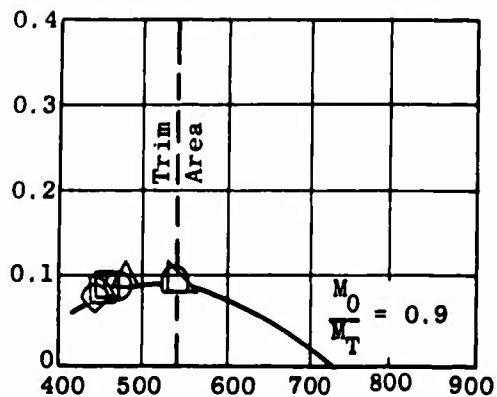
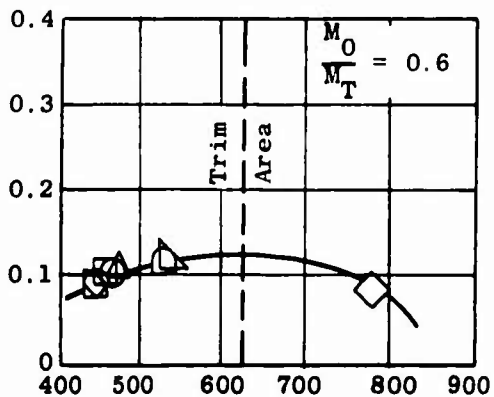
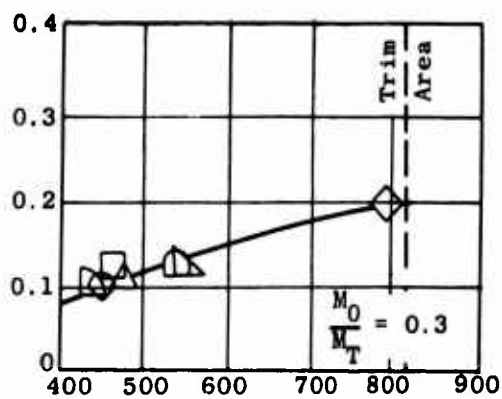
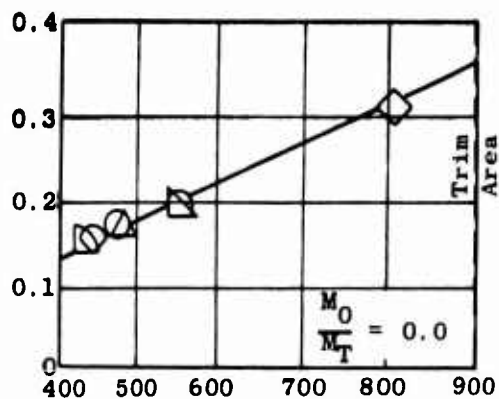


Figure 468. Variation of Flow Coefficient with Speed and Nozzle Area.

	Model
○	1
□	2
◇	3
△	4

	Model
▽	5
◐	6
◑	7
◒	8

Fan Net Thrust Coefficient, H_N



Nozzle Effective Area, $A_{12.0}$, Square Inches

Figure 469. Variation of Ideal Net Thrust with Speed and Nozzle Area.

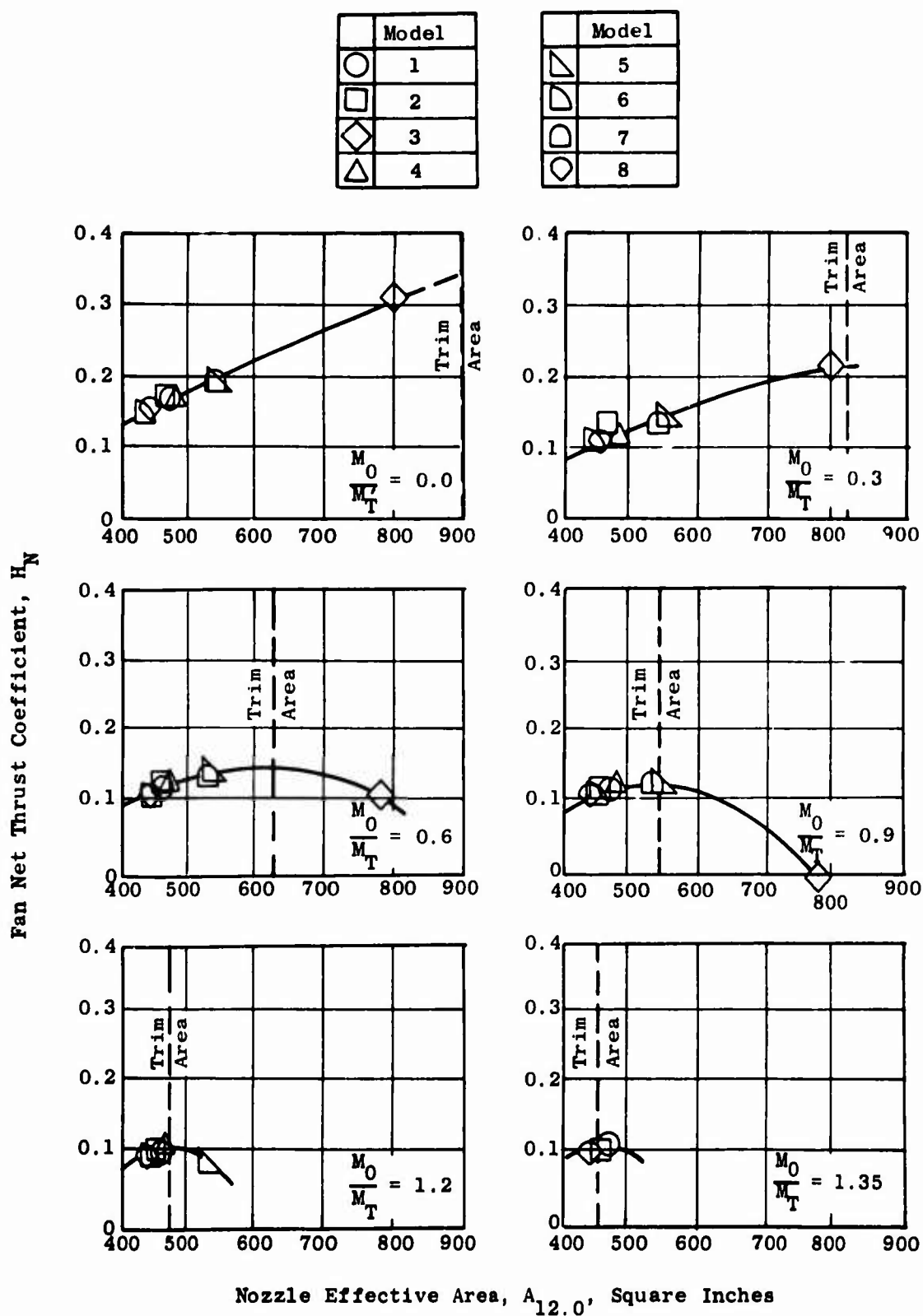


Figure 470. Variation of Net Thrust with Speed and Nozzle Area for a 0.95 Nozzle Thrust Coefficient.

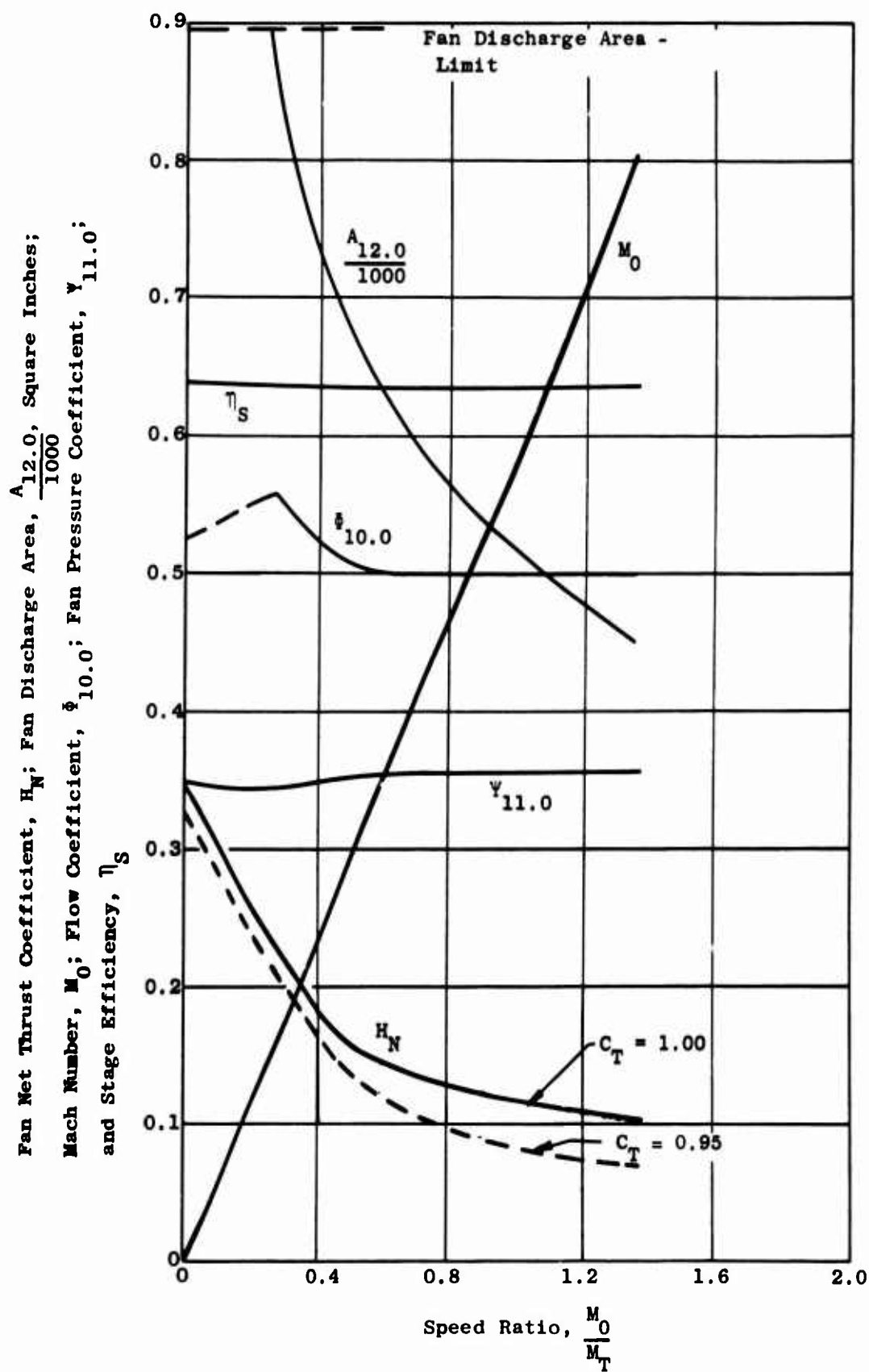


Figure 471. Fan Operating Characteristics for Optimum Nozzle Trim and 100% Fan Speed.

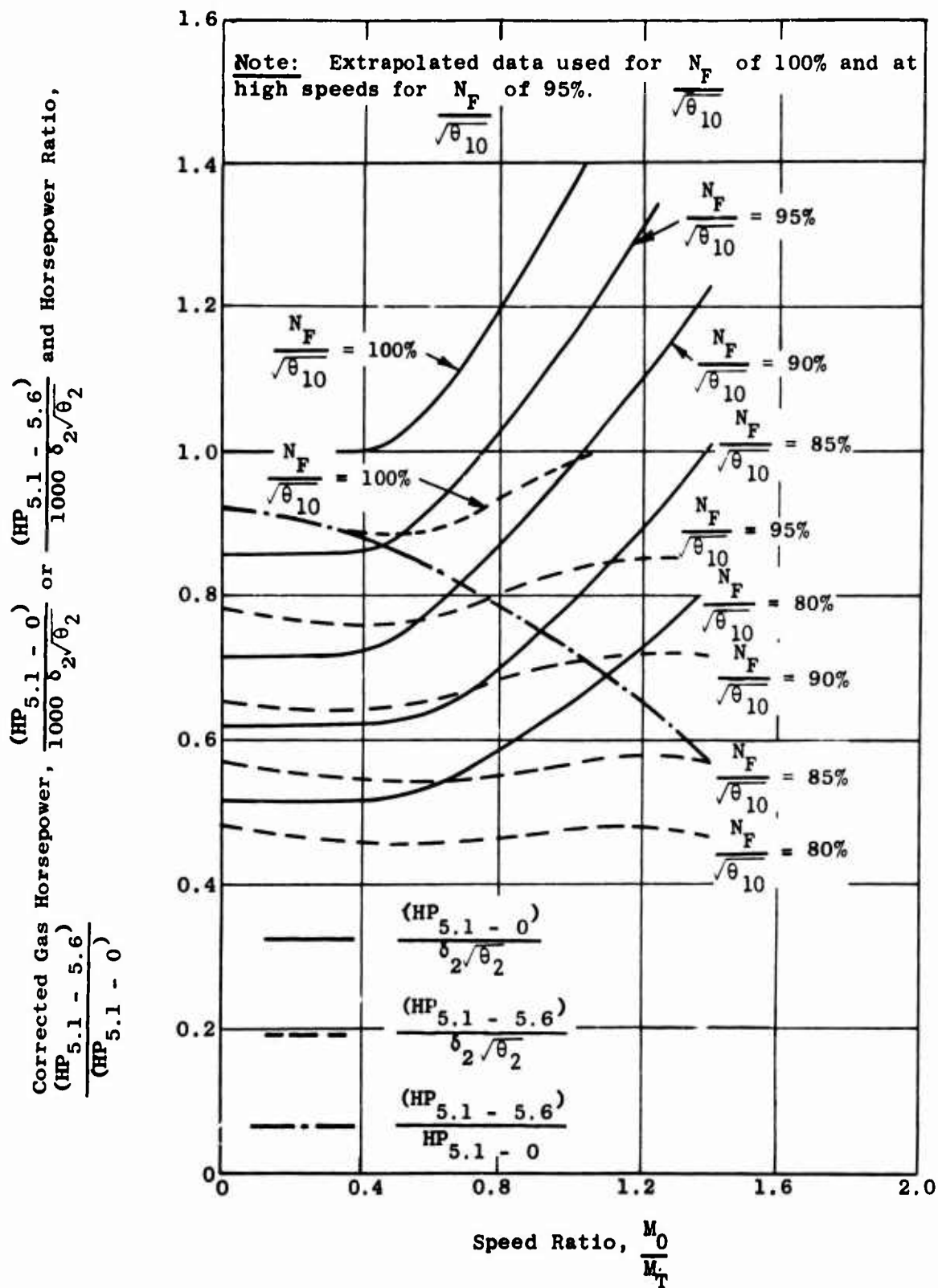


Figure 472. Fan Horsepower Requirements as a Function of Speed and Mach Number for Optimum Trim Area.

	Model
○	1
□	2
◇	3
△	4

	Model
▽	5
◐	6
◑	7
◒	8

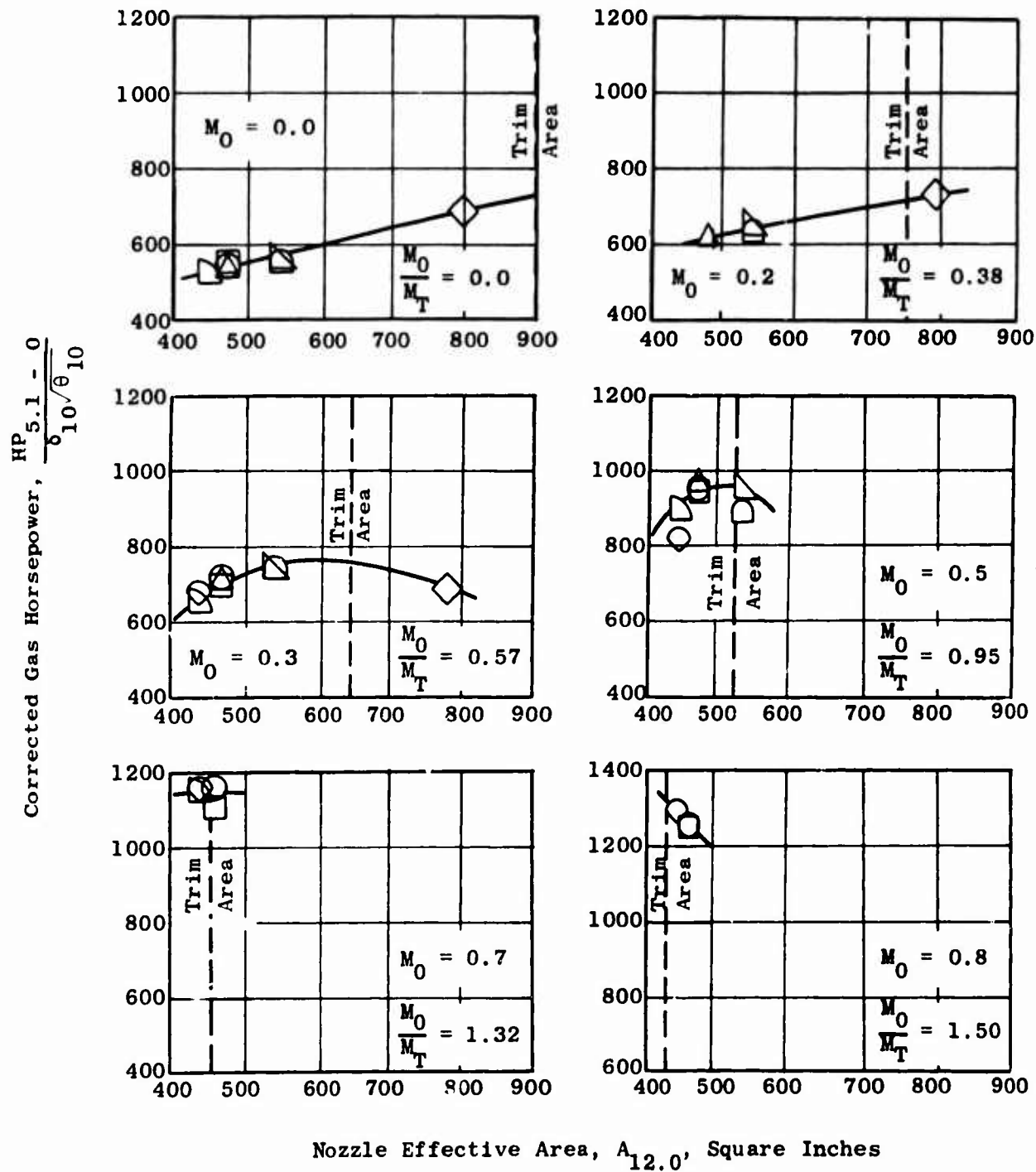


Figure 473. Variation of Fan Horsepower Requirements with Speed and Nozzle Area at a Fan Speed of 90%.

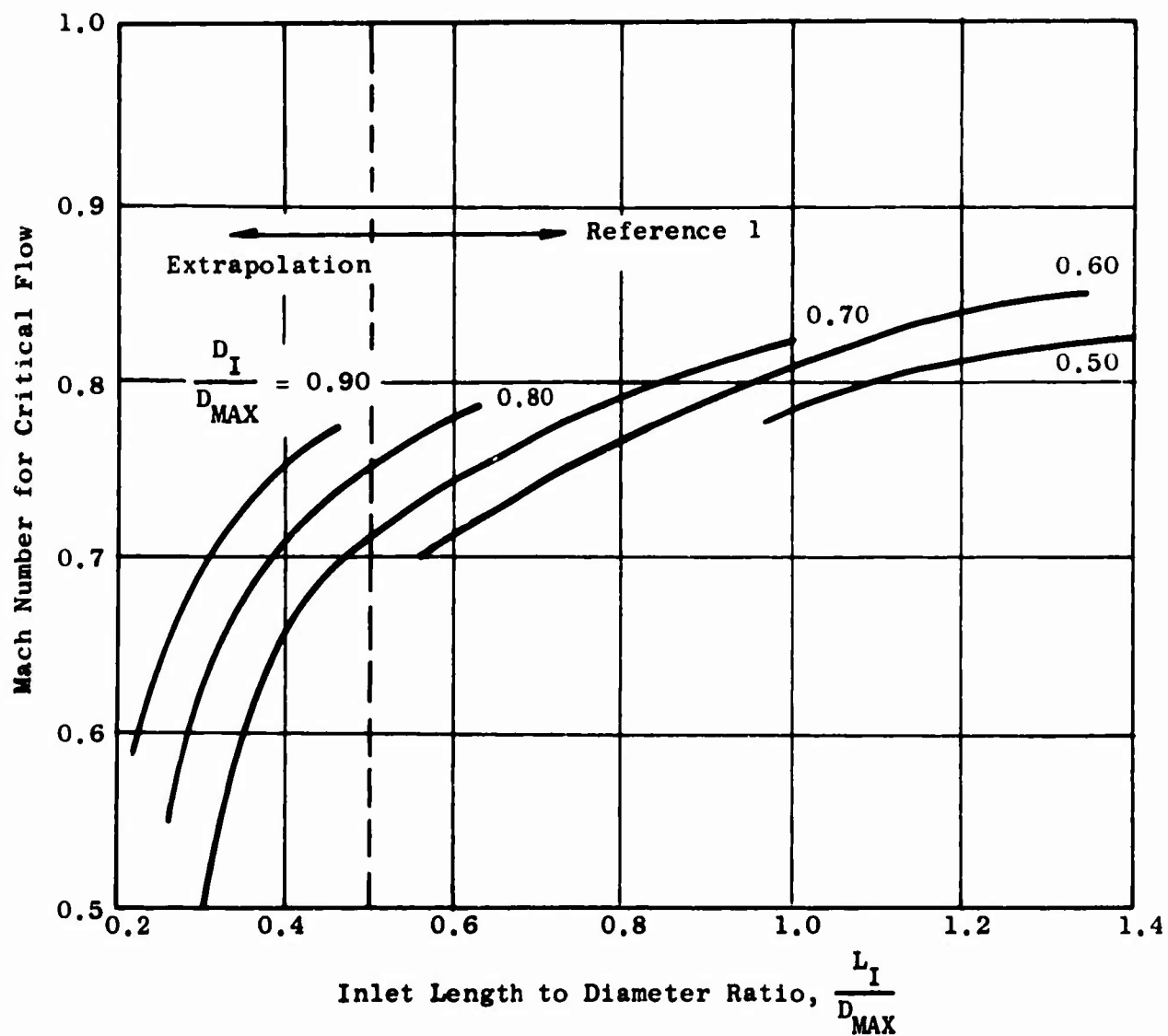


Figure 474. Predicted Nacelle Critical Mach Number as a Function of Inlet Length and Inlet Diameter.

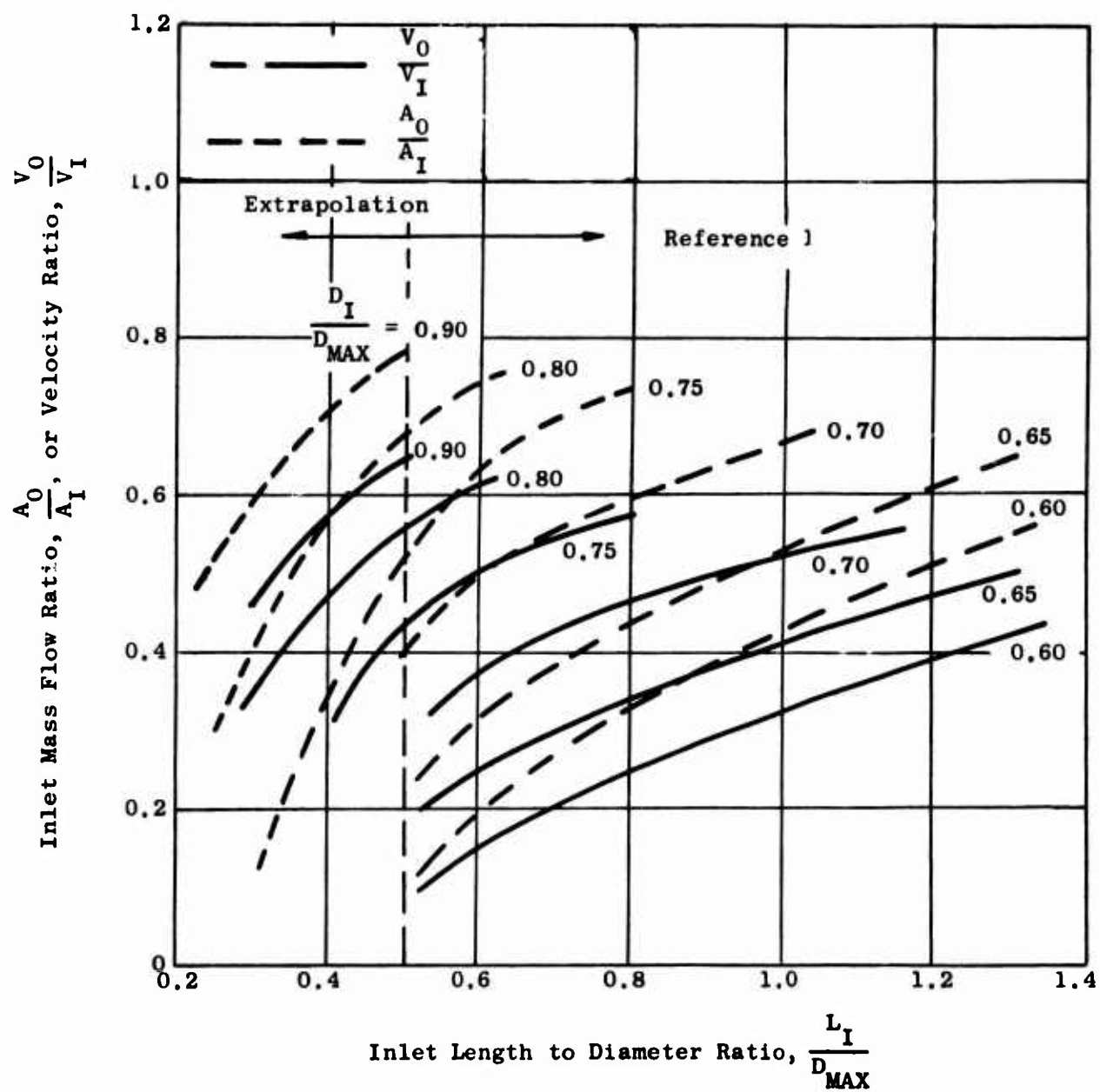


Figure 475. Predicted Minimum Mass Flow and Velocity Ratios as a Function of Inlet Length and Inlet Diameter.

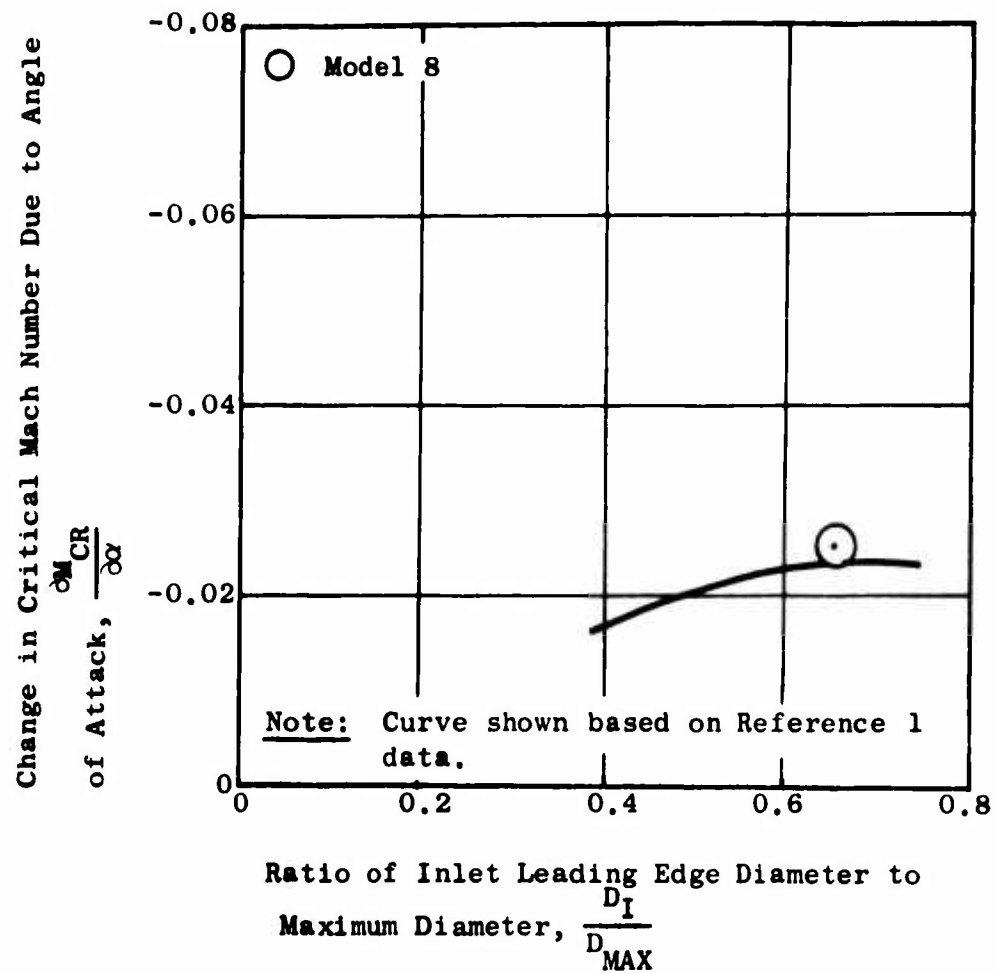


Figure 476. Estimated Correction to Critical Mach Number for Angle of Attack.

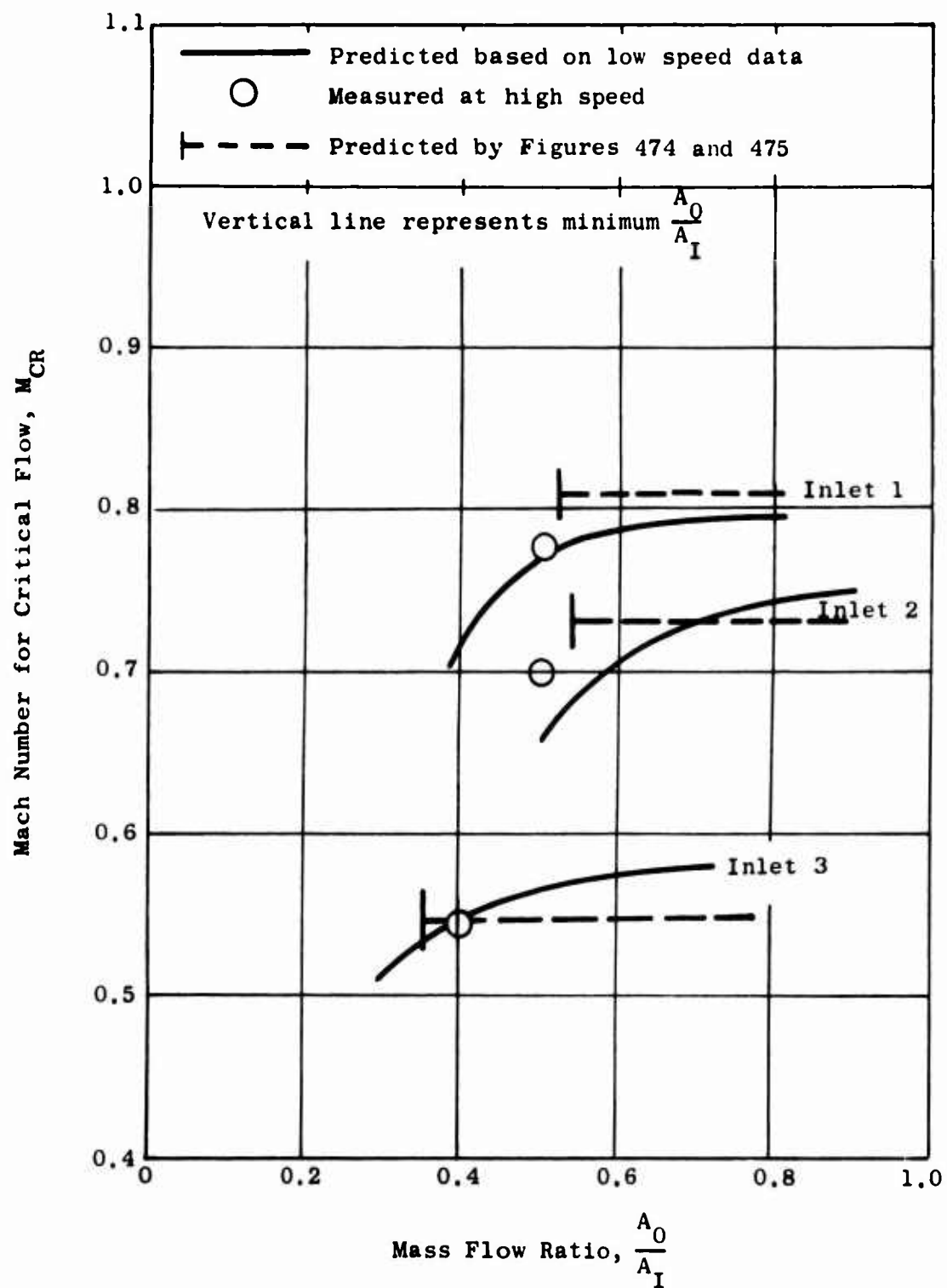


Figure 477. Comparison of Predicted and Measured Critical Mach Numbers for the Three Inlets.

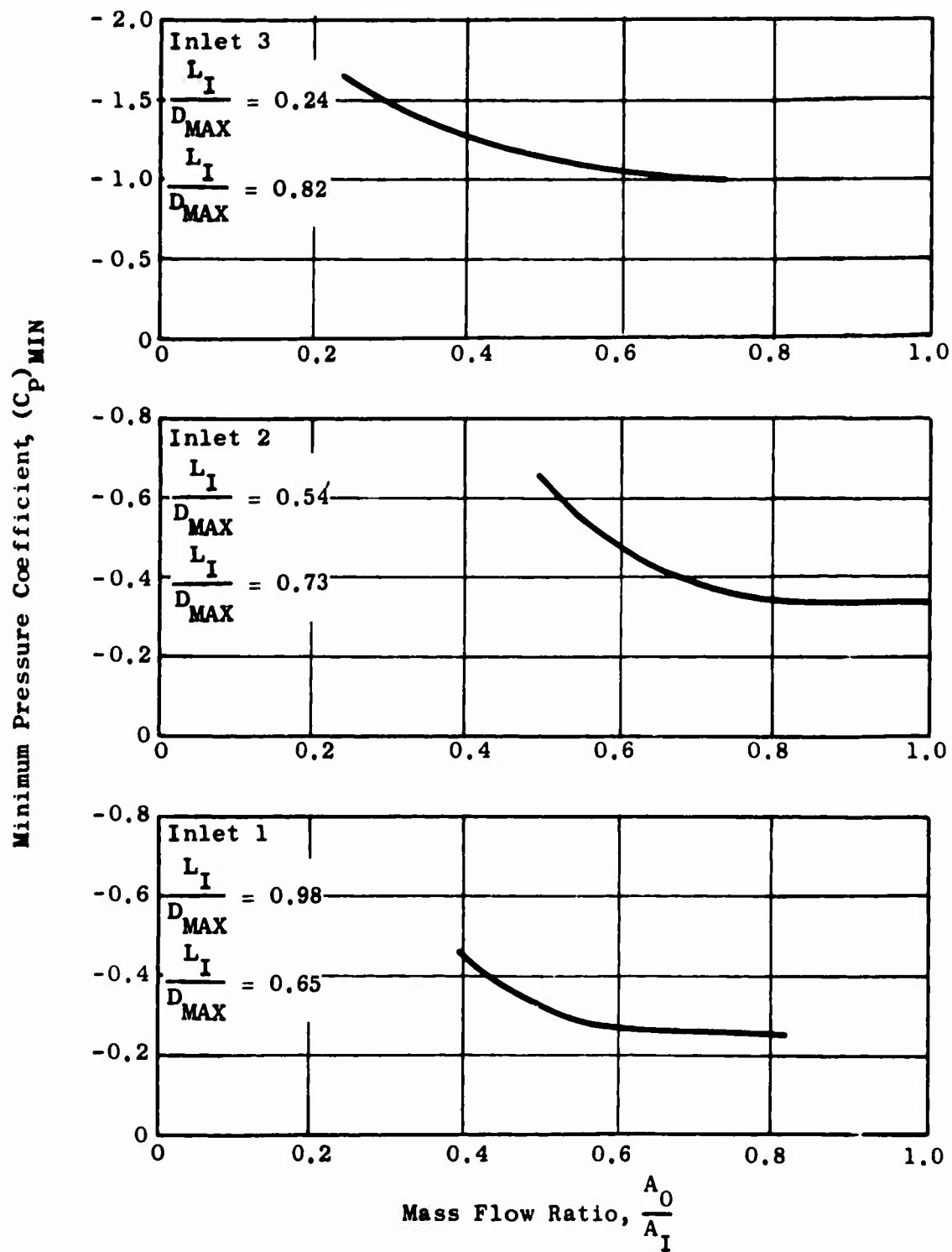


Figure 478. Variation of Low Speed Pressure Coefficient with Mass Flow Ratio for the Three Inlets Tested.

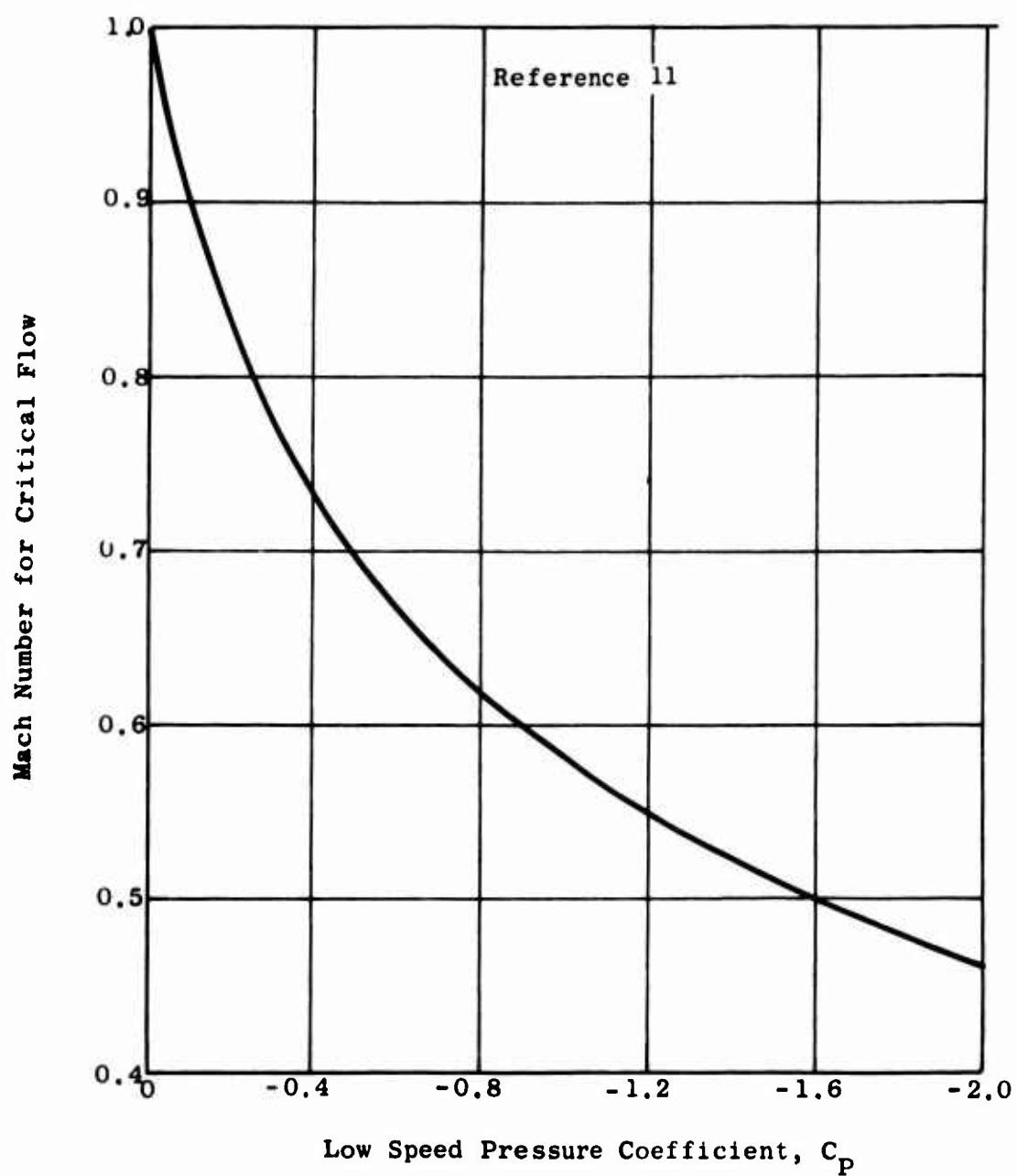


Figure 479. Compressibility Correction of Low Speed Pressure Coefficients.

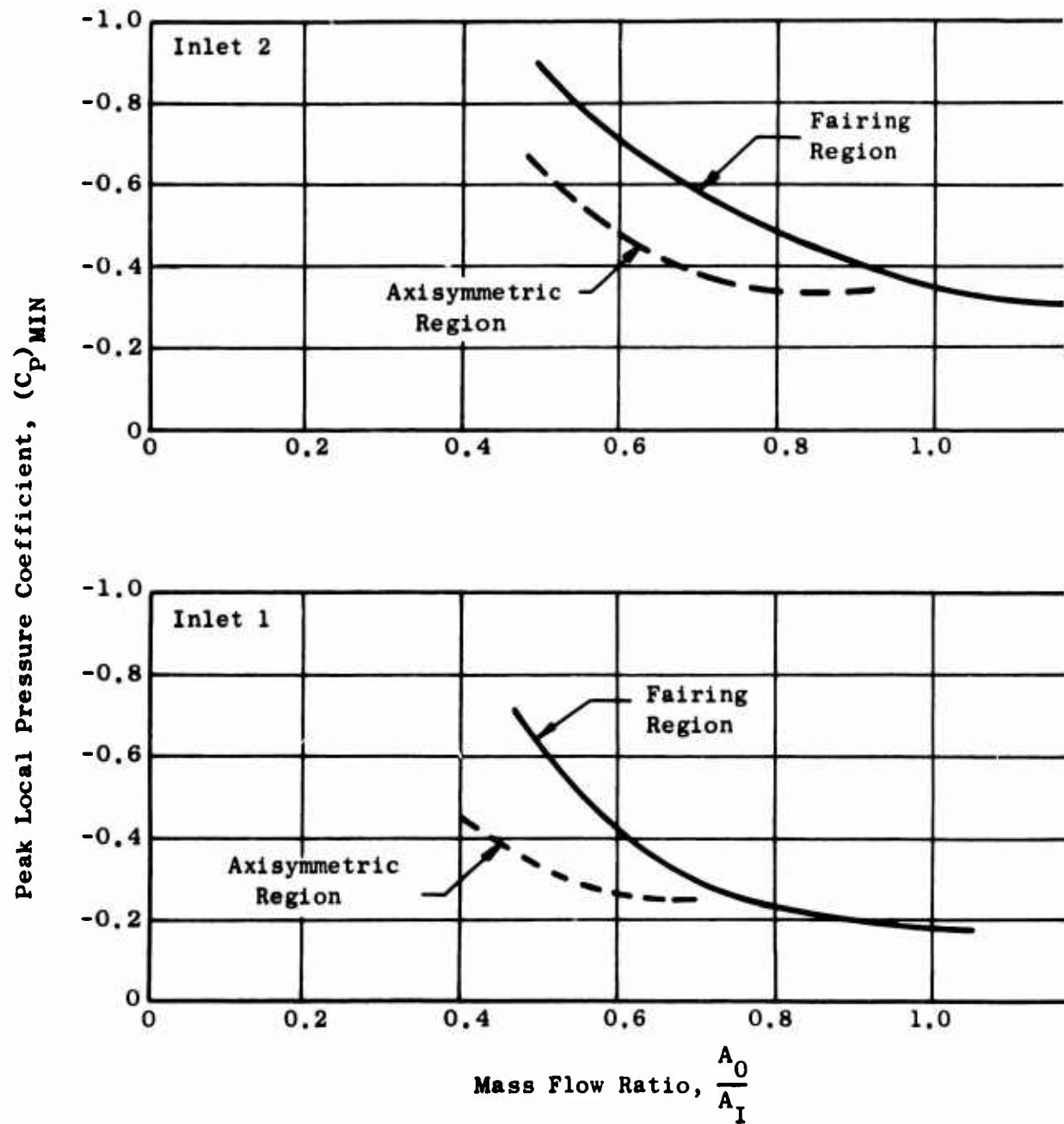


Figure 480. Comparison of Inlet Peak Pressure Coefficients for t Fairing and Axisymmetric Regions of Inlets.

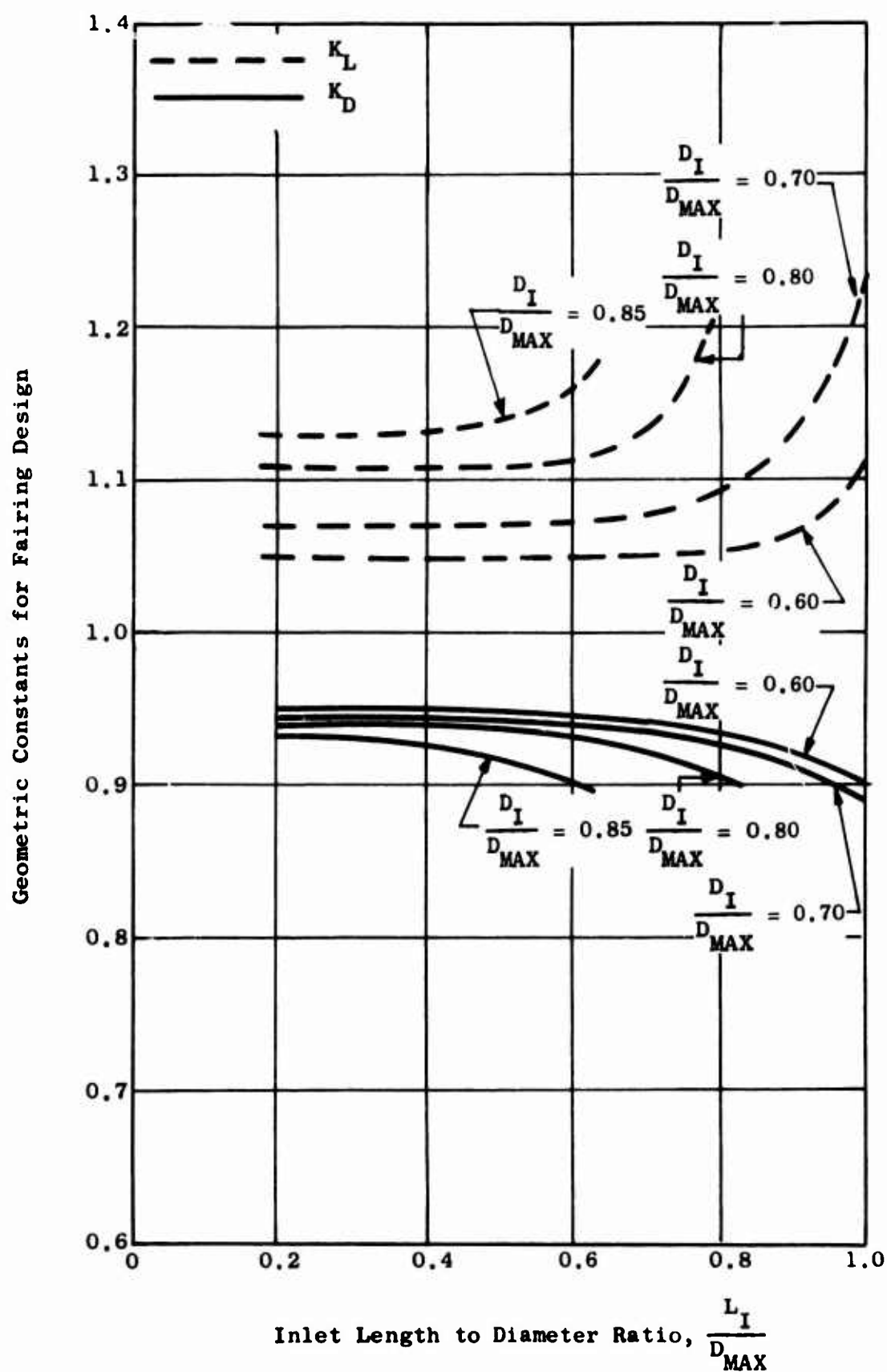


Figure 481. Geometric Constants for Design of Fan-Engine Nacelle Fairing.

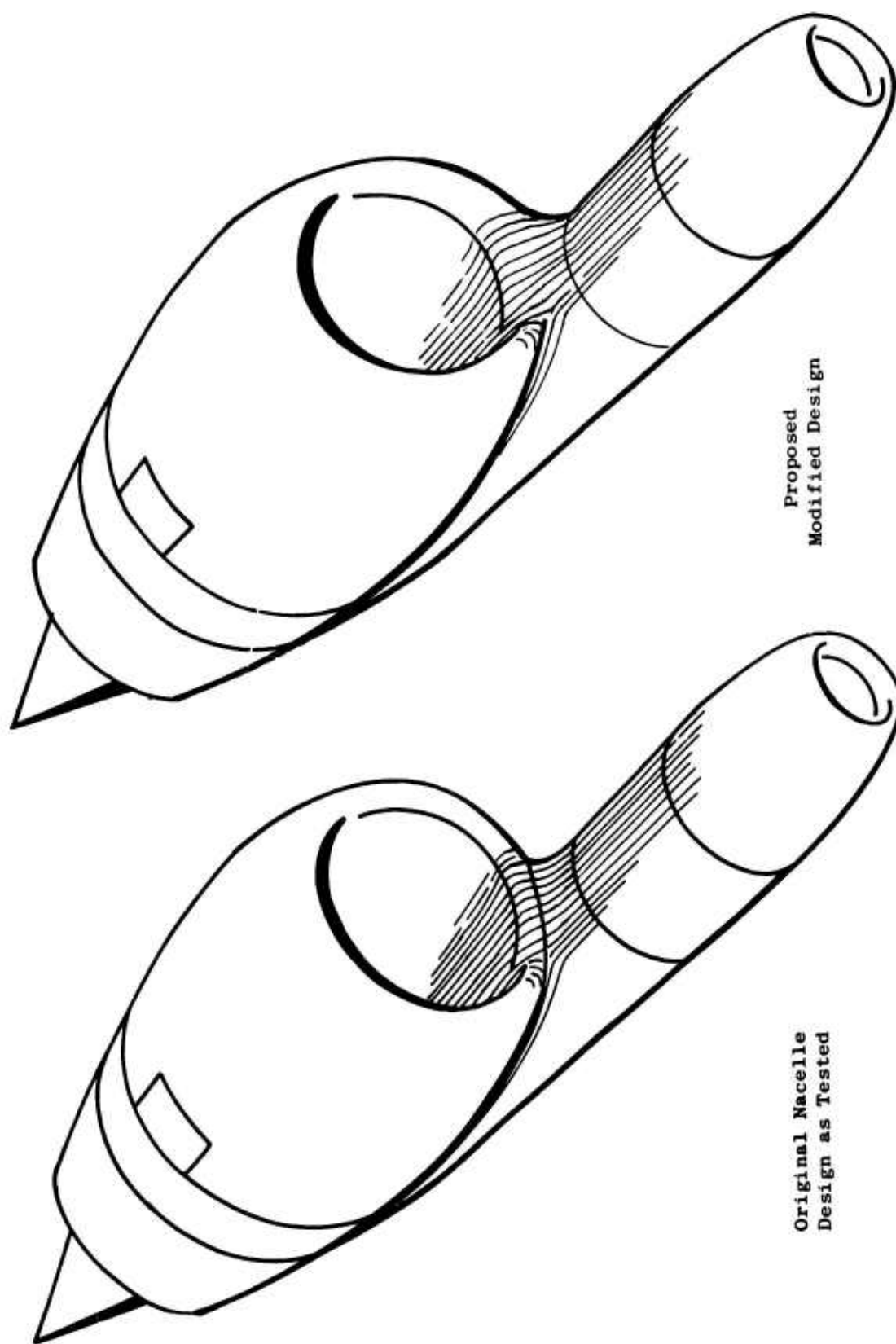


Figure 482. Sketch of Model 8 Showing Original and Modified Nacelle Designs.

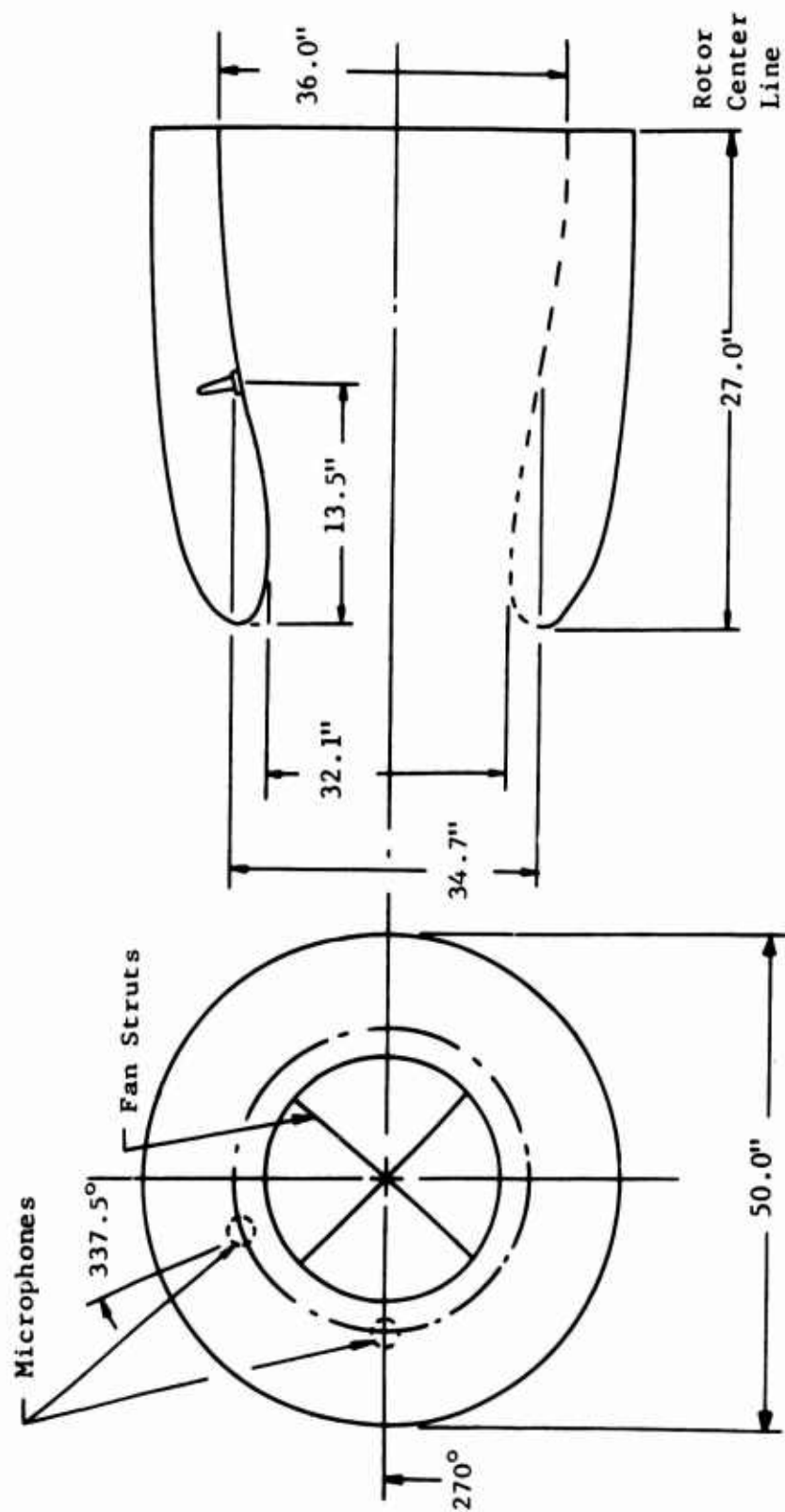


Figure 483. Microphone Installation in Model 3 Inlet.

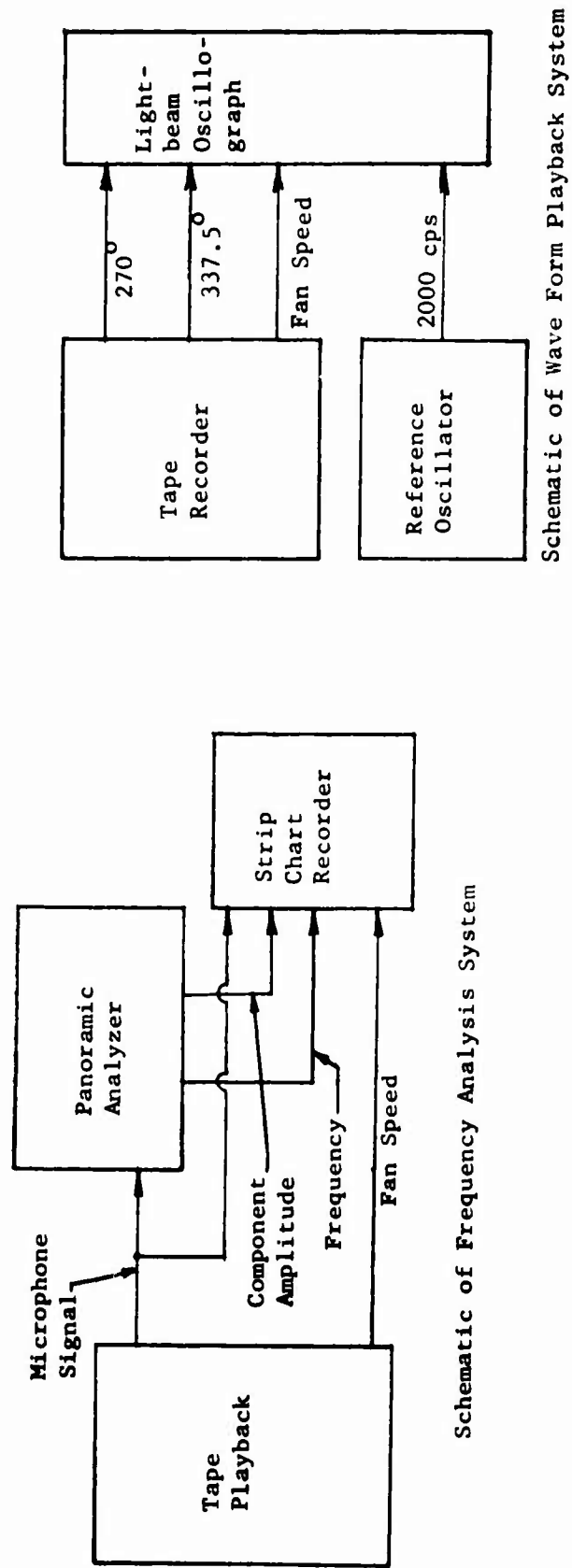
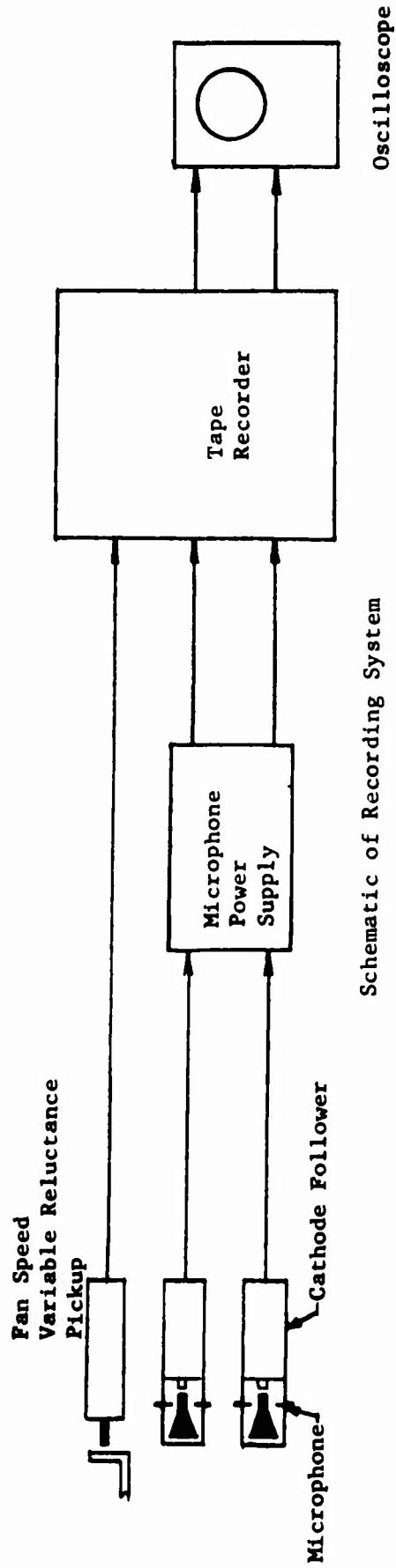


Figure 484. Schematic Diagram of Instrumentation and Data Reduction Systems.

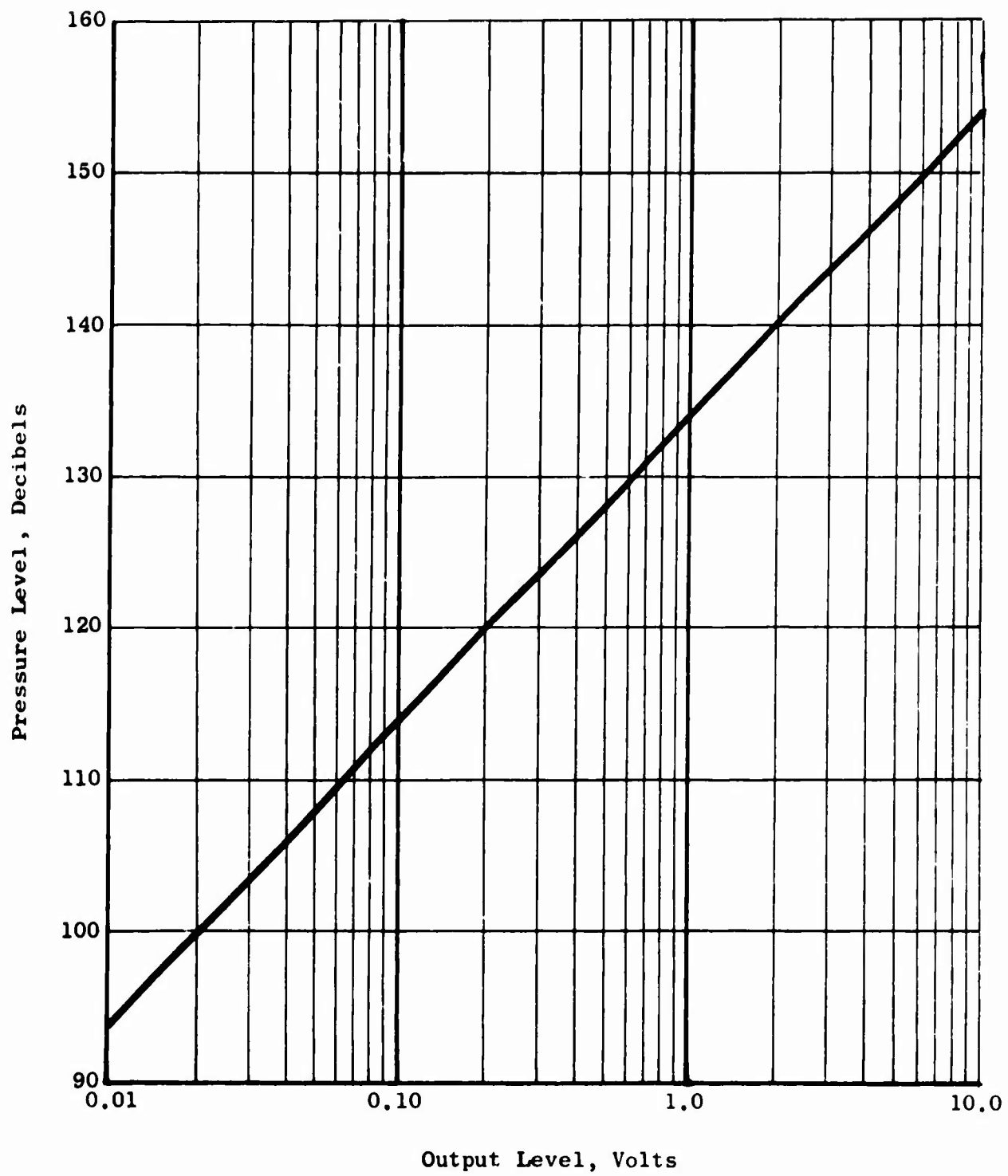


Figure 485. Conversion Chart - Output Level Versus Pressure Level in Decibels.

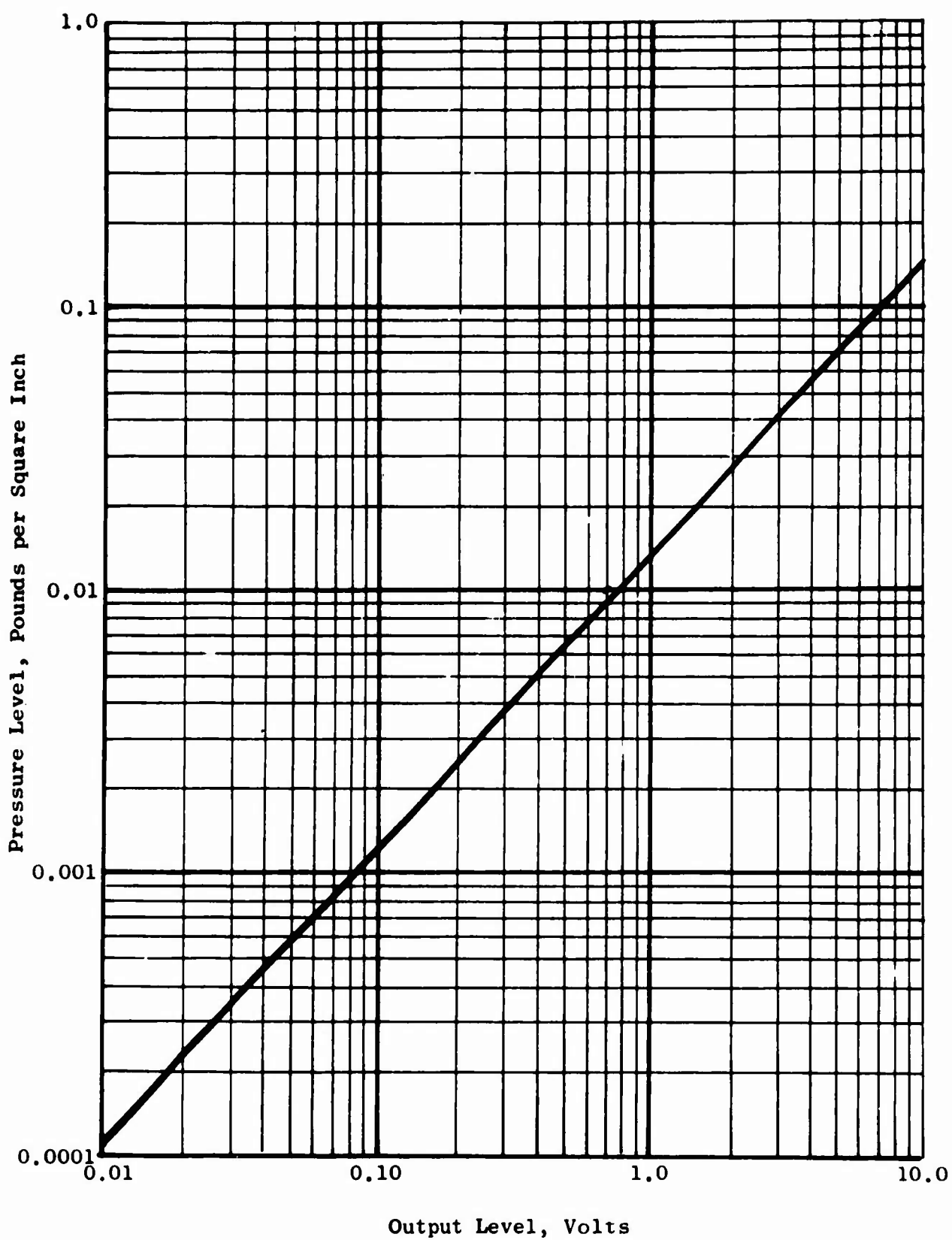
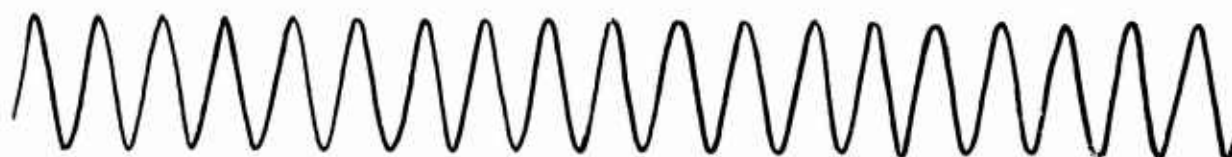


Figure 486. Conversion Chart - Output Level Versus Pressure Level in Pounds per Square Inch.



2000 c.p.s. reference



Speed pickup - 60 cycles per revolution



$\phi = 337\frac{1}{2}^\circ$ signal



$\phi = 270^\circ$ signal

Figure 487. Wave Form of Pressure Signal Data Point Number 1, $M_0 = 0.3$,
 $N_F = 1900$ Revolutions per Minute.

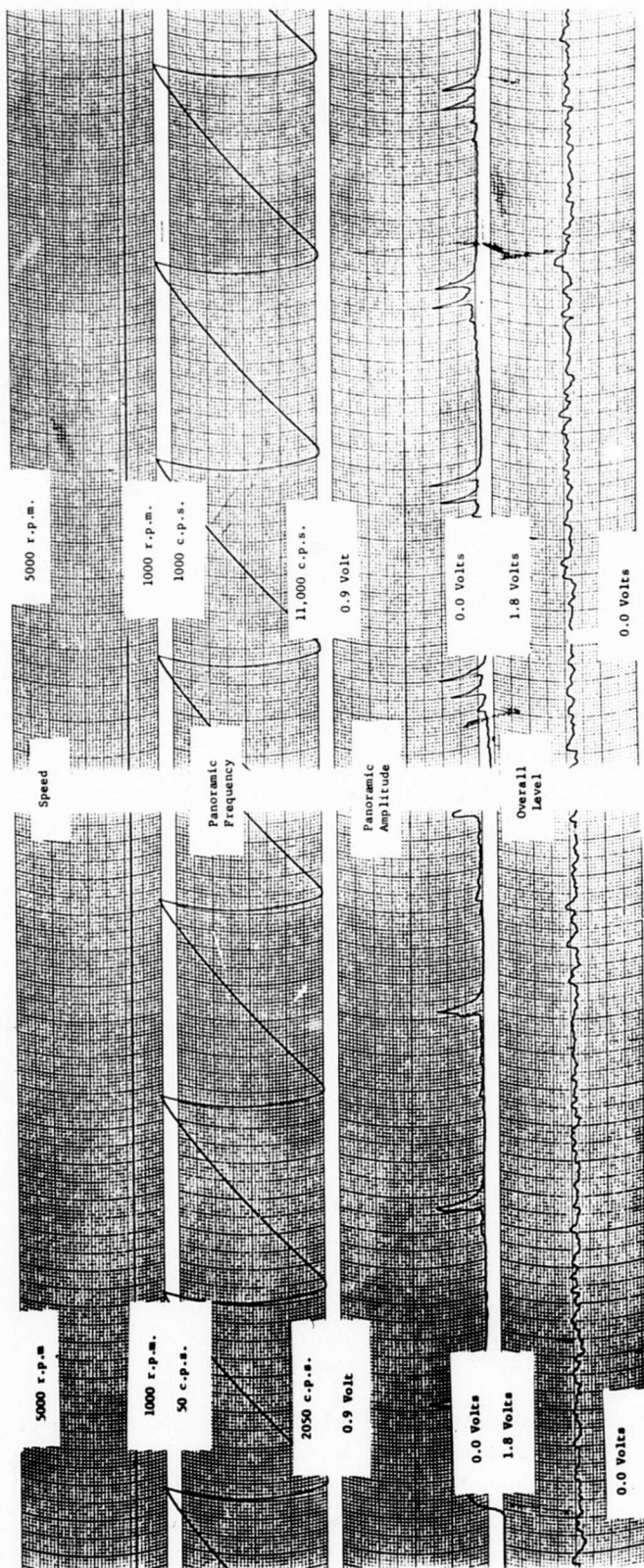
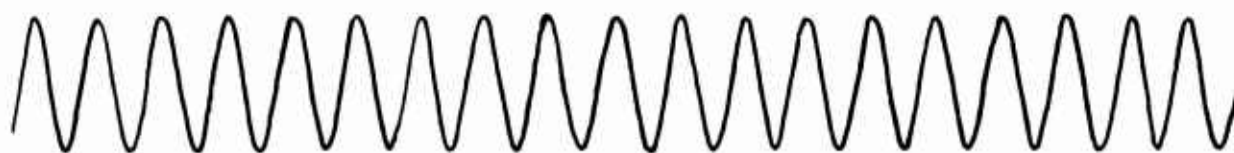
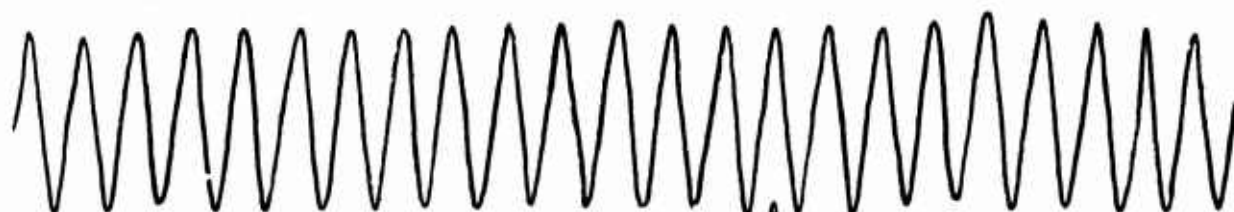


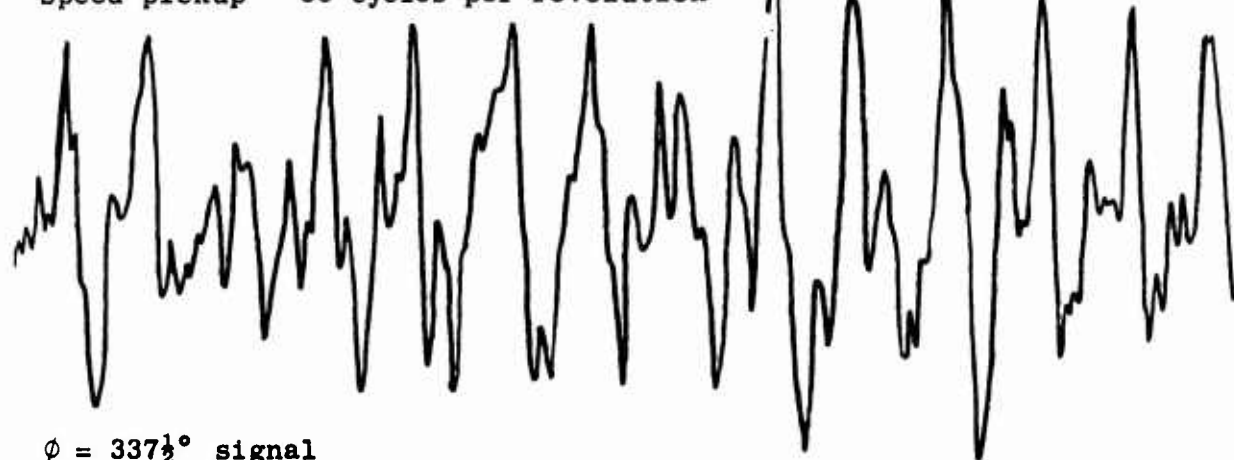
Figure 488. Amplitude and Frequency Analysis for Microphone Located at 337.5 Degrees, Data Point Number 1, $M_0 = 0.3$, $N_F = 1900$ Revolutions per Minute.



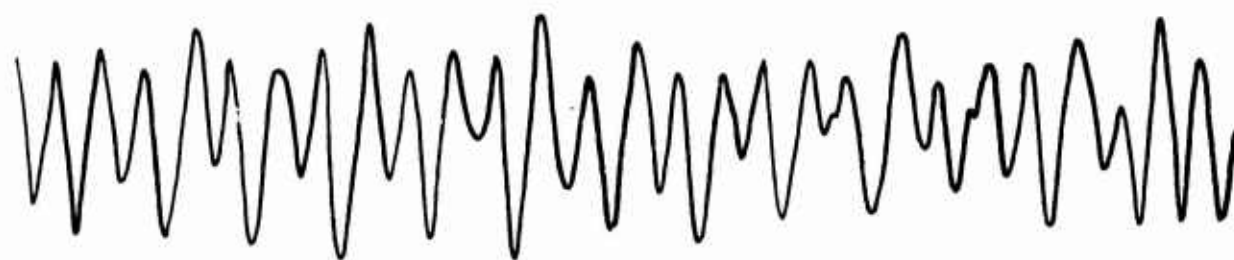
2000 c.p.s. reference



Speed pickup - 60 cycles per revolution



$\phi = 337\frac{1}{2}^\circ$ signal



$\phi = 270^\circ$ signal

Figure 489. Wave Form of Pressure Signal Data Point Number 2, $M_0 = 0.4$, $N_F = 2450$ Revolutions per Minute.

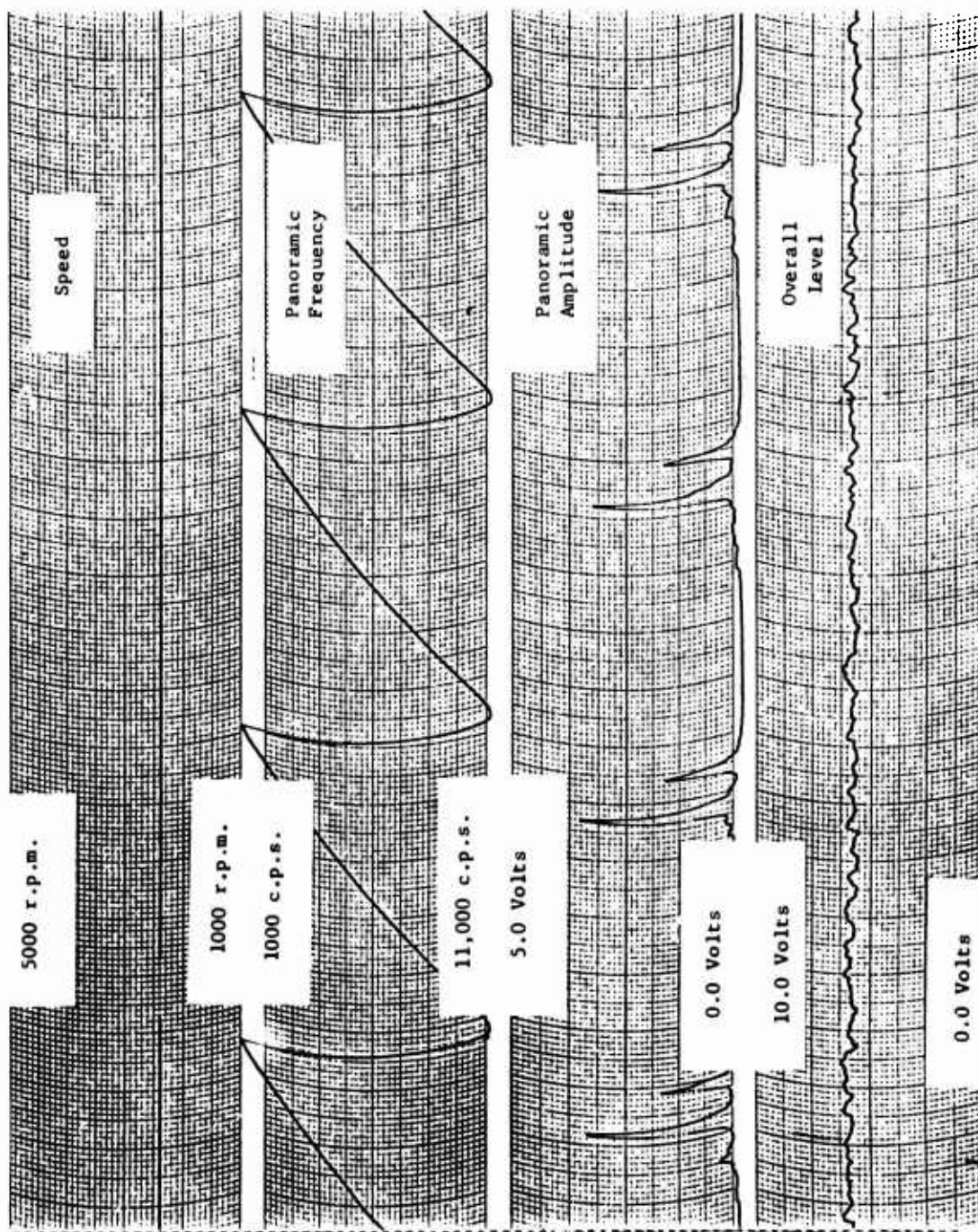


Figure 490. Amplitude and Frequency Analysis for Microphone Located at 270 Degrees, Data Point Number 2, $M_0 = 0.4$, $N_F = 1900$ Revolutions per Minute.

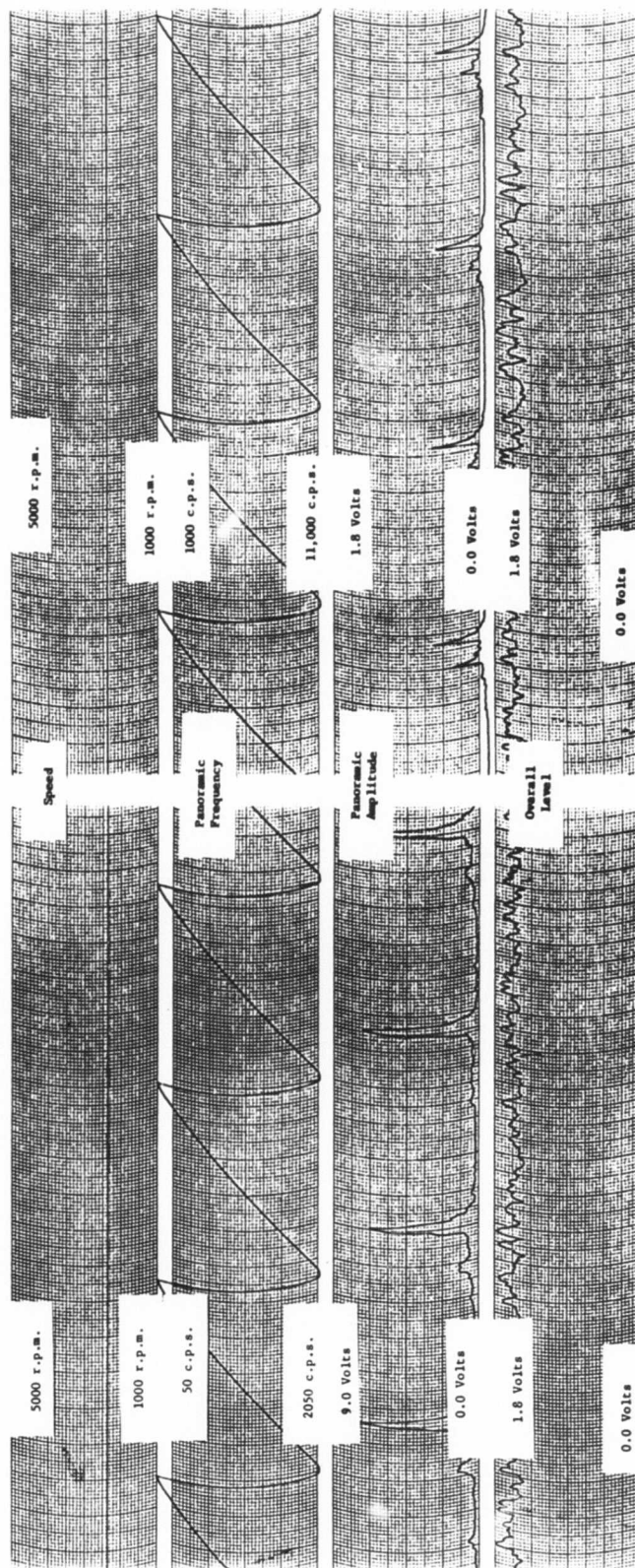
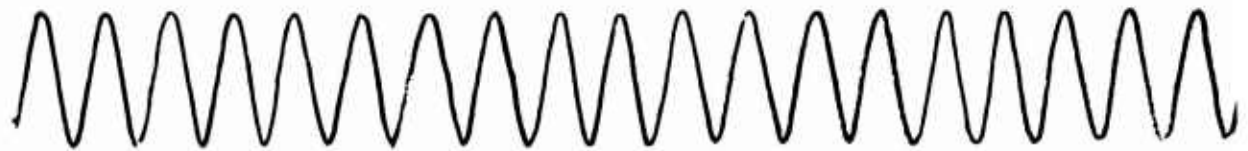
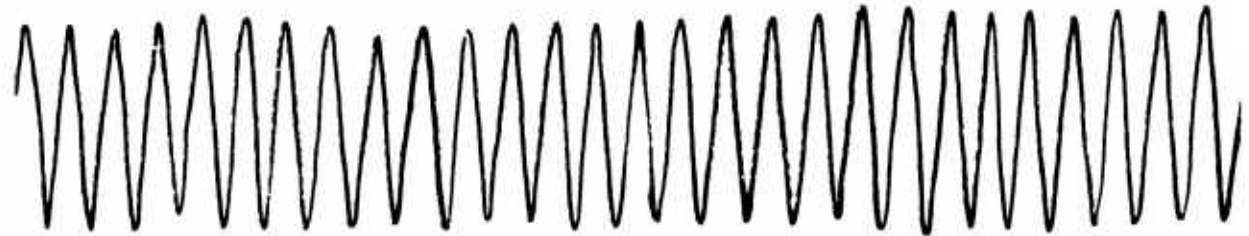


Figure 491. Amplitude and Frequency Analysis for Microphone Located at 337.5 Degrees, Data Point Number 2, $M_0 = 0.4$, $N_F = 1900$ Revolutions per Minute.



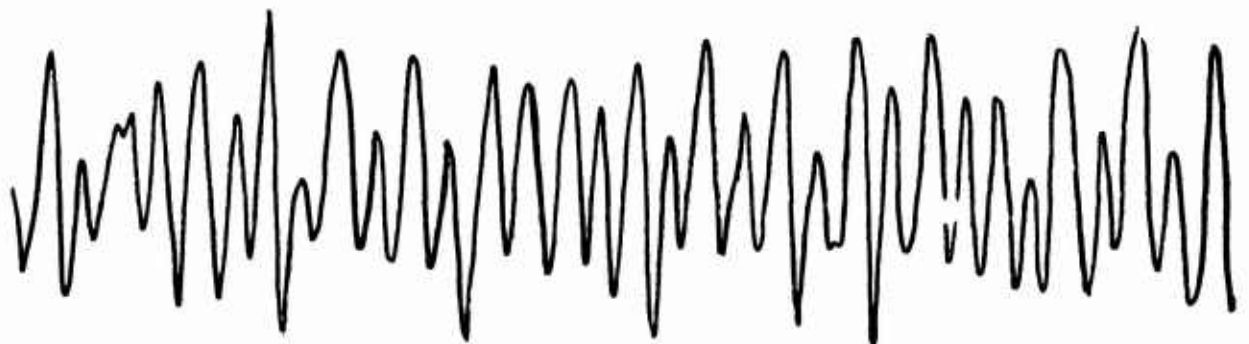
2000 c.p.s. reference



Speed pickup - 60 cycles per revolution



$\phi = 337\frac{1}{2}^\circ$ signal



$\phi = 270^\circ$ signal

Figure 492. Wave Form of Pressure Signal Data Point Number 3, $M_0 = 0.5$, $N_F = 2950$ Revolutions per Minute.

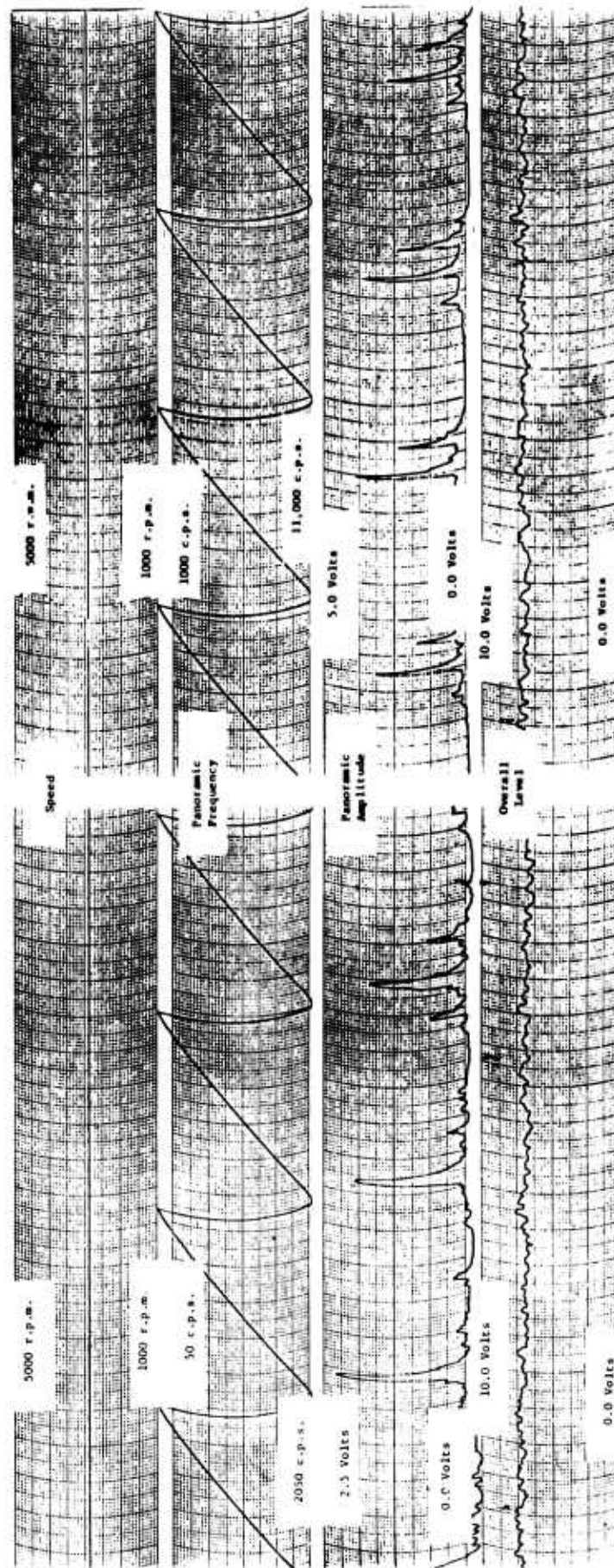


Figure 493. Amplitude and Frequency Analysis for Microphone Located at 270 Degrees, Data Point Number 3, $M_0 = 0.5$, $N_F = 2950$ Revolutions per Minute.

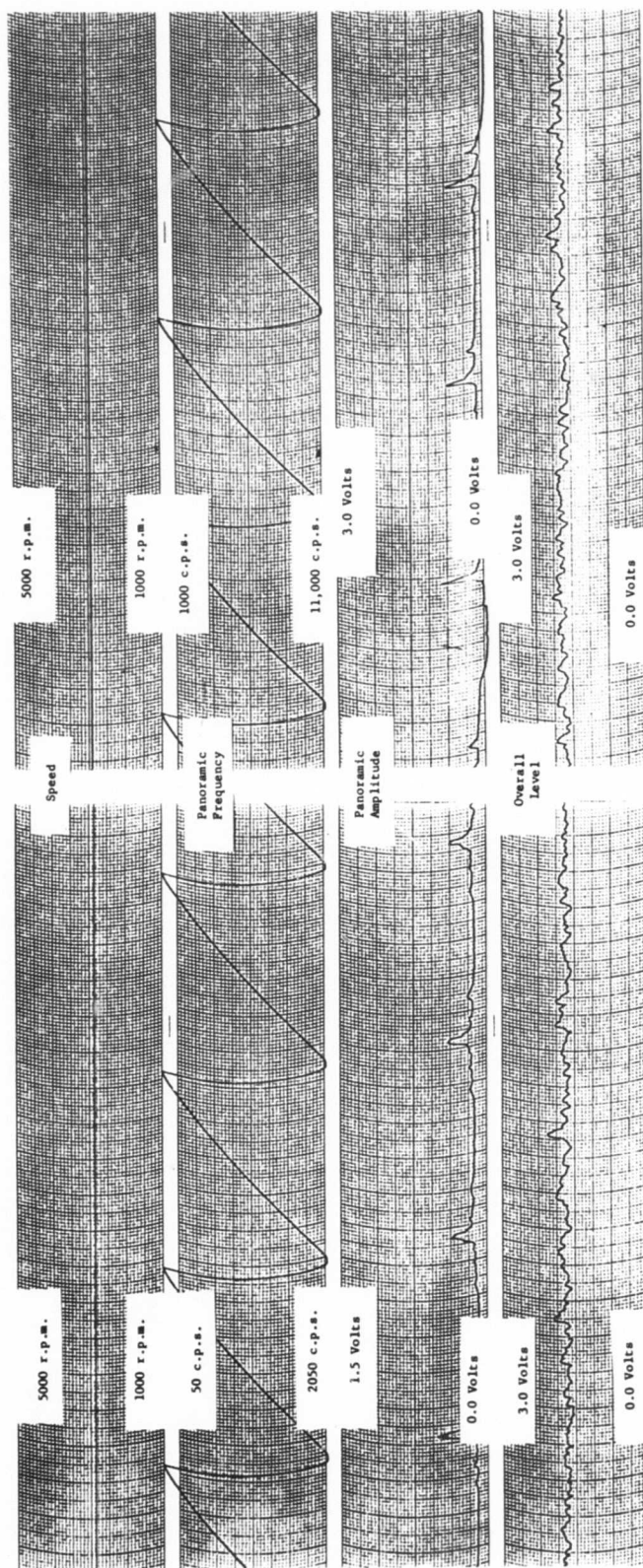
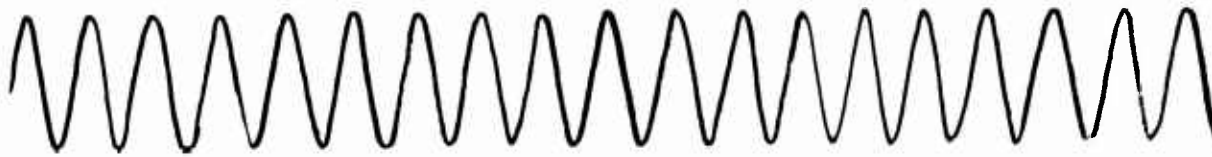
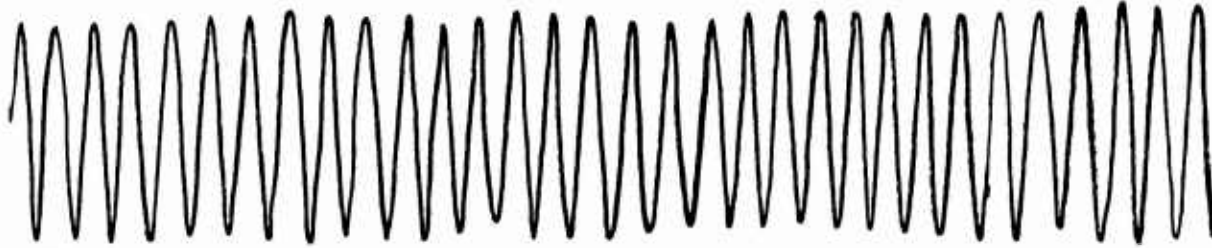


Figure 494. Amplitude and Frequency Analysis for Microphone Located at 337.5 Degrees, Data Point Number 3, $M_0 = 0.5$, $N_F = 2950$ Revolutions per Minute.



2000 c.p.s. reference



Speed pickup - 60 cycles per revolution



$\phi = 337\frac{1}{2}^\circ$ signal



$\phi = 270^\circ$ signal

Figure 495. Wave Form of Pressure Signal Data Point Number 4, $M_0 = 0.6$, $N_F = 3410$ Revolutions per Minute.

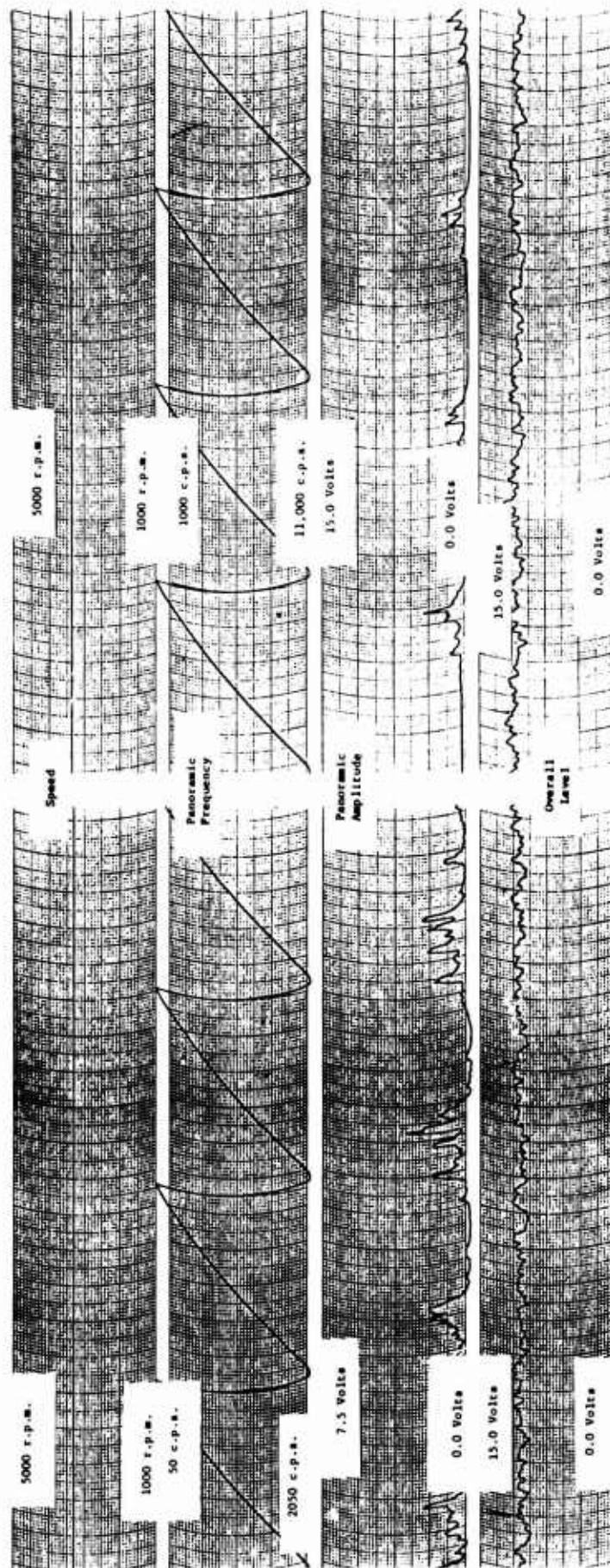


Figure 496. Amplitude and Frequency Analysis for Microphone Located at 370 Degrees, Data Point Number 4, $M_0 = 0.6$, $N_F = 3410$ Revolutions per Minute.

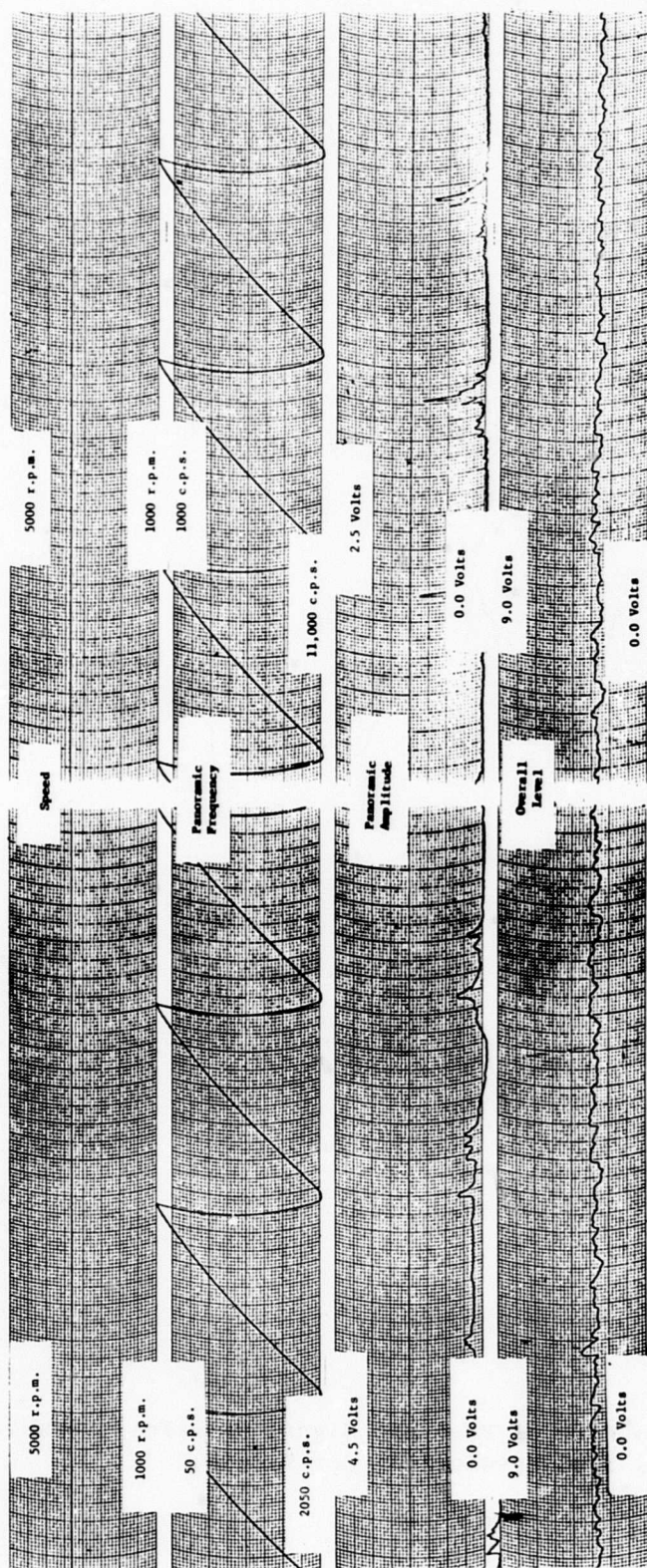


Figure 497. Amplitude and Frequency Analysis for Microphone Located at 337.5 Degrees, Data Point Number 4, $M_0 = 0.6$, $N_F = 3410$ Revolutions per Minute.

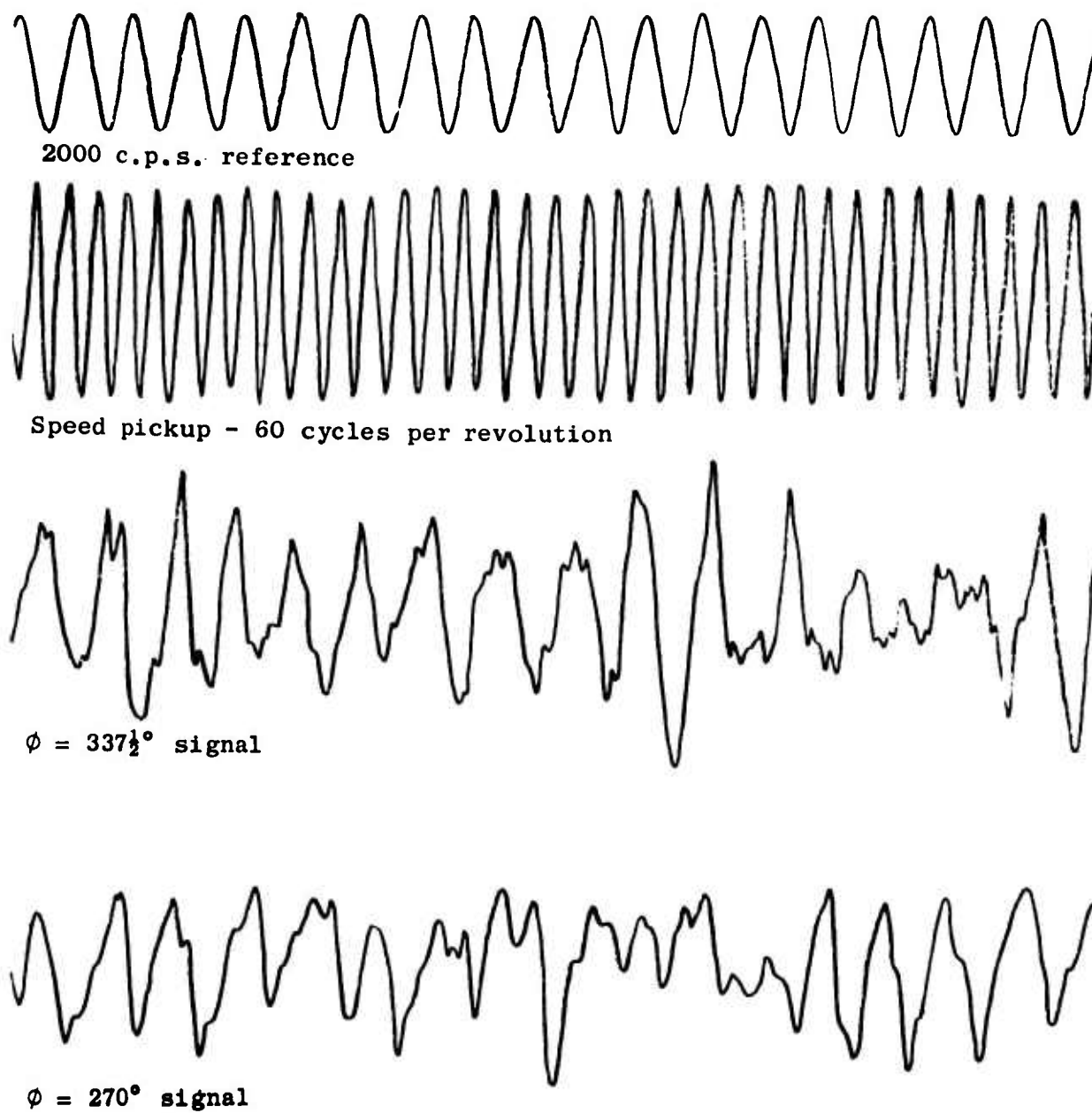


Figure 498. Wave Form of Pressure Signal Data Point Number 5, $M_0 = 0.7$, $N_F = 3760$ Revolutions per Minute.

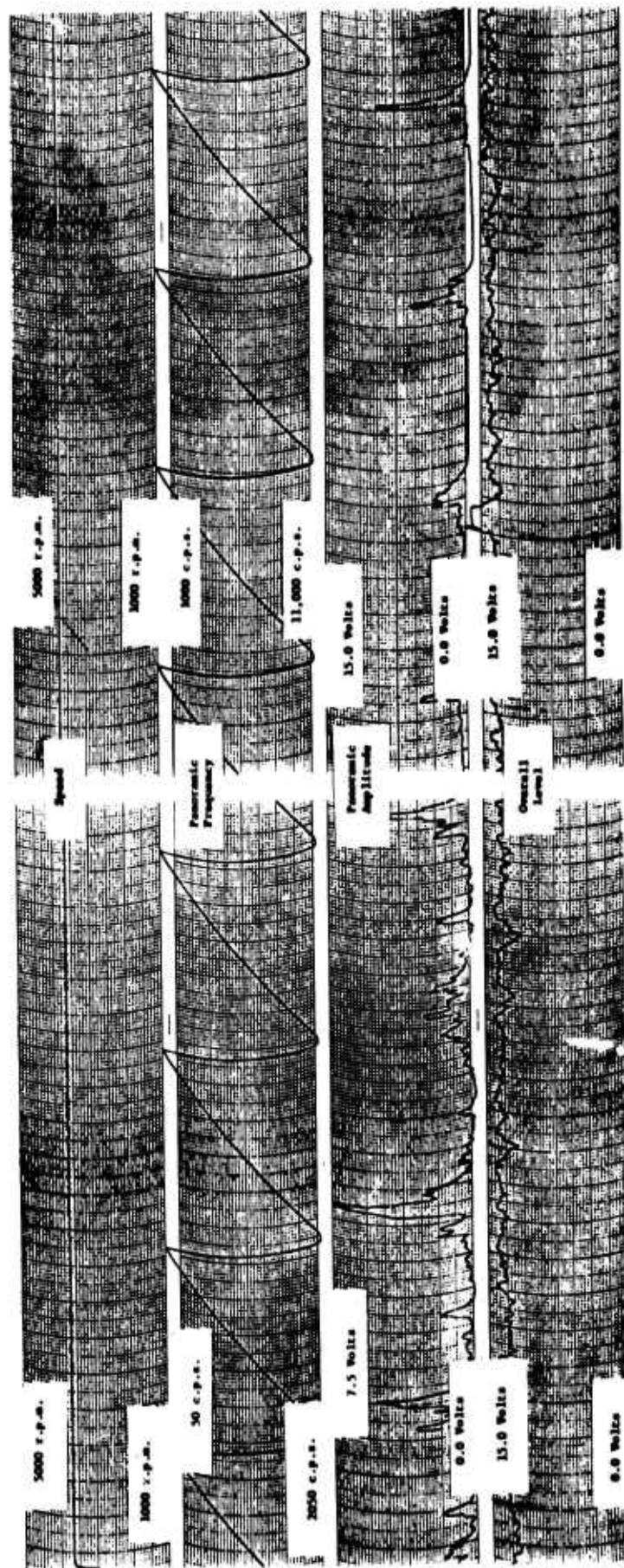


Figure 499. Amplitude and Frequency Analysis for Microphone Located at 270 Degrees, Data Point Number 5, $M_0 = 0.7$, $N_F = 3760$ Revolutions per Minute.

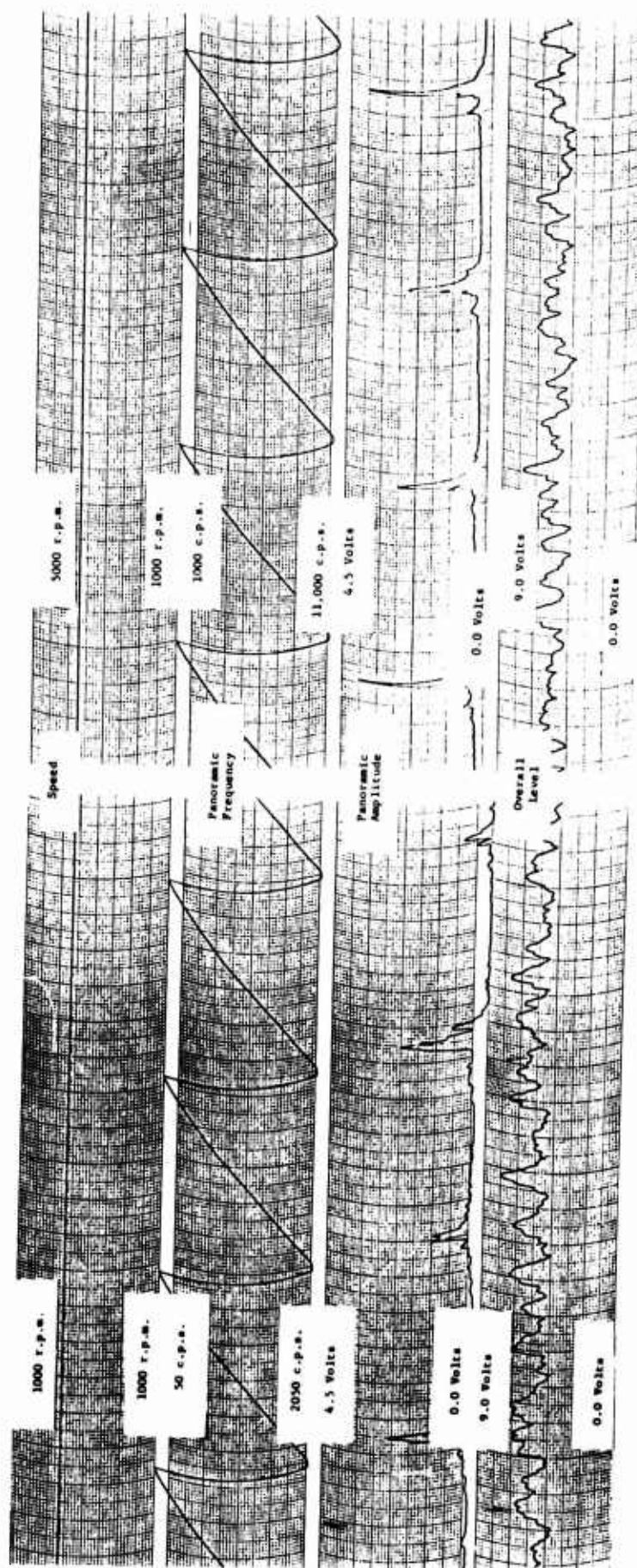


Figure 500. Amplitude and Frequency Analysis for Microphone Located at 337.5 Degrees, Data Point Number 5, $M_0 = 0.7$, $N_F = 3760$ Revolutions per Minute.

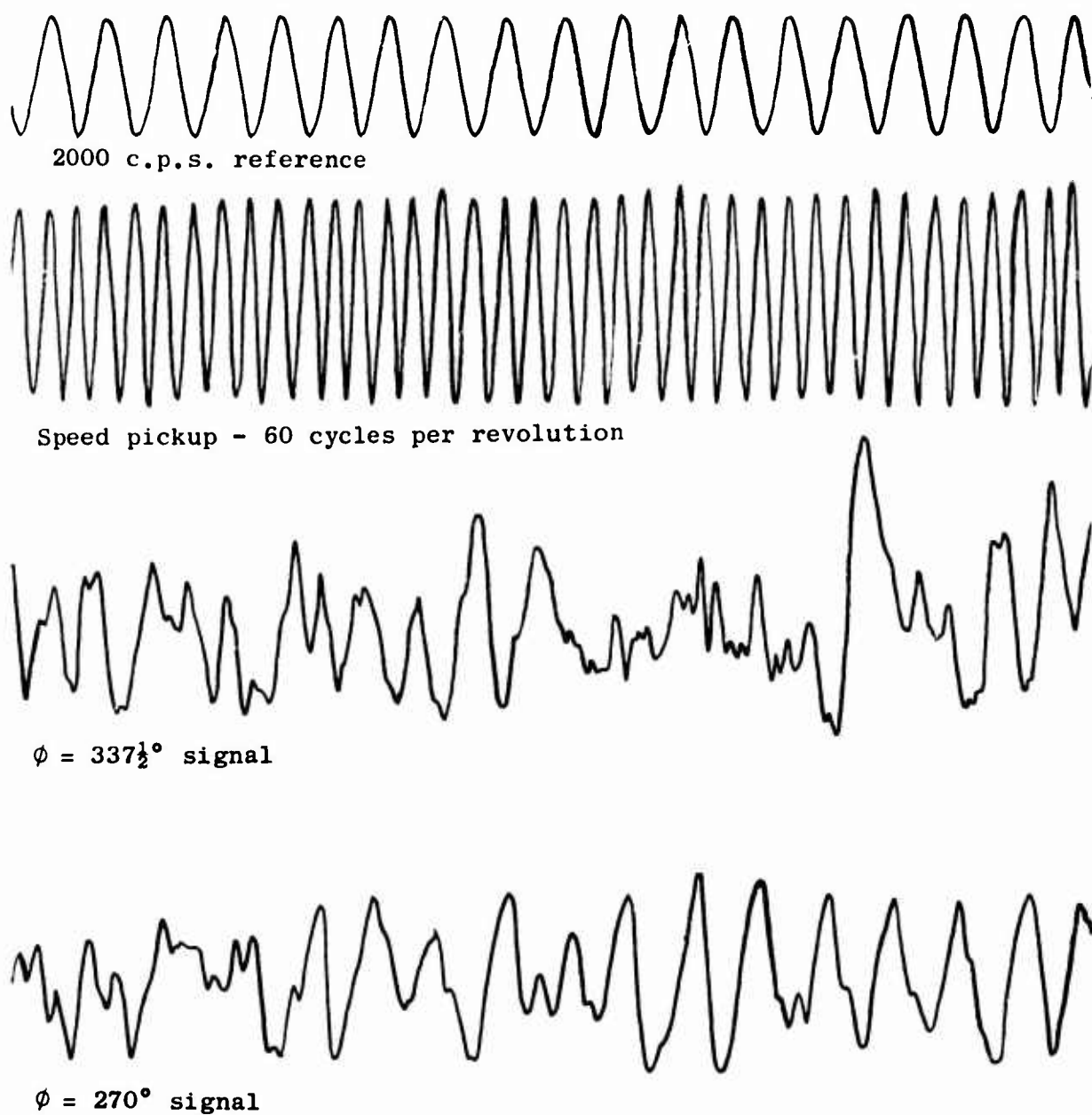


Figure 501. Wave Form of Pressure Signal Data Point Number 6, $M_0 = 0.8$, $N_F = 4050$ Revolutions per Minute.

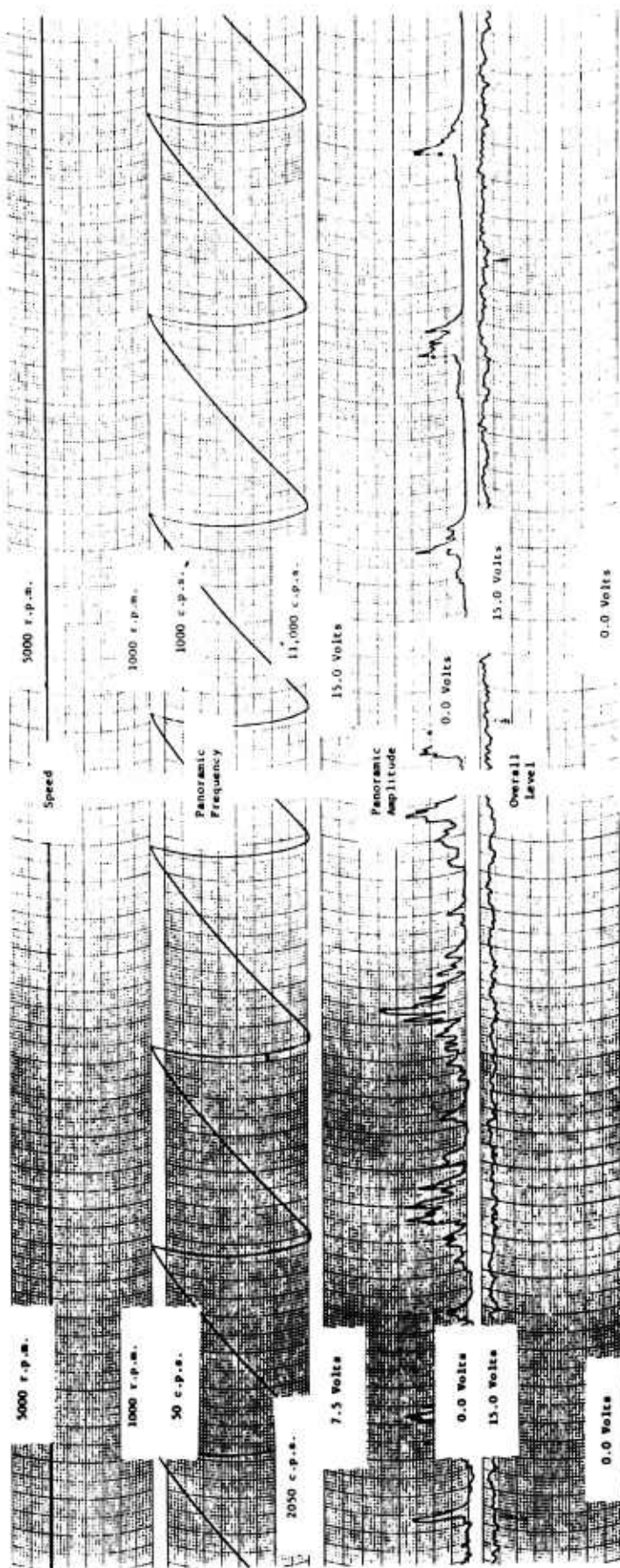


Figure 502. Amplitude and Frequency Analysis for Microphone Located at 270 Degrees, Data Point Number 6, $M_0 = 0.8$, $N_F = 4050$ Revolutions per Minute.

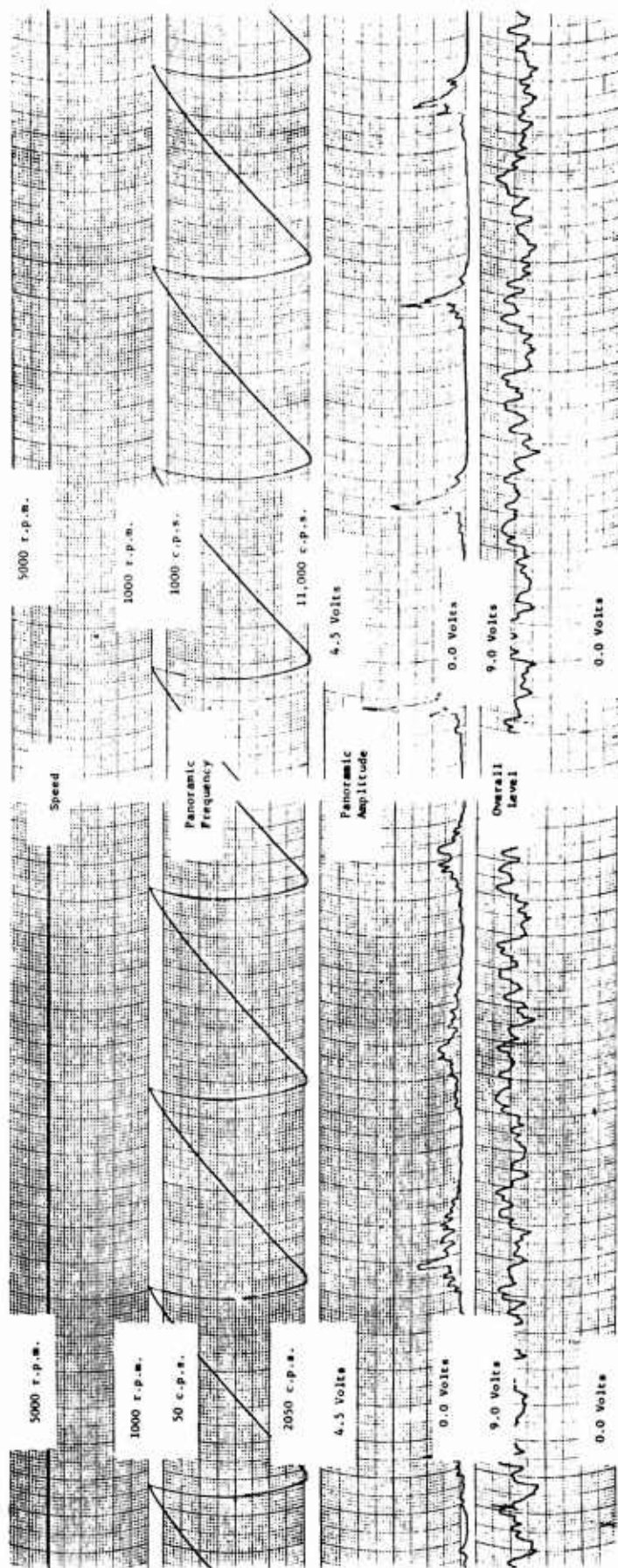
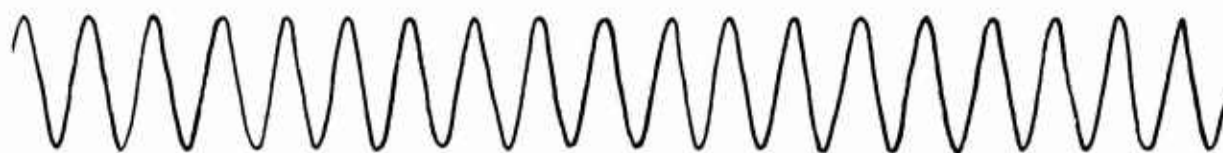
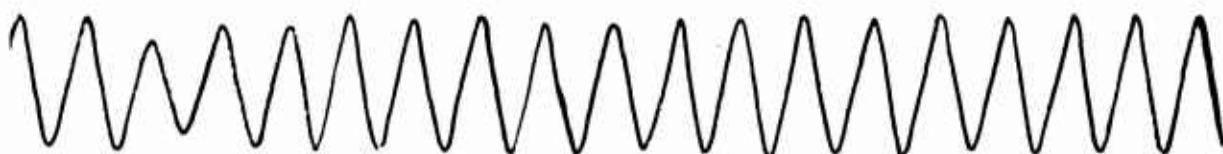


Figure 503. Amplitude and Frequency Analysis for Microphone Located at 337.5 Degrees, Data Point Number 6, $M_0 = 0.8$, $N_F = 4050$ Revolutions per Minute.



2000 c.p.s. reference



Speed pickup - 60 cycles per revolution



$\phi = 337\frac{1}{2}^\circ$ signal



$\phi = 270^\circ$ signal

Figure 504. Wave Form of Pressure Signal Data Point Number 7, $M_0 = 0.3$, $N_F = 1920$ Revolutions per Minute.

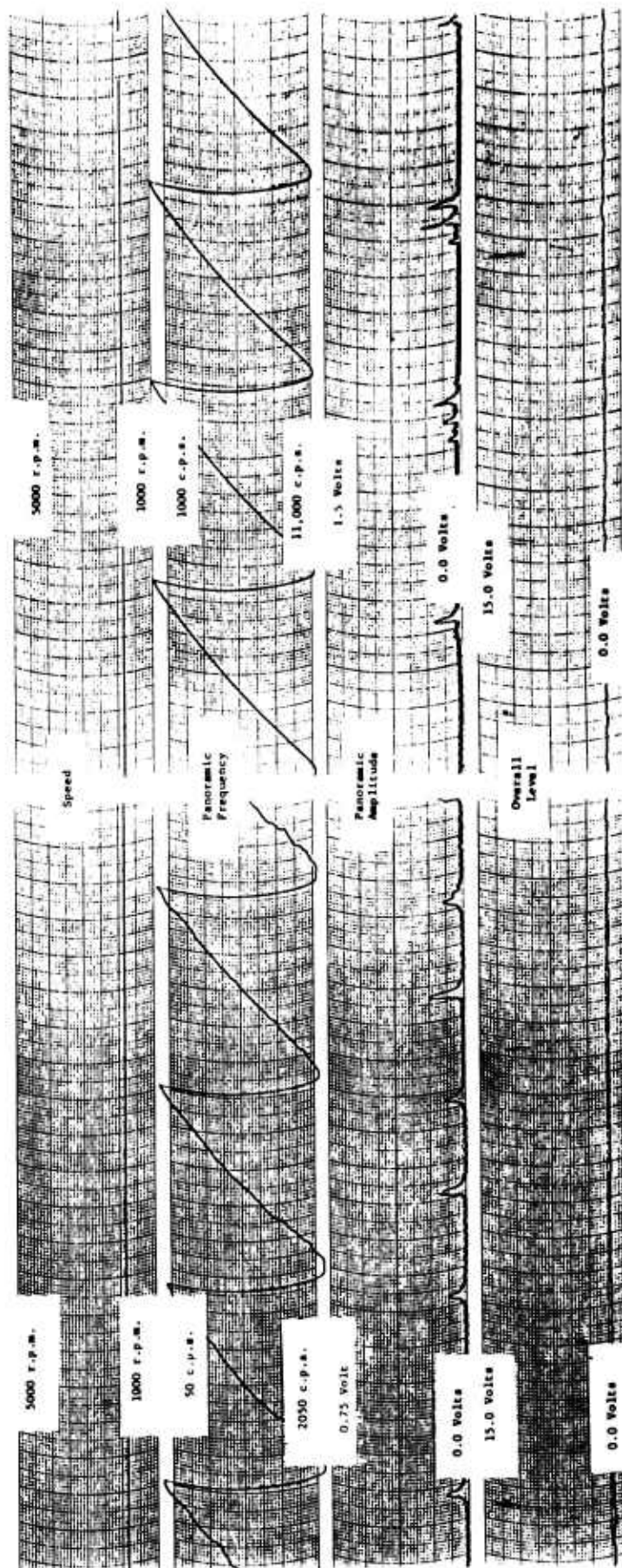


Figure 505. Amplitude and Frequency Analysis for Microphone Located at 270 Degrees, Data Point Number 7, $M_0 = 0.3$, $N_F = 1920$ Revolutions per Minute.

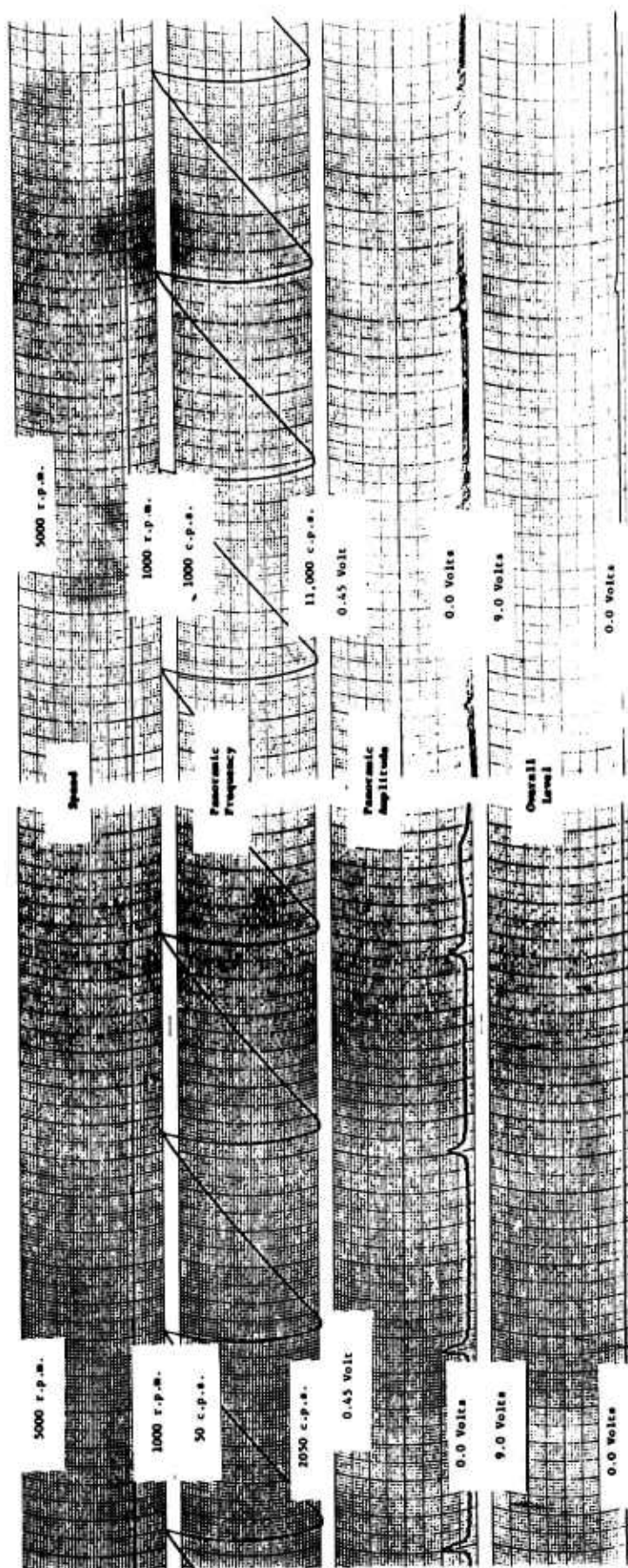


Figure 506. Amplitude and Frequency Analysis for Microphone Located at 337.5 Degrees, Data Point Number 7, $M_0 = 0.3$, $N_F = 1920$ revolutions per Minute.

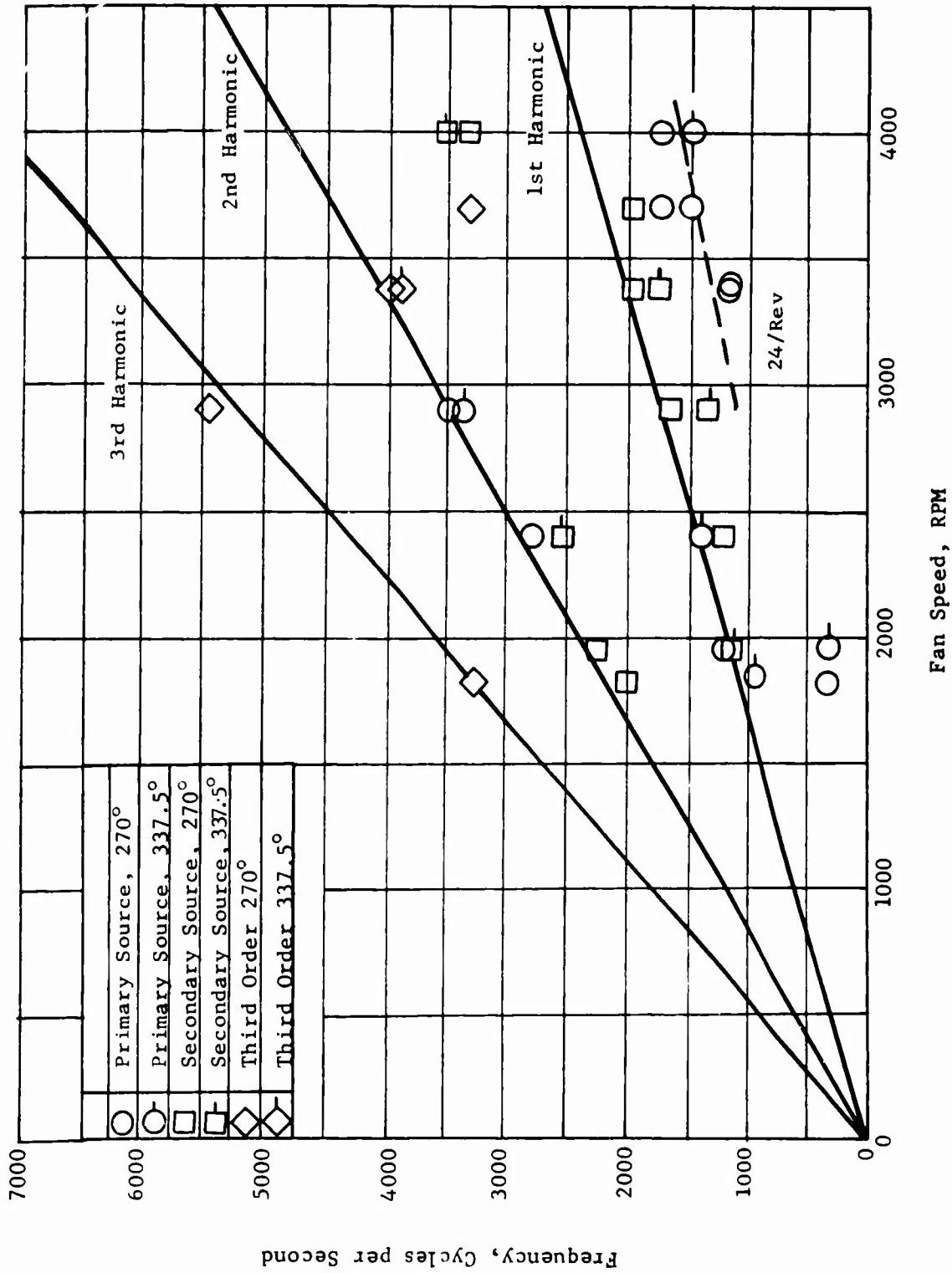


Figure 507. Data Showing Correlation of Microphone Frequencies with Harmonics of the Blade Passing Frequency.

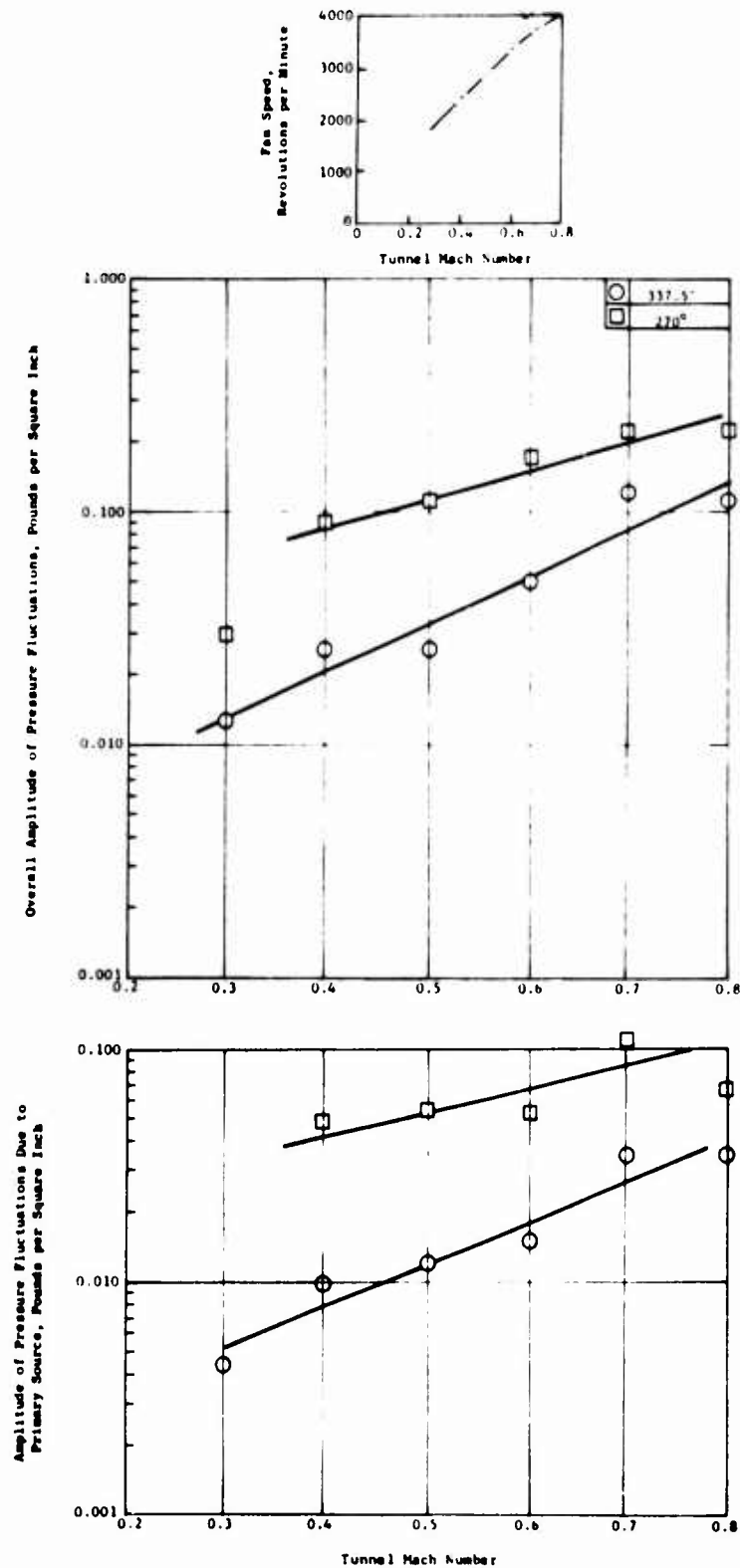


Figure 508. Amplitude of Overall Signal and Primary Source Signal Due to Pressure Fluctuations Shown as a Function of Mach Number.

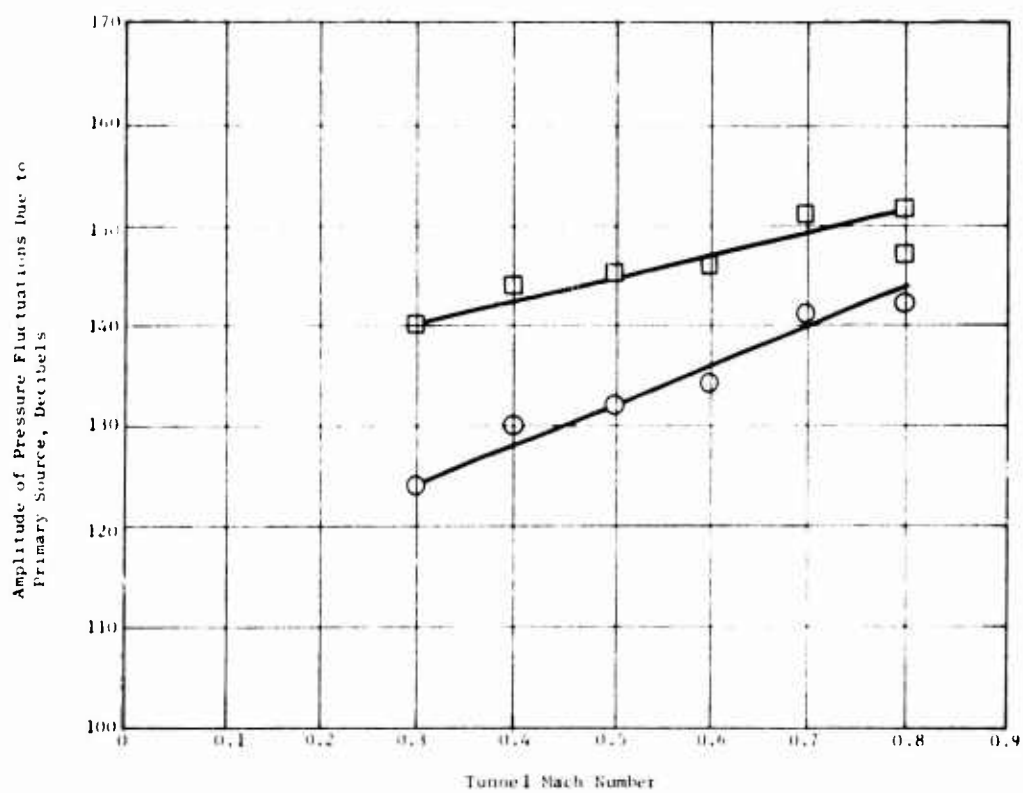
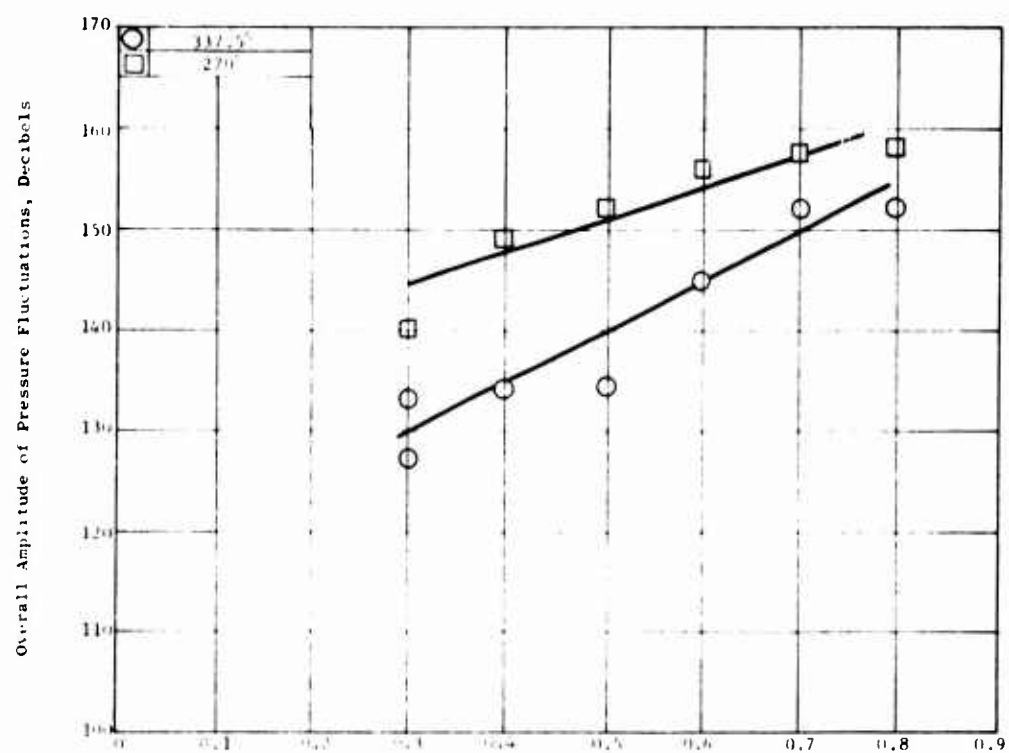


Figure 509. Amplitude of Overall Signal and Primary Source Signal Due to Pressure Fluctuations Expressed in Decibels and Shown as a Function of Mach Number.

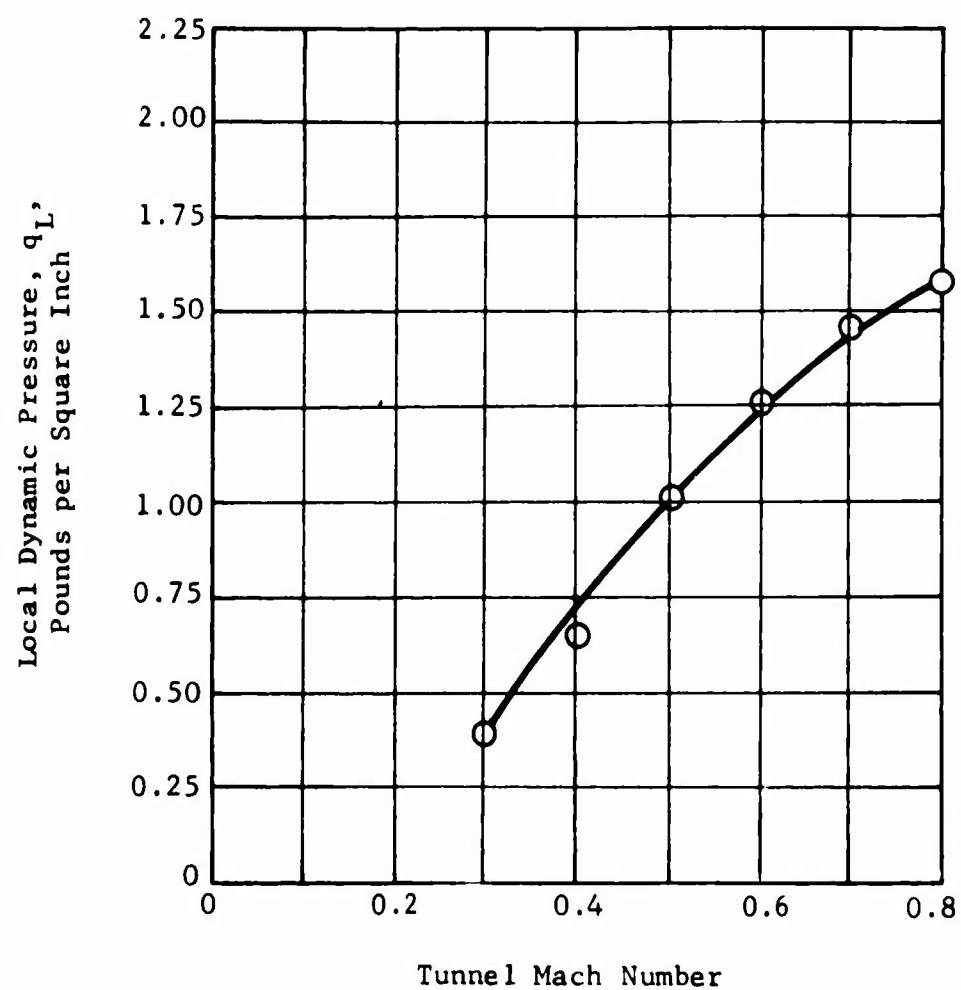


Figure 510. Local Dynamic Pressure at Axial Plane of Microphone Shown as a Function of Tunnel Mach Number.

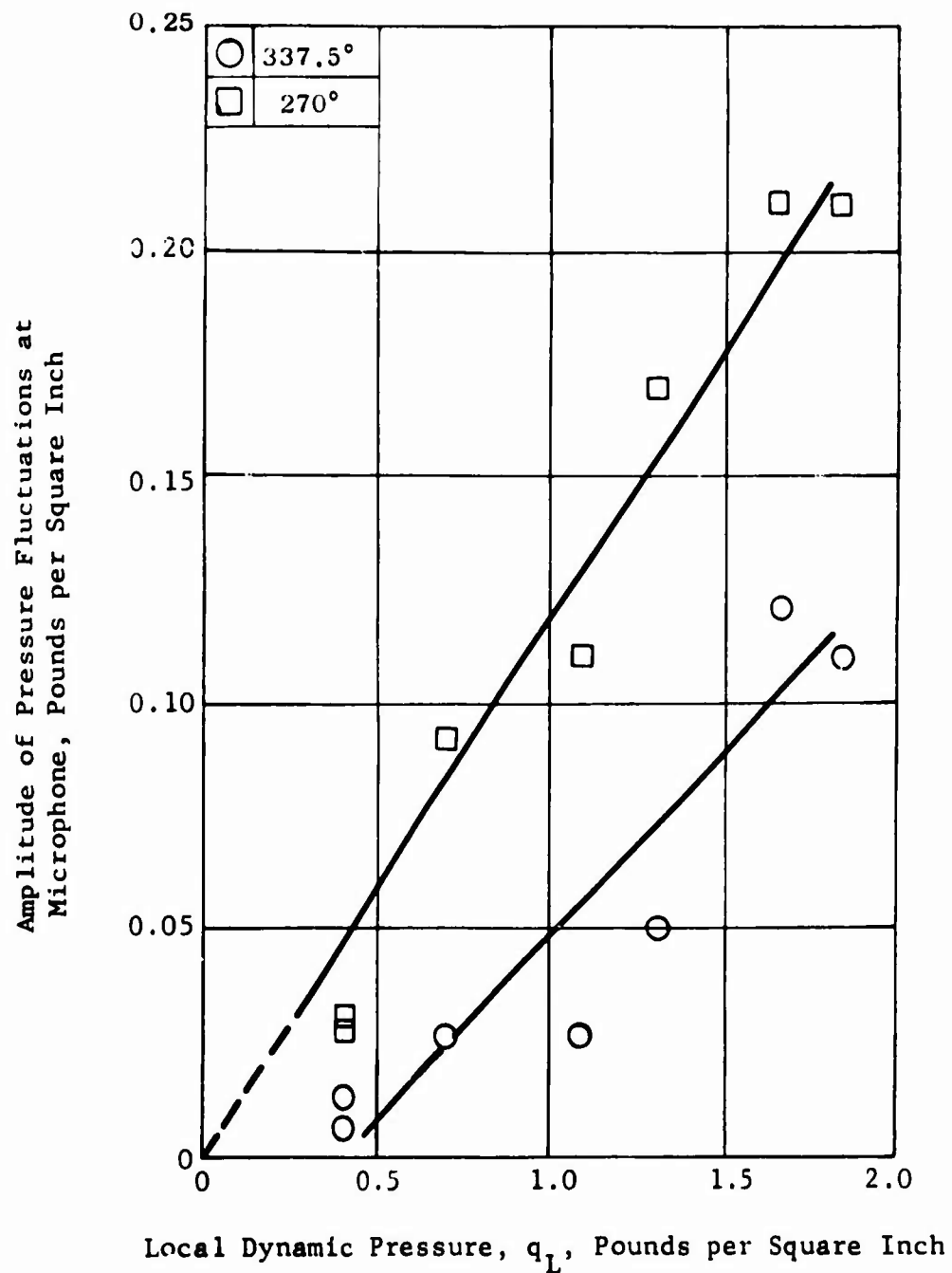


Figure 511. Amplitude of Pressure Fluctuations Shown as a Function of Local Dynamic Pressure.

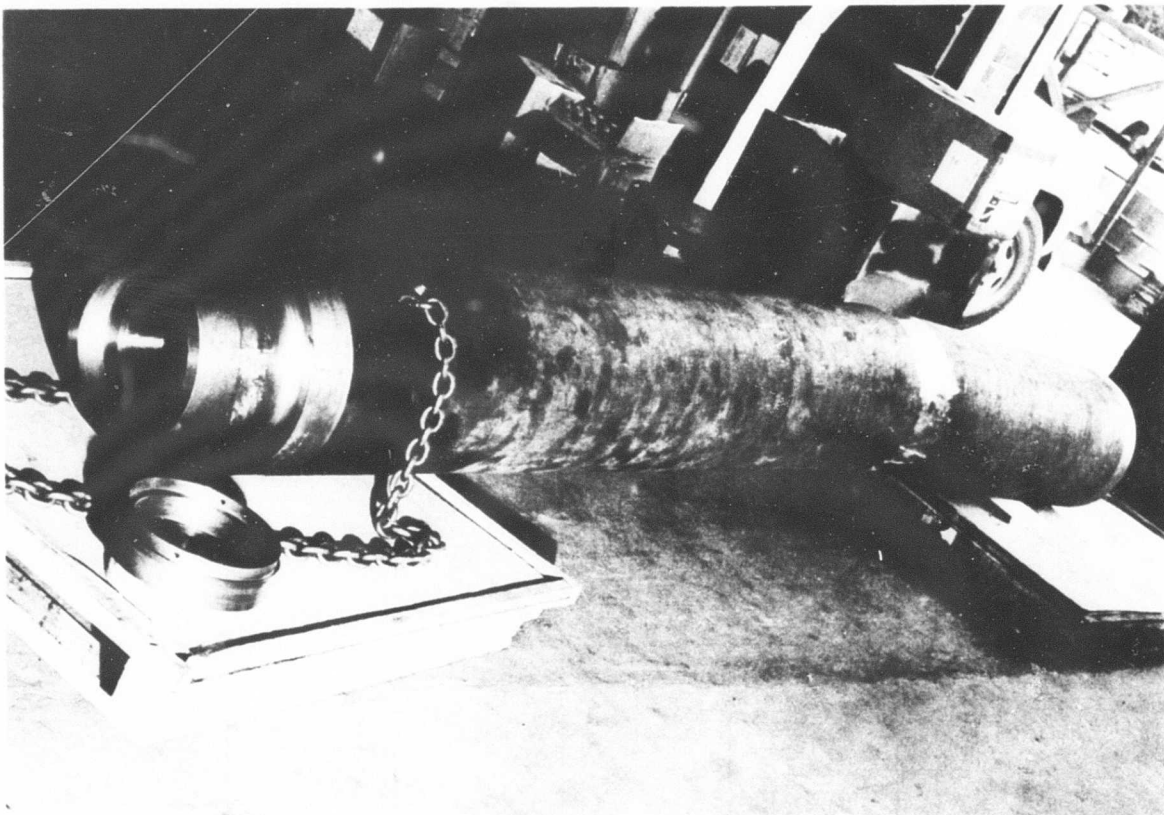


Figure 512. Photograph of Sting or Support Beam for Cruise Fan Model.

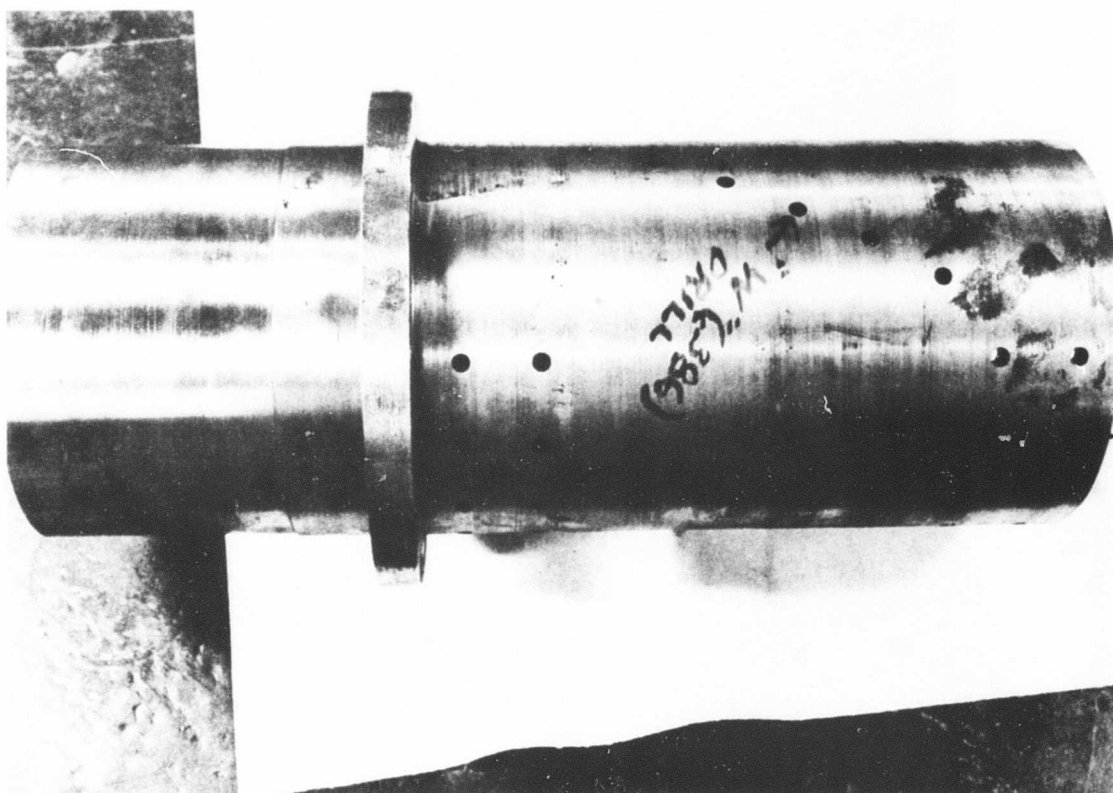


Figure 513. Photograph of Balance Adapter.

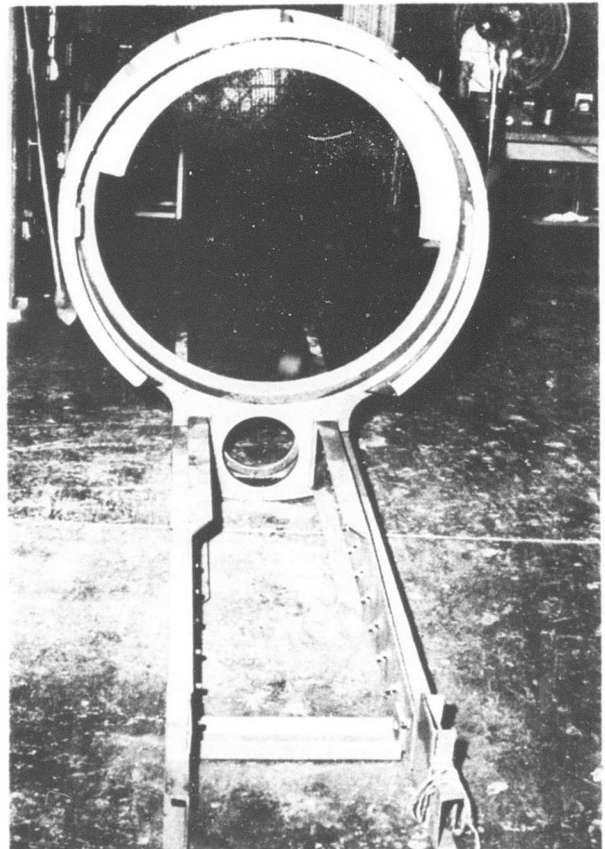
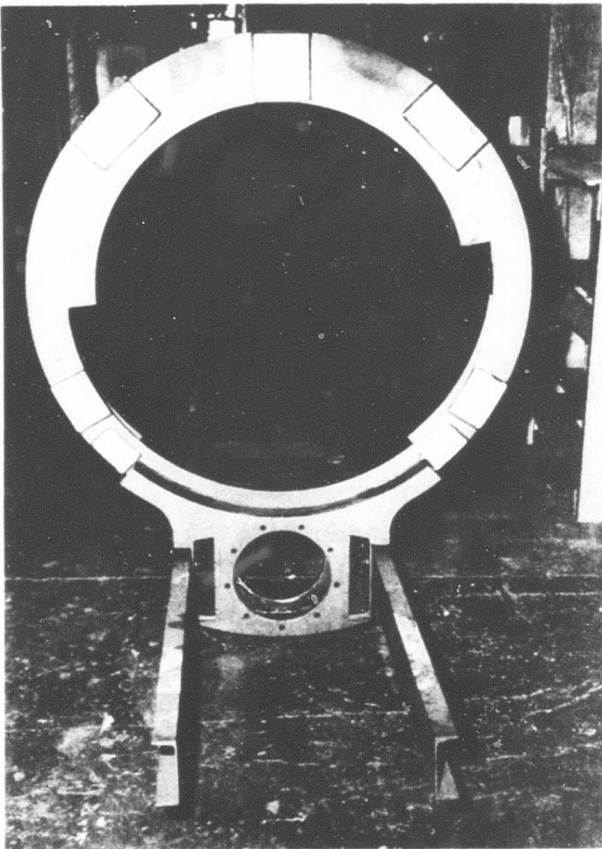
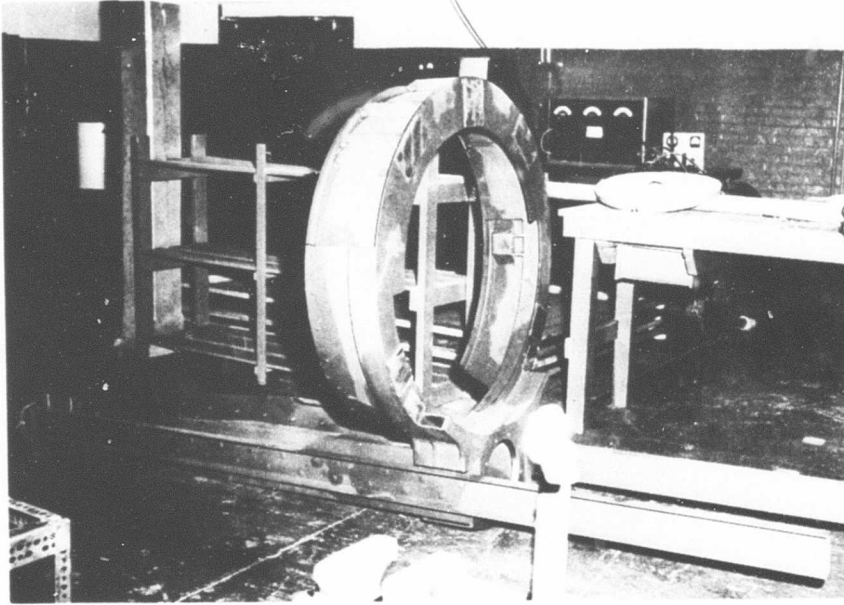


Figure 514. Photographs of Main Support Frame.

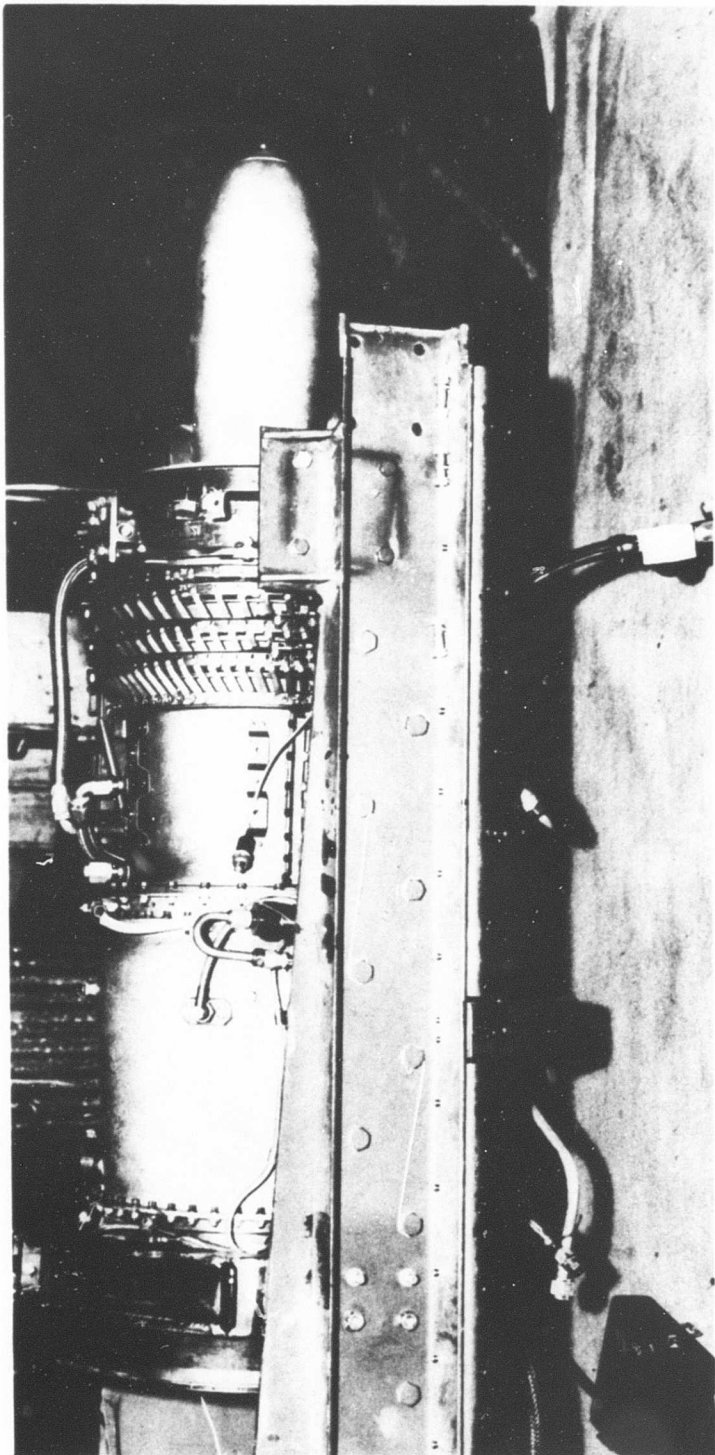


Figure 515. Photograph of T58-6A Engine Mounted in Engine Support Beams.

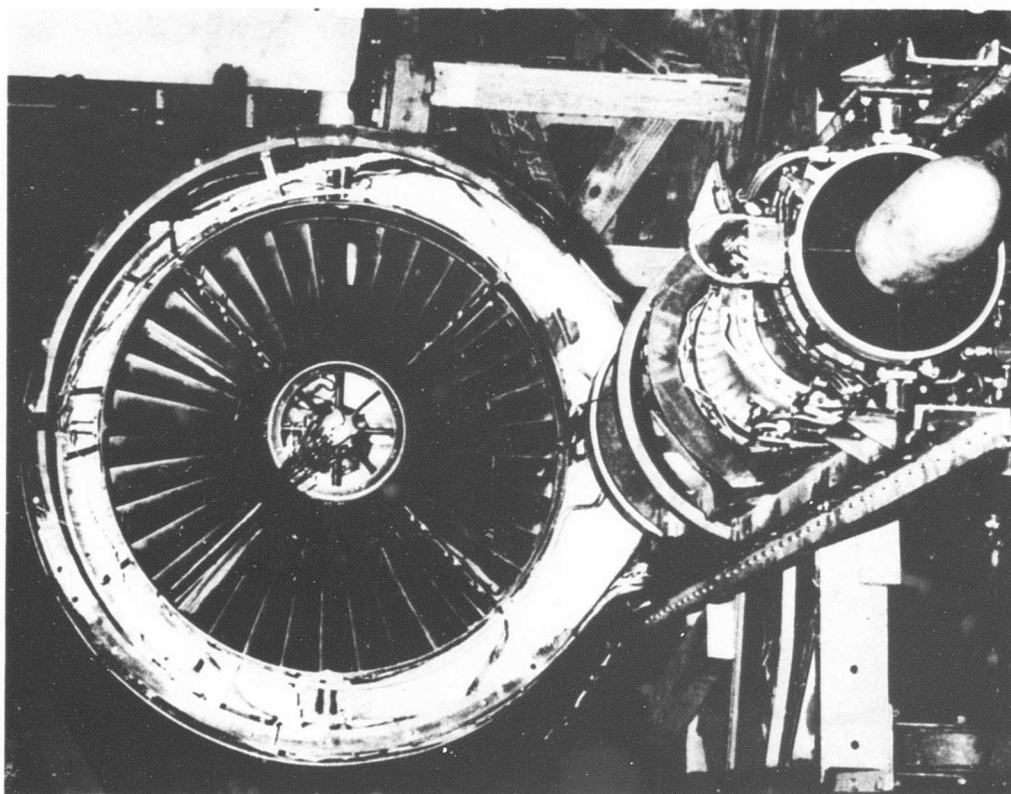
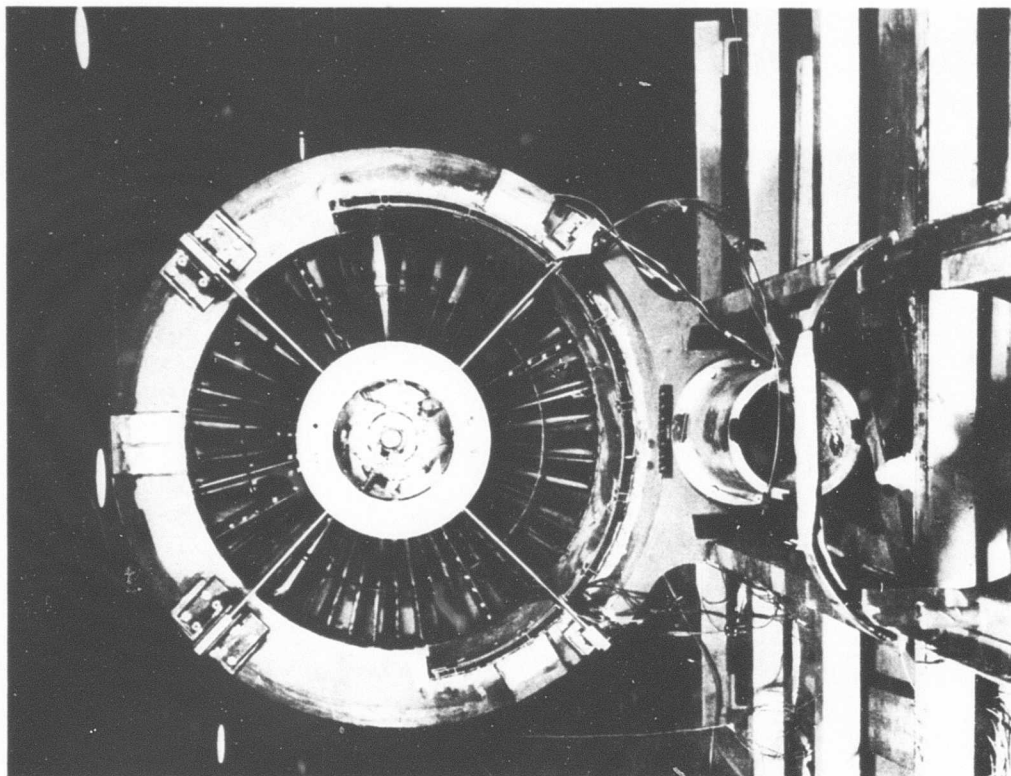
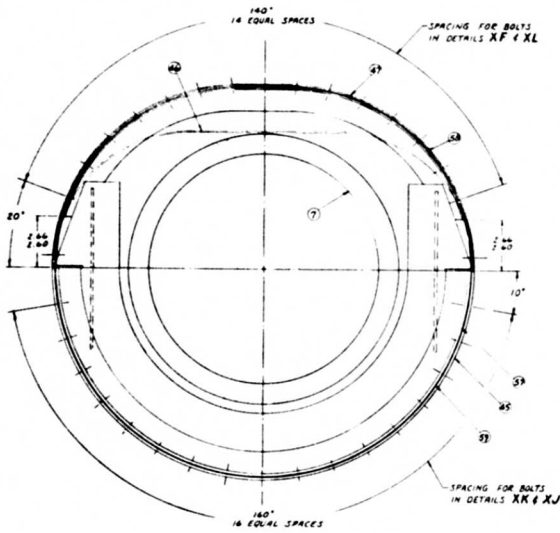
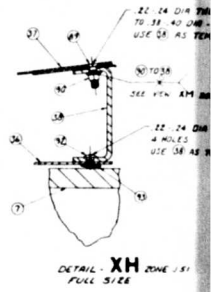
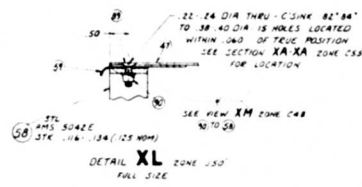


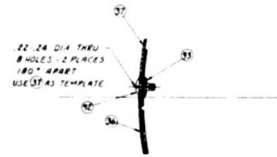
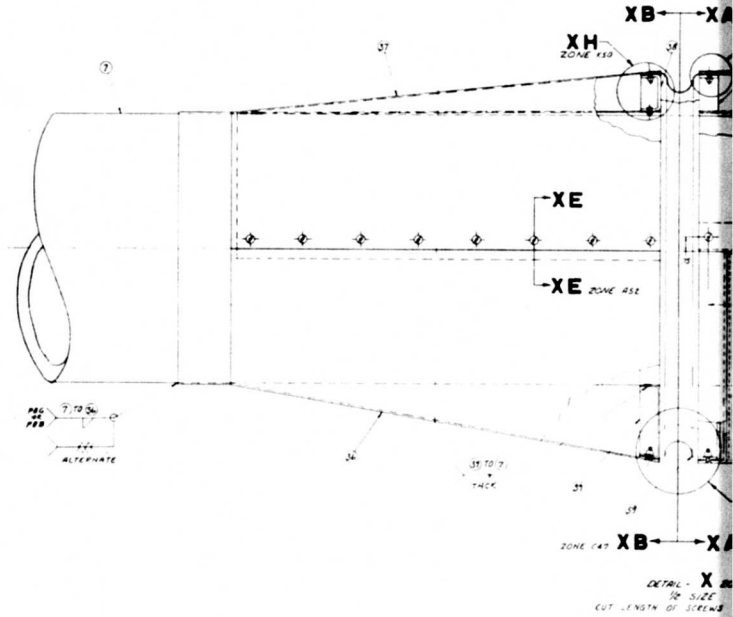
Figure 516. Photographs of X376 Fan Mounted in Main Support Frame.



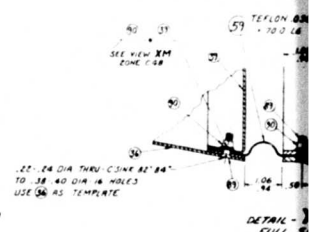
Figure 517. Photograph of Nozzle Plug for Cruise Fan Model.



SECTION - XA ~ XA ZONE D50 FULL SIZE



SECTION - XE ~ XE ZONE J51 FULL SIZE



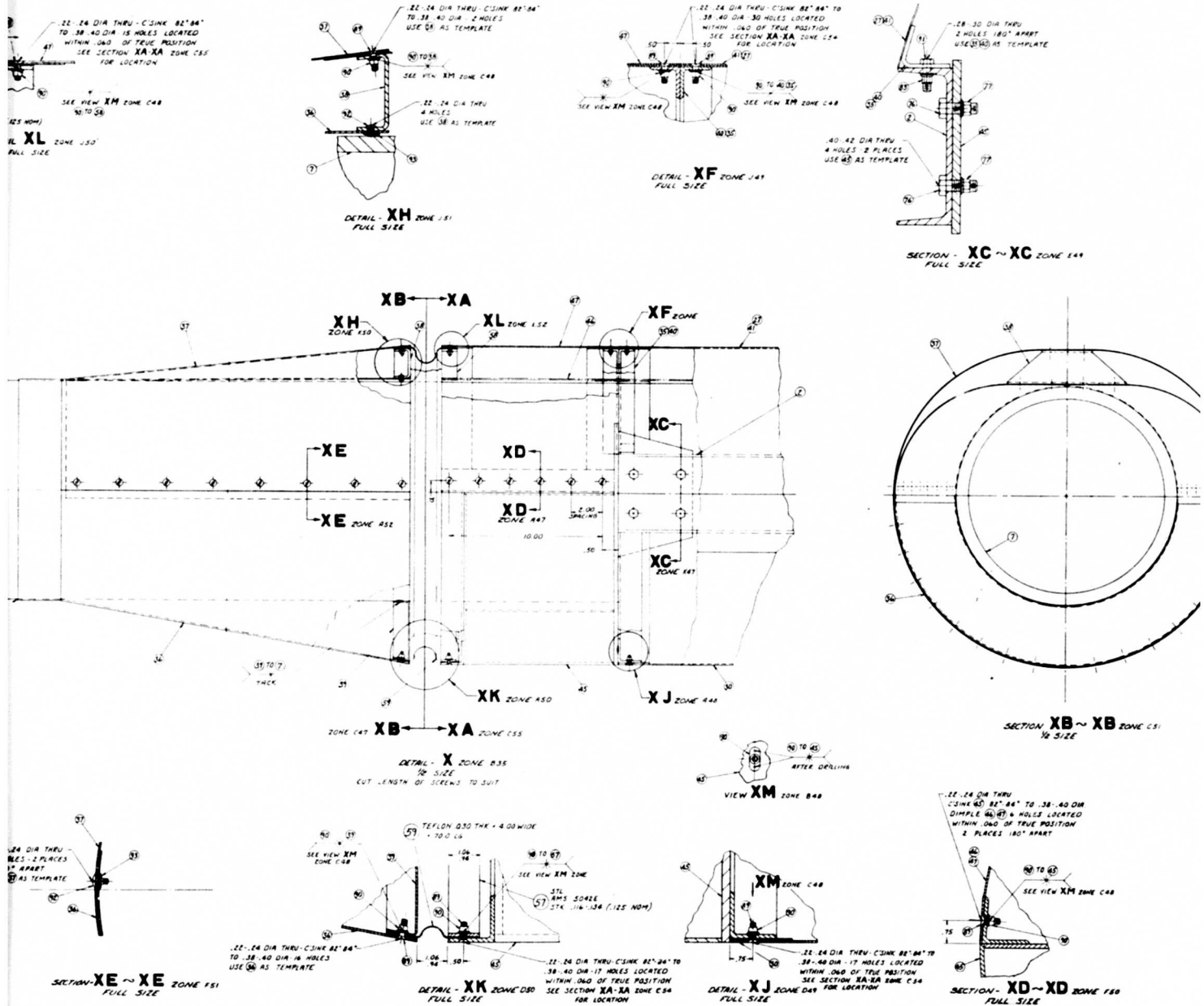


Figure 518. Model Assembly Drawing.



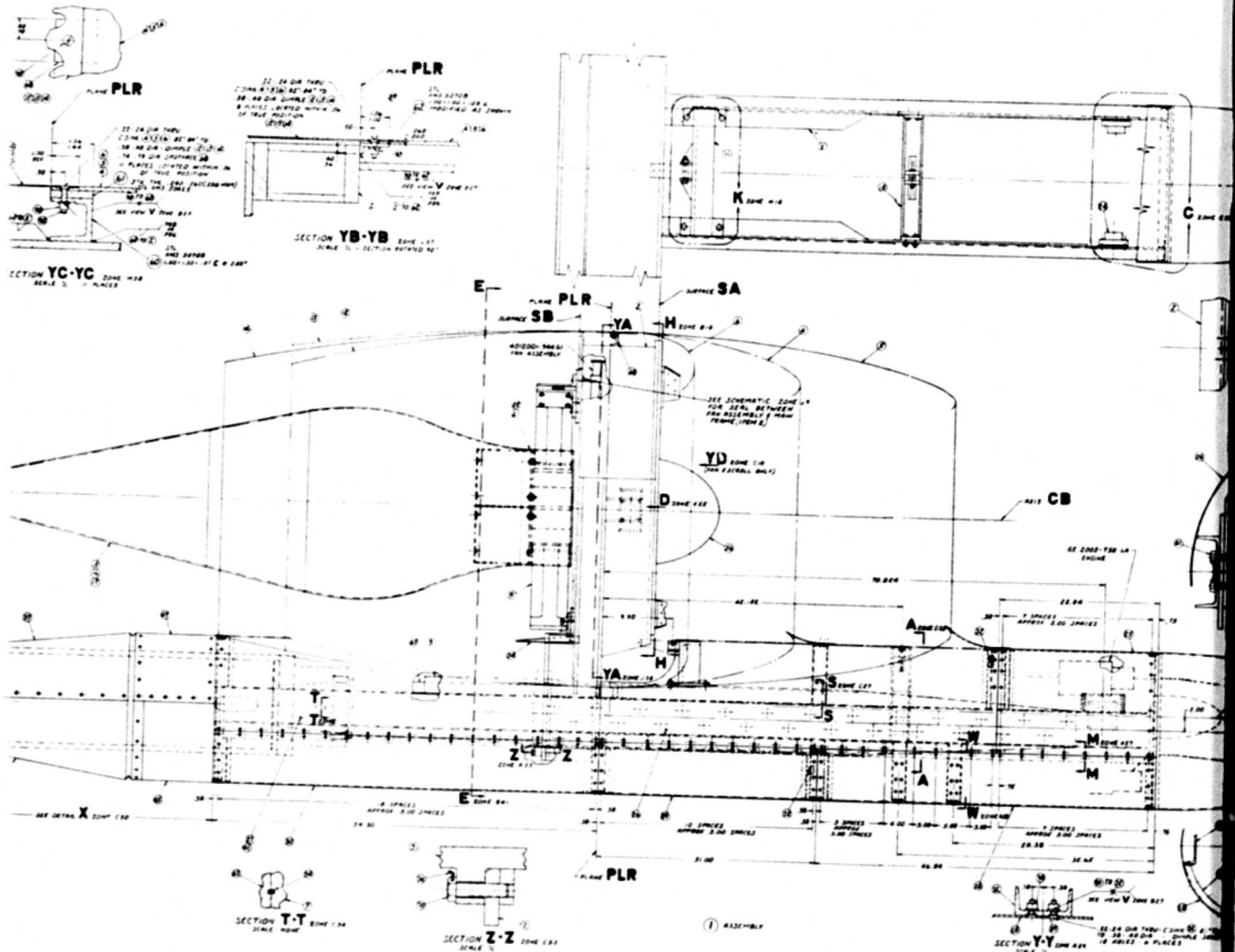


Figure 518. Model Assembly Drawing (Continued).

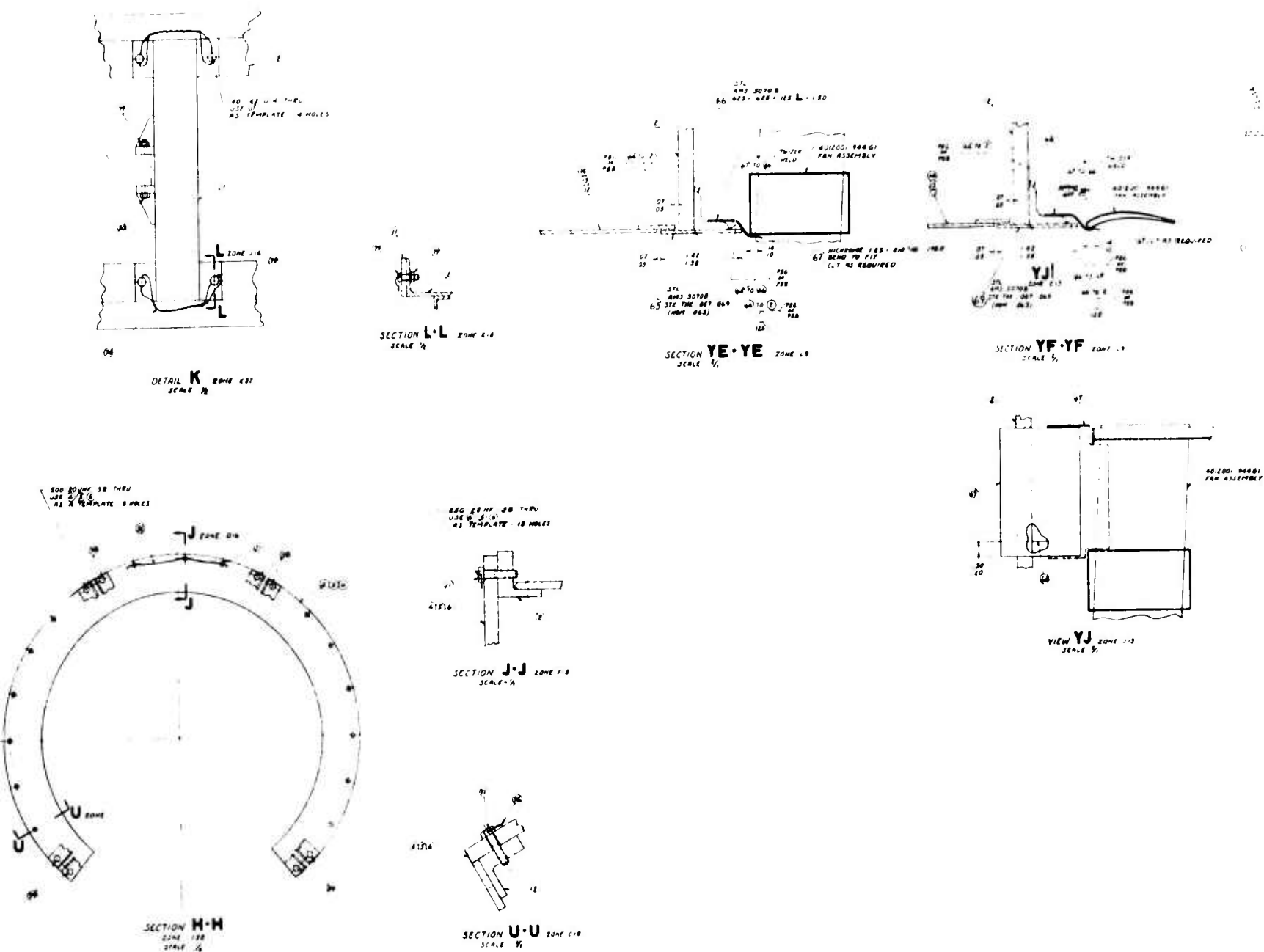
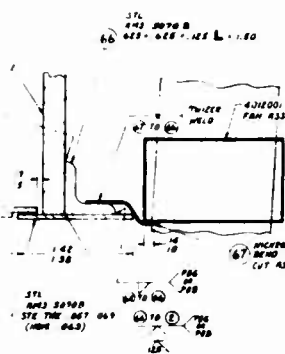
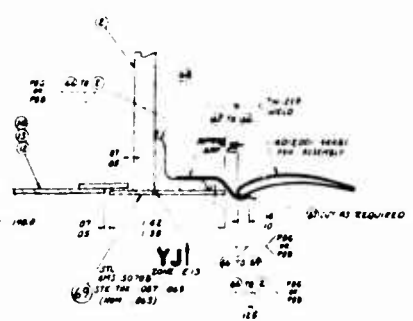


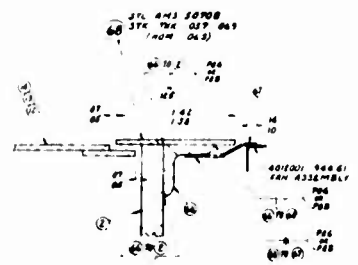
Figure 518. Model Assembly Drawing (Continued).



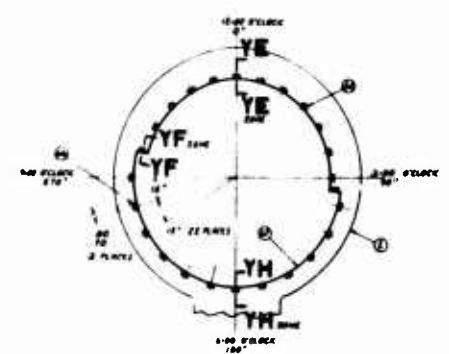
SECTION YE-YE ZONE 1.9
SCALE 1/2



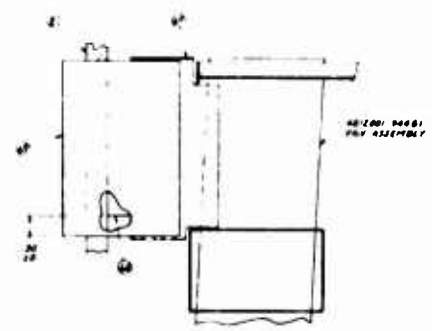
SECTION YF-YF ZONE 1.9
SCALE 1/2



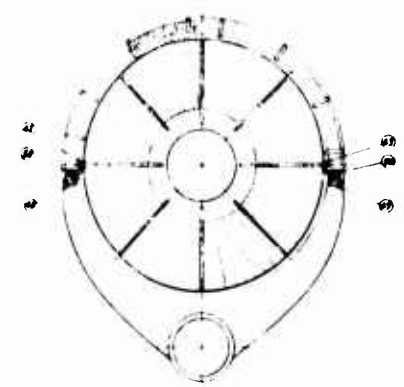
SECTION YH-YH ZONE 1.9
SCALE 1/2



SCHEMATIC OF SEAL
SCALE 1/2



VIEW YJ ZONE 1.9
SCALE 1/2



VIEW YD ZONE 1.9
SCALE 1/2

FAN ASSEMBLY
SAME AS 4-212001 944 61 WITH THE FOLLOWING EXCEPTIONS
1. ITEM 42 REPLACES ITEM 33 ON FAN ASSEMBLY
2. 1 43 1 33
3. 1 44 1 34
4. 1 45 1 35
5. ITEM 50 REPLACES ITEM 37 ON FAN ASSEMBLY
6. SCROLL INLET AIRBOX STAGE MODIFIED PER
ENGINEERING DRAWING TDR-150 100 01

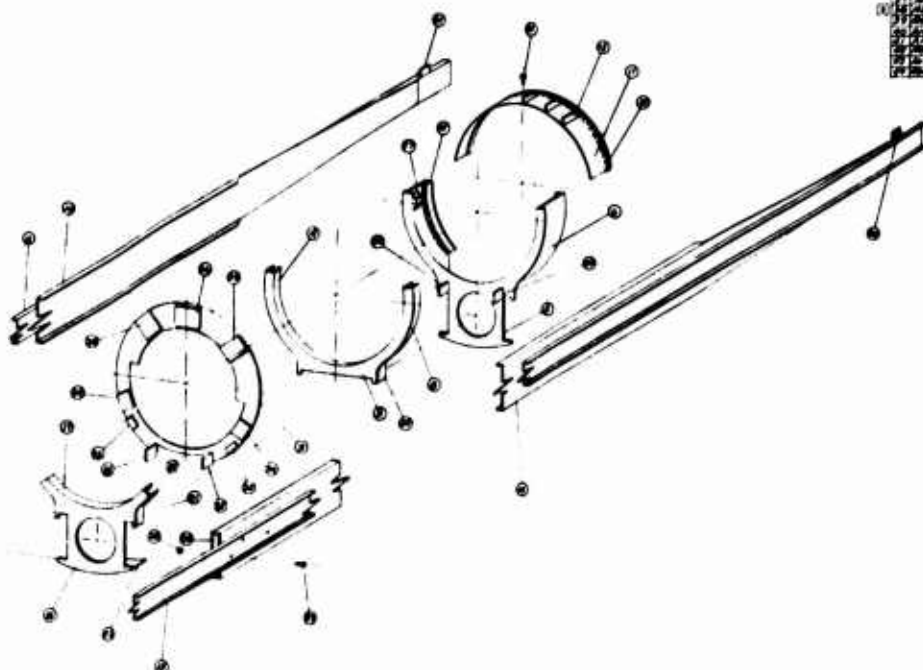
(Continued).

2. S.E.-INTERVIEW TO DETERMINE WHEN USED IN ASSEMBLY
 3. PDB FILLER MATL. **ONE SDB**
 4. PDB FILLER MATL. **ONE SDB**
 5. ALL WELDING MUST CONFORM TO REQUIREMENTS OF **W-207**
 6. SEE **31 31 207** FOR INTERPRETATION OF ONE

LAMBLEY CRUISE
FOR ASSEMBLY

631

ITEM	DESCRIPTION	QTY	UNIT	REMARKS
1	ASSEMBLY	1	EA	
2	FLANGE PLATE	1	EA	
3	FLANGE PLATE	1	EA	
4	FLANGE PLATE	1	EA	
5	FLANGE PLATE	1	EA	
6	FLANGE PLATE	1	EA	
7	FLANGE PLATE	1	EA	
8	FLANGE PLATE	1	EA	
9	FLANGE PLATE	1	EA	
10	FLANGE PLATE	1	EA	
11	FLANGE PLATE	1	EA	
12	FLANGE PLATE	1	EA	
13	FLANGE PLATE	1	EA	
14	FLANGE PLATE	1	EA	
15	FLANGE PLATE	1	EA	
16	FLANGE PLATE	1	EA	
17	FLANGE PLATE	1	EA	
18	FLANGE PLATE	1	EA	
19	FLANGE PLATE	1	EA	
20	FLANGE PLATE	1	EA	
21	FLANGE PLATE	1	EA	
22	FLANGE PLATE	1	EA	
23	FLANGE PLATE	1	EA	
24	FLANGE PLATE	1	EA	
25	FLANGE PLATE	1	EA	
26	FLANGE PLATE	1	EA	
27	FLANGE PLATE	1	EA	
28	FLANGE PLATE	1	EA	
29	FLANGE PLATE	1	EA	
30	FLANGE PLATE	1	EA	
31	FLANGE PLATE	1	EA	
32	FLANGE PLATE	1	EA	
33	FLANGE PLATE	1	EA	
34	FLANGE PLATE	1	EA	
35	FLANGE PLATE	1	EA	
36	FLANGE PLATE	1	EA	
37	FLANGE PLATE	1	EA	
38	FLANGE PLATE	1	EA	
39	FLANGE PLATE	1	EA	
40	FLANGE PLATE	1	EA	
41	FLANGE PLATE	1	EA	
42	FLANGE PLATE	1	EA	
43	FLANGE PLATE	1	EA	
44	FLANGE PLATE	1	EA	
45	FLANGE PLATE	1	EA	
46	FLANGE PLATE	1	EA	
47	FLANGE PLATE	1	EA	
48	FLANGE PLATE	1	EA	
49	FLANGE PLATE	1	EA	
50	FLANGE PLATE	1	EA	
51	FLANGE PLATE	1	EA	
52	FLANGE PLATE	1	EA	
53	FLANGE PLATE	1	EA	
54	FLANGE PLATE	1	EA	
55	FLANGE PLATE	1	EA	
56	FLANGE PLATE	1	EA	
57	FLANGE PLATE	1	EA	
58	FLANGE PLATE	1	EA	
59	FLANGE PLATE	1	EA	
60	FLANGE PLATE	1	EA	
61	FLANGE PLATE	1	EA	
62	FLANGE PLATE	1	EA	
63	FLANGE PLATE	1	EA	
64	FLANGE PLATE	1	EA	
65	FLANGE PLATE	1	EA	
66	FLANGE PLATE	1	EA	
67	FLANGE PLATE	1	EA	
68	FLANGE PLATE	1	EA	
69	FLANGE PLATE	1	EA	
70	FLANGE PLATE	1	EA	
71	FLANGE PLATE	1	EA	
72	FLANGE PLATE	1	EA	
73	FLANGE PLATE	1	EA	
74	FLANGE PLATE	1	EA	
75	FLANGE PLATE	1	EA	
76	FLANGE PLATE	1	EA	
77	FLANGE PLATE	1	EA	
78	FLANGE PLATE	1	EA	
79	FLANGE PLATE	1	EA	
80	FLANGE PLATE	1	EA	
81	FLANGE PLATE	1	EA	
82	FLANGE PLATE	1	EA	
83	FLANGE PLATE	1	EA	
84	FLANGE PLATE	1	EA	
85	FLANGE PLATE	1	EA	
86	FLANGE PLATE	1	EA	
87	FLANGE PLATE	1	EA	
88	FLANGE PLATE	1	EA	
89	FLANGE PLATE	1	EA	
90	FLANGE PLATE	1	EA	
91	FLANGE PLATE	1	EA	
92	FLANGE PLATE	1	EA	
93	FLANGE PLATE	1	EA	
94	FLANGE PLATE	1	EA	
95	FLANGE PLATE	1	EA	
96	FLANGE PLATE	1	EA	
97	FLANGE PLATE	1	EA	
98	FLANGE PLATE	1	EA	
99	FLANGE PLATE	1	EA	
100	FLANGE PLATE	1	EA	

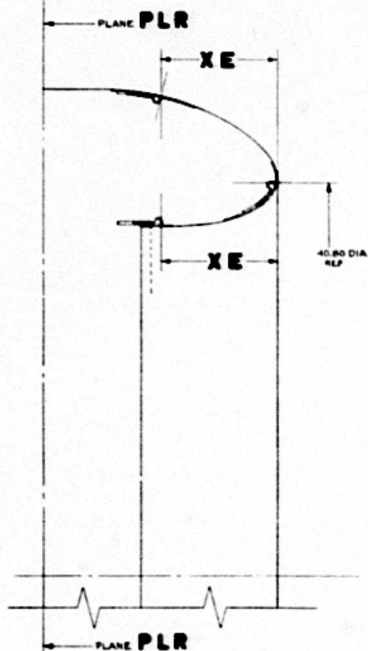


- A (IF REQD) AFTER WELDING & PRIOR TO FINAL PAINTING, ASSEMBLY SHALL BE STRESSED RELIEVED BY INDUSTRY PRACTICES & AIR COOLED.
- B ITEMS 18, 19, 18 HAVE 2 REQD WHICH ARE IDENTICAL BEFORE MATEN DRILLING.
- C HOLES TO BE DRILL AFTER ESTABLISHING 26.80 DIM (INCHES)
- D CLEAN SURFACES AND APPLY COAT OF ZINC CHROMATE PRIMER
- E ALL WELDS SHALL BE DYE PENETRANT INSPECTED PER AMS 2636 NO CRACKS ALLOWED.
- F (ITEM 26 LOCKWAS) SHALL BE SUPPLIED BY G.E.
- G WELDERS MUST BE CERTIFIED PER AMS 2636
- H ALL WELDS SHALL BE 100% PENETRATION.
- I SEE AMS 2636 FOR INTERPRETATION OF WELDING.
- J SEE AMS 2636 FOR THE FOLLOWING
- K ALL SURFACES SHALL BE PERPENDICULAR WITH SURFACE INDICATOR READING.
- L SURFACE AMS 2636 TO BE PARALLEL WITHIN .000 OF FULL INDICATOR READING.
- M DELINEATED RIGHT ANGLES ARE 90° PLUS OR MINUS (.2) 30 MINUTES.
- N BREAK SHARP EDGES AND REMOVE ALL BURRS.
- O SEE AMS 2636 FOR INTERPRETATION OF DIMS.

ITEM	DESCRIPTION	QTY	UNIT	REMARKS
1	MAIN FRAME	1	EA	
2	ANGLE CRUISE (IN)	1	EA	
3	ANGLE CRUISE (IN)	1	EA	
4	ANGLE CRUISE (IN)	1	EA	
5	ANGLE CRUISE (IN)	1	EA	
6	ANGLE CRUISE (IN)	1	EA	
7	ANGLE CRUISE (IN)	1	EA	
8	ANGLE CRUISE (IN)	1	EA	
9	ANGLE CRUISE (IN)	1	EA	
10	ANGLE CRUISE (IN)	1	EA	
11	ANGLE CRUISE (IN)	1	EA	
12	ANGLE CRUISE (IN)	1	EA	
13	ANGLE CRUISE (IN)	1	EA	
14	ANGLE CRUISE (IN)	1	EA	
15	ANGLE CRUISE (IN)	1	EA	
16	ANGLE CRUISE (IN)	1	EA	
17	ANGLE CRUISE (IN)	1	EA	
18	ANGLE CRUISE (IN)	1	EA	
19	ANGLE CRUISE (IN)	1	EA	
20	ANGLE CRUISE (IN)	1	EA	
21	ANGLE CRUISE (IN)	1	EA	
22	ANGLE CRUISE (IN)	1	EA	
23	ANGLE CRUISE (IN)	1	EA	
24	ANGLE CRUISE (IN)	1	EA	
25	ANGLE CRUISE (IN)	1	EA	
26	ANGLE CRUISE (IN)	1	EA	
27	ANGLE CRUISE (IN)	1	EA	
28	ANGLE CRUISE (IN)	1	EA	
29	ANGLE CRUISE (IN)	1	EA	
30	ANGLE CRUISE (IN)	1	EA	
31	ANGLE CRUISE (IN)	1	EA	
32	ANGLE CRUISE (IN)	1	EA	
33	ANGLE CRUISE (IN)	1	EA	
34	ANGLE CRUISE (IN)	1	EA	
35	ANGLE CRUISE (IN)	1	EA	
36	ANGLE CRUISE (IN)	1	EA	
37	ANGLE CRUISE (IN)	1	EA	
38	ANGLE CRUISE (IN)	1	EA	
39	ANGLE CRUISE (IN)	1	EA	
40	ANGLE CRUISE (IN)	1	EA	
41	ANGLE CRUISE (IN)	1	EA	
42	ANGLE CRUISE (IN)	1	EA	
43	ANGLE CRUISE (IN)	1	EA	
44	ANGLE CRUISE (IN)	1	EA	
45	ANGLE CRUISE (IN)	1	EA	
46	ANGLE CRUISE (IN)	1	EA	
47	ANGLE CRUISE (IN)	1	EA	
48	ANGLE CRUISE (IN)	1	EA	
49	ANGLE CRUISE (IN)	1	EA	
50	ANGLE CRUISE (IN)	1	EA	
51	ANGLE CRUISE (IN)	1	EA	
52	ANGLE CRUISE (IN)	1	EA	
53	ANGLE CRUISE (IN)	1	EA	
54	ANGLE CRUISE (IN)	1	EA	
55	ANGLE CRUISE (IN)	1	EA	
56	ANGLE CRUISE (IN)	1	EA	
57	ANGLE CRUISE (IN)	1	EA	
58	ANGLE CRUISE (IN)	1	EA	
59	ANGLE CRUISE (IN)	1	EA	
60	ANGLE CRUISE (IN)	1	EA	
61	ANGLE CRUISE (IN)	1	EA	
62	ANGLE CRUISE (IN)	1	EA	
63	ANGLE CRUISE (IN)	1	EA	
64	ANGLE CRUISE (IN)	1	EA	
65	ANGLE CRUISE (IN)	1	EA	
66	ANGLE CRUISE (IN)	1	EA	
67	ANGLE CRUISE (IN)	1	EA	
68	ANGLE CRUISE (IN)	1	EA	
69	ANGLE CRUISE (IN)	1	EA	
70	ANGLE CRUISE (IN)	1	EA	
71	ANGLE CRUISE (IN)	1	EA	
72	ANGLE CRUISE (IN)	1	EA	
73	ANGLE CRUISE (IN)	1	EA	
74	ANGLE CRUISE (IN)	1	EA	
75	ANGLE CRUISE (IN)	1	EA	
76	ANGLE CRUISE (IN)	1	EA	
77	ANGLE CRUISE (IN)	1	EA	
78	ANGLE CRUISE (IN)	1	EA	
79	ANGLE CRUISE (IN)	1	EA	
80	ANGLE CRUISE (IN)	1	EA	
81	ANGLE CRUISE (IN)	1	EA	
82	ANGLE CRUISE (IN)	1	EA	
83	ANGLE CRUISE (IN)	1	EA	
84	ANGLE CRUISE (IN)	1	EA	
85	ANGLE CRUISE (IN)	1	EA	
86	ANGLE CRUISE (IN)	1	EA	
87	ANGLE CRUISE (IN)	1	EA	
88	ANGLE CRUISE (IN)	1	EA	
89	ANGLE CRUISE (IN)	1	EA	
90	ANGLE CRUISE (IN)	1	EA	
91	ANGLE CRUISE (IN)	1	EA	
92	ANGLE CRUISE (IN)	1	EA	
93	ANGLE CRUISE (IN)	1	EA	
94	ANGLE CRUISE (IN)	1	EA	
95	ANGLE CRUISE (IN)	1	EA	
96	ANGLE CRUISE (IN)	1	EA	
97	ANGLE CRUISE (IN)	1	EA	
98	ANGLE CRUISE (IN)	1	EA	
99	ANGLE CRUISE (IN)	1	EA	
100	ANGLE CRUISE (IN)	1	EA	

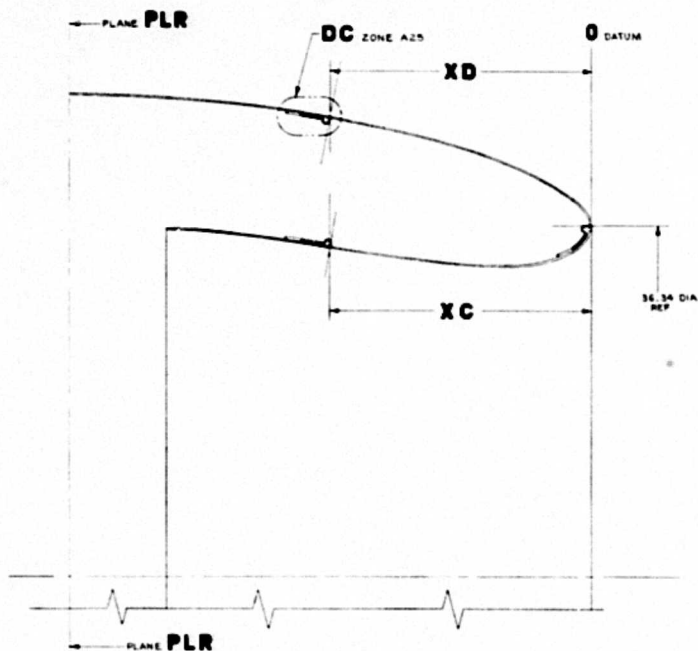
of Main Frame (Continued).

STA 01.950

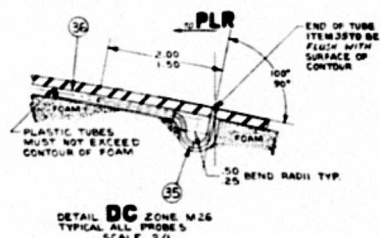


PROBE NUMBER	DISTANCE XE	ANGLE IN DEGREES	PROBE NUMBER	DISTANCE XF	ANGLE IN DEGREES
130	0.00	0	182	0.36	0
132	0.00	90	184	0.36	90
134	0.00	180	185	0.36	137
136	0.36	0	186	0.72	0
138	0.36	90	190	0.72	90
140	0.36	180	191	0.72	137
141	0.72	0	193	1.08	0
143	0.72	90	195	1.08	90
145	0.72	180	196	1.08	137
147	1.08	0	199	1.80	0
149	1.08	90	201	1.80	90
151	1.08	180	202	1.80	137
152	1.80	0	204	3.60	0
154	1.80	90	207	3.60	90
156	1.80	180	210	6.00	0
158	3.60	0	212	6.00	90
160	3.60	90	213	6.00	137
162	3.60	180	215	9.00	0
163	4.70	0	217	9.00	90
165	4.70	90	218	9.00	137
167	6.00	22.5	221	11.40	0
			223	11.40	90
			224	11.40	137

STA 10.350



PROBE NUMBER	DISTANCE XC	ANGLE IN DEGREES	PROBE NUMBER	DISTANCE XD	ANGLE IN DEGREES
130	0.00	0	182	0.36	0
132	0.00	90	184	0.36	90
134	0.00	180	185	0.36	137
136	0.36	0	186	0.72	0
138	0.36	90	190	0.72	90
140	0.36	180	191	0.72	137
141	0.72	0	193	1.08	0
143	0.72	90	195	1.08	90
145	0.72	180	196	1.08	137
147	1.08	0	199	1.80	0
149	1.08	90	201	1.80	90
151	1.08	180	202	1.80	137
152	1.80	0	204	3.60	0
154	1.80	90	207	3.60	90
156	1.80	180	210	6.00	0
158	3.60	0	212	6.00	90
160	3.60	90	213	6.00	137
162	3.60	180	215	9.00	0
163	4.70	0	217	9.00	90
165	4.70	90	218	9.00	137
167	6.00	22.5	221	11.40	0
			223	11.40	90
			224	11.40	137



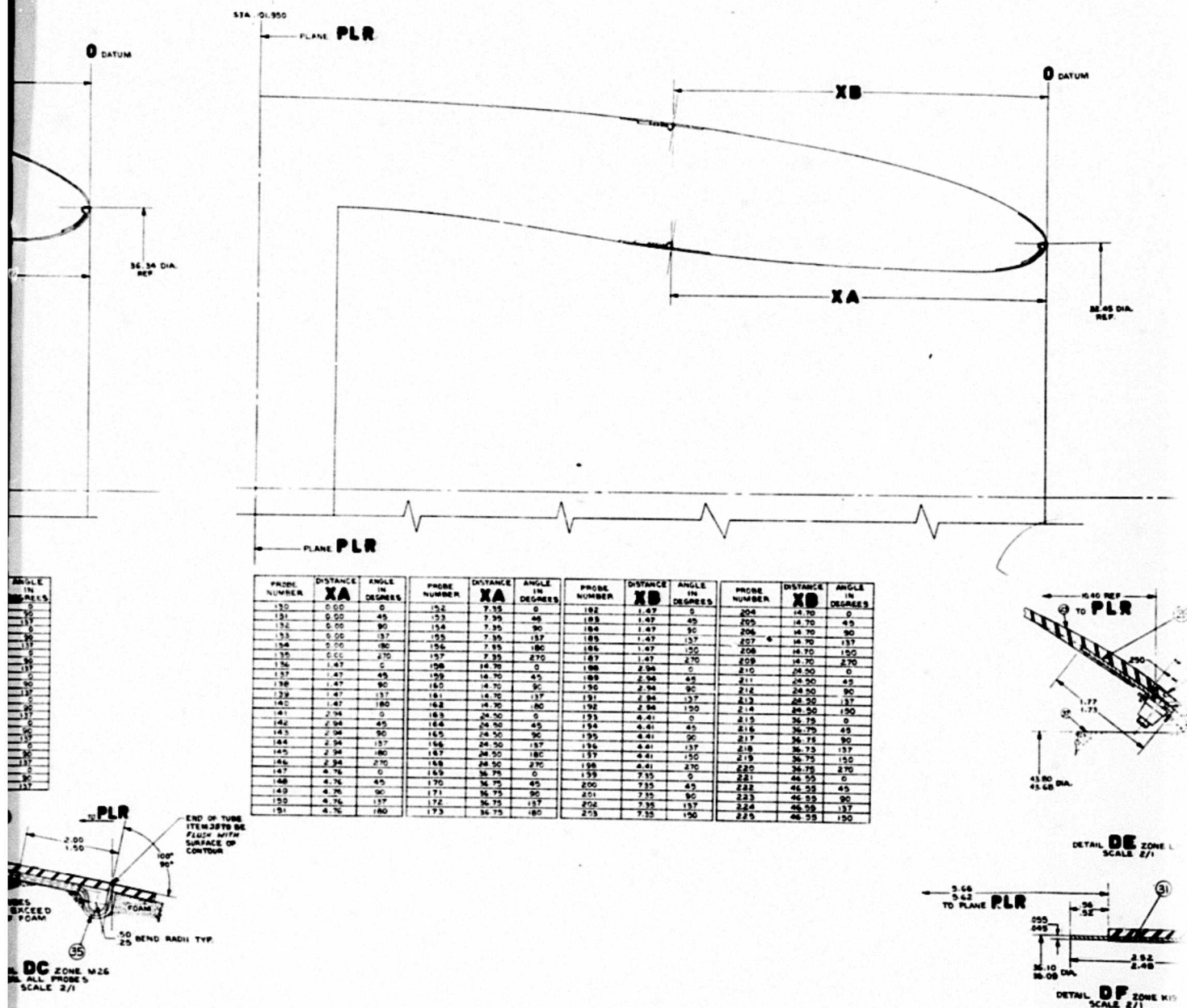


Figure 520. Detail Drawing of Nacelle Inlets.

Technical drawing of a ship's hull showing three views: a side profile view on the left, a plan view (top) in the center, and a cross-section view (right) on the right.

Side Profile View (Left): Shows the hull's curvature. A vertical line is labeled "0 DATUM". Horizontal reference lines are labeled "XB" and "XA". A dimension "34 45 DIA. REF." is indicated.

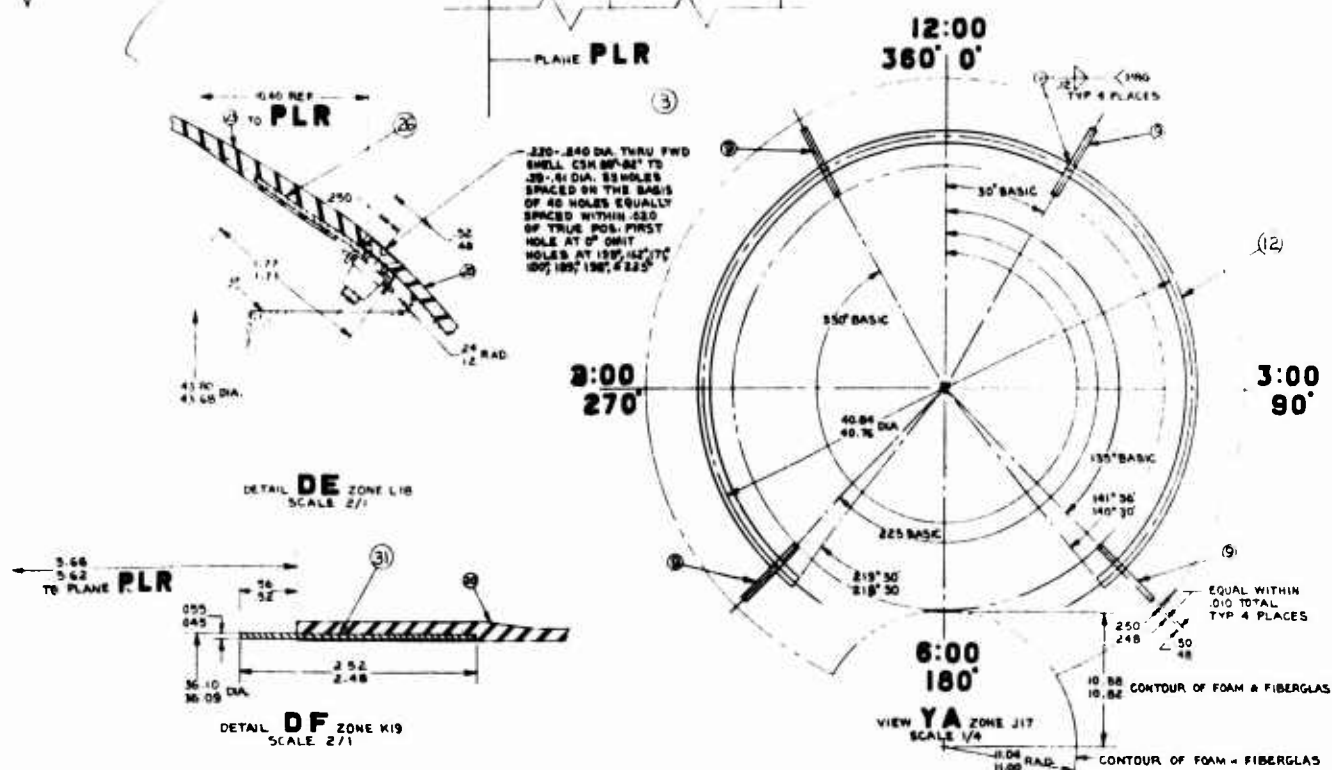
Plan View (Top): Shows the hull's footprint. Key features include:

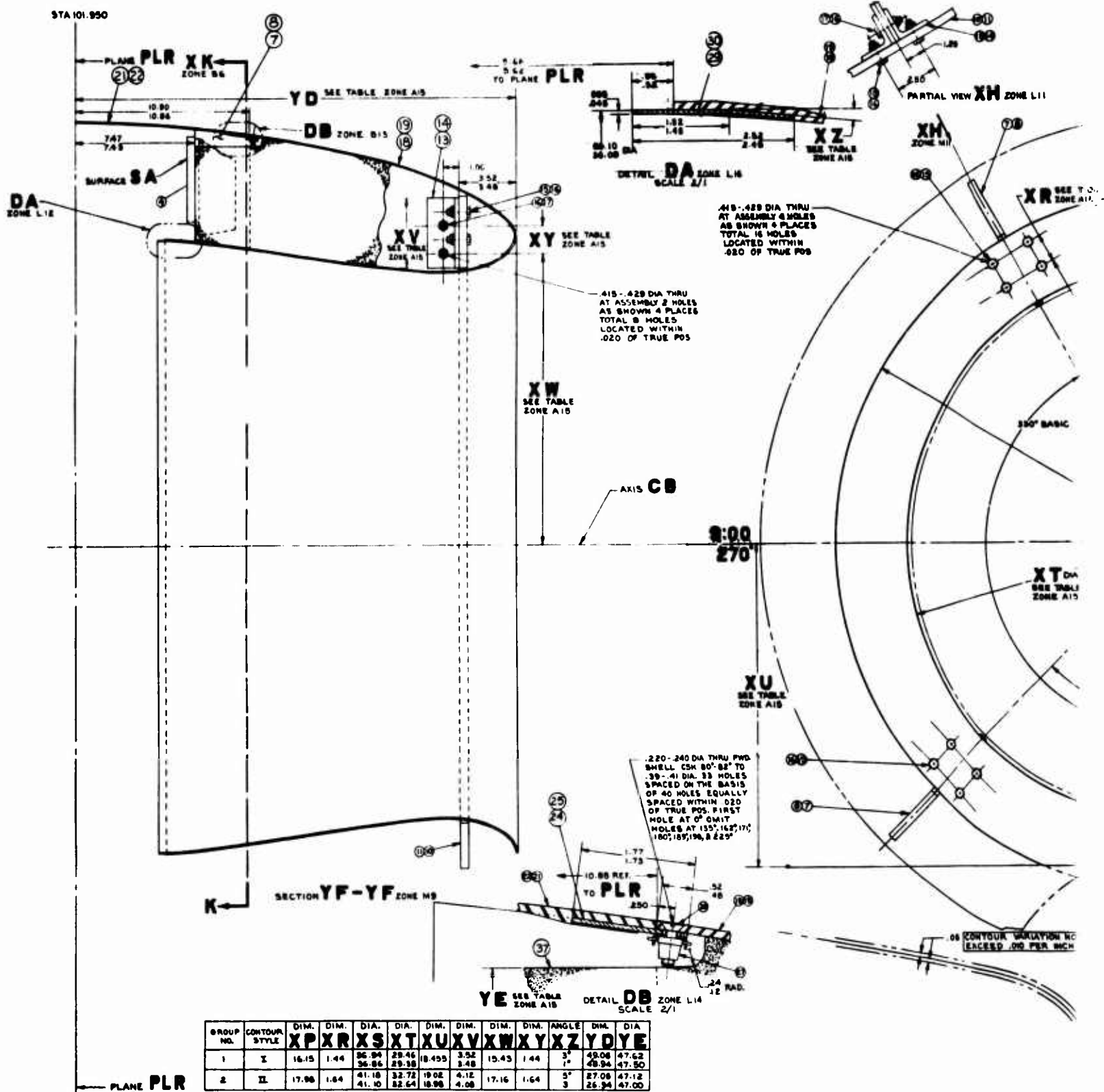
- PLR** (Plane of Reference Line)
- YB ZONE J17**
- DE ZONE C19**
- DF ZONE A19**
- SURFACE SA**
- Dimensions: 12 52, 11 98, 10 44, 10 36, 23.

Cross-section View (Right): Shows the internal structure of the hull. Key features include:

- VIEW YB ZONE M B**
- SURFACE SA**
- Dimensions: 5 44, 5 52, 1 06, 1 34, 1 24, 1 24, 1 24.

INSTANCE XD	ANGLE IN DEGREES
14.70	0
14.70	45
14.70	90
14.70	137
14.70	150
24.50	270
24.50	45
24.50	90
24.50	137
24.50	150
36.75	0
36.75	45
36.75	90
36.75	137
36.75	150
36.75	270
46.55	0
46.55	45
46.55	90
46.55	137
46.55	150



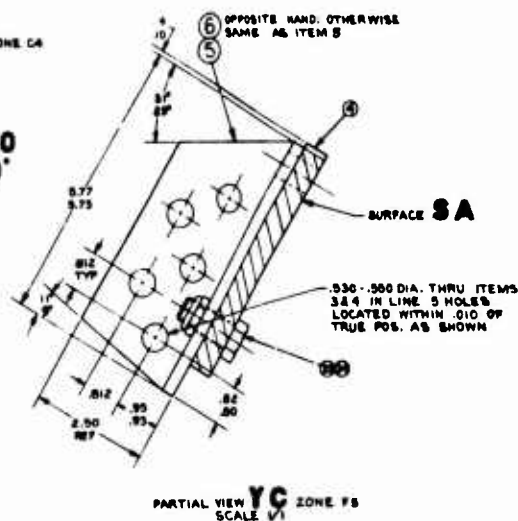
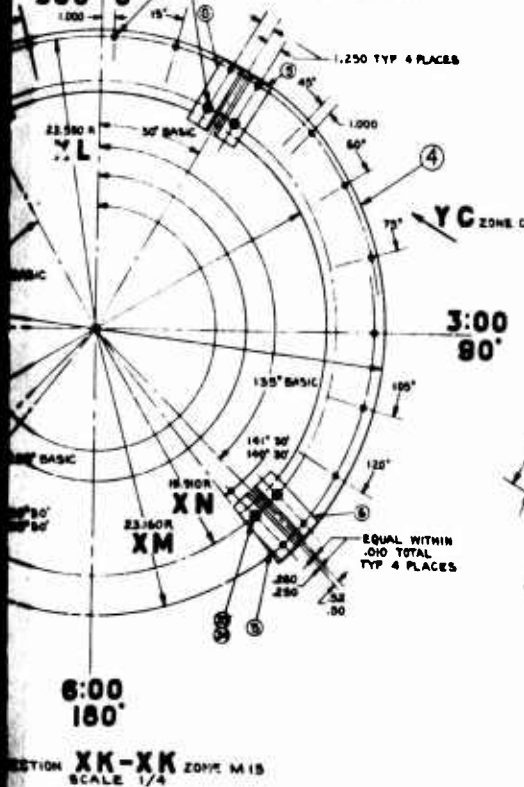


ITEM	DESCRIPTION	QTY	UNIT	GROUP
1	RESIN GLIDPOL 1027 - GLIDDEN CO.	1	LB	1
2	CATALYST - 6% COBALT NAPHTHANATE	1	LB	1
3	STYRENE MONOMER	1	LB	1
4	FIBERGLAS CLOTH 10 OR BORT CLOTH TMS M-14	1	LB	1
5	FOAM - AROTHANE FOAM 8764 BF 8750AF	1	LB	1
6	ACROR DANIELS MIDLAND CO.	1	LB	1
7	STEEL - SAE 1008	1	LB	1
8	ALUMINUM - 6061-T6	1	LB	1
9	BRASS - 360	1	LB	1
10	BRASS - 360	1	LB	1
11	BRASS - 360	1	LB	1
12	BRASS - 360	1	LB	1
13	BRASS - 360	1	LB	1
14	BRASS - 360	1	LB	1
15	BRASS - 360	1	LB	1
16	BRASS - 360	1	LB	1
17	BRASS - 360	1	LB	1
18	BRASS - 360	1	LB	1
19	BRASS - 360	1	LB	1
20	BRASS - 360	1	LB	1
21	BRASS - 360	1	LB	1
22	BRASS - 360	1	LB	1
23	BRASS - 360	1	LB	1
24	BRASS - 360	1	LB	1
25	BRASS - 360	1	LB	1
26	BRASS - 360	1	LB	1
27	BRASS - 360	1	LB	1
28	BRASS - 360	1	LB	1
29	BRASS - 360	1	LB	1
30	BRASS - 360	1	LB	1
31	BRASS - 360	1	LB	1
32	BRASS - 360	1	LB	1
33	BRASS - 360	1	LB	1
34	BRASS - 360	1	LB	1
35	BRASS - 360	1	LB	1
36	BRASS - 360	1	LB	1
37	BRASS - 360	1	LB	1

BESNA UNION NEW JERSEY OR EQUIV

280-.300 DIA THRU LOCATED AND MATCHED AT FINAL ASSY. MATCH DRILL BRACKETS AS SHOWN

18 HOLES ON RAD XL
10 HOLES ON RAD XM
8 HOLES ON RAD XN
TOTAL 36 HOLES



4 RESIN GLIDPOL 1027 - GLIDDEN CO.
CATALYST - 6% COBALT NAPHTHANATE
STYRENE MONOMER
FIBERGLAS CLOTH 10 OR BORT CLOTH TMS M-14
3. FOAM - AROTHANE FOAM 8764 BF 8750AF
ACROR DANIELS MIDLAND CO.
2. ALUMINUM - 6061-T6
1. STEEL - SAE 1008

CADILLAC PLASTIC

3 NACELLE CONTOUR PRECISION MASTER DUG NO FOR TYPES I, II, III IS 202017-327
2 PERMANENT MARK WITH DUG NO GROUP NO

SEE SPL 212010 FOR INTERPRETATION OF DRAWING

CHECKED BY DESIGNED BY DRAWN BY DATE	APPROVED BY DATE	FAN NACELLE- FORWARD	REVISIONS 1. 202017-327 2. 202017-327
-----------------------------------------------	---------------------	-------------------------	---------------------------------------------

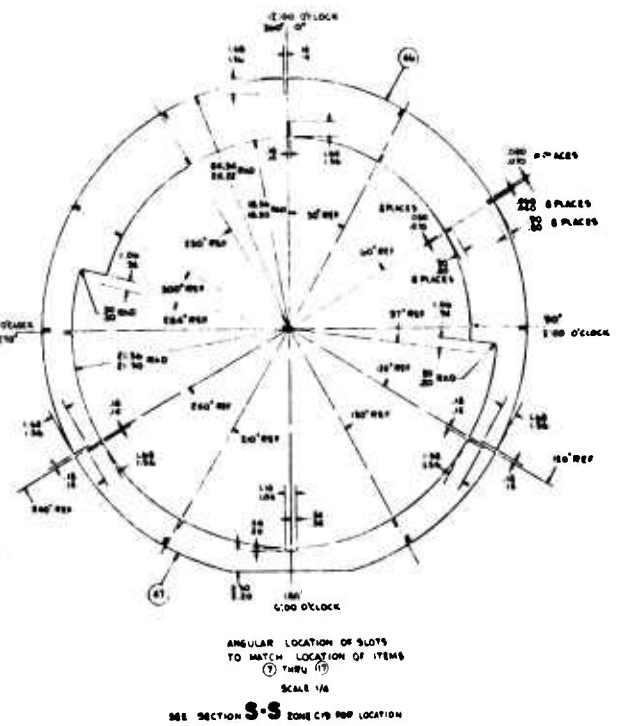
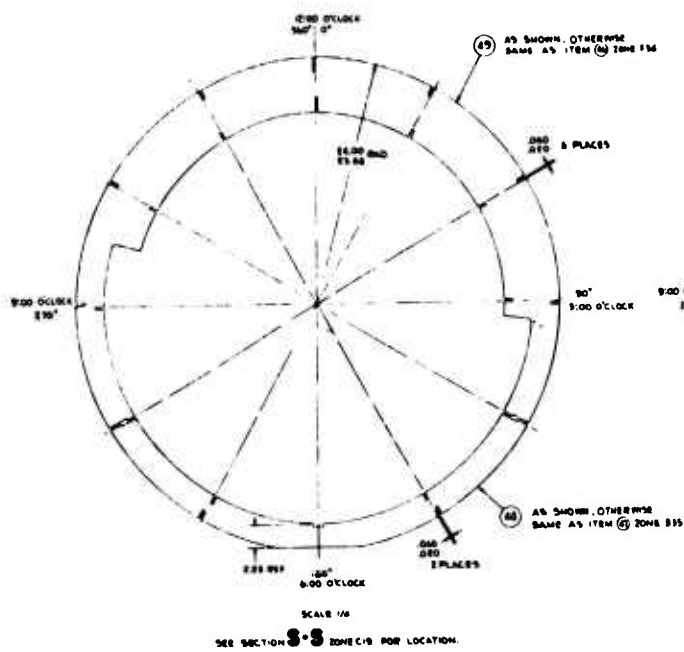
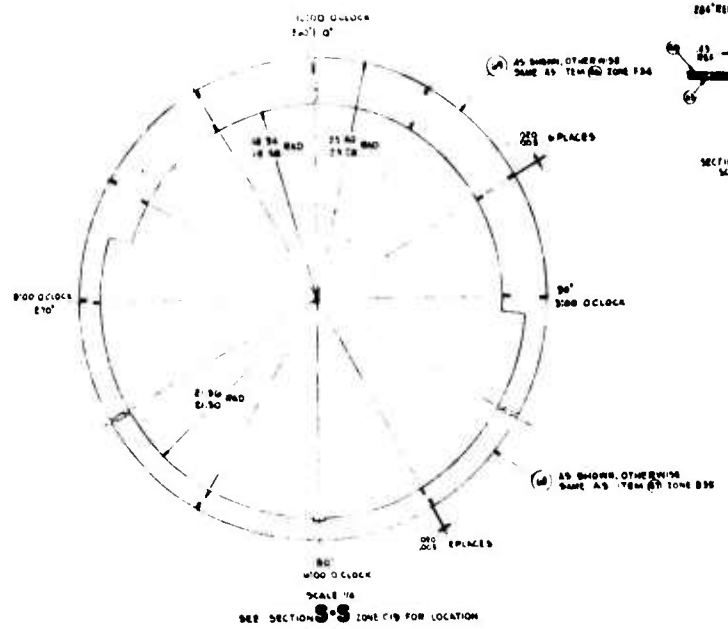
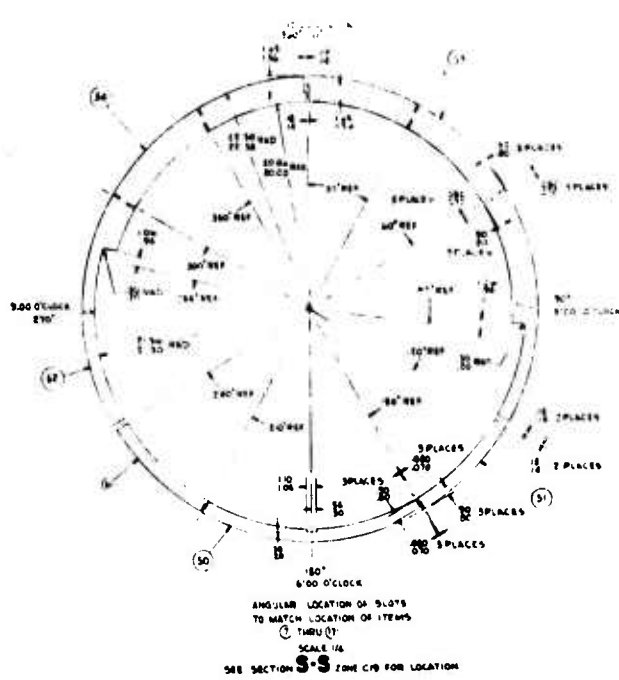


Figure 5

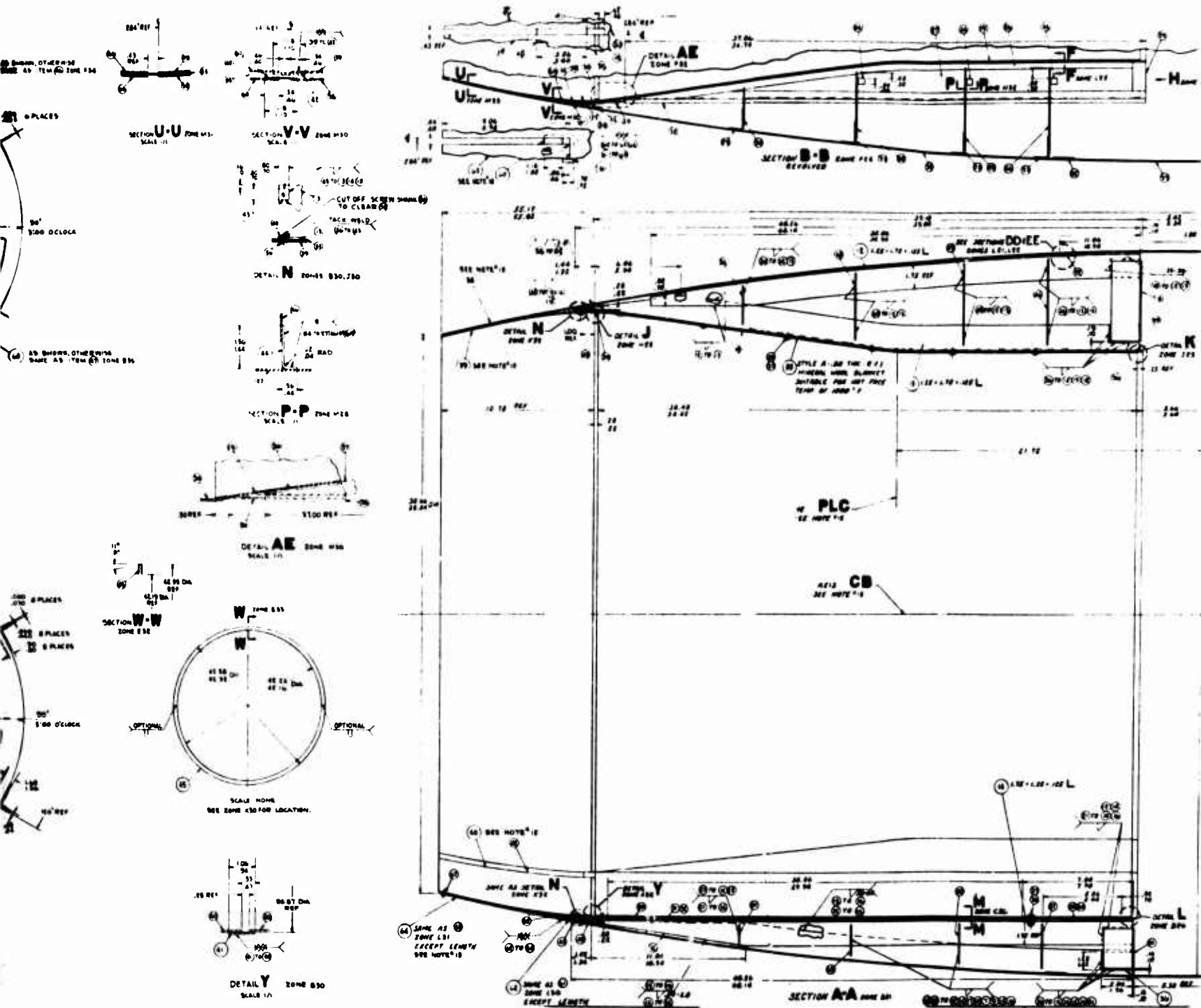
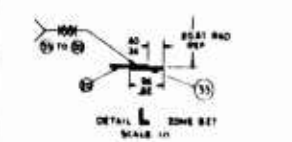
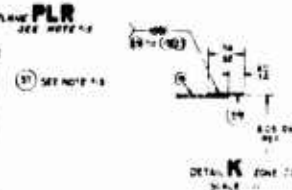
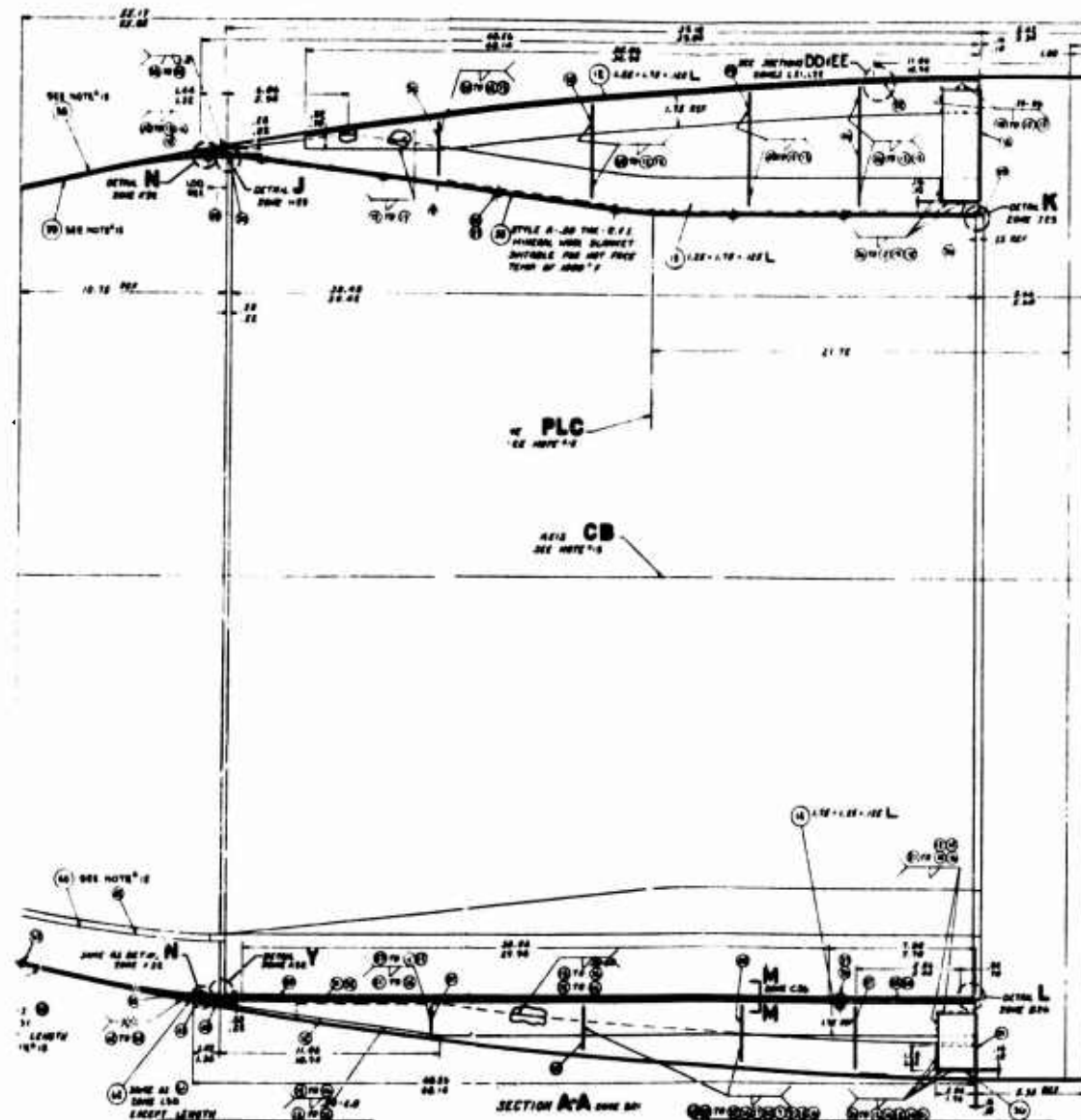
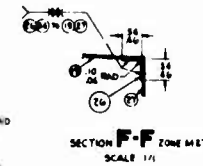
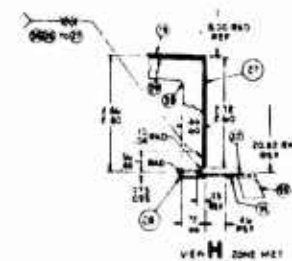
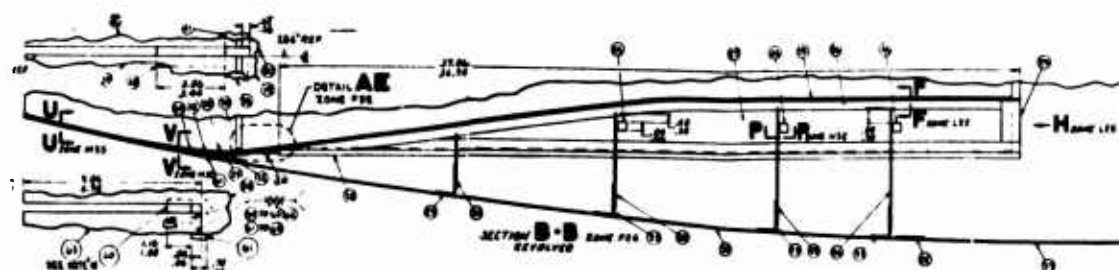


Figure 521. Detail Drawing of Aft Nacelle 1.



① ASSEMBLY

of Aft Nacelle 1.

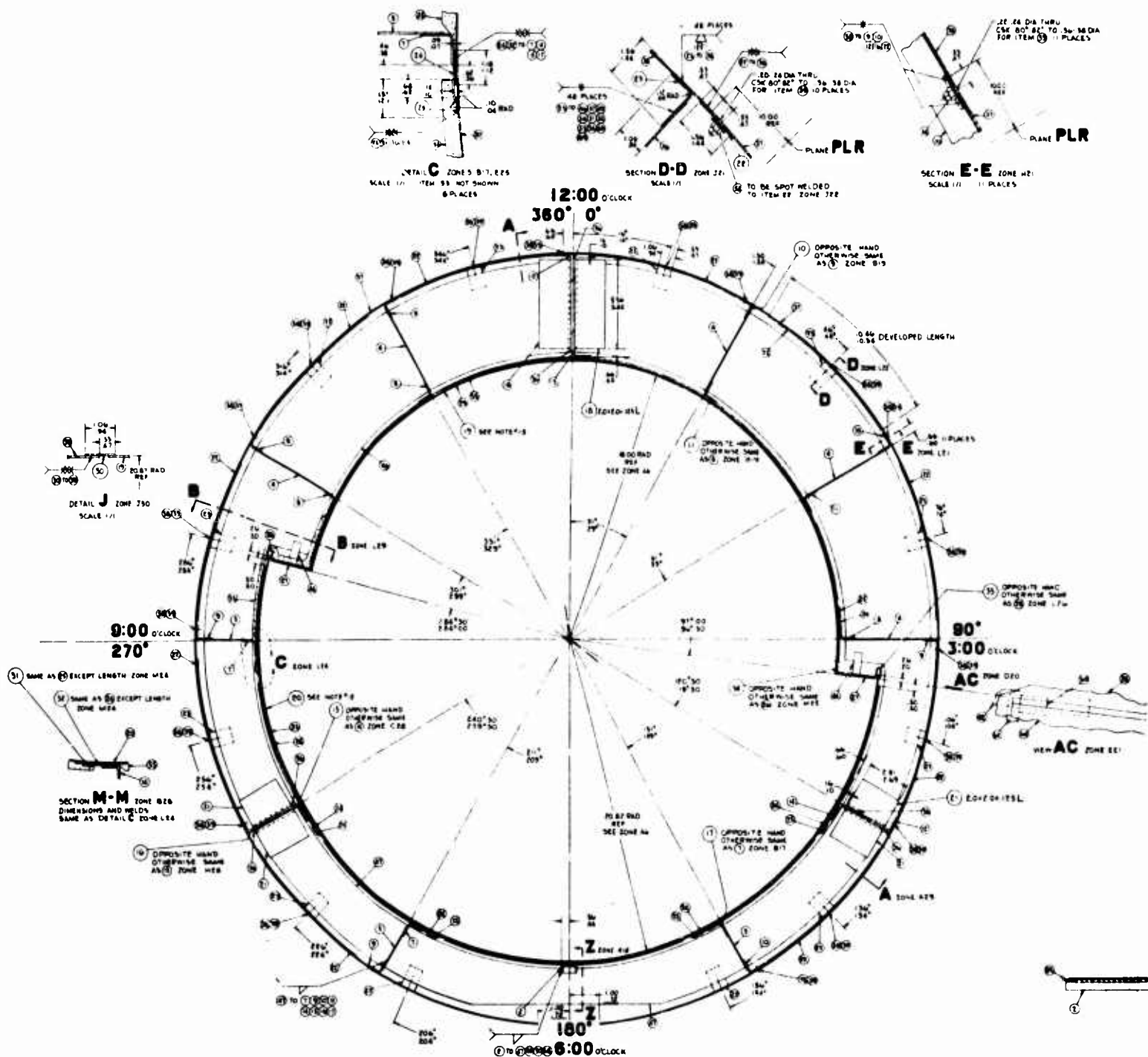


Figure 521. Detail Drawing of Aft Nacelle 1 (Co

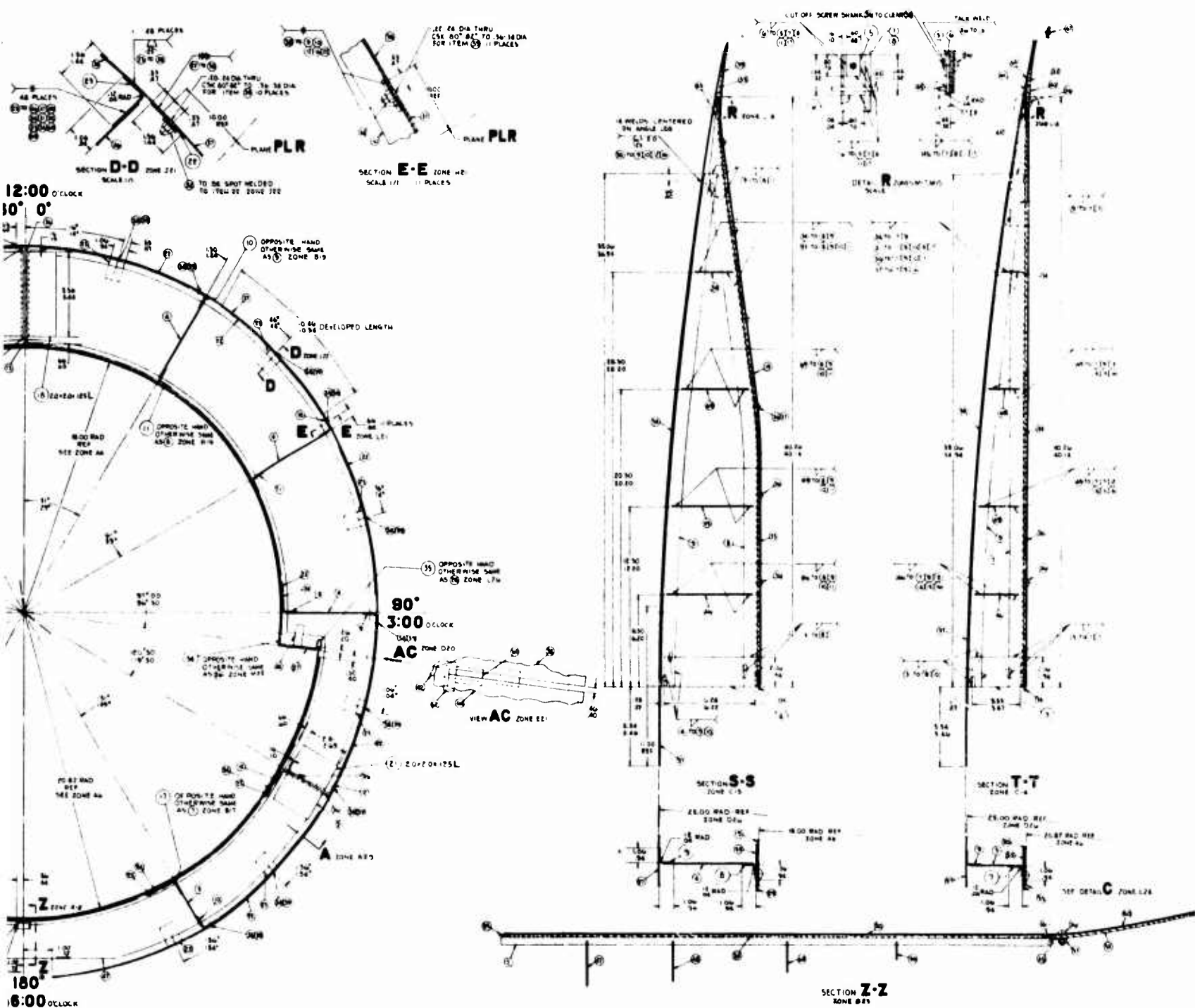
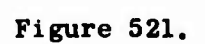


Figure 521. Detail Drawing of Aft Nacelle 1 (Continued).



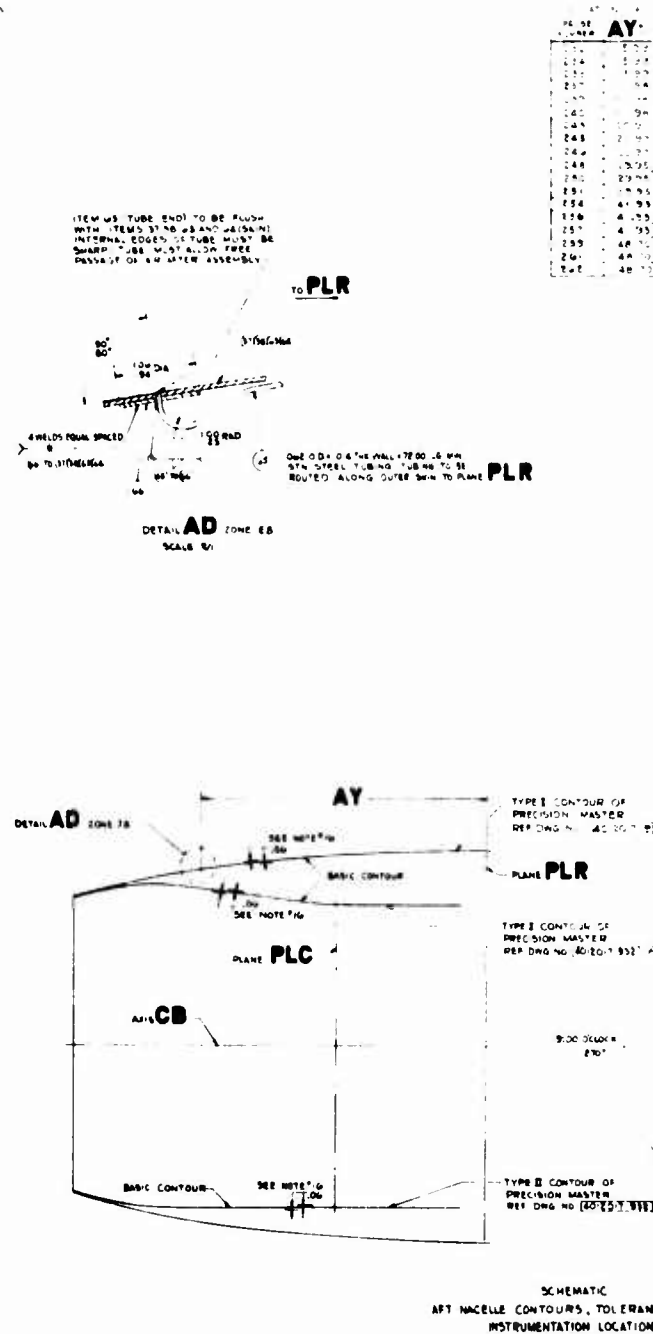
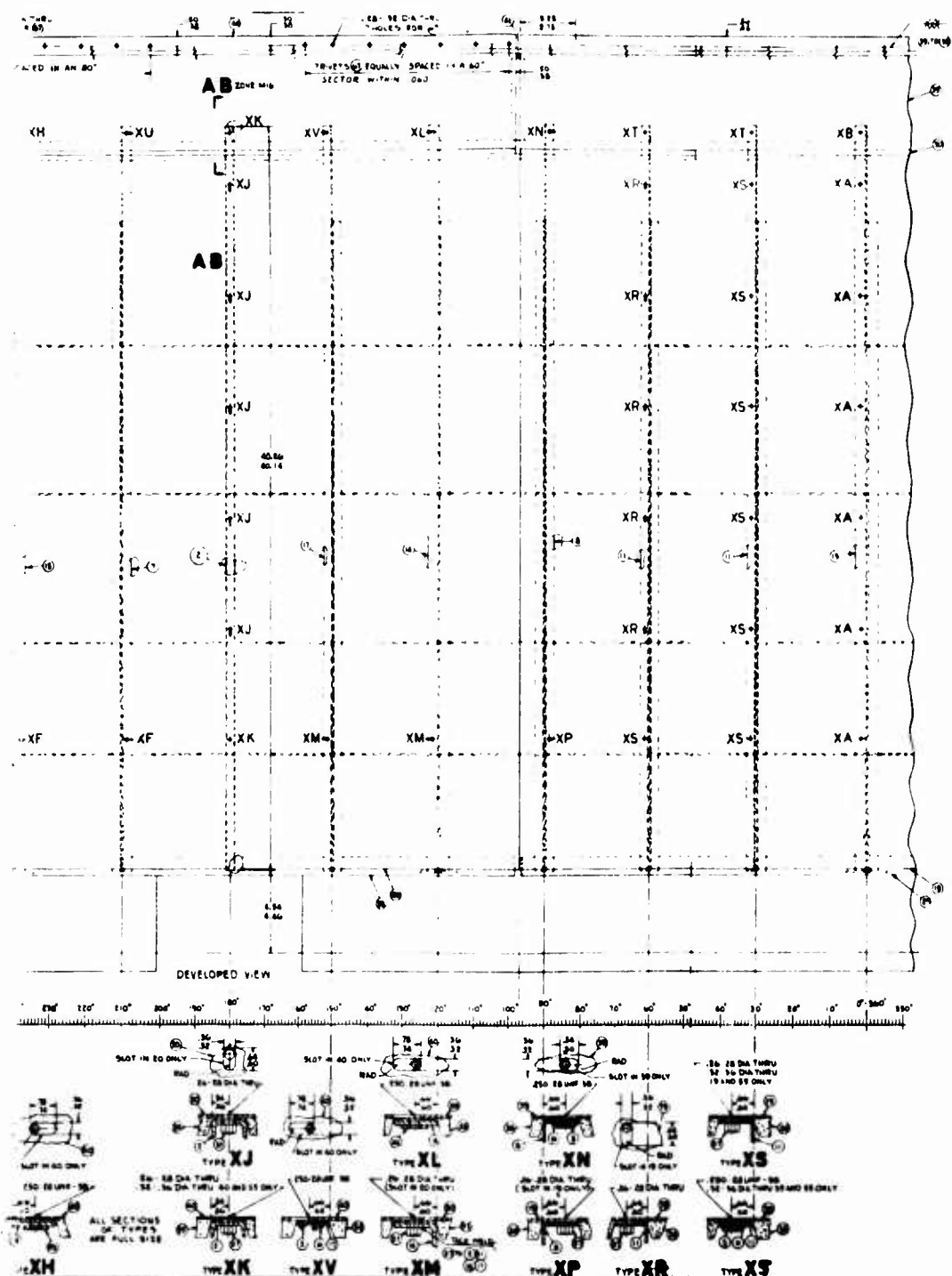
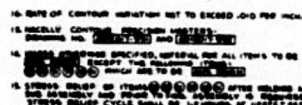
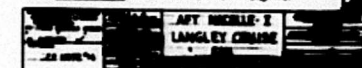


Figure 521. Detail Drawing of Aft Nacelle 1 (Continued).

[illegible]

- ③ REFRACTORY AND INSULATION CORP., CINCINNATI, OHIO OR EQUIV.
- ④ SP4, JERKINTOWN, PENNSYLVANIA OR EQUIV.
- ⑤ TONG, UNION, NEW JERSEY OR EQUIV.
- ⑥ BOOTS AIRCRAFT HUT CORP., NORWALK, CONNECTICUT OR EQUIV.

- [illegible]



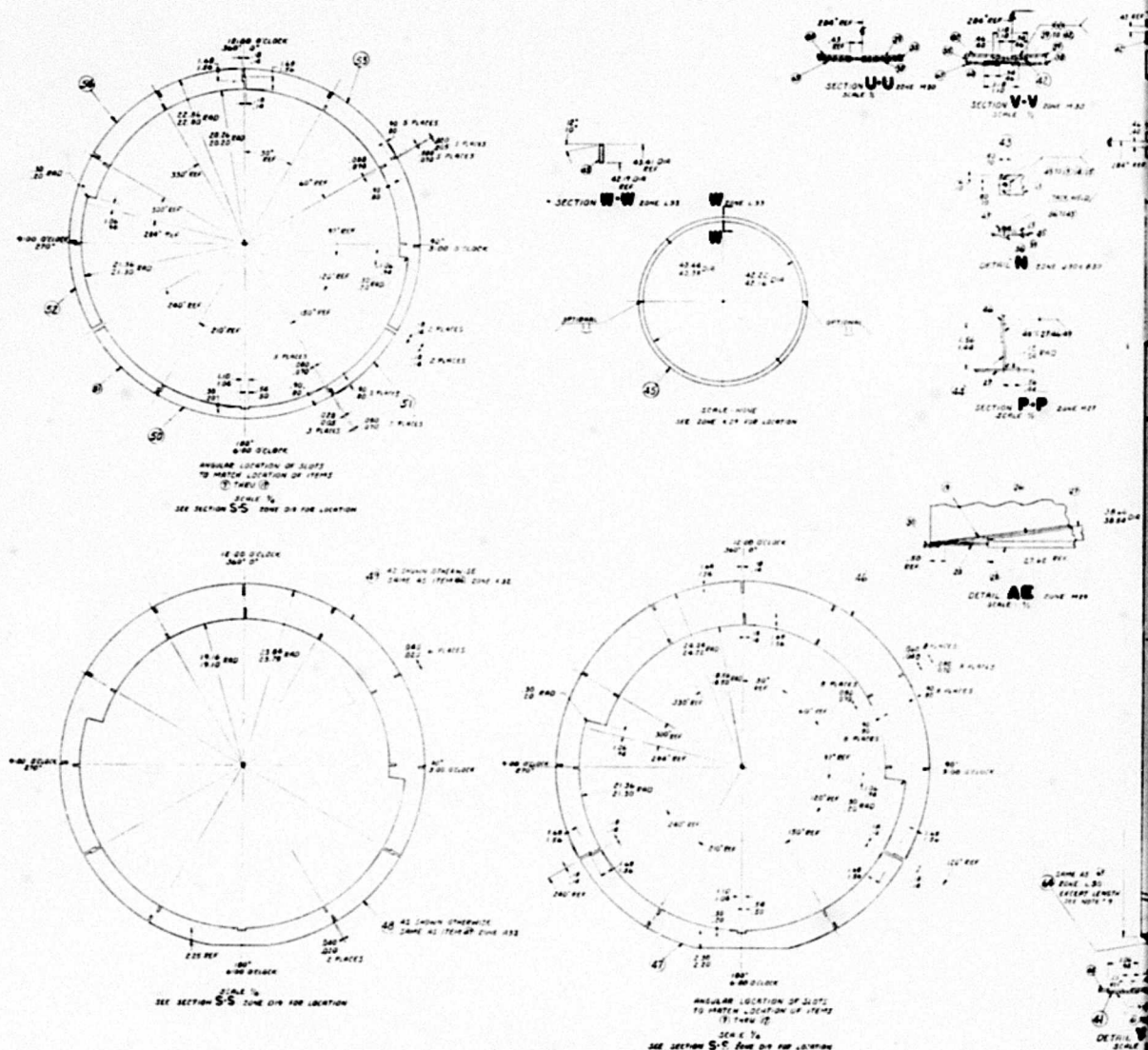
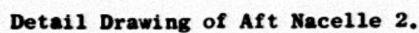


Figure 522. Detail Drawing of



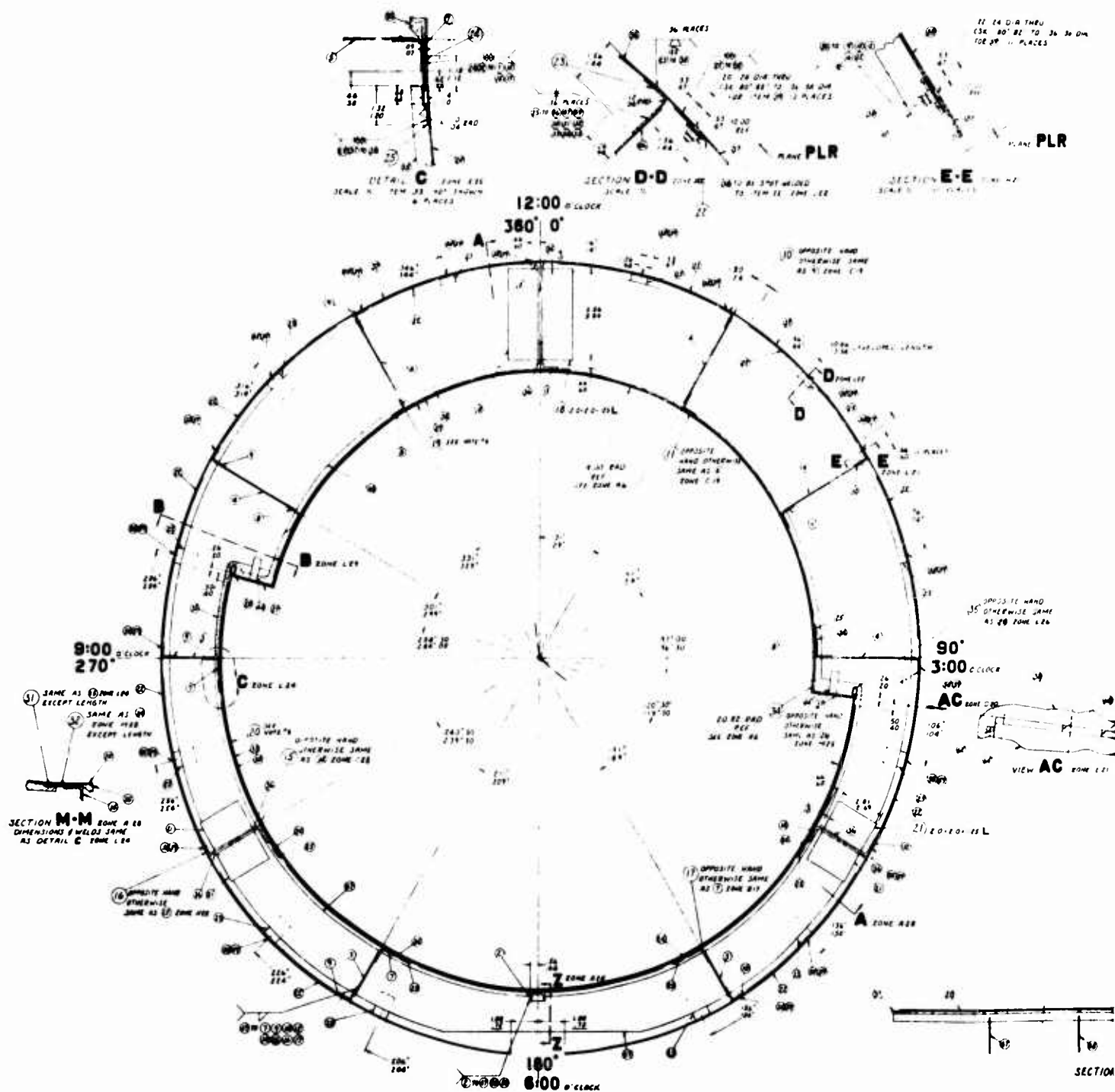
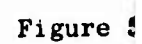
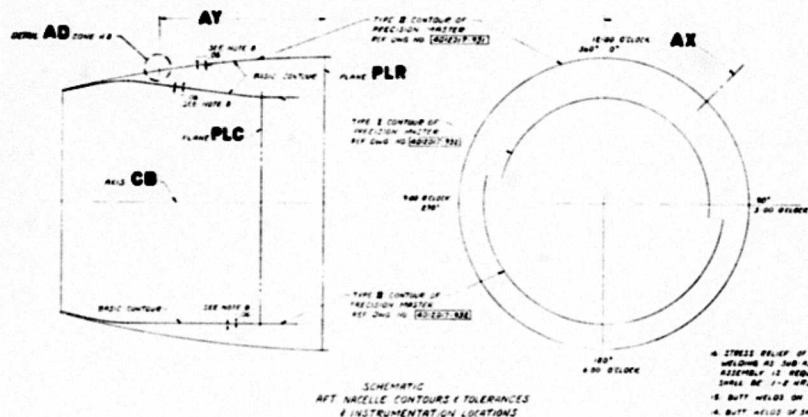


Figure 522. Detail Drawing of Aft Nacelle 2 (C)



[illegible][illegible]

- A. IAS, JENNIFER L. HENNINGSON, DE EDU
- B. IAS, JENNIFER L. HENNINGSON, DE EDU
- C. IAS, JENNIFER L. HENNINGSON, DE EDU
- D. IAS, JENNIFER L. HENNINGSON, DE EDU

1. PRO FILLER METAL 60-40 FOR AMS 5022
2. PRO FILLER METAL AMS 5022 FOR AMS 5022
3. WAREHOUSE STOCK: 1000-1000 INVENTORY AND NO
60-40 60-40
4. RATE OF CONSUMPTION: VARIATION NOT TO EXCEED 10% AND PRO INCH
5. SPOT WELDS ARE OPTIONAL FOR ALL FILLER METALS
6. PRO FILLER METAL AMS 5022 FOR AMS 5022
7. PRO FILLER METAL AMS 5022 FOR AMS 5022
8. WELDING PROCESS: PRO OF PRO
9. ALL WELDING MUST CONFORM TO REQUIREMENTS OF AMS
10. ELECTRICITY: 1000-1000 INVENTORY AND NO GROUP NO
11. SEE MS 22-10 AND INTERPRETATION OF DATA

ALL INFORMATION CONTAINED HEREIN IS UNCLASSIFIED DATE 11-19-01 BY 60322 UCBAW	APT MACELLE-2 LANDLEY CRUISE PAN	44-38861-1000 44-38861-1000
-------------------------------------------------------------------------------	----------------------------------------	--------------------------------

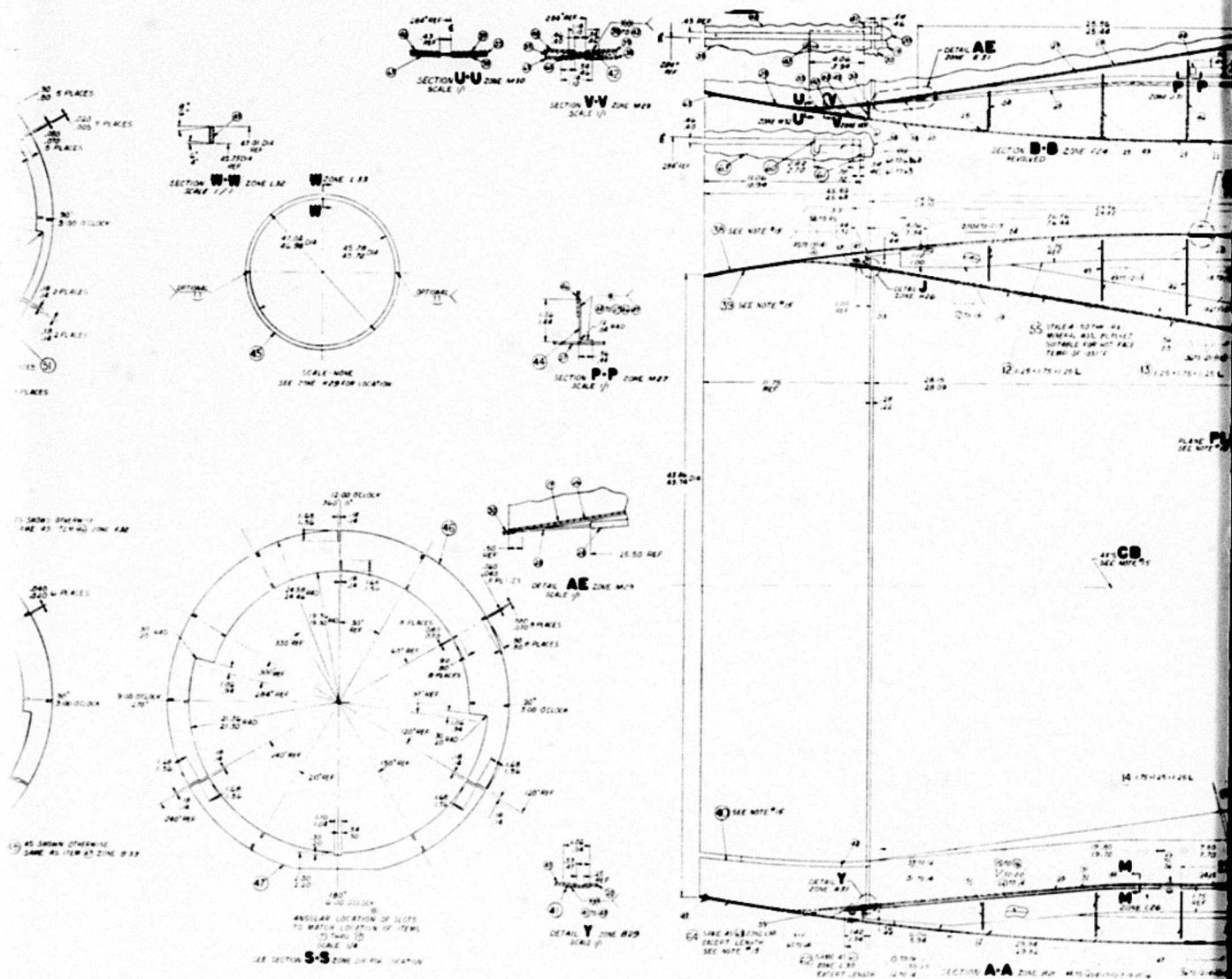


Figure 523. Detail Drawing of Aft Nacelle 4.

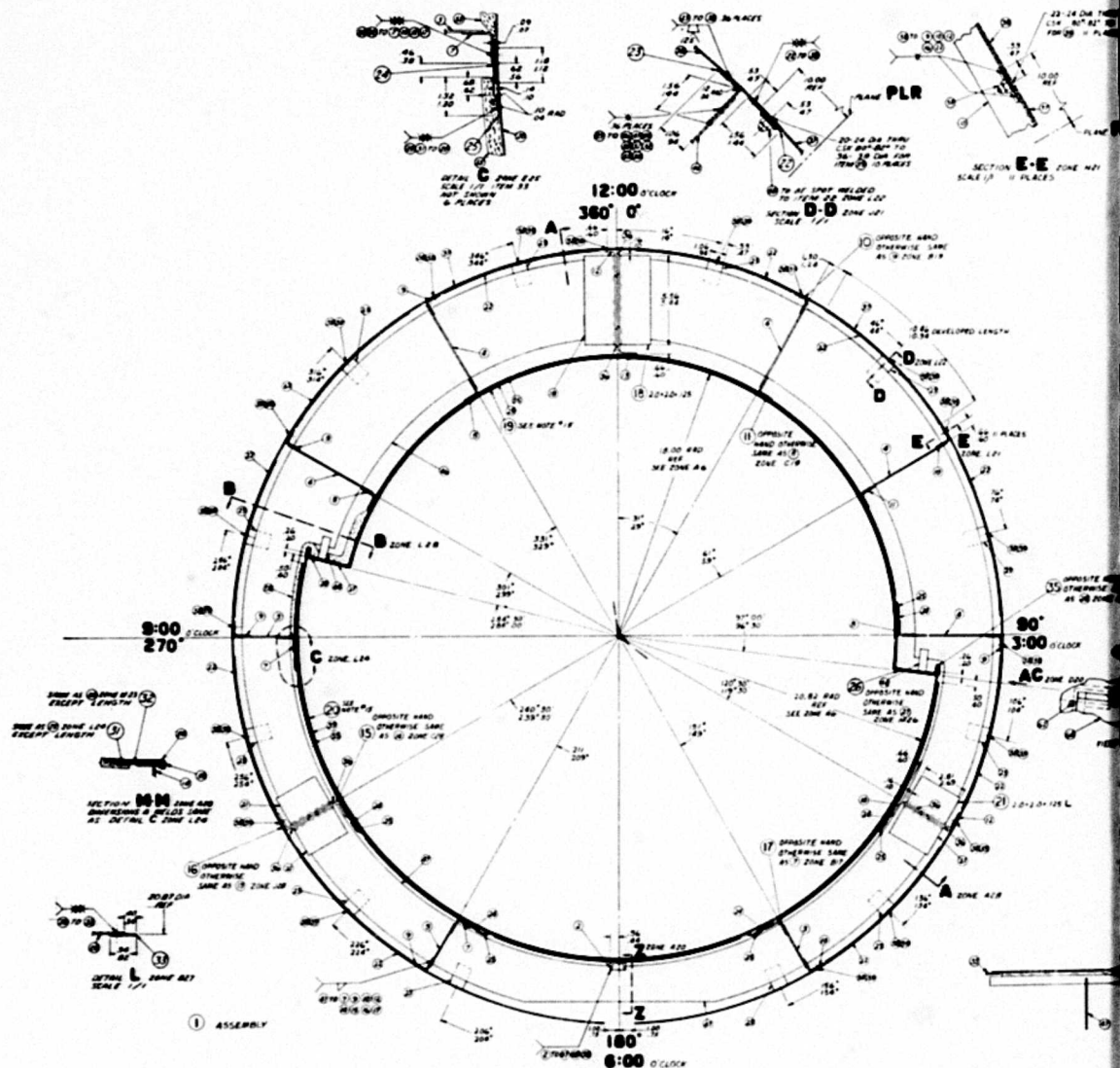
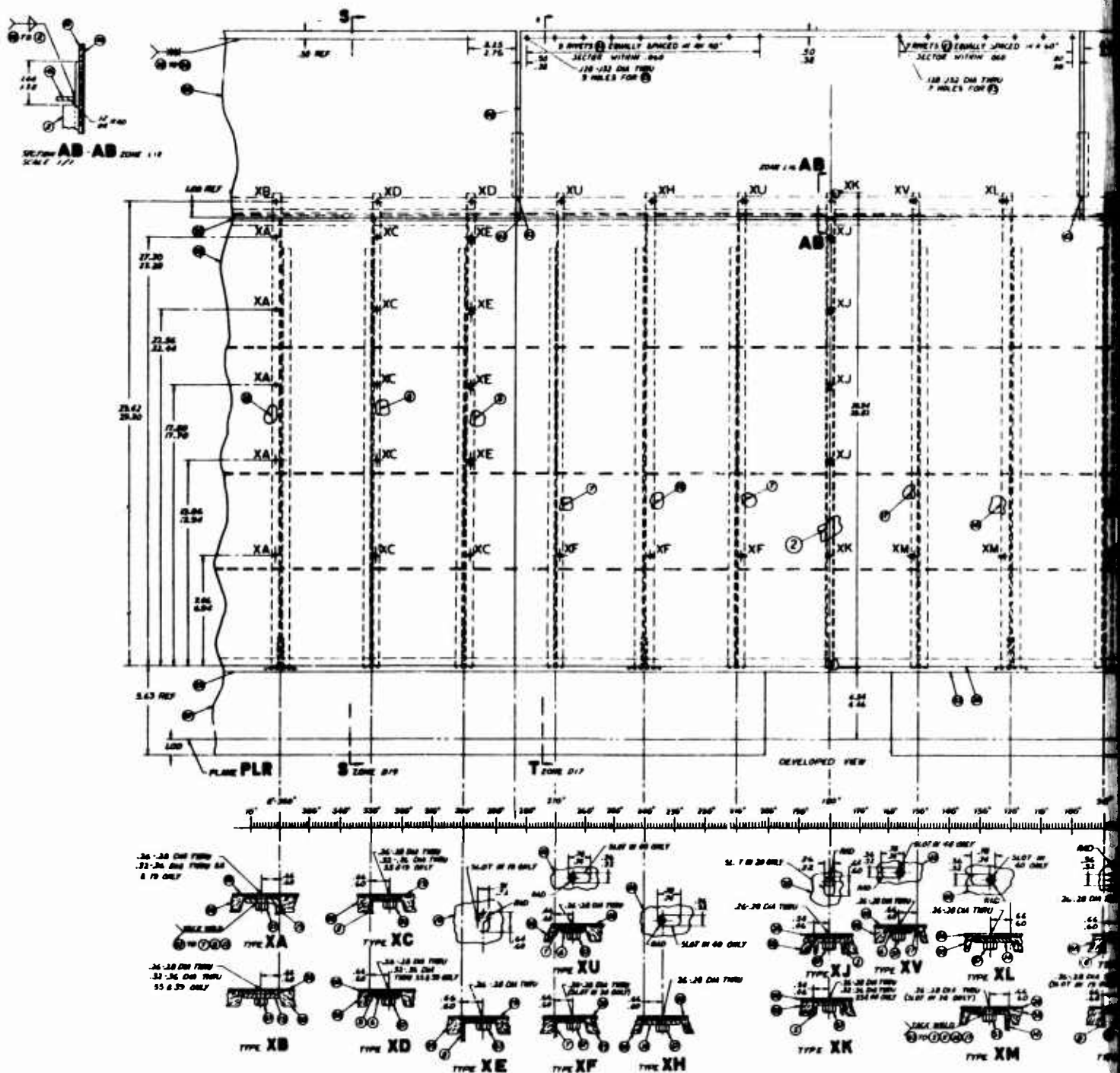
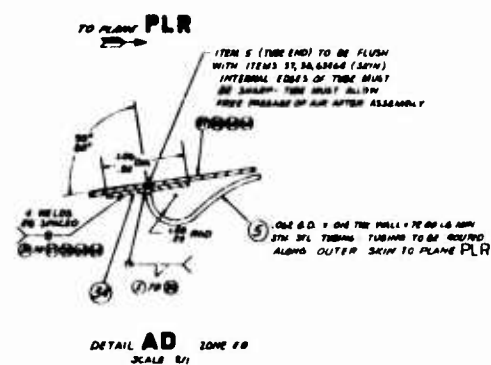
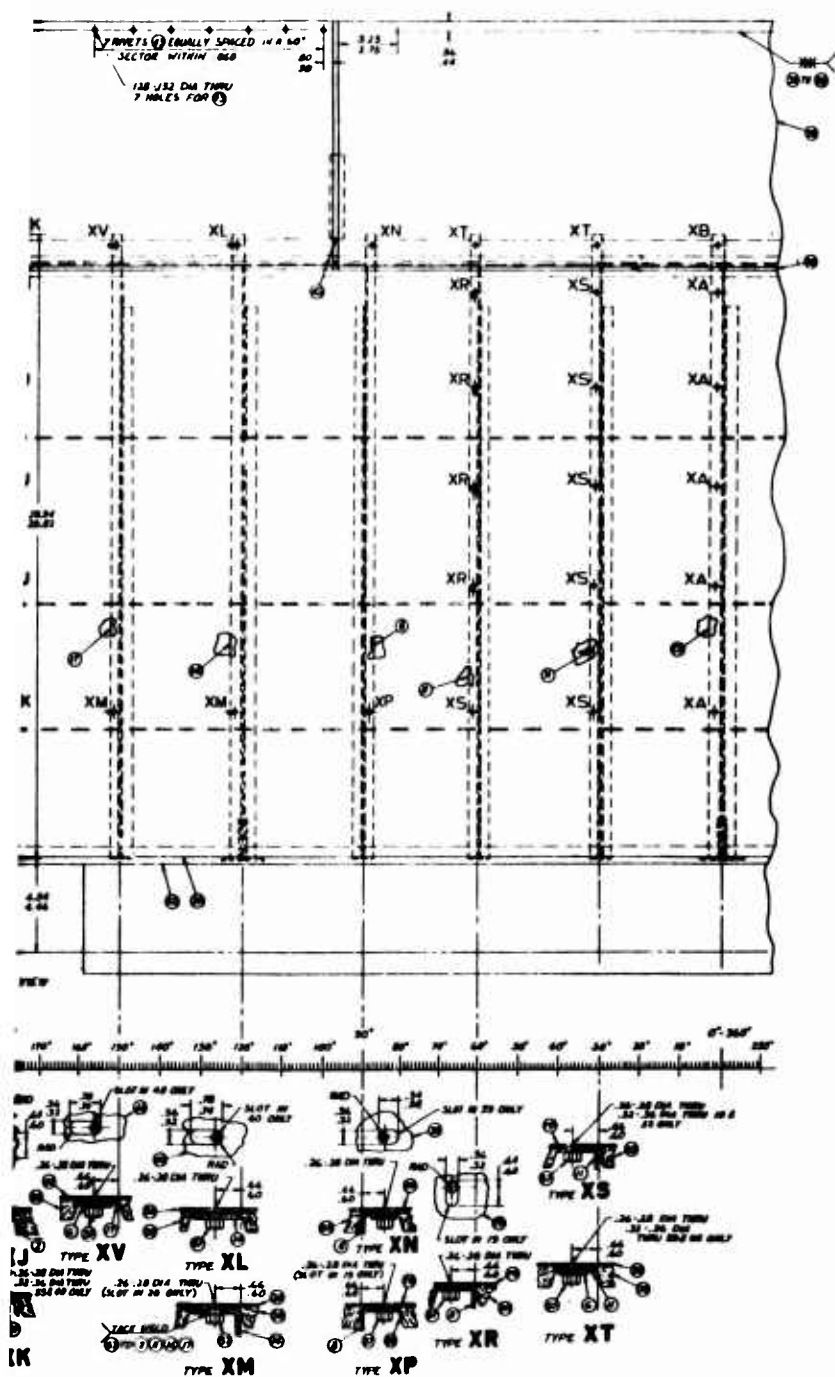


Figure 523. Detail Drawing





LOCATIONS OF ITEMS 26 & 27

ITEM	AY 1/8"	AX 1/8"
222	0.22	17.22
223	0.22	17.22
224	0.22	17.22
225	0.22	17.22
226	0.22	17.22
227	0.22	17.22
228	0.22	17.22
229	0.22	17.22
230	0.22	17.22
231	0.22	17.22
232	0.22	17.22
233	0.22	17.22
234	0.22	17.22
235	0.22	17.22
236	0.22	17.22
237	0.22	17.22
238	0.22	17.22
239	0.22	17.22
240	0.22	17.22
241	0.22	17.22
242	0.22	17.22
243	0.22	17.22
244	0.22	17.22
245	0.22	17.22
246	0.22	17.22
247	0.22	17.22
248	0.22	17.22
249	0.22	17.22
250	0.22	17.22
251	0.22	17.22
252	0.22	17.22
253	0.22	17.22
254	0.22	17.22
255	0.22	17.22
256	0.22	17.22
257	0.22	17.22
258	0.22	17.22
259	0.22	17.22
260	0.22	17.22
261	0.22	17.22
262	0.22	17.22
263	0.22	17.22
264	0.22	17.22
265	0.22	17.22
266	0.22	17.22
267	0.22	17.22
268	0.22	17.22
269	0.22	17.22
270	0.22	17.22
271	0.22	17.22
272	0.22	17.22
273	0.22	17.22
274	0.22	17.22
275	0.22	17.22
276	0.22	17.22
277	0.22	17.22
278	0.22	17.22
279	0.22	17.22
280	0.22	17.22
281	0.22	17.22
282	0.22	17.22
283	0.22	17.22
284	0.22	17.22
285	0.22	17.22
286	0.22	17.22
287	0.22	17.22
288	0.22	17.22
289	0.22	17.22
290	0.22	17.22
291	0.22	17.22
292	0.22	17.22
293	0.22	17.22
294	0.22	17.22
295	0.22	17.22
296	0.22	17.22
297	0.22	17.22
298	0.22	17.22
299	0.22	17.22
300	0.22	17.22

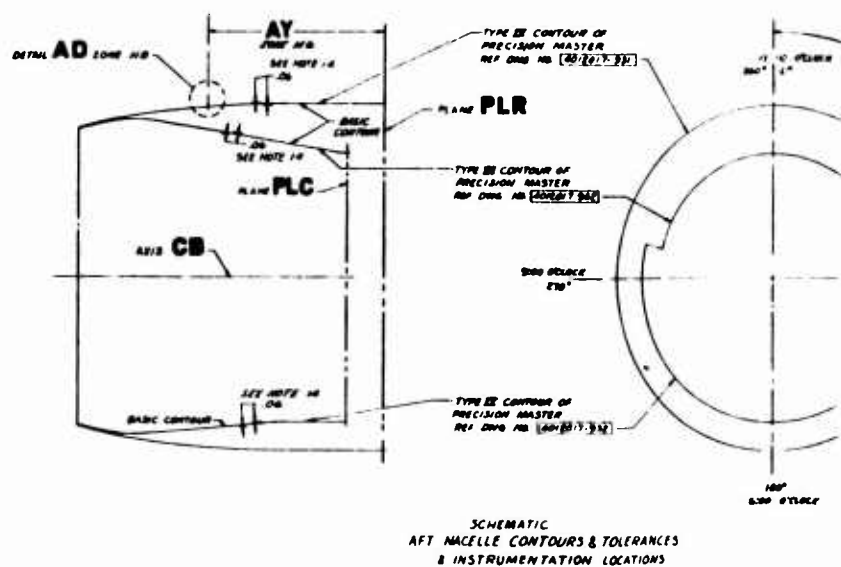
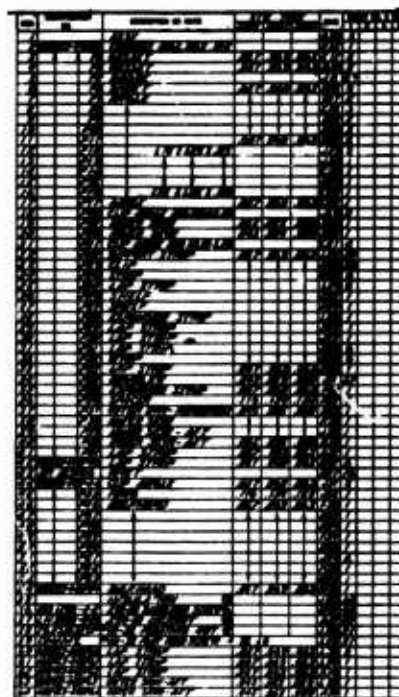


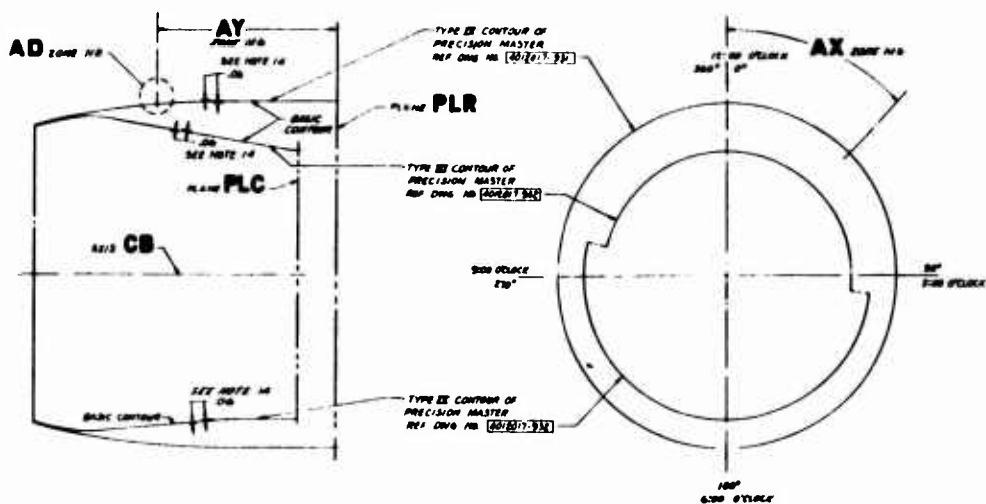
Figure 523. Detail Drawing of Aft Nacelle 4 (Continued).



DATE	AX	AX	AX
101	1.00	1.00	1.00
102	1.00	1.00	1.00
103	1.00	1.00	1.00
104	1.00	1.00	1.00
105	1.00	1.00	1.00
106	1.00	1.00	1.00
107	1.00	1.00	1.00
108	1.00	1.00	1.00
109	1.00	1.00	1.00
110	1.00	1.00	1.00
111	1.00	1.00	1.00
112	1.00	1.00	1.00
113	1.00	1.00	1.00
114	1.00	1.00	1.00
115	1.00	1.00	1.00
116	1.00	1.00	1.00
117	1.00	1.00	1.00
118	1.00	1.00	1.00
119	1.00	1.00	1.00
120	1.00	1.00	1.00
121	1.00	1.00	1.00
122	1.00	1.00	1.00
123	1.00	1.00	1.00
124	1.00	1.00	1.00
125	1.00	1.00	1.00
126	1.00	1.00	1.00
127	1.00	1.00	1.00
128	1.00	1.00	1.00
129	1.00	1.00	1.00
130	1.00	1.00	1.00
131	1.00	1.00	1.00
132	1.00	1.00	1.00
133	1.00	1.00	1.00
134	1.00	1.00	1.00
135	1.00	1.00	1.00
136	1.00	1.00	1.00
137	1.00	1.00	1.00
138	1.00	1.00	1.00
139	1.00	1.00	1.00
140	1.00	1.00	1.00
141	1.00	1.00	1.00
142	1.00	1.00	1.00
143	1.00	1.00	1.00
144	1.00	1.00	1.00
145	1.00	1.00	1.00
146	1.00	1.00	1.00
147	1.00	1.00	1.00
148	1.00	1.00	1.00
149	1.00	1.00	1.00
150	1.00	1.00	1.00
151	1.00	1.00	1.00
152	1.00	1.00	1.00
153	1.00	1.00	1.00
154	1.00	1.00	1.00
155	1.00	1.00	1.00
156	1.00	1.00	1.00
157	1.00	1.00	1.00
158	1.00	1.00	1.00
159	1.00	1.00	1.00
160	1.00	1.00	1.00
161	1.00	1.00	1.00
162	1.00	1.00	1.00
163	1.00	1.00	1.00
164	1.00	1.00	1.00
165	1.00	1.00	1.00
166	1.00	1.00	1.00
167	1.00	1.00	1.00
168	1.00	1.00	1.00
169	1.00	1.00	1.00
170	1.00	1.00	1.00
171	1.00	1.00	1.00
172	1.00	1.00	1.00
173	1.00	1.00	1.00
174	1.00	1.00	1.00
175	1.00	1.00	1.00
176	1.00	1.00	1.00
177	1.00	1.00	1.00
178	1.00	1.00	1.00
179	1.00	1.00	1.00
180	1.00	1.00	1.00
181	1.00	1.00	1.00
182	1.00	1.00	1.00
183	1.00	1.00	1.00
184	1.00	1.00	1.00
185	1.00	1.00	1.00
186	1.00	1.00	1.00
187	1.00	1.00	1.00
188	1.00	1.00	1.00
189	1.00	1.00	1.00
190	1.00	1.00	1.00
191	1.00	1.00	1.00
192	1.00	1.00	1.00
193	1.00	1.00	1.00
194	1.00	1.00	1.00
195	1.00	1.00	1.00
196	1.00	1.00	1.00
197	1.00	1.00	1.00
198	1.00	1.00	1.00
199	1.00	1.00	1.00
200	1.00	1.00	1.00



A IPS, JERKINTOWN, PENNSYLVANIA OR PENN
 B EARN, UNION, NEW JERSEY OR PENN
 C BOOTS AIRCRAFT ANY COLOR, HARTFORD, CONN OR PENN
 D REFRACTORY & MODULATION COIN, CINCINNATI, OHIO OR PENN



SCHEMATIC
AFT NACELLE CONTOURS & TOLERANCES
& INSTRUMENTATION LOCATIONS

- [illegible]





1.60	20.20	22.00	33.80	6.84	5.00
1.60	23.90	41.00	42.50	4.58	7.12

PLAN 11

START OF ANGLE

18°30' REF

25° INCL ANG REF

K DIA

J

M

SEE NOTE #3

BASIC CONTOUR

P

SEE NOTE 'S

44-38861-1000

12.90

85° 1426 AMS
R.F.

SCHEMATIC
PLUG CONTOUR TOLERANCES
INSTRUMENTATION LOCATIONS

PLANE PLC

-TYPE IV CONTOUR OF PRECISION
MASTER REF. DWG No 404-017-935

- A03-A23 DIA THRU ALL
3 ITEMS 4 ROWS OF
4 HOLES TOTAL OF 16 HOLES
SPACED AS SHOWN WITHIN
06 OF TRUE POSITION.

PLR

4 SLOTS TO 20
WITHIN 0.00 CI
TRUE POSITION

S *See* **Section C**

DETAIL **P** ZONE NO
NO SCALE

248-1

220 240 DIA THRU
4 VENTS EQ SPACED
25 SPACIN WITHIN
64 OF TRUE POSITION

WE I CONTOUR OF PRECISION
MASTER REF DWG NO 42027-939

BOUTOUR OF PRECISION
 MASTER REF CDS NO 4012017-033

PRECISION
F OWS M. 1012017.999

SECTION T-T ZONE 63
P.W. SIDE

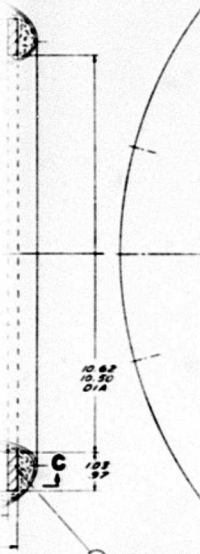
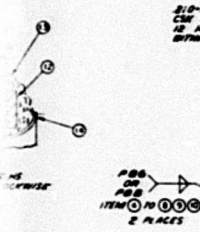
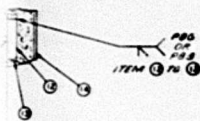
NOZZLE NUMBER	TYPE	SIZE	ANGLE	DISTANCE FROM NOZZLE	DISTANCE FROM NOZZLE	DISTANCE FROM NOZZLE	DISTANCE FROM NOZZLE
268	X	1/2	0	40	40	40	40
269	X	1/2	180	40	40	40	40
270	X	1/2	0	40	40	40	40
271	X	1/2	180	40	40	40	40
272	X	1/2	0	40	40	40	40
273	X	1/2	180	40	40	40	40
274	X	1/2	0	40	40	40	40
275	X	1/2	180	40	40	40	40
276	X	1/2	0	40	40	40	40
277	X	1/2	180	40	40	40	40
278	X	1/2	0	40	40	40	40
279	X	1/2	180	40	40	40	40
280	X	1/2	0	40	40	40	40
281	X	1/2	180	40	40	40	40
282	X	1/2	0	40	40	40	40
283	X	1/2	180	40	40	40	40
284	X	1/2	0	40	40	40	40
285	X	1/2	180	40	40	40	40
286	X	1/2	0	40	40	40	40
287	X	1/2	180	40	40	40	40
288	X	1/2	0	40	40	40	40
289	X	1/2	180	40	40	40	40
290	X	1/2	0	40	40	40	40
291	X	1/2	180	40	40	40	40
292	X	1/2	0	40	40	40	40
293	X	1/2	180	40	40	40	40
294	X	1/2	0	40	40	40	40
295	X	1/2	180	40	40	40	40
296	X	1/2	0	40	40	40	40
297	X	1/2	180	40	40	40	40
298	X	1/2	0	40	40	40	40
299	X	1/2	180	40	40	40	40
300	X	1/2	0	40	40	40	40
301	X	1/2	180	40	40	40	40
302	X	1/2	0	40	40	40	40
303	X	1/2	180	40	40	40	40
304	X	1/2	0	40	40	40	40
305	X	1/2	180	40	40	40	40
306	X	1/2	0	40	40	40	40

NOZZLE NUMBER	TYPE	SIZE	ANGLE	DISTANCE FROM NOZZLE	DISTANCE FROM NOZZLE	DISTANCE FROM NOZZLE	DISTANCE FROM NOZZLE
307	X	1/2	0	40	40	40	40
308	X	1/2	180	40	40	40	40
309	X	1/2	0	40	40	40	40
310	X	1/2	180	40	40	40	40
311	X	1/2	0	40	40	40	40
312	X	1/2	180	40	40	40	40
313	X	1/2	0	40	40	40	40
314	X	1/2	180	40	40	40	40
315	X	1/2	0	40	40	40	40
316	X	1/2	180	40	40	40	40
317	X	1/2	0	40	40	40	40
318	X	1/2	180	40	40	40	40
319	X	1/2	0	40	40	40	40
320	X	1/2	180	40	40	40	40
321	X	1/2	0	40	40	40	40
322	X	1/2	180	40	40	40	40
323	X	1/2	0	40	40	40	40
324	X	1/2	180	40	40	40	40
325	X	1/2	0	40	40	40	40
326	X	1/2	180	40	40	40	40
327	X	1/2	0	40	40	40	40
328	X	1/2	180	40	40	40	40
329	X	1/2	0	40	40	40	40
330	X	1/2	180	40	40	40	40
331	X	1/2	0	40	40	40	40
332	X	1/2	180	40	40	40	40
333	X	1/2	0	40	40	40	40
334	X	1/2	180	40	40	40	40
335	X	1/2	0	40	40	40	40
336	X	1/2	180	40	40	40	40
337	X	1/2	0	40	40	40	40
338	X	1/2	180	40	40	40	40
339	X	1/2	0	40	40	40	40
340	X	1/2	180	40	40	40	40
341	X	1/2	0	40	40	40	40
342	X	1/2	180	40	40	40	40
343	X	1/2	0	40	40	40	40
344	X	1/2	180	40	40	40	40
345	X	1/2	0	40	40	40	40
346	X	1/2	180	40	40	40	40
347	X	1/2	0	40	40	40	40
348	X	1/2	180	40	40	40	40
349	X	1/2	0	40	40	40	40
350	X	1/2	180	40	40	40	40

ESNA UNION, NEW JERSEY. OR EQUIV.

5. FOAM
APOTANE FOAM 8764 B7 & 8750AF
ARCHER DANIELS MIDLAND CO.
4. HARDWOOD
3. ALUMINUM - 6061-T6
2. STEEL - AISI 1020
1. FIBERGLAS
RESIN - GLIDPOL 1027 - GLIDDEN CO.
CATALYST - 6% COBALT NAPHTHANATE - CADILLAC PLASTICS
METHYL ETHYL KETONE PEROXIDE -
STYRENE MONOMER
FIBERGLAS CLOTH - 10 OZ. BOWT CLOTH THIS 16" X 16" -
MATERIAL:

6. PLUG CONTOUR PRECISION MASTER DWG. NO. FOR
TYPES 1, 2, 3, 4, 5, 6, 7, 8, 9, 10, 11, 12, 13, 14, 15, 16, 17, 18, 19, 20, 21, 22, 23, 24, 25, 26, 27, 28, 29, 30, 31, 32, 33, 34, 35, 36, 37, 38, 39, 40, 41, 42, 43, 44, 45, 46, 47, 48, 49, 50, 51, 52, 53, 54, 55, 56, 57, 58, 59, 60, 61, 62, 63, 64, 65, 66, 67, 68, 69, 70, 71, 72, 73, 74, 75, 76, 77, 78, 79, 80, 81, 82, 83, 84, 85, 86, 87, 88, 89, 90, 91, 92, 93, 94, 95, 96, 97, 98, 99, 100, 101, 102, 103, 104, 105, 106, 107, 108, 109, 110, 111, 112, 113, 114, 115, 116, 117, 118, 119, 120, 121, 122, 123, 124, 125, 126, 127, 128, 129, 130, 131, 132, 133, 134, 135, 136, 137, 138, 139, 140, 141, 142, 143, 144, 145, 146, 147, 148, 149, 150, 151, 152, 153, 154, 155, 156, 157, 158, 159, 160, 161, 162, 163, 164, 165, 166, 167, 168, 169, 170, 171, 172, 173, 174, 175, 176, 177, 178, 179, 180, 181, 182, 183, 184, 185, 186, 187, 188, 189, 190, 191, 192, 193, 194, 195, 196, 197, 198, 199, 200, 201, 202, 203, 204, 205, 206, 207, 208, 209, 210, 211, 212, 213, 214, 215, 216, 217, 218, 219, 220, 221, 222, 223, 224, 225, 226, 227, 228, 229, 230, 231, 232, 233, 234, 235, 236, 237, 238, 239, 240, 241, 242, 243, 244, 245, 246, 247, 248, 249, 250, 251, 252, 253, 254, 255, 256, 257, 258, 259, 260, 261, 262, 263, 264, 265, 266, 267, 268, 269, 270, 271, 272, 273, 274, 275, 276, 277, 278, 279, 280, 281, 282, 283, 284, 285, 286, 287, 288, 289, 290, 291, 292, 293, 294, 295, 296, 297, 298, 299, 300, 301, 302, 303, 304, 305, 306, 307, 308, 309, 310, 311, 312, 313, 314, 315, 316, 317, 318, 319, 320, 321, 322, 323, 324, 325, 326, 327, 328, 329, 330, 331, 332, 333, 334, 335, 336, 337, 338, 339, 340, 341, 342, 343, 344, 345, 346, 347, 348, 349, 350, 351, 352, 353, 354, 355, 356, 357, 358, 359, 360, 361, 362, 363, 364, 365, 366, 367, 368, 369, 370, 371, 372, 373, 374, 375, 376, 377, 378, 379, 380, 381, 382, 383, 384, 385, 386, 387, 388, 389, 390, 391, 392, 393, 394, 395, 396, 397, 398, 399, 400, 401, 402, 403, 404, 405, 406, 407, 408, 409, 410, 411, 412, 413, 414, 415, 416, 417, 418, 419, 420, 421, 422, 423, 424, 425, 426, 427, 428, 429, 430, 431, 432, 433, 434, 435, 436, 437, 438, 439, 440, 441, 442, 443, 444, 445, 446, 447, 448, 449, 450, 451, 452, 453, 454, 455, 456, 457, 458, 459, 460, 461, 462, 463, 464, 465, 466, 467, 468, 469, 470, 471, 472, 473, 474, 475, 476, 477, 478, 479, 480, 481, 482, 483, 484, 485, 486, 487, 488, 489, 490, 491, 492, 493, 494, 495, 496, 497, 498, 499, 500, 501, 502, 503, 504, 505, 506, 507, 508, 509, 510, 511, 512, 513, 514, 515, 516, 517, 518, 519, 520, 521, 522, 523, 524, 525, 526, 527, 528, 529, 530, 531, 532, 533, 534, 535, 536, 537, 538, 539, 540, 541, 542, 543, 544, 545, 546, 547, 548, 549, 550, 551, 552, 553, 554, 555, 556, 557, 558, 559, 560, 561, 562, 563, 564, 565, 566, 567, 568, 569, 570, 571, 572, 573, 574, 575, 576, 577, 578, 579, 580, 581, 582, 583, 584, 585, 586, 587, 588, 589, 590, 591, 592, 593, 594, 595, 596, 597, 598, 599, 600, 601, 602, 603, 604, 605, 606, 607, 608, 609, 610, 611, 612, 613, 614, 615, 616, 617, 618, 619, 620, 621, 622, 623, 624, 625, 626, 627, 628, 629, 630, 631, 632, 633, 634, 635, 636, 637, 638, 639, 640, 641, 642, 643, 644, 645, 646, 647, 648, 649, 650, 651, 652, 653, 654, 655, 656, 657, 658, 659, 660, 661, 662, 663, 664, 665, 666, 667, 668, 669, 670, 671, 672, 673, 674, 675, 676, 677, 678, 679, 680, 681, 682, 683, 684, 685, 686, 687, 688, 689, 690, 691, 692, 693, 694, 695, 696, 697, 698, 699, 700, 701, 702, 703, 704, 705, 706, 707, 708, 709, 710, 711, 712, 713, 714, 715, 716, 717, 718, 719, 720, 721, 722, 723, 724, 725, 726, 727, 728, 729, 730, 731, 732, 733, 734, 735, 736, 737, 738, 739, 740, 741, 742, 743, 744, 745, 746, 747, 748, 749, 750, 751, 752, 753, 754, 755, 756, 757, 758, 759, 760, 761, 762, 763, 764, 765, 766, 767, 768, 769, 770, 771, 772, 773, 774, 775, 776, 777, 778, 779, 780, 781, 782, 783, 784, 785, 786, 787, 788, 789, 790, 791, 792, 793, 794, 795, 796, 797, 798, 799, 800, 801, 802, 803, 804, 805, 806, 807, 808, 809, 810, 811, 812, 813, 814, 815, 816, 817, 818, 819, 820, 821, 822, 823, 824, 825, 826, 827, 828, 829, 830, 831, 832, 833, 834, 835, 836, 837, 838, 839, 840, 841, 842, 843, 844, 845, 846, 847, 848, 849, 850, 851, 852, 853, 854, 855, 856, 857, 858, 859, 860, 861, 862, 863, 864, 865, 866, 867, 868, 869, 870, 871, 872, 873, 874, 875, 876, 877, 878, 879, 880, 881, 882, 883, 884, 885, 886, 887, 888, 889, 890, 891, 892, 893, 894, 895, 896, 897, 898, 899, 900, 901, 902, 903, 904, 905, 906, 907, 908, 909, 910, 911, 912, 913, 914, 915, 916, 917, 918, 919, 920, 921, 922, 923, 924, 925, 926, 927, 928, 929, 930, 931, 932, 933, 934, 935, 936, 937, 938, 939, 940, 941, 942, 943, 944, 945, 946, 947, 948, 949, 950, 951, 952, 953, 954, 955, 956, 957, 958, 959, 960, 961, 962, 963, 964, 965, 966, 967, 968, 969, 970, 971, 972, 973, 974, 975, 976, 977, 978, 979, 980, 981, 982, 983, 984, 985, 986, 987, 988, 989, 990, 991, 992, 993, 994, 995, 996, 997, 998, 999, 1000, 1001, 1002, 1003, 1004, 1005, 1006, 1007, 1008, 1009, 1010, 1011, 1012, 1013, 1014, 1015, 1016, 1017, 1018, 1019, 1020, 1021, 1022, 1023, 1024, 1025, 1026, 1027, 1028, 1029, 1030, 1031, 1032, 1033, 1034, 1035, 1036, 1037, 1038, 1039, 1040, 1041, 1042, 1043, 1044, 1045, 1046, 1047, 1048, 1049, 1050, 1051, 1052, 1053, 1054, 1055, 1056, 1057, 1058, 1059, 1060, 1061, 1062, 1063, 1064, 1065, 1066, 1067, 1068, 1069, 1070, 1071, 1072, 1073, 1074, 1075, 1076, 1077, 1078, 1079, 1080, 1081, 1082, 1083, 1084, 1085, 1086, 1087, 1088, 1089, 1090, 1091, 1092, 1093, 1094, 1095, 1096, 1097, 1098, 1099, 1100, 1101, 1102, 1103, 1104, 1105, 1106, 1107, 1108, 1109, 1110, 1111, 1112, 1113, 1114, 1115, 1116, 1117, 1118, 1119, 1120, 1121, 1122, 1123, 1124, 1125, 1126, 1127, 1128, 1129, 1130, 1131, 1132, 1133, 1134, 1135, 1136, 1137, 1138, 1139, 1140, 1141, 1142, 1143, 1144, 1145, 1146, 1147, 1148, 1149, 1150, 1151, 1152, 1153, 1154, 1155, 1156, 1157, 1158, 1159, 1160, 1161, 1162, 1163, 1164, 1165, 1166, 1167, 1168, 1169, 1170, 1171, 1172, 1173, 1174, 1175, 1176, 1177, 1178, 1179, 1180, 1181, 1182, 1183, 1184, 1185, 1186, 1187, 1188, 1189, 1190, 1191, 1192, 1193, 1194, 1195, 1196, 1197, 1198, 1199, 1200, 1201, 1202, 1203, 1204, 1205, 1206, 1207, 1208, 1209, 1210, 1211, 1212, 1213, 1214, 1215, 1216, 1217, 1218, 1219, 1220, 1221, 1222, 1223, 1224, 1225, 1226, 1227, 1228, 1229, 1230, 1231, 1232, 1233, 1234, 1235, 1236, 1237, 1238, 1239, 1240, 1241, 1242, 1243, 1244, 1245, 1246, 1247, 1248, 1249, 1250, 1251, 1252, 1253, 1254, 1255, 1256, 1257, 1258, 1259, 1260, 1261, 1262, 1263, 1264, 1265, 1266, 1267, 1268, 1269, 1270, 1271, 1272, 1273, 1274, 1275, 1276, 1277, 1278, 1279, 1280, 1281, 1282, 1283, 1284, 1285, 1286, 1287, 1288, 1289, 1290, 1291, 1292, 1293, 1294, 1295, 1296, 1297, 1298, 1299,



- FOAM 876-B & 876-BF
MIDLAND CO.
- GLIDDEN CO.
MIDLAND CO.
TYPE SETTING PASTE - CADILLAC PLASTICS
MONOMER
BOAT CLOTH THICK 1/8 IN.



3/16-3/32 DIA THRU ITEMS 1 & 2
CIR 80-100 TO 34-48 DIA
12 HOLES IN SP & LOCATED
WITHIN 90° OF TRUE POSITION

ITEM 1 TO 12
12 PLACES IN FINAL ASSEMBLY

PDB
OR
PDB
ITEM 3 TO 12

LOCATE WITHIN 0.6
EITHER SIDE OF
TRUE POSITION
2 PLACES

PDB
OR
PDB
ITEM 3 TO 12

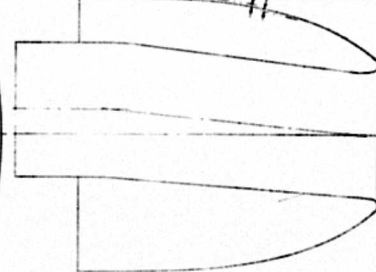
LOCATE WITHIN 0.6
EITHER SIDE OF
TRUE POSITION

ITEM NO.	DESCRIPTION	QTY	UNIT
1	ITEM 1 TO 12	12	PLACES
2	ITEM 1 TO 12	12	PLACES
3	ITEM 1 TO 12	12	PLACES
4	ITEM 1 TO 12	12	PLACES
5	ITEM 1 TO 12	12	PLACES
6	ITEM 1 TO 12	12	PLACES
7	ITEM 1 TO 12	12	PLACES
8	ITEM 1 TO 12	12	PLACES
9	ITEM 1 TO 12	12	PLACES
10	ITEM 1 TO 12	12	PLACES
11	ITEM 1 TO 12	12	PLACES
12	ITEM 1 TO 12	12	PLACES

1/4" ROOTS AIRCRAFT NUT CORR. NORMALLY CORR
OR EQUIV

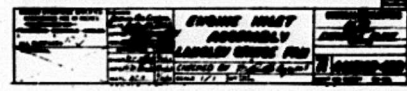
BASIC CONTOUR
SEE NOTE NO. 5

OR
SEE NOTE NO. 6



SCHEMATIC OF
ENGINE INLET CONTOUR & TOLERANCES

6. RATE OF CONTOUR VARIATION NOT TO EXCEED .010 PER INCH
7. INLET CONTOUR PRECISION MASTER DRAWING NO. 001-17-310
8. ALL WELDS SHALL BE DYE PENETRANT INSPECTED
PER 100% TEST. NO CRACKS ALLOWED
9. PDB FILLER MATERIAL 3/16" 304 STAINLESS
PDB FILLER MATERIAL 3/16" 304 STAINLESS
10. ALL WELDS MUST CONFORM TO REQUIREMENTS OF 100% TEST
11. SEE 100% TEST FOR INTERPRETATION OF DRAWING



UNCLASSIFIED

Security Classification

DOCUMENT CONTROL DATA - R&D		
(Security classification of title, body of abstract and indexing annotation must be entered when the overall report is classified)		
1 ORIGINATING ACTIVITY (Corporate author) General Electric Company Flight Propulsion Division Cincinnati, Ohio		2a REPORT SECURITY CLASSIFICATION
		2b GROUP
3 REPORT TITLE High-Speed Wind Tunnel Tests of a High Bypass Lift/Cruise Fan Propulsion System.		
4 DESCRIPTIVE NOTES (Type of report and inclusive dates) Final Report - March 1963 to January 1966		
5 AUTHOR(S) (Last name, first name, initial) Smith, Eugene G.		
6. REPORT DATE July 1966	7a. TOTAL NO. OF PAGES 713	7b. NO. OF REFS Eleven
8a. CONTRACT OR GRANT NO. DA 44-177-AMC-10(T)	9a. ORIGINATOR'S REPORT NUMBER(S) USAAVLABS Technical Report 66-40	
b. PROJECT NO. Task 1D131201D159		
c.	9b. OTHER REPORT NO(S) (Any other numbers that may be assigned this report) General Electric	
d.	Company Report R66FPD161	
10 AVAILABILITY/LIMITATION NOTICES Distribution of this document is unlimited.		
11 SUPPLEMENTARY NOTES	12. SPONSORING MILITARY ACTIVITY U. S. Army Aviation Materiel Laboratories Fort Eustis, Virginia	
13 ABSTRACT High-speed tests of a large scale, close coupled lift/cruise fan system were conducted in the NASA-Langley 16-foot wind tunnel. The X376 fan and a T58 core engine constituted the propulsion system. Test program included test Mach numbers from 0.0 to 0.85 and variable angle of attack. Extensive pressure measurements and balance force data were obtained.		

14. KEY WORDS	LINK A		LINK B		LINK C	
	ROLE	WT	ROLE	WT	ROLE	WT
<div>INSTRUCTIONS</div> <div><div><p>1. ORIGINATING ACTIVITY: Enter the name and address of the contractor, subcontractor, grantee, Department of Defense activity or other organization (<i>corporate author</i>) issuing the report.</p><p>2a. REPORT SECURITY CLASSIFICATION: Enter the overall security classification of the report. Indicate whether "Restricted Data" is included. Marking is to be in accordance with appropriate security regulations.</p><p>2b. GROUP: Automatic downgrading is specified in DoD Directive 5200.10 and Armed Forces Industrial Manual. Enter the group number. Also, when applicable, show that optional markings have been used for Group 3 and Group 4 as authorized.</p><p>3. REPORT TITLE: Enter the complete report title in all capital letters. Titles in all cases should be unclassified. If a meaningful title cannot be selected without classification, show title classification in all capitals in parenthesis immediately following the title.</p><p>4. DESCRIPTIVE NOTES: If appropriate, enter the type of report, e.g., interim, progress, summary, annual, or final. Give the inclusive dates when a specific reporting period is covered.</p><p>5. AUTHOR(S): Enter the name(s) of author(s) as shown on or in the report. Enter last name, first name, middle initial. If military, show rank and branch of service. The name of the principal author is an absolute minimum requirement.</p><p>6. REPORT DATE: Enter the date of the report as day, month, year; or month, year. If more than one date appears on the report, use date of publication.</p><p>7a. TOTAL NUMBER OF PAGES: The total page count should follow normal pagination procedures, i.e., enter the number of pages containing information.</p><p>7b. NUMBER OF REFERENCES: Enter the total number of references cited in the report.</p><p>8a. CONTRACT OR GRANT NUMBER: If appropriate, enter the applicable number of the contract or grant under which the report was written.</p><p>8b, 8c, & 8d. PROJECT NUMBER: Enter the appropriate military department identification, such as project number, subproject number, system numbers, task number, etc.</p><p>9a. ORIGINATOR'S REPORT NUMBER(S): Enter the official report number by which the document will be identified and controlled by the originating activity. This number must be unique to this report.</p><p>9b. OTHER REPORT NUMBER(S): If the report has been assigned any other report numbers (<i>either by the originator or by the sponsor</i>), also enter this number(s).</p></div><div><p>10. AVAILABILITY/LIMITATION NOTICES: Enter any limitations on further dissemination of the report, other than those imposed by security classification, using standard statements such as:</p><p>(1) "Qualified requesters may obtain copies of this report from DDC."</p><p>(2) "Foreign announcement and dissemination of this report by DDC is not authorized."</p><p>(3) "U. S. Government agencies may obtain copies of this report directly from DDC. Other qualified DDC users shall request through _____."</p><p>(4) "U. S. military agencies may obtain copies of this report directly from DDC. Other qualified users shall request through _____."</p><p>(5) "All distribution of this report is controlled. Qualified DDC users shall request through _____."</p><p>If the report has been furnished to the Office of Technical Services, Department of Commerce, for sale to the public, indicate this fact and enter the price, if known.</p><p>11. SUPPLEMENTARY NOTES: Use for additional explanatory notes.</p><p>12. SPONSORING MILITARY ACTIVITY: Enter the name of the departmental project office or laboratory sponsoring (<i>paying for</i>) the research and development. Include address.</p><p>13. ABSTRACT: Enter an abstract giving a brief and factual summary of the document indicative of the report, even though it may also appear elsewhere in the body of the technical report. If additional space is required, a continuation sheet shall be attached.</p><p>It is highly desirable that the abstract of classified reports be unclassified. Each paragraph of the abstract shall end with an indication of the military security classification of the information in the paragraph, represented as (TS), (S), (C), or (U).</p><p>There is no limitation on the length of the abstract. However, the suggested length is from 150 to 225 words.</p><p>14. KEY WORDS: Key words are technically meaningful terms or short phrases that characterize a report and may be used as index entries for cataloging the report. Key words must be selected so that no security classification is required. Identifiers, such as equipment model designation, trade name, military project code name, geographic location, may be used as key words but will be followed by an indication of technical context. The assignment of links, rules, and weights is optional.</p></div></div>						